

Advanced Structured Materials

Holm Altenbach
Victor Eremeyev *Editors*

Advances in Linear and Nonlinear Continuum and Structural Mechanics

 Springer


Advanced Structured Materials

Volume 198

Series Editors

Andreas Öchsner, Faculty of Mechanical Engineering, Esslingen University of Applied Sciences, Esslingen, Germany

Lucas F. M. da Silva, Department of Mechanical Engineering, Faculty of Engineering, University of Porto, Porto, Portugal

Holm Altenbach , Faculty of Mechanical Engineering, Otto von Guericke University Magdeburg, Magdeburg, Sachsen-Anhalt, Germany

Common engineering materials are reaching their limits in many applications, and new developments are required to meet the increasing demands on engineering materials. The performance of materials can be improved by combining different materials to achieve better properties than with a single constituent, or by shaping the material or constituents into a specific structure. The interaction between material and structure can occur at different length scales, such as the micro, meso, or macro scale, and offers potential applications in very different fields.

This book series addresses the fundamental relationships between materials and their structure on overall properties (e.g., mechanical, thermal, chemical, electrical, or magnetic properties, etc.). Experimental data and procedures are presented, as well as methods for modeling structures and materials using numerical and analytical approaches. In addition, the series shows how these materials engineering and design processes are implemented and how new technologies can be used to optimize materials and processes.

Advanced Structured Materials is indexed in Google Scholar and Scopus.

Holm Altenbach · Victor Eremeyev
Editors

Advances in Linear and Nonlinear Continuum and Structural Mechanics

 Springer

Editors

Holm Altenbach
Chair of Engineering Mechanics
Institute of Mechanics
Faculty of Mechanical Engineering
Otto-von-Guericke-Universität Magdeburg
Magdeburg, Germany

Victor Eremeyev
Department of Civil, Environmental
Engineering and Architecture
University of Cagliari
Cagliari, Italy

ISSN 1869-8433

Advanced Structured Materials

ISBN 978-3-031-43209-5

<https://doi.org/10.1007/978-3-031-43210-1>

ISSN 1869-8441 (electronic)

ISBN 978-3-031-43210-1 (eBook)

© The Editor(s) (if applicable) and The Author(s), under exclusive license to Springer Nature Switzerland AG 2023, corrected publication 2023

This work is subject to copyright. All rights are solely and exclusively licensed by the Publisher, whether the whole or part of the material is concerned, specifically the rights of translation, reprinting, reuse of illustrations, recitation, broadcasting, reproduction on microfilms or in any other physical way, and transmission or information storage and retrieval, electronic adaptation, computer software, or by similar or dissimilar methodology now known or hereafter developed.

The use of general descriptive names, registered names, trademarks, service marks, etc. in this publication does not imply, even in the absence of a specific statement, that such names are exempt from the relevant protective laws and regulations and therefore free for general use.

The publisher, the authors, and the editors are safe to assume that the advice and information in this book are believed to be true and accurate at the date of publication. Neither the publisher nor the authors or the editors give a warranty, expressed or implied, with respect to the material contained herein or for any errors or omissions that may have been made. The publisher remains neutral with regard to jurisdictional claims in published maps and institutional affiliations.

This Springer imprint is published by the registered company Springer Nature Switzerland AG
The registered company address is: Gewerbestrasse 11, 6330 Cham, Switzerland

Paper in this product is recyclable.

*Dedicated to our colleague, teacher and
friend Professor Leonid Mikhailovich Zubov
on the occasion of his 80th birthday.*

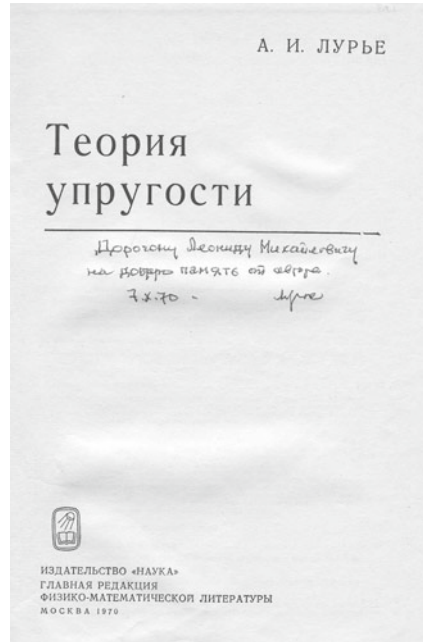
Preface



Leonid M. Zubov. (Photo by Alexey M. Kolesnikov)

Leonid Mikhailovich Zubov was born on September 1, 1943, in Yarensk, a small town near Arkhangelsk, Soviet Union. He graduated from the faculty of physics and mechanics of Leningrad Polytechnical Institute (now Peter the Great St. Petersburg Polytechnic University or simply Polytech). Later, Zubov became a Ph.D. student under supervision of Prof. Anatoliy Lurie. In 1970, Zubov defended his thesis entitled “*Bifurcation of Equilibrium of a Nonlinear Elastic Solid*” at Polytech. It is rather interesting that at that time it was not so common to publish papers with supervisors, so Zubov has no joint publications with Lurie. He published only single-authored papers related to elastic stability and to variational principles in the nonlinear elasticity. On the other hand, he was one of the first readers of Lurie’s book “Theory of elasticity” published in 1970. Moreover, some of his results were included in the

Fig. 1 Title page of Lurie’s “Theory of elasticity” with the dedication to Zubov by the author



book. This fact is mentioned in the book, see also the Lurie’s dedication in Fig. 1. Let us note that his paper on complementary energy in nonlinear elasticity Zubov (1970) found a response in the literature, see, e.g., de Veubeke (1972); Christoffersen (1973); Koiter (1973); Wempner (1980).

In 1970, Zubov moved to Rostov State University, Rostov on Don, in the department of elasticity chaired by Prof. Iosif Vorovich. That time it was not possible for him to stay in Leningrad. So it was a possibility to continue his research in a new department. That time, it was not so easy to find a position in a good university. The letter of recommendation from Prof. Lurie to Prof. Vorovich is given in Fig. 2 (in Russian), where Lurie underlined Zubov’s scientific and personal qualification. In Rostov on Don Zubov continued his research in nonlinear elasticity, theory of shells and started a new topic related to isolated and continuously distributed dislocations and disclinations in solids. In 1986, Zubov defended his doctoral thesis (habilitation), entitled *Semi-inverse and variational methods in nonlinear elasticity*, at Leningrad State University (now St. Petersburg State University).

Working at Rostov State University (now Southern Federal University) Leonid Zubov founded his school in nonlinear elasticity including simple and polar materials, nonlinear theory of shells. He has more than 20 Ph.D. students and two habilitated doctors, see Eremeyev et al. (2014) for more details. He has published more than 120 papers in peer-reviewed journals and several monographs (Zubov, 1982, 1997; Zubov and Karyakin, 2006; Eremeyev and Zubov, 2008, 2009; Zubov and Rudev, 2015).

Глубокоуважаемый Иосиф Израилевич,

обращаюсь к Вам со следующей просьбой. Этой осенью кончат аспирантуру по моей кафедре ("Механика и процессы управления" ЛПИ) Леонид Михайлович Зубов – Вы имели случай его видеть в Агверане. Это в высшей степени способный и трудолюбивый молодой человек. Занимается сейчас задачей устойчивости упругого тела, при чем исходит из строгих уравнений нелинейной теории. Диссертация будет закончена осенью. Частично о его достижениях в этом направлении я упоминал в своем докладе в Агверане. Могу еще добавить, что Л.М.Зубов очень эрудирован во всех разделах механики сплошной среды. Наконец, можно поручиться за его безупречные человеческие качества.

К сожалению, у меня нет возможности сохранить Л.М.Зубова у нас на кафедре – он не ленинградец и нет способа добиться прописки. Циническое разрешение этого вопроса (жениться на жилплощади) Л.М.Зубов отвергает.

Будет очень плохо, если по распределению он попадет на пустое место; поскольку у нас нет лучшего работающего научного коллектива, чем Ваша кафедра в Ростовском университете, я и беру на себя смелость предложить принять на работу Л.М.Зубова. Если Вы найдете это возможным и получите одобрение ректора, то просьба прислать соответствующее письмо, адресовав его ректору Ленинградского ордена Ленина Политехнического института им.М.И.Калинина члену-корреспонденту АН СССР В.С.Смирнову, копию – мне. Комиссия по распределению ожидается в апреле.

Ваш *Лurie*

10.III.1969 г.

Fig. 2 Letter of recommendation from Prof Anatolij Lurie to Prof. Iiosif Vorovich

Last years Prof. Zubov provided research in the following topics:

- Continuum theory of dislocations;
- Mechanics of micropolar solids under finite deformations;
- Nonlinear elasticity for solids with prestressed parts;

(see Zubov and Karyakin (2022a,b, 2023); Goloveshkina and Zubov (2019, 2020, 2021); Zubov (2019, 2021); Zingerman et al. (2023)) and the references therein for previous publications in the field.

This volume of the Advanced Structured Materials Series is devoted to current research in continuum and structural mechanics. It is dedicated to our friend and colleague, Prof. Leonid M. Zubov in occasion of his 80th birthday. With great pleasure that we—his colleagues and Friends—wish Professor Leonid M. Zubov many more creative years of interesting and important research.

Magdeburg, Germany
Cagliari, Italy
July 2023

Holm Altenbach
Victor Eremeyev

References

- Christoffersen J (1973) On Zubov's principle of stationary complementary energy and a related principle. Report 44, Danish Center for Appl. Math. and Mech., Department of Solid Mechanics, Technical University of Denmark
- de Veubeke BF (1972) A new variational principle for finite elastic displacements. *International Journal of Engineering Science* 10(9):745–763
- Eremeyev VA, Zubov LM (2008) *Mechanics of Elastic Shells* (in Russian). Nauka, Moscow
- Eremeyev VA, Zubov LM (2009) *Principles of Viscoelastic Micropolar Fluid Mechanics* (in Russian). SSC of RASci Publishers, Rostov on Don
- Eremeyev VA, Lebedev LP, Ogden RW (2014) Leonid M. Zubov: A life devoted to nonlinear mechanics. *International Journal of Engineering Science* 80:1–3, special issue on Nonlinear and Nonlocal Problems. In occasion of 70th birthday of Prof. Leonid Zubov
- Goloveshkina EV, Zubov LM (2019) Universal spherically symmetric solution of nonlinear dislocation theory for incompressible isotropic elastic medium. *Archive of Applied Mechanics* 89:409–424
- Goloveshkina EV, Zubov LM (2020) Equilibrium stability of nonlinear elastic sphere with distributed dislocations. *Continuum Mechanics and Thermodynamics* 32:1713–1725
- Goloveshkina EV, Zubov LM (2021) Spherically symmetric tensor fields and their application in nonlinear theory of dislocations. *Symmetry* 13(5):830
- Koiter WT (1973) On the principle of stationary complementary energy in the nonlinear theory of elasticity. *SIAM Journal on Applied Mathematics* 25(3):424–434
- Wempner G (1980) Complementary theorems of solid mechanics. In: *Variational Methods in the Mechanics of Solids*, Elsevier, pp 127–135
- Zingerman KM, Zubov LM, Belkin AE, Biryukov DR (2023) Torsion of a multilayer elastic cylinder with sequential attachment of layers with multiple superposition of large deformations. *Continuum Mechanics and Thermodynamics* 35(4):1235–1244
- Zubov L, Karyakin M (2022a) Large strains of cylindrical and spherical elastic shells with distributed dislocations. *Mechanics Research Communications* 124:103,911
- Zubov L, Karyakin M (2022b) Nonlinear deformations of a cylindrical pipe with pre-stressed thin coatings. *Mathematics and Mechanics of Solids* 27(9):1703–1720

- Zubov LM (1970) The stationary principle of complementary work in nonlinear theory of elasticity. *Journal of Applied Mathematics and Mechanics (PMM)* 34:228–232
- Zubov LM (1982) *Methods of Nonlinear Elasticity in the Theory of Shells* (in Russian). Rostov State University Press, Rostov on Don
- Zubov LM (1997) *Nonlinear Theory of Dislocations and Disclinations in Elastic Bodies*. No. 47 in *Lecture Notes in Physics*, Springer, Berlin
- Zubov LM (2019) Universal solution of nonlinear elasticity for a hollow cylinder with prestressed coatings. *Acta Mechanica* 230:4137–4143
- Zubov LM (2021) Spherically symmetric state of an elastic micropolar liquid. *Continuum Mechanics and Thermodynamics* 33:1199–1205
- Zubov LM, Karyakin MI (2006) *Tensor Calculus. Foundations of the Theory* (in Russian). Vuzovskaya Kniga, Moscow
- Zubov LM, Karyakin MI (2023) Large strains of a spherical shell with distributed dislocations and disclinations. In: Altenbach H, Berezovski A, dell’Isola F, Porubov A (eds) *Sixty Shades of Generalized Continua: Dedicated to the 60th Birthday of Prof. Victor A. Eremeyev*, Springer, Cham, pp 727–745
- Zubov LM, Rudev AN (2015) *Stong Ellipticity in the Elasticity of Anisotropic Materials* (in Russian). Southern Federal University, Rostov on Don

Contents

| | | |
|----------|--|-----------|
| 1 | On the Problem of Simulation of Ice–Floater Interaction Through Surface Waves | 1 |
| | Andrei K. Abramian, Nikolay M. Bessonov, and Anastasia A. Chevrichkina | |
| 1.1 | Introduction | 1 |
| 1.2 | The Problem Statement | 2 |
| 1.3 | Numerical Method | 4 |
| 1.4 | Results | 6 |
| 1.5 | Conclusion and Discussion | 10 |
| | References | 11 |
| 2 | Identification and Verification of the Soil Medium | |
| | S. S. Grigoryan’s Model for Dry Clay | 13 |
| | Vladimir Vas. Balandin, Vladimir VI. Balandin, Anatoly M. Bragov, Leonid A. Igumnov, Aleksandr Yu. Konstantinov, and Vasily L. Kotov | |
| 2.1 | Introduction | 14 |
| 2.2 | Methods of Experimental Research | 17 |
| 2.2.1 | Dynamic Testing of Clay Under Uniaxial Stress | 17 |
| 2.2.2 | Modified Kolsky Method for Testing Ground Media | 18 |
| 2.2.3 | The Reversed Experiment Technique | 20 |
| 2.3 | Sample Preparation Technique | 23 |
| 2.4 | Results of the Experimental Study | 24 |
| 2.4.1 | Results of Compression Tests According to the SHPB Method | 24 |
| 2.4.2 | Results of Modified SHPB Tests | 24 |
| 2.4.3 | Analysis of the Results of the Reversed Experiment | 28 |
| 2.5 | Numerical Simulation of Soil Sample Loading | 32 |
| 2.5.1 | Analysis of Experimental Results and Construction of a Mathematical Model of Clay Soil Deformation | 32 |

| | | |
|----------|--|-----------|
| 2.5.2 | Results of Numerical Simulation of Sample Compression in a Cage | 38 |
| 2.5.3 | Numerical Simulation of the Reversed Experiment | 40 |
| 2.6 | Conclusion | 43 |
| | References | 44 |
| 3 | Models of Defectness Medium for Bodies with Adhesion-Active Defective Surface | 47 |
| | P. A. Belov and S. A. Lurie | |
| 3.1 | Introduction | 47 |
| 3.2 | Kinematic Models of Defectness Bodies with Active Adhesion Surface | 49 |
| 3.3 | Force Model | 50 |
| 3.4 | Physical Model | 51 |
| 3.5 | Euler Equilibrium Equations and Spectrum of Boundary Value Problems | 52 |
| 3.6 | On Structure of Tensors of Adhesion Elastic Moduli | 54 |
| 3.7 | Classical Elastic Body with a Defectless Gradient Surface | 57 |
| 3.8 | Elastic Non-gradient Defectness Body with a Non-gradient Surface | 60 |
| 3.9 | Conclutions | 62 |
| | Appendix I | 62 |
| | Appendix II | 64 |
| | Appendix III | 66 |
| | References | 67 |
| 4 | On the Issue of the Stress in Incompressible and Rigid Media: Numerical Modeling | 69 |
| | N. Bessonov and Y. Litvinova | |
| 4.1 | Introduction | 69 |
| 4.2 | Modeling of Incompressible Liquids Flow | 70 |
| 4.2.1 | Newtonian Liquid | 70 |
| 4.2.2 | Convection Induced by Korteweg Stresses in Miscible Liquids | 75 |
| 4.3 | Rigid Body | 79 |
| | References | 84 |
| 5 | Numerical Estimation of Resistivity Contribution Tensor of a Concave Pore Embedded in a Transversely Isotropic Matrix | 87 |
| | Kou Du, Long Cheng, Jean-François Barthélémy, Igor Sevostianov, Albert Giraud, and Ayodele Adessina | |
| 5.1 | Introduction | 88 |
| 5.2 | Green Function-Based Correction of Boundary Conditions | 90 |
| 5.3 | Conductivity and Resistivity Contribution Tensors | 93 |
| 5.3.1 | Case of Homogeneous Inhomogeneity | 94 |

- 5.3.2 Case of Ellipsoidal Inhomogeneity 95
- 5.4 Numerical Framework of the Resistivity Contribution
 - Tensor Estimate 96
 - 5.4.1 Numerical Homogenization Method 98
 - 5.4.2 Assessment and Validation of the Proposed
 - Numerical Procedure 99
- 5.5 Numerical Estimation in the Case of Concave Pore
 - Embedded in Transversely Isotropic Matrix 103
 - 5.5.1 Superspherical Pore in Transversely Isotropic
 - Matrix 104
 - 5.5.2 Superspheroidal Pore in Transversely Isotropic
 - Matrix 106
- 5.6 Concluding Remarks 107
- Appendix A Three-Dimensional Green Function for Poisson’s
 Equation in Infinite Anisotropic Medium 111
- Appendix B Hill Polarization Tensor and Resistivity Contribution
 Tensor of a Spheroidal Inclusion Aligned in a Transversely
 Isotropic Host Matrix 111
- Appendix C Information of Meshes for the FEM Computations
 in the Case of Cubic Model Containing Concave Pore 112
- References 113
- 6 Effective Thermal Conductivity of Transversely Isotropic
 Materials with Concave Pores 115**
 - Kou Du, Long Cheng, Jean-François Barthélémy,
Igor Sevostianov, Albert Giraud, and Ayodele Adessina
 - 6.1 Introduction 115
 - 6.2 Resistivity Contribution Tensor of a Concave Pore 116
 - 6.3 Approximation Formula for Resistivity Contribution
 - Tensor of a Superspherical or Axisymmetrical
 - Superspheroidal Pore Embedded in a Transversely
 Isotropic Host Matrix 118
 - 6.3.1 Volume and Surface Area of Superspherical
 and Axisymmetrical Superspheroidal Pores 119
 - 6.3.2 Approximation Formula for Superspherical Pore 119
 - 6.3.3 Approximation Formula for Axisymmetrical
 Superspheroidal Pore 120
 - 6.4 Evaluation of the Effective Thermal Properties of Materials
 with Transversely Isotropic Matrices 121
 - 6.4.1 Comparisons with Oblate Spheroidal Pores
 of Same Volume 123
 - 6.4.2 Comparison of MTB, NIA and Maxwell
 Homogenization Schemes 126
 - 6.5 Concluding Remarks 128

Appendix A Background on Property Contribution Tensors 129

Appendix B Numerical Results for Approximation Formula
of Resistivity Contribution Tensors 132

References 133

**7 A Constitutive Model for Non-linear Basic Creep of Plain
Concrete 135**

Johanna Eisenträger and Holm Altenbach

7.1 Introduction 135

7.1.1 Creep in Concrete: Phenomenon and Experiments 135

7.1.2 Constitutive Models for Non-linear Basic Creep
in Concrete 138

7.1.3 Aim and Structure of the Current Contribution 142

7.2 Constitutive Model for Non-linear Basic Creep of Concrete 142

7.2.1 Governing Equations in One Dimension 142

7.2.2 Calibration 144

7.2.3 Governing Equations in Three Dimensions 148

7.2.4 Verification of the Constitutive Approach 150

7.3 Summary and Outlook 151

References 152

**8 On Tensile Instability of Elastic Structures with Elastic
Sliders of Different Stiffness 155**

Vadim V. Eremeev and Polina A. Lapina

8.1 Introduction 155

8.2 Elementary Cell Under Tension 156

8.3 Multiple Bifurcations 158

8.4 Conclusions 162

References 162

9 On Ellipticity in Nonlinear Elasticity 165

Victor A. Eremeyev

9.1 Introduction 165

9.2 Cauchy Nonlinear Elasticity 166

9.3 Incompressible Materials 168

9.4 Implicit Elasticity 168

9.5 Strain Gradient Elasticity 169

9.6 Media with Enhanced Kinematics 170

9.7 Conclusion 171

References 171

**10 Nonlinear Bending of Circular Beam with Distributed
Dislocations 175**

Evgeniya V. Goloveshkina

10.1 Introduction 175

10.2 Input Relations 177

10.3 Pure Bending of Circular Beam 178

10.4 Exact Solution for Harmonic Material 182

10.5 Numerical Analysis 184

10.6 Conclusion 190

References 190

11 Equilibrium Stability of Nonlinearly Elastic Cylindrical Tube with Distributed Dislocations Under Axial Compression 193

Evgeniya V. Goloveshkina

11.1 Introduction 193

11.2 Input Relations 195

11.3 Unperturbed State: Cylindrical Tube with Distributed Dislocations 196

11.4 Distribution of Straight Edge Dislocations 198

11.5 Exact Solution for Unperturbed State 198

11.6 Linearized Boundary Value Problem 200

11.7 Buckling Analysis 204

11.8 Conclusion 211

References 211

12 Simple Problems of Mechanical Equilibrium Applicable to the Synthesis and Modification of Materials 215

Anna G. Knyazeva

12.1 Introduction 216

12.2 Equilibrium Problems 217

12.3 Conclusion 239

References 239

13 Inflation of Hyperelastic Curved Tubes 245

Alexey M. Kolesnikov

13.1 Introduction 245

13.2 Inflation of Pressurized Curved Tube 246

13.3 Results 248

13.4 Conclusions 255

References 257

14 Analysis of the Homogenization Problem for Nonlinear Corrugated Plate 259

Alexander G. Kolpakov and Sergei I. Rakin

14.1 Introduction 259

14.2 Statement of the Problem and Dimension Reduction 260

 14.2.1 Periodicity Cell Problem 260

 14.2.2 Dimension Reduction for the Periodicity Cell Problem 262

14.3 Numerical Computations 263

 14.3.1 Overall In-Plane Deformation 263

 14.3.2 Strength of the Corrugated Plates 265

| | | |
|-----------|--|------------|
| 14.3.3 | Transition of the Geometric Nonlinearity at Microlevel into Physical Nonlinearity at Macrolevel | 267 |
| 14.3.4 | Overall Bending Deformation. Bending Deformation is Described by the Problem (1) with $e_{\alpha\beta} = 0$ | 268 |
| 14.4 | Conclusion | 270 |
| | References | 270 |
| 15 | Analysis of the Nanoindentation Results Using the Graded Coatings Information System | 273 |
| | Leonid I. Krenev, Evgeniy V. Sadyrin, Andrey L. Nikolaev, and Sergei M. Aizikovich | |
| 15.1 | Introduction | 273 |
| 15.2 | Materials and Methods | 275 |
| 15.3 | Results and Discussion | 277 |
| 15.4 | Conclusion | 280 |
| | References | 281 |
| 16 | On the Influence of Transversal Isotropy on the Exact Solution of a Problem of Imposing Finite Deformations in a Composite Nonlinear Elastic Slab with Prestressed Layers | 285 |
| | Vladimir A. Levin, Konstantin M. Zingerman, and Anton E. Belkin | |
| 16.1 | Introduction | 286 |
| 16.2 | Description of the Initial Configuration and Problem Statement | 287 |
| 16.3 | Mathematical Statement of the Problem | 288 |
| 16.4 | Determining the Coordinates of the Points of the Layers in the Intermediate and Final Configurations | 290 |
| 16.5 | Transformation of the Transversal Isotropy Vector | 291 |
| 16.6 | Stress Determination | 292 |
| 16.7 | Numerical Calculations | 293 |
| 16.8 | Conclusion | 294 |
| | References | 294 |
| 17 | Detection of the Poynting Effect in a Composite Hypoelastic Cylinder Under Multiple Imposition of Large Deformations | 297 |
| | Vladimir A. Levin, Konstantin M. Zingerman, and Danila R. Biryukov | |
| 17.1 | Introduction | 298 |
| 17.2 | Formulation of the Problem | 298 |
| 17.3 | The Algorithm for Problem Solving | 301 |
| 17.4 | Detection of the Poynting Effect in Numerical Analysis | 301 |
| 17.5 | Conclusion | 302 |
| | References | 303 |

18 Numerical Solution of Stress Concentration Problems in Elastic-Plastic Bodies Under the Superposition of Finite Deformations 305
 Vladimir A. Levin, Konstantin M. Zingerman,
 and Kirill Yu Krapivin

18.1 Introduction 307

18.2 The Statement of the Problems of Nonlinear Elastoplasticity at Large Deformations 308

 18.2.1 The Equilibrium Equation and Boundary Conditions 308

 18.2.2 Kinematic Relations 308

18.3 Constitutive Equations of Elasto-Plasticity 309

 18.3.1 Hypo-elastic Plasticity 309

 18.3.2 Hyperelastic Plasticity 310

18.4 Problem Statement of the Theory of Repeatedly Superimposed Large Deformations 311

 18.4.1 Modeling the Origin of Holes 311

 18.4.2 Mathematical Problem Statement 311

18.5 Examples 312

 18.5.1 Expansion of Thick-Walled Cylinder 313

 18.5.2 Necking of a Circular Bar 314

 18.5.3 Elongation of the Plate with Step-by-Step Removal of Inclusions 318

 18.5.4 Elongation of the Plate with a Step-by-Step Increase in the Circular Hole 320

18.6 Conclusion 320

References 322

19 Dynamic Buckling of Functionally Graded Plates and Shells Subjected to Thermal Shock 325
 Stanislav V. Levyakov

19.1 Introduction 325

19.2 Material Properties 328

19.3 Temperature Distribution 329

19.4 Shell Finite Element Formulation 331

 19.4.1 Invariant Representations 331

19.5 Reference Surface 333

 19.5.1 Kinematics of the Shell Element 333

 19.5.2 Strain Energy 334

 19.5.3 Kinetic Energy 337

19.6 Finite-Element Equations of Motion and Solution Method 337

19.7 Evaluation of Dynamic Buckling 339

19.8 Numerical Results and Discussion 339

 19.8.1 Comparison Studies 340

19.8.2 Dynamic Thermal Buckling of a Clamped Rectangular Plate 345

19.8.3 Dynamic Buckling of a Shallow Cylindrical Panel 348

19.8.4 Buckling of Simply Supported Cylindrical Shells 350

19.9 Concluding Remarks 352

References 353

20 Deposition and Characterization of Magnetron Sputtered AlN Coatings with Variable Stoichiometry 357

Andrey L. Nikolaev, Evgeniy V. Sadyrin, Ivan O. Kharchevnikov, Pavel E. Antipov, Vasilina A. Lapitskaya, Andrey S. Vasiliev, and Sergey S. Volkov

20.1 Introduction 358

20.2 Materials and Methods 359

20.3 Results and Discussion 360

20.4 Conclusion 365

References 365

21 Nonlinearity and Dispersion in Extended Mass-in-Mass Metamaterials 369

Alexey V. Porubov

21.1 Introduction 369

21.2 Extended Nonlinear Mass-in-Mass Models 370

21.2.1 Classic Mass-in-Mass Chain 370

21.2.2 Chain with Extra Attached Masses 371

21.2.3 Chain with Extra Internal Attached Masses 372

21.3 Continuum Limit of the Discrete Models 373

21.4 Derivation of Governing Equations 374

21.4.1 Asymptotic Decoupling of Continuum Equations 374

21.4.2 Single Equations for Longitudinal Strains 377

21.5 Localized Nonlinear Waves 377

21.6 Conclusions 381

References 382

22 Nonlinear Change of Young’s Modulus of Geomaterials Under Alternating Loads 385

Evgenii P. Riabokon, Mikhail S. Turbakov, Evgenii V. Kozhevnikov, Mikhail A. Guzev, and Hongwen Jing

22.1 Introduction 385

22.2 Materials and Methods 386

22.2.1 Materials for Study 386

22.2.2 Study Methods 387

22.3 Results and Discussion 389

22.4 Model Interpretations 390

22.5 Conclusion 393

References 394

23 Microstructural Model of Magnetic and Deformation Behavior of Single Crystals and Polycrystals of Ferromagnetic Shape-Memory Alloy 397
 Anatoli A. Rogovoy and Olga S. Stolbova

23.1 Introduction 397

23.2 The Main Relations of Micromagnetism 400

 23.2.1 Differential Equations 400

 23.2.2 Variational Equations 402

23.3 Detwinning Process 407

 23.3.1 Twin Structure 407

 23.3.2 Detwinning Condition 411

23.4 Statement of the Problem and Procedure for Its Numerical Implementation 416

 23.4.1 Computational Domain and Material Parameters 416

 23.4.2 Problem Formulation and Procedure for Its Numerical Realization 418

23.5 Results of Numerical Simulation 420

 23.5.1 A Monotwin Crystal 420

 23.5.2 A Polytwin Crystal 429

23.6 Conclusion 439

References 440

24 Stability of Circular Sandwich Plate with Porous Core and Prestressed Uniform Coatings 443
 Denis N. Sheydakov and Viacheslav A. Lyzhov

24.1 Introduction 443

24.2 Circular Sandwich Plate 444

24.3 Perturbed State of Sandwich Plate 449

24.4 Axisymmetric Buckling 455

24.5 Sandwich Plate with Identical Coatings 456

24.6 Conclusion 457

References 458

25 Localized Modes in a 1D Harmonic Crystal with a Mass-Spring Inclusion 461
 Ekaterina V. Shishkina and Serge N. Gavrilov

25.1 Introduction 461

25.2 The Mathematical Formulation for the Spectral Problem 463

25.3 The Case of a Symmetric Inclusion 464

 25.3.1 Symmetric Mode 465

 25.3.2 Antisymmetric Mode 468

 25.3.3 The Special Case $K = 1$ 469

25.4 The Case of an Asymmetric Inclusion 470

 25.4.1 The Special Case $m = 1$ 474

25.5 Discussion 475

Appendix 477

References 478

26 On Plate Buckling Induced by a Chemical Reaction 481
 Vladislav O. Shtegman, Alexander B. Freidin,
 and Alexander V. Morozov

26.1 Introduction 481

26.2 Modeling Kinetics of the Chemical Reaction Front 484

26.3 Loss of Plate Stability Due to the Chemical Reaction 487

26.4 Post-buckling of the Plate and Reaction Front Propagation 490

26.5 Conclusion 494

References 494

**27 On a Boundary Element Method for a Flow of Viscous Fluid
 Around a Cylinder 499**
 Mezhlum Sumbatyan and Rafael Zakaryan

27.1 Introduction 499

27.2 Mathematical Formulation 501

27.3 Specific Green’s Functions for the Exterior of the Cylinder 506

27.4 The BIE with the Specific Green’s Functions 507

27.5 Conclusions 512

References 512

**28 Interface Crack Starting From the Corner of a Wedge
 Attached to a Half-Plane 515**
 Konstantin B. Ustinov

28.1 Introduction 515

28.2 Geometry: Mathematical Formulation 517

28.3 Reduction of the Problem in Question to a Riemann Matrix
 Problem 518

28.4 Factorization of the Matrix Kernel 520

28.5 Asymptotics of the Involved Functions 522

28.6 Solution of the Riemann Problem 523

28.7 Some Numerical Results 525

28.8 Conclusion 527

References 528

**29 Static Thermomechanical Loading of Thermal Barrier
 Coatings: Compliance Functions 531**
 Andrey S. Vasiliev, Sergei M. Aizikovich, and Regina A. Bardakova

29.1 Introduction 532

29.2 Formulation of the Thermoelastic Problem 533

29.3 Compliance Functions 534

29.4 Numerical Results and Discussion 537

29.5 Closure 541

References 542

30 Sensitivity Analysis for Inhomogeneous and Prestressed Elastic Bodies 545

Alexander O. Vatulyan, Rostislav D. Nedin, and Victor O. Yurov

30.1 Introduction 545

30.2 Vibrations of an Isotropic Elastic Inhomogeneous Body in the Presence of Prestresses 547

30.3 General Structure of Relationships for Sensitivity Estimation 548

30.4 Sensitivity Characteristics for Problems I and II When Sounding by Concentrated Forces 552

30.5 Sensitivity Analysis for Longitudinal and Flexural Vibrations of Rods 553

30.6 Numerical Experiments 556

30.7 Conclusion 557

References 558

31 The Lowest Eigenfrequencies of an Immersed Thin Elastic Cylindrical Shell 559

Hazel Yücel, Barış Erbaş, Nihal Ege, and Julius Kaplunov

31.1 Introduction 560

31.2 Statement of the Problem 561

31.3 Asymptotic Scaling 563

31.4 Leading Order Approximation 565

31.5 First Order Approximation 566

31.6 Second Order Approximation 567

31.7 Discussion 569

31.8 Concluding Remarks 570

References 571

32 Grinding of Functionally Graded Coating Taking into Account Wear and Friction Heating 573

Vladimir B. Zelentsov, Polina A. Lapina, and Andrey L. Nikolaev

32.1 Introduction 574

32.2 Statement of the Problem of FGM Grinding 575

32.3 Exact Solution of the Problem for an Arbitrary $\mu(X)$ 577

32.4 Poles of Integrands 581

32.5 Asymptotic Analysis of the Obtained Solutions 582

32.6 Features of Wear of the FGM Coating 582

32.7 Grinding Process Control by Abrasive Settlement $\Delta(t)$ 586

32.8 Conclusion 588

References 589

**Correction to: On Tensile Instability of Elastic Structures
with Elastic Sliders of Different Stiffness C1**
Vadim V. Eremeev and Polina A. Lapina

Chapter 1

On the Problem of Simulation of Ice–Floater Interaction Through Surface Waves



Andrei K. Abramian, Nikolay M. Bessonov, and Anastasia A. Chevrichkina

Abstract The paper studies an approach to numerical simulation of a semi-infinite ice floe effect on floater dynamics. The authors have solved the problem numerically in a 2D formulation. The ice floe is considered as a semi-infinite beam with a bending stiffness equal to the cylindrical bending stiffness of a plate. The behavior of a floater under the actions of non-stationary and stationary harmonic moments is studied. Water is simulated as an ideal, incompressible fluid, and its flow is irrotational. The authors use nonlinear boundary conditions on the fluid-free surface. The values of displacements and angles of rotation of the floater are found. It is found that at non-stationary regimes maximum displacements and rotation angles of a floater can exceed their values at stationary regimes. The authors have revealed some cases when, at nonlinear conditions on a fluid-free surface, the pressure on a floater exceeds the values under linear conditions. The influence of the flexural rigidity of the body on the waves propagating in the system under consideration was studied.

Keywords Ice floe · Surface waves · Oscillation · Floater

1.1 Introduction

The operation of floating-type structures in the presence of ice floe in various loads acting on structures has been studied in many papers. Historically, the first studies were devoted to ships behavior near ice floe to ensure safe navigations (Kheisin 1967; Li and Wu 2021; Li et al. 2021; Nelli et al. 2017). Currently, floating oil platforms and nuclear power stations become the subject of research (Taylor and Ohkusu 2000; Sturova 2002; Tkacheva 2005; Keijdener 2019). For the problem statement, a floating structure is simulated as a rigid body (Nelli et al. 2017; Taylor and Ohkusu 2000; Sturova 2002; Tkacheva 2005) or as a plate (beam) (Kheisin 1967; Li and Wu 2021; Li et al. 2021; Keijdener 2019). Harmonic force (Li and Wu 2021; Li et al. 2021;

A. K. Abramian (✉) · N. M. Bessonov · A. A. Chevrichkina
Institute for Problems in Mechanical Engineering, Saint Petersburg, Russia
e-mail: andabr33@yahoo.co.uk

© The Author(s), under exclusive license to Springer Nature Switzerland AG 2023
H. Altenbach and V. Eremeyev (eds.), *Advances in Linear and Nonlinear Continuum and Structural Mechanics*, Advanced Structured Materials 198,
https://doi.org/10.1007/978-3-031-43210-1_1

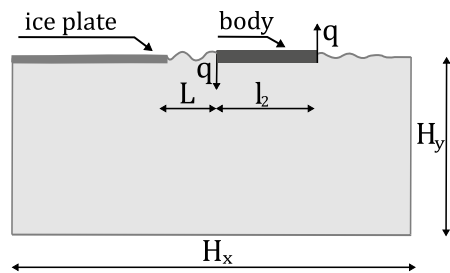
Nelli et al. 2017; Taylor and Ohkusu 2000; Sturova 2002; Tkacheva 2005), external forces moment (Keijndener 2019), and progressive waves (Li et al. 2021; Nelli et al. 2017; Taylor and Ohkusu 2000; Sturova 2002) are considered as external loads on a floating object. Water is considered as an ideal incompressible heavy fluid, and the ice floe as a plate floating on its surface. In papers (Kheisin 1967; Li and Wu 2021; Li et al. 2021; Nelli et al. 2017; Sturova 2002; Tkacheva 2005), the authors used linear boundary conditions on the fluid surface. In Kheisin (1967), Li and Wu (2021), Li et al. (2021), Nelli et al. (2017), Sturova (2002), Tkacheva (2005), various analytical methods were applied to obtain solutions and, in Keijndener (2019), Keijndener et al. (2017), Fox and Squire (1990) numerical methods were used. In the aforementioned papers, the displacement dependencies (including the angle of rotation) of both the floating body and the ice floe on the frequencies of the external forces and on the spatial coordinate were found. The present paper considers questions that have not been considered before for the best knowledge of the authors. One of the questions is a floater and an ice floe behavior in a non-stationary regime. The results obtained in this work reveal that the maximum displacements of a floater and an ice floe in the non-stationary regime can be significantly greater than in the stationary regime. The other question is the floater elasticity influence on the maximum displacements at external moment applied to it. The authors also found parameters of the considered system when nonlinear boundary conditions on the fluid surface are significant. In the present paper, the authors are solving the problem using the numerical method.

1.2 The Problem Statement

Consider the problem of the ice–floater interaction through surface waves (see Fig. 1.1).

The author simulates an ice floe as an elastic plate flowing an incompressible fluid (Kheisin (1967)). The floater is considered as an elastic plate with cylindrical rigidity much greater than that of ice. Elastic plates on the water surface are separated by regions with free surfaces. The problem is studied in 2D formulation. The model is assumed to be 2D, which implies that, the out-of-plane dimension of the floater is much bigger than the distance l between the ice floe and the floater. In this regard,

Fig. 1.1 Layout of the ice floe and the body simulating the floating structure in the calculated area



instead of the equations of the plates, the equations of the beam type are used. The cylindrical stiffness of the plate is taken as the bending stiffness of the beam. The Cartesian coordinate system in the (x, y) plane is used. The water is considered as an ideal, incompressible fluid, and its flow as irrotational (Kheisin (1967)). The potential of fluid velocities Φ satisfies the Laplace equation in the region occupied by the fluid:

$$\Delta \Phi = 0, \quad (1.1)$$

$$\frac{\partial \Phi}{\partial t} + \frac{|\nabla \Phi|^2}{2} = -\frac{1}{\rho} p - gy, \quad (1.2)$$

where $p(x, y, t)$ is the fluid pressure, ρ is the fluid density, and g acceleration of gravity.

Assume that here and below the pressure p is counted from the atmospheric pressure. Below, we confine ourselves to small transversal oscillations of the ice floe, thus the motion equation of the ice beam is

$$\rho_1 h \frac{\partial^2 w}{\partial t^2} = -D \frac{\partial^4 w}{\partial x^4} + p + q, \quad (1.3)$$

where $w(x, t)$ is vertical displacement of the surface from the equilibrium horizontal position, ρ_1 , h are ice density and thickness, $p(x, t)$ is the fluid pressure, $q(x, t)$ is the external load applied to the body, $D = Eh^3/(12(1 - \nu^2))$ is the cylindrical rigidity of the plate, and E , ν are Young's modulus and Poisson's ratio, respectively. Note that the cylindrical stiffness of the plate is given as a variable along the water surface $D = D(x)$ and it equals to either the cylindrical stiffness of the ice or the floating body. It can be taken on the fluid-free surface and it is small compared to the cylindrical stiffness of ice. Similarly, the density $\rho(x)$ and the thickness of the beam $h(x)$ are given as variables and equal to either the density and thickness of the ice or the floater. On the free surface, it is much less than the ice parameters. Test calculations have revealed that the ratio of the indicated quantities corresponding to the surface of the water and ice should be on the order of 10^4 or less. As a test problem, the problem of the dynamics of a single finite beam in contact with a basin of finite depth and infinite length along the x coordinate was taken. The harmonic moment (a couple of forces at the edges of the floater) is applied at the beam's center. This approach allows describing the ice beam, the free surface, and the floating body by the general equation (1.3) with boundary conditions on the surface, bottom, and side surfaces of the calculated region.

1.3 Numerical Method

The equations describing the motions of the system have the form:

$$\Delta \Phi = 0, \quad (1.4)$$

$$\frac{\partial \Phi}{\partial x} \Big|_{x=0} = 0, \quad \frac{\partial \Phi}{\partial x} \Big|_{x=H_x} = 0, \quad \frac{\partial \Phi}{\partial y} \Big|_{y=-H_y} = 0, \quad \frac{\partial \Phi}{\partial y} \Big|_{y=0} = \frac{dw}{dt}, \quad (1.5)$$

$$\rho_1 h \frac{\partial^2 w}{\partial t^2} = -D \frac{\partial^4 w}{\partial x^4} + q - \rho \left(\frac{\partial \Phi}{\partial t} + \alpha \frac{|\nabla \Phi|^2}{2} \right) - \rho g w - \mu \frac{\partial w}{\partial t}, \quad (1.6)$$

$$\frac{\partial w}{\partial x} \Big|_{x=0} = 0, \quad w \Big|_{x=0} = 0, \quad \frac{\partial w}{\partial x} \Big|_{x=H_x} = 0, \quad w \Big|_{x=H_x} = 0, \quad (1.7)$$

where H_x , and H_y are the width and depth of the calculated region, respectively.

The initial conditions are as follows:

$$\Phi \Big|_{t=0} = 0, \quad w \Big|_{t=0} = 0, \quad \frac{dw}{dt} \Big|_{t=0} = 0.$$

In the literature, the case of small surface displacement is usually considered, and it is assumed that

$$\frac{d\Phi}{dt} \approx \frac{\partial \Phi}{\partial t}. \quad (1.8)$$

This study considers a more general, nonlinear case when

$$\frac{d\Phi}{dt} = \frac{\partial \Phi}{\partial t} + \alpha \frac{|\nabla \Phi|^2}{2}. \quad (1.9)$$

Here, $\alpha = 0$ for the linear case, and $\alpha = 1$ for the nonlinear case. The system of equations (1.4)–(1.7) is solved numerically. A two-dimensional orthogonal non-uniform grid $I \times J$ is introduced with steps Δx_i and Δy_j in x and y , respectively, where $i = 1, \dots, I$, $j = 1, \dots, J$. To improve the accuracy of calculations, the grid thickens along the x axis in the vicinity of the body ends and the edges of the ice floe, it expands near the left and right sides of the computational domain. Vertically, the grid thickens near the water surface. In real life, the size of the x region extends to “infinity”. However, in numerical simulation one has to set these dimensions limited although they are as far apart as possible. To move away the boundaries of the computational domain without increasing the number of grid nodes, a non-uniform grid is used with a gradually increasing step toward the boundaries of the domain. However, starting from the moment equal to the time of the surface waves passage to the boundaries of the computational domain and back, the solution begins to be affected by the waves reflected from the boundaries of the domain. To reduce the

influence of the reflection effect, damping boundary conditions were introduced at the boundaries of the region, which damped the incoming waves. Such a numerical technique has proven itself in practice and is often used to reduce the influence of reflection from boundaries (Samarskiy and Nikolayev 1978; Potter 1973). To introduce damping boundary conditions, the term $-\mu \partial w / \partial t$ is added to the right side of Eq. (1.6), where μ is the coefficient of external damping. The experience of test calculations in study the μ effect on the degree of the wave reflection from the boundaries shows that the optimal solution reducing the effect of reflected waves by 85–95%, is to set μ on an area with a length of about 5% of the size of the entire area. In the rest (central) part of the computational domain, the value of μ is set equal to zero. Test calculations reveal that a very sharp change in the value of μ does not give the desired result, but, on the contrary, leads to the formation of additional reflected waves at the boundary. As test calculations show, a smooth change of μ from zero to $10^3 \dots 10^4$ kg/(m²s) near the calculation domain boundary is optimum. When calculating numerically, the system (1.4)–(1.7) is divided into two subsystems (1.4), (1.5), and (1.6), (1.7), which were solved sequentially in two stages at each time step. At each time step, the nodal values for the potential $\Phi_{i,j}^n$ are calculated, where n is the number of the time step. At the grid nodes corresponding to the fluid surface, the deviations of the surface from the equilibrium horizontal position w_i^n are determined. The sequence of calculations is as follows. Let the values potential $\Phi_{i,1}^n$ at all nodes and vertical deviations at near-surface nodes w_i^n and w_i^{n-1} are known from the previous time step Δt or taken from the initial conditions.

- Using the values $w_i^n \approx w_i^{n-1}$, we find the velocities $(dw/dt)^n \approx (w_i^n - w_i^{n-1})/\Delta t$, $i = 1 \dots I$ at all surface nodes.
- The found values $(dw/dt)^n$ are substituted into the boundary condition (1.5), then system (1.4), (1.5) is solved numerically and new values $\Phi_{i,j}^{n+1}$ are found at all grid nodes.
- Using the obtained values of $\Phi_{i,j}^{n+1}$ and the values of $\Phi_{i,j}^n$, j taken from the previous step time, the values $(d\Phi/dt)^{n+1}$ are calculated at all near-surface grid nodes using difference approximations of relations (1.8) or (1.9).
- The obtained values $(d\Phi/dt)^{n+1}$ are substituted into equation (1.6), which is solved numerically, and the values w_i^{n+1} are found at all near-surface nodes. Then the process is repeated.

The iterative method is used for solving the system (1.4) and (1.5) numerically). To solve equation (1.6) the substitution $M = \partial^2 w / \partial x^2$ is used. This allows replacing equation (1.6) of the fourth order in x , with the system of two second-order equations. This system is approximated by a three-point implicit difference scheme and solved using the matrix sweep method.

1.4 Results

As ice is present on one side of the floater, the problem is not symmetric with respect to the floater. The reflected waves only come from the left side of the floater, which leads to the floater displacement and its rotation because of an asymmetric pressure. The tangent of the floater rotation angle is calculated as the ratio of the difference in the displacements of its ends to its length. This is true in the case of a large bending rigidity of the floater. The displacement and rotation angle of the floater and ice are calculated for the case when a couple of non-stationary harmonic forces are applied in the center of the floater. It is given in the following form:

$$q = A \sin(\omega t) [\delta(x - H_x/2 - l_2/2) - \delta(x - H_x/2 + l_2/2)] H(t),$$

where A is the force amplitude, ω is the circular frequency of the force, $\delta(x)$ is the delta function, floater is located in the center of basin with the width H_x , and $H(t)$ is the Heaviside function:

$$H(t) = \begin{cases} 0, & t < 0 \\ 1, & t \geq 0 \end{cases}.$$

The forces and moment values are taken as in Keijndener (2019), which makes it possible to compare the results obtained in Keijndener (2019) with the results of our paper. The values of the main parameters are given in the Table 1.1.

Figures 1.2 and 1.3 show typical dependences of the maximum displacement of a floater on the moment frequency at different ice thicknesses in unsteady and stationary regimes, respectively. In these calculations, the non-stationary regime is the regime in which oscillations are established from the beginning of the countdown to the moment of their stabilization. A stationary regime is a regime when the maximum oscillation amplitude does not change for at least 10 periods. All figures show the maximum displacements or angles of rotation in stationary or non-stationary regimes.

The dependencies are obtained for the distance from the ice edge to the floater with $L = 15$ m. The dependence of the displacement of the right edge of the floater on the frequency in Fig. 1.3 shows that there are frequency ranges in which the effect of reflected waves on these movements is visible. The dependencies are obtained for the distance from the ice edge to the floater with $L = 15$ m. The non-symmetry of the problem leads to the fact that the displacements of the left edge of the body turn out to be slightly smaller than the right one. The dependence of the displacement of the

Table 1.1 Values of physical parameters, geometry parameters of the basin and the floater. l_2 is the length of the floater, $h_2\rho_2$ is the product of the thickness and density of the floater

| H_y , m | H_x , m | h, m | ρ_1 , kg/m ³ | v_{ice} | E_{ice} , GPa | $h_2\rho_2$, kg/m ² | l_2 , m |
|-----------|-----------|------|------------------------------|-----------|-----------------|---------------------------------|-----------|
| 100 | 200 | 1 | 925 | 0.3 | 5 | 3218 | 30 |

Fig. 1.2 Displacement of the right edge of the floater via the frequency of the moment with an amplitude of $A = 294300$ N/m in the non-stationary regime for different ice thicknesses h . Line 1 – $h = 0$ — no ice; line 2 – $h = 0.1$ m; line 3 – $h = 1$ m; line 4 – $h = 10$ m

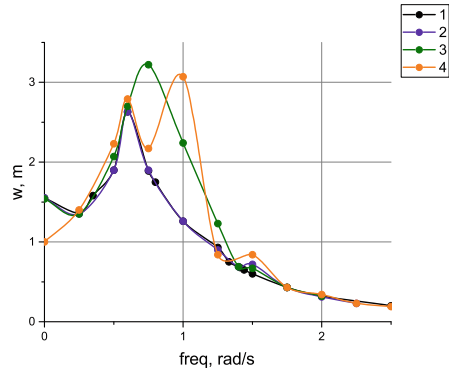
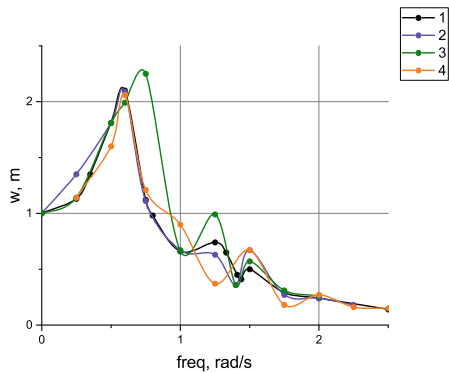


Fig. 1.3 Displacement of the right edge of the floater via the frequency of the moment with an amplitude of $A = 294300$ N/m in the stationary regime for different ice thicknesses h . Line 1 – $h = 0$ —no ice; line 2 – $h = 0.1$ m; line 3 – $h = 1$ m; line 4 – $h = 10$ m



right edge of the floater on the frequency in Fig. 1.3 shows that there are frequency ranges in which the effect of reflected waves on these movements is visible. The type of fluid surface waves is shown in Fig. 1.4. As can be seen from the figure, an almost stationary wave is formed in the space between the floater and the ice floe. In the figure, it corresponds to sinusoidal structures. The red color in the figure corresponds to large displacements, and blue to small ones. The graphs in Figs. 1.2 and 1.3 reveal that it is important to take into account the non-stationary regime since the maximum displacements in it exceed the maximum displacements in the stationary regime. It should be noted that, with an increase in the ice thickness, the displacement of the floater also increases. At the same time, calculations show that the displacements of the ice edge decrease with the ice thickness increase due to the plate cylindrical rigidity increase. The obtained results qualitatively coincide with the results obtained in Nelli et al. (2017) for the case of a free-floating plate.

The results of the linear problem performed by the authors are in good agreement with the results obtained in Keijdener (2019) with the help of the analytical method of expansion in terms of vertical eigenmodes in the steady state for a harmonic external excitation. Due to the good agreement between the values of the dependences obtained by numerical and analytical methods, the solution obtained by analytical

Fig. 1.4 Fluid surface waves between floater and ice for the moment with amplitude $A = 294300 \text{ N/m}$ in the stationary regime for ice thicknesses $h = 1 \text{ m}$

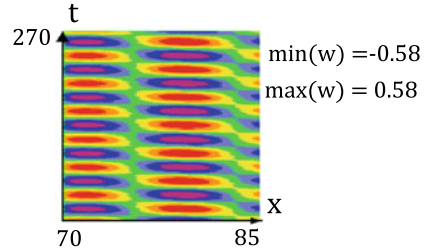
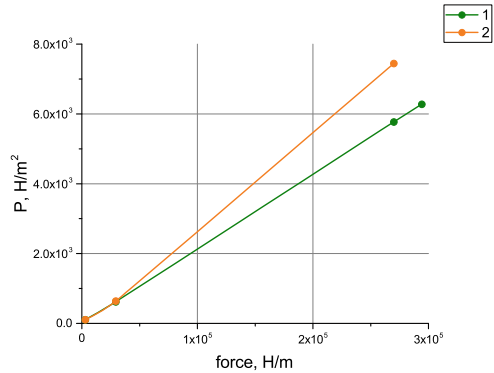


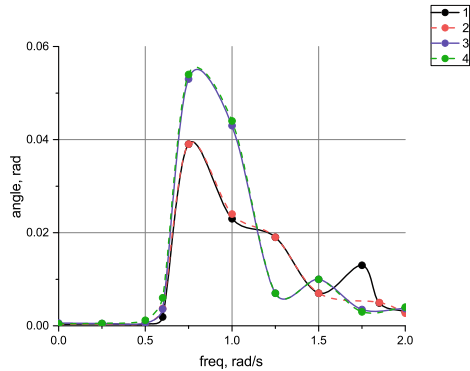
Fig. 1.5 Fluid pressure on the floater in the stationary regime for different amplitudes A , when $L = 10 \text{ m}$



formulas is not shown on the graphs. However, for some values of the parameters of the considered system, it occurs that the nonlinear boundary conditions lead to a difference from results obtained in the linear condition case. The fluid pressure on the floater at linear and nonlinear conditions on the fluid surface is shown in Fig. 1.5 for $L = 10 \text{ m}$ and different values of amplitudes. The graphs in Fig. 1.5 show that, for moment period $T = 3 \text{ s}$, the value of the fluid pressure in the nonlinear case is greater than in the linear case.

At the same time, the authors did not find the differences in the values of the floater maximum angle of rotation in the linear and nonlinear cases in the stationary regime in the range of frequencies $0.6\text{--}1.3 \text{ rad/s}$, as the curves in Fig. 1.6 present. As can be seen in Fig. 1.6, the maximum values of floater angle of rotation are larger when the gap between it and ice floe is smaller. The graphs in Fig. 1.6 show that the ice has little effect on the magnitude of the floater rotation angle up to the frequency $\omega = 0.55 \text{ rad/s}$. At frequencies greater than 0.55 rad/s , the effect of the ice is significant and manifests itself, among other things, by resonant peaks. The ice effect on the rotation angle is absent because of the reflected/incident wave interaction on the edge of the ice. The work Fox and Squire (1990) shows that, when a low-frequency wave is incident normal to the edge, its energy is transferred to a floating plate, while, in case a high-frequency wave is incident, its energy is completely reflected into the fluid. Figure 1.6 presents a similar behavior at frequencies below 0.55 rad/s , the waves are almost not reflected in this case. Non-propagating waves forming in the space between the ice and the floater decay quickly along the coordinate and do not affect

Fig. 1.6 Dependence of the floater angle of rotation in the linear and nonlinear cases via the frequency of the moment with $A = 250000$ N/m in stationary regime. Line 1 - $\alpha = 0$, and $L = 15$ m; line 2 - $\alpha = 1$ and $L = 15$ m; Line 3 - $\alpha = 0$, and $L = 1$ m; $\alpha = 1$, and $L = 1$ m



it. Therefore, the propagating reflected surface waves are the main in the process of a wave/floater interaction.

In contrast to the displacement behavior the angle of rotation dependence has some differences: the resonant peaks are not so pronounced, with the exception of one resonance. The nature of this resonance can be explained as follows. When the floater oscillates, it loses energy in the form of radiated waves and some of this energy is trapped in the gap between the floater and ice in the form of a standing wave (Keijdener 2019). Within these frequency bands, the length of a surface wave is approximately the same as gap length. Simultaneously, the amount of energy transferring to the wave significantly increases the floater displacement. When the reflected waves are in-phase with the vertical motions of the floater, resonance occurs and the floater’s response increases. If the reflected waves are in anti-phase with the floater, anti-resonance occurs and its response lowers. A couple of forces may create such anti-resonances. The last consideration explains the absence of pronounced resonant peaks at frequencies corresponding to displacement resonances. The authors consider another factor presumably affecting the displacement of the ice and the floater, namely, the floater’s cylindrical rigidity. The calculations revealed that the floater cylindrical rigidity starts affecting the maximum displacements of both the ice and the floater only if its value significantly decreases, by 1000 times compared with the parameters of offshore structures selected in Keijdener (2019). Therefore, we can consider the behavior of a real offshore structure in the problem under consideration as the behavior of a rigid body in case we are interested in the maximum values of the floater displacement only. At the same time, it should be noted that a change in the floater rigidity leads to a change in the wave patterns of the system under consideration. Figures 1.7 and 1.8 show how the floater wave patterns change with a change in the flexural rigidity of the floater. Figure 1.7 corresponds to the cylindrical stiffness $D = 10^5$ Nm, and Fig. 1.8 to the value $D = 10^8$ Nm. The red color in the figure corresponds to large displacements, and the blue to small ones.

Fig. 1.7 Floater waves patterns for the cylindrical stiffness $D = 10^5$ Nm

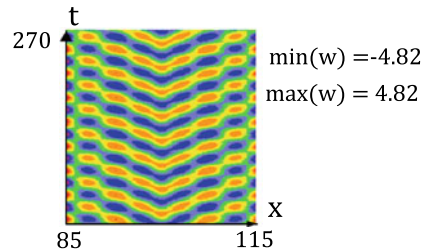
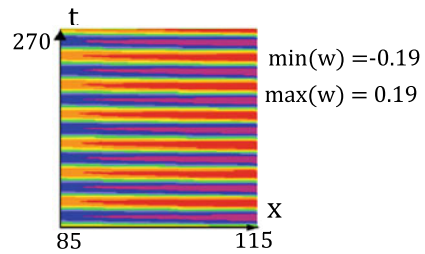


Fig. 1.8 Floater waves patterns for the cylindrical stiffness $D = 10^8$ Nm



1.5 Conclusion and Discussion

In the present paper, the authors propose an approach to the numerical solution of the problem of studying the effect of an ice cover and fluid surface waves on floater dynamics. Based on the numerical solution obtained, an analysis of the behavior of floater displacements and floater rotation angles under the action of a harmonic moment on the latter is carried out. It is shown that, in the non-stationary loading regime, the values of maximum displacements and rotation angles of the floater can differ significantly from the values determined in the stationary regime. It is shown that for a number of parameters and at certain frequencies, the nonlinear boundary conditions may lead to greater values of the fluid pressure acting on the floater than in the linear formulation. The flexural rigidity of a floater begins to affect its displacements and angles of rotation on a fluid surface at its values far from those that floating offshore structures can have. At the same time, a change in the rigidity of the body leads to a change in the wave patterns of the system under consideration. It should be noted that such important factors as the three-dimensional formulation of the problem, ice cover inhomogeneities (old ice inclusions, cavities filled with brine, etc.), slush, and speed of its approaching the ice have not been considered yet. The authors intend to take into account all these factors in their future works.

Acknowledgements This research is supported by the Russian Science Foundation via grant No 23-29-00459 (<https://rscf.ru/project/23-29-00459>).

References

- Fox C, Squire VA (1990) Reflection and transmission characteristics at the edge of shore fast sea ice. *J Geophys Res* 95(C7):11629–11639. <https://doi.org/10.1029/JC095iC07p11629>
- Keijndener C (2019) The effect of hydrodynamics on the interaction between floating structures and flexible ice floes. Thesis for: Ph.D., Delft University of Technology. <https://doi.org/10.4233/uuid:a66b84b9-6c66-4c9c-a2e1-87163244ae07>
- Keijndener C, Barbosaa JMO, Metrikine AV (2017) The influence of level ice on the frequency domain response of floaters. *Cold Regions Sci Technol* 143(1):112–125. <https://doi.org/10.1016/j.coldregions.2017.09.004>
- Kheisin DE (1967) Ice cover dynamics. Leningrad. *Gidrometeorologicheskoye izd-vo* (In Russian)
- Li ZF, Wu GX, Ren K (2021) Interactions of waves with a body floating in an open water channel confined by two semi-infinite ice sheets. *J Fluid Mech* 917:A19. <https://doi.org/10.1017/jfm.2021.274>
- Li ZF, Wu GX (2021) Hydrodynamic force on a ship floating on the water surface near a semi-infinite ice sheet. *Phys Fluids* 33(12):127101. <https://doi.org/10.1063/5.0071972>
- Nelli F, Bennetts LG, Skene DM, Monty JP, Lee JH, Meylan MH, Toffoli A (2017) Reflection and transmission of regular water waves by a thin, floating plate. *Wave Motion* 70:209–221. <https://doi.org/10.1016/j.wavemoti.2016.09.003>
- Potter D (1973) *Computational physics*. J Wiley
- Samarskiy AA, Nikolayev ES (1978) *Methods for solving grid equations* (In Russian). Nauka, Moscow
- Sturova IV (2002) The action of periodic surface pressures on a floating elastic platform. *J Appl Math Mech* 66(1):71–81. [https://doi.org/10.1016/S0021-8928\(02\)00010-2](https://doi.org/10.1016/S0021-8928(02)00010-2)
- Taylor RE, Ohkusu M (2000) Green functions for hydroelastic analysis of vibrating free-free beams and plates. *Appl Ocean Res* 22(5):295–314. [https://doi.org/10.1016/S0141-1187\(00\)00018-3](https://doi.org/10.1016/S0141-1187(00)00018-3)
- Tkacheva LA (2005) Impact of a periodic load on a floating elastic plate. *Izvestiya Rossiyskoy akademii nauk. Mekhanika Zhidkosti i Gaza* 2:132–146 (In Russian)

Chapter 2

Identification and Verification of the Soil Medium S. S. Grigoryan's Model for Dry Clay



Vladimir Vas. Balandin, Vladimir Vl. Balandin, Anatoly M. Bragov,
Leonid A. Igumnov, Aleksandr Yu. Konstantinov, and Vasily L. Kotov

Abstract Dynamic tests of dry clay were carried out to identify the parameters of the soil medium model of S.S. Grigoryan. To study the dynamic compressive strength under a uniaxial stress in the samples, the experiments were carried out on a PG-20 setup that implements the classical SHPB method. The modified SHPB method with a sample in a rigid holder was used in tests under conditions close to one-dimensional deformation. Based on the results of these experiments, the compressive strength of clay was determined at various strain rates up to 1200 1/s. In experiments with uniaxial deformation in the range of longitudinal stresses up to 400 MPa, strain diagrams, compressibility curves, and pressure dependences of the yield stress were obtained. The analysis of the results showed that the strain rate has practically no effect on the course of the strain diagrams and compressibility curves of the studied soil. The shear strength of the studied soil obeys the Mohr–Coulomb law both under loading and unloading. Based on the results of the experiments, the parameters of the mathematical model of S.S. Grigoryan for dry clay were obtained. Using this model in the LS-Dyna software package, the process of sample deformation was simulated under conditions corresponding to a real experiment. A good agreement between numerical and experimental results is obtained. To verify the model of the

V. Vas. Balandin · V. Vl. Balandin · A. M. Bragov · L. A. Igumnov (✉) · A. Yu. Konstantinov · V. L. Kotov

Gagarina Av, National Research Lobachevsky State University of Nizhny Novgorod, 23/6, Nizhny Novgorod 603022, Russia

e-mail: igumnov@mech.unn.ru

V. Vas. Balandin

e-mail: balandin@mech.unn.ru

V. Vl. Balandin

e-mail: balandin@mech.unn.ru

A. M. Bragov

e-mail: bragov@mech.unn.ru

V. L. Kotov

e-mail: vkotov@inbox.ru

soil environment, model experiments were carried out on the penetration of conical tips into dry clay in a reversed formulation. Using this identified model in the LS-Dyna software package, numerical simulation of penetration was carried out under conditions similar to those carried out using the reversed experiment. Comparison of the results of model and numerical experiments showed their satisfactory agreement at a dry friction coefficient of 0.5.

Keywords Dry clay · Strain rate · Split Hopkinson pressure bar · Volumetric compressibility · Identification · Verification · Penetration · Reversed experiment · Numerical simulation

2.1 Introduction

The study of the impact interaction of deformable and solid bodies with soil media is of significant scientific and applied importance. Computational methods are widely used to study the mechanisms of penetration into soils. These methods make it possible to comprehensively simulate the processes of penetration into soil barriers. To calculate the penetration into soil media, various software packages are widely used: LS-Dyna, Ansys, Logos, Abaqus, etc. However, two problems arise, when calculating the impact interaction. The first is the choice of models of the dynamic behavior of interacting media and the identification of their parameters. The second problem is the verification of the obtained numerical results by comparing them with the experimental results. A wide range of experimental studies requires to solve these problems. To select models and equip them with the necessary parameters, a large number of experimental studies of the dynamic properties of soil media in a wide range of strain rates and load amplitudes are required. Verification of the calculation results requires experimental studies of the penetration of deformable and solid bodies with the different shapes into soil media with various impact velocities. It should be noted that for a number of soil media, the dynamic properties have been studied quite fully. In particular, for sand, using two complementary techniques—a plane-wave impact experiment and a modified Kolsky method with tests in a rigid cage, compressibility curves were obtained in a wide range of load amplitudes (Lagunov and Stepanov 1963; Bragov et al. 2006; Bragov and Grushevskii 1993; Arlery et al. 2010; Bragov et al. 2008; Song et al. 2009; Martin et al. 2009, 2013; Chapman et al. 2006; Luo et al. 2014; Dianov et al. 1977), and its shear properties were studied (Bragov et al. 1994, 1996a, 2004). In these works, for a sandy medium, the influence of humidity, granulometric composition on the parameters of the shock adiabat, deformation diagrams, and shear resistance at high strain rates of 10^2 – 10^5 s⁻¹ and load levels up to 5 GPa were studied. The data obtained make it possible to equip mathematical models of sand deformation and accurately set their parameters in a wide range of load changes depending on its initial physical and mechanical characteristics of sand. A detailed review of experimental studies of the dynamic properties of sand is given in Omidvar et al. (2012).

Data on the deformation of clay soils under dynamic impacts are much less. In Yang et al. (2017), in experiments using the Kolsky method (SHPB), deformation diagrams were determined under uniaxial stress for clay samples. Clay samples were preliminarily statically loaded at various levels up to 4 MPa. The experiments were carried out at strain rates from 60 to 600 s⁻¹. An increase in the dynamic strength of the specimens and in the fracture strain with an increase in the strain rate and preload was found. The authors of He et al. (2010) conducted a study of wet clay using the SHPB method in the stress range up to 12 MPa. Based on the data obtained, the parameters of the soil fluidity criterion in the Mohr–Coulomb form are determined. In Buharev et al. (1991), in the pressure range up to 3.5 GPa, the impact compressibility of clay with different water content (0, 4.8, 7.5, and 10%) was studied. According to the results of the experiments, the parameters of the shock adiabats were determined, which turned out to be practically the same for different water contents in the samples. In Li et al. (2018), plane-wave experiments were carried out to determine the shock compressibility of loess, the density of which was 1.8 g/cm³, and the degree of saturation with water was 22%. The shock adiabat was obtained at stress levels from 0.2 to 1.6 GPa. The paper Bragov et al. (1996b) presents the results of a dynamic study by the Kolsky method for plasticine simulating wet clay soil. Diagrams of deformation of samples in a rigid cage in the range of longitudinal stresses up to 150 MPa are obtained. The parameters of the Mohr–Coulomb equation for the yield strength of plasticine are determined. In Bragov et al. (2002), the dynamic properties of wet clay samples in a rigid holder were studied. The experiments were carried out on an SHPB setup in the range of longitudinal stresses up to 200 MPa. Compressibility curves and dependences of shear stresses on pressure in the Mohr–Coulomb form are obtained. Plane-wave experiments were also carried out to determine the shock adiabat of wet clay in the pressure range up to 2 GPa. An analysis of the above results shows that the dynamic properties of clay at different moisture content have not been studied enough, in particular, there are no data on the dynamic properties of dry clay. An analysis of the above results shows that the dynamic properties of clay at different moisture content have not been studied enough, in particular, there are no data on the dynamic properties of dry clay.

As noted above, to solve the problem of verifying the model of the soil medium, it is necessary to conduct experiments on the penetration of solid and deformable bodies into the soil. The analysis performed showed that there are a fairly large number of experimental results on the penetration into sand with different moisture content (Balandin et al. 2016; Bragov et al. 2018; Omidvar et al. 2014). However, for clayey soils, data on penetration are insufficient (Veldanov et al. 2011; Bivin et al. 1978, 1980, 1982; Buharev and Gandurin 1995; Buharev et al. 1991, 1995; Balandin et al. 2020; Dayal et al. 1980). Existing data on the penetration of solids into clayey soils are limited mainly by experiments with a model medium—plasticine. In Veldanov et al. (2011) experiments were carried out on the penetration of conical tips with opening angles of 30° and 60° into a plasticine target in a direct formulation with the velocity up to 200 m/s. An accelerometer placed on the penetrating body was used to determine the penetration resistance force. In Bivin et al. (1978), the penetration resistance forces were determined for cones with opening angles 2α equal to 30°, 60°,

90°, 180° in the speed range up to 20 m/s. It was noted that the maximum drag force is achieved when the conical part of the striker is completely immersed and is a power-law function of the impact velocity. In Bivin et al. (1980), the penetration of conical impactors into plasticine was studied in the range of impact velocities of 30–300 m/s. A method was proposed for determining the maximum shear stresses τ_s arising in the soil during the penetration of cones, according to the experimental dependences of the maximum penetration depth on the impact velocity. It is assumed that the penetration resistance force is determined only by the action of tangential stresses on the surface of the penetrating body, and the velocity head (proportional to the square of the velocity) can be neglected. In Bivin et al. (1982), based on the results of measuring the final penetration depth of cones with half-opening angles of 15°, 30°, 45°, and 90° into plasticine, the parameters of the two-term penetration equation in the Poncelet form were determined. The experiments were carried out at impact velocities from 50 to 400 m/s. In works (Buharev and Gandurin 1995; Buharev et al. 1991, 1995), a study was made of the penetration of conical impactors into plasticine. Experiments with conical impactors (opening angle $2\alpha = 30^\circ$) were carried out at impact velocities from 20 to 86 m/s. The resistance forces were measured in different stages of penetration (non-stationary and quasi-stationary). Based on the data obtained, the dependences of the resistance coefficient and the soil shear strength parameter on the velocity in the two-term Poncelet equation were constructed. In Balandin et al. (2020), in the reversed experiments, the penetration of a hemispherical head and cones with different vertex angles into plasticine was studied. The impact velocities varied in the range from 80 to 460 m/s. The maximum forces acting on the heads in the initial, non-stationary section of penetration are determined. The maximum forces increase according to a power law with an increase in the impact velocity. It should be noted that plasticine models the behavior of water-saturated clay soil. There are practically no experimental data on penetration for clay. It is worth noting the work (Dayal et al. 1980), in which the forces acting on a cylindrical projectile with a conical tip (cone opening angle 60°) were experimentally determined when it penetrated clay in the range of impact velocities from 3 to 6.1 m/s. An analytical penetration model was proposed that takes into account the shear strength of the soil and friction on the surface of the projectile. Since the impact velocities were low, the soil was considered incompressible. The obtained analytical dependencies were numerically integrated. The authors noted good agreement between experimental and analytical results and suggested that this technique may be suitable for determining shear strength from a known impact velocity and maximum penetration depth. Experimental data on the impact interaction of solids with dry clay targets are not available in the literature.

2.2 Methods of Experimental Research

2.2.1 Dynamic Testing of Clay Under Uniaxial Stress

Since clay, unlike sand, has structural strength, to determine it, samples of dry clay were tested using the Kolsky method (Split Hopkinson Pressure Bar, SHPB method) under conditions of a uniaxial stress state (Kolsky 1949). In the mathematical model of the SHPB method, a system of three bars is considered: two infinitely strong, infinite and thin and one “soft” and very short (sample) between them (Fig. 2.1). It is assumed that there is no wave dispersion and that the deformation is uniform over the bar cross section. Lateral vibrations of the bar particles are neglected. In one of the bars, a one-dimensional elastic wave $\varepsilon^I(t)$ is generated, which propagates in the bars at a speed C . Wave propagation in the bars is represented by the $x \sim t$ diagram in Fig. 2.1. When the wave reaches the sample, it is divided into two, since the materials of the bar and the sample have different acoustic hardness ρC . The first wave $\varepsilon^R(t)$ is reflected back, and the second wave $\varepsilon^T(t)$ passes through the sample and enters the second (reference) bar. The sample experiences elastic–plastic deformation, while the bars experience elastic deformation. The amplitudes and waveforms $\varepsilon^R(t)$ and $\varepsilon^T(t)$ depend on the ratio of the acoustic stiffness of the bar and the sample and the response of the sample material to the applied dynamic load. By registering these elastic waves with the help of sensors and using the formulas proposed by H. Kolsky, we can determine the time dependences of stress, strain, and strain rate in the sample. Stresses, strain rate, and strain in the test sample were determined by the formulas:

$$\varepsilon_s(t) = \frac{C}{L_0} \int_0^t [\varepsilon^I(t) - \varepsilon^R(t) - \varepsilon^T(t)] \cdot dt, \quad (2.1)$$

$$\dot{\varepsilon}_s(t) = \frac{C}{L_0} \cdot (\varepsilon^I(t) - \varepsilon^R(t) - \varepsilon^T(t)), \quad (2.2)$$

$$\sigma_s(t) = \frac{P}{A_s} = \frac{EA}{2A_s^0} [\varepsilon^I(t) + \varepsilon^R(t) + \varepsilon^T(t)], \quad (2.3)$$

where C is the speed of sound in the measuring bars, E is Young's modulus of the material of the bars, A is the cross-sectional area of the measuring bars, A_s^0 is the initial cross-sectional area of the sample, ε^I , ε^R , ε^T are the deformations in the incident, reflected and transmitted pulses in the measuring bars. Excluding time as a parameter from the dependencies given above, it is possible to obtain deformation diagrams $\sigma(\varepsilon)$ with a known history of the change in the strain rate. In the experiments, measuring bars with a diameter of 20 mm, made of D16T aluminum alloy, were used. Bars had a length of 1500 mm. Strain gauges were glued on the surface of the bars in the middle. Loading was carried out by impact of an aluminum bar 300 mm long and

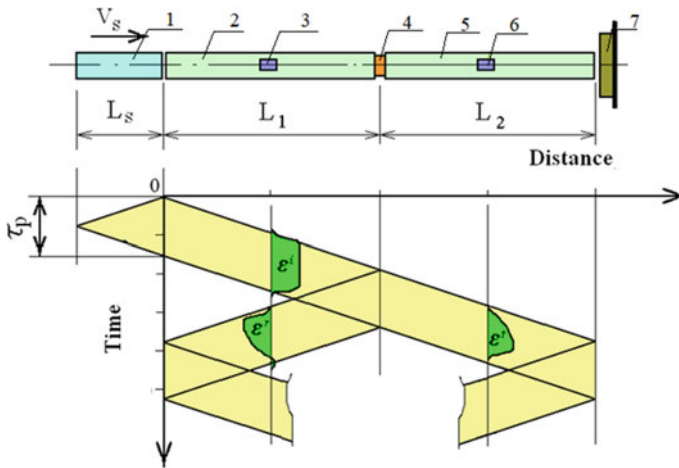


Fig. 2.1 Scheme of the Hopkinson Split Pressure Bar (SHPB) method and the pattern of wave propagation in measuring bars. 1–impactor, 2–incident bar, 3 and 6–strain gauges, 4–sample, 5–transmitting bar, 7–damper

19.8 mm in diameter on the end face of the incident bar. The striker was accelerated to the required speed in the barrel of a gas gun with a caliber of 20 mm.

2.2.2 Modified Kolsky Method for Testing Ground Media

To carry out dynamic tests of the soil medium under conditions of uniaxial deformation, the modified Kolsky method is used (Fig. 2.2) (Bragov et al. 1994, 1996a, 2004). The scheme of this method differs from the classical version of the Hopkinson split bar method in that the sample is enclosed in a rigid holder during testing, which limits its transverse deformation (Fig. 2.3). With the help of a gas gun with a caliber of 20 mm a compression pulse ε^I was created in incident bar. When this pulse has reached the soil sample and loads it, the first part of the pulse is reflected into the rod as a reflected pulse ε^R and the second part is passed through the sample into the second measuring bar as transmitted pulse ε^T . As a result of multiple reflection of waves in the sample, its stress–strain state becomes homogeneous, in a time noticeably shorter than the load duration. Since the radial strain of the sample is prevented by a rigid cage, and the radial strain is much less than the axial one, then after some time an axisymmetric volumetric stress and a one-dimensional strain appears in the sample.

Then the main components of the stress and strain tensors in the sample will have the form:

$$\sigma_1 = \sigma_x; \sigma_2 = \sigma_3 = \sigma_r; \varepsilon_1 = \varepsilon_x; \varepsilon_2 = \varepsilon_3 = 0$$

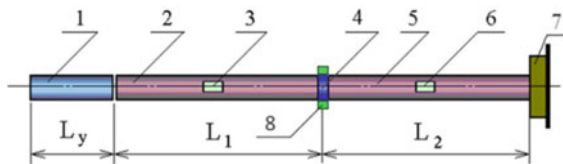
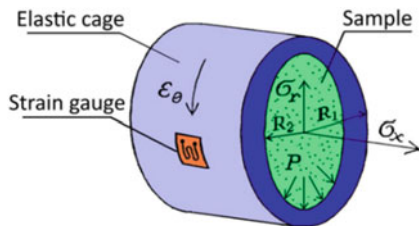


Fig. 2.2 Scheme of a setup of the modified Split Hopkinson Pressure Bar method: 1–striker, 2–incident bar, 3 and 6–strain gauges, 4–sample, 5–transmitting bar, 7–damper, 8–elastic cage

Fig. 2.3 Cage scheme



where σ_x and ε_x are longitudinal stresses and strains, σ_r are radial stresses. The axial components of stress $\sigma_x(t)$, strain $\varepsilon_x(t)$, and strain rate $\dot{\varepsilon}_x(t)$ in the sample are determined by registering strain pulses on measuring bars by strain gauges according to the traditional formulas of the SHPB method (1–3). The value of the radial component of the stress tensor can be obtained from solving the task of elastic deformation of a thick-walled cylinder under internal pressure. The relationship between the internal pressure P_i and the circumferential deformation of the casing $\varepsilon_\theta(t)$ has the form (Bragov et al. 1994).

$$\sigma_r(t) = P_i(t) = \frac{1}{2R_2^2} [E(R_1^2 - R_2^2)\varepsilon_\theta(t)] \quad (2.4)$$

where E is Young's modulus of the casing material, R_1 and R_2 are the outer and inner radii of the cage, respectively. The internal pressure P_i , under the influence of which the cage experiences small elastic deformations, are the desired radial stresses σ_r . Thus, according to the readings of strain gauges on the outer surface of the cage $\varepsilon_\theta(t)$, it is possible to determine the radial stress component $\sigma_r(t)$ in the sample. Further, from the obtained parametric dependences $\sigma_x(t)$, $\varepsilon_x(t)$, $\dot{\varepsilon}_x(t)$, and $\sigma_r(t)$, after their mutual synchronization, time is excluded as a parameter and a diagram of uniaxial deformation of the sample $\sigma_x \sim \varepsilon_x$ and a history of change in the strain rate $\dot{\varepsilon}_x \sim \varepsilon_x$ are constructed. The combination of two stress components in the sample, $\sigma_x(t)$ and $\sigma_r(t)$, makes it possible to calculate the basic properties of the material under test. The maximum shear stresses (shear resistance) will be on planes located at an angle of 45° to the X -axis, and their values on these planes will be equal to

$$\tau(t) = \frac{1}{2} [\sigma_x(t) - \sigma_r(t)] \quad (2.5)$$

The pressure $P(t)$ in the sample is determined through the principal stresses as follows:

$$P(t) = \frac{1}{3}[\sigma_x(t) + 2\sigma_r(t)] \quad (2.6)$$

Volumetric deformation will be equal to

$$\theta(t) = \varepsilon_x(t) \quad (2.7)$$

Thus, this technique makes it possible to calculate the following properties of the tested material: shear resistance $\tau(t)$, coefficient of lateral pressure (thrust) $\xi(t)$, pressure $P(t)$ in the sample, volumetric deformation $\theta(t)$, stress intensity $\sigma_i(t)$, and strain intensity $\varepsilon_i(t)$. Therefore, the used version of the Kolsky method, in addition to obtaining a diagram of uniaxial compression of a sample under conditions of passive limitation of radial deformation, is used to obtain a curve of volumetric compressibility $P \sim \theta$ and a dependence of shear resistance on pressure $\tau \sim P$. In the experiments, measuring bars with a diameter of 20 mm, made of steel with a yield strength of more than 2 GPa, were used. The incident bar had a length of 1500 mm, the transmitting bar had a length of 2900 mm. Strain gauges were glued on the surface of the incident bar at a distance of 810 mm from the sample, and on the transmitting bar at a distance of 420 mm from the sample. Loading was carried out by impact of a steel bar 300 mm long on the end face of the incident bar. A striker with a diameter of 19.8 mm was accelerated to the required speed in the barrel of a gas gun with a caliber of 20 mm. A pulse shaper made of annealed copper 0.8 mm thick was placed on the impacted end of the measuring bar. This made it possible to obtain sufficiently smooth leading and trailing edges of the incident pulse (Fig. 2.4). In Fig. 2.5, the synchronized strain pulses in the measuring bars are given. It is clearly seen that the sample is in a state close to homogeneous, since the strain values in the transmitted pulse are almost equal to the sum of the strains in the incident and reflected pulses, which indicates the equality of the forces acting on the sample from the incident and transmitting bars at each moment of time.

2.2.3 *The Reversed Experiment Technique*

The reversed experiments were carried out on a PG-57 setup (Bragov et al. 2018; Balandin et al. 2016). In these experiments, the resistance force was measured at the initial stage of penetration. This method for measuring the force of resistance to the penetration into the ground using a measuring bar is as follows. The container filled with soil accelerates to the required speeds and strikes a head of the appropriate shape, fixed on a measuring bar. The impact velocity and the material properties of the bar must be such that plastic deformations do not occur in the bar. In this case, an elastic strain impulse $\varepsilon(t)$ is formed in the bar. The registration of this pulse makes

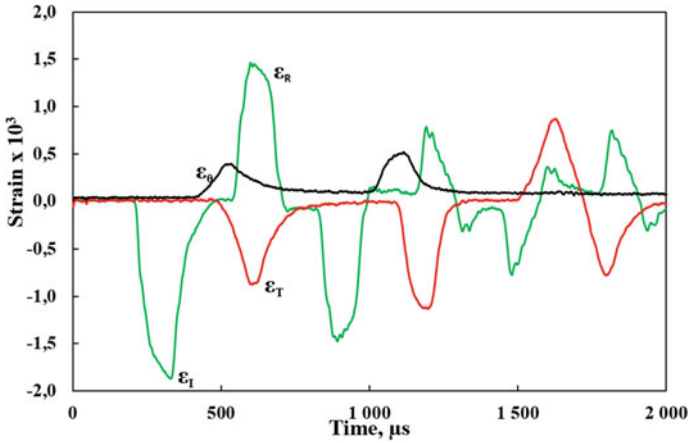
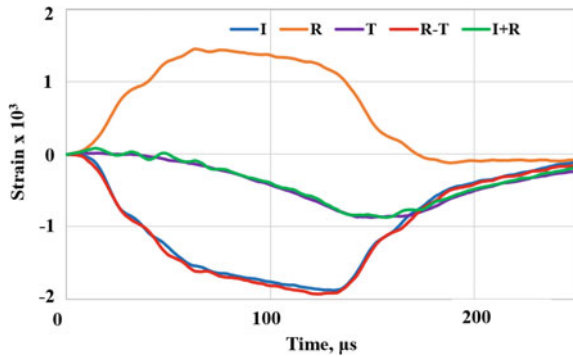


Fig. 2.4 Impulses of strain in measuring bars (ϵ^I , ϵ^R , ϵ^T) and in a holder (ϵ_θ) in experiment No. 51. (ϵ^I is an incident impulse, ϵ^R is a reflected impulse, ϵ^T is a transmitted impulse, ϵ_θ is a circumferential impulse of strain in a cage)

Fig. 2.5 Synchronized strain pulses in measuring bars (ϵ^I , ϵ^R , ϵ^T) in experiment No. 51



it possible to determine the force F acting on the head when interacting with the medium, according to the known relation $F(t) = E \epsilon(t) S$, where E is the elastic modulus of the bar, S is the area of its cross section. Thus, in this method, the task of measuring forces is greatly simplified and is reduced to registering the elastic strain impulse in the bar using strain gauges. The scheme of this technique is shown in Fig. 2.6. In the proposed version of the reversed experiment, a 57 mm caliber gas gun with a double-diaphragm shutter is used to accelerate a container with soil, which makes it possible to obtain stable and easily controlled impact velocities in the range from 50 to 500 m/s. The container is a cylinder made of polypropylene filled with soil medium. The bottom of the container is glued to the cylindrical part. The impact speed of the container was measured using two electro contact sensors located in the holes of the barrel, drilled in front of its muzzle. To close the contacts of the speed meter, an aluminum alloy ring was glued to the front edge of the container.

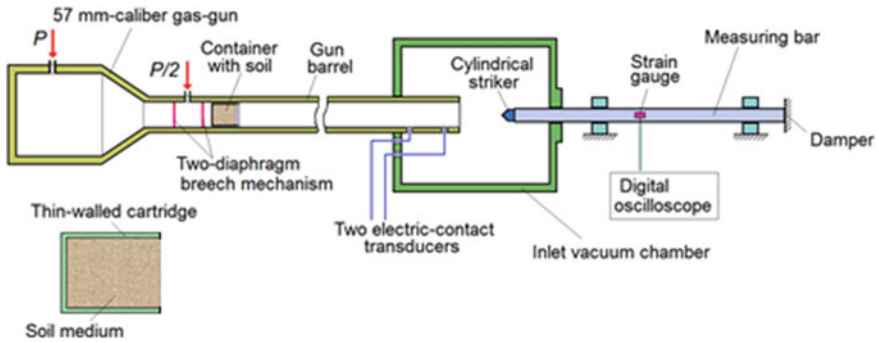


Fig. 2.6 Scheme of the reversed experiment technique

The distance between the contacts and the time of their closing determines the speed of the container before hitting the measuring bar.

A steel bar with a length of 1.5 m and a diameter of 12 mm with a yield strength of more than 600 MPa is used for measuring forces. The impact end of the measuring bar had a conical shape with an angle at the top of 60°. The bar is located at a certain distance from the muzzle of the barrel so that the impact occurs immediately after the full departure of the container from the barrel. The support, on which the bar is located, has adjusting supports, which allows to ensure the axisymmetric nature of the interaction. The bar with its rear end rests against a special stop, preventing its displacement and damping the impact energy. The impact occurs in a vacuum chamber to which the gun barrel is attached and into which a measuring bar is inserted. The geometric dimensions of containers with clay samples are shown in Fig. 2.7. The numbers indicate 1–clay sample, 2–polypropylene container, 3–fragment of a measuring bar with a head.

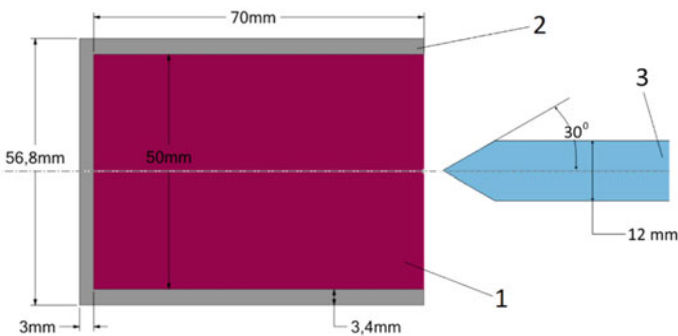


Fig. 2.7 Geometric dimensions of the sample

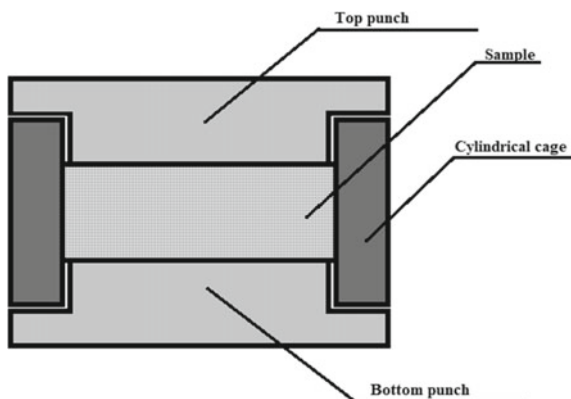
2.3 Sample Preparation Technique

Clay for testing was taken from a depth of 1 m in the Bogorodsky district of the Nizhny Novgorod region. The clay was dried in air at room temperature for a long time to completely remove moisture. Then pieces of dry clay were crushed to a powder. To form samples, ground clay was mixed with water in an amount of 20% by weight of the clay. The wet clay was thoroughly mixed to ensure uniformity. For tests according to the SHPB method, clay samples were molded in special cylindrical holders (Fig. 2.8). A strictly defined mass of wet clay was placed in a holder between two punches. Then the punches were brought as close as possible to obtain the required volume of the sample. After forming the sample, the upper punch was removed from the holder. Then the samples were dried in air until the added moisture was completely removed. It should be noted that, upon evaporation of moisture, the samples decreased in length and diameter. With complete evaporation of water, the diameter of the samples was 16.5–16.7 mm, and the length was 12.5–12.6 mm. The density of the samples was 1940–2000 kg/m³.

When tested according to the modified Kolsky method with a sample in a limiting cage, samples about 10 mm long were formed the same method. When moisture evaporated, the samples decreased in diameter; therefore, the diameter of the holder for the formation of samples was chosen so that, with complete evaporation of water, the diameter of the samples was 20.5 mm and corresponded to the inner diameter of the cage for testing. The density of the samples was 1950–1980 kg/m³.

Clay specimens with high of 70 mm were made for the reversed experiments. The samples were molded in aluminum cylindrical containers with an inner diameter of 54 mm. During the formation of the samples, the wet clay was compacted to eliminate possible voids. Then these samples were removed from the container and dried in air until the added moisture was completely removed. When the moisture evaporated, the samples decreased in diameter. Finally, when the water completely evaporated, the diameter of the samples was close to 50 mm and corresponded to the

Fig. 2.8 Scheme of the device for forming the sample



inner diameter of the polypropylene test container. The density of the samples was 1940–1980 kg/m³.

2.4 Results of the Experimental Study

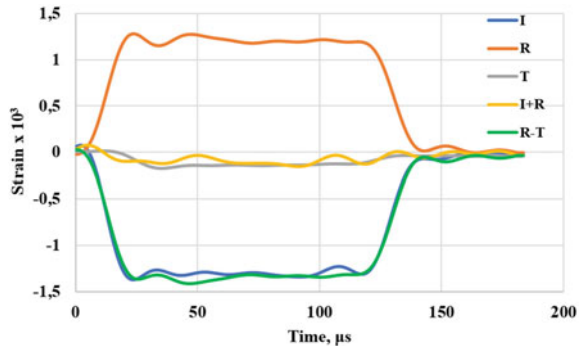
2.4.1 *Results of Compression Tests According to the SHPB Method*

Studies of dry clay samples under uniaxial stress were carried out using the traditional Kolsky method on a PG-20 setup. In the experiments, measuring bars with a diameter of 20 mm, made of D16T aluminum alloy, were used. The bars had a length of 1500 mm. The strain gauges were glued on the surfaces of the bars in the middle sections. Loading was carried out by impact of an aluminum bar 300 mm long and 19.8 mm in diameter on the end face of the incident bar. The striker was accelerated to the required speed in the barrel of a gas gun with a caliber of 20 mm. Figure 2.9 shows synchronized pulses in measuring bars in experiment s668-26. It is clearly seen that the sample is in a state close to homogeneous, since the strain values in the transmitted pulse are almost equal to the difference of the strains in the incident and reflected pulses, which indicates the equality of the forces acting on the sample from the loading and supporting bars at each moment of time. The loading conditions (strain rate) were varied by changing the impact speed. The experiments were carried out at strain rates close to 600 s⁻¹, 950 s⁻¹, and 1250 s⁻¹. Figure 2.10 shows a group of diagrams obtained under similar conditions at strain rates of about 950 s⁻¹ (top), and the bottom of the same figure shows the dependence of the strain rate on strain. It can be seen that the strain rates in the experiments are practically constant and close to 950 1/s. Diagrams of deformation of dry clay demonstrate a fairly large scatter. As the strain increases, the stress quickly reaches its maximum and then remains almost constant. This behavior indicates plastic deformation of the sample material after reaching a certain limiting stress. This stress corresponds to the yield strength of the material and increases from 10 to 22 MPa with an increase in the strain rate from 600 to 1250 s⁻¹ (Fig. 2.11). At the end of the process, the destruction of the sample material occurs, which is characterized by a drop in stress with increasing strain.

2.4.2 *Results of Modified SHPB Tests*

Tests of dry clay under conditions close to uniaxial deformation were carried out on a PG-20 setup using a modified SHPB technique with a sample in a bounding cage. After complete drying, the samples were inserted into a cage with strain gauges glued to the outer one to measure circumferential deformations ε_{θ} . The length of the

Fig. 2.9 Synchronized pulses (ε^I , ε^R , ε^T) in measuring bars in experiment s668-26



working part of the holder was 10 mm, so the samples had a length close to the length of the working part of the cage. The inner diameter of the holder was equal to 20.5 mm, which provided a sufficiently small gap between the holder and the side surface of the measuring bars. The outer diameter of cage was 35 mm. Since the length of the specimens and the working part of the cage practically coincided, thin-walled cylinders with a wall thickness of 1.85 mm (Fig. 2.12) and a length of 3 mm were left at the edges of the cages to ensure the centering relative to the bars. As shown in Bragov et al. (2004), these centering sleeves did not affect the measurement results.

The sample was placed inside the working part of the cage. Then the sample was pressed from both sides with measuring bars to eliminate gaps. The experiments were carried out under three loading modes, differing in the striker speed: ~ 20, 25, and 30 m/s. Correspondingly, the strain rate also differed: 1400, 1800, and 2500 s⁻¹. Five experiments were carried out for each loading mode. The parameters of the tested samples and the conditions for the experiments are shown in Table 2.1.

According to the results of experiments using formulas (2.1–2.3), the dependences on the time of longitudinal deformation, longitudinal stress, strain rate of the sample were determined. According to formula (2.4), the radial stress in the sample was determined as a function of time. These dependences were used to build strain diagrams, strain rate versus strain, pressure versus strain, and shear strength versus pressure. The pressure P and the shear stress τ were determined by formulas (2.5, 2.6). These dependences for each loading mode were averaged to obtain average curves and standard deviation. Strain diagrams were obtained in the stress range up to 400 MPa. An example of strain diagrams and dependences of strain rate on longitudinal strain, obtained at impactor velocities close to 20 m/s, is shown in Fig. 2.13 (Zel'dovich and Raizer, 2002). The abscissa shows the technical deformation. Comparison of the obtained average diagrams of clay deformation for different loading modes is shown in Fig. 2.14. It is clearly seen that the load branches of the obtained diagrams practically coincide within the scatter of the experimental data, i.e., do not depend on the strain rate, and the values of the achieved stresses and strains depend on the amplitude of the applied load. The slope of the unloading branches of the diagrams is close to linear for different experiments, and also does not depend on the strain rate.

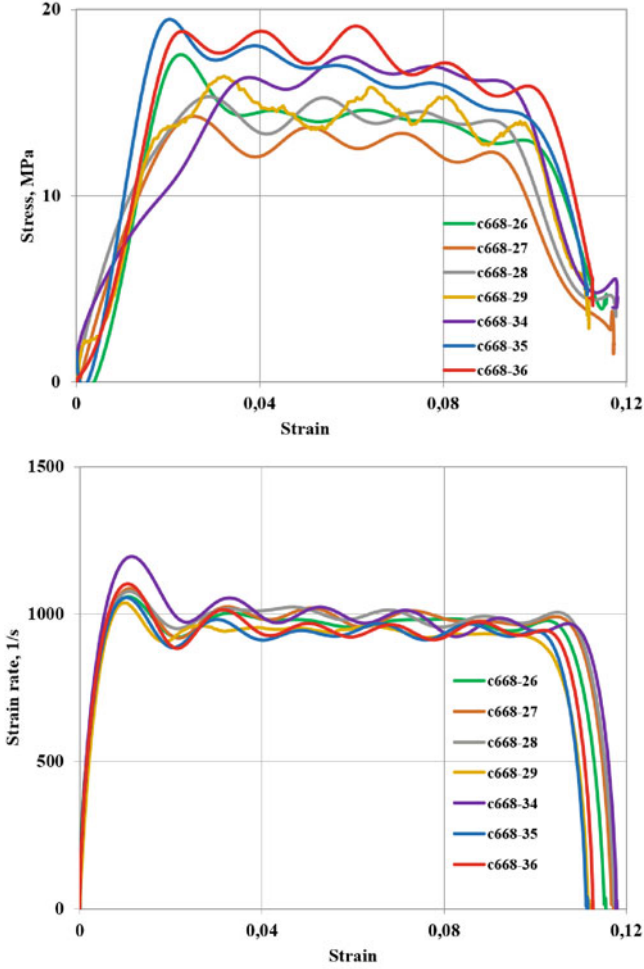


Fig. 2.10 Diagrams of dry clay deformation (top) and dependence of strain rate on strain at a strain rate of about 950 1/s under uniaxial stress conditions

The load branch of the dependence true deformation - longitudinal stress can be described by the expression (Zel' dovich and Raizer, 2002)

$$\sigma_x = \frac{\rho_0 A^2 \varepsilon_x}{(1 - B \varepsilon_x)^2}$$

where A and B are parameters of the shock adiabat written as $D = A + BU$ (D is the velocity of the shock wave, U is the mass velocity of matter behind the front). The load branches of the diagrams are well approximated by this dependence with the parameters $A = 500$ m/s, $B = 1.9$. The unloading branches of the diagrams have

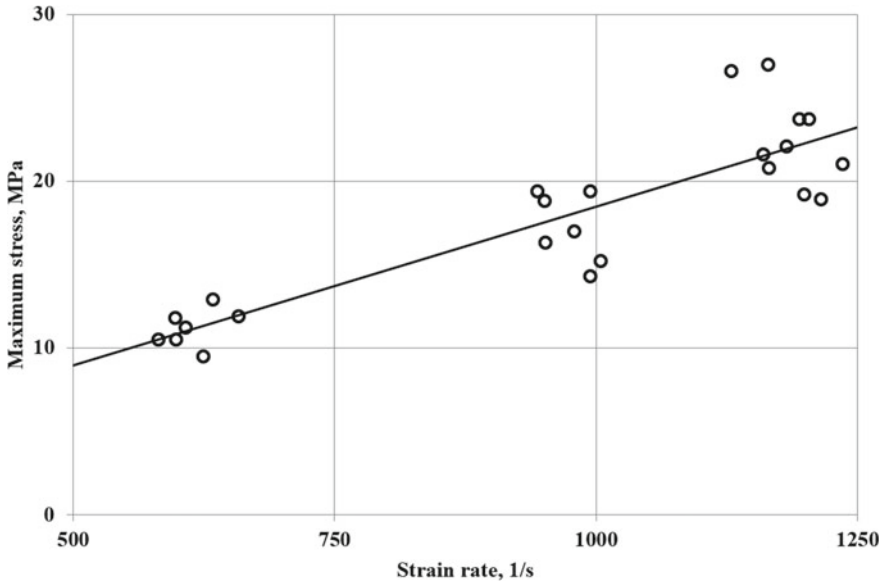
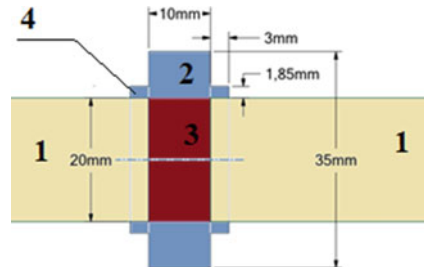


Fig. 2.11 Strain rate dependence of the flow stress of dry clay under uniaxial compression

Fig. 2.12 Measuring cage design. 1—measuring bars, 2—working part of the cage, 3—sample of the soil medium, 4—centering sleeves



a slope in the linear section, characterized by a modulus of 11,300 MPa. Since the volumetric deformation practically coincides with the longitudinal deformation—the difference is less than 2% of its value, then it is possible to construct a summary compressibility curve in true deformations. The course of the curves characterizing the dependence of pressure on volumetric deformation is also practically independent of the strain rate (Fig. 2.15).

Of considerable interest is the determination of the shear properties of the soil under study. For many soil media, the dependence of the yield strength on pressure can be described by the Mohr–Coulomb relation. The dependences $\tau \sim P$ determined in the experiments for the loading mode with an impact speed of 25 m/s are shown in Fig. 2.16. It is clearly seen that these dependencies have two different branches—loading and unloading, which have different slopes. Average dependences of shear strength τ on pressure P are shown in Fig. 2.17.

Table 2.1 The conditions of experiments using modified SHPB method

| Test no | Density of clay, g/sm ³ | Specimen length, mm | Remaining sample length, mm | Impact velocity, m/s | Maximum strain rate, s ⁻¹ |
|---------|------------------------------------|---------------------|-----------------------------|----------------------|--------------------------------------|
| 49 | 1,95 | 10,05 | 8,75 | 18,9 | 1470 |
| 51 | 1,96 | 10,05 | 8,7 | 19,4 | 1360 |
| 54 | 1,97 | 9,95 | 8,4 | 24,9 | 1710 |
| 55 | 1,98 | 9,9 | 8,4 | 24,9 | 1830 |
| 59 | 1,97 | 10,0 | 8,3 | 30,6 | 2630 |
| 61 | 1,98 | 9,95 | 8 | 30,3 | 2550 |
| 65 | 1,95 | 9,9 | 8,4 | 25,2 | 1910 |
| 66 | 1,95 | 9,7 | 8,1 | 24,6 | 1980 |
| 67 | 1,97 | 9,7 | 8,65 | 19,8 | 1380 |
| 68 | 1,96 | 9,7 | 8,4 | 19,8 | 1480 |
| 69 | 1,97 | 9,7 | 8,6 | 19,2 | 1520 |
| 70 | 1,98 | 9,7 | – | 30,8 | 2740 |
| 72 | 1,98 | 9,7 | 8,2 | 24,5 | 1920 |
| 73 | 1,98 | 9,7 | 8,2 | 24,5 | 2480 |
| 74 | 1,96 | 9,8 | – | 30,3 | 2480 |

The dependence of shear strength on pressure in the section of active load is described by a linear function of the form $\tau = C + kP$. At striker speeds of 20 and 25 m/s, $C = 2.5$ MPa, and $k = 0.4$, and at impact speeds of 30 m/s, $C = 0.5$ MPa, and $k = 0.38$. The branches of the dependence $\tau \sim P$ during unloading are also well approximated by straight lines that have different slopes for different test modes. At 20 m/s $C = -9$ MPa, and $k = 0.62$. At 25 m/s $C = -5$ MPa, and $k = 0.58$. At 30 m/s $C = -5$ MPa, and $k = 0.53$.

2.4.3 Analysis of the Results of the Reversed Experiment

Several reversed experiments were carried out on the penetration of conical head to verify the model of the soil medium. The head was a diameter of 12 mm. Container with dry clay was accelerated up to impact velocities of about 200 m/s. The conditions for the experiments are given in Table 2.2. The dependences of the resistance forces on time were obtained (Fig. 2.18). In the figure, the colored lines show the results of repeated tests. The black line corresponds to the average value. Confidence intervals with a probability of 0.95 are also shown. It can be noted that the increase in the resistance force during the penetration of a cone with an angle of $2\alpha = 60^\circ$ occurs along a curve close to a parabola. The maximum force during the penetration of the cone is reached at a moment close to the moment of immersion of the base of the

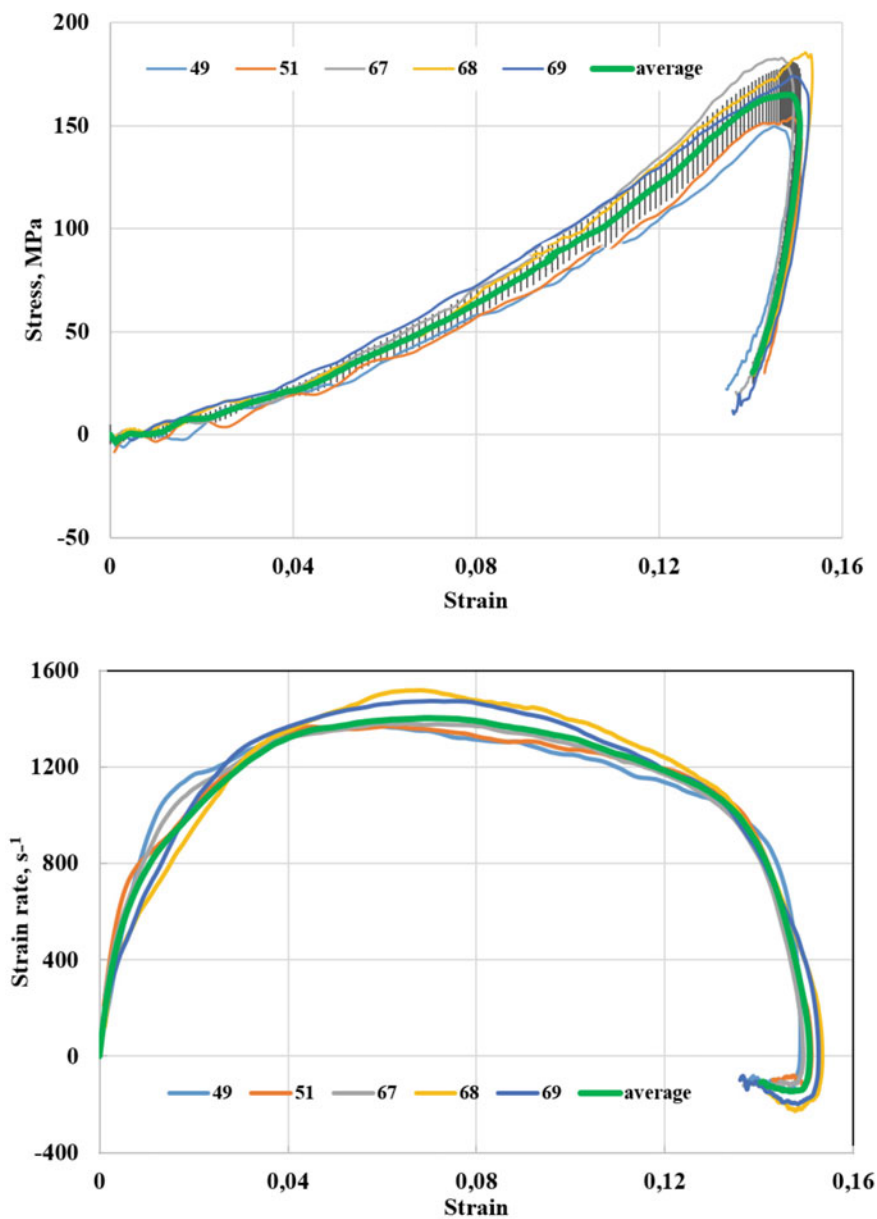


Fig. 2.13 Diagrams of deformation of clay samples at impact velocities of 20 m/s (a), the strain rate of clay samples at an impact velocity of about 20 m/s (b)

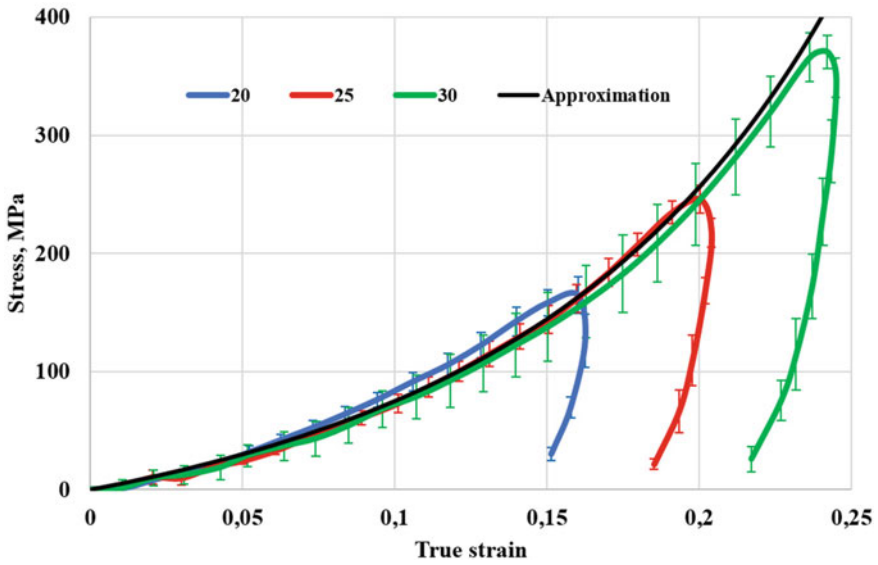


Fig. 2.14 Diagrams of strain of clay specimens at different impact velocities

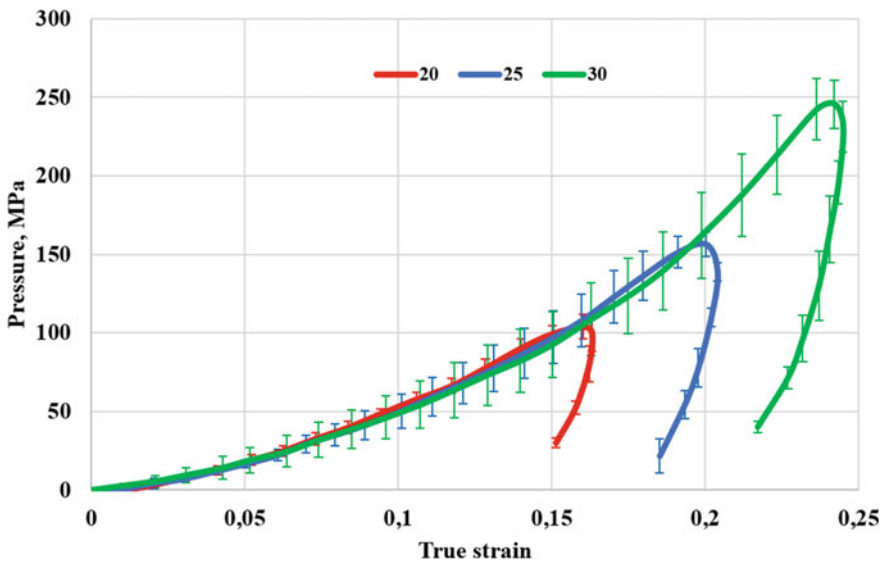


Fig. 2.15 Dependence of pressure on volumetric deformation at various impact velocities

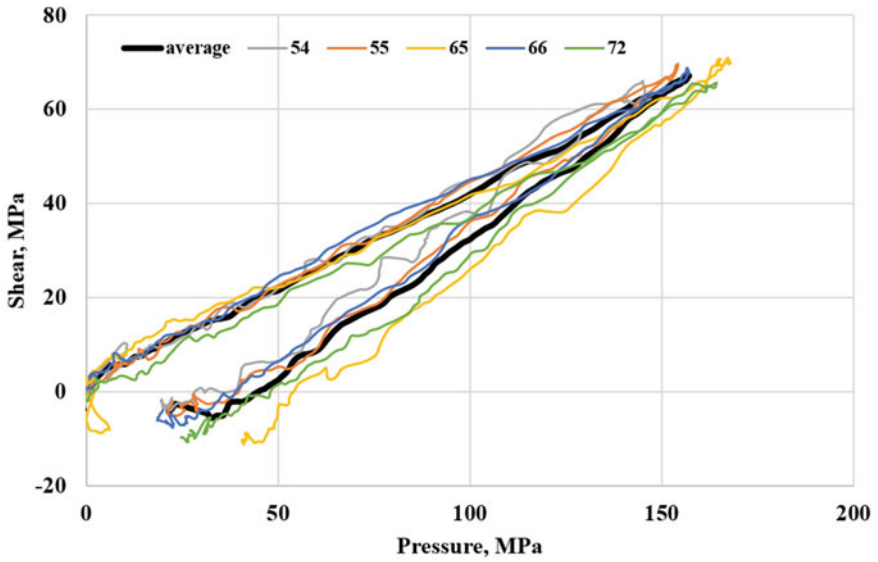


Fig. 2.16 Shear stress versus pressure at an impact velocity of 25 m/s

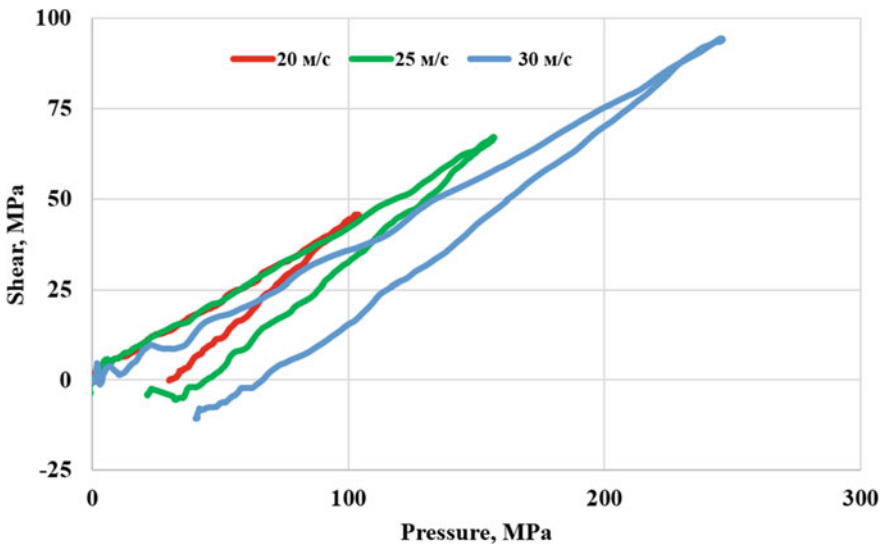


Fig. 2.17 Dependence of shear stress on pressure at different impact velocities

Table 2.2 The conditions of reversed experiments

| N ^o exp | Density, kg/m ³ | Velocity, m/s | F _{max} , kN |
|--------------------|----------------------------|---------------|-----------------------|
| 657 | 1940 | 188 | 20,6 |
| 659 | 1970 | 201 | 20 |
| 660 | 1980 | 208 | 20,2 |
| 661 | 1970 | 210 | 19 |

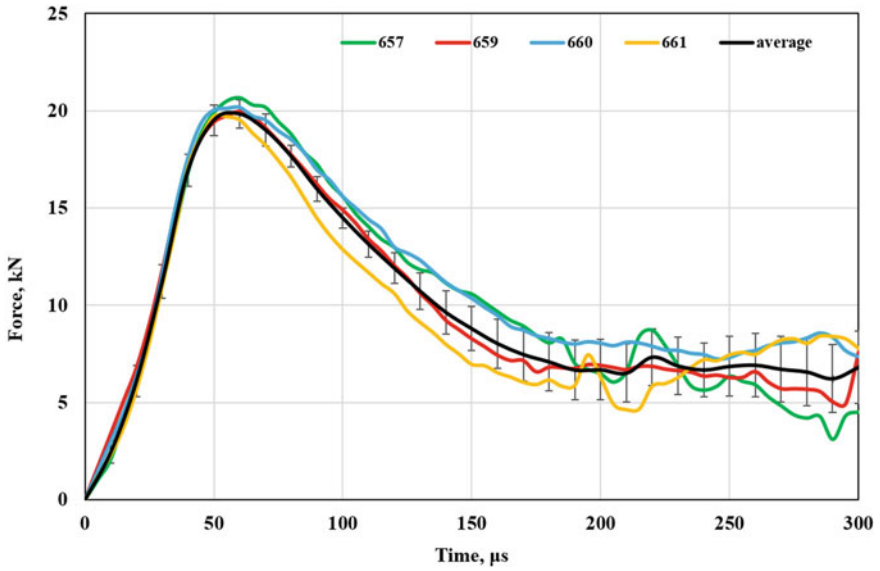


Fig. 2.18 Time dependence of penetration resistance forces

cone. The maximum resistance forces in all the experiments performed are close. After reaching the maximum, there is a gradual decrease in strength, because the influence of the walls of container on the resistance force is small.

2.5 Numerical Simulation of Soil Sample Loading

2.5.1 Analysis of Experimental Results and Construction of a Mathematical Model of Clay Soil Deformation

To model the behavior of clay, a constitutive relation in the form of Grigoryan’s model was chosen (Grigoryan 1960). This model is widely used to model the behavior of soft soil media under dynamic loads. Soft soil is considered as an elastoplastic medium that exhibits nonlinear resistance to compression and shear

(Bazhenov et al. 2014). In this model, to describe the nonlinear behavior of the soil medium, it is necessary to specify the dependence of pressure on volumetric deformation (or density), as well as the dependence of flow stress on pressure. In LS-DYNA software, such a model is implemented as a material: MAT_SOIL_AND_FOAM (LS-DYNA Keyword User's Manual). This is a fairly simple model that is recommended for describing soils, concretes, and foams. The volumetric compressibility curve is shown schematically in Fig. 2.19. As part of the implementation of the model in LS-DYNA, two options for the behavior of the material during unloading are provided. In the first case, unloading occurs along the same curve as the load (gray arrows in Fig. 2.19). In the second, unloading is performed in a straight line, the slope of which is set by the modulus of all-round compression K . In tension, the value of the maximum pressure is limited by the value of *Pressure Cutoff*.

The pressure is considered positive when compressed. Volumetric deformation is determined by the natural logarithm of the relative volume:

$$e = \ln \frac{V}{V_0}$$

here V is the current volume, V_0 is the initial volume. Curve $P(e)$ is given as a tabular function. The plastic behavior of the medium is described using the ideal plastic flow function:

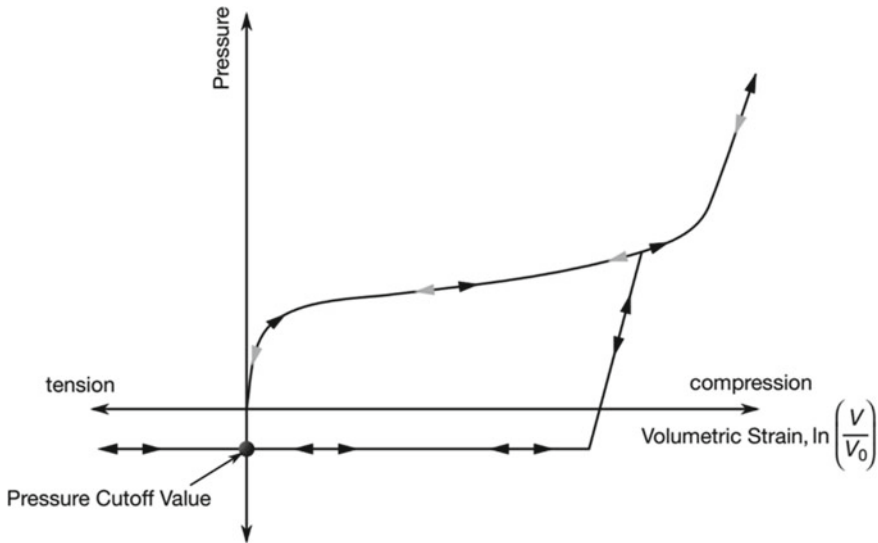


Fig. 2.19 Volumetric compressibility curve in the MAT_SOIL_AND_FOAM model (LS-DYNA Keyword User's Manual)

$$\phi = J_2 - [a_0 + a_1 P + a_2 P^2]$$

here J_2 is the second invariant of the stress tensor deviator:

$$J_2 = \frac{1}{2} s_{ij} s_{ij}$$

here s_{ij} are the components of the stress tensor deviator. On the flow surface:

$$J_2 = \frac{1}{3} \sigma_Y^2$$

where σ_Y is the flow stress in a uniaxial stress state. In this way:

$$\sigma_Y = [3(a_0 + a_1 P + a_2 P^2)]^{1/2}$$

The considered model does not assume strain hardening. The plastic behavior of the material is determined by the values of the material parameters a_0 , a_1 , a_2 . Model identification for clay was carried out on the basis of data obtained during the experimental determination of the dynamic compressibility of clay using a modification of the Kolsky method described above. As a result of the experimental studies performed, the dependences of pressure on volumetric deformation, as well as stress intensity on pressure for three loading modes were obtained, which correspond to striker velocities of 20, 25, and 30 m/s. The dependences of pressure on the logarithm of the relative volume of the sample, grouped by loading modes, are shown in Fig. 2.20. Good repeatability of the results of experiments carried out under the same conditions is visible. At the indicated striker speeds, in the corresponding experiments, axial strain rates of the order of 1200, 1500, and 2300 s⁻¹, respectively, were realized (Fig. 2.21).

Figure 2.22 shows the dependences of pressure on volumetric strain for three loading modes. It can be noted that the nature of the bulk compressibility curves is practically independent of the loading rate (left side of Fig. 2.22). It follows from the presented data that the mechanical properties of clay do not depend on the strain rate, but depend on the amplitude of the applied load, i.e., there is an exit to a single dynamic curve. It should be noted that in the deformation diagrams, the unloading curves differ significantly from the load ones. The load branches of the diagrams are actually repeated for different load intensities. Only the maximum deformation (and, accordingly, pressure) achieved in the test differs. At the highest strain rate, maximum pressures of the order of 250 MPa arise in the sample. The dependences of flow stress on pressure (right side of Fig. 2.22) in the loading area are practically linear. The slope of these sections is practically independent of the loading rate. The data shown in Fig. 2.22 was approximated to equip the MAT_SOIL_AND_FOAM model with the necessary parameters and constants. The left side of the figure shows the approximation of the volumetric compressibility curves by a tabular function. The table function is presented in Table 2.3.

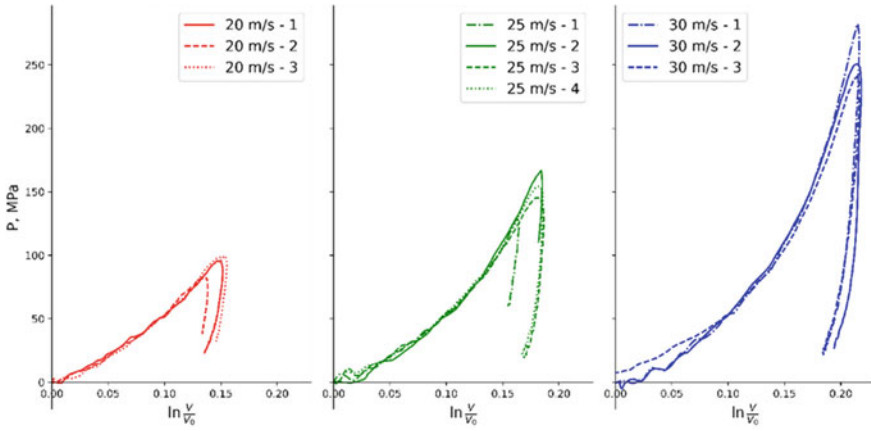


Fig. 2.20 Dependences of pressure on the logarithm of relative volume for three loading modes

Fig. 2.21 Axial strain rates

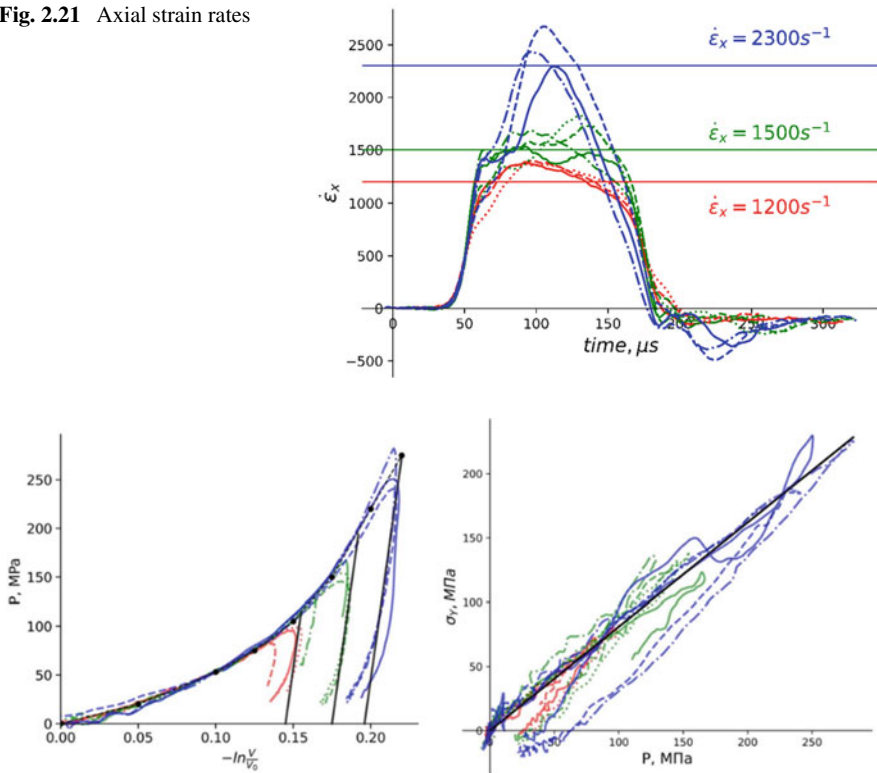


Fig. 2.22 On the left—approximation of the volumetric compressibility curve, on the right—approximation of the dependence of the flow stress on pressure

Table 2.3 The dependence of pressure on volumetric strain

| | | | | | | | | |
|---------------------|---|-------|------|--------|-------|--------|------|-------|
| $\ln \frac{V}{V_0}$ | 0 | -0.05 | -0.1 | -0.125 | -0.15 | -0.175 | -0.2 | -0.22 |
| P, MPa | 0 | 20 | 53 | 75 | 105 | 150 | 220 | 275 |

Unloading in the model under consideration is carried out in a straight line with a given angle of inclination. The module of the unloading branch was determined by approximating the experimental data (Fig. 2.22). The volumetric compression modulus K during unloading was 11,383 MPa. The procedure for determining the parameters of Grigoryan's model based on the data of tests of soft soils in a bounding cage is described in Dyanov and Kotov (2020). The parameters of the loading path on the stress plane under conditions of a uniaxial deformed state can be obtained analytically. The loading trajectory is formed by three segments. The first segment corresponds to the plastic loading of the soil from zero in the initial state to the maximum stress value determined by the amplitude of the load pulse. The second segment corresponds to the elastic deformation of the soil at the initial stage of unloading from the achieved state. The third segment is associated with the transition of the soil from the elastic to the plastic state. The slope of the first section is related to the lateral pressure coefficient (determined experimentally), which in turn is related to the coefficient in the linear dependence of the yield stress on pressure. The dependence of flow stress on pressure is well described by a linear function (Fig. 2.22, right).

$$\sigma_y = k \cdot P + b = 0.81 \cdot P$$

The slope of the first section of the loading trajectory:

$$K_I^\sigma = \frac{d\sigma_r}{d\sigma_x} = \frac{1 - k/3}{1 + 2 \cdot k/3}$$

For $k = 0.81$, we get $K_I^\sigma = 0.474$.

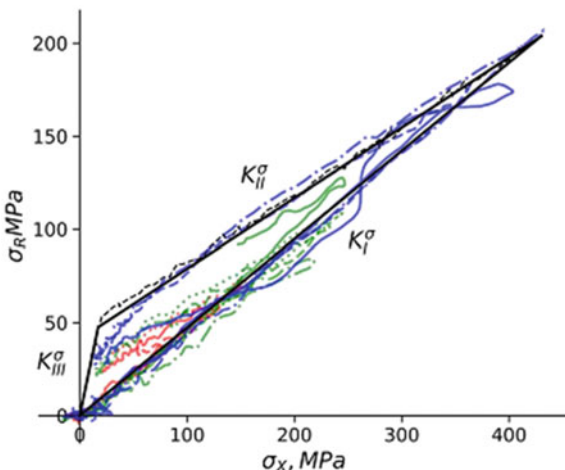
The slope of the second section (elastic) is determined by the formula, which at $G = \beta \cdot k \cdot K/2$, where K and G are the volumetric and shear unloading moduli, will have the form:

$$K_{II}^\sigma = \frac{K - 2G/3}{K + 4G/3} = \frac{1 - k \cdot \beta/3}{1 + 2 \cdot k \cdot \beta/3}$$

where β is a numerical parameter determined experimentally. In the case of the tested soil, the value $\beta = 1.32$ gives a good approximation of the experimental data on the elastic section of the unloading branch (Fig. 2.23). Thus $G = 6085$ MPa, $K_{II}^\sigma = 0.376$.

The third (plastic) section of the loading trajectory has a slope:

Fig. 2.23 Approximation of the trajectory of clay loading



$$K_{III}^{\sigma} = \frac{1 + k/3}{1 - 2 \cdot k/3}$$

With a value of $k = 0.81$, we get $K_{III}^{\sigma} = 2.76$. The approximation of the experimental loading trajectory by the three-link model constructed in this way is shown in Fig. 2.23.

It should be noted that this solution was obtained analytically for the case of one-dimensional deformation of the sample. Since the holder in real experiments is pliable and undergoes elastic deformations, the parameter β was determined by selection when simulating the process of deformation of the sample in the bounding holder. The value of the parameter obtained using the analytical solution was taken as the initial approximation. The simulation scheme is described in detail below. Figure 2.24 illustrates the sample deformation trajectory in the axes $\sigma_x - \sigma_r$ for different values of the parameter β . It can be seen that the best agreement with the experimental data is observed at $\beta = 1.13$, which corresponds to the unloading shear modulus $G = 5200$ MPa.

The coefficients of the MAT_SOIL_AND_FOAM model are defined as follows.

$$a_0 = \frac{\sigma_0^2}{3} = 75, a_1 = \frac{2 \cdot k \cdot \sigma_0^2}{3} = 8.26, a_2 = \frac{k^2}{3} = 0.2187$$

here σ_0 is the dynamic yield strength of clay, also determined using the classical version of the Kolsky method for compression under uniaxial stress conditions. The average value of this stress in the dynamic range of strain rates was about 15 MPa. A complete set of model constants, presented as an input map of the LS-DYNA software package, is shown in Fig. 2.25.

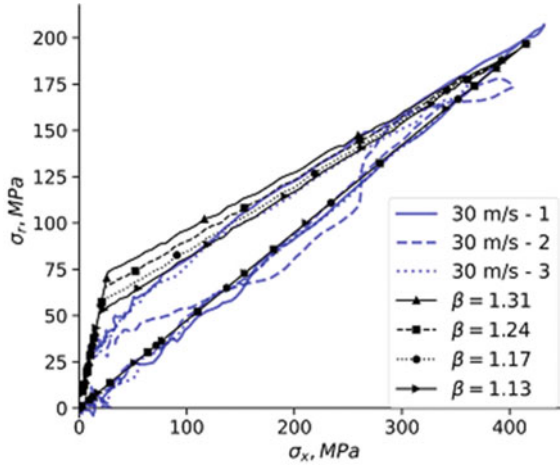


Fig. 2.24 Determination of the parameter β , taking into account the compliance of the cage

```
*MAT_SOIL_AND_FOAM_TITLE
glay
$#      mid      ro      g      bulk      a0      a1      a2      pc
      3      0.00198      5200      11383      75      8.26      0.227
$#      vcr      ref      lcid
      0.0      0.0      0
$#      eps1      eps2      eps3      eps4      eps5      eps6      eps7      eps8
      0.00e+00      -5.00e-02      -1.00e-01      -1.25e-01      -1.50e-01      -1.75e-01      -2.00e-01      -2.20e-01
$#      eps9      eps10
      0.0      0.0
$#      p1      p2      p3      p4      p5      p6      p7      p8
      0.000e+00      2.000e+01      5.300e+01      7.500e+01      1.050e+02      1.500e+02      2.200e+02      2.750e+02
$#      p9      p10
      0.0      0.0
```

Fig. 2.25 Clay model parameters for LS-DYNA

2.5.2 Results of Numerical Simulation of Sample Compression in a Cage

Experiments on dynamic compression of clay samples in a bounding cage were numerically reproduced using LS-DYNA software. Figure 2.26 shows a fragment of the model: the area near the sample in the bounding cage. The numbers indicate 1–cage, 2–measuring bars, 3–sample. Geometric dimensions are given on the right side of the figure. In the computational experiment, as well as in the full-scale test, the length of the incident bar was 1.5 m and the length of the transmitting bar was 3 m. Since the measuring bars and the cage work in the elastic region, their behavior was described by linear elastic MAT_ELASTIC models. Model parameters are given in Table 2.4.

As mentioned above, the behavior of the clay sample was described by the MAT_SOIL_AND_FOAM model, the parameters of which were defined earlier (Fig. 2.25).

Fig. 2.26 Fragment of the model

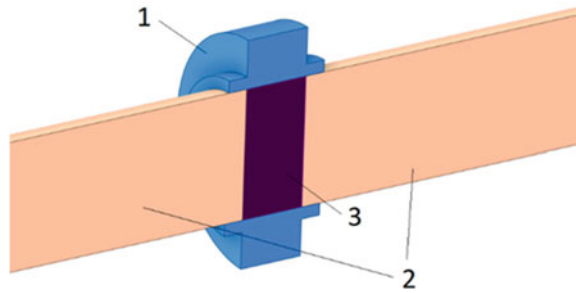


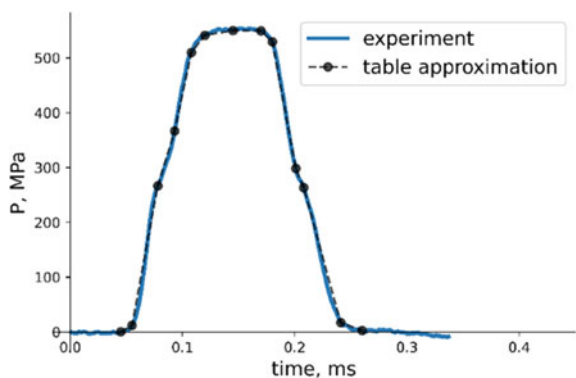
Table 2.4 Model parameters for describing the behavior of measuring bars and cage

| | Density, kg/m ³ | Young's module, MPa | Poisson's ratio |
|----------------|----------------------------|---------------------|-----------------|
| Measuring bars | 8050 | 185,000 | 0.28 |
| Cage | 7850 | 210,000 | 0.28 |

Since the behavior of the material did not show a dependence on the strain rate, the experiment was simulated with the maximum load amplitude (the impactor speed was 30 m/s). As a load, a stress pulse acting on the end of the incident bar was set. The shape of this pulse was determined from the incident strain pulse recorded in the corresponding full-scale test using the formula: $\sigma(t) = -E \cdot \varepsilon^I(t)$ here E is the modulus of elasticity of the measuring bar, $\varepsilon^I(t)$ is the strain impulse registered in the incident bar. The resulting time dependence of the stress pulse is shown in Fig. 2.27.

The problem was solved in an axisymmetric setting. An explicit scheme was used to integrate the equations over time. Area-weighted axisymmetric Lagrangian finite elements (type 14) were used to discretize the space. Figure 2.28(a-d) provides a comparison of simulation results and experimental data. The components of the stress tensor in the computational cell corresponding to the sample were determined numerically. The blue lines in the figures correspond to the experimental data, the black

Fig. 2.27 The stress pulse



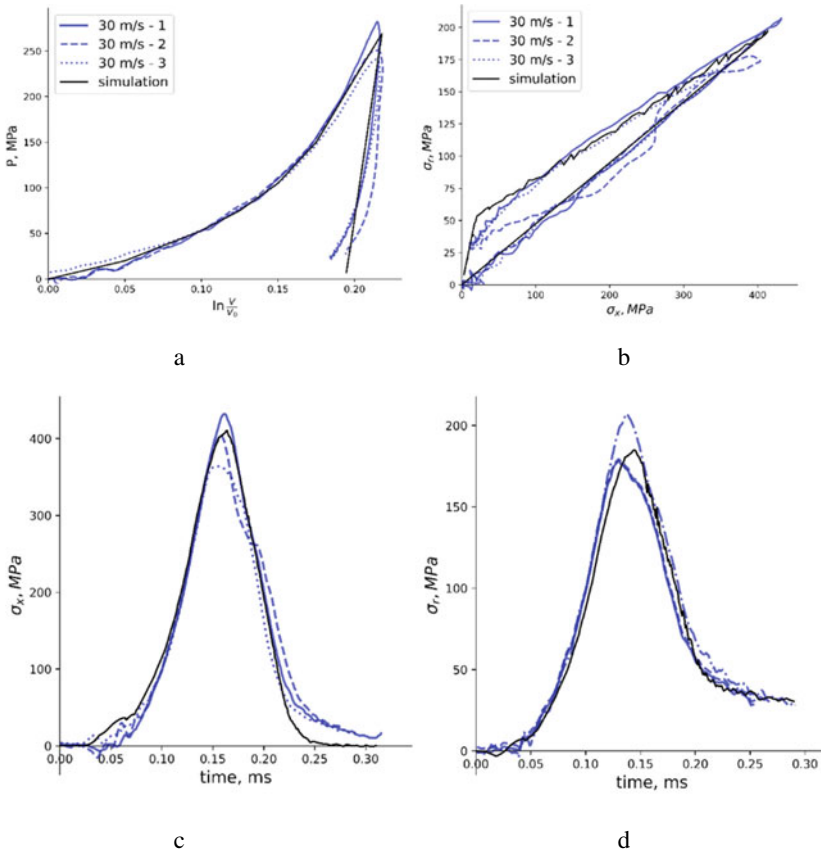


Fig. 2.28 Comparison of simulation results and experimental data

lines are the simulation results. Fig. 28a compares pressure versus strain. Fig. 28b shows the curves in the axial stress-radial stress axes. Fig. 28c and d compares the time dependences of the axial and radial stresses in the specimen, respectively. In general, it can be noted that the identified mathematical model based on the results of the experiment allows quite accurately, both qualitatively and quantitatively, to reproduce the main features (including nonlinear behavior) of the material under study.

2.5.3 Numerical Simulation of the Reversed Experiment

For a more reliable verification of the parameters of the model of the soil and their refinement, numerical simulation of the reversed experiment was carried out. The

geometric formulation of the task corresponds to the experimental scheme shown in Fig. 2.7. A sample 70 mm long and 50 mm in diameter was tested on a setup with a measuring bar 12 mm in diameter. The samples were placed in a polypropylene holder. In Fig. 2.7, the numbers indicate 1–sample, 2–container, and 3–fragment of a measuring bar with a conical tip. The opening of the cone is 60 degrees. Sample 1 in container 2 is accelerated with a gas gun. In the simulated experiments, the initial velocities of the sample are 200 m/s. The clay behavior was described by the MAT_SOIL_AND_FOAM model with the parameters defined earlier. The behavior of the material of the measuring bar was described by a linear elastic model (density 7850 kg/m³, Young's modulus 210 GPa, Poisson's ratio 0.28). The problem was solved in an axisymmetric formulation. An explicit scheme was used to integrate the equations over time. The discretization of the container and the measuring bar was carried out by Lagrangian area-weighted axisymmetric finite elements (type 14). Since large deformations occur in the clay sample during impact interaction with the measuring bar, the integration of the equations for the sample was carried out in Euler variables using the MMALE (Multi-material arbitrary Lagrange-Euler) setting. The interaction of the Lagrangian and Euler parts was carried out using a special contact CONSTRAINED_LAGRANGE_IN_SOLID. As in the experiments, the measuring bar had a zero initial speed, and the parts of the model representing the sample and the container were given initial speeds equal to the throwing speed in the real test. The Euler grid had the ability to move in space in the direction of the bar axis behind the center of mass of the sample material (control chart ALE_REFERENCE_SYSTEM_GROUP). This technique makes it possible to significantly save on computational resources (there is no need to cover a large area of space with an Eulerian grid, it is possible to cover only the area in the immediate vicinity of the sample) and improve the accuracy of calculations, since there are fewer calculation errors that occur when integrating the mass conservation equation when material flows from cell to cell.

Figure 2.29 shows the configuration of the computational domain at different times in the computational experiment.

It is obvious that the force of resistance to the penetration of the head into the clay depends on the coefficient of friction. In addition, as shown earlier, the values of the yield strength of the material at zero confining pressure have a certain spread. Since the value of the friction coefficient for dynamic contact is not exactly known, calculations were carried out with different values of the friction coefficient ($\alpha = 0, 0.25, 0.5, 0.75, \text{ and } 1$). To assess the influence of the initial clay yield stress on the simulation result, this value also varied from 15 to 25 MPa in the calculations. Comparison of the time dependences of the resistance forces obtained in a real experiment (black line) and computational experiments (colored lines, taking into account the spread of values of the uniaxial tensile strength) is shown in Fig. 2.30. The red lines show the dependences of the resistance forces obtained at a yield strength of 15 MPa, green—at a value of 25 MPa.

Numerical simulation showed that an increase in the friction coefficient above 0.5 does not change the calculation of the penetration resistance force versus time. At a friction coefficient close to 0.5, the values of the penetration resistance forces measured in the experiment and those obtained in the computational experiment

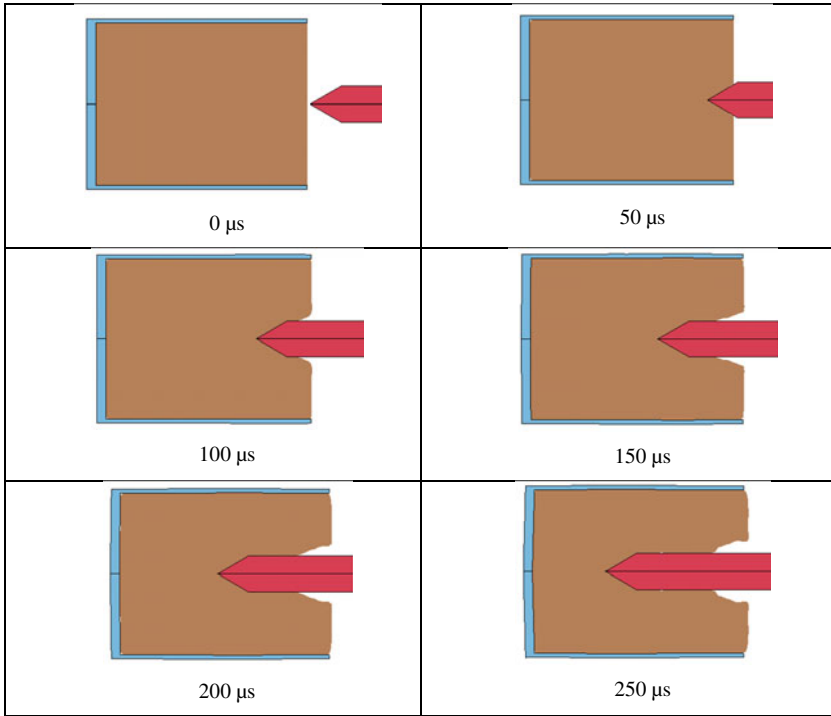


Fig. 2.29 The process of penetration of the bar with conical head into clay

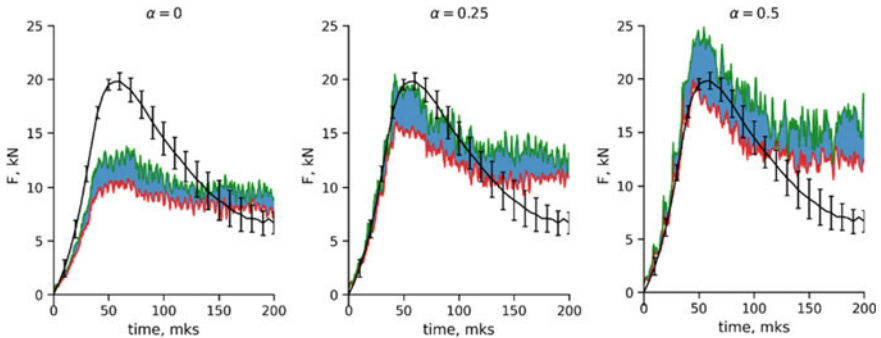


Fig. 2.30 Calculation results for different friction coefficients (0, 0.25, 0.5)

turned out to be quite close: the loading sections, the maximum values of the force, and the unloading sections up to a time of about 100 μs practically coincide, taking into account the scatter of the characteristics of the material and experimental data. It should be noted that the model used does not allow taking into account the effect of strain rate on clay characteristics. Therefore, in the calculations, a certain average

value was taken into account for the entire region of the material. In reality, different zones of the sample are deformed at different rates, and the maximum rate of deformation takes place in the zone of contact between the measuring bar and the sample. For more realistic modeling, it is necessary to use a model that takes into account the effect of the strain rate on the properties of the material, as well as experimentally determine the rate dependence of the strength of the material under uniaxial compression in a wider range of strain rates.

2.6 Conclusion

Using various versions of the Kolsky method, a study was made of the dynamic deformation of dry clay soil. Based on the results of this study, the parameters of the S.S. Grigoryan's model were determined. To verify this model, reversed ballistic experiments were carried out on the impact interaction of a dry clay barrier with a conical head at an impact velocity of ~ 200 m/s. Numerical calculations were carried out using the LS-Dyna. Comparison of the results of numerical and model experiments has shown that they are quite close within $100 \mu\text{s}$ from the onset of impact when the Coulomb friction coefficient of 0.5 is chosen in the calculations. Further, the results of numerical calculations lie above the results of inverted experiments. In our opinion, this phenomenon can be explained by the dependence of the initial clay strength on the strain rate. The initial compressive strength of clay at strain rates less than 1000 s^{-1} can be significantly less than 20 MPa, which will lead to a decrease in the resistance force with a decrease in the penetration velocity and, accordingly, the strain rate of the soil. In addition, it is possible that the coefficient of dry friction is not constant, and also depends on the penetration velocity. Based on the foregoing, it can be concluded that Grigoryan's model of the soil medium with experimentally determined parameters adequately describes the initial stage of the impact interaction of the conical head with the dry clay barrier. To refine the model, it is necessary to conduct additional studies of the effect of strain rate on the initial compressive strength and take this dependence into account in the model of the soil medium.

Acknowledgements This work was supported by the Russian Science Foundation (grant no. 22-19-00138).

References

- Arlery M, Gardou M, Fleureau JM, Mariotti C (2010) Dynamic behaviour of dry and watersaturated sand under planar shock conditions. *Int J Imp Eng* 37:1–10. <https://doi.org/10.1016/j.ijimpeng.2009.07.009>
- Balandin VV, Balandin VIVI, Bragov AM, Kotov VL (2016) Experimental study of the dynamics of penetration of a solid body into a soil medium. *Tech Phys* 61(6):860–868
- Balandin VV, Balandin VIVI, Bragov AM (2020) Experimental study of the processes of penetration of axisymmetric bodies into soft soil media. *Nizhny Novgorod*, p. 163. ISBN 978–5–600–02899–9 (in Rus)
- Bazhenov VG, Balandin VV, Grigoryan SS, Kotov VL (2014) Analiz modeley rascheta dvizheniya tel vrashcheniya minimalnogo soprotivleniya v gruntovykh sredakh [Analysis of models for calculating the motion of solids of revolution of minimum resistance in soil media], *Prikladnaya Matematika i Mekhanika [J. Appl. Math. Mech.]*, 78:98–115 (In Russian)
- Bivin YK, Viktorov VV, Stepanov LP (1978) Study of body motion in a clay environment. *Izv Akad Nauk SSSR Mekh Tverd Tela* 2:159–165. [Mech. Solids (Engl. Transl.)]
- Bivin YK, Viktorov VV, Kovalenko BY (1980) Determination of dynamic characteristics of soils by the penetration method. *Mech Solids*, 15(3):105–110
- Bivin YK, Kolesnikov VA, Flitman LM (1982) Determining mechanical properties of a medium by the dynamic penetration method. *Izv Akad Nauk SSSR Mekh Tverd Tela* (5):182–185 (1982) [Mech. Solids (Engl. Transl.)]
- Bragov AM, Grushevskii GM (1993) Influence of the moisture content and granulometric composition on the shock compressibility of sand. *Tech Phys Lett* 19:385–386
- Bragov AM, Grushevsky GM, Lomunov AK (1996a) Use of the kolsky method for confined tests of soft soils. *Exp Mech* 36:237–242
- Bragov AM, Kotov VL, Lomunov AK, Sergeichev IV (2004) Measurement of the dynamic characteristics of soft soils using the Kolsky method. *J Appl Mech Tech Phys* 45(4):580–585. <https://doi.org/10.1023/B:JAMT.0000030338.66701.e9>
- Bragov AM, Balandin VV, Lomunov AK, Filippov AR (2006) Determining the impact compressibility of soft soils from reversed test results. *Tech Phys Lett* 32(6):487–488. <https://doi.org/10.1134/S1063785006060101>
- Bragov AM, Grushevsky GM, Lomunov AK (1994) Use of the Kolsky method for studying shear resistance of soils. *DYMAT J* 1(3): 253–259
- Bragov AM, Gandurin VP, Grushevskii GM, Lomunov AK (1996b) New potentials of kolskii's method for studying the dynamic properties of soft soils. *J Appl Mech Tech Phys*, 36(3): 476–481. <https://link.springer.com/article/10.1007/BF02369791>
- Bragov AM, Demenko PV, Kruszka L, Lomunov AK, Sergeichev IV (2002) Évaluation de la compressibilité dynamique et de la résistance au cisaillement pour une large gamme de pressions et de vitesses de déformation Investigation of dynamic compressibility and shear resistance of soft soils in a wide range of strain rate and pressure. In: Fifth European conference “Numerical methods in geotechnical engineering NUMGE, Mestat (ed.) 2002, Presses de l'ENPC/LCPC, Paris, pp 909–917
- Bragov AM, Lomunov AK, Sergeichev IV, Tsembelis K, Proud WG (2008) Determination of physicomechanical properties of soft soils from medium to high strain rates. *Int J Impact Eng* 35(9):967–76. <https://doi.org/10.1016/j.ijimpeng.2007.07.004>
- Bragov AM, Balandin VV, Igumnov LA, Kotov VL, Kruszka L, Lomunov AK (2018) Impact and penetration of cylindrical bodies into dry and water-saturated sand. *Int J Imp Eng* 122:197–208 (2018)
- Buharev YN, Gandurin VP (1995) Forces acting on a sharp cone in the non-stationary stage of penetration into water and soil (in Rus.). *Appl Probl Strength Plast.* (53): 46–55
- Buharev YN, Gandurin VP, Korablev AE, Morozov VA, Himovich MI (1991) An experimental study of the penetration of an undeformable striker into clay and snow (in Rus.). *Appl Probl Strength Plast:* 99–106

- Buharev YN, Korablev AE, Himovich MI (1995) Experimental determination of shear stresses on the surface of the impactor during dynamic penetration into the soil (In Rus). *Mech Solids* (2), C:186–188
- Chapman DJ, Tsembelis K, Proud WG (2006) The behavior of water saturated sand under shock-loading. In: *Proceedings of the 2006 SEM annual conference and exposition on experimental and applied mechanics.*, vol 2. pp 834–840
- Dayal U, Allen JH, Reddy DV (1980) Low velocity projectile penetration of clay. *J Geotherm Eng Div N* 8:919–937
- Dianov MD, Zlatin NA, Mochalov SM et al. (1977) Shock compressibility of dry and water saturated sand. *Appl Phys Lett* 2, 207–208
- Dyanov DY, Kotov VL (2020) Determination of nonlinear strength characteristics of sandy soil based on the grigoryan soil model. *Probl Strength Plast* 82:471–482 (2020). <https://doi.org/10.32326/1814-9146-2020-82-4-471-482>. (In Russian)
- Gang Z, Yunliang L, Jin L, Zutang W, Ke W, Jiyong J, Shunshun T, Bingwen Q, Yurong Z, Xiangrong Z (2019) Dynamic behavior of clay with different water content under planar shock conditions. *Int. J Imp Eng* 129: 57–65. ISSN 0734–743X. <https://doi.org/10.1016/j.ijimpeng.2019.03.001>
- Grigoryan SS (1960) Ob osnovnykh predstavleniyakh dinamiki gruntov [Basic concepts of soil dynamics]. *Prikladnaya Matematika i Mekhanika [J. Appl. Math. Mech.]*, 24(6):1057–1072 (In Russian)
- He Y-X, Luan G-B, Zhu Z-W (2010) Dynamic constitutive modeling of partially saturated clay under impact loading. *Int J Nonlinear Sci & Numer Simul*, 11:195–199. <https://doi.org/10.1515/IJNS.2010.11.S1.195>
- Kolsky H (1949) An investigation of the mechanical properties of materials at very high rates of loading. *Proc Phys Soc Lond B* 62:676–700
- Lagunov VA, Stepanov VA (1963) Measurements of the dynamic compressibility of sand under high pressures. *Zh Prikl Mekh Tekhn Fiz (J Appl Mech Tech Phys)* 1:88–96. (Engl. Transl.)
- Li Y, Zhu Y, Zhang X, Li J, Wu K, Jing J, Tan S, Zhou G (2018) Dynamic behavior of remolded loess under planar shock conditions. *Int J Impact Eng* 111:236–243. ISSN 0734–743X, <https://doi.org/10.1016/j.ijimpeng.2017.09.016>.
- LS-DYNA Keyword User's Manual, vol II, Material models, LS-DYNA R11 10/12/18 (r:10572). Livermore Software Technology Corporation (LSTC, pp 178–182)
- Luo H, Cooper WL, Lu H (2014) Effects of particle size and moisture on the compressive behavior of dense Eglin sand under confinement at high strain rates. *Int J Imp Eng* 65:40–55. <https://doi.org/10.1016/j.ijimpeng.2013.11.001>
- Martin BE, Chen W, Song B, Akers SA (2009) Moisture effects on the high strain-rate behavior of sand. *Mech Mater* 41:786–798. <https://doi.org/10.1016/j.mechmat.2009.01.014>
- Martin BE, Kabir ME, Chen W (2013) Undrained high-pressure and high strain-rate response of dry sand under triaxial loading. *Int J Imp Eng* 54:51–63. <https://doi.org/10.1016/j.ijimpeng.2012.10.008>
- Omidvar M, Iskander M, Bless S (2014) Response of granular media to rapid penetration. *Int J Imp Eng* 66:60–82
- Omidvar M, Iskander M, Bless S (2012) Stress-strain behavior of sand at high strain rates. *Int J Imp Eng.*, 49:192–213. ISSN 0734–743X. <https://doi.org/10.1016/j.ijimpeng.2012.03.004>
- Song B, Chen W, Luk V (2009) Impact compressive response of dry sand. *Mech Mater* 41:777–785. <https://doi.org/10.1016/j.mechmat.2009.01.003>
- Veldanov VA, Markov VA, Pusev VI, Ruchko AM, Sotskii MY, Fedorov SV (2011) Computation of non-deformable striker penetration into low strength obstacles using piezoelectric accelerometry data. *Tech Phys* 56(7):992–1002. <https://doi.org/10.1134/S1063784211070231>
- Yang R, Chen J, Yang L, Fang S, Liu J (2017) An experimental study of high strain-rate properties of clay under high consolidation stress. *Soil Dyn Earth Eng* 92:46–51. <https://doi.org/10.1016/j.soildyn.2016.09.036>

Zel'Dovich YB, Raizer YP (2002) Physics of shock waves and high-temperature hydrodynamic phenomena. Dover Publications; Annotated edition. ISBN-10 0486420027, ISBN-13 978-0486420028, p 944

Chapter 3

Models of Defectness Medium for Bodies with Adhesion-Active Defective Surface



P. A. Belov and S. A. Lurie

Abstract The most general model of a coupled gradient and defective medium with an adhesively active surface with gradient and defective properties (damage surface) is formulated. The kinematic state in the volume of the body is determined by a coupled system of 12 partial differential equations with respect to three components of the displacement vector and 9 components of the incompatible free distortion tensor. The presented model includes, as special cases, the classical elasticity, Tupin's gradient models, the model of media with fields of Mindlin's defects, and its known special cases. The formulated continuum model of an adhesively active surface is the basis for elaboration of the various adhesive interaction models on the surface of a medium. In particular, the Murdoch–Gurtin model follows from the general model for a defect-free non-gradient surface, and the Steigman–Ogden model is realized for a defect-free gradient surface. It is shown that the proposed theory can be used to model the mechanical properties of graphene and graphene-like 2D structures.

Keywords Gradient models · Defect fields · Mindlin's model · Coupled gradient-defectness models · Damaged surfaces · Generalized adhesion model

3.1 Introduction

Development of modern models of the adhesive properties of solid deformable bodies was probably initially justified by the need to adequately predict the effective properties of inhomogeneous structures with a high density of phase boundaries and composite materials with small-sized micro- and nano-inclusions (Duan et al. 2005, 2008; Altenbach et al. 2011; Wang et al. 2011; Huang and Wang 2013; Eremeyev 2016; Gurtin and Murdoch 1978). Further, the continuum models of adhesion

P. A. Belov · S. A. Lurie (✉)
Institute of Applied Mechanics RAS, Moscow, Russia
e-mail: salurie@mail.ru

P. A. Belov
e-mail: belovpa@yandex.ru

© The Author(s), under exclusive license to Springer Nature Switzerland AG 2023
H. Altenbach and V. Eremeyev (eds.), *Advances in Linear and Nonlinear Continuum and Structural Mechanics*, Advanced Structured Materials 198,
https://doi.org/10.1007/978-3-031-43210-1_3

and interfaces and some of their applications are discussed to develop body surface models that expand the understanding of the features of superficial interactions in solid mechanics, which go beyond the well-known simplest models of surface interactions in liquids, determined by surface tension (Murdoch 2005; Belov and Lurie 2007; Altenbach et al. 2010; Altenbach and Morozov 2013; Lurie et al. 2020; Mindlin 1965), etc. Initially, adhesion continuum theories were developed in the framework of the classical theory of elasticity (Gurtin and Murdoch 1975a, b; Steigmann and Ogden 1997, 1999; Belov and Lurie 2007; Altenbach et al. 2010; Altenbach and Morozov 2013). So, for example, in the works (Belov and Lurie 2007; Lurie et al. 2020), a generalization of adhesion Murdoch–Gurtin model was suggested. However, in fact, at the same time, models of surface interactions were developed within the framework of generalized models of elasticity. Here, it is necessary to note the early work Mindlin (1965). Somewhat later, the works Yerofeyev and Sheshenina (2005), Lurie et al. (2010), Lurie and Belov (2014), Lurie et al. (2016) appeared in which models of adhesive interactions were developed for gradient theories of elasticity. It can be explained by the fact that the elastic moduli of surface interactions take into account scale effects and are of the order of length, while gradient models include a small-scale parameter of the order of the square of length. Therefore, taking into account the adhesive interfacial interactions for modeling of the effective properties of materials with a micro-nanostructure is quite logical. Moreover, from a mathematical point of view, models of surface interactions of the Gurtin–Murdoch type in gradient elasticity lead to correct boundary value problems, in contrast to classical elasticity. Despite the fact that models of media with fields of defects have received significant development, there are actually no models related to the study of the surface properties of such media. Obviously, there are interesting results of studies of media and its surfaces with defects such as dislocations, disclinations, etc., leading to discontinuity, which is given in Zubov (1997, 2011), Karyakin and Zubov (2011). At the same time, it is recognized that the existence and interaction of individual defects can be replaced by a field representation. The implementation of such an approach, even within the framework of linear models, makes it possible to develop the mechanics of media with fields of defects as a natural generalization of the classical mechanics of deformable media—continuum nanomechanics. However, defects generally occur not only inside the body but also on its surface. The formation of a surface with a given defectiveness is theoretically possible with the involvement of various technologies for the physical and chemical processing of the original surface. From a mathematical point of view, individual surface properties are determined by various adhesive interactions on the surface (Belov and Lurie 2009, 2014). In contrast to the gradient properties inside the body, where non-classical modules differ from the classical ones by the square of the length, adhesive modules differ by the linear dimension of the length and higher (Lurie et al. 2016). As a result, the adhesion interaction models may be more important for description of the effective properties of heterogeneous materials than gradient models with multiscale effects. In addition, we must take into account that adhesive properties are determined not by isotropic property tensors, but by transversally isotropic ones. In this paper, the most general

model of a gradient and defect medium bounded by an adhesively active surface with gradient and defect properties is formulated.

3.2 Kinematic Models of Defectness Bodies with Active Adhesion Surface

The general kinematic theory of defective media is presented in Belov and Lurie (2009). Let us give the definitions of the main parameters which defined the kinematic models. The displacement vector R_i and the incompatible distortion tensor D_{ij}^2 are taken as independent kinematic variables inside the body. By definition, inconsistent distortions cannot be represented as a gradient of some vector, in particular, a displacement vector. Along with independent kinematic variables, the kinematic model contains dependent kinematic variables D_{ij}^1 which are connected with displacement field:

$$D_{ij}^1 = R_{i,j}. \quad (3.1)$$

In addition, we define curvatures of two types. The first-type curvature D_{ijk}^1 is defined as the gradient of the constrained distortion. The gradient of the free (incompatible) distortion, let's call the second-type curvature D_{ijk}^2

$$D_{ijk}^1 = D_{ij,k}^1 = R_{i,jk}, \quad (3.2)$$

$$D_{ijk}^2 = D_{ij,k}^2 \quad (3.3)$$

Thus, the kinematic model contains the following kinematic variables: displacement vector R_i ; tensors of the second rank which are distortions of two types, D_{ij}^1 and D_{ij}^2 ; the tensors of the third rank which are defined as the distortion gradients of two types, $D_{ij,k}^1$ and $D_{ij,k}^2$. Incompatible distortion and curvature of the second type, D_{ij}^2 and D_{ijk}^2 , are characteristics of the imperfection-defectiveness of the medium.

We assume that the considered kinematic variables R_i , D_{ij}^a , D_{ijk}^a , and $a = 1, 2$ are defined as the kinematic model not only in body but also are kinematic variables of two types on the surface of the body. Thus, the introduced variables, R_i , D_{ij}^a , D_{ijk}^a , and $a = 1, 2$ are defined as not only in the volume but also on the surface. Variables D_{ij}^2 , D_{ijk}^2 on the surface are the tensor functions of two surface coordinates. In particular, if the body surface has only "flat" defects, then the defect field on the surface is determined by kinematic variables of the form $D_{ij}^2 = D_{pq}^2 \delta_{ip}^* \delta_{jq}^*$, $D_{ijk}^2 = D_{pqr}^2 \delta_{ip}^* \delta_{jq}^* \delta_{kr}^*$, where $\delta_{ij}^* = \delta_{ij} - n_i n_j$ and $\delta_{ij}^* n_j = 0$. Nevertheless, defectiveness (D_{ij}^2 , D_{ijk}^2) can occur not only in the volume of the body but also on its surface.

3.3 Force Model

The force model for any considered kinematic model is uniquely determined based on the principle of possible displacements. For the kinematic model (3.1)–(3.3), we have

$$\delta A - \int_V (\sigma_{ij}^a \delta D_{ij}^a + \sigma_{ijk}^a \delta D_{ij,k}^a) dV - \int_F (a_{ij}^a \delta D_{ij}^a + a_{ijk}^a \delta D_{ij,k}^a) dF = 0, \quad (3.4)$$

where $A = \int_V (P_i^V R_i + M_{ij}^V D_{ij}^2) dV + \int_F (P_i^F R_i + M_{ij}^F D_{ij}^2) dF$ is the work of the external forces P_i^V , P_i^F and of the moments M_{ij}^V , M_{ij}^F on independent kinematic variables.

Note that, since the physical meaning of the force factors M_{ij}^V , M_{ij}^F is difficult to substantiate, we will further assume that $M_{ij}^V = M_{ij}^F = 0$.

We also omitted the expressions for external work on the surface of the body with terms containing normal derivatives of displacements, since it is difficult to give a physical meaning to the corresponding force factors. We consider only reversible processes, so the linear variational form (3.4) is integrable. As a result, the volume U^V and surface U^F densities of potential energy are determined. Sufficient conditions for the existence of these quantities are given by Green's formulas:

$$\sigma_{ij}^a = \frac{\partial U^V}{\partial D_{ij}^a}, \quad a = 1, 2 \quad (3.5)$$

$$\sigma_{ijk}^a = \frac{\partial U^V}{\partial D_{ij,k}^a}, \quad a = 1, 2. \quad (3.6)$$

Two types of stresses σ_{ij}^a and couple stresses σ_{ijk}^a (see (3.5), (3.6)) determine the force model of the process of deformation of an elastic body containing a defective field.

The potential energy density of the surface U^F determines the adhesion properties of the body. The generalized Green's formulas formulated for the surface F of the body are sufficient conditions for the existence of the surface potential energy density:

$$a_{ij}^a = \frac{\partial U^F}{\partial D_{ij}^a}, \quad a_{ijk}^a = \frac{\partial U^F}{\partial D_{ij,k}^a}, \quad a = 1, 2. \quad (3.7)$$

The adhesive properties of the surface of elastic bodies are characterized by surface stresses and surface double stresses of two types a_{ij}^a and a_{ijk}^a , $a = 1, 2$ (3.7).

The index equal to 1 in the kinematic and force factors determines the deformed defectless state, while the kinematic variables and the corresponding force factors with an index equal to 2 characterize the imperfection of the considered medium and its surface.

3.4 Physical Model

We introduce the following generalized physically linear isotropic model through the definition of potential energy densities in the volume “ V ”, on the surface “ F ” and on the edges “ S ” and angular points “ p ” of the surface:

$$\begin{aligned}
 L = & A - \frac{1}{2} \int_V [C_{ijmn}^{pq} D_{ij}^p D_{mn}^q + C_{ijkmln}^{pq} D_{ijk}^p D_{mnl}^q] dV - \\
 & - \frac{1}{2} \int_F [A_{ijmn}^{pq} D_{ij}^p D_{mn}^q + 2A_{ijmnl}^{pq} D_{ij}^p D_{mnl}^q + A_{ijkmln}^{pq} D_{ijk}^p D_{mnl}^q] dF - \\
 & - \sum_S \oint U^S ds + \sum_P U^P, \tag{3.8}
 \end{aligned}$$

where C_{ijmn}^{pq} , C_{ijkmln}^{pq} are the tensors of generalized elastic moduli of the body and A_{ijmn}^{pq} , A_{ijmnl}^{pq} , A_{ijkmln}^{pq} are the tensors elastic surface moduli which are defined the adhesion properties of the surface.

The proposed version of the generalized model, in contrast to Mindlin’s and Tupin’s models, is both a gradient model ($D_{ij,k}^1$) and, at the same time, a model of media with defect fields (D_{ij}^2 , $D_{ij,k}^2$) in which it is allowed to take into account the connection of deformation fields with defect fields in the volume and on the surface. The potential energy densities are the quadratic forms of their arguments, taking into account the corresponding anisotropy: $U^V = U^V(D_{ij}^p, D_{ijn}^p)$, $U^F = U^F(D_{ij}^p, D_{ijq}^p \delta_{qk}^*)$, $U^S = U^S(D_{ij}^p, D_{ijn}^p s_n)$, $U^P = U^P(D_{ij}^p)$, δ_{ij} is the Kronecker delta, $\delta_{ij}^* = (\delta_{ij} - n_i n_j)$ is the “flat” Kronecker delta, defined on a smooth surface of the body, n_i and s_i are consequently the vector normal to the surface and the vector tangent to the edge (co-normal) of the surface.

Note that in what follows we will assume that the surface is smooth, i.e., neglect the potential energies of edges and corner points. Let’s write Hook’s equations for stresses and double stresses in the body. Using (3.5)–(3.7), we find

$$\sigma_{ij}^p = C_{ijmn}^{pq} D_{mn}^q, \quad \sigma_{ijk}^p = C_{ijkmln}^{pq} D_{mnl}^q. \tag{3.9}$$

The Green equations (3.5)–(3.7) and equation for the potential energy (3.8) lead to the following definition of the adhesion stresses and adhesion double stresses consequently:

$$a_{ij}^p = A_{ijmn}^{pq} D_{mn}^q + A_{ijmnl}^{pq} D_{mnl}^q, \quad a_{mnl}^p = A_{ijmnl}^{pq} D_{ij}^q + A_{ijkmln}^{pq} D_{ijk}^q. \tag{3.10}$$

Generalized constitutive relations (3.9), (3.10) for force factors performing possible work on kinematic variables characterizing the deformation fields D_{mn}^1 , D_{mnl}^1 and defect fields D_{mn}^2 , D_{mnl}^2 , respectively, can be written in more detailed form:

$$\begin{cases} \sigma_{ij}^1 = C_{ijmn}^{11} D_{mn}^1 + C_{ijmn}^{12} D_{mn}^2, & \sigma_{ijk}^1 = C_{ijkmnl}^{11} D_{mnl}^1 + C_{ijkmnl}^{12} D_{mnl}^2, \\ \sigma_{ij}^2 = C_{ijmn}^{21} D_{mn}^1 + C_{ijmn}^{22} D_{mn}^2, & \sigma_{ijk}^2 = C_{ijkmnl}^{21} D_{mnl}^1 + C_{ijkmnl}^{22} D_{mnl}^2, \end{cases} \quad (3.11)$$

and

$$\begin{aligned} a_{ij}^a &= A_{ijmn}^{a1} D_{mn}^1 + A_{ijmn}^{a2} D_{mn}^2 + A_{ijmnl}^{a1} D_{mnl}^1 + A_{ijmnl}^{a2} D_{mnl}^2, & a &= 1, 2, \\ a_{ijk}^a &= A_{mnik}^{a1} D_{mn}^1 + A_{mnik}^{a2} D_{mn}^2 + A_{mnljk}^{a1} D_{mnl}^1 + A_{mnljk}^{a2} D_{mnl}^2, & a &= 1, 2. \end{aligned} \quad (3.12)$$

3.5 Euler Equilibrium Equations and Spectrum of Boundary Value Problems

Taking into account the equations of the generalized Hooke's law (3.9)–(3.12), the variational equation of the principle of possible displacements takes the form:

$$\delta L = \delta A - \int_V (\sigma_{ij}^p \delta D_{ij}^p + \sigma_{ijk}^p \delta D_{ijk}^p) dV - \int_F (a_{ij}^p \delta D_{ij}^p + a_{ijk}^p \delta D_{ijk}^p) dF = 0 \quad (3.13)$$

We use integration by parts and in terms containing distortion gradients in the (3.13), and take into account that distortion variations of the second type are independent kinematic variables, and distortion variations of the first type can be integrated by parts again. In the result, we can find the following variational equation:

$$\begin{aligned} \delta L &= \int_V [(\sigma_{ij}^1 - \sigma_{ijk,k}^1)_{,j} + P_i^V] \delta R_i dV + \\ &+ \int_F \{P_i^F - (\sigma_{ij}^1 - \sigma_{ijk,k}^1) n_j + [\sigma_{ijk}^1 n_k + (a_{ij}^1 - a_{ijk,r}^1 \delta_{rk}^*)]_{,a} \delta_{aj}^* \} \delta R_i dF - \\ &- \int_F [\sigma_{ijk}^1 n_j n_k + (a_{ij}^1 - a_{ijk,r}^1 \delta_{rk}^*) n_j + (a_{ijk}^1 n_k)_{,b} \delta_{bj}^*] \delta (R_{i,a} n_a) dF - \\ &- \int_F a_{ijk}^1 n_j n_k \delta (R_{i,ab} n_a n_b) dF - \int_V (\sigma_{ij}^2 - \sigma_{ijk,k}^2) \delta D_{ij}^2 dV - \\ &- \int_F \{[\sigma_{ijk}^2 n_k + (a_{ij}^2 - a_{ijk,r}^2 \delta_{rk}^*)] \delta D_{ij}^2 + a_{ijk}^2 n_k \delta (D_{ij,a}^2 n_a)\} dF = 0. \end{aligned} \quad (3.14)$$

Variational equation (3.14) allows to write formally equilibrium equations (Euler equations) of a defective gradient medium:

$$\begin{cases} \sigma_{ij,j}^1 - \sigma_{ijk,jk}^1 + P_i^V = 0, \\ \sigma_{ij}^2 - \sigma_{ijk,k}^2 = 0 \end{cases} \quad (3.15)$$

and, accordingly, the spectrum of boundary value problems, which is determined the pairs of alternative boundary conditions:

$$\int_F \{P_i^F - (\sigma_{ij}^1 - \sigma_{ijk,k}^1)n_j + [\sigma_{ijk}^1 n_k + (a_{ij}^1 - a_{ijk,r}^1 \delta_{rk}^*)]_a \delta_{aj}^*\} \delta R_i \, dF = 0, \quad (3.16)$$

$$\int_F [\sigma_{ijk}^1 n_j n_k + (a_{ij}^1 - a_{ijk,r}^1 \delta_{rk}^*)n_j + (a_{ijk}^1 n_k)_{,b} \delta_{bj}^*] \delta (R_i, a n_a) \, dF = 0, \quad (3.17)$$

$$\int_F a_{ijk}^1 n_j n_k \delta (R_i, ab n_a n_b) \, dF = 0, \quad (3.18)$$

$$\int_F [\sigma_{ijk}^2 n_k + (a_{ij}^2 - a_{ijk,r}^2 \delta_{rk}^*)] \delta D_{ij}^2 \, dF = 0, \quad (3.19)$$

$$\int_F a_{ijk}^2 n_k \delta (D_{ij,a}^2 n_a) \, dF = 0. \quad (3.20)$$

Note that the real list of formal arguments in variations equations (3.14) in specific problems can be smaller due to the fact that the kinematic variables in the body volume and on the surface have different properties and must be consistent. For example, in the case of a classical elastic body, only components of displacements from the general list of arguments on the surface are kinematic variables on the surface. Thus, the normal derivatives of the displacement vector components should be excluded. This is done by concretizing the tensor of the adhesive modules. In this case, the components of the displacement vector on the surface are functions of only the coordinates of the surface and do not depend on the normal coordinate.

Using the equations of Hooke's law (3.9) (or (3.11)), we can write the equilibrium equations (3.15) in terms of the main kinematic variables:

$$C_{ijmn}^{11} R_{m,nj} - C_{ijkml}^{11} R_{m,nlk} + C_{ijmn}^{12} D_{mn,j}^2 - C_{ijkml}^{12} D_{mn,ljk}^2 + P_i^V = 0, \quad (3.21)$$

$$C_{ijmn}^{21} R_{m,n} - C_{ijkml}^{21} R_{m,nlk} + C_{ijmn}^{22} D_{mn}^2 - C_{ijkml}^{22} D_{mn,lk}^2 = 0. \quad (3.22)$$

Similarly, the boundary conditions (3.16)–(3.20) can also be rewritten in terms of generalized variables using the constitutive relations (3.9), (3.10), (or (3.11) (3.12)). Particular cases of equilibrium equations and boundary conditions can be obtained from the general statement (3.14), (3.15) and (3.16)–(3.20) by removing the corresponding tensors of the elastic moduli from the general list of physical constants in the constitutive equations (3.9), (3.10). So, for example, equilibrium equations of Tupin's gradient elasticity can be obtained from (3.21), (3.22), if we accept $C_{ijmn}^{12} = 0$, $C_{ijkml}^{12} = 0$ and $C_{ijmn}^{2q} = C_{ijkml}^{2q} = 0$, $q = 1, 2$. The equilibrium equations of Mindlin's theory of defective media can be obtained from the equilibrium equations of the generalized model (3.21), (3.22) if we take $C_{ijkml}^{11} = C_{ijkml}^{12} = C_{ijkml}^{21} = 0$.

3.6 On Structure of Tensors of Adhesion Elastic Moduli

The analysis of potential energy densities (3.7) allows us to formulate the properties of bulk modulus tensors and the properties of adhesion modulus tensors. The most important are the properties that follow from the generalized Green's formulas. Indeed, from (3.5), (3.6) follows the symmetry of the tensors of modules of the fourth and sixth ranks when the upper indices are interchanged, as well as pairs and triples of indices, respectively:

$$C_{ijmn}^{pq} = C_{mnij}^{qp}, \quad C_{ijkmnl}^{pq} = C_{mnljik}^{qp}. \quad (3.23)$$

Relations (3.23) are necessary conditions for the reversibility of deformation processes inside the body for the proposed general model.

Similar symmetry properties are required to ensure potentiality conditions for adhesive modules as well. The properties of tensors of adhesive modules of the fourth and sixth ranks are determined from (3.7) as

$$A_{ijmn}^{pq} = A_{mnij}^{qp}, \quad A_{ijkmnl}^{pq} = A_{mnljik}^{qp}. \quad (3.24)$$

Note that the properties of potentiality do not require additional symmetry properties from tensors of the fifth rank. They have the same set of amplitude coefficients (modules) but with different basis tensors.

Conditions (3.23) and (3.24) are not exhaustive for the adhesive moduli of elasticity. They must satisfy additional symmetry properties that ensure the consistency of boundary value problems. As an example, let us study the structure of tensors of adhesive elastic properties that determine the possible adhesive properties of an elastic body that obeys the hypotheses of the classical theory of elasticity.

There is a theorem.

The tensors of adhesive properties that determine the properties of the surface of a classical elastic body must satisfy the following additional conditions:

1. Adhesive modules must ensure the independence of the components of the kinematic factors from the normal coordinate. These conditions in the sentence that the symmetry conditions in terms of potentiality are satisfied are written as

$$A_{ijmn}^{1q} n_j = A_{ijmn}^{1q} n_n = 0, \quad (3.25)$$

$$A_{ijkmnl}^{1q} n_j = A_{ijkmnl}^{1q} n_k = A_{ijmnl}^{1q} n_j = A_{ijmnl}^{11} n_n = A_{ijmnl}^{1q} n_l = 0.$$

2. The following symmetry conditions must be satisfied for the tensor of adhesion moduli:

$$A_{ijkm}^{11} e_{ijr} n_r = A_{ijmnl}^{11} e_{nlr} n_r = A_{ijmnl}^{11} e_{ijr} n_r. \quad (3.26)$$

3. The conditions of symmetry of the adhesive double stresses with respect to the last indices must be met

$$A_{ijk mnl}^{11} e_{nlr} n_r = A_{ijk mnl}^{21} e_{nlr} n_r = 0, \quad (3.27)$$

where e_{ijk} is the Levi-Civita tensor.

Proving. The first part of the theorem is almost obvious—for the classical elasticity the boundary kinematic conditions are set on the displacement vector. This also requires the fulfillment of the first part of the theorem.

The second part of the theorem follows from the fact that an elastic body with a symmetric stress tensor is considered. Then, in order to match the static conditions, the symmetry properties of the adhesive stress tensor must also be satisfied.

The validity of the third part of the theorem follows from the assumption that there is no field of defects at the boundary of the body. Hence, the generalized deformations must be continuous as a function of the surface coordinates. Therefore, the conditions of symmetry in the order of differentiation in the second derivatives of displacements on the surface must be satisfied as necessary conditions for the continuity of the strain tensor on the surface of the body. The theorem has been proven.

Potential energy densities in the volume and on the surface and the spectrum of boundary value problems following from the Lagrange principle allow us to formulate (3.23), (3.24), and a fairly wide range of consequences of type (3.25)–(3.27) that simplify the structure of adhesion modules.

The most important consequences are the following: for the classical model of elasticity on the surface of the medium, the density of adhesive interactions should not contain terms with the first and second normal derivatives of displacements, otherwise the classical boundary value problem (3.16) will be redefined by the boundary conditions (3.17) and (3.18) (see the theorem); similarly, for Tupin's gradient model of the medium, the potential energy density of adhesive interactions on the surface of the medium should not contain terms with second normal derivatives of displacements; otherwise, the corresponding boundary value problem (3.16), (3.17) will be redefined by the boundary conditions (3.18).

For a model of a defective medium, the density of adhesive interactions should not contain terms with normal derivatives of incompatible distortions, since the components of the incompatible distortion tensor must satisfy the homogeneous or inhomogeneous Helmholtz equation (second-order), which means that the boundary value problem (3.19) will be redefined by the boundary conditions (3.20). Thus, the chosen model of elastic properties inside the volume of the medium allows us to make a conclusion about the adhesive properties of the surface that bounds this body.

As an example, taking into account conditions (3.24)–(3.27), we give a complete list of conditions on the tensors of the elastic moduli (tensors of the fourth rank for non-gradient models and tensors of the fifth and sixth ranks for gradient models). These moduli are characterize adhesive interactions that can be implemented for a body considered in the framework of classical elasticity:

for “classical” adhesion:

$$A_{ijmn}^{pq} = A_{mni j}^{qp} \quad (p, q = 1, 2), \quad A_{ijmn}^{11} n_j = 0, \quad A_{ijmn}^{12} n_j = 0, \quad (3.28)$$

for “gradient” adhesion:

$$\begin{aligned}
 A_{ijmnl}^{11}n_j &= 0, & A_{ijmnl}^{11}n_n &= 0, & A_{ijmnl}^{11}n_l &= 0, & A_{ijmnl}^{11}e_{nlr}n_r &= 0, \\
 A_{ijmnl}^{12}n_j &= 0, & A_{ijmnl}^{12}n_l &= 0, & & & & \\
 A_{ijmnl}^{21}n_n &= 0, & A_{ijmnl}^{21}n_l &= 0, & A_{ijmnl}^{21}e_{nlr}n_r &= 0, & & \\
 A_{ijmnl}^{22}n_l &= 0 & & & & & &
 \end{aligned} \tag{3.29}$$

and

$$\begin{aligned}
 A_{ijkmnl}^{pq} &= A_{mnljik}^{qp} \quad (p, q = 1, 2), \\
 A_{ijkmnl}^{11}n_j &= 0, & A_{ijkmnl}^{11}n_k &= 0, & A_{ijkmnl}^{11}e_{jkr}n_r &= 0, \\
 A_{ijkmnl}^{12}n_j &= 0, & A_{ijkmnl}^{12}n_k &= 0, & A_{ijkmnl}^{12}e_{jkr}n_r &= 0, \\
 A_{ijkmnl}^{22}n_l &= 0 & & & &
 \end{aligned} \tag{3.30}$$

Similarly, additional conditions can be constructed for tensors that determine the possible adhesive properties of the surface of a body considered in the framework of Tupin’s gradient elasticity. It can be seen that these conditions for gradient elasticity with a generally asymmetric stress tensor are written as the following relations:

for “classical” adhesion part of the model:

$$\begin{aligned}
 A_{ijmn}^{pq} &= A_{mnij}^{qp} \\
 \left\{ \begin{array}{l} A_{ijmnl}^{11}n_l = 0, \\ A_{ijmnl}^{11}e_{nlr} = 0, \end{array} \right. & \left\{ \begin{array}{l} A_{ijmnl}^{12}n_l = 0, \\ A_{ijmnl}^{12}e_{nlr} = 0, \end{array} \right. & \left\{ \begin{array}{l} A_{ijmnl}^{21}n_l = 0, \\ A_{ijmnl}^{21}e_{nlr} = 0, \end{array} \right. & \left\{ \begin{array}{l} A_{ijmnl}^{22}n_l = 0 \end{array} \right.
 \end{aligned} \tag{3.31}$$

for “gradient” adhesion part of the model:

$$\left\{ \begin{array}{l} A_{ijkmnl}^{11}n_k = 0, \\ A_{ijkmnl}^{11}e_{jkr} = 0, \\ A_{ijkmnl}^{11}e_{nlr} = 0, \end{array} \right. \left\{ \begin{array}{l} A_{ijkmnl}^{12}n_k = 0, \\ A_{ijkmnl}^{12}e_{jkr} = 0, \end{array} \right. \left\{ \begin{array}{l} A_{ijkmnl}^{21}n_k = 0, \\ A_{ijkmnl}^{21}n_n = 0, \\ A_{ijkmnl}^{21}n_l = 0, \\ A_{ijkmnl}^{21}e_{nlr}n_r = 0, \end{array} \right. A_{ijkmnl}^{22}n_k = 0, \tag{3.32}$$

where e_{ijk} is the Levi-Civita tensor.

Note that, in contrast to the restrictions on the adhesion modulus tensor formulated for the classical elastic body (3.28)–(3.30), the restrictions formulated for the gradient model of the elastic body in the form of relations (3.31), (3.32) allow the presence of normal derivatives of the displacement vector. At the same time, restrictions remain that ensure the symmetry of the tensor of the adhesion moduli of elasticity defined on the surface of the body.

In conclusion, we note that the potential energy density of adhesion

$$\begin{aligned}
2U^F = & A_{ijmn}^{11} R_{i,j} R_{m,n} + 2A_{ijmnl}^{11} R_{i,j} R_{m,nl} + A_{ijkmnl}^{11} R_{i,jk} R_{m,nl} + \\
& + 2B_{ijmn}^{12} R_{i,j} D_{mn}^2 + 2B_{ijmnl}^{12} R_{i,j} D_{mn,l}^2 + 2B_{ijkmnl}^{12} R_{i,jk} D_{mnl}^2 + \\
& + A_{ijmn}^{22} D_{ij}^2 D_{mn}^2 + 2A_{ijmnl}^{22} D_{ij}^2 D_{mn,l}^2 + A_{ijkmnl}^{22} D_{ijk}^2 D_{mnl}^2
\end{aligned}$$

allows us to propose a physical interpretation for an arbitrary adhesively active surface as an insertion into each other of four different surfaces:

- defectless, non-gradient surface ($A_{ijmn}^{11} R_{i,j} R_{m,n}$);
- defectless, gradient surface ($A_{ijkmnl}^{11} R_{i,jk} R_{m,nl}$);
- defective, non-gradient surface ($A_{ijmn}^{22} D_{ij}^2 D_{mn}^2$);
- defective, gradient surface ($A_{ijkmnl}^{22} D_{ijk}^2 D_{mnl}^2$).

The introduced surfaces interact with each other through the corresponding bilinear terms, characterized by elastic moduli with different superscripts ($p \neq q$).

Below, as a specific example, we will consider a model of a classical elastic body with the most common admissible adhesively active defectless surface.

3.7 Classical Elastic Body with a Defectless Gradient Surface

We assume that the classical theory of elasticity is valid in the volume of the body, and the surface of the body is smooth and has no edges. The Lagrangian of such a model has the form:

$$\begin{aligned}
L = A - & \frac{1}{2} \int_V C_{ijmn}^{11} R_{i,j} R_{m,n} dV - \\
& - \frac{1}{2} \int_F [A_{ijmn}^{11} R_{i,j} R_{m,n} + 2A_{ijmnl}^{11} R_{i,j} R_{m,nl} + A_{ijkmnl}^{11} R_{i,jk} R_{m,nl}] dF, \quad (3.33)
\end{aligned}$$

where $C_{ijmn}^{11} = \lambda \delta_{ij} \delta_{mn} + \mu (\delta_{im} \delta_{jn} + \delta_{in} \delta_{jm})$.

The fourth-rank adhesion tensor of moduli for a defect-free gradient surface (see Appendix I) is a generalization of the Gurtin–Murdoch Model (see Gurtin and Murdoch 1975a, b, 1978; Murdoch 2005; Lurie et al. 2020):

$$A_{ijmn}^{11} = \lambda^F \delta_{ij}^* \delta_{mn}^* + \mu^F (\delta_{im}^* \delta_{jn}^* + \delta_{in}^* \delta_{jm}^*) + \delta^F \delta_{jn}^* n_i n_m, \quad (3.34)$$

here $\lambda^F = a_1^{11}$, $\mu^F = (a_2^{11} + a_3^{11})/2$, $\delta^F = a_8^{11}$.

Tensors of adhesion moduli of the fifth rank (Appendix II) and the sixth rank (Appendix III) for a defectless gradient surface are written taking into account the conditions (see Eqs. (3.30)–(3.32)) as

$$A_{ijmnl}^{11} = b_7^{11} \delta_{ij}^* \delta_{nl}^* n_m + b_8^{11} (\delta_{in}^* \delta_{jl}^* n_m + \delta_{il}^* \delta_{jn}^* n_m) + b_{13}^{11} \delta_{jm}^* \delta_{nl}^* n_i + b_{14}^{11} (\delta_{jn}^* \delta_{ml}^* n_i + \delta_{jl}^* \delta_{mn}^* n_i) \quad (3.35)$$

$$A_{ijkmln}^{11} = c_1 (\delta_{ij}^* \delta_{kn}^* \delta_{lm}^* + \delta_{ik}^* \delta_{jn}^* \delta_{lm}^* + \delta_{ij}^* \delta_{kl}^* \delta_{mn}^* + \delta_{ik}^* \delta_{jl}^* \delta_{mn}^*) + c_2 (\delta_{in}^* \delta_{km}^* \delta_{jl}^* + \delta_{in}^* \delta_{kl}^* \delta_{mj}^* + \delta_{il}^* \delta_{km}^* \delta_{nj}^* + \delta_{il}^* \delta_{kn}^* \delta_{jm}^*) + c_3 (\delta_{ij}^* \delta_{km}^* \delta_{nl}^* + \delta_{ik}^* \delta_{jm}^* \delta_{nl}^* + \delta_{in}^* \delta_{kj}^* \delta_{lm}^* + \delta_{il}^* \delta_{kj}^* \delta_{mn}^*) + c_4 (\delta_{im}^* \delta_{kn}^* \delta_{lj}^* + \delta_{im}^* \delta_{kl}^* \delta_{jn}^*) + c_5 \delta_{im}^* \delta_{kj}^* \delta_{nl}^* + c_6 n_i n_m \delta_{kj}^* \delta_{nl}^* + c_7 n_i n_m \delta_{kn}^* \delta_{lj}^* + c_8 n_i n_m \delta_{kl}^* \delta_{jn}^*. \quad (3.36)$$

Requirement of stationarity of Lagrangian (3.33) leads to the following variational equality:

$$\delta L = \int_M (C_{ijmn}^{11} R_{m,n} + P_i^V) \delta R_i dV + \int_F [P_i^F - C_{ijmn}^{11} n_j R_{m,n} + A_{ijmn}^{11} R_{m,nj} + (A_{ijmnl}^{11} - A_{mni jl}^{11}) R_{m,nlj} - A_{mnl ijk}^{11} R_{m,nlkj}] \delta R_i dF = 0. \quad (3.37)$$

The variational statement (3.37), (3.35) and (3.36) shows that the equilibrium equations coincide with the classical ones, however, the boundary value problem has changed. Under static boundary conditions, adhesion corrections appeared (with variations in the components of the displacement vector on the surface of the body). Let's study them one by one. We use the following decomposition of the displacement vector on the surface:

$$R_i = r_i + R n_i, \quad r_i = R_j \delta_{ji}^*, \quad R = R_j n_j \quad (r_i n_i = 0)$$

where r_i are components of displacement vector in the tangential directions to the surface, and R is the normal component of the displacement vector.

A non-gradient, correction to the boundary conditions is given by the model of "ideal" adhesion, Belov and Lurie (2007), Lurie et al. (2020):

$$A_{ijmn}^{11} R_{m,nj} = (a_2^{11} + a_3^{11}) \nabla^2 r_i / 2 + (a_1^{11} + a_2^{11} / 2 + a_3^{11} / 2) r_{m,mi} + a_8^{11} n_i \nabla^2 R \quad (3.38)$$

In the general case, there is a correction to the boundary conditions, which, following the above interpretation, is determined by the adhesion interaction between non-gradient and gradient surfaces:

$$(A_{ijmnl}^{11} - A_{mni jl}^{11}) R_{m,nlj} = (b_7^{11} + 2b_8^{11} - b_{13}^{11} + 2b_{14}^{11}) (\nabla^2 R_i - n_i \nabla^2 r_{j,j}). \quad (3.39)$$

Finally, the third adhesion correction in the boundary conditions is determined by the gradient defectless adhesion model:

$$A_{mnl ijk}^{11} R_{m,nlkj} = 4(c_1 + c_2 + c_3) \nabla^2 r_{m,mi} + (2c_4 + c_5) \nabla^2 \nabla^2 r_i + (c_6 + c_7 + c_8) n_i \nabla^2 \nabla^2 R. \quad (3.40)$$

Note that the corrections to the natural boundary conditions when varying the normal displacement component give only terms in (3.38)–(3.40) containing convolution with the normal. As a result, we obtain the following spectrum of boundary value problems:

$$\int_F [P_i^F - \mu(n_n r_{i,n} + R_{,i}) + 2\mu^F \nabla^2 r_i / 2 + (\lambda^F + \mu^F) r_{m,mi} + B \nabla^2 R_{,i} + C_1 \nabla^2 r_{m,mi} + C_2 \nabla^2 \nabla^2 r_i] \delta r_i dF = 0, \quad (3.41)$$

$$\int_F [P_i^F n_i - (\lambda R_{m,m} + 2\mu n_m n_n R_{m,n}) + \delta^F \nabla^2 R - B \nabla^2 r_{j,j} + C_3 \nabla^2 \nabla^2 R] \delta R dF = 0, \quad (3.42)$$

where $B = b_7^{11} + 2b_8^{11} - b_{13}^{11} + 2b_{14}^{11}$, $C_1 = -4(c_1 + c_2 + c_3)$, $C_2 = (2c_4 + c_5)$, $C_3 = (c_6 + c_7 + c_8)$.

In accordance with Eqs. (3.41) and (3.42), the adhesive properties of a defectless surface are determined by seven adhesive moduli. For a non-gradient surface ($b_i = c_i = 0$), the spectrum of boundary value problems is simplified and contains only three adhesive moduli:

$$\int_F [P_i^F - \mu(n_n r_{i,n} + R_{,i}) + \mu^F \nabla^2 r_i + (\lambda^F + \mu^F) r_{m,mi}] \delta r_i dF = 0, \quad (3.43)$$

$$\int_F [P_i^F n_i - (\lambda^F R_{m,m} + 2\mu^F n_m n_n R_{m,n}) + \delta^F \nabla^2 R] \delta R dF = 0. \quad (3.44)$$

Boundary conditions (3.43) in tangential directions to the surface coincide with the formulation obtained using the Murdoch–Gurtin model (Gurtin and Murdoch 1975a, b). At the same time, in the direction of the unit vector of the normal, the boundary condition in the formulation of the Murdoch–Gurtin theory ($\delta^F = 0$) remains classical. In the presented generalized adhesion model (3.44), all three static boundary conditions (3.43), (3.44) must contain adhesion corrections of non-gradient adhesion with three adhesion moduli λ^F , μ^F , δ^F . Moreover, the modulus characterizes the “flexural” rigidity of the body surface, which can probably be very important for applications. As a result, the adhesive properties of a non-gradient surface are determined by three adhesive modules, and only in the special case of the Murdoch–Gurtin theory of adhesion—by two adhesion moduli λ^F , μ^F .

A similar situation takes place for a gradient surface model. The static boundary condition (3.42) coincides with the formulation of the boundary conditions constructed using the Steigman–Ogden model (Steigmann and Ogden 1997, 1999; Eremeyev 2016), which is determined only by gradient moduli $C_3 = c_6 + c_7 + c_8$ ($b_i = 0$). Under boundary conditions (3.41), with variations δr_i , $i = 1, 2$ along the tangential directions of the surface, the Steigman–Ogden theory does not give adhe-

sion corrections. In the generalized model formulated here, there are adhesion corrections in all three static conditions.

The special interest is the problem of modeling the mechanical properties of ultrathin graphene-type plates and similar 2D structures as the limiting case when, $V \rightarrow 0$ and $\mu \rightarrow 0$, $\lambda \rightarrow 0$ ($\mu = \lambda = 0$), i.e., there is no volume density of potential energy (there is no volume). In accordance with (3.41) at or (3.42), we obtain the graphene sheet equilibrium equations:

$$P_i^F + \mu^F \nabla^2 r_i + (\lambda^F + \delta^F) r_{m,mi} + T_2 \nabla^2 \nabla^2 r_i + T_1 \nabla^2 r_{j,ji} + B \nabla^2 R_i = 0, \quad (3.45)$$

$$P_i^F n_i - B \nabla^2 r_{j,j} + \delta^F \nabla^2 R + C_3 \nabla^2 \nabla^2 R = 0. \quad (3.46)$$

It follows from (3.45), (3.46) that the properties of graphene-like 2D structures are determined exclusively by adhesive properties. The number of physical modules is seven. As can be seen, in the general case, the problem of tension–compression–shear in the plane of a graphene sheet and the problem of bending are related. In the case, $B = 0$, the system of the equilibrium equations and boundary value problem as all are separated:

$$P_i^F + \mu^F \nabla^2 r_i + (\lambda^F + \delta^F) r_{m,mi} + T_2 \nabla^2 \nabla^2 r_i + T_1 \nabla^2 r_{j,ji} = 0, \\ P_i^F n_i + \delta^F \nabla^2 R + C_3 \nabla^2 \nabla^2 R = 0.$$

3.8 Elastic Non-gradient Defectness Body with a Non-gradient Surface

Assume now that there are defect fields inside the elastic body and on its surface, and, therefore, the list of kinematic variables includes distortions of both types. This particular case allows us to give a physical interpretation of adhesive modules. The Lagrangian of such a model has the form:

$$L = A - \frac{1}{2} \int_V (C_{ijmn}^{11} R_{i,j} R_{m,n} + 2C_{ijmn}^{12} R_{i,j} D_{mn}^2 + C_{ijmn}^{22} D_{ij}^2 D_{mn}^2) dV - \\ - \frac{1}{2} \int_F [A_{ijmn}^{11} R_{i,j} R_{m,n} + 2A_{ijmn}^{12} R_{i,j} D_{mn}^2 + A_{ijmn}^{22} D_{ij}^2 D_{mn}^2] dF. \quad (3.47)$$

Then using (3.47), the variational Lagrange equality is written as

$$\begin{aligned}
\delta L = & \int_V [(C_{ijmn}^{11} R_{m,nj} + C_{ijmn}^{12} D_{mn,j}^2 + P_i^V) \delta R_i \\
& - (C_{ijmn}^{12} R_{i,j} + C_{ijmn}^{22} D_{ij}^2) \delta D_{mn}^2] dV + \\
& + \int_F \{ [P_i^F - (C_{ijmn}^{11} R_{m,n} + C_{ijmn}^{12} D_{mn}^2) n_j \\
& + (A_{ijmn}^{11} R_{m,n} + A_{ijmn}^{12} D_{mn}^2)_{,p} \delta_{pj}^*] \delta R_i + \\
& - (A_{ijmn}^{11} R_{m,n} + A_{ijmn}^{12} D_{mn}^2) n_j \delta (R_{i,p} n_p) - \\
& - (A_{ijmn}^{12} R_{i,j} + A_{ijmn}^{22} D_{ij}^2) \delta D_{mn}^2 \} dF = 0. \tag{3.48}
\end{aligned}$$

Following (3.48), we have the following equilibrium equations:

$$C_{ijmn}^{11} R_{m,nj} + C_{ijmn}^{12} D_{mn,j}^2 + P_i^V = 0, \tag{3.49}$$

$$C_{ijmn}^{12} R_{i,j} + C_{ijmn}^{22} D_{ij}^2 = 0. \tag{3.50}$$

The system of equations (3.49), (3.50) allows you to explicitly, algebraically, find free, incompatible distortions D_{rs}^2 through constrained distortions $R_{i,j}$

$$D_{pq}^2 = -C_{pqmn}^{-22} C_{ijmn}^{12} R_{i,j} = c_{pqij} R_{i,j}, \tag{3.51}$$

where $C_{pqmn}^{-22} C_{ijmn}^{22} = \delta_{ip} \delta_{jq}$ and $c_{pqij} = -C_{pqmn}^{-22} C_{ijmn}^{12}$.

Such a model will be called an algebraic model with respect to inconsistent, free distortions D_{pq}^2 . We note that relations (3.51) can be considered as a generalization of Aero–Kuvshinsky’s hypothesis, which was used for formulation of the moment quasi-continuum model with an asymmetric stress tensor.

Using (3.51), one can eliminate free distortion tensor in (3.47) and represent the considered model as a classical elastic continuum with elastic moduli damaged by given defect fields:

$$\begin{aligned}
L = & A - \frac{1}{2} \int_V [C_{abcd}^{11} + 2C_{abmn}^{12} c_{mncd} + C_{ijmn}^{22} c_{ijab} c_{mncd}] R_{a,b} R_{c,d} dV - \\
& - \frac{1}{2} \int_F [A_{abcd}^{11} + 2A_{abmn}^{12} c_{mncd} + A_{ijmn}^{22} c_{ijab} c_{mncd}] R_{a,b} R_{c,d} dF = \\
= & A - \frac{1}{2} \int_V C_{ijmn} R_{i,j} R_{m,n} dV - \frac{1}{2} \int_F A_{ijmn} R_{i,j} R_{m,n} dF, \tag{3.52}
\end{aligned}$$

where $C_{abcd} = C_{abcd}^{11} + 2C_{abmn}^{12} c_{mncd} + C_{ijmn}^{22} c_{ijab} c_{mncd}$, $A_{abcd} = A_{abcd}^{11} + 2A_{abmn}^{12} c_{mncd} + A_{ijmn}^{22} c_{ijab} c_{mncd}$ we will call tensors T_{abcd} , A_{abcd} as a moduli of elasticity, “damaged” by the field of defects.

Thus, the variational statement of a non-gradient medium with the field of defects with a non-gradient surface coincides with the statement for the model of a defectless non-gradient medium bounded by a defect-free non-gradient surface, but with damaged moduli.

3.9 Conclusions

The most general model of a gradient and defective medium with an adhesively active surface is formulated, which can also have defect fields and may be considered as a 2D gradient media. It is shown that the formulated model contains, as special cases, the defect-free non-gradient classical elasticity model, the Tupin gradient models, and the coupled model, which is a gradient generalization of the Mindlin media model with defect fields. The formulated model of surface interactions makes it possible to obtain, in particular, well-known particular models of adhesive interactions: the Murdoch–Gurtin model for a defect-free non-gradient surface, the Steigman–Ogden model for a defect-free gradient surface, etc.

Appendix I

Let us indicate the structure of the fourth rank tensor for the general case when an elastic body can be considered in terms of classical and gradient elasticity and can contain defect fields. The body surface can also have defect fields. Tensors of adhesion modules of the fourth rank have a structure in the form of expansion in space of ten basis tensors of the fourth rank. In this case, the space of basis tensors splits into a direct sum of three subspaces.

The first basis tensor is constructed as tensor product of two “flat” Kronecker tensors with all possible index permutations

$$\delta_{ij}^* \delta_{mn}^*; \quad \delta_{im}^* \delta_{jn}^*; \quad \delta_{in}^* \delta_{jm}^*.$$

The second subspace of basis tensors is constructed as a tensor product of the “flat” Kronecker tensor and two unit vectors of the surface normal with all possible permutations of indices: $\delta_{ij}^* n_m n_n$; $\delta_{im}^* n_j n_n$; $\delta_{in}^* n_j n_m$; $\delta_{jm}^* n_i n_n$; $\delta_{jn}^* n_i n_m$; $\delta_{mn}^* n_i n_j$.

The third subspace consists of a single basis tensor, constructed as the tensor product of the four unit vectors of the normal to the surface:

$$n_i n_j n_m n_n.$$

The decomposition of any tensor of adhesive properties of the surface of the fourth rank has the form:

$$\begin{aligned}
A_{ijmn}^{Pq} = & a_1^{Pq} \delta_{ij}^* \delta_{mn}^* + a_2^{Pq} \delta_{im}^* \delta_{jn}^* + a_3^{Pq} \delta_{in}^* \delta_{jm}^* + \\
& + a_4^{Pq} \delta_{ij}^* n_m n_n + a_5^{Pq} \delta_{im}^* n_j n_n + a_6^{Pq} \delta_{in}^* n_j n_m + a_7^{Pq} \delta_{jm}^* n_i n_n + \\
& + a_8^{Pq} \delta_{jn}^* n_i n_m + a_9^{Pq} \delta_{mn}^* n_i n_j + a_{10}^{Pq} n_i n_j n_m n_n.
\end{aligned} \tag{I.1}$$

The potentiality conditions lead to (3.26) a reduction in the number of modules from ten to eight:

$$\begin{aligned}
A_{ijmn}^{Pq} - A_{mni j}^{qP} = & (a_1^{Pq} - a_1^{qP}) \delta_{mn}^* \delta_{ij}^* + (a_2^{Pq} - a_2^{qP}) \delta_{im}^* \delta_{jn}^* + (a_3^{Pq} - a_3^{qP}) \delta_{in}^* \delta_{jm}^* + \\
& + (a_4^{Pq} - a_4^{qP}) (\delta_{ij}^* n_m n_n - \delta_{mn}^* n_i n_j) + (a_5^{Pq} - a_5^{qP}) \delta_{im}^* n_j n_n + \\
& + (a_6^{Pq} - a_6^{qP}) (\delta_{in}^* n_j n_m - \delta_{jm}^* n_i n_n) + \\
& + (a_8^{Pq} - a_8^{qP}) \delta_{jn}^* n_i n_m + (a_{10}^{Pq} - a_{10}^{qP}) n_i n_j n_m n_n = 0.
\end{aligned} \tag{I.2}$$

In the result, we have

$$\begin{aligned}
A_{ijmn}^{Pq} = & (a_1^{Pq} + a_1^{qP}) \delta_{ij}^* \delta_{mn}^* / 2 + (a_2^{Pq} + a_2^{qP}) \delta_{im}^* \delta_{jn}^* / 2 + (a_3^{Pq} + a_3^{qP}) \delta_{in}^* \delta_{jm}^* / 2 + \\
& + (a_9^{Pq} + a_9^{qP}) (\delta_{ij}^* n_m n_n + \delta_{mn}^* n_i n_j) / 2 + \\
& + (a_7^{Pq} + a_7^{qP}) (\delta_{in}^* n_j n_m + \delta_{jm}^* n_i n_n) / 2 + \\
& + (a_5^{Pq} + a_5^{qP}) \delta_{im}^* n_j n_n / 2 + (a_8^{Pq} + a_8^{qP}) \delta_{jn}^* n_i n_m / 2 + \\
& + (a_{10}^{Pq} + a_{10}^{qP}) n_i n_j n_m n_n / 2.
\end{aligned} \tag{I.3}$$

For a gradient elastic body (Tupin's model), the adhesion properties of the surface are not limited by anything. The tensor is reduced to the form:

$$\begin{aligned}
A_{ijmn}^{11} = & a_1^{11} \delta_{ij}^* \delta_{mn}^* + (a_2^{11} + a_3^{11}) (\delta_{im}^* \delta_{jn}^* + \delta_{in}^* \delta_{jm}^*) / 2 + \\
& + a_9^{11} (\delta_{ij}^* n_m n_n + \delta_{mn}^* n_i n_j) + a_7^{11} (\delta_{in}^* n_j n_m + \delta_{jm}^* n_i n_n) + \\
& + a_5^{11} \delta_{im}^* n_j n_n + a_8^{11} \delta_{jn}^* n_i n_m + a_{10}^{11} n_i n_j n_m n_n.
\end{aligned} \tag{I.4}$$

Then the tensor A_{ijmn}^{12} has form

$$\begin{aligned}
A_{ijmn}^{12} = & A_{ijmn}^{21} = \\
= & (a_1^{12} + a_1^{21}) \delta_{ij}^* \delta_{mn}^* / 2 + (a_2^{12} + a_2^{21} + a_3^{12} + a_3^{21}) (\delta_{im}^* \delta_{jn}^* + \delta_{in}^* \delta_{jm}^*) / 4 + \\
& + (a_9^{12} + a_9^{21}) (\delta_{ij}^* n_m n_n + \delta_{mn}^* n_i n_j) / 2 + \\
& + (a_7^{12} + a_7^{21}) (\delta_{in}^* n_j n_m + \delta_{jm}^* n_i n_n) / 2 + \\
& + (a_5^{12} + a_5^{21}) \delta_{im}^* n_j n_n / 2 + (a_8^{12} + a_8^{21}) \delta_{jn}^* n_i n_m / 2 + (a_{10}^{12} + \\
& + a_{10}^{21}) n_i n_j n_m n_n / 2.
\end{aligned} \tag{I.5}$$

Tensor A_{ijmn}^{22} is

$$\begin{aligned} A_{ijmn}^{22} = & a_1^{22} \delta_{ij}^* \delta_{mn}^* + (a_2^{22} + a_3^{22})(\delta_{in}^* \delta_{jm}^* + \delta_{im}^* \delta_{jn}^*)/2 + \\ & + a_9^{22} (\delta_{ij}^* n_m n_n + \delta_{mn}^* n_i n_j) + a_7^{22} (\delta_{in}^* n_j n_m + \delta_{jm}^* n_i n_n) + \\ & + a_5^{22} \delta_{im}^* n_j n_n + a_8^{22} \delta_{jn}^* n_i n_m + a_{10}^{22} n_i n_j n_m n_n. \end{aligned} \quad (\text{I.6})$$

For a classical elastic body, the potential energy density of adhesion should not contain normal derivatives of displacements. The adhesive properties of the surface are limited by the conditions $A_{ijmn}^{11} n_j = 0$, $A_{ijmn}^{12} n_j = 0$. Then we can find

$$\begin{aligned} A_{ijmn}^{11} = & a_1^{11} \delta_{ij}^* \delta_{mn}^* + (a_2^{11} + a_3^{11})(\delta_{im}^* \delta_{jn}^* + \delta_{in}^* \delta_{jm}^*)/2 + a_8^{11} \delta_{jn}^* n_i n_m, \\ A_{ijmn}^{12} = & a_1^{12} \delta_{ij}^* \delta_{mn}^* + (a_2^{12} + a_2^{21} + a_3^{12} + a_3^{21})(\delta_{im}^* \delta_{jn}^* + \delta_{in}^* \delta_{jm}^*)/4 + a_8^{12} \delta_{jn}^* n_i n_m, \\ A_{ijmn}^{21} = & a_1^{12} \delta_{ij}^* \delta_{mn}^* + (a_2^{21} + a_2^{12} + a_3^{21} + a_3^{12})(\delta_{im}^* \delta_{jn}^* + \delta_{in}^* \delta_{jm}^*)/4 + a_8^{12} \delta_{jn}^* n_i n_m, \\ A_{ijmn}^{22} = & a_1^{22} \delta_{ij}^* \delta_{mn}^* + (a_2^{22} + a_3^{22})(\delta_{im}^* \delta_{jn}^* + \delta_{in}^* \delta_{jm}^*)/2 + a_8^{22} \delta_{jn}^* n_i n_m. \end{aligned}$$

Appendix II

We can write the following general form for tensors of the fifth rank:

$$\begin{aligned} A_{ijmnl}^{pq} = & b_1^{pq} \delta_{ij}^* \delta_{mn}^* n_l + b_2^{pq} \delta_{im}^* \delta_{jn}^* n_l + b_3^{pq} \delta_{in}^* \delta_{jm}^* n_l + \\ & + b_4^{pq} \delta_{ij}^* \delta_{ml}^* n_n + b_5^{pq} \delta_{im}^* \delta_{jl}^* n_n + b_6^{pq} \delta_{il}^* \delta_{jm}^* n_n + \\ & + b_7^{pq} \delta_{ij}^* \delta_{nl}^* n_m + b_8^{pq} \delta_{in}^* \delta_{jl}^* n_m + b_9^{pq} \delta_{il}^* \delta_{jn}^* n_m + \\ & + b_{10}^{pq} \delta_{im}^* \delta_{nl}^* n_j + b_{11}^{pq} \delta_{in}^* \delta_{ml}^* n_j + b_{12}^{pq} \delta_{il}^* \delta_{mn}^* n_j + \\ & + b_{13}^{pq} \delta_{jm}^* \delta_{nl}^* n_i + b_{14}^{pq} \delta_{jn}^* \delta_{ml}^* n_i + b_{15}^{pq} \delta_{jl}^* \delta_{mn}^* n_i + \\ & + b_{16}^{pq} \delta_{ij}^* n_m n_n n_l + b_{17}^{pq} \delta_{im}^* n_j n_n n_l + b_{18}^{pq} \delta_{in}^* n_j n_m n_l + b_{19}^{pq} \delta_{il}^* n_j n_m n_n + \\ & + b_{20}^{pq} \delta_{jm}^* n_i n_n n_l + b_{21}^{pq} \delta_{jn}^* n_i n_m n_l + b_{22}^{pq} \delta_{jl}^* n_i n_m n_n + \\ & + b_{23}^{pq} \delta_{mn}^* n_i n_j n_l + b_{24}^{pq} \delta_{ml}^* n_i n_j n_n + b_{25}^{pq} \delta_{nl}^* n_i n_j n_m + \\ & + b_{26}^{pq} n_i n_j n_m n_n n_l. \end{aligned} \quad (\text{II.1})$$

The space of basis tensors for the tensor of adhesion moduli of the fifth rank decomposes into a direct sum of three subspaces. The first basis subspace is

$$\left\{ \begin{array}{l} \delta_{ij}^* \delta_{mn}^* n_l \\ \delta_{im}^* \delta_{jn}^* n_l \\ \delta_{in}^* \delta_{jm}^* n_l \end{array} \right\} \left\{ \begin{array}{l} \delta_{ij}^* \delta_{ml}^* n_n \\ \delta_{im}^* \delta_{jl}^* n_n \\ \delta_{il}^* \delta_{jm}^* n_n \end{array} \right\} \left\{ \begin{array}{l} \delta_{ij}^* \delta_{nl}^* n_m \\ \delta_{in}^* \delta_{jl}^* n_m \\ \delta_{il}^* \delta_{jn}^* n_m \end{array} \right\} \left\{ \begin{array}{l} \delta_{im}^* \delta_{nl}^* n_j \\ \delta_{in}^* \delta_{ml}^* n_j \\ \delta_{il}^* \delta_{mn}^* n_j \end{array} \right\} \left\{ \begin{array}{l} \delta_{jm}^* \delta_{nl}^* n_i \\ \delta_{jn}^* \delta_{ml}^* n_i \\ \delta_{jl}^* \delta_{mn}^* n_i \end{array} \right\}$$

The second basis tensor is written as

$$\begin{Bmatrix} \delta_{ij}^* n_m n_n n_l \\ \delta_{im}^* n_j n_n n_l \\ \delta_{in}^* n_j n_m n_l \\ \delta_{il}^* n_j n_m n_n \end{Bmatrix} \begin{Bmatrix} \delta_{jm}^* n_i n_n n_l \\ \delta_{jn}^* n_i n_m n_l \\ \delta_{jl}^* n_i n_m n_n \end{Bmatrix} \begin{Bmatrix} \delta_{mn}^* n_i n_j n_l \\ \delta_{ml}^* n_i n_j n_n \end{Bmatrix} \begin{Bmatrix} \delta_{nl}^* n_i n_j n_m \end{Bmatrix}$$

The third subspace consists of one tensor:

$$n_i n_j n_m n_n n_l.$$

Assume now that the deformed body is considered as non-gradient elastic body. Thus, one should introduce the condition

$$A_{ijmnl}^{pq} n_l = 0 \quad (\text{II.2})$$

Then, using (II.1), (II.2) we can find:

$$\begin{aligned} A_{ijmnl}^{pq} = & b_4^{pq} \delta_{ij}^* \delta_{ml}^* n_n + b_5^{pq} \delta_{im}^* \delta_{jl}^* n_n + b_6^{pq} \delta_{il}^* \delta_{jm}^* n_n + \\ & + b_7^{pq} \delta_{ij}^* \delta_{nl}^* n_m + b_8^{pq} \delta_{in}^* \delta_{jl}^* n_m + b_9^{pq} \delta_{il}^* \delta_{jn}^* n_m + \\ & + b_{10}^{pq} \delta_{im}^* \delta_{nl}^* n_j + b_{11}^{pq} \delta_{in}^* \delta_{ml}^* n_j + b_{12}^{pq} \delta_{il}^* \delta_{mn}^* n_j + \\ & + b_{13}^{pq} \delta_{jm}^* \delta_{nl}^* n_i + b_{14}^{pq} \delta_{jn}^* \delta_{ml}^* n_i + b_{15}^{pq} \delta_{jl}^* \delta_{mn}^* n_i + \\ & + b_{19}^{pq} \delta_{il}^* n_j n_m n_n + b_{22}^{pq} \delta_{jl}^* n_i n_m n_n + b_{24}^{pq} \delta_{ml}^* n_i n_j n_n + b_{25}^{pq} \delta_{nl}^* n_i n_j n_m. \end{aligned} \quad (\text{II.3})$$

In the result, we can establish the final structure of all tensors A_{ijmnl}^{pq} ($p, q = 1, 2$). Taking into account (II.2) and (II.3), we find for tensor A_{ijmnl}^{11} :

$$\begin{aligned} A_{ijmnl}^{11} = & b_7^{11} \delta_{ij}^* \delta_{nl}^* n_m + (b_8^{11} + b_9^{11})(\delta_{in}^* \delta_{jl}^* n_m + \delta_{il}^* \delta_{jn}^* n_m)/2 + \\ & + b_{13}^{11} \delta_{jm}^* \delta_{nl}^* n_i + (b_{14}^{11} + b_{15}^{11})(\delta_{jn}^* \delta_{ml}^* n_i + \delta_{jl}^* \delta_{mn}^* n_i)/2. \end{aligned}$$

The tensors A_{ijmnl}^{12} and A_{ijmnl}^{21} using (II.2) can be written as

$$\begin{aligned} A_{ijmnl}^{12} = & b_4^{12} \delta_{ij}^* \delta_{ml}^* n_n + (b_5^{12} + b_6^{12})(\delta_{im}^* \delta_{jl}^* n_n + \delta_{il}^* \delta_{jm}^* n_n)/2 + \\ & + b_7^{12} \delta_{ij}^* \delta_{nl}^* n_m + (b_8^{12} + b_9^{12})(\delta_{in}^* \delta_{jl}^* n_m + \delta_{il}^* \delta_{jn}^* n_m)/2 + \\ & + b_{13}^{12} \delta_{jm}^* \delta_{nl}^* n_i + b_{14}^{12} \delta_{jn}^* \delta_{ml}^* n_i + b_{15}^{12} \delta_{jl}^* \delta_{mn}^* n_i + b_{22}^{12} \delta_{jl}^* n_i n_m n_n \end{aligned}$$

$$\begin{aligned} A_{ijmnl}^{21} = & b_4^{21} \delta_{ij}^* \delta_{ml}^* n_n + b_5^{21} \delta_{im}^* \delta_{jl}^* n_n + b_6^{21} \delta_{il}^* \delta_{jm}^* n_n + \\ & + b_7^{21} \delta_{ij}^* \delta_{nl}^* n_m + b_8^{21} \delta_{in}^* \delta_{jl}^* n_m + b_9^{21} \delta_{il}^* \delta_{jn}^* n_m + \\ & + b_{10}^{21} \delta_{im}^* \delta_{nl}^* n_j + b_{11}^{21} \delta_{in}^* \delta_{ml}^* n_j + b_{12}^{21} \delta_{il}^* \delta_{mn}^* n_j + \\ & + b_{13}^{21} \delta_{jm}^* \delta_{nl}^* n_i + b_{14}^{21} \delta_{jn}^* \delta_{ml}^* n_i + b_{15}^{21} \delta_{jl}^* \delta_{mn}^* n_i + \\ & + b_{19}^{21} \delta_{il}^* n_j n_m n_n + b_{22}^{21} \delta_{jl}^* n_i n_m n_n + b_{24}^{21} \delta_{ml}^* n_i n_j n_n + b_{25}^{21} \delta_{nl}^* n_i n_j n_m. \end{aligned}$$

The tensor A_{ijmnl}^{22} retains its structure

$$\begin{aligned}
 A_{ijmnl}^{22} = & b_4^{22} \delta_{ij}^* \delta_{ml}^* n_n + b_5^{22} \delta_{im}^* \delta_{jl}^* n_n + b_6^{22} \delta_{il}^* \delta_{jm}^* n_n + \\
 & + b_7^{22} \delta_{ij}^* \delta_{nl}^* n_m + b_8^{22} \delta_{in}^* \delta_{jl}^* n_m + b_9^{22} \delta_{il}^* \delta_{jn}^* n_m + \\
 & + b_{10}^{22} \delta_{im}^* \delta_{nl}^* n_j + b_{11}^{22} \delta_{in}^* \delta_{ml}^* n_j + b_{12}^{22} \delta_{il}^* \delta_{mn}^* n_j + \\
 & + b_{13}^{22} \delta_{im}^* \delta_{nl}^* n_i + b_{14}^{22} \delta_{jn}^* \delta_{ml}^* n_i + b_{15}^{22} \delta_{jl}^* \delta_{mn}^* n_i + \\
 & + b_{19}^{22} \delta_{il}^* n_j n_m n_n + b_{22}^{22} \delta_{jl}^* n_i n_m n_n + b_{24}^{22} \delta_{ml}^* n_i n_j n_n + b_{25}^{22} \delta_{nl}^* n_i n_j n_m.
 \end{aligned}$$

Appendix III

The space of basis tensors of the sixth rank decomposes into a direct sum of four subspaces:

$$A_{ijkmln} = A_{ijkmln}^{****} + A_{ijkmln}^{**} + A_{ijkmln}^* + A_{ijkmln}^{\circ}. \quad (\text{III.1})$$

These subspaces are defined in an obvious way and have the following structure:
first subspace

$$\left\{ \begin{array}{l} \delta_{ij}^* \delta_{km}^* \delta_{nl}^* \\ \delta_{ij}^* \delta_{kn}^* \delta_{lm}^* \\ \delta_{ij}^* \delta_{kl}^* \delta_{mn}^* \end{array} \right\} \left\{ \begin{array}{l} \delta_{ik}^* \delta_{jm}^* \delta_{nl}^* \\ \delta_{ik}^* \delta_{jn}^* \delta_{lm}^* \\ \delta_{ik}^* \delta_{jl}^* \delta_{mn}^* \end{array} \right\} \left\{ \begin{array}{l} \delta_{im}^* \delta_{kj}^* \delta_{nl}^* \\ \delta_{im}^* \delta_{kn}^* \delta_{lj}^* \\ \delta_{im}^* \delta_{kl}^* \delta_{jn}^* \end{array} \right\} \left\{ \begin{array}{l} \delta_{in}^* \delta_{km}^* \delta_{jl}^* \\ \delta_{in}^* \delta_{kj}^* \delta_{lm}^* \\ \delta_{in}^* \delta_{kl}^* \delta_{mj}^* \end{array} \right\} \left\{ \begin{array}{l} \delta_{il}^* \delta_{km}^* \delta_{nj}^* \\ \delta_{il}^* \delta_{kn}^* \delta_{jm}^* \\ \delta_{il}^* \delta_{kj}^* \delta_{mn}^* \end{array} \right\}$$

– second subspace

$$\left\{ \begin{array}{l} n_i n_j \delta_{km}^* \delta_{nl}^* \\ n_i n_j \delta_{kn}^* \delta_{lm}^* \\ n_i n_j \delta_{kl}^* \delta_{mn}^* \end{array} \right\} \left\{ \begin{array}{l} n_i n_k \delta_{jm}^* \delta_{nl}^* \\ n_i n_k \delta_{jn}^* \delta_{lm}^* \\ n_i n_k \delta_{jl}^* \delta_{mn}^* \end{array} \right\} \left\{ \begin{array}{l} n_i n_m \delta_{kj}^* \delta_{nl}^* \\ n_i n_m \delta_{kn}^* \delta_{lj}^* \\ n_i n_m \delta_{kl}^* \delta_{jn}^* \end{array} \right\} \left\{ \begin{array}{l} n_i n_n \delta_{km}^* \delta_{jl}^* \\ n_i n_n \delta_{kj}^* \delta_{lm}^* \\ n_i n_n \delta_{kl}^* \delta_{mj}^* \end{array} \right\} \left\{ \begin{array}{l} n_i n_l \delta_{km}^* \delta_{nj}^* \\ n_i n_l \delta_{kn}^* \delta_{jm}^* \\ n_i n_l \delta_{kj}^* \delta_{mn}^* \end{array} \right\} \\
 \left\{ \begin{array}{l} n_n n_l \delta_{ij}^* \delta_{km}^* \\ n_n n_l \delta_{ik}^* \delta_{mj}^* \\ n_n n_l \delta_{il}^* \delta_{jk}^* \end{array} \right\} \left\{ \begin{array}{l} n_j n_k \delta_{im}^* \delta_{nl}^* \\ n_j n_k \delta_{in}^* \delta_{lm}^* \\ n_j n_k \delta_{il}^* \delta_{mn}^* \end{array} \right\} \left\{ \begin{array}{l} n_j n_m \delta_{ik}^* \delta_{nl}^* \\ n_j n_m \delta_{in}^* \delta_{lk}^* \\ n_j n_m \delta_{il}^* \delta_{kn}^* \end{array} \right\} \left\{ \begin{array}{l} n_j n_n \delta_{ki}^* \delta_{ml}^* \\ n_j n_n \delta_{km}^* \delta_{li}^* \\ n_j n_n \delta_{kl}^* \delta_{im}^* \end{array} \right\} \left\{ \begin{array}{l} n_j n_l \delta_{km}^* \delta_{in}^* \\ n_j n_l \delta_{ki}^* \delta_{mn}^* \\ n_j n_l \delta_{kn}^* \delta_{mi}^* \end{array} \right\} \\
 \left\{ \begin{array}{l} n_m n_n \delta_{ij}^* \delta_{kl}^* \\ n_m n_n \delta_{ik}^* \delta_{lj}^* \\ n_m n_n \delta_{il}^* \delta_{jk}^* \end{array} \right\} \left\{ \begin{array}{l} n_m n_l \delta_{ij}^* \delta_{kn}^* \\ n_m n_l \delta_{ik}^* \delta_{nj}^* \\ n_m n_l \delta_{il}^* \delta_{jk}^* \end{array} \right\} \left\{ \begin{array}{l} n_k n_m \delta_{ij}^* \delta_{nl}^* \\ n_k n_m \delta_{in}^* \delta_{lj}^* \\ n_k n_m \delta_{il}^* \delta_{jn}^* \end{array} \right\} \left\{ \begin{array}{l} n_k n_n \delta_{ij}^* \delta_{ml}^* \\ n_k n_n \delta_{ik}^* \delta_{lj}^* \\ n_k n_n \delta_{il}^* \delta_{jm}^* \end{array} \right\} \left\{ \begin{array}{l} n_k n_l \delta_{ji}^* \delta_{mn}^* \\ n_k n_l \delta_{jm}^* \delta_{ni}^* \\ n_k n_l \delta_{jn}^* \delta_{im}^* \end{array} \right\}$$

– third subspace

$$\left\{ \begin{array}{l} \delta_{ij}^* n_k n_m n_n n_l \\ \delta_{ik}^* n_j n_m n_n n_l \\ \delta_{im}^* n_k n_j n_n n_l \\ \delta_{in}^* n_k n_m n_j n_l \\ \delta_{il}^* n_k n_m n_n n_j \end{array} \right\} \left\{ \begin{array}{l} \delta_{jk}^* n_i n_m n_n n_l \\ \delta_{jm}^* n_k n_i n_n n_l \\ \delta_{jn}^* n_k n_m n_i n_l \\ \delta_{jl}^* n_k n_m n_n n_i \end{array} \right\} \left\{ \begin{array}{l} \delta_{km}^* n_j n_i n_n n_l \\ \delta_{kn}^* n_j n_m n_i n_l \\ \delta_{kl}^* n_j n_m n_n n_i \end{array} \right\} \left\{ \begin{array}{l} \delta_{mn}^* n_j n_k n_i n_l \\ \delta_{ml}^* n_j n_k n_n n_i \end{array} \right\} \left\{ \begin{array}{l} \delta_{nl}^* n_j n_k n_m n_i \end{array} \right\}$$

– fourth subspace contains a single basis tensor:

$$n_i n_j n_k n_m n_n n_l.$$

Let's find the tensor moduli for the classical elasticity body. Using the constraints (3.30), including the symmetry properties of potentiality ($A_{ijkmln} = A_{mnljik}$), the number of basis tensors in the first subspace is reduced to five and in the second basis subspace to three:

$$\begin{aligned} A_{ijkmln}^{***} &= c_1(\delta_{ij}^* \delta_{kn}^* \delta_{lm}^* + \delta_{ik}^* \delta_{jn}^* \delta_{lm}^* + \delta_{ij}^* \delta_{kl}^* \delta_{mn}^* + \delta_{ik}^* \delta_{jl}^* \delta_{mn}^*) + \\ &+ c_2(\delta_{in}^* \delta_{km}^* \delta_{jl}^* + \delta_{in}^* \delta_{kl}^* \delta_{mj}^* + \delta_{il}^* \delta_{km}^* \delta_{nj}^* + \delta_{il}^* \delta_{kn}^* \delta_{jm}^*) + \\ &+ c_3(\delta_{ij}^* \delta_{km}^* \delta_{nl}^* + \delta_{ik}^* \delta_{jm}^* \delta_{nl}^* + \delta_{in}^* \delta_{kj}^* \delta_{lm}^* + \delta_{il}^* \delta_{kj}^* \delta_{mn}^*) + \\ &+ c_4(\delta_{im}^* \delta_{kn}^* \delta_{lj}^* + \delta_{im}^* \delta_{kl}^* \delta_{jn}^*) + \\ &+ c_5 \delta_{im}^* \delta_{kj}^* \delta_{nl}^*. \\ A_{ijkmln}^{**} &= g_1 n_i n_m \delta_{kj}^* \delta_{nl}^* + g_2 n_i n_m \delta_{kn}^* \delta_{lj}^* + g_3 n_i n_m \delta_{kl}^* \delta_{jn}^*. \end{aligned}$$

Using (3.30) including the reversibility of the deformation process, one can verify that the third and fourth subspaces are empty:

$$A_{ijkmln}^* \equiv 0, \quad A_{ijkmln}^{\circ} = 0.$$

In the result, we can find the final relations for the gradient elastic moduli:

$$\begin{aligned} A_{ijkmln} &= c_1(\delta_{ij}^* \delta_{kn}^* \delta_{lm}^* + \delta_{ik}^* \delta_{jn}^* \delta_{lm}^* + \delta_{ij}^* \delta_{kl}^* \delta_{mn}^* + \delta_{ik}^* \delta_{jl}^* \delta_{mn}^*) + \\ &+ c_2(\delta_{in}^* \delta_{km}^* \delta_{jl}^* + \delta_{in}^* \delta_{kl}^* \delta_{mj}^* + \delta_{il}^* \delta_{km}^* \delta_{nj}^* + \delta_{il}^* \delta_{kn}^* \delta_{jm}^*) + \\ &+ c_3(\delta_{ij}^* \delta_{km}^* \delta_{nl}^* + \delta_{ik}^* \delta_{jm}^* \delta_{nl}^* + \delta_{in}^* \delta_{kj}^* \delta_{lm}^* + \delta_{il}^* \delta_{kj}^* \delta_{mn}^*) + \\ &+ c_4(\delta_{im}^* \delta_{kn}^* \delta_{lj}^* + \delta_{im}^* \delta_{kl}^* \delta_{jn}^*) + c_5 \delta_{im}^* \delta_{kj}^* \delta_{nl}^* + \\ &+ c_6 n_i n_m \delta_{kj}^* \delta_{nl}^* + c_7 n_i n_m \delta_{kn}^* \delta_{lj}^* + c_8 n_i n_m \delta_{kl}^* \delta_{jn}^*. \end{aligned}$$

References

- Altenbach H, Eremeev V, Morozov NF (2010) On equations of the linear theory of shells with surface stresses taken into account. *Mech Solids* 45:331–342
- Altenbach H, Eremeyev VA, Lebedev LP (2011) On the spectrum and stiffness of an elastic body with surface stresses. *ZAMM* 91(9):699–710
- Altenbach H, Morozov NF (eds) *Surface effects in solid mechanics*. Springer, pp 135–153
- Belov PA, Lurie SA (2009) Continuum model of microheterogeneous media. *J Appl Math Mech* 73(5–73):599–608. <https://doi.org/10.1016/j.jappmathmech.2009>
- Belov PA, Lurie SA (2014) *Mathematic theory of damaged media. Gradient theory of elasticity. Formulations. Hierarchy. Comparative analysis*. Palmarium Academic Publishing, 337 p
- Belov PA, Lurie SA (2007) Theory of ideal adhesion interactions. *J Compos Mech Des* 14:545–561

- Duan HL, Wang J, Huang ZP, Karihaloo BL (2005) Size-dependent effective elastic constants of solids containing nano-inhomogeneities with interface stress. *J Mech Phys Solids* 53:1574–1596
- Duan HL, Wang J, Karihaloo BL (2008) Theory of elasticity at the nanoscale. In: Aref H, Van der Giessen E (eds) *Advances in applied mechanics*, vol 42. Elsevier, Amsterdam, pp 1–68
- Eremeyev VA (2016) On effective properties of materials at the nano- and microscales considering surface effects. *Acta Mech* 227(1):29–42. <https://doi.org/10.1007/s00707-015-1427-y>
- Gurtin ME, Murdoch AI (1975a) Addenda to our paper A continuum theory of elastic material surfaces. *Arch Rat Mech Anal* 59(4):389–390
- Gurtin ME, Murdoch AI (1975b) A continuum theory of elastic material surfaces. *Arch Rat Mech Anal* 57(4):291–323
- Gurtin ME, Murdoch AI (1978) Surface stress in solids. *Int J Solids Struct* 14:431–440
- Huang Z, Wang J (2013) Micromechanics of nanocomposites with interface energy effect. In: Li S, Gao XL (eds) *Handbook on micromechanics and nanomechanics*, pp 303–348. Pan Stanford Publishing, Stanford
- Karyakin MI, Zubov LM (2011) Theory of isolated and continuously distributed disclinations and dislocations in micropolar media. In: Altenbach H, Maugin GA, Erofeev V (eds) *Mechanics of generalized continua*. Berlin, Springer, pp 275–290
- Lurie SA, Belov PA, Tuchkova NP (2010) Gradient theory of media with conserved dislocations: application to microstructured materials. In: Maugin GA, Metrikine AV (eds) *One hundred years after the Cosserats*. Series: advances in mechanics and mathematics, vol 21. Springer, pp 223–234
- Lurie S, Belov P (2014) Gradient effects in fracture mechanics for nano-structured materials. In: *Engineering fracture mechanics*, vol 130. Pergamon Press Ltd. (United Kingdom), pp 3–11
- Lurie S, Belov P, Altenbach H (2016) Classification of gradient adhesion theories across length scale. *Advanced structured materials*. Springer International Publishing, pp 261–277
- Lurie S, Belov P, Lykosova E (2020) Extended model of surface-related effects in second-gradient elasticity. Surface waves related to the nature of adhesion. In: Altenbach H, Eremeyev V, Pavlov I, Porubov A (eds) *Nonlinear wave dynamics of materials and structures*. *Advanced structured materials*, vol 122. Springer, Cham. https://doi.org/10.1007/978-3-030-38708-2_13
- Mindlin RD (1965) Second gradient of strain and surface-tension in linear elasticity. *Int J Solids Struct* 1(4):417–438
- Murdoch AI (2005) Some fundamental aspects of surface modelling. *J Elast* 80:33–52
- Steigmann DJ, Ogden RW (1997) Plane deformations of elastic solids with intrinsic boundary elasticity. *Proc Roy Soc A* 453(1959):853–877
- Steigmann DJ, Ogden RW (1999) Elastic surface-substrate interactions. *Proc Roy Soc A* 455(1982):437–474
- Wang J, Huang Z, Duan H, Yu S, Feng X, Wang G, Zhang W, Wang T (2011) Surface stress effect in mechanics of nanostructured materials. *Acta Mech Solida Sin* 24(1):52–82
- Yerofeyev VI, Sheshenina OA (2005) Waves in a gradient-elastic medium with surface energy. *J Appl Math Mech* 69(1):57–69
- Zubov LM (1997) *Nonlinear theory of dislocations and disclinations in elastic bodies*. Springer, Berlin, p 205
- Zubov LM (2011) Continuum theory of dislocations and disclinations in nonlinearly elastic micropolar media. *Mech Solids* 46(3):348–356

Chapter 4

On the Issue of the Stress in Incompressible and Rigid Media: Numerical Modeling



N. Bessonov and Y. Litvinova

Abstract We evaluate issues related to the calculation of stresses in incompressible medium. Several examples of numerical modeling of the behavior of a classical Newtonian liquid are assessed, and the solution to the problem in miscible liquids in the presence of the Korteweg effect is studied. The problem of determining stresses in a absolutely solid (rigid) body is considered also. Examples are given.

4.1 Introduction

The model of an absolutely solid of perfectly rigid (or rigid for short) body is used in analytical mechanics when solving dynamic problems. But, analytical mechanics does not allow looking inside a rigid body and solving the problem of finding stresses. On the other hand, the theory of elasticity studies the stresses in elastic bodies in detail, but rarely does anyone ask the question of whether it is possible to determine the stresses in an absolutely solid body from the standpoint of the theory of elasticity.

It is a traditional opinion that for a rigid material, the stress is completely undetermined (Truesdell and Noll 1965). This idea arises also from the observation that no constitutive relation connecting the stress to the motion is necessary to determine the motion of the rigid body, unlike what happens for deformable continua.

We could find only a few articles devoted to the study of a rigid body from the point of view of the theory of elasticity. For example, the question of the limiting transition from an elastic to a rigid body was investigated in Grioni (1983), Roger and Gianni (2004). Here is an overview of this issue and a short bibliography in the articles.

N. Bessonov (✉)

Institute of Problems of Mechanical Engineering, Russian Academy of Sciences, Bol'shoy, 61,
199178 Saint Petersburg, Russia
e-mail: nickbessonov1@gmail.com

Y. Litvinova

Peter the Great St. Petersburg Polytechnic University, Polytechnicheskaya, 29, 195251 Saint
Petersburg, Russia

An Internet search for an answer to a question “is there and if there is, is it possible to find stresses in an absolutely solid body” gave two answers—the first one is: “What you are asking is not physical,” and the second one is: “If the stiffness is infinite and the strain is zero, then the stress is mathematically indeterminate.”

An absolutely solid body is a model concept of classical mechanics, denoting a set of material points, the distances between which are preserved in the process of any movements made by this body. In other words, an absolutely solid body not only does not change its shape but also keeps the distribution of mass inside unchanged.

In this article, we do not discuss the fundamental aspects of these problems in detail. Our goal is to consider this problem from the point of view of numerical modeling.

The model of an incompressible media can be considered as the part, or as the first approximation to the model of a perfectly rigid body. A large section of hydrodynamics deals with the description of the behavior of incompressible liquids. In Sect. 4.2 of the article, examples of the numerical solution of problems in the hydrodynamics of incompressible liquids are considered.

In Sect. 4.3, the possibility of determining stresses in a rigid body is described.

4.2 Modeling of Incompressible Liquids Flow

4.2.1 Newtonian Liquid

Let us consider how the problem of numerical modeling of incompressible media in hydrodynamics is solved, on the example of a model of an incompressible Newtonian viscous liquid (Fletcher 2006; Hirsch 2007; Roache 1998 and more). The restriction to incompressible flow introduces the computational difficulty that the continuity equation contains only velocity components, and there is no obvious link with the pressure as there is for compressible flow through the density ρ .

The equations of motion of an incompressible viscous liquid (Navie–Stokes equations) in nondimensional form for the 2D case are

$$\begin{cases} \frac{\partial u}{\partial t} + \frac{\partial uu}{\partial x} + \frac{\partial vu}{\partial y} = -\frac{\partial p}{\partial x} + \frac{1}{\text{Re}} \left(\frac{\partial^2 u}{\partial x^2} + \frac{\partial^2 u}{\partial y^2} \right) \\ \frac{\partial v}{\partial t} + \frac{\partial uv}{\partial x} + \frac{\partial vv}{\partial y} = -\frac{\partial p}{\partial y} + \frac{1}{\text{Re}} \left(\frac{\partial^2 v}{\partial x^2} + \frac{\partial^2 v}{\partial y^2} \right) \\ \frac{\partial u}{\partial x} + \frac{\partial v}{\partial y} = 0, \end{cases} \quad (4.1)$$

where u , v are the velocity components; Re is Reynolds numbers; t is the time; p is the pressure; and x , y are the space coordinates.

Two broad approaches to computing incompressible flow are available. First, the source (or elementary) variables, (u, v, p) in two dimensions, are used and special procedures are introduced to handle the continuity equation. The extension to three spatial dimensions creates no additional difficulty. Second, in two dimensions the

explicit treatment of the continuity equation can be avoided by introducing the stream function. In addition, the introduction of a transport equation for the vorticity leads to the stream function vorticity formulation. The extension of this formulation to three dimensions is not straightforward, since a three-dimensional stream function is not available (Fletcher 2006).

In the article Bessonov and Koleshko (1988), we use an approach based on the use of source variables. To solve the discretized equations, we use the iterative alternative direction implicit method similar to Hirsch (2007), Yanenko (1967). Consider the finite-difference equations approximating the system (4.1) in the compact form:

$$\Lambda(f) = 0, \quad (4.2)$$

where the finite-difference operator Λ includes also the discretization of the time derivative, the components of the vector f include (u, v, p) . Suppose that the initial distribution for f is given. It can be the initial condition or the values at the previous time step. The numerical method is based on the following iterative procedure. Let us introduce a parameter τ playing the role of the step of pseudo-time in the iterations and denote by k the iteration number.

First of all, we determine the residual ξ^k at every node of the mesh

$$\text{step 1: } \xi^k = \tau \Lambda(f^k). \quad (4.3)$$

For the boundary nodes, ξ^k is found from the boundary conditions. For example, the boundary condition $f^k = \text{const}$ implies to $\xi^k = 0$.

For 2D problem, we split Λ into two parts, Λ_1 and Λ_2

$$\Lambda = \Lambda_1 + \Lambda_2. \quad (4.4)$$

At the following steps, we find the values $\xi^{k+1/2}$ and ξ^{k+1} from the equations:

$$\text{step 2: } \frac{\xi^{k+1/2} - \xi^k}{\tau} = \Lambda_1(\xi^{k+1/2}), \quad (4.5)$$

$$\text{step 3: } \frac{\xi^{k+1} - \xi^{k+1/2}}{\tau} = \Lambda_2(\xi^{k+1}), \quad (4.6)$$

Finally, we find

$$\text{step 4: } f^{k+1} = f^k + \xi^{k+1}. \quad (4.7)$$

We continue to do steps 1–4 while ξ^k/τ (i.e. $\Lambda(f^k)$ (4.3)) becomes sufficiently small.

The method is quite flexible when choosing Λ_1 and Λ_2 and the fulfillment of the condition in the general case is not necessary, although it is very useful. It is easy to see that if you put Λ_1 and Λ_2 to zero, then steps 2 and 3 are excluded and steps 1 and 4 lead to the simplest explicit scheme:

$$\frac{f^{k+1} - f^k}{\tau} = \Lambda(f^k). \quad (4.8)$$

The most rational option is when Λ_1 and Λ_2 are one-dimensional finite-difference operators in spatial directions Λ_1 contains differences in direction only x and Λ_2 —only in the direction y . Exclude from (4.5) and (4.6) $\xi^{k+1/2}$,

$$(I - \tau \Lambda_1)(I - \tau \Lambda_2)\xi^{k+1} = \xi^k, \quad (4.9)$$

where I is the unit operator, or

$$(I - \tau \Lambda + \tau^2 \Lambda_1 \Lambda_2)\xi^{k+1} = \xi^k. \quad (4.10)$$

From (4.10) and (4.7), the following equation can be obtained:

$$\frac{f^{k+1} - f^k}{\tau} = \Lambda(f^{k+1}) + O(\tau^2). \quad (4.11)$$

The ratio (4.11) corresponds to the accuracy $O(\tau^2)$ to completely implicit scheme:

$$\frac{f^{k+1} - f^k}{\tau} = \Lambda(f^{k+1}). \quad (4.12)$$

Implicit scheme places much less demands on values τ . Unlike (4.12), the computational circuit (4.3)–(4.7) is economical, i.e., the number of required arithmetic operations at each iteration is proportional to the number of mesh nodes.

The application of the method (4.3)–(4.7) for solution of system (4.1) follow to:
Step 1:

$$\left\{ \begin{array}{l} \xi_u^k = \tau_v \left(-\left(\frac{u^k - u^n}{\Delta t} + \frac{\partial u^k u^k}{\partial x} + \frac{\partial v^k u^k}{\partial y}\right) - \frac{\partial p^k}{\partial x} + \frac{1}{\text{Re}} \left(\frac{\partial^2 u^k}{\partial x^2} + \frac{\partial^2 u^k}{\partial y^2} \right) \right) \\ \xi_v^k = \tau_v \left(-\left(\frac{v^k - v^n}{\Delta t} + \frac{\partial u^k v^k}{\partial x} + \frac{\partial v^k v^k}{\partial y}\right) - \frac{\partial p^k}{\partial y} + \frac{1}{\text{Re}} \left(\frac{\partial^2 v^k}{\partial x^2} + \frac{\partial^2 v^k}{\partial y^2} \right) \right) \\ \xi_p^k = -\tau_p \left(\frac{\partial u^k}{\partial x} + \frac{\partial v^k}{\partial y} \right), \end{array} \right. \quad (4.13)$$

where u^n, v^n, p^n were defined in the previous step in time, $u^k = u^n, v^k = v^n, p^k = p^n$ at $k = 0$, Δt is the time steps, and τ_v, τ_p are the pseudo-time steps.

Step 2:

$$\left\{ \begin{array}{l} \frac{\xi_u^{k+1/2} - \xi_u^k}{\tau_v} = -\frac{1}{2} \frac{\xi_u^{k+1/2}}{\Delta t} - \frac{\partial u^k \xi_u^{k+1/2}}{\partial x} - \frac{\partial \xi_p^{k+1/2}}{\partial x} + \frac{1}{\text{Re}} \frac{\partial^2 \xi_u^{k+1/2}}{\partial x^2} \\ \frac{\xi_v^{k+1/2} - \xi_v^k}{\tau_v} = -\frac{1}{2} \frac{\xi_v^{k+1/2}}{\Delta t} - \frac{\partial u^k \xi_v^{k+1/2}}{\partial x} + \frac{1}{\text{Re}} \frac{\partial^2 \xi_v^{k+1/2}}{\partial x^2} \\ \frac{\xi_p^{k+1/2} - \xi_p^k}{\tau_p} = -\frac{\partial \xi_u^{k+1/2}}{\partial x}. \end{array} \right. \quad (4.14)$$

Substitution $\xi_p^{k+1/2}$ from the last equation of system (4.14) to the first equation allows to decouple these equations, and solve them sequentially. For this reason, the step 2 can be converted to the next form:

$$\left\{ \begin{array}{l} \frac{\xi_u^{k+1/2} - \xi_u^k}{\tau_u} = -\frac{1}{2} \frac{\xi_u^{k+1/2}}{\Delta t} - \frac{\partial u^k \xi_u^{k+1/2}}{\partial x} - \frac{\partial \xi_p^k}{\partial x} + \left(\frac{1}{\text{Re}} + \tau_p \right) \frac{\partial^2 \xi_u^{k+1/2}}{\partial x^2} \\ \frac{\xi_v^{k+1/2} - \xi_v^k}{\tau_v} = -\frac{1}{2} \frac{\xi_v^{k+1/2}}{\Delta t} - \frac{\partial u^k \xi_v^{k+1/2}}{\partial x} + \frac{1}{\text{Re}} \frac{\partial^2 \xi_v^{k+1/2}}{\partial x^2} \\ \xi_p^{k+1/2} = \xi_p^k - \tau_p \frac{\partial \xi_u^{k+1/2}}{\partial x} . \end{array} \right. \quad (4.15)$$

With that remark, step 3 can be written as

Step 3:

$$\left\{ \begin{array}{l} \frac{\xi_u^{k+1} - \xi_u^{k+1/2}}{\tau} = -\frac{1}{2} \frac{\xi_u^{k+1}}{\Delta t} - \frac{\partial v^k \xi_u^{k+1}}{\partial y} + \frac{1}{\text{Re}} \frac{\partial^2 \xi_u^{k+1}}{\partial y^2} \\ \frac{\xi_v^{k+1} - \xi_v^{k+1/2}}{\tau} = -\frac{1}{2} \frac{\xi_v^{k+1}}{\Delta t} - \frac{\partial v^k \xi_v^{k+1}}{\partial y} - \frac{\partial \xi_p^{k+1/2}}{\partial y} + \left(\frac{1}{\text{Re}} + \tau_p \right) \frac{\partial^2 \xi_v^{k+1}}{\partial y^2} \\ \xi_p^{k+1} = \xi_p^{k+1/2} - \tau_p \frac{\partial \xi_v^{k+1}}{\partial y} , \end{array} \right. \quad (4.16)$$

Step 4:

$$u^{k+1} = u^k + \xi_u^{k+1} ,$$

$$v^{k+1} = v^k + \xi_v^{k+1} ,$$

$$p^{k+1} = p^k + \xi_p^{k+1} .$$

For Reynolds numbers Re above the critical value, a spontaneous unsteadiness appears, under the form of a periodic vortex shedding. This can be explained as follows Hirsch (2007): the backflow areas form a symmetrical pattern. The viscous boundary layers are the regions with the high vorticity. At the separation points of the upper and lower parts of the obstacle, the vortices are equal and have opposite signs, such that a symmetrical flow pattern arises. When the vortex intensities increase, a small perturbation, which would give the upper vortex, for instance, a slightly larger value than the lower one, that would influence the flow on the lower part and attract the lower vortex. This breaks the symmetry with the consequence that the upper vortex is not balanced anymore by the lower one of the opposite sign. This vortex is then convected by the flow away from the cylinder surface, leaving the lower vortex as the dominating one. This lower vortex attracts the flow to the lower side and after being at his turn convected by the flow away from the surface, handles back the dominating role to the upper vortex. This results in a periodic motion, known as the periodic von Karman street of shed vortices.

To illustrate the numerical method described above, this section presents the results of simulations of von Karman street flowing around a flat barrier. The problem was solved in a nondimensional form (4.1). Initial data: 2D channel, its height equal 1, and length equal 5, $\text{Re} = 1000$. A unit velocity profile was set at the inlet, boundary conditions $\partial u / \partial x = \partial v / \partial x = 0$ were set at the outlet.

Fig. 4.1 A von Karman vortex street and streamlines of the flow around a flat barrier. **a** $t = t_0$, **b** $t = t_0 + 0.3$, **c** $t = t_0 + 0.6$, **d** $t = t_0 + 0.9$, **e** $t = t_0 + 1.2$

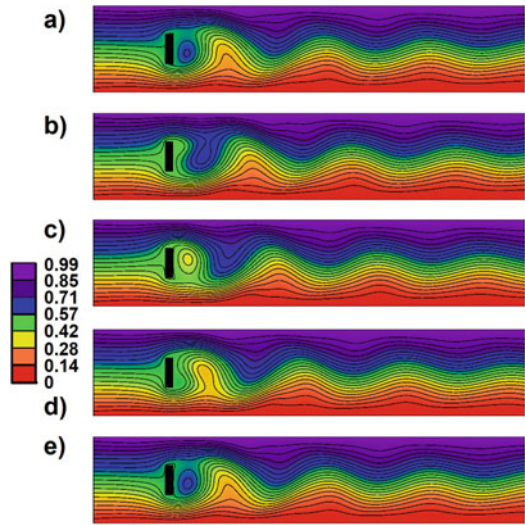
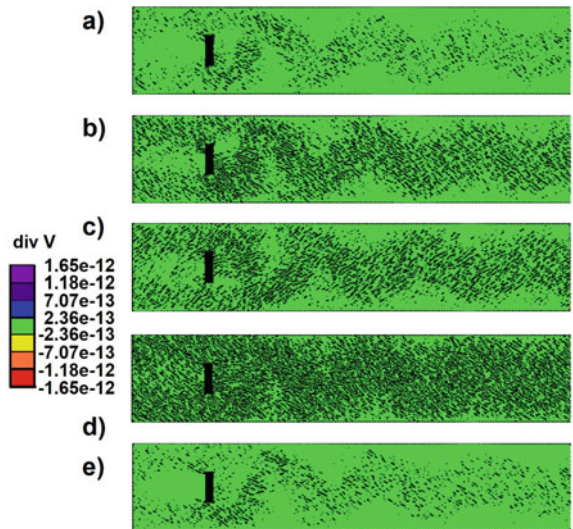


Fig. 4.2 A von Karman vortex street and distribution of the $\text{div } \mathbf{v}$ in the flow around a flat barrier. **a** $t = t_0$, **b** $t = t_0 + 0.3$, **c** $t = t_0 + 0.6$, **d** $t = t_0 + 0.9$, **e** $t = t_0 + 1.2$



The dimensionless time t_0 required for the formation of a stable von Karman track was equal or more than 100 dimensionless time units. Then, for every 1.2 dimensionless time unit, a new vortex is formed behind the barrier and the process repeats itself, dimensionless time step between slides equal 0.3. The streamlines corresponding to this are shown in Fig. 4.1. A distribution of the $\text{div } \mathbf{v}$ in shown in the Fig. 4.2. As can be seen from the Fig. 4.2, the value of $\text{div } \mathbf{v}$ characterizing the incompressibility condition does not exceed $2 \cdot 10^{-12}$.

4.2.2 Convection Induced by Korteweg Stresses in Miscible Liquids

Numerical simulation of the flow of a more complex model of a viscous incompressible liquid, was considered in articles Bessonov et al. (2004), Bessonov (2008), Pojman et al. (2009). The model includes The Navier–Stokes equations with an additional term, the Korteweg stress term arising from non-local interactions in the fluid (Korteweg 1901). The problem formulated in a Lagrangian form that is better adapted to describe the numerical method based on Lagrangian mesh:

$$\nabla \cdot \mathbf{v} = 0, \quad (4.17)$$

$$\rho \frac{d\mathbf{v}}{dt} = \nabla \cdot (\boldsymbol{\sigma} + \mathbf{K}), \quad (4.18)$$

$$\rho \frac{dc}{dt} = \nabla \cdot (D\nabla c), \quad (4.19)$$

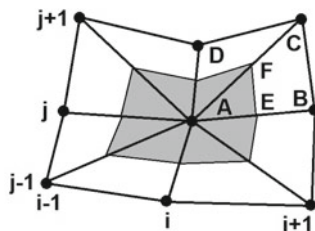
$$\rho c_p \frac{dT}{dt} = \nabla \cdot (\lambda \nabla T), \quad (4.20)$$

where $\boldsymbol{\sigma} = -p\mathbf{I} + \mu(\nabla\mathbf{v} + \mathbf{v}\nabla)$ is the viscous stress tensor; $\mathbf{K} = k[(\nabla c \cdot \nabla c)\mathbf{I} + (\nabla c \nabla c)]$ is the Korteweg stress tensor; \mathbf{v} is the velocity; ρ is the density; c the composition, i.e., the function which changes between 0 and 1 such that $c = 0$ corresponds to one liquid and $c = 1$ to the other; D is the diffusion coefficient; c_p is the heat capacity; T is the nondimensional temperature; λ is thermal conductivity; p is the pressure; μ is the dynamic viscosity; k is the Korteweg coefficient depends of the c and T (Bessonov et al. 2004; Bessonov 2008; Pojman et al. 2009); $\mathbf{a} \cdot \mathbf{b}$ is the scalar product; \mathbf{ab} is a dyadic product; \mathbf{I} is the unit tensor; $d(\dots)/dt = \partial(\dots)/\partial t + \nabla \cdot (\mathbf{v}(\dots))$.

For numerical simulations of the problem (4.17)–(4.20), the finite-volume method was applied. We use an adaptive nonorthogonal Lagrangian mesh $I \times J$ ($i = 1, \dots, I$, $j = 1, \dots, J$). Its fragment is shown in Fig. 4.3.

Each cell of the mesh (ABCD in Fig. 4.3) consists of two triangular elements (ABC and ACD). The direction of the cell diagonal alternates in the neighboring cell.

Fig. 4.3 A fragment of the mesh. The control volume V_A is gray



The structure of the equations suggests defining the velocity, the composition, and the temperature at the nodes of the mesh (nodal variables), and the component of the stress tensors $\boldsymbol{\sigma}$ and \mathbf{K} are defined inside the triangular elements. Equation (4.17) is also solved at triangular elements.

For each node of the mesh, we introduce a control volume as a polyhedron with the sides passing through the middle points of the sides and diagonals of the cells. In Fig. 4.3, the control volume V_A is shown for the node A .

We integrate the Eqs. (4.18)–(4.20) over each control volume. We have for the node A :

$$\rho \frac{d}{dt} \int_{V_A} \mathbf{v} dV = \int_{S_A} \mathbf{n} \cdot (-p\mathbf{I} + \mu(\nabla \mathbf{v} + \mathbf{v}\nabla) + k[(\nabla c \cdot \nabla c)\mathbf{I} + (\nabla c \nabla c)])^{n+1} dS, \quad (4.21)$$

$$\rho \frac{d}{dt} \int_{V_A} c dV = \int_{S_A} D\mathbf{n} \cdot \nabla c^{n+1} dS, \quad (4.22)$$

$$\rho \frac{d}{dt} \int_{V_A} c_p T dV = \int_{S_A} \lambda \mathbf{n} \cdot \nabla T^{n+1} dS, \quad (4.23)$$

where S_A is a boundary of a V_A ; \mathbf{n} is an external normal to S_A ; and n is the number of the time step. Note that the flux terms in the right-hand sides of (4.21)–(4.23) are taken implicitly in time.

The left-hand sides of the Eqs. (4.21)–(4.23) are approximated as follows:

$$\rho \frac{d}{dt} \int_{V_A} \mathbf{v} dV \approx \rho \frac{\mathbf{v}_A^{n+1} - \mathbf{v}_A^n}{\Delta t} \sum_i V_i, \quad (4.24)$$

$$\rho \frac{d}{dt} \int_{V_A} c dV \approx \rho \frac{c_A^{n+1} - c_A^n}{\Delta t} \sum_i V_i, \quad (4.25)$$

$$\rho \frac{d}{dt} \int_{V_A} c_p T dV \approx \rho \frac{T_A^{n+1} - T_A^n}{\Delta t} \sum_i V_i c_p, \quad (4.26)$$

where \sum_i is a sum over all triangles in the control volume V_A (obviously $\sum_i V_i \equiv V_A$).

The integrals in the right-hand sides of the Eqs. (4.21)–(4.23) are taken over the surfaces of control volumes. To compute these, we need to know the components of the stress tensors and the components of the temperature and concentration gradients. In what follows, we will use a discretization of ∇c , ∇T , $\nabla \cdot \mathbf{v}$, and $\nabla \mathbf{v}$ in triangular elements. For the sake of brevity, we introduce the notation:

$$\nabla \odot \Phi, \quad (4.27)$$

where Φ is the 2D vector or scalar nodal variable; \odot denotes a distributive operation admissible for Φ . We use a linear interpolation of the nodal variable Φ inside each triangle ABC (Bessonov and Song 2001):

$$\Phi = \mathbf{A} \cdot \mathbf{r} + \mathbf{b}, \quad (4.28)$$

where $\mathbf{r} = \mathbf{i}_n x_n$, (summation convention over dummy subscript is used); \mathbf{i}_i are the unit vectors ($i = 1, 2$); and \mathbf{A} and \mathbf{b} are parameters of interpolation. Types of \mathbf{A} (2D tensor or 2D vector) and \mathbf{b} (2D vector or scalar) depend from type of Φ (vector or scalar) reciprocally.

Substituting (4.28) in (4.27) gives

$$\nabla \odot \Phi = \mathbf{i}_n \odot \frac{\partial (\mathbf{A} \cdot \mathbf{i}_m x_m + \mathbf{b})}{\partial x_n} = \mathbf{i}_n \odot (\mathbf{A} \cdot \mathbf{i}_n). \quad (4.29)$$

For the vertices of the triangle ABC, we can write

$$\begin{cases} \Phi_A = \mathbf{A} \cdot \mathbf{r}_A + \mathbf{b} \\ \Phi_B = \mathbf{A} \cdot \mathbf{r}_B + \mathbf{b} \\ \Phi_C = \mathbf{A} \cdot \mathbf{r}_C + \mathbf{b} \end{cases}, \quad (4.30)$$

or

$$\begin{cases} \Phi_1 = \mathbf{A} \cdot \mathbf{r}_1 \\ \Phi_2 = \mathbf{A} \cdot \mathbf{r}_2 \end{cases}, \quad (4.31)$$

where $\Phi_1 = \Phi_B - \Phi_A$, $\Phi_2 = \Phi_C - \Phi_A$, $\mathbf{r}_1 = \mathbf{r}_B - \mathbf{r}_A$, $\mathbf{r}_2 = \mathbf{r}_C - \mathbf{r}_A$. From (4.31), we obtain that

$$\mathbf{A} = \Phi_m \mathbf{r}^m. \quad (4.32)$$

The vectors \mathbf{r}_1 , \mathbf{r}_2 and \mathbf{r}^1 , \mathbf{r}^2 are called reciprocal vectors. It is known that $\mathbf{r}_k \cdot \mathbf{r}^m = \delta_{km}$ and $\mathbf{r}_m \cdot \mathbf{r}^m = \mathbf{r}^m \cdot \mathbf{r}_m = \mathbf{I}$, where δ_{km} is the Kronecker delta symbol. For Cartesian coordinates \mathbf{r}_1 , \mathbf{r}_2 can be written in the form:

$$\mathbf{r}^1 = \frac{1}{D} \begin{vmatrix} \mathbf{i}_1 & \mathbf{i}_2 \\ r_{21} & r_{22} \end{vmatrix}, \quad \mathbf{r}^2 = \frac{1}{D} \begin{vmatrix} r_{11} & r_{12} \\ \mathbf{i}_1 & \mathbf{i}_2 \end{vmatrix}, \quad D = \begin{vmatrix} r_{11} & r_{12} \\ r_{21} & r_{22} \end{vmatrix}. \quad (4.33)$$

Substituting (4.32) in (4.33), we obtain finite-difference approximation for $\nabla \odot \Phi$:

$$\nabla \odot \Phi \approx \mathbf{r}^m \odot \Phi_m, \quad (4.34)$$

or, explicitly

$$\nabla \odot \Phi \approx \mathbf{r}^1 \odot \Phi_1 + \mathbf{r}^2 \odot \Phi_2. \quad (4.35)$$

The discretization of $\nabla \odot \Phi$ in (4.35) given in the triangle ABC is a linear combination of the differences of its values at the vertices.

In particular, for the orthogonal Cartesian mesh, the formula (4.35) looks like

$$\nabla \odot \Phi \approx \mathbf{i}_1 \odot \frac{\Phi_B - \Phi_A}{\Delta x} + \mathbf{i}_2 \odot \frac{\Phi_C - \Phi_A}{\Delta y}, \quad (4.36)$$

where $\Delta x = x_B - x_A$, $\Delta y = y_B - y_A$. We emphasize that similar to the case of the orthogonal mesh (4.36) the differences of nodal values in (4.35) are taken along the mesh lines. It will allow us to use for the nonorthogonal mesh the same algorithms as for the orthogonal mesh.

Let us define the approximation of the integrals in the right-hand sides of the equations (4.21)–(4.23) over the interval FE at the boundary S_A . The outward normal vector to it has the form:

$$\mathbf{n} = \frac{\mathbf{r}^1}{|\mathbf{r}^1|}. \quad (4.37)$$

Using (4.35) and (4.37), we can obtain the finite-difference approximation of the right-hand sides of the equations (4.21)–(4.23) over FE. For example, we obtain the following approximation for (4.23):

$$\int_{FE} \lambda \mathbf{n} \cdot \nabla T \, dS = \frac{1}{2} \lambda \mathbf{r}^1 \cdot (\mathbf{r}^1 T_1 + \mathbf{r}^2 T_2). \quad (4.38)$$

Approximation of the integrals in right-hand sides of (4.21) and (4.22) can be obtained similarly.

Taking into account (4.35), we can represent the approximation of the continuity equation (4.17) in the form:

$$\nabla \cdot \mathbf{v} = \mathbf{r}^1 \cdot \mathbf{v}_1 + \mathbf{r}^2 \cdot \mathbf{v}_2, \quad (4.39)$$

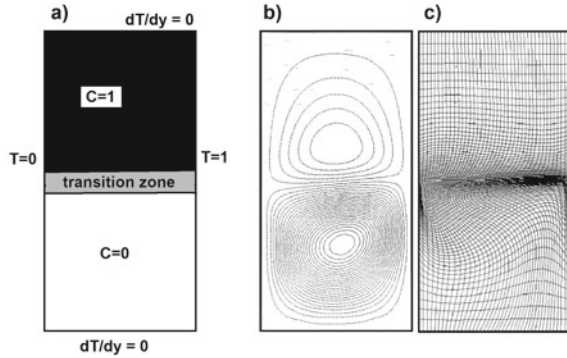
where $\mathbf{v}_1 = \mathbf{v}_B - \mathbf{v}_A$, $\mathbf{v}_2 = \mathbf{v}_C - \mathbf{v}_A$.

For the solution of the discretized equations, we use the iterative method (see Sect. 4.2.1). In Bessonov et al. (2004), Bessonov (2008), the numerical simulations of the system (4.18)–(4.20) in the rectangular domain with the plane transition was done (Fig. 4.4).

The no-slip boundary conditions for the velocity and the no-flux boundary conditions for the concentration were considered.

The stream function field and the numerical mesh (with each second mesh line) are shown in Fig. 4.4b and c. There is one vortex from each side of the transition zone with the upper vortex being essentially weaker than the lower one because of the viscosity dependence on c . The deformation of the numerical mesh in the lower part of the domain is stronger than in the upper part because the liquid velocity there is larger.

Fig. 4.4 a Computational domain and initial composition configuration; b steam function and shape of Lagrangian mesh at time = 1000 s



This sample provides an example of numerical modeling of an incompressible viscous liquid, taking into account the Korteweg effects and using a Lagrangian mesh.

4.3 Rigid Body

The question of finding stresses in the absolutely solid (rigid) body was discussed in literature (Roger and Gianni 2004; Grioni 1983), and more. They relied on the idea that the concept of a rigid body, although different from the concept of an elastic body, it is possible to imagine the development of the former as the limit of the sequence of the latter. In this article, we will try to approach the solution to the problem from the point of view of numerical simulation and numerical experimentation.

The model of a rigid body is used in analytical mechanics when solving dynamic problems that do not include the problem of finding stresses. An absolutely solid body is an ideal structure obtained as the limit of deformable bodies. The determining relation between binding stresses and displacements is not necessary to determine the motion of a solid, unlike deformable continuous media.

In elastic body mechanics, the incompressible condition is used, for example, for the simulation of rubber-like bodies, for which the incompressible condition determines the immutability of the volume, but the shear deformations remain. A large section of hydrodynamics is engaged in describing the behavior of incompressible liquids.

Consider an equation of momentum and constitutive relation for the elastic body (Hooke’s law):

$$\begin{aligned}
 \nabla \cdot \boldsymbol{\sigma} &= 0, \\
 p &= -K(\nabla \cdot \mathbf{u}), \\
 \mathbf{S} &= G(\nabla \mathbf{u} + \mathbf{u} \nabla - 2/3\mathbf{I}(\nabla \cdot \mathbf{u})),
 \end{aligned}
 \tag{4.40}$$

where $\boldsymbol{\sigma} = -p\mathbf{I} + \mathbf{S}$; \mathbf{u} is the displacement. Let stress be given on a part of the outer boundary of the body $\boldsymbol{\sigma}^*$.

Let us write the system in dimensionless form. Introduce the scales as follow: $[L]$ is for length, $[U]$ is for displacement, and $[|\boldsymbol{\sigma}^*|]$ is for stress. Substituting the scales in (4.40), we obtain dimensionless equations

$$\begin{aligned} \nabla \cdot \boldsymbol{\sigma} &= 0, \\ p &= -\frac{K[U]}{[L][|\boldsymbol{\sigma}^*|]}(\nabla \cdot \mathbf{u}), \\ \mathbf{S} &= \frac{G[U]}{[L][|\boldsymbol{\sigma}^*|]}(\nabla \mathbf{u} + \mathbf{u}\nabla - 2/3\mathbf{I}(\nabla \cdot \mathbf{u})). \end{aligned} \quad (4.41)$$

Here and below, the notation for dimensionless quantities (for simplicity) is retained.

Let $[U] = [L][|\boldsymbol{\sigma}^*|]/K$, then Eqs. (4.41) are rewritten in the form:

$$\begin{aligned} \nabla \cdot \boldsymbol{\sigma} &= 0, \\ p &= -\nabla \cdot \mathbf{u}, \\ \mathbf{S} &= \frac{G}{K}(\nabla \mathbf{u} + \mathbf{u}\nabla - 2/3\mathbf{I}(\nabla \cdot \mathbf{u})). \end{aligned} \quad (4.42)$$

In continuum mechanics, incompressibility is represented by the equation:

$$\nabla \cdot \mathbf{v} = 0 \quad (4.43)$$

for hydrodynamics (incompressible liquid) and

$$\nabla \cdot \mathbf{u} = 0 \quad (4.44)$$

for incompressible elastic media. Thus, the system (4.42) can be rewritten for an incompressible elastic media in the form:

$$\begin{aligned} \nabla \cdot \boldsymbol{\sigma} &= 0, \\ \nabla \cdot \mathbf{u} &= 0, \\ \mathbf{S} &= \frac{G}{K}(\nabla \mathbf{u} + \mathbf{u}\nabla - 2/3\mathbf{I}(\nabla \cdot \mathbf{u})). \end{aligned} \quad (4.45)$$

In this article, we propose to do the next step and define a rigid body as

$$\begin{aligned} \nabla \cdot \boldsymbol{\sigma} &= 0, \\ \nabla \cdot \mathbf{u} &= 0, \\ \nabla \mathbf{u} + \mathbf{u}\nabla - 2/3\mathbf{I}(\nabla \cdot \mathbf{u}) &= 0. \end{aligned} \quad (4.46)$$

In other words, in addition to the incompressibility condition (4.45) second equation, the condition associated with the unchanged shape of a body is introduced (4.46) in the third equation.

Let us ask the question: does there exist a nontrivial solution of system (4.46) such that the conditions

$$\mathbf{u} \equiv 0, \quad \boldsymbol{\sigma} \neq 0 \quad (4.47)$$

are satisfied? To answer this question, we have done several numerical experiments.

For the solution of the system (4.46), we applied the next explicit method. Let \mathbf{u}^k , p^k , \mathbf{S}^k , are an initial estimates of \mathbf{u} , p , \mathbf{S} for $k = 0$, where k is a number of iteration.

Step 1:

$$\xi_u^k = -\tau_u (\nabla \cdot \boldsymbol{\sigma}^k),$$

$$\xi_p^k = -\tau_p (\nabla \cdot \mathbf{u}^k),$$

$$\xi_S^k = \tau_S (\nabla \mathbf{u}^k + \mathbf{u}^k \nabla - 2/3 \mathbf{I} (\nabla \cdot \mathbf{u}^k)),$$

$$\max \left(\frac{|\xi_u^k|}{\tau_u}, \frac{|\xi_p^k|}{\tau_p}, \frac{|\xi_S^k|}{\tau_S} \right) < \varepsilon \rightarrow \text{yes} \rightarrow \mathbf{u}^k, p^k, \mathbf{S}^k \text{ are the solution of (46)} \rightarrow \text{STOP}$$

↓

no

↓

Step 2:

$$\mathbf{u}^{k+1} = \xi_u^k,$$

$$p^{k+1} = p^k + \xi_p^k,$$

$$\mathbf{S}^{k+1} = \mathbf{S}^k + \xi_S^k,$$

Go to Step 1.

Here, τ_u , τ_S , and τ_p are an iteration parameters; ε is a small parameter.

Numerical calculations were carried out with double precision. The value ε was chosen equal to $10^{-16} \dots 10^{-18}$ or less.

Consider the results of the numerical simulations.

First example: cylinder under compressive load. The simulation was done in cylindrical coordinates (R, z) (axisymmetric formulation of the problem). The length and diameter of the cylinder are equal to 1. The cylinder is mounted on a rigid base

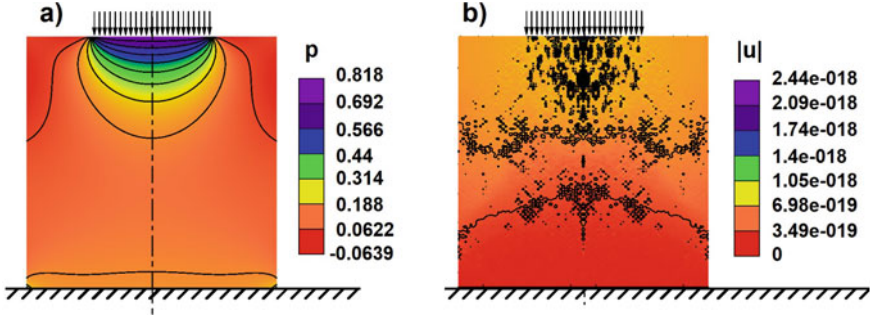


Fig. 4.5 Rigid cylinder. **a** Distribution of the pressure p , **b** Distribution of the displacement modulus $|u|$. $\tau_u = 10^{-6}$, $\tau_p = 2$, $\tau_S = 1$

with the possibility of slipping. A normal component of stress tensor equal to 1 and applied to a region with a radius of 0.5 (Fig. 4.5).

As a result of the simulations, a non-trivial solution was obtained for all components of stress tensor σ , with the complete absence of displacements in the entire computational domain. Figure 4.5 illustrates a distribution of pressure (Fig. 4.5a) and a modulus of displacement $|u|$ (Fig. 4.5b) for a loaded cylinder. As can be seen from the figure, the displacement values in the whole body are equal to or less than $\sim 10^{-18}$.

Such values correspond to zero for the range of numerical values of the quantities involved in the calculation and calculations with double precision.

The numerical experiments show that the results of modeling do not depend on the values of τ_u and depend on the ratio τ_S/τ_p . Different values of this ratio lead to a different distribution of stresses in the body (the displacement values remained below the given small value ε always).

For comparison, a numerical simulation of the same problem was done based on the system (4.42) (elastic body) using the explicit numerical scheme and the next method:

Step 1:

$$\xi_u^k = -\tau(\nabla \cdot \sigma^k),$$

$$\xi_p^k = -\nabla \cdot \mathbf{u}^k,$$

$$\xi_S^k = \frac{G}{K} (\nabla \mathbf{u}^k + \mathbf{u}^k \nabla - 2/3 \mathbf{I}(\nabla \cdot \mathbf{u}^k)),$$

$$\max(|\xi_u^k|/\tau) < \varepsilon \rightarrow \text{yes} \rightarrow \mathbf{u}^k, p^k, \mathbf{S}^k \text{ are the solution of (42)} \rightarrow \text{STOP}$$

↓

no

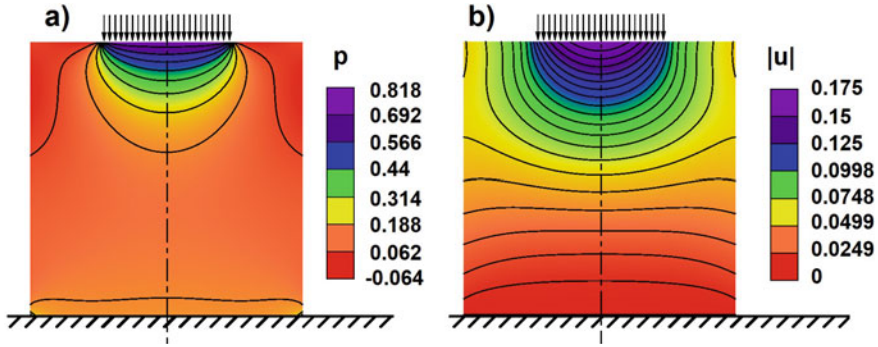


Fig. 4.6 Solid cylinder. **a** Distribution of the pressure p , **b** Distribution of the displacement modulus $|u|$. $\tau = 10^{-6}$, $K = 2$, $G = 1$

↓

Step 2:

$$\mathbf{u}^{k+1} = \mathbf{u}^k + \xi_u^k,$$

$$p^{k+1} = \xi_p^k,$$

$$S^{k+1} = \xi_S^k,$$

Go to Step 1.

Here, τ is an iteration parameter.

Figure 4.6 illustrates a distribution of pressure (Fig. 4.6a) and modulus of displacement $|u|$ (Fig. 4.6b) at the cylinder for $G/K = 0.5$.

We can see that the distributions of pressure in rigid (Fig. 4.5a) and solid (Fig. 4.6a) cylinders are identical. Calculations show that the values of other components of the stress tensor completely coincide.

In contrast, as can be seen from the comparison of (Fig. 4.5b) and (Fig. 4.6b), the distribution of displacement is completely different.

Second sample: I-beam and channel under compressive load (Fig. 4.7). The height and width of the I-beam are equal to 1 and 1 correspondingly. The height and width of the channel are equal to 1 and 0.5 correspondingly. The thickness of their walls equals 0.1. An external normal stress equal to 1 is applied to the top surfaces of the I-beam and channel. Their bottom is mounted on a rigid base with the possibility of slipping.

The simulation was done for Cartesian coordinates (x, y) (2D case, displacement along z axis equal to zero).

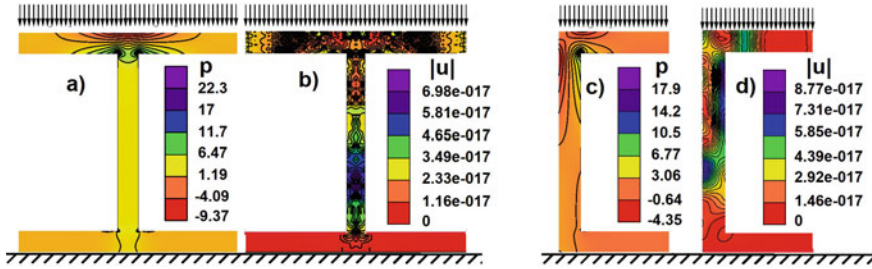


Fig. 4.7 a Distribution of the pressure p in a rigid I-beam, b Distribution of the displacement modulus $|u|$ in a rigid I-beam. c Distribution of the pressure p in a rigid channel, d Distribution of the displacement modulus $|u|$ in a rigid channel. $\tau_u = 10^{-6}$, $\tau_p = 2$, $\tau_s = 1$

Figure 4.7 shows a distribution of pressure in a rigid I-beam (Fig. 4.7a) and in a rigid channel (Fig. 4.7b). The highest values of pressure are observed at the junctions of the shelf and the wall. The pressure field of the I-beam is symmetrical.

As in the previous example, the calculations showed the complete coincidence of the components of the stress tensors calculated according to the model of a rigid body (4.46) and the model of an elastic body (4.42) provided that $\tau_s/\tau_p = G/K$.

The conclusion about the displacements is exactly the same as in the previous example. They are vanishingly small (Fig. 4.7b and d), respectively.

Conclusion. Numerical experiments have shown that stresses in a rigid body can be found, but this problem is ambiguous.

An unambiguous relationship between the stresses in the rigid body and the ratio of the iterative parameters of the numerical algorithm was found.

A correspondence between the ratio of these iterative parameters and the ratio of the elastic moduli of an elastic body is established.

Acknowledgements The authors would like to thank Professor A. M. Krivtsov for his help and many useful discussions.

References

- Bessonov NM, Koleshko SB (1988) Numerical simulation of stationary flow in artificial hearts valve on base of solution of Navier-Stokes equations on nonorthogonal grids. In: Simulation in mechanics, vol 2, p 19, Novosibirsk (by Russian)
- Bessonov NM, Song DJ (2001) Application of vector calculus to numerical simulation of continuum mechanics problems. *J Comput Phys* 167/1
- Bessonov N, Pojman J, Volpert V (2004) Modelling of diffuse interfaces with temperature gradients. *J Eng Math* 49(4):321–338
- Bessonov N, Pojman J, Viner G, Volpert V, Zoltowski B (2008) Instabilities of diffuse interfaces. *Math Model Nat Phenom* 3(1):108–125
- Fletcher CAJ (2006) Computational techniques for fluid dynamics, volume 2, specific techniques for different flow categories. Springer, pp 493

- Fosdick R, Royer-Carfagni G (2004) Stress as a constraint reaction in rigid bodies. *J Elast* 74:265–276
- Grioni G (1983) On the stress in rigid bodies. *Meccanica* 18(1):3–8
- Hirsch C (2007) Numerical computation of internal and external flows. Wiley, New-York, p 656
- Korteweg DJ (1901) Sur la forme que prennent les equations du mouvements des fluides si l'on tient compte des forces capillaires causees par des variations de densite considerables mais continues et sur la theorie de la capillarite dans l'hypothese d'une variation continue de la densite. *Arch Neerl Sci Exactes Nat* 6:1–24
- Pojman JA, Victor Wyatt Y, Bessonov N, Volpert V (2009) Numerical simulations of convection induced by Korteweg stresses in a miscible polymer-monomer system: effects of variable transport coefficients. *Polym Rat Vol Chang Microgravity Sci Technol* 21(3):225–237
- Roache PJ (1998) Fundamentals of computational fluid dynamics. Hermosa Publishers, p 648
- Truesdell C, Noll W (1965) Handbuch der Physik, Band IH/3. In: Die Nicht-Linearen Feldtheorien der Mechanik. Spfingier, Berlin
- Yanenko NN (1967) Method of fractionla steps. Springer, Berlin, p 156

Chapter 5

Numerical Estimation of Resistivity Contribution Tensor of a Concave Pore Embedded in a Transversely Isotropic Matrix



Kou Du, Long Cheng, Jean-François Barthélémy, Igor Sevostianov, Albert Giraud, and Ayodele Adessina

Abstract In this work, we focus on the effect of non-ellipsoidal concave pore on thermal conduction properties of porous media with an infinite transversely isotropic matrix. This effect is described by the resistivity contribution tensors that will be computed via the Finite Elements (FE)-based numerical homogenization. The FE computations will be carried out with some adapted and bounded boundary conditions that are formulated as dependent of the Green function and its gradient for the three-dimensional Poisson's equation in infinite anisotropic medium. It allows to incorporate the matrix anisotropy and the correction of the bias induced by the bounded character of the mesh domain. The boundary conditions are constructed and applied in such a way that they accelerate the convergence of numerical computations, and therefore preserve the accuracy of estimations. This is proved after several appropriate assessment and validation by comparing its predictions, in some particular cases, with analytical results and some available numerical ones. Finally, the effect of the pore concavity as well as that of the matrix anisotropy on the resistivity contribution tensor are quantitatively illustrated.

Keywords Concave shape · Supersphere · Superspheroid · Resistivity contribution tensor · Effective thermal properties · Transversely isotropic matrix

Igor Sevostianov is deceased.

K. Du · L. Cheng · A. Giraud (✉)
GeoResources Laboratory, Université de Lorraine (ENSG), CNRS, CREGU,
Vandoeuvre-lès-Nancy 54518, France
e-mail: albert.giraud@univ-lorraine.fr

J.-F. Barthélémy · A. Adessina
Cerema, Université Gustave Eiffel, UMR MCD, Sourdun 77171, France

I. Sevostianov
Department of Mechanical and Aerospace Engineering, New Mexico State University, Las Cruces
88001, NM, USA

5.1 Introduction

The resistivity contribution tensor has been introduced by Sevostianov and Kachanov (2002) in the context of the cross-property connection between elastic and conductive properties of heterogeneous materials. They have also reported the fact that inclusion shapes affect the elasticity and the conductivity differently.

Recently, an adapted boundary conditions-based numerical method has been proposed by Adessina et al. (2017) dedicated to the numerical resolution of the arbitrary shaped inhomogeneity problem, which induces in practice less expensive time-consuming costs. The resulting estimations can be found to converge for a relatively small matrix domain and the process is shown to be less time-consuming by holding a sufficiently accurate precision. The corrected boundary conditions in this method depend on the elastic properties of the matrix and the method, initially formulated for isotropic matrix only, is extended in the recent work Du et al. (2020) in the case of a transversely isotropic matrix. Application to the diffusion properties of materials with complex microstructures and isotropic matrix is carried out by Adessina et al. (2020). The present work focuses on the conductivity properties of the anisotropic porous materials by estimating the contribution tensor of the concave pore inhomogeneity surrounded by a transversely isotropic matrix. Specifically, superspherical and axisymmetric superspheroidal pores will be particularly considered, whose geometries are respectively described as (Figs. 5.1 and 5.2):

- superspheroidal pore

$$\left| \frac{x_1}{a} \right|^{2p} + \left| \frac{x_2}{a} \right|^{2p} + \left| \frac{x_3}{\zeta a} \right|^{2p} = 1 \quad (5.1)$$

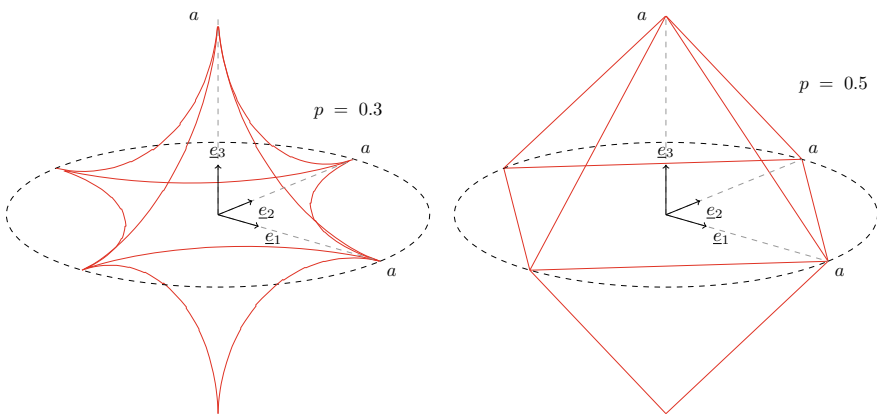


Fig. 5.1 Superspherical pore (relation (5.1) with $\zeta = 1$)

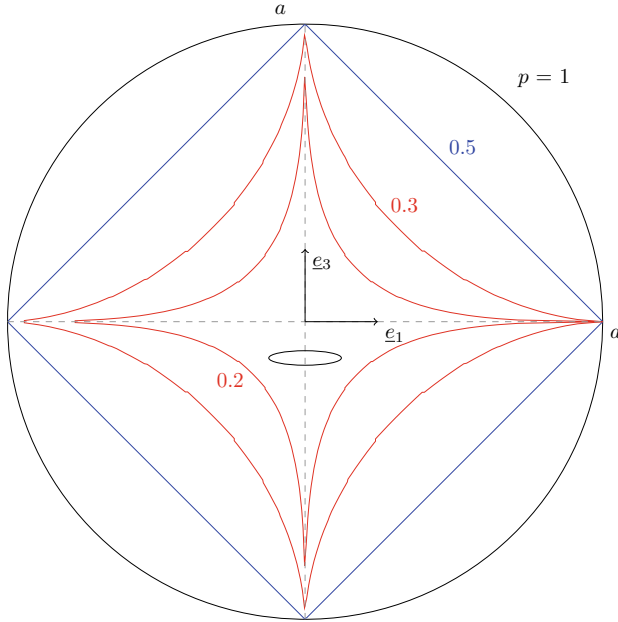


Fig. 5.2 2D representation in diametral plane of a 3D axisymmetrical superspheroidal pore, with $\varsigma = 1$ and symmetry axis x_3

- axisymmetrical superspheroidal pore

$$\left(\frac{x_1^2 + x_2^2}{a^2}\right)^p + \left|\frac{x_3}{\varsigma a}\right|^{2p} = 1 \tag{5.2}$$

p , ς , and a respectively denote non-dimensional concavity parameter, aspect ratio, and semi-lengths in plane $0x_1x_2$. These shapes are convex in the range $p > 0.5$ and concave for $p < 0.5$. Both shapes degenerate into a spheroid when $p = 1$. In what follows we will only consider $\varsigma = 1$ and $a = 1$, the first shape is then a supersphere of unit semi-lengths on x_i axes, and the second shape obtained by a rotation about symmetry axis x_3 . Supersphere and axisymmetrical superspheroid coincide with sphere in the case $p = 1$ but strongly differ in the limiting case $p \rightarrow 0$.

This paper is organized as follows. In Sect. 5.2, the classical concerned problem with an infinite transversely isotropic matrix is reformulated for an inhomogeneity embedded in a finite one by introducing the Green tensor-based correction of boundary conditions. It is then applied in Sect. 5.3 to the reformulation of the contribution tensors. Next, an adapted boundary conditions-based numerical framework is proposed by adopting the numerical homogenization method, which is also assessed and validated by comparing its predictions with some analytical and available numerical results to systematically justify its efficiency and accuracy with respect to the pore

concavity and the material anisotropy. The whole procedure leads to some numerical estimations, as presented in Sect. 5.5, in the cases of the superspheroidal and superspherical voids planted in the transversely isotropic matrix. Particular attention should be paid to the significant combined effect of the material anisotropy and the shape of pore especially when it is concave. We finally present some concluding remarks in Sect. 5.6.

5.2 Green Function-Based Correction of Boundary Conditions

We consider an infinite domain Ω comprising an inhomogeneity \mathcal{E} of arbitrary shape surrounded by a matrix. The matrix is thermally conductive obeying the Fourier law:

$$\underline{\sigma} = -\underline{\lambda} \cdot \underline{\varepsilon} \quad (5.3)$$

where $\underline{\sigma}$, $\underline{\lambda}$, and $\underline{\varepsilon}$ respectively denote the heat flux vector, the thermal conductivity tensor, and thermal gradient with T being the temperature field. Assuming that the infinite domain Ω is submitted to remote Hashin-type boundary condition:

$$T(\underline{x}) \underset{\|\underline{x}\| \rightarrow \infty}{\sim} \underline{E} \cdot \underline{x} \quad (5.4)$$

with $T(\underline{x})$ being the temperature field at the position \underline{x} and \underline{E} denoting the remote homogeneous thermal gradient, the above mentioned problem is described as

$$(\mathcal{P})_{\text{unbounded}} \begin{cases} \operatorname{div}(\underline{\sigma}(\underline{x})) = 0 & (\underline{x} \in \Omega) \\ \underline{\sigma}(\underline{x}) = -\underline{\lambda}(\underline{x}) \cdot \underline{\varepsilon}(\underline{x}) & (\underline{x} \in \Omega) \\ \underline{\varepsilon} = \underline{\operatorname{grad}}T & (\underline{x} \in \Omega) \\ T(\underline{x}) = \underline{E} \cdot \underline{x} & (\underline{x} \in \partial\Omega) \end{cases} \quad (5.5)$$

Borrowing ideas from Adessina et al. (2017) (see also Du et al. 2020), the temperature solution of Eq. (5.5) can be calculated as

$$T(\underline{x}) = \underline{E} \cdot \underline{x} + \int_{\underline{x}' \in \mathcal{E}} \underline{\operatorname{grad}}G_0(\underline{x} - \underline{x}') \cdot \underline{p}(\underline{x}') \, d\Omega_{\underline{x}'} \quad (5.6)$$

with the polarization vector (Ammari and Kang 2007):

$$\underline{p}(\underline{x}) = -[\underline{\lambda}(\underline{x}) - \underline{\lambda}_0] \cdot \underline{\varepsilon}(\underline{x}) \quad (5.7)$$

which is non-zero only in the inhomogeneity \mathcal{E} , and the Green function G_0 for the three-dimensional Poisson equation of the infinite medium with thermal conductivity

λ_0 . The expression of G_0 as well as its gradient $\underline{\text{grad}}G_0$ are briefly recalled in Appendix A. Note that the first term in the r.h.s. of Eq. (5.6) represents the remote temperature field and the second one corresponds to the disturbance caused by the inhomogeneity. We perform an approximation by assuming at the remote location of \underline{x}' (i.e., $\|\underline{x}\| \gg \|\underline{x}'\|$) that

$$G_0(\underline{x} - \underline{x}') \underset{\|\underline{x}\| \rightarrow \infty}{\sim} G_0(\underline{x}) \quad \forall \underline{x}' \in \mathcal{E} \quad (5.8)$$

Eq. (5.6) can then be rewritten as

$$T(\underline{x}) = \underline{E} \cdot \underline{x} + |\mathcal{E}| \underline{\text{grad}} G_0(\underline{x}) \cdot \underline{P} \quad (5.9)$$

in which \underline{P} is the average polarization vector inside the inhomogeneity, reading as

$$\underline{P} = \langle \underline{p} \rangle^{\mathcal{E}} = \frac{1}{|\mathcal{E}|} \int_{\underline{x}' \in \mathcal{E}} \underline{p}(\underline{x}') d\Omega_{\underline{x}'} = \underbrace{\frac{1}{|\mathcal{E}|} \int_{\underline{x}' \in \mathcal{E}} -\lambda(\underline{x}') \cdot \underline{\varepsilon}(\underline{x}') d\Omega_{\underline{x}'}}_{\langle \underline{\sigma} \rangle^{\mathcal{E}}} \quad (5.10)$$

$$+ \lambda_0 \cdot \underbrace{\left[\frac{1}{|\mathcal{E}|} \int_{\underline{x}' \in \mathcal{E}} \underline{\varepsilon}(\underline{x}') d\Omega_{\underline{x}'} \right]}_{\langle \underline{\varepsilon} \rangle^{\mathcal{E}}} \quad (5.11)$$

hence

$$\underline{P} = \langle \underline{\sigma} \rangle^{\mathcal{E}} + \lambda_0 \cdot \langle \underline{\varepsilon} \rangle^{\mathcal{E}} \quad (5.12)$$

with $\langle \underline{\sigma} \rangle^{\mathcal{E}}$ and $\langle \underline{\varepsilon} \rangle^{\mathcal{E}}$ being the averages heat flux and thermal gradient vector of the inhomogeneity, respectively.

In this context, it is crucial to remark that a careful attention should be paid on the approximation given by Eq. (5.8) which is theoretically true when $\|\underline{x}\| \gg \|\underline{x}'\|$. In fact, by developing the Taylor expansion of the remote temperature at \underline{x} , the higher order of the asymptotic behavior (i.e., $\underline{E} \cdot \underline{x}$) may lack of accuracy. Nevertheless, in the perspective of the FE computations, it is convenient to define an appropriate finite mesh scale that we will show in the next sections this approximation delivers very accurate results and thus is used here as well.

Based on Eq. (5.9), the approach of the corrected boundary conditions consist in reformulating the Eshelby like problem Eq. (5.5) into the one on a finite domain \mathcal{D} , which can be expediently written as

$$(\mathcal{P})_{\text{bounded}} \begin{cases} \text{div}(\underline{\sigma}(\underline{x})) = \underline{0} & (\mathcal{D}) \\ \underline{\sigma}(\underline{x}) = -\lambda(\underline{x}) \cdot \underline{\varepsilon}(\underline{x}) & (\mathcal{D}) \\ \underline{\varepsilon} = \underline{\text{grad}} \underline{T} & (\mathcal{D}) \\ T(\underline{x}) = \underline{E} \cdot \underline{x} + |\mathcal{E}| \underline{\text{grad}} G_0(\underline{x}) \cdot \underline{P} & (\partial \mathcal{D}) \end{cases} \quad (5.13)$$

At this point, it is emphasized that the following developments do not require any limitation on the material symmetry of the matrix nor on the shape or content of the inhomogeneity, see for instance (Du et al. 2020) in the context of linear anisotropic elasticity. Due to the linearity of Eq. (5.13), it can be considered as the superposition of two elementary linear thermal problems with different boundary conditions: one is composed by the remote Hashin-type boundary condition $T(\underline{x}) = \underline{E} \cdot \underline{x}$, denoted as the $(\mathcal{P})_{\text{bounded}}^E$ problem:

$$(\mathcal{P})_{\text{bounded}}^E \quad \begin{cases} \operatorname{div}(\underline{\sigma}(\underline{x})) = \underline{0} & (\mathcal{D}) \\ \underline{\sigma}(\underline{x}) = -\underline{\lambda}(\underline{x}) \cdot \underline{\varepsilon}(\underline{x}) & (\mathcal{D}) \\ \underline{\varepsilon} = \underline{\operatorname{grad}} \mathbf{T} & (\mathcal{D}) \\ T(\underline{x}) = \underline{E} \cdot \underline{x} & (\partial\mathcal{D}) \end{cases} \quad (5.14)$$

and according to the polarization field, another one depends on the gradient of the Green function $\underline{\operatorname{grad}}G_0$, named as the $(\mathcal{P})_{\text{bounded}}^P$ problem

$$(\mathcal{P})_{\text{bounded}}^P \quad \begin{cases} \operatorname{div}(\underline{\sigma}(\underline{x})) = \underline{0} & (\mathcal{D}) \\ \underline{\sigma}(\underline{x}) = -\underline{\lambda}(\underline{x}) \cdot \underline{\varepsilon}(\underline{x}) & (\mathcal{D}) \\ \underline{\varepsilon} = \underline{\operatorname{grad}} \mathbf{T} & (\mathcal{D}) \\ T(\underline{x}) = |\mathcal{E}| \underline{\operatorname{grad}}G_0(\underline{x}) \cdot \underline{P} & (\partial\mathcal{D}) \end{cases} \quad (5.15)$$

A direct consequence from the resolution of Eqs. (5.14) and (5.15) is that

$$\langle \underline{\varepsilon} \rangle^E = \mathbf{A}^E \cdot \underline{E}, \quad \langle \underline{\sigma} \rangle^E = -\mathbf{B}^E \cdot \underline{E} \quad (5.16)$$

$$\langle \underline{\varepsilon} \rangle^P = \mathbf{A}^P \cdot \underline{P}, \quad \langle \underline{\sigma} \rangle^P = -\mathbf{B}^P \cdot \underline{P} \quad (5.17)$$

where $\langle \underline{\varepsilon} \rangle^E$, $\langle \underline{\varepsilon} \rangle^P$, $\langle \underline{\sigma} \rangle^E$ and $\langle \underline{\sigma} \rangle^P$ respectively denote the average thermal gradient and heat flux vectors over the inhomogeneity, and \mathbf{A}^E , \mathbf{A}^P , \mathbf{B}^E , and \mathbf{B}^P are the second-order concentration tensors.

By taking into account the linearity of Eqs. (5.13)–(5.15) and combining Eqs. (5.16) and (5.17), one has

$$\begin{cases} \langle \underline{\varepsilon} \rangle^{\mathcal{E}} = \mathbf{A}^E \cdot \underline{E} + \mathbf{A}^P \cdot \underline{P} \\ \langle \underline{\sigma} \rangle^{\mathcal{E}} = -\mathbf{B}^E \cdot \underline{E} - \mathbf{B}^P \cdot \underline{P} \end{cases} \quad (5.18)$$

Next, substituting expression (5.18) in (5.11) renders

$$\underline{P} = \mathbf{D} \cdot \underline{E} \quad (5.19)$$

where

$$\mathbf{D} = (\mathbf{i} + \mathbf{B}^p - \lambda_0 \cdot \mathbf{A}^p)^{-1} \cdot (\lambda_0 \cdot \mathbf{A}^E - \mathbf{B}^E) \quad (5.20)$$

with \mathbf{i} being the second order identity tensor. At this stage, it is a simple matter to combine Eqs. (5.18)–(5.20) to finally establish the main result of this section:

$$\begin{cases} \langle \underline{\varepsilon} \rangle^\mathcal{E} = \mathbf{A}_0^\mathcal{E} \cdot \underline{E}, & \mathbf{A}_0^\mathcal{E} = \mathbf{A}^E + \mathbf{A}^p \cdot \mathbf{D} \\ \langle \underline{\sigma} \rangle^\mathcal{E} = -\mathbf{B}_0^\mathcal{E} \cdot \underline{E}, & \mathbf{B}_0^\mathcal{E} = \mathbf{B}^E + \mathbf{B}^p \cdot \mathbf{D} \end{cases} \quad (5.21)$$

where $\mathbf{A}_0^\mathcal{E}$ and $\mathbf{B}_0^\mathcal{E}$ denote respectively the average thermal gradient and heat flux concentration tensors of the bounded problem Eq. (5.13).

5.3 Conductivity and Resistivity Contribution Tensors

We closely followed in this section the presentation of property contribution tensors given in Kachanov and Sevostianov (2018) and recalled in recent paper (Du et al. 2020) devoted to elastic problem. Still in the context of linear conduction law, the extra thermal gradient (denoted by $\Delta \underline{\varepsilon}$) and heat flux vector (denoted by $\Delta \underline{\sigma}$) induced by the presence of inhomogeneity can be calculated in the dilute scheme as

$$\Delta \underline{\varepsilon} = -f \mathbf{H}_0^\mathcal{E} \cdot \underline{\Sigma}, \quad \Delta \underline{\sigma} = -f \mathbf{N}_0^\mathcal{E} \cdot \underline{E} \quad \text{with } f = \frac{|\mathcal{E}|}{|\Omega|} \quad (5.22)$$

where f denotes the volume fraction of the inhomogeneity and, $\mathbf{H}_0^\mathcal{E}$ and $\mathbf{N}_0^\mathcal{E}$ are both symmetric second rank tensors called the resistivity and conductivity contribution tensors, respectively¹. Moreover, the consistency laws ensuring that $\underline{\Sigma}$ and \underline{E} are also the average heat flux and thermal gradient vectors within a representative elementary volume (REV):

$$\underline{\Sigma} = (1 - f) \langle \underline{\sigma} \rangle^{\text{matrix}} + f \langle \underline{\sigma} \rangle^\mathcal{E} \quad (5.23)$$

$$\underline{E} = (1 - f) \langle \underline{\varepsilon} \rangle^{\text{matrix}} + f \langle \underline{\varepsilon} \rangle^\mathcal{E} \quad (5.24)$$

As matrix being homogeneous, by applying the Fourier Law, the average heat flux of the matrix can be written as

$$\langle \underline{\sigma} \rangle^{\text{matrix}} = -\lambda_0 \cdot \langle \underline{\varepsilon} \rangle^{\text{matrix}} = \frac{1}{1 - f} (-\lambda_0 \cdot \underline{E} + f \lambda_0 \cdot \langle \underline{\varepsilon} \rangle^\mathcal{E}) \quad (5.25)$$

Combining Eqs. (5.23) and (5.25), one has

$$\underline{\Sigma} = (1 - f) \langle \underline{\sigma} \rangle^{\text{matrix}} + f \langle \underline{\sigma} \rangle^\mathcal{E} = -\lambda_0 \cdot \underline{E} + f \lambda_0 \cdot \langle \underline{\varepsilon} \rangle^\mathcal{E} + f \langle \underline{\sigma} \rangle^\mathcal{E} \quad (5.26)$$

¹ The property contribution tensors then turn into conductivity \mathbf{N} and resistivity \mathbf{H} contribution tensors in contrast with the elasticity, the reader is referred for instance to Du et al. (2020).

and then

$$\underline{\Sigma} = -\lambda_0 \cdot \underline{E} + \underbrace{f \left(\langle \underline{\sigma} \rangle^{\mathcal{E}} + \lambda_0 \cdot \langle \underline{\varepsilon} \rangle^{\mathcal{E}} \right)}_{\Delta \underline{\sigma}} \quad (5.27)$$

By taking into account the polarization vector \underline{P} inside the inhomogeneity \mathcal{E} given in relation Eq. (5.11), consistency equation rewrites

$$\underline{\Sigma} = -\lambda_0 \cdot \underline{E} + \underbrace{f \underline{P}}_{\Delta \underline{\sigma}} \quad (5.28)$$

Comparison with relation Eqs. (5.22) and (5.19) allows to obtain a new expression of the conductivity contribution tensor $\mathbf{N}_0^{\mathcal{E}}$ which is approximated here by \mathbf{D} uniquely:

$$\mathbf{N}_0^{\mathcal{E}} = -\mathbf{D} = -(\mathbf{i} + \mathbf{B}^P - \lambda_0 \cdot \mathbf{A}^P)^{-1} \cdot (\lambda_0 \cdot \mathbf{A}^E - \mathbf{B}^E) \quad (5.29)$$

The contribution tensors $\mathbf{H}_0^{\mathcal{E}}$ and $\mathbf{N}_0^{\mathcal{E}}$ of a given inhomogeneity of any shape are interrelated as follows Sevostianov et al. (2008):

$$\mathbf{H}_0^{\mathcal{E}} = -\mathbf{r}_0 \cdot \mathbf{N}_0^{\mathcal{E}} \cdot \mathbf{r}_0, \quad \mathbf{N}_0^{\mathcal{E}} = -\lambda_0 \cdot \mathbf{H}_0^{\mathcal{E}} \cdot \lambda_0 \quad (5.30)$$

5.3.1 Case of Homogeneous Inhomogeneity

In the case of a homogeneous material with thermal conductivity tensor $\lambda(\underline{x}) = \lambda_{\mathcal{E}}$ in the inhomogeneity $\underline{x} \in \mathcal{E}$, by applying the Fourier Law on average heat flux and thermal gradient $\langle \underline{\sigma} \rangle^{\mathcal{E}} = -\lambda_{\mathcal{E}} \cdot \langle \underline{\varepsilon} \rangle^{\mathcal{E}}$, the partial concentration tensors have the following relations:

$$\mathbf{B}^E = \lambda_{\mathcal{E}} \cdot \mathbf{A}^E, \quad \mathbf{B}^P = \lambda_{\mathcal{E}} \cdot \mathbf{A}^P \quad (5.31)$$

It follows that Eq.(5.29) becomes

$$\mathbf{N}_0^{\mathcal{E}} = -\mathbf{D} = [(\lambda_{\mathcal{E}} - \lambda_0)^{-1} + \mathbf{A}^P]^{-1} \cdot \mathbf{A}^E \quad (5.32)$$

By using relations (5.22–5.27), one has

$$\Delta \underline{\sigma} = f \left(\langle \underline{\sigma} \rangle^{\mathcal{E}} + \lambda_0 \cdot \langle \underline{\varepsilon} \rangle^{\mathcal{E}} \right) = -f \mathbf{N}_0^{\mathcal{E}} \cdot \underline{E} \quad (5.33)$$

and consequently

$$\langle \underline{\sigma} \rangle^{\mathcal{E}} + \lambda_0 \cdot \langle \underline{\varepsilon} \rangle^{\mathcal{E}} = -\mathbf{N}_0^{\mathcal{E}} \cdot \underline{E} \quad (5.34)$$

and then combining with the Fourier law, the average thermal gradient is derived in the form:

$$\langle \underline{\varepsilon} \rangle^{\mathcal{E}} = (\lambda_{\mathcal{E}} - \lambda_0)^{-1} \cdot \mathbf{N}_0^{\mathcal{E}} \cdot \underline{E} \quad (5.35)$$

Finally, we get the following connection between the concentration and contribution tensors by comparing to relation (5.21):

$$\mathbf{A}_0^{\mathcal{E}} = (\lambda_{\mathcal{E}} - \lambda_0)^{-1} \cdot \mathbf{N}_0^{\mathcal{E}}, \quad \mathbf{B}_0^{\mathcal{E}} = \lambda_{\mathcal{E}} \cdot \mathbf{A}_0^{\mathcal{E}} \quad (5.36)$$

So that the concentration and contribution tensors can be calculated from each other.

Note that the particular consideration of the *perfectly insulating inhomogeneity* $\lambda_{\mathcal{E}} \rightarrow 0$ leads to the fact that the heat flux concentration tensors \mathbf{B}^E and \mathbf{B}^P both vanish. In practical applications, pore inhomogeneities fully saturated by dry air can be approximated, in a first approach, by the limiting case of the perfectly insulating inhomogeneity, due to the low thermal conductivity of dry air compared to most of solids constituting geomaterials. Consequently, the conductivity contribution tensor $\mathbf{N}_0^{\mathcal{E}}$ (see Eq. (5.32)) and the resistivity contribution tensor $\mathbf{H}_0^{\mathcal{E}}$ can be simplified as

$$\mathbf{N}_0^{\mathcal{E}} = (-\mathbf{r}_0 + \mathbf{A}^P)^{-1} \cdot \mathbf{A}^E, \quad \mathbf{H}_0^{\mathcal{E}} = \mathbf{r}_0 \cdot (\mathbf{r}_0 - \mathbf{A}^P)^{-1} \cdot \mathbf{A}^E \cdot \mathbf{r}_0 \quad (5.37)$$

And average thermal gradient concentration tensor $\mathbf{A}_0^{\mathcal{E}}$ may be deduced from relation Eq. (5.36)

$$\mathbf{A}_0^{\mathcal{E}} = -\mathbf{r}_0 \cdot \mathbf{N}_0^{\mathcal{E}} = \mathbf{r}_0 \cdot (\mathbf{r}_0 - \mathbf{A}^P)^{-1} \cdot \mathbf{A}^E \quad (5.38)$$

In the case of an infinity conductivity inhomogeneity $\lambda_{\mathcal{E}} \rightarrow \infty$, the thermal gradient concentration tensors \mathbf{A}^E and \mathbf{A}^P both vanish. Equation (5.29) becomes

$$\mathbf{N}_0^{\mathcal{E}} = -\mathbf{D} = (\mathbf{i} + \mathbf{B}^P)^{-1} \cdot \mathbf{B}^E \quad (5.39)$$

and the dual resistivity contribution tensor becomes

$$\mathbf{H}_0^{\mathcal{E}} = -\mathbf{r}_0 \cdot (\mathbf{i} + \mathbf{B}^P)^{-1} \cdot \mathbf{B}^E \cdot \mathbf{r}_0 \quad (5.40)$$

and the thermal gradient concentration tensor $\mathbf{A}_0^{\mathcal{E}}$ vanishes.

5.3.2 Case of Ellipsoidal Inhomogeneity

For a general isolated ellipsoidal inclusion, the conductivity $\mathbf{N}_0^{\mathcal{E}}$ and resistivity $\mathbf{H}_0^{\mathcal{E}}$ contribution tensors have explicit forms in terms of Hill polarization tensors:

$$\mathbf{N}_0^\mathcal{E} = [\mathbf{P}_0^\mathcal{E} + (\lambda_\mathcal{E} - \lambda_0)^{-1}]^{-1}, \quad \mathbf{H}_0^\mathcal{E} = [\mathbf{Q}_0^\mathcal{E} + (\mathbf{r}_\mathcal{E} - \mathbf{r}_0)^{-1}]^{-1} \quad (5.41)$$

where $\mathbf{Q}_0^\mathcal{E}$ and $\mathbf{P}_0^\mathcal{E}$ are Hill polarization tensors. Their analytical expressions are available for inclusion in spheroidal shape (ellipsoid of revolution) embedded in a transversely isotropic matrix (see Appendix B).

The thermal gradient concentration tensor $\mathbf{A}_0^\mathcal{E}$ is then derived:

$$\mathbf{A}_0^\mathcal{E} = [\mathbf{i} + \mathbf{P}_0^\mathcal{E} \cdot (\lambda_\mathcal{E} - \lambda_0)]^{-1} \quad (5.42)$$

And analytical contribution tensors can be obtained by Eq.(5.36) which will be further compared to the numerical results to validate the methodology.

5.4 Numerical Framework of the Resistivity Contribution Tensor Estimate

In this section, the focus is on the numerical procedure for the computation of the resistivity contribution tensors $\mathbf{H}_0^\mathcal{E}$. In order to simplify the notation, we drop the subscript 0 and the superscript \mathcal{E} with the understanding that H_{ij} represents the components of $\mathbf{H}_0^\mathcal{E}$. Moreover, for the sake of keeping this work focused and concise, we especially consider here the inhomogeneity in the case of individual and perfectly insulating pore (denoted also by \mathcal{E}) implemented in the center of a cubically bounded REV \mathcal{D} with a transversely isotropic matrix² $\mathcal{D}_M = \mathcal{D} \setminus \mathcal{E}$. Different shapes of the pore, in particular the non-ellipsoidal concave ones, will be considered whose 3D geometries, as shown in Fig. 5.3, are realized by adopting a user-defined Matlab script. Note that directions of the symmetry between the matrix anisotropy and that of the pore are both aligned on the axis \underline{e}_3 .

Moreover, the REV is meshed by use of the software *Netgen* (Schöberl 1997) with quadratic 3D thermal elements (*DC3D10*) that are compatible with the Finite Elements computations via Abaqus/Standard software (Smith 2009). An example in the case of superspherical pore with $p = 0.4$ is shown in Fig. 5.4. As discussed in Sect. 5.3, such a $(\mathcal{P})_{\text{bounded}}$ problem (e.g., Eq. (5.13)) can be decoupled into $(\mathcal{P})_{\text{bounded}}^E$ and $(\mathcal{P})_{\text{bounded}}^P$ (e.g., Eqs. (5.14) and (5.15)). Hence, the simulation procedure will be simultaneously carried out in two groups that due to the transversely anisotropy, each of them requires two computations. More specifically,

- for $(\mathcal{P})_{\text{bounded}}^E$ problem, temperature loading T^E with boundary thermal gradient respectively along \underline{e}_1 and \underline{e}_3 :

$$T^E = E_i x_i, \quad \underline{E} = E_0 \underline{e}_1 \quad \text{or} \quad \underline{E} = E_0 \underline{e}_3 \quad (5.43)$$

² It is important to emphasize that the proposed approach can be applied to any form of the bounded media and any type of matrix anisotropy.

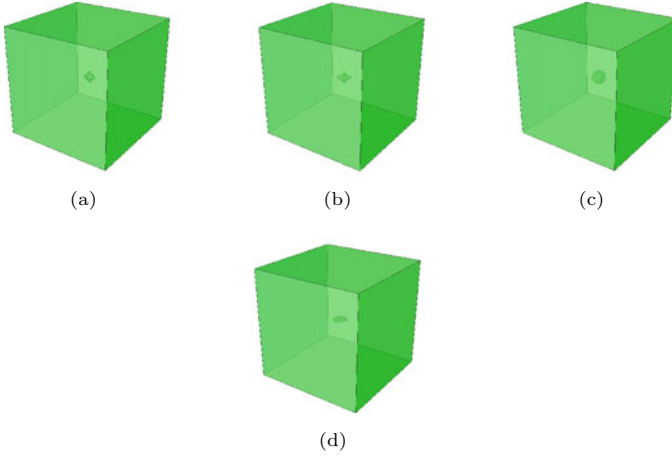
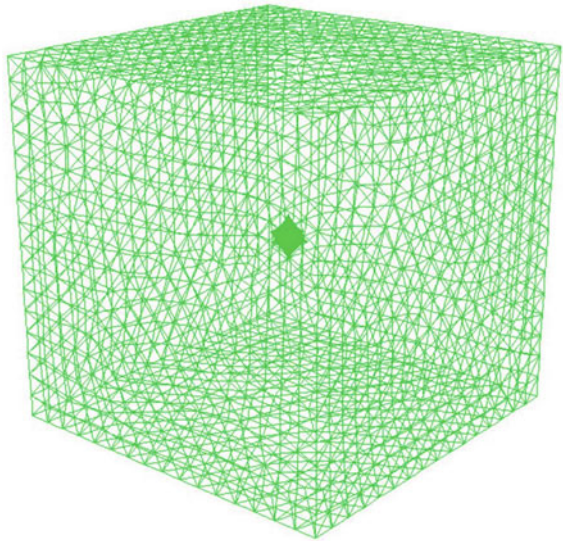


Fig. 5.3 Geometries of different representative models: **a** superspherical pore $p = 0.4$; **b** superspheroidal pore $p = 0.4$; **c** spherical pore $p = 1.0$; **d** aligned penny shaped crack

Fig. 5.4 Mesh of the superspherical pore with the concavity $p = 0.4$ in the center of cuboid matrix



- for $(\mathcal{P})_{\text{bounded}}^p$ problem, temperature loading T^P with boundary polarization vector respectively along \underline{e}_1 and \underline{e}_3 :

$$T^P = |\mathcal{E}| \frac{\partial G}{\partial x_i} P_i, \quad \underline{P} = P_0 \underline{e}_1 \quad \text{or} \quad \underline{P} = P_0 \underline{e}_3 \quad (5.44)$$

5.4.1 Numerical Homogenization Method

As the considered media being defined in a finite domain (i.e., porous media), the numerical homogenization method is adopted for the estimation of the resistivity contribution tensor $\mathbf{H}_0^{\mathcal{E}}$. Following Eq.(5.37), the resistivity concentration tensors \mathbf{A}^E and \mathbf{A}^P will be firstly computed. The consistency laws ensure that the subjected macroscopic thermal gradients are also the average ones, one has

$$\begin{aligned}\langle \underline{\varepsilon} \rangle_{\mathcal{D}}^E &= \underline{E} = (1-f) \langle \underline{\varepsilon} \rangle_{\mathcal{D}_M}^E + f \langle \underline{\varepsilon} \rangle_{\mathcal{E}}^E \\ \langle \underline{\varepsilon} \rangle_{\mathcal{D}}^P &= (1-f) \langle \underline{\varepsilon} \rangle_{\mathcal{D}_M}^P + f \langle \underline{\varepsilon} \rangle_{\mathcal{E}}^P\end{aligned}\quad (5.45)$$

where $\langle \underline{\varepsilon} \rangle_{\mathcal{D}}^E$ and $\langle \underline{\varepsilon} \rangle_{\mathcal{D}}^P$ denote the subjected macroscopic thermal gradient respectively for the $(\mathcal{P})_{\text{bounded}}^E$ and $(\mathcal{P})_{\text{bounded}}^P$ problems, $\langle \underline{\varepsilon} \rangle_{\mathcal{E}}^E$, $\langle \underline{\varepsilon} \rangle_{\mathcal{E}}^P$, $\langle \underline{\varepsilon} \rangle_{\mathcal{D}_M}^E$, and $\langle \underline{\varepsilon} \rangle_{\mathcal{D}_M}^P$ are the corresponding average thermal gradient in the porous phase and those in the matrix one.

Note that in Eq.(5.45), the macroscopic thermal gradient $\langle \underline{\varepsilon} \rangle_{\mathcal{D}}^E$ of the $(\mathcal{P})_{\text{bounded}}^E$ problem is known as predefined, while $\langle \underline{\varepsilon} \rangle_{\mathcal{D}}^P$ of the $(\mathcal{P})_{\text{bounded}}^P$ problem should be calculated. Following the Gauss theorem, the latter one can be obtained as an integral over the external boundary $\partial\mathcal{D}$:

$$\langle \varepsilon_i \rangle_{\mathcal{D}}^P = \frac{1}{|\mathcal{D}|} \sum_{m=1}^{\mathcal{M}} (T^P n_i)^{(m)} S^{(m)} \quad (5.46)$$

where \mathcal{M} is the total number of the surface elements, T^P denotes the nodal temperature of integration points, $S^{(m)}$ is the area of the m-th one, and n_i defines the unit normal of the outer surfaces.

Since the pore is insulated, the heat flux in the porous phase vanishes (i.e., $\langle \underline{\sigma} \rangle_{\mathcal{E}}^E = \langle \underline{\sigma} \rangle_{\mathcal{E}}^P = \mathbf{0}$), it follows that

$$\langle \sigma_i \rangle_{\mathcal{D}_M} = \langle \sigma_i \rangle_{\mathcal{D}} = \frac{1}{|\mathcal{D}_M|} \sum_{n=1}^{\mathcal{N}} (\sigma_i)^{(n)} V^n \quad (5.47)$$

with \mathcal{N} being the total number of the volume elements and $V^{(n)}$ giving the volume of the n-th one.

Following Fourier's Laws, $\langle \varepsilon_i \rangle_{\mathcal{D}_M}^E$ and $\langle \varepsilon_i \rangle_{\mathcal{D}_M}^P$ can then be calculated through

$$\langle \varepsilon_i \rangle_{\mathcal{D}_M} = -r_{ij} \cdot \langle \sigma_j \rangle_{\mathcal{D}_M}$$

Having in hand the above computed quantities, the average thermal gradient fields in the porous phase are expressed as

$$\begin{aligned}\langle \underline{\varepsilon} \rangle_{\mathcal{E}}^E &= \frac{\underline{E} - (1-f) \langle \underline{\varepsilon} \rangle_{\mathcal{D}_M}^E}{f} \\ \langle \underline{\varepsilon} \rangle_{\mathcal{E}}^P &= \frac{\langle \underline{\varepsilon} \rangle_{\mathcal{D}}^P - (1-f) \langle \underline{\varepsilon} \rangle_{\mathcal{D}_M}^P}{f}\end{aligned}\tag{5.48}$$

The concentration and contribution tensors can then be computed by Eqs. (5.21) and (5.37). Due to the transversely isotropy, both of them have 3 non-zero components which are $A_{11} = A_{22}$, A_{33} , $H_{11} = H_{22}$, H_{33} in the present study.

5.4.2 Assessment and Validation of the Proposed Numerical Procedure

In this section, the proposed numerical procedure will be assessed and validated by comparing its predictions of the resistivity contribution tensor $\mathbf{H}_0^{\mathcal{E}}$ with some analytical and numerical results in literature. To this end, a preliminary step aiming at defining an appropriate scale of the bounded REV will be first carried out. It will be accomplished by studying the accuracy and the efficiency of the proposed numerical procedure in the case of a spherical pore planted in an isotropic matrix. Next, we will systematically consider the superspherical pores embedded in an isotropic matrix as well as the spheroidal ones surrounded by a transversely isotropic matrix to respectively justify its accuracy on the concavity of the pores and that on the anisotropy of the matrix material.

5.4.2.1 Spherical Pore in Isotropic Matrix

Let us consider a spherical pore of radius a embedded in the center of a cubic REV with side length $2L$. By varying the so-called scale ratio a/L , the same mesh of each geometry with fixed a/L will be separately subjected to the corrected boundary conditions and the uncorrected ones (i.e., classical Hashin-type boundary conditions). Due to the symmetry of the problem, only one independent component of resistivity contribution tensor H_{11} is numerically computed that will be next compared to the corresponding analytical solution Eq. (B9). The relative errors are displayed in Fig. 5.5. It can be observed that the computation convergence with the corrected boundary conditions occurs and stabilizes even when $a/L \simeq 3$ with an excellent accuracy that the relative errors are around the value of 10^{-4} . Whereas it seems like that those obtained from the classical modeling just begin stabilize when the scale ratio a/L is much bigger (e.g., $a/L \geq 10$) and present important relative errors with respect to the former ones. This can be interpreted as, on one hand the corrections of the boundary conditions allow to accelerate the numerical convergence without degrading the computation accuracy, on the other hand when the scale ratio a/L is

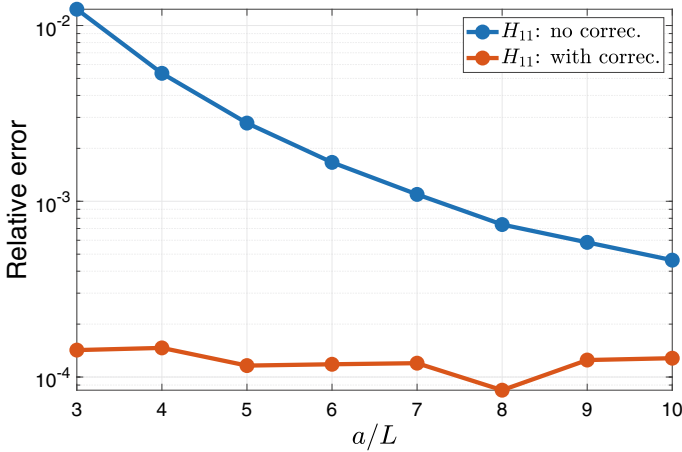


Fig. 5.5 Relative errors of H_{11} with respect to the analytical results for the spherical pore embedded in an isotropic matrix for different scale ratios $a/L \in [3, 10]$

sufficiently big, the representative bounded model tends to be an infinite one such that the correction of the boundary conditions is hence less efficient or might be useless in the numerical modeling. By considering the computation results as illustrated in Fig. 5.5, we adopt in an ad-hoc manner the scale ratio $a/L = 8$ in the next part of this work. This is of course an approximation but will be shown as sufficiently accurate in the following numerical estimations.

5.4.2.2 Superspheroidal Pore in Isotropic Matrix

Table 5.1 displays the numerical results of the resistivity contribution tensor for the superspheroidal pores surrounded by an isotropic matrix as well as their comparisons with the numerical results obtained by Sevostianov et al. (2016). Different geometries and meshes are realized by varying the value of the concavity parameter $p \in [0.2, 1]$. We pay our first attention to the particular case with $p = 1$ (i.e., spherical pore). It can be observed that, by comparing with the computations of Sevostianov et al. (2016), the FEM results obtained in this work present much smaller relative errors with respect to the analytical ones (i.e., $H_{11} = H_{33} = 1.5$). Moreover, the relative error of the FEM results with respect to those of Sevostianov et al. (2016) is shown to be increased as we decrease the concavity parameter p toward the limit value of 0. This difference becomes much significant and cannot be ignored especially for the estimation of H_{11} in the case of the concave pores (i.e., $p < 0.5$). In addition to the corrected boundary conditions that accelerate the computation convergence and preserve the accuracy of estimations, this might also be due to the fact that, as shown in Fig. 5.4, the meshes realized in this work are sufficiently refined in the transition zone between the matrix and porous phases that allows to reduce the effect of the

Table 5.1 Numerical estimations for H_{ij} for the superspheroidal pore embedded in isotropic host matrix with respect to Sevostianov et al. (2016)

| p | H_{11}^{FEM} | H_{33}^{FEM} | $H_{11}^{(2016)^1}$ | $H_{33}^{(2016)^1}$ | $R.E.(H_{11})^2$ (%) | $R.E.(H_{33})^2$ (%) |
|-----------------------|----------------|----------------|---------------------|---------------------|-------------------------|-------------------------|
| 0.2 | 1.4027 | 14.8636 | 2.0247 | 15.1972 | 44.345 | 2.244 |
| 0.25 | 1.3486 | 6.4986 | 1.7156 | 6.6319 | 27.212 | 2.052 |
| 0.3 | 1.3655 | 3.8970 | 1.6400 | 3.9392 | 20.102 | 1.083 |
| 0.35 | 1.3900 | 2.8087 | 1.5486 | 2.8234 | 11.412 | 0.522 |
| 0.4 | 1.4108 | 2.2794 | 1.5290 | 2.2896 | 8.377 | 0.450 |
| 0.5 | 1.4410 | 1.8303 | 1.5063 | 1.8322 | 4.528 | 0.106 |
| 0.7 | 1.4750 | 1.5828 | 1.5091 | 1.5880 | 2.310 | 0.330 |
| 1 | 1.4998 | 1.4998 | 1.5012 | 1.4963 | 0.095 | 0.238 |
| 1^3 | 1.5 | 1.5 | 1.5 | 1.5 | | |
| R.E. ⁴ (%) | 0.012 | 0.012 | 0.083 | 0.250 | | |

¹Numerical results obtained in Sevostianov et al. (2016)

² Relative error of FEM results with respect to those of Sevostianov et al. (2016)

³ Theory

⁴ Relative error of FEM results with respect to the analytical one for $p = 1$

geometric singularity as much as possible³. In return, it reveals that the numerical estimations obtained in the present work from the proposed numerical procedure and the refined meshes can be considered as accurate and precise in the case of isotropic matrix.

Table 5.2 shows the numerical estimation of the resistivity contribution tensor for the superspherical pores surrounded by an isotropic matrix as well as its comparison with respect to that obtained by Chen (2016a). It is worthy to mention that, unlike the superspheroid pores that present the axisymmetry, the superspherical ones are symmetric in all of the three principal directions. Consequently, only H_{11} is displayed in Table 5.2 since its three principal components are identical (i.e., $H_{11} = H_{22} = H_{33}$) and, according to the boundary conditions, the deviatoric ones are all null (i.e., $H_{ij} = 0$ if $i \neq j$). Once again, it can be observed that the FE computation realized in the present work is much more rigorous especially when the pore is concave (i.e., $p < 0.5$).

In order to understand better the aforementioned conclusion, as the superspheroidal pore tends to be a penny crack crossed by a perpendicular needle along the symmetry axis x_3 when the concavity $p \rightarrow 0$, we show in Table 5.3 the comparison between the FEM computations in a *limiting* case with $p = 0.2$, the associated results of Sevostianov et al. (2016) and the analytical ones of an aligned penny crack embedded in the isotropic host matrix. The geometry of the latter one is approximated by considering a very small thickness e such that $e/L = 0.002$ (see Fig. 5.3d) and the corresponding analytical solution can be calculated from Eq. (B10) with the

³ For more details on the mesh information, readers are referred to Appendix C and the Table B.2 of Sevostianov et al. (2016).

Table 5.2 Numerical estimations of H_{11} for the superspherical pore embedded in isotropic host matrix with respect to Chen (2016a)

| p | H_{11}^{FEM} | $H_{11}^{Chen}{}^1$ | $H_{11}^{R.E.}{}^2$ (%) |
|-----------------------|----------------|---------------------|-------------------------|
| 0.2 | 3.9379 | 2.8465 | 27.715 |
| 0.25 | 2.6193 | 2.1166 | 19.191 |
| 0.3 | 2.0892 | 1.7603 | 15.743 |
| 0.35 | 1.8385 | 1.6689 | 9.226 |
| 0.4 | 1.7065 | 1.6421 | 3.776 |
| 0.5 | 1.5856 | 1.5719 | 0.860 |
| 1 | 1.4999 | 1.5111 | 0.749 |
| 3 | 1.5531 | 1.5588 | 0.369 |
| 1^3 | 1.5000 | 1.5000 | |
| R.E. ⁴ (%) | 0.008 | 0.740 | |

¹ Chen (2016a)² Relative error of numerical H_{11} with respect to Chen (2016a)³ Theory⁴ Relative error of FEM results with respect to the analytical one for $p = 1$ **Table 5.3** Numerical estimations for H_{ij} for the crack embedded in isotropic host matrix with respect to the analytical results

| Models | Theory | FE crack Fig. 5.3d | FE superspheroid $p = 0.2$ | Ref. superspheroid ¹ |
|-------------------------|--------|--------------------|----------------------------|---------------------------------|
| H_{11} | 0 | 0.0015 | 0.0598 | 0.0863 |
| H_{33} | 0.6366 | 0.6403 | 0.6336 | 0.6478 |
| Relative Error H_{33} | NA | 0.582% | 0.483% | 1.751% |

¹ Normalized results of Superspheroidal case with $p = 0.2$ in Sevostianov et al. (2016)

anisotropy parameter $\nu = 1$. It is convenient to note here that the obtained resistivity contribution tensor is normalized by the volume fraction $\frac{V^{crack}}{V^{sphere}}$ to avoid the volume effect.. According to the comparison, although a good agreement can be observed among all of the three numerical results and the analytical one, the FE computation obtained from the proposed numerical model presents a very small relative error than the one calculated by Sevostianov et al. (2016).

5.4.2.3 Spherical Pore in Transversely Isotropic Matrix

This section deals with the assessment and validation of the numerical procedure by paying particular attention to the matrix anisotropy. In this light, we switch off the effect of the concavity parameter p by considering that the pore is in a spherical form and the matrix is transversely isotropic. Note once again that the proposed numerical procedure can also be applied to any type of anisotropy, which probably requires

Table 5.4 Numerical estimations for H_{ij} for the spherical pore embedded in transversely isotropic host matrix ($\kappa \in [0.1, 10]$) with respect to the analytical results

| κ | H_{11}^{FEM} | H_{33}^{FEM} | H_{11}^{theory} | H_{33}^{theory} | $H_{11}^{R.E.^1}$ (%) | $H_{33}^{R.E.}$ (%) |
|----------|----------------|----------------|-------------------|-------------------|-----------------------|---------------------|
| 0.1 | 12.1317 | 2.8453 | 12.1322 | 2.8450 | 0.004 | 0.013 |
| 0.2 | 6.4179 | 2.2625 | 6.4184 | 2.2626 | 0.007 | 0.005 |
| 0.5 | 2.7985 | 1.7518 | 2.7988 | 1.7519 | 0.008 | 0.008 |
| 0.8 | 1.8333 | 1.5710 | 1.8335 | 1.5712 | 0.008 | 0.008 |
| 1 | 1.4999 | 1.4999 | 1.5000 | 1.5000 | 0.008 | 0.008 |
| 2 | 0.8022 | 1.3269 | 0.8023 | 1.3271 | 0.008 | 0.008 |
| 5 | 0.3467 | 1.1813 | 0.3468 | 1.1813 | 0.008 | 0.008 |
| 8 | 0.2238 | 1.1321 | 0.2239 | 1.1322 | 0.008 | 0.008 |
| 10 | 0.1815 | 1.1133 | 0.1815 | 1.1134 | 0.008 | 0.008 |

¹ Relative error of numerical H_{11} with respect to analytical one

supplementary simulations and is not further pursued here. Table 5.4 shows the FE computation by varying the anisotropy parameter of the matrix $\kappa = \lambda_0^1/\lambda_0^3$ in the interval $\kappa \in [0.1, 10]$ as well as its comparison with respect to the analytical results (see for instance Sects. 5.3.2 and Appendix B). A very good agreement can be found and the relative errors are shown to be minor. It justifies that the accuracy of the proposed numerical method is unaffected by the matrix anisotropy.

5.5 Numerical Estimation in the Case of Concave Pore Embedded in Transversely Isotropic Matrix

In this section, we propose to carry out the study of the resistivity contribution tensor $\mathbf{H}_0^{\mathcal{E}}$ in the case of transversely isotropic matrix comprising concave pore to understand in more detail their combined effect. This will be carried out by separately varying the anisotropy parameter of the matrix, denoted by κ , and the concavity one p of the concave pores (i.e., superspheroidal and superspherical pores) that will both be defined in relatively large intervals such as $\kappa \in [0.1, 10]$ and $p \in [0.2, 5]$. Again, we restrict the study, particularly in the superspheroidal cases which verify the symmetry of revolution, to the assumption that the directions of the symmetry between the matrix anisotropy and that of the pore are aligned on the same direction \underline{e}_3 (see for instance Fig. 5.3a and b).

In return, for the FE computations, two non-zero and independent components of $\mathbf{H}_0^{\mathcal{E}}$ (i.e., H_{11} and H_{33}) will be computed. This is achieved by the proposed numerical procedure that was described in Sect. 5.4 by fixing the scale ratio of the REV $a/L = 8$. For the sake of prediction accuracy, the numerical computation will be carried out based on the sufficiently refined meshes, for which the numbers of nodes and elements are detailed in Appendix C.

Specifically, Sect. 5.5.1 investigates first the predictions in the case of superspherical pores. As expected, the combined effect of the matrix anisotropy and that of the pore concavity is quantitatively obtained. This effect on the response of the resistivity contribution tensor is also clearly illustrated in the $p - \kappa - H_{ij}$ spaces. In the remaining Sect. 5.5.2, similar study is realized for the superspheroidal pore embedded in the transversely isotropic matrix.

5.5.1 *Superspherical Pore in Transversely Isotropic Matrix*

Tables 5.5 and 5.6 respectively summarize the numerical estimations of H_{11} and H_{33} for the superspherical pores. First of all, it can be found that, by fixing the concavity parameter p , their predictions increase with the decrease of the anisotropy parameter κ . A second very interesting result, observed in any case of a fixed value κ , is that the influence of the concavity parameter p is not monotone. More specifically, the predictions of H_{11} and those of H_{33} both increase with the decrease of the concavity when $p \in [0.2, 1]$, in which this dependence becomes more significant especially when the pore is concave (i.e., $p < 0.5$). While this effect becomes opposite when the pore is severely convex (i.e., $p \in [1, 5]$). Similar observations were done in the numerical study of Chen (2016b), albeit for an isotropic matrix. Moreover, we present in Tables 5.5 and 5.6 the comparison between the numerical estimations of spherical pores $p = 1$ with the corresponding theoretical results. An excellent agreement can be found with the relative error being around 10^{-5} that could indirectly justify the accuracy of the proposed numerical model.

For completeness, Figs. 5.6 and 5.7 illustrate clearly the combined effect of the matrix anisotropy κ and the concavity parameter p . Each of their influences is also projected in the planes $\kappa - H_{ij}$ and $p - H_{ij}$, respectively. As discussed before, these effects are found to be much significant when the pore is concave with an important anisotropy of the matrix.⁴ Specifically, in Fig. 5.6, we observe that the prediction of H_{11} presents a more important evolution and a slower subsequent saturation in the plane $\kappa - H_{11}$ than that in the plane $p - H_{11}$, which quantitatively and qualitatively reveals that the effect of the matrix anisotropy κ seems to be more important than that of the pore concavity p on the component H_{11} . However, unlike the previous observation, Fig. 5.7 illustrates that the matrix anisotropy plays an important role in the estimation of the component H_{33} , which is, as expected, logical due to the colinearity between the geometrical symmetry and the one of the matrix anisotropy.

⁴ It is worthy to emphasize that the so-called important anisotropy is defined in the present work with a small value of κ and in the direction of \mathbf{e}_3 , which is aligned with the symmetry of the concave pore.

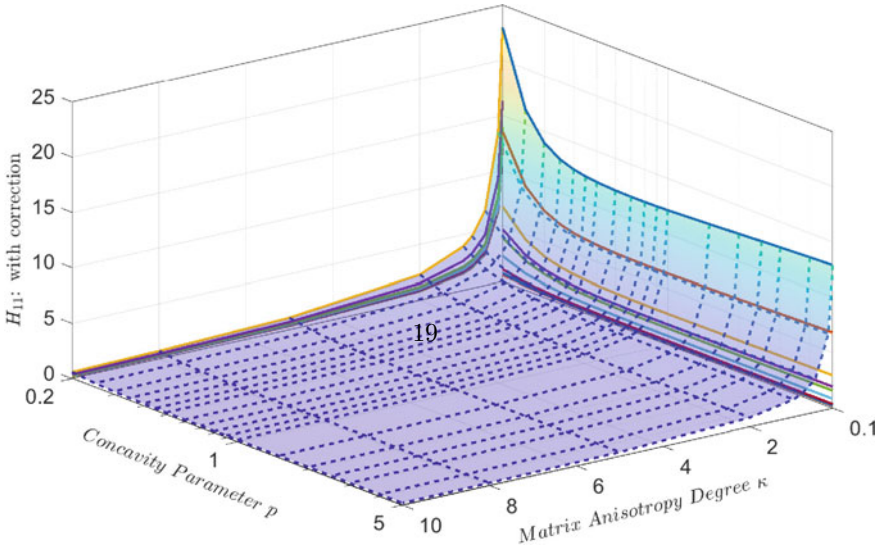


Fig. 5.6 Numerical estimation of H_{11} for the superspherical pore embedded in transversely isotropic corrected model with different concavity parameters $p \in [0.2, 5]$ and anisotropic degrees of matrix $\kappa \in [0.1, 10]$

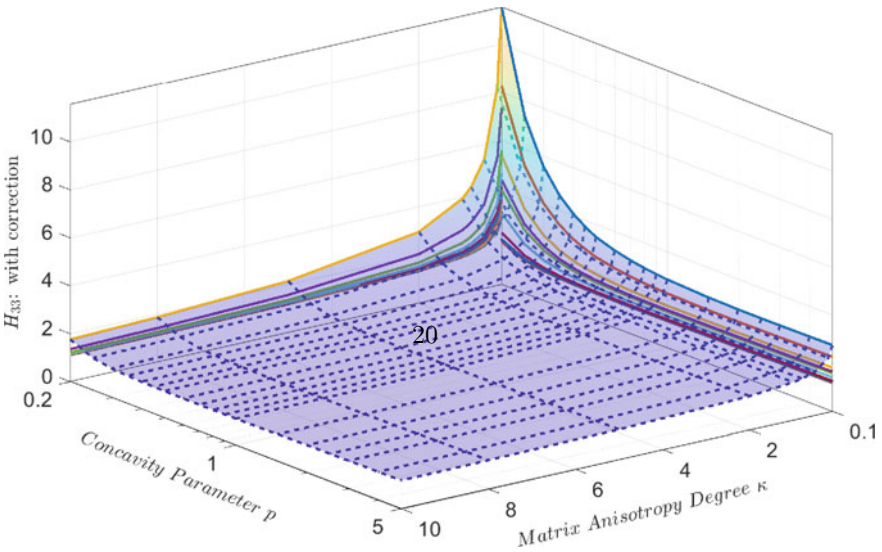


Fig. 5.7 Numerical estimation of H_{33} for the superspherical pore embedded in transversely isotropic corrected model with different concavity parameters $p \in [0.2, 5]$ and anisotropic degrees of matrix $\kappa \in [0.1, 10]$

Table 5.5 Numerical estimation of H_{11} for the superspherical pore embedded in transversely isotropic corrected model with different concavity parameters $p \in [0.2, 5]$ and anisotropic degrees of matrix $\kappa \in [0.1, 10]$

| H_{11} | κ | | | | | | | | |
|-------------------|----------|---------|--------|--------|--------|--------|--------|--------|--------|
| p | 0.1 | 0.2 | 0.5 | 0.8 | 1 | 2 | 5 | 8 | 10 |
| 0.2 | 22.9617 | 13.5471 | 6.7398 | 4.6880 | 3.9382 | 2.2709 | 1.0697 | 0.7186 | 0.5932 |
| 0.25 | 16.3178 | 9.3695 | 4.5467 | 3.1314 | 2.6193 | 1.4907 | 0.6896 | 0.4586 | 0.3767 |
| 0.3 | 13.9588 | 7.8041 | 3.6846 | 2.5097 | 2.0892 | 1.1727 | 0.5332 | 0.3514 | 0.2875 |
| 0.35 | 13.0014 | 7.1289 | 3.2891 | 2.2181 | 1.8385 | 1.0192 | 0.4564 | 0.2987 | 0.2435 |
| 0.4 | 12.5620 | 6.8031 | 3.0872 | 2.0660 | 1.7066 | 0.9369 | 0.4148 | 0.2700 | 0.2196 |
| 0.45 | 12.3382 | 6.6320 | 2.9761 | 1.9807 | 1.6320 | 0.8897 | 0.3908 | 0.2535 | 0.2059 |
| 0.5 | 12.2135 | 6.5328 | 2.9086 | 1.9278 | 1.5856 | 0.8600 | 0.3758 | 0.2432 | 0.1974 |
| 0.6 | 12.1030 | 6.4402 | 2.8420 | 1.8749 | 1.5388 | 0.8301 | 0.3610 | 0.2333 | 0.1892 |
| 0.7 | 12.0720 | 6.4059 | 2.8122 | 1.8499 | 1.5163 | 0.8152 | 0.3536 | 0.2284 | 0.1852 |
| 0.8 | 12.0769 | 6.3984 | 2.7999 | 1.8383 | 1.5055 | 0.8076 | 0.3498 | 0.2259 | 0.1831 |
| 0.9 | 12.0997 | 6.4046 | 2.7967 | 1.8339 | 1.5010 | 0.8038 | 0.3478 | 0.2245 | 0.1820 |
| 1 | 12.1317 | 6.4179 | 2.7985 | 1.8333 | 1.4999 | 0.8022 | 0.3467 | 0.2238 | 0.1815 |
| 1.5 | 12.3122 | 6.5087 | 2.8297 | 1.8496 | 1.5115 | 0.8057 | 0.3472 | 0.2240 | 0.1816 |
| 2 | 12.4641 | 6.5907 | 2.8633 | 1.8702 | 1.5276 | 0.8131 | 0.3498 | 0.2255 | 0.1828 |
| 2.5 | 12.5826 | 6.6559 | 2.8912 | 1.8877 | 1.5416 | 0.8199 | 0.3523 | 0.2271 | 0.1841 |
| 3 | 12.6751 | 6.7071 | 2.9136 | 1.9020 | 1.5531 | 0.8256 | 0.3545 | 0.2284 | 0.1851 |
| 4 | 12.8083 | 6.7815 | 2.9465 | 1.9232 | 1.5702 | 0.8342 | 0.3579 | 0.2305 | 0.1868 |
| 5 | 12.8961 | 6.8316 | 2.9690 | 1.9378 | 1.5820 | 0.8402 | 0.3603 | 0.2320 | 0.1879 |
| 1^{theory} | 12.1322 | 6.4184 | 2.7988 | 1.8335 | 1.5000 | 0.8023 | 0.3468 | 0.2239 | 0.1815 |
| R.E. ¹ | 0.004% | 0.007% | 0.008% | 0.008% | 0.008% | 0.008% | 0.008% | 0.008% | 0.008% |

¹ Relative error of numerical H_{11} with respect to analytical one for $p = 1$

5.5.2 Superspheroidal Pore in Transversely Isotropic Matrix

In this section, we investigate the combined effect of the concavity of the superspheroidal pore and the matrix anisotropy on the resistivity contribution tensor $\mathbf{H}_0^{\mathcal{E}}$, whose non-zero and independent components H_{11} and H_{33} are computed and summarized in Tables 5.7 and 5.8, respectively. Similar to the previous superspherical case discussed in Sect. 5.5.1, the estimations of both H_{11} and H_{33} components increase with the decrease of the anisotropy parameter κ and, present a non-monotone evolution due to the effect of the concavity parameter p . Even this non-monotonicity is so slight that can be neglected, it is worthy to note here that, unlike the superspherical pores discussed before, it occurs when the pore is “*extremely concave*” (e.g., $p \simeq 0.3$) for the component H_{11} and when the pore is “*very severely convex*” for H_{33} (e.g., $p \simeq 3$). A possible interpretation is that, unlike the superspherical cases, the superspheroidal pores present a symmetry of revolution that is colinear

Table 5.6 Numerical estimation of H_{33} for the superspherical pore embedded in transversely isotropic corrected model with different concavity parameters $p \in [0.2, 5]$ and anisotropic degrees of matrix $\kappa \in [0.1, 10]$

| H_{33} | κ | | | | | | | | |
|-------------------|----------|--------|--------|--------|--------|--------|--------|--------|--------|
| p | 0.1 | 0.2 | 0.5 | 0.8 | 1 | 2 | 5 | 8 | 10 |
| 0.2 | 11.5639 | 8.2715 | 5.3713 | 4.3437 | 3.9396 | 2.9602 | 2.1411 | 1.8668 | 1.7623 |
| 0.25 | 7.3694 | 5.3032 | 3.4967 | 2.8651 | 2.6193 | 2.0332 | 1.5619 | 1.4109 | 1.3545 |
| 0.3 | 5.5813 | 4.0483 | 2.7219 | 2.2652 | 2.0893 | 1.6765 | 1.3552 | 1.2551 | 1.2182 |
| 0.35 | 4.6424 | 3.4034 | 2.3392 | 1.9770 | 1.8386 | 1.5170 | 1.2699 | 1.1933 | 1.1650 |
| 0.4 | 4.0904 | 3.0316 | 2.1281 | 1.8229 | 1.7066 | 1.4368 | 1.2290 | 1.1639 | 1.1398 |
| 0.45 | 3.7383 | 2.8009 | 2.0038 | 1.7347 | 1.6321 | 1.3930 | 1.2069 | 1.1480 | 1.1261 |
| 0.5 | 3.4728 | 2.6374 | 1.9223 | 1.6789 | 1.5855 | 1.3664 | 1.1937 | 1.1386 | 1.1181 |
| 0.6 | 3.2161 | 2.4739 | 1.8399 | 1.6227 | 1.5388 | 1.3403 | 1.1811 | 1.1297 | 1.1104 |
| 0.7 | 3.0550 | 2.3784 | 1.7962 | 1.5946 | 1.5163 | 1.3292 | 1.1768 | 1.1270 | 1.1083 |
| 0.8 | 2.9553 | 2.3215 | 1.7723 | 1.5805 | 1.5055 | 1.3253 | 1.1766 | 1.1274 | 1.1087 |
| 0.9 | 2.8900 | 2.2857 | 1.7590 | 1.5737 | 1.5010 | 1.3251 | 1.1784 | 1.1293 | 1.1107 |
| 1 | 2.8453 | 2.2625 | 1.7518 | 1.5710 | 1.4999 | 1.3269 | 1.1813 | 1.1321 | 1.1133 |
| 1.5 | 2.7528 | 2.2223 | 1.7498 | 1.5793 | 1.5115 | 1.3442 | 1.1989 | 1.1483 | 1.1287 |
| 2 | 2.7321 | 2.2212 | 1.7619 | 1.5945 | 1.5276 | 1.3612 | 1.2143 | 1.1623 | 1.1418 |
| 2.5 | 2.7304 | 2.2283 | 1.7746 | 1.6083 | 1.5416 | 1.3750 | 1.2264 | 1.1733 | 1.1522 |
| 3 | 2.7342 | 2.2368 | 1.7857 | 1.6198 | 1.5531 | 1.3859 | 1.2360 | 1.1819 | 1.1604 |
| 4 | 2.7459 | 2.2523 | 1.8031 | 1.6371 | 1.5702 | 1.4019 | 1.2497 | 1.1943 | 1.1723 |
| 5 | 2.7548 | 2.2640 | 1.8154 | 1.6492 | 1.5820 | 1.4127 | 1.2590 | 1.2027 | 1.1801 |
| 1^{theory} | 2.8450 | 2.2626 | 1.7519 | 1.5712 | 1.5000 | 1.3271 | 1.1813 | 1.1322 | 1.1134 |
| R.E. ¹ | 0.013% | 0.005% | 0.008% | 0.008% | 0.008% | 0.008% | 0.008% | 0.008% | 0.008% |

¹ Relative error of numerical H_{33} with respect to analytical one for $p = 1$

with the direction of the matrix anisotropy, which induces an augmentation of the macroscopic anisotropic response of the REV in the direction of \mathbf{e}_3 .

Figures 5.8 and 5.9 show the evolution of the H_{ij} components on the concavity parameter p and the one of the matrix anisotropy κ . As same as the superspherical cases, it can also be finally concluded that both of them significantly affect the resistivity contribution tensor \mathbf{H}_0^ξ .

5.6 Concluding Remarks

In the present work, we have numerically evaluated the resistivity contribution tensor of the concave pore inhomogeneity embedded in a transversely isotropic matrix. This has been realized by use of an original developed numerical homogenization method complying with the adapted boundary conditions-based method recently for-

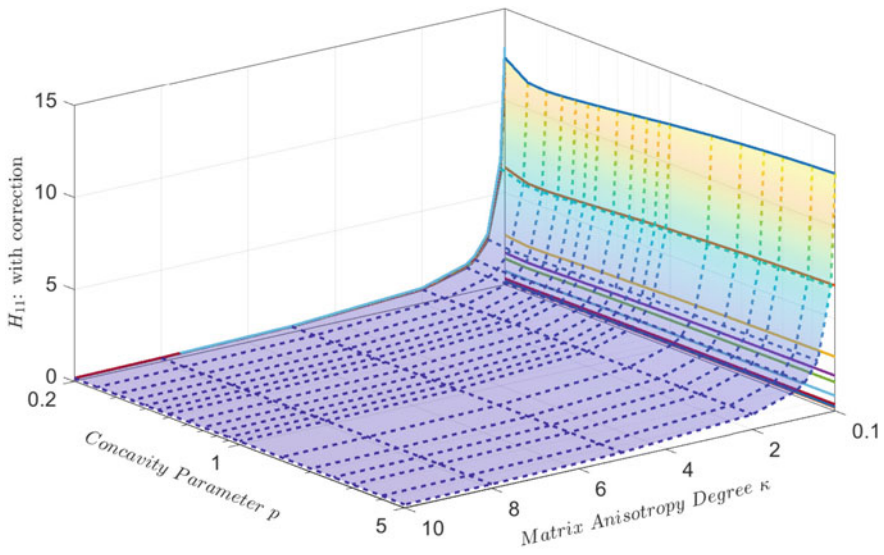


Fig. 5.8 Numerical estimation of H_{11} for the superspheroidal pore embedded in transversely isotropic corrected model with different concavity parameters $p \in [0.2, 5]$ and anisotropic degrees of matrix $\kappa \in [0.1, 10]$

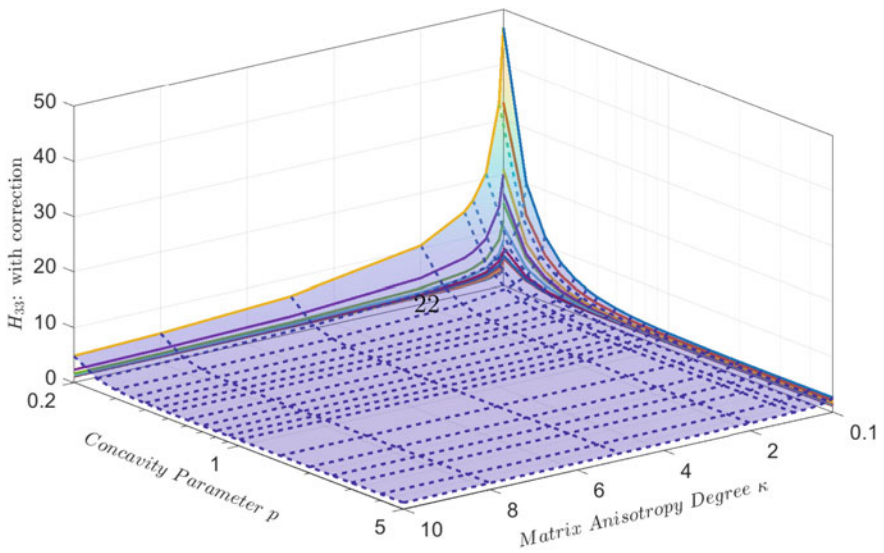


Fig. 5.9 Numerical estimation of H_{33} for the superspheroidal pore embedded in transversely isotropic corrected model with different concavity parameters $p \in [0.2, 5]$ and anisotropic degrees of matrix $\kappa \in [0.1, 10]$

Table 5.7 Numerical estimation of H_{11} for the superspheroidal pore embedded in transversely isotropic corrected model with different concavity parameters $p \in [0.2, 5]$ and anisotropic degrees of matrix $\kappa \in [0.1, 10]$

| H_{11} | κ | | | | | | | | |
|-------------------|----------|--------|--------|--------|--------|--------|--------|--------|--------|
| p | 0.1 | 0.2 | 0.5 | 0.8 | 1 | 2 | 5 | 8 | 10 |
| 0.2 | 12.3240 | 6.3573 | 2.6783 | 1.7264 | 1.4027 | 0.7377 | 0.3163 | 0.2048 | 0.1665 |
| 0.25 | 11.4445 | 5.9539 | 2.5443 | 1.6534 | 1.3486 | 0.7174 | 0.3112 | 0.2022 | 0.1646 |
| 0.3 | 11.3603 | 5.9383 | 2.5587 | 1.6705 | 1.3655 | 0.7308 | 0.3184 | 0.2069 | 0.1684 |
| 0.35 | 11.4181 | 5.9869 | 2.5934 | 1.6982 | 1.3900 | 0.7463 | 0.3257 | 0.2115 | 0.1720 |
| 0.4 | 11.4928 | 6.0393 | 2.6253 | 1.7222 | 1.4108 | 0.7590 | 0.3313 | 0.2150 | 0.1747 |
| 0.45 | 11.5676 | 6.0882 | 2.6526 | 1.7420 | 1.4276 | 0.7687 | 0.3354 | 0.2175 | 0.1767 |
| 0.5 | 11.6357 | 6.1325 | 2.6758 | 1.7581 | 1.4410 | 0.7761 | 0.3384 | 0.2193 | 0.1781 |
| 0.6 | 11.7629 | 6.2106 | 2.7132 | 1.7827 | 1.4610 | 0.7862 | 0.3423 | 0.2216 | 0.1798 |
| 0.7 | 11.8747 | 6.2762 | 2.7420 | 1.8005 | 1.4750 | 0.7926 | 0.3444 | 0.2228 | 0.1807 |
| 0.8 | 11.9718 | 6.3311 | 2.7647 | 1.8140 | 1.4854 | 0.7968 | 0.3456 | 0.2234 | 0.1812 |
| 0.9 | 12.0565 | 6.3777 | 2.7832 | 1.8247 | 1.4934 | 0.7999 | 0.3463 | 0.2237 | 0.1814 |
| 1 | 12.1309 | 6.4176 | 2.7984 | 1.8333 | 1.4998 | 0.8022 | 0.3467 | 0.2238 | 0.1815 |
| 1.5 | 12.3902 | 6.5533 | 2.8482 | 1.8605 | 1.5197 | 0.8086 | 0.3473 | 0.2237 | 0.1812 |
| 2 | 12.5480 | 6.6335 | 2.8767 | 1.8758 | 1.5308 | 0.8121 | 0.3475 | 0.2235 | 0.1810 |
| 2.5 | 12.6529 | 6.6863 | 2.8953 | 1.8859 | 1.5382 | 0.8144 | 0.3477 | 0.2234 | 0.1808 |
| 3 | 12.7291 | 6.7246 | 2.9090 | 1.8934 | 1.5437 | 0.8162 | 0.3479 | 0.2234 | 0.1807 |
| 4 | 12.8302 | 6.7753 | 2.9272 | 1.9035 | 1.5511 | 0.8188 | 0.3483 | 0.2234 | 0.1807 |
| 5 | 12.8947 | 6.8078 | 2.9390 | 1.9101 | 1.5560 | 0.8206 | 0.3486 | 0.2235 | 0.1807 |
| 1 ¹ | 12.1322 | 6.4184 | 2.7988 | 1.8335 | 1.5000 | 0.8023 | 0.3468 | 0.2239 | 0.1815 |
| R.E. ² | 0.011% | 0.012% | 0.012% | 0.012% | 0.012% | 0.012% | 0.013% | 0.014% | 0.014% |

¹ Theory

² Relative error of numerical H_{11} with respect to analytical one for $p = 1$

mulated by Adessina et al. (2017) (see also Du et al. 2020). The proposed numerical procedure was carried out for a bounded representative elementary volume and is shown to be efficient and accurate in the numerical modeling. By paying particular attentions to the pore concavity and the matrix anisotropy, a major contribution of this work is found as the sufficiently exact computation results and analysis that illustrate their significant effect on the thermal conductivity properties. Specifically, the adapted boundary conditions-based method was extended in the context of the matrix anisotropy thanks to the Green function and its gradients applied in the correction of the boundary conditions. The numerical homogenization method has been utilized in the proposed numerical procedure that has been firstly assessed and validated by comparing its predictions with the analytical and existing analytical and numerical results in particular cases. It is then used to the investigate the effect of the pore concavity on different transversely isotropic matrix from the quantitative estimates of the resistivity contribution tensor, which was found to be of critical importance especially in the case of concave pores.

Table 5.8 Numerical estimation of H_{33} for the superspheroidal pore embedded in transversely isotropic corrected model with different parameters $p \in [0.2, 5]$ and anisotropic degrees of matrix $\kappa \in [0.1, 10]$

| H_{33} | κ | | | | | | | | |
|-------------------|----------|---------|---------|---------|---------|---------|--------|--------|--------|
| p | 0.1 | 0.2 | 0.5 | 0.8 | 1 | 2 | 5 | 8 | 10 |
| 0.2 | 46.6772 | 33.0741 | 20.9710 | 16.6040 | 14.8636 | 10.5488 | 6.7387 | 5.3793 | 4.8420 |
| 0.25 | 20.0777 | 14.2620 | 9.0958 | 7.2373 | 6.4986 | 4.6769 | 3.0961 | 2.5473 | 2.3345 |
| 0.3 | 11.6980 | 8.3431 | 5.3758 | 4.3159 | 3.8970 | 2.8752 | 2.0155 | 1.7295 | 1.6214 |
| 0.35 | 8.0643 | 5.7939 | 3.7938 | 3.0862 | 2.8087 | 2.1410 | 1.5982 | 1.4244 | 1.3598 |
| 0.4 | 6.1965 | 4.4925 | 3.0029 | 2.4820 | 2.2794 | 1.7979 | 1.4158 | 1.2955 | 1.2510 |
| 0.45 | 5.1157 | 3.7483 | 2.5636 | 2.1535 | 1.9949 | 1.6207 | 1.3258 | 1.2326 | 1.1980 |
| 0.5 | 4.4280 | 3.2872 | 2.3012 | 1.9614 | 1.8303 | 1.5207 | 1.2753 | 1.1970 | 1.1677 |
| 0.6 | 3.6805 | 2.7923 | 2.0280 | 1.7644 | 1.6623 | 1.4199 | 1.2245 | 1.1611 | 1.1373 |
| 0.7 | 3.2956 | 2.5447 | 1.8958 | 1.6704 | 1.5827 | 1.3728 | 1.2011 | 1.1448 | 1.1235 |
| 0.8 | 3.0741 | 2.4047 | 1.8229 | 1.6194 | 1.5398 | 1.3481 | 1.1895 | 1.1369 | 1.1169 |
| 0.9 | 2.9359 | 2.3185 | 1.7793 | 1.5894 | 1.5148 | 1.3345 | 1.1838 | 1.1333 | 1.1141 |
| 1 | 2.8450 | 2.2623 | 1.7517 | 1.5710 | 1.4998 | 1.3269 | 1.1812 | 1.1321 | 1.1133 |
| 1.5 | 2.6565 | 2.1541 | 1.7061 | 1.5446 | 1.4805 | 1.3224 | 1.1854 | 1.1379 | 1.1194 |
| 2 | 2.6107 | 2.1336 | 1.7047 | 1.5487 | 1.4864 | 1.3317 | 1.1958 | 1.1478 | 1.1290 |
| 2.5 | 2.5980 | 2.1326 | 1.7115 | 1.5574 | 1.4957 | 1.3418 | 1.2052 | 1.1565 | 1.1373 |
| 3 | 2.5978 | 2.1373 | 1.7197 | 1.5664 | 1.5048 | 1.3509 | 1.2133 | 1.1639 | 1.1443 |
| 4 | 2.6048 | 2.1495 | 1.7343 | 1.5812 | 1.5196 | 1.3648 | 1.2255 | 1.1749 | 1.1548 |
| 5 | 2.6141 | 2.1604 | 1.7457 | 1.5923 | 1.5304 | 1.3748 | 1.2340 | 1.1827 | 1.1622 |
| 1 ¹ | 2.8450 | 2.2626 | 1.7519 | 1.5712 | 1.5000 | 1.3271 | 1.1813 | 1.1322 | 1.1134 |
| R.E. ² | 0.001% | 0.011% | 0.012% | 0.012% | 0.012% | 0.012% | 0.012% | 0.012% | 0.013% |

¹ Theory

² Relative error of numerical H_{33} with respect to analytical one for $p = 1$

Finally, the proposed numerical method is able to deal with any general anisotropy of the matrix material but such a study has not been attempted here for the sake of keeping the work focused and concise. In the perspective point of view, it is clear from the previous simulations that the effective properties such as those predicted from semi-analytical homogenization models could be further developed.

Acknowledgements This paper puts an end to a work carried out in collaboration with our late friend, Professor Igor Sevostianov, and is dedicated to his memory.

Appendix A Three-Dimensional Green Function for Poisson's Equation in Infinite Anisotropic Medium

As shown previously, the corrected boundary condition Eq. (5.13) relies on the gradient of Green function. It is worthy to recall that the three-dimensional Green function $G_0(\underline{x})$ for Poisson's equation in infinite anisotropic medium could be analytically calculated by

$$G_0(\underline{x}) = -\frac{1}{4\pi\sqrt{\det(\boldsymbol{\lambda}^0)}} \frac{1}{\sqrt{\underline{x} \cdot (\boldsymbol{\lambda}^0)^{-1} \cdot \underline{x}}} \quad (\text{A1})$$

and its gradient vector is

$$\underline{\text{grad}}G_0(\underline{x}) = \frac{(\boldsymbol{\lambda}_0)^{-1} \cdot \underline{x}}{4\pi\sqrt{\det(\boldsymbol{\lambda}_0)} [\underline{x} \cdot (\boldsymbol{\lambda}_0)^{-1} \cdot \underline{x}]^{3/2}} \quad (\text{A2})$$

The expanded formula for $\text{grad}G_0^i$ component writes

$$\text{grad}G_0^i = \frac{1}{4\pi\sqrt{\lambda_0^1\lambda_0^2\lambda_0^3}} \frac{x_i}{\lambda_0^i} \frac{1}{\left(\frac{x_1^2}{\lambda_0^1} + \frac{x_2^2}{\lambda_0^2} + \frac{x_3^2}{\lambda_0^3}\right)^{3/2}} \quad (\text{A3})$$

where λ_0^1 , λ_0^2 , and λ_0^3 are the three conductivity parameters of anisotropic matrix.

In particular isotropic case which means $\lambda_0^i = \lambda_0$ ($i = 1, 3$), the equations Eqs. (A1)–(A2) reduce to

$$G_0(\underline{x}) = -\frac{1}{4\pi\lambda_0} \frac{1}{\|\underline{x}\|}, \quad \underline{\text{grad}}G_0(\underline{x}) = \frac{1}{4\pi\lambda_0} \frac{\underline{x}}{\|\underline{x}\|^2} \quad (\text{A4})$$

Appendix B Hill Polarization Tensor and Resistivity Contribution Tensor of a Spheroidal Inclusion Aligned in a Transversely Isotropic Host Matrix

One considers a transversely isotropic matrix of conductivity tensor λ_0 (\underline{n} denotes unit vector on the symmetry axis, in this paper $\underline{n} = \underline{e}_3$):

$$\boldsymbol{\lambda}_0 = \lambda_0 (\nu^2 \mathbf{i}_T + \mathbf{i}_N), \quad \mathbf{i}_N = \underline{n} \otimes \underline{n}, \quad \mathbf{i}_T = \mathbf{i} - \mathbf{i}_N \quad (\text{B5})$$

The Hill polarization tensor $\mathbf{P}_0^\mathcal{E}$ of an spheroidal inclusion aligned in the directions of a transversely isotropic matrix (i.e., spheroid and matrix have the same symmetry axis) writes

$$\mathbf{P}_0^\mathcal{E} = \frac{g(\nu\gamma)}{\nu^2\lambda_0}\mathbf{i}_T + \frac{1-2g(\nu\gamma)}{\lambda_0}\mathbf{i}_N \quad (\text{B6})$$

where γ is the aspect ratio of radius and with shape function $g(\xi)$ (see Barthélémy 2008; Giraud et al. 2019)

$$g(\xi) = \begin{cases} \frac{1}{2} \left(1 + \frac{1}{\xi^2 - 1} \left(1 - \frac{\xi}{\sqrt{1 - \xi^2}} \arctan \left(\frac{\sqrt{1 - \xi^2}}{\xi} \right) \right) \right) & \text{if } \xi < 1 \\ \frac{1}{3} & \text{if } \xi = 1 \\ \frac{1}{2} \left(1 + \frac{1}{\xi^2 - 1} \left(1 - \frac{\xi}{2\sqrt{\xi^2 - 1}} \ln \left(\frac{\xi + \sqrt{\xi^2 - 1}}{\xi - \sqrt{\xi^2 - 1}} \right) \right) \right) & \text{if } \xi > 1 \end{cases} \quad (\text{B7})$$

By inserting (B6) into (5.41) and with the relationship (5.30), resistivity contribution tensor $\mathbf{H}_0^\mathcal{E}$ of an insulating $\lambda_\mathcal{E} = \mathbf{0}$ aligned spheroidal pore writes

$$\mathbf{H}_0^\mathcal{E} = \frac{1}{\nu^2\lambda_0(1-g(\nu\gamma))}\mathbf{i}_T + \frac{1}{2\lambda_0g(\nu\gamma)}\mathbf{i}_N \quad (\text{B8})$$

and the particular case of the spherical pore $\gamma = 1$ embedded in an isotropic matrix $\nu = 1$ is recovered

$$\mathbf{H}_0^\mathcal{E} = \frac{3}{2\lambda_0}\mathbf{i} \quad (\text{B9})$$

For the limiting case of an aligned penny shaped crack embedded in a TI matrix, the resistivity contribution tensor writes

$$\mathbf{H}_0^\mathcal{E} = \frac{2}{\pi\lambda_0\nu}\mathbf{i}_N \quad (\text{B10})$$

Appendix C Information of Meshes for the FEM Computations in the Case of Cubic Model Containing Concave Pore

We provide in Tables C1 and C2 the mesh information during the FEM computation for cubically bounded representative elementary volume containing respectively the superspheroidal and the superspherical pore. The displayed numbers of nodes and

Table C1 Number of nodes and elements in the meshes of the cubic models comprising different superspheroidal pores

| | | | | | | | | | |
|------------------------|---------|---------|---------|---------|---------|---------|---------|---------|---------|
| p | 0.2 | 0.25 | 0.3 | 0.35 | 0.4 | 0.45 | 0.5 | 0.6 | 0.7 |
| Num. N. ^[1] | 5580080 | 5062346 | 4246894 | 3412606 | 3777016 | 1965376 | 1272710 | 2049212 | 2125594 |
| Num. E. ^[2] | 3949744 | 3243744 | 2958504 | 2289744 | 2575736 | 1377480 | 843280 | 1361640 | 1419840 |
| p | 0.8 | 0.9 | 1 | 1.5 | 2 | 2.5 | 3 | 4 | 5 |
| Num. N. | 1047473 | 1716790 | 798157 | 2284278 | 2724190 | 2072024 | 2233528 | 2422684 | 2668330 |
| Num. E. | 1177376 | 1146672 | 545358 | 1531896 | 1823384 | 1395296 | 1501464 | 1629936 | 1801512 |

Number of nodes

Number of elements

Table C2 Number of nodes and elements in the meshes of the cubic models comprising different superspheroidal pores

| | | | | | | | | | |
|---------|---------|---------|---------|---------|---------|---------|---------|---------|---------|
| p | 0.2 | 0.25 | 0.3 | 0.35 | 0.4 | 0.45 | 0.5 | 0.6 | 0.7 |
| Num. N. | 4829072 | 2859018 | 3539342 | 3025846 | 3087712 | 2166076 | 1029954 | 1893940 | 2447226 |
| Num. E. | 3260176 | 1924360 | 2473320 | 2020488 | 2049608 | 1437104 | 762880 | 1309424 | 1716608 |
| p | 0.8 | 0.9 | 1 | 1.5 | 2 | 2.5 | 3 | 4 | 5 |
| Num. N. | 2487370 | 2288388 | 682512 | 1079731 | 2769712 | 2789860 | 3094708 | 1281679 | 749678 |
| Num. E. | 1716568 | 1579872 | 481944 | 739903 | 1866728 | 1883248 | 2091464 | 889557 | 505988 |

those of 3D quadratic elements show that each mesh is well refined for the corresponding computations to obtain a precision of computation as accurate as possible.

References

Adessina A, Barthélémy J-F, Lavergne F, Fraj AB (2017) Effective elastic properties of materials with inclusions of complex structure. *Int J Eng Sci* 119:1–15

Adessina A, Barthélémy J-F, Fraj AB (2020) Micromechanical model for the diffusion properties of materials embedding complex structures. *Mech Mater* 103404

Ammari H, Kang H (2007) Polarization and moment tensors: with applications to inverse problems and effective medium theory. Springer, Berlin

Barthélémy JF (2008) Effective permeability of media with a dense network of long and micro fractures. *Transp Porous Media* 76(1):153–178

Chen F (2016a) Micromechanical modelling of heterogenous porous materials with application to oolitic rocks. PhD thesis

Chen F (2016b) Modélisation micromécanique de milieux poreux hétérogènes et applications aux roches oolithiques. PhD thesis, Université de Lorraine, France

Du K, Cheng L, Barthélémy JF, Sevostianov I, Giraud A, Adessina A (2020) Numerical computation of compliance contribution tensor of a concave pore embedded in a transversely isotropic matrix. *Int J Eng Sci* 152:103306

Giraud A, Sevostianov I, Kushch VI, Cosenza P, Prêt D, Barthélémy JF, Trofimov A (2019) Effective electrical conductivity of transversely isotropic rocks with arbitrarily oriented ellipsoidal inclusions. *Mech Mater* 133:174–192

- Kachanov M, Sevostianov I (2018) *Micromechanics of materials, with applications. Solid mechanics and its applications*, vol 249. Springer, Berlin (2018)
- Schöberl J (1997) Netgen an advancing front 2d/3d-mesh generator based on abstract rules. *Comput Visual Sci* 1:41–52
- Sevostianov I, Kachanov M (2002) Explicit cross-property correlations for anisotropic two-phase composite materials. *J Mech Phys Solids* 50(2):253–282
- Sevostianov I, Kachanov M, Zohdi T (2008) On computation of the compliance and stiffness contribution tensors of non ellipsoidal inhomogeneities. *Int J Solids Struct* 45(16):4375–4383
- Sevostianov I, Chen F, Giraud A, Grgic D (2016) Compliance and resistivity contribution tensors of axisymmetric concave pores. *Int J Eng Sci* 101:14–28
- Smith M (2009) *ABAQUS/standard user's manual*, version 6.9. Dassault Systèmes Simulia Corp, United States

Chapter 6

Effective Thermal Conductivity of Transversely Isotropic Materials with Concave Pores



Kou Du, Long Cheng, Jean-François Barthélémy, Igor Sevostianov, Albert Giraud, and Ayodele Adessina

Abstract The aim of this paper is to extend recent elastic work to thermal problem. In the first part of the paper, approximate relations for the resistivity contribution tensor of pores of two reference shapes, supersphere and axisymmetrical superspheroid, are developed on the basis of 3D Finite Element Modelling, presented in the companion paper, and known exact solutions for the limiting cases of spherical pores. In the second part application to effective elastic coefficients of transversely isotropic materials such as clay rocks, in the frame of homogenization theory, is presented to illustrate the impact of concavity parameter on overall properties.

Keywords Concave shape · Supersphere · Superspheroid · Resistivity contribution tensor · Effective thermal properties · Transversely isotropic matrix

6.1 Introduction

In the present paper, we analyse the effect of the concavity of pores on the overall thermal properties of a porous material with transversely isotropic solid phase. For this goal, we use three homogenization techniques: Non-interaction approximation, Mori-Tanaka-Benveniste and Maxwell schemes. Both of them are based on the solu-

Igor Sevostianov is deceased.

K. Du · L. Cheng · A. Giraud (✉)
GeoResources Laboratory, Université de Lorraine (ENSG), CNRS, CREGU,
Vandoeuvre-lès-Nancy 54518, France
e-mail: albert.giraud@univ-lorraine.fr

J.-F. Barthélémy · A. Adessina
Cerema, Université Gustave Eiffel, UMR MCD, Sourdun 77171, France

I. Sevostianov
Department of Mechanical and Aerospace Engineering, New Mexico State University, Las Cruces 88001, NM, USA

tion for a single inhomogeneity problem and can be easily formulated for ellipsoidal inhomogeneities using Eshelby results (Eshelby 1961; Wu 1966).

Effective conductivity tensor of heterogeneous transversely isotropic materials has been extensively studied in the frame of multiscale homogenization method, by using single inclusion approach and considering inclusions of ellipsoidal shapes. See among many others (Giraud et al. 2007, 2019) for application to electrical and thermal conductivity of transversely isotropic mudstone rocks, and in Barthélémy (2008) for the case of an arbitrarily oriented ellipsoidal inhomogeneity embedded in an orthotropic matrix (application to conductivity of cracked porous anisotropic materials are presented).

By using multipole expansion of perturbation fields of inhomogeneities in terms of ellipsoidal harmonics, a full-field semi-analytical solution has been obtained for the conductivity problem of a composite with anisotropic matrix and arbitrarily oriented anisotropic ellipsoidal inhomogeneities in Kushch et al. (2017) (see also applications to conductivity in Kushch 2013; Kushch and Sevostianov 2014).

Experimental characterization and multiscale modelling of effective thermal conductivity of heterogeneous transversely isotropic porous material such as fired clay bricks have been recently investigated in Kiefer et al. (2020), Buchner et al. (2021), Tian et al. (2019). Transversely isotropic host matrix is taken into account and assumption of ellipsoidal shapes is considered for inclusion phases.

In the frame of single inclusion homogenization approach, by using property contribution tensors (Kachanov and Sevostianov 2018), effect of concavity of 3D inclusions on effective properties (elastic coefficients and conductivity) of isotropic composites have been studied in Giraud et al. (2015), Chen et al. (2015, 2017), Sevostianov et al. (2016), Trofimov et al. (2018), Markov et al. (2020). It has been recently extended to the case of a transversely isotropic matrix in Du et al. (2020, 2021) for the elastic problem. Recent theoretical and numerical (3D full field) modelling of elastic properties and thermal conductivity of isotropic cracked porous media, by multiscale homogenization, have been presented in Meynard et al. (2022) (see also Meynard 2019 for experimental characterizations and microstructural observations).

The objective of the present paper is to extend the approach to the conduction problem, in transversely isotropic composites with pores of concave 3D shapes, embedded in a transversely isotropic matrix. We use the recent numerical results presented in companion paper (Du et al. 2022) where resistivity contribution tensors of concave pores in a transversely isotropic material are obtained.

6.2 Resistivity Contribution Tensor of a Concave Pore

Refer to Appendix A for background on tensors and property contribution tensors. Superspheroidal and axisymmetrical superspheroidal shapes are defined by following implicit equations (Figs. 6.1 and 6.2):

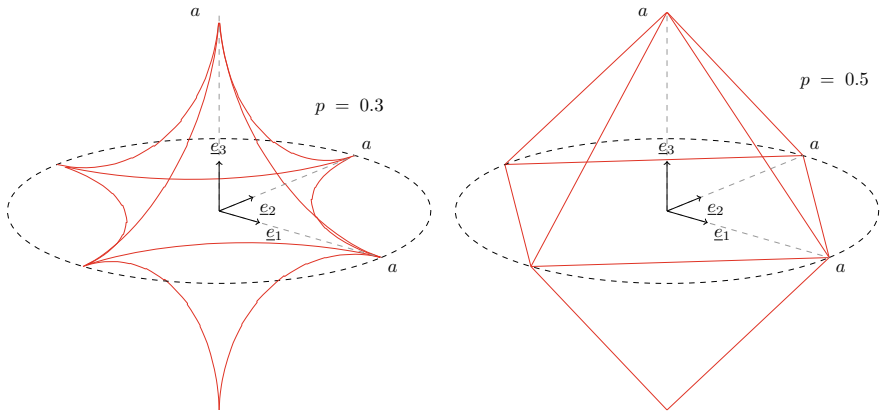


Fig. 6.1 Superspherical pore (relation (6.1) with $\zeta = 1$)

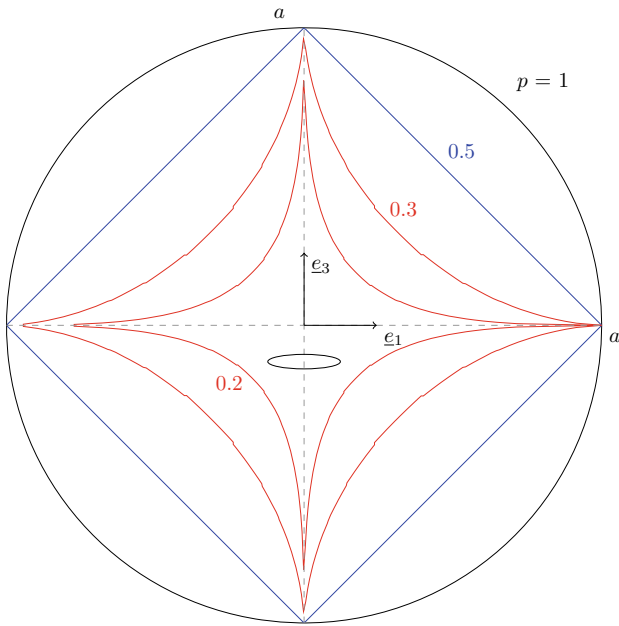


Fig. 6.2 2D representation in diametral plane of a 3D axisymmetrical superspheroidal pore, with $\zeta = 1$ and symmetry axis x_3

- superspheroidal pore

$$\left|\frac{x_1}{a}\right|^{2p} + \left|\frac{x_2}{a}\right|^{2p} + \left|\frac{x_3}{\zeta a}\right|^{2p} = 1 \quad (6.1)$$

- axisymmetrical superspheroidal pore

$$\left(\frac{x_1^2 + x_2^2}{a^2}\right)^p + \left|\frac{x_3}{\zeta a}\right|^{2p} = 1 \quad (6.2)$$

p , ζ and a respectively denote non-dimensional concavity parameter, aspect ratio and semi-lengths in plane $0x_1x_2$. These shapes are convex in the range $p > 0.5$ and concave for $p < 0.5$. Both shapes degenerate into a spheroid when $p = 1$. In what follows we will only consider $\zeta = 1$ and $a = 1$, the first shape is then a supersphere of unit semi-lengths on x_i axes, and the second shape obtained by a rotation about symmetry axis x_3 . Supersphere and axisymmetrical superspheroid coincide with sphere in the case $p = 1$ but strongly differ in the limiting case $p \rightarrow 0$. For thermal conductivity problem, the resistivity contribution tensors $\mathbf{H}_0^\mathcal{E}$ have two independent thermal coefficients: $H_{11}^\mathcal{E}$ and $H_{33}^\mathcal{E}$. Components of the resistivity contribution tensors of superspheroidal and axisymmetric superspheroidal pores embedded in a transversely isotropic material have been calculated by using Finite Element Method (FEM) and detailed numerical results are given in companion paper (Du et al. 2022). In the next section, we approximate these results analytically and then use it to estimate overall thermal properties of transversely isotropic matrix containing multiple concave pores, in the frame of single inclusion homogenization approach.

6.3 Approximation Formula for Resistivity Contribution Tensor of a Superspherical or Axisymmetrical Superspheroidal Pore Embedded in a Transversely Isotropic Host Matrix

We investigate in this section the extension to transverse isotropy of approximation formula for the resistivity contribution tensor of 3D pores of particular shapes previously presented. We restrict the study to the case of pores aligned in the direction of the host TI matrix and the two major parameters are the concavity parameter p characterizing the shape and the anisotropic ratio of the thermal conductivity tensor of the host TI matrix $\kappa = \frac{\lambda_1^0}{\lambda_3^0}$.

6.3.1 Volume and Surface Area of Superspherical and Axisymmetrical Superspheroidal Pores

Approximation formula may be obtained by using basic geometric information related to the considered reference shapes, supersphere and axisymmetrical superspheroid, defined in relations (6.1–6.2), with aspect ratio $\zeta = 1$ and $a = 1$. These information are volume, total surface area and corresponding volumes write (Γ denotes Euler *Gamma* function, see Trofimov et al. 2018; Du et al. 2021 for details)

$$V^{\text{se}}(p) = \frac{2}{3} \frac{\left(\Gamma\left[\frac{1}{2p}\right]\right)^3}{p^2 \Gamma\left[\frac{3}{2p}\right]}, \quad V^{\text{so}}(p) = \frac{4\pi}{3} \frac{\Gamma\left(\frac{1+2p}{2p}\right) \Gamma\left(\frac{1}{p}\right)}{\Gamma\left(\frac{3}{2p}\right)} \quad (6.3)$$

where superscripts se and so respectively refer to supersphere and superspheroid, p denotes the concavity parameter. Except for some particular values of concavity parameter ($p = \frac{1}{4}, \frac{1}{2}, 1$), the total surface area needs to be calculated by numerical integration. As in Du et al. (2021), we use the surface area of the supersphere $A^{\text{se}}(p)$ and the surface area $A^{\text{so}}(p)$ of the axisymmetrical superspheroid is given by the single integral accounting symmetry of revolution

$$A^{\text{so}}(p) = \int_0^1 (1-x^{2p})^{\frac{1}{2p}} \left(1+x^{-2(1+2p)}(1-x^{2p})^{\frac{1-2p}{p}}\right)^{\frac{1}{2}} dx \quad (6.4)$$

6.3.2 Approximation Formula for Superspherical Pore

We restrict this study to the range $0.2 \leq p \leq 1.0$ and $0.1 \leq \kappa \leq 10$. It allows to study concavity effect in a large extent ($p < 0.5$) avoiding needle type shape singularity when $p \rightarrow 0$. Anisotropic ratio $0.1 \leq \kappa \leq 10$ allows to take into account a wide range of transversely anisotropic materials, in particular many natural and man-made materials (sedimentary rocks, laminated composites, unidirectional fibre-matrix composites, clay bricks, wood, biomaterials as dentin, etc.).

On the basis of Trofimov et al. (2018), we propose approximation formula

$$H_{ii}^{\text{se}}(\kappa, p) = \frac{A^{\text{se}}(p)/(V^{\text{se}}(p))^{2/3}}{A^{\text{sphere}}/(V^{\text{sphere}})^{2/3}} f_{ii}^{\text{se}}(\kappa, p) H_{ii}^{\text{sphere}}, \quad \text{no sum over } i, i \in [1, 3] \quad (6.5)$$

where *sphere* denotes spherical case (particular case when $p = 1$). Semi-analytical approximations using the limiting cases of sphere $p = 1$ may be used for components H_{11} and H_{33} (with x_3 symmetry axis of *TI* matrix). Functions $f_{ii}^{\text{se}}(\kappa, p)$ are given in Eq. (6.6) by fitting the numerical results. They are piecewise functions in polynomial forms related to both variables κ and p . The polynomial coefficients of f_{11}^{se} and f_{33}^{se}

Table 6.1 Maximal relative errors of approximate results compared to *FEM* results, $\|(H_{ii}^{Aprox} - H_{ii}^{FEM})/H_{ii}^{FEM}\|$

| H_{11}^{se} | H_{33}^{se} | H_{11}^{so} | H_{33}^{so} |
|---------------|---------------|---------------|---------------|
| 0.877% | 0.796% | 0.500% | 1.675% |

are presented in Table B1 with different piecewise ranges of κ and p .

$$\begin{aligned}
 f_{ii}^{se}(\kappa, p) = & L_{00}^{(i)} + L_{10}^{(i)} \kappa + L_{01}^{(i)} p + L_{20}^{(i)} \kappa^2 + L_{11}^{(i)} \kappa p + L_{02}^{(i)} p^2 \\
 & + L_{30}^{(i)} \kappa^3 + L_{21}^{(i)} \kappa^2 p + L_{12}^{(i)} \kappa p^2 + L_{03}^{(i)} p^3 \\
 & + L_{40}^{(i)} \kappa^4 + L_{31}^{(i)} \kappa^3 p + L_{22}^{(i)} \kappa^2 p^2 + L_{13}^{(i)} \kappa p^3 + L_{04}^{(i)} p^4
 \end{aligned} \tag{6.6}$$

no sum over i , $i \in [1, 3]$

Comparisons between approximate relation Eq. (6.5) and finite element results are presented in Fig. 6.3. Maximal relative errors of approximate results compared to *FEM* results of superspherical pore are given in Table 6.1, and they are lower than 0.9%.

6.3.3 Approximation Formula for Axisymmetrical Superspheroidal Pore

Similar approximation formula Eq. (6.7) is proposed for components H_{11} and H_{33} of axisymmetrical superspheroidal pore (with x_3 symmetry axis of axisymmetrical superspheroid and *TI* matrix).

$$H_{ii}^{so}(\kappa, p) = \frac{A^{so}(p)/(V^{so}(p))^{2/3}}{A^{sphere}/(V^{sphere})^{2/3}} f_{ii}^{so}(\kappa, p) H_{ii}^{sphere}, \text{ no sum over } i, i \in [1, 3] \tag{6.7}$$

where *sphere* denotes spherical case (particular case when $p = 1$). Functions $f_{ii}^{so}(\kappa, p)$ are the same formula as Eq. (6.6). The polynomial coefficients of f_{11}^{so} and f_{33}^{so} are presented in Table B2 with different piecewise ranges of κ and p . Comparisons between approximate relation Eq. (6.7) and finite element results are presented in Fig. 6.4. Maximal relative errors of approximate results compared to *FEM* results are given in Table 6.1, and they are lower than 1.7%.

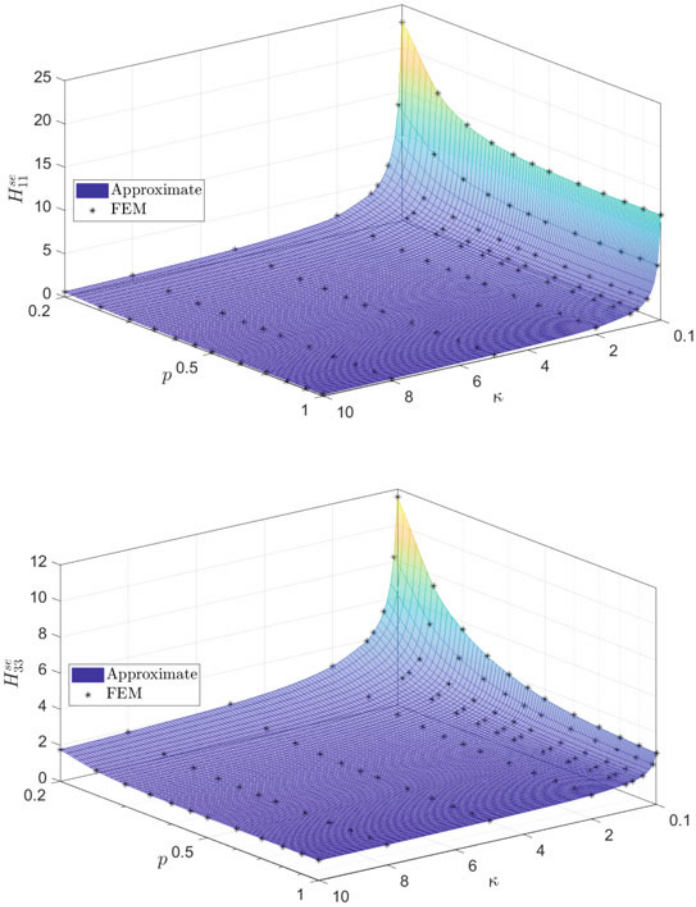


Fig. 6.3 The 2 independent components H_{11}^{se} and H_{33}^{se} of the resistivity contribution tensor of a superspherical pore embedded in *TI* matrix, as a function of concavity parameter p and anisotropic ratio of host matrix κ . Comparison between *FEM* results (star points) and approximate relations (plain surface)

6.4 Evaluation of the Effective Thermal Properties of Materials with Transversely Isotropic Matrices

In this section, we calculate effective thermal properties using three homogenization techniques: Non-Interaction Approximation, Mori Tanaka-Benveniste and Maxwell schemes (respectively referred with superscripts *NIA*, *MTB* and *MX*), see Benveniste 1987; Kachanov and Sevostianov 2018)

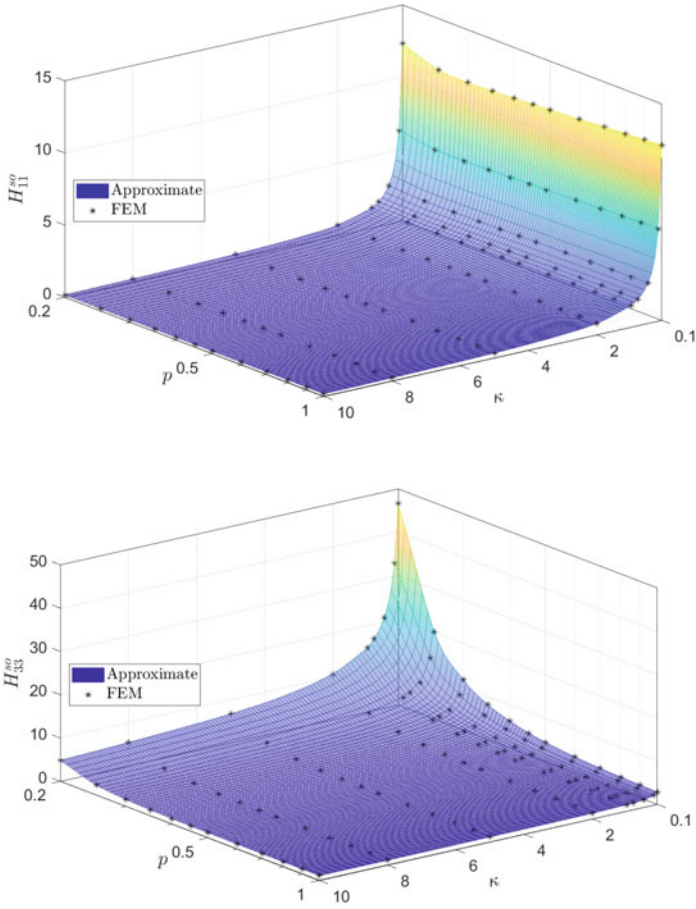


Fig. 6.4 The 2 independent components H_{11}^{so} and H_{33}^{so} of the resistivity contribution tensor of a superspheroidal pore embedded in TI matrix, as a function of concavity parameter p and anisotropic ratio of host matrix κ . Comparison between FEM results (star points) and approximate relations (plain surface)

$$\mathbf{r}^{\text{NIA}} = \mathbf{r}_0 + \varphi \mathbf{r}_0^{\mathcal{E}}, \quad \mathbf{r}^{\text{MTB}} = \mathbf{r}_0 + \frac{\varphi}{1 - \varphi} \mathbf{r}_0^{\mathcal{E}}, \quad \mathbf{r}^{\text{MX}} = \mathbf{r}_0 + \left[\frac{1}{\varphi} [\mathbf{r}_0^{\mathcal{E}}]^{-1} - \mathbf{Q}_0^{\Omega} \right]^{-1} \quad (6.8)$$

where φ denotes the porosity. \mathbf{Q}_0^{Ω} denotes the Hill tensor of the effective inclusion of the Maxwell scheme, which is supposed of spheroidal shape (with aspect ratio γ_e) and aligned with the directions of the TI host matrix. \mathbf{Q}_0^{Ω} is related to the strain Hill tensor \mathbf{P}_0^{Ω} by the relation:

$$\mathbf{Q}_0^{\Omega} = \lambda_0 \cdot (\mathbf{i} - \mathbf{P}_0^{\Omega} \cdot \lambda_0) \quad (6.9)$$

where λ_0 denotes the conductivity tensor of matrix. The porosity of clay matrix φ (denoted f_p^I in Giraud et al. 2008) is approximately comprised in the range $\varphi \leq 0.30$ for the sensitivity analysis.

6.4.1 Comparisons with Oblate Spheroidal Pores of Same Volume

Effective thermal coefficients λ_1^{MTB} and λ_3^{MTB} obtained with Mori-Tanaka-Benveniste (*MTB*) approximation of an aligned distribution of superspherical pores and axisymmetrical superspheroidal pores are respectively presented in Figs. 6.5, 6.6 and 6.7. Approximation formulae Eqs. 6.5–6.7 deduced from *FEM* are compared to approximation of resistivity contribution tensor of an oblate spheroidal pore of same volume (and same semi-axes lengths) Eq. (6.10):

$$H_{ij}(p) \approx H_{ij}^{\text{spheroid}}(\gamma(p)), \quad 0.2 \leq p \leq 1 \quad (6.10)$$

where aspect ratio $\gamma(p)$ of an oblate spheroidal pore of same volume (and semi axes) than a superspherical and an axisymmetrical superspheroidal pore of concavity parameter p are respectively given by

- superspherical pore:

$$\gamma(p) = \frac{V^{\text{se}}(p)}{V^{\text{sphere}}} = \frac{1}{2\pi} \frac{\left(\Gamma\left[\frac{1}{2p}\right]\right)^3}{p^2 \Gamma\left[\frac{3}{2p}\right]} \quad (6.11)$$

- axisymmetrical superspheroidal pore:

$$\gamma(p) = \frac{V^{\text{so}}(p)}{V^{\text{sphere}}} = \frac{\Gamma\left(\frac{1+2p}{2p}\right) \Gamma\left(\frac{1}{p}\right)}{\Gamma\left(\frac{3}{2p}\right)} \quad (6.12)$$

This comparison allows to underline a shape effect, and more precisely concavity effect on the effective thermal conductivities. It may be noticed that

- both the anisotropic ratio of host matrix κ and concavity parameter p have significant importance when estimating effective thermal coefficients λ_1^{MTB} and λ_3^{MTB} obtained with Mori-Tanaka-Benveniste (*MTB*) approximation of axisymmetric superspheroidal pores are presented in Figs. 6.6–6.7. Approximation formula Eq. 6.7 deduced from *FEM* are compared to approximation of resistivity contribution tensor of an oblate spheroidal pore of same volume (and same semi-axes lengths) Eqs. (6.10) and (6.12). properties and it is impossible to match effect of

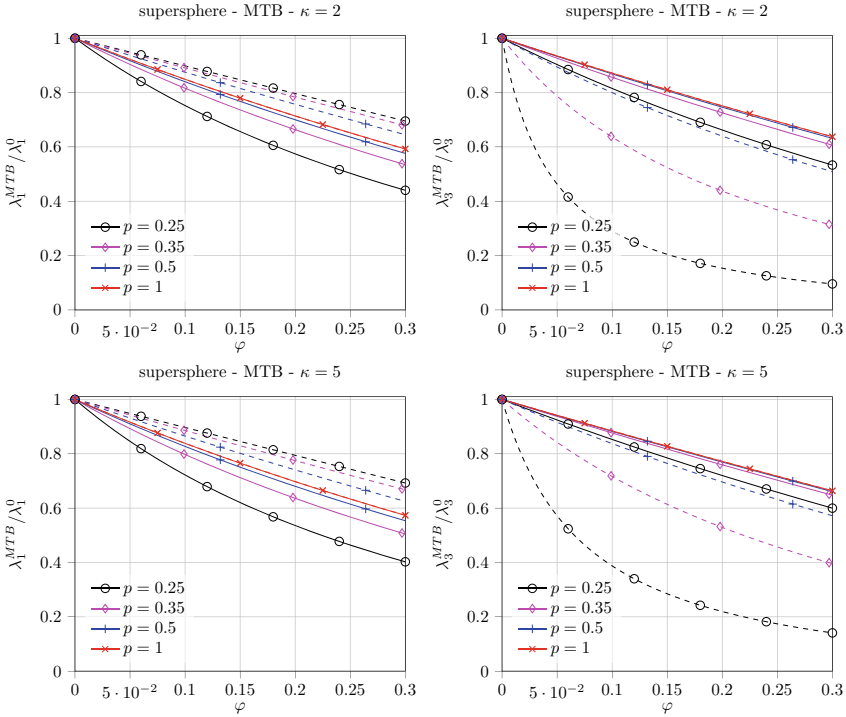


Fig. 6.5 Effective conductivity λ_1^{MTB} and λ_3^{MTB} as a function of porosity φ , MTB approximation, comparison between approximation formula Eq. (6.5) (plain lines) and oblate spheroid with same volume Eq. (6.10) (dashed lines)

concave pores by oblate spheroidal pores. It's not possible to separate effect of anisotropy from the effect of concavity.

- as expected, this concavity effect is different on normal and transverse conductivity and depends on the shape (supersphere and axisymmetrical superspheroid). The approximation of the pore shape by an oblate spheroid of same volume (and great semi-axis) could be relevant only for the transverse component in the case of the axisymmetrical shape and it is significantly irrelevant for the supersphere in the concave range. It may be emphasized that the limiting case $p \rightarrow 0$ (we only consider, due to numerical singularity, $p > 0.2$), is strongly different between these two shapes, the supersphere which respects cubic symmetry, tend to three perpendicular needles of unit semi length whereas the axisymmetrical superspheroids tend to an unit disc cross by a needle of unit semi length on symmetry axis. In the case of axisymmetrical shape, the effect of central needle becomes negligible compared to the unit disc. Both limiting cases of oblate spheroids when aspect ratio tends to zero on the one hand, and axisymmetrical superspheroid when p tends to zero on the other hand, coincide.

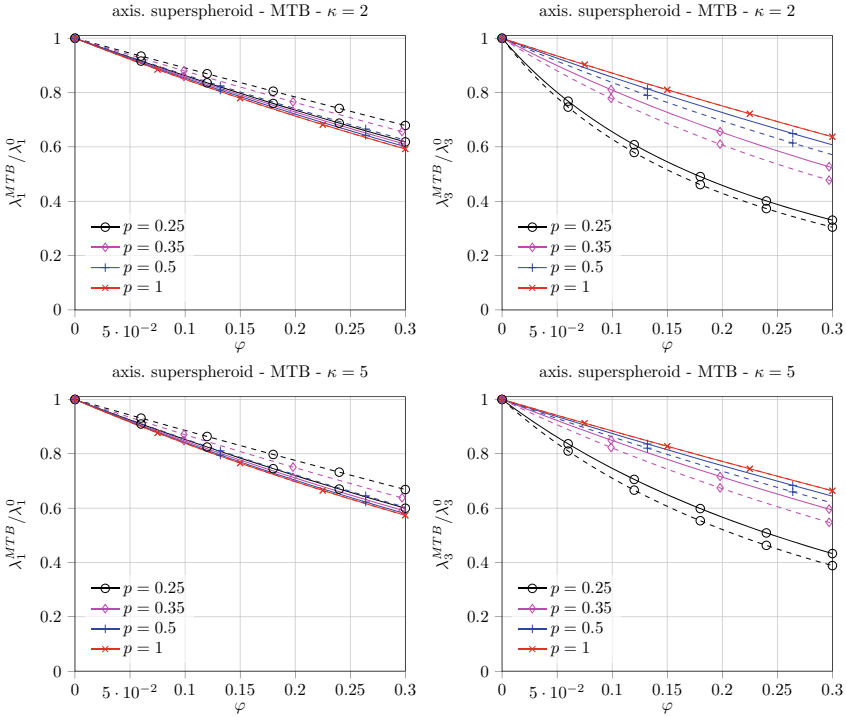


Fig. 6.6 Effective conductivity λ_1^{MTB} and λ_3^{MTB} as a function of porosity φ , MTB approximation, comparison between approximation formula Eq. (6.5) (plain lines) and oblate spheroid with same volume Eq. (6.10) (dashed lines)

- as porosity φ increases, effective conductivity gradually decreases. This is obviously expected because the thermal conductivity of insulating inhomogeneities tends to be zero. The increase in volume proportion of inhomogeneities will increase its impact.
- changes in variables κ and p have a greater impact on effective normal thermal conductivity λ_3^{MTB} than transverse λ_1^{MTB} thermal conductivity, in the case of the axisymmetrical spheroidal pore, and not for the superspherical pore. It must be emphasized that for practical applications to many anisotropic materials, the supersphere is certainly more realistic than the axisymmetrical shape, as it may approximately represents concave shapes filling the space between grains of convex shape.

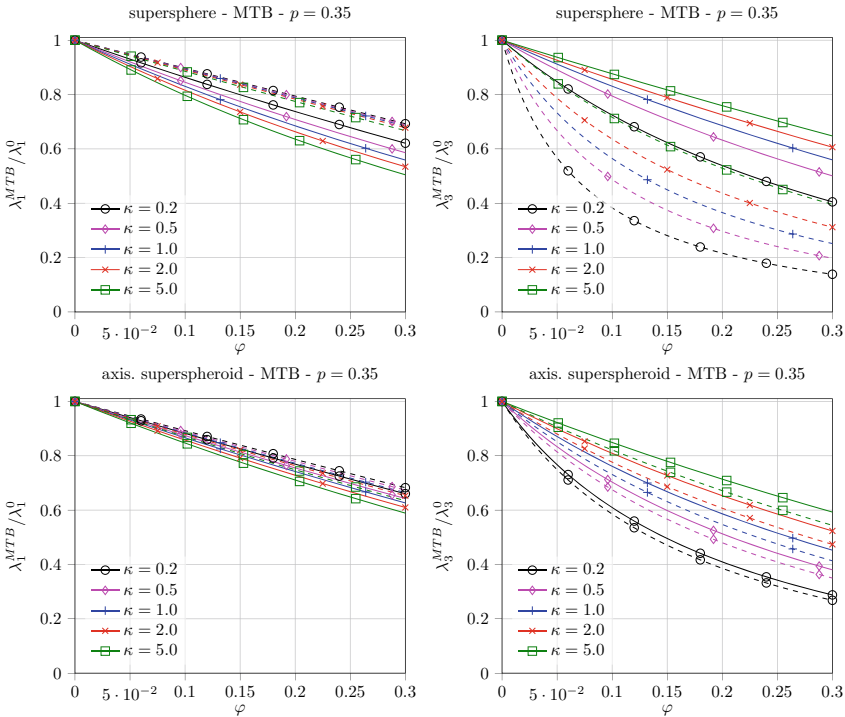


Fig. 6.7 Effective conductivity λ_1^{MTB} and λ_3^{MTB} as a function of porosity φ , MTB approximation, comparison between approximation formula (plain lines) and oblate spheroid with same volume Eq.(6.10) (dashed lines)

6.4.2 Comparison of MTB, NIA and Maxwell Homogenization Schemes

Effective thermal conductivity obtained with (NIA) approximation for aligned axisymmetrical superspheroidal pores and randomly oriented superspherical pores in the transverse plane are presented in Fig.6.8. Obtained effective porous material is transversely isotropic with same symmetry axis than matrix.

It may be observed that

- effects of these two shapes on thermal effective properties are strongly different in the concave range $0.2 < p < 0.5$. It is expected that the supersphere tends to three orthogonal needles (with zero volume and zero surface) when p tends to zero, whereas the axisymmetrical superspheroid tends to a circular crack with one central orthogonal needle (the latter has zero volume but non-zero surface).
- a significant anisotropic degree in the case of aligned axisymmetrical superspheroidal pores, in the limit $p \rightarrow 0$, it is similar to an aligned distribution of penny shaped cracks in *TI* matrix.

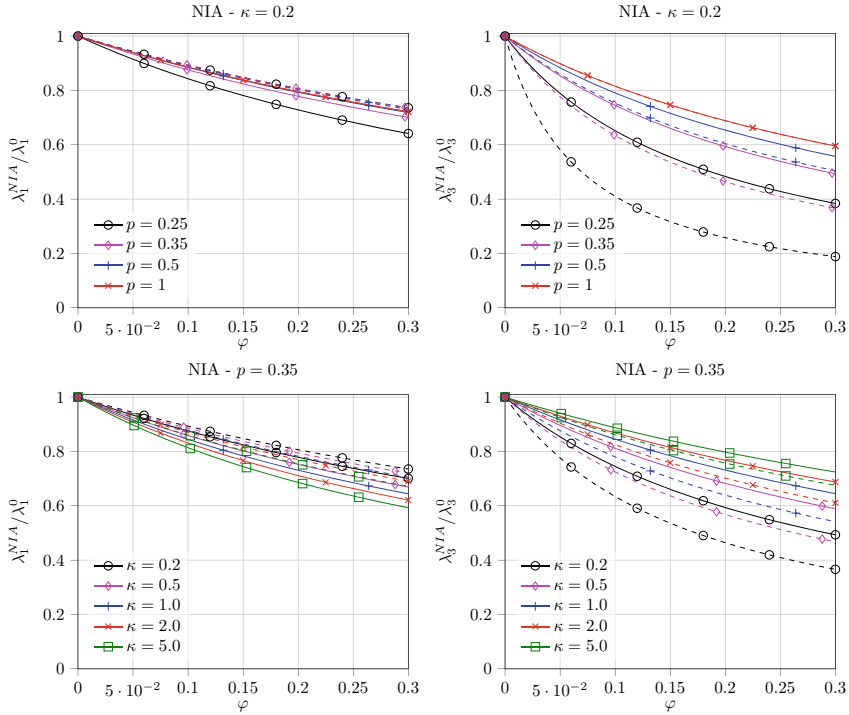


Fig. 6.8 Effective conductivity λ_1^{NIA} and λ_3^{NIA} as a function of porosity φ , NIA approximation, with constant anisotropic ratio of host matrix $\kappa = 0.2$ or concavity parameter $p = 0.35$. Comparison between superspherical pores (plain lines) and axisymmetric superspheroidal pores (dashed lines)

Effective thermal properties predicted by Maxwell, *MTB*, *NIA* are presented in Fig. 6.9 for respectively for superspherical pores randomly oriented in transverse plane and axisymmetrical superspheroidal. The shape of the effective inclusion of the Maxwell scheme is still an open issue when host matrix is anisotropic (see Sevostianov 2014; Giraud et al. 2019; Sevostianov et al. 2019). The sensitivity study on the shape of the effective inclusion and oblate spheroid of aspect ratio $\gamma_e = 0.5 - 1$ confirms that it is a parameter of major importance.

Compared to experimental data investigated in Giraud et al. (2007), and relative to transversely isotropic shale type rocks, anisotropic ratio $\kappa = 2$ is the most representative (and more generally one has $1 \leq \kappa$).

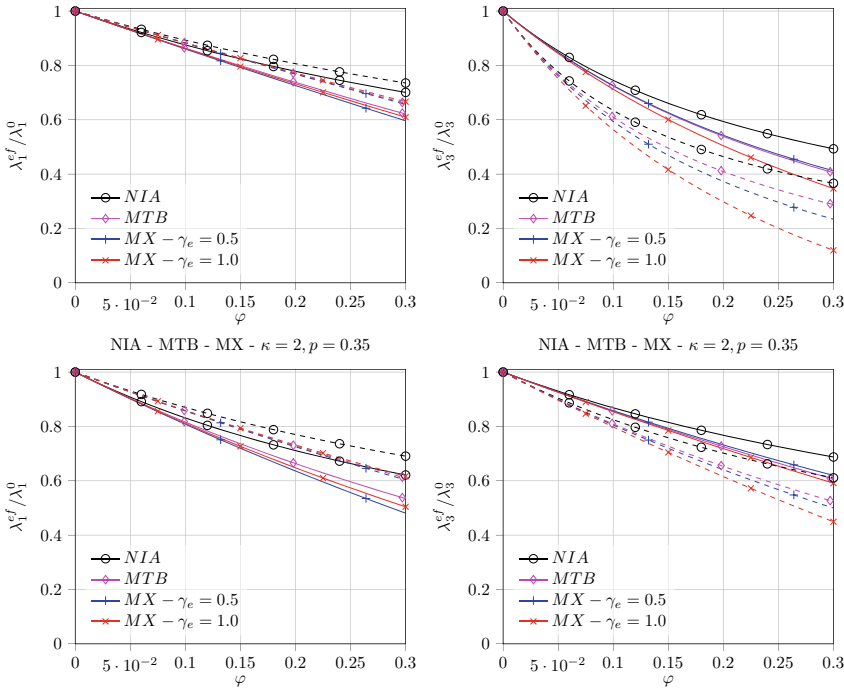


Fig. 6.9 Effective thermal conductivities as a function of porosity φ (plain lines: supersphere, dashed lines: axisymmetrical superspheroid), with different approximations, with constant anisotropic ratio of host matrix $\kappa = 0.2, 2$ and fixed concavity parameter $p = 0.35$

6.5 Concluding Remarks

In the present work, effective conductivity of a TI material containing aligned concave pores is discussed. Compared to previous studies on the subject, the novelty is the account of transverse isotropy of the host matrix. Two sources of overall anisotropy may be distinguished, matrix on the one hand, and pores on the other hand. Non-interaction approximation, Mori-Tanaka-Benveniste and Maxwell homogenization schemes have been considered by using explicit analytical representation of the resistivity contribution tensor for a single pore. These tensors were calculated for the set of superspherical and axisymmetrical superspheroidal pores with concavity parameter p in the range $0.2 \leq p \leq 1$ which covers both concave ($0.2 \leq p < 0.5$) and convex shapes ($0.5 \leq p \leq 1$) using FEM. Analytical approximations of the resistivity contribution tensor in terms of the pore concavity parameter p and of the anisotropic ratio κ of matrix conductivity tensor have been proposed. Similar to the elastic case, respectively numerical and analytical solutions for octahedron ($p = 0.5$) and sphere ($p = 1$) are used as a reference to built analytical approximations of the resistivity contribution tensor. An extensive sensitive study on the anisotropic degree of matrix

conductivity tensor is performed to cover a wide range of materials (for application to thermal conductivity) and accuracy of this approximation is better than 1.7% for all the tensor components. We show that the concavity parameter is the most important geometrical shape factor affecting the overall thermal conductivity.

Among the future extensions of this work one may cite:

- more complex and realistic orientation distributions could be considered and not only the aligned case investigated in this paper. It would need to solve numerically the problem of the arbitrarily oriented pore inclusion embedded in an orthotropic matrix.
- influence of pore interaction in TI matrix on overall thermal conductivity could be studied by comparing to full field modellings, which remains a challenging task for such 3D complex concave shapes
- the methodology could apply to inclusions of 3D shapes defined or not by implicit or parametric equations, perspectives are open as property contribution tensors may be numerically computed by using FEM (and then approximate relations could be developed differently)

Acknowledgements This paper puts an end to a work carried out in collaboration with our late friend, Professor Igor Sevostianov, and is dedicated to his memory.

Appendix A Background on Property Contribution Tensors

Property contribution tensors are used in micromechanics to describe the contribution of a single inhomogeneity to the property of interest (Kachanov and Sevostianov 2018). The average strain, over representative volume $|\Omega|$, can be represented as a sum

$$\underline{\varepsilon} = \mathbf{r}_0 : \underline{\Sigma} + \Delta \underline{\varepsilon} \quad (\text{A1})$$

where \mathbf{r}_0 where is the resistivity tensor of the matrix and $\underline{\Sigma}$ is uniform remotely applied heat flux vector. The material is assumed to be linear; hence, the extra thermal gradient $\Delta \underline{\varepsilon}$ due to presence of an inhomogeneity \mathcal{E} is a linear function of the applied heat flux vector

$$\Delta \underline{\varepsilon} = f \mathbf{H}_0^{\mathcal{E}} : \underline{\Sigma}, \quad \text{with } f = \frac{|\mathcal{E}|}{|\Omega|} \quad (\text{A2})$$

where $|\mathcal{E}|$ is the pore volume and $\mathbf{H}_0^{\mathcal{E}}$ is second-rank resistivity contribution tensor of the pore. The $\mathbf{H}_0^{\mathcal{E}}$ tensor is determined by the shape and size of the inhomogeneity, as well as properties of the matrix and of the inhomogeneity material. This tensor is also affected by conductive interactions. In the non-interaction approximation, it is taken by treating the inhomogeneities as isolated ones. In the case

of multiple inhomogeneities, the extra strain produced by m -th inhomogeneity is $\Delta \underline{\varepsilon}^{(m)} = f^{(m)} \mathbf{H}_0^{\varepsilon(m)} : \underline{\Sigma}$ so that the extra thermal resistivity due to all the inhomogeneities is given by

$$\Delta \underline{\varepsilon} = \left[\sum f^{(m)} \mathbf{H}_0^{\varepsilon(m)} \right] : \underline{\Sigma} \quad (\text{A3})$$

Formula (A3) highlights the fundamental importance of the resistivity contribution tensors: these tensors have to be summed up and averaged in the context of the effective conductive properties. The sum

$$\sum f^{(m)} \mathbf{H}_0^{\varepsilon(m)} \quad (\text{A4})$$

properly reflects compliance contributions of individual inhomogeneities and constitutes the general microstructural parameters in whose terms the effective compliance should be expressed. The conductivity contribution tensor denoted respectively by $\mathbf{N}_0^{\varepsilon}$ allows to calculate the extra heat flux vector induced by the presence of the inhomogeneity in a dilute situation such that

$$\Delta \underline{\sigma} = -f \mathbf{N}_0^{\varepsilon} \cdot \underline{E} \quad (\text{A5})$$

where \underline{E} is the remotely applied thermal gradient vector. We recall that the average concentration tensors $\mathbf{A}_0^{\varepsilon}$ and $\mathbf{B}_0^{\varepsilon}$ are defined as

$$\langle \underline{\varepsilon} \rangle^{\varepsilon} = \mathbf{A}_0^{\varepsilon} \cdot \underline{E}, \quad \langle \underline{\sigma} \rangle^{\varepsilon} = -\mathbf{B}_0^{\varepsilon} \cdot \underline{E} \quad (\text{A6})$$

with

$$\mathbf{A}_0^{\varepsilon} = (\lambda_{\varepsilon} - \lambda_0)^{-1} \cdot \mathbf{N}_0^{\varepsilon}, \quad \mathbf{B}_0^{\varepsilon} = \lambda_{\varepsilon} \cdot \mathbf{A}_0^{\varepsilon} \quad (\text{A7})$$

In the general case of non-ellipsoidal shapes, contribution and concentration tensors related to an inhomogeneity need to be calculated numerically. $\mathbf{H}_0^{\varepsilon}$ and $\mathbf{N}_0^{\varepsilon}$ can be interrelated as

$$\mathbf{H}_0^{\varepsilon} = -\mathbf{r}_0 \cdot \mathbf{N}_0^{\varepsilon} \cdot \mathbf{r}_0, \quad \mathbf{N}_0^{\varepsilon} = -\lambda_0 \cdot \mathbf{H}_0^{\varepsilon} \cdot \lambda_0 \quad (\text{A8})$$

In the case of a homogeneous inhomogeneity one has

$$\mathbf{A}_0^{\varepsilon} = (\lambda_{\varepsilon} - \lambda_0)^{-1} \cdot \mathbf{N}_0^{\varepsilon}, \quad \mathbf{B}_0^{\varepsilon} = \lambda_{\varepsilon} \cdot \mathbf{A}_0^{\varepsilon} \quad (\text{A9})$$

Appendix A.1 Case of an Ellipsoidal Homogeneous Inhomogeneity

The ellipsoidal homogeneous inhomogeneity is of particular interest in the present since analytical expressions of contribution and concentration tensors are available

and can then further be compared to the numerical ones to validate the methodology presented to calculate property contribution tensors and concentration tensors. In the particular case of an ellipsoidal inhomogeneity \mathcal{E} embedded in an infinite matrix $\mathbf{0}$ of conductivity λ_0 and resistivity \mathbf{r}_0 tensors, resistivity $\mathbf{H}_0^\mathcal{E}$ and conductivity $\mathbf{N}_0^\mathcal{E}$ contribution tensors write (see Kachanov and Sevostianov 2018 for details):

$$\mathbf{H}_0^\mathcal{E} = [(\mathbf{r}_\mathcal{E} - \mathbf{r}_0)^{-1} + \mathbf{Q}_0^\mathcal{E}]^{-1}, \quad \mathbf{N}_0^\mathcal{E} = [(\lambda_\mathcal{E} - \lambda_0)^{-1} + \mathbf{P}_0^\mathcal{E}]^{-1} \quad (\text{A10})$$

where $\mathbf{P}_0^\mathcal{E}$ and $\mathbf{Q}_0^\mathcal{E}$ denote the second order Hill's tensors of the inhomogeneity. Thermal gradient concentration tensor of the ellipsoidal inhomogeneity writes

$$\mathbf{A}_0^\mathcal{E} = [\mathbf{i} + \mathbf{P}_0^\mathcal{E} : (\lambda_\mathcal{E} - \lambda_0)]^{-1} \quad (\text{A11})$$

The Hill polarization tensor and resistivity contribution tensor of a spheroidal inclusion aligned in a transversely isotropic host matrix is detailed below. See Giraud et al. (2019), Barthélémy (2008) for the complete solution of arbitrarily oriented ellipsoidal inhomogeneity embedded in an orthotropic matrix. One considers a transversely isotropic matrix of conductivity tensor λ_0 (\underline{n} denotes unit vector on the symmetry axis, in this paper $\underline{n} = \underline{e}_3$)

$$\lambda_0 = \lambda_0 (\nu^2 \mathbf{i}_T + \mathbf{i}_N), \quad \mathbf{i}_N = \underline{n} \otimes \underline{n}, \quad \mathbf{i}_T = \mathbf{i} - \mathbf{i}_N \quad (\text{A12})$$

The Hill polarization tensor $\mathbf{P}_0^\mathcal{E}$ of a spheroidal inclusion aligned in the directions of a transversely isotropic matrix (spheroid and matrix have the same symmetry axis) writes

$$\mathbf{P}_0^\mathcal{E} = \frac{g(\nu\gamma)}{\nu^2 \lambda_0} \mathbf{i}_T + \frac{1 - 2g(\nu\gamma)}{\lambda_0} \mathbf{i}_N \quad (\text{A13})$$

with shape function $g(\xi)$ (see Barthélémy 2008; Giraud et al. 2019)

$$g(\xi) = \begin{cases} \frac{1}{2} \left(1 + \frac{1}{\xi^2 - 1} \left(1 - \frac{\xi}{\sqrt{1 - \xi^2}} \arctan \left(\frac{\sqrt{1 - \xi^2}}{\xi} \right) \right) \right) & \text{if } \xi < 1 \\ \frac{1}{3} & \text{if } \xi = 1 \\ \frac{1}{2} \left(1 + \frac{1}{\xi^2 - 1} \left(1 - \frac{\xi}{2\sqrt{\xi^2 - 1}} \ln \left(\frac{\xi + \sqrt{\xi^2 - 1}}{\xi - \sqrt{\xi^2 - 1}} \right) \right) \right) & \text{if } \xi > 1 \end{cases} \quad (\text{A14})$$

Resistivity contribution tensor $\mathbf{H}_0^\mathcal{E}$ of an insulating $\lambda_\mathcal{E} = \mathbf{0}$ aligned spheroidal pore writes

$$\mathbf{H}_0^\mathcal{E} = \frac{1}{\nu^2 \lambda_0 (1 - g(\nu\gamma))} \mathbf{i}_T + \frac{1}{2 \lambda_0 g(\nu\gamma)} \mathbf{i}_N \quad (\text{A15})$$

and the limiting case of the spherical pore $\gamma = 1$ embedded in an isotropic matrix $\nu = 1$ is recovered

$$\mathbf{H}_0^\mathcal{E} = \frac{3}{2\lambda_0} \mathbf{i} \tag{A16}$$

Resistivity contribution tensor of an aligned penny shaped crack embedded in a TI matrix writes

$$\mathbf{H}_0^\mathcal{E} = \frac{2}{\pi \lambda_0 \nu} \mathbf{i}_N \tag{A17}$$

Appendix B Numerical Results for Approximation Formula of Resistivity Contribution Tensors

Finite element results of a superspherical pore embedded in a TI matrix are given in table 4 of paper Du et al. (2020), and recalled in Table B1.

Finite element results of an axisymmetrical superspheroidal pore embedded in a TI matrix are given in table 3 of paper Du et al. (2020) and recalled in Table B2.

Table B1 Coefficients of piecewise functions f_{11}^{se} and f_{33}^{se} of superspherical pore

| coef | f_{11}^{se} | | | | f_{33}^{se} | | | |
|--------------------|-------------------------|------------------------|-------------------------|------------------------|-------------------------|------------------------|-------------------------|------------------------|
| | $\kappa \in [0.1, 1.0]$ | $\kappa \in [1.0, 10]$ | $\kappa \in [0.1, 1.0]$ | $\kappa \in [1.0, 10]$ | $\kappa \in [0.1, 1.0]$ | $\kappa \in [1.0, 10]$ | $\kappa \in [0.1, 1.0]$ | $\kappa \in [1.0, 10]$ |
| $p \in [0.2, 0.5]$ | [0.2, 0.5] | [0.2, 0.5] | [0.5, 1.0] | [0.5, 1.0] | [0.2, 0.5] | [0.2, 0.5] | [0.5, 1.0] | [0.5, 1.0] |
| $L_{00}^{(i)}$ | 0.87508 | 1.02996 | -0.29380 | -0.04144 | 1.55862 | 1.42940 | 0.44977 | -0.14596 |
| $L_{10}^{(i)}$ | 0.92838 | 0.08748 | 0.25650 | 0.02001 | -1.16012 | -0.22928 | -0.89815 | -0.03549 |
| $L_{01}^{(i)}$ | -7.76403 | -7.14286 | 4.02037 | 3.34072 | -7.43012 | -9.26201 | 2.55206 | 3.83896 |
| $L_{20}^{(i)}$ | -1.10309 | -0.00979 | -0.07315 | -0.00095 | 1.38766 | 0.03786 | 0.38652 | 0.00165 |
| $L_{11}^{(i)}$ | -1.59432 | -0.16284 | -0.43345 | -0.03018 | -0.42393 | 0.42521 | 1.29267 | 0.05476 |
| $L_{02}^{(i)}$ | 35.38743 | 31.16683 | -4.24305 | -3.60753 | 30.86098 | 38.22527 | -3.34516 | -4.29555 |
| $L_{30}^{(i)}$ | 0.44168 | 0.00042 | 0 | 0 | -0.66622 | -0.00310 | 0 | 0 |
| $L_{21}^{(i)}$ | 2.46194 | 0.01608 | 0.07852 | 0.00099 | -0.25478 | -0.04060 | -0.40081 | -0.00174 |
| $L_{12}^{(i)}$ | -1.28934 | -0.00314 | 0.17175 | 0.00977 | 3.12396 | -0.19939 | -0.37989 | -0.01839 |
| $L_{03}^{(i)}$ | -53.72084 | -47.14355 | 1.51744 | 1.30895 | -48.63572 | -59.63922 | 1.34169 | 1.60178 |
| $L_{40}^{(i)}$ | 0 | 0 | 0 | 0 | 0 | 0.00010 | 0 | 0 |
| $L_{31}^{(i)}$ | -0.86332 | -0.00063 | 0 | 0 | 0.60461 | 0.00147 | 0 | 0 |
| $L_{22}^{(i)}$ | -0.73579 | -0.00210 | 0 | 0 | -1.80085 | 0.01061 | 0 | 0 |
| $L_{13}^{(i)}$ | 2.30732 | 0.08566 | 0 | 0 | -0.39836 | -0.04774 | 0 | 0 |
| $L_{04}^{(i)}$ | 27.48389 | 24.38060 | 0 | 0 | 25.72938 | 32.79942 | 0 | 0 |

Table B2 Coefficients of piecewise functions f_{11}^{SO} and f_{33}^{SO} of axisymmetrical superspheroidal pore

| coef | f_{11}^{SO} | | | | f_{33}^{SO} | | | |
|----------------|---------------|------------|------------|------------|---------------|------------|------------|------------|
| | [0.1, 1.0] | [1.0, 10] | [0.1, 1.0] | [1.0, 10] | [0.1, 1.0] | [1.0, 10] | [0.1, 1.0] | [1.0, 10] |
| $\kappa \in$ | [0.2, 0.5] | [0.2, 0.5] | [0.5, 1.0] | [0.5, 1.0] | [0.2, 0.5] | [0.2, 0.5] | [0.5, 1.0] | [0.5, 1.0] |
| $L_{00}^{(i)}$ | 0.26483 | 0.31506 | -0.25095 | -0.33687 | 19.00314 | 11.76301 | 4.33631 | 1.29115 |
| $L_{10}^{(i)}$ | -0.00238 | -0.01251 | -0.05148 | 0.00924 | -11.92622 | -1.45203 | -4.57413 | -0.31561 |
| $L_{01}^{(i)}$ | -4.87821 | -5.68135 | 3.96451 | 4.28190 | -141.94940 | -84.24440 | -10.88093 | 0.41270 |
| $L_{20}^{(i)}$ | 0.01106 | 0.00069 | 0.02711 | -0.00055 | 8.97971 | 0.17599 | 3.30432 | 0.02697 |
| $L_{11}^{(i)}$ | -0.47228 | 0.06239 | 0.11204 | -0.00771 | 49.14392 | 5.02357 | 10.33640 | 0.71128 |
| $L_{02}^{(i)}$ | 36.00467 | 39.01536 | -4.30156 | -4.67035 | 463.93148 | 268.14315 | 14.16878 | -2.63909 |
| $L_{30}^{(i)}$ | 0 | 0 | 0 | 0 | -3.17077 | -0.01212 | -1.08391 | -0.00095 |
| $L_{21}^{(i)}$ | 0.11231 | -0.00302 | -0.02921 | 0.00054 | -22.09062 | -0.30483 | -4.87185 | -0.03998 |
| $L_{12}^{(i)}$ | 1.47851 | -0.05392 | -0.05868 | -0.00141 | -80.78645 | -6.96489 | -7.98576 | -0.54316 |
| $L_{03}^{(i)}$ | -70.65161 | -74.94268 | 1.58820 | 1.72562 | -704.18395 | -394.21125 | -8.68698 | 3.02476 |
| $L_{40}^{(i)}$ | 0 | 0 | 0 | 0 | 0 | 0.00034 | 0 | 0 |
| $L_{31}^{(i)}$ | 0 | 0 | 0 | 0 | 5.51144 | 0.00850 | 1.14473 | 0.00102 |
| $L_{22}^{(i)}$ | -0.21038 | 0.00223 | 0 | 0 | 12.74062 | 0.16059 | 1.47231 | 0.01196 |
| $L_{13}^{(i)}$ | -1.15256 | -0.00330 | 0 | 0 | 51.70313 | 3.68239 | 2.26321 | 0.15184 |
| $L_{04}^{(i)}$ | 45.74778 | 47.86995 | 0 | 0 | 407.85909 | 221.70354 | 2.05902 | -1.09374 |

References

Barthélemy JF (2008) Effective permeability of media with a dense network of long and micro fractures. *Transport in Porous Media* 76(1):153–178

Benveniste Y (1987) A new approach to the application of Mori-Tanaka’s theory in composite materials. *Mechanics of Materials* 6(2):147–157

Buchner T, Kiefer T, Königsberger M, Jäger A, Füssl J (2021) Continuum micromechanics model for fired clay bricks: Upscaling of experimentally identified microstructural features to macroscopic elastic stiffness and thermal conductivity. *Materials and Design* 212:110212

Chen F, Sevostianov I, Giraud A, Grgic D (2015) Evaluation of the effective elastic and conductive properties of a material containing concave pores. *International Journal of Engineering Science* 97:60–68

Chen F, Sevostianov I, Giraud A, Grgic D (2017) Accuracy of the replacement relations for materials with non-ellipsoidal inhomogeneities. *International Journal of Solids and Structures* 104–105:73–80

Du, K., Cheng, L., Barthélemy, J.F., Sevostianov, I., Giraud, A., Adessina, A.: Numerical estimation of resistivity contribution tensor of a concave pore embedded in a transversely isotropic matrix. In: Altenbach, H., Bruno, G., Eremeyev, V., Gutkin, M., Müller, W. (eds.) *Mechanics of Heterogeneous Materials*, pp. 1–25. Book series *Advanced Structured Materials*. Springer, ??? (2022)

Du K, Cheng L, Barthélemy JF, Sevostianov I, Giraud A, Adessina A (2020) Numerical computation of compliance contribution tensor of a concave pore embedded in a transversely isotropic matrix. *International Journal of Engineering Science* 152:103306

Du K, Cheng L, Barthélemy JF, Sevostianov I, Giraud A, Adessina A (2021) Effective elastic properties of transversely isotropic materials with concave pores. *Mechanics of Materials* 153:103665

Eshelby, J.D.: Elastic inclusions and inhomogeneities. In: *Progress in Solid Mechanics* 2, I.N. Sneddon and R. Hill Editors, pp. 89–140. North-Holland, Amsterdam, ??? (1961)

- Giraud A, Gruescu C, Do DP, Homand F, Kondo D (2007) Effective thermal conductivity of transversely isotropic media with arbitrary oriented ellipsoidal inhomogeneities. *International Journal of Solids and Structures* 44(11):2627–2647
- Giraud A, Hoxha D, Huynh QV, Do DP, Magneet V (2008) Effective porothermoelastic properties of transversely isotropic rock-like composites. *International Journal of Engineering Science* 46:527–550
- Giraud A, Sevostianov I, Chen F, Grgic D (2015) Effective thermal conductivity of oolitic rocks using the Maxwell homogenization method. *International Journal of Rock Mechanics and Mining Sciences* 80:379–387
- Giraud A, Sevostianov I, Kushch VI, Cosenza P, Prêt D, Barthélémy JF, Trofimov A (2019) Effective electrical conductivity of transversely isotropic rocks with arbitrarily oriented ellipsoidal inclusions. *Mechanics of Materials* 133:174–192
- Kachanov, M., Sevostianov, I.: *Micromechanics of Materials, with Applications. Solid Mechanics and Its Applications*, vol. 249. Springer, ??? (2018)
- Kiefer T, Füssl J, Kariem H, Konnerth J, Gaggl W, Hellmich C (2020) A multi-scale material model for the estimation of the transversely isotropic thermal conductivity tensor of fired clay bricks. *Journal of the European Ceramic Society* 40(15):6200–6217
- Kushch, V.: *Micromechanics of Composites. Multipole Expansion Approach*. Elsevier, ??? (2013)
- Kushch VI, Sevostianov I (2014) Dipole moments, property contribution tensors and effective conductivity of anisotropic particulate composites. *International Journal of Engineering Science* 74:15–34
- Kushch VI, Sevostianov I, Giraud A (2017) Local fields and effective conductivity tensor of ellipsoidal particle composite with anisotropic constituents. *Proceedings of the Royal Society A*. 473(1):53–77
- Markov A, Trofimov A, Sevostianov I (2020) A unified methodology for calculation of compliance and stiffness contribution tensors of inhomogeneities of arbitrary 2d and 3d shapes embedded in isotropic matrix - open access software. *International Journal of Engineering Science* 157:103390
- Meynard, J., Ibrahim, M., Monnier, A., Bornert, M., Castelier, E., Duguay, C., Gărăjeu, M., Masson, R.: Effective properties of an isotropic solid weakened by micro-cracks located at inter-granular boundaries. *Journal of the Mechanics and Physics of Solids* 158, 104647 (2022)
- Meynard, J.: Influence de la taille, de la morphologie et de la distribution spatiale des pores sur la conductivité thermique de céramiques UO₂ (in french), Effect of pore size, morphology and spatial distribution on the thermal conductivity of UO₂ ceramics. PhD thesis, Aix-Marseille Université, Marseille (France) (2019)
- Sevostianov I (2014) On the shape of effective inclusion in the Maxwell homogenization scheme for anisotropic elastic composites. *Mechanics of Materials* 75:45–59
- Sevostianov I, Chen F, Giraud A, Grgic D (2016) Compliance and resistivity contribution tensors of axisymmetric concave pores. *International Journal of Engineering Science* 101:14–28
- Sevostianov I, Mogilevskaya SG, Kushch VI (2019) Maxwell's methodology of estimating effective properties: Alive and well. *International Journal of Engineering Science* 140:35–88
- Tian, Z., Abou-Chakra, A., Geoffroy, S., Kondo, D.: The effective elastic properties and thermal conductivity of porous fired clay bricks. *European Journal of Environmental and Civil Engineering* 0(0), 1–15 (2019)
- Trofimov A, Markov A, Abaimov SG, Akhatov I, Sevostianov I (2018) Overall elastic properties of a material containing inhomogeneities of concave shape. *International Journal of Engineering Science* 132:30–44
- Wu TT (1966) The effect of inclusion shape on the elastic moduli of a two-phase material. *International Journal of Solids and Structures* 2(1):1–8

Chapter 7

A Constitutive Model for Non-linear Basic Creep of Plain Concrete



Johanna Eisenträger and Holm Altenbach

Abstract It is well known that plain concrete suffers from creep under sustained loads. Although various constitutive models have been proposed in the last years, these approaches are often restricted to linear creep of concrete at low load levels, face difficulties regarding multiaxial stress and deformation states, or involve a large number of parameters. The current contribution aims at closing this gap and presents a new robust modelling approach for the non-linear basic creep of plain concrete. Coupled non-linear evolution equations are formulated with respect to the creep strain and a backstress variable, which allows for the consideration of hardening effects. Both uniaxial and multiaxial stress conditions are taken into account, and the Drucker-Prager equivalent stress is utilized. Material parameters are determined based on compressive and tensile creep tests. Furthermore, the model is verified against an additional set of creep tests, which demonstrates that the proposed concept provides an accurate prediction for basic creep of concrete. Thereby, the concept is applicable for loads up to 70% of the short-term strength, while requiring a relatively low number of material parameters.

7.1 Introduction

7.1.1 Creep in Concrete: Phenomenon and Experiments

If concrete is subjected to sustained loads, creep deformations occur in the long term. According to Neville (1995), creep describes the increase of deformations over time under a sustained load. A creep-related phenomenon is relaxation, i.e., stress maxima in a component decrease under constant strain. While one usually aims at keeping

J. Eisenträger (✉) · H. Altenbach
Institute of Mechanics, Otto von Guericke University Magdeburg, Magdeburg, Germany
e-mail: johanna.eisentraeger@ovgu.de

H. Altenbach
e-mail: holm.altenbach@ovgu.de

© The Author(s), under exclusive license to Springer Nature Switzerland AG 2023
H. Altenbach and V. Eremeyev (eds.), *Advances in Linear and Nonlinear Continuum and Structural Mechanics*, Advanced Structured Materials 198,
https://doi.org/10.1007/978-3-031-43210-1_7

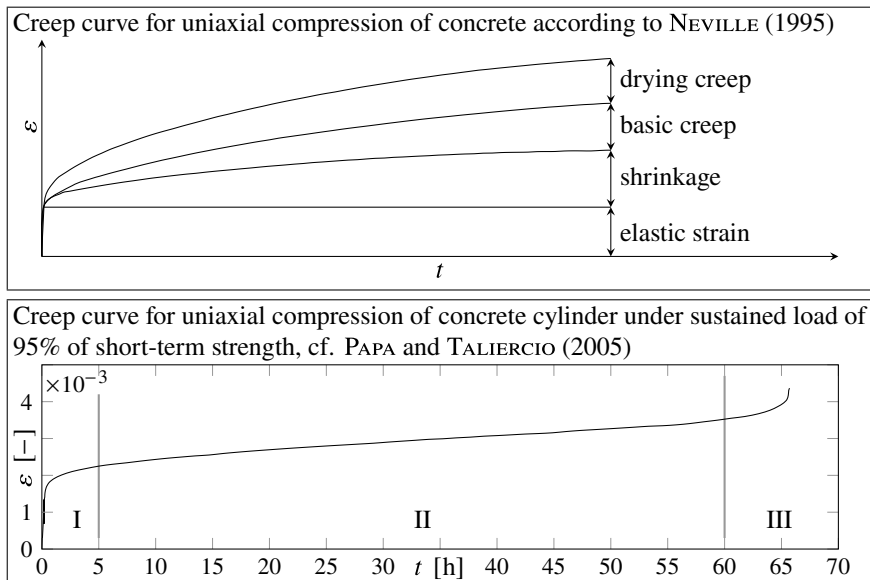


Fig. 7.1 Typical creep curves for concrete: different creep mechanisms in concrete under sustained compressive loads, cf. Neville (1995) (top), and creep curve for uniaxial compression of concrete cylinder under sustained load of 95% of short-term strength; cf. Papa and Taliercio (2005) (bottom)

creep strains at a minimum, relaxation can extend the lifetime of components in some cases, e.g., by reducing stresses in a component due to restrained shrinkage; cf. Bissonnette and Pigeon (1995). Typical creep tests under sustained compressive loads result in a creep curve, as depicted in Fig. 7.1. As an instantaneous reaction to the applied load, concrete exhibits elastic deformations followed by a continuous growth of strain over time. Note that the increase in creep strain is highest directly after applying the load such that approximately 70–80% of the entire creep deformation occurs within the first six months after loading (Gu et al. 2016). While the creep strain increases continuously, the change in creep deformation with time, i.e., the creep rate, decreases.

As depicted in the top picture of Fig. 7.1, one distinguishes basic creep, i.e., creep *without* a change in moisture content, and drying creep, i.e., creep *with* changing moisture content (Neville 1995). Creep in concrete is primarily based on microstructural processes in the cement paste since the deformations of aggregates are negligible. According to Bažant and Jirásek (2018), drying creep is due to the diffusion of water from pores, which increases local stress concentrations in the cement paste such that atomic bonds break, resulting in macroscopic deformations of concrete. At stress levels below 40% of the short-term compressive strength, concrete exhibits basic creep since atomic bands break and reconnect at highly stressed points in the hydrated cement paste. Under higher loads, basic creep is predominantly based on

the formation and growth of micro-cracks in the cement paste. Based on these complex microstructural processes, the influence of several macroscopic parameters on creep of concrete can be explained, for instance, the increase of creep strains under increasing stresses and temperatures as well as higher water-to-cement ratios. Furthermore, environmental factors during cement hydration, such as air humidity and temperature, exert a significant influence on the creep strength of concrete.

Next, let us discuss the different creep stages based on the creep curve shown in the bottom diagram of Fig. 7.1. The experimental data from Papa and Taliercio (2005) refers to a uniaxial compressive creep test under a very high stress level which is equivalent to 95% of the short-term compressive strength. Three different stages, marked with I, II, and III in Fig. 7.1, are identified: primary, secondary, and tertiary creep. During primary creep, the strain starts to increase with time, whereas the strain rate decreases until a constant minimum value is attained. This point marks the onset of the secondary stage, where the creep rate is constant. Under very high loads, i.e., above 70% of the compressive strength, tertiary creep can be observed. Due to an unstable development of micro-cracks, the strain rate increases until the failure of the specimen (Ren et al. 2020). It is worth noting that creep in concrete is often classified according to the load level. At loads below 40% of the short-term compressive strength, creep in concrete is linear, i.e., the amount of creep strain is proportional to the stress. For loads between 40 and 70% of the compressive strength, creep in concrete becomes non-linear and is primarily based on the growth and development of micro-cracks. Nevertheless, at these load levels, only primary and secondary creep occur, whereas tertiary creep is only observed for loads higher than 70% of the compressive strength (Ren et al. 2020).

Particularly for uniaxial creep of concrete under compression, a broad range of experimental results is available; cf., for example, Ross (1958), Roll (1964), Atrushi (2003), Ruiz et al. (2007), Ranaivomanana et al. (2013), Hamed (2015), and Charpin et al. (2018). Since concrete is a quasi-brittle material, conducting tensile creep tests requires more effort than applying compressive loads. Nevertheless, corresponding data has been published as well, e.g., Domone (1974), Bissonnette and Pigeon (1995), Kovler (1995), Kovler et al. (1999), Østergaard et al. (2001), Atrushi (2003), and Ranaivomanana et al. (2013). In contrast, experimental creep data for biaxial and triaxial stress states is rare; cf. Charpin et al. (2018), Liang and Wei (2019) for biaxial and Jordaán and Illston (1969), Kennedy (1975), and Kim et al. (2005) for triaxial stress states.

Among those experimental results, Roll (1964), Ruiz et al. (2007), Atrushi (2003), Ranaivomanana et al. (2013), and Hamed (2015) consider high loads such that non-linear creep occurs. Particularly high load levels of 80 and 90% of the compressive strength are chosen in Ruiz et al. (2007) for uniaxial compressive creep tests. The authors conclude that non-linear creep strains result from micro-cracking and also observe a tertiary creep stage. By using uniaxial compressive creep tests as well, it is found in Ranaivomanana et al. (2013) that non-linear creep starts at load levels between 30–50% of the short-term compressive strength. Note that although service load levels for most concrete structures are low such that creep strains are linear to the stress level, higher stresses occur in certain applications, such as dams, retaining

walls, columns, arches, containment vessels, cooling towers, prestressed concrete members, and reinforced concrete structures with high-strength steel (Hamed 2015). Additionally, short-term high loads can occur, e.g., the passing of a heavy load vehicle over a bridge. This local and temporary overload influences indirectly the creep behaviour by accelerating the growth of micro-cracks (Bockhold and Stangenberg 2004). Consequently, in these cases, non-linear creep has to be taken into account.

Furthermore, Ostergaard et al. have found that the age of loading is crucial particularly for tensile creep, i.e., tensile creep strains are very high when concrete is loaded within 24 h after mixing. If specimens are loaded after three days, tensile creep is significantly reduced, and the concrete mix exhibits a higher stiffness (Østergaard et al. 2001). Moreover, according to Charpin et al. (2018), the long-term evolution of basic creep follows a logarithmic trend over time, what has been concluded after conducting a long-term creep test over 12 years. Another interesting aspect is the multiaxial behaviour of concrete. Although the majority of concrete structures, such as slabs, columns, shell, and thin-walled structures, are usually subjected to multiaxial stress conditions, particularly due to restrained shrinkage deformation (Liang and Wei 2019), the experimental database for multiaxial creep tests of concrete is very limited. According to Liang and Wei (2019), biaxial creep is significantly lower than uniaxial creep, and the stress state is a key factor affecting the creep property of concrete. Furthermore, it has been found that Poisson's ratio does not change significantly during creep tests (Jordaan and Illston 1969; Charpin et al. 2018). In addition, Poisson's ratio is neither influenced by time nor by the stress state (Kennedy 1975; Kim et al. 2005). It is also worth pointing out that volumetric and deviatoric creep are both independent processes (Jordaan and Illston 1969).

7.1.2 Constitutive Models for Non-linear Basic Creep in Concrete

The current section provides a short review about constitutive models for non-linear basic creep in concrete. Modelling non-linear creep in concrete poses several challenges, such as the non-linear stress-strain relation in compression, the interaction with cracks in tension, or stress-dependent creep characteristics at high load levels (Hamed 2014). In contrast, relatively simple approaches, mainly based on linear viscoelasticity, are usually used to account for linear creep in concrete. Since various papers about linear creep in concrete have been published already, and a large number of constitutive models has been formulated, cf. Bažant and Jirásek (2018), the current review focuses on non-linear creep of concrete. Up to the present day, various constitutive models for non-linear creep in concrete have been formulated, either restricted to uniaxial stress states, cf. Carol and Murcia (1989), Bažant and Jirásek (1993), Bažant (2001), Barpi and Valente (2002), Ruiz et al. (2007), Fan et al. (2013), Hamed (2014), and Yu et al. (2020), or including multiaxial stress states, cf. Argyris et al. (1977), de Borst (1987), Papa and Taliercio (1996), Bažant

et al. (1997), Mazzotti and Savoia (2003), Bockhold and Stangenberg (2004), Papa and Taliervo (2005), Challamel et al. (2005), Contrafatto and Cuomo (2006), Bockhold (2007), Luzio (2009), Dutra et al. (2010), Gernay et al. (2013), Kindrachuk et al. (2015), Sellier et al. (2016), Bažant and Jirásek (2018), Boumakis et al. (2018), Huang et al. (2019), and Ren et al. (2020). Interestingly, Bažant identified already in 2001 the modelling of non-linear multiaxial creep at high stresses as an important direction for future research; cf. Bažant (2001).

The earliest and also simplest models for creep in concrete are based on linear viscoelasticity; cf., e.g., Argyris et al. (1977), Bažant (2001), Dutra et al. (2010), Fan et al. (2013), and Bažant and Jirásek (2018). Usually, these approaches make use of rheological systems, cf. Altenbach and Eisenträger (2021), Palmov (1998), Reiner (1960), and Giesekus (1994), such as Maxwell (Fan et al. 2013) or Kelvin chains (Argyris et al. 1977; Dutra et al. 2010; Bažant and Jirásek 2018), and derive the corresponding compliance functions. One of the earliest attempts to extend these linear viscoelastic models to non-linear creep was presented by Carol and Murcia in 1989 (1989). The authors formulated an incremental model based on an ageing Maxwell chain, which accounts for non-linear compressive creep of concrete and reduces to a linear viscoelastic model at low stress levels. Another frequently used approach to extend viscoelastic models to non-linear creep is the introduction of a stress-dependent creep coefficient, as done for example in Ruiz et al. (2007) and Hamed (2014). In Ruiz et al. (2007), non-linear creep and failure of concrete under sustained compression are simulated based on the affinity hypothesis, which states that linear and non-linear creep strains are related through the ratio of the applied stress level to the short-term compressive strength. Alternatively, Hamed makes use of a generalized Maxwell model in combination with a modified principle of superposition and a stress-dependent creep coefficient to account for non-linear creep of concrete (Hamed 2014). While models based on linear viscoelasticity are straightforward to formulate and usually require a limited number of material parameters, these approaches suffer from two drawbacks: First, viscoelastic models with compliance functions do not allow for the consideration of load cycles or the description of the non-linear behaviour under higher loads (Bockhold and Stangenberg 2004). Second, it is stated in Ren et al. (2020) that the extension based on stress-dependent creep coefficient is not suitable for multiaxial stress states.

Due to the limitations given above, alternative formulations have been proposed. In the literature, a few attempts based on fracture mechanics can be found; cf., for instance, Bažant and Jirásek (1993) and Barpi and Valente (2002). In Bažant and Jirásek (1993), the framework of linear elastic fracture mechanics is utilized to model non-linear creep in concrete, rock, and other quasi-brittle materials by replacing the elastic constants by linear viscoelastic operators. Barpi and Valente couple a viscoelastic rheological model with a fictitious (cohesive) crack model to account for creep and fracture in concrete (Barpi and Valente 2002). Another important group of constitutive models for non-linear creep of concrete is based on the microprestress-solidification (MPS) theory (Bažant et al. 1997; Mazzotti and Savoia 2003; Yu et al. 2020). Within this theory, the age dependence of concrete compliance is assumed to result from changes in the composition of the concrete mix, i.e., the *concentrations*

of constituents change, while the properties of the constituents themselves remain constant. Ageing of concrete is modelled based on two mechanisms: the relaxation of the microprestress and the volume growth of hydration products. Mazzotti and Savoia formulate a creep damage model based on a non-linear MPS theory (Mazzotti and Savoia 2003), while in Yu et al. (2020), the MPS approach is modified to account for the size effect in drying creep and to improve the description of the influence of humidity on transient thermal creep. Note that two drawbacks of the MPS theory are pointed out in Bockhold (2007): on the one hand, material non-linearities are accounted for based on an artificial extension of the formulation. On the other hand, the consideration of multiaxial stress and strain states is problematic.

By far, the largest group of constitutive models for non-linear creep of concrete, formulated particularly within the last twenty years, combines rheological models from viscoelasticity with approaches from classical plasticity theory and continuum damage mechanics (CDM). Typical representatives for these models are presented in de Borst (1987), Papa and Taliercio (1996), Papa and Taliercio (2005), Bockhold and Stangenberg (2004), Bockhold (2007), Challamel et al. (2005), Contrafatto and Cuomo (2006), Luzio (2009), Gernay et al. (2013), Kindrachuk et al. (2015), Huang et al. (2019), and Ren et al. (2020). These concepts usually consist of three parts: rheological systems such as Maxwell (de Borst 1987; Papa and Taliercio 2005; Luzio 2009) or Kelvin chains (Papa and Taliercio 2005; Bockhold 2007) to account for time-dependent creep deformation, a yield criterion and flow rule coupled with hardening variables to describe instantaneous plastic strains, and damage variables. For modelling plastic strains, the Drucker-Prager yield criterion is frequently applied for concrete, as done for instance in Bockhold and Stangenberg (2004), Bockhold (2007), Gernay et al. (2013), and Kindrachuk et al. (2015). Since the behaviour of concrete in tension differs significantly from the behaviour in compression, many formulations incorporate the Rankine yield criterion for the tensile regime of concrete (Bockhold and Stangenberg 2004; Bockhold 2007; Gernay et al. 2013). In addition, isotropic hardening variables are usually integrated into the constitutive models as well in order to allow for a refined representation of the evolution of inelastic strains (de Borst 1987; Bockhold and Stangenberg 2004; Bockhold 2007; Contrafatto and Cuomo 2006; Gernay et al. 2013; Kindrachuk et al. 2015; Huang et al. 2019). Note that in Gernay et al. (2013) and Huang et al. (2019) separate isotropic hardening variables for tension and compression are introduced in order to account for the anisotropic behaviour of concrete.

A variety of concepts is used by these constitutive models to account for damage. Most approaches make use of CDM since it represents a powerful modelling technique for concrete where deterioration is due to many micro-cracks (Kindrachuk et al. 2015). Thus, a phenomenological smeared crack approach is chosen to model damage in concrete, which is often interpreted as the time-dependent deterioration of the material characteristics. Various constitutive models introduce scalar damage variables as internal variables and formulate evolution equations, which is originally based on Kachanov's damage model (Kachanov 1958). Note that the formulations based on Kachanov's approach usually make use of Lemaitre and Chaboche's effective stress concept (Lemaitre 1996, 1971). To include internal damage variables into

a constitutive model, basically three different approaches are available, depending on the type of damage variable (Altenbach et al. 1990): scalar damage variables (Papa and Taliercio 1996; Challamel et al. 2005; Contrafatto and Cuomo 2006; Kindrachuk et al. 2015), second-order damage tensors (Papa and Taliercio 1996, 2005), and fourth-order damage tensors (de Borst 1987; Bockhold and Stangenberg 2004; Bockhold 2007; Gernay et al. 2013; Ren et al. 2020). Note that it is also possible to define damage tensors of eighth order, as explained in Murakami (2012)—a complex and, consequently, rarely applied approach. In contrast to Contrafatto and Cuomo (2006), where two separate scalar damage variables are introduced for tension and compression, most constitutive models with scalar damage variables only employ a single damage variable both for tension and compression for the sake of simplicity. It is also worth pointing out that although some approaches, such as the ones presented in Gernay et al. (2013), Ren et al. (2020), initially make use of fourth-order damage tensors, these tensors are only based on two scalar damage variables for tension and compression. Challamel et al. point out that isotropic damage models based on scalar variables face severe limitations since the dilatancy phenomenon, i.e., the inelastic volumetric expansion of concrete under compression, cannot be taken into account (Challamel et al. 2005). Furthermore, it is criticized in Papa and Taliercio (1996) that isotropic damage models are not able to account for damage-induced anisotropy. For this reason, the authors utilize a scalar variable for volumetric damage as well as two damage tensors of second order for tension and compression. On the other hand, various drawbacks of damage tensors and advantages of scalar damage variables are discussed in Contrafatto and Cuomo (2006), Gernay et al. (2013). First, isotropic damage variables help to overcome convergence problems when implementing non-isotropic damage models. Second, flow rules of anisotropic damage models with damage tensors are often established on an empirical basis. Third, scalar damage variables are often sufficient unless rapidly rotating stress states are present. Furthermore, the lack of experimental data on damage evolution of concrete under complex stress states also motivates the use of scalar damage variables.

In addition to the previously discussed constitutive models, two recent formulations are worth mentioning as well. First, Sellier et al. introduce a complex multi-mechanism model based on poro-mechanics to simulate non-linear basic creep and drying creep considering multiaxial loading states (Sellier et al. 2016). Second, a multi-physics model including hydration, moisture, and heat transport is proposed in Boumakis et al. (2018). The authors introduce a discrete element framework based on the lattice discrete particle method. This approach includes the MPS theory to account for ageing viscoelasticity. Since different mechanisms, such as long-term creep or fracturing rate-dependence, need to be calibrated independently, the model requires a large number of different experimental tests, which might be a practical limitation of the formulation, as it is also pointed out in Boumakis et al. (2018).

7.1.3 Aim and Structure of the Current Contribution

The discussion in the previous two sections has shown that a variety of constitutive models for creep of concrete has already been proposed. However, many of the existing approaches focus only on linear creep of concrete, face difficulties with respect to multiaxial stress and deformation states or involve a large number of parameters, which makes the parameter identification cumbersome. Consequently, the paper at hand aims at closing this gap by presenting a robust constitutive model for the non-linear basic creep of plain concrete. The model should have the following features:

- predict primary and secondary basic creep of plain concrete in a robust and accurate manner,
- account for the time-dependency of parameters due to the hardening of concrete,
- suitable for loads up to 70% of the short-term strength of concrete,
- applicable to multiaxial stress and strain states, and
- involve a low number of parameters.

In the following section, the proposed approach is discussed, whereby we start by presenting the governing equations in one-dimensional form in Sect. 7.2.1. This is succeeded by a description of the calibration procedure in Sect. 7.2.2 and the transformation of the governing equations to three dimensions in Sect. 7.2.3. Finally, the calibrated model is verified against additional creep tests from the literature in Sect. 7.2.4. The paper concludes with a summary and an outlook on future work in Sect. 7.3.

7.2 Constitutive Model for Non-linear Basic Creep of Concrete

This section introduces a novel constitutive model for non-linear basic creep of plain concrete. First, the governing equations are discussed in a one-dimensional form. Then, the model is calibrated based on uniaxial creep tests, i.e., all material parameters are determined. In Sect. 7.2.3, the constitutive model is referred to three-dimensional stress and strain states, which is followed by a verification against a different set of creep tests in Sect. 7.2.4.

7.2.1 Governing Equations in One Dimension

First, let us introduce the governing equations of the constitutive model in one-dimensional form since the calibration is also based on uniaxial material tests. Hooke's law for linear elasticity holds such that the stress σ depends linearly on

the elastic strain ε^{el} :

$$\sigma = E \varepsilon^{\text{el}} \quad (7.1)$$

with Young's modulus E . The strains are split additively into the corresponding elastic and inelastic parts:

$$\varepsilon = \varepsilon^{\text{el}} + \varepsilon^{\text{in}}. \quad (7.2)$$

As discussed in Sect. 7.1.1, creep tests with specimens made from plain concrete prove that concrete exhibits primary and secondary creep both under tensile and compressive loads; cf., e.g., Hamed (2015), Domone (1974). Subjected to higher loads, concrete also shows a tertiary creep stage; cf. Papa and Talierecio (2005). However, since these load levels are not of practical relevance, the current model will focus only on primary and secondary creep. To account for the decrease of the strain rate during the primary creep stage, a kinematic hardening model involving the backstress β is adopted from Naumenko et al. (2011), Naumenko and Altenbach (2016), and Eisenträger (2018). The following evolution equations hold for the inelastic strain ε^{in} and the backstress:

$$\dot{\varepsilon}^{\text{in}} = \text{sgn}(\sigma - \beta) f_{\sigma}(|\sigma - \beta|) - \frac{\partial}{\partial t} \left(\frac{\beta}{E} \right), \quad (7.3)$$

$$\dot{\beta} = \frac{1}{E} \dot{E} \beta + E \frac{\alpha}{1 - \alpha} \left(\dot{\varepsilon}^{\text{in}} - \frac{\beta}{\beta_{\star}} |\dot{\varepsilon}^{\text{in}}| \right), \quad (7.4)$$

where the dot $\dot{\square} = \frac{\partial \square}{\partial t}$ denotes the partial derivative with respect to time. Note that the backstress is similar to the one introduced by Armstrong and Frederick (1966), as demonstrated in Naumenko et al. (2011). Furthermore, f_{σ} denotes the stress response function, and α as well as β_{\star} are two stress-dependent material parameters.

The last term in Eq. (7.3) describes the change in backstress and Young's modulus with respect to the time t . While this term is usually neglected when using the constitutive model to describe the behaviour of metals, cf. Eisenträger (2018), it is crucial to take this term into account for concrete due to the time-dependence of Young's modulus while concrete hardens (Gilbert and Ranzi 2011). By evaluating the last term in Eq. (7.3) and exploiting Eq. (7.4), Eq. (7.3) is transformed as follows:

$$\dot{\varepsilon}^{\text{in}} + \frac{\alpha}{1 - \alpha} \left(1 - \frac{\beta}{\beta_{\star}} \text{sgn}|\dot{\varepsilon}^{\text{in}}| \right) \dot{\varepsilon}^{\text{in}} = \text{sgn}(\sigma - \beta) f_{\sigma}(|\sigma - \beta|). \quad (7.5)$$

Finally, the evolution of Young's modulus during the hydration of concrete is described by the following equation extracted from Gilbert and Ranzi (2011):

$$E(t) = E_{28} \left[\exp \left[C_1 \left(1 - \sqrt{\frac{C_2}{t - t_0}} \right) \right] \right]^{C_3}, \quad (7.6)$$

where E_{28} denotes Young's modulus of concrete at an age of 28 d, and C_1 , C_2 , C_3 , and t_0 are further material parameters. The time derivative of Young's modulus is obtained as follows:

$$\dot{E}(t) = \frac{1}{2} E(t) C_1 \sqrt{C_2} C_3 (t - t_0)^{-1.5}. \quad (7.7)$$

7.2.2 Calibration

Due to the limited availability of experimental data, the constitutive model is first calibrated in its one-dimensional form based on both compressive and tensile creep tests. Afterwards, the one-dimensional equations are referred to multiaxial stress and strain states by introducing equivalent stress and strain measures.

The calibration of the one-dimensional creep model is based on the uniaxial compressive and tensile creep tests presented in Hamed (2015) and Domone (1974), respectively. For the compressive creep tests, cylindrical specimens made from plain concrete (water/cement ratio = 0.54) are loaded at an age of 64 d, considering four different stress levels, i.e., 30, 50, 60, and 70% of the compressive strength $f_c = -36$ MPa at the age of loading. Young's modulus and the short-term compressive strength at 28 d are given as $E_{28} = 26700$ MPa and $f_c^{28} = -32$ MPa (Hamed 2015). In addition, experimental data sets for tensile creep tests are extracted from Domone (1974) because these creep tests with specimens made from plain concrete are conducted at similar relative load levels, i.e., 25, 40, 55, 65, and 70% of the short-term strength $f_t^{28} = 2.12$ MPa. Furthermore, the water/cement ratio (0.55) of the concrete mixture is similar to the mixture used for the compressive creep tests in Hamed (2015). Note that the tensile creep tests are conducted at an age of 28 d.

Calibrating the creep model closely follows the procedure presented in Eisenträger (2018) and Eisenträger et al. (2018). In the first step, the stress response function f_σ is found, which is based on the initial state of deformation. At the very beginning of a creep test, the influence of hardening is negligible ($\beta \approx 0$, $\alpha \approx 0$) such that Eq. (7.5) can be simplified as follows:

$$\dot{\varepsilon}_{\text{init}}^{\text{in}} \approx \text{sgn}(\sigma) f_\sigma(|\sigma|). \quad (7.8)$$

Thus, the initial inelastic strain rate $\dot{\varepsilon}_{\text{init}}^{\text{in}}$ is determined for every creep test, both in tension and compression, as described in Eisenträger (2018) and Eisenträger et al. (2018). The resulting data is represented by red points in Fig. 7.2, whereby the upper diagram displays the absolute value of the initial inelastic strain rate depending on the absolute stress values for all compressive creep tests. The lower diagram summarizes the equivalent results for the tensile creep tests. Figure 7.2 also demonstrates that the experimental data is approximated with high accuracy by the power law function

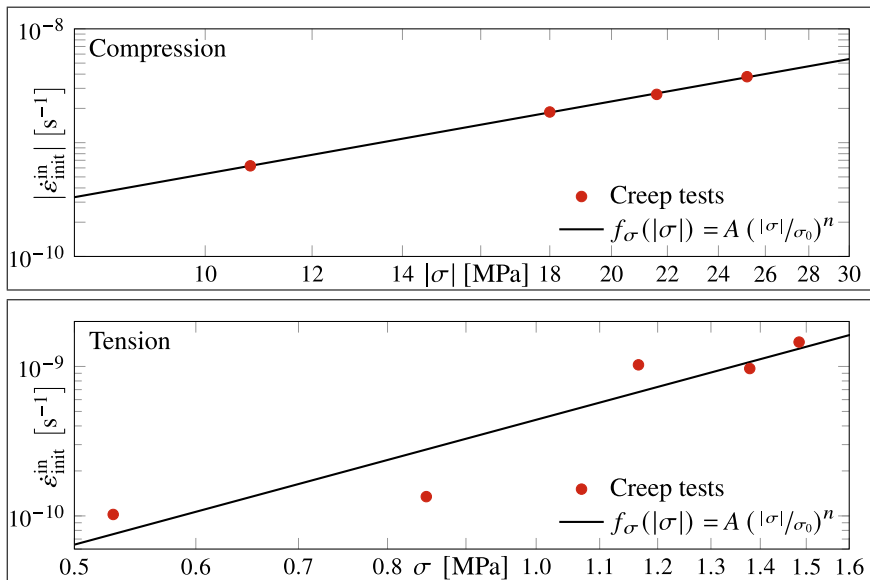


Fig. 7.2 Initial inelastic strain rates $\dot{\epsilon}_{\text{init}}^{\text{in}}$ versus stress σ for compressive and tensile creep tests

$$f_{\sigma}(|\sigma|) = A \left(\frac{|\sigma|}{\sigma_0} \right)^n \quad (7.9)$$

with the material parameters A , σ_0 , and n . The following values for these parameters are obtained via the optimization procedure described in Eisenträger (2018): $A_t = 3.009 \times 10^{-9} \text{ s}^{-1}$, $A_c = 5.317 \times 10^{-10} \text{ s}^{-1}$, $\sigma_{0_t} = 2.000 \text{ MPa}$, $\sigma_{0_c} = 10.000 \text{ MPa}$, $n_t = 2.775$, $n_c = 2.115$, while the subscripts \square_t and \square_c indicate whether the parameter is valid for tension or compression, respectively.

In addition to the stress response function, the parameters α and β_* must be determined. Both parameters describe the evolution of kinematic hardening, taking place particularly during the primary creep stage, and they are obtained via a parameter sensitivity study. Thereby, the tensile and compressive creep tests are simulated with the constitutive model by solving the system of equations, i.e., Eqs. (7.1), (7.2), (7.4), and (7.5), numerically with Matlab's solver `ode45`, which is based upon an explicit Runge-Kutta method (The MathWorks, Inc. 2021). For the simulation, the stress is prescribed as constant external load $\sigma = \bar{\sigma}$, and both the inelastic strain and the backstress are set to zero at the beginning of a creep test, i.e., $\epsilon^{\text{in}}(t = t_{\text{start}}) = 0$ and $\beta(t = t_{\text{start}}) = 0$. To obtain suitable values for β_* and α , both parameters are varied systematically, and the obtained creep curves are compared to the experimental results by using the following error $\Delta \epsilon^{\text{in}}$ in inelastic strain which is defined based on the L^2 norm:

$$\Delta \varepsilon^{\text{in}} = \sqrt{\frac{\int_{t_{\text{start}}}^{t_{\text{end}}} \left[\varepsilon_{\text{exp}}^{\text{in}}(t) - \varepsilon_{\text{num}}^{\text{in}}(t) \right]^2 dt}{\int_{t_{\text{start}}}^{t_{\text{end}}} \left[\varepsilon_{\text{exp}}^{\text{in}}(t) \right]^2 dt}}. \quad (7.10)$$

The subscript \square_{exp} denotes the experimental data, while the subscript \square_{num} refers to Matlab's results. Furthermore, the integrals with respect to time are computed via the trapezoidal rule, and t_{start} and t_{end} are the start and end time of the individual creep test. An overall error measure for all tensile or compressive creep tests is obtained as mean average of the errors in inelastic strain of the individual creep tests in tension or compression, respectively. Then, values for the parameters α and β_* , which result in a minimal error in inelastic strain for all tests, are found and interpolated with the following functions to obtain the stress dependence:

$$\alpha(|\sigma|) = A_1 \left(\frac{2}{1 + \exp(-A_2 |\sigma|)} - 1 \right) + A_3 \left(\frac{2}{1 + \exp(-A_4 (|\sigma| - A_5))} - 1 \right) + A_6, \quad (7.11)$$

$$\beta_*(|\sigma|) = B_1 + B_2 |\sigma|. \quad (7.12)$$

In Eqs. (7.11) and (7.12), the parameters $A_1, A_2, A_3, A_4, A_5, A_6, B_1,$ and B_2 are introduced. Note that the actual values of these parameters differ depending on the type of loading, as can be seen from Table 7.1, which provides an overview of all material parameters used in the one-dimensional formulation of the constitutive model for basic creep of plain concrete. The parameters $C_1, C_2, C_3,$ and t_0 are adopted from Gilbert and Ranzi (2011), and the value for Young's modulus at an age of 28 d is taken from Hamed (2015).

Finally, both the compressive and tensile creep tests are simulated with the constitutive model, applying the found set of parameters and functions. The results are summarized in Fig. 7.3, whereby the top diagram contains the compressive creep tests and the lower diagram displays the results of the tensile tests. Note that the experimental results are depicted as solid black lines, whereas dashed red lines are used for the results of simulation. It becomes obvious that the constitutive model provides an accurate approximation of the compressive creep tests and a good-quality approximation of the tensile creep tests with slightly higher deviations compared to the compressive tests. This effect can partly be explained by the higher scatter of the tensile creep tests, as becomes obvious in Fig. 7.2. While the initial creep rates in compression can be fitted by the stress response function with high accuracy, the data resulting from the tensile creep tests shows larger deviations from the power law stress response function.

Table 7.1 Material parameters in the one-dimensional constitutive model for basic creep of plain concrete

| Variable | Value | Value (compression) | Value (tension) | Unit |
|------------|-----------|-------------------------|------------------------|------------|
| C_1 | 0.380 | — | — | — |
| C_2 | 28.000 | — | — | d |
| C_3 | 0.500 | — | — | — |
| t_0 | 0.000 | — | — | s |
| E_{28} | 26700.000 | — | — | MPa |
| A | — | 5.317×10^{-10} | 3.009×10^{-9} | s^{-1} |
| σ_0 | — | 10.000 | 2.000 | MPa |
| n | — | 2.115 | 2.775 | — |
| B_1 | — | 12.400 | 0.000 | MPa |
| B_2 | — | 0.488 | 0.882 | — |
| A_1 | — | 0.000 | 1.000 | — |
| A_2 | — | 0.000 | 2.300 | MPa^{-1} |
| A_3 | — | 0.000 | -0.250 | — |
| A_4 | — | 0.000 | 5.000 | MPa^{-1} |
| A_5 | — | 0.000 | 1.320 | MPa |
| A_6 | — | 0.360 | -0.240 | — |

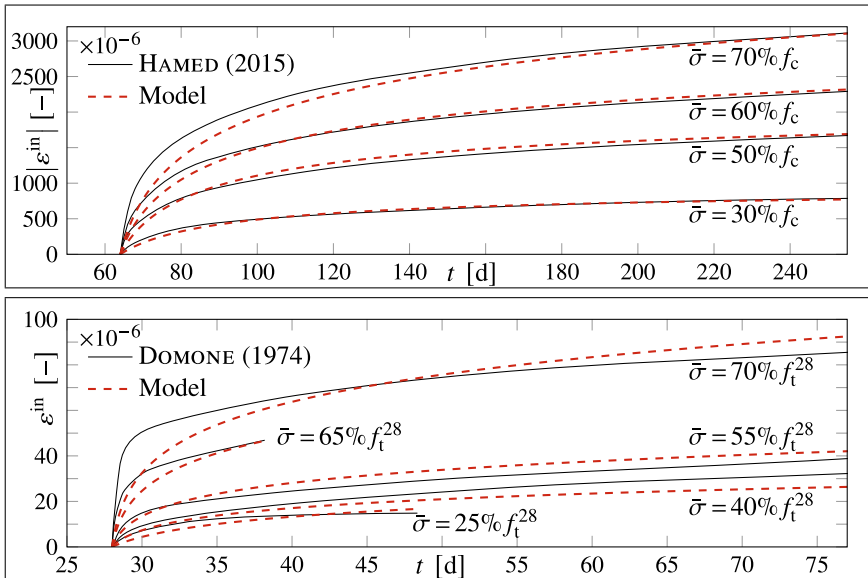


Fig. 7.3 Inelastic strain ϵ^{in} versus time t for creep tests. Compressive creep tests (top) with experimental data from Hamed (2015) and tensile creep tests (bottom) with experimental data from Domone (1974)

7.2.3 Governing Equations in Three Dimensions

To allow for the consideration of complex structures and loading scenarios, the current section extends the constitutive model presented as a one-dimensional formulation in Sect. 7.2.1 to multiaxial stress and strain states. This is primarily done by transforming the governing equations of the uniaxial model into a tensor notation and introducing adequate equivalent stress and strain measures. For plain concrete, the Drucker-Prager equivalent stress (Drucker and Prager 1952) is frequently used because it accounts for the influence of the deviatoric as well as hydrostatic stresses and has been proven to provide an accurate description for biaxial stress and strain states (Bockhold 2005). The Drucker-Prager equivalent stress is defined as follows Drucker and Prager (1952):

$$\sigma_{\text{eq}} = \gamma \left[\mu \text{tr}(\boldsymbol{\sigma}) + \sqrt{\frac{1}{2} \boldsymbol{\sigma}' : \boldsymbol{\sigma}'} \right] \quad (7.13)$$

with the biaxiality parameter μ and the abbreviation $\gamma = \left(\frac{1}{\sqrt{3}} - \mu \right)^{-1}$. Note that the parameter μ accounts for the influence of biaxial stresses and is obtained based on numerical tests in Krätzig and Pölling (2004) as $\mu = 0.050$, which is adopted by the current paper. Furthermore, the variable $\boldsymbol{\sigma}$ denotes the Cauchy stress tensor, and $\text{tr}(\square)$ represents the trace operator. The deviatoric part of a second-order tensor is marked by the prime $\square' = \square - \frac{1}{3} \text{tr}(\square) \mathbf{I}$ with the identity tensor $\mathbf{I} = \mathbf{e}_i \otimes \mathbf{e}_i$ with respect to an orthonormal vector basis $\{\mathbf{e}_i\}$. In Eq. (7.13), the double scalar product has been introduced which is defined via $\mathbf{A} : \mathbf{B} = A_{kl} B_{lk}$ for the two second-order tensors $\mathbf{A} = A_{kl} \mathbf{e}_k \otimes \mathbf{e}_l$ and $\mathbf{B} = B_{mn} \mathbf{e}_m \otimes \mathbf{e}_n$. Note that we make use of the Einstein summation convention.

As a next step, Eq. (7.1), i.e., Hooke's law for isotropic elasticity, is formulated for three dimensions:

$$\boldsymbol{\sigma} = K \varepsilon_{\text{V}}^{\text{el}} \mathbf{I} + 2G \boldsymbol{\varepsilon}^{\text{el}} \quad (7.14)$$

with the elastic strain tensor $\boldsymbol{\varepsilon}^{\text{el}}$, the volumetric strain $\varepsilon_{\text{V}} = \text{tr}(\boldsymbol{\varepsilon})$, as well as the bulk and shear modulus K and G , respectively. For three-dimensional elasticity, two independent material parameters are required. We make use of Poisson's ratio and assume that it is constant over time, i.e., $\nu = 0.2$, as proposed in Aili et al. (2016). Then, the shear and bulk moduli are obtained as follows based on the time-dependent function of Young's modulus in Eq. (7.6) and Poisson's ratio:

$$G(t) = \frac{E(t)}{2(1+\nu)}, \quad (7.15)$$

$$K(t) = \frac{E(t)}{3(1-2\nu)}. \quad (7.16)$$

Equation (7.14) can also be rewritten as follows:

$$\boldsymbol{\sigma} = \mathcal{C} : \boldsymbol{\varepsilon}^{\text{el}} \quad (7.17)$$

by introducing the elastic stiffness tetrad:

$$\mathcal{C} = \frac{1}{3} (3K - 2G) \mathbf{I} \otimes \mathbf{I} + 2G\mathcal{I}, \quad (7.18)$$

whereby $\mathcal{I} = \frac{1}{2} (\mathbf{e}_i \otimes \mathbf{e}_j \otimes \mathbf{e}_j \otimes \mathbf{e}_i + \mathbf{e}_i \otimes \mathbf{e}_j \otimes \mathbf{e}_i \otimes \mathbf{e}_j)$ is the symmetric unit tetrad. The split of strains into the elastic and inelastic parts, cf. Eq. (7.2), is obtained as follows after introducing the tensor of inelastic strains $\boldsymbol{\varepsilon}^{\text{in}}$:

$$\boldsymbol{\varepsilon} = \boldsymbol{\varepsilon}^{\text{el}} + \boldsymbol{\varepsilon}^{\text{in}}. \quad (7.19)$$

Additionally, the evolution equation for the inelastic strain, cf. Eq. (7.5), is transformed as follows by introducing the equivalent Drucker-Prager stress σ_{eq} , the backstress tensor $\boldsymbol{\beta}$, and the effective stress tensor $\tilde{\boldsymbol{\sigma}} = \boldsymbol{\sigma} - \boldsymbol{\beta}$:

$$\dot{\boldsymbol{\varepsilon}}^{\text{in}} = \gamma f_{\sigma}(\tilde{\sigma}_{\text{eq}}) \left[\mu \mathbf{I} + [1 - \alpha(\sigma_{\text{eq}})] \tilde{J}_2 \tilde{\boldsymbol{\sigma}}' + \frac{\gamma \alpha(\sigma_{\text{eq}})}{2\beta_{\star}(\sigma_{\text{eq}})} \boldsymbol{\beta}' \right]. \quad (7.20)$$

Note that the following abbreviation has been used in Eq. (7.20):

$$\tilde{J}_2 = \left(2\sqrt{\frac{1}{2} \tilde{\boldsymbol{\sigma}}' : \tilde{\boldsymbol{\sigma}}'} \right)^{-1}. \quad (7.21)$$

Furthermore, the equivalent effective stress $\tilde{\sigma}_{\text{eq}}$ is used in Eq. (7.20) and defined in analogy to Eq. (7.13):

$$\tilde{\sigma}_{\text{eq}} = \gamma \left[\mu \text{tr}(\tilde{\boldsymbol{\sigma}}) + \sqrt{\frac{1}{2} \tilde{\boldsymbol{\sigma}}' : \tilde{\boldsymbol{\sigma}}'} \right]. \quad (7.22)$$

The evolution equation for the backstress, cf. Eq. (7.4), is referred to three-dimensional stress and strain states, too:

$$\begin{aligned} \dot{\boldsymbol{\beta}} = & \frac{\dot{G}}{G} \boldsymbol{\beta}' + \frac{\dot{K}}{3K} \text{tr}(\boldsymbol{\beta}) \mathbf{I} + \frac{\alpha(\sigma_{\text{eq}})}{1 - \alpha(\sigma_{\text{eq}})} \left[2G (\dot{\boldsymbol{\varepsilon}}^{\text{in}})' + K \text{tr}(\dot{\boldsymbol{\varepsilon}}^{\text{in}}) \mathbf{I} \right. \\ & \left. - \gamma f_{\sigma}(\tilde{\sigma}_{\text{eq}}) \left(3K\mu \mathbf{I} + \frac{\gamma G}{\beta_{\star}(\sigma_{\text{eq}})} \boldsymbol{\beta}' \right) \right]. \end{aligned} \quad (7.23)$$

Note that in three dimensions, the equivalent stress measures are used as arguments for the stress response function f_{σ} as well as the parameters α and β_{\star} . The original functions according to Eqs. (7.9), (7.11), and (7.12) are not changed.

The three-dimensional formulation of the constitutive model makes use of the material parameters determined in Sect. 7.2.2; cf. Table 7.1. In the one-dimensional formulation of the model, some parameters vary depending on the type of loading, i.e., whether tension or compression occurs. For three-dimensional loading scenarios, the following criterion to distinguish tension and compression is suggested in Contrafatto and Cuomo (2006):

$$\text{tr}(\mathbf{e}^{\text{el}}) < 0 \Rightarrow \text{compression}, \quad (7.24)$$

$$\text{tr}(\mathbf{e}^{\text{el}}) > 0 \Rightarrow \text{tension}. \quad (7.25)$$

7.2.4 Verification of the Constitutive Approach

To verify the calibrated constitutive model, an additional set of experiments, i.e., the compressive creep tests from Roll (1964), is simulated. Creep tests at four different compressive load levels, i.e., $\bar{\sigma} = \{20\%, 35\%, 50\%, 65\%\} f_c^{28}$, are conducted at an age of 28 d. The compressive strength and Young's modulus account for $f_c^{28} = -42$ MPa and $E_{28} = 21500$ MPa, respectively. Figure 7.4 displays the obtained creep curves, i.e., the absolute value of the inelastic strain depending on time, whereby the experimental results marked as dots and dashed lines represent the simulation

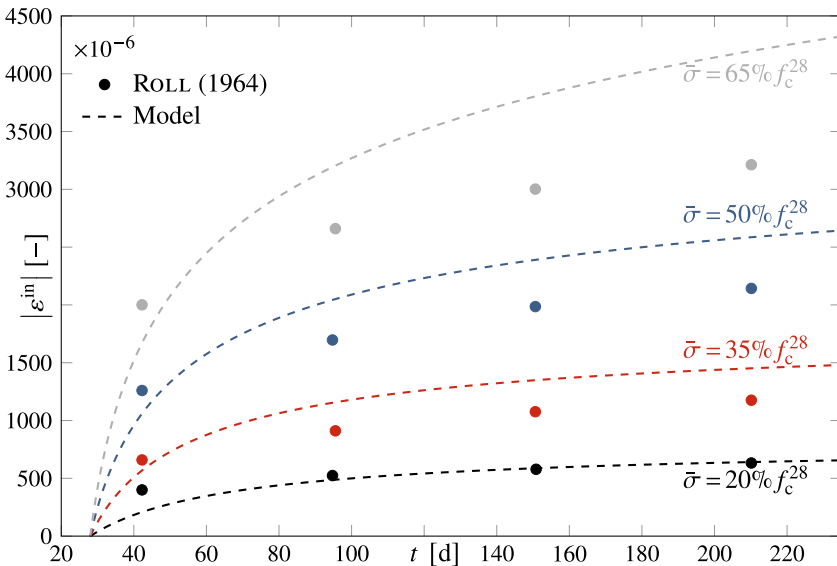


Fig. 7.4 Inelastic strain ε^{in} versus time t for compressive creep tests (experimental data from Roll 1964)

results. Note that Roll (1964) provides only limited information such that the experimental data is restricted to a low amount of data points. Nevertheless, it becomes evident that the constitutive model provides an adequate description of the experimental creep curves, and that the verification of the calibrated model has been successful. The lower the stress level, the more accurate the approximation by the constitutive model. However, it must be pointed out that creep of concrete varies to a high degree depending on the used mixture, the age at loading, the load level, curing conditions, etc. Therefore, it is highly recommended to apply utmost caution when using the calibrated model for other concrete mixes under varying conditions. In many cases, the constitutive model at hand must be recalibrated using different experimental results obtained with the same concrete mixture under similar conditions.

7.3 Summary and Outlook

The contribution at hand presents a constitutive model for non-linear basic creep of plain concrete. The governing equations are first formulated in one-dimensional form since material parameters are determined in a calibration procedure against uniaxial tensile and compressive creep tests from the literature. Coupled non-linear evolution equations are formulated with respect to the creep strain and a backstress variable, which allows for the consideration of kinematic hardening effects. To extend the analysis to complex structures, the constitutive model is referred to multiaxial stress and deformation states by applying a tensor notation and introducing the Drucker-Prager equivalent stress concept.

It has been demonstrated that the constitutive model is able to predict primary and secondary basic creep of plain concrete with high accuracy for loads up to 70% of the short-term strength. This holds both for tensile and compressive loading. The verification against an additional set of creep tests from the literature confirms the robustness of the developed approach, which involves a relatively low total number of material parameters.

The authors aim at implementing the constitutive model into a numerical framework such that the analysis of complex structures under realistic boundary conditions is feasible. Nowadays, plain concrete is rarely used without any reinforcement, which is why one has to consider both prestressed concrete (with continuous reinforcement) and short-fibre reinforced concrete. The numerical analysis of these structures poses several challenges. In previous analyses, cf. e.g., Zhang et al. (2020), Ya et al. (2023), the scaled boundary finite element method (SBFEM) has been identified as a powerful tool to simulate the behaviour of these structures and materials. The implementation of the presented constitutive model into the SBFEM can be realized in two different ways: either directly into an SBFEM code, as done for example in Eisenträger et al. (2020), or by implementing the constitutive model as a User Material (UMAT) subroutine into the commercial FE code Abaqus. Within the latter approach, the UMAT is combined with the User Element (UEL) presented in Ya et al. (2021, 2023). This would also allow for the consideration of fibre-pullout and damage.

Acknowledgements Johanna Eisenträger acknowledges the funding by the German Research Foundation (Deutsche Forschungsgemeinschaft—DFG) in context of the Project 422068083.

References

- Aili A, Vandamme M, Torrenti JM, Masson B, Sanahuja J (2016) *Cem Concr Res* 90:144. <https://doi.org/10.1016/j.cemconres.2016.09.014>
- Altenbach H, Eisenträger J (2021) *Lect Notes TICMI* 22:13
- Altenbach H, Altenbach J, Schießle P (1990) *Tech Mech-Eur J Eng Mech* 11(2):81
- Argyris JH, Pister KS, Szimmat J, Willam KJ (1977) *Comput Methods Appl Mech Eng* 10(2):199. [https://doi.org/10.1016/0045-7825\(77\)90006-8](https://doi.org/10.1016/0045-7825(77)90006-8)
- Armstrong PJ, Frederick CO (1966) A mathematical representation of the multiaxial Bauschinger effect. Tech. rep, Berkeley Nuclear Laboratories
- Atrushi DS (2003) Tensile and compressive creep of early age concrete: testing and modelling. PhD thesis, The Norwegian University of Science and Technology, Trondheim, Norway. <https://brage.bibsys.no/xmlui/handle/11250/231168>
- Barpi F, Valente S (2002) *Eng Fract Mech* 70(5):611. [https://doi.org/10.1016/s0013-7944\(02\)00041-3](https://doi.org/10.1016/s0013-7944(02)00041-3)
- Bažant ZP (2001) *Nucl Eng Des* 203(1):27. [https://doi.org/10.1016/S0029-5493\(00\)00299-5](https://doi.org/10.1016/S0029-5493(00)00299-5)
- Bažant ZP, Jirásek M (1993) *Int J Fract* 62:355
- Bažant ZP, Jirásek M (2018) Creep and hygrothermal effects in concrete structures, vol 225. Springer, Netherlands. <https://doi.org/10.1007/978-94-024-1138-6>
- Bažant ZP, Haugaard AB, Baweja S, Ulm FJ (1997) *J Eng Mech* 123(11):1188. [https://doi.org/10.1061/\(asce\)0733-9399\(1997\)123:11\(1188\)](https://doi.org/10.1061/(asce)0733-9399(1997)123:11(1188))
- Bissonnette B, Pigeon M (1995) *Cem Concr Res* 25(5):1075. [https://doi.org/10.1016/0008-8846\(95\)00102-1](https://doi.org/10.1016/0008-8846(95)00102-1)
- Bockhold J (2005) Modellbildung und numerische Analyse nichtlinearer Kriechprozesse in Stahlbetonkonstruktionen unter Schädigungsaspekten. PhD thesis, Ruhr-Universität Bochum
- Bockhold J (2007) *Comput Concr* 4(2):101
- Bockhold J, Stangenberg F (2004) *Beton- und Stahlbetonbau* 99(3):209. <https://doi.org/10.1002/best.200490098>
- Boumakis I, Luzio GD, Marcon M, Vorel J, Wan-Wendner R (2018) *Eng Fract Mech* 200:263. <https://doi.org/10.1016/j.engfracmech.2018.07.006>
- Carol I, Murcia J (1989) *Mater Struct* 22(3):176. <https://doi.org/10.1007/bf02472185>
- Challamel N, Lanos C, Casandjian C (2005) *Eur J Mech A/Solids* 24(4):593. <https://doi.org/10.1016/j.euromechsol.2005.05.003>
- Charpin L, Pape YL, Coustabeau É, Toppani É, Heinfling G, Bellego CL, Masson B, Montalvo J, Courtois A, Sanahuja J, Reviron N (2018) *Cem Concr Res* 103:140. <https://doi.org/10.1016/j.cemconres.2017.10.009>
- Contrafatto L, Cuomo M (2006) *Int J Plast* 22(12):2272. <https://doi.org/10.1016/j.ijplas.2006.03.011>
- de Borst R (1987) *Comput Methods Appl Mech Eng* 62(1):89. [https://doi.org/10.1016/0045-7825\(87\)90091-0](https://doi.org/10.1016/0045-7825(87)90091-0)
- Domone PL (1974) *Mag Concr Res* 26(88):144. <https://doi.org/10.1680/macr.1974.26.88.144>
- Drucker DC, Prager W (1952) *Q Appl Math* 10(2):157
- Dutra VFP, Maghous S, Filho AC, Pacheco AR (2010) *Cem Concr Res* 40(3):460. <https://doi.org/10.1016/j.cemconres.2009.10.018>
- Eisenträger J (2018) A framework for modeling the mechanical behavior of tempered martensitic steels at high temperatures. PhD thesis, Otto von Guericke University Magdeburg

- Eisenträger J, Naumenko K, Altenbach H (2018) *J Strain Anal Eng Des* 53:156. <https://doi.org/10.1177/0309324718755956>
- Eisenträger J, Zhang J, Song C, Eisenträger S (2020) *Int J Mech Sci* 182:105778. <https://doi.org/10.1016/j.ijmecsci.2020.105778>
- Fan LF, Wong LNY, Ma GW (2013) *Constr Build Mater* 48:814. <https://doi.org/10.1016/j.conbuildmat.2013.07.010>
- Gernay T, Millard A, Franssen JM (2013) *Int J Solids Struct* 50(22–23):3659. <https://doi.org/10.1016/j.ijsolstr.2013.07.013>
- Giesekus H (1994) *Phänomenologische Rheologie*. Springer, Berlin
- Gilbert RI, Ranzi G (2011) *Time-dependent behaviour of concrete structures*. Taylor & Francis Ltd
- Gu X, Jin X, Zhou Y (2016) *Basic principles of concrete structures*. Springer, Berlin. <https://doi.org/10.1007/978-3-662-48565-1>
- Hamed E (2014) *Mech Time-Depend Mater* 18(3):589. <https://doi.org/10.1007/s11043-014-9243-7>
- Hamed E (2015) *Mag Concr Res* 67(16):876. <https://doi.org/10.1680/macrc.14.00307>
- Huang H, Garcia R, Huang SS, Guadagnini M, Pilakoutas K (2019) *Mater Struct* 52(6). 10.1617/s11527-019-1432-z
- Jordaan JJ, Illston JM (1969) *Mag Concr Res* 21(69):195. <https://doi.org/10.1680/macrc.1969.21.69.195>
- Kachanov LM (1958) *Izv AN SSSR Otd Tekh Nauk* 8:26
- Kennedy TW (1975) *Evaluation and summary of a study of the long-term multiaxial creep behavior of concrete*. Technical report, Oak Ridge National Laboratory. <https://doi.org/10.2172/7353378>
- Kim JK, Kwon SH, Kim SY, Kim YY (2005) *Mag Concr Res* 57(10):623. <https://doi.org/10.1680/macrc.2005.57.10.623>
- Kindrachuk VM, Thiele M, Unger JF (2015) *Int J Fatigue* 78:81. <https://doi.org/10.1016/j.ijfatigue.2015.03.026>
- Kovler K (1995) *J Mater Civ Eng* 7(2):96. [https://doi.org/10.1061/\(ASCE\)0899-1561\(1995\)7:2\(96\)](https://doi.org/10.1061/(ASCE)0899-1561(1995)7:2(96))
- Kovler K, Igarashi S, Bentur A (1999) *Mater Struct* 32(5):383. <https://doi.org/10.1007/BF02479631>
- Krätzig WB, Pölling R (2004) *Comput Struct* 82(15–16):1201. <https://doi.org/10.1016/j.compstruc.2004.03.002>
- Lemaitre J (1971) *Proceedings I. C. M.* 1
- Lemaitre J (1996) *A course on damage mechanics*. Springer Science & Business Media
- Liang S, Wei Y (2019) *Cem Concr Compos* 104:103421. <https://doi.org/10.1016/j.cemconcomp.2019.103421>
- Luzio GD (2009) *J Eng Mech* 135(7):632. [https://doi.org/10.1061/\(asce\)0733-9399\(2009\)135:7\(632\)](https://doi.org/10.1061/(asce)0733-9399(2009)135:7(632))
- Mazzotti C, Savoia M (2003) *J Eng Mech* 129(9):1065. [https://doi.org/10.1061/\(asce\)0733-9399\(2003\)129:9\(1065\)](https://doi.org/10.1061/(asce)0733-9399(2003)129:9(1065))
- Murakami S (2012) *Continuum damage mechanics*. In: *A continuum mechanics approach to the analysis of damage and fracture*. Springer, Dordrecht. 10.1007/978-94-007-2666-6
- Naumenko K, Altenbach H (2016) *Modeling high temperature materials behavior for structural analysis: part I: continuum mechanics foundations and constitutive models*. Springer International Publishing, *Advanced structured materials*. <https://doi.org/10.1007/978-3-319-31629-1>
- Naumenko K, Altenbach H, Kutschke A (2011) *Int J Damage Mech* 20(4):578. <https://doi.org/10.1177/1056789510386851>
- Neville AM (1995) *Properties of concrete*. Pearson Education Limited
- Østergaard L, Lange DA, Altoubat SA, Stang H (2001) *Cem Concr Res* 31(12):1895. [https://doi.org/10.1016/s0008-8846\(01\)00691-3](https://doi.org/10.1016/s0008-8846(01)00691-3)
- Palmov VA (1998) *Vibrations of elasto-plastic bodies*. Springer, Berlin, *Foundations of engineering mechanics*. <https://doi.org/10.1007/978-3-540-69636-0>
- Papa E, Talierecio A (1996) *Eng Fract Mech* 55(2):163. [https://doi.org/10.1016/0013-7944\(96\)00004-5](https://doi.org/10.1016/0013-7944(96)00004-5)

- Papa E, Taliercio A (2005) *Int J Numer Anal Methods Geomech* 29(3):287. <https://doi.org/10.1002/nag.415>
- Ranaivomanana N, Multon S, Turatsinze A (2013) *Cem Concr Res* 52:1. <https://doi.org/10.1016/j.cemconres.2013.05.001>
- Reiner M (1960) *Deformation, strain and flow: an elementary introduction to rheology*. H. K, Lewis, London
- Ren X, Wang Q, Ballarini R, Gao X (2020) *J Eng Mech* 146(5):04020027. [https://doi.org/10.1061/\(asce\)em.1943-7889.0001748](https://doi.org/10.1061/(asce)em.1943-7889.0001748)
- Roll F (1964) Symposium paper, vol 9, p 95
- Ross AD (1958) *J Am Concr Inst* 54(3):739
- Ruiz MF, Muttoni A, Gambarova PG (2007) *J Adv Concr Technol* 5(3):383. <https://doi.org/10.3151/jact.5.383>
- Sellier A, Multon S, Buffo-Lacarrière L, Vidal T, Bourbon X, Camps G (2016) *Cem Concr Res* 79:301. <https://doi.org/10.1016/j.cemconres.2015.10.001>
- The MathWorks, Inc. (2021) MATLAB R2021a Documentation
- Ya S, Eisenträger S, Song C, Li J (2021) *Comput Methods Appl Mech Eng* 381:113766. <https://doi.org/10.1016/j.cma.2021.113766>
- Ya S, Eisenträger S, Qu Y, Zhang J, Kuen T, Song C (2023) *Soil Dyn Earthq Eng* 164:107620. <https://doi.org/10.1016/j.soildyn.2022.107620>
- Yu P, Duan YH, Fan QX, Tang SW (2020) *Constr Build Mater* 243:118183. <https://doi.org/10.1016/j.conbuildmat.2020.118183>
- Zhang J, Eisenträger J, Duczek S, Song C (2020) *Compos Struct* 235:111744. <https://doi.org/10.1016/j.compstruct.2019.111744>

Chapter 8

On Tensile Instability of Elastic Structures with Elastic Sliders of Different Stiffness



Vadim V. Eremeev and Polina A. Lapina

Abstract We analyze interesting phenomena of elastic instability under tension. For example, such an instability relates to neck formations in thin rods. It can also be observed in systems with sliders. Here we discuss a response of a one-dimensional elastic structure with sliders having different stiffness. As a result of multiple bucklings, we get a softening regime under tension.

Keywords Bifurcation · Stability · Slider · Instability under tension

8.1 Introduction

Nowadays the interest is growing to new microstructured or architected materials such as beam-lattice materials. They may demonstrate interesting unusual behavior such as instability under tension. Indeed, the most known is buckling behavior under compression. Some elastic structures with observed instability under tension were discussed by Zaccaria et al. (2011), Bertoldi et al. (2017), Bigoni et al. (2018), Eremeyev and Turco (2020), Chróścielewski et al. (2020). The peculiarity of the latter structures consists of the existence of particular elements called sliders. Possible sliding brings a certain nonlinearity and further bifurcations. Let us note that sliding plays a crucial role also in other microstructured materials such as masonries, see, e.g., Rios et al. (2022a); Rios et al. (2022b).

Here we modify the model proposed by Chróścielewski et al. (2020), Eremeyev and Turco (2020) in order to have multiple sliders of different shear stiffness. The

The original version of this chapter has been revised: The author name has been amended. The correction to this chapter is available at https://doi.org/10.1007/978-3-031-43210-1_33

V. V. Eremeev (✉) · P. A. Lapina

Research and Education Center “Materials”, Don State Technical University, Rostov-on-Don 344000, Russia
e-mail: er.vadim@gmail.com

P. A. Lapina

e-mail: polina-azarova86@mail.ru

© The Author(s), under exclusive license to Springer Nature Switzerland AG 2023, corrected publication 2023

155

H. Altenbach and V. Eremeyev (eds.), *Advances in Linear and Nonlinear Continuum and Structural Mechanics*, Advanced Structured Materials 198,
https://doi.org/10.1007/978-3-031-43210-1_8

structure under consideration consists of n elements (elementary cells). Each cell consists of two elastic bars of the same length and stiffness and a slider. The latter possesses a shear stiffness.

The chapter is organized as follows. First, we discuss the tension of an elementary cell. The loading diagram is plotted and a critical force is determined. Then we discuss a system of n parallel connected elementary cells. We assume that all elastic bars have the same stiffness whereas the shear stiffnesses of sliders are different, in general. As a result, we obtain a force-displacement diagram for this system.

8.2 Elementary Cell Under Tension

Following Chróscielewski et al. (2020), Eremeyev and Turco (2020), let us consider the tension of an elastic structure shown in Fig. 8.1. It consists of two elastic bars connected through a slider. The latter consists of two rigid bars and has a shear spring that prevents the free sliding of these bars. The upper elastic bar is loaded by tensile dead force P , whereas the second bar is fixed at the end. For this system, we have two kinematical descriptors, elongation $\lambda = l - l_0$ and the angle of slider rotation ϕ . So the cell has two degrees of freedom, translational and rotational ones. This structure can exhibit so-called rotation instability related to the appearance of a rotational mode of deformation.

In the following, we use a variational approach. The total potential energy has the form

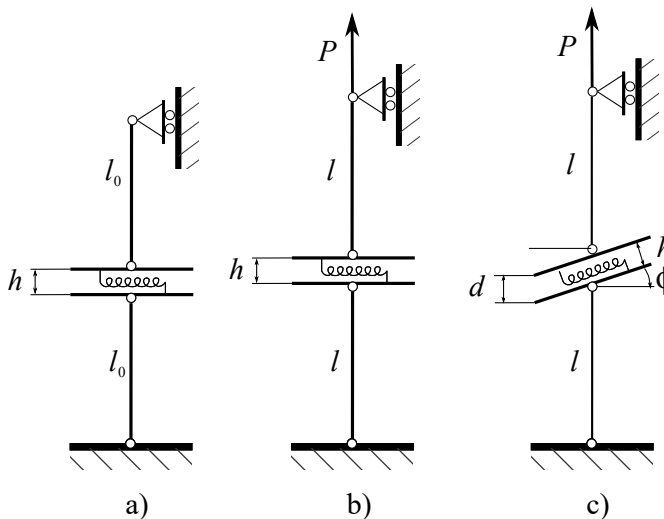


Fig. 8.1 Elementary cell with slider: **a** reference placement; **b** current placement without rotation; **c** current placement with rotation

$$E = U - V,$$

where U is an elastic energy, whereas V is the potential of external loads. U and V are given by the following formulae

$$\begin{aligned} U &= 2U_b + U_s, \quad V = Pu, \quad u = L - L_0, \quad L_0 = 2l_0 + h, \quad L = 2l + d, \\ U_b &= \frac{1}{2}C\lambda^2, \quad \lambda = l - l_0, \quad d = \frac{h}{\cos \phi} - h, \\ U_s &= \frac{1}{2}k\gamma^2, \quad \gamma = h \tan \phi. \end{aligned}$$

Hereinafter C is the stiffness of the bars, u is the displacement of the upper end, l and l_0 are lengths of the bars in reference and current placements, respectively, k is the stiffness of a shear spring. In addition, h is the distance between the faces of the slider. Note that we assume that h is constant during deformation. As a result, we have the formula

$$E = C\lambda^2 + \frac{1}{2}kh^2 \tan^2 \phi - P \left(2\lambda + \frac{h}{\cos \phi} - h \right). \quad (8.1)$$

Equilibrium equations follow from the stationarity conditions

$$\frac{\partial E}{\partial \lambda} = 2C\lambda - 2P = 0, \quad (8.2)$$

$$\frac{\partial E}{\partial \phi} = \frac{h \sin \phi}{\cos^2 \phi} \left[\frac{kh}{\cos \phi} - P \right] = 0. \quad (8.3)$$

Obviously, Eqs. (8.2) and (8.3) have two solutions. The first one is trivial and relates to straight configuration shown in Fig. 8.1b. It is given by

$$\lambda = P/C, \quad \phi = 0.$$

The second one is non-trivial and corresponds to so-called rotational instability, see Chróścielewski et al. (2020). It is given by the formulae

$$\lambda = \frac{P}{C}, \quad P = \frac{kh}{\cos \phi}.$$

We can show that the second solution is energetically preferable.

For the first solution, we have the following $P - u$ dependence

$$P = \frac{C}{2}u, \quad (8.4)$$

whereas the second solution results in the formula

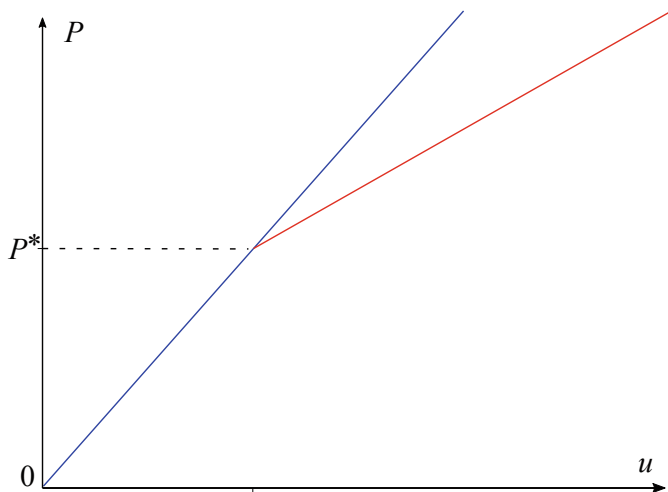


Fig. 8.2 Force–displacement diagram with bifurcation point at $P = P^*$

$$P = \frac{C}{2 + C/k}u - \frac{h}{1 + C/2k}. \quad (8.5)$$

The force–displacement diagram is given in Fig. 8.2. The second solution exists if and only if $P > P^* \equiv kh$. It is shown in red in Fig. 8.2, whereas the primary solution corresponds to the blue line which starts at the origin of the coordinate system. Obviously, we have a bifurcation here and P^* is a critical force.

8.3 Multiple Bifurcations

Let us now consider a system of n cells such as shown in Fig. 8.3. Here only vertical displacements are assumed. For simplicity, we assume that all elastic bars have the same stiffness C , whereas shear springs are different in stiffness. Without loss of generality, we assume that they are ordered as follows

$$k_1 \leq k_2 \dots \leq k_n.$$

The elastic energy U became a sum

$$U = \sum_{i=1}^n C\lambda_i^2 + \frac{1}{2} \sum_{i=1}^n k_i h^2 \tan^2 \phi_i, \quad (8.6)$$

whereas the work of external force has the same form $V = Pu$ with u given by

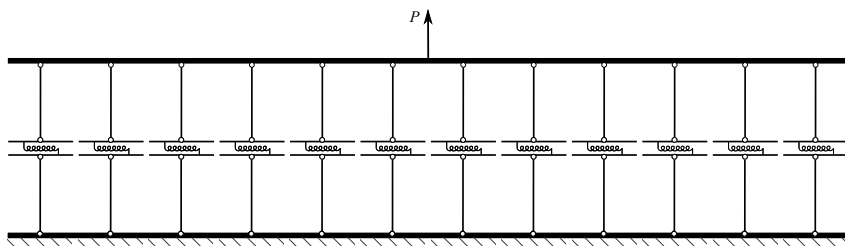


Fig. 8.3 Structure with n elementary cells. Here $n = 12$

$$u = 2\lambda_i + \frac{h}{\cos \phi_i} - h, \quad i = 1, \dots, n.$$

So this system has $n + 1$ degrees of freedom, for example, u and ϕ_i can be chosen as for λ_i we have the relation $\lambda_i = u/2 + h/2 - h/2\cos \phi_i$. As a result, the stationarity conditions of the total potential energy take the form

$$\begin{aligned} \frac{\partial E}{\partial u} &= \sum_{i=1}^n 2C\lambda_i \frac{\partial \lambda_i}{\partial u} - P \\ &= \sum_{i=1}^n \frac{C}{2} \left[u + h - \frac{h}{\cos \phi_i} \right] - P = 0, \end{aligned} \quad (8.7)$$

$$\begin{aligned} \frac{\partial E}{\partial \phi_i} &\equiv \frac{\partial U}{\partial \phi_i} = \sum_{j=1}^n 2C\lambda_j \frac{\partial \lambda_j}{\partial \phi_i} + h^2 k_i \tan \phi_i \frac{1}{\cos^2 \phi_i} \\ &= -Ch \left[u + h - \frac{h}{\cos \phi_i} \right] \frac{\sin \phi_i}{\cos^2 \phi_i} + h^2 k_i \frac{\sin \phi_i}{\cos^3 \phi_i} = 0. \end{aligned} \quad (8.8)$$

As in the previous case we have the primary solution in the form

$$P = n \frac{C}{2} u, \quad \phi_i = 0, \quad i = 1, \dots, n, \quad (8.9)$$

and a series of non-trivial solutions with $\phi_i \neq 0$ given by

$$P = \sum_{i=1}^n \frac{C}{2} \left[u + h - \frac{h}{\cos \phi_i} \right], \quad (8.10)$$

$$\frac{H \sin \phi_i}{\cos^2 \phi_i} \left[\frac{hk_i}{\cos \phi_i} - C(u + h) + \frac{Ch}{\cos \phi_i} \right] = 0, \quad i = 1, \dots, n. \quad (8.11)$$

The last equation results in more simple dependence

$$\frac{h}{\cos \phi_i} = \frac{C}{C + k_i}(u + h). \quad (8.12)$$

From (8.12) it follows that a solution exists when the following inequality is fulfilled

$$\frac{u}{h} \geq \frac{k_i}{C}. \quad (8.13)$$

This means that in the range $u < k_1/C$ there exists only the primary solution. In the range

$$\frac{hk_1}{C} \leq u < \frac{hk_2}{C}$$

we have two solutions, the primary and secondary ones. Finally, for $u > hk_n/C$ we have $n + 1$ solutions.

The effective stiffness of the structure under consideration depends on the chosen solution. For the primary solution, it is a stiffness of n parallel bars. So we have

$$S_0 = \frac{nC}{2}. \quad (8.14)$$

For the second solution, we get

$$S_1 = (n - 1) \frac{C}{2} + \frac{C}{2} \frac{k_1}{C + k_1}, \quad (8.15)$$

for the tertiary solution we obtain

$$S_2 = (n - 2) \frac{C}{2} + \frac{C}{2} \frac{k_1}{C + k_1} + \frac{C}{2} \frac{k_2}{C + k_2}. \quad (8.16)$$

Finally, it becomes

$$S_n = \frac{C}{2} \sum_{i=1}^n \frac{k_i}{C + k_i}. \quad (8.17)$$

Obviously, the effective stiffness parameters are ordered as follows

$$S_n < S_{n-1} < \dots < S_2 < S_1 < S_0. \quad (8.18)$$

So consequent bucklings result in the softening of the structure.

The corresponding force–displacement graph is shown in Fig. 8.4. Here $u_i^* = hk_i/C$. u_i^* is the abscissa of intersections of lines $P_{i-1}(u)$ and $P_i(u)$. As any new solution is energetically preferable, the force–displacement curve became a broken line shown in Fig. 8.5.

So one can see that sliding brings a softening in tension. Let us also note that similar behavior for a system of parallel bars one can obtain considering elastoplas-

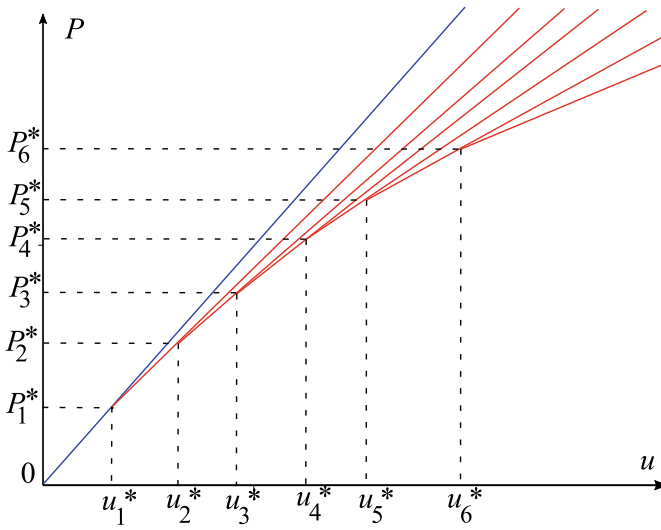


Fig. 8.4 Force–displacement diagram with bifurcation points at $P = P_i^*$. Here only six points are shown

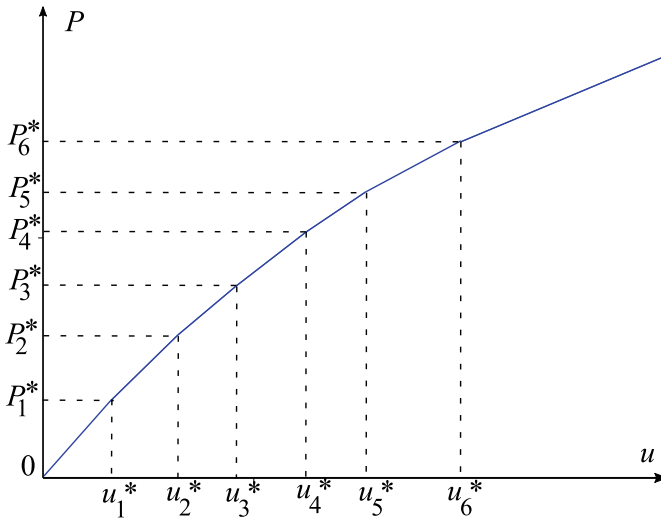


Fig. 8.5 Resulting force–displacement diagram

tic behavior. Indeed, in the case of elastoplasticity with hardening an elastoplastic bar exhibits a behavior similar to that given in Fig. 8.2. So a system of parallel elastoplastic bars may have the same behavior as in Fig. 8.5. Similar and even more complex behavior one can observe in media with damage, see, e.g., Lemaitre (1992, pp. 90–94). Unlike these structures, here we have a pure elastic regime.

8.4 Conclusions

We presented a one-dimensional elastic structure that consists of n elements. Each element consists of two elastic bars connected through a slider with shear stiffness. Considering a range of shear stiffness we obtained a loading diagram with a softening part. Note that for $n \rightarrow \infty$ we have an almost smooth transition regime related to a cascade of bifurcations.

The discussed above model could be also extended for more complex structures with a dominant shear response such as some beam-lattice materials or elastic networks. Nowadays, the beam-lattice materials and elastic networks lie on the cutting edge of mechanics of materials, see, e.g., Fleck et al. (2010), Picu (2022) and the reference therein. Often these materials were modeled within generalized models of continuum such as strain gradient (Berkache et al. 2017; dell’Isola and Steigmann 2020) or micropolar (Dos Reis and Ganghoffer 2012; Eremeyev et al. 2013; Eremeyev 2019; Eremeyev and Reccia 2022; Molnár and Blal 2023) and micromorphic media (Neff and Forest 2007; Hütter 2019; Biswas et al. 2020). So one may expect various regimes of instability such as discussed here buckling due to sliding.

Let us note that the analysis of instabilities under tension is closely related to the scientific interests of Prof. Leonid M. Zubov, to whom this chapter is devoted. He provided such an analysis using methods of the three-dimensional nonlinear elasticity, see, e.g., Zubov and Rudev (1994, 1996), Lastenko and Zubov (2002), Zubov and Lastenko (2004), Zubov and Sheidakov (2005, 2007) and related works from Rostov’s school of mechanics (Sheidakov 2007; Eremeyev et al. 2007).

Acknowledgements The second author acknowledges the support by the Russian Sciencebreak Foundation within grant No. 22-49-08014.

References

- Berkache K, Deogekar S, Goda I, Picu RC, Ganghoffer JF (2017) Construction of second gradient continuum models for random fibrous networks and analysis of size effects. *Compos Struct* 181:347–357
- Bertoldi K, Vitelli V, Christensen J, van Hecke M (2017) Flexible mechanical metamaterials. *Nat Rev Mater* 2(11):17,066

- Bigoni D, Bordignon N, Piccolroaz A, Stupkiewicz S (2018) Bifurcation of elastic solids with sliding interfaces. *Proc R Soc A: Math Phys Eng Sci* 474(2209):20170,681
- Biswas R, Poh LH, Shedbale AS (2020) A micromorphic computational homogenization framework for auxetic tetra-chiral structures. *J Mech Phys Solids* 135(103):801
- Chróścielewski J, dell'Isola F, Eremeyev VA, Sabik A (2020) On rotational instability within the nonlinear six-parameter shell theory. *Int J Solids Struct* 196:179–189
- dell'Isola F, Steigmann DJ (2020) *Discrete and continuum models for complex metamaterials*. Cambridge University Press, Cambridge
- Dos Reis F, Ganghoffer J (2012) Construction of micropolar continua from the asymptotic homogenization of beam lattices. *Comput Struct* 112:354–363
- Eremeyev VA (2019) Two- and three-dimensional elastic networks with rigid junctions: modeling within the theory of micropolar shells and solids. *Acta Mech* 230(11):3875–3887
- Eremeyev VA, Reccia E (2022) On dynamics of elastic networks with rigid junctions within nonlinear micro-polar elasticity. *Int J Multiscale Comput Eng* 20(6):1–11
- Eremeyev VA, Turco E (2020) Enriched buckling for beam-lattice metamaterials. *Mech Res Commun* 103(103):458
- Eremeyev VA, Freidin AB, Pavlyuchenko VN, Ivanchev SS (2007) Instability of hollow polymeric microspheres upon swelling. *Dokl Phys* 52(1):37–40
- Eremeyev VA, Lebedev LP, Altenbach H (2013) *Foundations of micropolar mechanics*. Springer-briefs in applied sciences and technologies. Springer, Heidelberg
- Fleck NA, Deshpande VS, Ashby MF (2010) Micro-architected materials: past, present and future. *Proc R Soc A: Math Phys Eng Sci* 466(2121):2495–2516
- Hütter G (2019) On the micro-macro relation for the microdeformation in the homogenization towards micromorphic and micropolar continua. *J Mech Phys Solids* 127:62–79
- Lastenko MS, Zubov LM (2002) A model of neck formation on a rod under tension. *Rev Colomb Mat* 36(1):49–57
- Lemaitre J (1992) *A course on damage mechanics*. Springer, Berlin
- Molnár G, Blal N (2023) Topology optimization of periodic beam lattices using Cosserat elasticity. *Comput Struct* 281(107):037
- Neff P, Forest S (2007) A geometrically exact micromorphic model for elastic metallic foams accounting for affine microstructure. modelling, existence of minimizers, identification of moduli and computational results. *J Elast* 87(2–3):239–276
- Picu CR (2022) *Network materials: structure and properties*. Cambridge University Press, Cambridge
- Rios AJ, Nela B, Pingaro M, Reccia E, Trovalusci P (2022a) Rotation and sliding collapse mechanisms for in plane masonry pointed arches: statistical parametric assessment. *Eng Struct* 262(114):338
- Rios AJ, Pingaro M, Reccia E, Trovalusci P (2022b) Statistical assessment of in-plane masonry panels using limit analysis with sliding mechanism. *J Eng Mech* 148(2):04021,158
- Sheidakov DN (2007) Stability of a rectangular plate under biaxial tension. *J Appl Mech Tech Phys* 48:547–555
- Zaccaria D, Bigoni D, Noselli G, Misseroni D (2011) Structures buckling under tensile dead load. *Proc R Soc A: Math Phys Eng Sci* 467(2130):1686–1700
- Zubov LM, Lastenko MS (2004) On the instability of equilibrium of a cylinder made of a hardening material subjected to tension. *Mech Solids* 39(3):109–116
- Zubov LM, Rudev AN (1994) Forms of stability loss in an elastic beam under tension. *Dokl Math* 39(10):715–718
- Zubov LM, Rudev AN (1996) The instability of a non-linearly elastic beam under tension. *J Appl Math Mech* 60(5):777–788
- Zubov LM, Sheidakov DN (2005) The effect of torsion on the stability of an elastic cylinder under tension. *J Appl Math Mech* 69(1):49–56
- Zubov LM, Sheidakov DN (2007) Instability of a hollow elastic cylinder under tension, torsion, and inflation. *Trans ASME J Appl Mech* 75(1)

Chapter 9

On Ellipticity in Nonlinear Elasticity



Victor A. Eremeyev

Abstract In this note we discuss ellipticity properties in elastic media under finite deformations. Ellipticity could be considered as an additional so-called constitutive inequality. The loss of ellipticity may indicate material instabilities, so its analysis constitutes an important problem in material modelling. Here we briefly recall some definitions of ellipticity and discuss their consequences in nonlinear elasticity of simple and non-simple elastic media.

Keywords Ellipticity · Nonlinear elasticity · Generalized media

9.1 Introduction

According to Truesdell (1966), Truesdell and Noll (2004) the formulation of constitutive equations is a crucial problem of continuum mechanics. In order to restrict the possible forms of constitutive relations some general principles were proposed such as the principle of material frame indifference, determinism, local action, and some others. In addition to the latter, in the literature several constitutive inequalities were discussed, see Truesdell and Noll (2004), Ogden (1997), Lurie (1990). Among them, ellipticity of equilibrium equations plays an important role. For example, Hill (1962) and Rice (1976) considered the loss of ellipticity as a possible criterion of material instability. Moreover, for simple elastic materials it can be proven that the infinitesimal stability, i.e. positive definiteness of the second variation of a total energy functional, implies the weak form of the strong ellipticity condition called the Hadamard inequality (Ogden 1997; Lurie 1990). So the Hadamard inequality is a necessary condition of infinitesimal instability. Converse statement can be proved for affine deformations of a homogeneous solid and for Dirichlet's boundary conditions.

V. A. Eremeyev (✉)

Department of Civil, Environmental Engineering and Architecture, University of Cagliari, via Marengo 2, 09123 Cagliari, Italy
e-mail: victor.ereameev@unica.it

In the mathematical literature there exist various definitions of ellipticity such as ordinary or Petrowsky ellipticity (Petrowsky 1939), strong ellipticity (Vishik 1951; Nirenberg 1955), Douglis–Nirenberg ellipticity (Douglis and Nirenberg 1955), and some others, see Volevich (1965), Egorov and Shubin (1998), Agranovich (1997). Ellipticity provides such properties as a regularity of solutions and well-posedness of the problems under consideration.

The aim of this note is to bring attention to ellipticity conditions in nonlinear elasticity. The chapter is organized as follows. First, we briefly recall definitions of ordinary and strong ellipticity in Cauchy-type nonlinear elasticity. In addition we give an example of the Douglis–Nirenberg ellipticity considering incompressible elasticity. We also mention ellipticity within implicit elasticity. Finally, we discuss ellipticity conditions in higher-order models of continua and media with enhanced kinematics.

9.2 Cauchy Nonlinear Elasticity

Governing equations of nonlinear elasticity consists of the Lagrangian equilibrium equations (Lurie 1990)

$$\nabla \cdot \mathbf{P} + \rho \mathbf{f} = \mathbf{0}, \quad (9.1)$$

and constitutive relations

$$\mathbf{P} = \mathbf{P}(\mathbf{F}), \quad \mathbf{F} = \nabla \mathbf{x}. \quad (9.2)$$

Here \mathbf{P} is the first Piola–Kirchhoff stress tensor, ∇ is the 3D nabla-operator, \cdot is the dot product, ρ is a mass density in a reference placement, \mathbf{f} is a mass force vector, \mathbf{F} is the deformation gradient, and \mathbf{x} is a position vector in a current placement. Let us note that hereinafter we use the direct tensor calculus as in Wilson (1901), Lurie (1990), Simmonds (1994), Eremeyev et al. (2018a).

Equations (9.1) and (9.2) constitute a nonlinear system of partial differential equations (PDEs) of the first order with respect to \mathbf{P} and \mathbf{x} . Substituting (9.2) into (9.1) we get a system of PDEs of second order with respect to \mathbf{x}

$$\nabla \cdot \mathbf{P}(\nabla \mathbf{x}) + \rho \mathbf{f} = \mathbf{0}. \quad (9.3)$$

We call (9.3) *ordinary elliptic* or *strongly elliptic* if the following inequalities are fulfilled, respectively,

$$\det \mathbb{Q}(\mathbf{k}) \neq 0, \quad \forall \mathbf{k} \neq \mathbf{0}, \quad (9.4)$$

$$\mathbf{a} \cdot \mathbb{Q}(\mathbf{k}) \cdot \mathbf{a} \geq C \mathbf{a} \cdot \mathbf{a} \mathbf{k} \cdot \mathbf{k}, \quad \forall \mathbf{a}, \mathbf{k}, \quad (9.5)$$

where C is a positive constant independent on \mathbf{k} and \mathbf{a} , whereas \mathbf{k} and \mathbf{a} are arbitrary vectors. $\mathbb{Q}(\mathbf{k})$ is called acoustic tensor and can be determined through the formula

$$\mathbf{a} \cdot \mathbb{Q}(\mathbf{k}) \cdot \mathbf{a} = (\mathbf{k} \otimes \mathbf{a}) : \frac{d\mathbf{P}}{d\mathbf{F}} : (\mathbf{k} \otimes \mathbf{a}), \quad (9.6)$$

where \otimes and $:$ are the dyadic and double dot products, respectively. Obviously, the strong ellipticity implies the ordinary ellipticity. Note that these inequalities are point-wise, i.e. they may depend on the position vector \mathbf{X} in a reference placement. Moreover, they depend on deformations, i.e. on \mathbf{F} , in general. As result, ellipticity conditions (9.4) and (9.5) may restrict admissible deformations. Violation of (9.4) and (9.5) is not forbidden, in general, but this situation may indicate some material instabilities, strain localization, appearance of non-smooth solutions.

From the mathematical point of view $\mathbb{Q}(\mathbf{k})$ is the *principal symbol* of the linearized equilibrium equations. It can be derived considering higher-order derivatives, i.e. the second ones in the case of simple materials.

For the Green-type elasticity, i.e. for hyper-elastic materials, there is a strain energy density $W = W(\mathbf{F})$ such that

$$\mathbf{P} = \frac{dW}{d\mathbf{F}}, \quad (9.7)$$

so (9.6) takes the form

$$\mathbf{a} \cdot \mathbb{Q}(\mathbf{k}) \cdot \mathbf{a} = (\mathbf{k} \otimes \mathbf{a}) : \frac{d^2 W}{d\mathbf{F}^2} : (\mathbf{k} \otimes \mathbf{a}). \quad (9.8)$$

Inequalities (9.4) and (9.5) can be relatively easily checked in the case of small deformations for isotropic solids. They reduce to the inequalities

$$\mu \neq 0, \quad \lambda + 2\mu \neq 0, \quad (9.9)$$

and

$$\mu > 0, \quad \lambda + 2\mu > 0, \quad (9.10)$$

respectively. Here λ and μ are Lamé elastic moduli. The case of anisotropic materials is much more complex even in the case of small strains, see e.g. Zubov and Rudev (2016a, b), where for 19 classes of anisotropic materials the strong ellipticity conditions were reduced to sets of elementary inequalities in terms of elastic moduli.

For finite deformations the analysis of ellipticity conditions is a certain challenge. Some results are summarized in Ogden (1997), Lurie (1990), see also more recent papers by Horgan and Saccomandi (2005), Merodio and Ogden (2005a, b, c), Quintanilla and Saccomandi (2009), Soldatos (2012), Soldatos et al. (2021), Merodio and Ogden (2023) and the references therein.

9.3 Incompressible Materials

Incompressibility is very often used as a constraint for rubber-like materials and biological tissues (Ogden 1997; Lurie 1990; Holzapfel and Ogden 2006). For these materials the governing equations have the form

$$\nabla \cdot \mathbf{P}_E - \nabla p \cdot \mathbf{F}^{-T} + \rho \mathbf{f} = \mathbf{0}, \quad \mathbf{P}_E = \mathbf{P}_E(\mathbf{F}), \quad \mathbf{F} = \nabla \mathbf{x}, \quad (9.11)$$

$$\det \mathbf{F} \equiv \det \nabla \mathbf{x} = 1. \quad (9.12)$$

Here the stress tensor is determined through deformations up to a hydrostatic part. So we have to introduce a pressure function p as a response to constraint (9.12). In fact, p is a Lagrange multiplier related to (9.12).

In this case we have a system of PDEs with respect to \mathbf{x} and p , which have different order of differentiation. So the standard definition of ellipticity should be modified accordingly. Here the Douglis–Nirenberg ellipticity can be applied as in the case of incompressible fluids, see Volevich (1965), Hayes and Horgan (1974). Omitting mathematical details we came to the following principal symbol

$$\mathbb{Q}_I(\mathbf{k}) = \begin{pmatrix} \mathbb{Q}(\mathbf{k}) & -i\mathbf{k} \cdot \mathbf{F}^{-T} \\ i\mathbf{k} \cdot \mathbf{F}^{-T} & 0 \end{pmatrix}, \quad (9.13)$$

where \mathbb{Q} is given by (9.6) with $\mathbf{P} = \mathbf{P}_E$, $i = \sqrt{-1}$. The Douglis–Nirenberg ellipticity condition consists of the inequality

$$\det \mathbb{Q}_I \neq 0, \quad \forall \mathbf{k} \neq \mathbf{0}. \quad (9.14)$$

Zee and Sternberg (1983) obtained the same inequality analyzing propagation of acceleration waves.

9.4 Implicit Elasticity

Another form of governing equations of elastic materials called implicit elasticity was proposed by Rajagopal (2007, 2010, 2011). Within this approach stresses and strains are related through an implicit relation such as

$$\mathbf{K}(\mathbf{F}, \mathbf{P}) = \mathbf{0}. \quad (9.15)$$

Here \mathbf{K} is a given tensor-valued function. Another incremental form of (9.15) was discussed in Rajagopal and Srinivasa (2007). The strong ellipticity in the form of inequality (9.5) was analyzed in Mai and Walton (2015b), where the theorem on

implicit functions was applied. Monotonicity of implicit constitutive relations was studied by Mai and Walton (2015a).

9.5 Strain Gradient Elasticity

For generalized media such as gradient elastic continua and micropolar or micromorphic media, ellipticity properties play a similar role as in classic nonlinear elasticity, in general. Let us briefly recall definitions of ordinary and strong ellipticity for the strain gradient elasticity. Within the strain gradient model Lagrangian equilibrium equations and constitutive relations have the form Bertram (2023), Bertram and Forest (2020), Eremeyev et al. (2018a)

$$\nabla \cdot \mathbf{T} + \rho \mathbf{f} = \mathbf{0}, \quad \mathbf{T} = \mathbf{P} - \nabla \cdot \mathbf{P}_2 \quad (9.16)$$

$$\mathbf{P} = \mathbf{P}(\mathbf{F}, \mathbf{G}), \quad \mathbf{P}_2 = \mathbf{P}_2(\mathbf{F}, \mathbf{G}), \quad \mathbf{G} = \nabla \mathbf{F}, \quad (9.17)$$

where \mathbf{T} is the first Piola–Kirchhoff total stress tensor, \mathbf{P}_2 is the first Piola–Kirchhoff hyper-stress third-order tensor, and \mathbf{G} is the second deformation gradient. Equations (9.16) constitute a system of nonlinear PDEs of the fourth order.

The principal symbol of (9.16) is given by the formula

$$\mathbf{a} \cdot \mathbb{Q}_{SG}(\mathbf{k}) \cdot \mathbf{a} = (\mathbf{k} \otimes \mathbf{k} \otimes \mathbf{a}) : \frac{d\mathbf{P}_2}{d\mathbf{G}} : (\mathbf{k} \otimes \mathbf{k} \otimes \mathbf{a}), \quad (9.18)$$

where $\dot{}$ stands for the triple dot product. As a result, the ordinary ellipticity is given by

$$\det \mathbb{Q}_{SG}(\mathbf{k}) \neq 0, \quad \forall \mathbf{k} \neq \mathbf{0}, \quad (9.19)$$

whereas the strong ellipticity takes the form

$$\mathbf{a} \cdot \mathbb{Q}_{SG}(\mathbf{k}) \cdot \mathbf{a} \geq C \mathbf{a} \cdot \mathbf{a} (\mathbf{k} \cdot \mathbf{k})^2, \quad \forall \mathbf{a}, \mathbf{k}, \quad (9.20)$$

where again C is a positive constant independent on \mathbf{a} and \mathbf{k} . Obviously, inequalities (9.19) and (9.20) imply constraints only on the dependence on the second deformation gradient. As in the case of simple materials the strong ellipticity is essential for existence of solutions (Mareno and Healey 2006).

Unlike the case of simple materials the relations between ellipticity and material instability is more complex. This analysis was provided in Eremeyev (2021), Eremeyev and Reccia (2022b). It was shown that the infinitesimal stability implies the weak for of strong ellipticity condition. On the other hand, the strong ellipticity does not guarantee stability. It requires additional constitutive inequalities for constitutive relations. In general, strain gradient elasticity can be treated as a gradi-

ent regularization of constitutive relations of simple materials after loss of ellipticity. Similar analysis of the strong ellipticity and infinitesimal instability was extended for third-order (Eremeyev 2022, 2023b) and n th-order (Eremeyev 2023d) strain gradient elasticity, where sufficient conditions of stability were formulated.

Within the linear Toupin–Mindlin strain gradient model of isotropic elastic solids ellipticity results in a few elementary inequalities for higher order elastic moduli (Eremeyev and Lazar 2022), whereas there are no requirements for Lamé’s moduli. Considering existence and uniqueness of weak solutions of the linear boundary-value problem with the Dirichlet’s boundary conditions, two constraints for μ and λ are also formulated. The latter take the form of inequalities (Eremeyev 2023c)

$$\mu > -c_1, \quad \lambda + 2\mu > -c_2, \quad (9.21)$$

where positive constants c_1 and c_2 are size-dependent. Moreover, exact bounds depend also on the spatial dimension of the problem under consideration, see Eremeyev (2023b) for an one-dimensional case.

Considering strain gradient models it is worth to mention gradient incomplete models such as couple-stress theory, which neither elliptic nor strongly elliptic, see Gourgiotis and Bigoni (2016a, b), Eremeyev et al. (2023), where also some regularizations towards elliptic systems were proposed. Extensive studies of the loss of ellipticity and material instabilities were provided by Gourgiotis and Bigoni (2016a, b), Bigoni and Gourgiotis (2016), Gourgiotis and Bigoni (2017). Another gradient incomplete model, called dilatational strain gradient elasticity, is also not elliptic, see Eremeyev (2023a), but it can be transformed into a Douglis–Nirenberg elliptic system of PDEs.

Finally, let us mention gradient incomplete models which appear as a continuum models of beam-lattice metamaterials (dell’Isola and Steigmann 2020; dell’Isola et al. 2019; Rahali et al. 2015). From the mathematical point of view these models may be not elliptic in a standard sense, but some of them belong to the class of hypoelliptic systems (Eremeyev et al. 2018b).

9.6 Media with Enhanced Kinematics

Mathematical theory of elliptic PDEs can be also applied to other generalized media. Ellipticity conditions were studied for materials with additional kinematical fields such as micropolar and micromorphic media. Within the micropolar elasticity ellipticity and acceleration waves were studied in Eremeyev (2005). The analysis was extended to thermoelastic materials in Altenbach et al. (2010). The loss of ellipticity in micropolar media and related problems such as strain localization, wave propagation, instabilities, and transition to plasticity were considered by Lakes (2018), Lakes (2021), Steinmann and Willam (1991), Passarella et al. (2011), De Borst (1991), De Borst et al. (1993), De Borst and Mühlhaus (1992), Dietsche et al.

(1993), Hasanyan and Waas (2018), Russo et al. (2020). Ellipticity condition for elastic micropolar fluids was introduced in Yermeyev and Zubov (1999).

For micromorphic media ellipticity conditions and related conditions of propagation of acceleration waves were analyzed in Eremeyev et al. (2018c). Comparison of micromorphic and strain gradient continue from the point of view of ellipticity conditions was provided in Eremeyev and Reccia (2022a), where some similarities and differences were underlined.

Strong ellipticity in materials with voids was discussed in Chiriță and Ghiba (2010).

9.7 Conclusion

We discussed ellipticity conditions such as ordinary and strong ellipticity, the Douglis–Nirenberg ellipticity considering Cauchy continua and their generalizations. Among the latter we consider strain gradient elasticity and media with additional kinematical descriptors.

Let us note that this brief review reflects some of the interests of Prof. Leonid M. Zubov, to whom it is devoted. In fact, he and his coworkers paid attention to the analysis of ellipticity within linear (Zubov and Rudev 2016a, b) and nonlinear elasticity (Zubov and Rudev 1992, 1995, 2011), shell theory (Eremeyev and Zubov 2007), micropolar hydrodynamics (Yermeyev and Zubov 1999). Recently the results on ellipticity of anisotropic materials were summarized in Zubov and Rudev (2015).

Acknowledgements The author acknowledges the support within the European Union’s Horizon 2020 research and 105 innovation programme under the Marie Skłodowska-Curie grant agreement EffectFact No 101008140.

References

- Agranovich M (1997) Elliptic boundary problems. In: Agranovich M, Egorov Y, Shubin M (eds) Partial differential equations IX: elliptic boundary problems. Encyclopaedia of mathematical sciences, vol 79. Springer, Berlin, pp 1–144
- Altenbach H, Eremeyev VA, Lebedev LP, Rendón LA (2010) Acceleration waves and ellipticity in thermoelastic micropolar media. *Arch Appl Mech* 80(3):217–227
- Bertram A (2023) *Compendium on gradient materials*. Springer, Cham
- Bertram A, Forest S (eds) (2020) *Mechanics of strain gradient materials*. Springer International Publishing, Cham
- Bigoni D, Gourgiotis PA (2016) Folding and faulting of an elastic continuum. *Proc R Soc A: Math Phys Eng Sci* 472(2187):20160,018
- Chiriță S, Ghiba ID, (2010) Strong ellipticity and progressive waves in elastic materials with voids. *Proc R Soc A: Math Phys Eng Sci* 466(2114):439–458
- De Borst R (1991) Simulation of strain localization: a reappraisal of the Cosserat continuum. *Eng Comput* 8(4):317–332

- De Borst R, Muhlhaus HB (1992) Finite deformation analysis of inelastic materials with micro-structure. In: *Finite inelastic deformations-theory and applications*, Springer, pp 313–322
- De Borst R, Sluys LJ, Muhlhaus HB, Pamin J (1993) Fundamental issues in finite element analyses of localization of deformation. *Eng Comput* 10:99–121
- dell'Isola F, Steigmann DJ (2020) *Discrete and continuum models for complex metamaterials*. Cambridge University Press, Cambridge
- dell'Isola F, Seppecher P, Alibert JJ, Lekszycki T, Grygoruk R, Pawlikowski M, Steigmann D, Giorgio I, Andreaus U, Turco E, Gołaszewski M, Rizzi N, Boutin C, Eremeyev VA, Misra A, Placidi L, Barchiesi E, Greco L, Cuomo M, Cazzani A, Corte AD, Battista A, Scerrato D, Eremeeva IZ, Rahali Y, Ganghoffer JF, Müller W, Ganzosch G, Spagnuolo M, Pfaff A, Barcz K, Hoschke K, Negggers J, Hild F (2019) Pantographic metamaterials: an example of mathematically driven design and of its technological challenges. *Contin Mech Thermodyn* 31(4):851–884
- Dietsche A, Steinmann P, Willam K (1993) Micropolar elastoplasticity and its role in localization. *Int J Plast* 9(7):813–831
- Douglis A, Nirenberg L (1955) Interior estimates for elliptic systems of partial differential equations. *Commun Pure Appl Math* 8(4):503–538
- Egorov YV, Shubin MA (1998) *Foundations of the classical theory of partial differential equations, encyclopaedia of mathematical sciences vol 30, 1st edn*. Springer, Berlin
- Eremeyev VA (2005) Acceleration waves in micropolar elastic media. *Dokl Phys* 50(4):204–206
- Eremeyev VA (2021) Strong ellipticity conditions and infinitesimal stability within nonlinear strain gradient elasticity. *Mech Res Commun* 117(103):782
- Eremeyev VA (2022) On strong ellipticity and infinitesimal stability in third-order nonlinear strain gradient elasticity. *Mech Solids* 57(8):1953–1957
- Eremeyev VA (2023a) Ellipticity of gradient poroelasticity. *Int J Eng Sci* 190(103):885
- Eremeyev VA (2023b) On the ellipticity of static equations of strain gradient elasticity and infinitesimal stability. *Vestn St Petersburg Univ Math* 56(1):77–83
- Eremeyev VA (2023c) On well-posedness of the first boundary-value problem within linear isotropic Toupin–Mindlin strain gradient elasticity and constraints for elastic moduli. *ZAMM* 103(6):e202200474
- Eremeyev VA (2023d) Strong ellipticity and infinitesimal stability within n th-order gradient elasticity. *Mathematics* 11(4):1024
- Eremeyev VA, Lazar M (2022) Strong ellipticity within the toupin-mindlin first strain gradient elasticity theory. *Mech Res Commun* 124(103):944
- Eremeyev VA, Reccia E (2022a) Nonlinear strain gradient and micromorphic one-dimensional elastic continua: comparison through strong ellipticity conditions. *Mech Res Commun* 124(103):909
- Eremeyev VA, Reccia E (2022b) Strong ellipticity within the strain gradient elasticity: Elastic bar case. In: *Theoretical analyses, computations, and experiments of multiscale materials: a tribute to Francesco dell'Isola*, Springer, pp 137–144
- Eremeyev VA, Zubov LM (2007) On constitutive inequalities in nonlinear theory of elastic shells. *ZAMM* 87(2):94–101
- Eremeyev VA, Cloud MJ, Lebedev LP (2018a) *Applications of tensor analysis in continuum mechanics*. World Scientific, New Jersey
- Eremeyev VA, Dell'Isola F, Boutin C, Steigmann D (2018b) Linear pantographic sheets: existence and uniqueness of weak solutions. *J Elast* 132:175–196
- Eremeyev VA, Lebedev LP, Cloud MJ (2018c) Acceleration waves in the nonlinear micromorphic continuum. *Mech Res Commun* 93:70–74
- Eremeyev VA, Scerrato D, Konopińska-Zmysłowska V (2023) Ellipticity in couple-stress elasticity. *Zeitschrift für angewandte Mathematik und Physik* 74(1):18
- Gourgiotis PA, Bigoni D (2016a) Stress channelling in extreme couple-stress materials Part I: Strong ellipticity, wave propagation, ellipticity, and discontinuity relations. *J Mech Phys Solids* 88:150–168

- Gourgiotis PA, Bigoni D (2016b) Stress channelling in extreme couple-stress materials Part II: localized folding vs faulting of a continuum in single and cross geometries. *J Mech Phys Solids* 88:169–185
- Gourgiotis PA, Bigoni D (2017) The dynamics of folding instability in a constrained cosserat medium. *Philos Trans R Soc A: Math, Phys Eng Sci* 375(2093):20160,159
- Hasanyan AD, Waas AM (2018) Localization in anisotropic elastoplastic micropolar media: application to fiber reinforced composites. *J Mech Phys Solids* 121:1–22
- Hayes M, Horgan CO (1974) On the Dirichlet problem for incompressible elastic materials. *J Elast* 4(1):17–25
- Hill R (1962) Acceleration waves in solids. *J Mech Phys Solids* 10(1):1–16
- Holzappel GA, Ogden RW (eds) (2006) *Mechanics of biological tissue*. Springer, Berlin
- Horgan CO, Saccomandi G (2005) A new constitutive theory for fiber-reinforced incompressible nonlinearly elastic solids. *J Mech Phys Solids* 53(9):1985–2015
- Lakes RS (2018) Stability of cosserat solids: size effects, ellipticity and waves. *J Mech Mater Struct* 13(1):83–91
- Lakes RS (2021) Softening of Cosserat sensitivity in a foam: warp effects. *Int J Mech Sci* 192(106):125
- Lurie AI (1990) *Non-linear theory of elasticity*. North-Holland, Amsterdam
- Mai T, Walton JR (2015a) On monotonicity for strain-limiting theories of elasticity. *J Elast* 120:39–65
- Mai T, Walton JR (2015b) On strong ellipticity for implicit and strain-limiting theories of elasticity. *Math Mech Solids* 20(2):121–139
- Mareno A, Healey TJ (2006) Global continuation in second-gradient nonlinear elasticity. *SIAM J Math Anal* 38(1):103–115
- Merodio J, Ogden R (2005a) On tensile instabilities and ellipticity loss in fiber-reinforced incompressible non-linearly elastic solids. *Mech Res Commun* 32(3):290–299
- Merodio J, Ogden R (2005b) Remarks on instabilities and ellipticity for a fiber-reinforced compressible nonlinearly elastic solid under plane deformation. *Q Appl Math* 63(2):325–333
- Merodio J, Ogden R (2005c) Tensile instabilities and ellipticity in fiber-reinforced compressible non-linearly elastic solids. *Int J Eng Sci* 43(8–9):697–706
- Merodio J, Ogden RW (2023) Instabilities associated with loss of ellipticity in fiber-reinforced nonlinearly elastic solids. In: *Mathematical methods and models in composites*. World Scientific, pp 295–332
- Nirenberg L (1955) Remarks on strongly elliptic partial differential equations. *Commun Pure Appl Math* 8(4):648–674
- Ogden RW (1997) *Non-linear elastic deformations*. Dover, Mineola
- Passarella F, Tibullo V, Zampoli V (2011) On the strong ellipticity for orthotropic micropolar elastic bodies in a plane strain state. *Mech Res Commun* 38(7):512–517
- Petrowsky IG (1939) Sur l'analyticité des solutions des systèmes d'équations différentielles. *Recueil Mathématique (Mat Sbornik)* 5(47)(1):3
- Quintanilla R, Saccomandi G (2009) Some qualitative properties for the equations of pre-stressed viscoelastic solids. *Mech Res Commun* 36(5):547–555
- Rahali Y, Giorgio I, Ganghoffer JF, dell'Isola F (2015) Homogenization à la Piola produces second gradient continuum models for linear pantographic lattices. *Int J Eng Sci* 97:148–172
- Rajagopal K (2010) On a new class of models in elasticity. *Math Comput Appl* 15(4):506–528
- Rajagopal K (2011) Conspectus of concepts of elasticity. *Math Mech Solids* 16(5):536–562
- Rajagopal KR (2007) The elasticity of elasticity. *Zeitschrift für angewandte Mathematik und Physik* 58:309–317
- Rajagopal KR, Srinivasa AR (2007) On the response of non-dissipative solids. *Proc R Soc A: Math Phys Eng Sci* 463(2078):357–367
- Rice JR (1976) The localization of plastic deformation. In: Koiter WT (ed) *Theoretical and applied mechanics (Proceedings of the 14th international congress on theoretical and applied mechanics)*, North-Holland Publ. Co, Delft, pp 207–220

- Russo R, Forest S, Girot Mata FA (2020) Thermomechanics of Cosserat medium: modeling adiabatic shear bands in metals. *Contin Mech Thermodyn* 1–20
- Simmonds JG (1994) A brief on tensor analysis, 2nd edn. Springer, New York
- Soldatos KP (2012) On loss of ellipticity in second-gradient hyper-elasticity of fibre-reinforced materials. *Int J Non-Linear Mech* 47(2):117–127
- Soldatos KP, Shariff MHB, Merodio J (2021) On the constitution of polar fiber-reinforced materials. *Mech Adv Mater Struct* 28(21):2255–2266
- Steinmann P, Willam K (1991) Localization within the framework of micropolar elasto-plasticity. In: *Advances in continuum mechanics*, Springer, pp 296–313
- Truesdell C (1966) *The elements of continuum mechanics*. Springer, New York
- Truesdell C, Noll W (2004) *The non-linear field theories of mechanics*, 3rd edn. Springer, Berlin
- Vishik MI (1951) On strongly elliptic systems of differential equations (in Russian). *Sb: Math* 29(71):615–657
- Volevich LR (1965) Solubility of boundary value problems for general elliptic systems (in Russian). *Sb: Math* 68(110):373–416
- Wilson EB (1901) *Vector analysis*. Yale University Press, New Haven, Founded upon the Lectures of G. W. Gibbs
- Yeremeyev VA, Zubov LM (1999) The theory of elastic and viscoelastic micropolar liquids. *J Appl Math Mech* 63(5):755–767
- Zee L, Sternberg E (1983) Ordinary and strong ellipticity in the equilibrium theory of incompressible hyperelastic solids. *Arch Rat Mech Anal* 83(1):53–90
- Zubov LM, Rudev AN (1992) An effective method of verifying Hadamard's condition for a non-linearly elastic compressible medium. *J Appl Math Mech* 56(2):252–260
- Zubov LM, Rudev AN (1995) Necessary and sufficient criteria for ellipticity of the equilibrium equations of a non-linearly elastic medium. *J Appl Math Mech* 59(2):197–208
- Zubov LM, Rudev AN (2011) A criterion for the strong ellipticity of the equilibrium equations of an isotropic non-linearly elastic material. *J Appl Math Mech* 75(4):432–446
- Zubov LM, Rudev AN (2015) Strong ellipticity in the elasticity of anisotropic materials. Southern Federal University, Rostov on Don (in Russian)
- Zubov LM, Rudev AN (2016a) Criterion for the strong ellipticity of the equations of motion of an anisotropic linear-elastic material. *J Appl Math Mech* 80(6):485–509
- Zubov LM, Rudev AN (2016b) On necessary and sufficient conditions of strong ellipticity of equilibrium equations for certain classes of anisotropic linearly elastic materials. *ZAMM* 96(9):1096–1102

Chapter 10

Nonlinear Bending of Circular Beam with Distributed Dislocations



Evgeniya V. Goloveshkina

Abstract A plane problem of the nonlinear theory of elasticity on pure bending of a circular beam in the form of a sector of a hollow circular cylinder containing continuously distributed straight edge dislocations, specified by the tensor field of dislocation density, is considered. The beam is loaded at the ends with a bending moment, the curved edges are stress-free. The boundary conditions at the ends of the beam are fulfilled in the integral sense of Saint-Venant. Within the framework of the model of a compressible semi-linear material, an exact solution is found. An explicit formula is obtained for the bending moment depending on the curvature of the deformed beam. The influence of dislocations on stresses and external bending moment is analyzed.

Keywords Nonlinear elasticity · Pure bending · Hollow circular cylinder · Edge dislocations · Semi-linear material · Exact solution

10.1 Introduction

Taking into account the physical imperfections of the material makes it possible to more adequately describe the behavior of a nonlinearly elastic body. In this work, such imperfections of the crystal structure as dislocations are taken into account. Dislocation models can be used both in the presence of dislocations and to describe other defects in crystalline bodies and features of their deformation (Gutkin and Ovid'ko 2004; Clayton 2011; Maugin 2013), for example, discontinuous stress and strain fields (Zhbánova and Zubov 2016). When the number of dislocations in a body is large enough, their continuous distribution, characterized by the dislocation density tensor, is used, and the continuum theory of dislocations (Kondo 1952; Kröner 1960; Bilby et al. 1955; Eshelby 1956; Berdichevsky and Sedov 1967; Goloveshkina and

E. V. Goloveshkina (✉)

Institute of Mathematics, Mechanics, and Computer Science of Southern Federal University, Milchakova Str. 8a, Rostov-on-Don 344090, Russia
e-mail: evgeniya.goloveshkina@yandex.ru

© The Author(s), under exclusive license to Springer Nature Switzerland AG 2023
H. Altenbach and V. Eremeyev (eds.), *Advances in Linear and Nonlinear Continuum and Structural Mechanics*, Advanced Structured Materials 198,
https://doi.org/10.1007/978-3-031-43210-1_10

175

Zubov 2019; Derezin and Zubov 2011; Clayton 2011; Teodosiu 2013; Le and Stumpf 1996) is used to model the behavior of such a body. In this paper, in the framework of this theory, we study the plane deformation of a pure bending of an elastic body that has the shape of a sector of a hollow circular cylinder.

This work takes into account the nonlinearity factor due to large deformations and therefore uses the nonlinear theory of elasticity. A number of solutions to problems for nonlinear elastic bodies with isolated dislocations and disclinations were obtained by Professor L. M. Zubov in his book (Zubov 1997). Physical and geometric nonlinearity must often be taken into account for such a type of deformation as bending. Large deformations occur, for example, during strong bending of elastic-plastic bodies, and to describe their behavior under conditions of active loading, it is advisable to use the model of a nonlinearly elastic material. The problem of nonlinear bending of an elastic body with dislocations was first considered in Zelenina and Zubov (2009). In the work (Zelenina and Zubov 2013), within the framework of the nonlinear theory, the plane deformation of a rectangular beam made of a semi-linear material with edge dislocations was studied. Without taking into account dislocations, the problem of the nonlinear theory of elasticity of pure bending of a circular beam was studied in Zubov and Popov (2007), where an exact solution was found for the model of a semi-linear material.

The problem of bending a beam with dislocations, considered in this paper, is reduced to a nonlinear boundary value problem for an ordinary differential equation. In this case, the differential equations of equilibrium and incompatibility in the volume of the body are fulfilled exactly. The boundary conditions on the curvilinear boundaries of the beam are also exactly satisfied. The boundary conditions at the ends of the beam are fulfilled approximately, in the integral sense of Saint-Venant. After solving the formulated one-dimensional boundary value problem for a given dislocation density, the moment becomes a known function of the bending parameter. The dependence of the moment on the bending parameter is a load diagram for a curved beam in nonlinear bending, which can be used to determine the value of the bending parameter for a given value of the external moment.

In the work, a bending parameter is found at which the beam bends without the appearance of stresses and without the application of an external bending moment. Such a deformation is called a quasi-solid state. The spherically symmetric quasi-solid state of a sphere with dislocations is considered in the paper Goloveshkina and Zubov (2018). The bending of a rectangular beam without the appearance of stresses is considered in Zelenina and Zubov (2013).

In this work, within the framework of the model of a compressible harmonic (semi-linear) material, an exact solution to the problem of nonlinear bending of a curved beam is found, and the effect of dislocations on the resulting stresses and external bending moment is also studied.

10.2 Input Relations

The system of equations describing the nonlinear deformation of an elastic body with distributed dislocations consists of Lurie (1990), Zubov (2004, 2011) incompatibility equations

$$\operatorname{rot} \mathbf{F} = \boldsymbol{\alpha}, \quad (10.1)$$

equilibrium equations

$$\operatorname{div} \mathbf{D} = 0, \quad (10.2)$$

and constitutive relations

$$\mathbf{D} = \frac{dW}{d\mathbf{F}}, \quad W = W(\mathbf{F}), \quad \mathbf{G} = \mathbf{F} \cdot \mathbf{F}^T. \quad (10.3)$$

Here, \mathbf{F} is the distortion tensor, \mathbf{D} is the asymmetric Piola stress tensor, also called the first Piola–Kirchhoff stress tensor, \mathbf{G} is the metric tensor, also called the Cauchy strain measure, W is the specific strain energy, and $\boldsymbol{\alpha}$ is the dislocation density tensor satisfying the solenoidality requirement:

$$\operatorname{div} \boldsymbol{\alpha} = 0. \quad (10.4)$$

The gradient, curl, and divergence operations (Lurie 1990; Lebedev et al. 2010) used in this paper are defined by the formulas:

$$\begin{aligned} \operatorname{grad} \Psi &= \mathbf{r}^s \otimes \frac{\partial \Psi}{\partial q^s}, \quad \operatorname{curl} \Psi = \mathbf{r}^s \times \frac{\partial \Psi}{\partial q^s}, \\ \operatorname{div} \Psi &= \mathbf{r}^s \cdot \frac{\partial \Psi}{\partial q^s}, \quad \mathbf{r}^s = \mathbf{i}_k \frac{\partial q^k}{\partial x_s} \quad (s, k = 1, 2, 3). \end{aligned} \quad (10.5)$$

In (10.5), x_k are the Cartesian coordinates of the reference configuration of the elastic body, \mathbf{i}_k are the coordinate vectors corresponding to them, q^s are some curvilinear Lagrangian coordinates, Ψ is an arbitrary differentiable tensor field of any order. In (10.2), an assumption was made about the possibility of neglecting the action of body forces.

If there are no dislocations in the body, i.e., $\boldsymbol{\alpha} \equiv 0$, then the distortion tensor is called the deformation gradient and Zubov (1997) is expressed as $\mathbf{F} = \operatorname{grad} \mathbf{R}$, where $\mathbf{R} = X_k \mathbf{i}_k$ is the radius vector of a point of the body in the deformed configuration and X_k are the Cartesian coordinates of the deformed state. For $\boldsymbol{\alpha} \neq 0$, the vector field $\mathbf{R}(q^s)$ does not exist.

In what follows, the elastic material will be considered isotropic. In this case, the specific energy is some function of the \mathbf{G} tensor invariants:

$$W(\mathbf{G}) = W(I_1, I_2, I_3), \quad (10.6)$$

$$I_1 = \operatorname{tr} \mathbf{G}, \quad I_2 = \frac{1}{2} (\operatorname{tr}^2 \mathbf{G} - \operatorname{tr} \mathbf{G}^2), \quad I_3 = \det \mathbf{G} = (\det \mathbf{F})^2,$$

and the Piola stress tensor is expressed as follows Zubov and Karyakin (2006)

$$\mathbf{D} = (\tau_1 + I_1 \tau_2) \mathbf{F} - \tau_2 \mathbf{G} \cdot \mathbf{F} + I_3 \tau_3 \mathbf{F}^{-\mathrm{T}}, \quad (10.7)$$

$$\tau_k(I_1, I_2, I_3) = \frac{\partial W}{\partial I_k}; \quad \mathbf{F}^{-\mathrm{T}} \triangleq (\mathbf{F}^{\mathrm{T}})^{-1} = (\mathbf{F}^{-1})^{\mathrm{T}}.$$

In the nonlinear theory of elasticity, models of isotropic materials are also used, in which the specific energy is given as a function of the invariants of the stretch tensor \mathbf{U} , which is a positive definite square root of the metric tensor \mathbf{G} :

$$W(\mathbf{G}) = W(J_1, J_2, J_3),$$

$$J_1 = \operatorname{tr} \mathbf{U}, \quad J_2 = \frac{1}{2} (\operatorname{tr}^2 \mathbf{U} - \operatorname{tr} \mathbf{U}^2), \quad J_3 = \det \mathbf{U}, \quad (10.8)$$

$$\mathbf{U} = (\mathbf{F} \cdot \mathbf{F}^{\mathrm{T}})^{1/2}.$$

Based on (10.3) and (10.8), a representation of the Piola stress tensor is derived

$$\mathbf{D} = \left(\frac{\partial W}{\partial J_1} + J_1 \frac{\partial W}{\partial J_2} \right) \mathbf{A} - \frac{\partial W}{\partial J_2} \mathbf{F} + J_3 \frac{\partial W}{\partial J_3} \mathbf{F}^{-\mathrm{T}}, \quad (10.9)$$

$$\mathbf{A} = \mathbf{U}^{-1} \cdot \mathbf{F},$$

where \mathbf{A} is the rotation tensor. The positive definite symmetric tensor \mathbf{U} and the proper orthogonal tensor \mathbf{A} form a polar decomposition of the distortion tensor

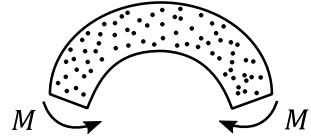
$$\mathbf{F} = \mathbf{U} \cdot \mathbf{A}. \quad (10.10)$$

10.3 Pure Bending of Circular Beam

Let us consider a plane deformation of an elastic body having the shape of a sector of a hollow circular cylinder in the reference configuration. The body occupies the region $r_1 \leq r \leq r_0, 0 \leq \varphi \leq \varphi_0, 0 \leq z \leq l$, where r, φ , and z are the cylindrical coordinates of the reference configuration. Since the deformation occurs in the $z = \text{const}$ plane, the size of l does not matter.

This circular beam is loaded at the ends $\varphi = 0$ and $\varphi = \varphi_0$ with a bending moment M (Fig. 10.1). Surfaces $r = r_0$ and $r = r_1$ are free from external load.

Fig. 10.1 Loading a beam with a bending moment M



Let us introduce the unit vectors

$$\begin{aligned} \mathbf{e}_r &= \mathbf{i}_1 \cos \varphi + \mathbf{i}_2 \sin \varphi, & \mathbf{e}_\varphi &= -\mathbf{i}_1 \sin \varphi + \mathbf{i}_2 \cos \varphi, \\ \mathbf{e}_R &= \mathbf{i}_1 \cos \varkappa\varphi + \mathbf{i}_2 \sin \varkappa\varphi, & \mathbf{e}_\Phi &= -\mathbf{i}_1 \sin \varkappa\varphi + \mathbf{i}_2 \cos \varkappa\varphi. \end{aligned} \quad (10.11)$$

The positive constant \varkappa will be called the bending parameter. The vectors \mathbf{e}_r , \mathbf{e}_φ , and \mathbf{i}_3 form an orthonormal basis. Another orthonormal basis is the vectors \mathbf{e}_R , \mathbf{e}_Φ , and \mathbf{i}_3 .

Let us assume that the dislocation density tensor is given as follows:

$$\boldsymbol{\alpha} = \beta(r)\mathbf{i}_3 \otimes \mathbf{e}_\Phi. \quad (10.12)$$

The expression (10.12) satisfies the solenoidality condition (10.4) for any function $\beta(r)$ and describes the distribution of straight edge dislocations with the z axis.

The solution of the system of equations (10.1)–(10.3) of the nonlinear theory of dislocations will be sought in the form:

$$\mathbf{F} = F_1(r)\mathbf{e}_r \otimes \mathbf{e}_R + F_2(r)\mathbf{e}_\varphi \otimes \mathbf{e}_\Phi + \mathbf{i}_3 \otimes \mathbf{i}_3. \quad (10.13)$$

The physically realizable deformation of a continuous medium at each point must satisfy the condition $\det \mathbf{F} > 0$. This requirement will be satisfied if the desired solution is subject to the inequalities

$$F_1(r) > 0, \quad F_2(r) > 0. \quad (10.14)$$

Based on (10.13), the metric tensor and its invariants are determined as

$$\begin{aligned} \mathbf{G} &= F_1^2 \mathbf{e}_r \otimes \mathbf{e}_r + F_2^2 \mathbf{e}_\varphi \otimes \mathbf{e}_\varphi + \mathbf{i}_3 \otimes \mathbf{i}_3, \\ I_1 &= F_1^2 + F_2^2 + 1, \quad I_2 = F_1^2 + F_2^2 + F_1^2 F_2^2, \quad I_3 = F_1^2 F_2^2. \end{aligned} \quad (10.15)$$

By virtue of (10.13) and (10.14), the stretch tensor and its invariants have the form:

$$\begin{aligned} \mathbf{U} &= F_1 \mathbf{e}_r \otimes \mathbf{e}_r + F_2 \mathbf{e}_\varphi \otimes \mathbf{e}_\varphi + \mathbf{i}_3 \otimes \mathbf{i}_3, \\ J_1 &= F_1 + F_2 + 1, \quad I_2 = F_1 F_2 + F_1 + F_2, \quad I_3 = F_1 F_2. \end{aligned} \quad (10.16)$$

The rotation tensor defined using (10.10), unlike the \mathbf{F} , \mathbf{G} , and \mathbf{U} tensors, does not depend on the r coordinate and is written as

$$\mathbf{A} = \mathbf{e}_r \otimes \mathbf{e}_R + \mathbf{e}_\varphi \otimes \mathbf{e}_\varphi + \mathbf{i}_3 \otimes \mathbf{i}_3. \quad (10.17)$$

The (10.17) expression allows us to find out the geometric meaning of the \varkappa parameter. Indeed, using the formulas (10.11), we transform the representation (10.17) to the form:

$$\mathbf{A} = (\mathbf{i}_1 \otimes \mathbf{i}_1 + \mathbf{i}_2 \otimes \mathbf{i}_2) \cos [(\varkappa - 1)\varphi] + (\mathbf{i}_1 \otimes \mathbf{i}_2 - \mathbf{i}_2 \otimes \mathbf{i}_1) \sin [(\varkappa - 1)\varphi] + \mathbf{i}_3 \otimes \mathbf{i}_3. \quad (10.18)$$

According to the well-known properties of proper orthogonal tensors Zubov and Karyakin (2006), the tensor (10.18) describes a rotation around the vector \mathbf{i}_3 by an angle $(\varkappa - 1)\varphi$. This means that the beam section $\varphi = \text{const}$ rotates around an axis parallel to the z axis, and the angle of rotation is proportional to the angular distance of the given section from the section $\varphi = 0$. In addition to rotation, the section $\varphi = \text{const}$ experiences tension–compression in the radial direction.

It follows from (10.7), (10.9), (10.13), (10.15)–(10.17) that in an isotropic homogeneous body under the considered deformation, the Piola stress tensor is described by the expression:

$$\mathbf{D} = D_1(r)\mathbf{e}_r \otimes \mathbf{e}_R + D_2(r)\mathbf{e}_\varphi \otimes \mathbf{e}_\varphi + D_3\mathbf{i}_3 \otimes \mathbf{i}_3. \quad (10.19)$$

By virtue of (10.11) and (10.19), the vector equilibrium equation (10.2) reduces to a single scalar equation:

$$\frac{dD_1}{dr} + \frac{D_1 - \varkappa D_2}{r} = 0. \quad (10.20)$$

Based on (10.11)–(10.13), the tensor incompatibility equation (10.1) is also reduced to one scalar relation:

$$\frac{dF_2}{dr} + \frac{F_2 - \varkappa F_1}{r} = \beta(r). \quad (10.21)$$

From (10.21), we find

$$F_1 = \frac{1}{\varkappa} \frac{d}{dr}(rF_2) - \frac{r\beta(r)}{\varkappa}. \quad (10.22)$$

Using the constitutive relations (10.7) or (10.9), the stresses D_1 and D_2 can be expressed as nonlinear functions of F_1 and F_2 . Substituting these expressions into the equilibrium equation (10.20) and using (10.22), we arrive at a nonlinear ordinary differential equation of the second order with respect to the function $F_2(r)$. The boundary conditions for this equation are the requirements of unloaded curved edges of the beam:

$$D_1(r_1) = 0, \quad D_2(r_0) = 0. \quad (10.23)$$

The density of edge dislocations $\beta(r)$ is considered to be a known (given) function.

Thus, due to the substitution (10.13), the problem of bending an elastic curved beam with dislocations is reduced to a nonlinear boundary value problem for an ordinary differential equation. In this case, the differential equations of equilibrium

and incompatibility in the volume of the body are fulfilled exactly. The boundary conditions on the curvilinear boundaries of the beam $r = r_1$ and $r = r_0$ are also exactly satisfied. The boundary conditions at the ends of the beam $\varphi = 0$ and $\varphi = \varphi_0$ can be satisfied approximately, in the integral sense of Saint-Venant.

The consequence of the equilibrium equation (10.20) is the equality:

$$D_2 = \frac{1}{\varkappa} \frac{d}{dr} (r D_1). \quad (10.24)$$

We integrate the relation (10.24) over the variable r and take into account the boundary conditions (10.23). Get

$$\int_{r_1}^{r_0} D_2 dr = 0. \quad (10.25)$$

Since, according to (10.19) $\mathbf{e}_\varphi \cdot \mathbf{D} = D_2 \mathbf{e}_\varphi$, the relation (10.25) means that the principal vector of forces acting in any section of the beam $\varphi = \text{const}$ is equal to zero. Thus, the implementation of the obtained solution on the deformation of a curved flat beam requires applying only bending moments to the ends of the beam $\varphi = 0$ and $\varphi = \varphi_0$, the vectors of which have the direction of the vector \mathbf{i}_3 .

To calculate the value of the bending moment, let's compare the solution obtained above with the solution to the problem of pure bending of a circular beam that does not contain distributed dislocations (Zubov and Popov 2007). In the absence of distributed dislocations, there is a field of displacement of body particles. Therefore, the deformation can be described as a dependence of the spatial (Eulerian) coordinates on the material (Lagrangian) coordinates. If we denote cylindrical Euler coordinates by R , Φ , and Z , then the deformation of a pure bending of a sector of a circular ring is written as Zubov and Popov (2007)

$$R = R(r), \quad \Phi = \varkappa\varphi, \quad Z = z. \quad (10.26)$$

The distortion tensor defined according to (10.26) is

$$\mathbf{F} = \text{grad } \mathbf{R} = \frac{dR}{dr} \mathbf{e}_r \otimes \mathbf{e}_R + \frac{\varkappa R}{r} \mathbf{e}_\varphi \otimes \mathbf{e}_\Phi + \mathbf{i}_3 \otimes \mathbf{i}_3, \quad (10.27)$$

i.e.

$$F_1(r) = \frac{dR}{dr}, \quad F_2(r) = \frac{\varkappa R}{r}. \quad (10.28)$$

It is easy to check that the functions (10.28) satisfy the equation (10.21) with zero right side, i.e. in the absence of distributed dislocations.

Since the principal vector of forces acting in an arbitrary azimuth section of the beam is equal to zero, the principal moment \mathbf{M} does not depend on the reduction point. Therefore, the principal moment in the last section $\varphi = \varphi_0$ will be equal to

$$\mathbf{M} = \int_{r_1}^{r_0} \mathbf{R} \times D_2 \mathbf{e}_\phi \, dr = \int_{r_1}^{r_0} R \mathbf{e}_R \times D_2 \mathbf{e}_\phi \, dr = M \mathbf{i}_3, \quad (10.29)$$

where M denotes the magnitude of the bending moment

$$M = \int_{r_1}^{r_0} R(r) D_2(r) \, dr. \quad (10.30)$$

Based on (10.28), the formula (10.30) can be rewritten as

$$M = \int_{r_1}^{r_0} \frac{r}{\varkappa} F_2(r) D_2(r) \, dr. \quad (10.31)$$

In the presence of distributed dislocations, the formula (10.30) is inapplicable, since the function $R(r)$ does not exist. Therefore, the bending moment for a beam with dislocations should be calculated using the formula (10.31).

After solving the one-dimensional boundary value problem formulated above for a given dislocation density $\beta(r)$, the moment M becomes, according to (10.31), a known function of the bending parameter \varkappa . Dependence $M(\varkappa)$ is a curved beam loading diagram for nonlinear bending. Using this diagram, one can, in particular, determine the value of the parameter \varkappa for a given value of the external moment M .

10.4 Exact Solution for Harmonic Material

As a model of an elastic compressible body, we take a harmonic (semi-linear) material (John 1960; Lurie 1990; Ogden 1997), whose specific energy has the expression

$$W = \frac{\mu \nu}{1 - 2\nu} (J_1 - 3)^2 + \mu (J_1^2 - 2J_1 - 2J_2 + 3). \quad (10.32)$$

In the region of small deformations, this model transforms into Hooke's law for an isotropic body with shear modulus μ and Poisson's ratio ν . The constitutive relation for the Piola stress tensor based on (10.9) and (10.32) is written as

$$\mathbf{D} = \frac{2\mu}{1 - 2\nu} (\nu J_1 - 1 - \nu) \mathbf{A} + 2\mu \mathbf{F}. \quad (10.33)$$

As applied to the bending problem, from (10.13), (10.16), (10.17), and (10.19), we obtain

$$\begin{aligned}
 D_1 &= \frac{2\mu}{1-2\nu}[(1-\nu)F_1 + \nu F_2 - 1], & D_2 &= \frac{2\mu}{1-2\nu}[\nu F_1 + (1-\nu)F_2 - 1], \\
 D_3 &= \frac{2\mu\nu}{1-2\nu}[F_1 + F_2 - 2].
 \end{aligned}
 \tag{10.34}$$

For this material, it is more convenient to reduce the bending problem to an equation with respect to the function $D_1(r)$, rather than with respect to the function $F_2(r)$. Let us reverse the relations (10.34), i.e., let us express the distortion components in terms of stresses

$$F_1 = 1 + \frac{1}{2\mu}[(1-\nu)D_1 - \nu D_2], \quad F_2 = 1 + \frac{1}{2\mu}[-\nu D_1 + (1-\nu)D_2]. \tag{10.35}$$

Let's express D_2 in terms of D_1 using the formula (10.24), then the distortion components according to (10.35) will be represented in terms of the function $D_1(r)$ and its derivative. Substituting these representations into the incompatibility equation (10.21), we obtain a differential equation with respect to $D_1(r)$:

$$\begin{aligned}
 \frac{d^2 D_1}{dr^2} + \frac{3}{r} \frac{dD_1}{dr} + \frac{1-\varkappa^2}{r^2} D_1 &= \gamma(r), \\
 \gamma(r) &\triangleq \frac{2\mu\varkappa}{(1-\nu)r^2} [r\beta(r) + \varkappa - 1].
 \end{aligned}
 \tag{10.36}$$

The solution of the equation (10.36) that satisfies the boundary conditions (10.23) has the form:

$$D_1(r) = \frac{r^{\varkappa-1}}{2\varkappa} \int_{r_1}^r \rho^{2-\varkappa} \gamma(\rho) d\rho - \frac{r^{-\varkappa-1}}{2\varkappa} \int_{r_1}^r \rho^{2+\varkappa} \gamma(\rho) d\rho + C_1 r^{\varkappa-1} + C_2 r^{-\varkappa-1}, \tag{10.37}$$

$$C_1 = \frac{r_0^{\varkappa}}{2\varkappa(r_0^{2\varkappa} - r_1^{2\varkappa})} \left[r_0^{-\varkappa} \int_{r_1}^{r_0} \rho^{2+\varkappa} \gamma(\rho) d\rho - r_0^{\varkappa} \int_{r_1}^{r_0} \rho^{2-\varkappa} \gamma(\rho) d\rho \right],$$

$$C_2 = -r_1^{2\varkappa} C_1.$$

The stress $D_2(r)$ and the distortion components $F_1(r)$ and $F_2(r)$ are determined from the found solution (10.37) using formulas (10.24) and (10.35). Thus, the solution to the problem of strong bending of a circular beam in a closed form is found in the case when the density of edge dislocations is an arbitrary function of the radial coordinate. This solution, in particular, makes it possible to construct a loading diagram for the beam $M(\varkappa)$ according to the formula (10.31).

As an example, consider the case when $\beta(r) = \beta_0 r^{-1}$, $\beta_0 = \text{const}$. Then the expression for the stress D_1 will be as follows:

$$D_1(r) = \frac{2\mu\kappa(\beta_0 + \kappa - 1)}{(1-\nu)(\kappa^2 - 1)} \left[\frac{\left(r_0^{-\kappa-1} - r_1^{-\kappa-1} \right) r^{\kappa-1} + \left(r_1^{\kappa-1} - r_0^{\kappa-1} \right) r^{-\kappa-1}}{r_0^{-\kappa-1} r_1^{\kappa-1} - r_0^{\kappa-1} r_1^{-\kappa-1}} - 1 \right]. \quad (10.38)$$

It can be seen from (10.24), (10.35), and (10.38) that for $\beta_0 + \kappa - 1 = 0$ all stresses are equal to zero, and the distortion tensor is properly orthogonal: $\mathbf{F} = \mathbf{A}$. This is an example of a quasi-solid state (Zelenina and Zubov 2013; Goloveshkina and Zubov 2018) of a body with dislocations. An elastic beam is bent with the bending parameter $\kappa = 1 - \beta_0$ without the appearance of stresses and the application of an external bending moment.

10.5 Numerical Analysis

We refer the radial coordinate to the outer radius, that is, we will have $r_0 = 1$, the stresses to the material constant μ , and the moment to the value μr_0^2 , having $\mu = 1$; let $\nu = 0.3$.

Consider the dislocation density $\beta(r) = \beta_0/r$. For a thick beam $r_1 = 0.5$, as the bending parameter κ increases, the difference between the moments M at different dislocation density parameters β_0 decreases (Fig. 10.2), which, as can be shown, does not perform for a thin beam $r_1 = 0.9$. There are such values of the bending parameter at which the values of the external bending moment in the presence of dislocations coincide with the moment in the absence of dislocations. For a negative dislocation density parameter at a given moment, there are two solutions for the bending parameter (Fig. 10.2).

In Figs. 10.3 and 10.4 for a thick beam, as well as in Figs. 10.5 and 10.6 in the case of a thin beam, for a given dislocation density parameter $\beta_0 = -0.2$, stresses D_1 and D_2 are presented for different bending parameters κ . Inside the beam, there is a surface $r = r_*$ on which there is no stress D_2 for any bending parameter. An increase in the bending parameter can lead to both a decrease in stresses and an increase in them.

At a fixed bending parameter for different dislocation density parameters, the stresses are shown in Figs. 10.7 and 10.8 at $\kappa = 0.8$. Negative dislocation densities can either increase stresses (e.g., $\kappa = 0.1$, $\kappa = 0.8$) or decrease (e.g., at $\kappa = 2$).

Figures 10.7 and 10.8 show the case when the beam is bent with the bending parameter $\kappa = 1 - \beta_0$ without stress and without applying an external bending moment ($\kappa = 0.8$).

The results for a thin beam $r_1 = 0.9$ in the cases of dislocation densities $\beta(r) = \beta_0/r$ and $\beta(r) = \beta_0$ coincide with high accuracy.

Figures 10.9, 10.10, and 10.11 for a thick beam $r_1 = 0.5$ compare the results in the cases $\beta(r) = \beta_0/r$ and $\beta(r) = \beta_0$. With the same bending parameter, the value of the moment at a positive dislocation density is smaller for $\beta(r) = \beta_0$, except for a small range of κ values, and vice versa for a negative one. It can be shown that, for

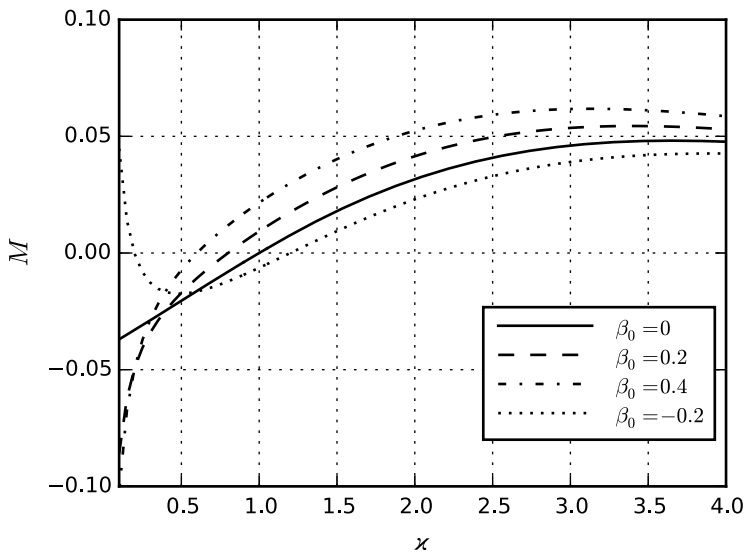


Fig. 10.2 Bending moment M for different dislocation parameters β_0 , thick beam $r_1 = 0.5$, and $\beta(r) = \beta_0/r$

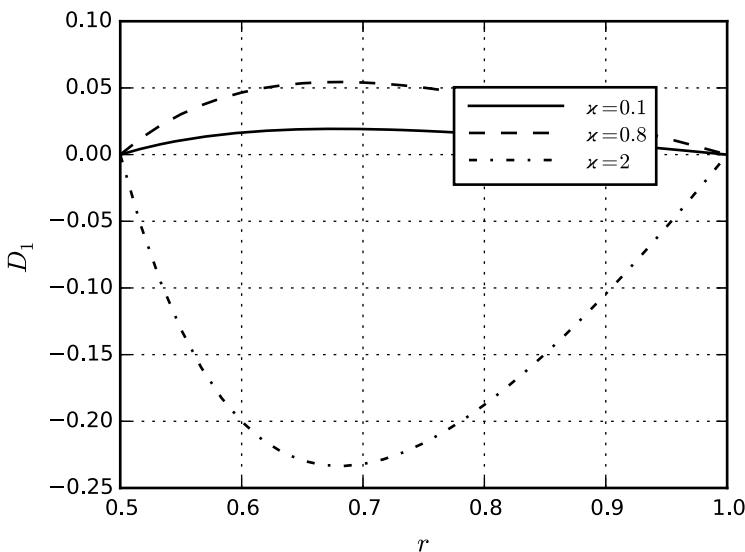


Fig. 10.3 Stress D_1 on a ground with normal \mathbf{e}_R for different bending parameters χ , thick beam $r_1 = 0.5$, $\beta(r) = \beta_0/r$, and $\beta_0 = -0.2$

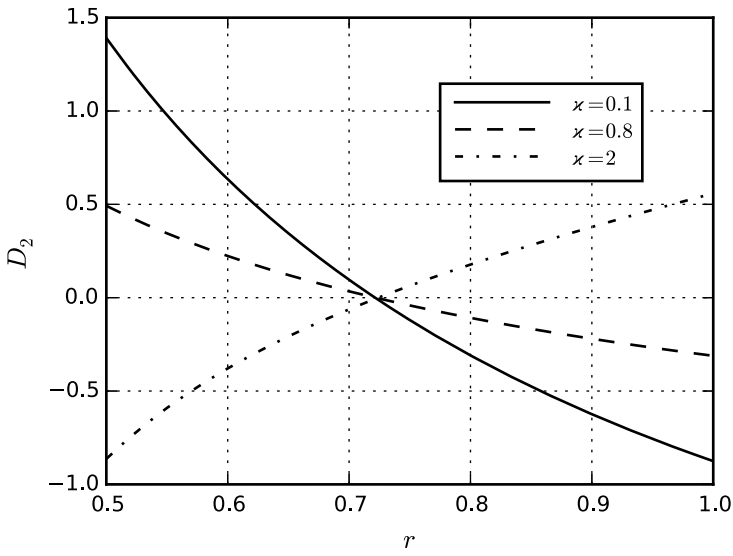


Fig. 10.4 Stress D_2 on a ground with normal \mathbf{e}_ϕ for different bending parameters \varkappa , thick beam $r_1 = 0.5$, $\beta(r) = \beta_0/r$, and $\beta_0 = -0.2$

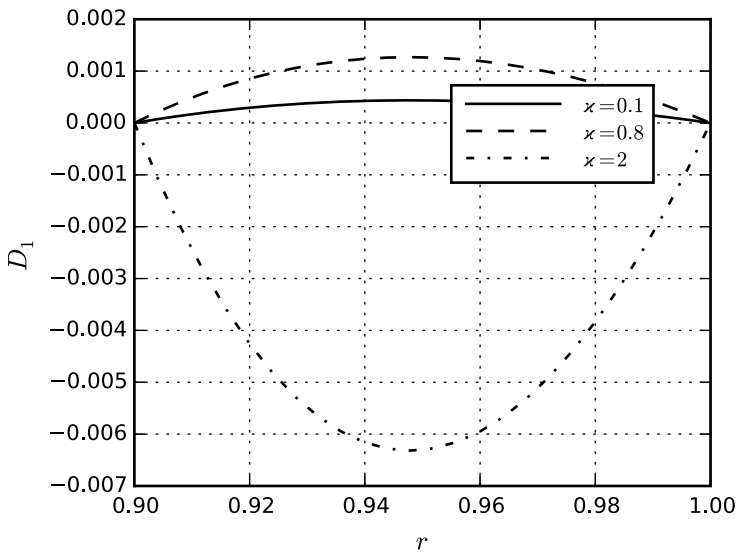


Fig. 10.5 Stress D_1 on a ground with normal \mathbf{e}_R for different bending parameters \varkappa , thin beam $r_1 = 0.9$, $\beta(r) = \beta_0/r$, and $\beta_0 = -0.2$

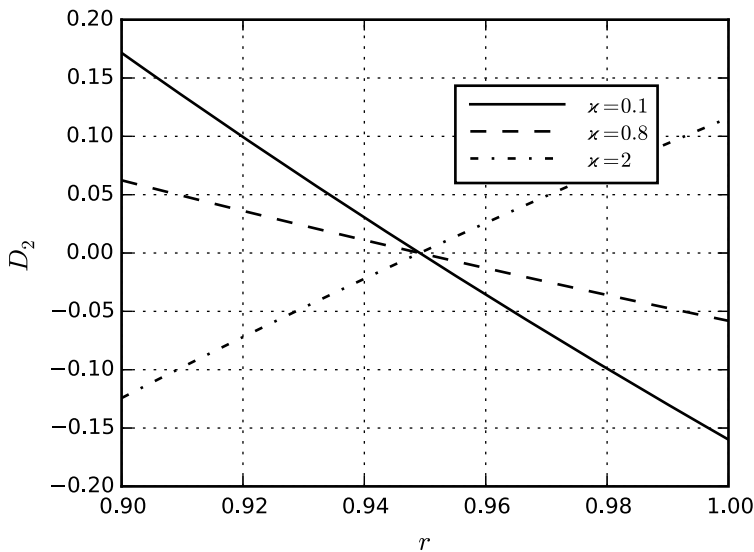


Fig. 10.6 Stress D_2 on a ground with normal \mathbf{e}_ϕ for different bending parameters ζ , thin beam $r_1 = 0.9$, $\beta(r) = \beta_0/r$, and $\beta_0 = -0.2$

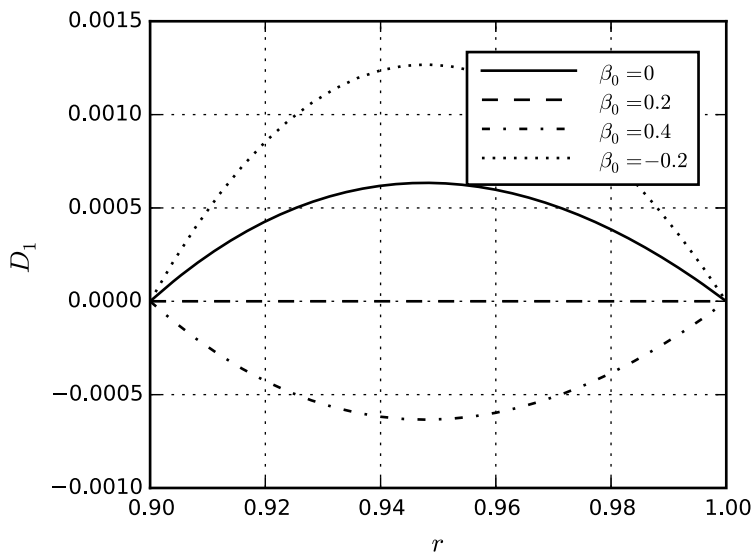


Fig. 10.7 Stress D_1 on a ground with normal \mathbf{e}_R for different dislocation parameters β_0 , thin beam $r_1 = 0.9$, $\beta(r) = \beta_0/r$, and $\zeta = 0.8$

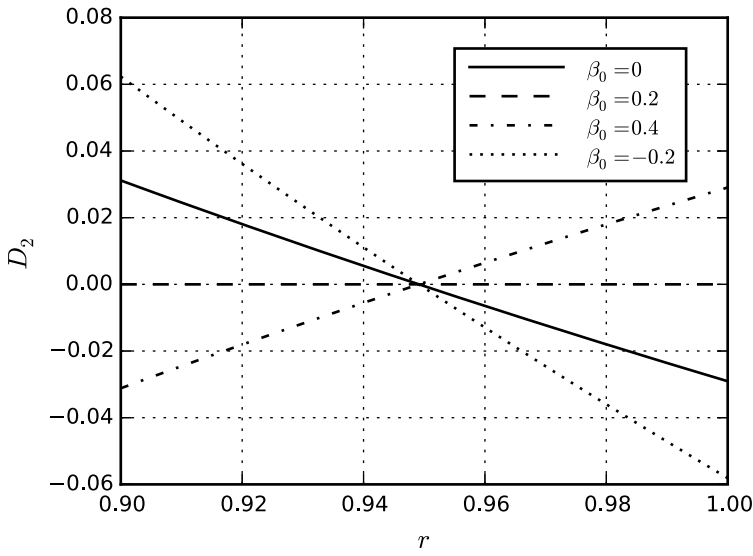


Fig. 10.8 Stress D_2 on a ground with normal \mathbf{e}_ϕ for different dislocation parameters β_0 , thin beam $r_1 = 0.9$, $\beta(r) = \beta_0/r$, and $\varkappa = 0.8$

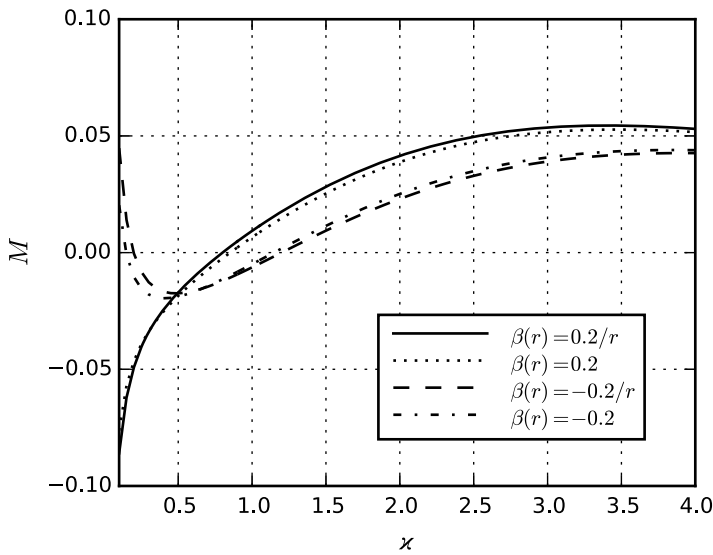


Fig. 10.9 Bending moment M for different dislocation parameters β_0 , comparison of densities $\beta = \beta_0/r$ and $\beta = \beta_0$, thick beam $r_1 = 0.5$, $\beta(r) = \beta_0$

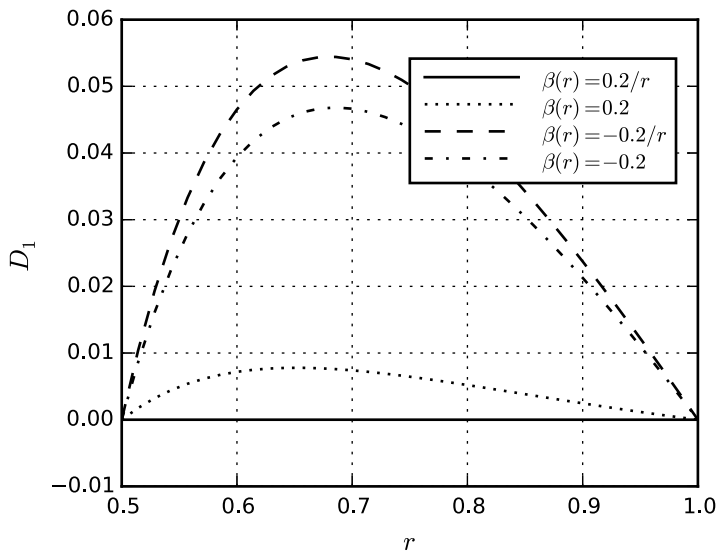


Fig. 10.10 Stress D_1 on a ground with normal \mathbf{e}_R for different dislocation parameters β_0 , comparison of densities $\beta = \beta_0/r$ and $\beta = \beta_0$, thick beam $r_1 = 0.5$, $\nu = 0.8$

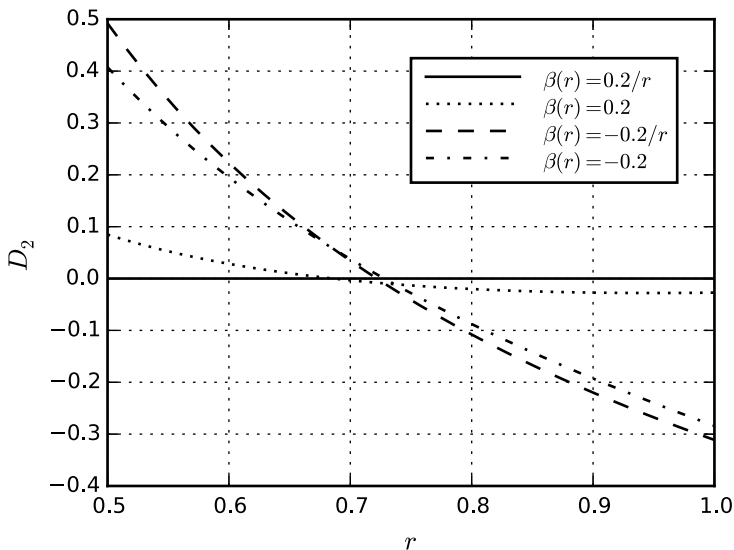


Fig. 10.11 Stress D_2 on a ground with normal \mathbf{e}_ϕ for different dislocation parameters β_0 , comparison of densities $\beta = \beta_0/r$ and $\beta = \beta_0$, thick beam $r_1 = 0.5$, $\nu = 0.8$

$\beta(r) = \beta_0$, the stress D_1 is less for $\varkappa = 0.1$ and greater in absolute value for $\varkappa = 2$, for $\varkappa = 0.8$, the differences are insignificant; the stress D_2 is less for $\varkappa = 0.1$ and $\varkappa = 0.8$, but greater for $\varkappa = 2$. For positive dislocation densities, the stresses D_1 and D_2 for the case $\beta(r) = \beta_0$ are greater, and at negative densities, they are less at $\varkappa = 0.1$ and $\varkappa = 0.8$ (Figs. 10.10 and 10.11), and vice versa, as can be shown for $\varkappa = 2$.

10.6 Conclusion

Within the framework of the nonlinear theory of dislocations, the problem of plane deformation of a pure bending of an elastic body in the form of a sector of a hollow circular cylinder with edge dislocations is solved. The original problem is reduced to a nonlinear boundary value problem for an ordinary differential equation. The differential equations of equilibrium and incompatibility in the volume of the body are fulfilled exactly. The boundary conditions on the curvilinear boundaries of the beam are satisfied exactly, and the boundary conditions on the ends of the beam are satisfied in the integral sense of Saint-Venant. After solving the formulated one-dimensional boundary value problem for a given dislocation density, the moment becomes a known function of the bending parameter. The density of edge dislocations is an arbitrary function of the radial coordinate. The dependence of the moment on the bending parameter is a loading diagram that determines the value of the bending parameter for a given value of the external moment. A quasi-solid state has been found, that is, a bending parameter has been obtained, at which the beam bends without the appearance of stresses and the application of an external bending moment. An exact solution is found for a compressible semi-linear material. The effect of dislocations on arising stresses and bending moment has been studied.

Acknowledgements The reported study was funded by the Russian Science Foundation, project number 23-21-00123, <https://rscf.ru/en/project/23-21-00123/>.

References

- Berdichevsky VL, Sedov LI (1967) Dynamic theory of continuously distributed dislocations. its relation to plasticity theory. *Prikl Mat Mekh* 31(6):989–1006
- Bilby BA, Bullough R, Smith E (1955) Continuous distributions of dislocations: a new application of the methods of non-Riemannian geometry. *Proc R Soc Lond A: Math Phys Eng Sci* A231:263–273
- Clayton JD (2011) *Nonlinear mechanics of crystals*. Springer, Dordrecht
- Derezin SV, Zubov LM (2011) Disclinations in nonlinear elasticity. *Ztsch Angew Math und Mech* 91:433–442
- Eshelby JD (1956) The continuum theory of lattice defects. In: Seitz F, Turnbull T (eds) *Solid state physics*, vol 3. Academic Press, New York, pp 79–144

- Goloveshkina E, Zubov LM (2018) Universal spherically symmetric solution of nonlinear dislocation theory for incompressible isotropic elastic medium. *Arch Appl Mech*. <https://doi.org/10.1007/s00419-018-1403-9>
- Goloveshkina EV, Zubov LM (2019) Universal spherically symmetric solution of nonlinear dislocation theory for incompressible isotropic elastic medium. *Arch Appl Mech* 89(3):409–424
- Gutkin MY, Ovid'ko IA (2004) Plastic deformation in nanocrystalline materials. Springer, Berlin
- John F (1960) Plane strain problems for a perfectly elastic material of harmonic type. *Commun Pure Appl Math* 13:239–296
- Kondo K (1952) On the geometrical and physical foundations in the theory of yielding. In: Proceedings of 2nd Japan national congress for applied mechanics, Tokyo, pp 41–47
- Kröner E (1960) Allgemeine Kontinuumstheorie der Versetzungen und Eigenspannungen. *Arch Ration Mech Anal* 4:273–334
- Le K, Stumpf H (1996) A model of elastoplastic bodies with continuously distributed dislocations. *Int J Plast* 12(5):611–627
- Lebedev LP, Cloud MJ, Eremeyev VA (2010) Tensor analysis with applications in mechanics. World Scientific, New Jersey
- Lurie AI (1990) Nonlinear theory of elasticity. North-Holland, Amsterdam
- Maugin GA (2013) Continuum mechanics through the twentieth century. Springer, Heidelberg
- Ogden RW (1997) Non-linear elastic deformations. Dover, New York
- Teodosiu C (2013) Elastic models of crystal defects. Springer, Berlin
- Zelenina A, Zubov LM (2009) Bending and torsion of nonlinear elastic bodies with continuously distributed dislocations (in Russian). *Vestnik Yuzhnogo Nauchnogo Tsentra Rossiyskoy Akademii Nauk* 5(4):15–22
- Zelenina A, Zubov LM (2013) Nonlinear effects during the tension, bend, and torsion of elastic bodies with distributed dislocations. *Dokl Phys* 58:354–357
- Zhbanova EV, Zubov LM (2016) The influence of distributed dislocations on large deformations of an elastic sphere. In: Naumenko K, Aßmus M (eds) Advanced methods of continuum mechanics for materials and structures, advanced structured materials, vol 60. Springer, Singapore, pp 61–76
- Zubov LM (1997) Nonlinear theory of dislocations and disclinations in elastic bodies. Springer, Berlin
- Zubov LM (2004) Continuously distributed dislocations and disclinations in nonlinearly elastic micropolar media. *Dokl Phys* 49(5):308–310
- Zubov LM (2011) The continuum theory of dislocations and disclinations in nonlinearly elastic micropolar media. *Mech Solids* 46(3):348–356
- Zubov LM, Karyakin MI (2006) Tensor calculus (in Russian). Vuzovskaya kniga, M
- Zubov LM, Popov AG (2007) Golovin's problem in the nonlinear theory of elasticity (in Russian). *Vestnik Yuzhnogo Nauchnogo Tsentra Rossiyskoy Akademii Nauk* 3(4):14–18

Chapter 11

Equilibrium Stability of Nonlinearly Elastic Cylindrical Tube with Distributed Dislocations Under Axial Compression



Evgeniya V. Goloveshkina

Abstract The problem of equilibrium stability of a nonlinearly elastic hollow circular cylinder under axial compression is considered. The cylinder contains continuously distributed edge dislocations specified by the tensor field of the dislocation density. The distribution of dislocations is axisymmetric. The unperturbed state is described by a system of nonlinear ordinary differential equations. In the study of stability, the bifurcation method is used to search for equilibrium positions that differ little from the unperturbed state. The critical values of the longitudinal force for thin-walled and thick-walled cylinders made of a compressible semi-linear material (John's model), at which the equilibrium bifurcation occurs, are determined. The buckling modes are investigated. The effect of dislocations on the loss of stability is analyzed.

Keywords Nonlinear elasticity · Equilibrium bifurcation · Hollow circular cylinder · Edge dislocations · Semi-linear material · Quasi-displacements

11.1 Introduction

The paper considers the stability under axial compression of a nonlinearly elastic cylinder. In the framework of the three-dimensional nonlinear theory of elasticity, the stability of elastic bodies that allow large deformations is considered, for example, in works (Green and Adkins 1960; Ogden 1997; Lurie 2005; Zubov and Moiseyenko 1983; Zubov 1997; Zelenin and Zubov 1985; Sensenig 1964; Biot 1965; Fu and Ogden 1999; Guz 1999). Instability under tensile stresses (Zubov and Rudev 1993; Ericksen 1975; Spector 1984; Haughton and Ogden 1979a; Zubov and Rudev 1996; Lastenko and Zubov 2002) is also a problem in which an elastic body in a subcritical state experiences large deformations. In Zubov and Sheidakov (2008), on the basis

E. V. Goloveshkina (✉)

Institute of Mathematics, Mechanics, and Computer Science of Southern Federal University, Milchakova Str. 8a, Rostov-on-Don 344090, Russia
e-mail: evgeniya.goloveshkina@yandex.ru

© The Author(s), under exclusive license to Springer Nature Switzerland AG 2023
H. Altenbach and V. Eremeyev (eds.), *Advances in Linear and Nonlinear Continuum and Structural Mechanics*, Advanced Structured Materials 198,
https://doi.org/10.1007/978-3-031-43210-1_11

193

of three-dimensional nonlinear elasticity, the stability of a hollow circular infinite cylinder is studied under three-parameter loading: axial tension, torsion, and inflation. The instability of a stretched hollow cylinder inflated by internal pressure is studied in Houghton and Ogden (1979a, b), Chen and Houghton (2003). The effect of torsion on the stability of a solid circular cylinder under stretching is analyzed in Zubov and Sheydaev (2005). Non-adjacent bending equilibrium forms are also considered in the problems of the nonlinear theory, that is, the supercritical behavior of shells, when, at low load levels, a sharp drop in load occurs after a change in the initial unperturbed equilibrium form. Some problems on the postcritical behavior of three-dimensional elastic bodies are considered in Zelenin and Zubov (1985, 1987, 1988).

In addition to the buckling of a thick-walled tube, the paper also studies the buckling of a thin shell. This solution can serve as a substantiation of the solution for a thick-walled tube, since in the absence of dislocations the results are in agreement with the theory of shells. Problems on the stability of the equilibrium of shells are considered in Singer et al. (2002), Samuelson and Eggwertz (1992), Grigolyuk and Kabanov (1978), Tovstik and Smirnov (2002), Timoshenko and Gere (1963), Volmir (1967), Tvergaard (1976), Budiansky and Hutchinson (1979), Houghton and Moiseyenko (2001).

To adequately describe the behavior of a nonlinear elastic body, one should take into account such factors as inhomogeneity, fluidity of the material, geometric, and physical imperfections. We study buckling phenomenon for an elastic body, taking into account microstructure defects in the form of dislocations. The nonlinear continuum theory of dislocations used in this paper, based on the works (Kondo 1952; Kröner 1960; Bilby et al. 1955; Berdichevsky and Sedov 1967; Eshelby 1956; Berdichevsky and Sedov 1967; Goloveshkina and Zubov 2019), was developed in the works (Derezin and Zubov 2011; Clayton 2011; Teodosiu 2013; Le and Stumpf 1996). Problems of stability of three-dimensional elastic bodies, taking into account distributed dislocations, are poorly covered in the literature. The stability of a nonlinearly elastic ball was studied in Goloveshkina and Zubov (2020). Professor Zubov L. M. in his monograph (Zubov 1997) obtained a number of solutions to problems for three-dimensional elastic bodies with isolated dislocations and disclinations, including stability problems.

In this paper, to determine the critical value of the parameter, which can be used to calculate the critical force, the bifurcation method (static Euler method) is used Lurie (2005, 1990), Ogden (1997), Green and Adkins (1960), Zubov and Moiseyenko (1983), Zelenin and Zubov (1985). According to the method, the critical load is considered to be the smallest load at which an adjacent form of equilibrium is statically possible, infinitely close to the original one. The stability analysis is reduced to solving a homogeneous boundary value problem linearized in the vicinity of the ground state. A necessary condition for the correctness of the bifurcation method is the conservatism of external loads.

After the separation of variables in the linearized boundary value problem, we arrive at two second-order linear differential equations with two boundary conditions. By solving a homogeneous linear boundary value problem, the minimum compres-

sion value is determined at which the cylinder loses its stability for the first time. We study how the dislocation density affects the buckling of a cylindrical body.

11.2 Input Relations

The system of equations describing large deformations of an elastic medium includes (Lurie 1990) equilibrium equations for stresses (without taking into account body forces)

$$\operatorname{div} \mathbf{D} = 0, \quad (11.1)$$

constitutive equations for the material

$$\mathbf{D} = \frac{dW(\mathbf{C})}{d\mathbf{C}}, \quad (11.2)$$

and geometric relations

$$\mathbf{C} = \operatorname{grad} \mathbf{R}. \quad (11.3)$$

Here, \mathbf{D} is the Piola asymmetric stress tensor (the first Piola–Kirchhoff stress tensor), \mathbf{C} is the deformation gradient, W is the specific strain energy, $\mathbf{R} = \mathbf{R}(q^s)$ is the radius vector of body points in the deformed state, and q^s ($s = 1, 2, 3$) are some curvilinear Lagrangian coordinates related to the Cartesian coordinates of the reference configuration x_1, x_2, x_3 by the relations $q^s = q^s(x_1, x_2, x_3)$. The operations of gradient and divergence (Lurie 1990; Lebedev et al. 2010) in curvilinear coordinates of the reference configuration of the body are defined by the expressions:

$$\operatorname{grad} \Phi = \mathbf{r}^n \otimes \frac{\partial \Phi}{\partial q^n}, \quad \operatorname{div} \Phi = \mathbf{r}^n \cdot \frac{\partial \Phi}{\partial q^n}, \quad \mathbf{r}^n = \mathbf{i}_k \frac{\partial q^n}{\partial x_k},$$

where Φ is an arbitrary differentiable tensor field of any order, \mathbf{i}_k is a constant orthonormal basis of Cartesian coordinates.

If dislocations with a tensor density α are distributed in a body, then the vector field $\mathbf{R}(q^s)$ does not exist and the geometric relations (11.3) are replaced by the incompatibility equation: (Zubov 2004, 2011)

$$\operatorname{rot} \mathbf{C} = \alpha, \quad (11.4)$$

where the α tensor must satisfy the solenoidality condition

$$\operatorname{div} \alpha = 0. \quad (11.5)$$

In this case, the \mathbf{C} tensor is called the distortion tensor. The physical meaning of the dislocation density is that the α tensor field flux through any surface is equal to the

total Burgers vector of all dislocations crossing this surface (Nye 1953; Vakulenko 1991; Landau and Lifshitz 1975).

The complete system of equilibrium equations for a nonlinearly elastic body with distributed dislocations contains the tensor distortion field \mathbf{C} as an unknown function.

11.3 Unperturbed State: Cylindrical Tube with Distributed Dislocations

In the reference configuration of a medium, we introduce cylindrical coordinates r , φ , and z , related to the Cartesian coordinates by the relations

$$x_1 = r \cos \varphi, \quad x_2 = r \sin \varphi, \quad x_3 = z.$$

Consider an elastic body in the form of a hollow circular cylinder with an outer radius r_0 , an inner radius r_1 , and an axis parallel to the vector \mathbf{i}_3 . As a vector basis, we will use the orts \mathbf{e}_r , \mathbf{e}_φ , \mathbf{i}_3 , which are directed along the tangents to the coordinate lines. There are relations

$$\mathbf{e}_r = \mathbf{i}_1 \cos \varphi + \mathbf{i}_2 \sin \varphi, \quad \mathbf{e}_\varphi = -\mathbf{i}_1 \sin \varphi + \mathbf{i}_2 \cos \varphi.$$

Let us assume that the dislocation density tensor is given as

$$\boldsymbol{\alpha} = \alpha_r(r) \mathbf{e}_r \otimes \mathbf{e}_r + \alpha_\varphi(r) \mathbf{e}_\varphi \otimes \mathbf{e}_\varphi + \alpha_{z\varphi}(r) \mathbf{i}_3 \otimes \mathbf{e}_\varphi + \alpha_z(r) \mathbf{i}_3 \otimes \mathbf{i}_3. \quad (11.6)$$

The functions $\alpha_r(r)$, $\alpha_\varphi(r)$, and $\alpha_z(r)$ are the scalar densities of screw dislocations in the radial, azimuthal, and axial directions, respectively, and the function $\alpha_{z\varphi}(r)$ is the scalar density of edge dislocations. Taking into account the condition of solenoidality (11.5) of the dislocation density tensor, we obtain the following equation:

$$\alpha_\varphi = \frac{d}{dr}(r\alpha_r). \quad (11.7)$$

This implies that the solenoidality condition does not impose restrictions on the functions $\alpha_{z\varphi}(r)$ and $\alpha_z(r)$.

The tensor field of distortion is found in the form

$$\mathbf{C}_0 = C_r(r) \mathbf{e}_r \otimes \mathbf{e}_r + C_\varphi(r) \mathbf{e}_\varphi \otimes \mathbf{e}_\varphi + C_{\varphi z}(r) \mathbf{e}_\varphi \otimes \mathbf{i}_3 + C_{z\varphi}(r) \mathbf{i}_3 \otimes \mathbf{e}_\varphi + \lambda \mathbf{i}_3 \otimes \mathbf{i}_3, \quad (11.8)$$

where λ is a real value.

By virtue of (11.6) and (11.8), the tensor incompatibility equation (11.4) is reduced to a system of ordinary differential equations:

$$C_{z\varphi} = -r\alpha_r, \quad \frac{dC_{z\varphi}}{dr} = -\alpha_\varphi, \quad (11.9)$$

$$\frac{d}{dr}(rC_{\varphi z}) = r\alpha_z, \quad (11.10)$$

$$\frac{dC_\varphi}{dr} + \frac{C_\varphi - C_r}{r} = \alpha_{z\varphi}. \quad (11.11)$$

In (11.9), the first equation determines the distortion component $C_{z\varphi}$, and the second equation is a consequence of the first one and the solenoidality condition (11.7). Integrating the equation (11.10), we find the distortion component

$$C_{\varphi z}(r) = \frac{1}{r} \int_{r_1}^r \alpha_z(r') dr' + \frac{b}{2\pi r}. \quad (11.12)$$

Here, b is the length of the Burgers vector of an isolated screw dislocation that can be contained in a hollow cylinder (Zubov 1997). The function $C_r(r)$ is expressed in terms of $C_\varphi(r)$ using (11.11):

$$C_r = \frac{d}{dr}(rC_\varphi) - r\alpha_{z\varphi}. \quad (11.13)$$

Thus, after the fulfillment of the incompatibility equations, only the C_φ distortion remains an unknown function, to find which one should refer to the equilibrium equations (11.1).

Taking into account the isotropy of the function W of tensor arguments, it can be shown Zubov and Karyakin (2006), Eremeyev et al. (2018) that for a homogeneous medium, the stresses do not depend on the coordinates φ and z . Using the formulas (11.8), we obtain the stress tensor

$$\begin{aligned} \mathbf{D}_0 = & D_r(r)\mathbf{e}_r \otimes \mathbf{e}_r + D_\varphi(r)\mathbf{e}_\varphi \otimes \mathbf{e}_\varphi + D_{\varphi z}(r)\mathbf{e}_\varphi \otimes \mathbf{i}_3 \\ & + D_{z\varphi}(r)\mathbf{i}_3 \otimes \mathbf{e}_\varphi + D_z(r)\mathbf{i}_3 \otimes \mathbf{i}_3. \end{aligned}$$

Then the vector equilibrium equation (11.1) is reduced to the scalar equation

$$\frac{dD_r}{dr} + \frac{D_r - D_\varphi}{r} = 0. \quad (11.14)$$

If the cylindrical tube is not loaded along the side surfaces $r = r_0$ and $r = r_1$, then the boundary conditions for the equation (11.14) will be as follows:

$$D_r(r_0) = 0, \quad (11.15)$$

$$D_r(r_1) = 0. \quad (11.16)$$

For a given multiplicity of longitudinal elongation λ , one can determine the resulting longitudinal force

$$Q = 2\pi \int_{r_1}^{r_0} D_z(r) r dr \quad (11.17)$$

applied to the ends of the tube.

So, the problem of large deformations of a cylindrical tube with distributed dislocations (11.6) is reduced to a nonlinear boundary value problem (11.14)–(11.16) for an ordinary differential equation. The unknown function in this problem is $C_\varphi(r)$.

11.4 Distribution of Straight Edge Dislocations

Consider the equilibrium of the cylindrical tube in the case when

$$\alpha_r = \alpha_\varphi = \alpha_z = 0, \quad b = 0.$$

Then the dislocation density tensor takes the form

$$\boldsymbol{\alpha} = \alpha_{z\varphi}(r) \mathbf{i}_3 \otimes \mathbf{e}_\varphi$$

and describes the distribution of edge dislocations whose axes are parallel to the cylinder axis \mathbf{i}_3 . The scalar dislocation density $\alpha_{z\varphi}(r)$ is an arbitrary function. From (11.9) and (11.12), it follows that the distortion tensor will be

$$\mathbf{C}_0 = C_r(r) \mathbf{e}_r \otimes \mathbf{e}_r + C_\varphi(r) \mathbf{e}_\varphi \otimes \mathbf{e}_\varphi + \lambda \mathbf{i}_3 \otimes \mathbf{i}_3. \quad (11.18)$$

Then the Piola stress tensor \mathbf{D} , due to the constitutive relations of the material (11.2), takes the form

$$\mathbf{D}_0 = D_r(r) \mathbf{e}_r \otimes \mathbf{e}_r + D_\varphi(r) \mathbf{e}_\varphi \otimes \mathbf{e}_\varphi + D_z(r) \mathbf{i}_3 \otimes \mathbf{i}_3. \quad (11.19)$$

The equilibrium equation (11.14), taking into account the expression for distortion C_r (11.13), serves to determine the function C_φ .

11.5 Exact Solution for Unperturbed State

As a specific model of an elastic material, we consider an isotropic semi-linear material (John's model) (John 1960; Lurie 1990; Ogden 1997), which corresponds to a function of the specific strain energy of the form

$$W = \frac{\mu\nu}{1-2\nu} \text{tr}^2(\mathbf{U} - \mathbf{E}) + \mu \text{tr}(\mathbf{U} - \mathbf{E})^2. \quad (11.20)$$

Here, \mathbf{E} is the unit tensor, μ and ν are the material constants. In the small strain region, the semi-linear material follows Hooke's law with a shear modulus μ and a Poisson's ratio ν . \mathbf{U} is the positive definite stretch tensor and \mathbf{A} is the proper orthogonal rotation tensor (Lurie 2005) from the polar decomposition $\mathbf{C} = \mathbf{U} \cdot \mathbf{A}$ of the distortion tensor.

The stress tensor (11.2) for such a specific energy (11.20) has the representation

$$\mathbf{D} = \frac{2\mu}{1-2\nu} (\nu \operatorname{tr} \mathbf{U} - 1 - \nu) \mathbf{A} + 2\mu \mathbf{C}. \quad (11.21)$$

In the equilibrium problem for a tube with straight edge dislocations based on (11.18) and (11.21), taking into account (11.19) and $\mathbf{U} = \mathbf{C}$ (since $\mathbf{A} = \mathbf{E}$ in the polar decomposition $\mathbf{C} = \mathbf{U} \cdot \mathbf{A}$), we obtain representations of stresses in terms of distortions:

$$\begin{aligned} D_r &= \frac{2\mu}{1-2\nu} [(1-\nu)C_r + \nu(C_\varphi + \lambda) - 1 - \nu], \\ D_\varphi &= \frac{2\mu}{1-2\nu} [\nu C_r + (1-\nu)C_\varphi + \nu\lambda - (1+\nu)], \\ D_z &= \frac{2\mu}{1-2\nu} [\nu C_r + \nu C_\varphi + (1-\nu)\lambda - (1+\nu)]. \end{aligned} \quad (11.22)$$

By means of (11.22), we express distortions in stresses D_r and D_φ :

$$\begin{aligned} C_r &= \frac{1-\nu}{2\mu} D_r - \frac{\nu}{2\mu} D_\varphi + 1 + \nu - \nu\lambda, \\ C_\varphi &= -\frac{\nu}{2\mu} D_r + \frac{1-\nu}{2\mu} D_\varphi + 1 + \nu - \nu\lambda. \end{aligned} \quad (11.23)$$

We express the stress D_φ in terms of D_r using the equilibrium equation (11.14) and assuming that the mass forces are absent:

$$D_\varphi = \frac{d}{dr}(r D_r). \quad (11.24)$$

Substituting the relations (11.23) into the incompatibility equation (11.13) and taking (11.24) into account, we arrive at a differential equation with respect to the function $D_r(r)$:

$$r^2 \frac{d^2 D_r}{dr^2} + 3r \frac{dD_r}{dr} = h(r), \quad h(r) \equiv \frac{2\mu}{1-\nu} r \alpha_{z\varphi}(r), \quad (11.25)$$

the solution of which has the form

$$D_r(r) = \frac{1}{2} \int_{r_1}^r \rho h(\rho) d\rho - \frac{1}{2r^2} \int_{r_1}^r \rho^3 h(\rho) d\rho + A + \frac{B}{r^2}.$$

The constants A and B are found from the boundary condition (11.16) and look like

$$A = -\frac{B}{r_1^2}, \quad B = \frac{-2\mu}{(1-2\nu)(r_0^{-2} - r_1^{-2}) - 2r_0^{-2}(1-\nu)} \left[1 + \nu - \nu\lambda - C_\varphi(r_0) + \frac{r_0^{-2}(1-\nu)}{2\mu} \int_{r_1}^{r_0} \rho^3 h(\rho) d\rho + \frac{1-2\nu}{4\mu} \left(\int_{r_1}^{r_0} \rho h(\rho) d\rho - r_0^{-2} \int_{r_1}^{r_0} \rho^3 h(\rho) d\rho \right) \right].$$

The constant $C_\varphi(r_0)$ is determined from the boundary condition (11.15). The quantity C_φ should be expressed in terms of D_r using (11.23) and (11.24):

$$C_\varphi = \frac{1-\nu}{2\mu} r \frac{dD_r}{dr} + \frac{1-2\nu}{2\mu} D_r + 1 + \nu - \nu\lambda.$$

11.6 Linearized Boundary Value Problem

The stability of the equilibrium of a nonlinearly elastic body can be studied using the static Euler method. It consists of determining the loading parameters under which the linearized boundary value problem has nontrivial solutions. A small deformation is imposed on the unperturbed (subcritical) state, and possible forms of equilibrium are determined.

Perturbed equilibrium equations should be derived by linearization of equilibrium equations (11.1), constitutive relations (11.2), and incompatibility equations (11.4), since if there are distributed dislocations in the body, the positions of the particles of the body cannot be found (the vector field $\mathbf{R}(q^s)$ does not exist).

To implement the linearization, we set

$$\mathbf{D} = \mathbf{D}_0 + \eta \dot{\mathbf{D}} + O(\eta^2), \quad \dot{\mathbf{D}} = \left. \frac{d}{d\eta} \mathbf{D}(\mathbf{C}_0 + \eta \mathbf{L}) \right|_{\eta=0},$$

$$\mathbf{C} = \mathbf{C}_0 + \eta \mathbf{L} + O(\eta^2),$$

where the subscript 0 marks the quantities related to the subcritical state. Leaving in these relations only terms of the first order with respect to η , we obtain the linearized equilibrium equation (11.1)

$$\operatorname{div} \dot{\mathbf{D}} = 0. \quad (11.26)$$

Assuming that the dislocation density tensor remains unchanged upon transition to a perturbed equilibrium state, from (11.4), we obtain the linearized incompatibility equation

$$\operatorname{rot} \mathbf{L} = 0,$$

the general solution of which can be represented as Zubov and Karyakin (2006)

$$\mathbf{L} = \text{grad } \mathbf{w}. \quad (11.27)$$

Here, \mathbf{w} is a differentiable vector field, called the quasi-displacement field.

In what follows, we confine ourselves to searching for axisymmetric solutions of the linearized problem when there is no dependence on φ . With an axisymmetric loss of stability, waves occur along z . Therefore, the quasi-displacement \mathbf{w} will be sought as a vector field in the plane defined by the coordinates r and z (radial and additional displacements), i.e.

$$\mathbf{w} = u(r, z)\mathbf{e}_r + w(r, z)\mathbf{e}_z. \quad (11.28)$$

Consider the finite deformation of a cylinder, for which the distortion tensor has the form

$$\mathbf{C} = C_\varphi \mathbf{e}_\varphi \otimes \mathbf{e}_\varphi + C_z \mathbf{e}_z \otimes \mathbf{e}_z + C_{rz} \mathbf{e}_r \otimes \mathbf{e}_z + C_{zr} \mathbf{e}_z \otimes \mathbf{e}_r + C_r \mathbf{e}_r \otimes \mathbf{e}_r. \quad (11.29)$$

The components of this tensor do not depend on the φ coordinate. Therefore, taking into account the relation

$$\mathbf{C} = \mathbf{U} \cdot \mathbf{A}, \quad (11.30)$$

we obtain the stretch and rotation tensors

$$\begin{aligned} \mathbf{U} &= U_\varphi \mathbf{e}_\varphi \otimes \mathbf{e}_\varphi + U_z \mathbf{e}_z \otimes \mathbf{e}_z + U_{rz} \mathbf{e}_r \otimes \mathbf{e}_z + U_{zr} \mathbf{e}_z \otimes \mathbf{e}_r + U_r \mathbf{e}_r \otimes \mathbf{e}_r, \\ \mathbf{A} &= (\mathbf{e}_z \otimes \mathbf{e}_r - \mathbf{e}_r \otimes \mathbf{e}_z) \sin \chi + (\mathbf{e}_z \otimes \mathbf{e}_z + \mathbf{e}_r \otimes \mathbf{e}_r) \cos \chi + \mathbf{e}_\varphi \otimes \mathbf{e}_\varphi. \end{aligned} \quad (11.31)$$

The geometric meaning of the formula (11.31) is that the elementary volumes of the cylinder rotate through the angle $\chi(r, z)$ around the vector \mathbf{e}_φ .

Since the tensor \mathbf{U} is symmetric, then

$$\mathbf{C} \cdot \mathbf{A}^T = \mathbf{A} \cdot \mathbf{C}^T. \quad (11.32)$$

Using (11.29), (11.31), and (11.32), we get the equation for determining the angle χ

$$(C_{zr} - C_{rz}) \cos \chi = (C_z + C_r) \sin \chi,$$

the solution of which is a pair of functions

$$\begin{aligned} \cos \chi &= \pm \frac{s}{\sqrt{s^2 + t^2}}, \quad \sin \chi = \pm \frac{t}{\sqrt{s^2 + t^2}}, \\ s &= C_z + C_r, \quad t = C_{zr} - C_{rz}. \end{aligned} \quad (11.33)$$

Here, the signs of the functions are taken either both upper or both lower. The sign is chosen according to the requirement that the tensor \mathbf{U} be positive definite, expressed by the inequality

$$(C_z \mathbf{e}_z \otimes \mathbf{e}_z + C_{rz} \mathbf{e}_r \otimes \mathbf{e}_z + C_{zr} \mathbf{e}_z \otimes \mathbf{e}_r + C_r \mathbf{e}_r \otimes \mathbf{e}_r) \odot \mathbf{A} > 0.$$

This condition is satisfied by a pair of solutions from (11.33) with a plus sign, i.e.,

$$\cos \chi = \frac{s}{\sqrt{s^2 + t^2}}, \quad \sin \chi = \frac{t}{\sqrt{s^2 + t^2}}. \quad (11.34)$$

Taking (11.34) into account, we write the rotation tensor

$$\mathbf{A} = \mathbf{e}_\varphi \otimes \mathbf{e}_\varphi + \frac{s}{\sqrt{s^2 + t^2}} (\mathbf{e}_z \otimes \mathbf{e}_z + \mathbf{e}_r \otimes \mathbf{e}_r) + \frac{t}{\sqrt{s^2 + t^2}} (\mathbf{e}_z \otimes \mathbf{e}_r - \mathbf{e}_r \otimes \mathbf{e}_z) \quad (11.35)$$

and the components of the stretch tensor

$$\begin{aligned} U_\varphi &= C_\varphi, \\ U_z &= \frac{sC_z + tC_{zr}}{\sqrt{s^2 + t^2}}, \quad U_r = \frac{sC_r - tC_{rz}}{\sqrt{s^2 + t^2}}, \\ U_{zr} &= U_{rz} = \frac{C_z C_{rz} + C_r C_{zr}}{\sqrt{s^2 + t^2}}. \end{aligned}$$

Since the unperturbed state is axisymmetric (no rotations, movement along the radial coordinate), then

$$\mathbf{A}_0 = \mathbf{E}. \quad (11.36)$$

Therefore, the linearized stress tensor for a semi-linear material given by the constitutive relations (11.21) has the form

$$\dot{\mathbf{D}} = \frac{2\mu}{1-2\nu} (\nu \operatorname{tr} \mathbf{U}_0 - 1 - \nu) \dot{\mathbf{A}} + \frac{2\mu}{1-2\nu} (\nu \operatorname{tr} \dot{\mathbf{U}}) \mathbf{E} + 2\mu \mathbf{L}. \quad (11.37)$$

By (11.36), the $\dot{\mathbf{A}}$ tensor is antisymmetric. This can be shown by differentiating the expression for the rotation tensor (11.35) with respect to η and taking into account that $t_0 = 0$ (because $C_{zr}^0 = C_{rz}^0 = 0$). Therefore, the linearized rotation tensor has the representation

$$\dot{\mathbf{A}} = \frac{\dot{t}}{s_0} (\mathbf{e}_z \otimes \mathbf{e}_r - \mathbf{e}_r \otimes \mathbf{e}_z) = \frac{L_{zr} - L_{rz}}{C_z^0 + C_r^0} (\mathbf{e}_z \otimes \mathbf{e}_r - \mathbf{e}_r \otimes \mathbf{e}_z).$$

Let us prove an auxiliary equality

$$\operatorname{tr} \dot{\mathbf{U}} = \operatorname{tr} \mathbf{L}. \quad (11.38)$$

To do this, we substitute as the stretch tensor its expression in terms of the distortion and rotation tensors according to (11.30) and differentiate with respect to the η parameter:

$$\operatorname{tr} \dot{\mathbf{U}} = [\operatorname{tr} (\mathbf{C} \cdot \mathbf{A}^T)]' = \operatorname{tr} (\mathbf{L} \cdot \mathbf{A}_0^T) + \operatorname{tr} (\mathbf{C}_0 \cdot \dot{\mathbf{A}}^T).$$

Since $\operatorname{tr} (\mathbf{C}_0 \cdot \dot{\mathbf{A}}^T) = 0$ due to the symmetry of the tensor \mathbf{C}_0 and the antisymmetry of the tensor $\dot{\mathbf{A}}$ and (11.36) holds, then we obtain the fulfillment of the relation (11.38).

Because the equality (11.36) is valid, as well as $\mathbf{U}_0 = \mathbf{C}_0 \cdot \mathbf{A}_0^T$, then

$$\mathbf{U}_0 = \mathbf{C}_0.$$

Therefore, we have linearized constitutive relations (11.37) in the form

$$\begin{aligned} \dot{\mathbf{D}} &= \frac{2\mu}{1-2\nu} (\nu \operatorname{tr} \mathbf{C}_0 - 1 - \nu) \frac{L_{zr} - L_{rz}}{C_z^0 + C_r^0} (\mathbf{e}_z \otimes \mathbf{e}_r - \mathbf{e}_r \otimes \mathbf{e}_z) \\ &+ \frac{2\mu}{1-2\nu} (\nu \operatorname{tr} \mathbf{L}) \mathbf{E} + 2\mu \mathbf{L}. \end{aligned} \quad (11.39)$$

Here, \mathbf{C}_0 is given by the formula (11.18), and the components of the linearized distortion tensor are determined according to the representation of this tensor

$$\begin{aligned} \mathbf{L} &= \frac{\partial u(r, z)}{\partial r} \mathbf{e}_r \otimes \mathbf{e}_r + \frac{u(r, z)}{r} \mathbf{e}_\varphi \otimes \mathbf{e}_\varphi + \frac{\partial w(r, z)}{\partial r} \mathbf{e}_r \otimes \mathbf{e}_z + \frac{\partial w(r, z)}{\partial z} \mathbf{e}_z \otimes \mathbf{e}_z \\ &+ \frac{\partial u(r, z)}{\partial z} \mathbf{e}_z \otimes \mathbf{e}_r, \end{aligned} \quad (11.40)$$

obtained taking into account (11.27) and (11.28).

Substituting the linearized stress tensor $\dot{\mathbf{D}}$ (11.39) into the linearized equilibrium equation (11.26), we obtain two equations for functions depending on the variables r and z .

The solution of the boundary value problem for the quasi-displacement vector \mathbf{w} will be sought in the form Lurie (2005)

$$u(r, z) = U(r) \sin \frac{\pi n z}{l}, \quad w(r, z) = W(r) \cos \frac{\pi n z}{l}, \quad n = 0, 1, 2, \dots \quad (11.41)$$

Here, l is the length of a cylinder, n is a number of half-waves along the length of a cylinder along which buckling occurs.

Substitution (11.41) allows you to separate the variable z in the linearized equations (11.26), (11.39), and (11.40).

As a result, we obtain the equilibrium equations

$$\begin{aligned} & \frac{\nu}{1-2\nu} \left(U'' + \frac{U'}{r} - \frac{U}{r^2} - \frac{\pi n}{l} W' \right) + U'' + \frac{1}{r} \left(U' - \frac{U}{r} \right) \\ & + \frac{[\nu(C_r + C_\varphi + \lambda) - 1 - \nu] \pi n}{(1-2\nu)(\lambda + C_r)l} \left(W' - \frac{\pi n}{l} U \right) - \frac{\pi^2 n^2}{l^2} U = 0, \end{aligned} \quad (11.42)$$

$$\begin{aligned} & \frac{1}{1-2\nu} \left[\frac{\nu(C_r' + C_\varphi')}{\lambda + C_r} \left(W' - \frac{\pi n}{l} U \right) \right. \\ & \left. + \frac{\nu(C_r + C_\varphi + \lambda) - 1 - \nu}{(\lambda + C_r)^2} \left[(\lambda + C_r) \left(W'' - \frac{\pi n}{l} U' \right) - C_r' \left(W' - \frac{\pi n}{l} U \right) \right] \right] \\ & + W'' + \frac{1}{r} \left[\frac{\nu(C_r + C_\varphi + \lambda) - 1 - \nu}{(1-2\nu)(\lambda + C_r)} \left(W' - \frac{\pi n}{l} U \right) + W' \right] \\ & + \frac{\nu \pi n}{(1-2\nu)l} \left(U' + \frac{U}{r} - \frac{\pi n}{l} W \right) - \frac{\pi^2 n^2}{l^2} W = 0 \end{aligned} \quad (11.43)$$

and boundary conditions in the absence of lateral load

$$\frac{\nu}{1-2\nu} \left(U' - \frac{U}{r} - \frac{\pi n}{l} W + U' \right) = 0, \quad (11.44)$$

$$\frac{[\nu(C_r + C_\varphi + \lambda) - 1 - \nu]}{(1-2\nu)(\lambda + C_r)} \left(W' - \frac{\pi n}{l} U \right) + W' = 0. \quad (11.45)$$

In the relations (11.42)–(11.45), the prime denotes derivatives with respect to r . Thus, the linearized problem for a cylinder with dislocations consists of a homogeneous system of two second-order ordinary linear differential equations (11.42) and (11.43) with respect to the functions $U(r)$ and $W(r)$ and boundary conditions (11.44) and (11.45). The homogeneous linear problem (11.42)–(11.45) was solved numerically. When a cylinder loses its stability, a buckling form is realized with the number n , which corresponds to the minimum of the axial elongation $1 - \lambda$. The longitudinal critical force is determined in terms of the elongation multiplicity λ using the formula (11.17).

11.7 Buckling Analysis

The cases of a thin shell ($r_1 = 0.95r_0$) and a thick-walled tube ($r_1 = 0.5r_0$) are considered. In what follows, the coordinate r will be assumed to be dimensionless, referred to the outer radius r_0 , so that $r_1 \leq r \leq 1$. Dimensionless stresses will be referred to the constant μ , which at small strains has the meaning of the shear modulus. Let $\nu = 0.3$, $l = 10$. The dislocation density is considered as $\beta(r) = \beta_0 r^\varkappa$, $\varkappa = 2$ and $\varkappa = -1$.

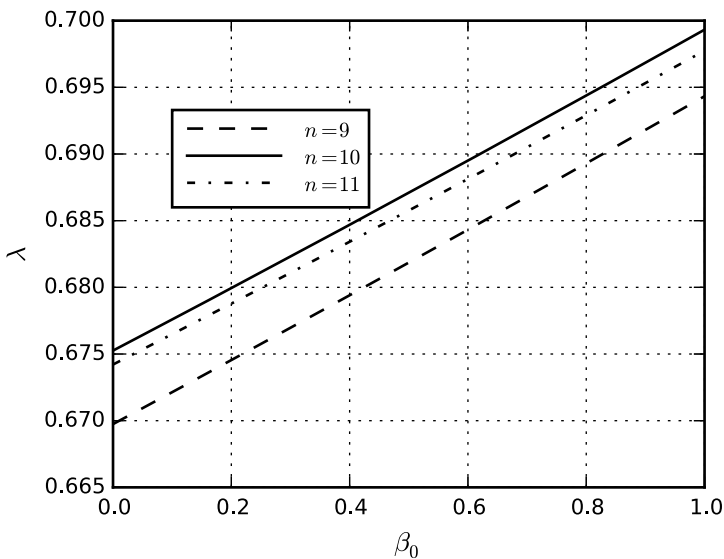


Fig. 11.1 Relationship between the elongation multiplicity λ and the dislocation density parameter β_0 , thick-walled tube, $\nu = -1$

A thick-walled tube $r_1 = 0.5r_0$ (Fig. 11.1) loses stability for the first time at $n = 10$, while a thin shell $r_1 = 0.95r_0$ (Fig. 11.2) loses stability for the first time at $n = 26$. For $\nu = 2$, the elongation multiplicity differs insignificantly from the elongation multiplicity in the case of $\nu = -1$, and this difference is the smaller, the smaller the parameter β_0 . For example, for $\beta_0 = 1$ in a thin shell for $\nu = 2$, we have $\lambda = 0.96976$, and for $\nu = -1$, we have $\lambda = 0.96978$. In a thick-walled tube with $\beta_0 = 1$ for $\nu = 2$, we have $\lambda = 0.6862$, and for $\nu = -1$, we have $\lambda = 0.6993$.

A critical resulting longitudinal force for a thick-walled tube and a thin shell is shown in Figs. 11.3 and 11.4. As the dislocation density increases, the critical force decreases in absolute value. For the case of the absence of dislocations, the results of this work are found to correspond with the results of the theory of shells Grigolyuk and Kabanov (1978). For example, for a shell $r_1 = 0.95r_0$, the longitudinal force $Q = -0.0243$ found by us corresponds to the longitudinal force $Q = -0.0241$ found by the theory of shells.

Consider the density of dislocations with $\nu = 2$. Figures 11.5 and 11.6 show that there are cylindrical surfaces inside the cylinder on which the buckling mode amplitudes U (along the vector \mathbf{e}_r) and W (along the vector \mathbf{e}_z) do not depend on the dislocation density. It can be shown that, for a thin shell, this is true for the amplitude U and is violated for the amplitude W . On the inner surface of a thick-walled tube and a thin shell, the amplitude U increases with an increase in the dislocation density, and on the outer surface—it decreases. As the dislocation density increases, the amplitude W decreases on the outer surface, increases in absolute value on the inner surface,

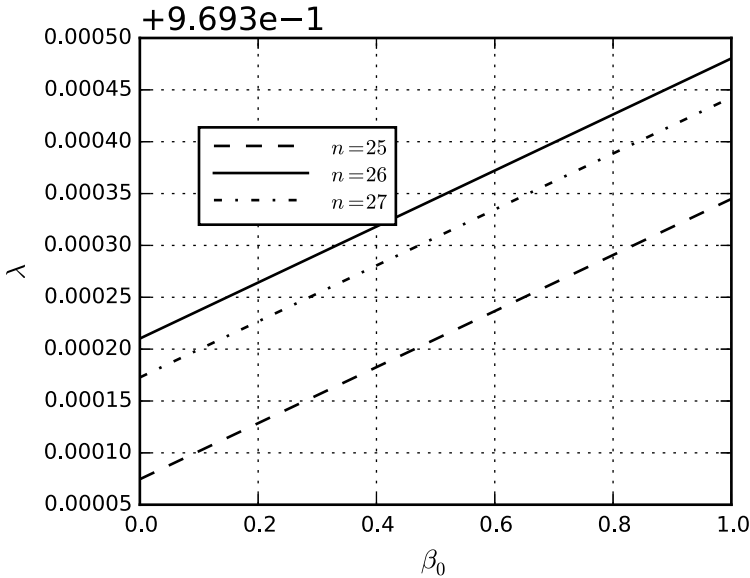


Fig. 11.2 Relationship between the elongation multiplicity λ and the dislocation density parameter β_0 , thin shell, $\nu = -1$

and, as it moves from the inner surface to the outer, first increases, then decreases, and then increases again.

In the case when $\nu = -1$, there is one cylindrical surface inside the thick-walled tube, on which the amplitude of the buckling mode U (Fig. 11.7) does not depend on the dislocation density, and two surfaces, on which the amplitude W (Fig. 11.8) does not depend on the dislocation density: closer to the body boundary is the one closer to the outer surface of the cylinder. The U buckling mode amplitude with increasing dislocation density decreases in absolute value on the outer surface and increases on the inner surface. With an increase in the dislocation density, the W buckling mode amplitude increases in absolute value on the inner surface, then, when moving from the inner surface to the outer surface, decreases in absolute value, and then increases, and decreases on the outer surface.

In a thin cylindrical shell with a distribution of dislocations with $\nu = -1$, the U buckling mode amplitude (Fig. 11.9; the curves for $\beta_0 = 0.4$ and $\beta_0 = 1$ are the same) is distributed over the thickness evenly. According to Fig. 11.10, an increase in the dislocation density can either decrease or increase the W buckling mode amplitude (the curves for $\beta_0 = 0.4$ and $\beta_0 = 1$ coincide). In addition, there is a cylindrical surface inside the shell, on which the buckling mode amplitude is zero for any dislocation density.

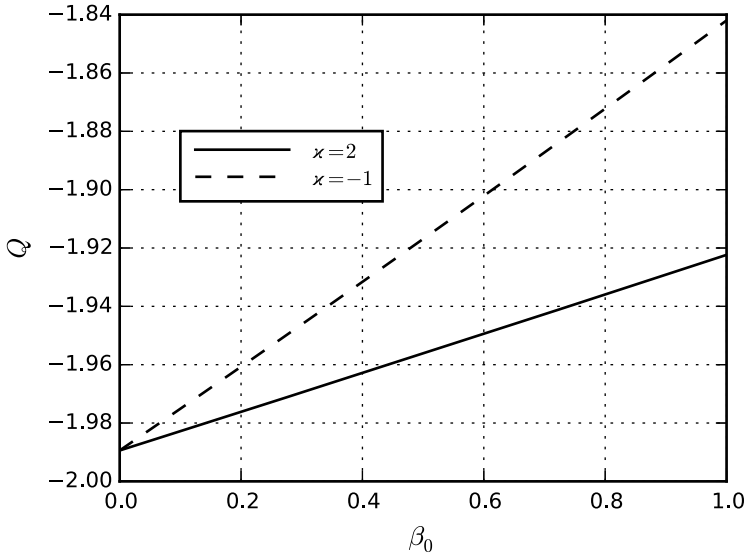


Fig. 11.3 Critical force, thick-walled tube, $n = 10$

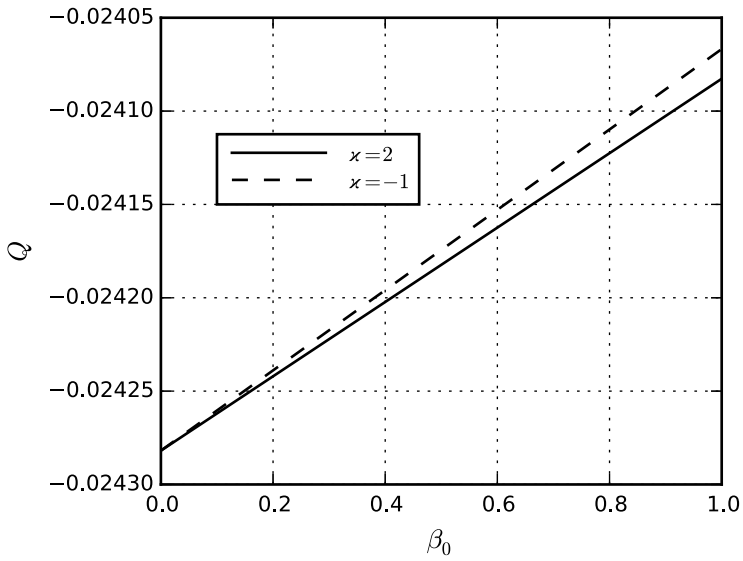


Fig. 11.4 Critical force, thin shell, $n = 26$

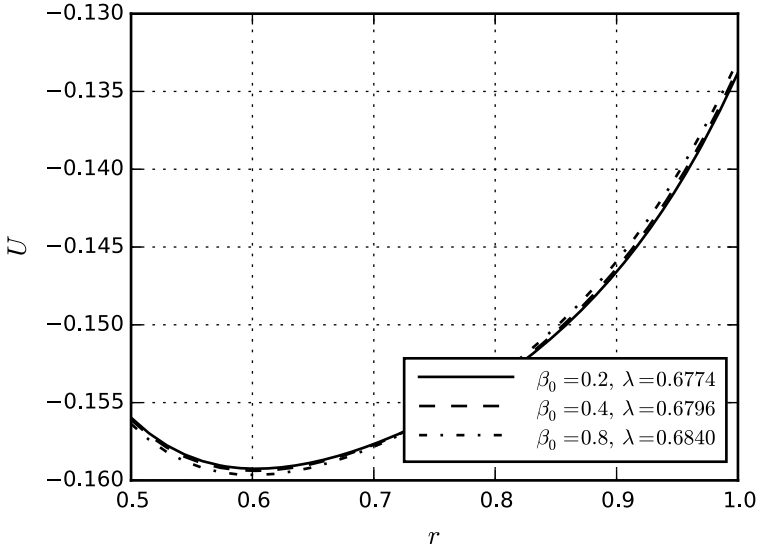


Fig. 11.5 Buckling mode amplitude along e_r , thick-walled tube, $\nu = 2, n = 10$

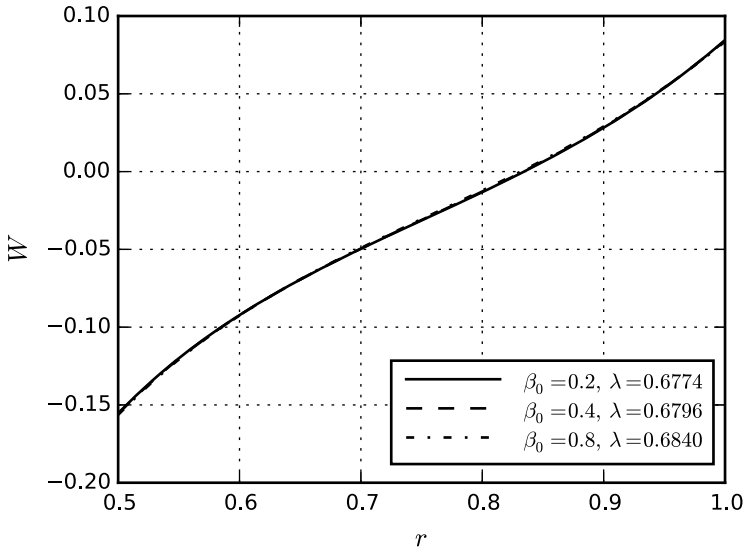


Fig. 11.6 Buckling mode amplitude along e_z , thick-walled tube, $\nu = 2, n = 10$

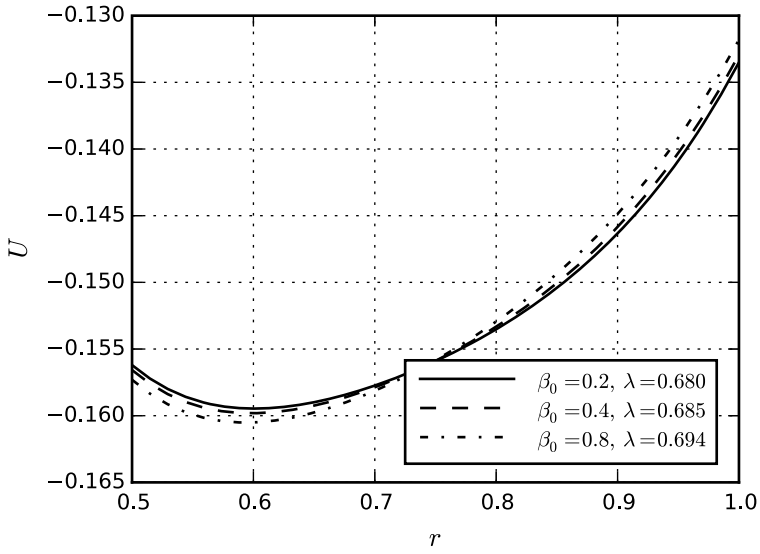


Fig. 11.7 Buckling mode amplitude along e_r , thick-walled tube, $\varkappa = -1, n = 10$

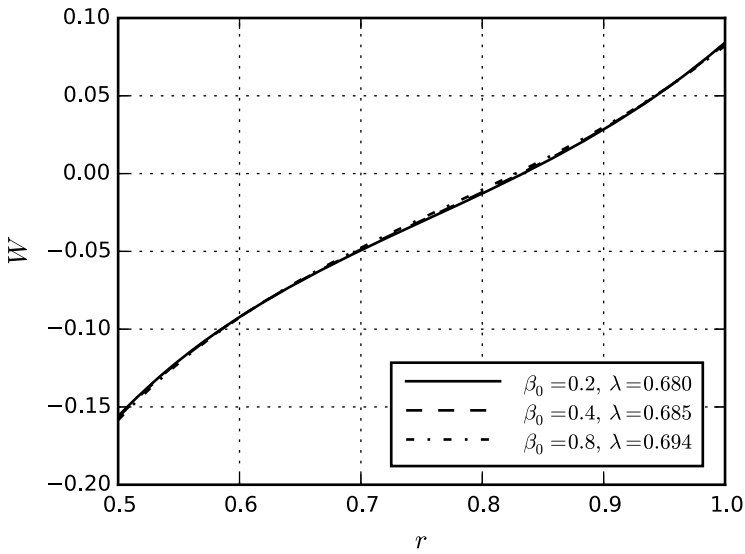


Fig. 11.8 Buckling mode amplitude along e_z , thick-walled tube, $\varkappa = -1, n = 10$

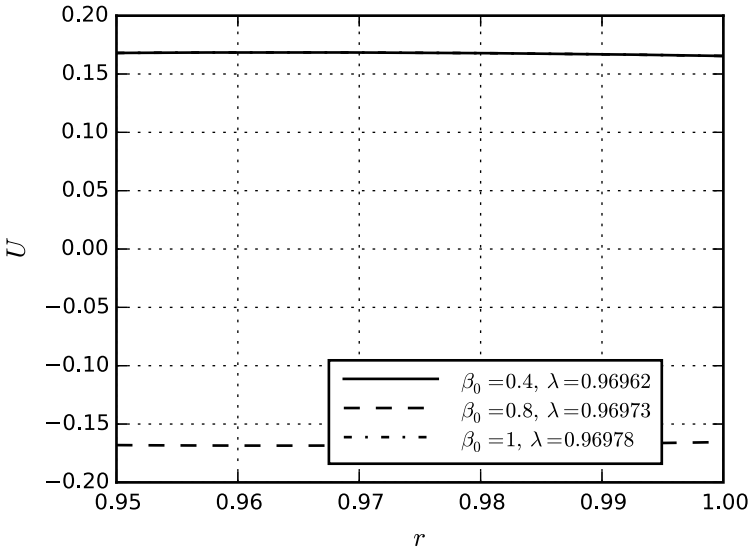


Fig. 11.9 Buckling mode amplitude along \mathbf{e}_r , thin shell, $\varkappa = -1, n = 26$

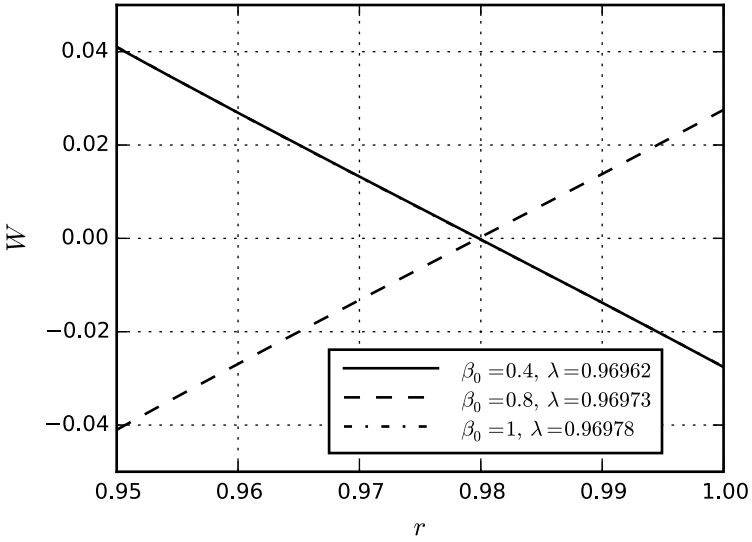


Fig. 11.10 Buckling mode amplitude along \mathbf{e}_z , thin shell, $\varkappa = -1, n = 26$

11.8 Conclusion

In this paper, we have studied the problem of equilibrium stability of an elastic hollow cylinder made of a semi-linear material, containing distributed dislocations. The problem is solved in the framework of the nonlinear three-dimensional theory of elasticity, taking into account continuously distributed dislocations. The distribution of edge dislocations, characterized by the scalar density of dislocations (an arbitrary function of the radial coordinate), is considered. The subcritical state of the cylinder is described by the exact solution. The critical values of the elongation multiplicity, which is used to determine the critical force, are found by solving a linearized homogeneous boundary value problem, which is obtained by linearizing the equilibrium equations, incompatibility equations, constitutive relations, and boundary conditions. Using a special substitution, the variables in the system of linear partial differential equations are separated. The resulting linear homogeneous boundary value problem for a system of ordinary differential equations is solved numerically. The cases of a thick-walled tube and a thin shell are considered. The effect of dislocations on the loss of stability is analyzed. In particular, it has been established that the presence of dislocations can both decrease and increase the critical force at which buckling occurs. It is shown that there is a dislocation density inversely proportional to the radius at which one of the buckling mode amplitudes in a thin shell is equal to zero. It has also been found that cylindrical surfaces can exist in a cylinder, on which the buckling mode amplitudes do not depend on the dislocation density.

Acknowledgements The reported study was funded by the Russian Science Foundation, project number 23-21-00123, <https://rscf.ru/en/project/23-21-00123/>.

References

- Berdichevsky VL, Sedov LI (1967) Dynamic theory of continuously distributed dislocations. its relation to plasticity theory. *Prikl Mat Mekh* 31(6):989–1006
- Bilby BA, Bullough R, Smith E (1955) Continuous distributions of dislocations: a new application of the methods of non-Riemannian geometry. *Proc R Soc Lond A: Math Phys Eng Sci* A231:263–273
- Biot MA (1965) *Mechanics of incremental deformations*. Wiley, New York
- Budiansky B, Hutchinson J (1979) *Buckling: progress and challenge*. NASA Conference Publication
- Chen YC, Haughton D (2003) Stability and bifurcation of inflation of elastic cylinders. *Proc R Soc Lond* 459:137–156
- Clayton JD (2011) *Nonlinear mechanics of crystals*. Springer, Dordrecht
- Derezin SV, Zubov LM (2011) Disclinations in nonlinear elasticity. *Ztsch Angew Math und Mech* 91:433–442
- Eremeyev VA, Cloud MJ, Lebedev LP (2018) *Applications of tensor analysis in continuum mechanics*. World Scientific, New Jersey
- Ericksen JL (1975) Equilibrium of bars. *J Elast* 5(3–4):191–201
- Eshelby JD (1956) The continuum theory of lattice defects. In: F Seitz DT (ed) *Solid state physics*, vol 3. Academic Press, New York, pp 79–144

- Fu YB, Ogden RW (1999) Nonlinear stability analysis of pre-stressed elastic bodies. *Contin Mech Thermodyn* 11:141–172
- Goloveshkina EV, Zubov LM (2019) Universal spherically symmetric solution of nonlinear dislocation theory for incompressible isotropic elastic medium. *Arch Appl Mech* 89(3):409–424
- Goloveshkina EV, Zubov LM (2020) Equilibrium stability of nonlinear elastic sphere with distributed dislocations. *Continuum Mech Thermodyn* 32(6):1713–1725
- Green AE, Adkins JE (1960) Large elastic deformations and non-linear continuum mechanics. Clarendon Press, Oxford
- Grigolyuk EI, Kabanov BB (1978) The stability of shells (in Russian). Nauka, M
- Guz A (1999) Fundamentals of the three-dimensional theory of stability of deformable bodies. Springer, Berlin
- Haughton D, Ogden R (1979a) Bifurcation of inflated circular cylinders of elastic material under axial loadingI. membrane theory for thin-walled tubes. *J Mech Phys Solids* 27(3):179–212
- Haughton D, Ogden R (1979b) Bifurcation of inflated circular cylinders of elastic material under axial loadingII. exact theory for thick-walled tubes. *J Mech Phys Solids* 27(5):489–512
- Haughton DM, Moiseyenko SI (2001) Elastic membranes. *Nonlinear elasticity: theory and applications*, pp 233–267
- John F (1960) Plane strain problems for a perfectly elastic material of harmonic type. *Commun Pure Appl Math* 13:239–296
- Kondo K (1952) On the geometrical and physical foundations in the theory of yielding. In: *Proceedings of 2nd Japan national congress for applied mechanics*, Tokyo, pp 41–47
- Kröner E (1960) Allgemeine Kontinuumstheorie der Versetzungen und Eigenspannungen. *Arch Ration Mech Anal* 4:273–334
- Landau LD, Lifshitz EM (1975) *Theory of elasticity, theoretical physics*, vol 7. Pergamon, Oxford
- Lastenko MS, Zubov LM (2002) A model of neck formation on a rod under tension. *Rev Colomb Mat* 36(1):49–57
- Le K, Stumpf H (1996) A model of elastoplastic bodies with continuously distributed dislocations. *Int J Plast* 12(5):611–627
- Lebedev LP, Cloud MJ, Eremeyev VA (2010) *Tensor analysis with applications in mechanics*. World Scientific, New Jersey
- Lurie AI (1990) *Nonlinear theory of elasticity*. North-Holland, Amsterdam
- Lurie AI (2005) *Theory of elasticity*. Springer, Berlin
- Nye JF (1953) Some geometrical relations in dislocated crystals. *Acta Metall* 1(2):153–162
- Ogden RW (1997) *Non-linear elastic deformations*. Dover, New York
- Samuelson LA, Eggwertz S (eds) (1992) *Shell stability handbook*. Elsevier Applied Science, London
- Sensenig CB (1964) Instability of thick elastic solids. *Commun Pure Appl Math* 17(4):451–491
- Singer J, Arbocz J, Weller T (2002) *Buckling experiments: experimental methods in buckling of thin-walled structures: shells, built-up structures, composites and additional topics*, vol 2. Wiley, New York
- Spector SJ (1984) On the absence of bifurcation for elastic bars in uniaxial tension. *Arch Ration Mech Anal* 85(2):171–199
- Teodosiu C (2013) *Elastic models of crystal defects*. Springer, Berlin
- Timoshenko SP, Gere JM (1963) *Theory of elastic stability*, 2nd edn. McGraw-Hill, Auckland
- Tovstik PE, Smirnov AL (2002) *Asymptotic methods in the buckling theory of thin shells*. World Scientific, Singapore
- Tvergaard V (1976) Buckling behaviour of plate and shell structures. In: Koiter WT (ed) *Proceedings of 14th IUTAM congress*, vol 72. North-Holland, pp 233–247
- Vakulenko AA (1991) The relationship of micro- and macroproperties in elastic-plastic media (in Russian). *Itogi Nauki Tekh, Ser: Mekh Deform Tverd Tela* 22(3):3–54
- Volmir AS (1967) *Stability of deformable systems*. Nauka, Moscow
- Zelenin AA, Zubov LM (1985) Supercritical deformations of the elastic sphere. *Izv Akad Nauk SSSR Mekh Tverd Tela (Proc Acad Sci USSR Mech solids)* 5:76–82

- Zelenin AA, Zubov LM (1987) Branching of solutions of the nonlinear elasticity theory static problems. *Prikl Mat Mech* 51(2):275–282
- Zelenin AA, Zubov LM (1988) The behaviour of a thick circular plate after stability loss. *Prikl Mat Mech* 52(4):642–650
- Zubov LM (1997) *Nonlinear theory of dislocations and disclinations in elastic bodies*. Springer, Berlin
- Zubov LM (2004) Continuously distributed dislocations and disclinations in nonlinearly elastic micropolar media. *Dokl Phys* 49(5):308–310
- Zubov LM (2011) The continuum theory of dislocations and disclinations in nonlinearly elastic micropolar media. *Mech Solids* 46(3):348–356
- Zubov LM, Karyakin MI (2006) *Tensor calculus (in Russian)*. Vuzovskaya kniga, M
- Zubov LM, Moiseyenko SI (1983) Stability of equilibrium of an elastic sphere turned inside out. *Izv Akad Nauk SSSR Mekh Tverd Tela (Proc Acad Sci USSR Mech solids)* 5:148–155
- Zubov LM, Rudev AN (1993) On the peculiarities of the loss of stability of a non-linear elastic rectangular bar. *Prikl Mat Mech* 57(3):65–83
- Zubov LM, Rudev AN (1996) The instability of a stretched non-linearly elastic beam. *Prikl Mat Mech* 60(5):786–798
- Zubov LM, Sheidakov DN (2008) Instability of a hollow elastic cylinder under tension, torsion, and inflation. *Trans ASME J Appl Mech* 75(1):0110021–0110026
- Zubov LM, Sheyidakov DN (2005) The effect of torsion on the stability of an elastic cylinder under tension. *Prikl Mat Mech* 69(1):53–60

Chapter 12

Simple Problems of Mechanical Equilibrium Applicable to the Synthesis and Modification of Materials



Anna G. Knyazeva

Abstract The paper presents examples of mechanical equilibrium problems that are used to characterize the stress–strain state of objects under conditions of surface treatment of materials and synthesis of coatings and allow constructing appropriate coupled models. In some practically interesting cases, solutions of coupled mechanical equilibrium problems are reduced to the solution of systems of linear equations, which is convenient both for constructing analytical evaluations and for numerical realization of coupled models, which is used by different authors in the physical and materials science literature. Examples of problems on the equilibrium of a three-layer plate under conditions of isothermal formation of transient diffusion zones and under conditions of isothermal annealing with simultaneous application of a mechanical load are described. The basic equations for the description of solid-phase combustion under flat stressed and flat deformed conditions and the basic equations for controlled synthesis of material on a substrate are presented. The possibilities of plate theory for description of synthesis of coating on a substrate are analyzed. The coupled equations of heat conduction and bending of a two-layer plate have been constructed taking into account the difference in the averaging approaches in heat conduction theory and in plate theory. Applications include modeling of transition zone formation under isothermal conditions, synthesis of materials in 3D technologies.

Keywords Coupled equilibrium problems · Analytical solutions · Materials modification

A. G. Knyazeva (✉)

Institute of Strength Physics and Materials Science of Siberian Branch of Russian Academy of Sciences, 2/4, Pr. Akademicheskii, Tomsk 634055, Russia

e-mail: anna-knyazeva@mail.ru

12.1 Introduction

It is no secret that composites attract attention with their properties different from those of their constituents, and sometimes exceeding them (Zheng et al. 2022; Shehryar et al. 2021; Koyanagi et al. 2018). They include layer composites with different properties, structure, and periodicity of layers. Quite many publications are devoted to modeling their behavior under thermomechanical loading conditions and calculating their effective properties. However, the formation of structure and properties occurs precisely in the process of creating composites. The simulation of the corresponding phenomena is paid little attention undeservedly.

In the technologies for obtaining layered materials or composites, including 3D technologies (Sun et al. 2023; You et al. 2023), both dissimilar (Fig. 12.1a) and identical materials (Fig. 12.1b) can be combined, special compositions can be used for their joining, which themselves undergo various transformations (Fig. 12.1c), which leads to a complex multilevel structure in the process of creating composites. Material bonding and synthesis of coatings can be carried out in air, in an oxidizing or inert atmosphere, in a vacuum; using external dynamic or static loading; can be controlled by an external energy source, etc. For example, if a laser or electron beam is expanded in line (and there is high-frequency scanning across the entire width of the sample), then processes in the thin surface layer and/or at the material-coating interface will be of interest in coating synthesis or surface treatment (Fig. 12.2a). In Laminated Object Manufacturing (LOM) technologies (Fig. 12.2b) or (Fig. 12.2c), the result will depend on both the applied load and the thermokinetic processes at the interfaces and structural transformations in the bonding composition (which depend on both temperature and stress). In all these cases, the chemical and phase composition, the structure of the interlayers and transition zones, and, consequently, the effective properties of the resulting composites will depend not only on the materials used, but also on the accompanying physical and chemical processes, the dynamics of which are different under different conditions.

The study of such objects in mechanics and physics uses different approaches. When building coupled models of synthesis, joining, and processing of materials, it is necessary to take into account the features of each particular technology individually. This is useful for identifying qualitative regularities that are sometimes impossible

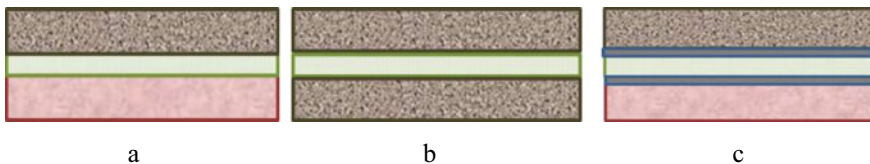


Fig. 12.1 Conditional schemes of joining materials in different technologies: **a** joining dissimilar materials; **b** joining the same materials **c** joining dissimilar materials using adhesives

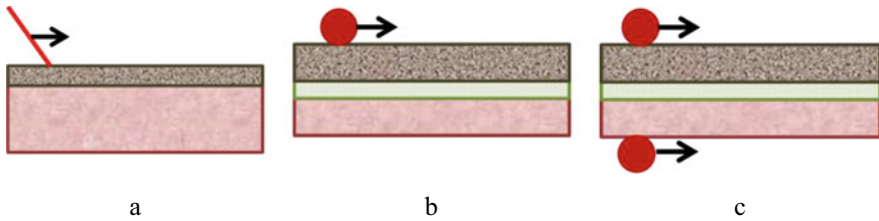


Fig. 12.2 Synthesis and joining of materials controlled by external action: **a** synthesis of coatings controlled by a moving heat source; **b** bonding of layers in LOM-technology; **c** Roll bonding technology scheme

to grasp with commercial packages. Below there are examples of simple equilibrium problems that are used or can be used in modeling of processes of materials modification and synthesis of composites.

12.2 Equilibrium Problems

Example 1 Let it be required to study the stress–strain state of a plate consisting of three layers with thicknesses h_A , h_B , and h_C (Fig. 12.1a). We denote the properties of the layers by the indices “A”, “B”, and “C”, respectively. In one of the plates (for example, the central one) chemical reactions or phase transitions may take place, the consequence of which may be a new phase composition (Chashchina and Knyazeva 2005, 2006). In the other situation, during homogeneous heating, diffusion interaction between the layers with the formation of diffusion zones is possible (Knyazeva et al. 2001, 2013). According to the Duhamel-Neumann relations for isotropic materials, we have

$$\sigma_{ij} = 2\mu\varepsilon_{ij} + \delta_{ij}[\lambda\varepsilon_{kk} - K\omega] \quad (12.1)$$

or

$$\sigma_{ij} = 2\frac{E}{2(1+\nu)}\varepsilon_{ij} + \delta_{ij}\left[\frac{E\nu}{(1-2\nu)(1+\nu)}\varepsilon_{kk} - \frac{E}{3(1-2\nu)}\omega\right],$$

where $i, j = x, y, z$; λ, μ —Lamé coefficients, $K = \lambda + \frac{2}{3}\mu$ —the bulk compression modulus, linked to the technical characteristics (elastic modulus E and Poisson’s coefficient ν) by the relations

$$K = \frac{E}{3(1-2\nu)}, \lambda = \frac{E\nu}{(1+\nu)(1-2\nu)}, \mu = \frac{E}{2(1+\nu)} \quad (12.2)$$

δ_{ij} -Kronecker delta

$$\begin{cases} \delta_{ij} = 1, & \text{if } i = j; \\ \delta_{ij} = 0, & \text{if } i \neq j, \end{cases}$$

ω is generally a function of concentration and temperature:

$$\omega = 3 \left[\alpha_T (T - T_0) + \sum_{k=1}^n \alpha_k (C_k - C_{k0}) \right], \quad (12.3)$$

α_T is linear thermal expansion coefficient; α_k are the coefficients of concentration expansion; index «0» relates to non-deformed state; n is a number of components (elements and compounds).

The properties of each layer are generally different.

Under the conditions of uniform along-surface heating or isothermal annealing (Boley et al. 1960) of a thin composite plate, it is logical to assume that the angular deformations and shear stresses are zero, while the remaining ones change only in the direction of the axis perpendicular to the plate surface. In addition, the stresses in this direction are also zero, $\sigma_{zz} = 0$. So we have

$$\begin{aligned} \varepsilon_{zz} = \varepsilon_{zz}(z), \quad \varepsilon_{yy} = \varepsilon_{xx} = \varepsilon(z), \\ \sigma_{yy} = \sigma_{xx} = \sigma(z). \end{aligned} \quad (12.4)$$

The shape of the plate in this case does not matter.

In this case, the equilibrium equations are fulfilled identically and do not allow us to find the components of the stress tensor. Therefore, it is necessary to involve the equations of deformation compatibility condition, of which in the described conditions two identical equations remain for ε_{yy} and ε_{xx} :

$$\frac{\partial^2 \varepsilon}{\partial z^2} = 0; \quad \varepsilon = \varepsilon_{yy} = \varepsilon_{xx}. \quad (12.5)$$

The solution of Eq. (12.2) is

$$\varepsilon = F_1 z + F_2, \quad (12.6)$$

where F_1 and F_2 are integration constants to be found.

From the Duhamel-Neiman relations (12.1), we find

$$\varepsilon_{zz} = \frac{1}{\lambda + 2\mu} [K\omega - 2\lambda\varepsilon] \equiv \frac{1}{3} \frac{1 + \nu}{1 - \nu} \omega - \frac{2\nu}{1 - \nu} \varepsilon \quad (12.7)$$

and

$$\sigma = -\frac{\omega}{3} \frac{E}{1-\nu} + \frac{E}{1-\nu} (F_1 z + F_2). \quad (12.8)$$

Hence, for a composite plate whose properties and composition change along the coordinate, we have

for $0 \leq x < h_A$:

$$\begin{aligned} \varepsilon_{zz}^A &= \frac{1}{3} \frac{1+\nu_A}{1-\nu_A} \omega_A - \frac{2\nu_A}{1-\nu_A} (F_1 z + F_2); \\ \sigma^A &= -\frac{\omega_A}{3} \frac{E_A}{1-\nu_A} + \frac{E_A}{1-\nu_A} (F_1 z + F_2); \\ \varepsilon^A &= F_1 z + F_2; \end{aligned}$$

for $h_A \leq x < h_A + h_B$:

$$\begin{aligned} \varepsilon_{zz}^B &= \frac{1}{3} \frac{1+\nu_B}{1-\nu_B} \omega_B - \frac{2\nu_B}{1-\nu_B} (F_1 z + F_2); \\ \sigma^B &= -\frac{\omega_B}{3} \frac{E_B}{1-\nu_B} + \frac{E_B}{1-\nu_B} (F_1 z + F_2); \\ \varepsilon^B &= F_1 z + F_2; \end{aligned}$$

and for $h_A + h_B \leq x < h_A + h_B + h_C$:

$$\begin{aligned} \varepsilon_{zz}^C &= \frac{1}{3} \frac{1+\nu_C}{1-\nu_C} \omega_C - \frac{2\nu_C}{1-\nu_C} (F_1 z + F_2); \\ \sigma^C &= -\frac{\omega_C}{3} \frac{E_C}{1-\nu_C} + \frac{E_C}{1-\nu_C} (F_1 z + F_2); \\ \varepsilon^C &= F_1 z + F_2. \end{aligned}$$

It remains to find the integration constants.

For a free unfixed homogeneous plate, the resultant force along the plate contour and the resultant moment of forces relative to the center of mass are zero (Boley et al. 1960). This is reflected by the equations:

$$\int_{-h/2}^{h/2} \sigma(z) dz = 0, \quad \int_{-h/2}^{h/2} \sigma(z) z dz = 0. \quad (12.9)$$

The stress σ acts perpendicular to the plate contour in the plane xy , h is the plate thickness. The center of mass is in the median plane of the plate (Fig. 12.3a).

If we move the origin of coordinates to the left by $h/2$, then instead of (9) we write

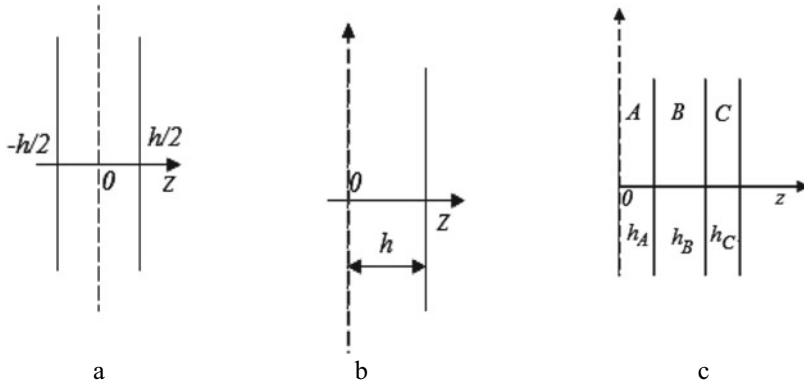


Fig. 12.3 Geometry problem 1

$$\int_0^h \sigma \left(z - \frac{h}{2} \right) dz = 0, \quad \int_0^h \sigma \left(z - \frac{h}{2} \right) \cdot \left(z - \frac{h}{2} \right) dz = 0. \quad (12.10)$$

For the three-layer plate (Fig. 12.3), we have

$$\int_0^{h_A+h_B+h_C} \sigma(z - z_*) dz = 0, \quad \int_0^{h_A+h_B+h_C} \sigma(z - z_*) \cdot (z - z_*) dz = 0 \quad (12.11)$$

where z_* —the position of the center of mass of the composite plate with respect to the plane $z = 0$. If necessary, this value can be easily calculated from the ratio

$$\langle \rho \rangle z_* = \rho_A z_A^* + \rho_B z_B^* + \rho_C z_C^*$$

or

$$z_* = \frac{\rho_A \frac{h_A}{2} + \rho_B \left(h_A + \frac{h_B}{2} \right) + \rho_C \left(h_A + h_B + \frac{h_C}{2} \right)}{\rho_A h_A + \rho_B h_B + \rho_C h_C} (h_A + h_B + h_C).$$

Substituting the found expressions for the stresses in (12.9), we find an equation system for determining the integration constants

$$\begin{aligned}
& - \int_0^{h_A+h_B+h_C} \frac{\omega(z, t)}{3} \frac{E}{1-\nu} dz + F_1 \int_0^{h_A+h_B+h_C} \frac{E}{1-\nu} z dz + F_2 \int_0^{h_A+h_B+h_C} \frac{E}{1-\nu} dz = 0, \\
& - \int_0^{h_A+h_B+h_C} \frac{\omega(z, t)}{3} \frac{E}{1-\nu} (z - z_*) dz + F_1 \int_0^{h_A+h_B+h_C} \frac{E}{1-\nu} z (z - z_*) dz + F_2 \\
& \int_0^{h_A+h_B+h_C} \frac{E}{1-\nu} (z - z_*) dz = 0.
\end{aligned}$$

If the properties do not depend on concentrations and coordinates, all but two integrals involving the function $\omega(z, t)$ are easily taken, and the system of equations is solved without difficulty.

If the properties cannot be considered constant over the thickness of the plate (for example, they are different in different materials, and, moreover, depend on the composition changing with time), it is convenient to present the system of equations for determining the integration constants as follows:

$$\begin{aligned}
-N + F_1\beta + F_2\alpha &= 0, \\
-(M - z_*N) + F_1(\gamma - z_*\beta) + F_2(\beta - z_*\alpha) &= 0,
\end{aligned} \tag{12.12}$$

where

$$\begin{aligned}
N &= \frac{1}{3} \left[\int_0^{h_A} \omega_A(z, t) \frac{E_A}{1-\nu_A} dz + \int_{h_A}^{h_A+h_B} \omega_B(z, t) \frac{E_B}{1-\nu_B} dz + \int_{h_A+h_B}^{h_A+h_B+h_C} \omega_C(z, t) \frac{E_C}{1-\nu_C} dz \right], \\
M &= \frac{1}{3} \left[\int_0^{h_A} \omega_A(z, t) z \frac{E_A}{1-\nu_A} dz + \int_{h_A}^{h_A+h_B} \omega_B(z, t) z \frac{E_B}{1-\nu_B} dz + \int_{h_A+h_B}^{h_A+h_B+h_C} \omega_C(z, t) z \frac{E_C}{1-\nu_C} dz \right], \\
\alpha &= \int_0^{h_A} \frac{E_A}{1-\nu_A} dz + \int_{h_A}^{h_A+h_B} \frac{E_B}{1-\nu_B} dz + \int_{h_A+h_B}^{h_A+h_B+h_C} \frac{E_C}{1-\nu_C} dz, \\
\beta &= \int_0^{h_A} \frac{E_A}{1-\nu_A} z dz + \int_{h_A}^{h_A+h_B} \frac{E_B}{1-\nu_B} z dz + \int_{h_A+h_B}^{h_A+h_B+h_C} \frac{E_C}{1-\nu_C} z dz, \\
\gamma &= \int_0^{h_A} \frac{E_A}{1-\nu_A} z^2 dz + \int_{h_A}^{h_A+h_B} \frac{E_B}{1-\nu_B} z^2 dz + \int_{h_A+h_B}^{h_A+h_B+h_C} \frac{E_C}{1-\nu_C} z^2 dz.
\end{aligned}$$

The solution to the system of Eqs. (12.12) is

$$F_1 = \frac{N\beta - M\alpha}{\beta^2 - \gamma\alpha}, \quad F_2 = -\frac{N\gamma - M\beta}{\beta^2 - \gamma\alpha}$$

and does not include the coordinate of the center of inertia. The solution of the thermokinetic problem is immediately in the required coordinate system.

A similar simple approach is used in various applied problems for objects of different geometry. For example, in Yang (2005) the stress distribution in a thin plate during boron diffusion in polycrystalline silicon is illustrated. In (Lee et al. 2000; Wang et al. 2002), the mutual influence of diffusion and stresses in a hollow cylinder is investigated. The authors investigated two variants of diffusion into the hollow cylinder at a constant stress level on the surface and at a constant surface potential and came to the conclusion that the character of stress influence is the same in both cases. In the paper (Pascalis 2022), the solution of the problem on diffusion saturation of some element of an isotropic sphere is presented. The spherically symmetric problem in the presence of volumetric reaction is presented in Hu et al. (2020). Stresses accompanying the diffusion process in the spherical geometry are calculated in Mikolaichuk and Knyazeva (2010) for different variants of arrangement of layers and so on.

Example 2 If the plate is under constant load (e.g., stretched in the direction of the OY axis), the average stress in z will also satisfy the loading conditions:

$$\begin{aligned} \langle \sigma_{xx} \rangle &= \frac{1}{h} \int_0^h \sigma_{xx}(x, y, z) dz; \quad \langle \sigma_{yy} \rangle = \frac{1}{h} \int_0^h \sigma_{yy}(x, y, z) dz; \\ \langle \tau_{xy} \rangle &= \frac{1}{h} \int_0^h \tau_{xy}(x, y, z) dz \end{aligned} \quad (12.13)$$

where $h = h_A + h_B + h_C$.

Stresses σ_{xx} and σ_{yy} , and also strains ε_{yy} and ε_{xx} will not equivalent.

In (Mikolaichuk and Knyazeva 2010; Knyazeva and Mikolaichuk 2011; Mikolaichuk et al. 2012), the loading conditions are formulated as follows:

$$\langle \sigma_{yy} \rangle = P; \quad \langle \sigma_{xx} \rangle = 0. \quad (12.14)$$

If only the stresses in the diffusion zone far from the plate edges are of interest for the study, the problem again becomes one-dimensional. Expressions for strains $\varepsilon_{yy} \neq \varepsilon_{xx}$ take the form

$$\varepsilon_{xx} = F_1 z + F_2;$$

$$\varepsilon_{yy} = F_3 z + F_4;$$

To find the four integration constants we use the conditions

$$\begin{aligned}\frac{1}{h} \int_0^h \sigma_{xx}(z) dz &= 0; \quad \frac{1}{h} \int_0^h \sigma_{yy}(z) dz = P; \\ \frac{1}{h} \int_0^h \sigma_{xx}(z) z dz &= 0; \quad \frac{1}{h} \int_0^h \sigma_{yy}(z) z dz = 0.\end{aligned}$$

The values τ_{xy} and ε_{xy} in this approximation turn equal to zero. From the Duhamel-Neiman relations, we find

$$\begin{aligned}\varepsilon_{kk} &= (F_1 + F_3)z + (F_2 + F_4) + \varepsilon_{zz}; \\ \varepsilon_{zz} &= -\frac{\lambda}{\lambda + 2\mu} [(F_1 + F_3)z + (F_2 + F_4)] + \frac{K}{\lambda + 2\mu} \omega; \\ \sigma_{xx} &= \frac{2\mu}{\lambda + 2\mu} [\lambda(F_3z + F_4) + 2(\lambda + \mu)(F_1z + F_2) - K\omega]; \\ \sigma_{yy} &= \frac{2\mu}{\lambda + 2\mu} [\lambda(F_1z + F_2) + 2(\lambda + \mu)(F_3z + F_4) - K\omega].\end{aligned}\tag{12.15}$$

Consequently, we come to a system of linear algebraic equations

$$\begin{aligned}M_1 F_1 + N_1 F_2 + M_2 F_3 + N_2 F_4 - \Omega &= 0; \\ M_2 F_1 + N_2 F_2 + M_1 F_3 + N_1 F_4 - \Omega &= Ph; \\ X F_1 + M_1 F_2 + Y F_3 + M_2 F_4 - \Phi &= 0; \\ Y F_1 + M_2 F_2 + X F_3 + M_1 F_4 - \Phi &= 0,\end{aligned}\tag{12.16}$$

where

$$\begin{aligned}M_1 &= \int_0^h \frac{4\mu(\lambda + \mu)}{\lambda + 2\mu} z dz; \quad M_2 = \int_0^h \frac{2\mu\lambda}{\lambda + 2\mu} z dz \\ N_1 &= \int_0^h \frac{4\mu(\lambda + \mu)}{\lambda + 2\mu} dz; \quad N_2 = \int_0^h \frac{2\mu\lambda}{\lambda + 2\mu} dz \\ X &= \int_0^h \frac{4\mu(\lambda + \mu)}{\lambda + 2\mu} z^2 dz; \quad Y = \int_0^h \frac{2\mu\lambda}{\lambda + 2\mu} z^2 dz \\ \Omega &= \int_0^h \frac{2\mu K}{\lambda + 2\mu} \omega dz; \quad \Phi = \int_0^h \frac{2\mu K}{\lambda + 2\mu} \omega z dz.\end{aligned}$$

All integrals are a function of the z coordinate.

Despite the presence of the same coefficients in (12.16), its solution turns out to be cumbersome and is not presented here.

If the formation of diffusion zones between materials is provided by diffusion of one of the components (for example, from the middle layer), then one equation for flux (and one diffusion equation for each layer) will be required to solve the diffusion problem. According to thermodynamic theory, the equation for diffusant flux in one-dimensional problem (Knyazeva 2005, 2003) has the form

$$J_i = -D^* f(\eta_i) \frac{\partial \eta_i}{\partial z} + B_i \eta_i \frac{\partial \sigma_{kk}^{(i)}}{\partial z}, \quad (12.17)$$

where $B_i = \alpha_i \frac{D^* m}{\rho_i R T}$ is transfer coefficient under stress action; η_i is diffusant concentration in i layer; $i = A, B, C D^*$ is self-diffusion coefficient; m is diffusant molar mass; ρ_i is layer density; α_i is the concentration expansion coefficient; R is universal gas constant.

Using (12.15), we find

$$\sigma_{kk}^{(i)} = \frac{k \mu_i K_i}{\lambda_i + 2 \mu_i} \left[(F_1 + F_3) z + (F_2 + F_4) - \frac{2}{3} \omega_i \right],$$

where $\omega_i = 3 \alpha_i (\eta_i - \eta_{i0})$.

If the properties within the layers can be considered unchanged, then

$$J_i = - \left[D^* f(\eta_i) + 2 \alpha_i B_i \eta_i \frac{k \mu_i K_i}{\lambda_i + 2 \mu_i} \right] \frac{\partial \eta_i}{\partial z} + B_i \eta_i \frac{k \mu_i K_i}{\lambda_i + 2 \mu_i} (F_1 + F_3). \quad (12.18)$$

Thus, the coupling of diffusion and mechanical processes manifests itself through a change in the effective diffusion coefficient (the second summand in brackets at the concentration derivative) and the appearance of additional convective transport (the second summand in (12.18)). When solving a particular problem, it is worth paying attention to the possibility of changing the diffusion transfer rate due to stress work (Mikolaichuk and Knyazeva xxxx).

Example 3 A somewhat different approach can be used when analyzing the influence of the stress–strain state on the dynamics of chemical transformations, for example, when synthesizing a coating on a substrate (Fig. 12.2a) or when synthesizing material in a layer between two inert plates (Fig. 12.1a, b). In the first case, we can assume that the reaction layer, loosely located on the substrate, is in a plane stress state, $\sigma_{zz} = 0$.

In this case

$$\sigma_{zz} = \sigma_{xy} = \sigma_{xz} = \sigma_{yz} = 0;$$

$$\begin{vmatrix} \varepsilon_{xx} & \varepsilon_{xy} & 0 \\ \varepsilon_{yx} & \varepsilon_{yy} & 0 \\ 0 & 0 & \varepsilon_{zz} \end{vmatrix}.$$

In the second case (Fig. 1a, b) –

$$\varepsilon_{zz} = 0.$$

This will be a planar deformation for which

$$\varepsilon_{zz} = \varepsilon_{xz} = \varepsilon_{zx} = \varepsilon_{yz} = \varepsilon_{zy} = 0$$

and

$$\begin{vmatrix} \sigma_{xx} & \sigma_{xy} & 0 \\ \sigma_{yx} & \sigma_{yy} & 0 \\ 0 & 0 & \sigma_{zz} \end{vmatrix}.$$

Here σ_{zz} and ε_{zz} are the components of stress and strain tensor in OZ axis direction.

If we assume that the substrate on which the thin powder layer is located is also thin, and in the second variant the thickness of the bounding plate is also small, then in the simplest approximation we can assume that all the quantities we will use in the theoretical description of the synthesis process do not depend on the z coordinate. This applies both to the components of the stress and strain tensors and to the temperature, concentrations, and rates of chemical reactions. Then to describe the synthesis process in a flat layer, we have a two-dimensional heat conduction equation

$$\rho c_\varepsilon \frac{\partial T}{\partial t} = \lambda_T \left(\frac{\partial^2 T}{\partial x^2} + \frac{\partial^2 T}{\partial y^2} \right) + W_{ch} + W_{ext} - H - 3K\alpha_T T \frac{\partial \varepsilon_{kk}}{\partial t} \quad (12.19)$$

with boundary and initial conditions

$$\begin{aligned} t = 0 : T &= T_0; \\ y = 0 : \partial T / \partial y &= 0 \end{aligned} \quad (12.20)$$

$$\begin{aligned} x = 0, \infty : \partial T / \partial x &= 0, \\ y \rightarrow \infty : \partial T / \partial y &= 0, \end{aligned} \quad (12.21)$$

where T —is the temperature; ρ —is the density; c_ε —is the heat capacity at constant strains; λ_T —is the thermal conductivity coefficient; W_{ch} —is summary chemical heat release, W_{ext} —is the external heat source; $H = \alpha_{eff}(T - T_0) + \sigma_0 \varepsilon_0 (T^4 - T_w^4)$; the first term in H describes the heat losses in a substrate, to the surrounding material layers, and/or to the environment (α_{eff} —is effective heat transfer coefficient in

Newton's law); the second term describes the heat loss from the plate surface due to thermal radiation according to the Stefan-Boltzmann law, σ_0 —Stefan-Boltzmann constant, ε_0 —degree of blackness, T_w —is the vacuum chamber wall temperature). The other designations are the same as above. For physicochemical processes occurring in the solid phase, powder melting and porosity change (if we are talking about the synthesis of material in the powder layer) in the first approximation obviously can be not considered.

In the case of one total reaction, we add the kinetics equation to the thermal conductivity equation:

$$\frac{d\eta}{dt} = k_0(1 - \eta) \exp\left(-\frac{E_a}{RT}\right) = \Phi(T, \eta), \quad (12.22)$$

where η —is a conversion level, E_a —is activation energy for chemical reaction; k_0 —is pre-exponential factor.

Then

$$W_{ch} = Q_{ch} \Phi(T, \eta),$$

where Q_{ch} —is the heat release of summary chemical reaction.

The function (3) in the Duhamel-Neiman relation takes the form

$$\omega = 3[\alpha_T(T - T_0) + \alpha_C(\eta - \eta_0)].$$

The reaction can be activated not only by changing the temperature (internal energy), but also by performing work. This is answered by another exponential law, which leads to a more complex heat release function (Knyazeva 1993)

$$\Phi(T, \eta) = k_0(1 - \eta) \exp\left(-\frac{E_a + k_\sigma \Pi}{RT}\right),$$

where Π —is stress work; coefficient k_σ reflects the fact that this work, like activation energy, must be calculated per mole.

In the approximation of small deformations, we need two equations of motion.

$$\frac{\partial \sigma_{xx}}{\partial x} + \frac{\partial \sigma_{xy}}{\partial y} = \rho \frac{\partial^2 u_x}{\partial t^2};$$

$$\frac{\partial \sigma_{yx}}{\partial x} + \frac{\partial \sigma_{yy}}{\partial y} = \rho \frac{\partial^2 u_y}{\partial t^2},$$

where u_x, u_y are displacement vector components in the XY plane.

The equations of motion can be rewritten through deformations. Then in the case of a plane stress state we find

$$\frac{2\mu}{\lambda + 2\mu} \frac{\partial^2}{\partial x^2} [2(\lambda + \mu)\varepsilon_{xx} + \lambda\varepsilon_{yy} - K\omega] + \mu \left(\frac{\partial^2 \varepsilon_{xx}}{\partial y^2} + \frac{\partial^2 \varepsilon_{yy}}{\partial x^2} \right) = \rho \frac{\partial^2 \varepsilon_{xx}}{\partial t^2}; \quad (12.23)$$

$$\mu \left(\frac{\partial^2 \varepsilon_{xx}}{\partial y^2} + \frac{\partial^2 \varepsilon_{yy}}{\partial x^2} \right) + \frac{2\mu}{\lambda + 2\mu} \frac{\partial^2}{\partial y^2} [2(\lambda + \mu)\varepsilon_{yy} + \lambda\varepsilon_{xx} - K\omega] = \rho \frac{\partial^2 \varepsilon_{yy}}{\partial t^2}.$$

In this case, there is the ε_{zz} deformation:

$$\varepsilon_{zz} = -\frac{1}{\lambda + 2\mu} [\lambda(\varepsilon_{xx} + \varepsilon_{yy}) - K\omega].$$

In the case of planar deformation $\varepsilon_{zz} = 0$ and the equations are slightly different from (23)

$$\begin{aligned} \frac{\partial^2}{\partial x^2} [(\lambda + 2\mu)\varepsilon_{xx} + \lambda\varepsilon_{yy} - K\omega] + \mu \left(\frac{\partial^2 \varepsilon_{xx}}{\partial y^2} + \frac{\partial^2 \varepsilon_{yy}}{\partial x^2} \right) &= \rho \frac{\partial^2 \varepsilon_{xx}}{\partial t^2}; \\ \mu \left(\frac{\partial^2 \varepsilon_{xx}}{\partial y^2} + \frac{\partial^2 \varepsilon_{yy}}{\partial x^2} \right) + \frac{\partial^2}{\partial y^2} [(\lambda + 2\mu)\varepsilon_{yy} + \lambda\varepsilon_{xx} - K\omega] &= \rho \frac{\partial^2 \varepsilon_{yy}}{\partial t^2}. \end{aligned} \quad (12.24)$$

For the shear component of the stress tensor in any case we obtain

$$\frac{\partial^2 \sigma_{xy}}{\partial x \partial y} = 2\mu \frac{\partial^2 \varepsilon_{xy}}{\partial x \partial y} = 2\mu \frac{1}{2} \frac{\partial^2}{\partial x \partial y} \left(\frac{\partial u_x}{\partial y} + \frac{\partial u_y}{\partial x} \right) = \mu \left(\frac{\partial^2 \varepsilon_{xx}}{\partial y^2} + \frac{\partial^2 \varepsilon_{yy}}{\partial x^2} \right). \quad (12.25)$$

The work is calculated by the formula:

$$\Pi = -(\sigma_{xx}\varepsilon_{xx} + \sigma_{yy}\varepsilon_{yy} + 2\sigma_{xy}\varepsilon_{xy}).$$

If we now assume that the planar reaction front moves to the right with velocity V_n , we come to one-dimensional problems for both situations, including the heat conduction equation of the form

$$\begin{aligned} c_\varepsilon \rho \left[\frac{\partial T}{\partial t} - V_n \frac{\partial T}{\partial x} \right] &= \lambda_T \frac{\partial^2 T}{\partial x^2} + W_{ch} - \alpha_{eff}(T - T_0) \\ &\quad - 3K\alpha_T T \left(\frac{\partial \varepsilon_{kk}}{\partial t} - V_n \frac{\partial \varepsilon_{kk}}{\partial x} \right) \end{aligned}$$

and systems of motion equations, respectively, for the plane stress state

$$\begin{aligned} \frac{2\mu}{\lambda + 2\mu} \frac{\partial^2}{\partial x^2} [2(\lambda + \mu)\varepsilon_{xx} - K\omega] &= \rho \left[\frac{\partial^2 \varepsilon_{xx}}{\partial t^2} - 2V_n \frac{\partial^2 \varepsilon_{xx}}{\partial t \partial x} + V_n^2 \frac{\partial^2 \varepsilon_{xx}}{\partial x^2} \right] \\ \mu \frac{\partial^2 \varepsilon_{yy}}{\partial x^2} &= \rho \left[\frac{\partial^2 \varepsilon_{yy}}{\partial t^2} - 2V_n \frac{\partial^2 \varepsilon_{yy}}{\partial t \partial x} + V_n^2 \frac{\partial^2 \varepsilon_{yy}}{\partial x^2} \right] \end{aligned}$$

and for the plane deformed state

$$\begin{aligned} \frac{\partial^2}{\partial x^2} [(\lambda + 2\mu)\varepsilon_{xx} - K\omega] &= \rho \left[\frac{\partial^2 \varepsilon_{xx}}{\partial t^2} - 2V_n \frac{\partial^2 \varepsilon_{xx}}{\partial t \partial x} + V_n^2 \frac{\partial^2 \varepsilon_{xx}}{\partial x^2} \right], \\ \mu \frac{\partial^2 \varepsilon_{yy}}{\partial x^2} &= \rho \left[\frac{\partial^2 \varepsilon_{yy}}{\partial t^2} - 2V_n \frac{\partial^2 \varepsilon_{yy}}{\partial t \partial x} + V_n^2 \frac{\partial^2 \varepsilon_{yy}}{\partial x^2} \right]. \end{aligned}$$

As a result, for the stationary reaction wave, we find

$$-c_\varepsilon \rho V_n \frac{dT}{dx} = \lambda_T \frac{d^2 T}{dx^2} + W_{ch} - \alpha_{eff}(T - T_0) + 3K\alpha_T T V_n \frac{d\varepsilon_{kk}}{dx} \quad (12.26)$$

$$\varepsilon_{yy} = Ax + B,$$

where A , B are integration constants, which can be found from the additional condition that forces and moments along the plate contour are equal to zero.

For the two considered cases, we have

$$\frac{d\varepsilon_{kk}}{dx} = -\frac{2\lambda\gamma_1 - \rho V_n^2}{(\lambda + \mu)2\gamma_1 - \rho V_n^2} \frac{\gamma_1 K}{2\mu} \frac{d\omega}{dx} + A\gamma_1,$$

where $\gamma_1 = \frac{2\mu}{\lambda + 2\mu}$,
and

$$\frac{d\varepsilon_{kk}}{dx} = A + \frac{K}{(\lambda + 2\mu) - \rho V_n^2} \frac{d\omega}{dx} = A + \frac{K/(\lambda + 2\mu)}{1 - \rho V_n^2/(\lambda + 2\mu)} \frac{d\omega}{dx}.$$

For large plates, the value of A is small and can be neglected, which makes the solution much easier.

This is the approach used in Timokhin and Knyazeva (1996); Knyazeva and Sorokova 2006; Knyazeva and Dyukarev 1995) in constructing coupled models of solid-phase combustion, and in Knyazeva 2010a; Knyazeva 2010b) in studying the stability of the reaction front to mechanical perturbations. In (Knyazeva and Kryukova 2022), within the framework of the same approach, a coupled model of composite synthesis was presented under the condition of two total reactions, one of which corresponds to the formation of reinforcing particles and the other to the formation of the matrix. The process was controlled by laser radiation.

Example 4 If it is necessary in the synthesis model of the composite coating to take into account the properties of the substrate or surrounding layers, there are variants.

We will proceed from the three-dimensional equations of heat conduction and equations of motion:

$$c_\varepsilon \rho \frac{dT}{dt} = \lambda_T \left(\frac{\partial^2 T}{\partial x^2} + \frac{\partial^2 T}{\partial y^2} + \frac{\partial^2 T}{\partial z^2} \right) + W_{ch} + W_{ext} - 3K\alpha_T T \frac{d\varepsilon_{kk}}{dt}. \quad (12.27)$$

$$\begin{aligned} \frac{\partial \sigma_{xx}}{\partial x} + \frac{\partial \sigma_{xy}}{\partial y} + \frac{\partial \sigma_{xz}}{\partial z} &= \rho \frac{dV_x}{dt}; \\ \frac{\partial \sigma_{yx}}{\partial x} + \frac{\partial \sigma_{yy}}{\partial y} + \frac{\partial \sigma_{yz}}{\partial z} &= \rho \frac{dV_y}{dt}; \\ \frac{\partial \sigma_{zx}}{\partial x} + \frac{\partial \sigma_{zy}}{\partial y} + \frac{\partial \sigma_{zz}}{\partial z} &= \rho \frac{dV_z}{dt}. \end{aligned} \quad (12.28)$$

Here V_x , V_y , V_z are velocity vector components:

$$\frac{d\varepsilon_{xx}}{dt} = \frac{\partial V_x}{\partial x}; \quad \frac{d\varepsilon_{yy}}{dt} = \frac{\partial V_y}{\partial y}; \quad \frac{d\varepsilon_{xy}}{dt} = \frac{1}{2} \left(\frac{\partial V_x}{\partial y} + \frac{\partial V_y}{\partial x} \right), \text{ etc.}$$

In the general case, the continuity equation is also required.

The effective properties of the layers are considered to be unchanged.

These equations are valid for media with any rheological properties. In the case of viscous media, another term related to energy dissipation will appear in the heat transfer equation.

Let us integrate Eqs. (12.1), (12.27), and (12.28) over the thickness of the substrate (S) and the layer in which the reactions take place (R). We assume that heat losses by different mechanisms are possible on the outer surface, and the lower surface is thermally insulated. We consider the properties of the layers to be unchanged. There is no external mechanical load. As a result, we obtain

$$\begin{aligned} [(c_\varepsilon \rho)_S h_S + (c_\varepsilon \rho)_R h_R] \frac{dT}{dt} &= [\lambda_{T,S} h_S + \lambda_{T,R} h_R] \left(\frac{\partial^2 T}{\partial x^2} + \frac{\partial^2 T}{\partial y^2} \right) \\ + h_R W_{ch} + \int_0^{h_S+h_R} W_{ext} dz - 3[K_S \alpha_T h_S + K_R \alpha_T h_R] T \frac{d\varepsilon_{kk}}{dt}; \end{aligned} \quad (12.29)$$

$$(h_S + h_R) \left(\frac{\partial \sigma_{xx}}{\partial x} + \frac{\partial \sigma_{xy}}{\partial y} \right) = (\rho_S h_S + \rho_R h_R) \frac{dV_x}{dt}; \quad (12.30)$$

$$(h_S + h_R) \left(\frac{\partial \sigma_{yx}}{\partial x} + \frac{\partial \sigma_{yy}}{\partial y} \right) = (\rho_S h_S + \rho_R h_R) \frac{dV_y}{dt};$$

$$\sigma_{ij} = 2(\mu_S h_S + \mu_R h_R) \varepsilon_{ij} + [(\lambda_S h_S + \lambda_R h_R) \varepsilon_{kk} - (K_S h_S \langle \omega_S \rangle + K_R h_R \langle \omega_R \rangle)]. \quad (12.31)$$

Since the layers are thin in total, we have a planar stress state. Then for the average stresses and strains over the thickness of the layers, the relations similar to the previous version will be fulfilled. We have

$$\begin{aligned}
(c_\varepsilon \rho)_{eff} \frac{dT}{dt} &= \lambda_{T,eff} \left(\frac{\partial^2 T}{\partial x^2} + \frac{\partial^2 T}{\partial y^2} \right) + \frac{h_R}{h_S + h_R} W_{ch} + \frac{W_{ext,eff}}{h_S + h_R} \\
&\quad - 3(K\alpha_T)_{eff} T \frac{d\varepsilon_{kk}}{dt} \\
\frac{\partial \sigma_{xx}}{\partial x} + \frac{\partial \sigma_{xy}}{\partial y} &= \rho_{eff} \frac{dV_x}{dt}; \\
\frac{\partial \sigma_{yx}}{\partial x} + \frac{\partial \sigma_{yy}}{\partial y} &= \rho_{eff} \frac{dV_y}{dt}
\end{aligned}$$

and

$$\begin{aligned}
\sigma_{xx} &= 2\mu_{eff} \varepsilon_{xx} + [\lambda_{eff} \varepsilon_{kk} - \langle K\omega \rangle], \\
\sigma_{yy} &= 2\mu_{eff} \varepsilon_{yy} + [\lambda_{eff} \varepsilon_{kk} - \langle K\omega \rangle], \\
0 &= 2\mu_{eff} \varepsilon_{zz} + [\lambda_{eff} \varepsilon_{kk} - \langle K\omega \rangle], \\
\sigma_{xy} &= 2\mu_{eff} \varepsilon_{xy},
\end{aligned}$$

where

$$\begin{aligned}
\rho_{eff} &= \frac{\rho_S h_S + \rho_R h_R}{h_S + h_R}, \quad (c_\varepsilon \rho)_{eff} = \frac{(c_\varepsilon \rho)_S h_S + (c_\varepsilon \rho)_R h_R}{h_S + h_R}; \\
\lambda_{T,eff} &= \frac{\lambda_{T,S} h_S + \lambda_{T,R} h_R}{h_S + h_R}; \quad (K\alpha_T)_{eff} = \frac{K_S \alpha_{T,S} h_S + K_R \alpha_{T,R} h_R}{h_S + h_R}; \\
\langle K\omega \rangle &= \frac{(K_S h_S \omega_S + K_R h_R \omega_R)}{h_S + h_R}, \\
\omega_S &= 3\alpha_{T,S}(T - T_0); \quad \omega_R = 3\alpha_{T,R}(T - T_0) + \omega_{ch}.
\end{aligned}$$

The second summand in last expression depends on the type and method of solving the kinetic problem.

Then the procedure is similar to the previous one. We write the equations of motion through deformations. We neglect the forces of inertia and assume that the laser or electron beam is deployed in a line. In this case, all quantities do not depend on the y -coordinate. As a result, we arrive at the equilibrium equations:

$$\begin{aligned}
\frac{2\mu_{eff}}{\lambda_{eff} + 2\mu_{eff}} \frac{\partial^2}{\partial x^2} [2(\lambda_{eff} + \mu_{eff}) \varepsilon_{xx} - \langle K\omega \rangle] &= 0; \\
\mu_{eff} \frac{\partial^2 \varepsilon_{yy}}{\partial x^2} &= 0,
\end{aligned}$$

from which it follows that

$$\varepsilon_{xx} = \frac{\langle K\omega \rangle}{2(\lambda_{eff} + \mu_{eff})} + Ax + B$$

and

$$\varepsilon_{yy} = Cx + D.$$

Then we find the remaining values.

$$\varepsilon_{zz} = -\frac{\lambda_{eff}}{(\lambda_{eff} + 2\mu_{eff})}(\varepsilon_{yy} + \varepsilon_{xx}) + \frac{\langle K\omega \rangle}{(\lambda_{eff} + 2\mu_{eff})};$$

$$\sigma_{xx} = 2\gamma_1(\lambda_{eff} + \mu_{eff})(Ax + B) + \gamma_1\lambda_{eff}(Cx + D);$$

$$\sigma_{yy} = 2\gamma_1(\lambda_{eff} + \mu_{eff})(Cx + D) + \gamma_1\lambda_{eff}(Ax + B) - \frac{\mu_{eff}}{\lambda_{eff} + \mu_{eff}}\langle K\omega \rangle,$$

where $\gamma_1 = \frac{2\mu_{eff}}{(\lambda_{eff} + 2\mu_{eff})}$.

The conditions for finding the integration constants are written in the form.

$$\int_0^L \sigma_{xx} dx = 0; \quad \int_0^L \sigma_{yy} dx = 0; \quad \int_0^L \sigma_{xx} x dx = 0; \quad \int_0^L \sigma_{yy} x dx = 0,$$

where L is the size of the plate in the direction of the Ox axis. We do not give the system of linear equations and its cumbersome solution. But let us note that since all sub-integral functions are finite, the integrals of the form

$$\frac{1}{L^2} \frac{(\lambda_{eff} + 2\mu_{eff})}{2(\lambda_{eff} + \mu_{eff})} \int_0^L \langle K\omega \rangle dx;$$

$$\frac{1}{L^3} \frac{(\lambda_{eff} + 2\mu_{eff})}{2(\lambda_{eff} + \mu_{eff})} \int_0^L \langle K\omega \rangle x dx$$

decrease rapidly with increasing plate length. In this simplest case, the system of equations with respect to integration constants will have only a trivial solution and

$$\varepsilon_{xx} = \frac{\langle K\omega \rangle}{2(\lambda_{eff} + \mu_{eff})};$$

$$\varepsilon_{yy} = 0;$$

$$\varepsilon_{zz} = -\frac{\lambda_{eff}}{(\lambda_{eff} + 2\mu_{eff})}\varepsilon_{xx} + \frac{\langle K\omega \rangle}{(\lambda_{eff} + 2\mu_{eff})};$$

$$\sigma_{xx} = 0;$$

$$\sigma_{yy} = -\gamma_1 \frac{(\lambda_{eff} + 2\mu_{eff})}{2(\lambda_{eff} + \mu_{eff})} \langle K\omega \rangle.$$

As a result, the one-dimensional heat conduction equation associated with deformations takes the form

$$(c_\varepsilon \rho)_{eff} \frac{dT}{dt} = \lambda_{T,eff} \frac{\partial^2 T}{\partial x^2} + \frac{h_R}{h_S + h_R} W_{ch} + \frac{W_{ext,eff}}{h_S + h_R} - \frac{3(K\alpha_T)_{eff} T}{2(\lambda_{eff} + \mu_{eff})} \frac{d\langle K\omega \rangle}{dt}. \quad (12.32)$$

It was shown in Sorokova and Knyazeva (2010) that the coupling of processes of different nature can serve as a source of additional instabilities in the propagation of the reaction front.

The equilibrium problem can also be solved in stresses, as in Knyazeva and Kryukova (2022).

Example 5 Problems 3 and 4 did not take into account plate bending, which can occur in the case of inhomogeneous heating, a moving local heat source, and a propagating reaction front, where the composition and temperature change. In order to take into account in the models of synthesis of layered composites and coatings the change in shape of individual layers and the product as a whole, plate theory can be used. There are quite a few thermomechanical models of plates and shells in the literature. However, in pure form, their applicability to our problems is not obvious. Attempts to apply them to non-uniform temperature conditions encountered in the literature raise many questions.

The impossibility of constructing a unified theory of plates and shells equally well applicable to all materials and types of stress–strain states are mentioned, for example, in the two-part review (Galinshteyn 1970, 1967). Without aiming to give an overview of all the theories known to date, of which there is an enormous accumulation, here are some examples.

The classical Kirchhoff theory (which is described in detail in almost all textbooks and monographs) is based on the hypothesis of invariability of the normal to the midline surface. The median surface is treated as a neutral layer, which bends but does not experience linear and shear deformations. The displacements of points distant from the middle plane by distance z are represented in the form.

$$\begin{aligned} u_z(x, y, z) &= z\phi_x, \\ v_z(x, y, z) &= z\phi_y, \\ w &= w_0(x, y). \end{aligned} \quad (12.33)$$

In Kirchhoff's theory, the angles of rotation ϕ_x and ϕ_y , the normal to the deformed plane with respect to the axis Z are defined as the derivatives of the transverse deflection w_0 :

$$\phi_x = -\frac{\partial w_0}{\partial x}, \quad \phi_y = -\frac{\partial w_0}{\partial y}, \quad \phi_z = -\frac{\partial w_0}{\partial y}. \quad (12.34)$$

If we take into account the displacements of the middle plane u_0, v_0 , instead of (33) we have (Birger 1992; Sokolnikoff and Sokolnikoff 1939):

$$\begin{aligned} u_z(x, y, z) &= u_0(x, y) + z\phi_x, \\ v_z(x, y, z) &= v_0(x, y) + z\phi_y, \\ w &= w_0(x, y). \end{aligned} \quad (12.35)$$

The theory of thin plates uses the flat stress approximation, according to which

$$\sigma_{zz} = 0; \quad \tau_{zx} = 0; \quad \tau_{zy} = 0.$$

Then, using elastic relations, joint deformation condition and equilibrium equations, the equations for the force function and for the deflection are derived. Variants of the theory of thermoelastic plates are considered in Sokolnikoff and Sokolnikoff (1939), and in the book (Birger 1992) in the defining relations, besides thermal, there are additional deformations, which are related by phase and structural transformations.

Note that in the literature there are variants of linear and nonlinear theories for small deflections and deformations

$$\begin{aligned} \varepsilon_x &= \frac{\partial u_0}{\partial x} - z \frac{\partial^2 w_0}{\partial x^2}; \\ \varepsilon_y &= \frac{\partial v_0}{\partial y} - z \frac{\partial^2 w_0}{\partial y^2}; \\ \gamma_{xy} &= \frac{\partial u_0}{\partial y} + \frac{\partial v_0}{\partial x} - 2z \frac{\partial^2 w_0}{\partial x \partial y} \end{aligned} \quad (12.36)$$

and for large deflections, when the deformation determinations at points at a distance z from the midplane are used (Donnel 1982; Timoshenko and Woinovsky-Krieger 1959) in the form

$$\begin{aligned}\varepsilon_x &= \frac{\partial u_0}{\partial x} + \frac{1}{2} \left(\frac{\partial w_0}{\partial x} \right)^2 - z \frac{\partial^2 w_0}{\partial x^2}; \\ \varepsilon_y &= \frac{\partial v_0}{\partial y} + \frac{1}{2} \left(\frac{\partial w_0}{\partial y} \right)^2 - z \frac{\partial^2 w_0}{\partial y^2}; \\ \gamma_{xy} &= \frac{\partial u_0}{\partial y} + \frac{\partial v_0}{\partial x} + \frac{\partial w_0}{\partial x} \frac{\partial w_0}{\partial y} - 2z \frac{\partial^2 w_0}{\partial x \partial y}.\end{aligned}$$

In Mindlin's theory (Mindlin 1951) (or in the so-called First Order Shear Deformation Plate Theory—FSDT), rotations ϕ_x and ϕ_y along with deflection w_0 are the main (primary) variables for which the solving equations are formulated. The FSDT theory is the basis, for example, of the model (Kanase et al. 2015), where each layer is characterized by its own structure. According to different authors, first-order theory requires the introduction of correction coefficients (Pai 1995). High-order theories (Galinsh 1970, 1967) proceed from the preliminary setting of some of the quantities (e.g., the displacement vector components) in the form of finite series containing approximating functions and parameters, the physical meaning of which is not always clear (Reddy 1984; Rohwer et al. 2001; Ferreira et al. 2011; Talha and Singh 2010; Kant and Shiyekar 2013; Tran et al. 2017; Naik and Sayyad 2019). Some of them are found in the course of problem-solving. If we are talking about multilayered plates or layered composites, the number of unknown parameters increases with the number of layers (except for some theories).

In (Joshani et al. 2017), for example, the thermomechanical behavior of layered composite plates is investigated. The model is based on the inverse hyperbolic shear deformation theory (Grover et al. 2013), in which

$$\begin{aligned}u_z(x, y, z) &= u_0(x, y) - z \frac{\partial w_0}{\partial x} + f(z)\theta_x, \\ v_z(x, y, z) &= v_0(x, y) - z \frac{\partial w_0}{\partial y} + f(z)\theta_y, \\ w &= w_0(x, y)\end{aligned}$$

$f(z) = \sinh^{-1}\left(\frac{rz}{n}\right) + \Omega z$, θ_x, θ_y are shear rotations; n is number of layers; Ω, r are some parameters. The temperature distribution is specified as a function containing linear and nonlinear terms in z .

Thermoelastic theories for multilayer composite plates (Karama et al. 2009; Sayyad et al. 2016) contain exponential functions along the z coordinate (perpendicular to the middle plane) in the definition of displacements in order to account for shear deformation. In the second of these, the temperature is assumed to be distributed linearly or nonlinearly along the thickness. However, the possible temperature distribution in the (x, y) plane is not analyzed. The trigonometric shear strain theory is used in Sandhya and Yuwaraj (2021). A review of some nonlinear and high-order theories is presented in Xu et al. (2010).

Three-dimensional thermoelastic analysis of simply supported rectangular plates with variable thicknesses subjected to thermomechanical loads was investigated in Xu et al. (2010). A variable thickness plate of functionally graded material also appears in Amiri et al. (2022). The thermal steady-state load is given in the form of a temperature difference between the upper and lower surfaces of the plate. It is assumed that the mechanical properties of the plate change linearly along the thickness depending on the volume content in the ceramic and metal layers, which appears in the model in the setting of the variable stiffness. Third-order theory is used. A three-dimensional problem for an orthotropic functionally graded rectangular plate assuming an arbitrary distribution of properties along the plate thickness is studied in Liu and Zhong (2011). A number of nonlocal theories are known (Aghababaei and Reddy 2009; Lu et al. 2007, 2019), etc.

Thus, in all publications, the stationary temperature distribution is specified, either found from the solution of the stationary problem or specified as an approximation of some three-dimensional distribution. However, in modern technologies for synthesizing coatings or surface treatment of materials, the temperature distribution is heterogeneous and depends on the type of heat source, its velocity, and trajectory along the treated surface. On the one hand, one can simply move to solving three-dimensional problems, which entails new problems. On the other hand, for both qualitative and quantitative analysis, it is useful to use simplifications based on physical considerations that will allow the use of well-developed analytical and numerical methods (Birger 1992; Donnel 1982; Mindlin 1951; Wang et al. 2000; Lukasevich 1982; Vinson 1989), etc.

As in problems 3, 4, we will be interested in changes in temperature and composition in a thin coating located on a thin substrate, which allowed us to introduce an average over the total thickness of the object of temperature and effective properties. Since the characteristic times for thermal and mechanical processes differ by orders of magnitude, in the mechanical equilibrium problem time is considered to be a parameter: the thermokinetic part of the problem remains non-stationary and the mechanical part is considered in the quasi-static formulation (however, there are no fundamental problems for setting a completely non-stationary problem).

In the present work, we restrict ourselves to the Kirchhoff approximation.

Then

$$\varepsilon_{xx} = -z \frac{\partial^2 w_0}{\partial x^2}, \quad \varepsilon_{yy} = -z \frac{\partial^2 w_0}{\partial y^2},$$

$$\gamma_{xy} = 2\varepsilon_{xy} = -2z \frac{\partial^2 w_0}{\partial x \partial y}.$$

We assume that the effective mechanical properties of the materials may depend on the temperature (and the properties of the upper layer change with the change in the composition), and that the relationship between the effective Lamé coefficients and the effective technical characteristics remains the same. Then the averaged Duhamel-Neiman relations presented above for the flat stress state will take the form (we omit

the index “*eff*” for simplicity):

$$\begin{aligned}\sigma_{xx} &= \frac{E}{1-\nu^2} [\varepsilon_{xx} + \nu\varepsilon_{yy}] - \frac{1-2\nu}{1-\nu} \langle K\omega \rangle, \\ \sigma_{yy} &= \frac{E}{1-\nu^2} [\varepsilon_{yy} + \nu\varepsilon_{xx}] - \frac{1-2\nu}{1-\nu} \langle K\omega \rangle, \\ \sigma_{xy} &= \frac{E}{2(1+\nu)} \gamma_{xy}, \\ \varepsilon_{zz} &= \frac{1+\nu}{1-\nu} \frac{1-2\nu}{E} \langle K\omega \rangle - \frac{\nu}{1-\nu} (\varepsilon_{xx} + \varepsilon_{yy}).\end{aligned}$$

Or for a point at distance z from the midline, we find

$$\begin{aligned}\sigma_{xx} &= -\frac{E}{1-\nu^2} z \left[\frac{\partial^2 w_0}{\partial x^2} + \nu \frac{\partial^2 w_0}{\partial y^2} \right] - \frac{1-2\nu}{1-\nu} \langle K\omega \rangle_z, \\ \sigma_{yy} &= -\frac{E}{1-\nu^2} z \left[\frac{\partial^2 w_0}{\partial y^2} + \nu \frac{\partial^2 w_0}{\partial x^2} \right] - \frac{1-2\nu}{1-\nu} \langle K\omega \rangle_z, \\ \sigma_{xy} &= -\frac{E}{(1+\nu)} z \frac{\partial^2 w_0}{\partial x \partial y}, \\ \varepsilon_{zz} &= \frac{1+\nu}{1-\nu} \frac{1-2\nu}{E} \langle K\omega \rangle_z + \frac{\nu}{1-\nu} z \left(\frac{\partial^2 w_0}{\partial x^2} + \frac{\partial^2 w_0}{\partial y^2} \right).\end{aligned}\tag{12.37}$$

We find the first invariant of the strain tensor

$$\varepsilon_{kk} = \frac{1+\nu}{1-\nu} \frac{1-2\nu}{E} \langle K\omega \rangle_z - \frac{1-2\nu}{1-\nu} z \left(\frac{\partial^2 w_0}{\partial x^2} + \frac{\partial^2 w_0}{\partial y^2} \right)$$

and then determine its thickness average

$$\begin{aligned}\langle \varepsilon_{kk} \rangle &= \frac{1}{h} \int_0^h \varepsilon_{kk} dz = \frac{1+\nu}{1-\nu} \frac{1-2\nu}{E} \int_0^h \langle K\omega \rangle_z dz \\ &\quad - \frac{1-2\nu}{1-\nu} \frac{h_S + h_R}{2} \left(\frac{\partial^2 w_0}{\partial x^2} + \frac{\partial^2 w_0}{\partial y^2} \right).\end{aligned}\tag{12.38}$$

In the heat conduction problem, it is logical to assume

$$\langle K\omega \rangle_z = \langle K\omega \rangle.$$

As a result, the thermal conductivity equation coupled with deflections takes the form

$$\begin{aligned}
(c_{\varepsilon\rho})_{eff} \frac{\partial T}{\partial t} &= \lambda_{T,eff} \left(\frac{\partial^2 T}{\partial x^2} + \frac{\partial^2 T}{\partial y^2} \right) + \frac{h_R}{h_S + h_R} W_{ch} + \frac{W_{ext,eff}}{h_S + h_R} - \\
&- 3(K\alpha_T)_{eff} T \frac{\partial}{\partial t} \left[\frac{1+\nu}{1-\nu} \frac{1-2\nu}{E} \langle K\omega \rangle - \frac{1-2\nu}{1-\nu} \frac{h_S + h_R}{2} \left(\frac{\partial^2 w_0}{\partial x^2} + \frac{\partial^2 w_0}{\partial y^2} \right) \right].
\end{aligned} \tag{12.39}$$

There is a peculiarity in the plate deflection problem.

The equilibrium equation for the Kirchhoff plate following from the principle of virtual displacements (Wang et al. 2000; Lukasevich 1982) has the form

$$\frac{\partial^2 M_{xx}}{\partial x^2} + 2 \frac{\partial^2 M_{xy}}{\partial x \partial y} + \frac{\partial^2 M_{yy}}{\partial y^2} + q = 0, \tag{12.40}$$

where the moments are defined as follows

$$M_{xx} = \int_{-h/2}^{h/2} \sigma_{xx} z dz; \quad M_{yy} = \int_{-h/2}^{h/2} \sigma_{yy} z dz; \quad M_{xy} = \int_{-h/2}^{h/2} \sigma_{xy} z dz.$$

Substitute σ_{xx} from (37) into $M_{xx} M_{xx}$

$$\begin{aligned}
M_{xx} &= \int_{-h/2}^{h/2} \left[-\frac{E}{1-\nu^2} z \left(\frac{\partial^2 w_0}{\partial x^2} + \nu \frac{\partial^2 w_0}{\partial y^2} \right) - \frac{1-2\nu}{1-\nu} \langle K\omega \rangle_z \right] z dz \\
&= -\frac{E}{1-\nu^2} \left(\frac{\partial^2 w_0}{\partial x^2} + \nu \frac{\partial^2 w_0}{\partial y^2} \right) \int_{-h/2}^{h/2} z^2 dz - \frac{1-2\nu}{1-\nu} \int_{-h/2}^{h/2} \langle K\omega \rangle_z z dz.
\end{aligned} \tag{12.41}$$

If, as in the thermal problem, we take $\langle K\omega \rangle_z = \langle K\omega \rangle$, then the second integral in (41) will be equal to zero, i.e., the dependence of temperature on the coordinate z in the plate theory is fundamental. This should be “taken into account” in $\langle K\omega \rangle_z$. In static conditions for thin plates, between the surface temperatures of which there is a difference, the distribution can always be approximated by a straight line segment, which is used in many theories (Birger 1992; Lukasevich 1982). Since in the thermal part of the problem the mean section temperature and the mean composition are determined, and the last really changes only in the upper layer (the effect of changes in composition on temperature is taken into account in the thermal conductivity equation by weighting factors; the corresponding deformations are included also with weighting factors), then for the considered simplest approximation it will not be a big mistake to take in (40)

$$\langle K\omega \rangle_z \approx \langle K\omega \rangle_0 + \frac{z}{h} \langle K\omega \rangle \approx \langle K\omega \rangle_0 + \frac{z}{h} \frac{(K_S h_S \omega_S + K_R h_R \omega_R)}{h_S + h_R} \tag{12.42}$$

where the form of the first term (depending only on x, y) does not matter for this approximation.

Because

$$\frac{(K_S h_S \omega_S + K_R h_R \omega_R)}{h_S + h_R} = (K_T \alpha_T)_{eff} (T - T_0) + \frac{K_R h_R}{h_S + h_R} \omega_{ch},$$

so from (41) we find

$$M_{xx} = -D \left(\frac{\partial^2 w_0}{\partial x^2} + \nu \frac{\partial^2 w_0}{\partial y^2} \right) - \frac{1 - 2\nu}{1 - \nu} \frac{h^3}{12} \left[(K_T \alpha_T)_{eff} (T - T_0) + \frac{K_R h_R}{h_S + h_R} \omega_{ch} \right].$$

Similarly

$$M_{yy} = -D \left(\frac{\partial^2 w_0}{\partial y^2} + \nu \frac{\partial^2 w_0}{\partial x^2} \right) - \frac{1 - 2\nu}{1 - \nu} \frac{h^3}{12} \left[(K_T \alpha_T)_{eff} (T - T_0) + \frac{K_R h_R}{h_S + h_R} \omega_{ch} \right].$$

The remaining value does not change externally.

$$M_{xy} = -(1 - \nu) D \frac{\partial^2 w_0}{\partial x \partial y}.$$

Here

$$D = \frac{E}{1 - \nu^2} \frac{h^3}{12} \equiv \frac{E_{eff}}{1 - \nu_{eff}^2} \frac{h^3}{12}$$

is cylindrical rigidity;

$$h = h_S + h_R.$$

Substitute these expressions into (40) and come to the equation for deflection:

$$\begin{aligned} & \frac{\partial^2}{\partial x^2} \left[D \left(\frac{\partial^2 w_0}{\partial x^2} + \nu \frac{\partial^2 w_0}{\partial y^2} \right) \right] + \frac{\partial^2}{\partial y^2} \left[D \left(\frac{\partial^2 w_0}{\partial y^2} + \nu \frac{\partial^2 w_0}{\partial x^2} \right) \right] \\ & + 2 \frac{\partial^2}{\partial x \partial y} \left((1 - \nu) D \frac{\partial^2 w_0}{\partial x \partial y} \right) = \end{aligned} \quad (12.43)$$

$$= q - \frac{\partial^2}{\partial x^2} [A(T - T_0) + B\omega_{ch}] - \frac{\partial^2}{\partial y^2} [A(T - T_0) + B\omega_{ch}],$$

where

$$A = \frac{1 - 2\nu}{1 - \nu} \frac{h^3}{12} (K_T \alpha_T)_{eff}; \quad B = \frac{1 - 2\nu}{1 - \nu} \frac{h^3}{12} \frac{K_R h_R}{h_S + h_R}.$$

The obtained coupled nonlinear Eqs. (12.39) and (12.43) together with the system of equations of chemical kinetics require numerical methods. However, it is probable

that under some assumptions (for example, such as in problems 3 and 4) analytical estimates will be possible.

12.3 Conclusion

Thus, the simple mechanical equilibrium problems presented in the article allow the construction of related models of some technological processes. In particular, the model of composite synthesis on a substrate takes into account not only the properties of layers and peculiarities of process control in laser technology, but also possible ways of influence of accompanying stresses on the dynamics of the process. Models for the synthesis of new materials using different variants of mechanical equilibrium problems are not presented in this paper, but references to existing publications give an idea of the possibilities of the physical approach. Generalization of the model on the basis of plate theory allows modification of the equations taking into account deflections. Consistent application of the theory leads to more complex expressions than those used in the formal approach (Manthena and Kedar 2019; Deshmukh et al. 2014). More rigorous generalizations are possible, taking into account the nature of the contact between the layers, changes in thermophysical properties with temperature and composition, and changes in the size of the reaction layer based on different popular theories (Maji and Mahato 2022; Altenbach et al. 2020). If melting in local areas needs to be taken into account, viscoelastic medium models will be required. Such models have applications to the creation of three-dimensional objects in modern 3D technologies; synthesis of multilayer and gradient coatings; synthesis of layered composites, etc. More complex situations arise in technologies where the process is controlled both by external heating together with the application of a moving or stationary mechanical load. When studying the stress–strain state and stability of the processes of creating thin-walled structures in 3D technologies, it may be necessary to involve non-classical shell models (Zubov and Eremeev 2003; Altenbach and Eremeev 2009; Sarkisyan 2011; Annin and Volchkov 2016). However, the construction of related models on their basis is a nontrivial task.

Acknowledgements This work was performed according to Government Research Assignment Project FWRW-2022-0003 at the Institute of Strength Physics and Materials Science of Siberian Branch Russian Academy of Sciences.

References

- Aghababaei R, Reddy JN (2009) Nonlocal third-order shear deformation plate theory with application to bending and vibration of plates. *J Sound Vib* 326:277–289. <https://doi.org/10.1016/j.jsv.2009.04.044>

- Alfutov NA, Zinovev PA, Popov BG (1984) Calculation of multilayer plates and shells made of composite materials [Raschet mnogosloinnykh plastin i obolochek iz kompozitsionnykh materialov]. Mashinostroyeniye, Moscow [in Russian]
- Altenbach H, Eremeev VA (2009) On the equations of Cosserat-type shells [Ob uravneniyakh obolochek tipa Kosserra]. *Comput Mech Contin Media* [Vychislitel'naya Mech Sploshnykh sred] [In Russian] 2(4):11–18
- Altenbach H, Chinchaladze N, Kienzler R, Müller WH Eds. (2020) Analysis of shells, plates, and beams. A State of the art report. Springer, (2020). <https://doi.org/10.1007/978-3-030-47491-1b>
- Amiri M, Loghman A, Arefi M (2022) Thermoelastic analysis of rectangular plates with variable thickness made of FGM based on TSDT using DQ method. *Geomech. Eng.* 29(6):667–681
- Annin BD, Volchkov YuM (2016) Nonclassical models of the theory of plates and shells. *J Appl Mech Tech Phys* 57(5):769–776. <https://doi.org/10.1134/S0021894416050011>
- Birger IA (1992) Rods, plates and shells [Sterjni_ plastinki i obolochki]. Nauka, Moscow [in Russian]
- Boley BA, Weiner JH (1960) Wiley and Sons. J: Theory Therm Stress. Inc., New York, London
- Chashchina AA, Knyazeva AG (2005) Regimes of connecting materials with the help of Synthesis in solid phase. *Chem Sustain Dev* 13:339–346 (2005). https://sibran.ru/upload/iblock/b3b/regimes_of_connecting_materials_with_the_help_of_synthesis_in_the_solid_phase.pdf
- Chashchina AA, Knyazeva AG (2006) Stresses in the reaction zone at the materials conjugation using solid-phase synthesis (in Russian). *Izvestiya TPU* 309(5):107–113
- De Pascalis R (2022) Diffusion-induced stress in a functionally graded incompressible elastic sphere. *Int J Non-Linear Mech* 138:103850. <https://doi.org/10.1016/j.ijnonlinmec.2021.103850>
- Deshmukh KC, Khandait MV, Kumar R (2014) Thermal stresses in a simply supported plate with thermal bending moments with heat sources. *Mater Phys Mech* 21:135–146 (2014). https://www.ipme.ru/e-journals/MPM/no_22114/MPM221_05_deshmukh.pdf
- Donnel LG (1982) Beams, plates and shells [Balki_ plastini i obolochki] [in Russian]. Nauka, Moscow
- Ferreira AJM, Roque CMC, Neves AMA, Jorge RMN, Coares CMM, Reddy JN (2011) Buckling analysis of isotropic and laminated plates by radial basis functions according to a higher-order shear deformation theory. *Thin-Walled Struct* 49:804–811
- Galinsh AK (1967) Calculation of plates and shells using refined theories [Raschet plastin i obolochek po utochnennim teoriyam]. *Issled. Po Teor. Plast. I Oboloc.* [In Russian] 5:66–92 (1967). <https://www.mathnet.ru/links/c4ec911e60bc7ca68fc034f2c00d0eec/kutpo535.pdf>
- Galinsh AK (1970) Calculation of plates and shells using refined theories [Raschet plastin i obolochek po utochnennim teoriyam]. *Issledovaniya po teorii plastin i obolochek* [in Russian] 6–7, 23–64. <https://www.mathnet.ru/links/9c4265dec8b1fc815147cea154286cf/kutpo470.pdf>
- Grover N, Maiti DK, Singh BN (2013) A new inverse hyperbolic shear deformation theory for static and buckling analysis of laminated composite and sandwich plates. *Compos Struct* 95:667–675
- Hu H, Yu P, Suo Y (2020) Stress induced by diffusion and local chemical reaction in spherical composition-gradient electrodes. *Acta Mech* 231:2669–2678. <https://doi.org/10.1007/s00707-020-02652-4>
- Joshan YS, Grover N, Singh BN (2017) Analytical modelling for thermo-mechanical analysis of cross-ply and angle-ply laminated composite plates. *Aerosp Sci Technol* 70:137–151. <https://doi.org/10.1016/j.ast.2017.07.041>
- Kanase AK, Shiyekar SM, Shiyekar MR (2015) Thermal stress analysis of three layered symmetric laminated composite plate. *Int. J. Curr. Eng. Technol.* 5(6):3685–3691
- Kant T, Shiyekar SM (2013) An assessment of a higher order theory for composite laminates subjected to thermal gradient. *Compos Struct* 96, 698–707 (2013)
- Karama M, Afaq KS, Mistou S (2009) A new theory for laminated composite plates. *Proceedings of the Institution of Mechanical Engineers, Part L. J Mater: Des Appl* 223(2):53–62. <https://doi.org/10.1243/14644207JMDA189>
- Knyazeva AG (1993) Hot-spot thermal explosion in deformed solids. *Combust, Explos Shock Waves* 29:419–428. <https://doi.org/10.1007/BF00782966>

- Knyazeva AG (2003) Cross effects in solid media with diffusion. *J Appl Mech Tech Phys* 44(3):373–384. <https://doi.org/10.1023/A:1023485224031>
- Knyazeva AG (2005) Diffusion and rheology in local equilibrium thermodynamics (In Russian). *Math Model Syst Process* 13:45–60
- Knyazeva AG, Dyukarev EA (1995) Stationary wave of a chemical reaction in a deformable medium with finite relaxation time of the heat flux. *Combust Explos Shock Waves* 31:304–312. <https://doi.org/10.1007/BF00742675>
- Knyazeva AG, Kryukova ON (2022) A coupled model of controlled synthesis, of a composite on a substrate. *Lobachevskii J. Math.* 43(7):1878–1893. <https://doi.org/10.1134/S1995080222100183>
- Knyazeva AG, Sorokova SN (2006) Steady regimes of conversion in a viscoelastic medium. *Combust Explos Shock Waves* 42:549–558. <https://doi.org/10.1007/s10573-006-0087-6>
- Knyazeva AG, Romanova VA, Pobol IL (2001) Non-homogeneous stress field in the diffusion zone the diffusion zone of an electron-beam soldered joint (In Russian). *Phys Mesomech* 4(5):41–53
- Knyazeva AG, Pobol IL, Oleshchuck IG (2013) Redistribution of alloying elements between joined materials under isothermal brazing conditions and accompanying mechanical stresses (In Russian). *Izvestiya VUZov, Fizika* 56(7/2):14–24
- Knyazeva AG (2010a) Solid-phase combustion in a plane stress state. 1. Stationary combustion wave. *J Appl Mech Tech Phys* 51:164–173. <https://doi.org/10.1007/s10808-010-0025-y>
- Knyazeva AG (2010b) Solid-phase combustion in a plane stress state. 2. Stability to small perturbations. *J Appl Mech Tech Phys* 51, 317–323. <https://doi.org/10.1007/s10808-010-0043-9>
- Knyazeva AG, Mikolaichuk MA (2011) Saturation of the plate with impurities from the environment under mechanical loading (In Russian). *Izv RAN, MTT (Mechanics)* 5:43–57 (2011)
- Koyanagi T, Katoh Y, Nozawa T, Snead LL, Kondo S, Henager CH Jr, Ferraris M, Hinoki T, Huang Q (2018) Recent progress in the development of SiC composites for nuclear fusion applications. *J Nucl Mater* 511:544–555. <https://doi.org/10.1016/j.jnucmat.2018.06.017>
- Lee S, Wang WL, Chen JR (2000) Diffusion-induced stresses in a hollow cylinder. *Mater Sci Eng, A* 285:186–194
- Liu W, Zhong Z (2011) Three-dimensional thermoelastic analysis of functionally graded plate. *Acta Mech Solida Sin* 24(3):241–249. [https://doi.org/10.1016/S0894-9166\(11\)60025-6](https://doi.org/10.1016/S0894-9166(11)60025-6)
- Lu P, Zhang PQ, Lee HP, Wang CM, Reddy JN (2007) Non-local elastic plate theories. *Proc R Soc A* 463:3225–3240. <https://doi.org/10.1098/rspa.2007.1903>
- Lu L, Guo X, Zhao J (2019) A unified size-dependent plate model based on nonlocal strain gradient theory including surface effects. *Appl Math Model* 68, 583–602 (2019). <https://doi.org/10.1016/j.apm.2018.11.023>
- Lukasevich S (1982) Local loads in plates and shells [Lokálne nagruzki v plastinkah i obolochkah]. Mir, Moscow [in Russian]
- Maji A, Mahato PK (2022) Development and applications of shear deformation theories for laminated composite plates: An overview. *J Thermoplast Compos Mater* 35(12):2576–2619. <https://doi.org/10.1177/0892705720930765>
- Manthena VR, Kedar GD (2019) On thermoelastic problem of a thermosensitive functionally graded rectangular plate with instantaneous point heat source. *J Therm Stresses*. <https://doi.org/10.1080/01495739.2019.158732>
- Mikolaichuk MA, Knyazeva AG Model of impurity diffusion in a structurally inhomogeneous deformable medium (in Russian). *Izvestiya VUZov, Fizika* 55(5/2):74–79
- Mikolaichuk MA, Knyazeva AG (2010) Effect of stresses and strains on impurity redistribution in a plate under uniaxial loading. *J Appl Mech Tech Phys* 51:422–430. <https://doi.org/10.1007/s10808-010-0057-3>
- Mikolaychuk MA, Knyazeva AG, Grabovetskaya GP, Mishin IP (2012) Study of the influence of mechanical stresses on diffusion in a coated plate (In Russian). *Vestnik PNIPU, Mechanika, PermGTU* 3:131–135
- Mindlin RD (1951) Influence of rotatory inertia and shear deformation on flexural motions of isotropic elastic plates. *ASME J Appl Mech* 18:31–38

- Naik NS, Sayyad AS (2019) An accurate computational model for thermal analysis of laminated composite and sandwich plates. *J Therm Stresses* 42(5):559–579. <https://doi.org/10.1080/01495739.2018.1522986>
- Pai PF (1995) A new look at shear correction factors and warping functions of anisotropic laminates. *Int J Solids Struct* 32(16):2295–2313
- Reddy JN (1984) A simple higher order shear deformation theory for laminated composite plates. *J Appl Mech* 51:752–754
- Rohwer K, Rolfes R, Sparr H (2001) Higher-order theories for thermal stresses in layered plates. *Int J Solids Struct* 38:3673–3687(2001)
- Sandhya KS, Yuwaraj M (2021). Ghugal Thermoelastic bending analysis of laminated plates subjected to linear and nonlinear thermal loads. *Adv Aircr Spacecr Sci* 8(3):213–237 (2021). <https://doi.org/10.12989/aas.2021.8.3.213>
- Sarkisyan SO (2011) General theory of micropolar elastic thin shells [Obshchaya teoriya mikropolyarnykh uprugikh tonlikh obolochek]. *Phys Mesomech [In Russian]* 14(1):55–66
- Sayyad AS, Ghugal YuM, Shinde BM (2016) Thermal stress analysis of laminated composite plates using exponential shear deformation theory. *Int J Automot Compos* 2(1):23–40. <https://doi.org/10.1504/IJAUTO.2016.078100>
- Shehryar A, Sanan A, Muhammad S, Abrar HB (2021) A comparative study on the effect of carbon-based and ceramic additives on the properties of fiber reinforced polymer matrix composites for high temperature applications. *Ceram Int* 47:33956–33971. <https://doi.org/10.1016/j.ceramint.2021.08.356>
- Sokolnikoff IS, Sokolnikoff ES (1939) Thermal stresses in elastic plates. *Trans Am Math Soc* 45:235–255
- Sorokova SN, Knyazeva AG (2010) Numerical study of the influence of the technological parameters on the composition and stressed-deformed state of a coating synthesized under electron-beam heating. *Theor Found Chem Eng* 44:172–185. <https://doi.org/10.1134/S0040579510020089>
- Sun J, Ye D, Zou J, Chen X, Wang Y, Yuan J, Liang H, Qu H, Binner J, Bai J (2023) A review on additive manufacturing of ceramic matrix composites. *J Mater Sci Technol* 138:1–16. <https://doi.org/10.1016/j.jmst.2022.06.039>
- Talha M, Singh BN (2010) Static response and free vibration analysis of FGM plates using higher order shear deformation theory. *Appl Math Model* 34(12):3991–4011
- Timokhin AM, Knyazeva AG (1996) Regimes of reaction front propagation in a coupled thermomechanical model of solid-phase combustion (In Russian). *Khimicheskaya Fizika* 15(10):85–100
- Timoshenko S, Woinovsky-Krieger S (1959) *Theory of plates and shells*. McGRAW-Hill Book Company, INC, New Yurk-Toronto-London
- Tran LV, Abdel Wahab M, Kim S-E (2017) An isogeometric finite element approach for thermal bending and buckling analyses of laminated composite plates. *Compos Struct* 179:35–49. <https://doi.org/10.1016/j.compstruct.2017.07.056>
- Vinson JR (1989) The behavior of thin walled structures: beams, plates, and shells (Mechanics of surface structures, 8). In: Nash WA, Oravas GE (eds.). Kluwer Academic Publishers, Dordrecht, Boston, London
- Wang CM, Reddy JN, Lee KH (2000) *Shear deformable beams and plates: Relationships with Classical Solutions*. Elsevier, Amsterdam, Lausanne, New York, Oxford, Shannon, Singapore, Tokyo
- Wang WL, Lee S, Chen JR (2002) Effect of chemical stress on diffusion in a hollow cylinder. *J. Appl. Phys.* 91(12), (2002). <https://doi.org/10.1063/1.1477624>
- Xu Y, Ding Z, Kefu L (2010) Three-dimensional thermoelastic analysis of rectangular plates with variable thickness subjected to thermo-mechanical loads. *J Therm Stresses* 33:1136–1155
- Yang F (2005) Interaction between diffusion and chemical stresses. *Mater Sci Eng, A* 409:153–159. <https://doi.org/10.1016/j.msea.2005.05.117>

- You X, Zhang Q, Yang J, Dong S (2023) Review on 3D-printed graphene-reinforced composites for structural applications. *Composites: Part A* 167:107420. <https://doi.org/10.1016/j.compositesa.2022.107420>
- Zheng H, Zhang W, Li B, Zhu J, Wang C, Song G, Wu G, Yang X, Huang Y, Ma L (2022) Recent advances of interphases in carbon fiber-reinforced polymer composites: A review. *Compos B* 233:109639. <https://doi.org/10.1016/j.compositesb.2022.109639>
- Zubov LM, Eremeev VA (2003) Mechanics of elastic micropolar shells [Mekhanika uprugikh mikropolyarnykh obolochek]. *Dalnevostochnyi Mat Zhurnal [In Russian]* 4(2):182–225

Chapter 13

Inflation of Hyperelastic Curved Tubes



Alexey M. Kolesnikov

Abstract This paper deals with the problem of inflation of curved thin-walled hyperelastic tubes. Nonlinear elastic membrane theory and the Fung model of material are used. Tubes with elliptic cross-sections are considered. The influence of internal pressure on tube curvature and the shape of its cross-section is investigated.

Keywords Membrane · Nonlinear · Elastic · Curved tube · Pipe · Inflation · Torus

13.1 Introduction

Thin-walled straight and curved tubes are a structural element of many technical systems and living objects, such as vessel walls, pipelines, pneumatic structures, soft robots and devices. They are often loaded by internal pressure. A straight tube of constant thickness under internal pressure remains a straight tube with deformed cross-section and length. Inflation leads to change a cross-section and curvature of tube. This effect is widely used in Bourdon pressure tubes (Feodos'ev 1949).

At present, two directions of research can be distinguished in the inflation problem of a curved tube. In the first case, nonlinearity of the displacement problem is taken into account, but the linear strain theory is used Feodos'ev (1949), Levyakov (1997). In the second case, nonlinearity of displacements and strains is considered. In the framework of membrane theory, such a problem is presented in Kolesnikov (2011a), Kolesnikov (2015). This approach is valid for thin-walled tubes of hyperelastic material at large strains.

A. M. Kolesnikov (✉)

Southern Federal University, ul. Milchakova 8a, Rostov on Don 344090, Russian Federation
e-mail: Alexey.M.Kolesnikov@gmail.com

© The Author(s), under exclusive license to Springer Nature Switzerland AG 2023
H. Altenbach and V. Eremeyev (eds.), *Advances in Linear and Nonlinear Continuum and Structural Mechanics*, Advanced Structured Materials 198,
https://doi.org/10.1007/978-3-031-43210-1_13

245

The tube inflation problem is a special case of the more general problem of pure bending of a tube under internal pressure, Libai and Simmonds (1988), Zubov (2001). For straight tubes, this problem has been studied in Koga (1972), Haseganu and Steigmann (1994), Haughton and McKay (1996) and Kolesnikov and Zubov (2009). The curved tubes are considered in Kolesnikov (2011b), Levyakov (2017) and Kolesnikov et al. (2019). The works show that the internal pressure increases the bending stiffness of the tube.

Studies of inflation of curved thin-walled tubes made of hyperelastic material are presented in Kolesnikov (2011a), Kolesnikov (2015). In Kolesnikov (2011a), circular cross-section tubes made of Mooney–Rivlin and neo-Hookean material are considered. It is shown that the tube unbends under inflation. That is, the curvature of the centre line decreases. In Kolesnikov (2015), the tubes of neo-Hookean material with elliptical cross-section are investigated. It is shown that at the beginning of inflation the cross-section of the tube tends to a circular shape. Depending on the ratio of the semi-axes, the tube is either bent or unbent. After the cross-section becomes close to circular, the tube unbends under inflation. A peculiarity of the behaviour of the neo-Hookean material is its instability under biaxial tension. This appears, for example, in straight or curved tube inflation as the existence of two different shapes of the tube corresponding to the same pressure. And also the pressure has a maximum on the curve “pressure–cross-sectional radius”.

In this paper, we consider the inflation problem of curved thin-walled tubes of constant thickness made of Fung material. The problem is solved within the framework of the nonlinear theory of elastic membranes. The aim of this work is to investigate the influence of the cross-section shape and the material parameters of the tube on its behaviour under the internal pressure. The monitored parameters are the curvature of the centre line and the average radius of the cross-section.

13.2 Inflation of Pressurized Curved Tube

In this paper, we will base on the previously presented mathematical model of inflating of a curvilinear thin-walled tube (Kolesnikov 2015), which is a special case of pure bending of an inflated curvilinear tube (Kolesnikov et al. 2019). In this section, we give the basic relations of this model.

In the initial state, the membrane surface is defined by the following equations:

$$\begin{aligned} \mathbf{r} &= x_1(s)\mathbf{i}_1 + x_2(s)\mathbf{e}_2, \quad s \in [0; S], \quad t \in [0; T], \\ \mathbf{e}_2 &= \mathbf{i}_2 \cos \beta t + \mathbf{i}_3 \sin \beta t, \quad \mathbf{e}_3 = -\mathbf{i}_2 \sin \beta t + \mathbf{i}_3 \cos \beta t. \end{aligned}$$

The membrane remains a curvilinear tube with changed curvature and cross-section under internal pressure. Its surface can be described as Libai and Simmonds (1988), Zubov (2001)

$$\begin{aligned} \mathbf{R} &= X_1(s)\mathbf{i}_1 + X_2(s)\mathbf{E}_2, \\ \mathbf{E}_2 &= \mathbf{i}_2 \cos Bt + \mathbf{i}_3 \sin Bt, \quad \mathbf{E}_3 = -\mathbf{i}_2 \sin Bt + \mathbf{i}_3 \cos Bt. \end{aligned} \quad (13.1)$$

Here, B is the unknown new curvature of the central axis, and $X_1(s)$ and $X_2(s)$ are unknown functions describing the cross-section of the inflated tube.

Let's introduce the principal stretch ratios of elongation λ_1 , λ_2 and the angle of the tangent to the cross-section ψ :

$$\lambda_1(s) = \sqrt{\frac{X_1'^2 + X_2'^2}{x_1'^2 + x_2'^2}}, \quad \lambda_2(s) = \sqrt{\frac{B^2 X_2'^2}{\beta^2 x_2'^2}}, \quad \tan \psi(s) = \frac{X_2'}{X_1'}. \quad (13.2)$$

The equilibrium equations of the membrane in this case can be written in the form Kolesnikov (2015), Kolesnikov et al. (2019)

$$X_1'(s) = \sqrt{g_{11}}\lambda_1 \cos \psi, \quad X_2'(s) = \sqrt{g_{11}}\lambda_1 \sin \psi, \quad (13.3)$$

$$\lambda_2'(s) = B\sqrt{\frac{g_{11}}{g_{22}}}\lambda_1 \sin \psi - \frac{g'_{22}}{2g_{22}}\lambda_2. \quad (13.4)$$

$$\begin{aligned} \frac{\partial^2 W}{\partial \lambda_1^2} \lambda_1' &= \left(\frac{\partial W}{\partial \lambda_2} - \lambda_1 \frac{\partial^2 W}{\partial \lambda_1 \lambda_2} \right) B\sqrt{\frac{g_{11}}{g_{22}}} \sin \psi - \\ &- \left(\frac{\partial W}{\partial \lambda_1} - \lambda_2 \frac{\partial^2 W}{\partial \lambda_1 \lambda_2} \right) \frac{g'_{22}}{2g_{22}} - \frac{h'}{h} \frac{\partial W}{\partial \lambda_1}, \end{aligned} \quad (13.5)$$

$$\frac{\partial W}{\partial \lambda_1} \psi' = B\sqrt{\frac{g_{11}}{g_{22}}} \frac{\partial W}{\partial \lambda_2} \cos \psi + \frac{\xi}{h} \sqrt{g_{11}}\lambda_1 \lambda_2. \quad (13.6)$$

The principal stress resultants in the membrane are determined by the equations

$$L_1 = \frac{h}{\lambda_2} \frac{\partial W}{\partial \lambda_1}, \quad L_2 = \frac{h}{\lambda_1} \frac{\partial W}{\partial \lambda_2}. \quad (13.7)$$

We assume that the cross-section of the tube is closed. The boundary conditions for the unknown functions at the points $s = 0, S$ are their periodicity. The boundary conditions at the ends ($t = 0, T$) of the tube are satisfied in the integral sense. In this problem, the resultant force and the resultant couple of the stresses in the membrane and the internal pressure are equal to zero:

$$\int_0^S \sqrt{G_{11}} L_2 ds - \xi \Sigma = 0, \quad (13.8)$$

$$\int_0^S \sqrt{G_{11}} L_2 (X_2 - X_{C2}) ds = 0. \quad (13.9)$$

Here X_{2C} is the centre of mass of the area bounded by the membrane contour in the cross-sectional plane. For a given potential energy function of deformation, the static problem of an elastic membrane is reduced to the boundary value problem for the system of ordinary differential equations (13.3)–(13.6) with parameter B . The boundary value problem is solved numerically by the shooting method.

13.3 Results

In this paper, we consider a tube made from incompressible Fung material. The strain energy function is given as

$$W = \frac{\mu}{2\gamma} (e^{\gamma(I_1-3)} - 1), \quad I_1 = \lambda_1^2 + \lambda_2^2 + \frac{1}{\lambda_1^2 \lambda_2^2}. \quad (13.10)$$

A correct choice of dimensionless parameters will give results independent of the material parameter μ . Below results will be presented for the material parameter $\gamma = 5, 0.2$ and 0.05 . Also, for comparison, some results will be presented for the neo-Hookean material, including those from Kolesnikov (2015).

We assume that the thickness $h = 0.001$ is constant and that the cross-section of the curved tube is elliptical and defined by the equations

$$x_1(s) = r_1 \sin s, \quad x_2(s) = \beta^{-1} - r_2 \cos(s), \quad s \in [0; 2\pi].$$

Also we assume that $T = \pi/(2\beta)$.

Next we consider the curved tube with the curvature of the central axis $\beta = 0.1$. The cross-sectional dimensions r_1 and r_2 are given in Table 13.1. The number in the first line corresponds to the curve number in Figs. 13.1, 13.2, 13.3, 13.4, 13.5, 13.6, 13.7, 13.8 and 13.9. As will be shown below, the shape of the cross-section has a significant influence on the deformation of the curved tube. During inflation, the curved tube bends or unbends in the plane $\mathbf{e}_2\mathbf{e}_3$. The tube 5 has a circular cross-section. The cross-section of the tubes 1–4 is an ellipse extended along the axis \mathbf{i}_1 and flattened along the axis \mathbf{e}_2 . For the tubes 6–9, the cross-section is elongated along the \mathbf{e}_2 -axis and flattened along the \mathbf{i}_1 -axis.

To present the results, we introduce a dimensionless pressure p^* and a relative curvature B^* as follows:

Table 13.1 The cross-section parameters

| N | 1 | 2 | 3 | 4 | 5 | 6 | 7 | 8 | 9 |
|-------|-----|-----|-----|-----|---|-----|-----|-----|-----|
| r_1 | 1.9 | 1.7 | 1.5 | 1.3 | 1 | 0.7 | 0.5 | 0.3 | 0.1 |
| r_2 | 0.1 | 0.3 | 0.5 | 0.7 | 1 | 1.3 | 1.5 | 1.7 | 1.9 |

$$p^* = \frac{\xi r_0}{\mu h}, \quad B^* = \frac{B}{\beta}.$$

In addition, we introduce dimensionless parameters characterizing the deformed cross-section

$$R_1 = \max \left\{ \frac{2X_1(s)}{r_1 + r_2}, s \in [0; \pi] \right\}, \tag{13.11}$$

$$R_2 = \frac{X_2(\pi) - X_2(0)}{r_1 + r_2}, \quad R_0 = \frac{R_1 + R_2}{r_1 + r_2}. \tag{13.12}$$

The deformed cross-section is not an ellipse. However, we can correspond parameters R_1 and R_2 to the semi-axes r_1 and r_2 of the initial elliptical cross-section. The parameter R_0 will be called the mean radius of the deformed cross-section. In the present work, we consider the undeformed cross-sections such that their mean radii are 1, as can be seen from Table 13.1.

In this work, we investigate the effect of the material parameter γ and the elliptical cross-section on the curvature of the inflated tube B and the mean radius of cross-section R_0 . Figures 13.1, 13.2 and 13.3 show the relationship between the curvature of central axis B^* and pressure p^* . The solid lines correspond to the results for the Fung material with parameter $\gamma = 5, 0.2$ and 0.05 , respectively. The dotted lines correspond to the results for the neo-Hookean material. The curve numbers in the figures correspond to the column numbers in Table 13.1.

Up to a certain pressure p^* , the ‘‘curvature–pressure’’ curves for the tubes made of Fung material coincide with one for the tubes made of neo-Hookean material. At $\gamma = 5$, the magnitude of this pressure $p^* \approx 0.4$, at $\gamma = 0.2 - p^* \approx 0.5$, at $\gamma = 0.05 - p^* \approx 0.6$. The tube 5 with a circular cross-section gradually unbends under pressure increasing, i.e. the curvature decreases. For the tubes 1–4, for which $r_1 > r_2$, the curvature first decreases dramatically, i.e. the tubes unbend sharply under the internal pressure. The greater the ratio r_1/r_2 , the more the tube unbends. The curvature then continues to decrease, but at a much slower rate. For the tubes 6–9, for which $r_1 < r_2$, the curvature first increases dramatically, that is, the tubes bend sharply under the internal pressure. The smaller the ratio r_1/r_2 , the more the tube bends. Then the curvature begins to slowly decrease, i.e. the tube begins to unbend.

Further, the behaviour of a tube made of Fung material depends on the material parameter γ and differs significantly from that for neo-Hookean tube. At $\gamma = 5$ (Fig. 13.1) for pressures $p^* > 0.4$, the curvature slowly monotonically decreases with increasing pressure. At $\gamma = 0.2$ (Fig. 13.2) for pressures $p^* > 0.5$ the curvature

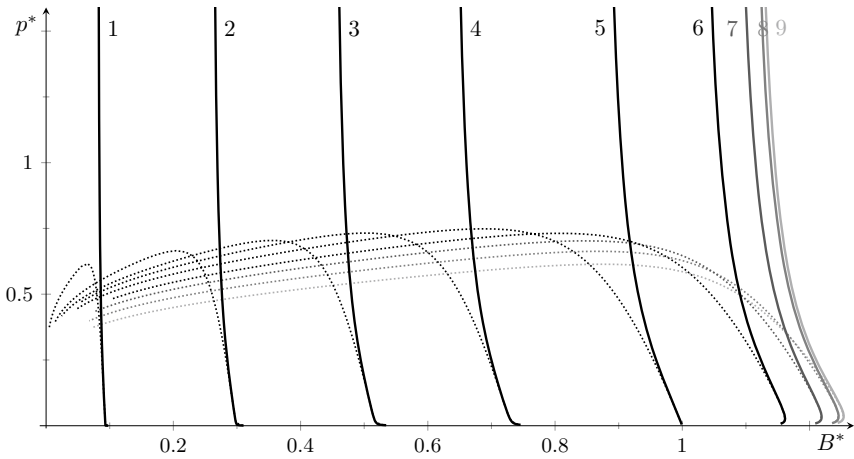


Fig. 13.1 The pressure p^* versus the curvature B^* ($\gamma = 5$)

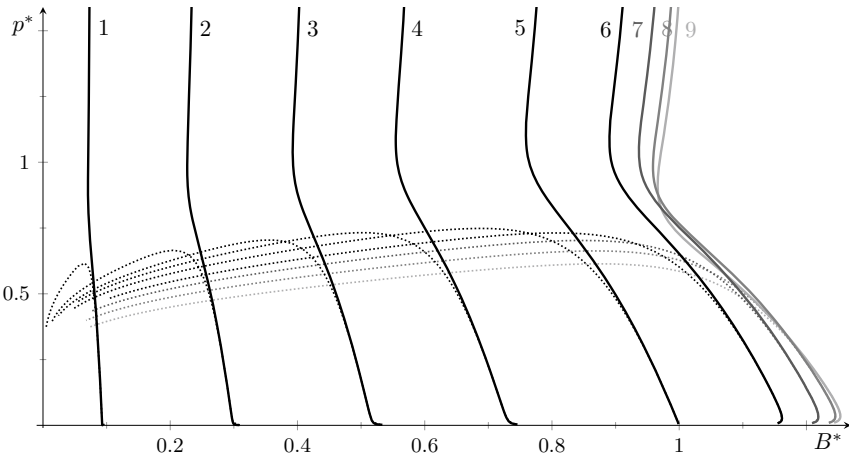


Fig. 13.2 The pressure p^* versus the curvature B^* ($\gamma = 0.2$)

first decreases, reaching a minimum, then slowly increases with increasing pressure. At $\gamma = 0.05$ (Fig. 13.3) for pressures $p^* > 0.6$ the curve “curvature–pressure” has a loop and a self-intersection point, after which the curvature increases with increasing pressure.

The change in curvature of the tube is related to the deformation of its cross-section. As it is shown in Kolesnikov (2015) that for a curvilinear tube of neo-Hookean material, for $r_1 \in [0.5, 1.5]$ and $r_2 \in [0.5, 1.5]$ the deviation from a circular shape is less than 5% at $p^* > 0.01$. Figures 13.4, 13.5 and 13.6 show the relationship between the ratio of characteristic cross-sectional dimensions R_1/R_2 and the pressure

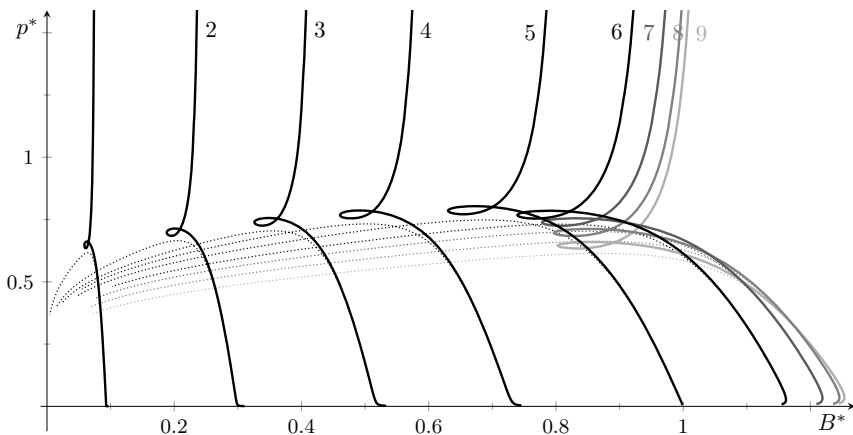


Fig. 13.3 The pressure p^* versus the curvature B^* ($\gamma = 0.05$)

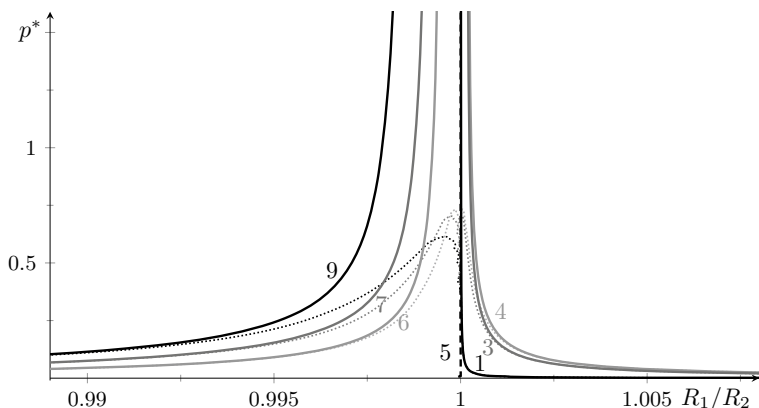


Fig. 13.4 The pressure p^* versus the ratio R_1/R_2 ($\gamma = 5$)

p^* . As we can see from the figures, the ratio of the characteristic dimensions of the cross-section tends rapidly towards 1. That is, the shape of the deformed cross-section of the curved tube tends to be circular. The elliptical cross-section flattened along the axis \mathbf{e}_2 (the tubes 1–4) tends the circular shape faster than the cross-section flattened along the axis \mathbf{i}_1 (the tubes 6–9).

Since the cross-section of the inflated tube is close to circular, let us consider the relationship between the average radius R_0 and pressure p^* shown in Figs. 13.7, 13.8 and 13.9. The solid black lines show the dependence R_0-p^* for the tubes made of Fung material at $r_1 \leq r_2$, and the solid grey lines correspond to $r_1 > r_2$. The thin dotted lines show the dependences of the mean radius for curvilinear tubes of neo-Hookean material. The thick grey dashed line in Figs. 13.7, 13.8 and 13.9, coinciding

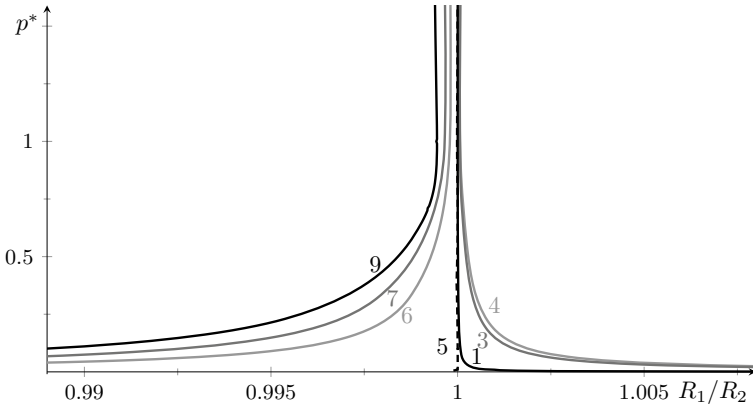


Fig. 13.5 The pressure p^* versus the ratio R_1/R_2 ($\gamma = 0.2$)

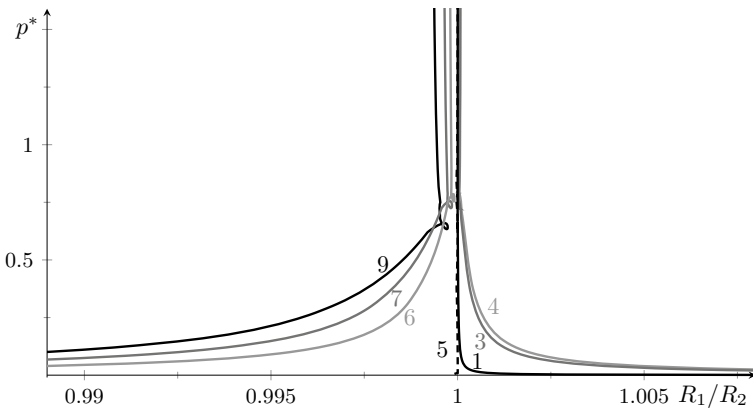


Fig. 13.6 The pressure p^* versus the ratio R_1/R_2 ($\gamma = 0.05$)

with the line 5, shows the relation between the radius of a straight tube (cylindrical membrane) and the pressure. That is, for circular curved tubes, a small curvature (in this work, the initial curvature $\beta = 0.1$) has little effect on the deformation of the cross-section.

At the start of inflation, the change in the mean radius depends on the ratio r_1/r_2 . For the tubes 1–4 with the elliptical cross-section flattened along the axis \mathbf{e}_2 ($r_1 > r_2$) the mean radius increases sharply, then the curve “mean radius–curvature” becomes similar to the relationship for the tube 5 with circular cross-section, but with a rightward shift (grey curves in Figs. 13.7, 13.8 and 13.9). The more r_1/r_2 differs from one, the greater the amount of shift. For the tubes 6–9 with the elliptical cross-section flattened along the axis \mathbf{i}_1 ($r_1 < r_2$), the dependence of the mean radius R_0 on pressure p^* decreases at the beginning of inflation (black curves in Fig. 13.7,

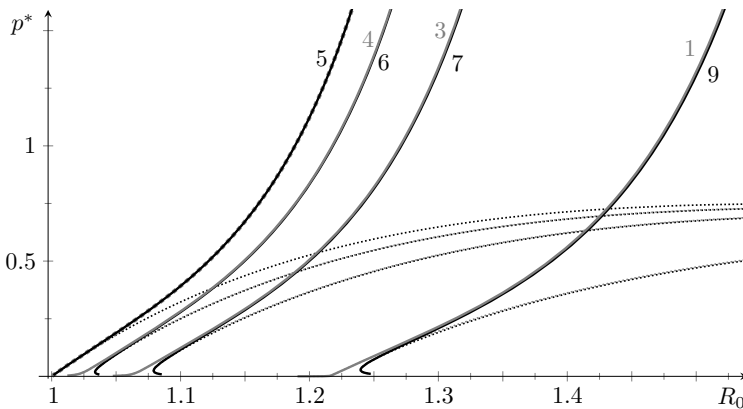


Fig. 13.7 The pressure p^* versus the average radius R_0 ($\gamma = 5$)

13.8 and 13.9), then it starts increasing with increasing pressure. For tubes where $r_1/r_2 = r_2/r_1$, the curves R_0-p^* become very close at $p^* > 0.1$. At $\gamma = 0.05$, the dependence of the mean radius R_0 has a descending region and a local minimum, as we can see in Fig. 13.9.

We note that for very small pressures and hence deformations we failed to obtain a numerical solution of the nonlinear differential equations, so for the tubes 1–4 and 6–9 in Figs. 13.1, 13.2 and 13.3 the curves do not start from point $B^* = 1$, and in Figs. 13.7, 13.8 and 13.9 the curves do not start from point $R_0 = 1$, which would correspond to the undeformed state of the tubes. Besides, for the tube 6–9 (Figs. 13.7, 13.8 and 13.9), the dependence R_0-p^* should have a sharp growth at very low pressures ($p^* < 0.01$) and reach a local maximum. After that the mean radius decreases, which has already been calculated numerically. We note that at very low pressures and hence deformations, the use of the membrane theory becomes incorrect, as the influence of the bending stiffness will be significant. In addition, at the beginning of inflation of curved tubes, areas of compression are formed in their, which quickly disappear with increasing pressure, as shown in Kolesnikov (2015). The inflation of curved tubes within small deformations has been previously investigated, e.g. by Feodos'ev (1949), Levyakov (1997). The effects of a significant change in curvature of a curved tube with a flattened cross-section is used in manometers (the Bourdon tube) (Feodos'ev 1949; Levyakov 1997).

Figures 13.10 and 13.11 show how the tube deforms during inflation using the tubes 9 and 1 as examples, respectively. The curves p^*-B^* show in the figures, on which the points P_k^m ($k = 1, 9, m = 1, \dots, 7$) are marked and the corresponding shapes of the longitudinal and cross-sections are shown. The grey lines show the initial shapes for comparison.

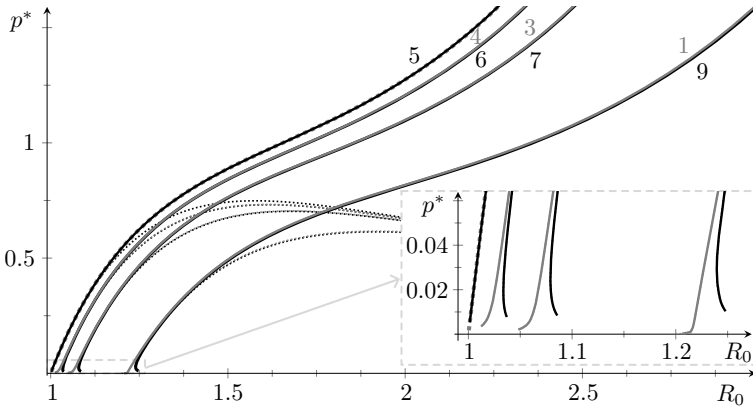


Fig. 13.8 The pressure p^* versus the average radius R_0 ($\gamma = 0.2$)

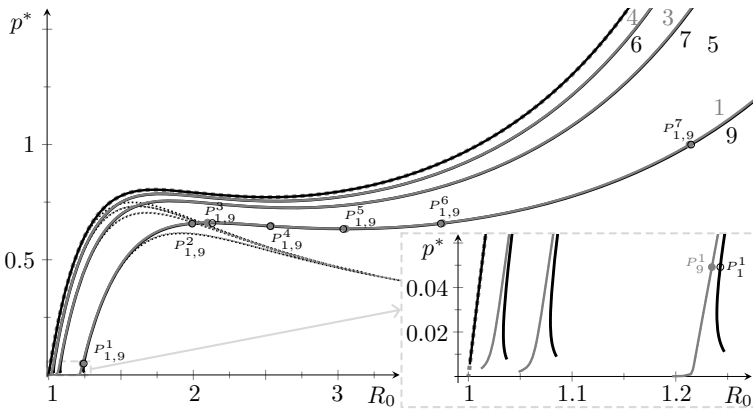


Fig. 13.9 The pressure p^* versus the average radius R_0 ($\gamma = 0.05$)

The points P^m_k ($k = 1, 9, m = 1, \dots, 7$) corresponding to the shapes shown in Figs. 13.10 and 13.11 are marked in Fig. 13.9. As we can see from Fig. 13.9, the points $P^3_{1,9}$ correspond to the local maximum pressure, after which the mean radius increases as the internal pressure decreases. The points $P^5_{1,9}$ correspond to the local minimum of the curves $R_0 - p^*$.

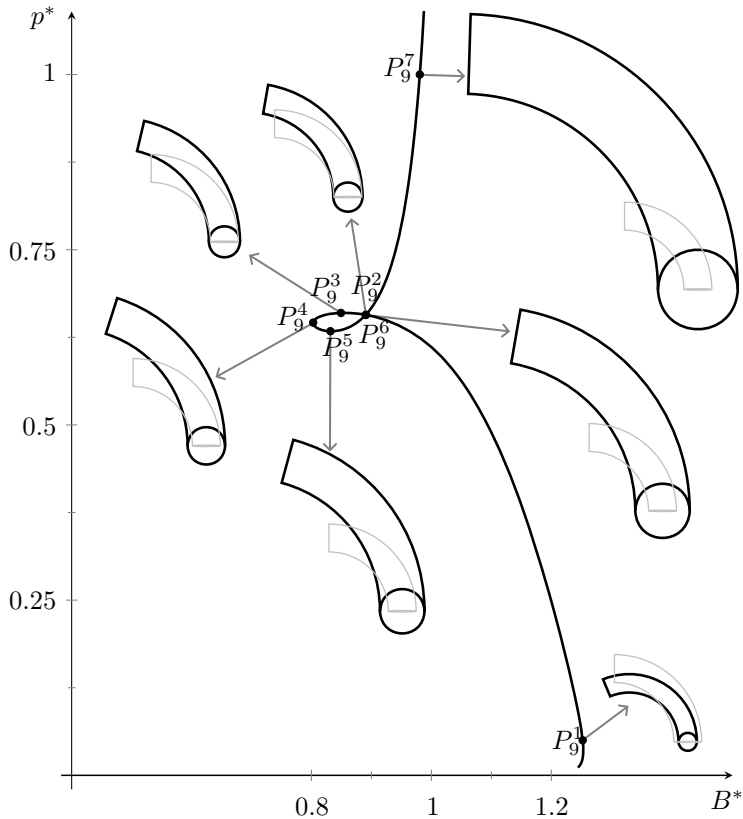


Fig. 13.10 Planform and cross-sectional views of a deformed tube 9 ($\gamma = 0.05$)

13.4 Conclusions

In this work, we consider the problem of an initially curved thin-walled tube made of hyperelastic material. Due to the small thickness and predominantly tensile stresses, the bending stiffness of the tube walls is neglected and the nonlinear theory of elastic membranes is used. The mechanical properties of the hyperelastic material are described by the Fung strain energy function.

A straight tube changes cross-section and length under inflation. A curved tube additionally changes the curvature. A tube made of neo-Hookean material has a specific behaviour. There is a maximum internal pressure after which the cross-section radius increases under the pressure decreases. This is usually associated with unstable of the tube (Gonçalves et al. 2008; Pearce and Fu 2010; Zubov and Karyakin 2011; Guo et al. 2016; Wang et al. 2019). For the curved tube made of the neo-Hookean material, the mean radius shows the same behaviour. Additionally, the curvature of the tube is reduced.

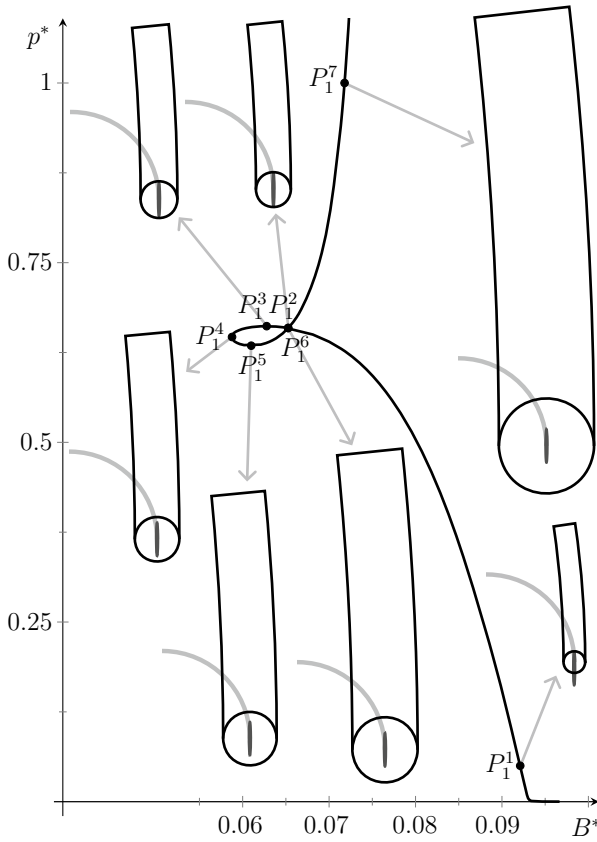


Fig. 13.11 Planform and cross-sectional views of a deformed tube 1 ($\gamma = 0.05$)

The elliptical cross-section of a thin-walled curved tube tends to circular shape when inflated. But as long as the pressures are small and they are not yet completely circular, the behaviour of the tubes is very different for different elliptical shapes. Some tubes are sharply unbent, other tubes are bent. This is a well-known effect, in particular used for pressure measurement with Bourdon tubes (Feodos'ev 1949; Levyakov 1997). But for thin-walled highly elastic tubes, rather quickly the cross-section becomes circular, as shown in this paper and in Kolesnikov (2015). Further, as the pressure increases, the behaviour of the tubes becomes similar to that of a tube with a circular cross-section. Their mean radius increases and the curvature decreases (for the neo-Hookean tubes). The difference in the initial shift of the curves “curvature–pressure” to one side or the other depends on the ratio of the semi-axes of the initial elliptical cross-section.

The Fung material has two material parameters. One parameter can be excluded by the introduction of dimensionless parameters, and the other parameter denoted as γ cannot be excluded. Up to a certain value of pressure and deformation, a tube

made of Fung material has a behaviour similar to the neo-Hookean tube. As the pressure increases, its behaviour begins to differ. The curvature–pressure relation exhibits three possible behaviours depending on the value of γ : monotonic decrease in curvature, decrease and then increase in curvature (for small γ); existence of a loop (for even smaller γ).

The change in curvature is associated with a change in the cross-section. For pressures that are not very small, the monotonicity of the “curvature–pressure” curve corresponds to the constant sign of the curvature of the “mean radius–pressure” curve. For the nonmonotonic “curvature–pressure” curve, the sign of the curvature of the “mean radius–pressure” curve changes, but the curvature itself remains monotonic. For the “curvature–pressure” curve that has a loop, the “mean radius–pressure” curve not only changes the sign of the curvature, but also ceases to be monotonically increasing. The local maximum and minimum on the “radius–pressure” curve is a known fact for straight tubes (Pearce and Fu 2010; Zubov and Karyakin 2011; Wang et al. 2019). This is usually associated with structural instability. According to the theory, the tube jumps from the maximum to the second ascending branch of the curve. In experiments, this is due to local bulging. When the cross-section of the tube increases locally and sharply. And then this extension is extended to the entire tube (Gonçalves et al. 2008; Guo et al. 2016; Wang et al. 2019). For the curved tube, the mechanisms appear to be the same. From the point of local maximum pressure, there will be a transition to the second ascending branch of the solution with an abrupt change in cross-section and curvature.

References

- Feodos'ev VI (1949) Elastic Elements in Precision Instrument making (In Russian). Oborongiz, Moscow
- Gonçalves PB, Pamplona D, Lopes SRX (2008) Finite deformations of an initially stressed cylindrical shell under internal pressure. *International Journal of Mechanical Sciences* 50(1):92–103
- Guo Z, Gattas J, Wang S, Li L, Albermani F (2016) Experimental and numerical investigation of bulging behaviour of hyperelastic textured tubes. *International Journal of Mechanical Sciences* 115:665–675
- Haseganu E, Steigmann D (1994) Theoretical flexure response of a pressurized cylindrical membrane. *International Journal of Solids and Structures* 31(1):27–50
- Haughton D, McKay B (1996) Wrinkling of inflated elastic cylindrical membranes under flexure. *International Journal of Engineering Science* 34(13):1531–1550
- Koga T (1972) Bending rigidity of an inflated circular cylindrical membrane of rubbery materials. *AIAA Journal* 10:1485–1489
- Kolesnikov AM (2011) Large bending deformations of pressurized curved tubes. *Archives of Mechanics* 63(5–6):507–516
- Kolesnikov AM (2011) Unbending of curved tube by internal pressure. In: Altenbach H, Eremeyeva VA (eds) *Advanced Structures Materials*. Springer-Verlag, Berlin, Shell-like Structures, pp 491–498
- Kolesnikov AM (2015) The finite inflation of a curved elastic tube. *Mathematics and Mechanics of Solids* 20:823–835. <https://doi.org/10.1177/1081286514553372>

- Kolesnikov AM, Zubov LM (2009) Large bending deformations of a cylindrical membrane with internal pressure. *ZAMM* 89:288–305
- Kolesnikov AM, Popov AV, Shubchinskaya NYu (2019) Bending of inflated curved hyperelastic tubes. *ZAMM-Journal of Applied Mathematics and Mechanics/Zeitschrift für Angewandte Mathematik und Mechanik* 99(7):e201800093
- Levyakov SV (1997) Nonlinear manometer effect for Bourdon tubes with arbitrary cross section. *Mechanics of Solids* 32(1):105–110
- Levyakov SV (2017) The effect of inflating pressure on the finite pure bending of hyperelastic tubes. *ZAMM - Journal of Applied Mathematics and Mechanics/Zeitschrift für Angewandte Mathematik und Mechanik* 97(5):561–575
- Libai A, Simmonds JS (1988) *The Nonlinear Theory of Elastic Shells*. Academic Press, San Diego
- Pearce SP, Fu YB (2010) Characterization and stability of localized bulging/necking in inflated membrane tubes. *IMA journal of applied mathematics* 75(4):581–602
- Wang S, Guo Z, Zhou L, Li L, Fu Y (2019) An experimental study of localized bulging in inflated cylindrical tubes guided by newly emerged analytical results. *Journal of the Mechanics and Physics of Solids* 124:536–554
- Zubov LM (2001) Semi-inverse solution in non-linear theory of elastic shells. *Archives of Mechanics* 53(4–5):599–610
- Zubov LM, Karyakin DM (2011) Instability of an elastic cylindrical membrane under tensile stresses (in Russian). *Izvestiya Vuzov. Severo-Kavkazskii Region. Natural Science* 4:31–33

Chapter 14

Analysis of the Homogenization Problem for Nonlinear Corrugated Plate



Alexander G. Kolpakov and Sergei I. Rakin

Abstract The numerical results of calculating the average stiffness of corrugated plates are given. The calculations are based on the transition from the three-dimensional (3-D) problem of the periodicity cells of the averaging theory to the corresponding two-dimensional (2-D) problem. We consider a physically linear-geometrically non-linear model at the microlevel and demonstrate this and find that the geometric nonlinearity at the microlevel is transformed into a physical (material) nonlinearity at the macrolevel.

Keywords Corrugated plate · Elasticity theory · Homogenization · Periodicity cell · Dimension reduction · Effective stiffnesses · Local stress/strain state · Nonlinearity

14.1 Introduction

The problem of computation of the homogenized (effective, macroscopic, etc. (Sab 2015; Dvorak 2013; Sanchez-Palencia 1980)) stiffness of corrugated plate attracted attention of numerous researchers for a long time. In (Sanchez-Palencia 1980), the beginning of the study is referred to 1923 (Huber 1923) and it is noted an existence of extensive literature on the subject. The use in modern engineering structures of corrugated plates and plates with corrugated core (Xia et al. 2012; Buannic et al. 2003; Talbi et al. 2009; Bartolozzi et al. 2013) gives additional stimulus for the studying the problem. The progress in the analysis of corrugated plates was made on the basis of shell theory (Andrianov et al. 1998; Lee and Yu 2011) and the homogenization theory (Caillerie 1984; Kohn and Vogelius 1984; Kalamkarov and Kolpakov 1997; Levinski 1995; Buannic et al. 2003; Kolpakov 2010).

A. G. Kolpakov (✉) · S. I. Rakin
SysAn (System Analysis in Engineering), A. Nevskogo Str., Bld.12a, 34, Novosibirsk 630075,
Russia
e-mail: algk@ngs.ru

Our homogenization analysis is based on the observation that three-dimensional corrugated plate is a cylinder and the 3-D periodicity cell problems of the homogenization theory for it can be reduced to 2-D problems on the cross-section of the periodicity cell. It makes possible numerical computation of the effective stiffnesses of the corrugated plate and the local strain/stress state in the plate with high accuracy.

Previously, a transition to a problem on the cross-section of plate was done in Annin et al. (2017); Kolpakov and Rakin (2016) for linear elasticity problem.

14.2 Statement of the Problem and Dimension Reduction

Consider a corrugated plate of periodic structure. The plate occupies a cylindrical domain with generatrix L perpendicularly 2-D domain S (the cross-section of the plate), see Fig. 14.1. Denote the periodicity cell of the plate by εP (drawn in bold in Fig. 14.1), where ε means the characteristic size of the periodicity cell (ε is also the characteristic thickness of the corrugated plate “in whole”, do not confuse ε with the thickness of the plate εh , see Fig. 14.1).

We assume that L is parallel to the axis Oy_1 , then the periodicity cell $\varepsilon P = [0, 1] \times \varepsilon P_0$, where εP_0 is the periodicity cell of the cross-section S .

If ε is small in comparison with the size of the plate, the plate may be substituted by a flat plate possessing so-called effective stiffness, see (Caillerie 1984; Kohn and Vogelius 1984; Kalamkarov and Kolpakov 1997).

14.2.1 Periodicity Cell Problem

To compute the effective stiffness, we use the homogenization method developed for linear plates originally in Caillerie (1984); Kohn and Vogelius (1984) and modified for the non-linear plates later (Hornung et al. 2014; Kalamkarov et al. 2017). In accordance with the homogenization method, we introduce the “fast” variables $\mathbf{y} = \mathbf{x}/\varepsilon$ (Sanchez-Palencia 1980) and the problems on the periodicity cell $P = [0, 1] \times P_0$ (see Fig. 14.2), that have the form: find function $\mathbf{N}^{ABv}(\mathbf{y})$ as solution of the

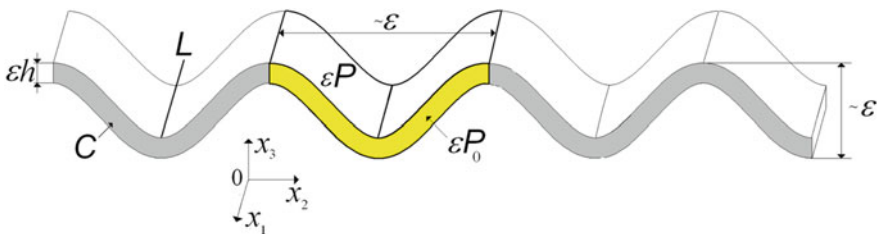


Fig. 14.1 Corrugated plate

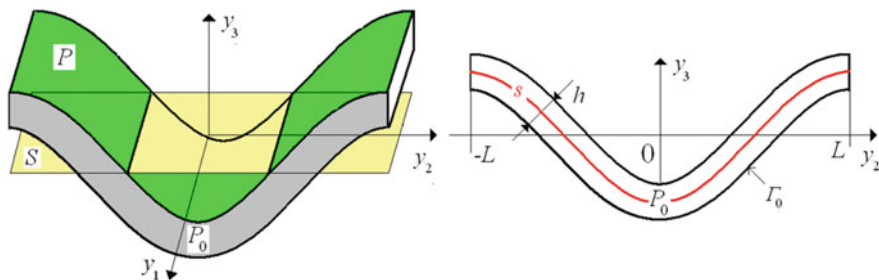


Fig. 14.2 Periodicity cell (top) and its cross-section (bottom) in the “fast” variables $\mathbf{y} = \mathbf{x}/\varepsilon$ (online version in color)

boundary-value problem

$$\begin{cases} \sigma_{ij} = 0 \text{ in } P, \\ \sigma_{ij}n_j = 0 \text{ in } \Gamma, \\ \sigma_{ij} = a_{ijkl}e_{kl}, \\ e_{ij} = 1/2(N_{i,j}^{ABCD} + N_{j,i}^{ABCD} + N_{n,i}^{ABCD}N_{n,j}^{ABCD}) \\ N^{ABCD}(\mathbf{y}) - e_{AB} - \rho_{CD}y_3 \text{ periodic in } y_1, y_2 \in S. \end{cases} \quad (14.1)$$

Here Γ is the free (lateral) surface of the periodicity cell; S is the projection of periodicity cell onto the Oy_1y_2 -plane, see Fig. 14.2; a_{ijkl} —elastic constants; \mathbf{n} —the outer vector-normal. Latin indices take the values 1, 2, 3; in (14.1) A and B take the values 1 and 2; μ and ν take the values 0 and 1.

We consider the plates made of isotropic material, in this case the elastic constants.

$$a_{ijkl} = \frac{E\nu_0}{(1 + \nu_0)(1 - 2\nu_0)}\delta_{ij}\delta_{kl} + \frac{E}{2(1 + \nu_0)}(\delta_{ik}\delta_{jl} + \delta_{il}\delta_{jk})$$

where E and ν_0 are Young’s modulus and Poisson ratio (Love 1929) (we use notation ν_0 in order to distinguish this from the index ν , traditionally used in the periodicity cell problem (Caillerie 1984; Kohn and Vogelius 1984; Kalamkarov and Kolpakov 1997)).

We solve the physically linear and geometrically non-linear problem, i.e., we assume that Young’s modulus E and the Poisson ratio ν_0 do not depend on the local deformations $e_{ij}^{loc} = 1/2(u_{i,j} + u_{j,i} + u_{n,i}u_{n,j})$. Having solved problem (14.1), we compute the elastic energy of the periodicity cell $E(e_{AB}, \rho_{CD})$. The corresponding homogenized governing equations of the plate are

$$\begin{aligned}\sigma_{AB} &= D_{ABCD}^0(e_{AB}, \rho_{AB})e_{CD} + D_{ABCD}^1(e_{AB}, \rho_{AB})\rho_{CD} = \frac{1}{|S|} \cdot \frac{\partial E}{\partial e_{AB}}(e_{AB}, \rho_{CD}) \\ M_{AB} &= D_{ABCD}^1(e_{AB}, \rho_{AB})e_{CD} + D_{ABCD}^2(e_{AB}, \rho_{AB})\rho_{CD} = \frac{1}{|S|} \cdot \frac{\partial E}{\partial \rho_{AB}}(e_{AB}, \rho_{CD})\end{aligned}\quad (14.2)$$

where $|S|$ means the area of S , see Fig. 14.2.

In (14.2), e_{AB} and ρ_{CD} are the homogenized (overall, macroscopic) in-plane deformations and curvatures of the plate considered a 2-D object. Eq. (14.2) introduces the homogenized in-plane stiffnesses D_{ABCD}^0 , and the homogenized bending stiffnesses D_{ABCD}^2 . The homogenized non-symmetric stiffnesses D_{ABCD}^1 are zero for plates of symmetric structure, in particular, for sinusoidal corrugated plate.

It is waiting that the homogenized stiffnesses D_{ABCD}^0 and D_{ABCD}^2 are non-linear functions of e_{AB} and ρ_{CD} . Remind that the original problem (14.1) is physically linear and the geometric non-linear. If the homogenized stiffnesses D_{ABCD}^0 and D_{ABCD}^2 really occurs non-linear functions of e_{AB} and ρ_{CD} , as it is waiting, it will means that we meet the effect of the transmission of the geometric nonlinearity into physical nonlinearity. Note that the effect of transmission of the geometric nonlinearity into physical nonlinearity as a result of homogenization was early reported in Kolpakov and Rakin (2010) for laminated bodies.

14.2.2 Dimension Reduction for the Periodicity Cell Problem

We assume that the elastic constants have the form $a_{ijkl}(y_2, y_3)$ —do not depend on the variable y_1 . This condition is satisfied by plates made of homogeneous materials ($a_{ijkl} = \text{const}$ in this case) and plates made of several homogeneous plates ($a_{ijkl}(y_2, y_3)$ is piecewise-constant function in this case).

In this case, problem (14.1) can be reduced to 2-D problems on the cross-section P_0 of the periodicity cell.

It means that $\mathbf{N}^{\text{ABv}}(\mathbf{y})$ does not depend on y_1 : $\mathbf{N}^{\text{ABv}}(\mathbf{y}) = \mathbf{N}^{\text{ABv}}(y_2, y_3)$. Then the periodicity cell problem (14.1) takes the form (in (14.3) $\delta, \kappa = 2, 3$; $i, k = 1, 2, 3$; A, B, C, D = 1, 2)

$$\begin{cases} \sigma_{\alpha\beta,\gamma} = 0 \text{ in } P, \\ \sigma_{\alpha\beta}n_\beta = 0 \text{ on } \Gamma, \\ \sigma_{\alpha\beta} = a_{\alpha\beta\gamma\delta}(\mathbf{y})e_{\gamma\delta}, \\ e_{\alpha\beta} = 1/2(N_{\alpha,\beta}^{\text{ABCD}} + N_{\beta,\alpha}^{\text{ABCD}} + N_{\eta,\beta}^{\text{ABCD}}N_{\eta,\alpha}^{\text{ABCD}}) \\ \mathbf{N}^{\text{ABCD}}(\mathbf{y}) - e_{AB} - \rho_{CD}y_3 \text{ periodic in } y_1, y_2 \in S. \end{cases}\quad (14.3)$$

14.3 Numerical Computations

We consider the corrugation of sinusoidal profile with period $T = 2L = 0.64$ m, see Fig. 14.2. Plate thickness of the corrugation is 0.04 m. Material characteristics of the material of the plate: Young’s modulus $E = 3 \cdot 10^{10}$ Pa, Poisson ratio $\nu_0 = 0.2$. ANSYS FEM (Thompson and Thompson 2017) software was used in computations. The finite elements PLANE42 and PLANE182 were used. The number of finite elements was about 3000.

14.3.1 Overall In-Plane Deformation

In-plane deformation is described by the problem (14.1) with $\rho_{CD} = 0$. We consider the tension of the plate in the direction 22. It means that in (14.1) $e_{22} \neq 0, e_{33} = 0$. We solved the geometrically non-linear problem (14.1) for values of the overall tension U in the range from 0.01 to 0.26 (from 1 to 26%). The deformed corrugation for several U is displayed in Figs. 14.3, 14.4, 14.5, 14.6 and 14.7. The scale and the colors in Figs. 14.3, 14.4, 14.5, 14.6 and 14.7 demonstrate the local von Mises stress in the plate.

For each value of the displacement U , elastic energy $E(U)$ of the deformed corrugation was computed by using the ANSYS option “Strain energy” *SENE* (Thompson and Thompson 2017). The computed energy values are presented in Table 14.1. The overall in-plane strain e_{11} was computed in accordance with 1-D formula for non-linear theory (Love 1929). By using the strain energy and *SENE* overall in-plane strain e_{11} , we determine the overall in-plane stiffness $D_{1111}^0(e_{11})$ from the equality.

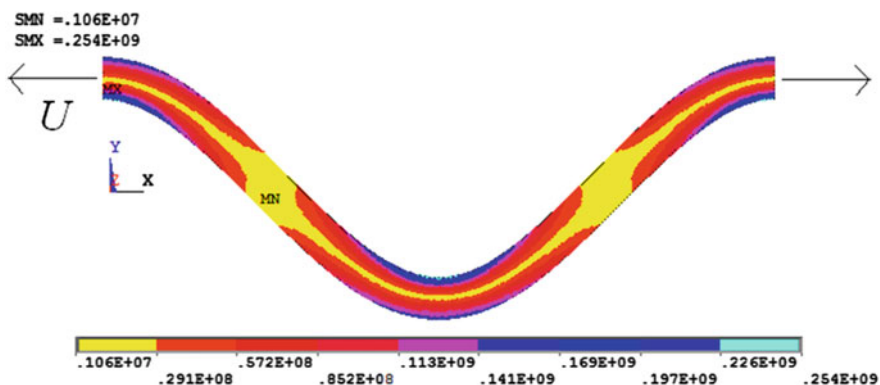


Fig. 14.3 Corrugation deformation corresponding to tension with $U = 2\%T$

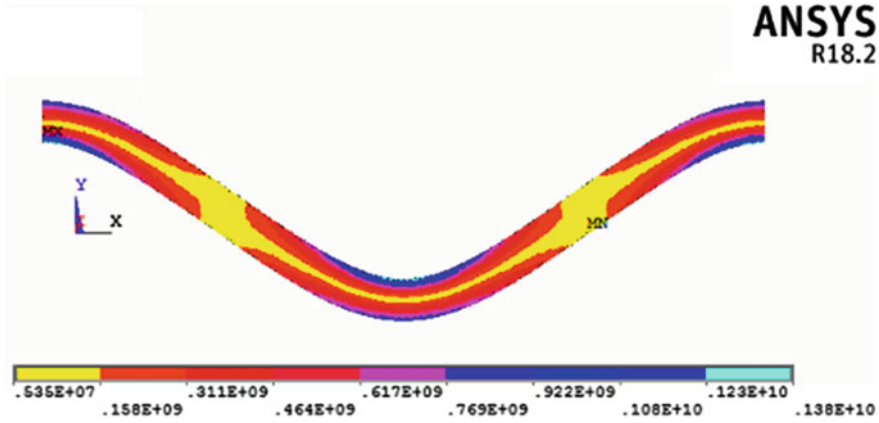


Fig. 14.4 Corrugation deformation corresponding to tension with $U = 10\%T$

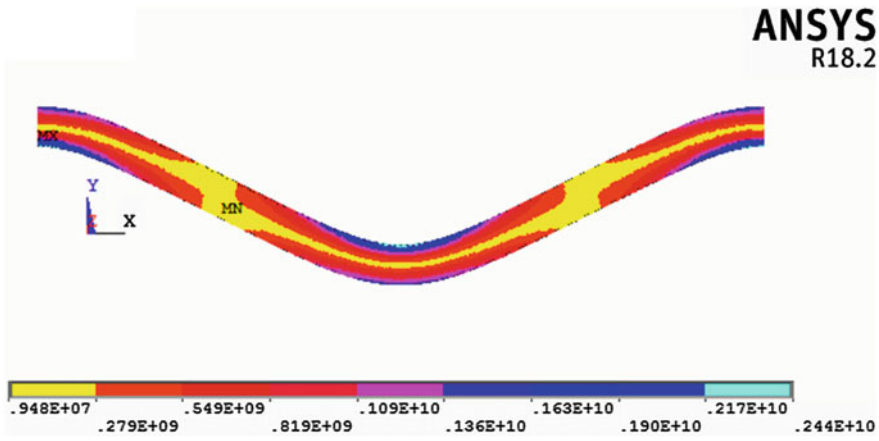


Fig. 14.5 Tension corresponding to $e_{11} = U = 2\%T$ 16%

$$SENE = \frac{1}{2} D_{1111}^0(e_{11}) e_{11}^2 2L$$

The computed values of $D_{1111}^0(e_{11})$ are presented in Table 14.1. The in-plane stiffness $D_{1111}^0(0) = 1,130E + 7$. In the last line of Table 14.1, ratio $r = \frac{D_{1111}^0(e_{11})}{D_{1111}^0(0)}$ is presented.

Recall that we consider physically linear elastic material and geometrically non-linear deformations. It is possible to consider a physically non-linear material. In this paper, we would like to pay attention to the phenomenon of transition of the geometric nonlinearity at microlevel into physical nonlinearity at macrolevel. This

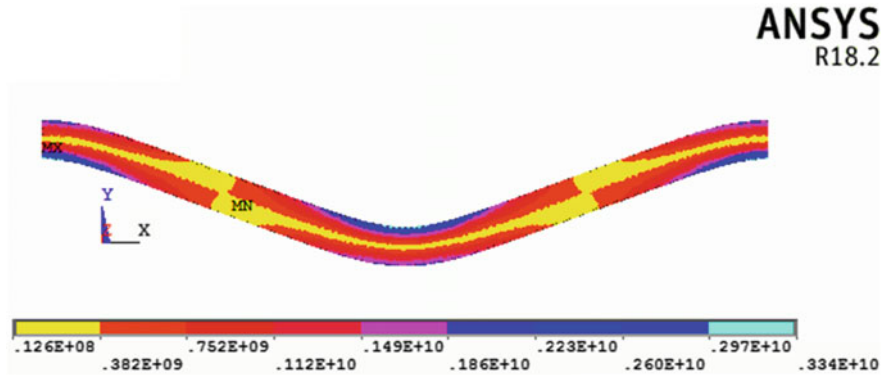


Fig. 14.6 Corrugation deformation corresponding to tension with $U = 20\%T$

SMN = .147E+08
 SMX = .455E+10

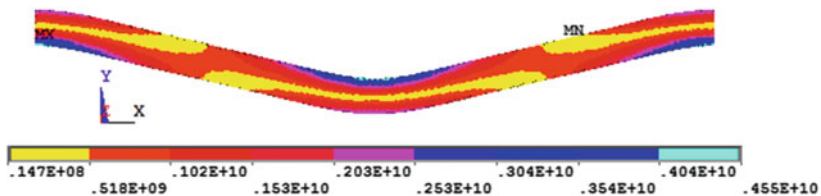


Fig. 14.7 Corrugation deformation corresponding to tension with $U = 24\%T$

is more pronounced if the material of the plate is physically linear. For this reason, we do not consider the physically non-linear material in this paper.

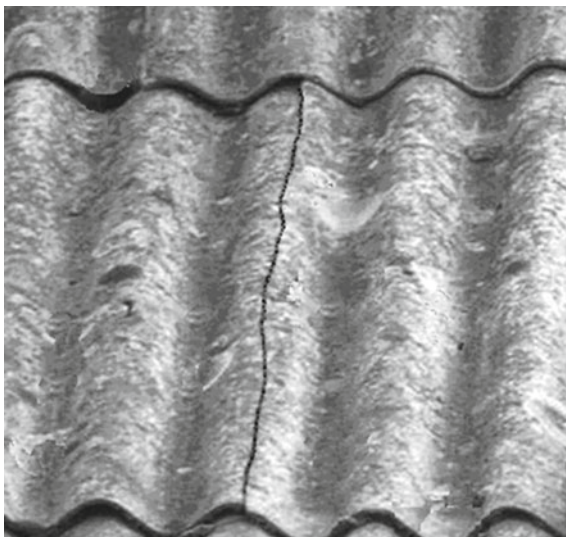
14.3.2 Strength of the Corrugated Plates

In Figs. 14.3, 14.4, 14.5, 14.6 and 14.7, we see that the maximum von Mises stress take place in the top of corrugation. As a consequence, we predict the failure of corrugated plates in the top of corrugation. Figure 14.8 presents a photo of failure of roofing slate. The crack in Fig. 14.8 has shapes close to right-lines and it is located at the top of the corrugation. It gives argument in the favor of our prediction. In Song et al. (2022), one can find an example of such a crack in a metal corrugated pipe.

Table 14.1 Energies and the in-plane overall stiffness $D_{1111}^0(e_{11})$ as function of e_{11}

| | | | | | | | | | |
|----------------------|-----------|-----------|-----------|-----------|-----------|-----------|-----------|-----------|-----------|
| U | 0,01 | 0,02 | 0,03 | 0,04 | 0,05 | 0,06 | 0,07 | 0,08 | 0,09 |
| e_{11} | 0,01 | 0,02 | 0,03 | 0,04 | 0,05 | 0,06 | 0,07 | 0,08 | 0,09 |
| $SENE$ | 7,47E + 2 | 3,04E + 3 | 6,97E + 3 | 1,26E + 4 | 2,02E + 4 | 2,97E + 4 | 4,13E + 4 | 5,52E + 4 | 7,15E + 4 |
| $D_{1111}^0(e_{11})$ | 1,17E + 7 | 1,19E + 7 | 1,21E + 7 | 1,24E + 7 | 1,26E + 7 | 1,29E + 7 | 1,32E + 7 | 1,35E + 7 | 1,38E + 7 |
| r | 1,02 | 1,04 | 1,06 | 1,08 | 1,1 | 1,12 | 1,15 | 1,17 | 1,2 |
| U | 0,1 | 0,11 | 0,12 | 0,13 | 0,14 | 0,15 | 0,16 | 0,17 | 0,18 |
| e_{11} | 0,11 | 0,12 | 0,13 | 0,14 | 0,15 | 0,16 | 0,17 | 0,18 | 0,2 |
| $SENE$ | 9,06E + 4 | 1,13E + 5 | 1,38E + 5 | 1,67E + 5 | 2,00E + 5 | 2,37E + 5 | 2,80E + 5 | 3,28E + 5 | 3,84E + 5 |
| $D_{1111}^0(e_{11})$ | 1,42E + 7 | 1,45E + 7 | 1,50E + 7 | 1,54E + 7 | 1,59E + 7 | 1,65E + 7 | 1,71E + 7 | 1,78E + 7 | 1,85E + 7 |
| R | 1,23 | 1,27 | 1,3 | 1,34 | 1,39 | 1,43 | 1,49 | 1,55 | 1,61 |
| U | 0,19 | 0,2 | 0,21 | 0,22 | 0,23 | 0,24 | 0,24 | 0,25 | 0,26 |
| e_{11} | 0,21 | 0,22 | 0,23 | 0,24 | 0,26 | 0,26 | 0,27 | 0,28 | 0,29 |
| $SENE$ | 4,47E + 5 | 5,21E + 5 | 6,06E + 5 | 7,05E + 5 | 8,22E + 5 | 9,61E + 5 | 9,61E + 5 | 1,13E + 6 | 1,33E + 6 |
| $D_{1111}^0(e_{11})$ | 1,94E + 7 | 2,03E + 7 | 2,15E + 7 | 2,28E + 7 | 2,43E + 7 | 2,43E + 7 | 2,61E + 7 | 2,82E + 7 | 3,07E + 7 |
| r | 1,69 | 1,77 | 1,87 | 1,98 | 2,12 | 2,12 | 2,27 | 2,46 | 2,68 |

Fig. 14.8 Cracks in roofing slate

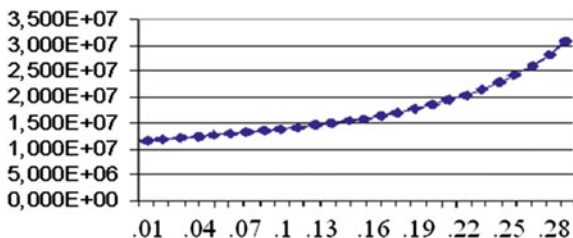


14.3.3 Transition of the Geometric Nonlinearity at Microlevel into Physical Nonlinearity at Macrolevel

Table 14.1 presents energy of the periodicity cell of corrugated plate for $e_{12} = e_{22} = 0$, $\rho_{CD} = 0$ and various (the axial tension along Ox -axis). The homogenized in-plane stiffness is computed by using formulas (14.2).

It is seen from Table 14.1 and Fig. 14.9 that the homogenized in-plane stiffness D_{1111}^0 is essentially non-linear functions of the in-plane homogenized strain e_{11} . It means that the effect of the transition of the geometric nonlinearity into physical nonlinearity as a result of homogenization really takes place for corrugated plates. Recall that in our computations the material of the plate is linear with constant Young’s modulus and Poisson ratio. The nonlinearity of the homogenized in-plane stiffness D_{1111}^0 is the result of the geometrical nonlinearity in the problem under consideration.

Fig. 14.9 The homogenized in-plane stiffness $D_{1111}^0(e_{11})$ as function of the homogenized strain e_{11}



14.3.4 Overall Bending Deformation. Bending Deformation is Described by the Problem (1) with $e_{\alpha\beta} = 0$

We consider the bending of the plate in the plane Oy_2y_3 perpendicular to the generatrix of the corrugation. It means that in (14.1) and (14.2) $e_{\alpha\beta} = 0$ and $\rho_{22} \neq 0$. We solved the geometrically non-linear problem (14.1) for values of the overall curvature ρ_{22} in the range from 0.3 to 3.1. The deformed corrugation for various curvatures is displayed in Figs. 14.10 and 14.11. The scale and the colors in Figs. 14.10 and 14.11 demonstrate the local von Mises stress.

For every overall curvature, the elastic energy (ANSYS option “Strain energy” *SENE*) of corrugation was computed by using the corresponding option of ANSYS. The computed values of the energy are presented in Table 14.2.

The distribution of the local von Mises stress in Figs. 14.10 and 14.11 look very similar to the distribution of the von Mises stress in a linear plate subjected to bending (Kolpakov and Kolpakov 2020). Nevertheless, the analysis of the data in Table 14.2 shows that the elastic energies in Table 14.2 differ from the corresponding values for the linear plate. The difference is not so strong like in the case of in-plane tension. Nevertheless, the effect of transition of the geometric nonlinearity into physical nonlinearity is clearly seen for the bending, too.

By using the strain energy *SENE* and overall curvature ρ_{11} , we determine the overall in-plane stiffness $D^2_{1111}(\rho_{11})$ from the equality

$$SENE = \frac{1}{2} D^2_{1111}(\rho_{11}) \rho_{11}^2 2L$$

The exact formulas for the stiffnesses of linear corrugated plates may be found in Ye et al. (2014); Kolpakov and Kolpakov (2020, 2014). In this paper, we do not

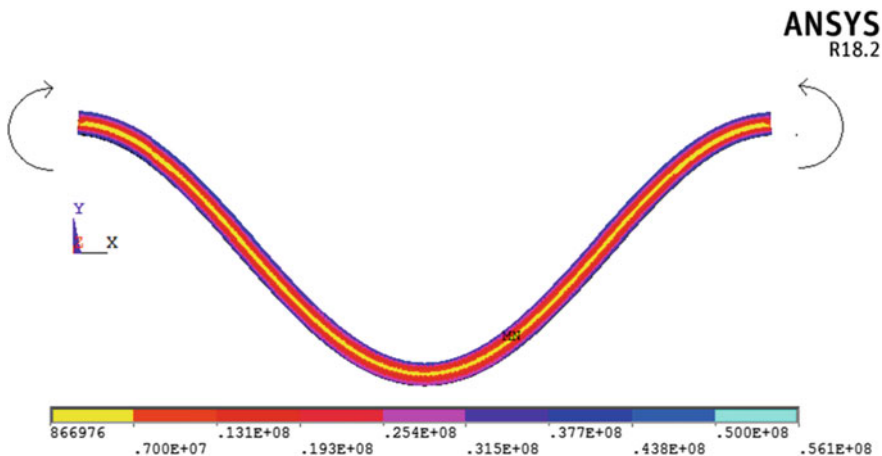


Fig. 14.10 Corrugation deformation corresponding to bending with $\rho_{11} = 0.3$

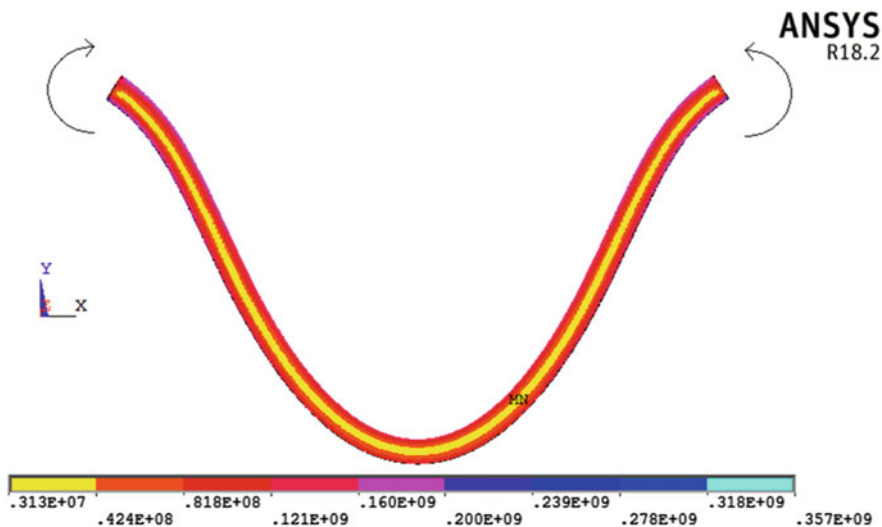


Fig. 14.11 Corrugation deformation corresponding to bending with $\rho_{11} = 1.6$

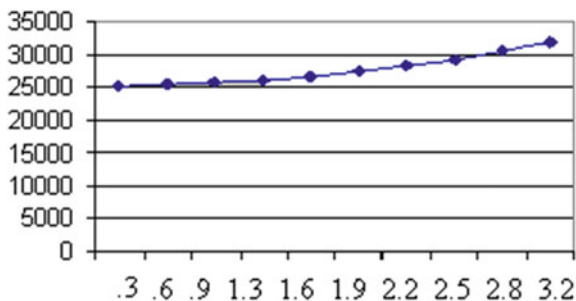
Table 14.2 The homogenized in-plane stiffness $D_{1111}^2(e_{11})$ as function of the overall curvature ρ_{11}

| ρ_{11} | 0,3 | 0,6 | 0,9 | 1,3 | 1,6 | 1,9 | 2,2 | 2,5 | 2,8 | 3,1 |
|-------------------------|--------|--------|--------|--------|--------|--------|--------|--------|--------|--------|
| SENE | 125 | 505 | 1151 | 2081 | 3322 | 4909 | 6890 | 9322 | 12,296 | 15,892 |
| $D_{1111}^2(\rho_{11})$ | 25,700 | 25,890 | 26,200 | 26,640 | 27,220 | 27,930 | 28,800 | 29,830 | 31,090 | 32,550 |
| r | 1,03 | 1,03 | 1,05 | 1,06 | 1,09 | 1,12 | 1,15 | 1,19 | 1,24 | 1,30 |

discuss the unsymmetrical (out of plane) stiffnesses $D_{ABCD}^1(e_{AB}, \rho_{AB})$. The general relations between the in-plane, the out-of-plane and the bending stiffnesses in linear plate may be found in Kolpakov (2010); Kolpakov (2007).

The computed values of $D_{1111}^2(\rho_{11})$ are presented in Table 14.2. The bending stiffness $D_{1111}^2(0) = 25,034$. In Table 14.2, $r = \frac{D_{1111}^2(\rho_{11})}{D_{1111}^2(0)}$.

Fig. 14.12 The homogenized in-plane stiffness $D_{1111}^0(e_{11})$ as function of the curvature ρ_{11}



14.4 Conclusion

Numerical analysis of the homogenized stiffnesses of a corrugated plate shows that the result of homogenization is the effect of the transition of geometric nonlinearity at the microlevel into physical (material) nonlinearity at the macrolevel. This effect is strong for the overall planar tension of the corrugated plate, and less pronounced, but still significant, for the overall bending.

For the case of non-linear deformation, as well as for linear deformation, the weakest point of the corrugated plate is the top of the corrugation.

References

- Andrianov IV, Diskovsky AA, Kholod EG (1998) Homogenization method in the theory of corrugated plates. *Tech Mech* 18:123–133
- Annin BD, Kolpakov AG, Rakin SI (2017) Homogenization of corrugated plates based on the dimension reduction for the periodicity cell problem. In: Altenbach H et al. (eds), *Mechanics for Materials and technologies. Advanced structured materials*. Springer International Publishing AG 2017, pp. 49–72
- Bartolozzi G, Pierini M, Orrenius U, Baldanzini N (2013) An equivalent material formulation for sinusoidal corrugated cores of structural sandwich panels. *Compos Struct* 100:173–185
- Buannic N, Cartraud P, Quesnel T (2003) Homogenization of corrugated core sandwich panels. *Compos Struct* 59:299–312
- Caillerie D (1984) Thin elastic and periodic plates. *Math Methods Appl Sci* 6:159–191
- Dvorak G (2013) *Micromechanics of composite materials*. Springer-Verlag, Berlin
- Hohe J, Becker W (2002) Effective stress-strain relations for two-dimensional cellular sandwich cores: Homogenization, material models, and properties. *Appl Mech Review* 55(1): 61–87
- Hornung P, Neukamm S, Velčić I (2014) Derivation of a homogenized nonlinear plate theory from 3d elasticity. *Calc Var Partial Differ Equ* 51:677–699
- Huber MT (1923) Die theorie des kreuzweise bewehrten eisenbetonplatten. *Der Bauingenieur* 4:354–360
- Kalamkarov AL, Kolpakov AG (1997) *Analysis, design and optimization of composite structures*. John Wiley & Sons, Chichester
- Kalamkarov AL, Tornabene F, Pacheco PMCL, Savi MA, Saha GC (2017) Geometrically non-linear elastic model for a thin composite layer with wavy surfaces *ZAMM—Z. Angew Math Mech* 97(11):1381–1392
- Kohn RV, Vogelius M (1984) A new model for thin plates with rapidly varying thickness. *Int J Solids Struct* 20:333–350
- Kolpakov AG (2010) *Stressed composite structures: Homogenized models for thin-walled nonhomogeneous structures with initial stresses*. Springer-Verlag, Berlin
- Kolpakov AG, Rakin SI (2016) Calculation of the effective stiffnesses of corrugated plates by solving the problem on the plate cross-section. *J Appl Mech Tech Phys* 57:757–767
- Kolpakov AA, Kolpakov AG (2019) Discussion of the effective stiffnesses in: Ye, Berdichevsky, and Yu [*Int. J. Solids Struct.* 51 (2014): 2073–2083. *Int J Solids Struct* 174–175:145–146
- Kolpakov, AA, Kolpakov AG (2020) On the effective stiffnesses of corrugated plates of various geometries. *Int J Eng Science*: 103327
- Kolpakov AG, Rakin, SI (2010) Overall and local effects in laminated elastic composite under nonlinear strains. *Mech Adv Mater Structures* 17(3): 165–175

- Kolpakov AA (2007) Design of a laminated plate possessing the required stiffness using the minimal number of materials and layers. *J Elast* 83(12/13): 964–975
- Lee CY, Yu W (2011) Homogenization and dimensional reduction of composite plates with in-plane heterogeneity. *Int J Solids Struct* 48:1474–1484
- Levinski T (1995) Effective stiffness of transversally non-homogeneous plates with unidirectional periodic structure. *Int J Solids Struct* 32(19):3261–3287
- Love AEH (1929) *A treatise on the mathematical theory of elasticity*. Cambridge University Press, London
- Sab K, Lebé A (2015) *Homogenization of thick and heterogeneous plates*. Wiley-ISTE, Hoboken
- Sanchez-Palencia E (1980) *Non-homogeneous media and vibration theory*. Springer, Berlin
- Song E, Jin Q, Cai K, Liu Y (2022) Failure analysis of the metal hose puncture and leakage in a natural gas reinjection station. *J Phys Conf Ser* 2022:012046
- Talbi N, Batti A, Ayad R, Guo YQ (2009) An analytical homogenization model for finite element modelling of corrugated cardboard. *Compos Struct* 88:280–289
- Thompson MK, Thompson JM (2017) *ANSYS Mechanical APDL for finite element analysis*. Butterworth-Heinemann, Oxford
- Xia Y, Friswell MI, Saavedra Flores EI (2012) Equivalent models of corrugated panels. *Int J Solids Struct*, 49(13):1453–1462
- Ye Z, Berdichevsky VL, Yu W (2014) An equivalent classical plate model of corrugated structures. *Int J Solids Struct* 51(11–12):2073–2083

Chapter 15

Analysis of the Nanoindentation Results Using the Graded Coatings Information System



Leonid I. Krenev, Evgeniy V. Sadyrin, Andrey L. Nikolaev,
and Sergei M. Aizikovich

Abstract The Graded Coatings information system is designed to construct solutions to a number of mixed axisymmetric boundary value problems in the theory of elasticity and thermoelasticity for continuously inhomogeneous coatings of complex structure. It can also be used to analyze the results of calculations and field experiments. The work with the information system is illustrated by the analysis of the nanoindentation results of coatings on silicon substrates obtained using pulsed laser sputtering.

15.1 Introduction

Zinc oxide is a promising semiconductor and piezoelectric material with a direct wide band gap (3.37 eV at room temperature) and a high exciton binding energy (60 meV) (Nikolaev et al. 2022). In recent years, ZnO nanostructures such as nanowires, nanorods, nanobelts, and coatings have attracted a lot of attention from various research groups (Ke et al. 2012; Liu et al. 2013) due to their unique physical properties and possible applications in nanoscale devices. ZnO nanostructures can be used as sensors (Nikolaev et al. 2019), photodetectors (Zhilin et al. 2014; Liu et al. 2019), devices based on surface acoustic waves (Karapetyan et al. 2022), actuators, displays and other NEMS elements as catalysts (Eremeyev 2016), in solar cells (Alhammedi et al. 2019), medical devices (Shetti et al. 2019), etc. ZnO nanostructures and coatings can be obtained using magnetron sputtering (Gao and Li 2004; Ellmer 2000), molec-

L. I. Krenev · E. V. Sadyrin (✉) · A. L. Nikolaev · S. M. Aizikovich
Don State Technical University, 1 Gagarin Square, 344000 Rostov-on-Don, Russia
e-mail: e.sadyrin@sci.donstu.ru

L. I. Krenev
e-mail: lkrenev@yandex.ru

A. L. Nikolaev
e-mail: andreynicolaev@eurosites.ru

S. M. Aizikovich
e-mail: saizikovich@gmail.com

© The Author(s), under exclusive license to Springer Nature Switzerland AG 2023
H. Altenbach and V. Eremeyev (eds.), *Advances in Linear and Nonlinear Continuum and Structural Mechanics*, Advanced Structured Materials 198,
https://doi.org/10.1007/978-3-031-43210-1_15

ular beam epitaxy (Chen et al. 1998; Look et al. 2002), sol-gel technology (Znaidi 2010; Hasnidawani et al. 2016), etc. However, the most flexible method is pulsed laser deposition (Jin et al. 2000; Nikolaev et al. 2021). Due to its widespread use in numerous industries, it is critical to correctly measure the mechanical properties of ZnO nanostructures (Vasiliev et al. 2018).

Over the past 50 years, the development of measuring technology has made it possible to widely use nanoindentation, that is, precision local force action on the material and registration of indenter displacement in the nanometer range (Golovin 2008; Fischer-Cripps and Nicholson 2004).

In their classic papers, Oliver and Pharr (1992, 2004) proposed a method for analyzing the results of indentation using the Berkovich indenter. This technique makes it possible to determine Young's modulus of a homogeneous sample based on the analysis of the indentation stiffness (the derivative of the load by the indentation depth) at the maximum indentation depth (Li and Bhushan 2002). In this case, the dependence of the contact area on the indentation depth is determined from calibration experiments on reference samples with previously known properties such as fused silica and sapphire.

When determining the mechanical properties of the coating, the international standard (ISO 2016) indicates that the thickness of the test sample should be large enough (or the indentation depth should be small enough) so that the influence of the substrate on the measurement result is small (Bull 2005). The thickness of the test sample must exceed the indentation depth at least 10 times or 3 times the diameter of the indentation area. When testing coatings, the thickness of the coating should be considered as the thickness of the test sample (Bouzakis et al. 2002). However, at low indentation depths, it is impossible to ensure high accuracy and repeatability of measurements (Saha and Nix 2002; Zhu et al. 2022).

To solve the problem of determining the properties of the coating and substrate, different authors mainly use numerical methods, for example, the finite element method (FEM) (Kot et al. 2013; Karimpour et al. 2013; Bouzakis et al. 2022).

Under the guidance of S. M. Aizikovich (Aizikovich et al. 2002, 2008; Krenev et al. 2015), an original numerical-analytical method for solving mixed static problems of the theory of elasticity and thermoelasticity for a continuously inhomogeneous half-space by depth with forces and sources specified on the surface was developed. Using this method in the Graded Coatings information system, it is possible to process experimental data, obtain the dependence of Young's modulus on the width of the contact area and, knowing the thickness of the coating, estimate the value of its Young's modulus.

In this paper, the results of nanoindentation of ZnO coatings of different thicknesses deposited on Si(001) substrates were analyzed.

15.2 Materials and Methods

The solution of mixed axisymmetric problems for indentation of a continuously inhomogeneous half-space is reduced to solving systems of dual integral equations, the kernel transforms of which are approximated by a quadratic rational expression. A dual integral equation with such a kernel has an exact analytical solution. When constructing kernel transforms of integral equations, the Hankel transform is used, and the system of ordinary differential equations with functional coefficients is solved numerically.

For practical application of the developed methods of numerical and analytical solution of a wide range of mixed and unmixed boundary problems of axisymmetric static theory of thermoelasticity, taking into account an arbitrary combination of laws of change of thermomechanical properties (Young's modulus, Poisson's ratio, thermal conductivity coefficient and coefficient of linear expansion), a set of programs in Fortran has been developed. The initial data for the calculation are formed in the form of a set of text files that contain tables of the values of the laws of inhomogeneous changes in thermomechanical properties, a description of the types of impacts (distributed pressure, various stamps, temperature or heat flow), a set of design parameters that affect the accuracy and time of calculation.

To preserve the results of calculations and carry out their multiparametric analysis in the future, as well as visualization of the stress-strain state of an inhomogeneous coating and its thermomechanical characteristics, a database has been developed that has been created and maintained in the PostgreSQL DBMS. The database stores the results of calculations, preceded by key attributes containing the task code and the code of the descriptor of the calculated information. In addition, there are fields for storing information about the ratio of the coating thickness to the radius of the coating impact zone, the radius and depth of the calculated points, and the calculated characteristics themselves. To process the results of experiments, the database stores descriptions of the types of indentors, a directory of materials, To carry out a multiparametric description of the materials under study with a list of properties of the substrate and layers, a module has been developed that allows creation of analytical queries to the database and visualization of the results using the Gnuplot package.

The web interface of the Graded Coatings information system is developed in Python using the Django library. The working version of the site is supported by the Apache server with the mod_wsgi module. The website is available at <http://109.195.227.87:8090>. The design of the site assumes the possibility to get acquainted with the description of the purpose of the IP and the list of tasks to be solved without registration. When registering, the user gets access to the main modes of the system, while, for the convenience of the user, samples of descriptions of the laws of changing the properties of coatings, impacts, coating themselves, and other objects are copied to the user. The site menu is shown in Fig. 15.1.

The first item is the informational one, the rest are interactive forms that allow you to work with lists of objects stored in the database. The "Theory" section presents a list of the laws of property change; a list of impacts (the punch introduction, the


Gradient coatings

Dear guest! The information system "Gradient coatings" is designed for:

- - constructing solutions to a number of mixed and unmixed boundary problems of thermoelasticity for continuously inhomogeneous coatings of complex structure simulating local thermomechanical effects on the coating;
- - analysis of the results of calculations and field experiments;
- - optimization of the process of development and creation of gradient coatings used as new materials.

More information about the site can be found [here](#)

Problems to be solved

| Thumbnail | ▲Code | Name |
|---|-----------------------|---|
|  | A | Hot smooth stamp with a flat sole. The temperature is set |
|  | P | Indentation of a smooth stamp with a flat sole |

« 1 | [2](#) »

Fig. 15.1 The main page of the website "Graded coatings". The "Service" mode is available for the administrator

growth of disc cracks, etc.); a list of various coatings; list of additional calculation parameters; list of calculation tasks with indication of specific coatings, impacts and additional parameters; lists of laws of inhomogeneity, coatings, impacts containing graphical thumbnails that help the user navigate when choosing. Each item in the list includes the "Edit" and "Delete" buttons, and there is an "Add" item in the header of the table. Thus, the user has the ability to add, modify, and delete any objects. In addition, there is a button "Add a copy", with its help it facilitates the creation of complex objects that differ little from the previous ones. The "Experiment" mode is designed to process the results of nanoindentation. The lists "Types of indentors" and "Materials Directory" contain common entries for the information system, which cannot be deleted or changed, but the user can make his or her own entries. The list of "Materials under study" allows one to describe the structure of the coating. When working with the "Research results" item, the user specifies a specific indenter and the material under study and must submit archived directories with "force-displacement-time" files for processing. The files must be in text format or in the original ".idr" format. Data processing is carried out using the Oliver-Pharr method. All parameters are editable. As a result, a table with calculated characteristics for all experiments grouped by source files is displayed. The user can withdraw individual experiments or files from consideration and recalculate the result. For a

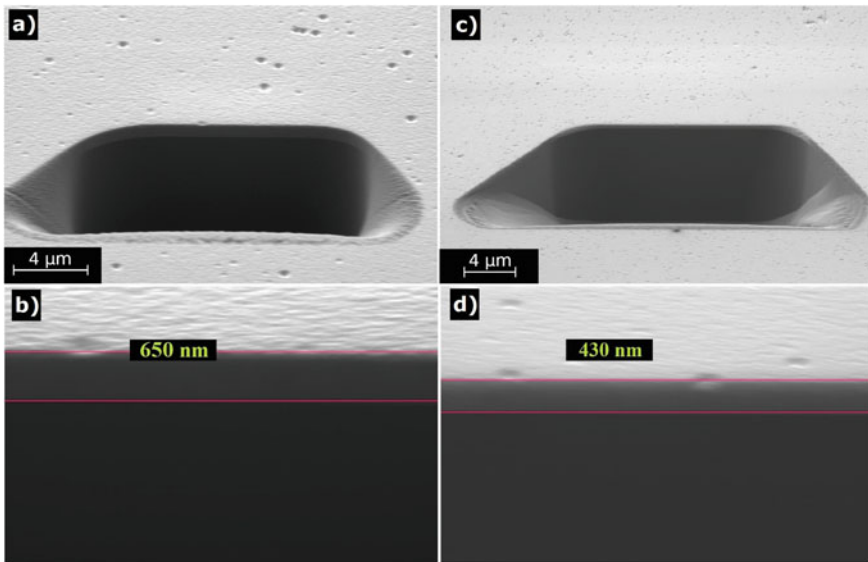


Fig. 15.2 Measurement of the thickness of the ZnO coating with a thickness of 650 nm (a, b) and 430 nm (c, d) using SEM

real experimental study, samples of ZnO coatings on Si (001) substrates obtained by pulsed laser sputtering were selected. The coating thickness was measured using a Crossbeam 340 scanning electron microscope (SEM, Carl Zeiss Microscopy GmbH, Germany) using an Everhart-Thornley detector and an accelerating voltage of 1.5 kV. To do this, a cross-section was made in the coating by means of a focused ion beam (Fig. 15.2).

To assess the mechanical properties of the coating, a series of nanoindentation experiments were carried out on the Nanotest 600 Platform 3 (Micro Materials, UK) unit using a Berkovich diamond indenter. To evaluate the properties of ZnO coatings, a series of 12 indentations with an increasing force from 1 to 200 mN were performed at a distance of at least 5 diameters of the indentation sites from each other, while the corresponding maximum indentation depth varied from 30 nm to 955 nm. The value of Poisson's ratio ZnO was assumed to be $\nu = 0.25$.

15.3 Results and Discussion

With the help of the Graded Coatings information system, using the example of the analysis of the results of indentation of Si substrates and ZnO coatings described earlier, Young's modulus of coatings was calculated. Figure 15.3 shows the results of determining Young's modulus for homogeneous silicon and silicon coated with zinc

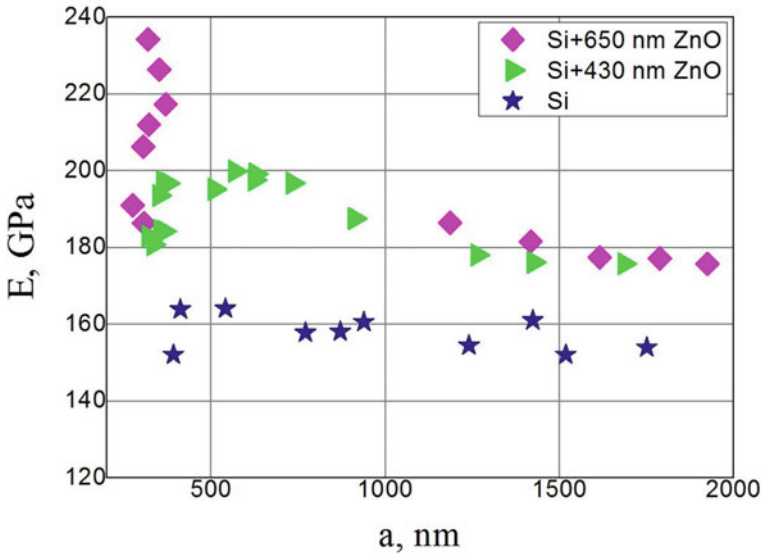


Fig. 15.3 Change in the calculated Young's modulus Si, Si+650 nm Zn and Si+430 nm ZnO depending on the radius of the calculated contact area

oxide with a thickness of 430 nm and 650 nm, depending on the calculated radius of the contact area.

In the "Theory" and "Calculations" mode, it is possible to set a series of calculation parameters. Using them, a series of calculations was carried out for the ratio of the coating modulus to the substrate modulus from 1/5 to 5, with a change in the ratio of the radius of the contact area to the coating thickness from 0 to 4. The results are shown in Fig. 15.4.

The table of calculation results shown on the graph is embedded in the calculation module of the "Research Results" mode. Understanding the coating thickness and Young's modulus of the substrate, one can estimate Young's modulus of the coating for each experiment. Figure 15.5 shows the results of calculating Young's modulus of coatings with a thickness of 650 nm and 430 nm, depending on the ratio of the radius of the contact area to the coating thickness. Despite the large spread at the beginning of the diagram, it can be assumed that Young's ZnO modulus is 250 GPa.

Figure 15.6 compares the theoretical curves of Young's modulus of the coating-substrate system and the results of nanoindentation. It is possible to note a good coincidence of the results in the area of a small spread of experimental data.

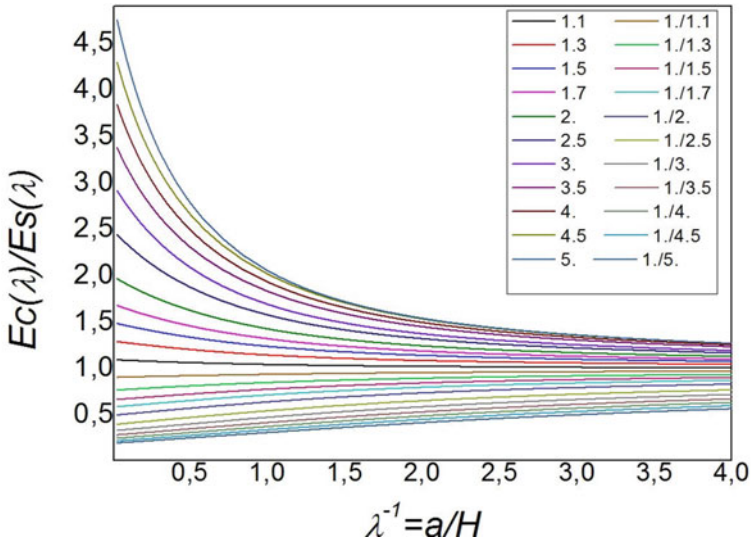


Fig. 15.4 Diagrams of the stiffness behavior for a series of relations of Young’s modulus of the coating and the substrate

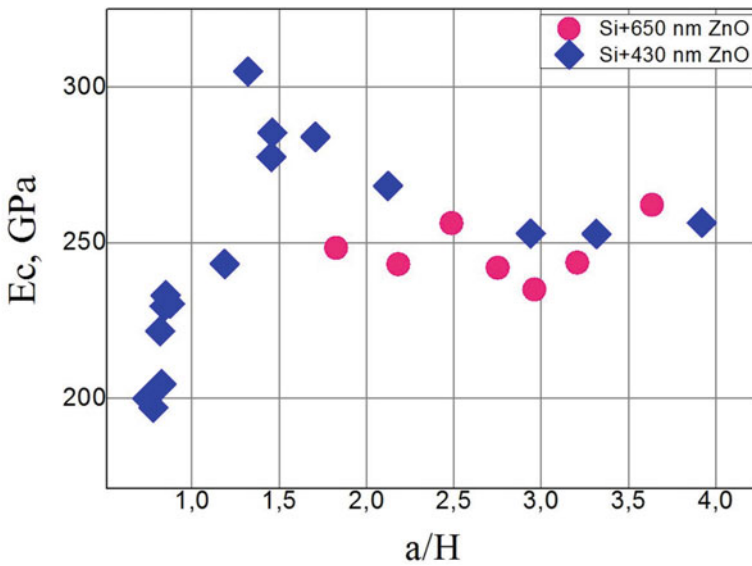


Fig. 15.5 The result of the evaluation of Young’s modulus of ZnO

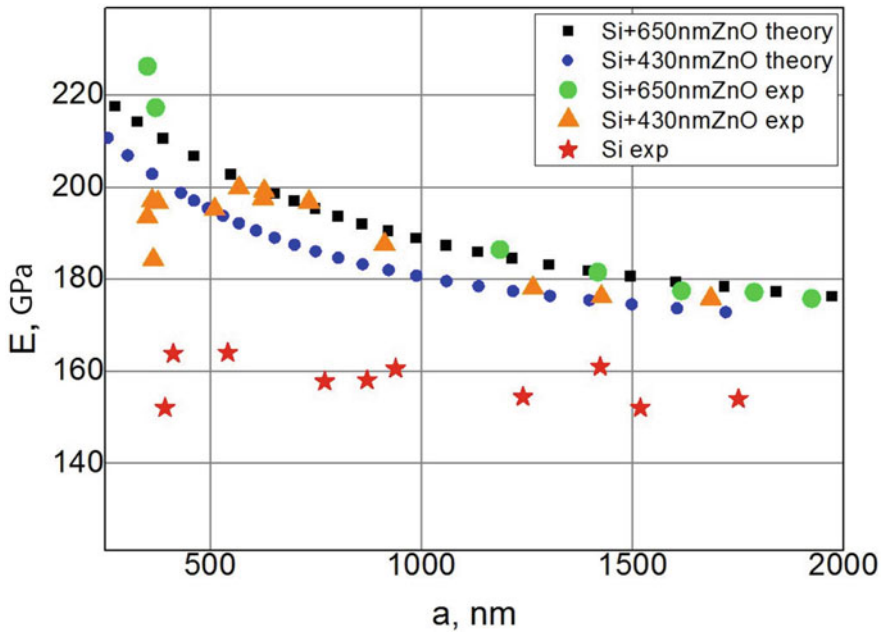


Fig. 15.6 Comparison of theoretical and experimental data with the value of Young's modulus ZnO equal to 250 GPa

15.4 Conclusion

The paper presents a brief description of the information system Graded Coatings, designed to construct solutions to mixed axisymmetric boundary problems of elasticity and thermoelasticity for continuously inhomogeneous coatings of complex structure, as well as to analyze the results of calculations and experimental data. The capabilities of the system in the analysis of experimental data are demonstrated. Based on the results of nanoindentation, the values of Young's modulus (250 GPa) of two ZnO coatings (430 nm and 650 nm) obtained by pulsed laser sputtering on Si (001) substrates were determined. The usage of the system may be further extended to other types of materials of the complex structure with the varying by depth mechanical characteristics such as artificial (Liu et al. 2021; Dubey et al. 2020) and natural (Zelentsov et al. 2023; Sadyrin 2022; Sadyrin et al. 2021) biomaterials.

Acknowledgements The work was supported by the Russian Science Foundation, grant number 22-49-08014, <https://rscf.ru/en/project/22-49-08014/>. All experiments were conducted in the Nanocenter of Don State Technical University (<http://nano.donstu.ru>).

References

- Aizikovich SM, Aleksandrov VM, Trubchik IS, Krenev LI (2008) Introduction of a spherical indenter into a half-space with a functionally graded elastic coating. *Dokl Phys* 53(1):29–33. <https://doi.org/10.1134/S1028335808010084>
- Aizikovich SM, Alexandrov VM, Kalker JJ, Krenev LI, Trubchik I (2002) Analytical solution of the spherical indentation problem for a half-space with gradients with the depth elastic properties. *Int J Solids Struct* 39(10):2745–2772. [https://doi.org/10.1016/S0020-7683\(02\)00124-5](https://doi.org/10.1016/S0020-7683(02)00124-5)
- Alhammadi S, Park H, Kim WK (2019) Optimization of intrinsic ZnO thickness in Cu (In, Ga) Se₂-based thin film solar cells. *Materials* 12(9):1365. <https://doi.org/10.3390/ma12091365>
- Bouzakis KD, Michailidis N, Hadjiyiannis S, Skordaris G, Erkens G (2002) The effect of specimen roughness and indenter tip geometry on the determination accuracy of thin hard coatings stress-strain laws by nanoindentation. *Mater Charact* 49(2):149–156. [https://doi.org/10.1016/S1044-5803\(02\)00361-3](https://doi.org/10.1016/S1044-5803(02)00361-3)
- Bouzakis KD, Michailidis N, Hadjiyiannis S, Skordaris G, Erkens G (2022) Continuous FEM simulation of the nanoindentation: actual indenter tip geometries, material elastoplastic deformation laws and universal hardness. *Int J Mater Res* 93(9):862–869
- Bull SJ (2005) Nanoindentation of coatings. *J Phys D: Appl Phys*, 38(24):R393. <https://doi.org/10.1088/0022-3727/38/24/R01>
- Chen Y, Bagnall DM, Koh HJ, Park KT, Hiraga K, Zhu Z, Yao T (1998) Plasma assisted molecular beam epitaxy of ZnO on c-plane sapphire: growth and characterization. *J Appl Phys* 84(7):3912–3918. <https://doi.org/10.1063/1.368595>
- Dubey A, Jaiswal S, Haldar S, Roy P, Lahiri D (2020) Functionally gradient magnesium-based composite for temporary orthopaedic implant with improved corrosion resistance and osteogenic properties. *Biomed Mater* 16(1):015017. <https://doi.org/10.1088/1748-605X/abb721>
- Ellmer K (2000) Magnetron sputtering of transparent conductive zinc oxide: relation between the sputtering parameters and the electronic properties. *J Phys D: Appl Phys* 33(4):R17. <https://doi.org/10.1088/0022-3727/33/4/201>
- Eremeyev VA (2016) On effective properties of materials at the nano- and microscales considering surface effects. *Acta Mech* 227(1):29–42. <https://doi.org/10.1007/s00707-015-1427-y>
- Fischer-Cripps AC, Nicholson DW (2004) Nanoindentation. Mechanical engineering series. *Appl Mech Rev* 57(2):B12-B12. <https://doi.org/10.1115/1.1704625>
- Gao W, Li Z (2004) ZnO thin films produced by magnetron sputtering. *Ceram Int* 30(7):1155–1159. <https://doi.org/10.1016/j.ceramint.2003.12.197>
- Golovin YI (2008) Nanoindentation and mechanical properties of solids in submicrovolumes, thin near-surface layers, and films: a Review. *Phys Solid State* 50(12):2205–2236. <https://doi.org/10.1134/S1063783408120019>
- Hasnidawani JN, Azlina HN, Norita H, Bonnia NN, Ratim S, Ali ES (2016) Synthesis of ZnO nanostructures using sol-gel method. *Procedia Chem* 19:211–216. <https://doi.org/10.1016/j.proche.2016.03.095>
- ISO 14577-4:2016 Metallic materials—Instrumented indentation test for hardness and materials parameters—Part 4: Test method for metallic and non-metallic coatings
- Jin BJ, Bae S, Lee SY, Im S (2000) Effects of native defects on optical and electrical properties of ZnO prepared by pulsed laser deposition. *Mater Sci Eng: B* 71(1–3):301–305. [https://doi.org/10.1016/S0921-5107\(99\)00395-5](https://doi.org/10.1016/S0921-5107(99)00395-5)
- Karapetyan GY, Kutepov ME, Kaidashev EM, Nikolaev AL (2022) Creation and research of the SAW transducer with a single-phase grid and a piezoelectric zinc oxide film. *J Adv Dielectr* 12(5):2250016–2250016. <https://doi.org/10.1142/S2010135X22500163>
- Karimpour M, Balint DS, Rzepiejewska-Malyska KA, Szerling A, Michler J, Lin J (2013) An inverse method for extracting the mechanical properties of the constituent materials of a multilayer from nanoindentation data. *Comput Mater Sci* 68:384–390. <https://doi.org/10.1016/j.commatsci.2012.11.007>

- Ke LL, Wang YS, Wang ZD (2012) Nonlinear vibration of the piezoelectric nanobeams based on the nonlocal theory. *Compos Struct* 94(6):2038–2047. <https://doi.org/10.1016/j.compstruct.2012.01.023>
- Kot M, Rakowski W, Lackner JM, Major, Ł (2013) Analysis of spherical indentations of coating-substrate systems: experiments and finite element modeling. *Mater Des* 43:99–111 (2013). <https://doi.org/10.1016/j.matdes.2012.06.040>
- Krenev LI, Aizikovich SM, Tokovyy YV, Wang YC (2015) Axisymmetric problem on the indentation of a hot circular punch into an arbitrarily nonhomogeneous half-space. *Int J Solids Struct* 59:18–28. <https://doi.org/10.1016/j.ijsolstr.2014.12.017>
- Li X, Bhushan B (2002) A review of nanoindentation continuous stiffness measurement technique and its applications. *Mater Charact* 48(1):11–36. [https://doi.org/10.1016/S1044-5803\(02\)00192-4](https://doi.org/10.1016/S1044-5803(02)00192-4)
- Liu C, Ke LL, Wang YS, Yang J, Kitipornchai S (2013) Thermo-electro-mechanical vibration of piezoelectric nanoplates based on the nonlocal theory. *Compos Struct* 106:167–174. <https://doi.org/10.1016/j.compstruct.2013.05.031>
- Liu D, Ma Z, Zhao H, Ren L, Zhang W (2021) Nano-indentation of biomimetic artificial bone material based on porous Ti6Al4V substrate with Fe₂₂Co₂₂Ni₂₂Ti₂₂Al₁₂ high entropy alloy coating. *Mater Today Commun* 28:102659. <https://doi.org/10.1016/j.mtcomm.2021.102659>
- Liu J, Wang Y, Ma J, Peng Y, Wang A (2019) A review on bidirectional analogies between the photocatalysis and antibacterial properties of ZnO. *J Alloy Compd* 783:898–918. <https://doi.org/10.1016/j.jallcom.2018.12.330>
- Look DC, Reynolds DC, Litton CW, Jones RL, Eason DB, Cantwell G (2002) Characterization of homoepitaxial p-type ZnO grown by molecular beam epitaxy. *Appl Phys Lett* 81(10):1830–1832. <https://doi.org/10.1063/1.1504875>
- Nikolaev AL, Kaidashev EM, Kamencev AS (2019) Morphology and photoluminescence of zinc oxide nanorods obtained by carbothermal synthesis at different temperatures. In: *Advanced materials: proceedings of the international conference on “physics and mechanics of new materials and their applications”, PHENMA 2018*. Springer International Publishing, pp 103–113. https://doi.org/10.1007/978-3-030-19894-7_9
- Nikolaev AL, Kamencev AS, Lyanguzov NV, Aizikovich SM (2021) Pulsed laser deposition of Au nanoparticles on ZnO nanostructures. In: *IOP conference series: materials science and engineering*, vol 1029, p 012064 (2021). <https://doi.org/10.1088/1757-899X/1029/1/012064>
- Nikolaev AL, Kazmina MA, Lyanguzov NV, Abdulvakhidov KG, Kaidashev EM (2022) Synthesis of ZnO nanorods for piezoelectric resonators and sensors. *J Adv Dielectr* 12(01):2160020. <https://doi.org/10.1142/S2010135X21600201>
- Oliver WC, Pharr GM (1992) An improved technique for determining hardness and elastic modulus using load and displacement sensing indentation experiments. *J Mater Res* 7(6):1564–1583. <https://doi.org/10.1557/JMR.1992.1564>
- Oliver WC, Pharr GM (2004) Measurement of hardness and elastic modulus by instrumented indentation: Advances in understanding and refinements to methodology. *J Mater Res* 19(1):3–20. <https://doi.org/10.1557/jmr.2004.19.1.3>
- Sadyrin EV, Mitrin BI, Yogina DV, Swain MV (2021) Preliminary study of distribution of mechanical properties and mineral density by depth of liquid saturated carious dentine. *IOP Conf Ser: Mater Sci Eng* 1029(1):012056; IOP Publishing. <https://doi.org/10.1088/1757-899X/1029/1/012056>
- Sadyrin EV (2022) Correlating the mechanical properties to the mineral density of brown spot lesion in dentine using nanoindentation and x-ray micro-tomography. In: *Advanced materials modelling for mechanical, medical and biological applications*. Springer International Publishing, pp 389–398. https://doi.org/10.1007/978-3-030-81705-3_21
- Saha R, Nix WD (2002) Effects of the substrate on the determination of thin film mechanical properties by nanoindentation. *Acta Mater* 50(1):23–38. [https://doi.org/10.1016/S1359-6454\(01\)00328-7](https://doi.org/10.1016/S1359-6454(01)00328-7)

- Shetti NP, Bukkitgar SD, Reddy KR, Reddy CV, Aminabhavi TM (2019) ZnO-based nanostructured electrodes for electrochemical sensors and biosensors in biomedical applications. *Biosens Bioelectron* 141:111417. <https://doi.org/10.1016/j.bios.2019.111417>
- Vasiliev AS, Sadyrin EV, Mitrin BI, Aizikovich SM, Nikolaev AL (2018) Nanoindentation of ZrN coatings on silicon and copper substrates. *Russ Eng Res* 38:735–737. <https://doi.org/10.3103/S1068798X18090289>
- Zelentsov VB, Sadyrin EV, Mitrin BI, Swain MV (2023) Mathematical tools for recovery of the load on the fissure according to the micro-CT results. *J Mech Behav Biomed Mater* 138:105625. <https://doi.org/10.1016/j.jmbbm.2022.105625>
- Zhilin DA, Lyanguzov NV, Nikolaev LA, Pushkariov VI, Kaidashev EM (2014) Photoelectric properties of MSM structure based on ZnO nanorods, received by thermal evaporation and carbothermal synthesis. *J Phys: Conf Ser* 541:012038. <https://doi.org/10.1088/1742-6596/541/1/012038>
- Zhu P, Zhao Y, Agarwal S, Henry J, Zinkle SJ (2022) Toward accurate evaluation of bulk hardness from nanoindentation testing at low indent depths. *Mater Des* 213:110317 (2022). <https://doi.org/10.1016/j.matdes.2021.110317>
- Znaidi L (2010) Sol-gel-deposited ZnO thin films: a review. *Mater Sci Eng: B* 174(1–3):18–30. <https://doi.org/10.1016/j.mseb.2010.07.001>

Chapter 16

On the Influence of Transversal Isotropy on the Exact Solution of a Problem of Imposing Finite Deformations in a Composite Nonlinear Elastic Slab with Prestressed Layers



Vladimir A. Levin, Konstantin M. Zingerman, and Anton E. Belkin

Abstract The paper presents a mathematical statement and obtains an exact analytical solution to the problem of the theory of finite deformations imposition on the equilibrium of a composite plate made by joining cylindrical layers of nonlinear elastic incompressible transversally isotropic materials. Initially unstressed layers go through two stages of deformation. The first stage corresponds to straightening and joining the layers. The second stage corresponds to the stretching of the formed single plate. Expressions for the stresses in the slab in the final state are obtained and restrictions on the directions of transversal isotropy are revealed, under which the exact analytical solution of the problem can be obtained.

Keywords Finite deformations · Transversal isotropy · Nonlinear elasticity · Analytical solution · Deformation imposition

These authors contributed equally to this work.

V. A. Levin (✉)

Mechanics and Mathematics Department, Lomonosov Moscow State University, Moscow, Russian Federation

e-mail: v.a.levin@mail.ru

K. M. Zingerman

Mechanics and Mathematics Department, Tver State University, Tver, Russian Federation

e-mail: zingerman@rambler.ru

A. E. Belkin

Mechanics and Mathematics Department, Tula State University, Tula, Russian Federation

e-mail: antonedurd2020@mail.ru

16.1 Introduction

One of the most important and relevant sections of solid mechanics is the theory of finite deformations. This branch of mechanics deals with such motions of bodies in which the deformations of the particles are large enough so that the assumptions inherent in the theory of small deformations, for example, the principle of linear superposition, were not applicable. Accounting for nonlinear effects associated with the finiteness of deformations is important in formulating the constitutive relations of continuum mechanics (Truesdell 1972; Lurie 1990).

The development of research in the field of finite deformations is the theory of multiple imposition of finite deformations, designed to model the deformation of bodies in several stages, when finite deformations occur in the body at each stage.

Many works are devoted to problems related to the repeated imposition of large deformations on bodies that are not linearly elastic.

In Levin (1998), the main constitutive relations and boundary value problems of the theory of multiple imposition of large deformations of elastic and viscoelastic materials are presented. Another class of problems of the imposition of additional finite deformations is solved by Levin and Zingerman (1998). In this work, the elastic interaction of holes, micropores, and narrow slots (cracks) introduced (arising) sequentially or simultaneously in preloaded bodies at finite deformations is analyzed.

It is of large importance to find exact analytical solutions to problems in the theory of superposition of large deformations (Zingerman et al. 2022). Among the problems for which exact solutions are obtained is the problem of tension-compression of a composite slab obtained by joining pre-deformed layers, which initially have the shape of sectors of hollow circular cylinders. For a special class of micropolar physically linear compressible isotropic elastic materials, the exact analytical solution of this problem was found in Levin et al. (2021). For incompressible isotropic nonlinear elastic materials whose mechanical properties are described by the Treloar (neo-Hookean) potential (Treloar 1975), the solution to this problem was obtained in Levin et al. (2020). In this article, a solution to a similar problem in a slightly different formulation is obtained. In contrast to Levin et al. (2020, 2021), where the axes of the sectors of circular cylinders in the initial state are mutually orthogonal, in this article it is assumed that these axes are parallel. The solution is obtained for incompressible transversally isotropic nonlinear elastic materials. The constitutive relations proposed in Merodio and Ogden (2002, 2005) are used.

In the work Levin et al. (2015), a method and algorithm for numerical evaluation of the effective mechanical properties of rubber-cord compositions are developed, taking into account finite deformations and low compressibility of rubber. The work Levin et al. (2018) is devoted to the model of a compressible orthotropic nonlinear elastic material, for which a number of exact analytical solutions are possible at large deformations. Using this model of elastic materials, an exact solution to the problem of bending a composite beam with pre-deformed layers under large deformations is obtained. The solution was obtained using the theory of superposition of large deformations. Numerical results are shown. Nonlinear effects and anisotropy effects are

investigated. The article Levin et al. (2014) deals with the static problem of torsion of a cylinder made of incompressible nonlinear elastic materials under large deformations. The cylinder contains a central round cylindrical inclusion, initially twisted, and stretched (or compressed) along the axis and fastened to a non-deformable outer hollow cylinder.

16.2 Description of the Initial Configuration and Problem Statement

The deformable elastic bodies considered in the problem are M cylindrical incompressible transversally isotropic layers, numbered from 1 to M and each equipped with its own cylindrical coordinate system (r_i, φ_i, z_i) , where i is the layer number. Layer S_i in its coordinate system in the initial configuration is described as a set:

$$S_i = \{(r_i, \varphi_i, z_i)\}$$

where

$$r_{si} \leq r_i \leq r_{fi},$$

$$\varphi_{si} \leq \varphi_i \leq \varphi_{fi},$$

$$z_{si} \leq z_i \leq z_{fi},$$

$r_{si}, r_{fi}, \varphi_{si}, \varphi_{fi}, z_{si}, z_{fi}$ are the given boundary values that determine the layer size for each coordinate. Each layer is associated with a rectangular Cartesian coordinate system (x_i, y_i, z_i) , that is associated with the cylindrical coordinate system by relations:

$$x_i = r_i \cos \varphi_i, y_i = r_i \sin \varphi_i, z_i = z_i \quad (16.1)$$

The material of each i th layer is transversely isotropic, its properties are described by the constitutive relation (Merodio and Ogden 2002, 2005)

$$\mathbf{T}_i = \mu_i \mathbf{F}_i + 2\mu_i \gamma_i (\mathbf{A}_i \cdot \mathbf{A}_i - 1) \mathbf{A}_i \otimes \mathbf{A}_i - p_i \mathbf{I} \quad (16.2)$$

where \mathbf{I} is unit tensor; μ_i and γ_i are material constants; \mathbf{T}_i —true stress tensor; \mathbf{P}_i —deformation gradient; $\mathbf{F}_i = \mathbf{P}_i \cdot \mathbf{P}_i^T$ —the Finger deformation measure; p_i —the Lagrange multiplier; \otimes —tensor product.

Vector $\mathbf{A}_i = \mathbf{P}_i \cdot \mathbf{A}_i^0$ determines the direction of transversal isotropy in the deformed state, and vector \mathbf{A}_i^0 determines the direction of transversal isotropy in the initial (undeformed) state (Merodio and Ogden 2002, 2005). In other words, vector \mathbf{A}_i^0 is directed perpendicular to the isotropy surfaces. In a cylindrical coordinate system (r_i, φ_i, z_i) vector \mathbf{A}_i^0 can be written as

$$\mathbf{A}_i^0 = A_{r_i} \mathbf{e}_r + A_{\varphi_i} \mathbf{e}_\varphi + A_{z_i} \mathbf{e}_z \quad (16.3)$$

One of the goals of work is to clarify the restrictions imposed on the components of the vector \mathbf{A}_i^0 , under which an exact analytical solution of the problem can be obtained.

Layers go through three states—initial, intermediate, and final. The transition from the initial state to the intermediate state and from the intermediate to the final state are, respectively, the first and second stages (phases) of deformation. At the first stage, all cylindrical layers are unbent in such a way that their outer and inner boundaries become flat. At the same time, the layers are connected, forming a single composite slab in the intermediate state. At the second stage, an additional deformation is applied. The composite plate is subjected to tension-compression in two directions, orthogonal to the direction of connection of the initial layers. A more detailed description of the stages of deformation is given below when listing the equations included in the mathematical formulation of the problem.

In what follows, the gradients of initial, additional, and total deformation are denoted by $\mathbf{P}_i^{\text{init}}$, $\mathbf{P}_i^{\text{add}}$, $\mathbf{P}_i^{\text{fin}}$, respectively. For the remaining tensors in equation (2) related to the intermediate configuration, the designation “int” is used; for tensors related to the final configuration—the designation “fin” is used.

The goal of the solution is to calculate the components of the stress tensor in the final state.

16.3 Mathematical Statement of the Problem

Let us present the mathematical formulation of the problem, which includes the following equations describing the deformation of the layers at both stages:

The equations describing the motion of layers for the first and second stages of deformation, respectively:

$$x = u_i(r_i), y = \tau_i \varphi_i, z = \alpha_i z_i \quad (16.4)$$

$$X = U(x) = U_i(r_i), Y = \beta_1 y, Z = \beta_2 z \quad (16.5)$$

where τ_i, α_i are the given constants of the first stage of deformation (i is the layer number); β_1, β_2 are given constants of the second stage of deformation; u_i, U, U_i are unknown functions.

Deformation gradient expression (Truesdell 1972; Levin 1998) for the first and second stages of deformation, respectively:

$$\mathbf{P}_i^{\text{init}} = \begin{pmatrix} \frac{\partial x}{\partial x_i} & \frac{\partial x}{\partial y_i} & \frac{\partial x}{\partial z_i} \\ \frac{\partial y}{\partial x_i} & \frac{\partial y}{\partial y_i} & \frac{\partial y}{\partial z_i} \\ \frac{\partial z}{\partial x_i} & \frac{\partial z}{\partial y_i} & \frac{\partial z}{\partial z_i} \end{pmatrix} \mathbf{P}_i^{\text{fin}} = \mathbf{P}_i^{\text{add}} \cdot \mathbf{P}_i^{\text{init}} = \begin{pmatrix} \frac{\partial X}{\partial x} & \frac{\partial X}{\partial y} & \frac{\partial X}{\partial z} \\ \frac{\partial Y}{\partial x} & \frac{\partial Y}{\partial y} & \frac{\partial Y}{\partial z} \\ \frac{\partial Z}{\partial x} & \frac{\partial Z}{\partial y} & \frac{\partial Z}{\partial z} \end{pmatrix} \cdot \mathbf{P}_i^{\text{init}}, \quad (16.6)$$

Incompressibility constraint for the first and second stages of deformation, respectively:

$$\det \mathbf{P}_i^{\text{init}} = 1, \det \mathbf{P}_i^{\text{add}} = 1 \quad (16.7)$$

Boundary conditions for gluing layers for the first and second stages of deformation, respectively:

$$u_1(r_{s1}) = 0 \quad (16.8)$$

$$u_{i-1}(r_{f_{i-1}}) = u_i(r_{s_i}), i = 2, \dots, M \quad (16.9)$$

$$U_1(r_{s1}) = 0 \quad (16.10)$$

$$U_{i-1}(r_{f_{i-1}}) = U_i(r_{s_i}), i = 2, \dots, M \quad (16.11)$$

Constitutive relation for intermediate and final states:

$$\mathbf{T}_i^{\text{int}} = \mu_i \mathbf{F}_i^{\text{int}} + 2\mu_i \gamma_i (\mathbf{A}_i^{\text{int}} \cdot \mathbf{A}_i^{\text{int}} - 1) \mathbf{A}_i^{\text{int}} \otimes \mathbf{A}_i^{\text{int}} - p_i \mathbf{I} \quad (16.12)$$

$$\mathbf{T}_i^{\text{fin}} = \mu_i \mathbf{F}_i^{\text{fin}} + 2\mu_i \gamma_i (\mathbf{A}_i^{\text{fin}} \cdot \mathbf{A}_i^{\text{fin}} - 1) \mathbf{A}_i^{\text{fin}} \otimes \mathbf{A}_i^{\text{fin}} - p_i \mathbf{I} \quad (16.13)$$

$$\mathbf{F}_i^{\text{init}} = \mathbf{P}_i^{\text{init}} \cdot (\mathbf{P}_i^{\text{init}})^T, \mathbf{F}_i^{\text{fin}} = \mathbf{P}_i^{\text{fin}} \cdot (\mathbf{P}_i^{\text{fin}})^T, \quad (16.14)$$

Change in the direction of the vector characterizing the transversal isotropy after the initial and additional deformation:

$$\mathbf{A}_i^{\text{init}} = \mathbf{P}_i^{\text{init}} \cdot \mathbf{A}_i, \mathbf{A}_i^{\text{fin}} = \mathbf{P}_i^{\text{add}} \cdot \mathbf{A}_i^{\text{init}} \quad (16.15)$$

Equilibrium equation for intermediate and final states:

$$\nabla^{\text{int}} \cdot \mathbf{T}_i^{\text{int}} = 0, \nabla^{\text{fin}} \cdot \mathbf{T}_i^{\text{fin}} = 0, \quad (16.16)$$

Boundary conditions for intermediate and final states:

$$\mathbf{N}^{\text{int}} \cdot \mathbf{T}_1^{\text{int}} \Big|_{x=u_1(r_{s1})} = 0, \mathbf{N}^{\text{fin}} \cdot \mathbf{T}_{X=U_1}^{\text{fin}} \Big|_{x=U_1(r_{s1})} = 0, \quad (16.17)$$

$$\mathbf{N}^{\text{int}} \cdot \mathbf{T}_{x=u_M}^{\text{int}} \Big|_{x=u_M(r_{fM})} = 0, \mathbf{N}^{\text{fin}} \cdot \mathbf{T}_{X=U_M}^{\text{fin}} \Big|_{X=U_M(r_{fM})} = 0, \quad (16.18)$$

$$\mathbf{N}^{\text{int}} \cdot \mathbf{T}_{x=u_{i-1}}^{\text{int}} \Big|_{x=u_{i-1}(r_{fi-1})} = \mathbf{N}^{\text{int}} \cdot \mathbf{T}_{x=u_i}^{\text{int}} \Big|_{x=u_i(r_{si})}, i = 2, \dots, M-1 \quad (16.19)$$

$$\mathbf{N}^{\text{fin}} \cdot \mathbf{T}_{X=U_{i-1}}^{\text{fin}} \Big|_{X=U_{i-1}(r_{fi-1})} = \mathbf{N}^{\text{fin}} \cdot \mathbf{T}_{X=U_i}^{\text{fin}} \Big|_{X=U_i(r_{si})}, i = 2, \dots, M-1 \quad (16.20)$$

16.4 Determining the Coordinates of the Points of the Layers in the Intermediate and Final Configurations

The deformation gradient $\mathbf{P}_i^{\text{init}}$, based on the first formula (16.6), is written as follows

$$\mathbf{P}_i^{\text{init}} = \begin{pmatrix} u'_i(r_i) \cos \varphi_i & u'_i(r_i) \sin \varphi^{(i)} & 0 \\ -\frac{\tau_i \sin \varphi_i}{r_i} & \frac{\tau_i \cos \varphi_i}{r_i} & 0 \\ 0 & 0 & \alpha_i \end{pmatrix} \quad (16.21)$$

where $u'_i(r_i) = \frac{du_i(r_i)}{dr_i}$.

Then the first equation (16.7) takes the form of an ordinary linear differential equation of the first order:

$$u'_i(r_i) = \frac{r_i}{\alpha_i \tau_i} \quad (16.22)$$

For $i = 1$, equation (16.22) is supplemented with the initial condition (16.8), for $i > 1$ —with condition (16.9). The solution of the Cauchy problem (16.22), (16.8) and (16.9) allows us to determine the radial deformation function at the first stage

$$u_1(r_1) = \frac{(r_1)^2 - (r_{s1})^2}{2\alpha_1 \tau_1} \quad (16.23)$$

$$u_i(r_i) = \frac{(r_i)^2 - (r_{s1})^2}{2\alpha_i \tau_i} + u_{i-1}(r_{s_{i-1}}), \quad i = 2, \dots, M \quad (16.24)$$

The deformation gradient $\mathbf{P}_i^{\text{add}}$, based on the second formula (16.6), is written as follows:

$$\mathbf{P}_i^{\text{add}} = \begin{pmatrix} U'_i(r_i) (u'_i(r_i))^{-1} & 0 & 0 \\ 0 & \beta_1 & 0 \\ 0 & 0 & \beta_2 \end{pmatrix} \quad (16.25)$$

where $U'_i(r_i) = \frac{dU_i(r_i)}{dr_i}$.

Then the second equation (16.7) takes the form of an ordinary linear differential equation of the first order:

$$U'_i(r_i) = \frac{u'_i(r_i)}{\beta_1 \beta_2} \quad (16.26)$$

For $i = 1$, equation (16.26) is supplemented with the initial condition (16.10), for $i > 1$ —with condition (16.11). The solution of the Cauchy problem (16.26), (16.10) and (16.11) allows us to determine the radial deformation function at the second stage:

$$U_1(r_1) = \frac{(r_1)^2 - (r_{s1})^2}{2\alpha_1 \tau_1 \beta_1 \beta_2} \quad (16.27)$$

$$U_i(r_i) = \frac{(r_i)^2 - (r_{s1})^2}{2\alpha_i \tau_i \beta_1 \beta_2} + U_{i-1}(r_{s_{i-1}}), \quad i = 2, \dots, M \quad (16.28)$$

16.5 Transformation of the Transversal Isotropy Vector

Using the first formula (16.15), one can obtain expressions for the components of the transversal isotropy vector in the intermediate state:

$$\mathbf{A}_i^{\text{int}} = A_{r_i} u'_i(r_i) \mathbf{i}_x + \frac{A_{\varphi_i} \tau_i}{r_i} \mathbf{i}_y + A_{z_i} \alpha_i \mathbf{i}_z \quad (16.29)$$

Similarly, using the second formula (16.15), one can obtain expressions for the components of the transversal isotropy vector in the final state:

$$\mathbf{A}_i^{\text{fn}} = A_{r_i} U'_i(r_i) \mathbf{i}_x + \frac{A_{\varphi_i} \beta_1 \tau_i}{r_i} \mathbf{i}_y + A_{z_i} \beta_2 \alpha_i \mathbf{i}_z \quad (16.30)$$

The vectors \mathbf{i}_x , \mathbf{i}_y , \mathbf{i}_z are the orthonormal basis of the rectangular Cartesian coordinate system. Representations (16.29) and (16.30) allow us to calculate $\mathbf{A}_i^{\text{init}} \cdot \mathbf{A}_i^{\text{int}}$, $\mathbf{A}_i^{\text{int}} \otimes \mathbf{A}_i^{\text{int}}$, $\mathbf{A}_i^{\text{fin}} \cdot \mathbf{A}_i^{\text{fin}}$, $\mathbf{A}_i^{\text{fin}} \otimes \mathbf{A}_i^{\text{fin}}$. For example, the tensor $\mathbf{A}_i^{\text{fin}} \otimes \mathbf{A}_i^{\text{fin}}$ has the following form:

$$\begin{pmatrix} A_{r_i}^2 (U_i'(r_i))^2 & \frac{A_{r_i} A_{\varphi_i} \beta_1 \tau_i f_i'(r_i)}{r_i} & A_{r_i} A_{z_i} \beta_2 \alpha_i u_i'(r_i) \\ \frac{A_{r_i} A_{\varphi_i} \beta_1 \tau_i f_i'(r_i)}{r_i} & \frac{A_{\varphi_i}^2 \beta_1^2 \tau_i^2}{r_i^2} & \frac{A_{\varphi_i} A_{z_i} \beta_1 \beta_2 \alpha_i \tau_i}{r_i} \\ A_{r_i} A_{z_i} \beta_2 \alpha_i u_i'(r_i) & \frac{A_{\varphi_i} A_{z_i} \beta_1 \beta_2 \alpha_i \tau_i}{r_i} & A_{z_i}^2 \beta_2^2 \alpha_i^2 \end{pmatrix}$$

The tensors $\mathbf{A}_i^{\text{init}} \otimes \mathbf{A}_i^{\text{init}}$, $\mathbf{A}_i^{\text{fin}} \otimes \mathbf{A}_i^{\text{fin}}$ are among the terms that make up $\mathbf{T}_i^{\text{int}}$ and $\mathbf{T}_i^{\text{fin}}$. In addition, expressions (16.12) and (16.13) for these stress tensors include the tensors $\mathbf{F}_i^{\text{init}}$ and $\mathbf{F}_i^{\text{fin}}$, which will be diagonal. In particular,

$$\mathbf{F}_i^{\text{init}} = \begin{pmatrix} [u_i'(r_i)]^2 & 0 & 0 \\ 0 & \left(\frac{\tau_i}{r_i}\right)^2 & 0 \\ 0 & 0 & \alpha_i^2 \end{pmatrix} \quad (16.31)$$

The components of the tensors $\mathbf{F}_i^{\text{init}}$ and $\mathbf{F}_i^{\text{fin}}$ depend only on r_i . If we consider the dependence of these tensors on the coordinates in the intermediate or final states, then they will depend only on x or X , respectively. In addition, if we assume that the Lagrange multiplier depends only on x or X , respectively, then the stresses will depend only on this coordinate. In this case, it follows from the equilibrium equations and boundary conditions that the shear stresses $(\mathbf{T}_i^{\text{fin}})_{XY}$, $(\mathbf{T}_i^{\text{fin}})_{XZ}$ are equal to zero. Therefore, either A_{r_i} or one of the components A_{φ_i} , A_{z_i} must be zero. If the shear stress $(\mathbf{T}_i^{\text{fin}})_{YZ}$ is also zero, then only one of the components of the vector \mathbf{A}_i^0 is non-zero.

16.6 Stress Determination

Calculating the deformation gradient $\mathbf{P}_i^{\text{fin}} = \mathbf{P}_i^{\text{add}} \cdot \mathbf{P}_i^{\text{init}}$ and substituting (16.27), (16.28) and (16.31) into (16.22), as well as applying the second condition (16.16), we determine the components of the stress tensor:

$$\begin{aligned}
 (\mathbf{T}_i^{\text{fin}})_{XX} &= 0 \\
 (\mathbf{T}_i^{\text{fin}})_{YY} &= \frac{\mu_i \beta_1^2 \tau_i^2}{r_i^2} + \frac{2\mu_i \gamma_i A_{\varphi_1}^2 \beta_1^2 \tau_i^2}{r_i^2} \left(A_{r_i}^2 (U_i'(r_i))^2 + \frac{A_{\varphi_1}^2 \beta_1^2 \tau_i^2}{r_i^2} + \right. \\
 &+ A_{z_i}^2 \beta_2^2 \alpha_i^2 - 1) - \mu_i (U_i'(r_i))^2 - 2\mu_i \gamma_i A_{r_i}^2 \left(A_{r_i}^2 (U_i'(r_i))^2 + \right. \\
 &\quad \left. + \frac{A_{\varphi_1}^2 \beta_1^2 \tau_i^2}{r_i^2} + A_{z_i}^2 \beta_2^2 \alpha_i^2 - 1) (U_i'(r_i))^2 \right. \\
 &\quad \left. + \frac{A_{\varphi_1}^2 \tau_i^2}{r_i^2} + A_{z_i}^2 \alpha_i^2 \right) (U_i'(r_i))^2 \\
 (\mathbf{T}_i^{\text{fin}})_{ZZ} &= \alpha_i^2 \mu_i + 2A_{z_i}^2 \alpha_i^2 \mu_i \gamma_i \left(A_{r_i}^2 (U_i'(r_i))^2 + \frac{A_{\varphi_1}^2 \tau_i^2}{r_i^2} + \right. \\
 &+ A_{z_i}^2 \alpha_i^2 - 1) - \mu_i (U_i'(r_i))^2 - 2\mu_i \gamma_i A_{r_i}^2 \left(A_{r_i}^2 (U_i'(r_i))^2 + \right. \\
 &\quad \left. + \frac{A_{\varphi_1}^2 \tau_i^2}{r_i^2} + A_{z_i}^2 \alpha_i^2 \right) (U_i'(r_i))^2
 \end{aligned} \tag{16.32}$$

Formulas (16.32) make it possible to calculate all non-zero components of the stress tensor in each layer in the final state.

16.7 Numerical Calculations

The algorithm for solving the problem given above is implemented as a program written using the Maple computer algebra system. Below are the results of numerical studies performed using the written program, in the form of graphs. These graphs demonstrate the difference in the resulting stresses depending on the nature of the transversal isotropy of the material.

The dependences of the stresses $\frac{(\mathbf{T}_i^{\text{fin}})_{YY}}{\mu_1}$ and $\frac{(\mathbf{T}_i^{\text{fin}})_{ZZ}}{\mu_1}$ of the first layer in the final state on the coordinate r_1 in the initial state are shown on Figs. 16.1 and 16.2, respectively. These dependences are presented for various types of transversal isotropy of the material (solid line corresponds to $A_{r_1} = 1$; dotted line— $A_{\varphi_1} = 1$; dashed

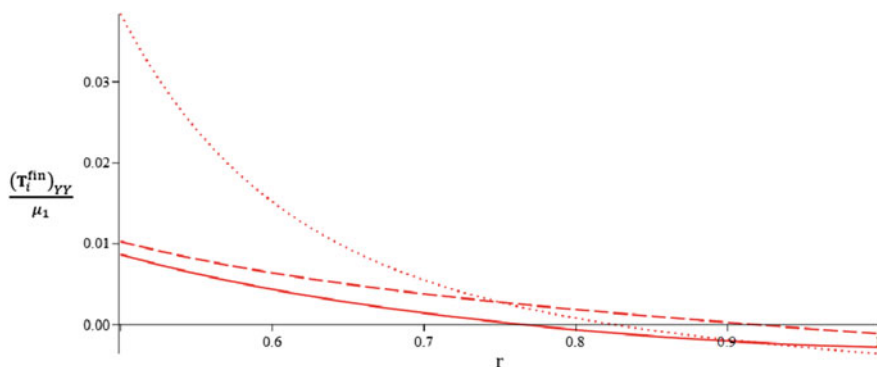


Fig. 16.1 $\frac{(\mathbf{T}_i^{\text{fin}})_{YY}}{\mu_1}$ in the final state on the coordinate in the initial state for various types of transversal isotropy

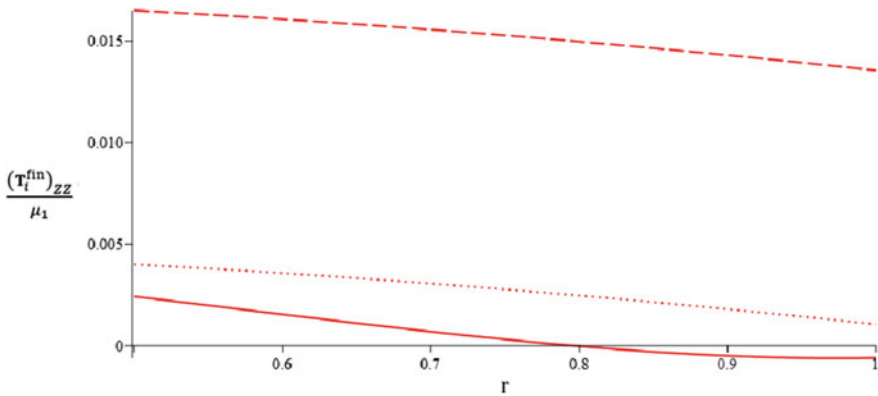


Fig. 16.2 $\frac{(T_i^{\text{fin}})_{ZZ}}{\mu_1}$ in the final state on the coordinate in the initial state for various types of transversal isotropy

line— $A_{z_1} = 1$). The inner radius of the layer in the initial state is taken equal to 0.5, the outer one is equal to 1. Parameters $\alpha_1 = 1, \tau_1 = 1, 7, \beta_1 = 1, 5, \beta_2 = 1, 5$.

16.8 Conclusion

The paper presents a mathematical formulation of the problem of imposing finite deformations on cylindrical layers made of incompressible nonlinear elastic transversally isotropic materials. The main steps of the analytical solution of the problem are described. The restrictions on the directions of transversal isotropy are analyzed those permit one to obtain exact analytical solution of the problem. The obtained results can be further used for the computation of effective properties of composite nonlinear-elastic plates with initial stresses (Altenbach and Eremeyev 2010).

Acknowledgements The work was carried out at Lomonosov Moscow State University with the support of the Russian Science Foundation (project 22-11-00110).

References

Altenbach H, Eremeyev V (2010) On the effective stiffness of plates made of hyperelastic materials with initial stresses. *Int J Non-Linear Mech* 45(10):976–981. <https://doi.org/10.1016/j.ijnonlinmec.2010.04.007>

Levin V, Zubov L, Zingerman K (2021) An exact solution to the problem of biaxial loading of a micropolar elastic plate made by joining two prestrained arc-shaped layers under large strains. *Eur J Mech-A/Solids* 88(104):237

- Levin VA (1998) Theory of repeated superposition of large deformations: Elastic and viscoelastic bodies. *Int J Solids Struct* 35(20):2585–2600
- Levin VA, Zingerman KM (1998) Interaction and Microfracturing Pattern for Successive Origination (Introduction) of Pores in Elastic Bodies: Finite Deformation. *Appl Mech* 65(2):431–435
- Levin VA, Zubov LM, Zingerman KM (2014) The torsion of a composite, nonlinear-elastic cylinder with an inclusion having initial large strains. *Int J Solids Struct* 51(6):1403–1409
- Levin VA, Zingerman KM, Vershinin AV et al (2015) Numerical analysis of effective mechanical properties of rubber-cord composites under finite strains. *Compos Struct* 131(3)
- Levin VA, Zubov LM, Zingerman KM (2018) Multiple joined prestressed orthotropic layers under large strains. *Int J Eng Sci* 131(1):47–59
- Levin VA, Zingerman KM, Zubov LM et al (2020) Large deformations of biaxial tension-compression of the plate, consisting two pre-deformed layers made of incompressible treloar material. *Lecture notes in computational science and engineering*, pp 609–618
- Lurie AI (1990) *Nonlinear theory of elasticity*. North Holland, Amsterdam
- Merodio J, Ogden RW (2002) Material instabilities in fiber-reinforced nonlinearly elastic solids under plane deformation. *Arch Mech* 54:525–552
- Merodio J, Ogden RW (2005) Mechanical response of fiber-reinforced incompressible non-linearly elastic solids. *Int J Non-Linear Mech* 40:213–227
- Treloar LRG (1975) *The physics of rubber elasticity*. Oxford University Press
- Truesdell C (1972) *A first course in rational continuum mechanics*. The Johns Hopkins University, Baltimore, Maryland
- Zingerman KM, Zubov LM, Belkin AE et al (2022) Torsion of a multilayer elastic cylinder with sequential attachment of layers with multiple superposition of large deformations. *Contin Mech Thermodyn*. <https://doi.org/10.1007/s00161-022-01110-x>

Chapter 17

Detection of the Poynting Effect in a Composite Hypoelastic Cylinder Under Multiple Imposition of Large Deformations



Vladimir A. Levin, Konstantin M. Zingerman, and Danila R. Biryukov

Abstract The paper investigates nonlinear effects found in the exact analytical solution of problem of multiple superimposition of large tensile-compressive and torsion strains for a sequentially formed multilayer cylinder, each layer of which is made of a hypoelastic incompressible material. After attaching each layer, tension-compression and torsion of the composite cylinder are performed. The material of each layer constituting the cylinder is characterized by a constitutive relationship, including the objective corotational derivative of Jaumann or Dienes. Based on the description of the formation and deformation of the cylinder, a mathematical statement of the problem is given and the main steps of its analytical solution are described. Some numerical results are given. The presence of the Poynting effect is demonstrated.

Keywords Hypoelastic material · Large deformations · Multi-stage deformation · Objective derivatives · Poynting effect · Exact solution

Vladimir A. Levin, Konstantin M. Zingerman and Danila R. Biryukov: These authors contributed equally to this work.

V. A. Levin (✉)

Mechanics and Mathematics Department, Lomonosov Moscow State University, Moscow, Russian Federation

e-mail: v.a.levin@mail.ru

K. M. Zingerman

Department of Applied Mathematics Cybernetics, Tver State University, Tver, Russian Federation

e-mail: zingerman@rambler.ru

D. R. Biryukov

Mechanics and Mathematics Department, Tula State University, Tula, Russian Federation

e-mail: danilabirukov@rambler.ru

17.1 Introduction

This work is devoted to the construction and study of an analytical solution to the problem of the theory of multiple superimposition of large deformations on the stage-by-stage quasi-static tension-compression and torsion of a multilayer hypoelastic cylinder manufactured by sequentially attaching layers. Several configurations (states) of a composite cylinder are considered; the transition from the previous configuration to the next corresponds to the attachment of a new layer to the cylinder, followed by tension-compression and torsion.

Works Truesdell (1972), Lurie (1990), Green and Adkins (1960) are devoted to general formulations of problems in the mechanics of a deformable solid body under large deformations and analytical methods for solving these problems. Statements and methods for solving problems of multiple imposition of large strains in deformable solids are given in Levin (1998), Levin and Zingerman (2008, 2009). Problems of torsion of nonlinearly elastic cylinders under large deformations were studied in Zubov and Bogachkova (1995), Zubov (2006). Joint torsion and tension-compression of a composite nonlinearly elastic rod with a circular cross-section with a pre-deformed inclusion was studied in Levin et al. (2013, 2014) in the framework of the theory of superposition of large deformations. In Levin et al. (2014), the influence of preliminary deformation on the manifestation of the Poynting effect (Truesdell 1972; Poynting 1909) was revealed and it was found that in the absence of an axial force, both tension and compression of the rod are possible, depending on the preliminary deformation. The solution of a similar problem for a multilayer nonlinearly elastic rod was obtained in Zingerman et al. (2022).

It is of interest to generalize the approach to the study of the imposition of large strains in torsion and tension-compression of a composite rod, proposed in Levin et al. (2013, 2014), Zingerman et al. (2022), to the case of inelastic materials. In particular, hypoelasticity models are one of the classes of inelastic materials (Truesdell 1972; Green and Adkins 1960; Brovko et al. 2009). In Ovchinnikova (2020), an exact analytical solution was obtained for the quasi-static problem of torsion of a circular cylinder made of an isotropic incompressible hypoelastic material. In Levin et al. (2022), based on the theory of multiple superposition of large strains, the quasi-static problem of joint torsion and tension-compression of a two-layer circular cylinder made of an isotropic incompressible hypoelastic material with a preliminarily deformed inclusion was solved. In this article, the solution obtained in Levin et al. (2022) is generalized to the case of an arbitrary number of layers and one of the versions of the Poynting effect is studied.

17.2 Formulation of the Problem

The process considered in the problem includes N stages (the set of stages is discrete, that is, continuous processes are not considered). Each stage corresponds to a cylindrical layer, these layers are sequentially attached to the inner cylinder (which is

conventionally considered the first layer). The total number of layers is thus the same as the number of steps, hereinafter referred to as deformation steps. The moment of time corresponding to the beginning of the deformation stage with the number j is denoted by $t^{(j-1)}$, and the moment of time corresponding to the end of this stage is denoted by $t^{(j)}$. The beginning of the deformation process $t^{(0)} = 0$. At the moment $t^{(j-1)}$ the cylinder (obtained at the previous stages) is supplemented with a new j th layer, and its inner radius $\tilde{r}_{j,j}$ must coincide with the outer radius $\tilde{R}_{j,j-1}$ previous layer. Further, during the j th stage, the cylinder is subjected to tension-compression and torsion, deforming as a whole.

The entire cylinder as a whole during the j th stage of deformation is supplied with rectangular Cartesian and cylindrical coordinate systems, connected at each moment of time by the relations:

$$\begin{cases} x^{(j)} = r^{(j)} \cos \varphi^{(j)} \\ y^{(j)} = r^{(j)} \sin \varphi^{(j)} \\ z^{(j)} = z^{(j)} \end{cases} \quad (17.1)$$

The coordinates of the particles of the cylinder during the j th stage of deformation are related to the coordinates of these particles in the previous state as follows:

$$\begin{cases} r^{(j)} = \lambda_j \cdot r^{(j-1)} \\ \varphi^{(j)} = \varphi^{(j-1)} + \alpha_j \\ z^{(j)} = z^{(j-1)} \cdot \lambda_j^{-2} \end{cases} \quad (17.2)$$

where λ_j is the characteristic of radial deformation (multiplicity of elongation); $\alpha_j = k_j z^{(j-1)}$; k_j is the characteristic of torsional deformation. Equation (17.2) automatically ensure the fulfillment of the incompressibility condition. The following notation will be used:

$$\Lambda_{j,i} = \lambda_i \lambda_{i+1} \dots \lambda_{j-1} \lambda_j$$

To characterize the deformation of the i th layer during the j th stage, the deformation gradient is used:

$$\begin{cases} \Psi_{j,i} = \frac{\partial(x^{(j)}, y^{(j)}, z^{(j)})}{\partial(x^{(j-1)}, y^{(j-1)}, z^{(j-1)})}, & i = j \\ \Psi_{j,i} = \Psi_{j-1,i} \cdot \frac{\partial(x^{(j)}, y^{(j)}, z^{(j)})}{\partial(x^{(j-1)}, y^{(j-1)}, z^{(j-1)})}, & i > j \end{cases} \quad (17.3)$$

The compound cylinder material is hypoelastic. The constitutive relation describing the mechanical behavior of the hypoelastic material for the i th layer during the j th stage of deformation is written below

$$\begin{cases} D(\mathbf{S}_{j,i}) = 2G_i \mathbf{C}_{j,i} \\ \boldsymbol{\sigma}_{j,i} = \mathbf{S}_{j,i} + p_{j,i} \mathbf{E} \end{cases} \quad (17.4)$$

where \mathbf{E} is the metric tensor, $\boldsymbol{\sigma}_{j,i}$ is the true Cauchy stress tensor, $\mathbf{S}_{j,i}$ is the stress deviator, D is the objective derivative (Jaumann or Dienes) with respect to time, $\mathbf{C}_{j,i}$ is the strain rate tensor, G_i —shear modulus, $p_{j,i}$ —pressure.

$$\mathbf{C}_{j,i} = \frac{1}{2} \left(\frac{\partial \boldsymbol{\Psi}_{j,i}}{\partial t} \cdot \boldsymbol{\Psi}_{j,i}^{-1} + \left(\frac{\partial \boldsymbol{\Psi}_{j,i}}{\partial t} \cdot \boldsymbol{\Psi}_{j,i}^{-1} \right)^T \right) \quad (17.5)$$

The objective derivatives of Jaumann and Dienes (Truesdell 1972; Dienes 1979) are defined by the following expression:

$$D(\mathbf{S}_{j,i}) = \frac{\partial \mathbf{S}_{j,i}}{\partial t} - \mathbf{B}_{j,i} \cdot \mathbf{S}_{j,i} + \mathbf{S}_{j,i} \cdot \mathbf{B}_{j,i} \quad (17.6)$$

where for the case of the Jaumann derivative the tensor $\mathbf{B}_{j,i}$ is defined as

$$\mathbf{B}_{j,i} = \frac{1}{2} \left(\frac{\partial \boldsymbol{\Psi}_{j,i}}{\partial t} \cdot \boldsymbol{\Psi}_{j,i}^{-1} - \left(\frac{\partial \boldsymbol{\Psi}_{j,i}}{\partial t} \cdot \boldsymbol{\Psi}_{j,i}^{-1} \right)^T \right) \quad (17.7)$$

for the case of the Dienes derivative, the tensor $\mathbf{B}_{j,i}$ is defined differently:

$$\mathbf{B}_{j,i} = \frac{\partial \mathbf{A}_{j,i}}{\partial t} \cdot \mathbf{A}_{j,i}^T \quad (17.8)$$

where $\mathbf{A}_{j,i}$ is the rotation tensor in the polar decomposition of the deformation gradient $\boldsymbol{\Psi}_{j,i}$.

The mathematical statement of the problem is supplemented by the equilibrium equations of layer i at the j th stage:

$$\frac{\partial ((\mathbf{S}_{j,i})_{11} + p_{j,i})}{\partial r^{(j-1)}} + \frac{(\mathbf{S}_{j,i})_{11} - (\mathbf{S}_{j,i})_{22}}{r^{(j-1)}} = 0 \quad (17.9)$$

The problem statement also includes the initial conditions at the j th stage

$$\mathbf{S}_{j,i} = 0, t = 0, j = 1 \quad (17.10)$$

$$\mathbf{S}_{j,i} \Big|_{t=t^{(j-1)}} = \mathbf{S}_{j,i} \Big|_{t=t^{(j-1)}}, j > 1 \quad (17.11)$$

and boundary conditions at the boundary of layer i with layer $i + 1$ during the j th stage of deformation:

$$\left\{ \begin{array}{l} ((\mathbf{S}_{j,i})_{11} + p_{j,i}) \Big|_{r^{(i-1)} = \frac{\bar{r}_{j,i}}{\lambda_{j,i}}} = 0, i = j \\ ((\mathbf{S}_{j,i})_{11} + p_{j,i}) \Big|_{r^{(i-1)} = \frac{\bar{r}_{j,i}}{\lambda_{j,i}}} = ((\mathbf{S}_{j,i})_{11} + p_{j,i+1}) \Big|_{r^{(i-1)} = \frac{\bar{r}_{j,i+1}}{\lambda_{j,i+1}}}, i \neq j \end{array} \right. \quad (17.12)$$

Equations and conditions (17.2)–(17.11) constitute the mathematical formulation of the problem. The desired value is the stress tensor $\sigma_{j,i}$.

17.3 The Algorithm for Problem Solving

Deformation gradient (17.3)–(17.4) using formulas (17.1)–(17.2) can be written in the form

$$\Psi_{j,i} = \begin{pmatrix} \Lambda_{j,i} \cos(\alpha_{j,i}) & -\Lambda_{j,i} \sin(\alpha_{j,i}) & -\Lambda_{j,i} k_{j,i} r^{(j-1)} \sin(\varphi_{i-1} + \alpha_{j,i}) \\ \Lambda_{j,i} \sin(\alpha_{j,i}) & \Lambda_{j,i} \cos(\alpha_{j,i}) & \Lambda_{j,i} k_{j,i} r^{(j-1)} \cos(\varphi_{i-1} + \alpha_{j,i}) \\ 0 & 0 & \frac{1}{(\Lambda_{j,i})^2} \end{pmatrix} \quad (17.13)$$

where

$$\alpha_{j,i} = \alpha_i + \alpha_{i+1} + \cdots + \alpha_{j-1} + \alpha_j$$

$$k_{j,i} = \frac{k_i + k_{i+1} + \cdots + k_{j-1} + k_j}{(\Lambda_{j-1,i-1})^2}$$

The algorithm for solving the problem includes the following steps:

Step 1. For each layer i in each state $j \geq i$, the deformation gradients $\Psi_{j,i}$ are calculated.

Step 2. For each layer i in each state $j \geq i$, $\mathbf{C}_{j,i}$ are calculated, formulas for the objective derivative $D(\mathbf{S}_{j,i})$ considered in this problem are substituted.

Step 3. In each state $j = 1 \dots N$, the deviator of the Cauchy stress tensor $\mathbf{S}_{j,i}$ is calculated for each layer $i \leq j$ by solving the Cauchy problem (17.6), (17.10).

Step 4. Calculate $p_{j,i}$ by solving the Cauchy problem (17.9), (17.11).

Step 5. The Cauchy stress tensor is calculated using formula (17.4).

17.4 Detection of the Poynting Effect in Numerical Analysis

The analytical solution of the problem was implemented using a program developed in Maple. The program made it possible to carry out a number of numerical studies and discover the Poynting effect in the case of gradual deformation of a compound cylinder.

The graphs in Fig. 17.1 show the dependence of the axial force on the deformation parameter α_2 of the second layer for a composite cylinder consisting of $N = 3$ layers. The material of the layers is hypoelastic, and the Dienes derivative is used as an objec-

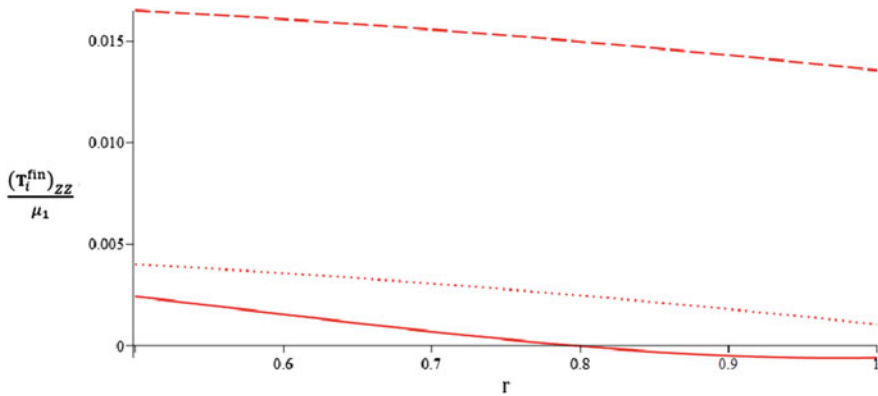


Fig. 17.1 Dependence of the axial force on the deformation parameter λ_2 of the second layer (out of three) for the case of the Dienes derivative

tive derivative. The input data for particular cases of the problem for which graphs are constructed are as follows: $k_1 = k_2 = C_k t^2$; $C_k = 1 \text{ s}^{-2}$; $\tilde{R}_{1,0} = 1 \text{ m}$; $\tilde{R}_{2,1} = 1, 1 \text{ m}$; $\tilde{R}_{3,2} = 1, 2 \text{ m}$; $t_1 = 1 \text{ s}$; $t_2 = 2 \text{ s}$; $\lambda_1 = \lambda_2 = \lambda_3 = 1$.

For solid plot, the deformation parameters are $\alpha_1 = \frac{1}{R_{1,0}}$, $\alpha_3 = \frac{-0,3}{R_{3,2}}$. For scatter graph, the deformation parameters are $\alpha_1 = \frac{1,5}{R_{1,0}}$, $\alpha_3 = \frac{-0,5}{R_{3,2}}$. For dotted graph, the deformation parameters are $\alpha_1 = \frac{1,9}{R_{1,0}}$, $\alpha_3 = \frac{-0,7}{R_{3,2}}$. The values of these parameters are chosen in such a way that the lines are clearly distinguished on the graph.

Graphs in Fig. 17.1 make it possible to observe the Poynting effect in a compound cylinder. This effect manifests itself in the presence of an axial force in the absence of deformation in the axial direction. At the same time, it was demonstrated that the value of the axial force depends on the parameters that determine the torsional deformation. The obtained results can be further generalized for models of micropolar inelasticity (Altenbach and Eremeyev 2014).

17.5 Conclusion

In this work, the problem of stage-by-stage tension-compression and torsional deformations of a body, which is a composite cylinder, is posed. A feature of the problem is taking into account the sequence of manufacturing the body, in each configuration supplemented with new elements.

A mathematical formulation of the problem is presented, including equations and boundary and initial conditions. The statement is considered in two versions—for the case of the Jaumann and Dienes derivatives. An algorithm is described that makes it possible to obtain an exact analytical solution.

To implement the algorithm, a program was developed, the use of which made it possible to detect the Poynting effect for the gradual deformation of a compound cylinder.

Acknowledgements The work was carried out at Lomonosov Moscow State University with the support of the Russian Science Foundation (project 22-11-00110)

References

- Altenbach H, Eremeyev V (2014) Strain rate tensors and constitutive equations of inelastic micropolar materials. *Int J Plast* 63:3–17. <https://doi.org/10.1016/j.ijplas.2014.05.009>
- Brovko GL, Ivanova OA, Finoshkina AS (2009) On geometrical and analytical aspects in formulations of problems of classic and non-classic continuum mechanics. *Mod Anal Appl Oper Theory: Adv Appl* 191:51–79
- Dienes JK (1979) On the analysis of rotation and stress rate in deforming bodies. *Acta Mech* 32:217–232
- Green AE, Adkins JE (1960) *Large elastic deformations and non-linear continuum mechanics*. Clarendon Press, Oxford
- Levin VA (1998) Theory of repeated superposition of large deformations: elastic and viscoelastic bodies. *Int J Solids Struct* 35:2585–2600
- Levin VA, Zingerman KM (2008) A class of methods and algorithms for the analysis of successive origination of holes in a pre-stressed viscoelastic body. *Finite strains. Commun Numer Methods Eng* 24:2240–2251
- Levin VA, Zingerman KM (2009) Redistribution of finite elastic strains after the formation of inclusions. Approximate analytical solution. *J Appl Math Mech* 73:710–721
- Levin VA, Zubov LM, Zingerman KM (2013) Torsion of a composite nonlinear elastic cylinder with a prestressed inclusion. *Dokl Phys* 58(12):540–543
- Levin VA, Zubov LM, Zingerman KM (2014) The torsion of a composite, nonlinear-elastic cylinder with an inclusion having initial large strains. *Int J Solids Struct* 51(6):1403–1409
- Levin VA, Zingerman KM, Belkin AE, et al (2022) Exact solution for a problem of the theory of repeatedly superimposed finite strains. Torsion and tension of a compound hypoelastic rod. In: *AIP Conference Proceedings*, vol 2533
- Lurie AI (1990) *Nonlinear theory of elasticity*. North Holland, Amsterdam
- Ovchinnikova NV (2020) The problem of torsion of a hypoelastic incompressible cylinder. In: Zubchaninov VG, Alekseev AA (eds) *Mathematical modeling and experimental mechanics of deformable solid: interuniversity collection of scientific papers*. 3, Tver: Tverskoy State Technical University, pp 65–72
- Poynting JH (1909) On pressure perpendicular to the shear planes in finite pure shears, and on the lengthening of loaded wires when twisted. *Proc R Soc Lond* 82:546–559
- Truesdell C (1972) *A first course in rational continuum mechanics*. The Johns Hopkins University, Baltimore, Maryland
- Zingerman KM, Zubov LM, Belkin AE et al (2022) Torsion of a multilayer elastic cylinder with sequential attachment of layers with multiple superposition of large deformations. *Contin Mech Thermodyn*. <https://doi.org/10.1007/s00161-022-01110-x>
- Zubov LM (2006) Non-linear Saint-Venant's problem for torsion, tension, and bending of the naturally twisted rod. *J Appl Math Mech* 70:300–310
- Zubov LM, Bogachkova LU (1995) Theory of torsion of elastic noncircular cylinders under large deformations. *J Appl Mech* 62:373–379

Chapter 18

Numerical Solution of Stress Concentration Problems in Elastic-Plastic Bodies Under the Superposition of Finite Deformations



Vladimir A. Levin, Konstantin M. Zingerman, and Kirill Yu Krapivin

Abstract This paper deals with numerical simulations of the elasto-plastic behavior of isotropic materials undergoing large deformations. The attention is focused on the state of stress and strain of previously loaded elasto-plastic bodies with holes originating in them. The problem statement and solution are based on the theory of repeatedly imposed large deformations within the framework of hyperelastic plasticity. The problem-solving is based on the finite-element and spectral-element methods. The validity of the model was tested on two test problems, and it was found that the numerical results were in good agreement either with the exact solution or with experimental data. Another two problems are strain localization problems in media with step-by-step exclusion of geometrical parts. These problems are characterized by the origination of localized shear bands (slip lines). It is shown that a new family of slip lines is originated at each step of deformation. This is the qualitative effect related with multiple superpositions of finite strains.

Keywords Superimposed finite strains · Finite strain plasticity · Hyperelasticity · Hyporelasticity · Finite elements · Spectral elements · Shear bands

These authors contributed equally to this work.

V. A. Levin (✉) · K. Y. Krapivin

Mechanics and Mathematics Department, Lomonosov Moscow State University, Moscow, Russian Federation

e-mail: v.a.levin@mail.ru

K. M. Zingerman

Department of Applied Mathematics and Cybernetics, Tver State University, Tver, Russian Federation

e-mail: zingerman@rambler.ru

Nomenclature

| | |
|--------------|---|
| \cdot | is the sign of tensor contraction, |
| $:$ | is the sign of double tensor contraction, |
| \mathbf{I} | is the second-rank identity tensor. |

Notation for the case when deformations are not superimposed

| | |
|--|---|
| $\overset{0}{\nabla}$ | is a gradient operator in coordinates of the initial state; |
| $\overset{0}{\Gamma}$ | is a boundary of a body in the initial (undeformed) state; |
| \mathbf{n} | is a normal to $\overset{0}{\Gamma}$; |
| \mathbf{N} | is a normal to the deformed boundary; |
| \mathbf{u} | is a displacement vector; |
| \mathbf{v} | is a velocity vector; |
| \mathbf{L} | is a velocity gradient; |
| $\boldsymbol{\omega}$ | is a <i>vorticity</i> tensor; |
| \mathbf{d} | is the rate of deformation tensor; |
| \mathbf{F} | is the deformation gradient; |
| J | is the relative volume variation; |
| $\mathbf{C} = \mathbf{F}^T \cdot \mathbf{F}$ | is the right Cauchy–Green deformation tensor; |
| $\mathbf{b} = \mathbf{F} \cdot \mathbf{F}^T$ | is the left Cauchy–Green deformation tensor; |
| $\boldsymbol{\sigma}$ | is the Cauchy stress tensor; |
| $\boldsymbol{\Pi}$ | is the second Piola–Kirchhoff stress tensor; |
| Φ | is a stress measure governing plasticity (yielding function); |
| \mathcal{D} | is a material tangent (fourth order tensor); |

Notation of the theory of repeatedly superimposed large deformations

| | |
|---------------------------|---|
| $\overset{n}{\nabla}$ | is a gradient operator in coordinates of the n -state; |
| $\overset{n}{\mathbf{R}}$ | is the position vector of a particle in the n th state; |
| $\overset{n}{\Gamma}$ | is a boundary of a body in the n -state; |
| \mathbf{u}_{n+1} | is a displacement vector defining the transition from the n th state to the $(n + 1)$ th state; |
| $\mathbf{F}_{m,n}$ | is the deformation gradient in transition from the m th state to the n th state; |
| $J_{m,n}$ | is the relative volume variation in transition from the m th state to the n th state; |

| | |
|--|--|
| $\mathbf{C}_{m,n} = \mathbf{F}_{m,n}^T \cdot \mathbf{F}_{m,n}$ | is a tensor defining the strains associated with the transition of a body from the m th state to the n -th state ($\mathbf{C}_{0,1} = \mathbf{C}$ is the right Cauchy–Green deformation tensor); |
| $\mathbf{b}_{m,n} = \mathbf{F}_{m,n} \cdot \mathbf{F}_{m,n}^T$ | is a tensor defining the strains associated with the transition of a body from the m -th state to the n -th state ($\mathbf{b}_{0,1} = \mathbf{b}$ is the left Cauchy–Green deformation tensor); |
| $\sigma_{0,n}$ | is the Cauchy stress tensor for the n -th state; |
| $\Pi_{0,n+1}^m$ | is the second Piola–Kirchhoff stress tensor in the base of the m -th state under transition from the initial state to the $(n + 1)$ -th state; at $m = 0$, this tensor is the second Piola–Kirchhoff stress tensor; |

18.1 Introduction

Often in problems of mechanical engineering, it is necessary to simulate the processes of the stress–strain state when changing the geometric shape, layer-by-layer addition of material, removal or addition of inclusions, for example, this occurs in technologies of additively manufactured materials. It is also worth considering significant loads, for example, when exposed to high temperatures, causing irreversible plastic deformations in the material. Under these conditions, it is necessary to resort to the theory of finite elastic-plastic deformations.

Previously, the problem was formulated using the theory of superimposed large deformations in elastic and viscoelastic bodies (Levin 1987, 1998)

The scope of this work is to revisit constitutive equations of finite strain elastoplasticity and to extend the previous solutions in the field of nonlinear elasticity (Levin et al. 2013; Levin and Zingerman 2008) to the plastic domain.

Despite the fact that there is no consensus on the most favorable final elastic-plastic kinematics, the developed numerical algorithms mainly focused on the following two approaches: *Rate-additive hypoelastic plasticity* (Hibbitt et al. 1970; McMeeking and Rice 1975; Nemat-Nasser 1979, 1982 and others); *Multiplicative hyperelastic plasticity* (Simo and Ortiz 1985; Simo 1988a, b; Simo and Hughes 1998; Lee 1969, 1981; Fish and Shek 2000 and others)

In this paper isotropic material is considered within the framework of multiplicative hyperelastic plasticity. The validity of the model will be examined for the following four problems: (a) necking; (b) expansion of an elasto-plastic thick-walled cylinder for which the exact solution has been reported in Hill (1998); (c) (d) strain localization problems in media with step-by-step exclusion of geometrical parts.

Note that strain localization (shear banding) is a plastic instability in large deformation of solids where the flow becomes concentrated in narrow layers (Yadav and Sagapuram 2020). Another forms of instability are considered, for example, by Zubov and Sheidakov (2007); Eremeyev (2021).

18.2 The Statement of the Problems of Nonlinear Elastoplasticity at Large Deformations

18.2.1 The Equilibrium Equation and Boundary Conditions

The equilibrium equation is written in the form

$$\overset{0}{\nabla} \cdot [J^{-1} \boldsymbol{\Pi} \cdot \mathbf{F}] = 0, \quad (18.1)$$

where $\overset{0}{\nabla}$ is a gradient operator in coordinates of the initial state; J is the relative volume variation; $\boldsymbol{\Pi}$ is the second Piola–Kirchhoff stress tensor; \mathbf{F} is the deformation gradient.

The boundary conditions are

$$\mathbf{n} \cdot \boldsymbol{\Pi}|_{\overset{0}{\Gamma}} = \mathbf{P} J \mathbf{F}^{-1} \cdot \mathbf{F}^{T^{-1}}, \quad (18.2)$$

where $\overset{0}{\Gamma}$ is a boundary of a body in the initial (undeformed) state, \mathbf{n} is a normal to this boundary, $\mathbf{P} = P \mathbf{N}$ is a pressure vector at the boundary, and \mathbf{N} is a normal to the deformed boundary.

The relation between the second Piola–Kirchhoff stress tensor $\boldsymbol{\Pi}$ and the Cauchy stress tensor $\boldsymbol{\sigma}$ is

$$\boldsymbol{\Pi} = J \mathbf{F}^{-1} \cdot \boldsymbol{\sigma} \cdot \mathbf{F}^{T^{-1}}. \quad (18.3)$$

18.2.2 Kinematic Relations

The mapping $\varphi: \Omega \in \mathcal{R}^3 \rightarrow \omega \in \mathcal{R}^3$ matches the vector $X \in \Omega$ of each material point in the initial coordinate system to the vector $x \in \omega$ in the new coordinate system: $x = \varphi(X)$.

The deformation gradient is defined as Lurie (1990)

$$F(X) = \frac{\partial \varphi(X)}{\partial X} \quad (18.4)$$

The relative volume variation is

$$J = \det \mathbf{F}, \quad \mathbf{F} = \mathbf{I} + \overset{0}{\nabla} \mathbf{u} = (\mathbf{I} - \nabla \mathbf{u})^{-1}, \quad (18.5)$$

where \mathbf{I} is an identity tensor.

$\mathbf{E} = \frac{1}{2} (\mathbf{C} - \mathbf{I})$ —Green–Largange strain tensor, $\mathbf{e} = \frac{1}{2} (\mathbf{I} - \mathbf{b}^{-1})$ —Euler–Almansi strain tensor.

The multiplicative decomposition of deformation gradient:

$$\mathbf{F} = \mathbf{F}^e \mathbf{F}^p \quad (18.6)$$

From here it follows directly

$$\mathbf{b}^e = \mathbf{F} \mathbf{C}^{p-1} \mathbf{F}^T. \quad (18.7)$$

Velocity gradient

$$\mathbf{L} = \nabla_x \mathbf{v} = \dot{\mathbf{F}} \mathbf{F}^{-1} \quad (18.8)$$

The straightforward differentiation of the above formula gives the additive decomposition of velocity gradient:

$$\mathbf{L} = \mathbf{L}^e + \mathbf{F}^e \mathbf{L}^p \mathbf{F}^{e-1} \quad (18.9)$$

Rate of deformation tensor:

$$\mathbf{d} = \frac{1}{2} (\mathbf{L} + \mathbf{L}^T) \quad (18.10)$$

Skew-symmetric part is called the *spin*, or *vorticity* tensor

$$\boldsymbol{\omega} = \frac{1}{2} (\mathbf{L} - \mathbf{L}^T) \quad (18.11)$$

Hence, the Lie derivative of the left Cauchy–Green elastic deformation tensor is written in terms of the right Cauchy–Green plastic deformation tensor

$$\begin{aligned} \mathcal{L}_v \mathbf{b}^e &= \mathbf{F} \left\{ \frac{\partial}{\partial t} \mathbf{F}^{-1} \mathbf{b}^e \mathbf{F}^{-T} \right\} \mathbf{F}^T \\ &= \mathbf{F} \dot{\mathbf{C}}^{p-1} \mathbf{F}^T. \end{aligned} \quad (18.12)$$

18.3 Constitutive Equations of Elasto-Plasticity

18.3.1 Hypo-elastic Plasticity

The model of hypoelastic plasticity is based on the additive decomposition of the strain rate tensor into elastic and plastic parts

$$\mathbf{d} = \mathbf{d}^e + \mathbf{d}^p. \quad (18.13)$$

Hyper elasto-plastic material models take the form:

$$\begin{aligned}\dot{\Sigma} &= \mathcal{D}^e (\mathbf{d} - \mathbf{d}^p) \\ &= \mathcal{D}^{ep} \mathbf{d},\end{aligned}\tag{18.14}$$

where $\dot{\Sigma}$ denotes any objective stress rate.

Closed-form expressions for various rates—including the Jaumann rate, the Truesdell rate, and the Green–Naghdi rate—have been derived by Moss (1984)

Lie derivative of stress

$$\mathcal{L}_v \sigma = \dot{\sigma} - \mathbf{L}\sigma - \sigma \mathbf{L}^T\tag{18.15}$$

The *Jaumann–Zaremba* stress rate

$$\overset{\nabla}{\sigma} = \dot{\sigma} - \omega \sigma - \sigma \omega^T\tag{18.16}$$

$$\mathbf{d}^p = \dot{\gamma} \frac{\partial \Phi(\sigma)}{\partial \sigma},\tag{18.17}$$

18.3.2 Hyperelastic Plasticity

Hyperelastic material models are a type of constitutive model for ideally elastic material for which the stress–strain relationship derives from a strain energy density function W . The Cauchy stress in elastic domain is given by

$$\sigma = \frac{1}{J} \frac{\partial W}{\partial \mathbf{F}^e} \cdot \mathbf{F}^{eT}\tag{18.18}$$

The hyperelastic model is based on the existence of a function W and multiplicative decomposition (18.6).

The associated flow law is considered

$$-\mathcal{L}_v \mathbf{b}^e = \dot{\gamma} \frac{\partial \Phi(\sigma)}{\partial \sigma} \mathbf{b}^e,\tag{18.19}$$

which, together with the complementarity condition

$$\Phi \leq 0, \dot{\gamma} \geq 0, \dot{\gamma} \Phi = 0,\tag{18.20}$$

consistency condition

$$\dot{\Phi} = 0\tag{18.21}$$

and equation (18.12), following the radial return algorithm, gives an explicit expression for the consistent elastic-plastic tangent tensor \mathcal{D}^{ep} . As in the infinitesimal-deformation, the use of consistent (algorithmic) tangent moduli is essential in order to achieve a quadratic rate of asymptotic convergence within Newton's iterations.

18.4 Problem Statement of the Theory of Repeatedly Superimposed Large Deformations

18.4.1 Modeling the Origin of Holes

The origination of holes is described as follows Levin (1987, 1998). Initial strains take place in a body due to the action of external forces. The body passes to the first intermediate state.

Then a closed surface is outlined in a body (the future boundary of the first hole). A part of the body limited by this surface is mentally removed, and its effect on the remaining part is replaced with the forces distributed along this surface. Then, the forces are changed "immediately" (in particular, reduced to zero). As a result, additional finite strains originate in the body. These strains are superimposed on the initial ones. The shape of the boundary surface also varies. The body passes to the second intermediate state.

After that, the second surface is outlined in the body, and the second hole originates in the same way. New additional strains and stresses are brought about in the body and are superimposed on the existing ones. The shape of holes also varies. The body passes to the next state.

The origin of the next holes can be described similarly.

18.4.2 Mathematical Problem Statement

According to the theory of superimposed large deformations (Levin 1987, 1998), the states of the body are numbered from 0 to N .

Consider the mathematical problem statement of transition from the n th state to the $(n + 1)$ th (current) state. The problem is formulated in coordinates of the n th state.

The equilibrium equation is written in the form

$$\overset{n}{\nabla} \cdot [(J_{0,n})^{-1} \overset{n}{\Pi}_{0,n+1} \cdot \mathbf{F}_{n,n+1}] = 0, \quad (18.22)$$

The boundary conditions are

$$\left[\mathbf{N} \cdot \mathbf{\bar{\Pi}}_{n,n+1} \right]_{\Gamma}^n = \mathbf{P} \cdot J_{0,n+1} [\mathbf{F}_{n,n+1}]^{-1} \cdot [\mathbf{F}_{n,n+1}^T]^{-1}, \quad (18.23)$$

where Γ^n is a boundary of a body in coordinates of the n th state (including the boundary of the hole originating in this state), \mathbf{N} is a normal to this boundary, and $\mathbf{P}_{n+1} = P \mathbf{N}$ is a pressure vector at the boundary.

The relation between the second Piola–Kirchhoff stress tensor in the base of the m th state $\mathbf{\bar{\Pi}}_{0,n+1}^m$ and the total true stress tensor $\boldsymbol{\sigma}_{0,n+1}$ is

$$\mathbf{\bar{\Pi}}_{0,n+1}^0 = J_{0,n+1} [\mathbf{F}_{0,n+1}]^{-1} \cdot \boldsymbol{\sigma}_{0,n+1} \cdot [\mathbf{F}_{0,n+1}^T]^{-1}. \quad (18.24)$$

The relation between the second Piola–Kirchhoff stress tensors in the bases of different states is

$$\mathbf{\bar{\Pi}}_{0,n+1}^l = \mathbf{F}_{m,l} \cdot \mathbf{\bar{\Pi}}_{0,n+1}^m \cdot \mathbf{F}_{m,l}^T. \quad (18.25)$$

The kinematic relations are

$$\mathbf{F}_{0,n} = \mathbf{F}_{k,n} \cdot \mathbf{F}_{0,k}, \quad (18.26)$$

$$J_{k,n} = \det \mathbf{F}_{k,n}, \quad (18.27)$$

$$\mathbf{F}_{k,n} = \mathbf{\nabla}^k \mathbf{R}^n = \mathbf{I} + \sum_{i=k+1}^n \mathbf{\nabla}^k \mathbf{u}_i = \left(\mathbf{\nabla}^n \mathbf{R}^k \right)^{-1} = \left(\mathbf{I} - \sum_{i=k+1}^n \mathbf{\nabla}^n \mathbf{u}_i \right)^{-1}, \quad (18.28)$$

where \mathbf{R}^k and \mathbf{R}^n are the position vectors of a particle in the k th and n th states, respectively; \mathbf{u}_i is a displacement vector in transition from the $(i - 1)$ th state to the i th state.

$\mathbf{C}_{0,n} = \mathbf{F}_{0,n}^T \cdot \mathbf{F}_{0,n}$ and $\mathbf{b}_{0,n} = \mathbf{F}_{0,n} \cdot \mathbf{F}_{0,n}^T$ are tensors defining the strains associated with the transition of a body from the initial state to the n th state (with $n = 1$, $\mathbf{C}_{0,1} = \mathbf{C}$ and $\mathbf{b}_{0,1} = \mathbf{b}$ are the right and the left Cauchy–Green deformation tensors, respectively (Lurie 1990).

18.5 Examples

In this paper, the solution of the problems is carried out within the framework of hyperelastic plasticity. We consider the following explicit forms of strain energy potential for isotropic elastic domain (Lurie 1990; Truesdell 1972):

$$\begin{aligned} W &= U(J^e) + \bar{W}(\bar{\mathbf{b}}^e) \\ \bar{\mathbf{b}}^e &= J^{e-2/3} \mathbf{b}^e, \end{aligned} \quad (18.29)$$

$$\begin{aligned} U(J^e) &= \frac{1}{2} K \left[\frac{1}{2} (J^{e2} - 1) - \ln J^e \right] \\ \bar{W}(\bar{\mathbf{b}}^e) &= \frac{1}{2} \mu (tr[\bar{\mathbf{b}}^e] - 3), \end{aligned} \quad (18.30)$$

where K and μ are elastic bulk and shear moduli, for elastic domain and von-Mises yield function for plastic domain.

All calculations were performed by the finite and spectral-element methods using the multi-purpose software package (FIDESYS LLC 2023)

The first two examples are given in order to examine the numerical algorithm; the next two demonstrate the possibility of accurate calculations with step-by-step geometry changes.

18.5.1 Expansion of Thick-Walled Cylinder

This example was considered in Simo and Ortiz (1985) and Simo (1988b). A thick-walled cylinder with an inner radius of 1 units and an outer radius of 2 units is subjected to prescribed displacement at the internal radius up to 7.5 units, Fig. 18.1.

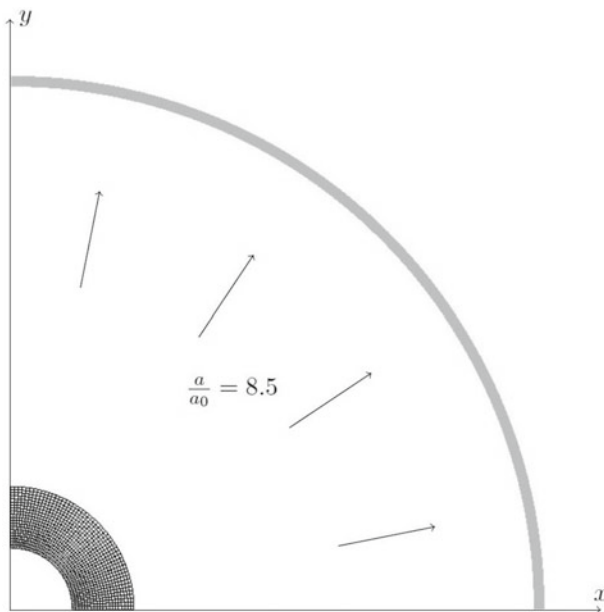


Fig. 18.1 Cylinder expansion

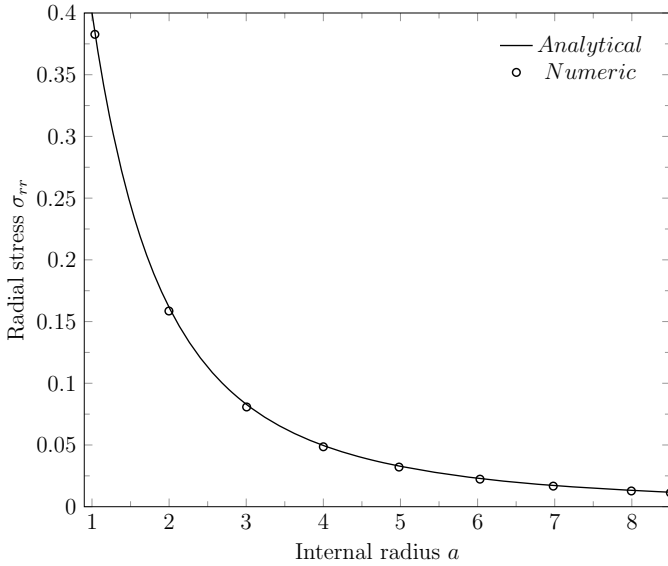


Fig. 18.2 The Cauchy stress σ_{rr} at the internal boundary as a function of internal radius

The values of the material constants shown are chosen to replicate rigid plastic behavior to allow a comparison with the exact solution (Hill 1998): bulk modulus $K = 40$ GPa, shear modulus $\mu = 3.8$ GPa, yield stress $k = 0.5$ MPa. Bi-linear isoparametric elements are used (Figs. 18.2 and 18.3).

18.5.2 Necking of a Circular Bar

The one shown here describes the necking of a circular bar with a radius of 6.413 mm, length of 53.334 mm made of a nonlinearly hardening material. This is experimentally well-documented example given by Simo and Hughes (1998). Material parameters are: Young modulus $E = 207$ GPa, Poisson's ratio $\nu = 0.3$.

The initial meshes are shown in Fig. 18.4 for four cases of 240, 1920, 3840, and 5760 elements. Isoparametric elements with midside nodes are used. The final deformed configurations with imposed edge displacement $u = 7.0$ mm obtained for all meshes are shown in Fig. 18.5, in three dimension for 5760 elements—Fig. 18.6. It is seen that there are no significant differences among the three. Figure 18.7 shows the ratio of the neck radius to the initial radius plotted against the relative elongation of the bar; the centered symbols represent experimental results, the solid curve represents results calculated by the *hyperelastic plasticity* in 15-time steps. The numerical results are in excellent agreement with the experimental ones. Stresses and deformations are shown in Fig. 18.8.

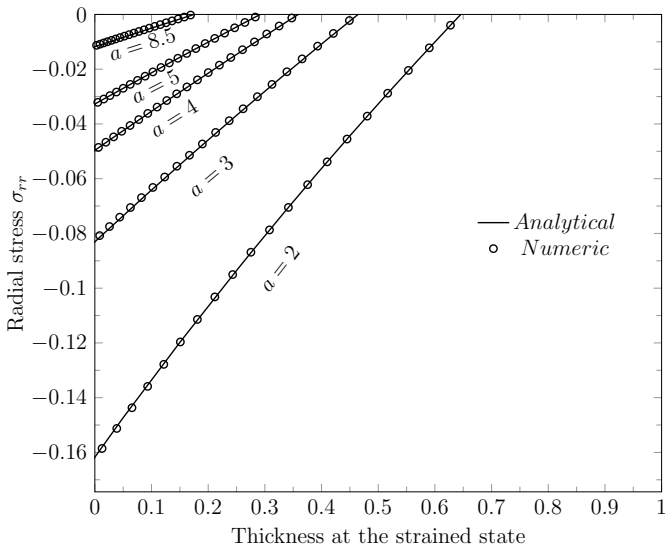


Fig. 18.3 Distribution of the Cauchy stress σ_{rr} over the thickness for the following values of the internal radius: $a = 2, 3, 4, 5, 8.5$

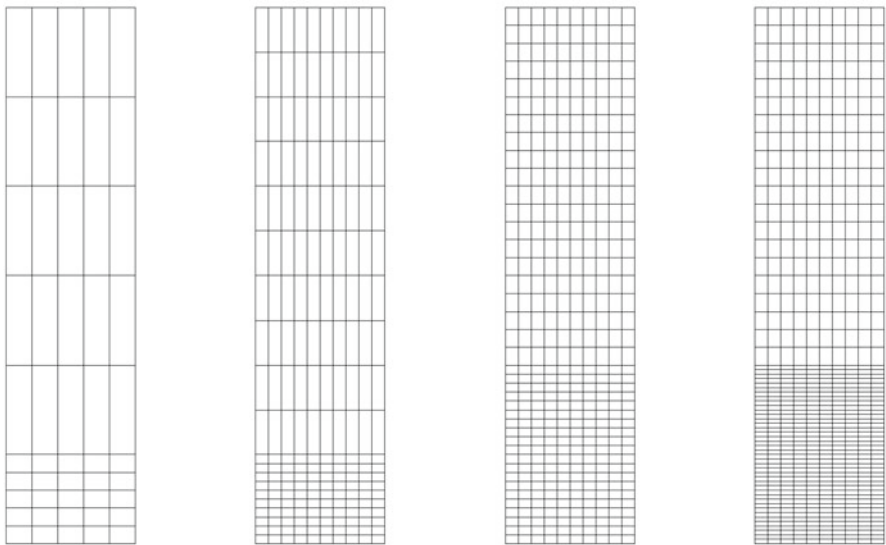


Fig. 18.4 Calculated finite-element meshes, initial view. Calculations have been carried out for the mesh of 240, 1920, 3840, and 5760 elements with refinement in the center

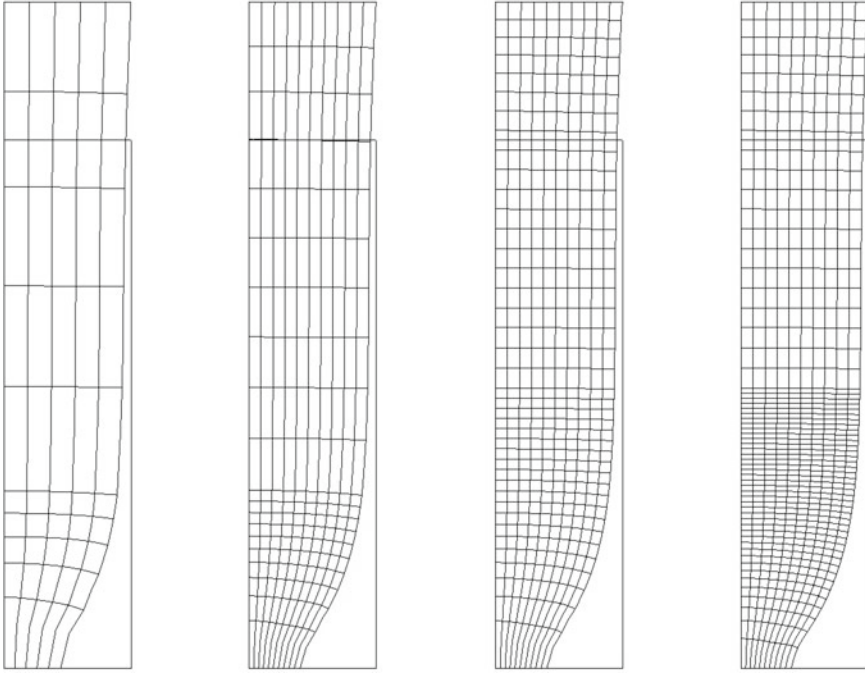
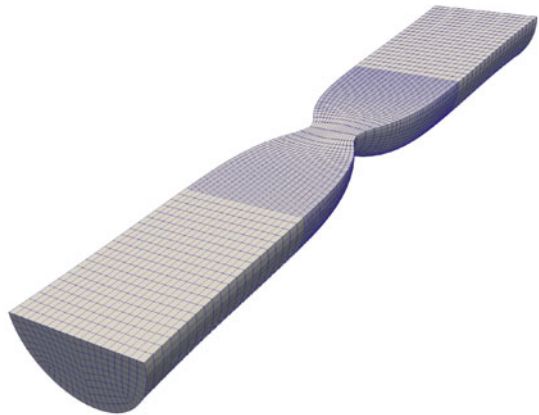


Fig. 18.5 Calculated finite-element meshes. The view of meshes shown above (Fig. 18.4) after deformation

Fig. 18.6 Volumetric mesh for the problem of necking. View after deformation



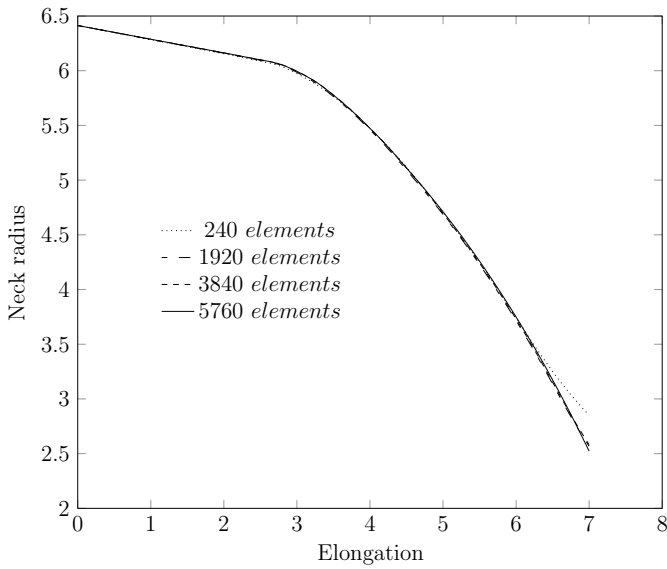


Fig. 18.7 The radius of the sample in the neck area as a function of stretch

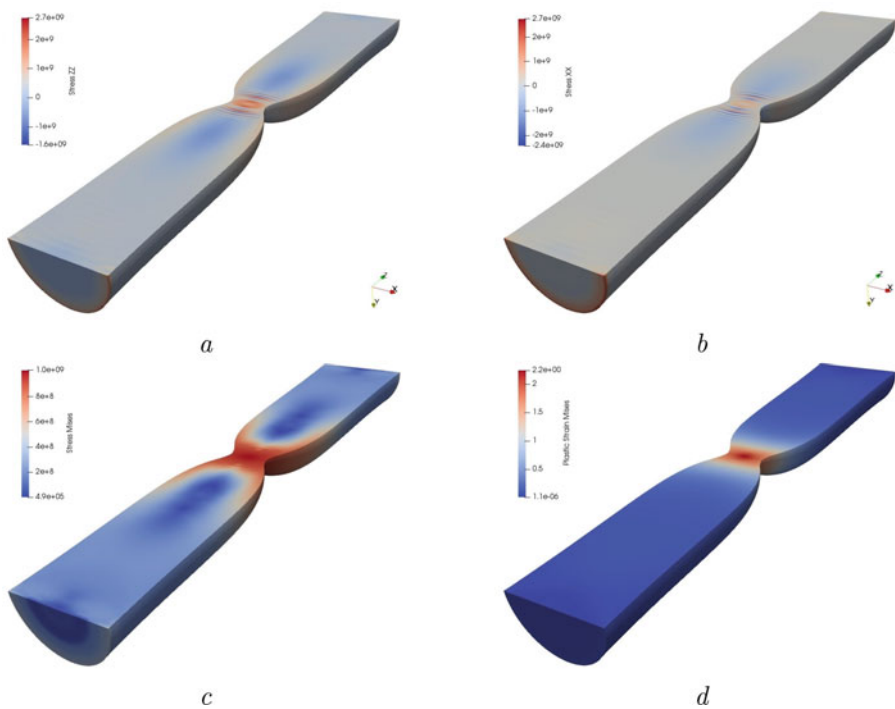


Fig. 18.8 Stress and strain state in the problem of necking. **a**—stress σ_z , **b**— σ_x , **c**—stress intensity, **d**—intensity of plastic strains

18.5.3 *Elongation of the Plate with Step-by-Step Removal of Inclusions*

The step-by-step elongation of the plate with a free circular cutout with the appearance of additional circular cutouts during loading is considered. The side boundaries are free of load, Fig. 18.9.

Previously this task was considered only in case of elastic deformation in Levin et al. (2013), Levin and Zingerman (2008).

This example is characterized by the possible presence of localized shear bands and discontinuous displacements along them. The accuracy of the solution with high-order elements in localization problems is quite well studied, see, for example, Solin et al. (2003), Jeremić and Xenophontos (1999). 4th order spectral elements are used in this study to capture plastic localization (Levin and Krapivin 2022).

Slip-line analysis gives an exact solution to the directions of the plastic flow fields, Hill (1998), Kachanov (1971). A family of logarithmic spirals expressed in polar coordinates as

$$\theta - \theta_0 = \pm \frac{\ln \frac{r}{a}}{\arctan \zeta / 2} \quad (18.31)$$

can adjoin a load-free circular boundary, and a family of straight-line segments can adjoin a load-free rectilinear boundary. Spirals intersect the radius vector at a constant angle $\zeta/2$.

Figure 18.10 shows the evolution of the slip lines. Initially, the slip lines are straight-line segments. When additional circular holes appear in the deformed state, additional lines appear in the form of logarithmic spirals. Thus, an overlap of two patterns of plastic flow is formed.

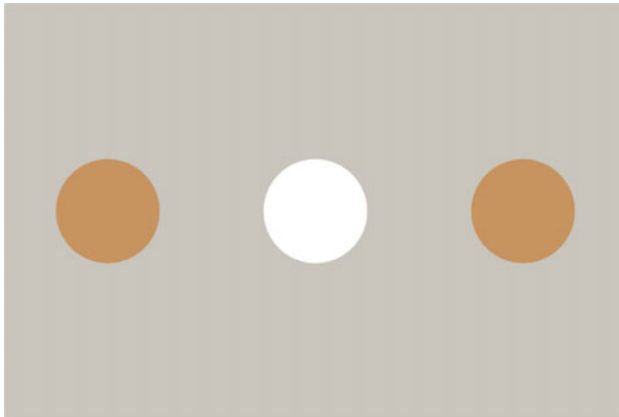


Fig. 18.9 Example 3. Circular inclusions

Fig. 18.10 Shear bands evolution

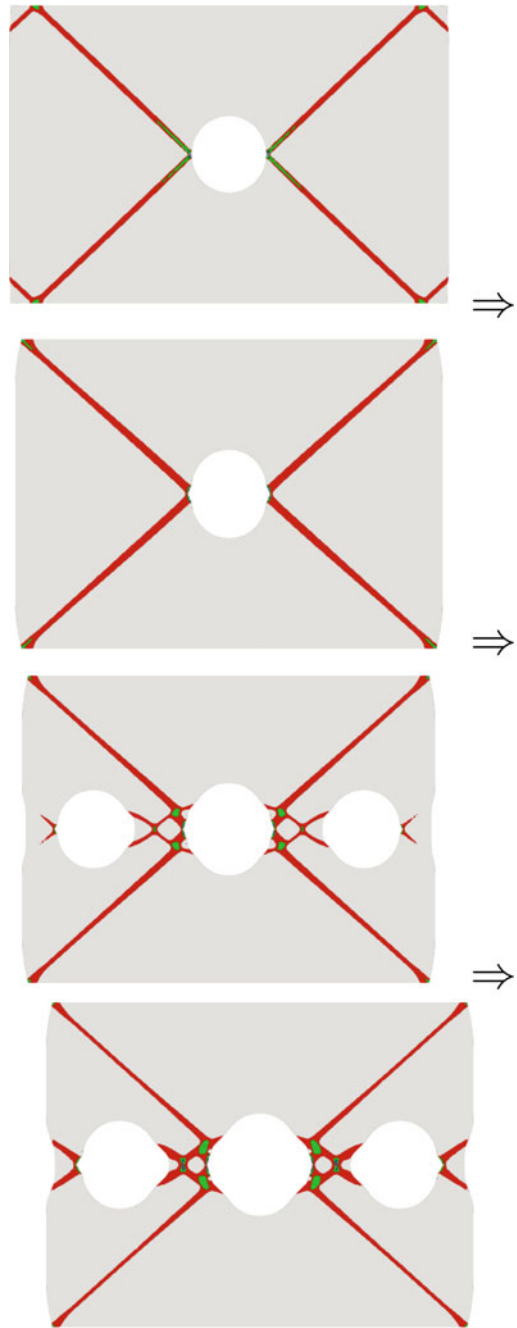
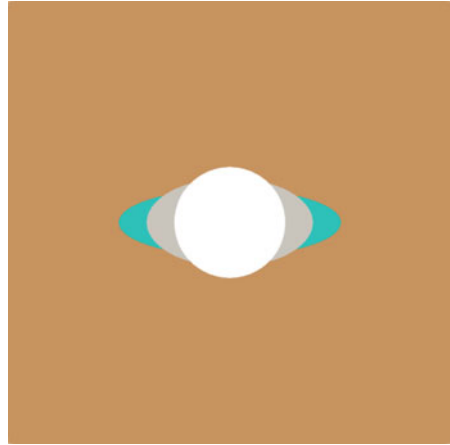


Fig. 18.11 Example 4.
Increasing circular hole



18.5.4 Elongation of the Plate with a Step-by-Step Increase in the Circular Hole

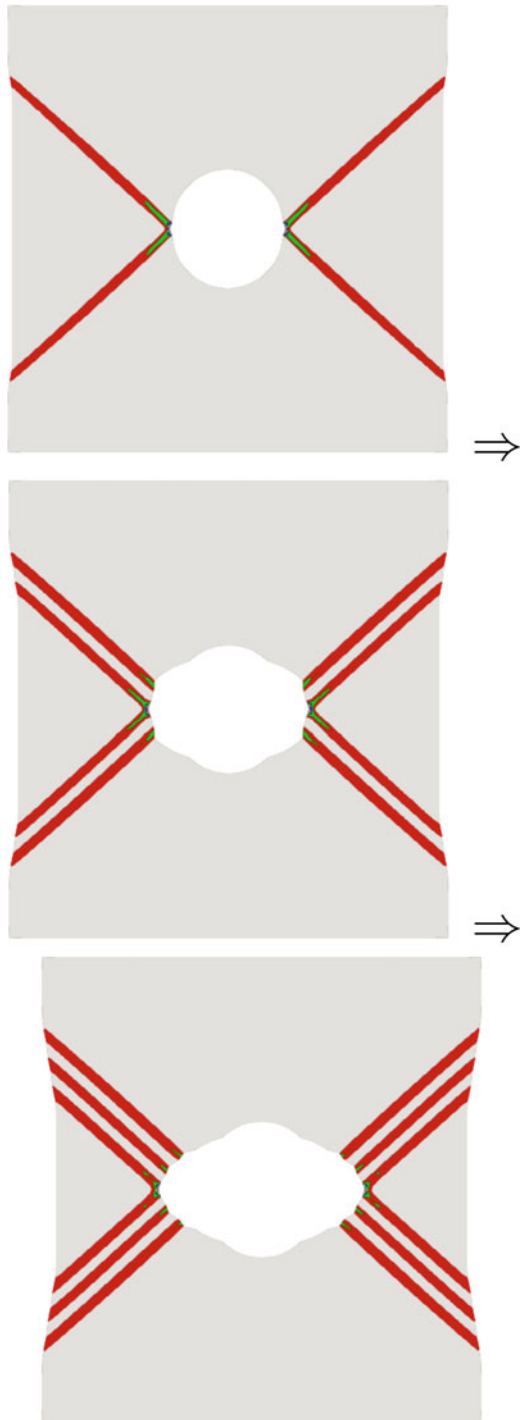
A step-by-step elongation of a plate with a free circular cutout with the removal of blocks in the area of stress concentration during loading is considered. The side boundaries are free of load, Fig. 18.11. In the elastic formulation, this problem is solved in Levin and Morozov (2007). Calculations are performed in three steps. Evolution and geometrical place of shear bands is shown in Fig. 18.12. Example can be useful for researchers of crack initiation and propagation.

18.6 Conclusion

Hyperelastic-based plasticity demonstrates a fast (small number of incremental steps is enough) numerical solutions of the strain localization problems in media with step-by-step exclusion of geometrical parts. The qualitative effect related with multiple superposition of finite strains is that a new family of slip lines is originated at each step of deformation. Thus, an overlap of some plastic flow patterns is formed.

Acknowledgements The research for this article was performed at Lomonosov Moscow State University and was financially supported by the Russian Science Foundation under grants 22-11-00110 (sections 1, 2, 4.3, 4.4) and 19-71-10008 (Sections 3, 4.1, 4.2, 5).

Fig. 18.12 Shear bands evolution



References

- Eremeyev VA (2021) Strong ellipticity conditions and infinitesimal stability within nonlinear strain gradient elasticity. *Mech Res Commun* 117(103):782. <https://doi.org/10.1016/j.mechrescom.2021.103782>
- FIDESYS LLC (2023) CAE FIDESYS. <https://cae-fidesys.com>. Accessed 15 March 2023
- Fish J, Shek K (2000) Finite deformation plasticity based on the additive split of the rate of deformation and hyperelasticity. *Comput Methods Appl Mech Eng* 190(1):75–93. [https://doi.org/10.1016/S0045-7825\(99\)00415-6](https://doi.org/10.1016/S0045-7825(99)00415-6)
- Hibbitt H, Marcal P, Rice J (1970) A finite element formulation for problems of large strain and large displacement. *Int J Solids Struct* 6(8):1069–1086. [https://doi.org/10.1016/0020-7683\(70\)90048-X](https://doi.org/10.1016/0020-7683(70)90048-X)
- Hill R (1998) *The mathematical theory of plasticity*, vol 11. Oxford University Press
- Jeremić B, Xenophontos C (1999) Application of the p-version of the finite element method to elastoplasticity with localization of deformation. *Commun Numer Meth Engng* 15:867–876. [https://doi.org/10.1002/\(SICI\)1099-0887\(199912\)15:12<867::AID-CNM296>3.0.CO;2-9](https://doi.org/10.1002/(SICI)1099-0887(199912)15:12<867::AID-CNM296>3.0.CO;2-9)
- Kachanov LM (1971) *Foundations of the theory of plasticity*. North-Holland, Amsterdam
- Lee EH (1969) Elastic-plastic deformation at finite strains. *J Appl Mech* 36(1):1–6. <https://doi.org/10.1115/1.3564580>
- Lee EH (1981) Some comments on elastic-plastic analysis. *Int J Solids Struct* 17(9):859–872. [https://doi.org/10.1016/0020-7683\(81\)90101-3](https://doi.org/10.1016/0020-7683(81)90101-3)
- Levin VA (1987) Using the method of successive approximations in problems of superposition of finite deformations. *Sov Appl Mech* 23(5):472–476. <https://doi.org/10.1007/BF00888060>
- Levin VA, Krapivin KY (2022) Theoretical and numerical plastic strain localization analysis of isotropic dilating non-associated media at plane strain conditions. *Chebyshevskii Sb* 23(4):285–307. [10.22405/2226-8383-2022-23-4-285-307](https://doi.org/10.22405/2226-8383-2022-23-4-285-307)
- Levin VA, Zingerman KM (2008) A class of methods and algorithms for the analysis of successive origination of holes in a pre-stressed viscoelastic body. finite strains. *Commun Numer Methods Eng* 24(12):2240–2251. [10.1002/cnm.1080](https://doi.org/10.1002/cnm.1080)
- Levin V (1998) Theory of repeated superposition of large deformations: elastic and viscoelastic bodies. *Int J Solids Struct* 35(20):2585–2600. [https://doi.org/10.1016/S0020-7683\(98\)80032-2](https://doi.org/10.1016/S0020-7683(98)80032-2)
- Levin VA, Morozov EM (2007) Nonlocal criteria for determining a prefracture zone in the process of defect growth for finite strains. *Dokl Phys* 52(7):391–393. <https://doi.org/10.1134/S1028335807070129>
- Levin VA, Zingerman KM, Vershinin AV et al (2013) Numerical analysis of the stress concentration near holes originating in previously loaded viscoelastic bodies at finite strains. *Int J Solids Struct* 50(20):3119–3135. <https://doi.org/10.1016/j.ijsolstr.2013.05.019>
- Lurie AI (1990) *Nonlinear theory of elasticity*. North Holland
- McMeeking R, Rice J (1975) Finite-element formulations for problems of large elastic-plastic deformation. *Int J Solids Struct* 11(5):601–616. [https://doi.org/10.1016/0020-7683\(75\)90033-5](https://doi.org/10.1016/0020-7683(75)90033-5)
- Moss WC (1984) On instabilities in large deformation simple shear loading. *Comput Methods Appl Mech Eng* 46(3):329–338. [https://doi.org/10.1016/0045-7825\(84\)90108-7](https://doi.org/10.1016/0045-7825(84)90108-7)
- Nemat-Nasser S (1979) Decomposition of strain measures and their rates in finite deformation elastoplasticity. *Int J Solids Struct* 15(2):155–166. [https://doi.org/10.1016/0020-7683\(79\)90019-2](https://doi.org/10.1016/0020-7683(79)90019-2)
- Nemat-Nasser S (1982) On finite deformation elasto-plasticity. *Int J Solids Struct* 18(10):857–872. [https://doi.org/10.1016/0020-7683\(82\)90070-1](https://doi.org/10.1016/0020-7683(82)90070-1)
- Simo JC (1988a) A framework for finite strain elastoplasticity based on maximum plastic dissipation and the multiplicative decomposition: part I. Continuum formulation. *Comput Methods Appl Mech Eng* 66(2):199–219. [10.1016/0045-7825\(88\)90076-X](https://doi.org/10.1016/0045-7825(88)90076-X)
- Simo JC (1988b) A framework for finite strain elastoplasticity based on maximum plastic dissipation and the multiplicative decomposition. part II: computational aspects. *Comput Methods Appl Mech Eng* 68(1):1–31. [10.1016/0045-7825\(88\)90104-1](https://doi.org/10.1016/0045-7825(88)90104-1)

- Simo JC, Hughes TJR (1998) Computational inelasticity. Springer, New York
- Simo J, Ortiz M (1985) A unified approach to finite deformation elastoplastic analysis based on the use of hyperelastic constitutive equations. *Comput Methods Appl Mech Eng* 49(2):221–245. [https://doi.org/10.1016/0045-7825\(85\)90061-1](https://doi.org/10.1016/0045-7825(85)90061-1)
- Solin P, Segeth K, Dolezel I (2003) Higher-order finite element methods. Chapman and Hall/CRC
- Truesdell C (1972) A first course in rational continuum mechanics. The Johns Hopkins University, Baltimore, Maryland
- Yadav S, Sagapuram D (2020) In situ analysis of shear bands and boundary layer formation in metals. *Proc R Soc A* 476(20190):519. <https://doi.org/10.1098/rspa.2019.0519>
- Zubov LM, Sheidakov DN (2007) Instability of a hollow elastic cylinder under tension, torsion, and inflation. *J Appl Mech* 75(1):011002. <https://doi.org/10.1115/1.2723824>

Chapter 19

Dynamic Buckling of Functionally Graded Plates and Shells Subjected to Thermal Shock



Stanislav V. Levyakov

Abstract In this work, the nonlinear dynamic response of suddenly heated functionally graded shells is studied through nonlinear transient analysis. To this end, a triangular shell finite element with 15 degrees of freedom is developed using the invariant-based approach and the concept of the surface of mass. Equations of motion of the shell finite-element model are integrated numerically by the Newmark method combined with iterative refinement of the solution using the Newton–Raphson procedure. For each time increment, the transient temperature field across the shell thickness is determined by iteratively solving the unsteady heat-conduction equation taking into account temperature-dependent properties of the material. The predicted temperature profile is used to compute the nodal thermal loads and temperature-dependent stiffness characteristics of the shell element. The proposed finite-element formulation is validated against the available solutions of dynamic problems of plates and shells. A number of examples are given to demonstrate nonlinear capabilities of the proposed formulation and to estimate the effect of dynamic thermal loading on buckling instability of FGM plates and shells.

Keywords Functionally graded material · Shells · Thermal shock · Unsteady heat conduction · Nonlinear dynamic buckling · Finite-element modeling

19.1 Introduction

In various fields of engineering, structural members have to operate in thermal environment characterized by elevated temperatures and high thermal gradients. Aerospace technology and nuclear engineering are modern areas of engineering where structures may be subjected to rapid surface heating, which leads to unsteady heat conduction and high thermal stresses referred to as thermal shock. Thin-walled

S. V. Levyakov (✉)

Department of Engineering Mathematics, Novosibirsk State Technical University, 630092
Novosibirsk, Russian Federation
e-mail: stan-levyakov@yandex.ru

© The Author(s), under exclusive license to Springer Nature Switzerland AG 2023
H. Altenbach and V. Eremeyev (eds.), *Advances in Linear and Nonlinear Continuum and Structural Mechanics*, Advanced Structured Materials 198,
https://doi.org/10.1007/978-3-031-43210-1_19

325

members subjected to thermal shock may experience large-amplitude motion and even exhibit unstable behavior that affects the performance of the structure.

Boley (1956) was the first to provide theoretical analysis of thermally induced vibrations of a thin beam subjected to step heating. Based on the linear beam bending theory, he obtained the exact analytical solution governing forced lateral vibrations caused by thermal moment that occurs due to transient non-uniform temperature distribution through the beam cross-section. Jones (1966), Seibert and Rice (1973) refined the solution of the problem by taking into account transverse shear effects and rotary inertia. One of the earliest finite-element formulations for dynamic analysis of beams and plates under unsteady heat conduction was proposed by Mason (1968). Stroud and Mayers (1971) studied the effect of temperature-dependent material properties on the dynamic response of a rapidly heated plate. It was shown that neglect or even incomplete consideration of the temperature dependence can lead to dangerously unconservative results. Das (1983) reported on vibrations of thin polygonal plates subjected to thermal shock through the complex variable theory. Irie and Yamada (1978) obtained analytical solution governing thermally induced axisymmetric vibrations of circular and annular plates subjected to a sinusoidally varying heat flux. Based on coupled equations of thermoelasticity, Al-Huniti et al. (2003) studied small transient deflections of a thin simply supported rectangular plate subjected to suddenly applied laser pulse of short duration. Nakajo and Hayashi (1988) studied dynamic axisymmetric response of circular plates under thermal impact by analytical and finite-element methods. They emphasized the significance of geometric nonlinearity in the analysis of plates with immovable edge. The studies mentioned above deal with homogeneous isotropic plates.

Tauchert (1989) investigated thermally induced vibrations of homogeneous orthotropic rectangular plates having two parallel simply supported edges. Chang et al. (1992) developed a finite element for linear analysis of thermally-induced vibrations of shear deformable laminated plates under thermal impact. Based on the finite-element results, they discussed the effect of boundary conditions and stacking sequence of laminates on the magnitude of vibrations. Adams and Bert (1999) studied the effect of orthotropic mechanical and thermal properties of the material on small-amplitude vibrations of a thin symmetrically laminated rectangular plate subjected to a step heat flux. The transient stresses and displacements in a thin orthotropic cylindrical shell subjected to instantaneous thermal shock were discussed by Huan and Wo (1980). Using the Donnell shell theory, Birman (1990) presented the analysis of dynamic response of linear and geometrically nonlinear reinforced cylindrical shells manufactured from composite materials. For various reinforcements, he evaluated the critical temperature at which the shells exhibit dynamic buckling behavior.

There has been a renewed interest in the analysis of thermally induced vibrations after the advent of functionally gradient materials (FGM) representing new class of advanced composite materials. Owing to high thermal resistance, FGMs are used in the design of structures operating under ultrahigh temperatures and large thermal gradients. There exists a large body of literature on stresses, vibrations, and buckling of mechanically and thermally loaded structural elements fabricated of FGMs. In

what follows, we confine our review to those contributions that deal with thermally induced vibrations of rapidly heated thin-walled structures.

Ma and Lee (2011) reported on small-amplitude lateral vibrations of a shear-deformable FG beam about thermally bent configuration caused by uniform temperature distribution. Based on the numerical solution of the governing equations, they studied the effect of thermal load on the beam frequencies taking into account temperature-dependent material properties. A more accurate approach based on nonlinear transient analysis of FG beams was proposed by Ghiasian et al. (2014). Nonlinear equations of motion were solved by the multi-term p-Ritz method combined with the Newmark integration scheme in the time domain. The issue of dynamic buckling of beams subjected to uniform rapid heating was briefly discussed by Ghiasian et al. (2015) based on the Budiansky-Roth criterion. Using a finite-element formulation, Malik and Kadoli (2017, 2018) studied thermally induced vibrations of FG beams taking into account geometrical nonlinearity and temperature-dependent properties of the material. Javani et al. (2019a) presented nonlinear dynamic analysis of suddenly heated shallow circular arches. The governing differential equations based on the first-order shear deformation theory and strain–displacement relations of the von Karman type were discretized and solved by the hybrid generalized differential quadrature method combined with the Newmark time integration scheme. A similar approach was used to investigate large-amplitude thermally induced vibrations of annular sector plates (Javani et al. 2021) and circular plates (Kiani and Eslami 2014; Javani et al. 2019b). Axisymmetric dynamic response of suddenly heated shallow cylindrical and conical shells was studied in Esmaili et al. (2019); Javani et al. (2019c), respectively. Javani et al. (2020) and Taleb et al. (2022) addressed the dynamic snap-through instability of shallow spherical caps.

Prakash et al. (2007) employed a finite-element procedure to investigate nonlinear dynamic buckling of shear-flexible FG spherical caps subjected to step heating. Zhang et al. (2019) dealt with axisymmetric dynamic thermal buckling of annular plates with small initial geometric imperfections. The governing equations based on the classical plate theory were solved by expanding the deflections in power series and integrating numerically in the time domain. Zhang et al. (2015) examined the effect of grading material properties on axisymmetric transient displacements of rapidly heated thin cylindrical shells by the differential quadrature method. Dynamic thermal buckling of geometrically perfect cylindrical shells was studied by Zhang et al. (2020) using the symplectic method. Pandey and Pradyumna (2018) proposed a finite-element formulation for transient stress analysis of FGM plates and panels based on the higher-order layerwise theory. Using a 20-node solid finite element, Czechowski (2015) studied dynamic buckling of a clamped rectangular plate FGM plate subjected to thermal heat flux loading of short duration.

The dynamic response of rapidly heated thin-walled structures made of FGMs represents a relatively new area of investigation. As can be seen from the existing literature, only a limited number of works have so far been reported on thermally induced nonlinear vibrations and dynamic buckling of suddenly heated plates and shells. The available results are confined to circular plates and shallow shells of revolution undergoing axisymmetric deformations. The effect of initial geometric

imperfections, which play an important role in the dynamic buckling behavior, has been discussed only briefly.

It is of interest to examine the dynamic stability of suddenly heated FGM shells through nonlinear transient analysis, which appears to be the most realistic approach to the problem. Transient analysis of nonlinear shells can be efficiently carried out using time marching schemes combined with iterative determination of deformed configuration at each time increment. Among available numerical approaches, the finite element method is one of the most successful and powerful tools. Typically, a finite-element model of a shell of relatively simple geometry involves thousands and even more solution variables to be operated on. Hence, much computer memory and time is required to repeatedly solve large system of equations governing dynamic response of the model. In most cases, the computational process is very time-consuming even for the current state-of-the-art computers. It is therefore of importance to develop effective numerical techniques that would allow one to reduce computational effort while providing reasonable accuracy in the calculations.

Our goal in this work is to develop a computationally-effective finite-element formulation for geometrically nonlinear analysis of thermally induced motion of functionally graded shells. To this end, we revisit the formulation reported in Levyakov and Kuznetsov (2011, 2014) to take into account inertia forces, thermal loads due to unsteady heat conduction, and temperature-dependent material properties.

19.2 Material Properties

We consider a shell made of a functionally graded material consisting of metal and ceramic constituents. The material properties are assumed to be graded in the thickness direction according to the power law (Shen 2009)

$$P(z, T) = P_m(T) + [P_c(T) - P_m(T)](0.5 + z/h)^n$$

$$(-h/2 \leq z \leq h/2) \quad (19.1)$$

where P denotes mechanical or thermal property of the material (Young's modulus, Poisson's ratio, coefficient of linear thermal expansion, etc.), T is the current temperature, h is the shell thickness, z is the distance measured from the shell middle surface, subscripts m and c refer to metal and ceramic phases, respectively, and n is a positive constant referred to as the grading index.

Dependence of material properties on temperature is commonly described by the power law

$$P_i = P_0(P_{-1}T^{-1} + 1 + P_1T + P_2T^2 + P_3T^3), \quad (i = c, m) \quad (19.2)$$

where P_{-1}, P_0, \dots, P_3 are coefficients determined for each constituent material.

19.3 Temperature Distribution

We consider non-steady one-dimensional problem of heat transfer through the thickness of a shell with temperature dependent material properties, assuming that heat transfer does not depend on a deformed configuration of the shell. The one-dimensional Fourier-Biot heat conduction equation to be solved for the temperature field $T = T(z, t)$ is given by

$$(\kappa T')' - \rho c_p \dot{T} = 0$$

$$0 \leq t, \quad -h/2 \leq z \leq h/2 \quad (19.3.1)$$

where $\kappa = \kappa(z, T)$ is the thermal conductivity, $\rho = \rho(z)$ is the density of the material, $c_p = c_p(z, T)$ is the specific heat capacity, and prime and superposed dot denote partial derivatives with respect to the transverse coordinate z and time t , respectively. Since the temperature profile varies with time, the material properties mentioned above are functions of z and t .

The initial condition is assumed to be

$$T(z, 0) = T_{ref} \quad (19.3.2)$$

where T_{ref} is the reference temperature at which the shell is stress free. We confine our attention to the following three types of thermal boundary conditions:

$$T(-h/2, t) = f(t)$$

$$T(h/2, t) = f(t) \quad (19.3.3)$$

$$T(-h/2, t) = T_{ref}$$

$$T(h/2, t) = f(t) \quad (19.3.4)$$

$$T'(-h/2, t) = 0$$

$$T(h/2, t) = f(t) \quad (19.3.5)$$

in which $f(t)$ is a prescribed boundary temperature.

The two common representations of the thermal shock are given by

$$f(t) = \Delta T \cdot H(t) \quad (19.3.6)$$

$$f(t) = \Delta T(1 - e^{-\sigma t}), \quad \sigma > 0 \quad (19.3.7)$$

where $H(t)$ is the Heaviside unit step function and σ is the loading parameter.

Because of inhomogeneous structure of the material and temperature-dependent properties, the solution of the heat-conduction problem (19.3.1)–(19.3.5) by analytical methods encounters serious mathematical difficulties. To solve the problem, we employ the finite-element method with step-by-step computations in the time domain. Equation (19.3.1) is multiplied by a test function and then integrated to obtain the variational form of the problem. We divide the shell thickness into elements of equal length Δz and assume that the material properties κ , ρ , and c_p are constant within each element.

Following the standard approximation procedure (see, e.g. (Zienkiewicz and Morgan 1983) and (Reddy 2004)), we use piecewise linear test functions and integrate over z . As a result, we arrive at a system of nonlinear ordinary differential equations, which can be converted to matrix form

$$\mathbf{K}(T)\mathbf{T} + \mathbf{R}(T)\dot{\mathbf{T}} = \mathbf{0} \quad (19.3.8)$$

where \mathbf{T} is the vector representing nodal temperatures, \mathbf{K} and \mathbf{R} are tridiagonal symmetric matrices depending on the nodal temperatures.

Let the time domain be represented by a sequence of finite elements of length Δt . Within the n -th time element, the temperature field can be approximated by the linear shape functions

$$\begin{aligned} \mathbf{T} &= \mathbf{T}^n N_1 + \mathbf{T}^{n+1} N_2 \\ N_1 &= 1 - (t - t^n)/\Delta t \\ N_2 &= (t - t^n)/\Delta t \end{aligned} \quad (19.3.9)$$

where $t^n < t < t^{n+1}$.

Using the weighted residual method to solve Eqs. (19.3.8), we require that the equations be satisfied at collocation points $t = t^n + \tau \Delta t$ ($0 < \tau < 1$). After integration of the equations, we obtain

$$(\tau \Delta t \mathbf{K}^{n+\tau} + \mathbf{R}^{n+\tau})\mathbf{T}^{n+1} + ((1 - \tau)\Delta t \mathbf{K}^{n+\tau} - \mathbf{R}^{n+\tau})\mathbf{T}^n = \mathbf{0} \quad (19.3.10)$$

where $\mathbf{K}^{n+\tau} = \mathbf{K}(\mathbf{T}^{n+\tau})$, $\mathbf{R}^{n+\tau} = \mathbf{R}(\mathbf{T}^{n+\tau})$, and $\mathbf{T}^{n+\tau} = (1 - \tau)\mathbf{T}^n + \tau\mathbf{T}^{n+1}$.

The matrices $\mathbf{K}^{n+\tau}$ and $\mathbf{R}^{n+\tau}$ are assembled from the elemental matrices

$$\mathbf{K}_e^{n+\tau} = \frac{1}{\Delta z} \kappa^{\tau+n} \begin{pmatrix} 1 & -1 \\ -1 & 1 \end{pmatrix}$$

$$\mathbf{R}_e^{n+\tau} = \frac{1}{6\Delta z} \rho c_p^{n+\tau} \begin{pmatrix} 2 & 1 \\ 1 & 2 \end{pmatrix} \quad (19.3.11)$$

where the material properties are calculated at the point $z_\eta = (1 - \eta)z_e + \eta z_{e+1}$ ($0 < \eta < 1$) within the element at instant $t = t^n + \tau \Delta t$.

Temperature at which the material properties are evaluated is given by

$$T_\eta^{n+\tau} = (1 - \tau)(1 - \eta)T_e^n + (1 - \tau)\eta T_{e+1}^n + \tau(1 - \eta)T_e^{n+1} + \tau\eta T_{e+1}^{n+1} \quad (19.3.12)$$

In the computations, we set $\tau = \eta = 1/2$, which gives errors of $O(\Delta t^2)$ and $O(\Delta z^2)$ in determining the temperature profile. To solve Eqs. (19.3.10), we use the iterative Newton–Raphson procedure assuming the Hessian to be constant at each time step. The computation scheme is given by

$$\begin{aligned} &(\tau \Delta t \mathbf{K}_{(i)}^{n+\tau} + \mathbf{R}_{(i)}^{n+\tau}) \delta \mathbf{T}_{(i)}^{n+1} + (\tau \Delta t \mathbf{K}_{(i)}^{n+\tau} + \mathbf{R}_{(i)}^{n+\tau}) \mathbf{T}_{(i)}^{n+1} + \\ &+ ((1 - \tau) \Delta t \mathbf{K}_{(i)}^{n+\tau} - \mathbf{R}_{(i)}^{n+\tau}) \mathbf{T}^n = \mathbf{0} \end{aligned} \quad (19.3.13)$$

$$\mathbf{T}_{(i+1)}^{n+1} = \mathbf{T}_{(i)}^{n+1} + \delta \mathbf{T}_{(i)}^{n+1}$$

where $\delta \mathbf{T}$ is the increment in the nodal temperatures and subscript i enumerates iterations in the time domain.

19.4 Shell Finite Element Formulation

We develop a shell finite element formulation for nonlinear dynamic analysis of FGM shells using the invariant-based approach proposed in Levyakov and Kuznetsov (2011); Levyakov and Kuznetsov (2014). We recall some basic statements of the approach.

19.4.1 Invariant Representations

Given two tensors u_{mn} and v_{mn} ($m, n = 1, 2$) referred to Cartesian system of reference $\xi_1 O \xi_2$, the combined invariant is defined as

$$I_{uv} = \frac{1}{2} e_{mp} e_{nq} u_{mn} v_{pq} \quad (19.4.1)$$

where e_{mp} is the permutation tensor with the components $e_{11} = e_{22} = 0, e_{12} = -e_{21} = 1$ and summation is performed over dummy indices unless otherwise specified.

It is worth noting that Eq. (19.4.1) implies the well-known results. Namely, setting $v_{mn} = 2\delta_{mn}$ (δ_{mn} being the Kronecker delta) and $v_{mn} = u_{mn}$, from Eq. (19.4.1) we, respectively, obtain the first and second invariants of the tensor u_{mn}

$$I_u = u_{11} + u_{22}$$

$$I_{uu} = u_{11}u_{22} - u_{12}^2 \tag{19.4.2}$$

When dealing with a triangular domain, it is reasonable to introduce three natural coordinates γ_i ($i = 1, 2, 3$) defined by three directions along the triangle's edges (see Fig. 19.1). Then the tensor u_{mn} can be represented by three natural components u_i ($i = 1, 2, 3$) determined in the three directions (no summation over i).

$$u_i = \alpha_{mni}u_{mn} \tag{19.4.3}$$

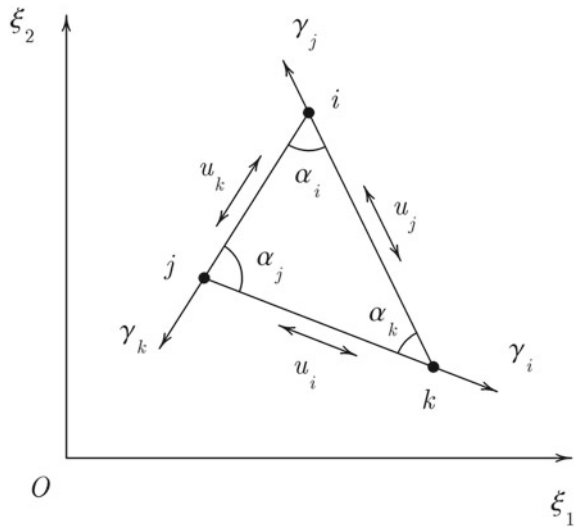
$$\alpha_{mni} = \lambda_{mi}\lambda_{ni}, \lambda_{mi} = \frac{1}{l_i}(\xi_{mk} - \xi_{mj}), (m, n = 1, 2; i, j, k = 1, 2, 3),$$

where ξ_{mk} is the m -th coordinate of the k -th vertex, l_i is the length of the side opposite to the i -th vertex, and the subscripts i, j , and k obey the rule of cyclic permutation.

Using matrix notation, the invariants (19.4.1) and (19.4.2) can be written in terms of the natural components as

$$I_u = \mathbf{u}^T \boldsymbol{\tau}, I_{uu} = \mathbf{u}^T (\mathbf{a}\mathbf{a}^T - \boldsymbol{\rho})\mathbf{u}, I_{uv} = \mathbf{u}^T (\mathbf{a}\mathbf{a}^T - \boldsymbol{\rho})\mathbf{v} \tag{19.4.4}$$

Fig. 19.1 Natural coordinates of a triangular element



$$\begin{aligned} \mathbf{u} &= \{u_1, u_2, u_3\}^T, \quad \mathbf{v} = \{v_1, v_2, v_3\}^T, \quad \mathbf{a} = \{a_1, a_2, a_3\}^T, \quad \boldsymbol{\tau} = \\ &2\{a_1(a - 2a_1), a_2(a - 2a_2), a_3(a - 2a_3)\}^T, \quad \boldsymbol{\rho} = \text{diag}(2a_1^2, 2a_2^2, 2a_3^2), \\ \Delta &= (l_p l_p)^2 - 2l_p^2 l_p^2, \quad a_p = \frac{(l_p)^2}{\sqrt{\Delta}} \text{ (no summation over } p), \\ a &= \frac{l_p l_q}{\sqrt{\Delta}} \quad (p, q = 1, 2, 3), \end{aligned}$$

where superscript T is a transpose of the matrix.

19.5 Reference Surface

To formulate kinematic relations of the finite element, we use the surface of mass as a reference surface whose position is given by

$$z_R = \int_{-h/2}^{h/2} \rho z dz \left(\int_{-h/2}^{h/2} \rho dz \right)^{-1} \quad (19.4.5)$$

where $\rho = \rho(z)$ is the density of the material.

The concept of the surface of mass is adopted here to decouple translations and rotations in the expression for the kinetic energy of FGM shell with non-uniform distribution of material properties across the thickness.

Under the assumptions of the first-order shear deformation theory, the position vectors of a material particle of the shell in the initial and deformed configurations are, respectively, written as

$$\mathbf{r}^z = \mathbf{r} + (z - z_R)\mathbf{d}, \quad \mathbf{r}^{*z} = \mathbf{r}^* + (z - z_R)\mathbf{d}^* \quad (19.4.6)$$

where \mathbf{r} is the position vector of the surface of mass, \mathbf{d} is the unit vector (director) normal to the undeformed middle surface, and the asterisk denotes variables that refer to a deformed state of the shell.

19.5.1 Kinematics of the Shell Element

A three-node triangular finite element proposed in Levyakov and Kuznetsov (2011); Levyakov and Kuznetsov (2014) is modified in the present work to incorporate inertia effects. The element geometry is determined by three nodal position vectors \mathbf{r}_i , \mathbf{r}_j , and \mathbf{r}_k and three nodal directors \mathbf{d}_i , \mathbf{d}_j , and \mathbf{d}_k normal to the reference surface in the undeformed state (see Fig. 19.2). We note that the three nodes and adjoined directors constitute a kinematic group which plays an important role in the formulation of the shell element.

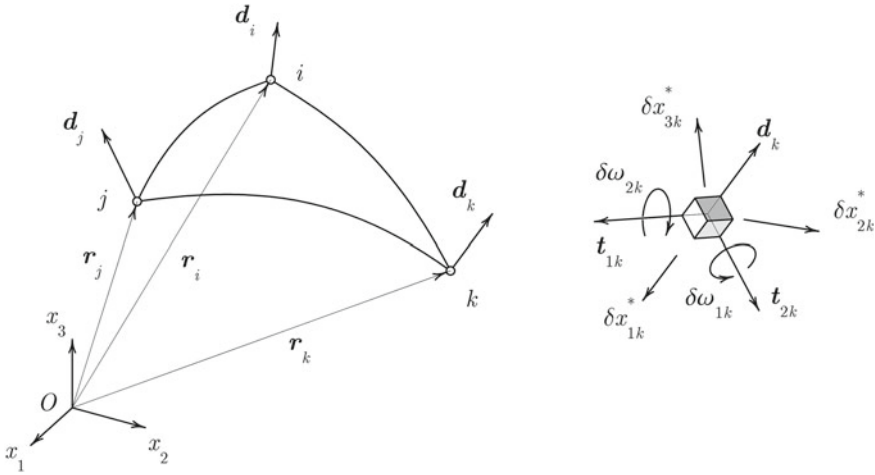


Fig. 19.2 Shell element and nodal degrees of freedom

In accordance with the first-order shear deformation theory of plates and shells, the directors are not necessarily normal to the surface but do not change in length. The element possesses 5 degrees of freedom (DOF) per node: three translations in the coordinate directions and two rotations of the nodal director. A total number of DOFs is equal to 15, which represent 9 straining modes and 6 rigid-body modes of motion.

Possible changes in the position and configuration of the element are characterized by the vector of generalized coordinates

$$\delta \mathbf{q}_e = [\delta \mathbf{q}_1^T, \delta \mathbf{q}_2^T, \delta \mathbf{q}_3^T]^T, \delta \mathbf{q}_n^T = [\delta x_{1n}^*, \delta x_{2n}^*, \delta x_{3n}^*, \delta \omega_{1n}, \delta \omega_{2n}] \quad (n = 1, 2, 3) \tag{19.4.7}$$

where x_{mn}^* are the components of the nodal position vector \mathbf{r}_n^* in a deformed state and ω_{mn} are the components of the rotation vector of the nodal director \mathbf{d}_n^* .

19.5.2 Strain Energy

Using the assumptions of the first-order shear deformation theory, we write the strains of the heated shell as

$$S_{mn} = \varepsilon_{mn} + (z - z_R)\kappa_{mn} - \alpha(T - T_{ref})$$

$$S_{m3} = \gamma_{m3} \quad (m, n = 1, 2) \tag{19.4.8}$$

where ε_{mn} and κ_{mn} are the membrane strains and curvature changes of the reference surface $z = z_R$, respectively, $\alpha = \alpha(z, T)$ is the coefficient of linear thermal expansion, and γ_{13} and γ_{23} are the transverse shear strains.

The strain energy density of the shell can be expressed in terms of invariants as

$$\Pi_V = \frac{1}{2} \frac{E}{1 - \nu^2} \left(I_S^2 - 2(1 - \nu)I_{SS} + \frac{1 - \nu}{2} I_\Gamma \right) \tag{19.4.9}$$

where I_S and I_{SS} are the first and second invariants of the strain tensor S_{mn} , respectively, I_Γ is the first invariant of the tensor $\Gamma_{mn} = S_{m3}S_{n3}$, $E = E(z, T)$ is Young’s modulus, and $\nu = \nu(z, T)$ is Poisson’s ratio of the material. The invariants appearing in Eq. (19.4.8) are determined using the template Eqs. (19.4.2) or (19.4.3).

Substituting Eqs. (19.4.7) into Eq. (19.4.8) and integrating over the shell thickness, we obtain the strain energy

$$\begin{aligned} \Pi = \frac{1}{2} \iint_A & (B_1 I_\varepsilon^2 - 2B_2 I_{\varepsilon\varepsilon} + D_1 I_\kappa^2 - 2D_2 I_{\kappa\kappa} + \\ & 2G_1 I_\varepsilon I_\kappa - 4G_2 I_{\varepsilon\kappa} + C_\Gamma I_\Gamma - 2N_T I_\varepsilon - 2M_T I_\kappa + 2\alpha_0) dA \end{aligned} \tag{19.4.10}$$

where

$$(B_1, G_1, D_1) = \int_{-\frac{h}{2}}^{\frac{h}{2}} (1, z - z_R, (z - z_R)^2) \frac{E}{1 - \nu^2} dz \tag{19.4.11}$$

$$(B_2, G_2, D_2) = \int_{-\frac{h}{2}}^{\frac{h}{2}} (1, z - z_R, (z - z_R)^2) \frac{E}{1 + \nu} dz \tag{19.4.12}$$

$$(N_T, M_T) = \int_{-\frac{h}{2}}^{\frac{h}{2}} (1, z - z_R) \frac{E}{1 - \nu} \alpha(T - T_{ref}) dz \tag{19.4.13}$$

$$C_\Gamma = k \int_{-\frac{h}{2}}^{\frac{h}{2}} G dz$$

$$\alpha_0 = \int_{-\frac{h}{2}}^{\frac{h}{2}} \frac{E}{1 - \nu} \alpha^2(T - T_{ref})^2 dz \tag{19.4.14}$$

Here A is the area of the shell middle surface, $G = 0.5E/(1+\nu)$ is the shear modulus, k is the shear correction factor introduced to account for non-uniform distribution of transverse shear stresses in the thickness direction.

Since the material properties are functions of the coordinate z and time t , the integrals in Eqs. (19.4.11)–(19.4.14) can be evaluated by numerical methods only. We employ the trapezoidal rule for this purpose.

Using Eqs. (19.4.3), we express the strain energy (19.4.9) of the triangular element in terms of the natural components of the strain tensors

$$\begin{aligned} \Pi_e = \frac{1}{2} \iint_{A_e} \{ \boldsymbol{\varepsilon}^T [B_1 \boldsymbol{\tau} \boldsymbol{\tau}^T - 2B_2(\mathbf{a}\mathbf{a}^T - \boldsymbol{\rho})] \boldsymbol{\varepsilon} + \boldsymbol{\kappa}^T [D_1 \boldsymbol{\tau} \boldsymbol{\tau}^T - 2D_2(\mathbf{a}\mathbf{a}^T - \boldsymbol{\rho})] \boldsymbol{\kappa} + \\ 2\boldsymbol{\varepsilon}^T [G_1 \boldsymbol{\tau} \boldsymbol{\tau}^T - 2G_2(\mathbf{a}\mathbf{a}^T - \boldsymbol{\rho})] \boldsymbol{\kappa} + C_\Gamma \boldsymbol{\tau}^T \boldsymbol{\Gamma} - 2\boldsymbol{\tau}^T (N_T \boldsymbol{\varepsilon} + M_T \boldsymbol{\kappa}) + 2\alpha_0 \} dA_e \end{aligned} \quad (19.4.15)$$

where $\boldsymbol{\varepsilon}^T = \{ \varepsilon_1, \varepsilon_2, \varepsilon_3 \}^T$, $\boldsymbol{\kappa}^T = \{ \kappa_1, \kappa_2, \kappa_3 \}^T$, $\boldsymbol{\Gamma}^T = \{ \Gamma_1, \Gamma_2, \Gamma_3 \}^T$ are vectors of the natural strains, and A_e is the element area computed by the formula $A_e = \frac{1}{4}\sqrt{\Delta}$, in which Δ is computed using Eqs. (19.4.4).

Using approximations of the natural strains considered in Levyakov and Kuznetsov (2011), after integration over the element area in Eq. (19.4.14), we obtain the strain energy of the element.

$$\Pi_e = \frac{1}{2} \mathbf{u}^T \mathbf{K} \mathbf{u} - \mathbf{u}^T \mathbf{P} + \alpha_0 A_e \quad (19.4.16)$$

where \mathbf{u} is the 9×1 vector of the generalized elastic strains, \mathbf{K} is the 9×9 stiffness matrix, \mathbf{P} is the 9×1 vector of thermal loads (for detailed derivation, the reader is referred to Levyakov and Kuznetsov (2011)).

To formulate algorithm for determining the deformed configuration of the shell, it is necessary to find the first and second variations of the strain energy.

$$\begin{aligned} \delta \Pi_e &= \mathbf{g}_e^T \delta \mathbf{q}_e \\ \delta^2 \Pi_e &= \delta \mathbf{q}_e^T \mathbf{H}_e \delta \mathbf{q}_e \end{aligned} \quad (19.4.17)$$

where is \mathbf{g}_e and \mathbf{H}_e the gradient and the Hessian of the element, respectively, and $\delta \mathbf{q}_e$ is given by Eq. (19.4.7).

19.5.3 Kinetic Energy

Using Eq. (19.4.6) and taking into account Eq. (19.4.5), we write the kinetic energy of the shell element

$$T_e = \frac{1}{2} \iint_A (I_0 \dot{\mathbf{r}}^{*2} + I_2 \dot{\mathbf{d}}^{*2}) dA_e$$

$$(I_0, I_2) = \int_{-h/2}^{h/2} (1, (z - z_R)^2) \rho dz \quad (19.4.18)$$

We determine the mass matrix of the triangular finite element using the direct mass lumping. Assuming that nodal contribution of the mass distribution over the element is proportional to the angle at the node, we obtain the 15×15 diagonal mass matrix

$$\mathbf{M}_e = \text{diag}(\boldsymbol{\mu}_1^T, \boldsymbol{\mu}_2^T, \boldsymbol{\mu}_3^T)$$

$$\boldsymbol{\mu}_i^T = A_e (\alpha_i / \pi) \{I_0, I_0, I_0, I_2, I_2\} \quad (19.4.19)$$

where α_i is the angle at the i -th vertex of the element. In what follows, we ignore the terms I_2 representing rotary inertia.

Assuming that rotary inertia I_2 is of minor significance compared to translational inertia I_0 , we set $I_2 = 0$.

19.6 Finite-Element Equations of Motion and Solution Method

The equations of motion of the shell finite-element model can be obtained using Hamilton's principle

$$\delta \int_{t_1}^{t_2} \sum_e (T_e - \Pi_e) dt = 0 \quad (19.5.1)$$

where t_1 and t_2 are instants of time and summation is performed over the finite elements.

Substituting expressions for the strain energy (19.4.15) and the kinetic energy (19.4.16) of the element into Eq. (19.5.1) and integrating by parts, we obtain nonlinear equations of motion

$$\mathbf{M}\ddot{\mathbf{q}} + \mathbf{C}\dot{\mathbf{q}} + \mathbf{g} = \mathbf{0} \quad (19.5.2)$$

in which \mathbf{M} , \mathbf{C} , \mathbf{g} , and \mathbf{q} are the mass matrix, the damping matrix, the gradient, and the vector of the generalized coordinates of the strain energy of the finite-element assemblage, respectively.

To integrate Eqs. (19.5.2) in the time domain, we employ Newmark's implicit scheme. At each moment $t + \Delta t$, where Δt is the time increment, solution of the dynamic equations is found iteratively using the Newton–Raphson procedure:

$$\left(\mathbf{H}_{(p)}^{t+\Delta t} + a_1 \mathbf{M} + a_4 \mathbf{C} \right) \delta \mathbf{q}_{(p+1)}^{t+\Delta t} = -\mathbf{g}_{(p)}^{t+\Delta t} - (a_1 \mathbf{M} + a_4 \mathbf{C}) \left(\mathbf{q}_{(p)}^{t+\Delta t} - \mathbf{q}^t \right) + \quad (19.5.3)$$

$$+ (a_2 \mathbf{M} - a_5 \mathbf{C}) \dot{\mathbf{q}}^t + (a_3 \mathbf{M} - a_6 \mathbf{C}) \ddot{\mathbf{q}}^t,$$

$$a_1 = \frac{1}{\alpha \Delta t^2}, a_2 = \frac{1}{\alpha \Delta t}, a_3 = \frac{1-2\alpha}{2\alpha}, a_4 = \frac{\beta}{\alpha \Delta t}, a_5 = 1 - \frac{\alpha}{\beta}, a_6 = \left(1 - \frac{\beta}{2\alpha} \right) \Delta t,$$

where \mathbf{H} is the Hessian of the finite-element model of the shell, $\delta \mathbf{q}$ is the increment in the vector of generalized coordinates, the subscript p enumerates iterations, and α and β are the parameters taken to be equal to 1/4 and 1/2, respectively (Bathe and Wilson 1976). The procedure for computing the gradient and Hessian of the shell element can be found in Levyakov and Kuznetsov (2011).

After the increment $\delta \mathbf{q}_{(p)}^{t+\Delta t}$ has been found from Eqs. (5.3), we update the nodal vectors using the formulas

$$\mathbf{r}_s^{*(p+1)} = \mathbf{r}_s^{*(p)} + \delta \mathbf{r}_s^{*(p)} \quad (19.5.4)$$

$$\mathbf{d}_s^{*(p+1)} = c_1^{(p)} \mathbf{d}_s^{*(p)} + c_2^{(p)} \left(\mathbf{t}_{1s}^{*(p)} \delta \omega_{1s}^{(p)} + \mathbf{t}_{2s}^{*(p)} \delta \omega_{2s}^{(p)} \right)$$

$$\mathbf{t}_{ms}^{*(p+1)} = \mathbf{t}_{ms}^{*(p)} - \delta \omega_{ms}^{(p)} \left[c_2^{(p)} \mathbf{d}_s^{*(p)} + c_3^{(p)} \left(\mathbf{t}_{1s}^{*(p)} \delta \omega_{1s}^{(p)} + \mathbf{t}_{2s}^{*(p)} \delta \omega_{2s}^{(p)} \right) \right]$$

$$\delta \omega_s^{(p)} = \left(\delta \omega_{1s}^{(p)2} + \delta \omega_{2s}^{(p)2} \right)^{1/2}$$

$$c_1^{(p)} = \cos \delta \omega_s^{(p)}, c_2^{(p)} = \frac{\sin \delta \omega_s^{(p)}}{\delta \omega_s^{(p)}}, c_3^{(p)} = \frac{1 - \cos \delta \omega_s^{(p)}}{\delta \omega_s^{(p)2}}$$

where \mathbf{t}_{1s}^* and \mathbf{t}_{2s}^* are two auxiliary unit vectors normal to the director \mathbf{d}_s^* .

After the solution of Eqs. (19.5.2) has been found with a required accuracy, the nodal velocities and accelerations at each time step are computed using formulas (Bathe and Wilson 1976)

$$\ddot{\mathbf{q}}^{t+\Delta t} = a_1 \mathbf{q}^{t+\Delta t} - a_1 \mathbf{q}^t - a_2 \dot{\mathbf{q}}^t - a_3 \ddot{\mathbf{q}} \quad (19.5.5)$$

$$\dot{\mathbf{q}}^{t+\Delta t} = a_4 \mathbf{q}^{t+\Delta t} - a_4 \mathbf{q}^t + a_5 \dot{\mathbf{q}}^t + a_6 \ddot{\mathbf{q}}^t$$

19.7 Evaluation of Dynamic Buckling

After thermal shock of magnitude ΔT is applied to a surface of a shell, the stress resultants N_T and M_T (see Eqs. (19.4.12)) increase monotonically with time due to heat transfer through the wall thickness. The rate at which the thermal loads increase depends on the (1) magnitude of thermal shock, (2) material properties, (3) wall thickness, and (4) thermal boundary conditions. If the shell is restrained against thermal expansion, thermally induced compressive stresses can result in buckling. As the stresses reach the critical level, the shell jumps to oscillations about new equilibrium configuration. Volmir (1967) proposed the following simple criterion for dynamic buckling of plates and shells: given the time history of deflection at a certain characteristic point of the shell, the critical time is defined as a moment of the highest buckling rate, which corresponds to the inflection point on the time-deflection curve. In the general case, however, this approach is difficult to implement, since the location of the characteristic point is not known in advance. For this reason, to investigate dynamic buckling, we use the time history of the kinetic energy rather than deflection at a single point.

It is well known that initial geometric imperfections unavoidable in real structures play an important role in the stability of thin plates and shells. In the nonlinear analysis of imperfection-sensitive thin-walled structure, the dynamic buckling instability is interpreted as rapid development of the initial deflections under the time-dependent loads. Since the amplitude and pattern of deviation from ideal geometric shape are random, it is common practice to assume that the initial imperfection is similar in shape to eigenmodes obtained from the static buckling analysis.

19.8 Numerical Results and Discussion

The sample problems considered below deal with FGM plates and shells composed of silicon nitride Si_3N_4 (ceramic phase) and SUS304 stainless steel (metal phase) unless otherwise specified. Mechanical and physical properties of the phases are listed in Tables 19.1 and 19.2 (see, e.g. (Shen 2009)). Temperature-dependent properties are taken into account unless otherwise specified.

In all the problems, transient analysis of the structures is performed under zero initial conditions. To determine temperature distribution across the wall thickness, we use a uniform mesh of 200 elements of equal size.

Table 19.1 Temperature-dependent properties of Si₃N₄

| Property | Dimension | P_0 | P_{-1} | P_1 | P_2 | P_3 |
|------------|---------------------|-------------------------|----------|-------------------------|------------------------|--------------------------|
| E_c | Pa | 348.43×10^9 | 0 | -3.07×10^{-4} | 2.16×10^{-7} | -8.946×10^{-11} |
| ν_c | – | 0.24 | 0 | 0 | 0 | 0 |
| α_c | K ⁻¹ | 5.8723×10^{-6} | 0 | 9.095×10^{-4} | 0 | 0 |
| κ_c | W(mK) ⁻¹ | 13.723 | 0 | -1.032×10^{-3} | 5.466×10^{-7} | -7.876×10^{-11} |
| c_{pc} | J/(kgK) | 555.11 | 0 | 1.016×10^{-3} | 2.92×10^{-7} | -1.67×10^{-10} |
| ρ_c | kg/m ³ | 2370 | 0 | 0 | 0 | 0 |

Table 19.2 Temperature-dependent properties of SUS304

| Property | Dimension | P_0 | P_{-1} | P_1 | P_2 | P_3 |
|------------|---------------------|------------------------|----------|-------------------------|-------------------------|--------------------------|
| E_m | Pa | 201.04×10^9 | 0 | 3.079×10^{-4} | -6.534×10^{-7} | 0 |
| ν_m | – | 0.3262 | 0 | -2.002×10^{-4} | 3.797×10^{-7} | 0 |
| α_m | K ⁻¹ | 12.33×10^{-6} | 0 | 8.086×10^{-4} | 0 | 0 |
| κ_m | W(mK) ⁻¹ | 15.379 | 0 | -1.264×10^{-3} | 2.092×10^{-6} | -7.223×10^{-10} |
| c_{pm} | J/(kgK) | 496.56 | 0 | -1.151×10^{-3} | 1.636×10^{-6} | -5.863×10^{-10} |
| ρ_m | kg/m ³ | 8166 | 0 | 0 | 0 | 0 |

19.8.1 Comparison Studies

In this section, the present finite-element formulation is validated by considering free vibration and transient problems for which analytical or numerical solutions are available in the literature.

19.8.1.1 Free Vibration of FGM Shells

The first example is free small-amplitude vibrations of a circular cylindrical panel of square plan form. The outer surface of the panel is ceramic rich and the inner surface is metal rich. The properties of the material are determined at the reference temperature $T_{ref} = 300$ K. The grading index in Eq. (19.2.1) is set equal to $n = 2$. The geometric parameters are: wall thickness $h = 0.01$ m, side length $a = 10h$, radius of the middle surface $R = 10a$, and subtended angle $\theta = 0.05$.

The aim is to verify the mass matrix of the proposed shell element. We determine free-vibration frequencies ω of the shells with fully clamped and simply supported

Table 19.3 Frequency parameter λ of the FGM cylindrical panel for $n = 2$

| Boundary conditions | Mode number | Present solution | | | Zhao et al. (2009) | ANSYS |
|---------------------|-------------|------------------|----------------|----------------|--------------------|----------------|
| | | 8×8 | 16×16 | 32×32 | 15×15 | 24×24 |
| CCCC | 1 | 40.078 | 40.556 | 40.670 | 40.670 | 41.166 |
| | 2 | 75.731 | 77.359 | 77.705 | 76.823 | 79.046 |
| | 3 | 75.820 | 77.443 | 77.788 | 76.885 | 79.136 |
| SSSS | 1 | 23.692 | 23.711 | 23.609 | – | 23.884 |
| | 2 | 55.562 | 56.117 | 56.086 | – | 56.758 |
| | 3 | 55.718 | 56.268 | 56.238 | – | 56.970 |

immovable boundary contour. Table 19.3 lists the nondimensional frequency parameter $\lambda = (\omega a^2/h)\sqrt{12(1 - \nu_m^2)\rho_m/E_m}$ computed for the first three vibration modes using uniform union-jack meshes. The computation results agree well with the numerical solution obtained by the element-free kp-Ritz method (Zhao et al. 2009) and with the finite-element solution obtained by the ANSYS software where the grading properties of the material were modeled using the Shell181 multilayered element.

19.8.1.2 Dynamic Response of an Isotropic Beam to Thermal Shock

The second example deals with thermally-induced vibrations of a simply supported isotropic beam made of the Si_3N_4 material, which corresponds to $n = 0$ in Eq. (19.2.1). The length, thickness, and width of the beam are $l = 1$ m, $h = 0.01$ m, and $b = 0.1$ m, respectively. The upper surface of the beam is exposed to step temperature rise $\Delta T = 100$ K, whereas the lower surface is kept at a reference temperature of 300 K (see Eqs. (19.3.4) and (19.3.6)).

For small-amplitude vibrations, the dynamic response of the beam with temperature-independent properties can be predicted using the analytical solution.

$$w = \sum_{m=1,3,5,\dots}^{\infty} \alpha_m(t) \sin \frac{m\pi x}{l} - \frac{M_T}{2D}(x^2 - lx) \tag{19.7.1}$$

$$\alpha_m(t) = \frac{8l^2 b E \alpha h^2 \Delta T}{D \pi^5 m^3} \sum_{k=2,4,6,\dots}^{\infty} \frac{1}{k^2} \frac{e^{-\gamma_k t} - (\omega_m/\gamma_k) \sin \omega_m t - \cos \omega_m t}{1 + (\omega_m/\gamma_k)^2}$$

$$M_T = b E \alpha h^2 \Delta T \left(\frac{1}{12} - \frac{2}{\pi^2} \sum_{k=2,4,6,\dots}^{\infty} \frac{1}{k^2} e^{-\gamma_k t} \right)$$

$$\gamma_k = \frac{\kappa}{c_p \rho} \left(\frac{k\pi}{h} \right)^2, \omega_m = (m\pi/l)^2 \sqrt{D/I}, D = \frac{E b h^3}{12}, I = \rho b h$$

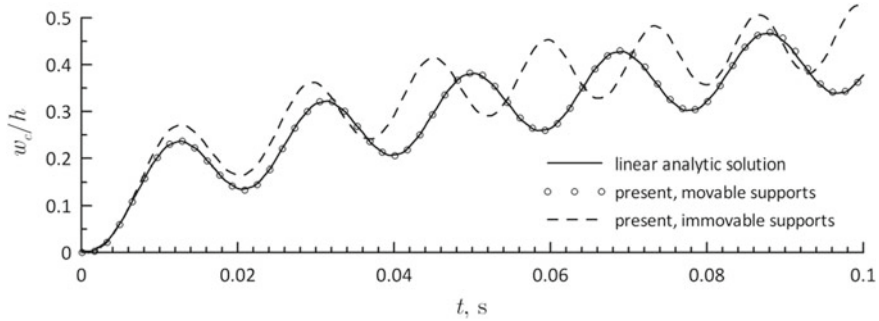


Fig. 19.3 Time history of the midspan deflection for the simply supported isotropic beam

where w is the lateral deflection and x is the axial coordinate.

The finite-element solution predicting dynamic response of the beam was obtained using the following data: a 4×40 uniform union-jack mesh with 320 elements, and the time increment in the Newmark integration scheme $\Delta t = 10^{-4}$ s.

The midspan deflection w_c versus time is shown in Fig. 19.2. The finite-element results agree favorably with the linear analytical solution (19.7.1) in the case where the end supports are allowed to move in the axial direction. For axially immovable supports, the linear solution fails to predict the beam response adequately because of geometrically nonlinear effects. It is seen from Fig. 19.2 that the frequency of vibrations increases due to the additional constraints at the beam ends.

19.8.1.3 Dynamic Response of a Circular Plate to Thermal Shock

The third example is the thermally induced vibrations of a simply supported FGM circular plate with immovable edge. The upper surface of the plate is exposed to step temperature rise $\Delta T = 10$ K, whereas the lower surface is kept at a reference temperature of 300 K (see Eqs. (19.3.4) and (19.3.6)). The radius and thickness of the plate are $a = 0.080$ m and $h = 0.001$ m, respectively.

To determine the dynamic axisymmetric deflections of the plate, we consider a quarter of the plate using the following data: number of elements $N = 16$ and the time increment in the Newmark integration scheme $\Delta t = 0.5 \times 10^{-4}$ s.

The predicted central deflection w_c versus time is shown in Fig. 19.3 for the grading index $n = 5$. The finite-element results are very close to the solution of Kiani and Eslami (2014) obtained by the Ritz method with simple polynomial functions.

19.8.1.4 Snap-Through of a Shallow Spherical Cap

The next example deals with the snap-through instability of a suddenly heated isotropic spherical cap with immovable simply supported edge. This problem has

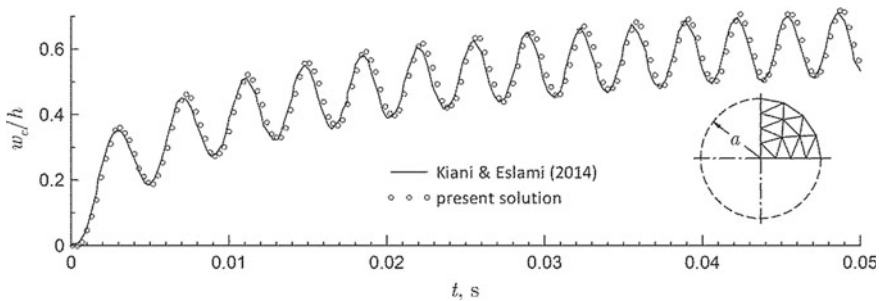


Fig. 19.4 Time history of the central deflection of the simply supported circular FGM plate

recently been considered by Javani et al. (Javani et al. 2020). Given the wall thickness h , the geometry of the cap is determined by two nondimensional parameters

$$\lambda = \sqrt{12} \frac{R\theta^2}{h}, \quad \mu = 2\sqrt{12} \frac{R\theta}{h}$$

where R is the radius of curvature and θ is the half opening angle.

The cap is made of the SUS304 steel with temperature-independent properties. The inner surface of the cap is suddenly heated, whereas the outer surface is kept at the reference temperature (see Eqs. (19.3.4) and (19.3.6)). Under these loading conditions, the cap can jump to inverted position. Assuming that axisymmetric deformation occurs, we consider a quarter of the cap and impose symmetry conditions along two radial directions. In Fig. 19.5, we plot time histories of the normalized central deflection w/f for $h = 1$ mm, $\lambda = 1.7$ and $\mu = 150$, where $f = R\theta^2/2$ is the rise of the cap. Using the model consisting of 400 elements, we found that snap-through instability occurs if $68.6K < \Delta T < 68.65K$. The same range was obtained using a finer mesh consisting of 1 600 elements. The present results agree well with the calculation results of Javani et al. (Javani et al. 2020) who found that the critical temperature rise lies in the range $68.25 K < \Delta T < 68.5 K$.

19.8.1.5 Large Thermal Displacements of an FGM Plate

Now we verify nonlinear capabilities of the proposed finite-element model in the dynamic analysis of large displacements and rotations. To this end, we consider thermal finite bending of a cantilevered thin narrow plate of length $L = 1$ m, width $b = L/80$, and thickness $h = L/200$. The grading index of the FGM is $n = 1$. The plate is heated according to Eqs. (3.4) and (3.7), where $\Delta T = 1\ 880$ K. Due to the increasing thermal bending moment M_T , the plate is rolled up into a circular cylindrical shape. The computation results are shown in Fig. 19.6 for two heating rates determined by parameters $\sigma = 1\ s^{-1}$ (slow heating) and $\sigma = 10\ s^{-1}$ (rapid heating) that enter Eq. (3.7). It is seen that, for slow heating, the plate is bent nearly

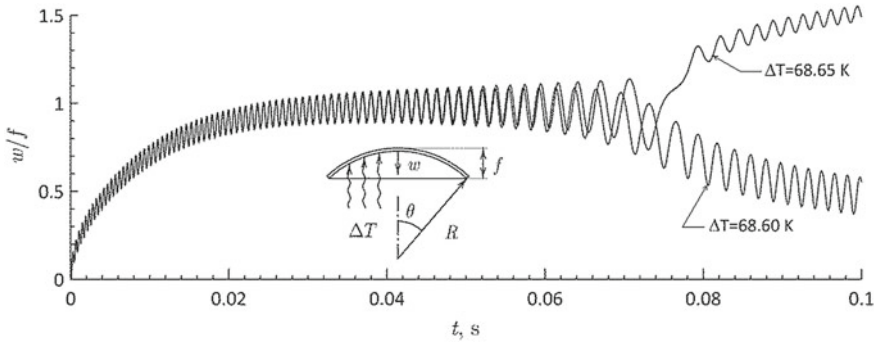


Fig. 19.5 Time history of the central deflection of the simply supported spherical cap

statically performing small-amplitude oscillations about the deformed configuration. With time, the plate tends to assume closed circular shape (see Fig. 19.7), where the tip displacements approach their limiting values, i.e. $u/L \rightarrow 1$ and $w/L \rightarrow 0$. As a reference solution, we take the analytical solution based on the beam model and steady-state temperature distribution over the plate (Levyakov and Kuznetsov 2014). Using this solution, one finds that the temperature rise required to roll the plate into a closed circle is $\Delta T = 1\,814$ K, which is 3.5% lower than the above-mentioned magnitude. A slightly stiffer response of the present finite-element model compared to the beam model can be attributed to the fact that under non-uniform heating the plate is deformed into a doubly curved surface rather than into a cylindrical surface. The effect of Poisson’s ratio on the dynamic thermal deflections was found to be of little significance. It is seen from Fig. 19.6 that under rapid heating, the pure thermal bending is accompanied by finite-amplitude oscillations. The solution obtained for 20×2 mesh agrees with that obtained for finer 80×2 mesh, the difference becomes noticeable after approximately 1 s. Deformed configurations of the rapidly heated plate are shown in Fig. 19.7. The effect of the time increment on accuracy of the solution is demonstrated by Table 19.4.

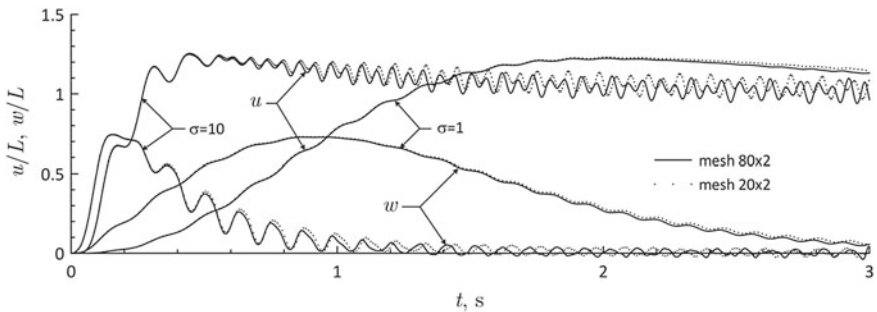


Fig. 19.6 Time histories of the tip displacements of the cantilevered FGM plate

Fig. 19.7 Equilibrium configurations of the cantilevered plate under rapid heating (80×2 mesh)

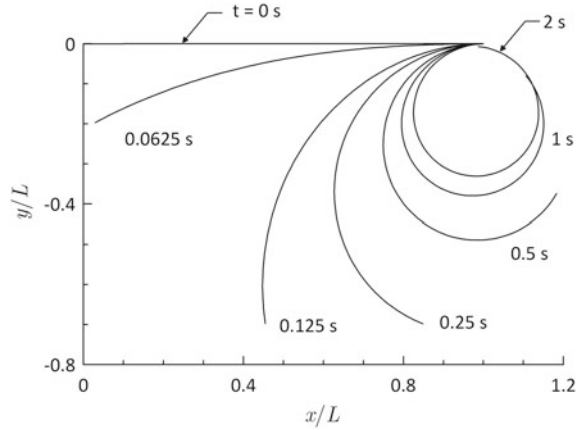


Table 19.4 Convergence study of the thermal bending of a rapidly heated cantilevered plate

| t, s | $\Delta t, s$ | u/L | w/L | T, J | $\Pi, N\cdot m$ |
|--------|-----------------------|-------------------------|----------------------------|-----------|--------------------------|
| 0.5 | 1.0×10^{-3} | 1.183040 | 0.3738415 | 0.2408254 | 0.3547774×10^3 |
| | 0.5×10^{-3} | 1.182904 | 0.3740037 | 0.2376331 | 0.3547818×10^3 |
| | 0.25×10^{-3} | 1.182890 | 0.3740629 | 0.2367167 | 0.3547828×10^3 |
| 1 | 1.0×10^{-3} | 1.107099 | 0.8054594×10^{-1} | 0.3501693 | 0.1925129×10^3 |
| | 0.5×10^{-3} | 1.106922 | 0.8062025×10^{-1} | 0.3339732 | 0.1925309×10^3 |
| | 0.25×10^{-3} | 1.106802 | 0.8066291×10^{-1} | 0.3301827 | $0.1925350D \times 10^3$ |
| 2 | 1.0×10^{-3} | 0.9783874 | 0.6896778×10^{-2} | 0.8386965 | 0.6026749×10^2 |
| | 0.5×10^{-3} | 0.9876465 | 0.6889352×10^{-2} | 0.6100725 | 0.5948815×10^2 |
| | 0.25×10^{-3} | 0.9874587 | 0.6621523×10^{-2} | 0.5892913 | 0.5950926×10^2 |
| 3 | 1.0×10^{-3} | diverges at $t = 2.1 s$ | | | |
| | 0.5×10^{-3} | 0.9944956 | 0.9535049×10^{-2} | 1.626111 | 0.3034419×10^2 |
| | 0.25×10^{-3} | 0.9932212 | 0.9230670×10^{-2} | 1.590626 | 0.3038009×10^2 |
| 4 | 1.0×10^{-3} | diverges at $t = 2.1 s$ | | | |
| | 0.5×10^{-3} | 1.060673 | 0.9872496×10^{-2} | 0.7590779 | 0.2422324×10^2 |
| | 0.25×10^{-3} | 1.058927 | 0.1021280×10^{-1} | 0.8333617 | 0.2414937×10^2 |

19.8.2 Dynamic Thermal Buckling of a Clamped Rectangular Plate

We consider a fully clamped rectangular FGM plate of length $a = 0.3$ m, width $b = 0.15$ m, and thickness $h = 0.001$ m. It is assumed that initial geometrical imperfection is of the form.

$$w_0 = \sum_{m,k} A_{mk} \varphi_m(x/a) \varphi_k(y/b) \quad (19.7.2)$$

where $\varphi_m(x)$ is the m -th eigenfunction governing the vibration mode of the clamped–clamped beam and A_{mk} represents amplitude of the imperfection mode. The eigenfunctions are normalized to unity.

We study nonlinear dynamic instability of the plate under thermal shock using the following discretization parameters: a uniform 32×16 union-jack mesh with 1 024 elements and the time increment $\Delta t = 0.5 \times 10^{-4}$ s. In thermal boundary conditions (19.3.3), (19.3.4), and (19.3.5), the loading function $f(t)$ is given by Eq. (19.3.6).

At the initial stage of heat transfer, the plate remains undisturbed. If the magnitude of thermal shock ΔT is high enough, the compressive stresses rapidly develop and reach the critical level. At this moment, the plate jumps to oscillations about new configuration. Figure 19.8 shows time histories of the deflection at point $A(a/2; b/4)$ for three types of thermal boundary conditions and for different magnitudes of thermal shock ΔT . The curves were obtained for $n = 1$ and nonzero coefficients $A_{11} = A_{12} = 10^{-2}h$ in Eq. (19.7.2).

Decreasing the magnitude of thermal shock ΔT leads to slower thermal loading. As a result, the critical time necessary for the plate to buckle increases and the amplitude of postbuckling vibrations becomes less and less pronounced. This result suggests that in the limit as $t \rightarrow \infty$, where steady-state temperature distribution is reached, the plate exhibits static buckling. It follows that the critical temperature rise ΔT_{cr} can be determined from the static buckling problem under steady-state temperature distribution.

In Fig. 19.8, the dark circles mark the critical moments where the kinetic energy of the plate reaches the first pronounced maximum. Given a magnitude of thermal shock $\Delta T > \Delta T_{cr}$, the shortest critical time occurs if the top and bottom surfaces are heated simultaneously (see Eqs. (19.3.3)). Comparing Figs. 8b and c, we infer that the curves obtained under thermal boundary conditions (3.4) and (3.5) differ only slightly.

In Fig. 19.9, we show normalized deflections of the plate subjected to thermal boundary conditions (19.3.4) for $\Delta T = 100$ K. The effect of the antisymmetric mode of imperfection A_{12} shows up only at the onset of buckling. After the critical moment $t > 0.005$ s, its effect vanishes and the plate oscillates about a doubly symmetric bent configuration.

It is of interest to estimate the effect of the rate of thermal loading on the dynamic buckling instability. Confining our attention thermal boundary conditions (19.3.4), we compute the dynamic load factor (DLF) using formula

$$DLF = \frac{N_{T,cr}^{dyn}}{N_{T,cr}^{stat}} \quad (19.7.3)$$

where $N_{T,cr}^{dyn}$ is the stress resultant at the critical moment and $N_{T,cr}^{stat}$ is the critical stress resultant obtained from the solution of the corresponding static buckling problem

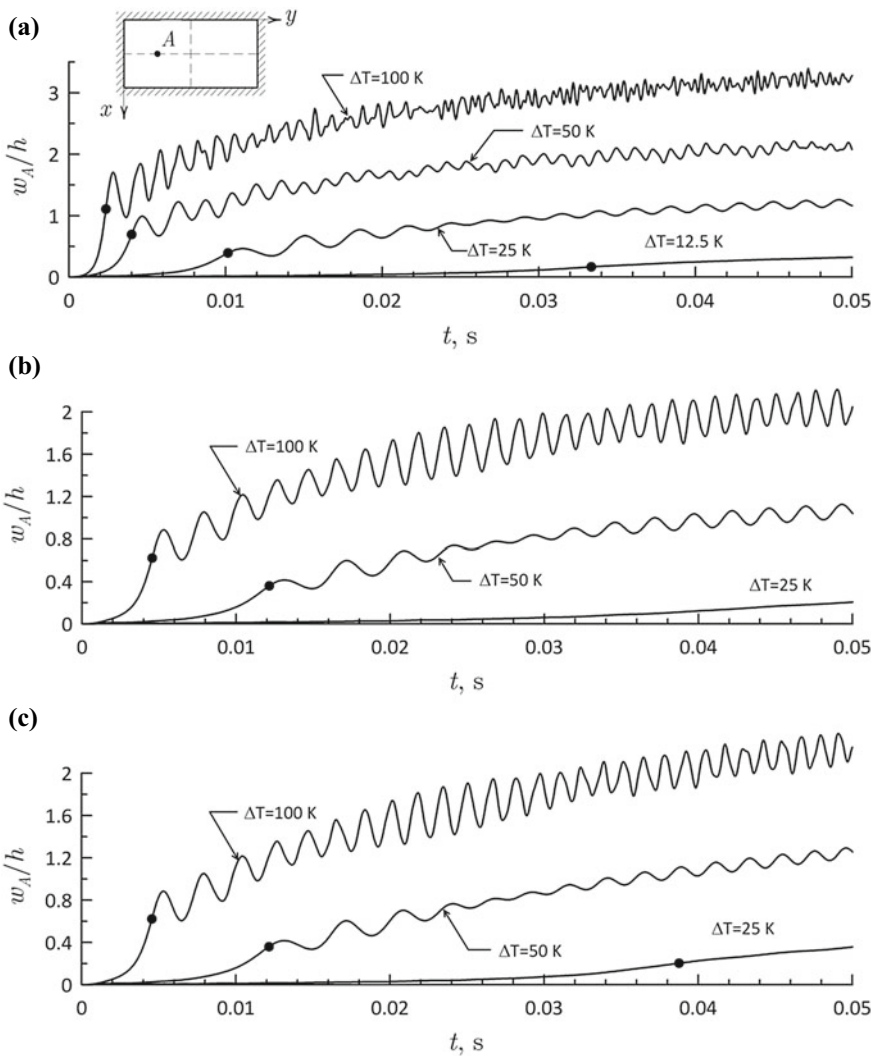


Fig. 19.8 Time histories of the deflection of the clamped rectangular FGM plate: **a** response under thermal boundary conditions (19.3.3); **b** response under thermal boundary conditions (19.3.4); **c** response under thermal boundary conditions (19.3.5).

under steady-state temperature distribution. The computation results are summarized in Table 19.5. It is seen that the dynamic buckling resistance of the plate increases as the grading index n and the magnitude of thermal shock ΔT increase. This effect can be attributed to inertia forces.

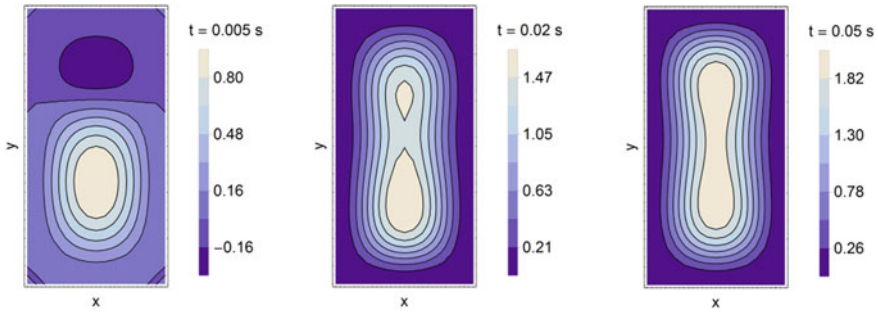


Fig. 19.9 Contour plots of the normalized deflections w/h of the rectangular plate

Table 19.5 Effect of thermal loading on the dynamic buckling of the clamped rectangular plate

| n | Steady-state solution | | $\Delta T / \Delta T_{cr}^{stat}$ | | | |
|-----|----------------------------|------------------------|-----------------------------------|-------|-------|-------|
| | ΔT_{cr}^{stat} , K | $N_{T,cr}^{stat}$, kN | 1.5 | 2 | 5 | 10 |
| | | | DLF | | | |
| 0.2 | 26.84 | 45.20 | 1.021 | 1.067 | 1.41 | 2.114 |
| 0.5 | 23.97 | 42.43 | 1.024 | 1.080 | 1.415 | 2.140 |
| 1 | 21.52 | 40.23 | 1.020 | 1.082 | 1.414 | 2.140 |
| 5 | 17.35 | 37.10 | 1.031 | 1.101 | 1.434 | 2.136 |
| 10 | 16.15 | 35.85 | 1.042 | 1.108 | 1.469 | 2.203 |

19.8.3 Dynamic Buckling of a Shallow Cylindrical Panel

We consider a shallow cylindrical panel whose boundary contour is simply supported and immovable. Dimensions of the panel are: radius of curvature $R = 1$ m, wall thickness h , half opening angle $\theta = 0.1$, and length $l = 0.2$ m (see Fig. 19.10).

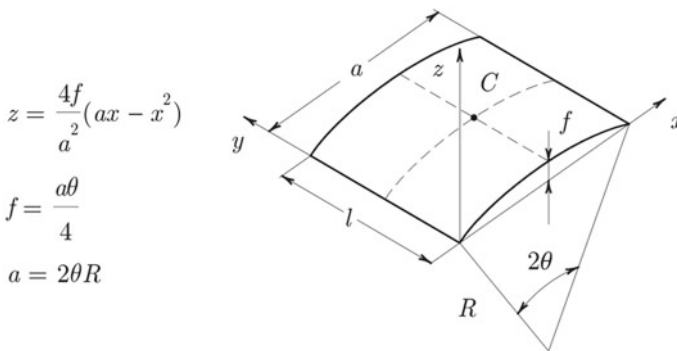


Fig. 19.10 Geometry of a shallow cylindrical panel

The initial imperfection is assumed to be of the form

$$w_0 = \sum_{m,k} A_{mk} \sin \frac{m\pi x}{a} \sin \frac{k\pi y}{l} \tag{19.7.4}$$

where m and k are the half-wave numbers in the coordinate directions. We consider two panels whose thicknesses are 0.5 mm and 1 mm. For $h = 0.5$ mm, the only nonzero coefficients in Eq. (7.3) are $A_{2,2} = -A_{3,2} = h/100$. For $h = 1$ mm, we set $A_{2,1} = -A_{2,3} = -h/100$, the remaining coefficients being zero. The imperfection shapes are roughly similar to the buckling mode shapes obtained by solving the corresponding static buckling problem under the steady-state temperature distribution across the thickness.

Using a uniform 32×32 mesh and setting $\Delta t = 3 \times 10^{-5}$ s, we study dynamics of the cylindrical panel under thermal boundary condition (3.4), in which the loading function $f(t)$ is given by Eq. (3.7) and $\sigma = 10^2 \text{ s}^{-1}$.

Figure 19.11 shows time histories of the normalized central deflection w_c/h and kinetic energy of thin cylindrical panel with $h = 0.5$ mm and $n = 1$. Contour plots of the normalized deflections are shown in Fig. 19.12. The first maximum of the kinetic energy occurs at $t = 0.01695$ s, where deformation of the panel changes from symmetric to asymmetric mode. The second, more pronounced maximum occurs at $t = 0.0269$ s, which is the evidence of the buckling mode switching. We note that, in contrast to plates, dynamic buckling of the panels occurs deeply in the region of large deflections. The results presented in Fig. 19.12 agree with the results obtained by static nonlinear analysis of the panel under static thermal loading (Levyakov and Kuznetsov 2014).

To estimate the effect of dynamic thermal loading on the buckling instability of the panel, we compute the dynamic load factor defined by Eq. (19.7.3). The calculation results obtained under thermal boundary conditions (3.4) are summarized in Table 19.6. It is seen from the results that the buckling resistance of the panel

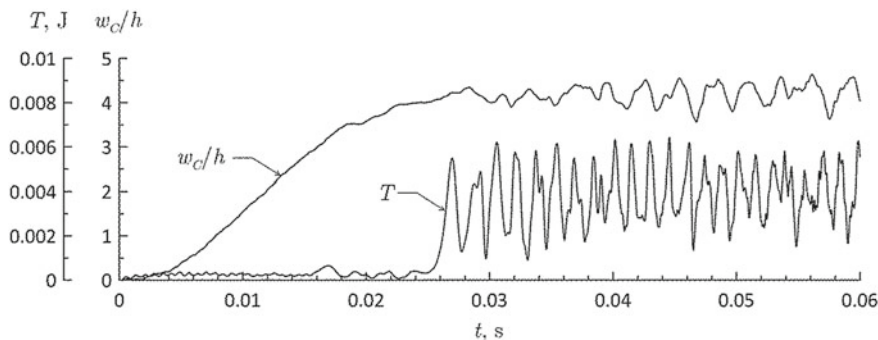


Fig. 19.11 Time histories of deflection and kinetic energy of thin cylindrical panel of thickness $h = 0.5$ mm under $\Delta T = 250$ K

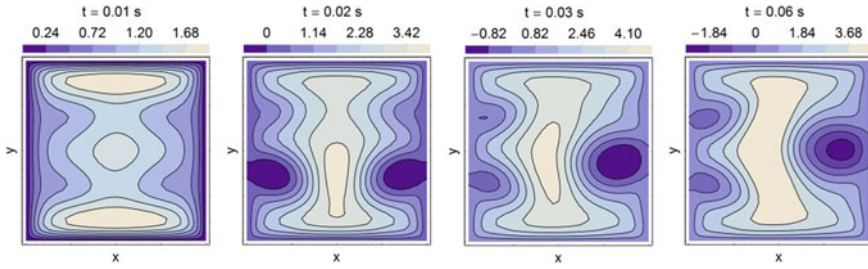


Fig. 19.12 Contour plots of the normalized deflections w/h of thin cylindrical panel

Table 19.6 Effect of dynamic thermal loading on buckling resistance of the simply supported cylindrical panel

| $h, \text{ mm}$ | n | Steady-state solution | | $\Delta T / \Delta T_{cr}^{stat}$ | | |
|-----------------|-----|-----------------------------------|-------------------------------|-----------------------------------|------|------|
| | | $\Delta T_{cr}^{stat}, \text{ K}$ | $N_{T,cr}^{stat}, \text{ kN}$ | 1.2 | 1.5 | 2.0 |
| | | | | DLF | | |
| 0.5 | 0.2 | 138.74 | 121.9 | 1.07 | 1.16 | 1.28 |
| | 0.5 | 123.35 | 112.4 | 1.07 | 1.09 | 1.34 |
| | 1 | 110.99 | 105.8 | 1.07 | 1.17 | 1.34 |
| | 5 | 98.169 | 105.5 | 1.08 | 1.19 | 1.39 |
| | 10 | 97.60 | 108.6 | 1.09 | 1.21 | 1.42 |
| 1.0 | 0.2 | 411.65 | 797.3 | 1.09 | 1.24 | 1.51 |
| | 0.5 | 375.29 | 735.3 | 1.09 | 1.23 | 1.54 |
| | 1 | 344.68 | 690.8 | 1.08 | 1.22 | 1.57 |
| | 5 | 321.45 | 702.1 | 1.11 | 1.25 | 1.66 |
| | 10 | 329.54 | 740.3 | 1.13 | 1.40 | 1.69 |

slightly increases with the magnitude of thermal shock ΔT and index n . This effect can be attributed to lateral inertia.

19.8.4 Buckling of Simply Supported Cylindrical Shells

Finally, we consider a closed cylindrical shell of radius $R = 0.4 \text{ m}$, length $L = \sqrt{3}/5 \text{ m}$, and wall thickness $h = 0.001 \text{ m}$. The outer surface of the shell is ceramic rich and the inner surface is metal rich. The edges are simply supported and immovable. The shell is meshed into 5 120 elements obtained by dividing the cylindrical surface into 160 segments in the circumferential direction and into 16 segments in the axial direction.

We assume that initial imperfection is of the form

$$w_0 = A_0(w_{01} + w_{02} + w_{03}) \quad (19.6.6)$$

where $A_0/h = 10^{-2}$ and w_{01} , w_{02} , and w_{03} are the first three buckling modes obtained from the nonlinear static analysis of the shell subjected to uniform temperature rise. Fourier series approximations of the buckling modes are given by

$$w_{01} = \sin 17\phi \sum_{k=1,3,\dots}^9 a_k \sin \frac{k\pi z}{L}$$

$$w_{02} = \sin 18\phi \sum_{k=1,3,\dots}^9 b_k \sin \frac{k\pi z}{L} \quad (19.6.7)$$

$$w_{03} = \sin 16\phi \sum_{k=2,4,\dots}^{10} c_k \sin \frac{k\pi z}{L},$$

where $a_1 = 0.270$, $a_3 = 1.0$, $a_5 = 0.061$, $a_7 = -0.315$, $a_9 = -0.136$, $b_1 = 0.188$, $b_3 = 1.0$, $b_5 = 0.071$, $b_7 = -0.372$, $b_9 = -0.171$, $c_2 = 1.0$, $c_4 = 0.398$, $c_6 = -0.165$, $c_8 = -0.270$, $c_{10} = -0.047$.

The nonlinear transient simulation was performed under thermal shock governed by Eqs. (19.3.4) and (19.3.7), in which $\sigma = 10^3 \text{s}^{-1}$. Figure 19.13 shows time histories of the axial reaction force F and kinetic energy T for the shell with grading index $n = 1$. It is seen that, due to unsteady heat conduction, the reaction force increases from zero and, after reaching a maximum, drops by approximately 45%. As the critical time, we take the moment at which the reaction force reaches a maximum.

Figure 19.14 shows deformed configurations of the shell computed for the moments marked by circles in Fig. 19.13. In the prebuckling state, the shell swells axisymmetrically near the immovable edges. In the postbuckling regime, the deflection pattern rapidly changes exhibiting no symmetry.

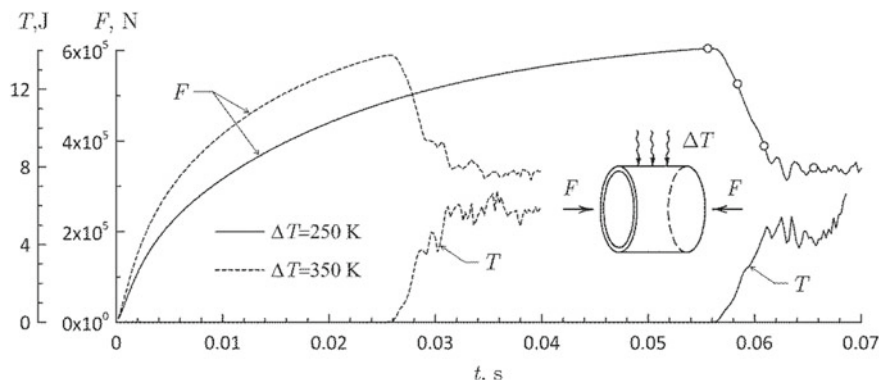


Fig. 19.13 Axial reaction force versus time for the simply supported cylindrical FGM shell with grading index $n = 1$

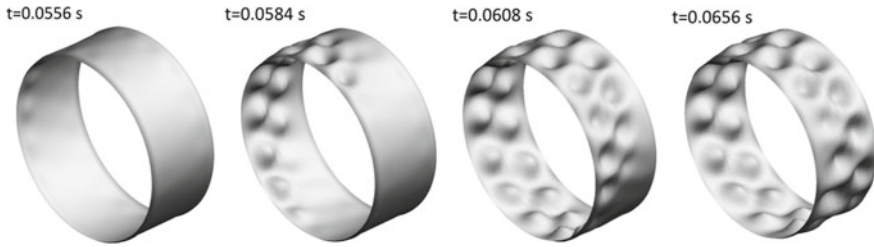


Fig. 19.14 Deformed configurations of the cylindrical FGM shell for states marked in Fig. 19.13 (deflection is magnified by a factor of 10)

Table 19.7 Effect of dynamic thermal loading on buckling resistance of the simply supported cylindrical shell

| n | Steady-state solution | | | $\Delta T / \Delta T_{cr}^{stat}$ | | | |
|-----|----------------------------|------------------------|-------|-----------------------------------|-------|-------|-------|
| | ΔT_{cr}^{stat} , K | $N_{T,cr}^{stat}$, kN | F, kN | 1.2 | 1.5 | 2.0 | 3.0 |
| | | | | DLF | | | |
| 0.2 | 271.3 | 500.7 | 770.5 | 0.919 | 0.931 | 0.970 | 1.021 |
| 1 | 236.2 | 462.6 | 686.1 | 0.917 | 0.941 | 0.978 | 1.046 |
| 5 | 200.5 | 434.1 | 615.7 | 0.924 | 0.947 | 0.996 | 1.068 |

Table 19.7 lists the dynamic load factor computed for various values of the grading index *n*. In contrast to the plates and shallow shells considered above, the dynamic load factor is less than unity. This can be attributed to high sensitivity of closed cylindrical shell to (1) initial imperfections introduced in the dynamic analysis and (2) time history of the stresses that develop under unsteady heat transfer through the shell thickness.

The critical time and buckling resistance increase with the grading index of the material since higher content of the ceramic phase results in higher stiffness of the FGM shell and lower rate of heat transfer through the shell thickness.

19.9 Concluding Remarks

A finite-element formulation has been proposed for nonlinear dynamic analysis of functionally graded plates and shells subjected to thermal shock. A triangular element with 15 degrees of freedom has been developed using the invariant-based approach and the concept of the surface of mass. Among the computational advantages of the shell finite element are (1) small number of degrees of freedom, (2) exact representation of six rigid body modes, and (3) compact and closed-form formulas for computing the gradient and Hessian, which are used to formulate the equations of motion. Performance of the element has been tested in several problems and good

agreement has been reported between the calculation results and solutions available in the open literature.

A nonlinear analysis of transient response of suddenly heated plates and shells fabricated of functionally graded materials has been performed. Based on the numerical results, the following conclusions can be drawn:

- (1) sudden heating of thin plates and shells leads to nonlinear vibrations and, under certain conditions, to dynamic buckling instability;
- (2) plates and shells with restrained edges exhibit dynamic buckling provided the magnitude of thermal shock is higher than the critical temperature rise obtained from the corresponding static buckling analysis under steady-state temperature distribution;
- (3) the critical buckling time at which dynamic buckling occurs decreases with an increase in the magnitude of thermal shock;
- (4) the dynamic load factor increases with the magnitude of thermal shock;
- (5) higher content of ceramic phase of the material tends to increase buckling resistance of FGM plates and shells.

References

- Adams RJ, Bert CW (1999) Thermoelastic vibrations of a laminated rectangular plate subjected to a thermal shock. *J Thermal Stresses* 22(9):875–895. <https://doi.org/10.1080/014957399280607>
- Al-Huniti NS, Al-Nimr MA, Meqdad MM (2003) Thermally induced vibration in a thin plate under the wave heat conduction model. *J Thermal Stresses* 26(10):943–962. <https://doi.org/10.1080/01495730306344>
- Bathe KJ, Wilson EL (1976) Numerical methods in finite element analysis. Prentice hall Englewood cliffs, N. J.
- Birman V (1990) Thermal dynamic problems of reinforced composite cylinders. *ASME, J Appl Mech* 57:941–947
- Boley BA (1956) Thermally induced vibrations of beams. *J Aeronaut Sci* 23(2):179–181. <https://doi.org/10.2514/8.3527>
- Chang JS, Wang JH, Tsai T (1992) Z: Thermally induced vibration of thin laminated plates by finite element method. *Comput Struct* 42(1):117–128. [https://doi.org/10.1016/0045-7949\(92\)90541-7](https://doi.org/10.1016/0045-7949(92)90541-7)
- Czechowski L (2015) Study of dynamic buckling of FG plate due to heat flux pulse. *Int J Appl Mech Eng* 20(1):19–31. <https://doi.org/10.1515/ijame-2015-0002>
- Das S (1983) Vibrations of polygonal plates due to thermal shock. *J Sound Vib* 89:471–476. [https://doi.org/10.1016/0022-460X\(83\)90348-6](https://doi.org/10.1016/0022-460X(83)90348-6)
- Esmaili HR, Arvin H, Kiani Y (2019) Axisymmetric nonlinear rapid heating of FGM cylindrical shells. *J Thermal Stresses* 42(4):490–505. <https://doi.org/10.1080/01495739.2018.1498756>
- Ghiasian SE, Kiani Y, Eslami MR (2014) Non-linear rapid heating of FGM beams. *Int J Non-Linear Mech* 67:74–84. <https://doi.org/10.1016/j.ijnonlinmec.2014.08.006>
- Ghiasian SE, Kiani Y, Eslami MR (2015) Nonlinear thermal dynamic buckling of FGM beams. *Eur J Mech A/Solids* 54:232–242. <https://doi.org/10.1016/j.euromechsol.2015.07.004>
- Huan CLD, Wo HK (1980) Thermal stresses and displacements induced in a finite, orthotropic, cylindrical, thin shell by an instantaneous thermal shock. *J Thermal Stresses* 3(N2):277–293 (1980). <https://doi.org/10.1080/01495738008926968>

- Irie T, Yamada G (1978) Thermally induced vibration of circular plate. *Bull JSME* 21(162):1703–1709
- Javani M, Kiani Y, Eslami MR (2019a) Geometrically nonlinear rapid surface heating of temperature-dependent FGM arches. *Aerosp Sci Technol* 90:264–274. <https://doi.org/10.1016/j.ast.2019.04.049>
- Javani M, Kiani Y, Eslami MR (2019b) Large amplitude thermally induced vibrations of temperature dependent annular FGM plates. *Composites Part B* 371–383 (2019b). <https://doi.org/10.1016/j.compositesb.2018.11.018>
- Javani M, Kiani Y, Eslami MR (2019c) Nonlinear axisymmetric response of temperature-dependent FGM conical shells under rapid heating. *Acta Mech* 230:3019–3039. <https://doi.org/10.1007/s00707-019-02459-y>
- Javani M, Kiani Y, Eslami MR (2020) Dynamic snap-through of shallow spherical shells subjected to thermal shock. *Int J Pressure Vessels Piping* 179:104028. <https://doi.org/10.1016/j.ijpvp.2019.104028>
- Javani M, Kiani Y, Eslami MR (2021) Rapid heating vibrations of FGM annular sector plates. *Eng Comput* 37:305–322. <https://doi.org/10.1007/s00366-019-00825-x>
- Jones JP (1966) Thermoelastic vibrations of a beam. *J Acoust Soc Am* 39(3):542–554
- Kiani Y, Eslami MR (2014) Geometrically non-linear rapid heating of temperature dependent circular FGM plates. *J Therm Stress* 37(12):1495–1518
- Levyakov SV, Kuznetsov VV (2014) Nonlinear stability analysis of functionally graded shells using the invariant-based triangular finite element. *ZAMM* 94(1–2):107–117. <https://doi.org/10.1002/zamm.201200188>
- Levyakov SV, Kuznetsov VV (2011) Application of triangular element invariants for geometrically nonlinear analysis of functionally graded shells. *Comput Mech* 48:499. <https://doi.org/10.1007/s00466-011-0603-8>
- Levyakov SV, Kuznetsov VV (2017) Invariant-based formulation of a triangular finite element for geometrically nonlinear thermal analysis of composite shells. *Compos Struct* 177:38–53. <https://doi.org/10.1016/j.compstruct.2017.06.006>
- Ma LS, Lee DW (2011) A further discussion of nonlinear mechanical behavior for FGM beams under in-plane thermal loading. *Compos Struct* 93(2):831–842. <https://doi.org/10.1016/j.compstruct.2010.07.011>
- Malik P, Kadoli R (2017) Thermo-elastic response of SUS316-Al₂O₃ functionally graded beams under various heat loads. *Int J Mech Sci* 128–129:206–223. <https://doi.org/10.1016/j.ijmecsci.2017.04.014>
- Malik P, Kadoli R (2018) Thermal induced motion of functionally graded beams subjected to surface heating. *Ain Shams Eng J* 9(1):149–160. <https://doi.org/10.1016/j.asej.2015.10.010>
- Mason JB (1968) Analysis of thermally induced structural vibrations by finite element techniques. *NASATM X-63488* (1968)
- Nakajo Y, Hayashi K (1988) Response of simply supported and clamped circular plates to thermal impact. *J Sound Vib* 122(2):347–356
- Pandey S, Pradyumna S (2018) Transient stress analysis of sandwich plate and shell panels with functionally graded material core under thermal shock. *J Thermal Stresses* 41(5):543–567. <https://doi.org/10.1080/01495739.2017.1422999>
- Prakash T, Singha MK, Ganapathi M (2007) Nonlinear dynamic thermal buckling of functionally graded spherical caps. *AIAA J* 45(2):505–508. <https://doi.org/10.2514/1.21578>
- Reddy JN (2004) *An Introduction to Nonlinear Finite Element Analysis*. Oxford University Press, Oxford
- Seibert AG, Rice JS (1973) Coupled thermally induced vibrations of beams. *AIAA J* 7(7):1033–1103. <https://doi.org/10.2514/3.6866>
- Shen HS (2009) *Functionally graded materials: nonlinear analysis of plates and shells*. CRC Press, Boca Raton, FL, USA
- Stroud RC, Mayers J (1971) Dynamic response of rapidly heated plate elements. *AIAA J* 9(1):76–83. <https://doi.org/10.2514/3.6126>

- Taleb S, Hedayati R, Sadighi M, Ashoori AR (2022) Dynamic thermal buckling of spherical porous shells. *Thin-Walled Struct* 172:108737. <https://doi.org/10.1016/j.tws.2021.108737>
- Tauchert TR (1989) Thermal shock of orthotropic rectangular plates. *J Thermal Stresses* 12(2):241–258. <https://doi.org/10.1080/01495738908961964>
- Volmir AS (1967) *Stability of deformable systems*. Nauka, Moscow (In Russian)
- Zhang JH, Li GZ, Li SR (2015) Analysis of transient displacements for a ceramic-metal functionally graded cylindrical shell under dynamic thermal loading. *Ceram Int* 41(9):12378–12385. <https://doi.org/10.1016/j.ceramint.2015.06.070>
- Zhang JH, Pan SC, Chen L (2019) Dynamic thermal buckling and postbuckling of clamped–clamped imperfect functionally graded annular plates. *Nonlinear Dyn* 95(2):565–577. <https://doi.org/10.1007/s11071-018-4583-5>
- Zhang JH, Chen S, Zheng W (2020) Dynamic buckling analysis of functionally graded material cylindrical shells under thermal shock. *Continuum Mech Thermodyn* 32:1095–1108. <https://doi.org/10.1007/s00161-019-00812-z>
- Zhao X, Lee YY, Liew KM (2009) Thermoelastic and vibration analysis of functionally graded cylindrical shells. *Int J Mech Sci* 51(9–10):694–707. <https://doi.org/10.1016/j.ijmecsci.2009.08.001>
- Zienkiewicz OC, Morgan K (1983) *Finite elements and approximation*. John Wiley & Sons, New York

Chapter 20

Deposition and Characterization of Magnetron Sputtered AlN Coatings with Variable Stoichiometry



Andrey L. Nikolaev, Evgeniy V. Sadyrin, Ivan O. Kharchevnikov,
Pavel E. Antipov, Vasilina A. Lapitskaya, Andrey S. Vasiliev,
and Sergey S. Volkov

Abstract In the present paper, a series of AlN coatings deposited using magnetron sputtering method were characterized in terms of their stoichiometry, microgeometry, and microstructure. The coatings were obtained at 1, 2, 3, 4 sccm N_2 flow. Their thickness and microstructure were studied using scanning electron microscopy and the stoichiometry was observed using energy dispersive X-ray analysis. The microgeometry of the coatings was obtained using atomic-force microscope. Stable modes of obtaining AlN coatings with nitrogen content from 6.31 to 25.48 atomic percent with an average deposition rate of about 3.3 angstroms per second were demonstrated. The results demonstrated an almost linear relationship between the composition of the coatings and the composition of the gas mixture during the deposition process. This observation can be used to predict the required composition of the gas mixture under the given process parameters to obtain AlN coatings of the required thickness and with the required elemental composition.

A. L. Nikolaev · E. V. Sadyrin (✉) · I. O. Kharchevnikov · P. E. Antipov · A. S. Vasiliev ·
S. S. Volkov
Don State Technical University, 1 Gagarin Square, 344000 Rostov-on-Don, Russia
e-mail: e.sadyrin@sci.donstu.ru

A. L. Nikolaev
e-mail: andreynicolaev@eurosites.ru

I. O. Kharchevnikov
e-mail: babaduksac@yandex.ru

P. E. Antipov
e-mail: sly_fox_03@mail.ru

S. S. Volkov
e-mail: fenix_rsu@mail.ru

V. A. Lapitskaya
Luikov Heat and Mass Transfer Institute of the National Academy of Sciences of Belarus, Minsk,
Belarus
e-mail: vasilinka.92@mail.ru

© The Author(s), under exclusive license to Springer Nature Switzerland AG 2023
H. Altenbach and V. Eremeyev (eds.), *Advances in Linear and Nonlinear Continuum
and Structural Mechanics*, Advanced Structured Materials 198,
https://doi.org/10.1007/978-3-031-43210-1_20

357

20.1 Introduction

Aluminum nitride (AlN) is a ceramic material, which finds various applications in modern medicine, science, and industry. One of the innovative ways to utilize AlN is the development of biosensors. Such devices are used in the applications where precise and selective detection of target molecules is required (Wingqvist 2010). The detection is performed via customized biomolecules, for example, antibodies, usually in viscous media (Wingqvist et al. 2007). Such sensors are also significant instruments for analytical researches of biomolecular interactions with solid surfaces. For example, such biosensors may be integrated on the extraluminal surface of implants for the continuous monitoring of the vascular graft (Natta et al. 2019; Mishra et al. 2022) providing vital information about the blood flow hemodynamics in the artificial vessel of the patient.

Due to the modern possibilities of magnetron sputtering techniques AlN biosensors may be of miniature size (Sadyrin et al. 2023, 2020), thus allowing high degree of manipulation during the implant construction. Moreover, AlN offers attractive physical properties such as high piezoelectric effect, high surface acoustic wave velocity, excellent dielectric permittivity, high thermal stability, wide band gap (6.2 eV), and chemical inertness (Mwema et al. 2020; Fei et al. 2018; Chen et al. 2019; Besleaga et al. 2017).

Recently, the AlN thin films were used (Murillo et al. 2019) for the development of the breast cancer biosensor demonstrating encouraging efficacy. The usage of AlN coatings in the fabrication of gravimetric biosensors, responding to species, like proteins, DNA chains, toxins, virus, or bacteria, of different molecular weights was proposed in García-Gancedo et al. (2011), DeMiguel-Ramos et al. (2017), Nikolaev et al. (2014). Construction of flexible piezoelectric pressure sensors using AlN thin films deposited on polymeric substrates has been reported in Akiyama et al. (2006). The use of such films for measuring human muscle movements (Bu et al. 2009) and monitoring the respiration and heartbeat during sleep (Bu et al. 2007) was suggested. AlN coatings as the elements of the biosensors have been recently employed to performing intravascular ultrasound imaging (Lu et al. 2014) and ultrasonic fingerprint sensing (Lu et al. 2015).

One of the possible ways to improve the mechanical properties of the AlN coating is to manage its stoichiometric composition during the sputtering process by varying the volume of nitrogen in the vacuum chamber (Gilewicz et al. 2022; Aizikovitch et al. 2022; Sadyrin et al. 2018). In the present paper, utilizing such an approach a range of AlN coatings was deposited followed by their characterization. Thus, their thickness and microstructure have been studied using scanning electron microscopy (SEM) and the stoichiometry—using energy dispersive X-ray (EDX) analysis (Zhilin et al. 2014; Pushkariov et al. 2014; Popenko et al. 2011). The microgeometry of the coatings was obtained using atomic-force microscope (AFM).

20.2 Materials and Methods

Three AlN coatings were deposited on the substrates made of Si (100) wafers $10 \times 15 \text{ mm}^2$. Prior to the preparation of the substrates the notch perpendicular to its face was applied using a diamond cutter. The sample preparation included successively keeping the substrates in the following liquids:

- analytical grade acetone brought to boil;
- hydrogen peroxide mixed with nitric acid 1:1 by volume brought to boil;
- 2% hydrofluoric acid at room temperature.

The deposition was carried out using Robvac VSM100 (Aktan Vacuum, Fryazino, Russia) magnetron sputtering unit.

Pure Al target (99.99% pure) was mechanically clamped to the magnetron cathode of the sputtering system. Substrates were mounted on the sample holder and a base pressure of 10^{-6} mbar was obtained. The target surface was sputter etched by Ar at 150 W for 15 min to avoid contamination before deposition. During deposition, N_2 and Ar were supplied to the vacuum chamber using mass flow controllers. Ar was supplied with a flow equal to 75 sccm. In this way, films were obtained at four different N_2 flow (1, 2, 3, 4 sccm). Let us denote them as the samples 1, 2, 3, 4. The remaining deposition parameters were kept quasi-constant. The working pressure varied from $7.7 \cdot 10^{-3}$ mbar to $8.1 \cdot 10^{-3}$ mbar. The deposition temperature was 100°C . The target was sputtered in the power stabilization mode at 150 W. Target to substrate distance was 8 cm. The voltage applied to the magnetron varied from 450 to 700 volts during the sputtering process. Deposition times were 40 min, 40 min, 32 min and 44 min for the samples 1, 2, 3, and 4 respectively.

Following deposition, the samples were chipped along the previously applied notch and their thickness was obtained in the SEM Crossbeam 340 (Carl Zeiss Microscopy, Oberkochen, Germany). During examination the samples were clamped in the special holder so that the chip surface was positioned normally under the electron beam. The research was conducted using the Everhart-Thornley secondary electron detector with electron high tension (EHT) voltage 3 kV. After that the samples were glued to the position table with the conductive tape and the microstructure of their surface was studied, EHT was 3 kV as well.

Chemical analysis conducted by EDS Oxford X-Max 80 (Oxford Instruments, Abingdon, UK) with 200x magnification and 20 kV voltage, from the surface of the sample over the total area with a wide coverage (approximately $150\text{--}200 \mu\text{m}$ by $400\text{--}500 \mu\text{m}$), as well as from individual contrasting crystals pointwise.

The microgeometry of the coatings was obtained using AFM Nanoeducator (NT-MDT, Zelenograd, Russia) equipped with the tungsten probe. The resolution was $270 \times 270 \text{ px}$ on the scanning fields $21 \times 21 \mu\text{m}$. The probe was checked using the calibration grid prior to each test.

20.3 Results and Discussion

Figure 20.1 demonstrates the results of thickness measurements on each of the samples. The images of the sample surface obtained using SEM are shown in Fig. 20.2 for the samples 1–4.

The obtained values for the coating thickness were 833.2, 788.7, 725.3, and 732.3 nm for the samples 1, 2, 3, and 4, respectively.

The microgeometrical research revealed that for the sample 1 the surface was formed by the aluminum particles in the form of three-dimensional polyhedra (Fig. 20.2a). At the same time, the surface of the sample 2 (Fig. 20.2b) was comprised of the sparse positioned particles of aluminum (Fig. 20.2b) between depressed AlN particles, whereas the surface of the samples 3 (Fig. 20.2c) and Fig. 20.4 (Fig. 20.2d) is comprised mostly of AlN particles. The particles are elongated resembling micro-pillars. Moreover, according to the examination of the faces of the notches (Fig. 20.1c and 20.1d) one can conclude, that these micro-pillars are higher for the case of the sample 4 (Fig. 20.2c).

The AFM-derived surface topography of the samples 1–4 is presented on the Fig. 20.3. The microgeometrical characteristics (average roughness R_a and average maximum roughness height R_z) were obtained for each sample by 20 profiles (Sadyrin et al. 2022): 5 in horizontal direction, 5 in vertical direction, 10 in diagonal direction. Additionally, each profile was averaged by the 10 nearest profiles. Thus, 200 profiles were analyzed for the study (Table 20.1). Maximum roughness height R_t was measured for the whole image.

Note, that the smallest values of R_a , R_z , and R_t were observed for the sample 1 (obtained at 1 sccm of N_2). The analysis of the results revealed the monotonic increase of the average maximum roughness height from sample 1 to sample 4. A sudden increase in the microgeometrical parameters from sample 1 to sample 2 is explained by the character of the surface relief—the sparse depressions between the high peaks of the freestanding aluminum particles, clearly visible on both the SEM (Fig. 20.2b) and AFM (Fig. 20.3b) images. The decrease of the R_a from the sample 3 to sample 4 (Fig. 20.4) can be explained by the close arrangement of relief elements in the form of micro-pillars to each other, which does not allow the tip of the probe to pass to their base.

Table 20.1 The microgeometrical characteristics of the samples 1–4

| Sample | R_a , nm | Standart deviation, nm | R_z , nm | Standart deviation, nm | R_t , nm |
|--------|------------|------------------------|------------|------------------------|------------|
| 1 | 65.7 | 18.7 | 257.8 | 61.9 | 920.0 |
| 2 | 105.1 | 41.2 | 395.1 | 181.4 | 980.0 |
| 3 | 104.0 | 17.3 | 406.6 | 86.3 | 1100.0 |
| 4 | 93.9 | 14.2 | 424.8 | 77.6 | 1000.0 |

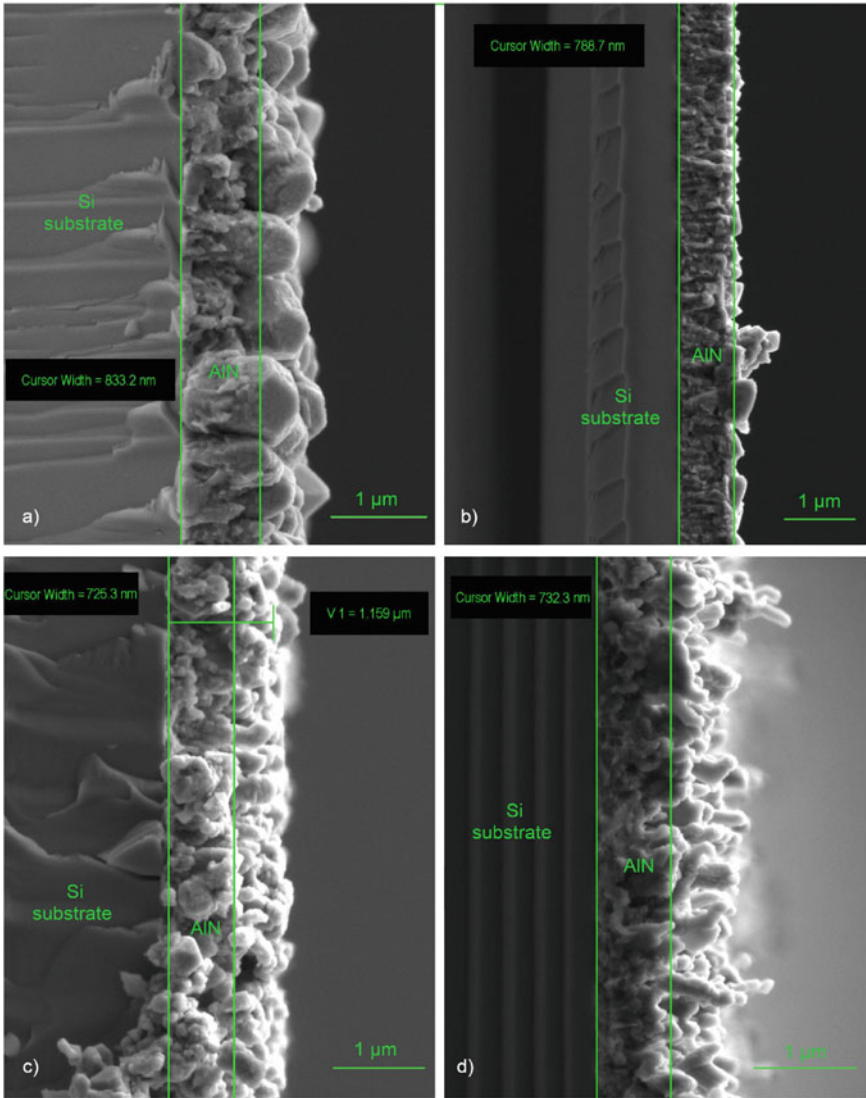


Fig. 20.1 Thickness measurements along the notch of the samples: **a** 1 (1 sccm of N_2); **b** 2 (2 sccm of N_2); **c** 3 (3 sccm of N_2); **d** 4 (4 sccm of N_2)

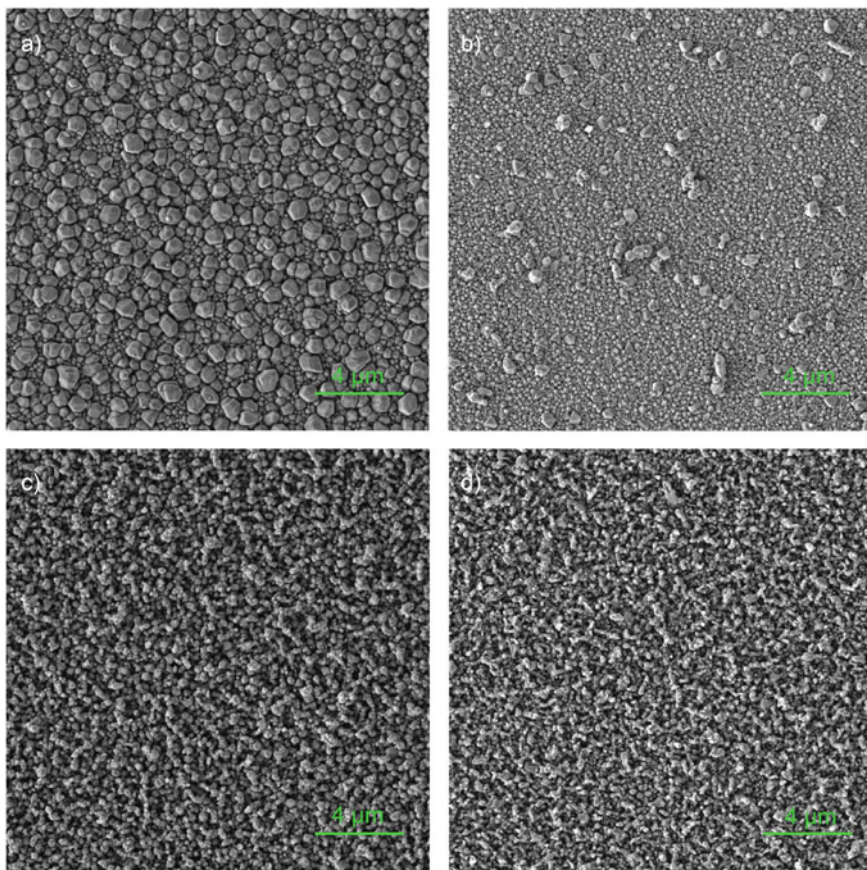


Fig. 20.2 SEM derived surface of the samples: **a** 1 (1 sccm of N_2); **b** 2 (2 sccm of N_2); **c** 3 (3 sccm of N_2); **d** 4 (4 sccm of N_2)

Table 20.2 The element composition for the sample 1–4

| Sample number | Al (atomic %) | O (atomic %) | N (atomic %) |
|---------------|---------------|--------------|--------------|
| 1 | 92.49 | 2 | 5.5 |
| 2 | 85.97 | 2.23 | 11.8 |
| 3 | 77.39 | 7 | 15.61 |
| 4 | 73.23 | 3.6 | 23.17 |

The element composition for each of the samples was measured for each sample by three rectangular $150 \times 300 \mu\text{m}$ areas, then the results were averaged across the areas (Table 20.2).

The Aztec 3.3 SP1 (Oxford Instruments, Abingdon, UK) software, which was used to analyze the EDX spectra, made it possible to recalculate the composition

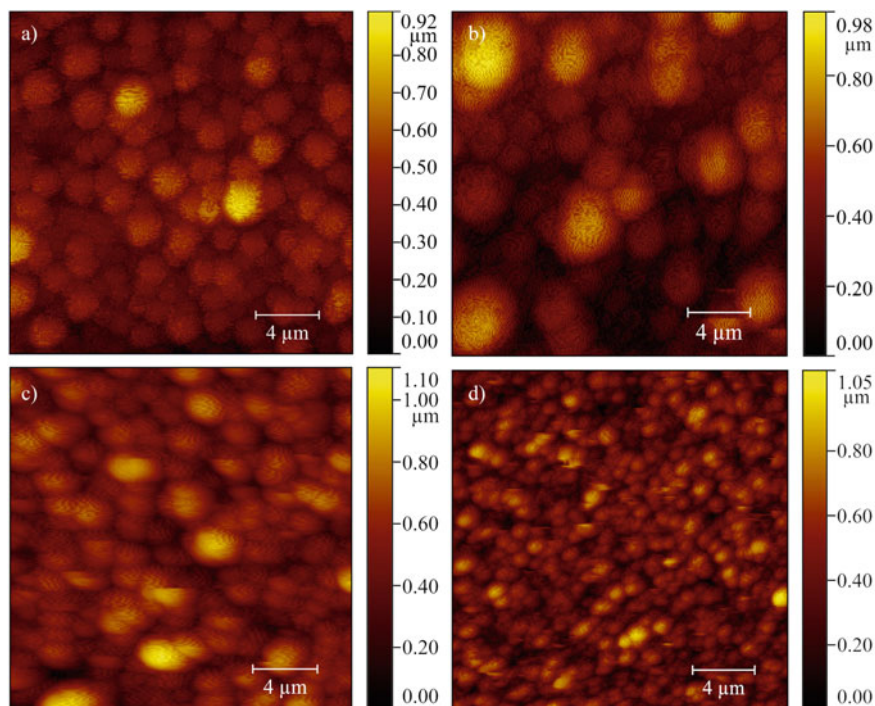


Fig. 20.3 AFM surface topography of the samples: **a** 1 (1 sccm of N_2); **b** 2 (2 sccm of N_2); **c** 3 (3 sccm of N_2); **d** 4 (4 sccm of N_2)

Table 20.3 The elemental composition for the sample 1–4 without oxygen

| Sample number | Al (atomic %) | N (atomic %) |
|---------------|---------------|--------------|
| 1 | 93.69 | 6.31 |
| 2 | 87.02 | 12.98 |
| 3 | 80.6 | 19.4 |
| 4 | 74.52 | 25.48 |

of chemical elements and remove elements that could be erroneously determined from the calculations. The composition of the coatings included oxygen in a typical amount. Oxygen, most likely, was adsorbed on the porous surface of the coatings during the transfer of samples from the magnetron chamber to the SEM. The surface topography of the samples obtained using AFM confirmed this assumption. A more developed coating structure corresponds to a larger amount of adsorbed oxygen. Table 20.3 shows the recalculation of the elements composition of coatings without taking into account adsorbed oxygen.

Analysis of the EDS results revealed an almost linear dependence of the elemental composition of the coatings on the nitrogen flow during the deposition process

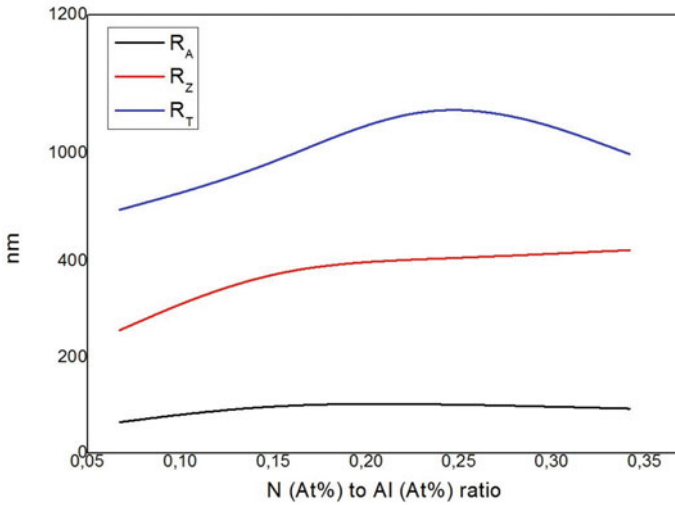


Fig. 20.4 Dependence of R_a , R_z and R_t values on the stoichiometric ratio of nitrogen to aluminum in AlN coatings

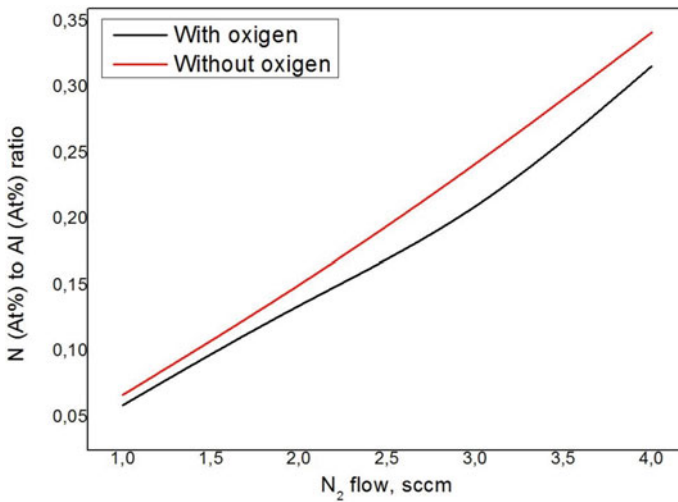


Fig. 20.5 Dependence of the elemental composition of the deposited coatings on the nitrogen flow during the deposition process

(Fig. 20.5). Note, that this material behavior is not typical for reactive magnetron sputtering.

20.4 Conclusion

In this work, we investigated a set of AlN coatings deposited with different nitrogen content (nitrogen flow). The deposition method was reactive magnetron sputtering. The influence of this factor on the elemental composition of the coatings and the microstructure of the coatings has been studied. Stable modes of obtaining AlN coatings with nitrogen content from 6.31 to 25.48 atomic percent with an average deposition rate of about 3.3 angstroms per second were demonstrated. The results show an almost linear relationship between the composition of the coatings and the composition of the gas mixture during the deposition process. This fact can be used to predict the required composition of the gas mixture under the given process parameters to obtain AlN coatings of the required thickness and with the required elemental composition. The next step of this study will be to establish relationships between the elements composition, mechanical and tribological properties of AlN coatings. As a result, this will make it possible to obtain functionally graded coatings with a smooth change in properties by depth.

Acknowledgements V. A. Lapitskaya acknowledges the support of the Belarus Republican Foundation for Fundamental Research (grant No. T23RNF-132), A. L. Nikolaev and Volkov S.S. acknowledges the support of the Russian Science Foundation (grant No. 23-49-10062, <https://rscf.ru/project/23-49-10062/>). The experiments were conducted in the Nanocenter of Research and Education Center “Materials”, Don State Technical University (<http://nano.donstu.ru>).

References

- Aizikovich SM, Nikolaev AL, Sadyrin EV, Krenev LI, Irkha VA, Galybin AN (2022) Indentation of thin coatings: theoretical and experimental investigation. *WIT Trans Eng Sci* 134:157–167. <https://doi.org/10.2495/BE450141>
- Akiyama M, Morofuji Y, Kamohara T, Nishikubo K, Tsubai M, Fukuda O, Ueno N (2006) Flexible piezoelectric pressure sensors using oriented aluminum nitride thin films prepared on polyethylene terephthalate films. *J Appl Phys* 100(11):114318. <https://doi.org/10.1063/1.2401312>
- Besleaga C, Dumitru V, Trinca LM, Popa AC, Negrila CC, Kołodziejczyk Ł, Luculescu C-R, Ionescu GC, Ripeanu, R-G, Vladescu A, Stan GE (2017) Mechanical, corrosion and biological properties of room-temperature sputtered aluminum nitride films with dissimilar nanostructure. *Nanomaterials* 7(11):394. <https://doi.org/10.3390/nano7110394>
- Bu N, Fukuda O, Ueno N, Inoue M (2009) A preliminary study on detection of muscle activity using a flexible AlN piezoelectric thin film sensor. In: 2009 IEEE international conference on robotics and biomimetics (ROBIO). IEEE, pp 944–948. <https://doi.org/10.1109/ROBIO.2009.5420447>
- Bu N, Ueno N, Fukuda O (2007) Monitoring of respiration and heartbeat during sleep using a flexible piezoelectric film sensor and empirical mode decomposition. In: 2007 29th annual international conference of the IEEE engineering in medicine and biology society. IEEE, pp 1362–1366. <https://doi.org/10.1109/IEMBS.2007.4352551>
- Chen J, Lv B, Zhang F, Wang Y, Liu X, Yan G, Shen Z, Wen Z, Wang L, Zhao W, Sun G, Liu C, Zeng Y (2019) The composition and interfacial properties of annealed AlN films deposited on 4H-SiC by atomic layer deposition. *Mater Sci Semicond Process* 94:107–115. <https://doi.org/10.1016/j.mssp.2019.01.045>

- DeMiguel-Ramos M, Díaz-Durán B, Escolano JM, Barba M, Mirea T, Olivares J, Clement M, Iborra E (2017) Gravimetric biosensor based on a 1.3 GHz AlN shear-mode solidly mounted resonator. *Sens Actuators B: Chem* 239:1282–1288. <https://doi.org/10.1016/j.snb.2016.09.079>
- Fei C, Liu X, Zhu B, Li D, Yang X, Yang Y, Zhou Q (2018) AlN piezoelectric thin films for energy harvesting and acoustic devices. *Nano Energy* 51:146–161. <https://doi.org/10.1016/j.nanoen.2018.06.062>
- García-Gancedo L, Zhu Z, Iborra E, Clement M, Olivares J, Flewitt AJ, Milne WI, Ashley GM, Luo JK, Zhao XB, Lu JR (2011) AlN-based BAW resonators with CNT electrodes for gravimetric biosensing. *Sens Actuators B: Chem* 160(1):1386–1393. <https://doi.org/10.1016/j.snb.2011.09.083>
- Gilewicz A, Kuznetsova T, Aizikovitch S, Lapitskaya V, Khabarava A, Nikolaev A, Warcholinski B (2021) Comparative investigations of AlCrN coatings formed by cathodic arc evaporation under different nitrogen pressure or arc current. *Materials* 14(2):304. <https://doi.org/10.3390/ma14020304>
- Lu Y, Heidari A, Horsley DA (2014) A high fill-factor annular array of high frequency piezoelectric micromachined ultrasonic transducers. *J Microelectromechanical Syst* 24(4):904–913 (2014). <https://doi.org/10.1109/JMEMS.2014.2358991>
- Lu Y, Tang H, Fung S, Wang Q, Tsai JM, Daneman M, Boser BE, Horsley DA (2015) Ultrasonic fingerprint sensor using a piezoelectric micromachined ultrasonic transducer array integrated with complementary metal oxide semiconductor electronics. *Appl Phys Lett* 106(26):263503. <https://doi.org/10.1063/1.4922915>
- Mishra S, Mohanty S, Ramadoss A (2022) Functionality of flexible pressure sensors in cardiovascular health monitoring: a review. *ACS Sens* 7(9):2495–2520. <https://doi.org/10.1021/acssensors.2c00942>
- Murillo AE, Melo-Maximo L, Garcia-Farrera B, Martínez OS, Melo-Máximo DV, Oliva-Ramirez J, García K, Huerta L, Oseguera J (2019) Development of AlN thin films for breast cancer acoustic biosensors. *J Mater Res Technol* 8(1):350–358. <https://doi.org/10.1016/j.jmrt.2018.02.007>
- Mwema FM, Akinlabi ET, Oladijo OP (2020) A systematic review of magnetron sputtering of AlN thin films for extreme condition sensing. *Mater Today: Proc* 26:1546–1550. <https://doi.org/10.1016/j.matpr.2020.02.317>
- Natta L, Mastronardi VM, Guido F, Algieri L, Puce S, Pisano F, Rizzi F, Pulli R, Quattier A, De Vittorio M (2019) Soft and flexible piezoelectric smart patch for vascular graft monitoring based on aluminum nitride thin film. *Sci Rep* 9(1):1–10. <https://doi.org/10.1038/s41598-019-44784-1>
- Nikolaev AL, Karapetyan GY, Nesvetaev DG, Lyanguzov NV, Dneprovski VG, Kaidashev EM (2014) Preparation and investigation of ZnO nanorods array based resistive and SAW CO gas sensors. In: *Advanced materials: physics, mechanics and applications*. Springer International Publishing, pp 27–36. https://doi.org/10.1007/978-3-319-03749-3_3
- Popenko EM, Gromov AA, Pautova YI, Chaplina EA, Ritzhaupt-Kleissl HJ (2011) SEM-EDX study of the crystal structure of the condensed combustion products of the aluminum nanopowder burned in air under the different pressures. *Appl Surf Sci* 257(8):3641–3644. <https://doi.org/10.1016/j.apsusc.2010.11.096>
- Pushkariov VI, Nikolaev AL, Kaidashev EM (2014) Synthesis and characterization of ZnO nanorods obtained by catalyst-free thermal technique. *J Phys Conf Ser* 541:012031. <https://doi.org/10.1088/1742-6596/541/1/012031>
- Sadyrin EV, Mitrin BI, Krenev LI, Nikolaev AL, Aizikovitch SM (2018) Evaluation of mechanical properties of the two-layer coating using nanoindentation and mathematical modeling. In: *Advanced materials: proceedings of the international conference on “physics and mechanics of new materials and their applications”*, PHENMA 2017. Springer International Publishing, pp 495–502. https://doi.org/10.1007/978-3-319-78919-4_39

- Sadyrin EV, Nikolaev AL, Bardakova RA, Kotova AA, Kharchevnikov IO, Zabyaka IY, Aizikovich SM (2023) Nanoindentation derived mechanical properties of TiN thin film deposited using magnetron sputtering method. In: Deformation and destruction of materials and structures under quasi-static and impulse loading. Springer, Cham, pp 245–254. https://doi.org/10.1007/978-3-031-22093-7_17
- Sadyrin E, Karotkiyan R, Sushentsov N, Stepanov S, Zabyaka I, Kislyakov E, Litvinenko A (2019) Mechanical properties derived by spherical indentation of TiN coating deposited by a method combining magnetron sputtering and Arc evaporation. In: Advanced materials: proceedings of the international conference on “physics and mechanics of new materials and their applications”, PHENMA 2019. Springer International Publishing, pp 85–95. https://doi.org/10.1007/978-3-030-45120-2_8
- Sadyrin E, Lapitskaya V, Kuznetsova T, Yogina D, Maksyukov S, Aizikovich S (2022) Nanoindentation and atomic force microscopy derived mechanical and microgeometrical properties of tooth root cementum. *Micro* 2(4):575–588. <https://doi.org/10.3390/micro2040038>
- Wingqvist G: AlN-based sputter-deposited shear mode thin film bulk acoustic resonator (FBAR) for biosensor applications a review. *Surf Coatings Technol* 205(5):1279–1286 (2010). <https://doi.org/10.1016/j.surfcoat.2010.08.109>
- Wingqvist G, Bjurström J, Liljeholm L, Yantchev V, Katardjiev I: Shear mode AlN thin film electroacoustic resonant sensor operation in viscous media. *Sens Actuators B: Chem* 123(1):466–473 (2007). <https://doi.org/10.1016/j.snb.2006.09.028>
- Zhang TY, Xu WH, Zhao MH (2004) The role of plastic deformation of rough surfaces in the size-dependent hardness. *Acta Mater* 52(1):57–68. <https://doi.org/10.1016/j.actamat.2003.08.026>
- Zhilin DA, Lyanguzov NV, Nikolaev LA, Pushkariov VI, Kaidashev EM (2014) Photoelectric properties of MSM structure based on ZnO nanorods, received by thermal evaporation and carbothermal synthesis. *J Phys: Conf Ser* 541:012038. <https://doi.org/10.1088/1742-6596/541/1/012038>

Chapter 21

Nonlinearity and Dispersion in Extended Mass-in-Mass Metamaterials



Alexey V. Porubov

Abstract Three nonlinearly elastic extended mass-in-mass metamaterial models are asymptotically studied using their long wavelength continuum limits. The governing nonlinear equations with dispersion are obtained for longitudinal strain including dispersion effects. Both nonlinear stiffness of the main chain spring and those of the attached masses are taken into account. It is shown that the nonlinearities and dispersion differently affect the dynamics of the longitudinal strain waves for the models considered.

Keywords Metamaterial · Continuum limit · Nonlinear wave · Localization · Dispersion

21.1 Introduction

Nonlinear strain waves transfer considerable strain energy and may reflect internal structure of a material. Nonlinear finite amplitude waves, being powerful, may affect durability of a material. The behavior of nonlinear strain waves is sensitive to the characteristics of the material. Of special interest are localized waves that can exist due to a balance between nonlinearity and dispersion. Metamaterials possess rich internal structure that give rise to variety of sources of nonlinearity and dispersion.

One of the simplest but instructive metamaterial models is the mass-in-mass lattice model, Huang et al. (2009), Ma and Sheng (2016), Eremeyev and Turco (2020), Lazarov and Jensen (2007), Cveticanin and Cveticanin (2018), Fang et al. (2017), Erofeev et al. (2020), Porubov and Antonov (2021), Porubov (2021), Porubov and Krivtsov (2022). Experimental realization of the metamaterial model with the internal resonators can be found in Yao et al. (2008), Zhou et al. (2015), Yang et al. (2017), Zhou et al. (2012). They provide directions to the possible extensions of the mass-in

A. V. Porubov (✉)

Institute for Problems in Mechanical Engineering, Bolshoy 61, V.O., Saint-Petersburg, Russian Federation

e-mail: alexey.porubov@gmail.com

-mass metamaterial model. Such extended models have been considered in Fang et al. (2017), Zhou et al. (2015), Oyelade and Akano (2020), Bukhari and Barry (2020), Liu and Reina (2018), Huang and Sun (2010), Hu et al. (2017). A nonlinearly elastic chain with masses when attached mass with are attached through two main masse has been studied in Fang et al. (2017). The model with additional attached masses has been considered in Zhou et al. (2015), Oyelade and Akano (2020), Bukhari and Barry (2020).

Discrete modeling based on the study of the difference governing equations is the most favorable method for finding the solution of the metamaterial problems. This is effective in the linear problems, however, nonlinear difference equations are much less solvable than the continuum differential ones. Nevertheless, the continuum modeling is used much less frequently (Erofeev et al. 2020; Porubov and Antonov 2021; Porubov 2021; Porubov and Krivtsov 2022). The usual transfer from discrete to continuum approach is based on the long wavelength continuum limit giving rise to the partial differential governing equations (Born and Huang 1954; Askar 1985; Ostoja-Starzewski 2002; Andrianov et al. 2010; Porubov 2023). It restricts the study by the long strain waves.

The plan of the current work is as follows. In Sect. 21.2, the nonlinear discrete models for extended mass-in-mass metamaterials are presented. Next Sect. 21.3 is devoted to the continuum approximation and obtaining coupled nonlinear differential equations for all three models. The asymptotic procedure for decoupling and obtaining single nonlinear equations for longitudinal strains is given in Sect. 21.4. A comparative analysis of the localized wave solution of the single equations is examined in Sect. 21.5. The Conclusions summarize the most important deviations in the nonlinear strain dynamics caused by each modification of the mass-in-mass model.

21.2 Extended Nonlinear Mass-in-Mass Models

21.2.1 Classic Mass-in-Mass Chain

The classic mass-in-mass chain is shown in Fig. 21.1.

We consider a one-dimensional lattice where interaction between the masses m is modeled by nonlinearly-elastic spring. The additional masses m_1 are attached to each mass m by the springs with another nonlinearly elastic stiffness. The quadratic nonlinearity appears as a result of an expansion of a more general potential of interaction in the weakly nonlinear case and by retaining the leading order nonlinear term. We assume that the masses m_1 are not connected by the springs.

Then the model equations are

$$\begin{aligned} \ddot{u}_n = & \beta_0(u_{n-1} - 2u_n + u_{n+1}) + \eta\beta_1(v_n - u_n) + \\ & + \eta\beta_2(v_n - u_n)^2 + \beta_3((u_{n+1} - u_n)^2 - (u_{n-1} - u_n)^2), \end{aligned} \quad (21.1)$$

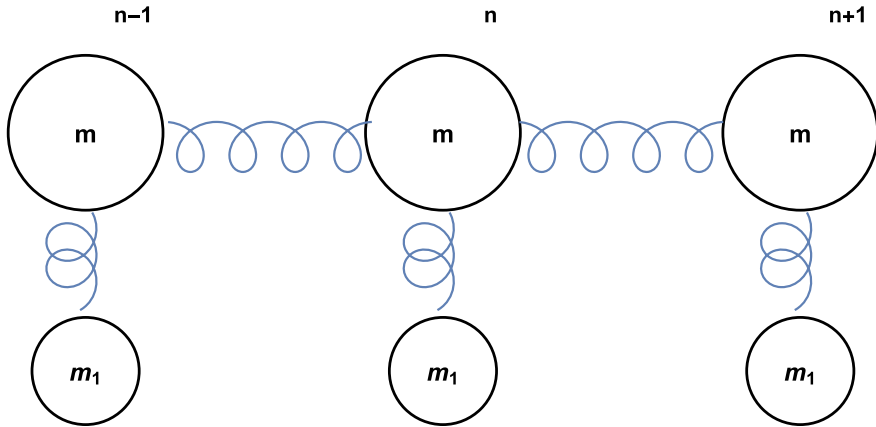


Fig. 21.1 Classic mass-in-mass chain

$$\ddot{v}_n = -\beta_1(v_n - u_n) - \beta_2(v_n - u_n)^2, \quad (21.2)$$

where the displacement of the mass m with the number n is denoted by u_n , while that of m_1 is denoted by v_n . Other notations are $\eta = m_1/m$, the linear stiffness of the spring in the chain is $\beta_0 m$, the nonlinear stiffness is $\beta_3 m$. The corresponding linear and nonlinear stiffnesses of the attached spring are $\beta_1 m_1$, $\beta_2 m_1$, respectively. We considered this problem in Porubov (2023) in detail. Here some results are used for comparison with the other models.

21.2.2 Chain with Extra Attached Masses

The chain with extra attached masses m_1 is shown in Fig. 21.2.

We considered different stiffnesses of the springs of the attached masses for the linearized problem in Porubov (2023). Now besides nonlinearity, we also take into account different attached masses, m_1 and m_2 . The model equations of motion are

$$\begin{aligned} \ddot{u}_n = & \beta_0(u_{n-1} - 2u_n + u_{n+1}) + \eta\beta_1(v_n - u_n) + \eta\gamma(w_n - u_n) + \\ & \beta_3((u_{n+1} - u_n)^2 - (u_{n-1} - u_n)^2) + \eta\beta_2(v_n - u_n)^2 + \chi\kappa(w_n - u_n)^2 \end{aligned} \quad (21.3)$$

$$\ddot{v}_n = -\beta_1(v_n - u_n) - \beta_2(v_n - u_n)^2. \quad (21.4)$$

$$\ddot{w}_n = -\gamma(w_n - u_n) - \kappa(w_n - u_n)^2. \quad (21.5)$$

Here $\chi = m_2/m$, $\gamma = m_2/m_1$, $\kappa = m_2/m_1$ account for linear and nonlinear stiffness of the additional attached spring respectively. The displacement of the mass m with the

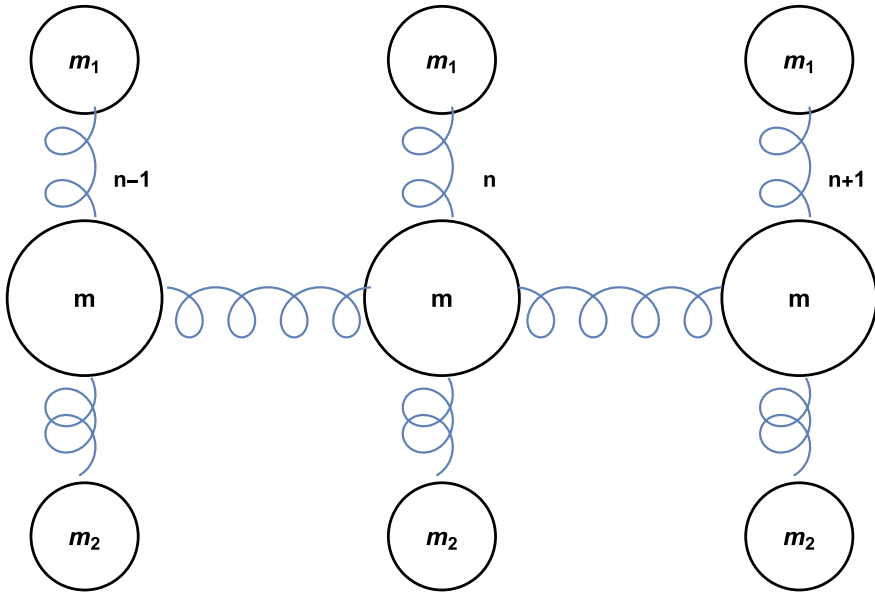


Fig. 21.2 Chain with extra attached masses

number n is denoted by u_n , that of m_1 (“upper” in Fig. 21.2), is denoted by v_n while that of m_2 (“lower” in Fig. 21.2) is denoted by w_n . We use these schematic notations but in reality this is one-dimensional model where attached masses are depicted upper and lower for better understanding.

21.2.3 Chain with Extra Internal Attached Masses

The chain with extra internal attached masses is shown in Fig. 21.3.

Now we use the notation w_n for the internal mass displacement, while the notations u_n, v_n have the same meaning as in the classic mass-in-mass model. The equations of motion are

$$\ddot{u}_n = \beta_0(u_{n-1} - 2u_n + u_{n+1}) + \eta\beta_1(v_n - u_n) + \beta_3((u_{n+1} - u_n)^2 - (u_{n-1} - u_n)^2) + \eta\beta_2(v_n - u_n)^2 \tag{21.6}$$

$$\ddot{v}_n = \beta_1(u_n - v_n) + f\gamma(w_n - u_n) - \beta_2(v_n - u_n)^2 + f\kappa(w_n - u_n)^2. \tag{21.7}$$

$$\ddot{w}_n = -\gamma(w_n - u_n) - \kappa(w_n - u_n)^2, \tag{21.8}$$

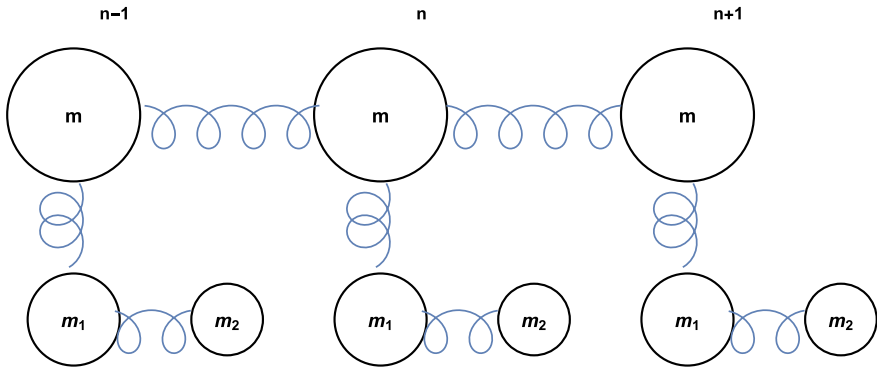


Fig. 21.3 Chain with extra internal attached masses

where f is the mass ratio, $f = m_2/m_1$, and κm_2 is the nonlinear stiffness of the internal spring.

21.3 Continuum Limit of the Discrete Models

Another description of the dynamic processes can be done using a continuum limit of Eqs. (21.1) and (21.2). The continuum functions $u(x, t)$, $v(x, t)$ are introduced for description of the displacements of the masses m_1 , m_2 . The continuum displacements of the neighboring masses are sought using the long-wave approximation (Born and Huang 1954), based on the Taylor series,

$$u_{n\pm 1} = u \pm h u_x + \frac{h^2}{2} u_{xx} \pm \frac{h^3}{6} u_{xxx} + \frac{h^4}{24} u_{xxxx} + \dots,$$

where the lattice step, h , is considered as an increment of the spatial variable, x .

Truncating the series by the fourth-order terms, we obtain from Eqs. (21.1), (21.2) of the classic mass-in-mass model,

$$u_{tt} = \beta_0 h^2 u_{xx} + \frac{\beta_0 h^4}{12} u_{xxxx} + \eta \beta_1 (v - u) + \eta \beta_2 (v - u)^2 + 2\beta_3 h^3 u_x u_{xx}, \quad (21.9)$$

$$v_{tt} = -\beta_1 (v - u) - \beta_2 (v - u)^2. \quad (21.10)$$

The continuum functions $u(x, t)$, $v(x, t)$, $w(x, t)$ are introduced for description of the displacements of the masses m , “upper,” m_1 , and “lower,” m_2 , respectively, in the model with the additional attached mass. Then the continuum limit of Eqs. (21.3)–(21.5) is

$$u_{tt} = a^2 u_{xx} + \frac{a^2 h^2}{12} u_{xxxx} + \eta \beta_1 (v - u) + \chi \gamma (w - u) + \eta \beta_2 (v - u)^2 + \chi \kappa (w - u)^2 + 2\beta_2 h^3 u_x u_{xx}, \quad (21.11)$$

$$v_{tt} = -\beta_1 (v - u) - \beta_2 (v - u)^2, \quad (21.12)$$

$$w_{tt} = -\gamma (w - u) - \kappa (w - u)^2. \quad (21.13)$$

The continuum limit of the equations of motion (21.6)–(21.8) for the model with an extra internal attached mass gives rise to

$$u_{tt} = a^2 u_{xx} + \frac{a^2 h^2}{12} u_{xxxx} + \eta \beta_1 (v - u) + \eta \beta_2 (v - u)^2 + 2\beta_3 h^3 u_x u_{xx}, \quad (21.14)$$

$$v_{tt} = \beta_1 (u - v) + f \gamma (w - u) - \beta_2 (v - u)^2 + f \kappa (w - u)^2, \quad (21.15)$$

$$w_{tt} = -\gamma (w - u) - \kappa (w - u)^2. \quad (21.16)$$

21.4 Derivation of Governing Equations

21.4.1 Asymptotic Decoupling of Continuum Equations

The asymptotic procedure of decoupling of continuum governing equations has been developed in Porubov (2023) for the classic mass-in-mass mode (21.9), (21.10). The procedure is applicable for the weakly nonlinear and the long wavelength case. The idea is to obtain single nonlinear equation with dispersion terms for the longitudinal displacement or strain of the main chain, while remaining displacements of the attached masses are expressed through it and its derivatives.

The series solution of the function v of Eq. (21.10), is suggested,

$$v = v_0 + v_1 + v_2 + \dots, \quad (21.17)$$

Then the weakly nonlinear and long wavelength consideration suggests in the leading order,

$$v_0 - u = 0.$$

Next order equation is

$$v_{0,tt} + \beta_1 v_1 = 0,$$

while in the second order we obtain

$$v_{1,tt} + \beta_1 v_2 + \beta_2 v_1^2 = 0.$$

Then the solutions of the equations are

$$v_0 = u, \quad v_1 = -\frac{1}{\beta_1} u_{tt}, \quad v_2 = \frac{1}{\beta_1^2} u_{tttt} - \frac{\beta_2}{\beta_1^3} u_{tt}^2.$$

Truncating series (21.17) by v_2 and substituting it into Eq. (21.9) we obtain single equation for the displacement u ,

$$(1 + \eta)u_{tt} = \beta_0 h^2 u_{xx} + \frac{\beta_0 h^4}{12} u_{xxxx} + \frac{\eta}{\beta_1} u_{tttt} + 2\beta_3 h^3 u_x u_{xx}. \quad (21.18)$$

One can see that nonlinearity, caused by nonlinear stiffness of the spring of the attached mass of the original model, is absent in Eq. (21.18). Also there are two dispersion terms in the equation.

This equation can be re-written for a longitudinal strain $q = u_x$,

$$(1 + \eta)q_{tt} = \beta_0 h^2 q_{xx} + \frac{\beta_0 h^4}{12} q_{xxxx} + \frac{\eta}{\beta_1} q_{tttt} + \beta_3 h^3 (q^2)_{xx}. \quad (21.19)$$

Next we can change the terms q_{xxxx} , q_{tttt} with the term w_{xxtt} using the relationship $f_{;ppwong}$ from the leading order of the equation.

$$q_{tt} = \frac{\beta_0 h^2}{1 + \eta} q_{xx}.$$

This, in general, approximate substitution can be used for dispersion terms q_{xxxx} , q_{tttt} as the exact substitution since Eq. (21.19) itself has been obtained approximately as a continuum limit neglecting sixth-order derivative terms. Then we arrive at the single governing equation for longitudinal strain waves to be presented in the next Section.

The model with extra attached mass consists of three coupled equations, and the asymptotic solution is sought as

$$v = v_0 + v_1 + v_2 + \dots, \quad w = w_0 + w_1 + w_2 + \dots, \quad (21.20)$$

Like for the previous model, we obtain from Eqs. (21.12), (21.13),

$$v_0 = u, \quad v_1 = -\frac{1}{\beta_1} u_{tt}, \quad v_2 = \frac{1}{\beta_1^2} u_{tttt} - \frac{\beta_2}{\beta_1^3} u_{tt}^2.$$

$$w_0 = u, \quad w_1 = -\frac{1}{\gamma}u_{tt}, \quad w_2 = \frac{1}{\gamma^2}u_{ttt} - \frac{\kappa}{\gamma^3}u_{tt}^2.$$

Then it follows from Eq. (21.11) that the longitudinal strain $q = u_x$

$$(1 + \eta + \chi)q_{tt} = \beta_0 h^2 q_{xx} + \frac{\beta_0 h^4}{12} q_{xxxx} + \left(\frac{\eta}{\beta_1} + \frac{\chi}{\gamma} \right) q_{ttt} + \beta_3 h^3 (q^2)_{xx}. \quad (21.21)$$

Here approximate substitution for transformation of the dispersion terms is

$$q_{tt} = \frac{\beta_0 h^2}{1 + \eta + \chi} q_{xx}.$$

Again the resulting equation will be presented in the next Section.

The asymptotic procedure for the model with an internal attached mass has the form of Eq. (21.20) We obtain from Eqs. (21.15) and (21.16) for v_i, w_i ,

$$v_0 = u, \quad v_1 = -\frac{1+f}{\beta_1}u_{tt}, \quad v_2 = a_1 u_{ttt} + a_2 u_{tt}^2.$$

$$w_0 = u, \quad w_1 = -\frac{\beta_1 + (1+f)\gamma}{\beta_1 \gamma} u_{tt},$$

where

$$a_1 = \frac{\beta_1 f + \gamma(1+f)^2}{\beta_1^2 \gamma},$$

$$a_2 = -\beta_2 \frac{(1+f)^2}{\beta_1^3}.$$

The equation for q follows from Eq. (21.14).

$$(1 + \eta(1 + \chi))q_{tt} = \beta_0 h^2 q_{xx} + \frac{\beta_0 h^4}{12} q_{xxxx} + \frac{\eta a_1}{\beta_1} q_{ttt} + \beta_3 h^3 (q^2)_{xx}. \quad (21.22)$$

Here approximate substitution is

$$q_{tt} = \frac{\beta_0 h^2}{1 + \eta(1 + f)} q_{xx},$$

it will be used for substitution both in derivative and nonlinear terms, and the final equation can be found in the next Section.

21.4.2 Single Equations for Longitudinal Strains

The single governing equation for the classic mass-in-mass model is Porubov (2023)

$$q_{tt} = \frac{\beta_0 h^2}{1 + \eta} q_{xx} + \frac{\beta_1 h^2 (1 + \eta)^2 + 12\eta\beta_0 h^2}{12\beta_1 (1 + \eta)^2} q_{xxtt} + \frac{\beta_3 h^3}{1 + \eta} (q^2)_{xx}. \quad (21.23)$$

The single governing equation for the mass-in-mass model with an extra attached mass is

$$q_{tt} = \frac{\beta_0 h^2}{1 + \eta + \chi} q_{xx} + \frac{h^2((1 + \eta + \chi)^2 \beta_1 \gamma + 12(\eta\gamma + \chi\beta_1)\beta_0)}{12(1 + \eta + \chi)\beta_1 \gamma} q_{xxtt} + \frac{\beta_3 h^3}{1 + \eta + \chi} (q^2)_{xx}. \quad (21.24)$$

After transformation of the dispersion terms the single governing equation for the mass-in-mass model with an extra internal attached mass is

$$q_{tt} = \frac{\beta_0 h^2}{1 + \eta(1 + f)} q_{xx} + \frac{h^2((1 + \eta(1 + f))^2 + 12\eta\beta_1\beta_0 a_1)}{12(1 + \eta(1 + f))} q_{xxtt} + \frac{\beta_3 h^3}{1 + \eta(1 + f)} (q^2)_{xx}. \quad (21.25)$$

Equations (21.23), (21.24) have the same functional form with the difference in the coefficients of the corresponding linear, nonlinear, and dispersion terms. Both equations doesn't contain any influence of the nonlinear stiffness of the attached masses. The linear stiffness coefficients affect the coefficients of the equations. The sign of the dispersion term in both equations is always positive while the sign of nonlinear term depends on the sign of the nonlinear stiffness coefficient β_3 .

One can note that modulational waves in the classic mass-jn-mass model the nonlinear stiffness of the attached mass results in the additional nonlinear term in the modulation equation giving rise to the bounded growth of the amplitude of the modulation wave (Porubov 2021).

21.5 Localized Nonlinear Waves

The analysis of the solutions of the linear model equations usually considers periodic wave solutions where the band gaps are the most important finding. However, localized waves do not demonstrate band gaps even in the linear case (Porubov and Krivtsov 2022).

Equations (21.23), (21.24) and (21.25) possess exact localized traveling wave solution,

$$q = A \operatorname{sech}^2(p(x - Vt - x_0)), \tag{21.26}$$

where for a classic mass-in-mass model (Porubov 2023),

$$A = \frac{3(V^2(1 + \eta) - \beta_0 h^2)}{2\beta_3 h^3(1 + \eta)}, \quad p = \sqrt{\frac{3\beta_1(1 + \eta)(V^2(1 + \eta) - \beta_0 h^2)}{(\beta_1(1 + \eta)^2 + 12\eta\beta_0)h^2 V^2}}. \tag{21.27}$$

Then the reality of p is achieved for the velocity V defined as

$$V > \sqrt{\frac{\beta_0 h^2}{1 + \eta}}.$$

The parameters of the solution of model with the additional attached mass are

$$A = \frac{3(V^2(1 + \eta + \chi) - \beta_0 h^2)}{2\beta_3 h^3}, \quad p = \sqrt{\frac{(V^2(1 + \eta + \chi) - \beta_0 h^2)}{4b_s V^2}} \tag{21.28}$$

where

$$b_s = \frac{h^2((1 + \eta + \chi)^2 \beta_1 \gamma + 12\beta_0(\eta\gamma + \chi\beta_1))}{12(1 + \eta + \chi)\beta_1 \gamma}.$$

Then the reality of p is achieved for the velocity V defined as

$$V > \sqrt{\frac{\beta_0 h^2}{1 + \eta + \chi}}.$$

The parameters of the solution of model with the additional internal attached mass are

$$A = \frac{3(V^2(1 + \eta(1 + f)) - \beta_0 h^2)}{2\beta_3 h^3}, \quad p = \sqrt{\frac{(V^2(1 + \eta(1 + f)) - \beta_0 h^2)}{4b_d V^2}} \tag{21.29}$$

where

$$b_d = \frac{h^2(1 + \eta(1 + f))}{12} + \frac{\beta_0 \beta_1 \eta h^2}{1 + \eta(1 + f)} \frac{\beta_1 f + \gamma(1 + f)^2}{\beta_1^2 \gamma}.$$

Then the reality of k is achieved for the velocity V

$$V > \sqrt{\frac{\beta_0 h^2}{1 + \eta(1 + f)}}.$$

The velocity intervals are different. Both extended models provide widening of the velocity interval. The sign of the amplitude is defined entirely by the sign of nonlinear stiffness coefficient β_3 of the main chain. Different dispersion term coefficients in the single model equations give rise to variation in the width of the solitary wave.

Numerical simulations reveal important differences in the evolution of the initial localized perturbation. We have chosen it in the form

$$\begin{aligned} q(x, 0) &= A_n \operatorname{sech}^2(p_n(x - x_0)), \\ q_t(x, 0) &= 2V_n p_n A_n \operatorname{sech}^2(p_n(x - x_0)) \tanh(k(x - x_0)), \end{aligned} \quad (21.30)$$

where

$$V_n = \sqrt{\beta_0 h^2 + \delta}, \quad A_n = \frac{3(V_n^2 - \beta_0 h^2)}{2\beta_3 h^3}, \quad p_n = 0.5 \sqrt{\frac{3(V_n^2 - \beta_0 h^2)}{h V_n}}.$$

This condition differs from that of any exact solutions given above. We use the Wolfram Mathematica 13 for numerical simulations using the sweep method or the three-diagonal matrix algorithm, see, e.g., Yu et al. (2009). Numerical simulations for Eq. (21.23) are performed in the region in the region $0 < x < x_N$, $0 < t < t_N$. The values of the parameters are chosen as

$$h = 0.7, \beta_0 = 0.5, \beta_1 = 0.5, \beta_2 = 0.2, \beta_3 = 0.5, \eta = 0.2, \chi = 0.4, \delta = 0.2.$$

$$x_N = 200, x_0 = x_N/3, t_N = 150.$$

Shown in Fig. 21.4 is a comparative localized waves evolution for the case of classic mass-in-mass model, Eq. (21.23), and the model with an extra attached mass, Eq. (21.24). Since the initial condition (21.30), Fig. 21.4, corresponds neither exact solution (21.27) nor (21.28) we don't observe stable single solitary wave (21.26) propagation. Shown by dashed line is the evolution in classic model. We see that the initial perturbation splits into two solitary waves marked by 1 and 3 in Fig. 21.4b–d. They propagate with their velocities, and the distance between them increases as time goes on. The amplitudes remain permanent. On the contrary, no splitting into the solitary waves is seen for the extended model shown by solid line. Only perturbation tail develops behind the solitary wave marked by 2. The amplitude and the velocity of the wave is smaller than that of the highest wave 1 of the classic model. The choice of non-zero initial velocity V_n provides unidirectional propagation.

Figure 21.5 demonstrates dependence of the amplitude and the velocity of localized wave on the mass ratio χ . One can see an increase in both parameters with the decrease in the value of χ . No more waves are generated, and the tails behind the localized wave are similar for all values of χ . Contrary to the previous figure here and in the following $x_0 = x_N/2$.

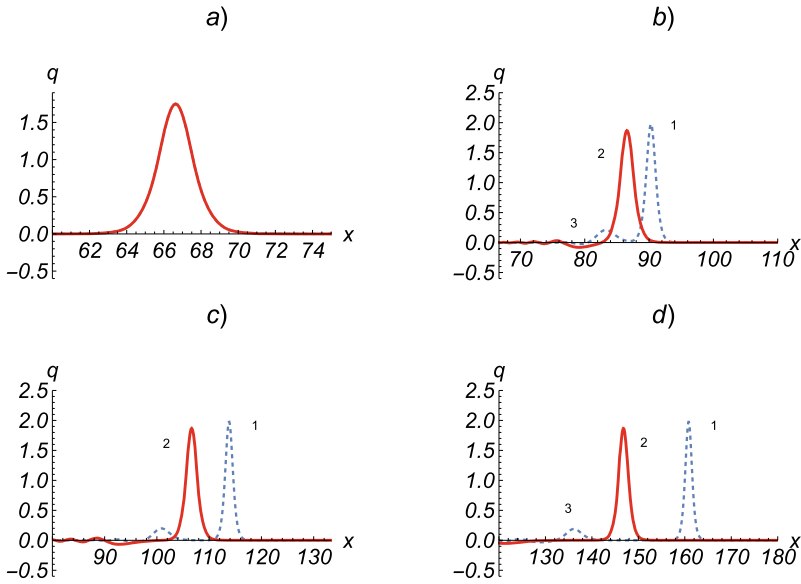


Fig. 21.4 Evolution of the localized input for the case of the classic mass-in-mass model (dashed line) and the model with extra attached mass (solid line). **a** $t = 0$, **b** $t = t_N/4$, **c** $t = t_N/2$, **d** $t = t_N$. Marked by 1, 2, 3 are the localized waves emerged form the initial perturbation

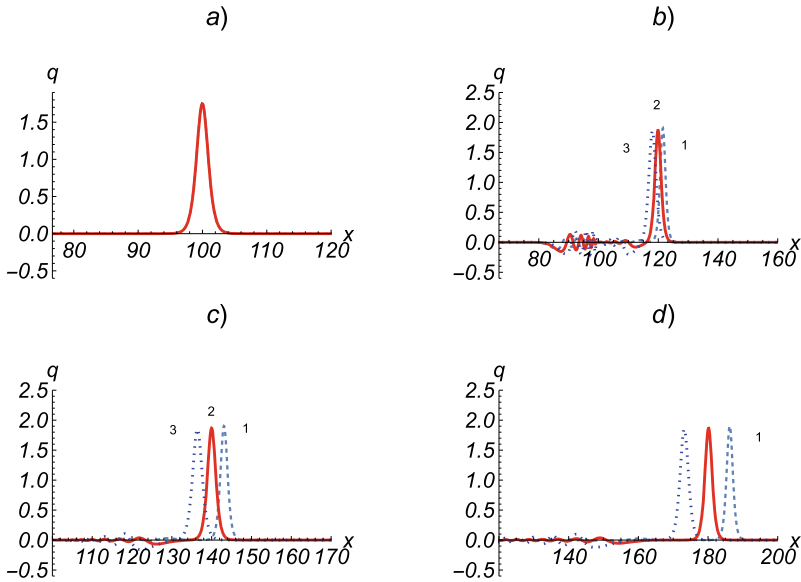


Fig. 21.5 Dependence on the mass ratio χ for the model with extra attached mass. Marked by 1 is the case $\chi = 0.2$, dashed line; marked by 2 is the case $\chi = 0.4$, solid line; 3 corresponds to $\chi = 0.7$, dotted line. **a** $t = 0$, **b** $t = t_N/4$, **c** $t = t_N/2$, **d** $t = t_N$

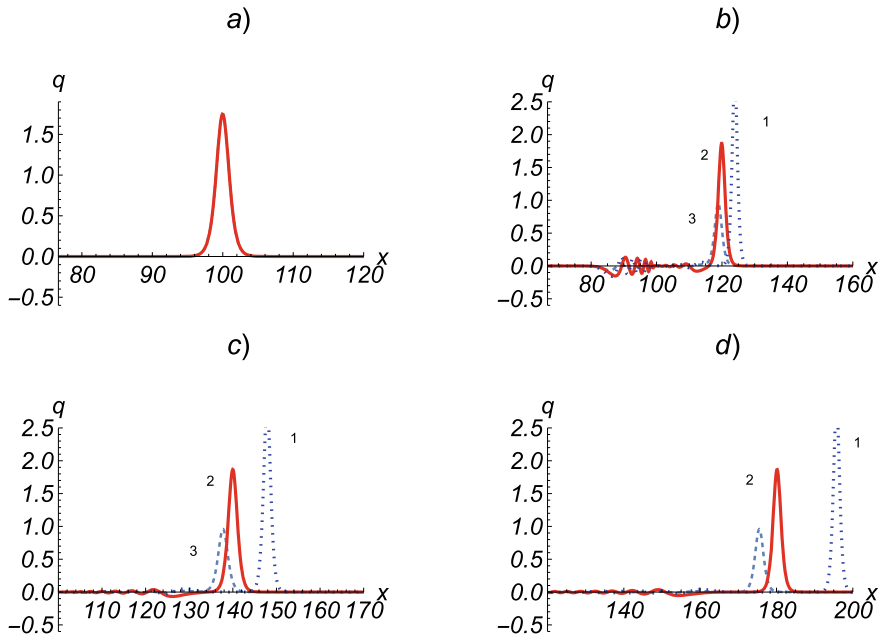


Fig. 21.6 Dependence on the initial velocity V_n for the model with extra attached mass. Marked by 1— $\delta = 0.4$, dotted line; 2— $\delta = 0.2$, solid line; 3— $\delta = 0.1$, dashed line. **a** $t = 0$, **b** $t = t_N/4$, **c** $t = t_N/2$, **d** $t = t_N$

Dependence on the value of initial velocity V_n is seen in Fig. 21.6. Again the number of the emerged solitary waves is the same. The velocity and the amplitude grow with an increase in the value of δ thus in the value of V_n .

21.6 Conclusions

Extended nonlinearly elastic metamaterial mass-in-mass models can be analyzed in the long wavelength continuum approximation. The model equations and their localized exact solutions reveal important features caused by the additional elements in the original models. Even variations in the dispersion term coefficients of the governing equations result in the serious differences in the dynamics of localized strain waves evolution. It concerns variations in the amplitude and velocity and the number of the emerged waves.

The nonlinear stiffness of the spring of the main chain only affects propagation of localized longitudinal waves for all models. Contribution of the nonlinear stiffness of the attached mass spring is found in the relationships for the displacements of the attached masses.

Acknowledgements The work was supported by the Ministry of Science and Higher Education of the Russian Federation in the framework of the state assignment under contract No. 12112500318-1.

References

- Andrianov IV, Awrejcewicz J, Weichert D (2010) Improved continuous models for discrete media. *Math Probl Eng* 2010:986242
- Askar A (1985) *Lattice dynamical foundations of continuum theories*. World Scientific, Singapore
- Belashov VY, Vladimirov SV (2009) *Solitary waves in dispersive complex media theory simulation applications*. Springer, Berlin
- Born M, Huang K (1954) *Dynamical theory of crystal lattices*. Clarendon Press, Oxford
- Bukhari M, Barry O (2020) Spectro-spatial analyses of a nonlinear metamaterial with multiple nonlinear local resonators. *Nonlinear Dyn* 99:1539–1560
- Cveticanin L, Cveticanin D (2018) Acoustic metamaterials: theory and application. In: Herisanu N, Marinica V (eds), *Acoustics and vibration of mechanical structures-AVMS-2017*, Springer proceedings in physics, vol 198, pp 21–32
- Eremeyev VA, Turco E (2020) Enriched buckling for beam-lattice metamaterials. *Mech Res Comm* 103:103458
- Erofeev V, Kolesov D, Malkhanov A (2020) Nonlinear strain waves in a metamaterial defined a mass-to-mass chain. *IOP Conf Ser: Mater Sci Eng* 709:033037
- Fang X, Wen J, Bonello B, Yin J, Yu D (2017) Wave propagation in one-dimensional nonlinear acoustic metamaterials. *New J Phys* 19:053007
- Hu G, Tang L, Das R, Gao S, Liu H (2017) Acoustic metamaterials with coupled local resonators for broadband vibration suppression. *AIP Adv* 7:025211
- Huang GL, Sun CT (2010) Band gaps in a multiresonator acoustic metamaterial. *J Vib Acoust* 132:031003
- Huang HH, Sun CT, Huang GL (2009) On the negative effective mass density in acoustic metamaterials. *Intern J Eng Sci* 47:610–617
- Lazarov BS, Jensen JS (2007) Low-frequency band gaps in chains with attached non-linear oscillators. *Intern J Non-Linear Mech* 42:1186–1193
- Liu C, Reina C (2018) Broadband locally resonant metamaterials with graded hierarchical architecture. *J Appl Phys* 123:095108
- Ma G, Sheng P (2016) Acoustic metamaterials: from local resonances to broad horizons. *Sci Adv* 2(2):1–16
- Ostoja-Starzewski M (2002) Lattice models in micromechanics. *Appl Mech Rev* 55:35–60
- Oyelade AO, Akano TT (2020) Graded hierarchical architecture metamaterial in vibration suppression. *UPB Sci Bull Ser D* 82(3):41–50
- Porubov AV (2023) Continuum description of extended mass-in-mass metamaterial models. In: Altenbach H, Berezovski A, dell’Isola F, Porubov A (eds) *Sixty shades of generalized continua. Advanced structured materials*, vol 170. Springer, Cham, pp 567–578
- Porubov AV (2021) Wave modulation in a nonlinear acoustic metamaterial. *Int J Non-Linear Mech* 137:103788
- Porubov AV (2023) Nonlinear wave localization in an acoustic metamaterial. *Commun Nonlinear Sci Numer Simul* 119:107095
- Porubov AV, Antonov ID (2021) On control of harmonic waves in an acoustic metamaterial. *Mech Res Commun* 116:103745
- Porubov AV, Krivtsov AM (2022) Dispersive propagation of localized waves in a mass-in-mass metamaterial lattice. *Continuum Mech Thermodyn* 34:1475–1483
- Yang T, Song Z-G, Clerkin E, Zhang Y-W, Sun J-H, Su Y-S, Chen L-Q, Hagedorn P (2017) A programmable nonlinear acoustic metamaterial. *AIP Adv* 7:095323

- Yao S, Zhou X, Hu G (2008) Experimental study on negative effective mass in a 1D mass-spring system. *New J Phys* 10:043020
- Zhou X, Liu X, Hu G (2012) Elastic metamaterials with local resonances: an overview. *Theor Appl Mech Lett* 2:041001
- Zhou J, Cheng Y, Zhang H, Huang G, Hu G (2015) Experimental study on interaction between a positive mass and a negative effective mass through a mass-spring system. *Theor Appl Mech Lett* 5:196–199

Chapter 22

Nonlinear Change of Young's Modulus of Geomaterials Under Alternating Loads



Evgenii P. Riabokon, Mikhail S. Turbakov, Evgenii V. Kozhevnikov, Mikhail A. Guzev, and Hongwen Jing

Abstract Young's modulus of the geomaterial is investigated experimentally under the alternating loads. With an increase in the frequency of the alternating load the strain amplitude of rock samples decreases, while Young's modulus increases. It was also found that Young's modulus behaves differently (according to different laws) in the low-frequency region (below 10 Hz) and in the high-frequency region (above 10 Hz).

Keywords Nonlinear young's modulus · Alternating load · Geomaterial

22.1 Introduction

Under the alternating loads the mechanical characteristics of rocks and Young's modulus in particular change. The nonlinearity of Young's modulus of sedimentary rocks is evidenced by both state-of-the-art and earlier experimental works. In particular, in Sun et al. (2020) a nonlinear dependence (increase) of Young's modulus of Bleurswiller sandstone on the frequency of the external applied axial load ranging from 10^{-2} Hz to 10^2 Hz was obtained. The work Li et al. (2020) also revealed an increase in Young's modulus of dense sandstone with an increase in the frequency of loading ranging from 10^0 Hz to 10^3 Hz. In the study of New Red sandstone on a small experimental rig (Guzev and Kozhevnikov 2020; Riabokon et al. 2021; Guzev et al. 2021a, b an increase in Young's modulus with an increase in the frequency of

E. P. Riabokon · M. S. Turbakov · E. V. Kozhevnikov · M. A. Guzev
Perm National Research Polytechnic University, Perm, Russia

M. A. Guzev (✉)
Institute for Applied Mathematics of the Far Eastern Branch of the Russian Academy of Sciences, Vladivostok, Russia
e-mail: guzev@iam.dvo.ru

H. Jing
State Key Laboratory for Geomechanics and Deep Underground Engineering, China University of Mining and Technology, Xuzhou, China

© The Author(s), under exclusive license to Springer Nature Switzerland AG 2023
H. Altenbach and V. Eremeyev (eds.), *Advances in Linear and Nonlinear Continuum and Structural Mechanics*, Advanced Structured Materials 198,
https://doi.org/10.1007/978-3-031-43210-1_22

385

the alternating load was revealed from 10 Hz to 40 Hz in accordance with the rational function. While studying the Opalinus Clay (Lozovyi and Bauer 2019) and Mancos shale (Szewczy et al. 2016) samples, a steady slow increase in Young's modulus was revealed with an increase in the load frequency ranging from 1 Hz to 100 Hz. During the study of Pierre clay, in Pimienta et al. (2015) the authors also revealed the dispersion of the elastic modulus with help of a dynamic loading rig. In earlier works, for example, in Batzle et al. (2006) and Tutuncu et al. (1998), the nonlinear behavior of Young's modulus with the increasing loading rate (frequency) was also obtained.

It is generally accepted that with an increase in the frequency of an alternating load Young's modulus increases in accordance with the same dependence at different frequencies. At the same time, the analysis of works shows that still less attention was paid to the low-frequency region (below 10 Hz), in which the change in Young's modulus may differ from the region of higher frequencies (above 10 Hz). In this regard, to study the behavior of Young's modulus both at low and high frequencies, experimental studies are performed using geomaterial samples.

The studies are carried out in the zone of linear elasticity of the geomaterial, in which the stress σ and the longitudinal strain ε are connected linearly by Young's modulus E in accordance with the ratio $\sigma = E \cdot \varepsilon$. The state of the linear elasticity was achieved by static preloading of the samples. The boundaries of the zone of linear elasticity of the rock were preliminary estimated in tests for uniaxial compressive strength. The behavior of Young's modulus of the geomaterial under loading was studied in the frequency range from 0.1 Hz to 60 Hz. As a result of the investigation, the nonlinear behavior of Young's modulus was revealed and two zones with different laws of change of Young's modulus were identified.

The paper is organized as follows. Section 22.2 describes the materials and methods for conducting an experimental investigation. Section 22.3 presents the research results and their discussion. Section 22.4 presents model interpretations of the obtained experimental data, followed by a conclusion.

22.2 Materials and Methods

22.2.1 Materials for Study

As a geomaterial for study, a limestone with a dense consolidated heterogeneous structure was chosen. The six samples with a diameter of 25 mm and a length of 50 mm were prepared for the investigation in accordance with the ASTM standard (ASTM 2001) (Fig. 22.1).

According to the analysis of a thin section, form components of limestone are represented by bioclasts, composed of micritic calcite, but more often clear-crystalline calcite 0.08–0.22 mm in size fills bioclast chambers or fills their walls (Fig. 22.2a). Single chambers of skeletal forms are filled with quartz, the grain size of which



Fig. 22.1 The photograph depicting six limestone samples prepared for the study

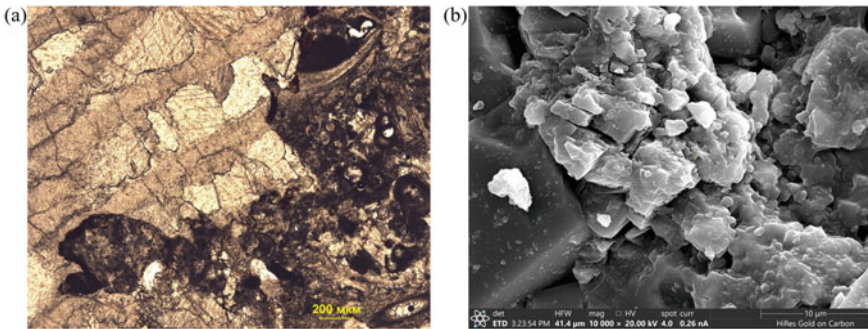


Fig. 22.2 Microphotographs of a limestone sample: **a** microphotograph of a thin section of a sample with a fragment of bryozoan with a chamber filled with medium-grained calcite; **b** electron microphotograph of a sample with rhombohedral calcite particles

is less than 0.04 mm. The matrix in the rock is micritic. Secondary calcite cement, sparite (30%), of different crystals with grain sizes of 0.08–0.3 mm, is developed in the intergranular space as a result of recrystallization of the matrix and bioclasts. The pores are intercrystalline, formed along organogenic voids, isolated, rounded, slit-like, irregularly shaped. The pores are 0.008–0.2 mm in size. The stylolite sutures are finely serrated and the veins of the seal are branching, filled with brown clay-organic matter. The results of electron microscopy revealed that the sample structure is represented by a microgranular framework with a rhombohedral calcite particle size of more than 0.1 mm (Fig. 22.2b).

22.2.2 Study Methods

The investigation was carried out on the Instron ElectroPuls E10000 servo-electric testing system (Fig. 22.3a), which met the experimental requirements such as: (a)

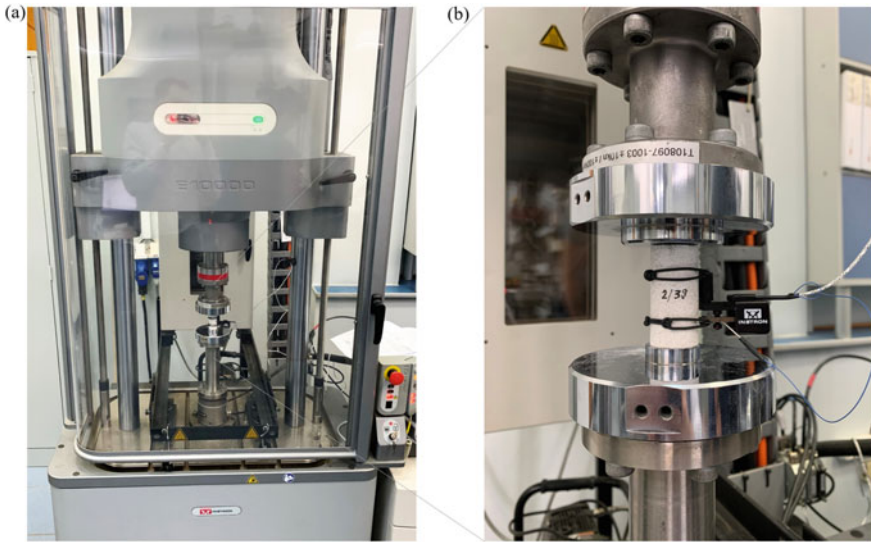


Fig. 22.3 Photographs of the Instron ElectroPuls E10000 test system depicting: **a** general view of the system; **b** geomechanical sample 2/39 between load plates with strain gauge installed.

is able to develop a load sufficient to transfer a full-size traditional core sample to a state of linear elasticity; (b) allows to create alternating loading of a full-sized rock sample in a wide frequency range. The deformation of the rock sample during the tests was recorded by an Instron 2620–603 mechanical strain gauge, which was supported on the sample by highly sensitive knives and pressed against the sample by rubber clamps (Fig. 22.3b).

Before the start of the experiment, each sample was loaded with a static preload $F_{st} = 6.9$ kN. During the experiment, each sample was additionally loaded with a dynamic load F_{dyn} of the amplitude $A = 850$ N applied at different frequencies.

The program of investigation included 12 steps (Fig. 22.4). After the first step of initializing the experiment to achieve the specified value of sample strain (control mode by digital position) at a frequency of 0.1 Hz, a gradual increase in the amplitude of the dynamic load begins at the second step. The waveform was sinusoidal. The duration of each step is chosen in such a way that the regime stabilizes and the deformation amplitude reaches a shelf (a certain constant value) (see Fig. 22.5a). For this, the duration of stabilization (the number of cycles required) was preliminarily estimated (Table 22.1). After the amplitude reached a constant value at the second step of the experiment, the load was instantly removed and the second loading mode was initialized until a constant amplitude value was reached again. The process was repeated ten times at all frequencies, after which the experiment was completed. The procedure was performed for each of the six samples. The data from the load cell of the testing system and the strain sensor were recorded in the WaveMatrix package.

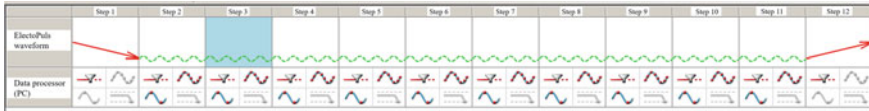


Fig. 22.4 The program of the dynamic loading of geomaterial samples including 12 steps such as step 1 is a stage of preloading the samples; steps 2–11 are stages of loading samples at frequencies of 0.1, 0.5, 1, 2, 5, 10, 20, 40, 60 and 100 Hz; step 12 is an unloading stage

Table 22.1 Duration (number of cycles) of loading in each mode

| | | | | | | | | | |
|------------------------------|-----|-----|----|----|-----|-----|-----|------|------|
| Load frequency ω , Hz | 0.1 | 0.5 | 1 | 2 | 5 | 10 | 20 | 40 | 60 |
| Number of cycles | 10 | 25 | 50 | 50 | 100 | 200 | 500 | 1000 | 1000 |

Despite the availability of experimental results at a frequency of 100 Hz, the data were not stable, and therefore it was decided not to use them.

22.3 Results and Discussion

Note that the strain amplitude decreases not with an increase in the number of cycles (duration of cyclic exposure) and possible fatigue effects, but with an increase in the frequency of the alternating load (Fig. 22.5a) at a constant value of the alternating load (Fig. 22.5b).

Taking the asymptotic values from Fig. 22.5a, it is not difficult to demonstrate the nonlinear dependence of the geomaterial strain amplitude on the frequency of the alternating applied load (Fig. 22.6).

The decrease in the amplitude of sample strain shown in Fig. 22.6 at the constant load and the stress consequently, indicates an increase in the resistance of the sample with an increase in the strain rate (load frequency).

At the same time, the stress-strain diagrams (Fig. 22.7) show that, for example, the rock sample 2/46 at all frequencies of the variable load behaves like an absolutely elastic body, which is confirmed by the absence of empty space inside the ellipse (the absence of hysteresis and energy dissipation), as a result, the ellipse becomes almost a straight line.

As a result of processing experimental data and calculating based on their dynamic Young’s modulus, two areas are visually distinguished in which Young’s modulus changes in accordance with different laws (Fig. 22.8).

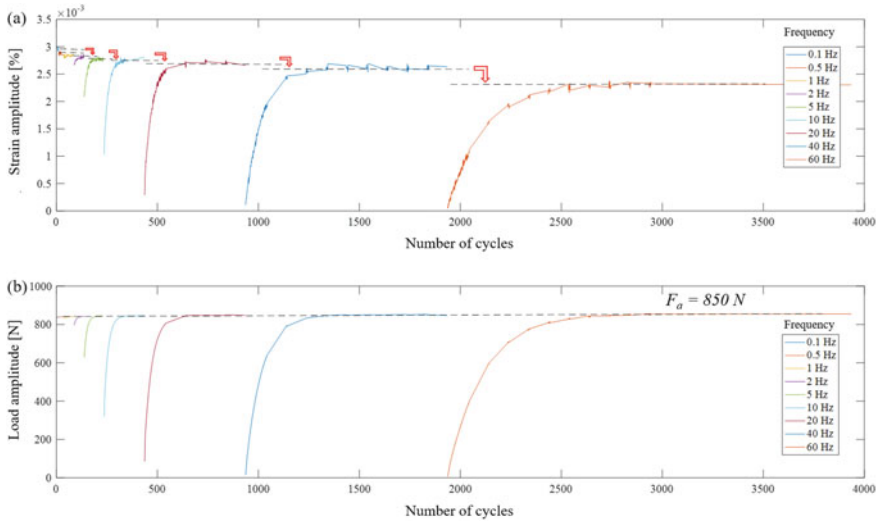
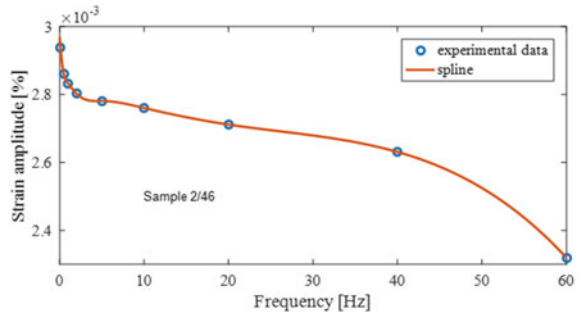


Fig. 22.5 Graphs of changes in experimental data under the influence of an alternating load with frequencies ranging from 0.1 Hz to 60 Hz load amplitude (on example of the sample 2/46): **a** strain amplitude; **b** load amplitude

Fig. 22.6 Dependence of the sample strain amplitude on the frequency of the alternating load ranging from 0.1 Hz to 60 Hz (on example of the sample 2/46)



22.4 Model Interpretations

The analysis of the dependencies obtained (Fig. 22.8) shows that for all rock samples the nature of the change in Young’s modulus is the same, only the specific values of the mechanical characteristic are different. There is an inflection is clearly visible in the frequency region of 10 Hz, where the law changes, in accordance with which Young’s modulus changes. In the frequency range from 10 Hz to 60 Hz the behavior of Young’s modulus is determined by a rational function (see Fig. 22.9). The change in Young’s modulus in accordance with a rational function in the range of frequencies ω from 10 Hz to 40 Hz of the applied load with an amplitude A was modeled by the authors in previous works. In particular, the work Guzev et al. (2020) presents a

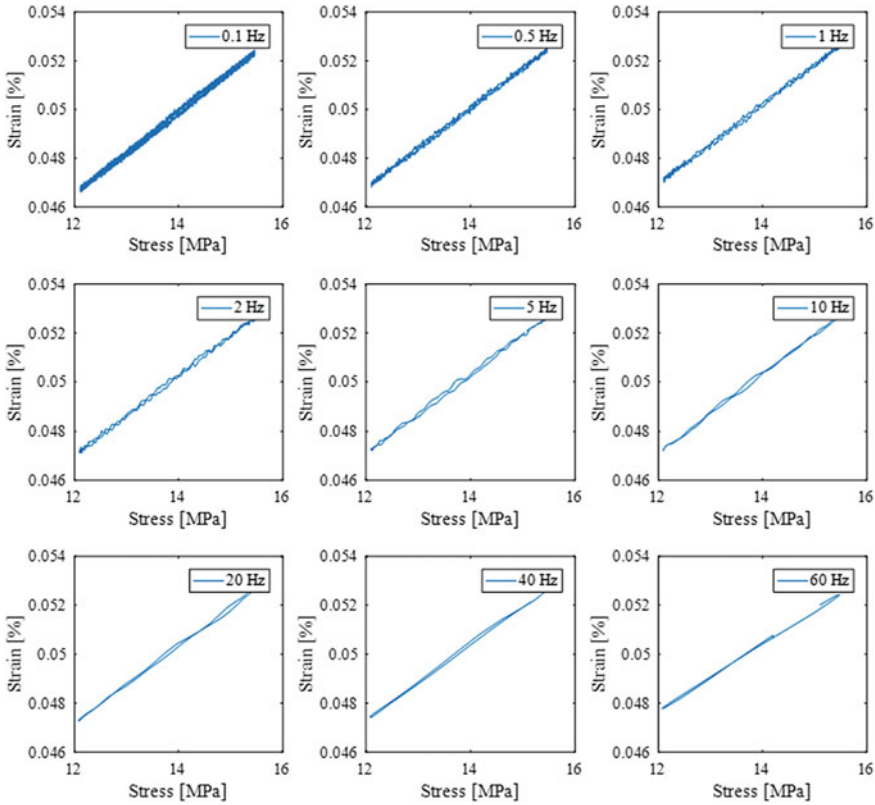


Fig. 22.7 Stress-strain diagrams of the sample under the influence of the alternating load at frequencies from 0.1 Hz to 60 Hz (on example of the sample 2/46)

mathematical model based on the classical idealized model of Jaeger J.C. “mass-on-spring” and built using Newton’s equation.

$$E_{dyn} = \frac{A}{\frac{S}{l} \left| \frac{A}{m[\alpha^2 - 1]\omega^2} - C \sin \frac{\pi\alpha}{2} \cos \pi\alpha \right|}. \tag{22.1}$$

Based on physical substantiated relationships, the classical model includes sample parameters such as mass m , length l and diameter d . The model also contains the parameter C , which takes into account the experimental conditions, and the parameter α , which reflects the ratio of the natural oscillation frequency of the geomaterial at the moment of loading to the frequency of the applied load. It can be said that the classical model corresponds to the continuum model.

In another work of the authors Guzev et al. (2021c), based on the gradient theory, a non-classical mathematical model of the change in Young’s modulus is presented, taking into account the scale (internal structure) of the sample,

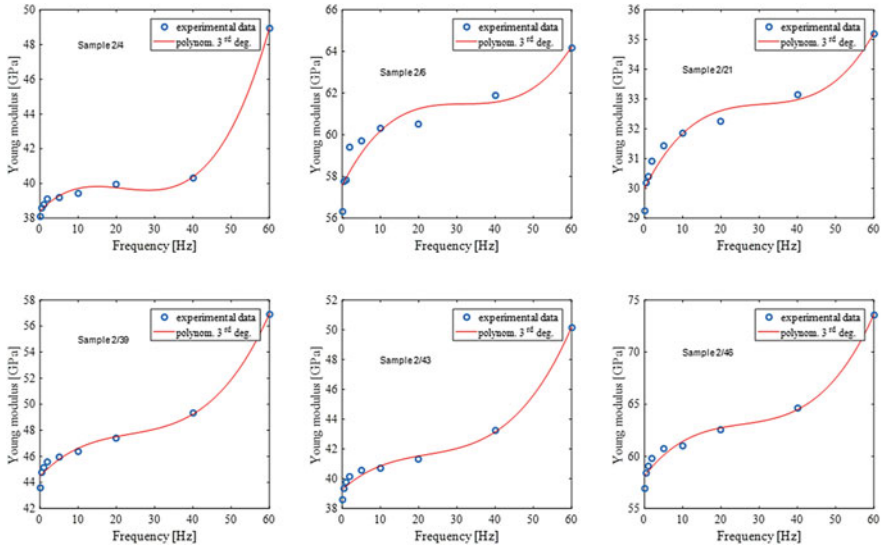
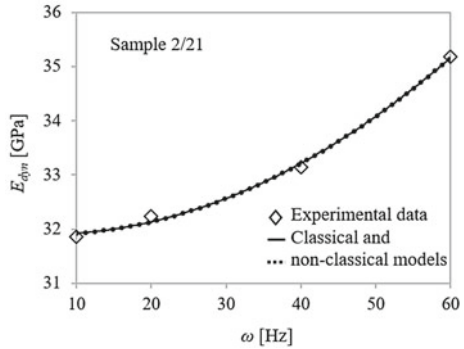


Fig. 22.8 Dependencies of Young’s modulus of rock samples on the frequency of the applied alternating load

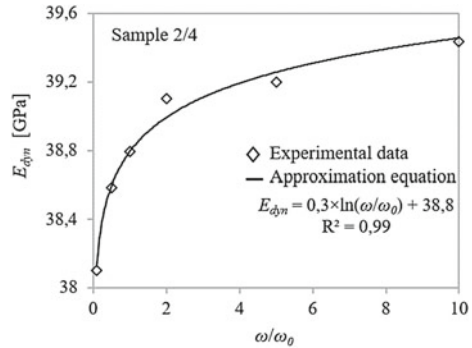
Fig. 22.9 Experimental data and the change in Young’s modulus calculated by the classical and non-classical models depending on the frequency of the applied dynamic load (on the example of sample 2/21)



$$E_{dyn} = E_{st} + \rho_0 \frac{-v_{st}^2 + \sqrt{v_{st}^4 - (4\gamma\omega^2)/\rho_0}}{2}. \tag{22.2}$$

The model contains a phenomenological parameter γ , which takes into account the internal heterogeneous structure of the geomaterial. In addition to the additive, the model takes into account the velocity of propagation of a sound wave v_{st} in the geomaterial, the density of the geomaterial ρ_0 and the frequency ω of the external applied load. Figure 22.9 shows the model dependences and experimental data on Young’s modulus in the frequency range from 10Hz to 60Hz.

Fig. 22.10 Approximation of experimental data on the change in Young’s modulus with an increase in the frequency of the alternating load from 0.1 Hz to 10 Hz (on example of the sample 2/4)



In the frequency range from 0.1 Hz to 10 Hz, the nature of the change in Young’s modulus for all samples is close to a certain logarithmic function (see Fig. 22.8). To identify the dependence of Young’s modulus of the rock on the frequency of the applied load, let us use the approximation of experimental data. On example of the experimental data obtained when loading the sample 2/4 it can be seen (Fig. 22.10) that the values of Young’s modulus are approximated by the natural logarithm function of the dimensionless frequency ($\omega_0 = 1$ Hz) of the applied load $E_{dyn} = a \cdot \ln(\omega/\omega_0) + E_{st}$. In the approximating equation, the dynamic Young’s modulus E_{dyn} , numerical coefficient a and the added static Young’s modulus E_{st} have the dimension of [GPa].

The nature of the change in Young’s modulus at frequencies below 10 Hz indicates a slightly different mechanism for the response of the geomaterial to an external applied load than in the previously proposed classical and non-classical models. In this regard, in further studies, the task will be to propose a mathematical model that would reflect the change in Young’s modulus over the entire frequency range, taking into account the change in the dispersion law.

22.5 Conclusion

An experimental investigation of the change in Young’s modulus of the geomaterial under the influence of an alternating load with a frequency ranging from 0.1 Hz to 60 Hz was carried out in the work. Heterogeneous limestone was used as the studied rock. Based on the results of the study, the following conclusions can be drawn:

- (1) under the influence of an alternating load the change in Young’s modulus of the geomaterial is carried out differently over the entire frequency range: in the low-frequency region (from 0.1 Hz to 10 Hz) the approximation of the calculated Young’s modulus is given by a certain logarithmic function, while in the high-frequency region (from 10 Hz to 60 Hz) the law of Young’s modulus change is close to a rational one;

(2) the experimental data obtained in this work on high-precision equipment confirmed the previous results of the authors obtained on a small experimental rig, according to which, with an increase in the strain rate (frequency of the applying dynamic load), a dispersion of Young's modulus of the geomaterial is observed;

(3) the classical and non-classical models previously developed by the authors, which reflect the change in Young's modulus at frequencies from 10 to 40 Hz, can be extended to 60 Hz and supplemented with a new revealed dependence of Young's modulus in the low-frequency region.

Acknowledgements The research was supported by a grant from the Russian Science Foundation No. 22-19-00447, <https://rscf.ru/project/22-19-00447/>.

References

- ASTM D4543: standard practices for preparing rock core specimens and determining dimensional and shape tolerances. West Conshohocken, PA, USA: American Society for Testing and Materials International, 2001
- Batzle ML, Han D-H, Hofmann R (2006) Fluid mobility and frequency-dependent seismic velocity—direct measurements. *Geophysics* 71:N1–N9. <https://doi.org/10.1190/1.2159053>
- Guzev MA, Kozhevnikov EV, Turbakov MS, Riabokon EP, Poplygin VV (2020) Experimental studies of the influence of dynamic loading on the elastic properties of sandstone. *Energies* 13:6195. <https://doi.org/10.3390/en13236195>
- Guzev MA, Kozhevnikov EV, Turbakov MS, Riabokon EP, Poplygin VV (2021a) Experimental investigation of the change of elastic moduli of clastic rocks under nonlinear loading. *Int J Eng Trans C: Asp* 34(3):750–755. <https://doi.org/10.5829/ije.2021.34.03c.21>
- Guzev MA, Riabokon EP, Turbakov MS, Kozhevnikov EV, Poplygin VV (2021b) Study on the effect of nonlinear dynamic loads on the elastic modulus of rocks during hydrocarbon fields development. In: 7th scientific exploration conference—Tyumen 2021: natural resources management as a cross-functional process. <https://doi.org/10.3997/2214-4609.202150026>
- Guzev MA, Riabokon EP, Turbakov MS, Poplygin VV (2021c) Non-classical model for description of the dynamic elasticity modulus of the material. *Mater Phys Mech* 47(5):720–726. <https://doi.org/10.18149/MPM.4752021-6>
- Guzev M, Riabokon E, Turbakov M, Kozhevnikov E, Poplygin V (2020) Modelling of the dynamic Young's modulus of a sedimentary rock subjected to nonstationary loading. *Energies* 13:6461. <https://doi.org/10.3390/en13236461>
- Li H, Wang D, Gao J, Zhang M, Wang Y, Zhao L, Yang Z (2020) Role of saturation on elastic dispersion and attenuation of tight rocks: an experimental study. *J Geophys Res: Solid Earth* 125:e2019JB018513. <https://doi.org/10.1029/2019JB018513>
- Lozovyi S, Bauer A (2019) From static to dynamic stiffness of shales: frequency and stress dependence. *Rock Mech Rock Eng* 52. <https://doi.org/10.1007/s00603-019-01934-1>
- Pimienta L, Fortin J, Gueguen Y (2015) Bulk modulus dispersion and attenuation in sandstones. *Geophysics* 80:D111–D127. <https://doi.org/10.1190/geo2014-0335.1>
- Riabokon E, Poplygin V, Turbakov M, Kozhevnikov E, Kobiakov D, Guzev M, Wiercigroch M (2021) Nonlinear Young's modulus of new red sandstone: experimental studies. *Acta Mech Solida Sin* 34(6):989–999. <https://doi.org/10.1007/s10338-021-00298-w>
- Sun C, Borgomano JVM, Fortin J, Wang SX (2020) Effect of pore collapse and grain crushing on the frequency dependence of elastic wave velocities in a porous sandstone. *Rock Mech Rock Eng* 53:5081–5093. <https://doi.org/10.1007/s00603-020-02213-0>

- Szewczyk D, Bauer A, Holt RM (2016) A new laboratory apparatus for the measurement of seismic dispersion under deviatoric stress conditions. *Geophys Prospect* 64. <https://doi.org/10.1111/1365-2478.12425>
- Tutuncu AN, Podio AL, Gregory AR, Sharma MM (1998) Nonlinear viscoelastic behavior of sedimentary rocks, Part I: effect of frequency and strain amplitude. *Geophysics* 63:184–194. <https://doi.org/10.1190/1.1444311>

Chapter 23

Microstructural Model of Magnetic and Deformation Behavior of Single Crystals and Polycrystals of Ferromagnetic Shape-Memory Alloy



Anatoli A. Rogovoy and Olga S. Stolbova

Abstract Based on the microstructural approach, a model of the Heusler alloy with magnetic shape-memory behavior is constructed using the theory of micromagnetism. The Landau–Lifshitz–Gilbert equation is utilized to describe the dynamics of the magnetization process. The problem of magnetization of single crystals of the Ni_2MnGa alloy, which has a “herringbone”-type martensitic structure (a twinned variant of martensite), is considered. A condition for the detwinning of a ferromagnetic shape-memory alloy in a magnetic field is proposed, and the effect of the reorientation (detwinning) of martensitic variants forming a twin on the magnetization of the material and the occurrence of structural (detwinning) deformations in it are taken into account. First, the process of magnetization and occurrence of the structural deformation of a single grain is considered, when an external magnetic field is applied at different angles to the anisotropy axes of twinned variants. Then, based on the obtained results, magnetization curves for various (isotropic and texture-oriented) polycrystalline samples are constructed and the deformed states of these materials are determined.

23.1 Introduction

Recently, the Ni_2MnGa Heusler alloy has become the object of a large number of studies aimed at developing new functional materials that can change their size and shape when exposed to an external magnetic field (see, for example, Bachaga et al. 2019; Khan et al. 2018; Vasil’ev et al. 2003). When this material is cooled from a

A. A. Rogovoy (✉) · O. S. Stolbova
ICMM UB RAS, A. Korolev Street, 1, Perm, Russia
e-mail: rogovoy@icmm.ru

O. S. Stolbova
e-mail: sos@icmm.ru

high-temperature phase with a cubic crystal lattice (austenite state) without applying a mechanical load, then, in the process of a direct first-order phase transition, twin structures are formed in a low-temperature phase with a tetragonal crystal lattice (martensitic state). To detwin these structures, a stress and/or an external magnetic field is applied, while deformation of up to 6–10% occurs in the material.

In the martensitic state at temperatures below the Curie point (376 K for Ni_2MnGa), Heusler alloys are ferromagnets, which means they have spontaneous magnetization even in the absence of an external magnetic field. Each variant of martensite has an easy magnetization axis, and this axis is an energetically favorable direction of the spontaneous magnetization vector. Magnetic domains are formed in regions consisting of interrelated variants of martensite with the same direction of magnetization vectors. Thus, magnetic domains with different directions of the magnetization vectors are formed in the martensitic phase, and these domains are located in such a way that the alloy is non-magnetized in the absence of a magnetic field. In a magnetic field, the walls of magnetic domains move, the magnetization vectors rotate, and the martensitic variants are reoriented (detwinned).

The processes described above occur at the level of the material structure; therefore, microstructural modeling, which is the subject of the works of Kazaryan and Wang (2002), Mennerich et al. (2011), Wan et al. (2006), Zhang and Chen (2005), allow to write constitutive equations without additional assumptions, in contrast to the phenomenological approach, to which many publications are devoted (Bustamante et al. 2007; Haldar et al. 2011; Rogovoy and Stolbova 2016). To describe the evolution of the magnetization vector, there are two approaches within the framework of the theory of micromagnetism (Brown 1963). The first approach is to minimize the magnetic energy density functional with additional restrictions on the parameters. In this case, the Euler–Ostrogradsky equation is solved, which corresponds to the minimum of this functional, or this functional is minimized directly. In the second, the Landau–Lifshitz–Gilbert equation is used, and the effective field strength vector is found as a result of applying the Euler–Ostrogradsky operator to the total magnetic energy density functional. In the publication of Rogovoy et al. (2021a), the magnetic energy functional is minimized to describe the evolution of the magnetization and to perform numerical simulation of the motion and interaction of the Neel domain walls under the action of a magnetic field for a Ni_2MnGa single crystal. In another article (Rogovoy et al. 2001b), the Landau–Lifshitz–Gilbert equation was used for the twinned variant of martensite, which is a more complex structure. In this publication, the variational equations corresponding to the Landau–Lifshitz–Gilbert differential equation and the equation for the scalar magnetic potential are written using the standard Galerkin procedure. Due to this, the requirements for the smoothness of the solution are reduced (weakened) in comparison with the original differential equations; therefore, such a formulation of the problem is called weak. The possibilities of approaches described above (minimization of the magnetic energy functional and solution of the Landau–Lifshitz–Gilbert equation) for describing magnetic processes are analyzed, and a conclusion is made about the advantage of utilizing the Landau–Lifshitz–Gilbert equation (Rogovoy and Stolbova 2021).

In a ferromagnetic material, purely magnetic Maxwellian stresses and mass (ponderomotive) purely magnetic forces and moments arise in an external magnetic field. These forces and moments cause in the body, in addition to Maxwell's, the usual elastic stress. It is believed that twinning or detwinning of the martensitic structure in a ferromagnetic material with shape memory occurs when these forces and moments reach critical values, resulting in significant deformations (6–10%). This deformation is not magnetostrictive, which is usually neglected due to its smallness. These critical values are reached when the motion of the walls of the magnetic domains ends (the magnetic domains favorably located to the external field have grown at the expense of the domains less favorably located to it) and the local magnetization vectors begin to turn in a direction favorable for the external magnetic field.

All the above processes occur in a single ferromagnetic alloy crystal with shape memory. But most of the real materials are polycrystalline materials, since they, unlike single crystals, are easier to manufacture. For example, polycrystalline films are used in spintronics, actuator, and sensor applications. But such materials can be not only isotropic but also textured. The structures of polycrystals, which are created from single-twin crystals of Ni–Mn–Ga alloys and correspond to different textures, can be found in many works (see, for example, Casoli et al. 2020; Kumar et al. 2012; Li et al. 2017; Musabirov et al. 2015; Rani et al. 2011). We will use this information when we model the behavior of polycrystalline material based on the behavior of single crystals.

In the present research, which is a continuation of the previous works of the authors (Rogovoy and Stolbova 2022a, b), a mesostructural model of the behavior of the Heusler alloy single-twin crystal with the shape memory in the magnetic field has been constructed to describe the such mentioned above processes, as the motion of the magnetic domain walls, the rotation of the magnetization vectors, and the reorientation (detwinning) of martensitic variants. Using this model, the magnetization curves for both the single-twin crystal and polytwin crystals are constructed and the deformation behavior of these structures has been described.

In this work, the new results of research are (a) using variational equations corresponding to the differential formulation of the problem of magnetization of the Heusler alloys in a magnetic field, (b) the detwinning condition for a ferromagnetic shape-memory alloy under the action of a magnetic field only, (c) the results obtained within the framework of the approach based on the use of variational equations and describing the behavior of a twin variant of martensite of Ni–Mn–Ga alloys in the magnetic field allowing for detwinning process, and (d) magnetization curves in polytwinned crystals consisting of single-twin crystals and deformed states of such structures.

We denote vectors in bold italic font, \mathbf{A} , tensors in bold straight font, \mathbf{A} , the scalar product between tensors and/or vectors as $\mathbf{A} \cdot \mathbf{B}$, the vector product as $\mathbf{A} \times \mathbf{B}$ and the tensor product, for which the notation \otimes is sometimes used, as $\mathbf{A}\mathbf{B}$. When the Hamilton operator $\nabla = \mathbf{r}^i \partial/\partial q^i$ is used, the basis vector of this operator is always in the first place on the left, $\nabla * \mathbf{A} = \mathbf{r}^i * \partial\mathbf{A}/\partial q^i$, where $*$ is scalar, vector, or tensor product, unlike some works in which the action of the Hamilton operator is

represented as $\nabla * \mathbf{A} = \partial \mathbf{A} / \partial q^i * \mathbf{r}^i$. The expression \mathbf{A}^T means the transpose of the second rank tensor \mathbf{A} .

23.2 The Main Relations of Micromagnetism

23.2.1 Differential Equations

According to Brown's work (1963), the magnetization of each cell of the crystal will be described by the spontaneous magnetization vector of constant length \mathbf{M} ($|\mathbf{M}| = M_s$, M_s is the saturation magnetization), oriented along one of the crystallographic directions (the easy magnetization axis) in two opposite directions. The Landau–Lifshitz–Gilbert equation describes the dynamics of this vector in a magnetic field:

$$\frac{\partial \mathbf{m}}{\partial t} = -\gamma(\mathbf{m} \times \mathbf{H}_{eff}) + \alpha \left(\mathbf{m} \times \frac{\partial \mathbf{m}}{\partial t} \right), \quad (23.1)$$

where γ is a gyromagnetic ratio, α is a damping (dissipation) parameter, $\mathbf{m} = \mathbf{M}/M_s$ is unit magnetization vector, \mathbf{H}_{eff} is a strength vector of effective field (external and internal (intrinsic) magnetic fields):

$$\mathbf{H}_{eff} = \mathbf{H}_{ext} + \mathbf{H}_{int} + \mathbf{H}_{exch} + \mathbf{H}_{anis} + \mathbf{H}_{m-el}. \quad (23.2)$$

Here, \mathbf{H}_{ext} is a strength vector of applied external field, \mathbf{H}_{int} is a strength vector of internal demagnetization field caused by an applied external field, \mathbf{H}_{exch} is the exchange field strength vector, \mathbf{H}_{anis} is the anisotropy field strength vector, \mathbf{H}_{m-el} is a strength vector of magneto-elastic field causing magnetostrictive strain, which is very small compared to the phase or structural (detwinning) one, due to which this strain and this magnetic field are usually neglected (Mennerich et al. 2011).

For the effective field \mathbf{H}_{eff} , the following expression takes place (Mennerich et al. 2011):

$$\mathbf{H}_{eff} = -\frac{1}{\mu_0 M_s} \frac{\delta \psi}{\delta \mathbf{m}}, \quad (23.3)$$

in which μ_0 is a magnetic constant. The variational derivative

$$\frac{\delta \psi}{\delta \mathbf{m}} = \frac{\partial \psi}{\partial \mathbf{m}} - \nabla \cdot \frac{\partial \psi}{\partial (\nabla \mathbf{m})} \quad (23.4)$$

is the Euler–Ostrogradsky operator, which gives the differential equation, that minimizes the total magnetic energy functional ψ with respect to variable \mathbf{m} , and the condition

$$\left[\mathbf{m} \times \left(\mathbf{N} \cdot \frac{\partial \psi}{\partial (\nabla \mathbf{m})} \right) \right] \Big|_{\Gamma} = \mathbf{0}, \quad (23.5)$$

where \mathbf{N} is the external unit normal to the body surface Γ in the actual state, is a natural boundary condition for this functional. The total magnetic energy density ψ can be written as (Mennerich et al. 2011)

$$\psi = \psi_{ext} + \psi_{int} + \psi_{exch} + \psi_{anis}.$$

Here, the first two terms are the density of magnetic energy from the action of an applied external magnetic field (Zeeman energy and demagnetization energy), and the last two terms are the density of internal magnetic energy (exchange energy and anisotropy energy):

$$\begin{aligned} \psi_{ext} &= -\mu_0 M_s \mathbf{H}_0 \cdot \mathbf{m}, & \psi_{int} &= -\frac{1}{2} \mu_0 M_s \mathbf{H}_{demag} \cdot \mathbf{m}, \\ \psi_{exch} &= A_{exch} |\nabla \mathbf{m}|^2, & \psi_{anis} &= K_{anis} (1 - (\mathbf{m} \cdot \mathbf{p}^\alpha)^2), \end{aligned} \quad (23.6)$$

where A_{exch} is the exchange constant, K_{anis} is the anisotropy constant, and \mathbf{p}^α is the direction of the easy axis of the variant α (for the case of the existence of several easy axes in the crystal. It is further assumed that there is only one easy axis in the crystal). Thus, it follows from the relations (23.3), (23.4) and (23.6) that (Mennerich et al. 2011)

$$\begin{aligned} \mathbf{H}_{ext} &= \mathbf{H}_0, & \mathbf{H}_{int} &= \mathbf{H}_{demag}, \\ \mathbf{H}_{exch} &= \frac{2A_{exch}}{\mu_0 M_s} \Delta \mathbf{m}, & \mathbf{H}_{anis} &= \frac{2K_{anis}}{\mu_0 M_s} (\mathbf{m} \cdot \mathbf{p}^\alpha) \mathbf{p}^\alpha. \end{aligned} \quad (23.7)$$

The boundary condition (23.5) with account for (23.7) will be written in the form:

$$2A_{exch} [\mathbf{m} \times (\mathbf{N} \cdot \nabla \mathbf{m})] \Big|_\Gamma = \mathbf{0}. \quad (23.8)$$

Since $\mathbf{m} \cdot \mathbf{m} = 1$, then it turns out that the normal derivative $\mathbf{N} \cdot \nabla (\mathbf{m} \cdot \mathbf{m}) = 0$, thereby $(\mathbf{N} \cdot \nabla \mathbf{m}) \cdot \mathbf{m} = 0$, so, the vector $(\mathbf{N} \cdot \nabla \mathbf{m})$ is perpendicular to the vector \mathbf{m} . The equality (23.8) will be true only if at least one of the multipliers is equal to zero. Since $\mathbf{m} \neq \mathbf{0}$, the second vector must be equal to zero, which is the Neumann boundary condition for the vector \mathbf{m} :

$$(\mathbf{N} \cdot \nabla \mathbf{m}) \Big|_\Gamma = \mathbf{0}.$$

The strength of the acting external field and the demagnetization field is determined by the equation $\mathbf{H} = \mathbf{H}_0 + \mathbf{H}_{demag}$. This field in the absence of electric currents should be vortex-free, $\nabla \times \mathbf{H} = \mathbf{0}$, which, at constant \mathbf{H}_0 , reduces to the equality $\nabla \times \mathbf{H}_{demag} = \mathbf{0}$, which will always be executed if we put $\mathbf{H}_{demag} = -\nabla \varphi$, where φ is a scalar depending on the vector coordinate \mathbf{x} . The magnetic field inductance \mathbf{B} , which must satisfy the equation $\nabla \cdot \mathbf{B} = 0$, is introduced by the relation $\mathbf{B}(\mathbf{x}) = \mu_0 (\mathbf{H} + M_s \mathbf{m})$ for $\mathbf{x} \in \Omega^{(in)}$, where $\Omega^{(in)}$ is the region occupied by the body and $\mathbf{B}(\mathbf{x}) = \mu_0 \mathbf{H}$ for $\mathbf{x} \in \Omega^{(ex)}$, where $\Omega^{(ex)}$ is the region occupied

by the medium surrounding the body. Therefore, given the above representations \mathbf{H} , \mathbf{H}_{demag} and the constancy of \mathbf{H}_0 , the Poisson and the Laplace equations for the function φ follow:

$$\nabla \cdot \nabla \varphi = M_s \nabla \cdot \mathbf{m} \quad \forall \mathbf{x} \in \Omega^{(in)}, \quad (23.9)$$

$$\nabla \cdot \nabla \varphi = 0 \quad \forall \mathbf{x} \in \Omega^{(ex)}. \quad (23.10)$$

The natural requirement that φ must obey is

$$\varphi \rightarrow 0 \quad \text{when } \mathbf{x} \rightarrow \infty. \quad (23.11)$$

On the surface Γ separating the body from its environment, the following equality is fulfilled:

$$\varphi^{(in)}|_{\Gamma} = \varphi^{(ex)}|_{\Gamma}, \quad (23.12)$$

wherein the superscript (*in*) corresponds to the body, and superscript (*ex*) denotes its environment.

Additional boundary conditions that the function φ should satisfy are related to the behavior of vectors \mathbf{H} and \mathbf{B} on the surface Γ (Rogovoy et al. 2001b, 2021a):

$$(\nabla \varphi^{(in)} - \nabla \varphi^{(ex)})|_{\Gamma} \cdot \mathcal{T} = 0, \quad (23.13)$$

where \mathcal{T} is the unit tangent vector to the surface of the body Γ in the actual configuration, and

$$(\nabla \varphi^{(in)} - \nabla \varphi^{(ex)})|_{\Gamma} \cdot \mathbf{N} = M_s \mathbf{m} \cdot \mathbf{N}. \quad (23.14)$$

From (23.7) and the representation of \mathbf{H}_{demag} in terms of the scalar potential φ , the effective field (23.2) is written as:

$$\mathbf{H}_{eff} = \mathbf{H}_0 - \nabla \varphi + \frac{2 A_{exch}}{\mu_0 M_s} \Delta \mathbf{m} + \frac{2 K_{anis}}{\mu_0 M_s} (\mathbf{m} \cdot \mathbf{p}^\alpha) \mathbf{p}^\alpha. \quad (23.15)$$

23.2.2 Variational Equations

To describe the distribution of the magnetization vector in the body, it is necessary to solve the differential equation (23.1) with boundary condition (23.8) and differential equations (23.9), (23.10) with boundary conditions (23.11)–(23.14). The strength vector of effective field \mathbf{H}_{eff} in equation (23.1) is determined by the relation (23.15). The relations (23.9), (23.10) require, at least, the existence of a second derivative with respect to the coordinates for the function φ , and the relation (23.15) for the function \mathbf{m} . Using the Galerkin procedure, we realize the so-called weak (variational) formulation of the problem and reduce the requirements for the smoothness of these functions. The obtained variational equations are solved by the finite element method.

According to the Galerkin procedure, the equations (23.1), (23.9), (23.10) and boundary conditions (23.8), (23.14) are first reduced to one or another homogeneous form: that is, the right part of the equation is transferred to the left part, or vice versa. Therefore, homogeneous equations can differ in sign and it is convenient to use this to significantly simplify the final expression. According to the Galerkin procedure, the equations acting on the volume of the body and the equations acting on the surface (boundary conditions) are processed separately. Since the areas in which these equations operate do not intersect, the equations obtained in accordance with the Galerkin procedure can be added (or subtracted) and each of them can have both a plus sign and a minus sign. As a result, we get

$$\int_{\Omega^{(in)}} \left[\frac{\partial \mathbf{m}}{\partial t} + \gamma (\mathbf{m} \times \mathbf{H}_{eff}) - \alpha \left(\mathbf{m} \times \frac{\partial \mathbf{m}}{\partial t} \right) \right] \cdot \delta \mathbf{m} d\Omega^{(in)} \pm \beta \int_{\Gamma} [\mathbf{m} \times (\mathbf{n} \cdot \nabla \mathbf{m})] \cdot \delta \mathbf{m} d\Gamma = 0, \tag{23.16}$$

where β is a constant coefficient, the value of which we define below, and

$$\int_{\Omega^{(in)}} (\nabla \cdot \nabla \varphi - M_s \nabla \cdot \mathbf{m}) \delta \varphi d\Omega^{(in)} + \int_{\Omega^{(ex)}} (\nabla \cdot \nabla \varphi) \delta \varphi d\Omega^{(ex)} \pm \int_{\Gamma} \mathbf{n} \cdot (\nabla \varphi^{(in)} - \nabla \varphi^{(ex)} - M_s \mathbf{m}) \delta \varphi d\Gamma = 0. \tag{23.17}$$

Here, $\delta \mathbf{m}$ and $\delta \varphi$ are arbitrary changes of the vector \mathbf{m} and of the scalar φ , that is their variations.

The first two integrals of the equation (23.17) include the second derivatives of φ with respect to the coordinates, which requires using at least the quadratic approximation for these quantities under the numerical solution. Using the easily proved equality $\nabla \cdot (A \mathbf{b}) = \mathbf{b} \cdot (\nabla A) + A (\nabla \cdot \mathbf{b})$, where A and \mathbf{b} are arbitrary scalar and vector, this requirement can be significantly weakened and the so-called weak formulation of the problem can be implemented. Rewriting this equality in the form $A (\nabla \cdot \mathbf{b}) = \nabla \cdot (A \mathbf{b}) - \mathbf{b} \cdot (\nabla A)$, accepting $A = \delta \varphi$, $\mathbf{b} = \nabla \varphi$ or $\mathbf{b} = M_s \mathbf{m}$ and applying the Ostrogradsky–Gauss theorem, we will convert the first line in (23.17), which we denote {1}, to the form

$$\begin{aligned}
\{1\} = & \int_{\Gamma} \mathbf{n}^{(in)} \cdot [(\nabla\varphi^{(in)} - M_s \mathbf{m}) \delta\varphi^{(in)}] d\Gamma + \\
& + \int_{\Gamma} \mathbf{n}^{(ex)} \cdot [(\nabla\varphi^{(ex)}) \delta\varphi^{(ex)}] d\Gamma + \int_{\Gamma_{\infty}} \mathbf{n}^{(\infty)} \cdot [(\nabla\varphi^{(\infty)}) \delta\varphi^{(\infty)}] d\Gamma_{\infty} - \\
& - \int_{\Omega^{(in)}} (\nabla\varphi - M_s \mathbf{m}) \cdot \nabla\delta\varphi d\Omega^{(in)} - \int_{\Omega^{(ex)}} \nabla\varphi \cdot \nabla\delta\varphi d\Omega^{(ex)}.
\end{aligned}$$

Taking into account that $\mathbf{n}^{(in)} = \mathbf{n}$, $\mathbf{n}^{(ex)} = -\mathbf{n}$, $\varphi \rightarrow 0$ when $\mathbf{x} \rightarrow \infty$ (see (23.11)) and $\varphi^{(in)}|_{\Gamma} = \varphi^{(ex)}|_{\Gamma}$ (see (23.12)), we transform the first two lines on the right side of this equality by combining integrals over the Γ surface, and then the expression $\{1\}$ is presented as

$$\begin{aligned}
& \int_{\Gamma} \mathbf{n} \cdot [(\nabla\varphi^{(in)} - \nabla\varphi^{(ex)} - M_s \mathbf{m}) \delta\varphi] d\Gamma - \\
& - \int_{\Omega^{(in)}} (\nabla\varphi - M_s \mathbf{m}) \cdot \nabla\delta\varphi d\Omega^{(in)} - \int_{\Omega^{(ex)}} \nabla\varphi \cdot \nabla\delta\varphi d\Omega^{(ex)}.
\end{aligned}$$

Taking the “minus” sign in the last integral of the equation (23.17), we obtain as a result the following weak form of the variational equation (23.17), which includes only the first derivatives from φ with respect to the coordinates:

$$\int_{\Omega^{(in)}} (\nabla\varphi - M_s \mathbf{m}) \cdot \nabla\delta\varphi d\Omega^{(in)} + \int_{\Omega^{(ex)}} \nabla\varphi \cdot \nabla\delta\varphi d\Omega^{(ex)} = 0. \quad (23.18)$$

Let's return now to the equation (23.16). From the equality $\mathbf{m} \cdot \mathbf{m} = 1$, it follows that $\delta(\mathbf{m} \cdot \mathbf{m}) = 2\mathbf{m} \cdot \delta\mathbf{m} = 0$, that is, the vectors $\delta\mathbf{m}$ and \mathbf{m} are mutually orthogonal, $\delta\mathbf{m} \perp \mathbf{m}$. This requirement can be satisfied by putting $\delta\mathbf{m} = \mathbf{m} \times \delta\xi$, where $\delta\xi$ are any trial vector-functions that do not coincide in direction with \mathbf{m} . As a result, we get

$$\begin{aligned}
& \int_{\Omega^{(in)}} \left[\frac{\partial\mathbf{m}}{\partial t} + \gamma(\mathbf{m} \times \mathbf{H}_{eff}) - \alpha\left(\mathbf{m} \times \frac{\partial\mathbf{m}}{\partial t}\right) \right] \cdot (\mathbf{m} \times \delta\xi) d\Omega^{(in)} \pm \\
& \pm \beta \int_{\Gamma} [\mathbf{m} \times (\mathbf{n} \cdot \nabla\mathbf{m})] \cdot (\mathbf{m} \times \delta\xi) d\Gamma = 0.
\end{aligned}$$

Using now the known properties of the mixed product of vectors and the scalar product of two vector products of vectors, choosing the functions $\delta\xi$ satisfying the condition $\delta\xi \perp \mathbf{m}$, from which the equality $\mathbf{m} \cdot \delta\xi = 0$ will follow, and given that $\mathbf{m} \cdot \mathbf{m} = 1$, we reduce this equation to the form

$$\int_{\Omega^{(in)}} \left[\left(\mathbf{m} \times \frac{\partial \mathbf{m}}{\partial t} \right) - \gamma \mathbf{H}_{eff} + \alpha \frac{\partial \mathbf{m}}{\partial t} \right] \cdot \delta \boldsymbol{\xi} d\Omega^{(in)} \mp \beta \int_{\Gamma} (\mathbf{n} \cdot \nabla \mathbf{m}) \cdot \delta \boldsymbol{\xi} d\Gamma = 0.$$

Substituting here the expression for the effective field (23.15), we will have

$$\int_{\Omega^{(in)}} \left[\left(\mathbf{m} \times \frac{\partial \mathbf{m}}{\partial t} \right) - \gamma \left(\mathbf{H}_0 - \nabla \varphi + \frac{2A_{exch}}{\mu_0 M_s} \Delta \mathbf{m} + \frac{2K_{anis}}{\mu_0 M_s} (\mathbf{m} \cdot \mathbf{p}^\alpha) \mathbf{p}^\alpha \right) + \alpha \frac{\partial \mathbf{m}}{\partial t} \right] \cdot \delta \boldsymbol{\xi} d\Omega^{(in)} \mp \beta \int_{\Gamma} (\mathbf{n} \cdot \nabla \mathbf{m}) \cdot \delta \boldsymbol{\xi} d\Gamma = 0. \quad (23.19)$$

Here, the integrand contains the quantity $\Delta \mathbf{m}$, which includes second derivatives with respect to the coordinates, that requires the usage of at least the quadratic approximation for this quantity under the numerical solution. Using the well-known equality $\nabla \cdot (\mathbf{A} \cdot \mathbf{b}) = (\nabla \cdot \mathbf{A}) \cdot \mathbf{b} + \mathbf{A}^T \cdot \nabla \mathbf{b}$, where \mathbf{A} and \mathbf{b} are an arbitrary tensor of the second rank and a vector, from which it follows that $(\nabla \cdot \mathbf{A}) \cdot \mathbf{b} = \nabla \cdot (\mathbf{A} \cdot \mathbf{b}) - \mathbf{A}^T \cdot \nabla \mathbf{b}$, assuming that $\mathbf{A} = \nabla \mathbf{m}$, $\mathbf{b} = \delta \boldsymbol{\xi}$ and applying the Ostrogradsky–Gauss theorem, we obtain

$$\begin{aligned} \int_{\Omega^{(in)}} (\nabla \cdot \nabla \mathbf{m}) \cdot \delta \boldsymbol{\xi} d\Omega^{(in)} &= \int_{\Omega^{(in)}} \left[\nabla \cdot (\nabla \mathbf{m} \cdot \delta \boldsymbol{\xi}) - (\nabla \mathbf{m})^T \cdot \nabla \delta \boldsymbol{\xi} \right] d\Omega^{(in)} = \\ &= \int_{\Gamma} (\mathbf{n} \cdot \nabla \mathbf{m}) \cdot \delta \boldsymbol{\xi} d\Gamma - \int_{\Omega^{(in)}} (\nabla \mathbf{m})^T \cdot \nabla \delta \boldsymbol{\xi} d\Omega^{(in)}. \end{aligned}$$

Taking the “plus” sign in the last integral of the equation (23.19) and assuming $\beta = (2\gamma A_{exch})/(\mu_0 M_s)$, we get

$$\begin{aligned} \int_{\Omega^{(in)}} \left[\left(\mathbf{m} \times \frac{\partial \mathbf{m}}{\partial t} \right) - \gamma \left(\mathbf{H}_0 - \nabla \varphi + \frac{2K_{anis}}{\mu_0 M_s} (\mathbf{m} \cdot \mathbf{p}^\alpha) \mathbf{p}^\alpha \right) + \alpha \frac{\partial \mathbf{m}}{\partial t} \right] \cdot \delta \boldsymbol{\xi} d\Omega^{(in)} + \\ + \frac{2\gamma A_{exch}}{\mu_0 M_s} \int_{\Omega^{(in)}} (\nabla \mathbf{m})^T \cdot \nabla \delta \boldsymbol{\xi} d\Omega^{(in)} = 0. \end{aligned}$$

When solving this variational equation, we will use the θ -scheme. To do this, let us represent $\mathbf{m}(t)$ at the current time t , as $\mathbf{m}_* + \theta \tau \mathbf{v}$, where $\mathbf{m}_* = \mathbf{m}(t_*)$ is the magnetization at the previous time moment t_* , $\tau = t - t_*$ is the time step, $\theta \in [0, 1]$, $\mathbf{v} = \partial \mathbf{m} / \partial t$. As a result, keeping only the linear terms relative to τ , we come to the equation

$$\begin{aligned}
& \int_{\Omega^{(in)}} (\mathbf{m}_* \times \mathbf{v} + \alpha \mathbf{v}) \cdot \delta \boldsymbol{\xi} d\Omega^{(in)} - \\
& - \gamma \int_{\Omega^{(in)}} \left(\mathbf{H}_0 - \nabla \varphi + \frac{2 K_{anis}}{\mu_0 M_s} [(\mathbf{m}_* + \theta \tau \mathbf{v}) \cdot \mathbf{p}^\alpha] \mathbf{p}^\alpha \right) \cdot \delta \boldsymbol{\xi} d\Omega^{(in)} + \\
& + \frac{2 \gamma A_{exch}}{\mu_0 M_s} \int_{\Omega^{(in)}} [(\nabla \mathbf{m})_*^T + \theta \tau (\nabla \mathbf{v})^T] \cdot \nabla \delta \boldsymbol{\xi} d\Omega^{(in)} = 0.
\end{aligned} \tag{23.20}$$

From the condition $\mathbf{m}(t) \cdot \mathbf{m}(t) = 1 \forall t$, it follows that $\mathbf{m}_* \cdot \mathbf{v} = 0$ and $\delta(\mathbf{m}_* \cdot \mathbf{v}) = \mathbf{m}_* \cdot \delta \mathbf{v} = 0$. Then, given that $\mathbf{m}_* \cdot \delta \boldsymbol{\xi} = 0$, we take as $\delta \boldsymbol{\xi}$ the quantity $\delta \mathbf{v}$, $\delta \boldsymbol{\xi} = \delta \mathbf{v}$. To meet the conditions $\mathbf{m}_* \cdot \mathbf{v} = 0$ and $\mathbf{m}_* \cdot \delta \mathbf{v} = 0$, we will use the Lagrange multiplier method. As a result, the equation (23.20) is presented in the following final form:

$$\begin{aligned}
& \int_{\Omega^{(in)}} (\mathbf{m}_* \times \mathbf{v} + \alpha \mathbf{v} + \lambda \mathbf{m}_*) \cdot \delta \mathbf{v} d\Omega^{(in)} - \\
& - \gamma \int_{\Omega^{(in)}} \left(\mathbf{H}_0 - \nabla \varphi + \frac{2 K_{anis}}{\mu_0 M_s} [(\mathbf{m}_* + \theta \tau \mathbf{v}) \cdot \mathbf{p}^\alpha] \mathbf{p}^\alpha \right) \cdot \delta \mathbf{v} d\Omega^{(in)} + \\
& + \frac{2 \gamma A_{exch}}{\mu_0 M_s} \int_{\Omega^{(in)}} [(\nabla \mathbf{m})_*^T + \theta \tau (\nabla \mathbf{v})^T] \cdot \nabla \delta \mathbf{v} d\Omega^{(in)} + \int_{\Omega^{(in)}} (\mathbf{m}_* \cdot \mathbf{v}) \delta \lambda d\Omega^{(in)} = 0,
\end{aligned} \tag{23.21}$$

where λ is the Lagrange multiplier.

The constructed related variational equations (23.18) and (23.21) allow us to determine φ , \mathbf{v} and λ . The external magnetic field is applied in accordance with the step-by-step procedure, and at each such step, the variational equations are solved. These equations describe the change in the magnetic field over time within each increment of the external field and use other, internal time steps. At the internal current step, the value \mathbf{m}_* is taken from the previous internal step.

After finding \mathbf{v} at the current step, in order to reduce the computational error, the vector \mathbf{m} is corrected so that its length remains unit:

$$\mathbf{m} = \frac{\mathbf{m}_* + \tau \mathbf{v}}{|\mathbf{m}_* + \tau \mathbf{v}|}.$$

Given that $|\mathbf{m}| = 1$, the process in internal steps is over when the condition $|\mathbf{m} - \mathbf{m}_*| < 10^{-3}$ is fulfilled. This happens in about 3000 internal steps.

At the first stage, in the absence of an external magnetic field, the initial magnetization distribution \mathbf{m} is set and, solving variational equations, the initial boundaries of the magnetic domains and distribution of the magnetization vectors in them are

determined. The resulting magnetic structure is the initial one for the subsequent application of an external magnetic field.

The stability of the numerical solution is provided by the choice of the parameter θ : if $\theta > 0.5$, the scheme will be stable for any steps in time and space.

23.3 Detwinning Process

23.3.1 Twin Structure

This section is devoted to a brief explanation of the detwinning process that occurs during the reorientation of martensitic variants that form a twin. A detailed consideration of this process can be found in another publication of the authors of this article (Rogovoy and Stolbova 2022b).

The symmetry of the crystal is characterized by the orthogonal tensors proper¹ \mathbf{R}_α forming a group of rotations \mathcal{P} , $\mathbf{R}_\alpha \in \mathcal{P}$, in which the shape of the crystal remains unchanged: a cube is transformed into a cube, a parallelepiped into the same parallelepiped, and so on. During the first-order phase transition, the cubic cell of austenite (high-temperature state) of the Ni_2MnGa shape-memory alloy transforms into a tetragonal martensite cell (low-temperature state). The rotation group for a cell in the austenitic state \mathcal{P}_a (for a cubic cell) consists of 24 orthogonal tensors, $\mathcal{V}_{\mathcal{P}_a} = 24$. The rotation group for a cell in the martensitic state \mathcal{P}_m (for a tetragonal cell) consists of eight orthogonal tensors, $\mathcal{V}_{\mathcal{P}_m} = 8$ (orthogonal tensors matching to these states are given, for example, in the work of Hane and Shield 1998). The number of independent variants of martensite that can form during a phase transition is given by $\mathcal{V} = \mathcal{V}_{\mathcal{P}_a} / \mathcal{V}_{\mathcal{P}_m}$, which is 3 for Ni_2MnGa .

The Bain strain tensor \mathbf{U}_i (the symmetric positive definite tensor of the pure strain in the polar decomposition of the deformation gradient $\mathbf{F}_i = \mathbf{R}_i \cdot \mathbf{U}_i$, where \mathbf{R}_i is the proper orthogonal tensor) describes the transformation of an austenitic crystal cell into a martensitic one. The cubic austenite cell in the Ni_2MnGa shape-memory alloy transforms into any of the three tetragonal martensite cells whose pure strain tensors \mathbf{U}_i , $i = 1, 2, 3$, have the following form in the orthonormal basis \mathbf{e}_k , $k = 1, 2, 3$, with vectors parallel to the edges of the cubic cell (Bhattacharya 1991; Hane and Shield 1998)

$$\begin{aligned} \mathbf{U}_1 &= \beta \mathbf{e}_1 \mathbf{e}_1 + \alpha (\mathbf{e}_2 \mathbf{e}_2 + \mathbf{e}_3 \mathbf{e}_3), & \mathbf{U}_2 &= \alpha (\mathbf{e}_1 \mathbf{e}_1 + \mathbf{e}_3 \mathbf{e}_3) + \beta \mathbf{e}_2 \mathbf{e}_2, \\ \mathbf{U}_3 &= \alpha (\mathbf{e}_1 \mathbf{e}_1 + \mathbf{e}_2 \mathbf{e}_2) + \beta \mathbf{e}_3 \mathbf{e}_3. \end{aligned} \quad (23.22)$$

¹ The tensor \mathbf{Q} for which $\mathbf{Q}^T = \mathbf{Q}^{-1}$ is called the orthogonal tensor. This tensor, when scalar multiplied by some vector, rotates it in space without changing its modulus. When acting on two vectors, this tensor also preserves the angle between them as they rotate in space. The determinant of the orthogonal tensor is ± 1 . The determinant of the orthogonal tensor proper is $+1$.

On the plane separating the two variants of martensite with the Bain strain tensors \mathbf{U}_i and \mathbf{U}_j , the Hadamard compatibility condition (Truesdell 1972) for deformation gradients \mathbf{F}_i and \mathbf{F}_j must be fulfilled, which in our case takes the form (Hane and Shield 1998)

$$\mathbf{F}_i - \mathbf{F}_j = \mathbf{a} \mathbf{n}. \quad (23.23)$$

Here, $\mathbf{F}_k = (\nabla \mathbf{R}_k)^T$, where ∇ is the Hamilton operator with respect to the initial configuration and \mathbf{R}_k is the radius-vector of the position of the point k in the actual configuration, \mathbf{n} is the unit vector of the normal to the surface separating the martensite variants in the initial, undeformed state, $\mathbf{a} = (\mathbf{F}_i - \mathbf{F}_j) \cdot \mathbf{n}$ is the projection onto the normal of the jump of the deformation gradient when passing through the separating surface.

The Hadamard condition is a consequence of the following reasoning. Let the surface S be a part of the inner surface of the body dividing it into volumes (denote them V_+ and V_-), in each of which the vector \mathbf{a} is continuous and differentiable along any path lying on S . Then there are continuous derivatives having in our notation the form (see the end of the Introduction) $d\mathbf{a}_+ = (\nabla \mathbf{a})_+^T \cdot d\mathbf{l}$ and $d\mathbf{a}_- = (\nabla \mathbf{a})_-^T \cdot d\mathbf{l}$, which characterize the changes of the vector \mathbf{a} in the direction of any vector \mathbf{l} lying on S under tending to the surface S from the side of the volumes V_+ and V_- . Subtracting one from the other, we get the Hadamard compatibility condition: $[d\mathbf{a}] = [\nabla \mathbf{a}]^T \cdot d\mathbf{l}$, where $[d\mathbf{a}] = d\mathbf{a}_+ - d\mathbf{a}_-$ and $[\nabla \mathbf{a}]^T = (\nabla \mathbf{a})_+^T - (\nabla \mathbf{a})_-^T$. If the vector \mathbf{a} is continuous in the body including the surface S , then $[d\mathbf{a}] = \mathbf{0}$ from which it follows that $[\nabla \mathbf{a}]^T \cdot d\mathbf{l} = \mathbf{0}$, and, as a result, the second-rank tensor $[\nabla \mathbf{a}]^T$ should have a dyadic representation in the form $[\nabla \mathbf{a}]^T = \mathbf{b} \mathbf{n}$, where \mathbf{n} is the normal to the surface S , which can be considered as unit, and \mathbf{b} is some vector that determines the projection of $[\nabla \mathbf{a}]^T$ on the normal, as it follows from the condition $[\nabla \mathbf{a}]^T \cdot \mathbf{n} = \mathbf{b} \mathbf{n} \cdot \mathbf{n} = \mathbf{b}$.

Rewriting (23.23) in the form $\mathbf{R}_i \cdot \mathbf{U}_i - \mathbf{R}_j \cdot \mathbf{U}_j = \mathbf{a} \mathbf{n}$, carrying out a scalar multiplication of this expression on the left by \mathbf{R}_j^T and introducing a vector $\hat{\mathbf{a}} = \mathbf{R}_j^T \cdot \mathbf{a}$, we get

$$\mathbf{R}_{ij} \cdot \mathbf{U}_i - \mathbf{U}_j = \hat{\mathbf{a}} \mathbf{n}, \quad (23.24)$$

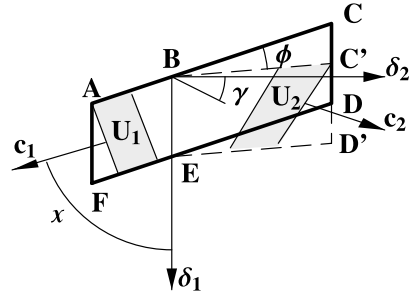
where $\mathbf{R}_{ij} = \mathbf{R}_j^T \cdot \mathbf{R}_i$. Representing (23.24) as

$$\mathbf{R}_{ij} \cdot \mathbf{U}_i = (\mathbf{g} + \hat{\mathbf{a}} \mathbf{n} \cdot \mathbf{U}_j^{-1}) \cdot \mathbf{U}_j, \quad (23.25)$$

where \mathbf{g} is the unit tensor, we conclude that $\det(\mathbf{g} + \hat{\mathbf{a}} \mathbf{n} \cdot \mathbf{U}_j^{-1}) = 1$, since the determinant of the product is equal to the product of the determinants, $\det \mathbf{R}_{ij} = 1$ and $\det \mathbf{U}_i = \det \mathbf{U}_j$ for the expressions (23.22). It follows from here that the tensor $\mathbf{g} + \hat{\mathbf{a}} \mathbf{n} \cdot \mathbf{U}_j^{-1}$ describes processes without changing the volume, namely, a simple shift, and this will be shown below. Following Hane and Shield (1998), Bhattacharya (1991), we will represent (23.25) in the form:

$$\mathbf{R}_{ij} \cdot \mathbf{U}_i = (\mathbf{g} + s \tilde{\mathbf{a}} \mathbf{N}) \cdot \mathbf{U}_j, \quad (23.26)$$

Fig. 23.1 The process of twin formation



where $s = |\hat{\mathbf{a}}| |\mathbf{U}_j^{-1} \cdot \mathbf{n}|$ is the magnitude of the shift, $\tilde{\mathbf{a}} = \hat{\mathbf{a}} / |\hat{\mathbf{a}}|$ is the direction of the shift and $\mathbf{N} = (\mathbf{U}_j^{-1} \cdot \mathbf{n}) / |\mathbf{U}_j^{-1} \cdot \mathbf{n}|$. The symmetry of the tensor \mathbf{U}_j^{-1} is taken into account here: $\mathbf{U}_j^{-1} \cdot \mathbf{n} = \mathbf{n} \cdot \mathbf{U}_j^{-1}$.

The relation (23.26) can be written as

$$\mathbf{R}_{ij} \cdot \mathbf{U}_i = \mathbf{f} \cdot \mathbf{U}_j, \quad \mathbf{f} = \mathbf{g} + s \delta_1 \delta_2, \quad (23.27)$$

where \mathbf{f} is the deformation gradient describing the process of simple shift (not to be confused with a pure shift) by an amount s (by an angle γ , $s = \tan \gamma$) in the plane with unit normal δ_2 in direction of the unit vector δ_1 . The fulfillment of this condition leads to the fact that the axes of the plates of two variants of martensite with the Bain strain, for example, \mathbf{U}_1 and \mathbf{U}_2 are located at a certain angle to each other, forming a twin, and such a structure for material under consideration can be obtained by a simple shift of part of one of the martensite plate in the direction of the δ_1 axis, as shown in Fig. 23.1.

Here, according to the Hadamard compatibility condition, a plate $ABCDEF$ with an axis \mathbf{c}_1 coinciding with the short axis of a tetragonal martensite cell with a Bain strain \mathbf{U}_1 , turns into a twin $ABC'D'EF$ by shifting of any cross section of part $BCDE$ of plate $ABCDEF$, parallel to the plane to which the vector δ_2 is normal, in the direction of the vector δ_1 , proportional to the distance of this cross section from the cross section of BE , and transformation of the part $BCDE$ into the part $BC'D'E$ shown in Fig. 23.1 by the dashed line.² This corresponds to a simple shift in the direction of the vector δ_1 relative to the vector δ_2 by an angle γ or the rotation of the plane BC (ED) by the angle ϕ to the position BC' (ED'). The angle χ here is the angle between vectors \mathbf{c}_1 and δ_1 . Again, in accordance with the Hadamard compatibility condition, tetragonal martensite cell in a plate $BC'D'E$ with a Bain strain \mathbf{U}_2 has a short axis \mathbf{c}_2 which is directed at a certain angle ψ to the vector \mathbf{c}_1 . This vector does not coincide with the axis of the plate $BC'D'E$, and the angle ψ is not, in general, 90° . So, for the ferromagnetic shape-memory alloy, it is necessary

² The tetragonal martensite cells are shown in Fig. 23.1 as the gray areas. Each tetragonal cell has two identical edges $a = b$ and one short edge, which is denoted as c . For this reason, the unit normal to the largest plane of the tetragonal cell is denoted as \mathbf{c} and this vector coincides with the vector of easy magnetization \mathbf{p} in the last relation (23.6).

to clearly distinguish the directions of the main axes of plates forming a twin and of the short axes of the tetragonal martensite cells with the Bain strains \mathbf{U}_i . These tetragonal martensite cells are formed in each of two structural elements that make up the twin (Planes et al. 2009) and the vectors of local spontaneous magnetization \mathbf{M} of the cells in a ferromagnetic material are directed along or against the short axes of the tetragonal martensite cells \mathbf{c}_i . Regions that include interconnected variants of martensite with the same direction of the magnetization vector form magnetic domains. In the martensitic state, many magnetic domains are formed with different directions of the magnetization vectors, while it is energetically favorable for these domains to coordinate with each other in such a way that the total magnetization of the material in the absence of an external magnetic field is zero. When a magnetic field is applied, the walls of magnetic domains begin to move, magnetization vectors rotate, and reorientation (detwinning) of the martensitic variants begins.

For Ni_2MnGa , the parameters of cubic and tetragonal cells are known (Lee et al. 2004; Velikohatny and Naumov 1999): a cubic cell has equal length of all edges $a = 0.5852$ nm, and for a tetragonal cell, the length of edges is $a = b = 0.5920$ nm, $c = 0.5566$ nm, $c/a = 0.94$. As a result, in the Bain tensors, $\alpha = 0.5920/0.5852 = 1.01162$, $\beta = 0.5566/0.5852 = 0.951128$. For these parameters, it was obtained (see Rogovoy and Stolbova, 2022 b) that $\chi = 46.8^\circ$, $\gamma \approx 7^\circ$, $\phi \approx 4^\circ$ and a deformation gradient which describes a simple shift and in the basis δ_1 , δ_2 , shown in Fig. 23.1, has a view $\mathbf{f} = \mathbf{g} + s \delta_1 \delta_2$ (see (23.27)), where $s = \tan \gamma = 0.123398$ from which it follows that $\gamma \approx 7^\circ$, in the basis \mathbf{e}_1 , \mathbf{e}_2 , coinciding with the vectors \mathbf{c}_1 , \mathbf{c}_2 , takes the following concrete form

$$\mathbf{f} = \mathbf{g} - 0.061582 (\mathbf{e}_1 \mathbf{e}_1 - \mathbf{e}_2 \mathbf{e}_2) + 0.057899 \mathbf{e}_1 \mathbf{e}_2 - 0.065498 \mathbf{e}_2 \mathbf{e}_1 \quad (23.28)$$

(regarding the relations between the basis vectors δ_1 , δ_2 and \mathbf{e}_1 , \mathbf{e}_2 see the right part of Fig. 23.2). For our material, the short axes \mathbf{c} of two tetragonal martensite cells forming a twin, which are also the axes of easy magnetization, are located at an angle 90° to each other, $\psi = 90^\circ$ and this is in a full accordance with the experimental results (Ge et al. 2004, 2005; Musabirov et al. 2012).³ Then, in the basis \mathbf{e}_k , in which the expressions (23.22) are presented, vectors \mathbf{c}_1 and \mathbf{c}_2 in Fig. 23.1 coincide with the vectors \mathbf{e}_1 and \mathbf{e}_2 respectively (at \mathbf{U}_1 short axis is directed along the vector \mathbf{e}_1 and at \mathbf{U}_2 along the vector \mathbf{e}_2) and this basis is convenient to use in describing the twin structure from material under consideration. The axis of the cell relative to which twinning occurs (here it is a tetragonal cell with deformation \mathbf{U}_1) is parallel to the boundary of the twin, and the axis of the other cell is not parallel.

³ Mennerich et al. (2011) indicated that the short axes of two tetragonal martensite cells forming a twin in the Ni_2MnGa alloy are at an angle of 86.5° to each other and reference is made to the experimental work of Solomon et al. (2005). But in the specified publication the $\text{Ni}_{51}\text{Mn}_{29}\text{Ga}_{20}$ alloy is considered. We assume that the difference in angles is due to this.

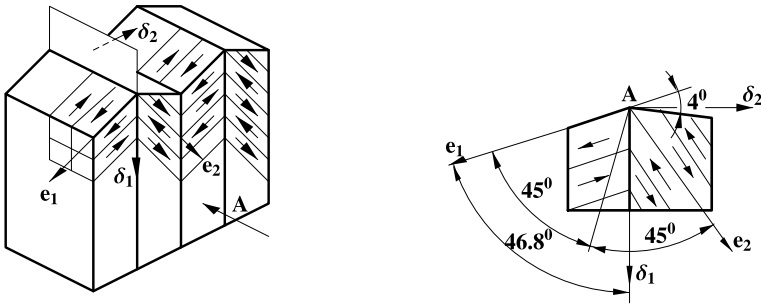


Fig. 23.2 The twin structure, spatial direction of the basis, and magnetization vectors in magnetic domains of tetragonal cells (at the left); the view in the direction of the arrow A (at the right)

Figure 23.2 shows a general view of twinned structure (“herringbone” structure) and presents the spatial direction of the vectors e_1 , e_2 , δ_1 and δ_2 and the magnetization vectors in the tetragonal magnetic domains located in structural elements forming a twin.

23.3.2 Detwinning Condition

Since in our case the twinning was produced by a simple shift, then the detwinning must also be produced by a shift. Detwinning will occur when the tangential force on the surface separating the martensitic variants reaches a certain value, which can be obtained from the experiment. As it was shown in the work of Rogovoy and Stolbova (2022b), to find this force it is necessary to solve a boundary value problem for the case of anisotropic moment theory of elasticity. If detwinning occurs under the simultaneous application of external forces and a magnetic field, then solving such a problem is the only way to describe the detwinning process. However, when only a magnetic field is applied, there is an easier way to simulate the detwinning process based on the calculation of the mass magnetic moment. This subsection is devoted to the description of such approach.

All variants of martensite have magnetic domains, the magnetization vectors that are directed along or against the short axes c , and this leads to zero overall magnetization of the entire structural element when there is no external magnetic field. If a magnetic field is applied and gradually increased, the following processes are realized. At the first stage, the walls of the magnetic domains move: the most favorably oriented domains in the direction of the applied external field increase due to the less favorably oriented domains. After that, the magnetization vectors in the domains try to rotate along the applied field. Besides the magnetic field induces mass (ponderomotive) forces $F_{mag} = \mu_0 \mathbf{M} \cdot \nabla \mathbf{H}$ and mass moments $L_{mag} = \mu_0 \mathbf{M} \times \mathbf{H}$, which act in the body volume. Since $\mu_0 \mathbf{H} = \mathbf{B} - \mu_0 \mathbf{M}$ (see Sect. 23.2) and $\mathbf{M} \times \mathbf{M} = \mathbf{0}$, then the last expression for the mass moments is

represented as $\mathbf{L}_{mag} = \mathbf{M} \times \mathbf{B}$. It should be noted that the magnetic field also induces forces $\mathbf{f}_{mag} = (1/2) \mu_0 M_N^2 \mathbf{N}$, $M_N = \mathbf{M} \cdot \mathbf{N}$, which are distributed over the actual body surface but this field does not produce magnetic moments \mathbf{l}_{mag} distributed over this surface, $\mathbf{l}_{mag} = \mathbf{0}$. These forces and moments create a stressed state in the material, and when this state and the corresponding magnetic forces and moments (if there are no forces and moments of a different physical nature) reach a certain critical value at any point of the material, the process of the twinned structure disappearance (detwinning process) takes place in this point, in addition to the two mentioned above the processes.

In our work, only purely magnetic processes are considered, it is assumed that $V^{(in)}$ coincides with all space, $V^{(ex)} = 0$, and the boundary condition is replaced by periodic ones. Therefore, only mass (ponderomotive) forces \mathbf{F}_{mag} and mass moments \mathbf{L}_{mag} act in the medium. There are no surface forces and moments.

The process of detwinning, in which the boundary between two differently oriented adjacent variants of martensite forming a twin, begins to move, has been experimentally studied for Ni–Mn–Ga alloys close to stoichiometric Ni₂MnGa by Heczko et al. (2001), Heczko and Straka (2003), Heczko (2005), Heczko and Bradshaw (2017). Cooling to the temperature of the austenite–martensite transformation in the absence of a magnetic and force field caused a shift in the (110) plane of the initial cubic austenite structure, and this led to the formation of twin structures. In this state, single-crystal prismatic samples were cut along the {100} planes. Thus, the directions [100], [010] and [001] in the martensitic variants that form the twin are easy magnetization axes \mathbf{c} and are parallel to the sides of the sample. A magnetic field was applied along one of these short axes and the magnetization along this axis of some Ni–Mn–Ga alloys close to stoichiometric Ni₂MnGa was measured, thus magnetization curves were plotted for these experiments. At the magnetic field $\mu_0 |\mathbf{H}_0| = 0.3 \div 0.5$ T a sharp jump in the magnetization is observed on these curves. Such a jump is explained by the reorientation of the martensitic variants that form the twin, or, in other words, by detwinning process. Similar experiments were carried out for shape-memory magnetic films of the same material, and magnetization curves were plotted (Thomas et al. 2009).

Under the action of only a magnetic field and the absence of forces and moments of a different physical nature, we believe that detwinning occurs when the mass magnetic moment reaches a certain value (found from the experiment) in the elements of the twin. It is convenient to consider this process in the short axes \mathbf{c}_i , $i = 1, 2$ of tetragonal martensitic cells forming these plates which are the axes of easy magnetization (the vectors of local spontaneous magnetization \mathbf{M} are directed along or against them in the absence of an external magnetic field) and coincide, as shown above, with the vectors of orthonormal basis \mathbf{e}_i , $i = 1, 2$.

Twins of the same shape can be formed in two ways. In the first of them, the structure arises from element 1 – 2 – 3' (see Fig. 23.3 on the left) by shifting its part 2 – 3' in the direction of the vector δ_1 to the position 2 – 3. This process was discussed in the previous subsection where, for specific parameters of cubic and tetragonal cells for Ni₂MnGa, connections are established between the quantities present in the Hadamard compatibility equation.

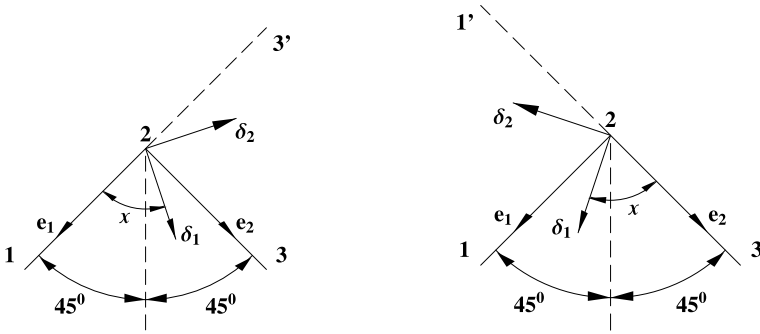


Fig. 23.3 The formation of twin, $\chi = 46.8^\circ$

As a result, the deformation gradient describing the kinematics of the process is constructed both for basis δ_i , $i = 1, 2$, in which it is convenient to represent the deformation of a simple shear, and for basis e_i , $i = 1, 2$, which coincides with both the axes of magnetic anisotropy of the material and the axes of easy magnetization. This gradient in the basis δ_i , shown in Fig. 23.3 on the left or in the right Fig. 23.2, is represented, as we know, by the expression $\mathbf{f} = \mathbf{g} + s \delta_1 \delta_2$, where s is the magnitude of the shift. As it follows from these figures,

$$\delta_1 = e_1 \cos \chi + e_2 \sin \chi, \quad \delta_2 = -e_1 \sin \chi + e_2 \cos \chi, \quad (23.29)$$

and then in the basis e_i tensor \mathbf{f} , which we will further denote as \mathbf{f}_1 indicating belonging to the first case, takes the form

$$\mathbf{f}_1 = \mathbf{g} - a(e_1 e_1 - e_2 e_2) + b e_1 e_2 - c e_2 e_1. \quad (23.30)$$

Here, for specific values of s and χ given above,

$$a = s \sin \chi \cos \chi = 0.061582, \quad b = s \cos^2 \chi = 0.057899, \quad (23.31)$$

$$c = s \sin^2 \chi = 0.065498$$

and \mathbf{f}_1 is represented as (see (23.28))

$$\mathbf{f}_1 = \mathbf{g} - 0.061582(e_1 e_1 - e_2 e_2) + 0.057899 e_1 e_2 - 0.065498 e_2 e_1. \quad (23.32)$$

The second way of twin formation is shown in Fig. 23.3 on the right. Here, twin occurs from element $1' - 2 - 3$ by shifting its part $1' - 2$ in direction of the vector δ_1 to the position $1 - 2$. Note that the vectors δ_1 and δ_2 on the right and left of Fig. 23.3 have different positions relative to the vectors e_1 and e_2 . As it follows from the solution of the Hadamard compatibility equation, the position of vector δ_1 , in direction of which the shift is taking place, is determined by the angle χ relative to the element from which the twin is formed. In the first case, it is element $1 - 2 - 3'$,

while in the second case, it is element $1' - 2 - 3$. So, the formation of twins in the second case is described by the expression the same as in the first case, but for the vectors δ_i shown in Fig. 23.3 on the right, $\mathbf{f} = \mathbf{g} + s \delta_1 \delta_2$. As it follows from this figure,

$$\delta_1 = \mathbf{e}_1 \sin \chi + \mathbf{e}_2 \cos \chi, \quad \delta_2 = \mathbf{e}_1 \cos \chi - \mathbf{e}_2 \sin \chi, \quad (23.33)$$

and then tensor \mathbf{f} , which we will further denote as \mathbf{f}_2 indicating belonging to the second case, takes for this case in the basis \mathbf{e}_i the form

$$\mathbf{f}_2 = \mathbf{g} + a (\mathbf{e}_1 \mathbf{e}_1 - \mathbf{e}_2 \mathbf{e}_2) - c \mathbf{e}_1 \mathbf{e}_2 + b \mathbf{e}_2 \mathbf{e}_1 \quad (23.34)$$

and is represented allowing for (23.31) as

$$\mathbf{f}_2 = \mathbf{g} + 0.061582 (\mathbf{e}_1 \mathbf{e}_1 - \mathbf{e}_2 \mathbf{e}_2) - 0.065498 \mathbf{e}_1 \mathbf{e}_2 + 0.057899 \mathbf{e}_2 \mathbf{e}_1. \quad (23.35)$$

In accordance with these two cases of twinning process, detwinning process will occur in two cases also: when element $2 - 3$ rotates in the plane of the drawing counterclockwise relative to the point 2 and takes the position $2 - 3'$ and when the element $1 - 2$ rotates in the plane of the drawing clockwise relative to point 2 and takes the position $1' - 2$. In the first case, the positive mass magnetic moment, which is perpendicular to the plane of Fig. 23.3 and has a necessary magnitude, should be applied to element $2 - 3$, and in the second case, the negative mass magnetic moment, which is perpendicular to the plane of Fig. 23.3 and has a necessary magnitude, must be applied to element $1 - 2$. In the third case, when these necessary conditions are met for two elements $1 - 2$ and $2 - 3$ at the same time, is unlikely due to all kinds of fluctuation processes accompanying magnetic, force, and temperature processes occurring in the body.

As mentioned above, for an external magnetic field applied along the easy magnetization axis, reorientation (detwinning) in the Heusler Ni_2MnGa alloy occurs, as follows from the experiments, when $\mu_0 |\mathbf{H}_0| = 0.3 \div 0.5$ T. To this moment, 180° walls separating magnetic domains disappear but the strength of the external magnetic field is still insufficient to rotate the vectors of local magnetization in elements of the twin mainly along the field. Therefore, a mass magnetic moment $\mathbf{L}_{mag} = \mu_0 \mathbf{M} \times \mathbf{H}$, acting on the elements of the twin $1 - 2$ and/or $2 - 3$ in Fig. 23.3, arises. We put in accordance with this moment the critical value of the external field when the detwinning process begins.

To realize the above, a magnetic problem is solved for the twinned state of the Ni_2MnGa Heusler alloy, when an external magnetic field is applied in the direction along or against element $1 - 2$ (easy axis \mathbf{c}_1 , problem C_1), or along or against element $2 - 3$ (easy axis \mathbf{c}_2 , problem C_2) in Fig. 23.3, that fully corresponds to the experiment described above. The obtained magnetization distribution allows us to determine the average value of the mass magnetic moment \mathbf{L}_{mag} in the regions occupied by elements $1 - 2$ and $2 - 3$ of the twin. For the problem C_1 , as a result of the motion of the magnetic domain walls, the magnetization vector \mathbf{M} almost coincides with the magnetic field vector \mathbf{H} in the element $1 - 2$. For this reason, the mass magnetic

moment L_{mag} in this element of the twin is a rather small magnitude. In the element 2 – 3, the vectors \mathbf{M} , as a result of the movement of the magnetic domain walls and rotation of this vector, occupy such a position with respect to the vector \mathbf{H} , that the mass magnetic moment implements counterclockwise rotation and its value we will call critical and denote as L_{mag}^{cr} for the above critical value of the applied external magnetic field $\mu_0 |\mathbf{H}_0| = 0.3 \div 0.5$ T. This situation has a simple interpretation: the positive magnetic moment acting counterclockwise on the element 2 – 3 of the twin (see Fig. 23.3) causes this element to rotate around point 2 counterclockwise also in the plane of the drawing. As a result, the element 2 – 3 becomes a linear continuation of the element 1 – 2 (the reorientation of martensite variants occurs in accordance with the first case considered above when discussing Fig. 23.3).

For the problem C_2 , as a result of the magnetic domain walls movement, the magnetization vector \mathbf{M} became almost coincident with the magnetic field vector \mathbf{H} in the element 2 – 3. For this reason, the mass magnetic moment L_{mag} in this element of the twin is a rather small magnitude. In the element 1 – 2, the vectors \mathbf{M} , as a result of the movement of the magnetic domain walls and rotation of this vector occupy such a position with respect to the vector \mathbf{H} , that the mass magnetic moment implements clockwise rotation when $|L_{mag}| = |L_{mag}^{cr}|$. This situation has a simple interpretation: the negative magnetic moment acting clockwise on the element 1 – 2 of the twin (see Fig. 23.3) causes the rotation of this element around point 2 clockwise also in the plane of the drawing. As a result, the element 1 – 2 becomes a linear continuation of the element 2 – 3 (the reorientation of the martensitic variants occurs in accordance with the second case considered above in the discussion of Fig. 23.3).

In the next section, following any of these algorithms, we will get a specific value of $|L_{mag}^{cr}|$ corresponding to the above-mentioned experiments performed by Heczko et al. (2001), Heczko and Straka (2003), Heczko (2005), Heczko and Bradshaw (2017). This critical value we use to determine the beginning of the detwinning process in the same material, but when an external magnetic field is applied in different directions relative to the c axis of each variant of martensite that makes up the twin. As noted above detwinning occurs when the module of mass magnetic moment $|L_{mag}|$ reaches a magnitude $|L_{mag}^{cr}|$ and will be positive in the element 2 – 3 of the twin with the easy axis c_2 or negative in the element 1 – 2 of the twin with the easy axis c_1 . In the first case element 2 – 3 will occupy position 2 – 3' and will be a continuation of element 1 – 2. In the second case element 1 – 2 will occupy position 1' – 2 (see Fig. 23.3) and will be a continuation of element 2 – 3. In any other cases, detwinning process does not occur.

Kinematics corresponding to detwinning process is described by the relations inverse (23.32), (23.35). It is easy to construct the latter based on the expression for the deformation gradient written in the basis δ_i , corresponding to the left or right Fig. 23.3, $\mathbf{f} = \mathbf{g} + s \delta_1 \delta_2$. As it is easy to check, the tensor inverse to \mathbf{f} , will have the form $\mathbf{f} = \mathbf{g} - s \delta_1 \delta_2$. Substituting representations (23.29) and (23.33) here, we will have

$$\begin{aligned} \mathbf{f}_1^{-1} &= \mathbf{g} + a(\mathbf{e}_1\mathbf{e}_1 - \mathbf{e}_2\mathbf{e}_2) - b\mathbf{e}_1\mathbf{e}_2 + c\mathbf{e}_2\mathbf{e}_1 \quad \text{for the first case,} \\ \mathbf{f}_2^{-1} &= \mathbf{g} - a(\mathbf{e}_1\mathbf{e}_1 - \mathbf{e}_2\mathbf{e}_2) + c\mathbf{e}_1\mathbf{e}_2 - b\mathbf{e}_2\mathbf{e}_1 \quad \text{for the second case,} \end{aligned} \quad (23.36)$$

and taking into account (23.31), we get the following specific expressions:

$$\begin{aligned} \mathbf{f}_1^{-1} &= \mathbf{g} + 0.061582(\mathbf{e}_1\mathbf{e}_1 - \mathbf{e}_2\mathbf{e}_2) - 0.057899\mathbf{e}_1\mathbf{e}_2 + 0.065498\mathbf{e}_2\mathbf{e}_1, \\ \mathbf{f}_2^{-1} &= \mathbf{g} - 0.061582(\mathbf{e}_1\mathbf{e}_1 - \mathbf{e}_2\mathbf{e}_2) + 0.065498\mathbf{e}_1\mathbf{e}_2 - 0.057899\mathbf{e}_2\mathbf{e}_1. \end{aligned} \quad (23.37)$$

By direct multiplication, it is easy to show that tensors (23.36) are the inverse to the tensors (23.30), (23.34) and tensors (23.37) are the inverse to the tensors (23.32), (23.35).

Remark As noted earlier, the element 2 – 3 of the twin 1 – 2 – 3 (see Fig. 23.3) passes into the element 2 – 3' and becomes a continuation of the element 1 – 2 for the first case of detwinning process. The result of this is the elongation of the material in the direction of the vector \mathbf{e}_1 and its shortening in the direction of the vector \mathbf{e}_2 . The element 1 – 2 of the twin 1 – 2 – 3 passes into the element 1' – 2 – 3 and becomes a continuation of the element 2 – 3 for the second case of detwinning process. The result of this is the elongation of the material in the direction of the vector \mathbf{e}_2 and its shortening in the direction of the vector \mathbf{e}_1 . As a result, the deformation process becomes most evident in this basis and the convenience of such a representation will be demonstrated below.

23.4 Statement of the Problem and Procedure for Its Numerical Implementation

23.4.1 Computational Domain and Material Parameters

The relations which were presented in the previous sections, we use to construct a model of magnetic and deformed behavior of a ferromagnetic Ni_2MnGa Heusler alloy in an external magnetic field. This alloy is considered both as a monotwin crystal and as a polytwin crystal, each grain of which is a twinned variant of martensite and has strong anisotropic properties. At the beginning, we consider the processes of magnetization and deformation of a single grain, when an external magnetic field is applied at different angles to the anisotropy axes of twinned variants, after which, using the results obtained, we plot magnetization curves for various polycrystalline samples and describe the deformation behavior of these materials in detwinning process. Figure 23.4 shows the structure of the twinned variant of martensite in a monotwin crystal.

As a characteristic size of martensitic plates in Heusler alloy is about 100–200 nm, the computational domain is chosen in the form of a square $L \times L$, where $L = 380$ nm. The 380 nm \times 380 nm domain under consideration (blue square in Fig. 23.4) is an elementary cell duplicated along the x and y axes. In the “herringbone” structure

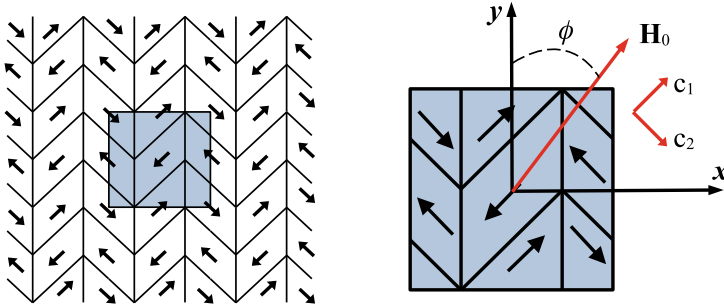


Fig. 23.4 Computational domain for the twinned variant of martensite in a monotwin crystal

under consideration, the axes of easy magnetization in the magnetic domains belonging to two variants of martensitic plates forming the twin, are located relative to the plane separating the martensitic variants (habitus plane) at an angle of 90° to each other. Inside each martensitic variant, these axes in the magnetic domains are located at an angle of 180° . The arrows in Fig. 23.4 show the magnetization vectors directed along or against the short axes (the axes of easy magnetization or the anisotropy axes) c_1 and c_2 in each variant of martensite when there is no external magnetic field. With this distribution, the sample is not magnetized as a whole.

For Ni_2MnGa alloy, the values of saturation magnetization M_s , magnetocrystalline anisotropy constant K_{anis} , exchange constant A_{exch} , gyromagnetic ratio γ and the damping (dissipation) parameter α are given in the Table 23.1. For the numerical implementation of the problem, we make all the relations dimensionless by introducing the characteristic size $l_0 = 3.8 \text{ nm}$ and energy $\psi_0 = \mu_0 M_s^2 = 4.55 \cdot 10^5 \text{ J/m}^3$. We estimate the thickness of the domain wall to determine the characteristic size of the finite element in the numerical calculation of the magnetization process. This size should be such that at least four to five elements fall on the domain wall. A large number of elements significantly increases the counting time, a smaller number significantly reduces the accuracy of the result. We determine the order of domain wall thickness by the relation $\delta \approx \sqrt{A_{exch}/K_{anis}}$ given in Brown's monograph (see Brown 1963), and for the Ni_2MnGa $\delta \approx 9 \text{ nm}$. The thickness by itself, Δ , is determined for a 180° wall in two ways: by the Lilly method $\Delta_L = \pi \delta$ and by the Landau–Lifshitz method $\Delta_{L-L} = 2 \delta$, which, taking into account the above value of δ , give $\Delta_L \approx 28 \text{ nm} \approx 7.4 l_0$ and $\Delta_{L-L} \approx 18 \text{ nm} \approx 4.7 l_0$. As a result, we obtain the following dimensionless parameters:

$$\tilde{M}_s = 1; \quad \tilde{K}_{anis} = \frac{K_{anis}}{\psi_0} \approx 0.54; \quad \tilde{A}_{exch} = \frac{A_{exch}}{\psi_0 l_0^2} \approx 3.$$

We also make dimensionless the external magnetic field $\tilde{\mathbf{H}}_0 = \mathbf{H}_0/M_s$ and introduce the notation $\tilde{H}_0 = |\tilde{\mathbf{H}}_0|$.

Table 23.1 Material parameters

| Parameter | Value | Dimension | Source |
|------------|--------------------|------------------|--|
| M_s | $6.015 \cdot 10^5$ | A/m | Mennerich et al. (2011), Tickle and James (1999) |
| K_{anis} | $2.5 \cdot 10^5$ | J/m ³ | Mennerich et al. (2011), Tickle and James (1999) |
| A_{exch} | $2 \cdot 10^{-11}$ | J/m | Mennerich et al. (2011), Zhang and Chen (2005) |
| γ | $2.21 \cdot 10^5$ | m/(A·s) | Mennerich et al. (2011) |
| α | 0.5 | – | Mennerich et al. (2011) |

23.4.2 Problem Formulation and Procedure for Its Numerical Realization

For the twinning structure, presented in Fig. 23.4, and the shape-memory ferromagnetic Ni₂MnGa Heusler alloy with the such parameters, we statement the problem to describe the magnetic and deformed behavior in a magnetic field both as a monotwin crystal and as a polytwin crystal. First, the behavior of a monotwin crystal is modeled. The periodicity conditions of the solution are imposed (Rogovoy et al. 2021a). For the computational domain shown in Fig. 23.4, these conditions for the any function φ have a view:

$$\text{if } y_0 - L/2 \leq y \leq y_0 + L/2 \text{ then } \begin{cases} \text{if } x_0 + L > x > x_0 + L/2 \text{ then } \varphi(x, y) = \varphi(x - L, y) \\ \text{if } x_0 - L < x < x_0 - L/2 \text{ then } \varphi(x, y) = \varphi(x + L, y) \end{cases}$$

$$\text{if } x_0 - L/2 \leq x \leq x_0 + L/2 \text{ then } \begin{cases} \text{if } y_0 + L > y > y_0 + L/2 \text{ then } \varphi(x, y) = \varphi(x, y - L) \\ \text{if } y_0 - L < y < y_0 - L/2 \text{ then } \varphi(x, y) = \varphi(x, y + L) \end{cases}$$

Here x_0, y_0 are the coordinates of the center of the computational domain shown in Fig. 23.4. To implement these conditions, it is necessary to consider the $2L \times 2L$ domain already, in the middle of which the domain $L \times L$ (blue square in Fig. 23.4) is located. The motion and interaction of the walls of magnetic domains, the rotation of the magnetization vectors and the detwinning process should be taken into account in this description. As noted earlier, we, based on the initial magnetization distribution \mathbf{m} and using the coupled variational equations (23.18) and (23.21), establish the initial boundaries of the magnetic domains and distribution of the magnetization vectors in them in the absence of an external magnetic field (Problem 1). The obtained magnetic structure is the initial one for the subsequent application of the magnetic field. Then,

applying an external magnetic field in the direction of vector \mathbf{c}_1 (see Fig. 23.4), that corresponds to the experiments given in the previous section (Heczko et al. 2001; Heczko and Straka 2003; Heczko 2005; Heczko and Bradshaw 2017), we determine the critical value of the mass magnetic moment L_{mag}^{cr} at which detwinning process is carried out (Problem 2). Now we have everything to solve the problem in full and to describe the movement of the domain walls, the rotation of the magnetization vector and detwinning process that will allow us to construct the magnetization curves and to define deformation states when an external magnetic field \mathbf{H}_0 is applied to the computational domain, shown in Fig. 23.4, at different angles to the y axis in the (x, y) plane (Problem 3). Thus, we obtain the evolution of the magnetization distribution in the sample with an increase in the external magnetic field, and magnetization curves for each direction (dependencies of the average value of the projection of the magnetization on the axis along which the external magnetic field is directed on the applied field) and deformation states.

When solving the variational equation (23.21), the time step was $\tau = \gamma M_s t = 0.05$ and $\theta = 0.6$. This problem was solved by the finite element method (FEM) using open source computing platform FEniCS (<https://fenicsproject.org>). A regular grid consisting of 5184 finite elements was set. The blue square in Fig. 23.4 was divided into 1296 equal squares, each of the resulting squares was divided diagonally into four equal triangles. Each element was triangle with sides 7.5 nm, 7.5 nm and 10.6 nm. As a result, there were from three to four finite elements per domain wall, which is quite enough to ensure the necessary accuracy of the solution. The specified above periodicity conditions of the solution are imposed. A quadratic approximation was set for the vector \mathbf{v} , and linear for φ and λ . \tilde{H}_0 increased from 0 to 1.5 with increments of $\tilde{h}_0 = 0.01$. Within each step of the applied magnetic field, 3000 time steps were realized to fulfill the condition of convergence of the solution.

Having a sufficient set of magnetization curves and deformed states of a single crystal for various directions of application of an external magnetic field to it,⁴ we describe the behavior of a polycrystal, each grain of which is a single crystal oriented in the plane of Fig. 23.4 in a certain way which determines the isotropic and anisotropic behavior of the polycrystal. As a result, we construct magnetization curves and determine deformed states in a polycrystal, which is a representative volume of the material under consideration (Problem 4).

The results obtained in solving Problems 1–4 are given in the next section.

⁴ The justification for the necessary sufficiency will be given in the following section.

23.5 Results of Numerical Simulation

23.5.1 A Monotwin Crystal

First of all, we will present results of calculating the evolution of the magnetization vector \mathbf{m} . This presentation demonstrates the movement and annihilation of the domain walls and the rotation of the vector \mathbf{m} , but does not yet take into account the detwinning process. Why this is done in this way, we hope, will become clear a little later. The results obtained in this direction describe the evolution of the magnetization vector when the external magnetic field is applied to the y axis at the angles ϕ (see Fig. 23.4) where $0^\circ \leq \phi \leq 90^\circ$. As will be shown below, this is enough to describe the magnetic and deformation behavior of various polytwin crystals. Among all the results obtained in this direction, we will give only three of the most representative. Figures 23.5, 23.6 and 23.7 demonstrate these three cases of the evolution of the magnetization vector in an external magnetic field. Although the problem under consideration is plane, but when solving the Landau–Lifshitz–Gilbert equation, the vector \mathbf{m} does not lie in the (x, y) plane of the computational domain shown in Fig. 23.4 and the arrows in these figures show the projections of the vector \mathbf{m} onto the plane (x, y) for various values of the external magnetic field \tilde{H}_0 applied at angles $\phi = 0^\circ$ (Fig. 23.5), $\phi = 45.84^\circ$ (Fig. 23.6) and $\phi = 90^\circ$ (Fig. 23.7) to the y axis. The color of the m_x component is rendered so that areas where $m_x = 1$ are red and areas where $m_x = -1$ are blue. Areas with other m_x values are shown in gradations of these colors according to the scales presented on the right.

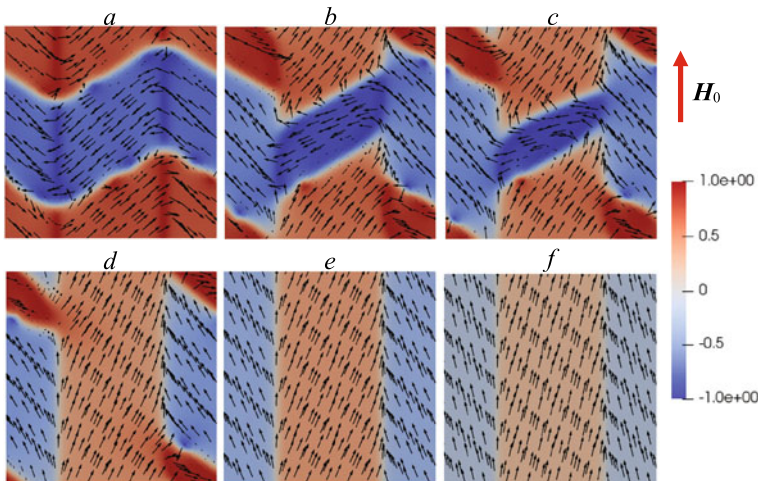


Fig. 23.5 The process of the magnetization vector evolution when a magnetic field is applied along the y axis: **a** $\tilde{H}_0 = 0$, **b** $\tilde{H}_0 = 0.25$, **c** $\tilde{H}_0 = 0.3$, **d** $\tilde{H}_0 = 0.32$, **e** $\tilde{H}_0 = 0.33$, **f** $\tilde{H}_0 = 1.5$

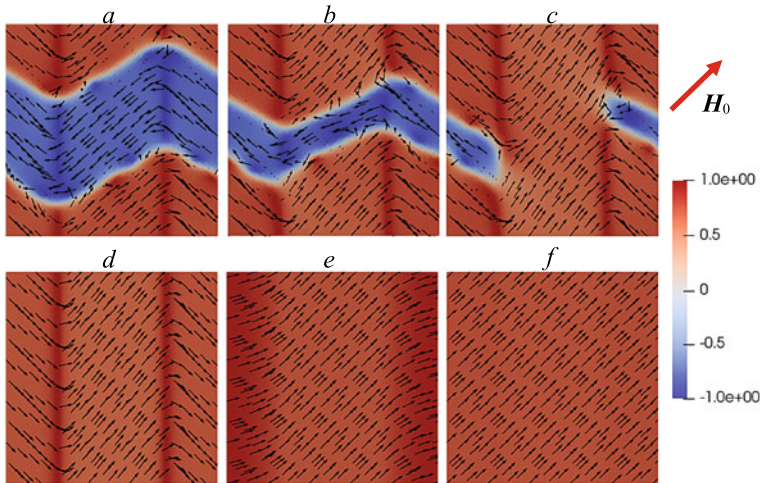
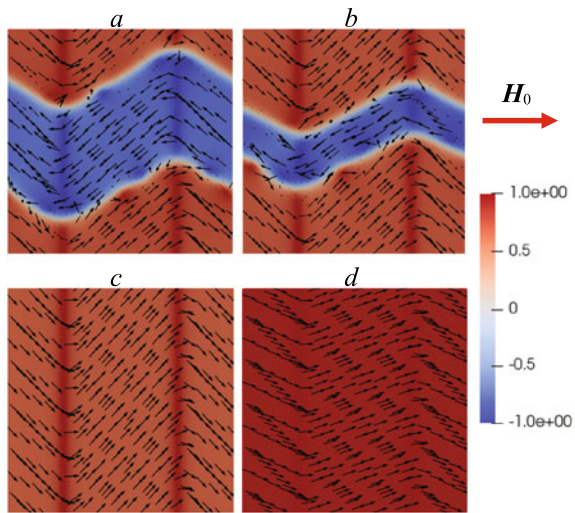


Fig. 23.6 The process of the magnetization vector evolution when a magnetic field is applied at an angle of 45.84° to the y axis: **a** $\tilde{H}_0 = 0$, **b** $\tilde{H}_0 = 0.15$, **c** $\tilde{H}_0 = 0.16$, **d** $\tilde{H}_0 = 0.17$, **e** $\tilde{H}_0 = 1.1$, **f** $\tilde{H}_0 = 1.5$

Fig. 23.7 The process of the magnetization vector evolution when a magnetic field is applied along the x axis: **a** $\tilde{H}_0 = 0$, **b** $\tilde{H}_0 = 0.11$, **c** $\tilde{H}_0 = 0.13$, **d** $\tilde{H}_0 = 1.5$



Figures 23.5a, 23.6a and 23.7a show the initial magnetic domains boundaries and the distribution of the magnetization vectors in them and in the computational domain in the absence of an external magnetic field, which is a solution to Problem 1 posed in Sect. 23.4.2. Such a picture is obtained by solving the coupled variational equations (23.18) and (23.21) for the initial distribution of the magnetization vector \mathbf{m} shown in Fig. 23.4. The resulting magnetic structure is the initial one for the subsequent application of a magnetic field in various directions relative to the computational

domain (Figs. 23.5, 23.6 and 23.7b, c and so on). It can be seen from these figures that, at the initial stage, the magnetization occurs due to the motion of the magnetic domains walls, and then due to the rotation of the magnetization vectors.

Knowing the distribution of the magnetization vector in the computational domain for the angles $0^\circ \leq \phi \leq 90^\circ$, we construct the dimensionless mass magnetic moments $\tilde{\mathbf{L}}_{mag} = \mathbf{L}_{mag}/\psi_0$ corresponding to these angles, where $\mathbf{L}_{mag} = \mu_0 \mathbf{M} \times \mathbf{H}$. $\tilde{\mathbf{L}}_{mag}$ is defined as the average value of the mass magnetic moment in elements 1 – 2 (see Fig. 23.3) corresponding to the middle of the computational domain in Fig. 23.4, for this domain, and in elements 2 – 3 corresponding to the periphery of this computational domain, for this domain. The key results for further explanation and use are shown in Fig. 23.8 depending on \tilde{H}_0 . The blue color shows the moment for element 1 – 2 (the middle area in Fig. 23.4), red for element 2 – 3 (the periphery area in Fig. 23.4). ϕ is the angle to the y axis in degrees.

The dependence of $\tilde{\mathbf{L}}_{mag}$ on \tilde{H}_0 , shown in Fig. 23.8 for the angle $\phi = 45.84^\circ$, allows us to solve Problem 2 of Sect. 23.4.2 and determine the critical value of the mass magnetic moment $\tilde{\mathbf{L}}_{mag}^{cr}$, in which the detwinning process is carried out. Here the vector of the external magnetic field \mathbf{H}_0 acts in the direction of the axis of easy magnetization \mathbf{c}_1 of one of the elements of the twin, located in the central region of Fig. 23.4, as in the experiments in which the magnetization curve is constructed taking into account the detwinning process (Heczko et al. 2001; Heczko and Straka 2003; Heczko 2005; Heczko and Bradshaw 2017).

As follows from Fig. 23.6, 180° walls separating magnetic domains disappear already at a value $\tilde{H}_0 = 0.17$ (see Fig. 23.6d), which corresponds to $\mu_0 |\mathbf{H}_0| = 0.13$ T, and the vector \mathbf{m} lies completely in the plane of this figure. The vector of the mass magnetic moment $\tilde{\mathbf{L}}_{mag}$ (its average value), as it follows from Fig. 23.8 for the angle $\phi = 45.84^\circ$, directed at the reader perpendicular to the plane of this figure (red line, counterclockwise rotation, positive moment $\tilde{\mathbf{L}}_{mag}$) in the peripheral region of Fig. 23.4, where the vector of easy magnetization is \mathbf{c}_2 , or from the reader also perpendicular to the plane of this figure (blue line, clockwise rotation, negative moment $\tilde{\mathbf{L}}_{mag}$) in the middle area of Fig. 23.4, where the vector of easy magnetization is \mathbf{c}_1 . Directions of these moments in these areas correspond to all detwinning cases discussed in Sect. 23.3.2. But the magnitude of $\tilde{\mathbf{L}}_{mag}$ in the central region is very small. Therefore, the detwinning will occur in accordance with the first case, when the mass magnetic moment in the peripheral area reaches a critical value $|\tilde{\mathbf{L}}_{mag}^{cr}|$. As follows from the experiments, presented in the works of Heczko et al. (2001), Heczko and Straka (2003), Heczko (2005), Heczko and Bradshaw (2017), detwinning begins when the external magnetic field reaches the value $\mu_0 |\mathbf{H}_0| = 0.3 \div 0.5$ T. Choosing the smallest value $\mu_0 |\mathbf{H}_0| = 0.3$, to which $\tilde{H}_0^{cr} = 0.41$ corresponds, we have from Fig. 23.8 for the angle $\phi = 45.84^\circ$ that $|\tilde{\mathbf{L}}_{mag}^{cr}| = 0.35$, $|\mathbf{L}_{mag}^{cr}| = 0.16 \cdot 10^6$ N·m/m³ and this is the solution to Problem 2 posed in Sect. 23.4.2.

Distributions of $\tilde{\mathbf{L}}_{mag}$, including that shown in Fig. 23.8, and the obtained critical value of the mass magnetic moment allow us to conclude that there is no detwinning until ϕ is less than $\approx 40^\circ$. In the field of $(\approx 40^\circ) \leq \phi \leq (\approx 89^\circ)$, detwinning occurs in accordance with the first case. At the same time, \tilde{H}_0^{cr} at which the critical value

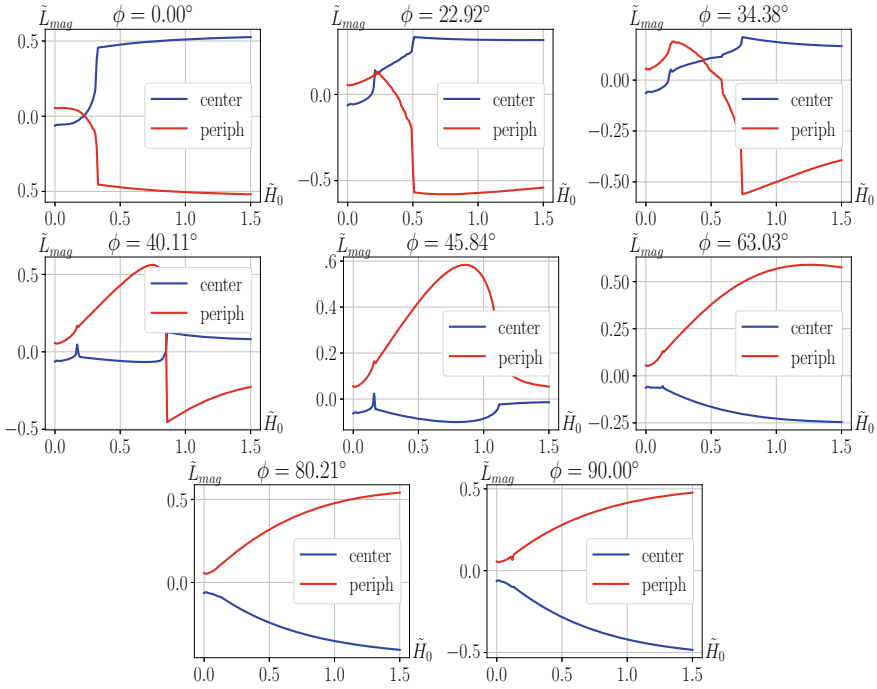


Fig. 23.8 Mass magnetic moments

$|\tilde{L}_{mag}^{cr}|$ is reached, varies from 0.40 at $\phi \approx 40^\circ$ to 0.72 at $\phi \approx 89^\circ$. At an angle of 90° , the curves of the dependence of \tilde{L}_{mag} on \tilde{H}_0 for element 1 – 2 (Fig. 23.3, the middle of the calculated area in Fig. 23.4) and for element 2 – 3 (the periphery of the computational domain in Fig. 23.4) differ only by a sign (see Fig. 23.8). This means that detwinning here can occur both in accordance with the first and in accordance with the second case but only when the external magnetic field reaches the value $\tilde{H}_0^{cr} = 0.72$. From the point of view of physics, the probability of any of these cases is the same due to all kinds of fluctuations accompanying magnetic, force and temperature processes occurring in the medium. But as shown below, at $\phi = 90^\circ + \gamma$, $0^\circ < \gamma < 90^\circ$ detwinning occurs in accordance with the second case. Therefore, from the point of view of mathematics, if we strive to an angle of 90° from the side $90^\circ -$, then detwinning occurs in accordance with the first case, but if from the side $90^\circ +$, then in accordance with the second one. We will continue to adhere to this position, without having any specifics from the point of view of physics.

To construct models of polytwin crystal behavior, dependencies \tilde{L}_{mag} on \tilde{H}_0 were calculated for 17 values of the angles ϕ , including 8, shown in Fig. 23.8. The segment along the angle ϕ from 0 to 1.5 radians was passed in increments of 0.1 radians, 1.5708 radians corresponded to 90° . Table 23.2 shows the values of \tilde{H}_0^{cr} at which the first or the second case of detwinning process occurs for the corresponding ϕ . As noted

Table 23.2 The values at which the detwinning process occurs

| | | | | | | | | | | |
|------------------|--------|-------|-------|-------|-------|-------|-------|-------|-------|-------------|
| ϕ , radians | 0.7 | 0.8 | 0.9 | 1.0 | 1.1 | 1.2 | 1.3 | 1.4 | 1.5 | 1.5708 |
| ϕ , degrees | 40.11 | 45.84 | 51.57 | 57.30 | 63.03 | 68.75 | 74.48 | 80.21 | 85.94 | 90.00 |
| \bar{H}_0^{cr} | 0.40 | 0.41 | 0.42 | 0.43 | 0.45 | 0.48 | 0.52 | 0.57 | 0.65 | 0.72 |
| Detwinning | 1 case | | | | | | | | | 1 or 2 case |

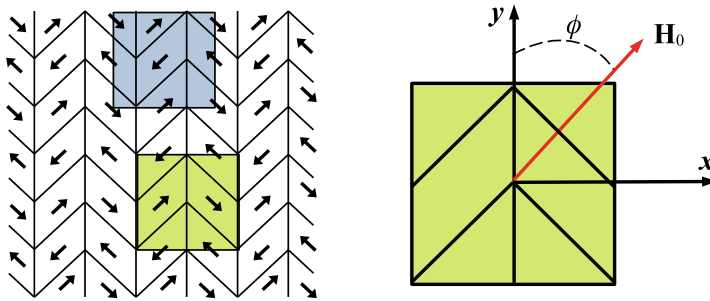


Fig. 23.9 Domain D_S containing a twin and having a certain symmetry

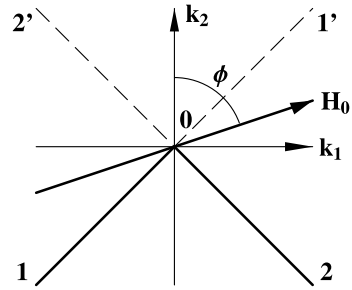
earlier, detwinning does not occur for angles ϕ less than 40° . Therefore, the table shows the results only for angles greater than 40° .

Such a change in the angle ϕ is sufficient to fully describe the magnetic and deformation reaction of the material to the application of an external magnetic field at angles from 0° to 360° , if we take into account the following. Figure 23.4 shows the computational domain, which is duplicated in the horizontal and vertical directions. This choice of the computational domain allows us to set the periodicity condition of the solution. But such a choice of domains repeating in space is not the only one. In Fig. 23.9, in addition to the computational domain, another domain containing a twin and having a certain symmetry is highlighted (let's denote it as D_S).

Based namely on the symmetry, we carry out analysis further. In Fig. 23.10 the magnetic structure of this symmetrical domain D_S is shown. Here, the k_2 axis is the vertical axis y of symmetry for domain D_S and axis k_1 is the axis x in Fig. 23.9. The angles between the axes $k_1, 01', k_2, 02', -k_1, 01, -k_2, 02, k_1$ are all 45° . The vectors of spontaneous magnetization m are directed from point 0 to points 1 and 2' for one group of magnetic domains and from point 0 to points 2 and 1' for another group (see Fig. 23.9).

The magnetic structure presented in Fig. 23.10 has four 180° axes of symmetry: k_1, k_2 and two diagonals $1 - 1'$ and $2 - 2'$. Symmetry with respect to diagonals replaces vectors k_1 and k_2 with vectors k_2 and k_1 or $-k_2$ and $-k_1$ accordingly. Symmetry with respect to vector k_1 replaces vector k_2 with vector $-k_2$ and symmetry with respect to vector k_2 replaces vector k_1 with vector $-k_1$. We will use symmetries with respect to vectors k_1 and k_2 based on the fact that mutual positions of the vectors m and H_0 correspond to the conditions of such symmetry. We will describe the

Fig. 23.10 The magnetic structure of symmetrical domain D_S . H_0 is a strength vector of external magnetic field applied to the domain at an angle ϕ



symmetry using an orthogonal tensor (Rogovoy 2020)

$$\mathbf{O}(\varphi, \mathbf{e}) = \mathbf{g} \cos \varphi + \mathbf{e}\mathbf{e} (1 - \cos \varphi) + (\mathbf{e} \times \mathbf{g}) \sin \varphi. \quad (23.38)$$

This tensor rotates any vector \mathbf{a} with respect to the vector \mathbf{e} by an angle φ counterclockwise, leaving its length unchanged: $\mathbf{a}' = \mathbf{O}(\varphi, \mathbf{e}) \cdot \mathbf{a}$, $|\mathbf{a}'| = |\mathbf{a}|$. In addition, with this transformation, the angle between the two vectors \mathbf{a} and \mathbf{b} remains unchanged: $\mathbf{a} \cdot \mathbf{b} = \mathbf{a}' \cdot \mathbf{b}'$.

Using expression (23.38), a 180° rotation relative to the k_1 axis is described by the orthogonal tensor $\mathbf{O}(k_1) = k_1 k_1 - k_2 k_2 - k_3 k_3$. As noted earlier, although the problem under consideration is plane, but when solving the Landau–Lifshitz–Gilbert equation, the vector \mathbf{m} has three components, $\mathbf{m} = m^1 k_1 + m^2 k_2 + m^3 k_3$. But m^3 does not make sense to take into account when calculating the magnetization curves and the mass magnetic moment for which we carry out this analysis. m^3 does not affect the magnetization curves at all, as will be shown below, and the magnitude of the mass magnetic moment necessary to determine its critical value is calculated when m^3 is already zero. Therefore, the components of any vector or tensor associated with the vector k_3 are not taken into account further. Bearing in mind the above, $\mathbf{O}(k_1) = k_1 k_1 - k_2 k_2$ and vectors

$$\mathbf{m} = m^1 k_1 + m^2 k_2, \quad \mathbf{H}_0 = H_0^1 k_1 + H_0^2 k_2, \quad \mathbf{H} = H^1 k_1 + H^2 k_2 \quad (23.39)$$

are transformed by such rotation into the vectors $\mathbf{m}' = \mathbf{O} \cdot \mathbf{m} = m^1 k_1 - m^2 k_2$, $\mathbf{H}'_0 = \mathbf{O} \cdot \mathbf{H}_0 = H_0^1 k_1 - H_0^2 k_2$ and $\mathbf{H}' = \mathbf{O} \cdot \mathbf{H} = H^1 k_1 - H^2 k_2$ (the vectors \mathbf{m}' , \mathbf{H}'_0 and \mathbf{H}' are a mirror image relative to the axis k_1 of the vectors \mathbf{m} , \mathbf{H}_0 and \mathbf{H}). The magnetization curves which is described by the relation $\tilde{m} = \mathbf{m} \cdot (\mathbf{H}_0/H_0)$ remain unchanged in this case since $\mathbf{m} \cdot (\mathbf{H}_0/H_0) = \mathbf{m}' \cdot (\mathbf{H}'_0/H'_0)$, but the vector $\mathbf{L}_{mag} = \mu_0 M_s \mathbf{m} \times \mathbf{H}$ changes its sign because $\mathbf{m} \times \mathbf{H} = -\mathbf{m}' \times \mathbf{H}'$ (both are easy to check with a simple substitution. Note that m^3 does not affect $\mathbf{m} \cdot (\mathbf{H}_0/H_0)$ at all). With such rotation, as it is easy to understand, the angle ϕ between the vector \mathbf{H}'_0 and the fixed vertical axis y (see Fig. 23.9), which was equal to β for the vector \mathbf{H}_0 , becomes equal to $\pi - \beta$, $0 \leq \beta \leq \pi/2$ (mathematically, this follows from the analysis of scalar products $k_2 \cdot \mathbf{H}_0$ and $k_2 \cdot \mathbf{H}'_0$). With that in mind and considering

the results of Sect. 23.3.2, we conclude that detwinning process for $\pi - \beta$ begins at the same \tilde{H}_0^{cr} as in Table 23.2 for the angle $\phi = \beta$ but instead of the first case it will be carried out in accordance with the second case discussed in above-mentioned Sect. 23.3.2. The magnetization curves will be exactly the same as for angle $\phi = \beta$.

Let's now perform a 180° rotation around the vector \mathbf{k}_2 , $\mathbf{O}(\mathbf{k}_2) = -\mathbf{k}_1\mathbf{k}_1 + \mathbf{k}_2\mathbf{k}_2$, in addition to the previous rotation: $\mathbf{O} = \mathbf{O}(\mathbf{k}_2) \cdot \mathbf{O}(\mathbf{k}_1) = -\mathbf{k}_1\mathbf{k}_1 - \mathbf{k}_2\mathbf{k}_2$. Note, this product is commutative, in contrast to the general case. As a result, the vectors \mathbf{m} , \mathbf{H}_0 and \mathbf{H} (23.39) are transformed by such rotation into the vectors $\mathbf{m}' = \mathbf{O} \cdot \mathbf{m} = -(m^1\mathbf{k}_1 + m^2\mathbf{k}_2)$, $\mathbf{H}'_0 = \mathbf{O} \cdot \mathbf{H}_0 = -(H_0^1\mathbf{k}_1 + H_0^2\mathbf{k}_2)$ and $\mathbf{H}' = \mathbf{O} \cdot \mathbf{H} = -(H^1\mathbf{k}_1 + H^2\mathbf{k}_2)$ that leads to the equalities $\tilde{m} = \tilde{m}'$ and $\mathbf{L}_{mag} = \mathbf{L}'_{mag}$. Given that the angle ϕ between the vector \mathbf{H}'_0 and the fixed vertical axis y shown in Fig. 23.9, which was equal to β for the vector \mathbf{H}_0 , becomes equal to $\pi + \beta$, $0 \leq \beta \leq \pi/2$, we conclude that detwinning process for $\pi + \beta$ begins at the same \tilde{H}_0^{cr} as in Table 23.2 for the angle $\phi = \beta$ and is carried out in accordance with the first case indicated in this table. The magnetization curves will be exactly the same as for angle $\phi = \beta$.

Finally, we will perform a 180° rotation only around the \mathbf{k}_2 axis: $\mathbf{O}(\mathbf{k}_2) = -\mathbf{k}_1\mathbf{k}_1 + \mathbf{k}_2\mathbf{k}_2$. Of course, this rotation is a 180° rotation around the vector \mathbf{k}_1 in addition to the previous rotation $\mathbf{O} = \mathbf{O}(\mathbf{k}_2) \cdot \mathbf{O}(\mathbf{k}_1)$. The vectors \mathbf{m} , \mathbf{H}_0 and \mathbf{H} (23.39) are transformed by such rotation into the vectors $\mathbf{m}' = \mathbf{O} \cdot \mathbf{m} = -m^1\mathbf{k}_1 + m^2\mathbf{k}_2$, $\mathbf{H}'_0 = \mathbf{O} \cdot \mathbf{H}_0 = -H_0^1\mathbf{k}_1 + H_0^2\mathbf{k}_2$ and $\mathbf{H}' = \mathbf{O} \cdot \mathbf{H} = -H^1\mathbf{k}_1 + H^2\mathbf{k}_2$ that leads to the equalities $\tilde{m} = \tilde{m}'$ and $\mathbf{L}_{mag} = -\mathbf{L}'_{mag}$. With such rotation, the angle ϕ between the vector \mathbf{H}'_0 and the fixed vertical axis y shown in Fig. 23.9, which was equal to β for the vector \mathbf{H}_0 , becomes equal to $2\pi - \beta$, $0 \leq \beta \leq \pi/2$. Considering this and the results of Sect. 23.3, we conclude that detwinning process for $2\pi - \beta$ begins at the same \tilde{H}_0^{cr} as in Table 23.2 for the angle $\phi = \beta$ but instead of the first case it will be carried out in accordance with the second case discussed in above-mentioned Sect. 23.3. The magnetization curves will be exactly the same as for angle $\phi = \beta$.

Let us construct the average value of the projection of the magnetization on the axis along which the external magnetic field is directed:

$$\tilde{m} = \langle m_{\parallel} \rangle = \frac{1}{S} \int_{\Omega^{(in)}} \left(\mathbf{m} \cdot \frac{\tilde{\mathbf{H}}_0}{\tilde{H}_0} \right) d\Omega^{(in)}, \quad (23.40)$$

where S is the area of the considered domain. Figure 23.11 demonstrates the dependencies of \tilde{m} on the modulus \tilde{H}_0 for various directions (angles ϕ) of an external magnetic field application, taking into account possible detwinning. Five stages of the magnetization process are distinguished on each of the presented curves. At the first stage, the 180° walls of the magnetic domains moves proportional to the applied magnetic field and the magnetization depends linearly on this field. At the second stage, a jump in magnetization occurs due to a significant increase in the speed of movement of these walls. At the third stage, these walls are annihilated in a critical field, magnitude of which \tilde{H}_0 , for example, is approximately 0.32 for Fig. 23.5e, or 0.17 for Fig. 23.6d, or 0.13 for Fig. 23.7c, and the magnetization vectors begin to turn gradually, trying to lie along the applied external magnetic field. At the fourth stage,

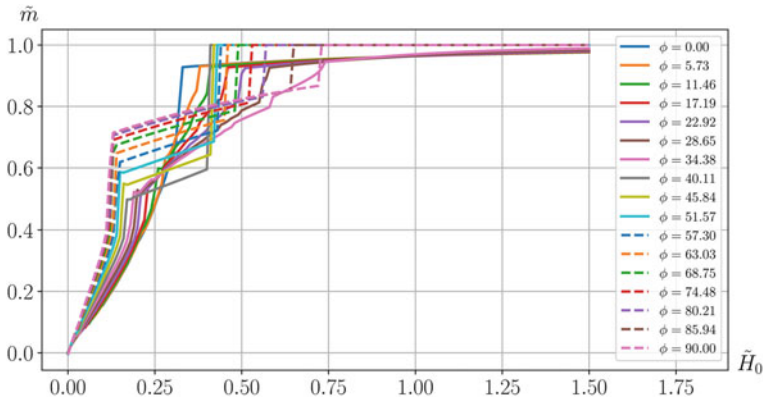


Fig. 23.11 The magnetization curves for different directions of application of the external magnetic field ϕ (in degrees)

which is observed only for ϕ greater than 40° , detwinning occurs and the magnetization increases sharply again by a jump. For the curves presented in Fig. 23.11 this takes place at the values of \tilde{H}_0 given in Table 23.2. At the last fifth stage, the magnetization reaches saturation. The magnetization curves obtained show essentially anisotropic magnetic properties in the twinned martensite of the Ni_2MnGa alloy. By this we solve the magnetic part of Problem 3, formulated in the Sect. 23.4.2.

The detwinning process, which accompanies the magnetization process at certain values of the angle ϕ , leads to the occurrence of the structural deformation and can be carried out, as it has been shown, in accordance with two cases. Let's construct a deformed state for these cases. For detwinning process the strain tensor has a form $\mathbf{e} = (\mathbf{f}^{-T} \cdot \mathbf{f}^{-1} - \mathbf{g})/2$, where $\mathbf{f}^{-1} = \mathbf{f}_1^{-1}$ or $\mathbf{f}^{-1} = \mathbf{f}_2^{-1}$ is defined in the basis $\mathbf{e}_1, \mathbf{e}_2$ by the relations (23.36) or (23.37). Using expressions (23.36), this form is concretized into an expression $\mathbf{e} = e^{11} \mathbf{e}_1 \mathbf{e}_1 + e^{22} \mathbf{e}_2 \mathbf{e}_2 + e^{12} (\mathbf{e}_1 \mathbf{e}_2 + \mathbf{e}_2 \mathbf{e}_1)$, where

$$e^{11} = (a^2 + c^2 + 2a)/2, \quad e^{22} = (a^2 + b^2 - 2a)/2, \\ e^{12} = [(1-a)c - (1+a)b]/2, \quad \text{for the first case;}$$

$$e^{11} = (a^2 + b^2 - 2a)/2, \quad e^{22} = (a^2 + c^2 + 2a)/2, \\ e^{12} = [(1-a)c - (1+a)b]/2, \quad \text{for the second case.}$$

Giving that $a = 0.061582$, $b = 0.057899$, $c = 0.065498$ (see (23.31)), we obtain

$$e^{11} \approx 0.06, \quad e^{22} \approx -0.06, \quad e^{12} \approx 0.00 \quad \text{for the first case;} \\ e^{11} \approx -0.06, \quad e^{22} \approx 0.06, \quad e^{12} \approx 0.00 \quad \text{for the second case.} \quad (23.41)$$

These results correspond to the actual behavior of the sample. Indeed, for detwinning process of the first case, element 2 – 3 of the twin 1 – 2 – 3 in Fig. 23.3 is converted to an element 2 – 3' which is a continuation of element 1 – 2. As a result the sample increases its size in the direction of element 1 – 2 – 3' (in direction of vector e_1) and decreases in the perpendicular direction (in direction of element 1' – 2 – 3 or vector e_2). Therefore, the component e^{11} of the strain tensor is positive, and e^{22} is negative (see the first line in (23.41)). For detwinning process of the second case, element 1 – 2 of the twin 1 – 2 – 3 in Fig. 23.3 is converted to an element 1' – 2 which is a continuation of element 2 – 3. As a result the sample increases its size in the direction of element 1' – 2 – 3 (in direction of vector e_2) and decreases in the perpendicular direction (in direction of element 1 – 2 – 3' or vector e_1). Therefore, the component e^{22} of the strain tensor is positive, and e^{11} is negative (see the second line in (23.41)), unlike the previous case. The magnitude of these strains is in a full accordance with the experimental data (see Heczko and Straka 2003; Heczko 2005) both in the first and in the second cases.

Since the detwinning in these two cases is carried out by a simple shift, this process should take place without changing the volume. The obtained values of the strain tensors components fully correspond to this position. In addition, it turned out that the vectors e_1, e_2 , coinciding with both the axes of easy magnetization c_1, c_2 of the crystal and the axes of its anisotropy p_1, p_2 , are the principal axes of the twinning and detwinning deformation processes.

We emphasize that deformations (23.41) occur only if the conditions given in Table 23.2 are met: to each angle ϕ , which determines the direction of action of the external magnetic field on the calculated area, a certain intensity of this field corresponds. If this intensity is less than that shown in Table 23.2, no detwinning occurs. To take into account everything that is said here, based on the analysis carried out after Table 23.2 for the angle ϕ varying from 90° to 360° , we rewrite represented in (23.41) as

$$e^{11} = 0.06 \Gamma(\phi, \tilde{H}_0), \quad e^{22} = -0.06 \Gamma(\phi, \tilde{H}_0), \quad e^{12} = 0.00,$$

$$\Gamma(\phi, \tilde{H}_0) = \begin{cases} H(\tilde{H}_0 - \tilde{H}_0^{cr}(\phi)) & \text{if } 0 \leq \phi \leq \pi/2 \\ -H(\tilde{H}_0 - \tilde{H}_0^{cr}(\pi - \phi)) & \text{if } \pi/2 \leq \phi \leq \pi \\ H(\tilde{H}_0 - \tilde{H}_0^{cr}(\phi - \pi)) & \text{if } \pi \leq \phi \leq 3\pi/2 \\ -H(\tilde{H}_0 - \tilde{H}_0^{cr}(2\pi - \phi)) & \text{if } 3\pi/2 \leq \phi \leq 2\pi \end{cases}, \quad (23.42)$$

where $\tilde{H}_0^{cr}(\zeta) = \infty$, if $0^\circ \leq \zeta \leq 40^\circ$ and $H(x)$ is the Heaviside's function:

$$H(x) = \begin{cases} 1 & \text{if } x \geq 0 \\ 0 & \text{if } x < 0 \end{cases}.$$

All of the above allows us to assert that the deformation part of Problem 3, formulated in the Sect. 23.4.2, has been solved.

23.5.2 A Polytwinned Crystal

A monotwin crystal was considered above, to which an external magnetic field was applied at different angles in the xy plane. Now fixing the direction of the external magnetic field and placing the same calculated region shown in Fig. 23.4 at different angles to it, we, using the curves shown in Fig. 23.11, describe the magnetization of this representative composite region, which models a polycrystal with a different arrangement of twins in the plane, and deformed state of a polycrystal arising as a result of the detwinning processes in single crystals. This will be the solution to Problem 4, formulated in Sect. 23.4.2. With this approach, as is customary in many structural models, the magnetic interaction, as well as the deformation interaction of these regions are not taken into account and the question of these effects remains open.

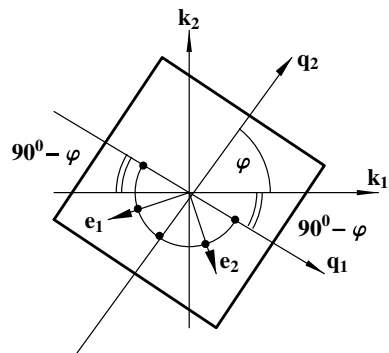
In order to specify the location of single crystals in a polycrystal, we introduce, in addition to the orthonormal coordinate systems (q_1, q_2) associated with single crystals, the general orthonormal coordinate system (k_1, k_2) associated with the polycrystal (see Fig. 23.12). The location of the single crystal in the polycrystal is determined by the angle φ between the axis q_2 of the single crystals and the vector k_1 of the general coordinate system. The arcs between the black dots in Fig. 23.12 cover equal angles of 45° .

To construct the magnetization curves for isotropic and anisotropic polycrystals we propose the following relation

$$m(\tilde{H}_0) = \left(\int_{\phi_1}^{\phi_2} \tilde{m}(\phi, \tilde{H}_0) d\phi \right) / \left(\int_{\phi_1}^{\phi_2} d\phi \right), \tag{23.43}$$

where $\tilde{m}(\phi, \tilde{H}_0)$ is the values of magnetization that correspond to the angle ϕ , shown in Fig. 23.4 for the single crystal, at the point \tilde{H}_0 . The angle ϕ , shown in Fig. 23.4, is defined through the angle φ , shown in Fig. 23.12, by the relation $\phi = \varphi - \varphi_H$,

Fig. 23.12 The position of a single crystal in a polycrystal



where φ is the angle between the vector \mathbf{k}_1 and the vector \mathbf{q}_2 and φ_H is the angle between the vector \mathbf{H}_0 and the vector \mathbf{k}_1 . The angle φ defines the position of the single crystal in polycrystal and φ_H defines the direction in which the vector of the external magnetic field \mathbf{H}_0 acts with respect to the polycrystal. The relation (23.43) describes the effect of the magnetization of single crystals for the angles ϕ belonging to the segment $[\phi_1, \phi_2]$ on the magnetization of a polycrystal, which corresponds to the unit of the angle ϕ .

For isotropic polycrystal relation (23.43) takes the form

$$m(\tilde{H}_0) = \left(\int_0^{2\pi} \tilde{m}(\phi, \tilde{H}_0) d\phi \right) / \left(\int_0^{2\pi} d\phi \right). \tag{23.44}$$

It is easy to see that this expression remains valid for any choice of φ_H . Indeed, let's choose any φ_H from the closed segment $[0, 2\pi]$ and fix it. Taking into account that $0 \leq \varphi \leq 2\pi$, we have:

$$\begin{aligned} &\text{if } \varphi_H \geq \varphi, \text{ then } 0 \leq \varphi \leq \varphi_H \text{ and } -\varphi_H \leq \phi \leq 0, \\ &\text{if } \varphi_H \leq \varphi, \text{ then } \varphi_H \leq \varphi \leq 2\pi \text{ and } 0 \leq \phi \leq 2\pi - \varphi_H, \\ &\text{and as a result } -\varphi_H \leq \phi \leq 2\pi - \varphi_H. \end{aligned}$$

In such case expression (23.43) for isotropic material takes a form

$$m(\tilde{H}_0) = \left(\int_{-\varphi_H}^{2\pi-\varphi_H} \tilde{m}(\phi, \tilde{H}_0) d\phi \right) / \left(\int_{-\varphi_H}^{2\pi-\varphi_H} d\phi \right) \tag{23.45}$$

and is a complete analogue of the equation (23.44). Since the established connection between (23.44) and (23.45) is valid for any φ_H , the relation (23.44) does not depend on φ_H .

Let's go back to the expression (23.43). Dividing the segment $[\phi_1, \phi_2]$ into n equal parts and believing \tilde{m} as a constant on each such part, we obtain from (23.43)

$$m(\tilde{H}_0) = \frac{1}{n} \sum_{j=1}^n \tilde{m}(\varphi_j - \varphi_H, \tilde{H}_0). \tag{23.46}$$

We consider three types of polycrystalline samples: isotropic polycrystal, texture-oriented polycrystal—structure 1 and texture-oriented polycrystal—structure 2.

It is assumed that an isotropic polycrystal consists of 17 twinned single crystals of the same volume located at angles $\varphi_j = 0^\circ, \dots, 90^\circ$ between the axis \mathbf{q}_2 of the single crystals and the vector \mathbf{k}_1 of the general coordinate system (see Fig. 23.12). The magnetization curves corresponding to these 17 positions are shown in Fig. 23.11 and are used to construct the magnetization curve for isotropic polycrystal. Let's show that such a change in the angle of φ is quite enough.

In connection with what is said in the paragraphs after Table 23.2,

$$\begin{aligned} \tilde{m}(2\pi - \phi_j, \tilde{H}_0) &= \tilde{m}(-\phi_j, \tilde{H}_0) = \tilde{m}(\phi_j, \tilde{H}_0), & \tilde{m}(\pi - \phi_j, \tilde{H}_0) &= \tilde{m}(\phi_j, \tilde{H}_0), \\ \tilde{m}(\pi + \phi_j, \tilde{H}_0) &= \tilde{m}(\phi_j, \tilde{H}_0), & \text{where } \phi_j &= \varphi_j - \varphi_H, \quad 0 \leq \phi_j \leq \pi/2. \end{aligned} \quad (23.47)$$

Let's represent (23.46) for an isotropic material in the form

$$\begin{aligned} m(\tilde{H}_0) &= \frac{1}{4n} \left[\sum_{j=1}^n \tilde{m}(\phi_j, \tilde{H}_0) + \sum_{j=1}^n \tilde{m}(\pi - \phi_j, \tilde{H}_0) + \right. \\ &\quad \left. + \sum_{j=1}^n \tilde{m}(\pi + \phi_j, \tilde{H}_0) + \sum_{j=1}^n \tilde{m}(2\pi - \phi_j, \tilde{H}_0) \right], \end{aligned}$$

where ϕ_j in each sum varies from 0° to 90° . This expression takes into account the uniform distribution of the direction of the \mathbf{q}_2 vector of single crystals along a circle from 0° to 360° , which must be performed for an isotropic polycrystal. Then, in accordance with (23.47), we will have four identical sums in square brackets and this expression will eventually take the following form for an isotropic material at the value $n = 17$ given above:

$$m(\tilde{H}_0) = \frac{1}{17} \sum_{j=1}^{17} \tilde{m}(\phi_j, \tilde{H}_0), \quad \text{where } 0 \leq \phi_j \leq \pi/2,$$

and it will be the simplest when $\varphi_H = 0$:

$$m(\tilde{H}_0) = \frac{1}{17} \sum_{j=1}^{17} \tilde{m}(\varphi_j, \tilde{H}_0). \quad (23.48)$$

Here $\tilde{m}(\varphi_j, \tilde{H}_0)$ is the values of magnetization at the point \tilde{H}_0 for the curve shown in Fig. 23.11 that correspond to the angle ϕ_j at which the external magnetic field acts on the calculated domain for the single crystal. We use expression (23.48) to construct the magnetization curve of an isotropic polycrystal, shown in Fig. 23.13.

There is a predominant direction of martensitic structures orientation for textured polycrystals. It is assumed that the structure 1 consists of 3 twinned single crystals and the structure 2 consists of 5 twinned single crystals of the same volume. These twinned crystals are located at angles $\varphi_j = 40.11^\circ, 45.84^\circ, 51.57^\circ$ for the structure 1 and $\varphi_j = 34.38^\circ, 40.11^\circ, 45.84^\circ, 51.57^\circ, 57.30^\circ$ for the structure 2 between the vectors \mathbf{q}_2 of the twinned single crystals and \mathbf{k}_1 of the general coordinate system.

Remark This arrangement of twin crystals is not randomly chosen. The sets of single-twin crystals, differently located in the space for the structure 1 and the structure 2, are grouped around a crystal whose angle φ is about 45° . This means that

for this crystal one element of the twin has the axis e_1 directed against the vector k_1 , and the other element of the twin has the axis e_2 directed against the vector k_2 (see Fig. 23.12). If an external magnetic field is applied along the axis k_1 and reaches a value of $\tilde{H}_0 \approx 0.4$ (see Table 23.2), this crystal will detwinned and the element, which was directed along the vector $-k_2$, will be directed along the vector k_1 . As a result, the magnetization in this crystal in the direction of the vector k_1 will increase by a jump. In addition, as it was shown above, detwinning process causes in this crystal a structural strain and in the direction of the vector k_1 its value is $e^{11} \approx 0.06$. The values of $\tilde{H}_0 \approx 0.4$ and $e^{11} \approx 0.06$ will be the control values for the magnetic and deformed behavior of the structures 1 and 2 under the action of an external magnetic field in the direction of the vector k_1 . Detwinning of other crystals in these structures under the action of a field in the same direction causes the same elongation as in the above case, but in a direction other than k_1 . This, in accordance with (23.40), will reduce the value of \tilde{m} compared to the previous case and this decrease will be stronger the stronger the angle φ_j will differ from 45° . As a result, the jump in the average value of magnetization, determined by the relation (23.43), should be less for structure 2 compared to structure 1, since the structure 2 is the structure 1, expanded by the two elements most distant from the element defined by an angle of 45° .

The magnetization curve for the above anisotropic structures is described by the expression

$$m(\tilde{H}_0) = \frac{1}{n} \sum_{j=1}^n \tilde{m}(\varphi_j - \varphi_H, \tilde{H}_0),$$

where $n = 3$ for the structure 1 and $n = 5$ for the structure 2, φ_H is the angle in the xy plane between the vectors H_0 and k_1 , $\tilde{m}(\varphi_j - \varphi_H, \tilde{H}_0)$ is the values of magnetization at the point \tilde{H}_0 for the curve shown in Fig. 23.11 that correspond to the angle $\varphi_j - \varphi_H$ at which the external magnetic field acts on the calculated domain for the single crystal. By applying an external magnetic field along the k_1 vector ($\varphi_H = 0$) and in the direction of 45° to this axis ($\varphi_H = 45^\circ$), we construct curves for an anisotropic polycrystalline material of structures 1 and 2 (see Fig. 23.13).

The solid lines in Fig. 23.13 show the curves for such polycrystals when an external magnetic field is applied along the k_1 vector of these polycrystals. The dashed lines show the magnetization curves for textured polycrystals when a magnetic field is applied at an angle of 45° to the vector k_1 (for an isotropic polycrystal, the magnetization curve completely coincided with the curve corresponding to the field acting along the k_1 vector).

When the external magnetic field is applied along the vector k_1 (the solid lines) the curves for anisotropic structures 1 and 2 have jumps in the region $\tilde{H}_0 = 0.4$. At that, the jump for structure 1 is greater than the jump for structure 2. All this is in full accordance with what was said above in the *Remark*. If for structures 1 and 2 detwinning occurs simultaneously in all single crystals that make up these structures, then in an isotropic material detwinning occurs sequentially in single crystals with an increase in the external magnetic field, since the intensity of this field is not

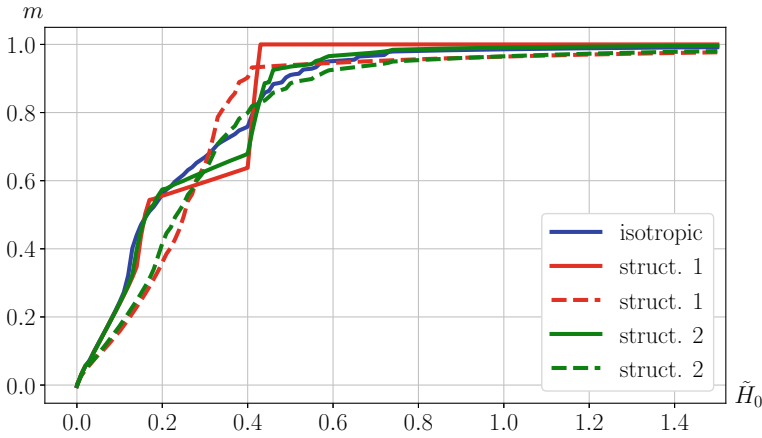


Fig. 23.13 Magnetization curves for different polycrystals

enough for simultaneous detwinning in all crystals. At a given time, detwinning occurs only in those crystals, position of which and field strength in which satisfy the conditions of Table 23.2. For this reason, the curve for an isotropic material in Fig. 23.13 (blue solid line) consists of a series of small jumps in magnetization in the interval $0.4 \leq \tilde{H}_0 \leq 0.7$.

If an external magnetic field is applied at an angle of 45° to the vector \mathbf{k}_1 , then, as will be shown below, detwinning does not occur in structures 1 and 2 and there are no jumps on the curves in Fig. 23.13 (dashed lines). The magnetization curves for these textured polycrystals differ depending on the direction of the applied magnetic field, because such polycrystals are anisotropic.

Let us now define the deformed state that occurs in isotropic and anisotropic (structures 1 and 2) polycrystalline materials in the detwinning process. As it defined at the end of the previous subsection, the deformations arising in detwinning process are represented in the basis $\mathbf{e}_1, \mathbf{e}_2$ as

$$\mathbf{e} = e^{11} \mathbf{e}_1 \mathbf{e}_1 + e^{22} \mathbf{e}_2 \mathbf{e}_2 + e^{12} (\mathbf{e}_1 \mathbf{e}_2 + \mathbf{e}_2 \mathbf{e}_1) \tag{23.49}$$

and have components (see (23.42))

$$e^{11} = 0.06 \Gamma(\phi, \tilde{H}_0), \quad e^{22} = -0.06 \Gamma(\phi, \tilde{H}_0), \quad e^{12} = 0.00. \tag{23.50}$$

In the basis of polycrystal $\mathbf{k}_1, \mathbf{k}_2$ (see Fig. 23.12), the tensor (23.49) has the form

$$\mathbf{e} = E^{11} \mathbf{k}_1 \mathbf{k}_1 + E^{22} \mathbf{k}_2 \mathbf{k}_2 + E^{12} (\mathbf{k}_1 \mathbf{k}_2 + \mathbf{k}_2 \mathbf{k}_1) \tag{23.51}$$

and from the equality of tensors in (23.49) and (23.51) we conclude that $E^{kp} = e^{ij} (\mathbf{e}_i \cdot \mathbf{k}_k)(\mathbf{e}_j \cdot \mathbf{k}_p)$ or, given that $e^{12} = 0$ for any case of detwinning process (see

(23.50)),

$$\begin{aligned}
 E^{11} &= e^{11} (\mathbf{e}_1 \cdot \mathbf{k}_1)(\mathbf{e}_1 \cdot \mathbf{k}_1) + e^{22} (\mathbf{e}_2 \cdot \mathbf{k}_1)(\mathbf{e}_2 \cdot \mathbf{k}_1), \\
 E^{22} &= e^{11} (\mathbf{e}_1 \cdot \mathbf{k}_2)(\mathbf{e}_1 \cdot \mathbf{k}_2) + e^{22} (\mathbf{e}_2 \cdot \mathbf{k}_2)(\mathbf{e}_2 \cdot \mathbf{k}_2), \\
 E^{12} &= e^{11} (\mathbf{e}_1 \cdot \mathbf{k}_1)(\mathbf{e}_1 \cdot \mathbf{k}_2) + e^{22} (\mathbf{e}_2 \cdot \mathbf{k}_1)(\mathbf{e}_2 \cdot \mathbf{k}_2).
 \end{aligned}
 \tag{23.52}$$

From Fig. 23.12 we have

$$\begin{aligned}
 \mathbf{e}_1 \cdot \mathbf{k}_1 &= -\cos(\varphi - 45^\circ), & \mathbf{e}_1 \cdot \mathbf{k}_2 &= -\sin(\varphi - 45^\circ), \\
 \mathbf{e}_2 \cdot \mathbf{k}_1 &= \sin(\varphi - 45^\circ), & \mathbf{e}_2 \cdot \mathbf{k}_2 &= -\cos(\varphi - 45^\circ)
 \end{aligned}$$

and then expressions in (23.52) take a view

$$\begin{aligned}
 E^{11} &= e^{11} \cos^2(\varphi - 45^\circ) + e^{22} \sin^2(\varphi - 45^\circ), \\
 E^{22} &= e^{11} \sin^2(\varphi - 45^\circ) + e^{22} \cos^2(\varphi - 45^\circ), \\
 E^{12} &= e^{11} \sin(\varphi - 45^\circ) \cos(\varphi - 45^\circ) - e^{22} \sin(\varphi - 45^\circ) \cos(\varphi - 45^\circ)
 \end{aligned}$$

or, given that $\cos^2 \alpha = [1 + \cos(2\alpha)]/2$, $\sin^2 \alpha = [1 - \cos(2\alpha)]/2$, $\sin \alpha \cos \alpha = (1/2) \sin(2\alpha)$,

$$\begin{aligned}
 E^{11} &= \frac{1}{2} (e^{11} + e^{22}) + \frac{1}{2} (e^{11} - e^{22}) \sin(2\varphi), \\
 E^{22} &= \frac{1}{2} (e^{11} + e^{22}) - \frac{1}{2} (e^{11} - e^{22}) \sin(2\varphi), \\
 E^{12} &= -\frac{1}{2} (e^{11} - e^{22}) \cos(2\varphi)
 \end{aligned}$$

and, considering (23.50), we obtain

$$\begin{aligned}
 E^{11}(\phi, \varphi, \tilde{H}_0) &= 0.06 \Gamma(\phi, \tilde{H}_0) \sin(2\varphi), & E^{22}(\phi, \varphi, \tilde{H}_0) &= -0.06 \Gamma(\phi, \tilde{H}_0) \sin(2\varphi), \\
 E^{12}(\phi, \varphi, \tilde{H}_0) &= -0.06 \Gamma(\phi, \tilde{H}_0) \cos(2\varphi).
 \end{aligned}
 \tag{23.53}$$

As explained earlier, $\phi = \varphi - \varphi_H$ (see the explanation after the relation (23.43)).

The relations (23.53) allow us to construct the deformed state that occurs in an isotropic or anisotropic polycrystal during the detwinning process in single crystals. To do this, we use a relation similar to (23.43),

$$\hat{E}^{ij}(\varphi_H) = \left(\int_{\varphi_1}^{\varphi_2} E^{ij}(\phi, \varphi, \tilde{H}_0) d\varphi \right) / \left(\int_{\varphi_1}^{\varphi_2} d\varphi \right). \tag{23.54}$$

Dividing here the segment $[\varphi_1, \varphi_2]$ into n equal parts, $\Delta\varphi = (\varphi_2 - \varphi_1)/n$, believing that $\varphi_j = \varphi_1 + (j + 0.5) \Delta\varphi$, calculating E^{ij} in these points and assuming it a constant on each such part, we obtain

$$\hat{E}^{ij}(\varphi_H) = \frac{1}{n} \sum_{j=0}^{n-1} E^{ij}(\varphi_j - \varphi_H, \varphi_j, \tilde{H}_0). \tag{23.55}$$

The expression (23.55) will be convenient for us to use for anisotropic material in some cases.

For the isotropic material we use the relation (23.54). Let's consider the cases when an external magnetic field with strengths of $\tilde{H}_0 = 0.46$ and $\tilde{H}_0 = 1.0$ is applied at angles of $\varphi_H = 0^\circ$ and $\varphi_H > 0^\circ$. Then, for $\varphi_H = 0^\circ$, $\phi = \varphi - \varphi_H = \varphi$ and in accordance with (23.42) and the Table 23.2 we have for $\tilde{H}_0 = 0.46$ that

$$\Gamma(\varphi) = \begin{cases} 0 & \text{if } 0 \leq \varphi \leq \alpha_1 \\ 1 & \text{if } \alpha_1 \leq \varphi \leq \alpha_2 \\ 0 & \text{if } \alpha_2 \leq \varphi \leq \pi/2 \end{cases}, \quad \Gamma(\varphi) = - \begin{cases} 0 & \text{if } \pi/2 \leq \varphi \leq \pi - \alpha_2 \\ 1 & \text{if } \pi - \alpha_2 \leq \varphi \leq \pi - \alpha_1 \\ 0 & \text{if } \pi - \alpha_1 \leq \varphi \leq \pi \end{cases},$$

$$\Gamma(\varphi) = \begin{cases} 0 & \text{if } \pi \leq \varphi \leq \pi + \alpha_1 \\ 1 & \text{if } \pi + \alpha_1 \leq \varphi \leq \pi + \alpha_2 \\ 0 & \text{if } \pi + \alpha_2 \leq \varphi \leq 3\pi/2 \end{cases}, \quad \Gamma(\varphi) = - \begin{cases} 0 & \text{if } 3\pi/2 \leq \varphi \leq 2\pi - \alpha_2 \\ 1 & \text{if } 2\pi - \alpha_2 \leq \varphi \leq 2\pi - \alpha_1 \\ 0 & \text{if } 2\pi - \alpha_1 \leq \varphi \leq 2\pi \end{cases},$$

where, as it follows from Table 23.2, $\alpha_1 = 40^\circ$, $\alpha_2 = 63.03^\circ$. With this in mind and substituting (23.53) into (23.54) we get

$$\hat{E}^{11} = \frac{0.06}{2\pi} \left(\int_{\alpha_1}^{\alpha_2} \sin(2\varphi) d\varphi - \int_{\pi-\alpha_2}^{\pi-\alpha_1} \sin(2\varphi) d\varphi + \int_{\pi+\alpha_1}^{\pi+\alpha_2} \sin(2\varphi) d\varphi - \int_{2\pi-\alpha_2}^{2\pi-\alpha_1} \sin(2\varphi) d\varphi \right). \quad (23.56)$$

It is easy to show that each of the last three integrals with their signs is equal to the first integral. As a result

$$\hat{E}^{11} = 2 \frac{0.06}{\pi} \int_{\alpha_1}^{\alpha_2} \sin(2\varphi) d\varphi = \frac{0.06}{\pi} [\cos(2\alpha_1) - \cos(2\alpha_2)]. \quad (23.57)$$

Substituting the above values of angles here, we get for $\varphi_H = 0^\circ$ and $\tilde{H}_0 = 0.46$ that $\hat{E}^{11} = 0.015$ and, as it follows from (23.53), that $\hat{E}^{22} = -0.015$. It also follows from (23.53) that \hat{E}^{12} is represented in the case under consideration as (23.56) with the replacement of the sine by the cosine and the addition of a minus sign before the entire expression. It is easy to show that the terms in the obtaining expression are mutually destroyed under any α_1 and α_2 and as a result $\hat{E}^{12} = 0$.

If now $\tilde{H}_0 = 1.0$, then, in accordance with Table 23.2, we have for $\varphi_H = 0^\circ$ that $\alpha_2 = \pi/2$ in the expression (23.56) for \hat{E}^{11} and as a result, $\hat{E}^{11} = 0.022$, $\hat{E}^{22} = -0.022$, $\hat{E}^{12} = 0$. The increase in the modulus of these components with the increasing the external magnetic field is explained by the inclusion of additional regions in detwinning process (see Table 23.2). The expression for $\Gamma(\varphi)$ which will

not be quite correct in this case, it is clear how to convert, but having the relation (23.56), it is now not necessary.

For $\varphi_H > 0^\circ$, $\phi = \varphi - \varphi_H$ and in accordance with (23.42) and the Table 23.2 we have for $\tilde{H}_0 = 0.46$ that

$$\Gamma(\varphi) = \begin{cases} 1 & \text{if } \varphi_H + \alpha_1 \leq \varphi \leq \varphi_H + \alpha_2 \\ -1 & \text{if } \pi + \varphi_H - \alpha_2 \leq \varphi \leq \pi + \varphi_H - \alpha_1 \\ 1 & \text{if } \pi + \varphi_H + \alpha_1 \leq \pi + \varphi_H + \alpha_2 \\ -1 & \text{if } \pi + \varphi_H - \alpha_2 \leq \pi + \varphi_H - \alpha_1 \end{cases},$$

and $\Gamma(\varphi) = 0$ for all other φ . Then, equation (23.54), in view of the relations (23.53), takes for \hat{E}^{11} the form

$$\hat{E}^{11} = \frac{0.06}{2\pi} \left(\int_{\varphi_H + \alpha_1}^{\varphi_H + \alpha_2} \sin(2\varphi) d\varphi - \int_{\pi + \varphi_H - \alpha_2}^{\pi + \varphi_H - \alpha_1} \sin(2\varphi) d\varphi + \int_{\pi + \varphi_H + \alpha_1}^{\pi + \varphi_H + \alpha_2} \sin(2\varphi) d\varphi - \int_{2\pi + \varphi_H - \alpha_2}^{2\pi + \varphi_H - \alpha_1} \sin(2\varphi) d\varphi \right). \tag{23.58}$$

It is easy to show that this equality can be represented as

$$\hat{E}^{11} = \frac{0.06}{\pi} \left(\int_{\alpha_1}^{\alpha_2} \sin(2\varphi + 2\varphi_H) d\varphi + \int_{\alpha_1}^{\alpha_2} \sin(2\varphi - 2\varphi_H) d\varphi \right),$$

or as

$$\hat{E}^{11} = \frac{0.06}{\pi} \int_{\alpha_1}^{\alpha_2} [\sin(2\varphi + 2\varphi_H) + \sin(2\varphi - 2\varphi_H)] d\varphi,$$

or at last, given that $\sin A + \sin B = 2 \sin \frac{A+B}{2} \cos \frac{A-B}{2}$, as

$$\hat{E}^{11}(\varphi_H) = 2 \frac{0.06}{\pi} \cos(2\varphi_H) \int_{\alpha_1}^{\alpha_2} \sin(2\varphi) d\varphi. \tag{23.59}$$

As it follows from (23.53) $\hat{E}^{22} = -\hat{E}^{11}$ and \hat{E}^{12} is represented in the case under consideration as (23.58) with the replacement of the sine by the cosine and the addition of a minus sign before the entire expression

$$\hat{E}^{12} = -\frac{0.06}{2\pi} \left(\int_{\varphi_H + \alpha_1}^{\varphi_H + \alpha_2} \cos(2\varphi) d\varphi - \int_{\pi + \varphi_H - \alpha_2}^{\pi + \varphi_H - \alpha_1} \cos(2\varphi) d\varphi + \int_{\pi + \varphi_H + \alpha_1}^{\pi + \varphi_H + \alpha_2} \cos(2\varphi) d\varphi - \int_{2\pi + \varphi_H - \alpha_2}^{2\pi + \varphi_H - \alpha_1} \cos(2\varphi) d\varphi \right).$$

This equality is reduced to

$$\hat{E}^{12} = \frac{0.06}{\pi} \int_{\alpha_1}^{\alpha_2} [\cos(2\varphi + 2\varphi_H) - \cos(2\varphi - 2\varphi_H)] d\varphi,$$

or, given that $\cos A - \cos B = 2 \sin \frac{A+B}{2} \sin \frac{B-A}{2}$, to

$$\hat{E}^{12}(\varphi_H) = 2 \frac{0.06}{\pi} \sin(2\varphi_H) \int_{\alpha_1}^{\alpha_2} \sin(2\varphi) d\varphi. \quad (23.60)$$

Relations (23.59) and (23.60) are the general expressions that defines the components of the strain tensor that occurs in an isotropic material with the shape memory when it is detwinned. The magnitudes of these components depend both on the magnitude of the applied external magnetic field, which in accordance with Table 23.2 determines the value of the angle α_2 , and on the direction of this field action (from the angle φ_H). As it follows from Table 23.2, $\alpha_2 = 63.03^\circ$ when $\tilde{H}_0 = 0.46$ and $\alpha_2 = 90^\circ$ when $\tilde{H}_0 = 1.00$. At the same time the angle α_1 remains unchanged, $\alpha_1 = 40^\circ$. When $\varphi_H = 0$ expression (23.59) is exactly the same as (23.57) and from the expression (23.60) it follows that $\hat{E}^{12} = 0$ as it was noted earlier. Although the components of the strain tensor in the orthonormal basis k_i (see Fig. 23.12) depend on the angle φ_H between vectors k_1 and H_0 , in the orthonormal basis γ_i in which vector γ_1 is directed along the vector H_0 , these components remain unchanged. This can easily be shown in the same way as the relationship was shown between e^{ij} and E^{kp} in the expressions (23.49) and (23.51). Therefore, the such material is called isotropic.

Let us now consider the deformed state of an anisotropic material with shape memory when it is detwinned. We assume that twinned single crystals of the same volume are continuously distributed in a polycrystal at $\varphi_1 \leq \varphi \leq \varphi_2$ and the external magnetic field is applied at an angle φ_H . We will consider two special cases of textured polycrystals for which magnetization curves were above constructed: the structure 1 when $\varphi_1 = 40.11^\circ$ and $\varphi_2 = 51.57^\circ$, and the structure 2 when $\varphi_1 = 34.38^\circ$ and $\varphi_2 = 57.30^\circ$. For these two cases we present an algorithm for determining the deformed state during the dissipation of twins (during detwinning) for the two angles φ_H of the action of an external magnetic field: $\varphi_H = 0$ and $\varphi_H = 45^\circ$, and two \tilde{H} : $\tilde{H}_0 = 0.46$ and $\tilde{H}_0 = 1.00$. The deformed state during detwinning for any

other case of anisotropy and the direction of action of the external magnetic field can be determined in accordance with this algorithm.

So, we analyze the deformation behavior of structure 1 at $\varphi_H = 0$, $\tilde{H}_0 = 0.46$. (1) Since $\phi = \varphi - \varphi_H$ then $\phi = \varphi$ and $\varphi_1 \leq \phi \leq \varphi_2$ where $\varphi_1 = 40.11^\circ$ and $\varphi_2 = 51.57^\circ$. (2) Such a change in ϕ corresponds to the first line in (23.42). As a result, we have $\Gamma(\phi, \tilde{H}_0) = H(0.46 - \tilde{H}_0^{cr}(\phi))$. (3) As it follows from Table 23.2, $\Gamma = 1$ for $\tilde{H}_0 = 0.46$ if $\phi = \varphi \in U$ where the set $U = [40^\circ, 63.03^\circ]$. Since for structure 1 $\varphi \in U_1$ where the set $U_1 = [40.11^\circ, 51.57^\circ]$ then it follows from the intersection of the sets U and U_1 , $U \cap U_1$, that $\varphi_1 = 40.11^\circ$ and $\varphi_2 = 51.57^\circ$. (4) As a result of the above, we obtain from the expressions (23.53) and (23.54) that

$$\hat{E}^{11} = a S, \quad \hat{E}^{22} = -a S, \quad \hat{E}^{12} = -a C, \tag{23.61}$$

$$a = 0.06/(\varphi_2 - \varphi_1), \quad S = \int_{\varphi_1}^{\varphi_2} \sin(2\varphi) d\varphi, \quad C = \int_{\varphi_1}^{\varphi_2} \cos(2\varphi) d\varphi$$

and for structure 1, $\varphi_H = 0$, $\tilde{H}_0 = 0.46$ the detwinning strain tensor has the following components in the basis k_i (see Fig. 23.12): $\hat{E}^{11} = 0.06$, $\hat{E} = -0.06$, $\hat{E}^{12} = 0.0017$.

Now, we analyze the deformation behavior of structure 1 at $\varphi_H = 0$, $\tilde{H}_0 = 1.00$. Everything that is said in item (1) of the previous case remains unchanged here. In accordance with item (2) $\Gamma(\phi, \tilde{H}_0) = H(1.00 - \tilde{H}_0^{cr}(\phi))$ and with item (3) the set U for $\tilde{H}_0 = 1.00$ has the form $U = [40^\circ, 90^\circ]$. Since the set U_1 remains unchanged, then the set that is the intersection of sets U and U_1 remains unchanged too. As a result, the angles φ_1 and φ_2 are the same as in the previous case and from item (4) we have the same components of the detwinning strain tensor as above.

If the external magnetic field acts on structure 1 at an angle $\varphi_H = 45^\circ$ then $\phi = \varphi - \varphi_H$ will be change, given that $\varphi \in U_1$ where the set $U_1 = [40.11^\circ, 51.57^\circ]$, in the interval $\phi \in [-4.89^\circ, 6.57^\circ]$ what corresponds to the first and fourth areas of change of ϕ in the expression (23.42): $\phi \in [0^\circ, 6.57^\circ]$ and $\phi \in [355.11^\circ, 360^\circ]$. Since $\tilde{H}_0^{cr}(\zeta) = \infty$, if $0^\circ \leq \zeta \leq 40^\circ$, where $\zeta = \phi$ for the first area and $\zeta = 2\pi - \phi$ for the second area, then $\Gamma = 0$ in the any of these cases and detwinning does not occur at any magnitude of the external magnetic field.

All of the above about the deformation behavior during the detwinning structure 1 at $\varphi_H = 0$ and $\tilde{H}_0 = 0.46$ remains valid for structure 2 with the replacement of the set U_1 by the set U_2 where the set $U_2 = [34.38^\circ, 57.30^\circ]$ is the set that describes the structure 2. The consequence of the intersection of the sets U and now U_2 (instead of U_1) will be the values of the angles $\varphi_1 = 40^\circ$ and $\varphi_2 = 57.30^\circ$ and, as a result, we obtain from the expressions (23.61) that $\hat{E}^{11} = 0.0586$, $\hat{E} = -0.0586$, $\hat{E}^{12} = 0.0075$.

By performing an analysis similar to that performed for structure 1 at $\varphi_H = 0$ and $\tilde{H}_0 = 1.00$, as well as at $\varphi_H = 45^\circ$, we obtain similar results for structure 2: at $\varphi_H = 0$ and $\tilde{H}_0 = 1.00$, the deformed state remains exactly the same as at $\varphi_H = 0$ and $\tilde{H}_0 = 0.46$, and at $\varphi_H = 45^\circ$, detwinning does not occur.

Table 23.3 Some results of the performed deformation analysis

| | $\varphi_H = 0$ | | $\varphi_H = 45^\circ$ | |
|-----------------------|----------------------|---------------------|------------------------|---------------------|
| | $\tilde{H}_0 = 0.46$ | $\tilde{H}_0 = 1.0$ | $\tilde{H}_0 = 0.46$ | $\tilde{H}_0 = 1.0$ |
| Isotrop., E^{11} | 0.015 | 0.022 | 0.015 | 0.022 |
| Structure 1, E^{11} | 0.06 | 0.06 | 0 | 0 |
| Structure 2, E^{11} | 0.0586 | 0.0586 | 0 | 0 |

The results of the deformation analysis carried out above are presented in Table 23.3. Here E^{11} is the average strain of elongation of the considered structure in the direction of the vector \mathbf{k}_1 (see Fig. 23.12) caused by the detwinning process (for an isotropic material, this vector can have any direction). As follows from this table, the detwinning of an isotropic material occurs sequentially and is determined by an increase in the strength of the applied external magnetic field. In structures 1 and 2, complete detwinning occurs when a field is applied along the vector \mathbf{k}_1 already at $\tilde{H}_0 = 0.46$ and the value of E^{11} for the first structure is greater than that of the second. When the field is applied at an angle of 45° to the vector \mathbf{k}_1 , the detwinning does not occur at any external field strength.

The results of the deformation analysis fully correspond to the explanations given above in the *Remark* and when discussing the curves in Fig. 23.13.

23.6 Conclusion

Within the framework of the theory of micromagnetism, the problem of magnetization of a single-twinned martensitic crystal of the Ni_2MnGa alloy with shape memory by the finite element method was solved. The dynamics of the magnetic process was described by the Landau–Lifshitz–Gilbert equation, for which, as for other differential equations and boundary conditions of the theory of micromagnetism, variational equations were put in correspondence. This made it possible to reduce the requirements for the smoothness of the problem solution. Magnetization curves were plotted for various angles of application of the magnetic field to the anisotropy axes of the twin variants.

A condition for the detwinning of a shape-memory ferromagnetic alloy in a magnetic field was proposed and the influence of the reorientation (detwinning) of the martensitic variants forming a twin on the magnetization of material and on the occurrence of the structural (detwinning) deformations in it were taken into account.

A change in the main mechanisms of magnetization, such as the movement and interaction of 180° magnetic domain walls, the rotation of the local magnetization vectors and the occurrence of the structural deformations connected with detwinning process, leads to kinks in the magnetization curves which occur at various values

of the external magnetic field depending on the direction of action of this magnetic field.

Based on the magnetization curves obtained for single crystal and deformation state which corresponds to detwinning state of such structure, the deformed states and the magnetization curves were constructed for various types of polycrystals (isotropic and textured) which are some structures from the single crystals. For texture-oriented polycrystals, the magnetization curves and deformation states differ depending on the direction of the applied magnetic field, because such polycrystals are anisotropic.

Acknowledgements This work was fulfilled under financial support of the Russian Foundation for Basic Research through Grant 20-01-00031. The author expresses his sincere thanks for these supports.

References

- Bachaga T, Zhang J, Khitouni M, Sunol JJ (2019) NiMn-based Heusler magnetic shape memory alloys: a review. *Int J Adv Manuf Technol* 103:2761–2772. 10.1007/s00170-019-03534-3
- Bhattacharya K (1991) Wedge-like microstructure in martensites. *Acta Metal Mater* 39(10):2431–2444. [http://dx.doi.org/10.1016/0956-7151\(91\)90023-T](http://dx.doi.org/10.1016/0956-7151(91)90023-T)
- Brown WF (1963) *Micromagnetics*. Interscience Publisher, New York, NY, USA
- Bustamante R, Dorfmann A, Ogden RW (2007) A nonlinear magnetoelastic tube under extension and inflation in an axial magnetic field: numerical solution. *J Eng Math* 59:139–153. <http://dx.doi.org/10.1007/s10665-006-9088-4>
- Casoli F, Varvaro G, Ghahfarokhi MT, Fabbri S, Albertini F (2020) Insight into the magnetisation process of martensitic Ni-Mn-Ga films: a micromagnetic and vector magnetometry study. *J Phys Mater* 3:045003. <https://doi.org/10.1088/2515-7639/abb0ee>
- Ge Y, Heczko O, Söderberg O, Lindroos VK (2004) Various magnetic domain structures in a Ni-Mn-Ga martensite exhibiting magnetic shape memory effect. *J Appl Phys* 96(4):2159–2163. <http://dx.doi.org/10.1063/1.1773381>
- Ge Y, Heczko O, Söderberg O, Hannula S-P, Lindroos VK (2005) Investigation of magnetic domains in Ni-Mn-Ga alloys with a scanning electron microscope. *Smart Mater Struct* 14(5):S211–S215. <http://dx.doi.org/10.1088/0964-1726/14/5/007>
- Haldar K, Kiefer B, Lagoudas DC (2011) Finite element analysis of the demagnetization effect and stress inhomogeneities in magnetic shape memory alloy samples. *Philos Mag* 91:4126–4157. <https://dx.doi.org/10.1080/14786435.2011.602031>
- Hane KF, Shield TW (1998) Symmetry and microstructure in martensites. *Philos Mag A* 78(6):1215–1252. <http://dx.doi.org/10.1080/01418619808239984>
- Heczko O, Jurek K, Ullakko K (2001) Magnetic properties and domain structure of magnetic shape memory Ni-Mn-Ga alloy. *J Magnetism Magn Mater* 226–230, 996–998. [http://dx.doi.org/10.1016/S0304-8853\(00\)01170-7](http://dx.doi.org/10.1016/S0304-8853(00)01170-7)
- Heczko O, Straka L (2003) Temperature dependence and temperature limits of magnetic shape memory effect. *J Appl Phys* 94(11):7139–7143. 10.1063/1.162 6800
- Heczko O (2005) Magnetic shape memory effect and magnetization reversal. *J Magnetism Magn Mater* 290–291, 787–794. <http://dx.doi.org/10.1016/j.jmmm.2004.11.397>
- Heczko O, Bradshaw V (2017) Magnetic domain structure and magnetically-induced reorientation in Ni-Mn-Ga magnetic shape memory alloy. *Acta Phys Pol A* 131(4):1063–1065. <http://dx.doi.org/10.12693/APhysPolA.131.1063>
- Kazaryan A, Wang Y (2002) Development of magnetic domains in hard ferromagnetic thin films of polytwinned microstructure. *J Appl Phys* 92:7408–7414. 10.1063/1.1522494

- Khan RAA, Ghomashchi R, Xie Z, Chen L (2018) Ferromagnetic shape memory Heusler materials: synthesis, microstructure characterization and magnetostructural properties. *Materials* 11:988. <https://doi.org/10.3390/ma11060988>
- Kumar SV, Vallalperuman K, Seenithurai S, Mahendran M (2012) Structural and magnetic characterization of martensitic Ni₂MnGa polycrystalline ferromagnetic shape memory alloy. *Elixir Magn Mater* 50:113920
- Lee N, Kim BJ, Huang MD, Lee YP, Rhee JY, Kudryavtsev YV (2004) Structural and temperature dependence of physical properties of Ni₂MnM (M=Al, Ga and In) Heusler alloys. *J Korean Phys Soc* 45(1):34–37
- Li Z, Yang B, Zou N, Zhang Y, Esling C, Gan W, Zhao X, Zuo L (2017) Crystallographic characterization on polycrystalline Ni-Mn-Ga alloys with strong preferred orientation. *Materials* 10:463. <http://dx.doi.org/10.3390/ma10050463>
- Mennerich C, Wendler F, Jainta M, Nestler B (2011) A phase-field model for the magnetic shape memory effect. *Arch Mech* 63(5–6):549–571
- Musabirov II, Mulyukov RR, Koledov VV (2015) Crystallographic texture and the preferential orientation of a martensite in the polycrystalline Ni_{2.08}Mn_{0.96}Ga_{0.96} alloy. *IOP Conf Ser Mater Sci Eng* 82:463. <http://dx.doi.org/10.1088/1757-899X/82/1/012064>
- Musabirov II, Mulyukov KY, Safarov IM (2012) Studies of the texture of a polycrystalline alloy ingot of the system Ni₂ MnGa. *Letts Mater* 2(3):157–160 (in Russian). <http://dx.doi.org/10.22226/2410-3535-2012-3-157-160>
- Planes A, Mañosa L, Acet M (2009) Magnetocaloric effect and its relation to shape-memory properties in ferromagnetic Heusler alloys. *J Phys: Condens Matter* 21:233201. <http://dx.doi.org/10.1088/0953-8984/21/23/233201>
- Rani RJ, Pandi RS, Seenithurai S, Kumar SV, Muthuraman M, Mahendran M (2011) Structural, thermal and magnetic characterization of Ni-Mn-Ga ferromagnetic shape memory alloys. *Am J Condens Matter Phys* 1:1–7. 10.5923/j.ajcmp.20110101.01
- Rogovoy AA (2020) A formalized approach to the construction of models of deformable solid mechanics. Part I. Basic relations of continuum mechanics, Perm, Ural branch of the Russian academy of sciences. <https://www.elibrary.ru/item.asp?id=44190094> (Rogovoy AA (2021) A formalized approach to the construction of models of deformable solid mechanics. Part I. Basic relations of continuum mechanics, 2nd edn. Moscow-Izhevsk: Institute of Computer Research) (in Russian)
- Rogovoy A, Stolbova O (2016) Modeling the magnetic field control of phase transition in ferromagnetic shape memory alloys. *Int J Plast* 85:130–155. 10.1016/j.ijplas.2016.07.006
- Rogovoy AA, Stolbov OV, Stolbova OS (2021a) The microstructural model of the ferromagnetic material behavior in an external magnetic field. *Magnetochemistry* 7:7. 10.3390/magnetochemistry7010007
- Rogovoy AA, Stolbova OS, Stolbov OV (2021b) Numerical simulation of evolution of magnetic microstructure in Heusler alloys. *J Appl Mech Technol Phys* 62(5):870–881. <http://dx.doi.org/10.1134/S0021894421050199>
- Rogovoy A, Stolbova O (2021) Comparison of two approaches for microstructural modeling of the ferromagnetic alloys behavior. *IEEE Magn Lett* 13:2500404. 10.1109/LMAG.2021.3127112
- Rogovoy AA, Stolbova OS (2022a) Microstructural modeling of the magnetization process in Ni₂ MnGa alloy polytwin crystals. *Magnetochemistry* 8:78. <https://doi.org/10.3390/magnetochemistry8080078>
- Rogovoy AA, Stolbova OS (2022b) Microstructural model of the behavior of a ferroalloy with shape memory in a magnetic field. *Mech Adv Mater Struct* (online publication). <https://doi.org/10.1080/15376494.2022.2114046>
- Solomon VC, McCartney MR, Smith DJ, Tang YJ, Berkowitz AE, O’Handley RC (2005) Magnetic domain configurations in spark-eroded ferromagnetic shape memory Ni-Mn-Ga particles. *Appl Phys Lett* 86(19):192503-1. <http://dx.doi.org/10.1063/1.1925319>
- Tickle R, James RD (1999) Magnetic and magnetomechanical properties of Ni₂ MnGa. *J Magnetism Magn Mater* 195:627–638. 10.1016/S0304-8853(99)002929

- Thomas M, Heczko O, Buschbeck J, Lai YW, McCord J, Kaufmann S, Schultz L, Föhle S (2009) Stray-field-induced actuation of free-standing magnetic shape-memory films. *Adv Mater* 21(36):3708–3711. <http://dx.doi.org/10.1002/adma.200900469>
- Truesdell C (1972) A first course in rational continuum mechanics. Johns Hopkins University Baltimore, Maryland
- Vasil'ev AN, Buchel'nikov VD, Takagi T, Kholvailo VV, Estrin EI (2003) Shape memory ferromagnets. *Uspekhi Fizicheskikh Nauk* 173(6):577–607 [*Phys-Uspekhi* 46(6):559–588]. <http://dx.doi.org/10.3367/UFNr.0173.200306a.0577>
- Velikohatny OI, Naumov II (1999) Electronic structure and instability of the compound Ni₂MnGa. *Solid State Phys* 41(4):684–690 (in Russian)
- Wan X-P, Wang K, Weinan E (2006) Simulations of 3-D domain wall structures in thin films. *Disc Cont Dyn Syst B* 6(2):373–389. <http://dx.doi.org/10.3934/dcdsb.2006.6.373>
- Zhang JX, Chen LQ (2005) Phase-field microelasticity theory and micromagnetic simulations of domain structures in giant magnetostrictive materials. *Acta Mater* 53:2845–2855. <https://dx.doi.org/10.1016/j.actamat.2005.03.002>

Chapter 24

Stability of Circular Sandwich Plate with Porous Core and Prestressed Uniform Coatings



Denis N. Sheydakov and Viacheslav A. Lyzhov

Abstract Within the framework of a general stability theory for three-dimensional bodies the buckling analysis is carried out for a three-layer circular plate under radial compression. The middle layer of the plate (core) is made of a highly porous material, and to describe its behavior the micropolar continuum model is used. The top and bottom layers (coatings) are made of classic non-polar materials. It is assumed that the coatings were attached to the porous core after preliminary deformations of radial tension-compression and contain internal stresses. When determining the subcritical state in the core and the coatings, writing of constitutive relations with respect to different reference configurations is used. For the physically linear material, the equations of neutral equilibrium are derived, which describes the behavior of the considered sandwich plate in a perturbed state. For a special case of axisymmetric perturbations the stability analysis of a circular sandwich plate with a porous core and prestressed uniform coatings is reduced to solving a linear homogeneous boundary value problem for a system of seven ordinary differential equations. It is also found that if top and bottom coatings are identical then the stability analysis can be reduced to solving two independent linear homogeneous boundary value problems for half of the sandwich plate.

Keywords Nonlinear elasticity · Deformation stability · Micropolar medium · Internal stresses · Sandwich plate · Porous core · Prestressed coating

24.1 Introduction

The problem of equilibrium stability for deformable bodies is of considerable interest from a practical point of view because the exhaustion of load-bearing capacity and the collapse of buildings and engineering structures quite often occur due to

D. N. Sheydakov (✉) · V. A. Lyzhov
Southern Scientific Centre of the Russian Academy of Sciences (SSC RAS), Chekhov Ave. 41,
344006 Rostov-on-Don, Russia
e-mail: sheidakov@mail.ru

© The Author(s), under exclusive license to Springer Nature Switzerland AG 2023
H. Altenbach and V. Eremeyev (eds.), *Advances in Linear and Nonlinear Continuum and Structural Mechanics*, Advanced Structured Materials 198,
https://doi.org/10.1007/978-3-031-43210-1_24

443

the buckling under external loads. The stability of classical elastic bodies has been extensively studied (Fu and Ogden 1999; Pignataro et al. 1991; Timoshenko and Gere 2009; Volmir 1970). However, due to the development of modern technologies and the emergence of new materials, the buckling analysis for bodies with a complex microstructure and internal stresses is becoming quite relevant. Particularly, in recent decades, various constructions made of highly porous materials such as metal and polymer foams (Ashby et al. 2000; Banhart 2000; Degischer and Kriszt 2002; Gibson and Ashby 1997) have become widely used in the aerospace and automotive industries. This is due to a number of their advantages: low weight, high specific strength, excellent possibilities to absorb energy, etc. As a rule, these constructions have a sandwich structure—a foam core is covered by hard and stiff shells (coatings). The latter are necessary for corrosion and thermal protection, as well as optimization of mechanical properties under loading. In addition, coatings often contain internal stresses, which can be both a side effect of the assembly process due to the plastic strains, heating, phase transitions, etc., and a required functional property.

The present paper is dedicated to studying the stability of nonlinearly elastic sandwich plates with a highly porous core and prestressed uniform coatings. First, it should be noted that the behavior of porous materials quite often cannot be adequately described within the framework of the classical elasticity theory due to the absence of internal size parameters. One approach to account for the microstructure influence is to use the model of a micropolar continuum (Cosserat continuum) (Altenbach et al. 2010; Cosserat and Cosserat 1909; Eringen 1999; Kafadar and Eringen 1971; Maugin 1998; Toupin 1964), i.e., medium with couple stresses and rotational degrees of freedom. It allows, in particular, describing the size effects observed experimentally for porous materials (Diebels 1999; Diebels and Steeb 2002; Lakes 1986, 1995). Next, a distinctive feature of sandwich plates with prestressed coatings is the lack of a unified natural (stress-free) reference configuration. For this reason, when deriving the governing equations for different parts of a sandwich plate, the writing of the constitutive relations with respect to different reference configurations is used (Eremeev and Zubov 2017; Merodio and Ogden 2016; Merodio et al. 2013; Zubov 2019). Given the above, we studied the bifurcation of equilibrium for a quite common structural element—a circular sandwich plate with a porous core and prestressed coatings. The static Euler method was used for the stability analysis. Within this method, the critical values of loading parameters are determined from the condition of existence for non-trivial solutions of a linearized boundary value problem.

24.2 Circular Sandwich Plate

We consider a three-layer circular plate of radius r_0 and thickness H . The middle layer of the plate (core) of thickness $2h$ is made of a highly porous material, and to describe its behavior the micropolar continuum model is used. The top and bottom layers (coatings) are formed from the circular panels made of classic non-polar materials. These panels are attached to the porous core after their preliminary

deformation. We assume that the coatings experienced initial deformations of radial tension-compression, described by the following relations (hereinafter, the superscripts “+” and “-” will denote the quantities related to the top coating and the bottom coating, respectively) (Lurie 1990; Sheydaikov 2013):

$$\begin{aligned} r &= a^\pm \rho^\pm, \quad 0 \leq \rho^\pm \leq \rho_0^\pm, \quad a^\pm \rho_0^\pm = r_0; \quad \varphi = \theta^\pm, \quad 0 \leq \theta^\pm \leq 2\pi; \\ z &= c^\pm \zeta^\pm + z_0^\pm, \quad 0 \leq \zeta^\pm \leq \zeta_0^\pm, \quad z_0^- = -c^- \zeta_0^- - h, \quad z_0^+ = h; \end{aligned} \quad (24.1)$$

$$\mathbf{C}_0^\pm = a^\pm \mathbf{e}_\rho^\pm \otimes \mathbf{e}_r + a^\pm \mathbf{e}_\theta^\pm \otimes \mathbf{e}_\varphi + c^\pm \mathbf{e}_\zeta^\pm \otimes \mathbf{e}_z, \quad (24.2)$$

where $\rho^\pm, \theta^\pm, \zeta^\pm$ and $\rho^-, \theta^-, \zeta^-$ are the cylindrical coordinates in natural reference configurations χ^+ and χ^- of circular panels acting as the top and bottom coatings, ρ_0^\pm, ζ_0^\pm and ρ_0^-, ζ_0^- are the radii and the thicknesses of these panels before the deformation; r, φ, z are the cylindrical coordinates in a prestressed state χ ; $\{\mathbf{e}_\rho^+, \mathbf{e}_\theta^+, \mathbf{e}_\zeta^+\}$, $\{\mathbf{e}_\rho^-, \mathbf{e}_\theta^-, \mathbf{e}_\zeta^-\}$ and $\{\mathbf{e}_r, \mathbf{e}_\varphi, \mathbf{e}_z\}$ are orthonormal vector bases of the corresponding cylindrical coordinates; a^+ and a^- are the given coefficients of radial tension-compression of the coating panels, c^+ and c^- are some constants characterizing the deformations in the thickness direction of these panels and determined from the absence of loads on their faces; \mathbf{C}_0^+ and \mathbf{C}_0^- are the deformation gradients corresponding to the transition from the natural reference configuration to the prestressed state of the top coating and the bottom coating, respectively ($\chi^\pm \rightarrow \chi$).

Next, we study the deformation of radial compression for the considered sandwich plate, choosing χ as the reference configuration, which is natural for the micropolar core, but prestressed for the non-polar coatings. This deformation is described by the relations (Lurie 1990; Sheydaikov 2013; Zubov 1997)

$$\begin{aligned} R &= \alpha r, \quad 0 \leq r \leq r_0; \quad \Phi = \varphi, \quad 0 \leq \varphi \leq 2\pi; \\ Z &= \begin{cases} f^-(z), & -h - h^- \leq z \leq -h, \\ f(z), & |z| \leq h, \\ f^+(z), & h \leq z \leq h + h^+, \end{cases} \quad h^\pm = c^\pm \zeta_0^\pm; \\ \mathbf{R} &= \alpha r \mathbf{e}_R + f(z) \mathbf{e}_Z, \quad \mathbf{R}^\pm = \alpha r \mathbf{e}_R + f^\pm(z) \mathbf{e}_Z. \end{aligned} \quad (24.3)$$

Here R, Φ, Z are the cylindrical coordinates in the actual (deformed) configuration X ; $\{\mathbf{e}_R, \mathbf{e}_\Phi, \mathbf{e}_Z\}$ is an orthonormal vector basis of the corresponding cylindrical coordinates; α is the given radial compression ratio; $f(z), f^+(z), f^-(z)$ are the unknown functions which characterize the thickness deformation of the sandwich plate; h^+ and h^- are the thicknesses of the prestressed coatings; R, R^+, R^- are the radius-vectors corresponding to the transition from the chosen reference to the actual configuration ($\chi \rightarrow X$) of the circular sandwich plate.

In addition, a proper orthogonal tensor of microrotation \mathbf{H} , which determines the rotation of medium particles, is given for the micropolar core ($|z| \leq h$):

$$\mathbf{H} = \mathbf{e}_r \otimes \mathbf{e}_R + \mathbf{e}_\varphi \otimes \mathbf{e}_\Phi + \mathbf{e}_z \otimes \mathbf{e}_Z. \quad (24.4)$$

According to the expressions (24.3), the deformation gradients \mathbf{C} , \mathbf{C}^+ , \mathbf{C}^- are (hereinafter the ' denotes the derivative with respect to z):

$$\begin{aligned}\mathbf{C} &= \overset{\circ}{\nabla} \mathbf{R} = \alpha \mathbf{e}_r \otimes \mathbf{e}_R + \alpha \mathbf{e}_\varphi \otimes \mathbf{e}_\Phi + f' \mathbf{e}_z \otimes \mathbf{e}_Z, \\ \mathbf{C}^\pm &= \overset{\circ}{\nabla} \mathbf{R}^\pm = \alpha \mathbf{e}_r \otimes \mathbf{e}_R + \alpha \mathbf{e}_\varphi \otimes \mathbf{e}_\Phi + f^{\pm'} \mathbf{e}_z \otimes \mathbf{e}_Z,\end{aligned}\quad (24.5)$$

where $\overset{\circ}{\nabla}$ is a nabla-operator in the reference configuration χ .

It follows from relations (24.4), (24.5) that the wryness tensor \mathbf{L} for the micropolar core of the sandwich plate ($|z| \leq h$) is equal to zero (\mathbf{I} is the unit tensor) (Nikitin and Zubov 1998; Pietraszkiewicz and Eremeyev 2009; Zubov 2016)

$$\mathbf{L} = \frac{1}{2} \text{tr} \left[\mathbf{H} \cdot \left(\overset{\circ}{\nabla} \times \mathbf{H} \right)^T \right] \mathbf{I} - \mathbf{H} \cdot \left(\overset{\circ}{\nabla} \times \mathbf{H} \right)^T = \mathbf{0}, \quad (24.6)$$

and the stretch tensor \mathbf{Y} is expressed as follows

$$\mathbf{Y} = \mathbf{C} \cdot \mathbf{H}^T = \alpha \mathbf{e}_r \otimes \mathbf{e}_r + \alpha \mathbf{e}_\varphi \otimes \mathbf{e}_\varphi + f' \mathbf{e}_z \otimes \mathbf{e}_z. \quad (24.7)$$

According to the Eqs. (24.5), the expressions of the stretch tensors \mathbf{U}^+ , \mathbf{U}^- and the macro rotation tensors \mathbf{A}^+ , \mathbf{A}^- for the top ($h \leq z \leq h + h^+$) and bottom ($-h - h^- \leq z \leq -h$) non-polar coatings have the form (Lurie 1990)

$$\begin{aligned}\mathbf{U}^\pm &= \left(\mathbf{C}^\pm \cdot \mathbf{C}^{\pm T} \right)^{\frac{1}{2}} = \alpha \mathbf{e}_r \otimes \mathbf{e}_r + \alpha \mathbf{e}_\varphi \otimes \mathbf{e}_\varphi + f^{\pm'} \mathbf{e}_z \otimes \mathbf{e}_z, \\ \mathbf{A}^\pm &= \mathbf{U}^{\pm-1} \cdot \mathbf{C}^\pm = \mathbf{e}_r \otimes \mathbf{e}_R + \mathbf{e}_\varphi \otimes \mathbf{e}_\Phi + \mathbf{e}_z \otimes \mathbf{e}_Z.\end{aligned}\quad (24.8)$$

We assume that the elastic properties of the sandwich plate are described by the model of a physically linear material. In this case, the specific strain energy W for the micropolar core is a quadratic form of the tensors $\mathbf{Y} - \mathbf{I}$ and \mathbf{L} (Eremeyev and Zubov 1994; Lakes 1995)

$$\begin{aligned}W &= \frac{1}{2} \lambda \text{tr}^2 (\mathbf{Y} - \mathbf{I}) + \frac{1}{2} (\mu + \kappa) \text{tr} \left((\mathbf{Y} - \mathbf{I}) \cdot (\mathbf{Y} - \mathbf{I})^T \right) + \\ &+ \frac{1}{2} \mu \text{tr} (\mathbf{Y} - \mathbf{I})^2 + \frac{1}{2} \gamma_1 \text{tr}^2 \mathbf{L} + \frac{1}{2} \gamma_2 \text{tr} (\mathbf{L} \cdot \mathbf{L}^T) + \frac{1}{2} \gamma_3 \text{tr} \mathbf{L}^2,\end{aligned}\quad (24.9)$$

$$\mu + \kappa > 0, \quad \lambda + 2\mu + \kappa > 0, \quad \gamma_2 > 0, \quad \gamma_1 + \gamma_2 + \gamma_3 > 0,$$

and the constitutive relations for the Piola-type stress and couple stress tensors \mathbf{D} and \mathbf{G} at $|z| \leq h$ have the form (Sheydakov 2013, 2016):

$$\begin{aligned} \mathbf{D} &= \frac{\partial W}{\partial \mathbf{Y}} \cdot \mathbf{H} = [\lambda \text{tr}(\mathbf{Y} - \mathbf{I}) \mathbf{I} + (\mu + \kappa)(\mathbf{Y} - \mathbf{I}) + \mu(\mathbf{Y}^T - \mathbf{I})] \cdot \mathbf{H}, \\ \mathbf{G} &= \frac{\partial W}{\partial \mathbf{L}} \cdot \mathbf{H} = [\gamma_1 (\text{tr} \mathbf{L}) \mathbf{I} + \gamma_2 \mathbf{L} + \gamma_3 \mathbf{L}^T] \cdot \mathbf{H}, \end{aligned} \quad (24.10)$$

where $\lambda, \mu, \kappa, \gamma_1, \gamma_2, \gamma_3$ are the micropolar elastic parameters of the porous core.

The specific strain energies W^+ and W^- for the top and bottom non-polar coatings are written as follows (Lurie 1990):

$$W^\pm = \frac{1}{2} \lambda^\pm \text{tr}^2(\mathbf{U}_1^\pm - \mathbf{I}) + \mu^\pm \text{tr}(\mathbf{U}_1^\pm - \mathbf{I}), \quad \mu^\pm > 0, \quad \lambda^\pm + 2\mu^\pm > 0. \quad (24.11)$$

Here λ^+, μ^+ and λ^-, μ^- are the elastic parameters of the uniform coatings; \mathbf{U}_1^+ and \mathbf{U}_1^- are the stretch tensors corresponding to the transition from the natural (stress-free) reference configuration to the actual (deformed) state of the top coating ($h \leq z \leq h + h^+$) and the bottom coating ($-h - h^- \leq z \leq -h$), respectively ($\chi^\pm \rightarrow \mathbf{X}$). To obtain expressions for these tensors, we use the formulae for transforming the deformation gradient when changing reference configuration (Eremeev and Zubov 2017; Lurie 1990; Truesdell 1977):

$$\begin{aligned} \mathbf{C}_1^\pm &= \mathbf{C}_0^\pm \cdot \mathbf{C}^\pm, \quad \mathbf{U}_1^\pm = \left(\mathbf{C}_0^\pm \cdot \mathbf{U}^{\pm 2} \cdot \mathbf{C}_0^{\pm T} \right)^{\frac{1}{2}}, \\ \mathbf{A}_1^\pm &= \left(\mathbf{C}_0^\pm \cdot \mathbf{U}^{\pm 2} \cdot \mathbf{C}_0^{\pm T} \right)^{-\frac{1}{2}} \cdot \mathbf{C}_0^\pm \cdot \mathbf{U}^\pm \cdot \mathbf{A}^\pm, \end{aligned} \quad (24.12)$$

where $\mathbf{C}_1^+, \mathbf{A}_1^+$ and $\mathbf{C}_1^-, \mathbf{A}_1^-$ are the deformation gradients and the macrorotation tensors for the transition from the corresponding natural reference configurations to the actual state of the coatings ($\chi^\pm \rightarrow \mathbf{X}$).

According to representation (24.11) for the non-polar coatings, the Piola stress tensors $\mathbf{D}_1^+, \mathbf{D}_1^-$ with respect to natural reference configurations χ^+ and χ^- have the form (Sheydaikov 2011a, b):

$$\mathbf{D}_1^\pm = \frac{\partial W^\pm}{\partial \mathbf{U}_1^\pm} \cdot \mathbf{A}_1^\pm = [\lambda^\pm \text{tr}(\mathbf{U}_1^\pm - \mathbf{I}) \mathbf{I} + 2\mu^\pm (\mathbf{U}_1^\pm - \mathbf{I})] \cdot \mathbf{A}_1^\pm. \quad (24.13)$$

The constitutive relations for the coatings with respect to the prestressed reference configuration χ are derived using the formulae connecting the Piola stress tensors in different reference configurations (Eremeev and Zubov 2017; Lurie 1990)

$$\mathbf{D}^\pm = J_0^{\pm-1} \mathbf{C}_0^{\pm T} \cdot \mathbf{D}_1^\pm, \quad J_0^\pm = \det \mathbf{C}_0^\pm. \quad (24.14)$$

Thus, according to Eqs. (24.12)–(24.14) for the top and bottom coatings, the Piola stress tensors $\mathbf{D}^+, \mathbf{D}^-$ relative to reference configuration χ have the form:

$$\begin{aligned} \mathbf{D}^\pm &= J_0^{\pm-1} \mathbf{C}_0^{\pm T} \cdot \left(\lambda^{\pm} \text{tr} \left[\left(\mathbf{C}_0^\pm \cdot \mathbf{U}^{\pm 2} \cdot \mathbf{C}_0^{\pm T} \right)^{\frac{1}{2}} - \mathbf{I} \right] \mathbf{I} + \right. \\ &\quad \left. + 2\mu^\pm \left[\left(\mathbf{C}_0^\pm \cdot \mathbf{U}^{\pm 2} \cdot \mathbf{C}_0^{\pm T} \right)^{\frac{1}{2}} - \mathbf{I} \right] \right) \cdot \left(\mathbf{C}_0^\pm \cdot \mathbf{U}^{\pm 2} \cdot \mathbf{C}_0^{\pm T} \right)^{-\frac{1}{2}} \cdot \mathbf{C}_0^\pm \cdot \mathbf{U}^\pm \cdot \mathbf{A}^\pm. \end{aligned} \quad (24.15)$$

It follows from expressions (24.4), (24.6), (24.7) and (24.10) that for the micropolar core the Piola-type couple stress tensor \mathbf{G} is equal to zero in the case of radial compression of a circular sandwich plate and the Piola-type stress tensor \mathbf{D} is

$$\begin{aligned} \mathbf{D} &= [\lambda s + \psi(\alpha - 1)] (\mathbf{e}_r \otimes \mathbf{e}_R + \mathbf{e}_\varphi \otimes \mathbf{e}_\Phi) + [\lambda s + \psi(f' - 1)] \mathbf{e}_z \otimes \mathbf{e}_Z, \\ s &= 2\alpha + f' - 3, \quad \psi = 2\mu + \kappa. \end{aligned} \quad (24.16)$$

According to the relations (24.2), (24.8) and (24.15), the expressions of the Piola stress tensors \mathbf{D}^+ and \mathbf{D}^- for the prestressed non-polar coatings have the form:

$$\begin{aligned} \mathbf{D}^\pm &= \frac{1}{a^\pm c^\pm} [\lambda^\pm s^\pm + 2\mu^\pm (\alpha a^\pm - 1)] (\mathbf{e}_r \otimes \mathbf{e}_R + \mathbf{e}_\varphi \otimes \mathbf{e}_\Phi) + \\ &\quad + \frac{1}{a^{\pm 2}} [\lambda^\pm s^\pm + 2\mu^\pm (f^{\pm'} c^\pm - 1)] \mathbf{e}_z \otimes \mathbf{e}_Z, \\ s^\pm &= 2\alpha a^\pm + f^{\pm'} c^\pm - 3. \end{aligned} \quad (24.17)$$

The equilibrium equations of the considered sandwich plate in the absence of mass forces and moments are written as follows (Eremeyev and Zubov 1994; Sheydaikov 2011b; Zubov 1997):

$$\begin{aligned} \overset{\circ}{\nabla} \cdot \mathbf{D}^- &= \mathbf{0}, & -h - h^- \leq z \leq -h, \\ \overset{\circ}{\nabla} \cdot \mathbf{D} &= \mathbf{0}, \quad \overset{\circ}{\nabla} \cdot \mathbf{G} + (\mathbf{C}^T \cdot \mathbf{D})_\times = \mathbf{0}, & |z| \leq h, \\ \overset{\circ}{\nabla} \cdot \mathbf{D}^+ &= \mathbf{0}, & h \leq z \leq h + h^+. \end{aligned} \quad (24.18)$$

The symbol \times represents the vector invariant of a second-order tensor. The boundary conditions

$$\begin{aligned} \mathbf{e}_z \cdot \mathbf{D}^\pm \Big|_{z=\pm h \pm h^\pm} &= \mathbf{0}, & \mathbf{e}_z \cdot \mathbf{D} \Big|_{z=\pm h} &= \mathbf{e}_z \cdot \mathbf{D}^\pm \Big|_{z=\pm h}, \\ f(0) &= 0, & f(\pm h) &= f^\pm(\pm h), \end{aligned} \quad (24.19)$$

express the absence of loads on the faces of the plate ($z = \pm h \pm h^\pm$), the rigid coupling of the prestressed coatings with the porous core ($z = \pm h$), and the absence of vertical displacement at $z = 0$.

By solving the boundary value problem (24.18), (24.19) while taking into account relations (24.5), (24.16) and (24.17), we find the unknown functions:

$$\begin{aligned}
 f(z) &= \xi z, & f^\pm(z) &= \xi^\pm z \pm h(\xi - \xi^\pm), \\
 \xi &= 1 - \frac{2\lambda(\alpha - 1)}{\lambda + \psi}, & \xi^\pm &= \frac{1}{c^\pm} - \frac{2\lambda^\pm(\alpha a^\pm - 1)}{c^\pm(\lambda^\pm + 2\mu^\pm)}.
 \end{aligned} \tag{24.20}$$

The coefficients c^+ and c^- in the case of a physically linear material (24.11) are expressed as follows:

$$c^\pm = 1 - \frac{2\lambda^\pm(a^\pm - 1)}{\lambda^\pm + 2\mu^\pm}.$$

24.3 Perturbed State of Sandwich Plate

We assume that in addition to the described subcritical state of equilibrium \mathbf{X} for the circular sandwich plate, there is an infinitely close perturbed equilibrium state under the same external loads, which is determined by the radius-vector $\mathbf{R} + \eta\mathbf{v}$ and the microrotation tensor $\mathbf{H} - \eta\mathbf{H} \times \boldsymbol{\omega}$ for the micropolar core, and by the radius-vectors $\mathbf{R}^+ + \eta\mathbf{v}^+$ and $\mathbf{R}^- + \eta\mathbf{v}^-$ for the prestressed non-polar coatings. Here η is a small parameter; \mathbf{v} , \mathbf{v}^+ , \mathbf{v}^- are the vectors of additional displacements; $\boldsymbol{\omega}$ is the linear incremental rotation vector, which characterize the small rotation of the micropolar medium particles, measured from the subcritical state. This perturbed state is described by the equations (Eremeyev and Zubov 1994; Green and Adkins 1960; Ogden et al. 1997):

$$\begin{aligned}
 \overset{\circ}{\nabla} \cdot \mathbf{D}^{-\bullet} &= \mathbf{0}, & -h - h^- &\leq z \leq -h, \\
 \overset{\circ}{\nabla} \cdot \mathbf{D}^\bullet &= \mathbf{0}, & \overset{\circ}{\nabla} \cdot \mathbf{G}^\bullet + \left[\overset{\circ}{\nabla} \mathbf{v}^T \cdot \mathbf{D} + \mathbf{C}^T \cdot \mathbf{D}^\bullet \right]_x &= \mathbf{0}, & |z| &\leq h, \\
 \overset{\circ}{\nabla} \cdot \mathbf{D}^{+\bullet} &= \mathbf{0}, & h &\leq z \leq h + h^+,
 \end{aligned} \tag{24.21}$$

where \mathbf{D}^\bullet and \mathbf{G}^\bullet are the linearized Piola-type stress and couple stress tensors for the porous core; $\mathbf{D}^{+\bullet}$ and $\mathbf{D}^{-\bullet}$ are the linearized Piola stress tensors for the top and bottom coatings. In the case of a physically linear micropolar material (24.9), the following relations are valid for the first two tensors (Eremeyev and Zubov 1994; Sheydkov 2011a):

$$\begin{aligned}
 \mathbf{D}^\bullet &= \left[\lambda(\text{tr}\mathbf{Y}^\bullet) \mathbf{I} + (\mu + \kappa) \mathbf{Y}^\bullet + \mu \mathbf{Y}^{\bullet T} \right] \cdot \mathbf{H} - \\
 &\quad - \left[\lambda \text{tr}(\mathbf{Y} - \mathbf{I}) \mathbf{I} + (\mu + \kappa)(\mathbf{Y} - \mathbf{I}) + \mu(\mathbf{Y}^T - \mathbf{I}) \right] \cdot \mathbf{H} \times \boldsymbol{\omega}, \\
 \mathbf{G}^\bullet &= \left[\gamma_1(\text{tr}\mathbf{L}^\bullet) \mathbf{I} + \gamma_2 \mathbf{L}^\bullet + \gamma_3 \mathbf{L}^{\bullet T} \right] \cdot \mathbf{H} - \\
 &\quad - \left[\gamma_1(\text{tr}\mathbf{L}) \mathbf{I} + \gamma_2 \mathbf{L} + \gamma_3 \mathbf{L}^T \right] \cdot \mathbf{H} \times \boldsymbol{\omega},
 \end{aligned} \tag{24.22}$$

$$\mathbf{Y}^\bullet = \left(\overset{\circ}{\nabla} \mathbf{v} + \mathbf{C} \times \boldsymbol{\omega} \right) \cdot \mathbf{H}^T, \quad \mathbf{L}^\bullet = \overset{\circ}{\nabla} \boldsymbol{\omega} \cdot \mathbf{H}^T. \tag{24.23}$$

Here \mathbf{Y}^\bullet is the linearized stretch tensor, and \mathbf{L}^\bullet is the linearized wryness tensor for the micropolar core of the sandwich plate.

According to the expressions (24.12)–(24.14), the representations of the linearized Piola stress tensors $\mathbf{D}^{+\bullet}$ and $\mathbf{D}^{-\bullet}$ for a physically linear non-polar material (24.11) have the form (Sheydakov 2011a, b):

$$\begin{aligned} \mathbf{D}^{\pm\bullet} = & J_0^{\pm-1} \mathbf{C}_0^{\pm T} \cdot [\lambda^\pm (\text{tr} \mathbf{U}_1^{\pm\bullet}) \mathbf{I} + 2\mu^\pm \mathbf{U}_1^{\pm\bullet}] \cdot (\mathbf{C}_0^\pm \cdot \mathbf{U}^{\pm 2} \cdot \mathbf{C}_0^{\pm T})^{-\frac{1}{2}} \cdot \mathbf{C}_0^\pm \cdot \mathbf{U}^\pm \cdot \mathbf{A}^\pm + \\ & + J_0^{\pm-1} \mathbf{C}_0^{\pm T} \cdot \left(\lambda^\pm \text{tr} \left[(\mathbf{C}_0^\pm \cdot \mathbf{U}^{\pm 2} \cdot \mathbf{C}_0^{\pm T})^{\frac{1}{2}} - \mathbf{I} \right] \mathbf{I} + \right. \\ & \left. + 2\mu^\pm \left[(\mathbf{C}_0^\pm \cdot \mathbf{U}^{\pm 2} \cdot \mathbf{C}_0^{\pm T})^{\frac{1}{2}} - \mathbf{I} \right] \right) \cdot \mathbf{A}_1^{\pm\bullet}, \end{aligned} \quad (24.24)$$

$$\begin{aligned} \mathbf{A}_1^{\pm\bullet} = & (\mathbf{C}_0^\pm \cdot \mathbf{U}^{\pm 2} \cdot \mathbf{C}_0^{\pm T})^{-\frac{1}{2}} \cdot \mathbf{C}_0^\pm \cdot \overset{\circ}{\nabla} \mathbf{v}^\pm - \\ & - (\mathbf{C}_0^\pm \cdot \mathbf{U}^{\pm 2} \cdot \mathbf{C}_0^{\pm T})^{-\frac{1}{2}} \cdot \mathbf{U}_1^{\pm\bullet} \cdot (\mathbf{C}_0^\pm \cdot \mathbf{U}^{\pm 2} \cdot \mathbf{C}_0^{\pm T})^{-\frac{1}{2}} \cdot \mathbf{C}_0^\pm \cdot \mathbf{U}^\pm \cdot \mathbf{A}^\pm, \end{aligned} \quad (24.25)$$

where $\mathbf{U}_1^{+\bullet}$, $\mathbf{U}_1^{-\bullet}$ are the linearized stretch tensors, and $\mathbf{A}_1^{+\bullet}$, $\mathbf{A}_1^{-\bullet}$ are the linearized macrorotation tensors with respect to the natural reference configurations χ^+ and χ^- of the non-polar coatings. The stretch tensors can be expressed in terms of linearized Cauchy-Green deformation tensors $\mathbf{g}_1^{+\bullet}$, $\mathbf{g}_1^{-\bullet}$:

$$\begin{aligned} \mathbf{g}_1^{\pm\bullet} = & (\mathbf{U}_1^\pm \cdot \mathbf{U}_1^\pm)^\bullet = \mathbf{U}_1^{\pm\bullet} \cdot (\mathbf{C}_0^\pm \cdot \mathbf{U}^{\pm 2} \cdot \mathbf{C}_0^{\pm T})^{\frac{1}{2}} + (\mathbf{C}_0^\pm \cdot \mathbf{U}^{\pm 2} \cdot \mathbf{C}_0^{\pm T})^{\frac{1}{2}} \cdot \mathbf{U}_1^{\pm\bullet}, \\ \mathbf{g}_1^{\pm\bullet} = & (\mathbf{C}_1^\pm \cdot \mathbf{C}_1^{\pm T})^\bullet = \mathbf{C}_0^\pm \cdot (\overset{\circ}{\nabla} \mathbf{v}^\pm \cdot \mathbf{C}^{\pm T} + \mathbf{C}^\pm \cdot \overset{\circ}{\nabla} \mathbf{v}^{\pm T}) \cdot \mathbf{C}_0^{\pm T}. \end{aligned}$$

Linearized boundary conditions on the faces of the sandwich plate ($z = \pm h \pm h^\pm$) and at the interfaces between the prestressed coatings and the porous core ($z = \pm h$) are written as follows (Sheydakov 2011b):

$$\begin{aligned} \mathbf{e}_z \cdot \mathbf{D}^{\pm\bullet} \Big|_{z=\pm h \pm h^\pm} = & 0; & \mathbf{e}_z \cdot \mathbf{D}^\bullet \Big|_{z=\pm h} = & \mathbf{e}_z \cdot \mathbf{D}^{\pm\bullet} \Big|_{z=\pm h}, \\ \mathbf{e}_z \cdot \mathbf{G}^\bullet \Big|_{z=\pm h} = & 0, & \mathbf{v} \Big|_{z=\pm h} = & \mathbf{v}^\pm \Big|_{z=\pm h}. \end{aligned} \quad (24.26)$$

We assume that there is no friction at the edge of the circular plate ($r = r_0$) and constant radial displacement is given. This leads to the following linearized edge conditions (Sheydakov 2013):

$$\begin{aligned} \mathbf{e}_r \cdot \mathbf{D}^\bullet \cdot \mathbf{e}_\Phi \Big|_{r=r_0} = & \mathbf{e}_r \cdot \mathbf{D}^\bullet \cdot \mathbf{e}_Z \Big|_{r=r_0} = \mathbf{e}_r \cdot \mathbf{v} \Big|_{r=r_0} = 0, \\ \mathbf{e}_r \cdot \mathbf{G}^\bullet \cdot \mathbf{e}_R \Big|_{r=r_0} = & \mathbf{e}_\varphi \cdot \boldsymbol{\omega} \Big|_{r=r_0} = \mathbf{e}_z \cdot \boldsymbol{\omega} \Big|_{r=r_0} = 0, \\ \mathbf{e}_r \cdot \mathbf{D}^{\pm\bullet} \cdot \mathbf{e}_\Phi \Big|_{r=r_0} = & \mathbf{e}_r \cdot \mathbf{D}^{\pm\bullet} \cdot \mathbf{e}_Z \Big|_{r=r_0} = \mathbf{e}_r \cdot \mathbf{v}^\pm \Big|_{r=r_0} = 0. \end{aligned} \quad (24.27)$$

The vectors of additional displacements \mathbf{v} , \mathbf{v}^+ , \mathbf{v}^- and the vector of incremental rotation $\boldsymbol{\omega}$ in the basis of Eulerian cylindrical coordinates are written as

$$\begin{aligned}\mathbf{v} &= v_R \mathbf{e}_R + v_\Phi \mathbf{e}_\Phi + v_Z \mathbf{e}_Z, & \boldsymbol{\omega} &= \omega_R \mathbf{e}_R + \omega_\Phi \mathbf{e}_\Phi + \omega_Z \mathbf{e}_Z. \\ \mathbf{v}^\pm &= v_R^\pm \mathbf{e}_R + v_\Phi^\pm \mathbf{e}_\Phi + v_Z^\pm \mathbf{e}_Z,\end{aligned}\quad (24.28)$$

Then, according to formulae (24.2), (24.4), (24.5), (24.8), (24.23), (24.25) and (24.28), the expressions for the linearized wryness tensor \mathbf{L}^\bullet , the linearized macro-rotation tensors $\mathbf{A}_1^{\pm\bullet}$, and the linearized stretch tensors \mathbf{Y}^\bullet and $\mathbf{U}_1^{\pm\bullet}$ have the form:

$$\begin{aligned}\mathbf{L}^\bullet &= \frac{\partial \omega_R}{\partial r} \mathbf{e}_r \otimes \mathbf{e}_r + \frac{1}{r} \left(\frac{\partial \omega_\Phi}{\partial \varphi} + \omega_R \right) \mathbf{e}_\varphi \otimes \mathbf{e}_\varphi + \frac{\partial \omega_Z}{\partial z} \mathbf{e}_z \otimes \mathbf{e}_z + \\ &+ \frac{\partial \omega_\Phi}{\partial r} \mathbf{e}_r \otimes \mathbf{e}_\varphi + \frac{1}{r} \left(\frac{\partial \omega_R}{\partial \varphi} - \omega_\Phi \right) \mathbf{e}_\varphi \otimes \mathbf{e}_r + \frac{\partial \omega_Z}{\partial r} \mathbf{e}_r \otimes \mathbf{e}_z + \\ &+ \frac{\partial \omega_R}{\partial z} \mathbf{e}_z \otimes \mathbf{e}_r + \frac{1}{r} \frac{\partial \omega_Z}{\partial \varphi} \mathbf{e}_\varphi \otimes \mathbf{e}_z + \frac{\partial \omega_\Phi}{\partial z} \mathbf{e}_z \otimes \mathbf{e}_\varphi,\end{aligned}\quad (24.29)$$

$$\begin{aligned}\mathbf{A}_1^{\pm\bullet} &= \frac{1}{2\alpha} \left(\frac{\partial v_\Phi^\pm}{\partial r} - \frac{1}{r} \frac{\partial v_R^\pm}{\partial \varphi} + \frac{v_\Phi^\pm}{r} \right) \mathbf{e}_r^\pm \otimes \mathbf{e}_\Phi + \frac{\varepsilon}{a^\pm} \left(\frac{a^\pm}{c^\pm} \frac{\partial v_Z^\pm}{\partial r} - \frac{\partial v_R^\pm}{\partial z} \right) \mathbf{e}_r^\pm \otimes \mathbf{e}_Z + \\ &+ \frac{1}{2\alpha} \left(\frac{1}{r} \frac{\partial v_R^\pm}{\partial \varphi} - \frac{v_\Phi^\pm}{r} - \frac{\partial v_\Phi^\pm}{\partial r} \right) \mathbf{e}_\theta^\pm \otimes \mathbf{e}_R + \frac{\varepsilon}{a^\pm} \left(\frac{a^\pm}{c^\pm r} \frac{\partial v_Z^\pm}{\partial \varphi} - \frac{\partial v_\Phi^\pm}{\partial z} \right) \mathbf{e}_\theta^\pm \otimes \mathbf{e}_Z + \\ &+ \frac{\varepsilon}{c^\pm} \left(\frac{c^\pm}{a^\pm} \frac{\partial v_R^\pm}{\partial z} - \frac{\partial v_Z^\pm}{\partial r} \right) \mathbf{e}_z^\pm \otimes \mathbf{e}_R + \frac{\varepsilon}{c^\pm} \left(\frac{c^\pm}{a^\pm} \frac{\partial v_\Phi^\pm}{\partial z} - \frac{1}{r} \frac{\partial v_Z^\pm}{\partial \varphi} \right) \mathbf{e}_z^\pm \otimes \mathbf{e}_\Phi,\end{aligned}\quad (24.30)$$

$$\begin{aligned}\mathbf{Y}^\bullet &= \frac{\partial v_R}{\partial r} \mathbf{e}_r \otimes \mathbf{e}_r + \frac{1}{r} \left(\frac{\partial v_\Phi}{\partial \varphi} + v_R \right) \mathbf{e}_\varphi \otimes \mathbf{e}_\varphi + \frac{\partial v_Z}{\partial z} \mathbf{e}_z \otimes \mathbf{e}_z + \\ &+ \left(\frac{\partial v_\Phi}{\partial r} - \alpha \omega_Z \right) \mathbf{e}_r \otimes \mathbf{e}_\varphi + \left(\frac{1}{r} \frac{\partial v_R}{\partial \varphi} - \frac{v_\Phi}{r} + \alpha \omega_Z \right) \mathbf{e}_\varphi \otimes \mathbf{e}_r + \\ &+ \left(\frac{\partial v_Z}{\partial r} + \alpha \omega_\Phi \right) \mathbf{e}_r \otimes \mathbf{e}_z + \left(\frac{\partial v_R}{\partial z} - \xi \omega_\Phi \right) \mathbf{e}_z \otimes \mathbf{e}_r + \\ &+ \left(\frac{1}{r} \frac{\partial v_Z}{\partial \varphi} - \alpha \omega_R \right) \mathbf{e}_\varphi \otimes \mathbf{e}_z + \left(\frac{\partial v_\Phi}{\partial z} + \xi \omega_R \right) \mathbf{e}_z \otimes \mathbf{e}_\varphi,\end{aligned}\quad (24.31)$$

$$\begin{aligned}
\mathbf{U}_1^{\pm\bullet} = & a^{\pm} \frac{\partial v_R^{\pm}}{\partial r} \mathbf{e}_{\rho}^{\pm} \otimes \mathbf{e}_{\rho}^{\pm} + \frac{a^{\pm}}{r} \left(\frac{\partial v_{\Phi}^{\pm}}{\partial \varphi} + v_R^{\pm} \right) \mathbf{e}_{\theta}^{\pm} \otimes \mathbf{e}_{\theta}^{\pm} + c^{\pm} \frac{\partial v_Z^{\pm}}{\partial z} \mathbf{e}_{\zeta}^{\pm} \otimes \mathbf{e}_{\zeta}^{\pm} + \\
& + \frac{a^{\pm}}{2} \left(\frac{1}{r} \frac{\partial v_R^{\pm}}{\partial \varphi} + \frac{\partial v_{\Phi}^{\pm}}{\partial r} - \frac{v_{\Phi}^{\pm}}{r} \right) (\mathbf{e}_{\rho}^{\pm} \otimes \mathbf{e}_{\theta}^{\pm} + \mathbf{e}_{\theta}^{\pm} \otimes \mathbf{e}_{\rho}^{\pm}) + \\
& + \varepsilon \left(\alpha \frac{\partial v_R^{\pm}}{\partial z} + \xi^{\pm} \frac{\partial v_Z^{\pm}}{\partial r} \right) (\mathbf{e}_{\rho}^{\pm} \otimes \mathbf{e}_{\zeta}^{\pm} + \mathbf{e}_{\zeta}^{\pm} \otimes \mathbf{e}_{\rho}^{\pm}) + \\
& + \varepsilon \left(\alpha \frac{\partial v_{\Phi}^{\pm}}{\partial z} + \frac{\xi^{\pm}}{r} \frac{\partial v_Z^{\pm}}{\partial \varphi} \right) (\mathbf{e}_{\theta}^{\pm} \otimes \mathbf{e}_{\zeta}^{\pm} + \mathbf{e}_{\zeta}^{\pm} \otimes \mathbf{e}_{\theta}^{\pm}); \quad \varepsilon = \frac{a^{\pm} c^{\pm}}{\alpha a^{\pm} + \xi^{\pm} c^{\pm}}.
\end{aligned} \tag{24.32}$$

Taking into account relations (24.2), (24.4), (24.6)–(24.8), (24.14), (24.22), (24.24), (24.28)–(24.32), the components of the linearized Piola-type stress and couple stress tensors \mathbf{D}^{\bullet} and \mathbf{G}^{\bullet} are written as follows (Sheydakov 2013):

$$\begin{aligned}
\mathbf{e}_r \cdot \mathbf{D}^{\bullet} \cdot \mathbf{e}_R &= (\lambda + \psi) \frac{\partial v_R}{\partial r} + \frac{\lambda}{r} \left(\frac{\partial v_{\Phi}}{\partial \varphi} + v_R \right) + \lambda \frac{\partial v_Z}{\partial z}, \\
\mathbf{e}_{\varphi} \cdot \mathbf{D}^{\bullet} \cdot \mathbf{e}_{\Phi} &= \lambda \frac{\partial v_R}{\partial r} + \frac{\lambda + \psi}{r} \left(\frac{\partial v_{\Phi}}{\partial \varphi} + v_R \right) + \lambda \frac{\partial v_Z}{\partial z}, \\
\mathbf{e}_z \cdot \mathbf{D}^{\bullet} \cdot \mathbf{e}_Z &= \lambda \frac{\partial v_R}{\partial r} + \frac{\lambda}{r} \left(\frac{\partial v_{\Phi}}{\partial \varphi} + v_R \right) + (\lambda + \psi) \frac{\partial v_Z}{\partial z}, \\
\mathbf{e}_r \cdot \mathbf{D}^{\bullet} \cdot \mathbf{e}_{\Phi} &= \tau \frac{\partial v_{\Phi}}{\partial r} + \frac{\mu}{r} \left(\frac{\partial v_R}{\partial \varphi} - v_{\Phi} \right) + B_Z \omega_Z, \\
\mathbf{e}_{\varphi} \cdot \mathbf{D}^{\bullet} \cdot \mathbf{e}_R &= \frac{\tau}{r} \left(\frac{\partial v_R}{\partial \varphi} - v_{\Phi} \right) + \mu \frac{\partial v_{\Phi}}{\partial r} - B_Z \omega_Z, \\
\mathbf{e}_r \cdot \mathbf{D}^{\bullet} \cdot \mathbf{e}_Z &= \tau \frac{\partial v_Z}{\partial r} + \mu \frac{\partial v_R}{\partial z} - B_{\Phi} \omega_{\Phi}, \quad \mathbf{e}_z \cdot \mathbf{D}^{\bullet} \cdot \mathbf{e}_R = \tau \frac{\partial v_R}{\partial z} + \mu \frac{\partial v_Z}{\partial r} + B_{\Phi} \omega_{\Phi}, \\
\mathbf{e}_{\varphi} \cdot \mathbf{D}^{\bullet} \cdot \mathbf{e}_Z &= \frac{\tau}{r} \frac{\partial v_Z}{\partial \varphi} + \mu \frac{\partial v_{\Phi}}{\partial z} + B_R \omega_R, \quad \mathbf{e}_z \cdot \mathbf{D}^{\bullet} \cdot \mathbf{e}_{\Phi} = \tau \frac{\partial v_{\Phi}}{\partial z} + \frac{\mu}{r} \frac{\partial v_Z}{\partial \varphi} - B_R \omega_R,
\end{aligned} \tag{24.33}$$

$$\begin{aligned}
\mathbf{e}_r \cdot \mathbf{G}^{\bullet} \cdot \mathbf{e}_R &= \gamma \frac{\partial \omega_R}{\partial r} + \frac{\gamma_1}{r} \left(\frac{\partial \omega_{\Phi}}{\partial \varphi} + \omega_R \right) + \gamma_1 \frac{\partial \omega_Z}{\partial z}, \\
\mathbf{e}_{\varphi} \cdot \mathbf{G}^{\bullet} \cdot \mathbf{e}_{\Phi} &= \gamma_1 \frac{\partial \omega_R}{\partial r} + \frac{\gamma}{r} \left(\frac{\partial \omega_{\Phi}}{\partial \varphi} + \omega_R \right) + \gamma_1 \frac{\partial \omega_Z}{\partial z}, \\
\mathbf{e}_z \cdot \mathbf{G}^{\bullet} \cdot \mathbf{e}_Z &= \gamma_1 \frac{\partial \omega_R}{\partial r} + \frac{\gamma_1}{r} \left(\frac{\partial \omega_{\Phi}}{\partial \varphi} + \omega_R \right) + \gamma \frac{\partial \omega_Z}{\partial z},
\end{aligned} \tag{24.34}$$

$$\begin{aligned}
\mathbf{e}_r \cdot \mathbf{G}^\bullet \cdot \mathbf{e}_\Phi &= \gamma_2 \frac{\partial \omega_\Phi}{\partial r} + \frac{\gamma_3}{r} \left(\frac{\partial \omega_R}{\partial \varphi} - \omega_\Phi \right), & \mathbf{e}_r \cdot \mathbf{G}^\bullet \cdot \mathbf{e}_Z &= \gamma_2 \frac{\partial \omega_Z}{\partial r} + \gamma_3 \frac{\partial \omega_R}{\partial z}, \\
\mathbf{e}_\varphi \cdot \mathbf{G}^\bullet \cdot \mathbf{e}_R &= \frac{\gamma_2}{r} \left(\frac{\partial \omega_R}{\partial \varphi} - \omega_\Phi \right) + \gamma_3 \frac{\partial \omega_\Phi}{\partial r}, & \mathbf{e}_\varphi \cdot \mathbf{G}^\bullet \cdot \mathbf{e}_z &= \frac{\gamma_2}{r} \frac{\partial \omega_Z}{\partial \varphi} + \gamma_3 \frac{\partial \omega_\Phi}{\partial z}, \\
\mathbf{e}_z \cdot \mathbf{G}^\bullet \cdot \mathbf{e}_R &= \gamma_2 \frac{\partial \omega_R}{\partial z} + \gamma_3 \frac{\partial \omega_Z}{\partial r}, & \mathbf{e}_z \cdot \mathbf{G}^\bullet \cdot \mathbf{e}_\Phi &= \gamma_2 \frac{\partial \omega_\Phi}{\partial z} + \frac{\gamma_3}{r} \frac{\partial \omega_Z}{\partial \varphi},
\end{aligned}$$

and the components of the linearized Piola stress tensors $\mathbf{D}^{+\bullet}$ and $\mathbf{D}^{-\bullet}$ are

$$\begin{aligned}
\mathbf{e}_r \cdot \mathbf{D}^{\pm\bullet} \cdot \mathbf{e}_R &= \frac{\lambda^\pm + 2\mu^\pm}{c^\pm} \frac{\partial v_R^\pm}{\partial r} + \frac{\lambda^\pm}{c^\pm r} \left(\frac{\partial v_\Phi^\pm}{\partial \varphi} + v_R^\pm \right) + \frac{\lambda^\pm}{a^\pm} \frac{\partial v_Z^\pm}{\partial z}, \\
\mathbf{e}_\varphi \cdot \mathbf{D}^{\pm\bullet} \cdot \mathbf{e}_\Phi &= \frac{\lambda^\pm}{c^\pm} \frac{\partial v_R^\pm}{\partial r} + \frac{\lambda^\pm + 2\mu^\pm}{c^\pm r} \left(\frac{\partial v_\Phi^\pm}{\partial \varphi} + v_R^\pm \right) + \frac{\lambda^\pm}{a^\pm} \frac{\partial v_Z^\pm}{\partial z}, \\
\mathbf{e}_z \cdot \mathbf{D}^{\pm\bullet} \cdot \mathbf{e}_Z &= \frac{\lambda^\pm}{a^\pm} \frac{\partial v_R^\pm}{\partial r} + \frac{\lambda^\pm}{a^\pm r} \left(\frac{\partial v_\Phi^\pm}{\partial \varphi} + v_R^\pm \right) + (\lambda^\pm + 2\mu^\pm) \frac{c^\pm}{a^{\pm 2}} \frac{\partial v_Z^\pm}{\partial z}, \\
\mathbf{e}_r \cdot \mathbf{D}^{\pm\bullet} \cdot \mathbf{e}_\Phi &= \frac{1}{2\alpha a^\pm c^\pm} \left[B_Z^\pm \frac{\partial v_\Phi^\pm}{\partial r} - \frac{S^\pm}{r} \left(\frac{\partial v_R^\pm}{\partial \varphi} - v_\Phi^\pm \right) \right], \\
\mathbf{e}_\varphi \cdot \mathbf{D}^{\pm\bullet} \cdot \mathbf{e}_R &= \frac{1}{2\alpha a^\pm c^\pm} \left[\frac{B_Z^\pm}{r} \left(\frac{\partial v_R^\pm}{\partial \varphi} - v_\Phi^\pm \right) - S^\pm \frac{\partial v_\Phi^\pm}{\partial r} \right], \\
\mathbf{e}_r \cdot \mathbf{D}^{\pm\bullet} \cdot \mathbf{e}_Z &= \frac{\varepsilon}{a^\pm c^\pm} \left(\frac{B_\Phi^\pm}{c^\pm} \frac{\partial v_Z^\pm}{\partial r} - \frac{S^\pm}{a^\pm} \frac{\partial v_\Phi^\pm}{\partial z} \right), \\
\mathbf{e}_z \cdot \mathbf{D}^{\pm\bullet} \cdot \mathbf{e}_R &= \frac{\varepsilon}{a^{\pm 2}} \left(\frac{B_\Phi^\pm}{a^\pm} \frac{\partial v_R^\pm}{\partial z} - \frac{S^\pm}{c^\pm} \frac{\partial v_Z^\pm}{\partial r} \right), \\
\mathbf{e}_\varphi \cdot \mathbf{D}^{\pm\bullet} \cdot \mathbf{e}_z &= \frac{\varepsilon}{a^\pm c^\pm} \left(\frac{B_R^\pm}{c^\pm r} \frac{\partial v_Z^\pm}{\partial \varphi} - \frac{S^\pm}{a^\pm} \frac{\partial v_\Phi^\pm}{\partial z} \right), \\
\mathbf{e}_z \cdot \mathbf{D}^{\pm\bullet} \cdot \mathbf{e}_\Phi &= \frac{\varepsilon}{a^{\pm 2}} \left(\frac{B_R^\pm}{a^\pm} \frac{\partial v_\Phi^\pm}{\partial z} - \frac{S^\pm}{c^\pm r} \frac{\partial v_Z^\pm}{\partial \varphi} \right).
\end{aligned} \tag{24.35}$$

The following notation is adopted here:

$$\begin{aligned}
B_R &= B_\Phi = \lambda s + \mu (\alpha + \xi) - \psi, & B_Z &= \lambda s + 2\mu\alpha - \psi, \\
B_R^\pm &= B_\Phi^\pm = S^\pm + 2\mu^\pm (\alpha a^\pm + \xi^\pm c^\pm), & B_Z^\pm &= S^\pm + 4\mu^\pm \alpha a^\pm, \\
\tau &= \mu + \kappa, & \gamma &= \gamma_1 + \gamma_2 + \gamma_3, & S^\pm &= \lambda^\pm s^\pm - 2\mu^\pm.
\end{aligned}$$

Using expressions (24.5), (24.16), (24.28), (24.33)–(24.35), we write the equations of neutral equilibrium (24.21) for the circular sandwich plate in scalar form:

$$\begin{aligned}
& \tau \left(\frac{1}{r^2} \frac{\partial^2 v_R}{\partial \varphi^2} + \frac{\partial^2 v_R}{\partial z^2} - \frac{1}{r^2} \frac{\partial v_\Phi}{\partial \varphi} \right) + (\lambda + \mu) \left(\frac{1}{r} \frac{\partial^2 v_\Phi}{\partial r \partial \varphi} + \frac{\partial^2 v_Z}{\partial r \partial z} \right) + \\
& + (\lambda + \psi) \left(\frac{\partial^2 v_R}{\partial r^2} + \frac{1}{r} \frac{\partial v_R}{\partial r} - \frac{v_R}{r^2} - \frac{1}{r^2} \frac{\partial v_\Phi}{\partial \varphi} \right) + B_\Phi \frac{\partial \omega_\Phi}{\partial z} - \frac{B_Z}{r} \frac{\partial \omega_Z}{\partial \varphi} = 0, \\
& \frac{\lambda + \psi}{r^2} \left(\frac{\partial^2 v_\Phi}{\partial \varphi^2} + \frac{\partial v_R}{\partial \varphi} \right) + \tau \left(\frac{\partial^2 v_\Phi}{\partial r^2} + \frac{1}{r} \frac{\partial v_\Phi}{\partial r} - \frac{v_\Phi}{r^2} + \frac{\partial^2 v_\Phi}{\partial z^2} + \frac{1}{r^2} \frac{\partial v_R}{\partial \varphi} \right) + \\
& + \frac{\lambda + \mu}{r} \left(\frac{\partial^2 v_R}{\partial r \partial \varphi} + \frac{\partial^2 v_Z}{\partial \varphi \partial z} \right) - B_R \frac{\partial \omega_R}{\partial z} + B_Z \frac{\partial \omega_Z}{\partial r} = 0, \\
& (\lambda + \psi) \frac{\partial^2 v_Z}{\partial z^2} + (\lambda + \mu) \left(\frac{\partial^2 v_R}{\partial r \partial z} + \frac{1}{r} \frac{\partial v_R}{\partial z} + \frac{1}{r} \frac{\partial^2 v_\Phi}{\partial \varphi \partial z} \right) + \\
& + \tau \left(\frac{\partial^2 v_Z}{\partial r^2} + \frac{1}{r} \frac{\partial v_Z}{\partial r} + \frac{1}{r^2} \frac{\partial^2 v_Z}{\partial \varphi^2} \right) + \frac{B_R}{r} \frac{\partial \omega_R}{\partial \varphi} - B_\Phi \left(\frac{\partial \omega_\Phi}{\partial r} + \frac{\omega_\Phi}{r} \right) = 0, \\
& \gamma \left(\frac{\partial^2 \omega_R}{\partial r^2} + \frac{1}{r} \frac{\partial \omega_R}{\partial r} - \frac{\omega_R}{r^2} - \frac{1}{r^2} \frac{\partial \omega_\Phi}{\partial \varphi} \right) + \\
& + \gamma_2 \left(\frac{1}{r^2} \frac{\partial^2 \omega_R}{\partial \varphi^2} - \frac{1}{r^2} \frac{\partial \omega_\Phi}{\partial \varphi} + \frac{\partial^2 \omega_R}{\partial z^2} \right) + \\
& + (\gamma_1 + \gamma_3) \left(\frac{1}{r} \frac{\partial^2 \omega_\Phi}{\partial r \partial \varphi} + \frac{\partial^2 \omega_Z}{\partial r \partial z} \right) + B_R \left[\frac{\partial v_\Phi}{\partial z} - \frac{1}{r} \frac{\partial v_Z}{\partial \varphi} + (\alpha + \xi) \omega_R \right] = 0, \\
& \frac{\gamma}{r^2} \left(\frac{\partial^2 \omega_\Phi}{\partial \varphi^2} + \frac{\partial \omega_R}{\partial \varphi} \right) + \frac{\gamma_1 + \gamma_3}{r} \left(\frac{\partial^2 \omega_R}{\partial r \partial \varphi} + \frac{\partial^2 \omega_Z}{\partial \varphi \partial z} \right) + \\
& + \gamma_2 \left(\frac{1}{r^2} \frac{\partial \omega_R}{\partial \varphi} + \frac{\partial^2 \omega_\Phi}{\partial r^2} + \frac{1}{r} \frac{\partial \omega_\Phi}{\partial r} - \frac{\omega_\Phi}{r^2} + \frac{\partial^2 \omega_\Phi}{\partial z^2} \right) + \\
& + B_\Phi \left[\frac{\partial v_Z}{\partial r} - \frac{\partial v_R}{\partial z} + (\alpha + \xi) \omega_\Phi \right] = 0, \\
& \gamma \frac{\partial^2 \omega_Z}{\partial z^2} + \gamma_2 \left(\frac{\partial^2 \omega_Z}{\partial r^2} + \frac{1}{r} \frac{\partial \omega_Z}{\partial r} + \frac{1}{r^2} \frac{\partial^2 \omega_Z}{\partial \varphi^2} \right) + \\
& + (\gamma_1 + \gamma_3) \left(\frac{\partial^2 \omega_R}{\partial r \partial z} + \frac{1}{r} \frac{\partial \omega_R}{\partial z} + \frac{1}{r} \frac{\partial^2 \omega_\Phi}{\partial \varphi \partial z} \right) + \\
& + B_Z \left[\frac{1}{r} \left(\frac{\partial v_R}{\partial \varphi} - v_\Phi \right) - \frac{\partial v_\Phi}{\partial r} + 2\alpha \omega_Z \right] = 0,
\end{aligned} \tag{24.36}$$

$$\begin{aligned}
& \frac{\lambda^\pm + 2\mu^\pm}{c^\pm} \left(\frac{\partial^2 v_R^\pm}{\partial r^2} + \frac{1}{r} \frac{\partial v_R^\pm}{\partial r} - \frac{1}{r^2} \frac{\partial v_\Phi^\pm}{\partial \varphi} - \frac{v_R^\pm}{r^2} \right) + \\
& + \frac{B_Z^\pm}{2\alpha a^\pm c^\pm r^2} \left(\frac{\partial^2 v_R^\pm}{\partial \varphi^2} - \frac{\partial v_\Phi^\pm}{\partial \varphi} \right) + \frac{\varepsilon B_\Phi^\pm}{a^{\pm 3}} \frac{\partial^2 v_R^\pm}{\partial z^2} + \\
& + \frac{1}{a^\pm} \left(\lambda^\pm - \frac{\varepsilon S^\pm}{a^\pm c^\pm} \right) \frac{\partial^2 v_Z^\pm}{\partial r \partial z} + \frac{1}{c^\pm r} \left(\lambda^\pm - \frac{S^\pm}{2\alpha a^\pm} \right) \frac{\partial^2 v_\Phi^\pm}{\partial r \partial \varphi} = 0, \\
& \frac{\varepsilon B_R^\pm}{a^{\pm 3}} \frac{\partial^2 v_\Phi^\pm}{\partial z^2} + \frac{\lambda^\pm + 2\mu^\pm}{c^\pm r^2} \left(\frac{\partial^2 v_\Phi^\pm}{\partial \varphi^2} + \frac{\partial v_R^\pm}{\partial \varphi} \right) + \\
& + \frac{B_Z^\pm}{2\alpha a^\pm c^\pm} \left(\frac{\partial^2 v_\Phi^\pm}{\partial r^2} + \frac{1}{r} \frac{\partial v_\Phi^\pm}{\partial r} - \frac{v_\Phi^\pm}{r^2} + \frac{1}{r^2} \frac{\partial v_R^\pm}{\partial \varphi} \right) + \\
& + \frac{1}{c^\pm r} \left(\lambda^\pm - \frac{S^\pm}{2\alpha a^\pm} \right) \frac{\partial^2 v_R^\pm}{\partial r \partial \varphi} + \frac{1}{a^\pm r} \left(\lambda^\pm - \frac{\varepsilon S^\pm}{a^\pm c^\pm} \right) \frac{\partial^2 v_Z^\pm}{\partial \varphi \partial z} = 0, \\
& (\lambda^\pm + 2\mu^\pm) \frac{c^\pm}{a^{\pm 2}} \frac{\partial^2 v_Z^\pm}{\partial z^2} + \frac{\varepsilon B_\Phi^\pm}{a^\pm c^{\pm 2}} \left(\frac{\partial^2 v_Z^\pm}{\partial r^2} + \frac{1}{r} \frac{\partial v_Z^\pm}{\partial r} \right) + \frac{\varepsilon B_R^\pm}{a^\pm c^{\pm 2} r^2} \frac{\partial^2 v_Z^\pm}{\partial \varphi^2} + \\
& + \frac{1}{a^\pm} \left(\lambda^\pm - \frac{\varepsilon S^\pm}{a^\pm c^\pm} \right) \left(\frac{\partial^2 v_R^\pm}{\partial r \partial z} + \frac{1}{r} \frac{\partial v_R^\pm}{\partial z} + \frac{1}{r} \frac{\partial^2 v_\Phi^\pm}{\partial \varphi \partial z} \right) = 0.
\end{aligned} \tag{24.37}$$

Substitution ($n = 0, 1, \dots$)

$$\begin{aligned}
v_R &= V_R(r, z) \cos n\varphi, & v_\Phi &= V_\Phi(r, z) \sin n\varphi, & v_Z &= V_Z(r, z) \cos n\varphi, \\
v_R^\pm &= V_R^\pm(r, z) \cos n\varphi, & v_\Phi^\pm &= V_\Phi^\pm(r, z) \sin n\varphi, & v_Z^\pm &= V_Z^\pm(r, z) \cos n\varphi, \\
\omega_R &= \Omega_R(r, z) \sin n\varphi, & \omega_\Phi &= \Omega_\Phi(r, z) \cos n\varphi, & \omega_Z &= \Omega_Z(r, z) \sin n\varphi,
\end{aligned}$$

allows us to separate the variable φ in these equations, reducing the stability analysis to the solution of a homogeneous boundary value problem (24.26), (24.27), (24.36), (24.37) for a system of twelve partial differential equations in the twelve unknown functions of two variables r, z .

24.4 Axisymmetric Buckling

In the special case of axisymmetric perturbations ($n = 0$) the use of substitution (Sheydakov 2013)

$$\begin{aligned}
v_R &= V_R(z) J_1(\beta r), & v_\Phi &= 0, & v_Z &= V_Z(z) J_0(\beta r), \\
v_R^\pm &= V_R^\pm(z) J_1(\beta r), & v_\Phi^\pm &= 0, & v_Z^\pm &= V_Z^\pm(z) J_0(\beta r), \\
\omega_R &= 0, & \omega_\Phi &= \Omega_\Phi(z) J_1(\beta r), & \omega_Z &= 0,
\end{aligned} \tag{24.38}$$

$$\beta = \sigma_m / r_0, \quad J_1(\sigma_m) = 0, \quad m = 1, 2, \dots$$

leads additionally to the separation of variable r in the linearized boundary value problem (24.26), (24.27), (24.36), (24.37) and allows satisfying the linearized edge conditions (24.27). Here J_0, J_1 are the Bessel functions of the first kind.

Taking into account relations (24.38), the equations of neutral equilibrium (24.36), (24.37) are written as follows:

$$\begin{aligned} \tau V_R'' - (\lambda + \psi) \beta^2 V_R - (\lambda + \mu) \beta V_Z' + B_\Phi \Omega_\Phi' &= 0, \\ (\lambda + \psi) V_Z'' - \tau \beta^2 V_Z + (\lambda + \mu) \beta V_R' - \beta B_\Phi \Omega_\Phi &= 0, \\ \gamma_2 \Omega_\Phi'' + [(\alpha + \xi) B_\Phi - \gamma_2 \beta^2] \Omega_\Phi - B_\Phi V_R' - \beta B_\Phi V_Z &= 0, \\ \frac{\varepsilon B_\Phi^\pm}{a^{\pm 3}} V_R^{\pm''} - \frac{(\lambda^\pm + 2\mu^\pm) \beta^2}{c^\pm} V_R^\pm - \frac{\beta}{a^\pm} \left(\lambda^\pm - \frac{\varepsilon S^\pm}{a^\pm c^\pm} \right) V_Z^{\pm'} &= 0, \\ (\lambda^\pm + 2\mu^\pm) \frac{c^\pm}{a^{\pm 2}} V_Z^{\pm''} - \frac{\varepsilon \beta^2 B_\Phi^\pm}{a^\pm c^{\pm 2}} V_Z^\pm + \frac{\beta}{a^\pm} \left(\lambda^\pm - \frac{\varepsilon S^\pm}{a^\pm c^\pm} \right) V_R^{\pm'} &= 0. \end{aligned} \tag{24.39}$$

The linearized boundary conditions (24.26) take the form:

(1) on the faces of the plate ($z = \pm h \pm h^\pm$)

$$\frac{B_\Phi^\pm}{a^\pm} V_R^{\pm'} + \frac{\beta S^\pm}{c^\pm} V_Z^\pm = 0, \quad \lambda^\pm \beta V_R^\pm + (\lambda^\pm + 2\mu^\pm) \frac{c^\pm}{a^\pm} V_Z^{\pm'} = 0; \tag{24.40}$$

(2) at the interfaces between the coatings and the core ($z = \pm h$)

$$\begin{aligned} \tau V_R' - \mu \beta V_Z + B_\Phi \Omega_\Phi &= \frac{\varepsilon B_\Phi^\pm}{a^{\pm 3}} V_R^{\pm'} + \frac{\varepsilon \beta S^\pm}{a^{\pm 2} c^\pm} V_Z^\pm, \\ \lambda \beta V_R + (\lambda + \psi) V_Z' &= \frac{\lambda^\pm \beta}{a^\pm} V_R^\pm + (\lambda^\pm + 2\mu^\pm) \frac{c^\pm}{a^{\pm 2}} V_Z^{\pm'}, \\ \Omega_\Phi' &= 0, \quad V_R = V_R^\pm, \quad V_Z = V_Z^\pm. \end{aligned} \tag{24.41}$$

Thus, in the case of axisymmetric perturbations, the stability analysis of a circular sandwich plate with a porous core and prestressed uniform coatings is reduced to solving a linear homogeneous boundary value problem (24.39)–(24.41) for a system of seven ordinary differential equations.

24.5 Sandwich Plate with Identical Coatings

It is easy to show that in the case of identical top and bottom coatings ($h^+ = h^-$, $a^+ = a^-$, $\lambda^+ = \lambda^-$, $\mu^+ = \mu^-$) the boundary value problem (24.39)–(24.41) has two independent sets of solutions (Sheydakov 2011b, 2013). The **First set** is formed

by solutions for which the deflection of a sandwich plate is an odd function of z (a symmetric buckling):

$$\begin{aligned} V_R(z) &= V_R(-z), & V_Z(z) &= -V_Z(-z), & \Omega_\Phi(z) &= -\Omega_\Phi(-z), & 0 \leq z \leq h, \\ V_R^+(z) &= V_R^-(z), & V_Z^+(z) &= -V_Z^-(z), & & & h \leq z \leq h + h^+. \end{aligned}$$

For the **Second set** of solutions, on the contrary, the deflection is an even function of z (a flexural buckling):

$$\begin{aligned} V_R(z) &= -V_R(-z), & V_Z(z) &= V_Z(-z), & \Omega_\Phi(z) &= \Omega_\Phi(-z), & 0 \leq z \leq h, \\ V_R^+(z) &= -V_R^-(z), & V_Z^+(z) &= V_Z^-(z), & & & h \leq z \leq h + h^+. \end{aligned}$$

Due to this property, it is sufficient to consider only half of the sandwich plate ($0 \leq z \leq h + h^+$) to study its stability. The boundary conditions at $z = 0$ follow from the evenness and oddness of the unknown functions V_R, V_Z, Ω_Φ :

(1) for the **First set** of solutions:

$$V'_R(0) = V_Z(0) = \Omega_\Phi(0) = 0, \tag{24.42}$$

(2) for the **Second set** of solutions:

$$V_R(0) = V'_Z(0) = \Omega'_\Phi(0) = 0. \tag{24.43}$$

Thus, the stability analysis of a circular sandwich plate with a porous core and identical prestressed coatings can be reduced to solving two linear homogeneous boundary value problems—(24.39)–(24.42) and (24.39)–(24.41), (24.43)—for a system of five ordinary differential equations.

24.6 Conclusion

In the framework of bifurcation approach, we have studied the stability of a circular sandwich plate under radial compression. The plate consists of a micropolar porous core and non-polar uniform coatings. The coatings were assumed to be subjected to preliminary deformations and contain internal stresses. When determining the subcritical deformed state in different parts of a sandwich plate, writing of constitutive relations with respect to different reference configurations was used. For the physically linear material, we have derived the equations of neutral equilibrium (24.36), (24.37), which describe the behavior of a circular sandwich plate with a porous core and prestressed uniform coatings in a perturbed state. Using a special substitution (24.38), these equations were simplified and the linearized boundary value problem was formulated for the case of axisymmetric perturbations. Thus, the stability analysis was reduced to solving a linear homogeneous boundary value prob-

lem (24.39)–(24.41) for a system of seven ordinary differential equations. It was also shown that for a circular sandwich plate with identical top and bottom coatings the stability analysis can be reduced to solving two linear homogeneous boundary value problems—(24.39)–(24.42) and (24.39)–(24.41), (24.43)—for a system of five ordinary differential equations. For specific materials of the porous core and the coatings all formulated boundary value problems can be solved numerically, using methods described by Sheydaikov (2016, 2021).

Acknowledgements The study was supported by the Russian Science Foundation grant No. 23-21-00462, <https://rscf.ru/en/project/23-21-00462/>.

References

- Altenbach J, Altenbach H, Eremeyev VA (2010) On generalized Cosserat-type theories of plates and shells: a short review and bibliography. *Arch Appl Mech* 80:73–92
- Ashby MF, Evans AG, Fleck NA, Gibson LJ, Hutchinson JW, Wadley HNG (2000) *Metal foams: a design guide*. Butterworth-Heinemann, Boston
- Banhart J (2000) Manufacturing routes for metallic foams. *JOM* 52(12):22–27
- Cosserat E, Cosserat F (1909) *Theorie des Corps Deformables*. Hermann et Fils, Paris
- Degischer HP, Kriszt B (eds) (2002) *Handbook of cellular metals. Production, processing, applications*. Wiley-VCH, Weinheim
- Diebels S (1999) A micropolar theory of porous media: constitutive modelling. *Trans Porous Media* 34(1–3):193–208
- Diebels S, Steeb H (2002) The size effect in foams and its theoretical and numerical investigation. *Proc R Soc Lond A* 458(3):2869–2883
- Eremeev VV, Zubov LM (2017) Buckling of a two-layered circular plate with a prestressed layer. *Math Mech Solid* 22(4):773–781
- Eremeyev VA, Zubov LM (1994) On the stability of elastic bodies with couple-stresses. *Mech Solids* 29(3):172–181
- Eringen AC (1999) *Microcontinuum field theory. I. Foundations and solids*, Springer, New York
- Fu YB, Ogden RW (1999) Nonlinear stability analysis of pre-stressed elastic bodies. *Contin Mech Thermodyn* 11:141–172
- Gibson LJ, Ashby MF (1997) *Cellular solids: structure and properties*, 2nd edn. Cambridge University Press, Cambridge, Cambridge solid state science series
- Green AE, Adkins JE (1960) *Large elastic deformations and non-linear continuum mechanics*. Clarendon Press, Oxford
- Kafadar CB, Eringen AC (1971) Micropolar media—I. The classical theory. *Int J Eng Sci* 9, 271–305 (1971)
- Lakes RS (1986) Experimental microelasticity of two porous solids. *Int J Solids Struct* 22:55–63
- Lakes RS (1995) Experimental methods for study of Cosserat elastic solids and other generalized elastic continua. In: Mühlhaus H (ed) *Continuum models for materials with micro-structure*. Wiley, New York, pp 1–22
- Lurie AI (1990) *Non-linear theory of elasticity*. North-Holland, Amsterdam
- Maugin GA (1998) On the structure of the theory of polar elasticity. *Philos Trans R Soc Lond A* 356:1367–1395
- Merodio J, Ogden RW (2016) Extension, inflation and torsion of a residually stressed circular cylindrical tube. *Contin Mech Thermodyn* 28:157–174
- Merodio J, Ogden RW, Rodriguez J (2013) The influence of residual stress on finite deformation elastic response. *Int J Nonlin Mech* 56:43–49

- Nikitin E, Zubov LM (1998) Conservation laws and conjugate solutions in the elasticity of simple materials and materials with couple stress. *J Elast* 51:1–22
- Ogden RW, Steigmann DJ, Haughton DM (1997) The effect of elastic surface coating on the finite deformation and bifurcation of a pressurized circular annulus. *J Elast* 47(2):121–145
- Pietraszkiewicz W, Eremeyev VA (2009) On natural strain measures of the non-linear micropolar continuum. *Int J Solids Struct* 46:774–787
- Pignataro M, Rizzi N, Luongo A (1991) *Stability*. Elsevier, bifurcation and postcritical behaviour of elastic structures
- Sheydakov DN (2011) Buckling of elastic composite rods made of micropolar material subjected to combined loads. In: Altenbach H, Erofeev V, Maugin G (eds) *Mechanics of generalized continua—from micromechanical basics to engineering applications, advanced structured materials*, vol 7. Springer, Berlin, pp 255–271
- Sheydakov DN (2011) On stability of elastic rectangular sandwich plate subject to biaxial compression. In: Altenbach H, Eremeyev VA (eds) *Shell-like Structures—non-classical theories and applications, advanced structured materials*, vol 15. Springer, Berlin, pp 203–216
- Sheydakov DN (2013) Buckling of inhomogeneous circular plate of micropolar material. In: Altenbach H, Forest S, Krivtsov A (eds) *Generalized continua as models for materials with multi-scale effects or under multi-field actions, advanced structured materials*, vol 22. Springer, Berlin, pp 291–302
- Sheydakov DN (2016) Size effect on buckling of non-uniform circular plate made of foam material. *Mater Phys Mech* 28(1–2):26–30
- Sheydakov DN (2021) Stability of circular micropolar rod with prestressed two-layer coating. *Contin Mech Thermodyn* 33:1313–1329
- Timoshenko SP, Gere JM (2009) *Theory of elastic stability*. Dover Publications, New York
- Toupin RA (1964) Theories of elasticity with couple-stress. *Arch Ration Mech Anal* 17:85–112
- Truesdell C (1977) *A first course in rational continuum mechanics*. Academic Press, New York
- Volmir AS (1970) *Stability of deformable systems*. Foreign technology division, Wright-Patterson AFB
- Zubov LM (1997) *Nonlinear theory of dislocations and disclinations in elastic bodies*. Springer, Berlin
- Zubov LM (2016) Universal deformations of micropolar isotropic elastic solids. *Math Mech Solid* 21(2):152–167
- Zubov LM (2019) Universal solution of nonlinear elasticity for a hollow cylinder with prestressed coatings. *Acta Mech* 230:4137–4143

Chapter 25

Localized Modes in a 1D Harmonic Crystal with a Mass-Spring Inclusion



Ekaterina V. Shishkina and Serge N. Gavrilov

Abstract The spectral problem concerning the existence of localized modes of oscillation in 1D harmonic crystal with a single mass-spring inclusion is investigated. A crystal is an infinite harmonic chain of particles with nearest-neighbor interaction. The bond stiffnesses are referred to as “springs”. Two types of inclusion are considered, namely, a symmetric and an asymmetric ones. The symmetric inclusion consists of the particle of an alternated mass with two springs of alternated stiffnesses attached. The asymmetric inclusion consists of the particle of an alternated mass with one alternated spring attached. Outside the inclusion the chain is assumed to be uniform. For both types of a mass-spring inclusion, the necessary and sufficient conditions for the existence of localized modes, as well as the corresponding frequencies of localized oscillation, are found.

25.1 Introduction

The phenomenon of localized modes of linear oscillation is well known for both continuum (Glushkov et al. 2011; Indeitsev et al. 2007; Kuznetsov et al. 2002; Ursell 1951) and discrete (Andrianov et al. 2012; Gendelman and Paul 2021; Kossevich 1999; Manevich et al. 1989; Maradudin et al. 1963; Montroll and Potts 1955; Rubin 1963; Teramoto and Takeno 1960; Yu 2019) systems. In discrete mechanical systems, to the best of our knowledge, this phenomenon was first time described in the classical study by Montroll and Potts (1955), though it was previously known in physics for non-mechanical systems (Conwell et al. 1950; Koster 1954; Koster and Slater 1954). In the discrete case, usually, isotopic (i.e., pure inertial) or pure elastic inclusions

E. V. Shishkina · S. N. Gavrilov (✉)
Institute for Problems in Mechanical Engineering RAS, V.O., Bolshoy pr. 61, St. Petersburg
199178, Russia
e-mail: serge@pdmi.ras.ru

E. V. Shishkina
e-mail: shishkina_k@mail.ru

are considered, though in the referenced above work (Montroll and Potts 1955) a mass-spring inclusion is also discussed.

To discover the existence of a localized mode in a system, one needs to consider a spectral problem, see, e.g., Indeitsev et al. (2007). If localized mode exists in a system, then one can observe (Shishkina et al. 2023) the localization of non-stationary waves.¹ Namely, some portions of the wave energy can be trapped forever near inhomogeneities (in the absence of dissipation). One can observe undamped localized vibration of an infinite system subjected to an impulse loading. For a discrete mechanical system this was shown first time by Teramoto and Tokeno (1960).

The localized modes essentially influence on another wave phenomenon, which we call the anti-localization of non-stationary waves (Shishkina and Gavrilov 2023; Shishkina et al. 2023). This is zeroing of the non-localized propagating component of the wave-field in a neighborhood of an inclusion. The anti-localization breaks at the boundary of the localization domain (the domain of existence for the localized mode in the problem parameters space). This fact can be discovered only by considering the systems, where the boundary of the localization domain does not correspond to a homogeneous system without any inclusion (Shishkina et al. 2023). This is our main motivation to investigate the problems involving mass-spring inclusions.

In the paper we systematically investigate the spectral problems concerning the existence of localized modes of oscillation in 1D harmonic crystal with a mass-spring inclusion. A crystal is an infinite harmonic chain of particles with nearest-neighbor interaction. The bond stiffnesses are referred to as “springs”. The chain contains a single mass-spring inclusion, which consists of a single particle with an alternated mass and two or one springs attached to this particle with an alternated stiffness. The first case is the case of a symmetric inclusion, whereas the second case is the case of an asymmetric inclusion. Outside the inclusion the chain is assumed to be uniform. The schematic of the system is presented in Fig. 25.1. For both types of a mass-spring inclusion, the necessary and sufficient conditions for the existence of localized modes are found, as well as the corresponding frequencies of localized oscillation. Note that

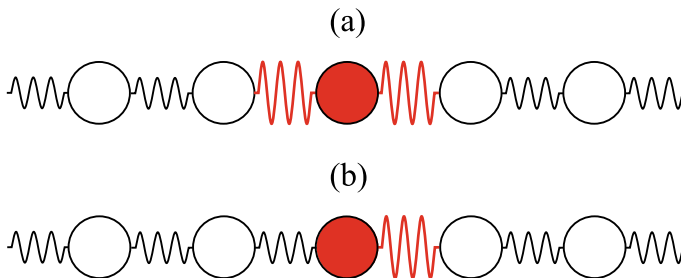


Fig. 25.1 The schematic of the system. **a** The case of a symmetric inclusion, **b** the case of an asymmetric inclusion

¹ In the discrete case it is more correct to speak about quasi-waves, since the perturbations propagate at an infinite speed.

the spectral problem for a continuum analogue of discrete problems considered in the paper is investigated in Glushkov et al. (2011), Gavrilov et al. (2019).

Note that the case of a symmetric mass-spring inclusion was previously considered by Montroll and Potts in (1955), who obtained the expression for the frequency of the antisymmetric localized mode and the frequency equation for the symmetric mode. For the symmetric oscillation the problem solution was not finalized, namely, neither the expression for the admissible frequency was explicitly derived, nor the domain of existence for the corresponding mode was obtained. In recent paper (Yu 2019) Yu considered a non-stationary problem for the case of a symmetric mass-spring inclusion and, in particular, obtained the frequency of the symmetric localized oscillation and its domain of existence. In our opinion, although the results obtained in Yu (2019) are correct, they have been derived by a wrong way. The more detailed comparison of the results obtained in this paper with the known results is given in Discussion (see Sect. 25.5).

25.2 The Mathematical Formulation for the Spectral Problem

The equations of motions in the dimensionless form can be expressed as the following infinite system of differential-difference equations:

$$\begin{aligned} \ddot{u}_n - (u_{n+1} - 2u_n + u_{n-1}) \\ = (- (m - 1)\ddot{u}_0 + (K - 1)((u_1 - u_0) + \gamma(u_{-1} - u_0)))\delta_n \\ - (K - 1)(u_1 - u_0)\delta_{n-1} + \gamma(K - 1)(u_0 - u_{-1})\delta_{n+1}, \end{aligned} \quad (25.1)$$

where $n \in \mathbb{Z}$, δ_n is the Kronecker delta, $u_n(t)$ is the dimensionless displacement of the particle with a number n , $n = 0$ corresponds to the particle with alternated dimensionless mass m , $\gamma = 1$ corresponds to the case of a symmetric inclusion, and $\gamma = 0$ corresponds to the case of an asymmetric inclusion. We assume that

$$m > 0 \quad \text{and} \quad K > 0; \quad (25.2)$$

$$m \neq 1 \quad \text{or} \quad K \neq 1. \quad (25.3)$$

The differential-difference operator in the left-hand side of Eq. (25.1) corresponds to a uniform chain of mass points of unit mass connected by springs of unit stiffness. The non-dimensionalization is discussed, e.g., in Shishkina and Gavrilov (2023). Assuming that $u_n(t)$ is a harmonic oscillation

$$u_n(t) = U_n(\Omega) e^{-i\Omega t}, \quad (25.4)$$

consider the steady-state problem concerning the natural localized oscillation at a frequency Ω . In what follows, we assume without loss of generality that

$$\Omega > 0. \tag{25.5}$$

Since we deal with a linear system, for the uniform chain ($m = 1, K = 1$) the corresponding solutions for amplitudes are

$$U_n = U_0 e^{-iqn}, \tag{25.6}$$

where q is the (quasi-)wave-number. The frequency Ω and wave-number q are related by the dispersion relation, which properties are discussed in Appendix.

In the case of the chain with the inclusion, we look for a mode with finite energy, and, therefore, we require that U_n satisfy conditions

$$\sum_{n=-\infty}^{\infty} U_n^2 < \infty, \quad \sum_{n=-\infty}^{\infty} (U_{n+1} - U_n)^2 < \infty, \tag{25.7}$$

and, hence, consider the frequencies inside the stop-band (25.79) (see Appendix). Due to Eq. (25.1) for the amplitudes U_n one gets:

$$-\Omega^2 U_n - (U_{n+1} - 2U_n + U_{n-1}) = ((m - 1)\Omega^2 U_0 + (K - 1)((U_1 - U_0) + \gamma(U_{-1} - U_0)))\delta_n - (K - 1)(U_1 - U_0)\delta_{n-1} + \gamma(K - 1)(U_0 - U_{-1})\delta_{n+1}. \tag{25.8}$$

The last equation can be treated as the equation of motion for the homogeneous chain with three-point loads expressed by terms in the right-hand side. Thus, the solution is

$$U_n = ((m - 1)\Omega^2 U_0 + (K - 1)((U_1 - U_0) + \gamma(U_{-1} - U_0)))G_n + (K - 1)(U_0 - U_1)G_{n-1} + \gamma(K - 1)(U_0 - U_{-1})G_{n+1}, \tag{25.9}$$

where G_n is the Green function for a uniform chain given by Eq. (25.82) (see Appendix).

25.3 The Case of a Symmetric Inclusion

Here we take $\gamma = 1$. Due to symmetry, the oscillation, without lost of generality, can be considered as the sum of symmetric and antisymmetric components:

$$U_n = U_n^s + U_n^a, \tag{25.10}$$

where $U_{-n}^s = U_n^s$, $U_{-n}^a = -U_n^a$. Hence, for the symmetric mode Eq. (25.9) can be rewritten as

$$U_n^s = (m-1)\Omega^2 U_0^s G_n + (K-1)(U_0^s - U_1^s)(G_{n+1} - 2G_n + G_{n-1}), \quad (25.11)$$

where $n \geq 0$. For the antisymmetric mode U_n^a , taking into account that $U_0^a = 0$, we rewrite Eq. (25.9) in the following form:

$$U_n^a = (K-1)U_1^a(G_{n+1} - G_{n-1}). \quad (25.12)$$

25.3.1 Symmetric Mode

Consider now the symmetric mode. We subsequently substitute $n = 0$ and $n = 1$ into Eq. (25.11) and obtain the following homogeneous set of linear algebraic equations for unknown U_0^s and U_1^s :

$$(1 - (m-1)\Omega^2 G_0 - 2(K-1)(G_1 - G_0))U_0^s + 2(K-1)(G_1 - G_0)U_1^s = 0, \quad (25.13)$$

$$\begin{aligned} &((m-1)\Omega^2 G_1 + (K-1)(G_2 - 2G_1 + G_0))U_0^s \\ &- (1 + (K-1)(G_2 - 2G_1 + G_0))U_1^s = 0. \end{aligned} \quad (25.14)$$

Here we have taken into account that $G_n = G_{-n}$. A non-trivial solutions exist if and only if the determinant of the set is zero. Substituting expression (25.82) for the Green function, calculating the determinant, and simplifying the complicated expression obtained lead to the frequency equation for the symmetric mode:

$$\Omega L(\Omega) = -\sqrt{\Omega^2 - 4R(\Omega)}, \quad (25.15)$$

where

$$L(\Omega) = m\Omega^6 - ((m+2)K + 5m)\Omega^4 + (2(2m+5)K + 5m)\Omega^2 - 2K(m+5), \quad (25.16)$$

$$R(\Omega) = m\Omega^6 - ((m+2)K + 3m)\Omega^4 + (2(m+3)K + m)\Omega^2 - 2K. \quad (25.17)$$

Here we have taken into account that (25.79) is fulfilled. Equation (25.15) after squaring, which is possible if and only if

$$L(\Omega)R(\Omega) \leq 0, \quad (25.18)$$

can be equivalently transformed to the form of the following bi-quadratic equation:

$$m^2(K - 1)\Omega^4 + Km(- (m + 2)K + 4)\Omega^2 - 4K^2 = 0. \tag{25.19}$$

The solution of the last equation (25.19) in the case

$$K \neq 1 \tag{25.20}$$

is

$$\Omega^2 = \Omega_{\pm}^2 \stackrel{\text{def}}{=} \frac{K \left(-4 + (m + 2)K \pm \sqrt{((m + 2)^2 K - 8m)K} \right)}{2(K - 1)m}. \tag{25.21}$$

The special case $K = 1$ is considered in Sect. 25.3.3. Since $\Omega \in \mathbb{R}$, the discriminant for Eq. (25.19) must be non-negative:

$$K \geq \frac{8m}{(m + 2)^2}. \tag{25.22}$$

Finally, the domain of existence for modes with corresponding frequencies Ω_{\pm} are areas in the two-dimensional parameter space,² where inequalities (25.79), (25.18), and (25.22) are fulfilled. For the mode with the frequency $\Omega = \Omega_+$ the domain of existence is plotted in Fig. 25.2 (see zone “4”). For the root Ω_- restriction (25.18) is never satisfied in the domain where Eq. (25.22) is fulfilled.

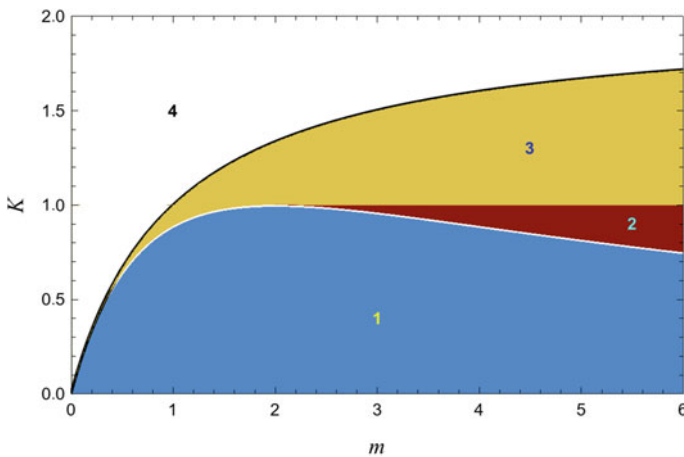


Fig. 25.2 The domain of existence (zone 4) for the symmetric mode with the frequency $\Omega = \Omega_+$ in the case of symmetric inclusion. Outside of zone “1” inequality (25.22) is true; in zone “2” inequality (25.77) is true; in zones “2” and “3” inequality (25.18) is false

² The parameters are m and K .

The boundary for the domain of existence for the mode with the frequency $\Omega = \Omega_+$ is the boundary between zones “3” and “4”, which corresponds to a common root of the equation

$$L(\Omega)R(\Omega) = 0, \quad (25.23)$$

and frequency equation (25.15). To find the analytic expression for the boundary we should prove the following lemma.

Lemma 1 *Provided that Eqs. (25.2), (25.3), (25.5), (25.20) are true, $\Omega = 2$ is the unique solution of set of Eqs. (25.23), (25.15), which exists if and only if*

$$K = \frac{2m}{1+m}. \quad (25.24)$$

Proof Clearly, the right-hand side of (25.15) is zero at $\Omega = 2$. Thus, $\Omega = 2$ is the solution of set (25.23), (25.15) if and only if $L(2) = 0$. Calculating $L(2)$ and putting the expression obtained to zero yields

$$-2Km - 2K + 4m = 0, \quad (25.25)$$

which is equivalent to Eq. (25.24).

Let positive $\Omega \neq 2$ satisfies Eqs. (25.23), (25.15). Then

$$L(\Omega) - R(\Omega) \equiv -2m\Omega^4 + 2(2m + K(2 + m))\Omega^2 - 2K(4 + m) = 0. \quad (25.26)$$

Since Eq. (25.23) is true, Eq. (25.19) follows from Eq. (25.15). Thus, Ω is a common root of two bi-quadratic equations, namely Eqs. (25.19), (25.26), hence, the left-hand sides of these equations must be proportional. Calculating the remainder of two polynomials, which equal to the left-hand sides of (25.19) and (25.26), and putting the result to zero, one gets for all Ω :

$$(Km(m+2) - 2m^2)\Omega^2 + Km^2 + 4Km - K^2(m+2)^2 \equiv 0, \quad (25.27)$$

which is equivalent to $m = 0$ and $K = 0$. □

Remark 1 One can easily prove that for $K > 0$ and $m > 0$ polynomials $L(\Omega)$ and $R(\Omega)$ do not have common roots by calculating the Gröbner basis (Buchberger 2002) for this set of polynomials.

Hence, the boundary between zones “3” and “4” corresponds to the curve, where Eq. (25.24) is fulfilled. Finally, there exists the unique symmetric localized mode with the frequency $\Omega = \Omega_+$, where Ω_+ is given by Eq. (25.21). The domain of existence for this mode is

$$K > \frac{2m}{1+m}. \quad (25.28)$$

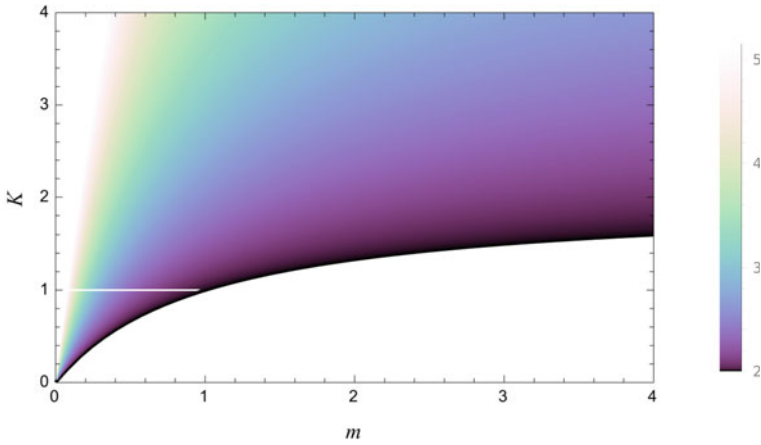


Fig. 25.3 The value of the trapped mode frequency $\Omega = \Omega_+$ defined according to Eq. (25.21) inside the domain of existence (25.28) in the case of a symmetric inclusion

The frequency equation in the form of bi-quadratic equation (25.19) was previously obtained by Montroll and Potts in (1955). The authors in Montroll and Potts (1955) do not find the explicit expressions for the roots of this equation and do not examine their properties, hence, they do not obtain the domain (25.28) of existence for the symmetric mode of localized oscillation.

In Fig. 25.3 one can see the plot of the value of the trapped mode frequency Ω_+ defined according to Eq. (25.21) inside the domain of existence (25.28).

25.3.2 Antisymmetric Mode

Consider now the antisymmetric mode. One substitutes $n = 1$ into Eq. (25.12) and gets

$$((K - 1)(G_2 - G_0) - 1)U_1^a = 0. \tag{25.29}$$

The non-trivial solution for U_1^a exists if and only if

$$(K - 1)(G_2 - G_0) - 1 = 0. \tag{25.30}$$

Substituting expression (25.82) for the Green function, and simplifying the complicated expression obtained yields the following frequency equation:

$$2K - \Omega^2 = \Omega\sqrt{\Omega^2 - 4}. \tag{25.31}$$

Equation (25.31) after squaring, which is possible if and only if

$$2K - \Omega^2 \geq 0, \quad (25.32)$$

can be equivalently transformed to the form of the following expression:

$$\Omega^2 = \frac{K^2}{K - 1}. \quad (25.33)$$

One can see that $\Omega \in \mathbb{R}$, if and only if

$$K > 1. \quad (25.34)$$

Finally, the domain of existence for the antisymmetric mode with frequency (25.33) is the area in the two-dimensional parameter space, where inequalities (25.32), (25.34), and (25.79) are fulfilled. Substituting Eq. (25.33) into restrictions (25.32), (25.79), respectively, leads to the following inequalities:

$$\frac{K(K - 2)}{K - 1} \geq 0, \quad (25.35)$$

$$\frac{K^2}{K - 1} > 4. \quad (25.36)$$

The solution of the set of inequalities (25.34)–(25.36) is

$$K > 2. \quad (25.37)$$

Thus, provided that (25.37) is true, there exists the unique antisymmetric localized mode with frequency given by (25.33).

Results of Sect. 25.3.2 re-obtain the ones derived by Montroll and Potts in (1955). Namely, in Montroll and Potts (1955) the authors obtained frequency equation (25.30), Eq. (25.33) for the frequency of antisymmetric localized mode and domain of its existence (25.37).

25.3.3 The Special Case $K = 1$

Consider the particular case $K = 1$. The antisymmetric mode in this case cannot exist. For the symmetric mode frequency equation (25.19) transforms to the following one:

$$m(2 - m)\Omega^2 - 4 = 0. \quad (25.38)$$

Hence, the frequency of the localized mode is

$$\Omega = \Omega_0 \stackrel{\text{def}}{=} \frac{2}{\sqrt{m(2 - m)}}. \quad (25.39)$$

Here, obviously, $m < 2$, since $\Omega \in \mathbb{R}$. The left-hand side of Eq. (25.18) with Ω given by (25.39) is

$$L(\Omega_0)R(\Omega_0) = \frac{4(m-1)m^6}{(m-2)^6}. \quad (25.40)$$

Thus, Eq. (25.18) is equivalent to

$$m \leq 1. \quad (25.41)$$

Taking into account that restriction (25.79) for Ω described by Eq. (25.39) is equivalent to the inequality

$$(m-1)^2 > 0, \quad (25.42)$$

which is true for all $m \neq 1$, one gets the expression for the domain of existence for the localized mode

$$m < 1. \quad (25.43)$$

Note that it is the particular case of Eq. (25.28) for $K = 1$.

These results for the particular case $K = 1$ are well known in the literature and coincide with the ones previously obtained in many studies, e.g., in Montroll and Potts (1955) or in recent paper (Shishkina and Gavrilov 2023).

25.4 The Case of an Asymmetric Inclusion

Let us take $\gamma = 0$ and substitute $n = 0$ and $n = 1$ into Eq. (25.9). We obtain the following homogeneous set of linear algebraic equations for unknown U_0 and U_1 :

$$((m-1)\Omega^2 G_0 - (K-1)(G_0 - G_1) - 1)U_0 + (K-1)(G_0 - G_1)U_1 = 0, \quad (25.44)$$

$$((m-1)\Omega^2 G_1 - (K-1)(G_1 - G_0))U_0 + ((K-1)(G_1 - G_0) - 1)U_1 = 0. \quad (25.45)$$

Here one has taken into account that $G_n = G_{-n}$. A non-trivial solutions exist if and only if the determinant of the set is zero. Substituting expression (25.82) for the Green function G_n , calculating the determinant, and simplifying the complicated expression obtained lead to the frequency equation for the localized mode:

$$\Omega L(\Omega) = -\sqrt{\Omega^2 - 4R(\Omega)}, \quad (25.46)$$

where

$$L(\Omega) = m\Omega^4 - (1 + K + 3m + Km)\Omega^2 + 2 + 4K + 2Km, \quad (25.47)$$

$$R(\Omega) = m\Omega^4 - (1 + K)(1 + m)\Omega^2 + 2K. \quad (25.48)$$

Here we have taken into account that (25.79) is fulfilled. Equation (25.46) after squaring, which is possible if and only if

$$L(\Omega)R(\Omega) \leq 0, \quad (25.49)$$

can be equivalently transformed to the form of the following bi-quadratic equation:

$$m(m-1)(K-1)\Omega^4 + (K^2 - (1-Km)^2)\Omega^2 - 4K^2 = 0. \quad (25.50)$$

In the case

$$m \neq 1 \quad \text{and} \quad K \neq 1 \quad (25.51)$$

the solution of Eq. (25.50) is

$$\Omega^2 = \Omega_{\pm}^2 \stackrel{\text{def}}{=} \frac{(1-Km)^2 - K^2 \pm \sqrt{(1+K(m-1))^2(1+K(2-6m+K(1+m)^2))}}{2(K-1)(m-1)m}. \quad (25.52)$$

The special case $K = 1$ is considered in Sect. 25.3.3. The case $m = 1$ is treated in Sect. 25.4.1. Since $\Omega \in \mathbb{R}$, the discriminant for Eq. (25.50) must be non-negative:

$$1 + K(m-1) = 0 \quad \text{or} \quad 1 + K(2-6m+K(1+m)^2) \geq 0. \quad (25.53)$$

The first expression in Eq. (25.53) is equivalent to

$$K = \frac{1}{1-m}. \quad (25.54)$$

For inequality (25.53) one can obtain the following equivalent one:

$$(1+m)^2 K^2 + 2(1-3m)K + 1 \geq 0. \quad (25.55)$$

We can demonstrate that this inequality is satisfied if and only if

$$\left(m \leq 1 \text{ and } K > 0\right) \quad \text{or} \quad \left(m > 1 \text{ and } K \in (0, K_-] \cup [K_+, +\infty)\right), \quad (25.56)$$

where

$$K_{\pm} \stackrel{\text{def}}{=} \frac{3m-1 \pm 2\sqrt{2m(m-1)}}{(1+m)^2}. \quad (25.57)$$

Note that $K_+ = K_- = 1/2$ at $m = 1$.

Finally, the domain of existence for modes with corresponding frequencies Ω_{\pm} are areas in the two-dimensional parameter space, where restrictions (25.79), (25.49), and (25.56) are fulfilled. For modes with frequency $\Omega = \Omega_-$ and $\Omega = \Omega_+$ the domains of existence are plotted in Fig. 25.4a, b, respectively (see zone “4” in each plot).

The boundaries for the domain of existence for the modes with the frequencies $\Omega = \Omega_{\pm}$ correspond to the common roots of the equation

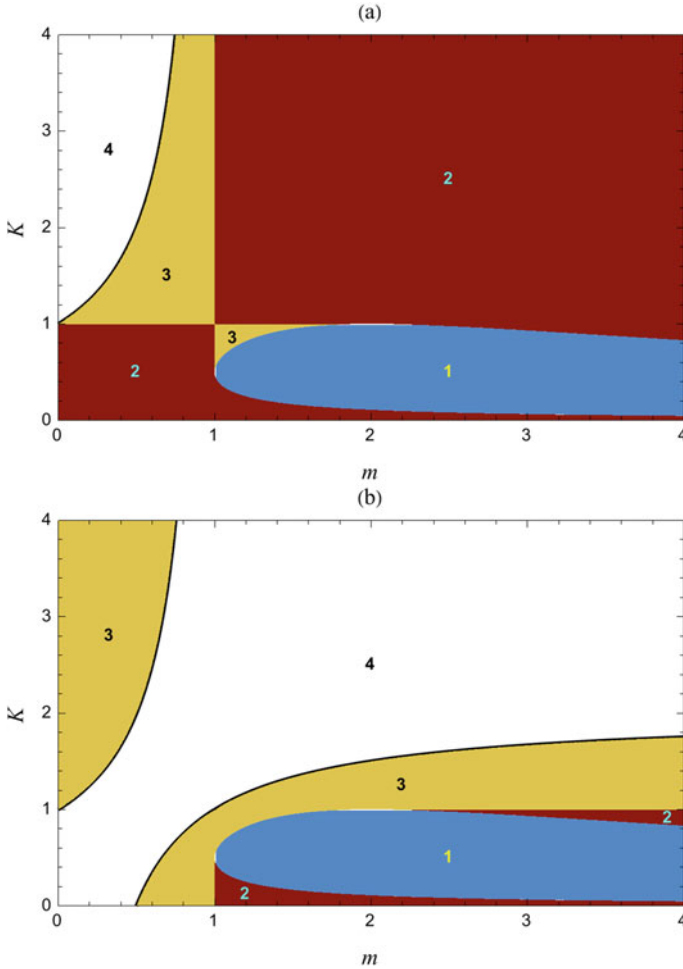


Fig. 25.4 The domain of existence (zone 4) for the mode with the frequency **a** $\Omega = \Omega_-$, **b** $\Omega = \Omega_+$ in the case of asymmetric inclusion. Outside of zone “1” restriction (25.56) is true; in zone “2” inequality (25.77) is true; in zones “2” and “3” inequality (25.49) is false

$$L(\Omega)R(\Omega) = 0, \quad (25.58)$$

and frequency equation (25.46).

Lemma 2 *Provided that Eqs. (25.2), (25.5), (25.51) are true, the solutions of set of Eqs. (25.58), (25.46) are*

1. $\Omega = 2$, which exists if and only if

$$K = 2 - \frac{1}{m}; \quad (25.59)$$

2.

$$\Omega = \sqrt{\frac{2}{(1-m)m}}, \quad (25.60)$$

which exists if and only if inequality

$$m < 1 \quad (25.61)$$

and Eq. (25.54) are fulfilled.

There are no more solutions.

Proof Clearly, the right-hand side of (25.46) is zero at $\Omega = 2$. Thus, $\Omega = 2$ is the solution of set (25.58), (25.46) if and only if $L(2) = 0$. Calculating $L(2)$ yields:

$$Km - 2m + 1 = 0, \quad (25.62)$$

which is equivalent to Eq. (25.59).

Let $\Omega \neq 2$ satisfies Eqs. (25.58), (25.46). Equation (25.58) can be fulfilled if and only if Ω is a common root of equations:

$$L(\Omega) = 0, \quad (25.63)$$

$$R(\Omega) = 0. \quad (25.64)$$

Therefore,

$$L(\Omega) - R(\Omega) = 2(-m\Omega^2 + K(1+m) + 1) = 0, \quad (25.65)$$

which is equivalent to

$$\Omega = \sqrt{\frac{1 + K(1+m)}{m}}. \quad (25.66)$$

Since Eq. (25.58) is true, Eq. (25.50) follows from Eq. (25.46). Thus, Eq. (25.66) should be a common root of Eq. (25.65) and bi-quadratic equation (25.50). Substituting Eq. (25.66) into Eq. (25.50) leads to

$$-4(1 + K(m - 1))^2 = 0, \quad (25.67)$$

which is equivalent to Eq. (25.54). For such values of K

$$\Omega = \Omega_{\pm} \Big|_{K=\frac{1}{1-m}} = \sqrt{\frac{2}{(1-m)m}}. \quad (25.68)$$

It is clear, that the root (25.68) exists only if $m < 1$. □

One can see that the root defined by Eq. (25.68) satisfies restriction (25.79):

$$\frac{2}{(1-m)m} > 4 \quad \iff \quad m^2 + (m - 1)^2 > 0. \quad (25.69)$$

Hence, the boundary between zones “3” and “4” in Fig. 25.4a corresponds to the curve, where Eq. (25.54) is fulfilled. The same boundary separates the left simply connected domain of zone “3” and zone “4” in Fig. 25.4b. The boundary between zone “4” and the right simply connected domain of zone “3” in Fig. 25.4b is defined by Eq. (25.59).

The final conclusion can be formulated as follows. Provided that inequality

$$K > 2 - \frac{1}{m} \quad (25.70)$$

is true, there exists the unique localized mode, which frequency equals $\Omega = \Omega_-$ if

$$m < 1 \quad \text{and} \quad K > \frac{1}{1-m}, \quad (25.71)$$

and equals $\Omega = \Omega_+$ otherwise. Note that for $m < 1$ and $K = 1/(1 - m)$ the localized mode exists, and the corresponding frequency is defined by Eq. (25.68).

In Fig. 25.5 one can see the plot of the value of the trapped mode frequency Ω_{\pm} defined according to Eq. (25.52) and the root selection condition (25.71) inside the domain of existence (25.70).

25.4.1 The Special Case $m = 1$

Consider the special case $m = 1$, $K \neq 1$. Frequency equation (25.46) transforms to the following one:

$$(2K - 1)\Omega^2 - 4K^2 = 0. \quad (25.72)$$

Hence, the frequency is

$$\Omega = \frac{2K}{\sqrt{2K - 1}}. \quad (25.73)$$

One can see that $\Omega \in \mathbb{R}$ if and only if $K > 1/2$. It is easy to show that the frequency defined by Eq. (25.73) satisfies restriction (25.79) if and only if $K \neq 1$.

Now we should verify restriction (25.49). Equations (25.47), (25.48) calculated at Ω given by (25.73) transform to the following ones:

$$L(\Omega) = \frac{2(1 - K)}{(2K - 1)^2}, \tag{25.74}$$

$$R(\Omega) = \frac{2K}{(2K - 1)^2}. \tag{25.75}$$

Obviously, inequality (25.49) is satisfied for $K \geq 1$. Since we consider $K \neq 1$, we conclude that the localized mode with frequency Eq. (25.73) exists if and only if $K > 1$.

The results of this particular case were previously obtained in Maradudin et al. (1963).

25.5 Discussion

The spectral problem concerning the existence of localized modes of oscillation in 1D harmonic crystal with a single mass-spring inclusion has been investigated in the paper. We have considered two types of inclusion, namely, a symmetric inclusion (Fig. 25.1a), and an asymmetric inclusion(Fig. 25.1b). Note that the obtained results were verified by numerical calculation of a fundamental solution for the corresponding non-stationary problems at a number of various values of the problem

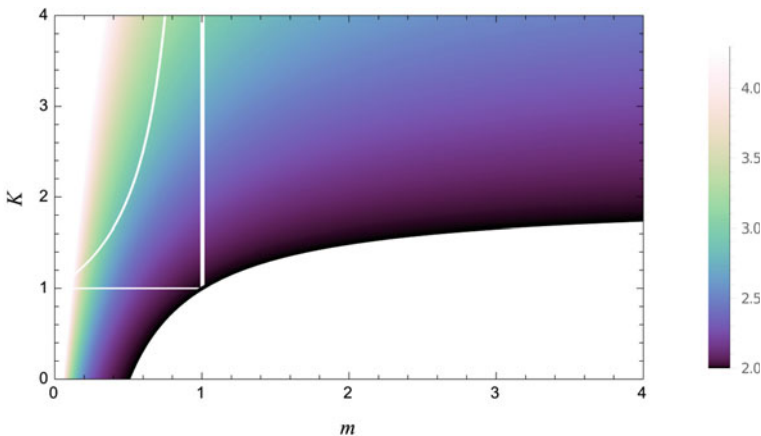


Fig. 25.5 The value of the trapped mode frequency $\Omega = \Omega_{\pm}$ defined according to Eq. (25.52) and the root selection condition (25.71) inside the domain of existence (25.70) in the case of an asymmetric inclusion

parameters m and K . The presence of a localized mode can be easily discovered in the non-stationary response of a system as a non-vanishing oscillation with corresponding frequency (Teramoto and Takeno 1960; Rubin 1963; Shishkina and Gavrilov 2023; Yu 2019; Shishkina et al. 2023). The perfect agreement was obtained.

For the case of a symmetric mass-spring inclusion (Sect. 25.3) oscillation can be uncoupled into two components, namely, the symmetric and antisymmetric ones. For the symmetric mode expression (25.21) for the natural frequency $\Omega = \Omega_+$ is obtained. For the symmetric mode the domain of existence is defined by Eq. (25.28), see Fig. 25.2 for details. The frequency of the antisymmetric mode is given by Eq. (25.33).

Note that the case of a symmetric mass-spring inclusion was previously considered by Montroll and Potts in their famous study (Montroll and Potts 1955), where the expression for the frequency of the antisymmetric localized mode in the form of Eq. (25.33), as well as the frequency equation for the symmetric mode, coinciding with bi-quadratic equation (25.19), were obtained. The solution of Eq. (25.19) was not derived, and the domains of existence for modes with frequencies Ω_{\pm} defined by Eq. (25.21) were not investigated. Note that, as far as we understand (see Remark 1), our unsquared frequency equation (25.15) cannot be reduced to the unsquared frequency equation in Montroll and Potts (1955) (see equation (3.22) in Montroll and Potts 1955). Moreover, in book (Maradudin et al. 1963) the corresponding problem concerning the symmetric localized mode is not accounted in the list of known analytically solvable 1D problems.

In study Yu (2019) the momentum autocorrelation function for the alternated mass in a chain with a symmetric defect is investigated. This function coincides with (Rubin 1963) a fundamental solution of the deterministic problem (with accuracy to a constant multiplier). The non-vanishing component of the momentum autocorrelation function consists of contributions from modes with frequencies Ω_{\pm} defined by Eq. (25.21). Restriction (25.18) is not introduced into consideration. In order to select the appropriate value of the frequency among two possible values given by (25.21), Yu calculates the amplitudes of the corresponding modes and rejects the mode with frequency Ω_- due to its “non-physical nature”, since its amplitude is greater than the initial particle velocity. In the present study we demonstrate that the criterion for the choice of the proper root (25.21) of the frequency equation in the form of bi-quadratic equation (25.19) is restriction (25.18), which makes possible the squaring of Eq. (25.15). We also demonstrate that the boundary of the domain of existence (25.28) corresponds to a root of Eqs. (25.23), whereas in Yu (2019) it is declared that the boundary corresponds to a minimal (in some sense) value of the frequency Ω_+ . In our opinion, although the results obtained in Yu (2019) are correct, they have been derived by a wrong way.

For the case of an asymmetric mass-spring inclusion (Sect. 25.4) the domain of existence for the localized mode defined by inequality (25.70) is divided into two areas, to which different roots $\Omega = \Omega_{\pm}$ (25.52) of frequency equation (25.50) correspond. The choice of the proper root should be done according to condition (25.71). We have not found any study where the spectral problem for an asymmetric inclusion was considered, although there may be some.

The special particular cases considered in Sects. 25.3.3, 25.4.1 were previously considered in Maradudin et al. (1963); Montroll and Potts (1955).

The plots for values of the localized modes frequencies inside the corresponding domains of existence are presented in Figs. 25.3 and 25.5 for the cases of a symmetric and an asymmetric inclusion, respectively. One can see that the plots have qualitatively similar structure, the essential difference can be observed only for enough small values of m and K .

The results of the paper can be used, in particular, in the investigation of non-stationary waves anti-localization (Shishkina et al. 2023) in infinite discrete systems.

Acknowledgements The paper is dedicated to the 80th anniversary of Prof. L.M. Zubov. The authors are grateful to A.M. Krivtsov, V.A. Kuzkin, Yu.A. Mochalova for useful and stimulating discussions. This work is supported by Russian Science Support Foundation (project 22-11-00338).

Appendix

Here we discuss the dispersion relation and the Green function in the frequency domain for the uniform chain. Assuming the solution to be in the form of Eqs. (25.4), (25.6) we get the dispersion relation for a uniform chain corresponding to the one described by Eq. (25.1):

$$\Omega^2 = 4 \sin^2 \frac{q}{2} \equiv 2(1 - \cos q), \quad (25.76)$$

where $\Omega \in \mathbb{R}$ is the frequency, q is the wave-number. The detailed analysis of the dispersion relation for a uniform chain is given, for example, in Shishkina and Gavrilov (2023).

The whole frequency band $\Omega \in \mathbb{R}$ can be divided to the pass-band, where

$$\Omega^2 < \Omega_*^2 \equiv 4, \quad (25.77)$$

$$q = \pm \arccos \frac{2 - \Omega^2}{2}, \quad (25.78)$$

i.e., the corresponding wave-numbers $q(\Omega)$ are reals, and the stop-band, where

$$\Omega^2 > \Omega_*^2 \equiv 4, \quad (25.79)$$

$$q = \pi \pm i \operatorname{arccosh} \frac{1}{2}(\Omega^2 - 2) = \pi \pm i \ln \left(\frac{1}{2}(\Omega^2 - 2) + \sqrt{\frac{1}{4}(\Omega^2 - 2)^2 - 1} \right), \quad (25.80)$$

i.e., the corresponding wave-numbers are imaginary. Here

$$\Omega_* \stackrel{\text{def}}{=} 2 \quad (25.81)$$

is the cut-off (or boundary) frequency, which separates the bands.

The Green function in the frequency domain for the corresponding uniform chain in the stop-band is Montroll and Potts (1955), Shishkina and Gavrilov (2023)

$$G_n(\Omega) = \frac{(-1)^{|n|} 2^{|n|}}{\Phi^{|n|-1}(\Omega)((-\Omega^2 + 2)\Phi(\Omega) + 4)}, \quad (25.82)$$

where

$$\Phi(\Omega) \stackrel{\text{def}}{=} \Omega^2 - 2 + |\Omega| \sqrt{\Omega^2 - 4}. \quad (25.83)$$

References

- Andrianov IV, Danishevs'kyy VV, Kalamkarov AL (2012) Vibration localization in one-dimensional linear and nonlinear lattices: discrete and continuum models. *Nonlinear Dyn* 72:37–48. <https://doi.org/10.1007/s11071-012-0688-4>
- Buchberger B (2002) Gröbner basis. In: *Encyclopedia of mathematics*. Kluwer Academic Publishers
- Conwell E, Weisskopf VF (1950) Theory of impurity scattering in semiconductors. *Phys Rev* 77(3):388–390. <https://doi.org/10.1103/PhysRev.77.388>
- Gavrilov SN, Shishkina EV, Mochalova YA (2019) An infinite-length system possessing a unique trapped mode versus a single degree of freedom system: a comparative study in the case of time-varying parameters. In: Altenbach H et al (eds) *Dynamical processes in generalized continua and structures, advanced structured materials*, vol 103, pp 231–251. Springer. https://doi.org/10.1007/978-3-030-11665-1_13
- Gendelman OV, Paul J (2021) Kapitza thermal resistance in linear and nonlinear chain models: isotopic defect. *Phys Rev E* 103(5):052113. <https://doi.org/10.1103/PhysRevE.103.052113>
- Glushkov E, Glushkova N, Wauer J (2011) Wave propagation in an elastically supported string with point-wise defects: gap-band and pass-band effects. *ZAMM* 91(1):4–22. <https://doi.org/10.1002/zamm.201000039>
- Indeitsev DA, Kuznetsov, NG, Motygin OV, Mochalova YA (2007) *Lokalizatsia lineynykh voln* [Localization of linear waves]. Izdatelstvo Sankt-Peterburgskogo universiteta [St. Petersburg University publishing house], St. Petersburg (in Russian)
- Koshevich AM (1999) *The crystal lattice: phonons, solitons, dislocations*. Wiley-VCH, Berlin
- Koster GF (1954) Theory of scattering in solids. *Phys Rev* 95(6):1436–1443. <https://doi.org/10.1103/PhysRev.95.1436>
- Koster GF, Slater JC (1954) Wave functions for impurity levels. *Phys Rev* 95(5):1167–1176. <https://doi.org/10.1103/PhysRev.95.1167>
- Kuznetsov N, Maz'ya V, Vainberg B (2002) *Linear water waves: a mathematical approach*. Cambridge University Press, Cambridge (2002). <https://doi.org/10.1017/CBO9780511546778>
- Manevich LI, Mikhlin YV, Pilipchuk VN (1989) *Metod normalnykh kolebaniy dlya suschestvenno nelineynykh system* [Method of normal modes for essentially nonlinear systems]. Nauka [Science], Moscow. In Russian
- Maradudin AA, Montroll EW, Weiss OH (1963) *Theory of lattice dynamics in the harmonic approximation*. Academic Press, New York and London
- Montroll EW, Potts RB (1955) Effect of defects on lattice vibrations. *Phys Rev* 100(2):525–543. <https://doi.org/10.1103/PhysRev.100.525>

- Rubin RJ (1963) Momentum autocorrelation functions and energy transport in harmonic crystals containing isotopic defects. *Phys Rev* 131(3):964–989. <https://doi.org/10.1103/PhysRev.131.964>
- Shishkina EV, Gavrilov SN (2023) Unsteady ballistic heat transport in a 1D harmonic crystal due to a source on an isotopic defect. *Contin Mech Thermodyn* 35(2):431–456. <https://doi.org/10.1007/s00161-023-01188-x>
- Shishkina EV, Gavrilov SN, Mochalova YA (2023) The anti-localization of non-stationary linear waves and its relation to the localization. The simplest illustrative problem. *J Sound Vib* 553:117673. <https://doi.org/10.1016/j.jsv.2023.117673>
- Teramoto E, Takeno S (1960) Time dependent problems of the localized lattice vibration. *Prog Theor Phys* 24(6):1349–1368. <https://doi.org/10.1143/PTP.24.1349>
- Ursell F (1951) Trapping modes in the theory of surface waves. *Math Proc Camb Philos Soc* 47(2):347–358. <https://doi.org/10.1017/S0305004100026700>
- Yu MB (2019) A monatomic chain with an impurity in mass and Hooke constant. *Eur Phys J B* 92:272. <https://doi.org/10.1140/epjb/e2019-100383-1>

Chapter 26

On Plate Buckling Induced by a Chemical Reaction



Vladislav O. Shtegman, Alexander B. Freidin, and Alexander V. Morozov

Abstract This paper is concerned with the study of a plate buckling caused by a chemical reaction and is motivated by the use of buckling as a stress relaxation mechanism in silicon-based anodes in lithium-ion batteries. Chemical reaction is localized at the sharp interface—reaction front—and is accompanied by the transformation strain, which generates internal stresses which, in turn, affect the front propagation. If the external supports limit the elongation of the plate, then the transformation strain creates compressive forces, which can lead to buckling of the plate and redistribution of the stresses in the plate. Coupling of stresses and chemical reaction rate is carried out using the concept of a chemical affinity tensor. A problem for a plate with two reaction fronts is considered. The kinetics of the reaction fronts before the loss of plate stability and during post-buckling is studied.

Keywords Buckling · Mechanochemistry · Configurational force · Chemical affinity tensor · Numerical simulations

26.1 Introduction

Environmentally friendly, cheap, and durable energy storage is necessary to meet the needs of its storage. Since first entering the market, Li-ion batteries (LiBs) became

V. O. Shtegman · A. B. Freidin (✉)
Institute for Problems in Mechanical Engineering of the Russian Academy of Sciences, St. Petersburg, Russia
e-mail: fab@ipme.ru

V. O. Shtegman
e-mail: shvo@ipme.ru

A. V. Morozov
Institute of Mechanics, Faculty of Mechanical Engineering, Berlin Institute of Technology, Berlin, Germany
e-mail: morozov@tu-berlin.de

© The Author(s), under exclusive license to Springer Nature Switzerland AG 2023
H. Altenbach and V. Eremeyev (eds.), *Advances in Linear and Nonlinear Continuum and Structural Mechanics*, Advanced Structured Materials 198,
https://doi.org/10.1007/978-3-031-43210-1_26

the promising source of energy storage for applications such as portable electronics, microchips, electro cars, and large-scale energy storage.

The Li-ion battery consists of the three main structural elements: anode, cathode, and electrolyte. Anode and cathode are the Li-ion absorbing materials, and electrolyte is used for the transfer of ions and electrons. Lithium ions flow through the electrolyte whereas the electrons generated from the reaction, $\text{Li} = \text{Li}^+ - e^-$ go through the external circuit. Liquid electrolytes used in LiBs are usually made of lithium salt, e.g., LiPF_6 , LiBF_4 , or LiClO_4 , in a liquid organic solvent, e.g., ethylene carbonate, diethyl carbonate (Teki et al. 2009). One of the main factors determining capacity of the LiBs is the choice of anode material. The capacity of LiBs with Si as the anode material is 9 times higher than the capacity of a battery with a widely used graphite anode, e.g., 3590 mAh/g versus 375 mAh/g, respectively (Wu and Cui 2012).

Lithiation of Si is a two-phase process (McDowell et al. 2013a; Liu et al. 2012b), which may occur at a sharp propagating interface (Liu et al. 2012a, b). Lithiated silicon is formed as a result of the chemical reaction, $\text{Si} + x\text{Li} \rightarrow \text{Li}_x\text{Si}$, where maximal theoretical value of x is 4.4 ($\text{Li}_{22}\text{Si}_5$). However, at a room temperature metastable phase of lithiated silicon $\text{Li}_{15}\text{Si}_4$ can be formed (McDowell et al. 2013b). In all cases, the lithiation is accompanied by a transformation strain (Kasavajjula et al. 2007) producing mechanical stresses, which could retard and block the lithiation (McDowell et al. 2013a; Liu et al. 2012b; Van Havenbergh et al. 2016) and destroy the anode (Liu et al. 2012a; Van Havenbergh et al. 2016). Thus, mechanism of stress relaxation is desirable.

Extensive research has been carried out on the development of new nanoscale structures of silicon-based anodes for lithium-ion batteries, e.g., Kasavajjula et al. (2007), Baggetto et al. (2011), Van Havenbergh et al. (2016), Esmanski and Ozin (2009), Cui et al. (2009), Park et al. (2009), Song et al. (2010), Chan et al. (2008). In Van Havenbergh et al. (2016), the formation of nanovoids in coated Si nanoparticles (NPs) during lithiation was reported. Nanovoids contributed to the stress relaxation during lithiation and prevented fracture of the NPs. In Cui et al. (2009), Chan et al. (2008), the authors reported on the capacity and cycle-life performance of 3D designs of Si anode for LiBs made of arrays of nanowires. In Park et al. (2009), Song et al. (2010), the capacity and cycle-life performance of Si-nanotube anode structures for LiBs was investigated. Baggetto et al. (2011) performed an experimental study in which a honeycomb periodic structure of the Si anode was fabricated which buckled during lithiation, releasing stored elastic energy (Fig. 26.1).

Note that the loss of stability of a structural element is present in many microelectronics applications and is usually considered undesirable due to the loss of the bearing capacity of the element. Over the past decades, various models have been developed describing the buckling of structural elements, and some examples are listed below. Buckling of a two-layered circular plate with a pre-stressed layer was studied in Eremeev and Zubov (2015) where three-dimensional linearized equilibrium equations for each layer and the equation for critical strains were derived. Non-linear buckling analysis of a three-layered rectangular plate with pre-stressed middle layer subjected to the lateral compression/stretching was presented in Eremeev and Zubov (2017) where critical values of a load parameter and the dependence of the

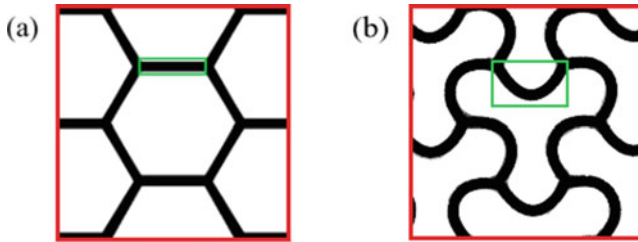


Fig. 26.1 Schematic representation of the honeycomb-structured Si anode: **a** unlithiated; **b** lithiated (designed basing on Baggetto et al. 2011)

critical stress on initial strains were obtained. Instability of the hollow elastic cylinder using bifurcation method was studied in Zubov and Sheydakov (2008) where the critical surface and the stability region in the space of loading parameters were defined, and the influence of the wall thickness on the instability was investigated, and the criterion of stability under tension was formulated. In Nikravesht et al. (2020) and Mei et al. (2007) it was reported on buckling and a numerical simulation of surface delamination and wrinkling of bi-layered composite thin films. The effects of stress accelerated corrosion on the loss of the stability of a spherical shell due to changing the thickness and the critical time prior to the stability loss were discussed in Gutman et al. (2016).

Buckling of a structural element due to stresses produced by a transformation of a material is presented by the loss of stability of a rod caused by martensitic transformations, see, e.g., Rahman et al. (2005), Movchan et al. (2020), Movchan et al. (2020), Dumanskii and Movchan (2019) and reference therein. Buckling-induced fracture and delamination of the supercapacitor due to the charge transfer was studied in Yang (2017). The effects of manufacturing process, geometric conditions, and charge/discharge rates on the stability of the electrode structure using geometrically nonlinear buckling theory were investigated in Zhu et al. (2022). In Kermani et al. (2021), the authors reported on an analytical and numerical study of buckling of a layered cell of a lithium-ion battery due to in-plane loading and examined the strength at buckling.

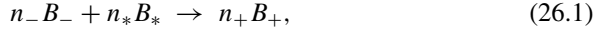
In the above examples, buckling is an undesirable phenomenon. The present study is inspired by the utilization of buckling as a mechanism of stress relaxation in a structural element of the Si-based honeycomb anode. We consider buckling of a pinned plate undergoing a chemical reaction as a model problem and make a step toward modeling the lithiation-induced buckling process in terms of a stress-affected chemical reaction by using the concept of the chemical affinity tensor (Freidin 2013). The concept of the chemical affinity tensor (Freidin 2013) is used to couple mechanical stresses and the reaction rate in a thermodynamically sound manner.

The paper is organized as follows. In Sect. 26.2, the overview of the chemical reaction front kinetics based on the chemical affinity tensor concept is given. In Sect. 26.3, a plate undergoing a chemical reaction is considered and the kinetics of chemical reaction fronts before the loss of the stability of the plate is described

analytically. Then, in Sect. 26.4, numerical investigation of post-buckling behavior of the plate and reaction fronts propagation at post-buckling stage are performed.

26.2 Modeling Kinetics of the Chemical Reaction Front

The chemical reaction of the following type is considered:



where B_- , B_* , and B_+ are the chemical formulae of the reaction constituents, n_- , n_* , and n_+ are the stoichiometric coefficients, the subscripts “-”, “*”, and “+” refer to the initial solid material, diffusing reactant, and solid reaction product, respectively. During further analysis stoichiometric coefficients n_* , n_- , n_+ are normalized by n_* : $n_- \rightarrow n_-/n_*$, $n_+ \rightarrow n_+/n_*$, $n_* \rightarrow 1$.

It is assumed that the chemical reaction is localized at the reaction front and the diffusing reactant is fully consumed by the reaction. Chemical reaction is accompanied by the transformation strain which is assumed to be a volume expansion: an elementary volume of initial material $dV_- = n_- M_- / \rho_-$ transforms into an elementary volume of the transformed material $dV_+ = n_+ M_+ / \rho_+$, where M_{\pm} and ρ_{\pm} are the molar masses and reference mass densities of the constituents B_{\pm} , respectively. The ratio $J_{\text{ch}} = dV_+ / dV_-$ represents the transformation strain at the reaction front if the diffusing constituent does not produce additional volume deformation (the case of a solid skeleton approach (Freidin 2013), but generally speaking the ratio of elementary volumes of materials on both sides of the reaction front, if they were stress-free, is given by the formula (Morozov et al. 2020)

$$J_{\text{ch}} = \frac{n_+ M_+ / \rho_+ + \beta M_* / \rho_*}{n_- M_- / \rho_-}, \quad (26.2)$$

where parameter β characterize deformational interaction between the diffusing reactant B_* and the reaction product B_+ ; $\beta = 0$ in the case of the solid skeleton approach, $\beta = 1$ if the diffusing reactant adds its volume to the reaction product. Note that J_{ch} depends on the concentration of the diffusing constituent if $\beta \neq 0$, but for the sake of simplicity further we consider J_{ch} as a given material parameter.

Kinetics of the chemical reaction front is modeled using the concept of the chemical affinity tensor. The chemical affinity tensor was derived as the consequence of the mass balance, linear momentum balance, energy balance, and the second law of thermodynamics in the form of the Clausius-Duhem inequality written for a moving reaction front (Freidin 2013), see also (Freidin et al. 2014; Freidin and Vilchevskaya 2020). Stresses produced by the transformation strain and external loading affect the reaction front velocity through the normal component of the chemical affinity tensor. The validity of the approach based on the chemical affinity tensor was demonstrated

by solution of a number of coupled mechanochemistry problem (see, e.g., Petrenko et al. 2022, Freidin et al. 2022 and reference therein).

The kinetic equation used in classical chemistry is based on the scalar chemical affinity (Prigogine and Defay 1954; Glansdorff et al. 1973). It can be reformulated for the reaction rate $\omega[\mathbf{n}]$ at the area element with normal \mathbf{n} as a function of the normal component of the affinity tensor as follows Freidin (2013):

$$\omega[\mathbf{n}] = k_* c \left\{ 1 - \exp\left(-\frac{A_{nn}}{RT}\right) \right\} \quad (26.3)$$

where k_* is a kinetic coefficient, c is the partial molar concentration of the diffusing reactant, R is the universal gas constant, T is the temperature, and A_{nn} is the normal component of the chemical affinity tensor acting as a configurational force. Then the normal component of the reaction front velocity W_n can be obtained from the mass balance at the reaction front:

$$W_n = \frac{n_- M_-}{\rho_-} \omega[\mathbf{n}]. \quad (26.4)$$

Further we consider the case of small strains. Then the expression for the normal component of the chemical affinity tensor takes the form:

$$A_{nn} = \frac{n_- M_-}{\rho_-} (\gamma - \zeta) + n_* RT \ln \frac{c}{c_*}, \quad (26.5)$$

where c_* is the solubility of B_* in B_+ ,

$$\zeta = w_+ - w_- - \boldsymbol{\sigma}_\pm : \llbracket \boldsymbol{\varepsilon} \rrbracket \quad (26.6)$$

represents the influence of the stress-strain state, w_\pm are the strain energies of the solid constituents per unit volume, $\llbracket \boldsymbol{\varepsilon} \rrbracket = \boldsymbol{\varepsilon}_+ - \boldsymbol{\varepsilon}_-$ is the jump of the strain tensor across reaction front, $\boldsymbol{\sigma}$ is the Cauchy stress tensor, and

$$\gamma = \eta_- - \eta_+ + \frac{\rho_-}{n_- M_-} \eta_* \quad (26.7)$$

is the temperature dependent chemical energy parameter, η_+ , η_- are the chemical energies in the stress-free state of the constituents B_+ , B_- , and η_* is the reference chemical energy of the diffusing reactant B_* .

An equilibrium concentration c_{eq} can be introduced at the reaction front such that $A_{nn}(c_{\text{eq}}) = 0$. From (26.5) it follows that $c_{\text{eq}} = \varkappa c_*$ where

$$\varkappa = \exp\left(-\frac{n_- M_- (\gamma - \zeta)}{\rho_- RT}\right). \quad (26.8)$$

Then the reaction rate (26.3) can be expressed as

$$\omega[\mathbf{n}] = k_* (c - \varkappa c_*), \tag{26.9}$$

where \varkappa represents the influence of the competition between chemical and mechanical factors on the reaction rate. If the stresses are such that $\varkappa = 1$, i.e., $\zeta = \gamma$, then the front propagation is blocked.

Hence, one has a coupling between mechanics, diffusion, and chemical reaction. In addition, effects of mechanical stresses can be accounted for through the stress-dependent diffusivity and the cross effects of stress gradient in the diffusion flux, see, e.g., Knyazeva (2003), Cui et al. (2013), Bower and Guduru (2012). However, in the present work, we focus only on the influence of stresses on the reaction rate and buckling due to reaction front propagation.

To calculate ζ and, therefore specify a kinetic equation defining the reaction front velocity one has to find stresses, strains, and the concentration of the diffusive reactant at the reaction front. Further following assumptions are used: we neglect the initial stage of the diffusion of B_* prior to the start of the reaction and separation of the reaction front from the outer boundary of the body. We also assume that the front propagation is controlled by the reaction rate rather than by diffusion, i.e., we assume that diffusion is much faster than the chemical reaction and is fast enough to consider a steady-state diffusion for each front position. Then the diffusion can be described by Fick’s equation:

$$\Delta c = 0 \tag{26.10}$$

with boundary conditions:

$$D\mathbf{n} \cdot \nabla c - \alpha(c_* - c) = 0 \text{ at } \Omega_+, \quad D\mathbf{n} \cdot \nabla c + \omega[\mathbf{n}] = 0 \text{ at } \Gamma, \tag{26.11}$$

where α is the surface mass transfer coefficient, Ω_+ is the outer boundary of the domain occupied by material B_+ . The first boundary condition states that if the solubility c_* is reached then the supply of the diffusing reactant stops. The second boundary condition follows from the mass balance at the reaction front and states that all the diffusing reactant is consumed by the reaction.

To find stresses and strains one has to solve the equilibrium equation

$$\nabla \cdot \boldsymbol{\sigma} = 0 \tag{26.12}$$

with boundary and interface conditions

$$\mathbf{u}|_{\Omega_1} = \mathbf{u}_0, \quad \boldsymbol{\sigma} \cdot \mathbf{n}|_{\Omega_2} = \mathbf{t}_0, \tag{26.13}$$

$$[[\mathbf{u}]]|_{\Gamma} = 0, \quad [[\boldsymbol{\sigma}]]|_{\Gamma} \cdot \mathbf{n} = 0, \tag{26.14}$$

where \mathbf{u}_0 and \mathbf{t}_0 are the displacement and traction prescribed at the parts Ω_1 and Ω_2 of the outer boundary of the body, respectively, Γ is the reaction front. We consider linear elastic solid constituents with constitutive relations

$$\sigma_- = \mathbf{C}_- : \boldsymbol{\varepsilon}_-, \quad \sigma_+ = \mathbf{C}_+ : (\boldsymbol{\varepsilon}_+ - \boldsymbol{\varepsilon}_{\text{ch}}), \quad (26.15)$$

where \mathbf{C}_\pm are the stiffness tensors, $\boldsymbol{\varepsilon}_{\text{ch}}$ is the chemical transformation strain. Then

$$\gamma - \zeta = \gamma - \frac{1}{2} \sigma_+ : (\boldsymbol{\varepsilon}_+ - \boldsymbol{\varepsilon}^{\text{ch}}) + \frac{1}{2} \sigma_- : \boldsymbol{\varepsilon}_- + \sigma_\pm : [\boldsymbol{\varepsilon}]. \quad (26.16)$$

Further we consider isotropic solid constituents and take

$$\mathbf{C}_\pm = \lambda_\pm \mathbf{E} \otimes \mathbf{E} + 2\mu_\pm \mathbf{I}, \quad \boldsymbol{\varepsilon}_{\text{ch}} = \varepsilon_{\text{ch}} \mathbf{E}, \quad (26.17)$$

where λ_\pm and μ_\pm are the Lamé constants, \mathbf{E} and \mathbf{I} are the second and forth rank unit tensors, respectively.

26.3 Loss of Plate Stability Due to the Chemical Reaction

A coupled problem “diffusion—chemistry—mechanics” for a pinned plate until its loss of stability was considered in Shtegman et al. (2021). Below, for completeness, the main points are presented.

We consider a plate of the width a , length $b \gg a$, and thickness $2H$, symmetric with respect to the middle plane, pinned at the edges $x = \pm a/2$ (Fig. 26.2, rectangular coordinates x, y, z are used). The upper and lower sides $y = \pm H$ are traction-free. A plane strain formulation is assumed with $\varepsilon_z^\pm = 0$. The chemical reaction starts simultaneously on both sides and two reaction fronts propagate toward the middle plane. The diffusing reactant is supplied through the upper and lower sides. The reac-

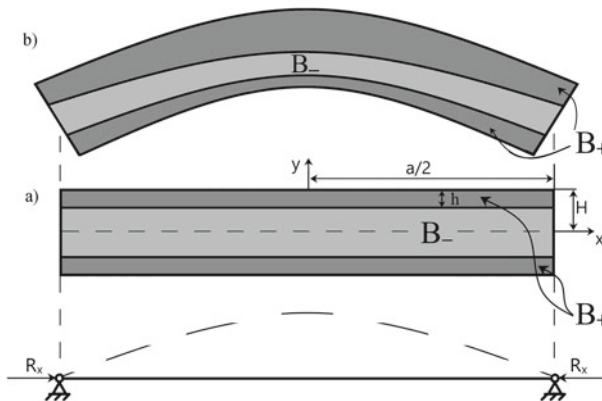


Fig. 26.2 Schematic representation of a plate with two chemical reaction fronts: **a** before buckling; **b** during post-buckling

tion fronts are planar before buckling, the top and bottom layers of the transformed material have the same thickness h . Due to pinning, $\varepsilon_x^\pm = 0$.

The stresses are induced by the transformation strain similar to thermal stresses. Since the upper and lower sides of the plate are traction-free and the traction continuity condition $[[\sigma_y]]|_{y=\pm(H-h)} = 0$ holds at the reaction fronts, one can accept that $\sigma_y^\pm = 0$ everywhere. Then non-zero stresses are

$$\sigma_x^+ = \sigma_z^+ = \frac{E_+ \varepsilon_{ch}}{1 - \nu_+}, \quad H - h < |y| < H, \tag{26.18}$$

where E_+ and ν_+ are Young's moduli and Poisson's ratio of the transformed material, respectively. The stresses do not depend on the front position until the loss of stability. Then ζ in (26.16) does not depend on the thickness of the transformed material layer,

$$\gamma - \zeta = \gamma - \frac{E_+ \varepsilon_{ch}^2}{1 - \nu_+}. \tag{26.19}$$

The planar chemical reaction front can propagate only if $\omega[\mathbf{n}] > 0$ which holds if $c > c_{eq}$ at the reaction front. On the other hand $c \leq c_*$. Thus, if the front propagates, then $c_{eq} < c_*$, $\varkappa < 1$ and $\gamma - \zeta > 0$, i.e., $\gamma/\gamma_* > 1$, where $\gamma_* = E_+ \varepsilon_{ch}^2 / (1 - \nu_+)$ is the critical value of γ .

The solution of the diffusion equation (26.10) with boundary and interface conditions (26.11) gives the concentrations at the upper and lower reaction fronts:

$$c(y)|_{|y|=H-h} = \frac{1 + \varkappa k_* (1/\alpha + h/D)}{1 + k_* (1/\alpha + h/D)} c_*. \tag{26.20}$$

Then, by (26.4) and (26.9), the reaction front velocity W_n is expressed as a function of the front position:

$$W_n(h) = dh/dt = \frac{n_- M_-}{\rho_-} \frac{c_*(1 - \varkappa)}{1/k_* + 1/\alpha + \xi H/D} \tag{26.21}$$

where $\xi = h/H$ is the relative thickness of the transformed layer. Integrating (26.21) gives the time of reaching the relative thickness ξ :

$$t(\xi) = \frac{\rho_-}{n_- M_-} \frac{\xi(1/k_* + 1/\alpha + \xi H/(2D))}{c_*(1 - \varkappa)} H \tag{26.22}$$

The time is inversely proportional to the kinetic coefficient k_* , the mass transfer coefficient α , and the diffusivity D . Internal stresses produced by the transformation strain affect the reaction front kinetics via parameter \varkappa . It is seen how the front decelerates if the ratio γ/γ_* decreases, i.e., if the mechanical factor γ_* increases relative to the chemical energy γ .

The reaction force R_x at the supports, bending stiffens D_{ef} and critical buckling load N_{cr} can be calculated as Timoshenko and Gere (1961), Eslami et al. (2013)

$$R_x(h) = \int_H^{-H} \sigma_x dy, \quad D_{\text{ef}}(h) = \int_H^{-H} C y^2 dy, \quad N_{\text{cr}}(h) = D_{\text{ef}}(h) \frac{\pi^2}{a^2}, \quad (26.23)$$

where σ_x is given by (26.18), $C = C_+$ if $H - h < |y| < H$, and $C = C_-$ if $|y| < h$, $C_{\pm} = E_{\pm}/(1 - \nu_{\pm}^2)$.

During the propagation of the front the reaction force increases and the bending stiffness changes. Buckling occurs at the critical thickness of the transformed layer h_{cr} such that $R_x(h_{\text{cr}}) = N_{\text{cr}}(h_{\text{cr}})$. Substitution of (26.23) into the buckling criterion leads to the equation

$$(C_-/C_+ - 1) \eta_{\text{cr}}^3 + G \eta_{\text{cr}} - G + 1 = 0, \quad (26.24)$$

where $\eta_{\text{cr}} = 1 - \xi_{\text{cr}}$, $\xi_{\text{cr}} = h_{\text{cr}}/H$, the ratio C_-/C_+ reflects the influence of the elasticity parameters of both solid constituents on the bending stiffness of a plate, dimensionless parameter G depends on the geometrical dimensions of the plate—the ratio a/H , the chemical transformation strain and Poisson’s ratio of the transformed material:

$$G = 3\varepsilon_{\text{ch}}(1 + \nu_+) \frac{a^2}{\pi^2 H^2}. \quad (26.25)$$

Buckling occurs if the solution of (26.24) is in range $\eta_{\text{cr}} \in [0, 1]$. Such a root exists if $G > 1$. For given transformation strain and elastic moduli, by adjusting the ratio a/H , one can achieve the buckling at prescribed ξ_{cr} . Then one can calculate the time t_{cr} prior buckling by (26.22).

Further calculations are performed at the reference values of the material parameters, which are given in Table 26.1. The dependencies of the critical relative thickness ξ_{cr} on parameter G for various values of the ratio C_-/C_+ are shown in Fig. 26.3.

The dependencies of critical time t_{cr} on parameter G at various values of energy parameter γ are shown in Fig. 26.4. The energy parameter depends on the temperature. Thus, it is possible to control $\gamma(T)$ and hence the reaction front velocity and the moment of buckling by changing the temperature. Note that temperature can cause thermal stresses affecting the kinetics of the reaction.

Table 26.1 Reference values of parameters

| Parameter | a/H | E_- [GPa] | E_+ [GPa] | ν_- | ν_+ | ε_{ch} |
|-----------|-------------------------------|--------------------------|------------------------------|--------------|-----------------|---------------------------------|
| Value | 11.6 | 86.4 | 59.2 | 0.33 | 0.25 | 0.017 |
| Parameter | γ [J/mm ³] | D [mm ² /s] | c_* [mol/mm ³] | k_* [mm/s] | α [mm/s] | γ_* [J/mm ³] |
| Value | 0.03 – 0.05 | 0.1 | 0.1 | 0.01 | 0.2 | 0.022 |

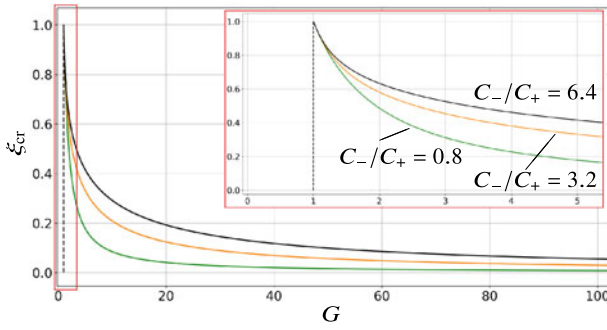


Fig. 26.3 Dependencies of the critical thickness of the reaction front on parameter G at various ratio C_-/C_+ ($\gamma = 0.03$)

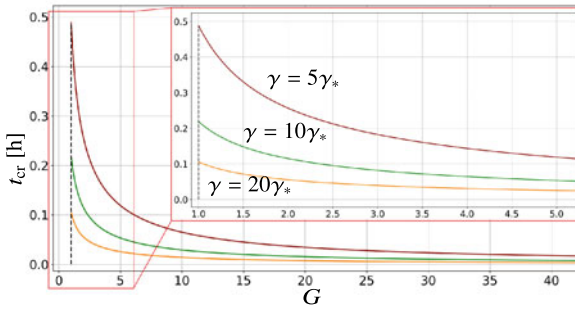


Fig. 26.4 Dependencies of the time prior buckling on the parameter G at various γ ($C_-/C_+ = 1.5$)

26.4 Post-buckling of the Plate and Reaction Front Propagation

Post-buckling behavior of a homogeneous beam or plate can be described analytically with the use of a geometrically nonlinear post-buckling theory developed by Timoshenko and Gere (1961), see also Eslami (2018), Li et al. (2002), Hauck et al. (2010), Eremeyev and Pietraszkiewicz (2011), Levin et al. (2015) and references therein. However, in order to model the propagation of two chemical reaction fronts during post-buckling one has to find stresses and strains at nonplanar fronts inside the bi-materials plate with changing thickness of the domains occupied by materials B_+ and B_- along coordinate axis x (Fig. 26.2b). Therefore, numerical modeling was implemented.

Previously, numerical simulations of the equilibrium and propagation of the sharp interface were carried out by finite element modeling (FEM) for the case of stress-induced phase transformations driving by the configurational force equal to the jump of the Eshelby stress tensor across the interface (see, e.g., Socrate and Parks 1993; Mueller and Gross 1998; Gross et al. 2002; Kabanova and Freidin 2022 and reference

therein). A numerical study of the propagation of the chemical reaction front with the reaction kinetics defined by the chemical affinity tensor was performed by FEM in Morozov et al. (2019), Freidin et al. (2022). Below we focus on the chemical reaction front propagation in the plate at the post-buckling stage. Due to the symmetry of the model with respect to axis $x = 0$ (see Fig. 26.2), only half of the plate was considered. The interface passed along the edges of the elements, and remeshing of the geometry in combination with a user-defined Python postprocessing algorithm was undertaken at each iteration.

Developed numerical procedure does not describe the nucleation of the new phase, therefore existence of an initial thin layer of material B_+ was assumed. Note that the FEM procedure for tracking the reaction front may be a time-costly procedure. A number of steps are to be done at each iteration: create model and mesh it, find stresses, strains, and concentration at each point of the reaction front, compute velocity of the reaction front by (26.3), (26.4), move the reaction front in accordance with the velocities of its points to the new position for the next iteration.

According to Euler's buckling criterion, $R_x(h) = N_{cr}(h)$, in numerical modeling, two stages can be distinguished: before and after the loss of stability. Before buckling, at $R_x(h) < N_{cr}(h)$, a flat plate with two planar reaction fronts propagated with equal velocities was observed, as expected.

At the post-buckling stage, the stress-strain state was no longer symmetrical with respect to the middle plane. This resulted in unequal velocities of the points of the upper and lower chemical reaction fronts. Figure 26.5 shows an image of a buckled plate consisting of the initial and transformed materials.

Positions of the chemical reaction fronts and the shape of the middle plane of the half of the bent plate at various iteration steps are shown in Fig. 26.6. By (26.8), the acceleration or retardation of the front is defined by the competition between chemical and mechanical factors, γ and ζ . The upper chemical reaction front is subjected to additional tension due to buckling, which results in acceleration of the front whereas the lower reaction front is subjected to the compressing strains, which retard the front and even can block it. Note that, depending on material parameters and the ranges of tension and compression values, tension can retard the front, and compression can accelerate it Freidin et al. (2014), Petrenko et al. (2022).

The impact of energy parameter γ on the front kinetics is represented in Fig. 26.7 where the position of the middle point of the front is shown in dependence on time

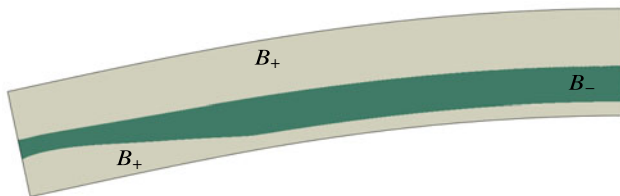


Fig. 26.5 FEM-image of a partially transformed plate in a post-buckling state

Fig. 26.6 Kinetics of the chemical reaction fronts and plate bending: **a** the upper and lower reaction fronts and **b** deflection w of the middle plane of the plate at various post-buckling moments; $E_+ = 59.2, E_- = 86.4, \nu_+ = 0.25, \nu_- = 0.33$ ($C_-/C_+ = 1.5$), $\gamma = 0.03$; $x' = (x + a/2)/H$, N is the iteration number

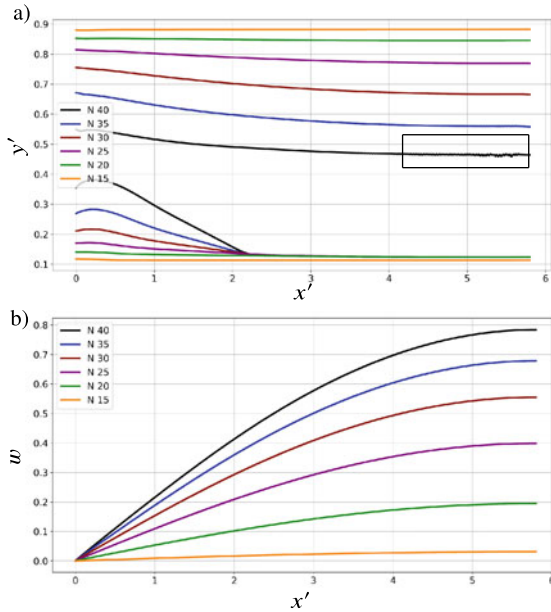
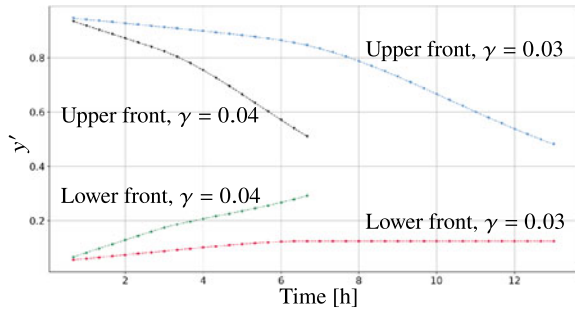


Fig. 26.7 Positions of the middle points (at $x = 0$) of upper and lower chemical reaction fronts v.s. time at various values of γ , $E_+ = 59.2, E_- = 86.4, \nu_+ = 0.25, \nu_- = 0.33$



for the same set of elasticity parameters as in Fig. 26.6 and two values of γ . One can see that 33% increase in the energy parameter (from $\gamma = 0.03$ to 0.04) results in 2 times acceleration of the lower chemical reaction front. At $\gamma = 0.03$ the propagation of the part of the lower front is blocked. In the case $\gamma = 0.04$ blocking of the lower chemical reaction front was not observed.

The kinetics of the front at the set of the elasticity parameters “exchanged” with respect to the parameters of Fig. 26.6 ($E_+ \leftrightarrow E_-, \nu_+ \leftrightarrow \nu_-$, i.e., $C_-/C_+ \leftrightarrow C_+/C_-$) but at higher γ is shown in Fig. 26.9. In this case $\gamma_* = 0.035$ and the front cannot start to propagate at the initial stage prior to buckling. That is why $\gamma = 0.05$ was taken. In both cases blocking of the propagation of the part of the lower front takes place but in the second case the blocking starts earlier than in the first case despite the higher value of γ .

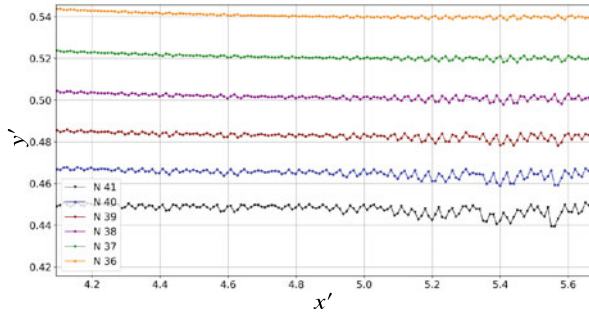


Fig. 26.8 Zoomed rectangle from Fig. 26.6a: development of instabilities of the upper reaction front (N is the iteration number)

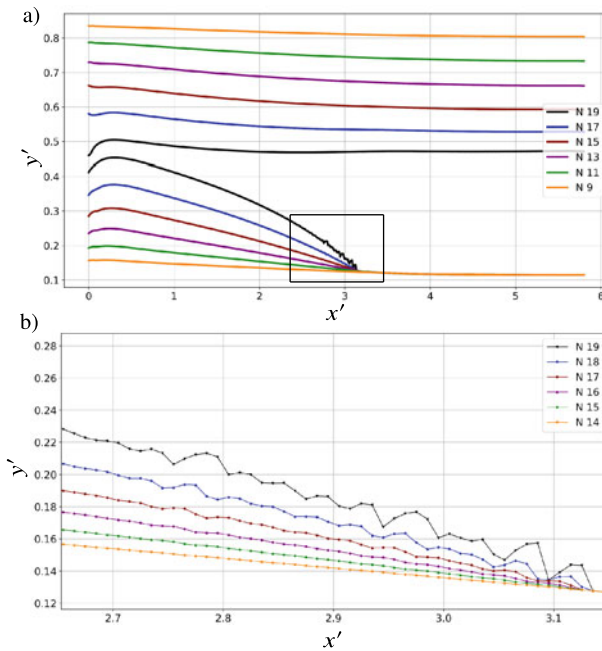


Fig. 26.9 The positions **a** of upper and lower chemical reaction fronts at various iterations N; **b** zoomed rectangle from **a**: development of reaction front instabilities; $E_+ = 86.4$, $E_- = 59.2$, $\nu_+ = 0.33$, $\nu_- = 0.25$ ($C_-/C_+ = 0.6$), $\gamma = 0.05$; $x' = (x + a/2)/H$

In both cases the loss of stability of the reaction front—the appearance and growth of wave-type perturbations—was observed after a number of iterations. In the first case it took place at the part of the upper reaction front, at $x' \approx 4 - 5.5$ (Figs. 26.6a, 26.8). However, if the elasticity parameters were exchanged, the loss of stability of the lower reaction front occurred at $x' \approx 2.5 - 3$ (Fig. 26.9).

Detailed examinations of the stability of the reaction front are out of the scope of the present paper. We only note that this may be the result of so-called kinetic instability according to which the front is unstable if front perturbations grow further due to kinetic equations (26.3), (26.4). The procedure of kinetic stability analysis was developed earlier for an equilibrium phase interface in the case of stress-induced phase transformations (see Yermeyev et al. 2007 and reference therein) and then for equilibrium and propagating chemical reaction fronts (Morozov et al. 2023) (see also Morozov et al. 2019). In this case, numerical inaccuracies caused by remeshing and numerical finding of the normal to the reaction front act as physical fluctuations.

26.5 Conclusion

In this paper, the plate buckling coupled with the propagation of chemical reaction fronts was studied. Two stages of the fronts propagation were considered: before and after the loss of stability of the plate. The influence of elasticity and energy parameters on the critical thickness of the transformed material layer and the time before buckling as well as on the propagation of the reaction front and deflection of the plate at the post-buckling stage was investigated. Differences in the behavior of the upper and lower reaction fronts were described. The blocking of the propagation of the parts of fronts and instability of the fronts were observed at the post-buckling stage.

Acknowledgements V.O. Shtegman and A.B. Freidin acknowledge the support of the Russian Science Foundation (Grant No. 19-19-00552-П).

References

- Baggetto L, Danilov D, Notten P (2011) Honeycomb-structured silicon: remarkable morphological changes induced by electrochemical (de)lithiation. *Adv Mater* 23:1563–1566. <https://doi.org/10.1002/adma.201003665>
- Bower A, Guduru P (2012) A simple finite element model of diffusion, finite deformation, plasticity and fracture in lithium ion insertion electrode materials. *Model Simul Mater Sci Eng* 20. <https://doi.org/10.1088/0965-0393/20/4/045004>
- Chan C, Peng H, Liu G, McIlwrath K, Zhang X, Huggins R, Cui Y (2008) High-performance lithium battery anodes using silicon nanowires. *Nat Nanotechnol* 3:31–5. <https://doi.org/10.1038/nnano.2007.411>
- Cui LF, Ruffo R, Chan C, Peng H, Cui Y (2009) Crystalline-amorphous core-shell silicon nanowires for high capacity and high current battery electrodes. *Nano Lett* 9:491–495. <https://doi.org/10.1021/nl8036323>
- Cui Z, Gao F, Qu J (2013) Interface-reaction controlled diffusion in binary solids with applications to lithiation of silicon in lithium-ion batteries. *J Mech Phys Solids* 61:293–310. <https://doi.org/10.1016/j.jmps.2012.11.001>

- Dumanskii S, Movchan A (2019) Loss of stability of a rod from a shape-memory alloy caused by reverse martensitic transformation. *Mech Solids* 54:929–940. <https://doi.org/10.3103/S0025654419060086>
- Eremeev V, Zubov L (2015) Buckling of a two-layered circular plate with a prestressed layer. *Math Mech Solids* 22:773–781. <https://doi.org/10.1177/1081286515612527>
- Eremeev V, Zubov L (2017) On instability of a three-layered nonlinear elastic rectangular plate with prestressed middle layer. In: Pietraszkiewicz W, Witkowski W (eds) *Shell structures: theory and applications*, vol 4. CRC Press, Boca Raton, London, New York, pp 215–218. <https://doi.org/10.1201/9781315166605-46>
- Eremeyev VA, Pietraszkiewicz W (2011) Thermomechanics of shells undergoing phase transition. *J Mech Phys Solids* 59:1395–1412. <https://doi.org/10.1016/j.jmps.2011.04.005>
- Eslami M (2018) *Buckling and postbuckling of beams, plates, and shells*. Springer. <https://doi.org/10.1007/978-3-319-62368-9>
- Eslami R, Hetnarski R, Ignaczak J, Noda N, Sumi N, Tanigawa Y (2013) *Theory of Elasticity and Thermal Stresses*. Springer. https://doi.org/10.1007/978-94-007-6356-2_21
- Esmanski A, Ozin G (2009) Silicon inverse-opal-based macroporous materials as negative electrodes for lithium ion batteries. *Adv Funct Mater* 19:1999–2010. <https://doi.org/10.1002/adfm.200900306>
- Freidin A, Vilchevskaya E (2020) Chemical affinity tensor in coupled problems of mechanochemistry. In: Altenbach H, Öchsner A (eds) *Encyclopedia of continuum mechanics*. Springer, Berlin. https://doi.org/10.1007/978-3-662-53605-6_143-1
- Freidin AB (2013) Chemical affinity tensor and stress-assist chemical reactions front propagation in solids. In: *Proceedings of the ASME 2013 international mechanical engineering congress and exposition*, vol 9, p V009T10A102. American Society of Mechanical Engineers. <https://doi.org/10.1115/IMECE2013-64957>
- Freidin AB, Korolev IK, Aleshchenko SP (2022) FEM-simulations of a chemical reaction front propagation in an elastic solid with a cylindrical hole. In: Polyanskiy VA, Belyaev AK (eds) *Mechanics and control of solids and structures. Advanced structured materials*, vol 164. Springer, pp 195–208. https://doi.org/10.1007/978-3-030-93076-9_10
- Freidin AB, Vilchevskaya EN, Korolev IK (2014) Stress-assist chemical reactions front propagation in deformable solids. *Int J Eng Sci* 83:57–75. [10.1016/j.ijengsci.2014.03.008](https://doi.org/10.1016/j.ijengsci.2014.03.008)
- Glandsdorff P, Prigogine I, Hill RN (1973) Thermodynamic theory of structure, stability and fluctuations. *Am J Phys* 41(1):147–148. <https://doi.org/10.1119/1.1987158>
- Gross D, Mueller R, Kolling S (2002) Configurational forces-morphology evolution and finite elements. *Mech Res Commun* 29(6):529–536. [https://doi.org/10.1016/S0093-6413\(02\)00296-3](https://doi.org/10.1016/S0093-6413(02)00296-3)
- Gutman E, Bergman R, Levitsky S (2016) Influence of internal uniform corrosion on stability loss of a thin-walled spherical shell subjected to external pressure. *Corros Sci* 111:212–215. <https://doi.org/10.1016/j.corsci.2016.04.018>
- Hauck T, Müller W, Schmadlak I (2010) Nonlinear buckling analysis of vertical wafer probe technology. *Microsystem technologies-micro-and nanosystems-information storage and processing systems. Microsyst Technol* 16:1909–1920. <https://doi.org/10.1007/s00542-010-1115-8>
- Kabanova PK, Freidin AB (2022) Numerical investigation of the evolution of new phase domains in an elastic solid. *Comput Contin Mech* 15(4):466–479. <https://doi.org/10.7242/1999-6691/2022.15.4.36>
- Kasavajjula U, Wang C, Appleby A (2007) Nano- and bulk-silicon-based insertion anodes for lithium-ion secondary cells. *J Power Sources* 163:1003–1039. <https://doi.org/10.1016/j.jpowsour.2006.09.084>
- Kermani G, Keshavarzi M, Sahraei E (2021) Deformation of lithium-ion batteries under axial loading: analytical model and representative volume element. *Energy Rep* 7:2849–2861. <https://doi.org/10.1016/j.egy.2021.05.015>
- Knyazeva AG (2003) Cross effects in solid media with diffusion. *J Appl Mech Tech Phys* 44:373–384. <https://doi.org/10.1023/A:1023485224031>

- Levin VA, Zubov LM, Zingerman KM (2015) Influence of the prestressed layer on the nonlinear flexure of a rectangular beam made of compressible material. *Dokl Phys* 60(4):167–170. <https://doi.org/10.1134/S1028335815040023>
- Li S, Zhou YH, Zheng X (2002) Thermal post-buckling of a heated elastic rod with pinned-fixed ends. *J Therm Stress* 25:45–56. <https://doi.org/10.1080/014957302753305862>
- Liu X, Zhong L, Huang S, Mao S, Zhu T, Huang J (2012a) Size-dependent fracture of silicon nanoparticles during lithiation. *ACS Nano* 6:1522–1531. <https://doi.org/10.1021/nn204476h>
- Liu XH, Fan F, Yang H, Zhang S, Huang J, Zhu T (2012b) Self-limiting lithiation in silicon nanowires. *ACS Nano* 7:1495–1503. <https://doi.org/10.1021/nn305282d>
- McDowell M, Lee SW, Harris J, Korgel B, Wang C, Nix W, Cui Y (2013a) In situ tem of two-phase lithiation of amorphous silicon nanospheres. *Nano Lett* 13:758–764. <https://doi.org/10.1021/nl3044508>
- McDowell M, Lee SW, Nix W, Cui Y (2013b) 25th anniversary article: understanding the lithiation of silicon and other alloying anodes for lithium-ion batteries. *Adv Mater* 25:4966–4985. <https://doi.org/10.1002/adma.201301795>
- Mei H, Huang R, Chung J, Stafford C, Yu Hh (2007) Buckling modes of elastic thin films on elastic substrates. *Appl Phys Lett* 90:151902–151902. <https://doi.org/10.1063/1.2720759>
- Morozov A, Freidin A, Müller W (2023) On stress-affected propagation and stability of chemical reaction fronts in solids. *Int J Eng Sci* 189:103876. <https://doi.org/10.1016/j.ijengsci.2023.103876>
- Morozov A, Freidin AB, Klinkov VA, Semench AV, Müller WH, Hauck T (2020) Experimental and theoretical studies of cu-sn intermetallic phase growth during high-temperature storage of eutectic snag interconnects. *J Electron Mater*. <https://doi.org/10.1007/s11664-020-08433-y>
- Morozov AV, Freidin AB, Müller WH (2019) Stability of chemical reaction fronts in the vicinity of a blocking state. *PNRPU Mech Bull* 3:58–64. <https://doi.org/10.15593/perm.mech/2019.3.06>
- Movchan A, Kazarina S, Silchenko A (2020) Experimental study of stability loss of titanium nickelide rods caused by reverse thermoelastic martensitic transformation. *Deform Fract Mater* 2–7. <https://doi.org/10.31044/1814-4632-2020-9-2-7>
- Movchan A, Kazarina S, Sil'chenko A (2020) Buckling of a rod with a circular cross section induced by a direct thermoelastic martensitic transformation. *Russ Metall (Metally)* 2020:298–304. <https://doi.org/10.1134/S0036029520040199>
- Mueller R, Gross D (1998) 3D simulation of equilibrium morphologies of precipitates. *Comput Mater Sci* 11(1):35–44. [https://doi.org/10.1016/S0927-0256\(97\)00193-6](https://doi.org/10.1016/S0927-0256(97)00193-6)
- Nikravesh S, Ryu D, Shen YL (2020) Instabilities of thin films on a compliant substrate: direct numerical simulations from surface wrinkling to global buckling. *Sci Rep* 10:5728. <https://doi.org/10.1038/s41598-020-62600-z>
- Park MH, Kim MG, Choo J, Kim K, Kim J, Ahn S, Cui Y, Cho J (2009) Silicon nanotube battery anodes. *Nano Lett* 9:3844–3847. <https://doi.org/10.1021/nl902058c>
- Petrenko S, Freidin AB, Charkaluk E (2022) On chemical reaction planar fronts in an elastic-viscoelastic mechanical framework. *Contin Mech Thermodyn* 34:137–163. <https://doi.org/10.1007/s00161-021-01051-x>
- Prigogine I, Defay R (1954) *Chemical thermodynamics*. Longmans, Green
- Rahman MA, Qiu J, Tani J (2005) Buckling and postbuckling characteristics of the superelastic sma columns - numerical simulation. *J Intell Mater Syst Struct* 16(9):691–702. <https://doi.org/10.1177/1045389X05054022>
- Shtegman V, Morozov A, Freidin A, Müller W (2021) On buckling induced by a chemical reaction. *Mater Phys Mech* 47. https://doi.org/10.18149/MPM.4712021_4
- Socrate S, Parks DM (1993) Numerical determination of the elastic driving force for directional coarsening in Ni-superalloys. *Acta Metall Mater* 47(7):2185–2209. [https://doi.org/10.1016/0956-7151\(93\)90389-A](https://doi.org/10.1016/0956-7151(93)90389-A)
- Song T, Xia J, Lee JH, Lee DH, Kwon MS, Choi JM, Wu J, Doo SG, Chang H, Park W, Zang D, Kim H, Huang Y, Hwang KC, Rogers J, Paik U (2010) Arrays of sealed silicon nanotubes as anodes for lithium ion batteries. *Nano Lett* 10:1710–1716. <https://doi.org/10.1021/nl100086e>

- Teki R, Datta M, Krishnan R, Parker T, Lu TM, Kumta P, Koratkar N (2009) Nanostructured silicon anodes for lithium ion rechargeable batteries. *Small* 5:2236–42. <https://doi.org/10.1002/sml.200900382>
- Timoshenko SP, Gere JM (1961) *Theory of elastic stability*, 2nd edn. McGraw-Hill, New York
- Van Havenbergh K, Turner S, Marx N, Van Tendeloo G (2016) The mechanical behavior during (de)lithiation of coated silicon nanoparticles as anode material for lithium-ion batteries studied by in situ transmission electron microscopy. *Energy Technol* 4. 10.1002/ente.201600057
- Wu H, Cui Y (2012) Designing nanostructured si anodes for high energy lithium ion batteries. *Nano Today* 7:414–429. <https://doi.org/10.1016/j.nantod.2012.08.004>
- Yang F (2017) Analysis of charging-induced structural damage in electrochemical systems. *Phys Chem Chem Phys* 19. <https://doi.org/10.1039/C7CP00026J>
- Yeremeyev VA, Freidin AB, Sharipova LL (2007) The stability of the equilibrium of two-phase elastic solids. *J Appl Math Mech* 71(1):61–84. <https://doi.org/10.1016/j.jappmathmech.2007.03.007>
- Zhu Z, Wan J, Wu T, Huang P (2022) Effect of electrode processing on the stability of electrode structure. *Acta Mech* 233. <https://doi.org/10.1007/s00707-022-03229-z>
- Zubov L, Sheydakov D (2008) Instability of a hollow elastic cylinder under tension, torsion, and inflation. *J Appl Mech (Trans ASME)* 75. <https://doi.org/10.1115/1.2723824>

Chapter 27

On a Boundary Element Method for a Flow of Viscous Fluid Around a Cylinder



Mezhlum Sumbatyan and Rafael Zakaryan

Abstract In the classical problem of hydrodynamics, for a cylinder placed in a flow of viscous incompressible fluid, we propose a new version of boundary integral equation (BIE), in the two-dimensional (2d) case. The proposed method is based on the Navier–Stokes equations formulated in terms of vorticity and stream functions. With this treatment, the most complex point is to satisfy correctly the no-slip boundary conditions on the surface of the cylinder, which all are written in terms of a stream function; hence, there is no boundary condition for the vorticity function. This obstacle is overcome in the present work by substituting an appropriate expression for vorticity to a certain expression for the stream function. Such an approach results in a specific system of BIEs for the boundary value of the vorticity function and its normal derivative, over the boundary line. By so doing, we demonstrate the application of this method by using two different forms of Green’s function—(i) for full 2d space; (ii) for the exterior of the cylinder, with the Dirichlet boundary condition over its surface. In the latter case, Green’s function is more complex, being expressed as an infinite series of the modified Bessel functions, but the treatment is simplified in this case to be reduced to a single BIE, instead of a traditional system of two BIEs. In a discrete form, the proposed approach generates a new Direct Numerical Simulation (DNS) method to the formulated problem.

Keywords Flow around a cylinder · Viscous fluid · Boundary integral equation · Boundary element method · Stream function · Vorticity function

27.1 Introduction

Standard DNS methods, like Finite Element Methods (FEM) (Zienkiewicz and Taylor 2000), Finite Volume Methods (FVM) (Moukalled et al. 2019), and others, have widely been applied to the problem about flows of viscous fluid around bodies. The BIE method, which is a subject of the present work, is used for viscous fluids less

M. Sumbatyan (✉) · R. Zakaryan
Vorovich Institute of Mathematics, Mechanics and Computer Science, Southern Federal University, Milchakova Street 8a, Rostov-on-Don 344090, Russia
e-mail: masumbatyan@sfnu.ru

© The Author(s), under exclusive license to Springer Nature Switzerland AG 2023
H. Altenbach and V. Eremeyev (eds.), *Advances in Linear and Nonlinear Continuum and Structural Mechanics*, Advanced Structured Materials 198,
https://doi.org/10.1007/978-3-031-43210-1_27

extensively, since their governing Navier–Stokes equations are strongly nonlinear. Among others, let us mention the works (Brebbia et al. 1984; Dargush and Banerjee 1991; Aydin and Fenner 2000; Grigoriev and Dargush 1999).

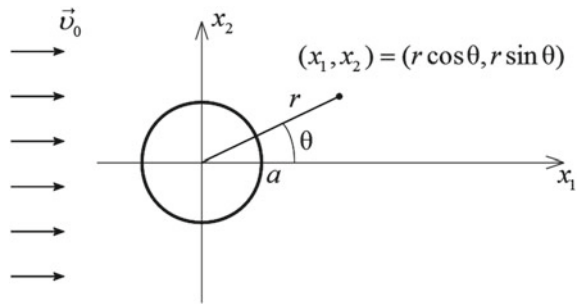
The BIE method is coupled with the Boundary Element Method (BEM), following from the classical potential theory. Initially, this method was applied to elastic problems, and some later—to the problems of fluids and gases. The method is based on the governing differential equations describing a certain physical problem, written in an integral form. The main advantage of the BIE method is observed in linear and linearized problems and consists of a decreasing dimension of the problem by unit. Many impressive examples such an efficiency can be found in the dynamics of non-viscous fluid, as well as in viscous fluid dynamics with the Stokes and the Oseen approximations. Thus, the solution to a three-dimensional (3d) problem can be reduced to a BIE over a 2d surface, and a solution to a 2d problem can be reduced to an integral equation over a boundary curve. Obviously, with nonlinear terms this advantage disappears, and one needs to discretize both 3d or 2d integrals, respectively. However, there are some other positive factors when applying the BIE method, discussed below.

Let us discuss the principal aspects of the BIE applied to flows of the viscous incompressible fluid. First of all, the application of the BIE depends on the choice of basic physical quantities: velocity—pressure or stream function—vorticity, or velocity—vorticity. Such a choice influences the choice of the initial and the boundary conditions, as well as the way of transformation of the Navier–Stokes and continuity equations to the integral form, which determines the form of integral equations themselves. If one the chosen physical quantities is the velocity, then the boundary conditions are rather simple. An attractive approach, at least in the 2d problems, is found in the Navier–Stokes equations written in terms of stream and vorticity functions, which in the 2d problems both are scalar functions, and the pressure function is excluded. With this treatment, the most complex point is to satisfy correctly the no-slip boundary conditions on the boundary, since they all are written in terms of the stream function. Therefore, there is a trouble when solving a respective boundary-value problem for the vorticity function, since there is no explicit boundary condition for the vorticity; see, for example, Roache 1976; Fletcher 1988.

The second important point is the choice between stationary and transient forms of the Navier–Stokes equations. In the transient case, one should choose an appropriate form for the derivative, respectively time. Then this derivative is represented either in integral form or by a finite-difference scheme. In the present work, we represent the time derivative as a finite difference by the Euler scheme (an implicit form), as in Tseng and Ferziger (2003).

The third important point is the choice of an appropriate representation for the nonlinear terms in the Navier–Stokes equations. For instance, with the Stokes approximation the nonlinear terms are neglected, and in the Oseen approximation there are neglected the small quantities of the second order. In other works, the authors propose some finite-difference schemes for the nonlinear terms, as well as penalty functions have been used for convective terms. Besides, some authors apply the divergence theorem and the dual reciprocity method (DRM) for the nonlinear terms (Aydin and

Fig. 27.1 A round cylinder of radius a placed in a uniform flow of viscous fluid



Fenner 2000). As a rule, these methods permit the study of flows with small and moderate Reynolds numbers. However, the improved formulation of the penalty function in Grigoriev and Dargush (1999) permits acceptable solutions for large Reynolds numbers, but as outlined in Aydin and Fenner (2000) the method itself looks more like a certain FEM.

The fourth important point is the used way to transform partial differential equations to a system of integral equations. Let us emphasize the two possible approaches: (i) the weighted residuals method with arbitrary weight function, and (ii) the method based on Green's function. In the first case, there is usually used the Green–Gauss theorem, but in the second case there is typically used the second Green's formula transforming the volumetric integral to an integral over the boundary.

Now let us describe the principal difference and expected advantage of the BIE method when compared with the FEM and the FVM. The main attention is paid to methods of development of integral equations and their reducing to an efficient form of discretization. The main advantage of the BIE method is that this provides a good convergence of the numerical process with a relatively small number of nodes on the mesh. Hence, this essentially reduces the time required to construct the solution. It should also be noted that the integral form of the equations permits to take into account singular points and breaking points of the solution, not by increasing the dimension of the mesh but by some mathematical transformations.

27.2 Mathematical Formulation

Let us consider a uniform flow of the incompressible viscous fluid around a circular disk; see Fig. 27.1. The governing equations are the Navier–Stokes equations, which we write in the 2d case in the Cartesian coordinate system (x_1, x_2) in terms of stream function ψ and vorticity function ω ; see Roache (1976), Fletcher (1988), and Cottet and Koumoutsakos (2000):

$$\begin{aligned} \frac{\partial \omega_f}{\partial t} &= -v_{f1} \frac{\partial \omega_f}{\partial x_1} - v_{f2} \frac{\partial \omega_f}{\partial x_2} + v \Delta \omega_f, \\ v_{f1} &= \frac{\partial \psi_f}{\partial x_2}, \quad v_{f2} = -\frac{\partial \psi_f}{\partial x_1}, \quad \omega_f = \frac{\partial v_{f1}}{\partial x_2} - \frac{\partial v_{f2}}{\partial x_1}, \quad \Delta \psi_f = \omega_f, \end{aligned} \quad (27.1)$$

where the subscript f indicates that the respective quantity is related to the full stream field. Here v_{f1} and v_{f2} are the components of the velocity vector. The equation of continuity $\partial v_{f1}/\partial x_1 + \partial v_{f2}/\partial x_2 = 0$ is satisfied here automatically.

Any full physical quantity is a sum of respective quantity in the incoming flow (marked with the subscript 0) and the perturbed one (free of any subscript):

$$v_{f1} = v_0 + v_1, \quad v_{f2} = v_2, \quad \psi_f = \psi_0 + \psi, \quad \omega_f = \omega, \quad \psi_0 = v_0 x_2. \quad (27.2)$$

The perturbed quantities are assumed to decay in the far zone.

If the initial values for $t = 0$ are known for both functions ψ and ω , then the first equation in (27.1) can be solved by iterations with respect to time. It is known (Roache 1976; Fletcher 1988) that stable numerical methods are provided with backward finite-difference schemes over time. In the simplest form, such an implicit iterative scheme is obtained from the Euler approximation $(\partial \omega / \partial t)_n \approx (\omega_n - \omega_{n-1}) / \tau$, where τ is a chosen time step. It is possible to apply finite-difference schemes of higher orders, but this does not change the essence of the algorithm and only modifies slightly the value of the small parameter ε below. In any way, the nonlinear term in Eq. (27.1) should be taken on the “previous” time layer, to avoid the nonlinear boundary-value problem at each iteration. The current time layer is associated with iteration number n which may appear as either a subscript or a superscript, for any physical quantity. With such a treatment, the iteration algorithm is convergent for a sufficiently small time step τ .

This approach yields the following iteration process for functions ω_n and ψ_n :

$$\begin{aligned} \omega_f^n - \varepsilon \Delta \omega_f^n &= g_f^{n-1} \sim \Delta \omega_f^n - k^2 \omega_f^n = -\frac{g_f^{n-1}}{\varepsilon}, \\ g_f^{n-1} &= \omega_f^{n-1} + \tau \left(\frac{\partial \psi_f}{\partial x_1} \frac{\partial \omega_f}{\partial x_2} - \frac{\partial \psi_f}{\partial x_2} \frac{\partial \omega_f}{\partial x_1} \right)_{n-1}, \\ \Delta \psi_f^n &= \omega_f^n, \quad (\varepsilon = v \tau, \quad k^2 = 1/\varepsilon). \end{aligned} \quad (27.3)$$

By a standard method related to the classical potential theory (Brebbia et al. 1984; Colton and Kress 1983), one can extract from two elliptic partial differential equations in (27.3) the following integral representations for functions ω_n and ψ_n :

$$\begin{aligned} \omega_n(x) &= \int_l \left[\frac{\partial G_\omega(y, x)}{\partial n_y} \omega_n(y) - G_\omega(y, x) \frac{\partial \omega_n(y)}{\partial n_y} \right] dl_y + \\ &+ \frac{1}{\varepsilon} \iint_S G_\omega(y, x) g_f^{n-1}(y) ds_y, \end{aligned} \tag{27.4}$$

$$\begin{aligned} \psi_n(x) &= \int_l \left[\frac{\partial G_\psi(y, x)}{\partial n_y} \psi_f^n(y) - G_\psi(y, x) \frac{\partial \psi_f^n(y)}{\partial n_y} \right] dl_y - \\ &- \iint_S G_\psi(y, x) \omega_n(y) ds_y, \end{aligned} \tag{27.5}$$

for any chosen point $x = (x_1, x_2)$ in the fluid. Here, S is the domain covered by the fluid, i.e. exterior of the cylinder, l is its circular boundary line, dl_y is the elemental arc length over the boundary line, ds_y is the elemental area in the fluid, and n_y is the unit normal to l directed toward the fluid (i.e. outside the cylinder). The subscript y means that the elemental quantities are taken at point $y = (y_1, y_2)$, not at point x . Besides, functions

$$\begin{aligned} G_\omega &= \frac{1}{2\pi} K_0(k|y - x|), \quad G_\psi = -\frac{1}{2\pi} \ln |y - x|, \\ |y - x| &= [(y_1 - x_1)^2 + (y_2 - x_2)^2]^{1/2} \end{aligned} \tag{27.6}$$

are Green’s functions in the unbounded space for Helmholtz operator $(\Delta_y - k^2)G_\omega$ and Laplace operator $\Delta_y G_\psi$, respectively. If $k \rightarrow +0$ then the first of them is transformed to the second one that is evident due to the asymptotic behavior of the Macdonald function K_0 (Abramowitz and Stegun 1964).

By using the no-through and no-slip boundary condition and taking into account that the stream function is defined up to arbitrary constant summand, one may write the following boundary conditions for function ψ :

$$\psi_f^n(x)|_l = 0, \implies \psi_n(x)|_l = -\psi_0|_l, \tag{27.7}$$

$$\left. \frac{\partial \psi_f^n(x)}{\partial n_x} \right|_l = 0, \implies \left. \frac{\partial \psi_n(x)}{\partial n_x} \right|_l = -\left. \frac{\partial \psi_0}{\partial n_x} \right|_l, \tag{27.8}$$

where l is a boundary line of the cylinder.

Equations (27.4) and (27.5) contain four functions over the boundary line l , on the current n -th time layer: ψ_n and $\partial \psi_n / \partial n$, as well as ω_n and $\partial \omega_n / \partial n$. Obviously, they should be defined from the boundary conditions. For a more efficient representation, let us calculate asymptotically in Eq. (27.4) the integral over domain S , along variable y with an arbitrary fixed $x \in S$, in the case when parameter ε is small:

$$\begin{aligned} \iint_S G_\omega(y, x) g_{n-1}(y) ds_y &= \frac{1}{2\pi} \iint_S K_0(k|y-x|) g_f^{n-1}(y) ds_y \sim \\ &\sim \left(\begin{matrix} y_1 - x_1 = \mu \cos \varphi \\ y_2 - x_2 = \mu \sin \varphi \end{matrix} \right) \sim \frac{g_f^{n-1}(x)}{2\pi} \int_0^{2\pi} \int_0^\infty K_0(k\mu) \mu d\mu d\varphi = \varepsilon g_f^{n-1}(x). \end{aligned} \tag{27.9}$$

Here, the above asymptotic function g_f^{n-1} could be extracted outside the integral with its value at point $y = x$, since the principal contribution to this integral is given by a small vicinity of this point, due to exponential decay of the Macdonald function with an increasing argument. Besides, the value of the last integral in (27.9), over variable μ , is tabulated; see Abramowitz and Stegun (1964).

Let us rewrite Eq. (27.4), by using (27.9), with variables $(y; \eta)$ instead of $(x; y)$:

$$\omega_n(y) = \int_l \left[\frac{\partial G_\omega(\eta, y)}{\partial n_\eta} \omega_n(\eta) - G_\omega(\eta, y) \frac{\partial \omega_n(\eta)}{\partial n_\eta} \right] dl_\eta + g_f^{n-1}(y). \tag{27.10}$$

Now, the obtained expression (27.10) for vorticity ω_n may be substituted into the dual integral in (27.5), by taking into account that the curvilinear integral in Eq. (27.5), containing the boundary value of a full stream function and of its normal derivative, is equal to zero, due to boundary conditions (27.7), (27.8):

$$\begin{aligned} \psi_n(x) &= - \iint_S G_\psi(y, x) g_f^{n-1}(y) ds_y - \int_l \omega_n(\eta) \frac{\partial}{\partial n_\eta} \left[\iint_S G_\psi(y, x) G_\omega(\eta, y) ds_y \right] \\ &\quad \times dl_\eta + \int_l \frac{\partial \omega_n(\eta)}{\partial n_\eta} \left[\iint_S G_\psi(y, x) G_\omega(\eta, y) ds_y \right] dl_\eta. \end{aligned} \tag{27.11}$$

The asymptotic estimate of Eq. (27.11) with small ε gives for the internal dual integral:

$$\iint_S G_\psi(y, x) G_\omega(\eta, y) ds_y \sim \frac{G_\psi(\eta, x)}{2\pi} \int_0^\pi \int_0^\infty K_0(k\mu) \mu d\mu d\varphi = \frac{\varepsilon}{2} G_\psi(\eta, x), \tag{27.12}$$

where we have taken into account that this integral should be applied over a half-plane for variable $\mu = |y - x|$, since point η belongs to the boundary contour: $\eta \in l$, and so the principal contribution to this integral is given by a small semi-circle whose diameter is tangential to contour l . Of course, such a treatment is valid only if the boundary line l is smooth.

Then, to come to integral equations, one should evaluate the behavior of respective integrals, as $x \rightarrow l$ (Colton and Kress 1983):

$$\begin{aligned}
 \int_l G(y, x) \frac{\partial f(y)}{\partial n_y} dl_y &\rightarrow \int_l G(y, x) \frac{\partial f(y)}{\partial n_y} dl_y, \\
 \int_l f(y) \frac{\partial G(y, x)}{\partial n_y} dl_y &\rightarrow \int_l f(y) \frac{\partial G(y, x)}{\partial n_y} dl_y + \frac{f(x)}{2}, \\
 \frac{\partial}{\partial n_x} \int_l G(y, x) \frac{\partial f(y)}{\partial n_y} dl_y &\rightarrow \int_l \frac{\partial G(y, x)}{\partial n_x} \frac{\partial f(y)}{\partial n_y} dl_y - \frac{1}{2} \frac{\partial f(x)}{\partial n_x}, \\
 \frac{\partial}{\partial n_x} \int_l f(y) \frac{\partial G(y, x)}{\partial n_y} dl_y &\rightarrow \int_l f(y) \frac{\partial^2 G(y, x)}{\partial n_x \partial n_y} dl_y,
 \end{aligned} \tag{27.13}$$

where f is an arbitrary smooth function.

This implies that two boundary conditions (27.7) and (27.8) applied to function (27.11), taking also into account relations (27.12) and (27.13), lead to a pair of BIEs, with respect to the two unknown functions ω_n and $\partial\omega_n/\partial n$, as follows:

$$\begin{aligned}
 \frac{\varepsilon}{4} \omega_n(x) + \frac{\varepsilon}{2} \int_l \frac{\partial G_\psi(y, x)}{\partial n_y} \omega_n(y) dl_y - \frac{\varepsilon}{2} \int_l G_\psi(y, x) \frac{\partial \omega_n(y)}{\partial n_y} dl_y = \\
 = \psi_0 - \iint_S G_\psi(y, x) g_f^{n-1}(y) ds_y,
 \end{aligned} \tag{27.14a}$$

$$\begin{aligned}
 \frac{\varepsilon}{4} \frac{\partial \omega_n(x)}{\partial n_x} - \frac{\varepsilon}{2} \int_l \frac{\partial G_\psi(y, x)}{\partial n_x} \frac{\partial \omega_n(y)}{\partial n_y} dl_y + \frac{\varepsilon}{2} \int_l \frac{\partial^2 G_\psi(y, x)}{\partial n_y \partial n_x} \omega_n(y) dl_y \\
 = \frac{\partial \psi_0}{\partial n_x} - \iint_S \frac{\partial G_\psi(y, x)}{\partial n_x} g_f^{n-1}(y) ds_y.
 \end{aligned} \tag{27.14b}$$

The developed system of BIEs in the discretization of the domain covered by the flow, with nodes of a boundary mesh, implies the subdivision of contour l to N small sub-intervals. This leads to a system of linear algebraic equations (SLAE) of dimension $2N \times 2N$. The known values of respective functions on the $(n - 1)$ th time layer permit, with the use of this SLAE, to define the unknown functions over the boundary contour l on the n th time layer. Then one can find, coming back to Eqs. (27.10) and (27.11), the unknown functions on the n th time layer in the total flow domain. This allows one to pass to the calculation of all physical quantities on the next time layer. If one sets on the initial 0-th layer the values of the physical functions corresponding say to a flow of non-viscous fluid around a cylinder, then one comes, after several iteration steps, to a flow field corresponding to the viscous flow around the cylinder.

Obviously, such an approach is applicable to any body of a rather general geometry placed in the flow of viscous incompressible fluid.

27.3 Specific Green's Functions for the Exterior of the Cylinder

Here, we construct Green's functions for both Poisson and Helmholtz equations, which satisfy the homogeneous Lagrange boundary condition over the cylinder. The derivation follows the classical book (Duffy 2001).

Let us start with the Poisson equation. First of all, let us pass to the polar coordinate system, with

$$x_1 = r_0 \cos \theta_0, \quad x_2 = r_0 \sin \theta_0, \quad y_1 = r \cos \theta, \quad y_2 = r \sin \theta. \quad (27.15)$$

One thus needs to solve the following equation:

$$\Delta G_\psi \equiv \frac{\partial^2 G_\psi}{\partial r^2} + \frac{1}{r} \frac{\partial G_\psi}{\partial r} + \frac{1}{r^2} \frac{\partial^2 G_\psi}{\partial \theta^2} = -\delta(y-x) \equiv -\frac{\delta(r-r_0)\delta(\theta-\theta_0)}{r}, \quad (27.16)$$

regarding function $G_\psi = G_\psi(y, x) = G_\psi(r, \theta; r_0, \theta_0)$ as a function of $y = (r, \theta)$ for any fixed point $x = (r_0, \theta_0)$ in the fluid, with the boundary condition $G_\psi|_{r=a} = 0$. Then, according to Duffy (2001), since

$$\delta(\theta - \theta_0) = \frac{1}{2\pi} \sum_{m=0}^{\infty} a_m \cos[m(\theta - \theta_0)], \quad a_0 = 1, \quad a_m = 2 \quad (m \geq 1), \quad (27.17)$$

one may seek function G_ψ , due to the orthogonality of the trigonometric functions, in the following form:

$$G_\psi = \sum_{m=0}^{\infty} G_m^\psi(r, r_0) \cos[m(\theta - \theta_0)]. \quad (27.18)$$

By so doing, Eq. (27.16) is reduced to the inhomogeneous ordinary differential equation (ODE) of the second order:

$$\frac{\partial^2 G_m^\psi}{\partial r^2} + \frac{1}{r} \frac{\partial G_m^\psi}{\partial r} - \frac{m^2}{r^2} G_m^\psi = -a_m \frac{\delta(r-r_0)}{2\pi r}, \quad (27.19)$$

whose solution, bounded at infinity and satisfying the boundary condition $G_m^\psi(a) = 0$, can simply be constructed in the following form:

$$G_m^\psi(r, r_0) = \frac{1}{2\pi m} \left[-\left(\frac{a^2}{r_0 r}\right)^m + H(r-r_0) \left(\frac{r_0}{r}\right)^m + H(r_0-r) \left(\frac{r}{r_0}\right)^m \right], \quad (m \geq 1), \quad (27.20a)$$

$$G_0^\psi(r, r_0) = \frac{1}{2\pi} \left[H(r-r_0) \ln \frac{r_0}{a} + H(r_0-r) \ln \frac{r}{a} \right], \quad (27.20b)$$

where H is the Heaviside function, whose derivative is Dirac's delta-function.

Green's function for the Helmholtz operator

$$\frac{\partial^2 G_\omega}{\partial r^2} + \frac{1}{r} \frac{\partial G_\omega}{\partial r} + \frac{1}{r^2} \frac{\partial^2 G_\omega}{\partial \theta^2} - k^2 G_\omega = - \frac{\delta(r - r_0) \delta(\theta - \theta_0)}{r}, \tag{27.21}$$

$$\left(k^2 = \frac{1}{\varepsilon}, \varepsilon = \nu \tau \right),$$

with a certain parameter $k > 0$, can be developed by analogy. If one applies the expansion as in (27.18)

$$G_\omega = \sum_{m=0}^{\infty} G_m^\omega(r, r_0) \cos[m(\theta - \theta_0)], \tag{27.22}$$

then for every coefficient in this expansion, Eq. (27.21) is again reduced to the ODE, as follows:

$$\frac{\partial^2 G_m^\omega}{\partial r^2} + \frac{1}{r} \frac{\partial G_m^\omega}{\partial r} - \left(\frac{m^2}{r^2} + k^2 \right) G_m^\omega = - a_m \frac{\delta(r - r_0)}{2\pi r}, \tag{27.23}$$

whose solution, bounded at infinity and satisfying the boundary condition $G_m^\omega(a) = 0$, is constructed in a similar way (Grigoriev and Dargush 1999):

$$G_m^\omega(r, r_0) = \frac{a_m}{4\pi} \left[- \frac{K_m(kr_0)}{K_m(ka)} K_m(kr) I_m(ka) + \right. \\ \left. + H(r - r_0) K_m(kr) I_m(kr_0) + H(r_0 - r) I_m(kr) K_m(kr_0) \right], \quad (m \geq 0). \tag{27.24}$$

It is interesting to notice that Green's function for the Poisson equation (3.6) can directly be obtained from Green's function for the Helmholtz equation (27.24) if one applies the limit $k \rightarrow +0$ in the latter, by taking the well-known asymptotic behavior of the modified Bessel functions for a small argument.

27.4 The BIE with the Specific Green's Functions

With so constructed specific Green's functions, the basic equations above can significantly be simplified. Thus, representation (27.4) is reduced to

$$\omega_n(x) = \int_l \frac{\partial G_\omega(y, x)}{\partial n_y} \omega_n(y) dl_y + \frac{1}{\varepsilon} \iint_S G_\omega(y, x) g_f^{n-1}(y) ds_y, \tag{27.25}$$

since $G_\omega(y, x) = 0, y \in l$. Besides, Eq. (27.5) is simplified to the following form:

$$\psi_n(x) = - \iint_S G_\psi(y, x) \omega_n(y) ds_y, \tag{27.26}$$

since $\psi_f(y) = 0, \partial\psi_f(y)/\partial n_y = 0, y \in l$ at each iteration step, due to no-through and no-slip boundary conditions (27.7) and (27.8). It is obvious that the second boundary condition means trivial tangential velocity on the boundary contour. The first one follows from the trivial normal velocity on the cylinder, which is equivalent to the trivial tangential derivative of the stream function. This leads to a constant value of function $\psi_f(y)$ over the boundary, which we accept as trivial. Then both terms in the boundary integrals in Eq. (27.5) become zero.

When looking at representations (27.25) and (27.26), it is obvious that if function g_f^{n-1} is known from the previous iteration step and boundary value of the vorticity ω_n is known over the boundary line l then Eq. (27.25) determines vorticity ω_n at an arbitrary point in the fluid. After that, by substituting this calculated function into Eq. (27.26) one thus can find also the stream function all over the flow. Therefore, here we are faced with the well-known key trouble—in which way the boundary value of the vorticity ω_n can be determined if there is no boundary condition formulated for this function? To overcome this obstacle, there were proposed many approximate formulas, starting from the work of Thom (1933), which locally connect boundary values of vorticity with boundary values of the stream function; a good survey is given in Weinan and Liu (1996).

In the present work, we propose a natural treatment of this point, which does not require any approximations. In the case of Green’s functions valid in the full 2d space, this has been applied above in Section 2. First of all, let us note that expression (27.5) is obtained from the Poisson equation $\Delta\psi = \omega$, see Eq. (27.1), where the boundary condition may be known either for ψ (Dirichlet problem) or for its normal derivative (Neumann problem). If one has homogeneous conditions for both these functions, one thus can use only one of them, for correct treatment of the Poisson equation. We assume that $\psi_f = 0, y \in l$. Therefore, the remaining condition $\partial\psi_f(y)/\partial n_y = 0$ is indeed the one which should be used to find the boundary value of vorticity ω . It is obvious that the most natural way is to substitute expression (27.25) into expression (27.26), and then to take the normal derivative of the so obtained function, $\partial\psi_f^n(y)/\partial n_y$, to put it equal to zero, that is equivalent to condition $\partial\psi_n(y)/\partial n_y = -\partial\psi_0/\partial n_y$.

The above-mentioned substitution leads to the following formula:

$$\begin{aligned} \psi_n(x) = & - \int_l \left[\iint_S G_\psi(y, x) \frac{\partial G_\omega(\eta, y)}{\partial n_\eta} ds_y \right] \omega_n(\eta) dl_\eta - \\ & - \frac{1}{\varepsilon} \iint_S \left[\iint_S G_\psi(y, x) G_\omega(\eta, y) ds_y \right] g_f^{n-1}(\eta) ds_\eta, \end{aligned} \tag{27.27}$$

where 2d points x, y, η can be expressed in both the Cartesian and the polar coordinate systems, as follows:

$$\begin{aligned} x &= (x_1, x_2) = (r_0 \cos \theta_0, r_0 \sin \theta_0), \\ y &= (y_1, y_2) = (r \cos \theta, r \sin \theta), \\ \eta &= (\eta_1, \eta_2) = (\rho \cos \beta, \rho \sin \beta). \end{aligned} \tag{27.28}$$

This allows one to write out representation (27.27) for the stream function in the polar coordinate system:

$$\begin{aligned} \psi_n(r_0, \theta_0) &= - \int_0^{2\pi} \left[\int_0^{2\pi} \int_a^\infty \left(\sum_{m=0}^\infty G_m^\psi(r, r_0) \cos[m(\theta - \theta_0)] \right) \times \right. \\ &\times \left. \left(\sum_{q=0}^\infty \frac{\partial G_q^\omega(a, r)}{\partial \rho} \cos[q(\beta - \theta)] \right) r dr d\theta \right] \omega_n(a, \beta) a d\beta - \\ &- \frac{1}{\varepsilon} \int_0^{2\pi} \int_a^\infty \left[\int_0^{2\pi} \int_a^\infty \left(\sum_{m=0}^\infty G_m^\psi(r, r_0) \cos[m(\theta - \theta_0)] \right) \times \right. \\ &\times \left. \left(\sum_{q=0}^\infty G_q^\omega(\rho, r) \cos[q(\beta - \theta)] \right) r dr d\theta \right] g_f^{n-1}(\rho, \beta) \rho d\rho d\beta. \end{aligned} \tag{27.29}$$

By taking into account the orthogonality of the trigonometric functions, the integration over variable θ significantly simplifies expression (27.29), as follows:

$$\begin{aligned} \psi_n(r_0, \theta_0) &= -\pi a \sum_{m=0}^\infty b_m \int_0^{2\pi} \int_a^\infty G_m^\psi(r, r_0) \frac{\partial G_m^\omega(a, r)}{\partial \rho} \cos[m(\beta - \theta_0)] \omega_n(a, \beta) r dr d\beta - \\ &- \frac{\pi}{\varepsilon} \sum_{m=0}^\infty b_m \int_0^{2\pi} \int_a^\infty \left[\int_a^\infty G_m^\psi(r, r_0) G_m^\omega(\rho, r) r dr \right] \cos[m(\beta - \theta_0)] g_f^{n-1}(\rho, \beta) \rho d\rho d\beta, \end{aligned} \tag{27.30}$$

where $b_0 = 2, b_m = 1 (m \geq 1)$.

Since the normal to the round cylinder is directed along the radius, the expression for the normal derivative of the stream function over the boundary line is directly obtained from (27.30):

$$\begin{aligned}
 & \frac{\partial \psi_n(a, \theta_0)}{\partial r_0} = \\
 & = -\pi a \sum_{m=0}^{\infty} b_m \int_0^{2\pi} \int_a^{\infty} \frac{\partial G_m^\psi(r, a)}{\partial r_0} \frac{\partial G_m^\omega(a, r)}{\partial \rho} \cos[m(\beta - \theta_0)] \omega_n(a, \beta) r dr d\beta - \\
 & \frac{\pi}{\varepsilon} \sum_{m=0}^{\infty} b_m \int_0^{2\pi} \int_a^{\infty} \left[\int_a^{\infty} \frac{\partial G_m^\psi(r, a)}{\partial r_0} G_m^\omega(\rho, r) r dr \right] \cos[m(\beta - \theta_0)] g_f^{n-1}(\rho, \beta) \rho d\rho d\beta.
 \end{aligned}
 \tag{27.31}$$

Some terms in the last formula can be calculated in explicit form:

$$\frac{\partial G_0^\psi(r, a)}{\partial r_0} = \frac{1}{2\pi a}, \quad \frac{\partial G_m^\psi(r, a)}{\partial r_0} = \frac{1}{\pi a} \left(\frac{a}{r}\right)^m, \quad (m \geq 1),
 \tag{27.32}$$

$$\begin{aligned}
 \frac{\partial G_m^\omega(a, r)}{\partial \rho} &= \frac{ka_m}{4\pi} \left[-K'_m(ka) I_m(ka) \frac{K_m(kr)}{K_m(ka)} + I'_m(ka) K_m(kr) \right] = \\
 &= \frac{a_m K_m(kr)}{4\pi a K_m(ka)},
 \end{aligned}
 \tag{27.33}$$

where we have used the equality $I_m(z)K'_m(z) - K_m(z)I'_m(z) = -1/z$; see Prudnikov et al. (1986).

On the basis of (27.32) and (27.33), one can calculate explicitly two integrals on a semi-infinite interval over variable r in Eq. (27.31). In the second line of (27.31), this implies

$$\begin{aligned}
 \int_a^\infty \frac{\partial G_m^\psi(r, a)}{\partial r_0} G_m^\omega(\rho, r) r dr &= \frac{a_m \varepsilon}{4\pi^2 a} \left[\left(\frac{a}{\rho}\right)^m - \frac{K_m(k\rho)}{K_m(ka)} \right], \quad (m \geq 1), \\
 \int_a^\infty \frac{\partial G_0^\psi(r, a)}{\partial r_0} G_0^\omega(\rho, r) r dr &= \frac{a_0 \varepsilon}{8\pi^2 a} \left[1 - \frac{K_0(k\rho)}{K_0(ka)} \right],
 \end{aligned}
 \tag{27.34}$$

where we have used the following tabulated integrals (Colton and Kress 1983):

$$\int K_m(z) z^{1-m} dz = -z^{1-m} K_{m-1}(z), \quad \int I_m(z) z^{1-m} dz = z^{1-m} I_{m-1}(z),
 \tag{27.35}$$

as well as the following equality: $K_m(z)I_{m-1}(z) + I_m(z)K_{m-1}(z) = 1/z$.

By analogy, the semi-infinite integral in the first line of (27.31) implies

$$\int_a^\infty \frac{\partial G_m^\psi(r, a)}{\partial r_0} \frac{\partial G_m^\omega(a, r)}{\partial \rho} r dr = \frac{a_m \sqrt{\varepsilon}}{4\pi^2 a} \frac{K_{m-1}(ka)}{K_m(ka)}, \quad (m \geq 1),$$

$$\int_a^\infty \frac{\partial G_0^\psi(r, a)}{\partial r_0} \frac{\partial G_0^\omega(a, r)}{\partial \rho} r dr = \frac{a_0 \sqrt{\varepsilon}}{8\pi^2 a} \frac{K_{-1}(ka)}{K_0(ka)} = \frac{a_0 \sqrt{\varepsilon}}{8\pi^2 a} \frac{K_1(ka)}{K_0(ka)},$$
(27.36)

since for Macdonald's functions $K_{-1} = K_1$.

Then representation (27.31) reads

$$\frac{\partial \psi_n(a, \theta_0)}{\partial r_0} = - \int_0^{2\pi} K(\beta - \theta_0) \omega_n(a, \beta) d\beta - \int_0^{2\pi} \int_a^\infty K_g(\rho, \beta - \theta_0) g_f^{n-1}(\rho, \beta) \rho d\rho d\beta,$$
(27.37a)

where

$$K(\beta - \theta_0) = \frac{\sqrt{\varepsilon}}{4\pi} \sum_{m=0}^\infty a_m \frac{K_{m-1}(ak)}{K_m(ak)} \cos[m(\beta - \theta_0)],$$

$$K_g(\rho, \beta - \theta_0) = \frac{1}{4\pi a} \sum_{m=0}^\infty a_m \left[\left(\frac{a}{\rho} \right)^m - \frac{K_m(k\rho)}{K_m(ka)} \right] \cos[m(\beta - \theta_0)].$$
(27.37b)

Now, by taking into account that $\psi_0 = v_0 x_2 = v_0 r_0 \sin \theta_0$, and satisfying the boundary condition $\partial \psi_n(a, \theta_0) / \partial r_0 = -\partial \psi_0(a, \theta_0) / \partial r_0 = -v_0 \sin \theta_0$, Eq. (27.37a) is reduced to the basic BIE of the first kind for the boundary value of the vorticity at each iteration step ($0 \leq \theta_0 \leq 2\pi$):

$$\int_0^{2\pi} K(\beta - \theta_0) \omega_n(a, \beta) d\beta = v_0 \sin \theta_0 - \int_0^{2\pi} \int_a^\infty K_g(\rho, \beta - \theta_0) g_f^{n-1}(\rho, \beta) \rho d\rho d\beta.$$
(27.38)

As soon as this boundary value $\omega(a, \beta)$ is found, both stream and vorticity functions can easily be determined all over the volume occupied by the fluid stream—by Eqs. (27.30) and (27.25), respectively.

27.5 Conclusions

The following conclusions may be drawn from the above study:

1. In the 2d problem about a rigid body placed in the uniform stream of the viscous incompressible fluid, we apply a standard implicit scheme in time, which reduces the nonlinear Navier–Stokes equations to an iterative process, where at each iteration step there is a need to solve two linear elliptic boundary-value problems, if the convective terms are taken at the previous temporal layer. The two linear partial differential equations (PDEs) are the Laplace equation for the stream function and the Helmholtz equation for the vorticity function.
2. To solve those PDEs, we propose two alternative approaches, to construct some BIEs over the obstacle’s boundary contour. By an appropriate discretization, these can be reduced to a certain form of the BEM.
3. The proposed approach allows the authors to overcome the well-known difficulty connected with the fact that there is no appropriate boundary condition for the vorticity function. Based on Green’s functions for the unbounded 2d-space, the proposed method reduces the problem, at each iteration step, to a system of two BIEs. On the contrary, Green’s function which satisfies the homogeneous Dirichlet boundary condition permits reducing the problem to a single integral equation only, which is more preferable from the numerical point of view.

Acknowledgements The first author is grateful to the Russian Foundation for Basic Research (RFBR), for the support through Project No. 19-29-06013.

References

- Abramowitz M, Stegun I (1964) Handbook of mathematical functions with formulas, graphs, and mathematical tables. National Bureau of Standards, New York
- Aydin M, Fenner RT (2000) Boundary element analysis of driven cavity flow for low and moderate Reynolds numbers. *Int J Numer Meth Fluids* 37:45–64
- Brebbia CA, Telles JCF, Wrobel LC (1984) Boundary element techniques: theory and applications in engineering. Springer, Berlin
- Colton D, Kress R (1983) Integral equations methods in scattering theory. Wiley, New York
- Cottet G-H, Koumoutsakos PD (2000) Vortex Methods: theory and Practice. Cambridge University Press, Cambridge
- Dargush GF, Banerjee PK (1991) A time-dependent incompressible viscous BEM for moderate Reynolds numbers. *Int J Numer Meth Eng* 31:1627–1648
- Duffy DG (2001) Green’s functions with applications. Boca Raton, Florida, Chapman & Hall/CRC
- Fletcher CAJ (1988) Computational techniques for fluid dynamics, vol. 1, 2. Springer, Berlin
- Grigoriev MM, Dargush AV (1999) A poly-region boundary element method for incompressible viscous fluid flows. *Int J Numer Meth Eng* 46:1127–1158
- Moukalled F, Mangani L, Mangani L (2019) The finite volume method in computational fluid dynamics: an advanced introduction with OpenFOAM and Matlab. Springer International, Heidelberg

- Prudnikov AP, Brychkov YA, Marichev OI (1986) Integrals and series, Vol. 2: special functions. Gordon and Breach, New York
- Roache PJ (1976) Computational fluid dynamics. Hermosa Publ, Albuquerque
- Tseng Y-H, Ferziger JH (2003) A ghost-cell immersed boundary method for flow in complex geometry. *J Comput Phys* 192:593–623
- Weinan E, Liu J-G (1996) Vorticity boundary condition and related issues for finite difference schemes. *J Comput Phys* 124:368–382
- Zienkiewicz OC, Taylor RL (2000) The finite element method. Vol. 3: Fluid dynamics. Butterworth-Heinemann, Oxford

Chapter 28

Interface Crack Starting From the Corner of a Wedge Attached to a Half-Plane



Konstantin B. Ustinov

Abstract An analytical solution has been obtained for a problem of an edge crack between a wedge and half-plane of different elastic isotropic materials with the zero second Dundurs parameter of elastic mismatch. The solution has been obtained with the help of the Mellin transform and by reducing the problem to the matrix Wiener-Hopf problem. The kernel of the problem allowed factorization by Khrapkov's technique, however for zero second Dundurs parameter only. A particular case of uniform loading applied to the crack faces is considered in detail. Expressions for stress intensity factors for both opening and shear modes are obtained in terms of combinations of three single integrals of algebraic functions.

Keywords Wiener-Hopf technique · Matrix factorization · Mellin transform · Interface crack

28.1 Introduction

The problem in question belongs to a category of problems on contacting wedges with cracks. An elegant way to obtain analytical solutions for a class of 2-D elasticity problems of uniform bodies composed by two wedges with cracks was obtained by Khrapkov (1971a, b, c, 2001). This class covers the following cases: (i) two wedges forming a half-plane (an inclined edge crack in a half-plane); (ii) two wedges forming a plane (a semi-infinite crack with an arbitrarily oriented branch); (iii) one of the wedges forming a half-plane (the crack lying on the line of the contact of an arbitrary wedge and a half-plane). The method consists in reducing the problems to vector Riemann problems by applying the Mellin transform, followed by factorization of the matrix coefficient. Later, this technique was successfully used for solving similar problems including the problems of wedges of different materials (Kuliev 1979; Kipnis 1978), problem of semi-infinite crack parallel to a free rectilinear boundary

K. B. Ustinov (✉)

Department, IPMech RAS, Vernadskogo 101-1, Moscow 119526, Russia
e-mail: ustinov@ipmnet.ru

(Zlatin and Khrapkov 1990; Khrapkov 2001), problems of a semi-infinite interface cracks between layers and half-plane (Ustinov 2015), and in bi-material elastic layer (Ustinov 2019). In Ustinov (2020), it was demonstrated that the way to obtain solutions for all cases considered by Khrapkov (1971a, b, c, 2001) may be applied for similar cases of the wedges composed by different elastic materials, although with a restriction imposed on the elastic constants. The current article is devoted to obtaining a solution of this type, namely a wedge and half-plane of different elastic isotropic materials glued together everywhere except a finite region at the wedge corner, where both normal and tangential discontinuity of displacement take place.

Problems of bodies composed of wedges of different materials even without cracks attract attention by many research due to their importance from both the theoretical and practical points of view; such problems appear when studying processes of fracture of polycrystalline media, coating delamination, and others. Thus, bodies composed of two quadrant wedges of different materials were considered in Bogy (1970). In Bogy (1971b), the solution was generalized for a half-plane composed of two non-quadrant wedges. The contact and the crack problems for an elastic wedge of arbitrary angle were considered in Erdogan and Gupta (1976).

The next step was considering composed bodies with cracks terminating at the interface. A semi-infinite crack in a plane normal to a rectilinear interface and terminating on it was considered in Zak and Williams (1963). Similar problems for an inclined crack and for a crack terminating at the corner of a kinked interface were solved in Bogy (1971a, b), respectively. A review may be found in Sinclair (2004).

In the case of interfacial cracks, i.e. when the crack locates along the interface, causing additional difficulties when considering the stress field near its tip. The necessary information about the distribution of stresses and strains near the interface cracks may be found in Hutchinson and Suo (1991), Begley and Hutchinson (2017). Apart from purely geometrical parameters, solutions of problems of interface crack are determined by two Dundurs parameters α , β (Dundurs 1964), characterizing the mismatch of the elastic properties, written here in the form of Ustinov and Massabò (2022)

$$\alpha = \frac{\bar{E}_1 - \bar{E}_2}{\bar{E}_1 + \bar{E}_2} = \left(\frac{1}{\bar{E}_2} - \frac{1}{\bar{E}_1} \right) \left(\frac{1}{\bar{E}_1} + \frac{1}{\bar{E}_2} \right)^{-1}, \quad (28.1)$$

$$\beta = \frac{1}{2} \left(\frac{1 - \bar{\nu}_2}{\bar{E}_2} - \frac{1 - \bar{\nu}_1}{\bar{E}_1} \right) \left(\frac{1}{\bar{E}_2} + \frac{1}{\bar{E}_1} \right)^{-1}$$

Here, $\bar{E}_i = E_i$, $\bar{\nu}_i = \nu_i$ for plane stress, and $\bar{E}_i = E_i/(1 - \nu_i^2)$, $\bar{\nu}_i = \nu_i/(1 - \nu_i)$ for plane strain; E_k , ν_k , $k = 1, 2$ are Young's moduli and Poisson's ratios of media 1,2; $-1 \leq \alpha \leq 1$, and $-1/8 + 3\alpha/8 \leq \beta \leq 1/8 + 3\alpha/8$ for plane stress, $-1/2 + \alpha/2 \leq \beta \leq 1/2 + \alpha/2$ for plane strain. Thus, the condition of vanishing of the second Dundurs parameter $\beta = 0$ to be used further may be satisfied for any α for plane strain and for $-1/3 \leq \alpha \leq 1/3$ for plane stress.

The current study is devoted to obtaining an analytical solution of a problem of an edge crack between a wedge of arbitrary angle $0 < \theta_0 \leq \pi$ and half-plane of different elastic isotropic materials with zero second Dundurs parameter of elastic mismatch.

The solution is obtained by applying the Mellin transform to the equations of elasticity and boundary conditions and reducing the problem under consideration to a matrix Riemann problem. It is the fulfillment of the above-mentioned restrictive condition $\beta = 0$ that allows the application of Khrapkov’s method of matrix factorization. For arbitrary combinations of elastic constants, effective approximate methods may be used, e.g. Rogosin and Mishuris (2016), Abrahams et al. (2008a, b).

28.2 Geometry: Mathematical Formulation

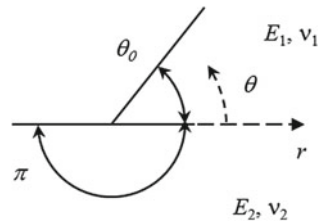
Consider an infinite wedge of angle $\theta_0 \leq \pi$ attached to a half-plane with a finite interface crack of unit length starting from the vertex of the wedge. Without loss of generality, the crack length may be set equal to unity. In polar coordinate frame r, θ with the origin of the vertex, the geometry may be considered as two wedges $0 \leq \theta \leq \theta_0$ and $-\pi \leq \theta \leq 0$ attached perfectly along the ray $1 \leq r < \infty$ and separated along the line segment $0 \leq r \leq 1$ (Fig. 28.1). The wedge and half-plane are isotropic and elastic, with Young’s moduli and Poisson’s ratios being E_1, ν_1 and E_2, ν_2 , respectively.

For both the wedge and the half-plane, the system of equations of elasticity has to be satisfied. In the introduced polar coordinate system r, θ , it has the form

$$\begin{aligned} \frac{\partial \sigma_{rr}}{\partial r} + \frac{1}{r} \frac{\partial \sigma_{r\theta}}{\partial \theta} + \frac{\sigma_{rr} - \sigma_{\theta\theta}}{r} &= 0; & \frac{\partial \sigma_{r\theta}}{\partial r} + \frac{1}{r} \frac{\partial \sigma_{\theta\theta}}{\partial \theta} + 2 \frac{\sigma_{r\theta}}{r} &= 0; \\ \epsilon_{rr} = \frac{\partial u_r}{\partial r}; & \quad \epsilon_{\theta\theta} = \frac{u_r}{r} + \frac{1}{r} \frac{\partial u_\theta}{\partial \theta}; & \quad \epsilon_{r\theta} = \frac{1}{2} \left(\frac{\partial u_\theta}{\partial r} - \frac{u_\theta}{r} + \frac{1}{r} \frac{\partial u_r}{\partial \theta} \right) & \quad (28.2) \\ \epsilon_{rr} = \frac{1}{E_k} \sigma_{rr} - \frac{\nu_k}{E_k} \sigma_{\theta\theta}; & \quad \epsilon_{\theta\theta} = \frac{1}{E_k} \sigma_{\theta\theta} - \frac{\nu_k}{E_k} \sigma_{rr}; & \quad \epsilon_{r\theta} = \frac{1 + \nu_k}{2E_k} \sigma_{r\theta} \end{aligned}$$

Here, subscripts $k = 1, 2$ correspond to the wedge and half-plane, respectively; u_r, u_θ are the components of displacement vector; $\sigma_{rr}, \sigma_{\theta\theta}, \sigma_{r\theta}, \epsilon_{rr}, \epsilon_{\theta\theta}, \epsilon_{r\theta}$ are components of stress and strain tensors.

Fig. 28.1 Wedge attached to a half-plane with a finite interface crack starting from the wedge corner



Together with the boundary conditions,

$$\begin{aligned} \sigma_{\theta\theta}(r, \theta_0) = \sigma_{\theta\theta}(r, -\pi) = \sigma_{r\theta}(r, \theta_0) = \sigma_{r\theta}(r, -\pi) = 0 \\ \sigma_{\theta\theta}(r, 0) = \sigma_{\theta\theta}^{(0)}(r), \quad \sigma_{r\theta}(r, 0) = \sigma_{r\theta}^{(0)}(r), \quad 0 \leq r \leq 1 \\ u_r^{(1)}(0, r) - u_r^{(2)}(0, r) = 0, \quad u_\theta^{(1)}(0, r) - u_\theta^{(2)}(0, r) = 0, \quad r \geq 1 \end{aligned} \tag{28.3}$$

the above equations form a closed system.

28.3 Reduction of the Problem in Question to a Riemann Matrix Problem

Consider Mellin transforms (note that this definition follows Uflyand 1968; Khrapkov 1971a, b, c, 2001 and differs from Sneddon 1979):

$$\hat{f}(p) = \int_0^\infty f(r) r^p dr, \quad f(r) = \frac{1}{2\pi i} \int_{c-i\infty}^{c+i\infty} \hat{f}(p) r^{-p-1} dp, \quad -\delta_0 < c < 0 \tag{28.4}$$

Here, δ_0 is the distance of the closest to the imaginary axis singularity of $\hat{f}(p)$, located in the left half-plane of p .

The relations between transforms of the displacement derivatives and stresses along the ray $0 \leq r < \infty, \theta = 0$ for the wedge are Khrapkov (1971a, b, c, 2001)

$$\begin{aligned} \frac{\partial \hat{u}_\theta}{\partial r}(0, p) = \frac{2}{E_1} \left[\frac{\sin \theta_0 p \cos \theta_0 p + p \sin \theta_0 \cos \theta_0}{p^2 \sin^2 \theta_0 - \sin^2 \theta_0 p} \hat{\sigma}_{\theta\theta}(0, p) + \right. \\ \left. \left(\frac{p(p-1) \sin^2 \theta_0}{p^2 \sin^2 \theta_0 - \sin^2 \theta_0 p} - \frac{1-\nu_1}{2} \right) \hat{\sigma}_{r\theta}(0, p) \right] \end{aligned} \tag{28.5}$$

$$\begin{aligned} \frac{\partial \hat{u}_r}{\partial r}(0, p) = \frac{2}{E_1} \left[\left(-\frac{p(p+1) \sin^2 \theta_0}{p^2 \sin^2 \theta_0 - \sin^2 \theta_0 p} + \frac{1-\nu_1}{2} \right) \hat{\sigma}_{\theta\theta}(0, p) + \right. \\ \left. \frac{\sin \theta_0 p \cos \theta_0 p - p \sin \theta_0 \cos \theta_0}{p^2 \sin^2 \theta_0 - \sin^2 \theta_0 p} \hat{\sigma}_{r\theta}(0, p) \right] \end{aligned} \tag{28.6}$$

A similar relation for the half-plane is obtained from (28.6) by replacing E_1, ν_1 with E_2, ν_2 and θ_0 with $-\pi$. From here, the relations between transforms of derivatives of relative displacements of the contacting edges and stresses are obtained as follows:

$$\mathbf{X}_+ = \mathbf{K}(\mathbf{X}_- + \mathbf{Z}_+) \quad (28.7)$$

Here,

$$\begin{aligned} \mathbf{X}_+ &= \frac{E_1 E_2}{2(E_1 + E_2)} \int_0^1 \frac{\partial}{\partial r} \begin{pmatrix} u_\theta^{(1)}(0, p) - u_\theta^{(2)}(0, p) \\ u_r^{(1)}(0, p) - u_r^{(2)}(0, p) \end{pmatrix} r^p dr \\ \mathbf{X}_- &= \int_1^\infty \begin{pmatrix} \sigma_{\theta\theta}(0, p) \\ \sigma_{r\theta}(0, p) \end{pmatrix} r^p dr, \quad \mathbf{Z}_+ = \int_0^1 \begin{pmatrix} \sigma_{\theta\theta}(0, p) \\ \sigma_{r\theta}(0, p) \end{pmatrix} r^p dr \end{aligned} \quad (28.8)$$

The intervals of integration were reduced owing to vanishing of the integrands beyond the specified bounds. The components of the matrix kernel \mathbf{K} are

$$\begin{aligned} K_{11} &= \frac{1 - \alpha}{4d_1} (\sin 2p\theta_0 + p \sin 2\theta_0) + \frac{1 + \alpha}{4d_2} \sin 2p\pi \\ K_{12} &= \left(\frac{1 - \alpha}{2d_1} \sin^2 \theta_0 \right) p(p - 1) + \beta \\ K_{21} &= - \left(\frac{1 - \alpha}{2d_0} \sin^2 \theta_0 \right) p(p + 1) - \beta \\ K_{22} &= \frac{1 - \alpha}{4d_1} (\sin 2p\theta_0 - p \sin 2\theta_0) + \frac{1 + \alpha}{4d_2} \sin 2p\pi \end{aligned} \quad (28.9)$$

$$d_1 = p^2 \sin^2 \theta_0 - \sin^2 p\theta_0; \quad d_2 = -\sin^2 p\pi \quad (28.10)$$

In order to formulate the Riemann problem, the behavior of the vector-functions to be determined has to be specified in key points (corresponding to zero, unity, and infinity of the original problem). In order to have elastic energy bounded near the crack tip both stresses and displacements derivatives at $r \rightarrow 1$ should grow no faster than $(r - 1)^{-1/2}$, which corresponds to

$$\mathbf{X}_\pm = O(p^{-1/2}); \quad p \rightarrow \pm\infty \quad (28.11)$$

Singularities of vector-functions \mathbf{X}_+ and \mathbf{Z}_+ corresponding to bounded derivatives of displacements and bounded stresses lay within the left half-plane of p with the closest to the imaginary axis simple pole located at $p = -1$:

$$\mathbf{X}_+ = O(p^{-1}); \quad \mathbf{Z}_+ = O(p^{-1}); \quad p \rightarrow -1 \quad (28.12)$$

Therefore, vector-functions \mathbf{X}_+ and \mathbf{Z}_+ are holomorphic in the half-plane $\text{Re } p > -1$, which is why the lower index + is used.

Behavior of function \mathbf{X}_- depends on the applied loads. If no load is applied at infinity, the stresses $\sigma_{\theta\theta}(0, r)$ and $\sigma_{r\theta}(0, r)$ tend to zero at $r \rightarrow \infty$. If the load applied at the crack faces is self-balanced, then the stresses will tend to zero faster than r^{-1} .

Thus, vector-function \mathbf{X}_- has no singularities (is holomorphic) in the left half-plane $\text{Re } p \leq 0$ (therefore the lower index “-” is used) and

$$\mathbf{X}_- = O(1); \quad p \rightarrow 0 \quad (28.13)$$

A uniform load applied at infinity results in a pole at $p = -1$ in \mathbf{X}_-

$$\mathbf{X}_- = O(p^{-1}); \quad p \rightarrow -1 \quad (28.14)$$

Thus, in case of load applied to the crack faces the vector-functions \mathbf{X}_{\pm} have an overlapping range of regularity $-1 < \text{Re } p < 0$, and a traditional non-uniform Wiener-Hopf problem may be posed.

In case of free of loading crack faces ($\mathbf{Z}_+ = 0$) and uniform stress σ_{∞} applied at infinity, the vector-functions \mathbf{X}_{\pm} have only a common line of regularity (except the point $p = -1$, where they may have simple poles), and a uniform Riemann problem may be formulated for finding the eigen solution.

28.4 Factorization of the Matrix Kernel

The main point of the solution consists in the factorization of the matrix coefficient $K(p)$, i.e. its representation in the form

$$\mathbf{K}(p) = \mathbf{K}_+(p) \mathbf{K}_-^{-1}(p) \quad (28.15)$$

where matrix-functions $\mathbf{K}_{\pm}(p)$ are holomorphic in the right and left half-planes of complex plane $\text{Re } p \geq \delta_0$ and $\text{Re } p \leq \delta_0$, respectively, and $\det \mathbf{K}_{\pm}(p) \neq 0$ in the corresponding domains up to the boundary. The general solution for an arbitrary kernel is still unknown. However, kernel (28.9) being a particular case of the matrix-functions described in Ustinov (2020) may be effectively factorized by Khrapkov's method (Khrapkov 1971a, b, c, 2001) for $\beta = 0$:

$$\begin{aligned} \mathbf{K}_+^{\pm 1}(p) &= \Lambda_{\pm}^{\pm 1}(p) [\mathbf{I} \cosh(\phi \beta_{\pm}) \pm \mathbf{B}(p) \sinh(\phi \beta_{\pm})] \\ \mathbf{K}_-^{\pm 1}(p) &= \Lambda_{\pm}^{\pm 1}(p) [\mathbf{I} \cosh(\phi \beta_{\mp}) \pm \mathbf{B}(p) \sinh(\phi \beta_{\mp})] \end{aligned} \quad (28.16)$$

Here \mathbf{I} is the unity matrix; matrix-function $\mathbf{B}(p)$ called the commutant (Khrapkov 1971a, b, c, 2001) and function $\phi(p)$ are

$$\mathbf{B}(p) = \phi^{-1}(p) \begin{pmatrix} \cos \theta_0 & (p-1) \sin \theta_0 \\ -(p+1) \sin \theta_0 & -\cos \theta_0 \end{pmatrix}, \quad \phi(p) = \sqrt{1 - p^2 \sin^2 \theta_0} \tag{28.17}$$

Functions $\Lambda_{\pm}(p)$, $\beta_{\pm}(p)$ are the solutions of scalar Riemann problems (the latter should not be confused with the second Dundurs parameter, which will not appear hereafter):

$$\Lambda_{-}^{-1}(p) \Lambda_{+}(p) = \Delta^{1/2}(p), \quad p \in L \tag{28.18}$$

$$\beta_{+}(p) - \beta_{-}(p) = \phi^{-1}(p) \varepsilon(p), \quad p \in L \tag{28.19}$$

Here, determinant $\Delta(p)$ and exponent $\varepsilon(p)$ of matrix $\mathbf{K}(p)$ are

$$\Delta(p) = \lambda_1(p) \lambda_2(p), \quad \varepsilon(p) = \frac{1}{2} \log \frac{\lambda_1(p)}{\lambda_2(p)} \tag{28.20}$$

Eigenvalues $\lambda_1(p)$, $\lambda_2(p)$ of matrix $\mathbf{K}(p)$ are

$$\lambda_{1,2}(p) = \cot p A_{1,2}(\tau) \tag{28.21}$$

Here $A_{1,2}(\tau)$ are expressed in terms of the argument corresponding to the imaginary axis $p = i\tau$

$$A_{1,2}(\tau) = \frac{1}{4} \tanh \tau \left[\frac{1 - \alpha}{d_3} \sinh 2\tau\theta_0 + \frac{1 + \alpha}{d_4} \sinh 2\pi\tau \pm 2\tau \sin \theta_0 \sqrt{1 + \tau^2 \sin^2 \theta_0} \frac{1 - \alpha}{d_3} \right] \tag{28.22}$$

$$d_3 = \tau^2 \sin^2 \theta_0 - \sinh^2 \theta_0\tau; \quad d_4 = -\sinh^2 \pi\tau$$

Solutions of (28.18), (28.19) may be written similar to Khrapkov (1971a, b, c, 2001) in terms of Cauchy type integrals and factorization of cotangent in terms of gamma function:

$$\Lambda_{+}(p) = \frac{\sqrt{\pi} \Gamma(1 + p/\pi)}{\Gamma(1/2 + p/\pi)} J_{+}(p), \quad \Lambda_{-}(p) = \frac{p\Gamma(1/2 - p/\pi)}{\sqrt{\pi}\Gamma(1 - p/\pi)} J_{-}(p) \tag{28.23}$$

$$J_{\pm}(p) = \exp \left\{ -\frac{1}{4\pi} \int_{-\infty}^{\infty} \log [A_1(\tau) A_2(\tau)] \frac{d\tau}{i\tau - p} \right\} \tag{28.24}$$

$$\beta_{\pm}(p) = -\frac{1}{4\pi} \int_{-\infty}^{\infty} \frac{1}{\sqrt{1 + \tau^2 \sin^2 \theta_0}} \log \frac{A_1(\tau)}{A_2(\tau)} \frac{d\tau}{i\tau - p} \tag{28.25}$$

According to the rule of calculation of contour integrals, the integration contour may be transformed to the imaginary axis of p . For equal properties of the wedge and half-plane ($\alpha = \beta = 0$), the above formulae are reduced to formulae due to Khrapkov (1971a, b, c, 2001).

Note that the obtained factorization may be used for solving a problem with a similar geometry but with the locations of the intact part of the interface and the crack being exchanged. Such a problem for a homogeneous body was solved in Kipnis (1979).

28.5 Asymptotics of the Involved Functions

Let us write the asymptotics of the involved functions that will be used further. Using the representation of Cauchy type integrals at infinity (Noble 1959; Khrapkov 2001), the following asymptotics for (28.25) are obtained:

$$\beta_{\pm}(p) = \frac{q \cot \theta_0}{p} \tag{28.26}$$

where

$$q(\theta_0, \alpha) = \frac{\sin \theta_0}{2\pi} \int_0^{\infty} \frac{1}{\sqrt{1 + \tau^2 \sin^2 \theta_0}} \log \frac{A_1(\tau)}{A_2(\tau)} d\tau, \quad p \rightarrow \pm\infty \tag{28.27}$$

Substituting (28.26) into (28.16) gives

$$\mathbf{K}_{\pm}^{\pm 1}(p) = (-p)^{\pm 1/2} \mathbf{Q}_{\infty}^{\pm 1} \tag{28.28}$$

where

$$\mathbf{Q}_{\infty}^{\pm 1} = \begin{pmatrix} \cos q & \pm \sin q \\ \mp \sin q & \cos q \end{pmatrix}, \quad p \rightarrow -\infty \tag{28.29}$$

It follows from (28.16) that vector-functions $\mathbf{K}_{\pm}^{\pm 1}(p)$ are regular at $p = -1$ (except for $\alpha = 0, \alpha = \pi$). Therefore

$$\mathbf{K}_{-1}^{\pm 1} \equiv \mathbf{K}_{-1}^{\pm 1}(-1) = -\Lambda_{-1}^{\pm 1} \mathbf{Q}_{-1}^{\pm 1} \tag{28.30}$$

where¹

$$\mathbf{Q}_{-1}^{\pm 1} = \mathbf{I} \cosh q_{-1} \pm \begin{pmatrix} 1 & -2 \tan \theta_0 \\ 0 & -1 \end{pmatrix} \sinh q_{-1} \tag{28.31}$$

$$\Lambda_{-1} \equiv \Lambda_{-}(-1) = -\frac{\Gamma(1/2 + 1/\pi)}{\sqrt{\pi}\Gamma(1 + 1/\pi)} \exp \left\{ -\frac{1}{2\pi} \int_0^\infty \log [A_1(\tau) A_2(\tau)] \frac{d\tau}{\tau^2 + 1} \right\} \tag{28.32}$$

$$q_{-1} \equiv \phi(-1)\beta_{-}(-1) = -\frac{\cos \theta_0}{2\pi} \int_0^\infty \frac{1}{\sqrt{1 + \tau^2 \sin^2 \theta_0}} \log \frac{A_1(\tau)}{A_2(\tau)} \frac{d\tau}{\tau^2 + 1} \tag{28.33}$$

For an important case $\theta = \pi/2$, expression (28.31) becomes formally undetermined since $\cos \theta_0 \rightarrow 0$. By performing the proper limit transition, one has

$$\mathbf{Q}_{-1}^{\pm 1}(\theta = \pi/2) = \mathbf{I} \pm \begin{pmatrix} 0 & 1 \\ 0 & 0 \end{pmatrix} \frac{1}{\pi} \int_0^\infty \frac{1}{\sqrt{1 + \tau^2}} \log \frac{A_1(\tau)}{A_2(\tau)} \frac{d\tau}{\tau^2 + 1} \tag{28.34}$$

28.6 Solution of the Riemann Problem

Let us consider the non-homogeneous problem, consisting in solving Eq. (28.7) where vector-functions \mathbf{X}_{\pm} have an overlapping range of regularity $-1 < \text{Re } p < 0$. Substituting (28.15) into (28.7) yields

$$\mathbf{K}_{+}^{-1}\mathbf{X}_{+} - \mathbf{Y}_{+} = \mathbf{K}_{-}^{-1}\mathbf{X}_{-} - \mathbf{Y}_{-} \tag{28.35}$$

Here \mathbf{Y}_{\pm} represents product $\mathbf{K}_{\pm}^{-1}\mathbf{Z}_{\pm}$ as a sum of parts, holomorphic in the right and left half-planes of complex plane p , respectively

$$\mathbf{Y}_{+} - \mathbf{Y}_{-} = -\mathbf{K}_{-}^{-1}\mathbf{Z}_{+} \tag{28.36}$$

According to Liouville theorem (e.g. Noble 1959; Khrapkov 2001), both the left- and right-hand sides of equation (28.35) are equal to a single function, holomorphic in the whole plane p . Moreover, it may be concluded from (28.28) and (28.11) that both sides of (28.35) tend to zero as $p \rightarrow \infty$ in both half-planes $\text{Re } p > 0$ and

¹ There were a misprint in Ustinov (2020) in the formula similar to (28.31) not affecting further results: the sign “-” before tangent was missed.

Re $p < 0$; and hence, this holomorphic function should be equal to zero. Thus, the general solution is

$$\mathbf{X}_{\pm} = \mathbf{K}_{\pm} \mathbf{Y}_{\pm} \quad (28.37)$$

Consider the load being a power function

$$\begin{pmatrix} \sigma_{\theta\theta}(0, p) \\ \sigma_{r\theta}(0, p) \end{pmatrix} = \mathbf{S}_m x^m, \quad 0 < r < 1, \quad m > -1 \quad (28.38)$$

where \mathbf{S}_m is a real constant vector. The Mellin transform is

$$\mathbf{Z}_+ = \mathbf{S}_m (p + m + 1)^{-1} \quad (28.39)$$

By adding and subtracting the term $\frac{1}{p+m+1} \mathbf{K}_-^{-1}(p = -m - 1) \mathbf{S}_0$ in (28.36), one has

$$\begin{aligned} \mathbf{Y}_+ &= -\frac{1}{p+m+1} \mathbf{K}_-^{-1}(p = -m - 1) \mathbf{S}_0 \\ \mathbf{Y}_- &= \frac{1}{p+m+1} [\mathbf{K}_-^{-1}(p) - \mathbf{K}_-^{-1}(p = -m - 1)] \mathbf{S}_0 \end{aligned} \quad (28.40)$$

Substitution of (28.40) into (28.37) finally yields

$$\begin{aligned} \mathbf{X}_+ &= -\frac{1}{p+m+1} \mathbf{K}_+(p) \mathbf{K}_-^{-1}(p = -m - 1) \mathbf{S}_0 \\ \mathbf{X}_- &= \frac{1}{p+m+1} [\mathbf{I} - \mathbf{K}_-(p) \mathbf{K}_-^{-1}(p = -m - 1)] \mathbf{S}_0 \end{aligned} \quad (28.41)$$

The most important values that could be extracted from the obtained solution are the stress intensity factors, SIFs, (K_1, K_2) , i.e. coefficients at inverse square root singularities at $r = 1$ corresponding to similar singularities at infinity for the transforms (e.g. Khrapkov 1971a, b, c)

$$\mathbf{X}_- = \frac{1}{\sqrt{-2p}} \begin{pmatrix} K_1 \\ K_2 \end{pmatrix}, \quad p \rightarrow -\infty \quad (28.42)$$

Comparison of (28.42) and (28.41) using (28.28), (28.31) gives

$$\begin{pmatrix} K_1 \\ K_2 \end{pmatrix} = -\sqrt{2} \Lambda_-^{-1}(p = -m - 1) \mathbf{Q}_{\infty} \mathbf{Q}_-^{-1}(p = -m - 1) \mathbf{S}_0 \quad (28.43)$$

The obtained solution may be applied to a load being a superposition of power functions. Moreover, a rather general function may be approximated by a power series.

The solution is especially simple in the case of the uniform load applied to the crack faces: $\sigma_0 = \sigma_{\theta\theta} = const, \tau_0 = \sigma_{r\theta} = const$. Thus, (28.41) reduces to

$$Y_+ = -\frac{1}{p+1} \mathbf{K}_{-1}^{-1} \mathbf{S}_0, \quad Y_- = \frac{1}{p+1} [\mathbf{K}_{-1}^{-1}(p) - \mathbf{K}_{-1}^{-1}] \mathbf{S}_0 \tag{28.44}$$

and (28.43) reduces to

$$\begin{pmatrix} K_1 \\ K_2 \end{pmatrix} = -\sqrt{2} \Lambda_{-1}^{-1} \mathbf{Q}_{\infty} \mathbf{Q}_{-1}^{-1} \mathbf{S}_0 \tag{28.45}$$

28.7 Some Numerical Results

Consider the crack of length a with faces loaded with the constant normal unit stresses, so that $\mathbf{S}_0 = \begin{pmatrix} 1 \\ 0 \end{pmatrix}$. The SIFs are determined by algebraic functions of three integrals: (28.27), (28.32), and (28.33). Substituting their values into (28.29), (28.31) and then into (28.45) yields the values of SIFs. The results are presented in Figs. 28.2, 28.3, 28.4, and 28.5. Figures 28.2 and 28.3 depict dependencies of mode I and mode II SIFs versus the wedge angle for various values of α . Solid lines correspond to $\alpha = 0$, dashed lines correspond to $\alpha = 0.9$, and dotted lines correspond to $\alpha = -0.9$. Figures 28.4 and 28.5 depict dependencies of mode I and mode II SIFs versus parameter α for various wedge angles. Solid lines correspond to $\theta = \pi/2$, dashed lines correspond to $\theta = 3\pi/4$, dotted lines correspond to $\theta = \pi/4$, and dot-dashed lines correspond to $\theta = \pi/3$.

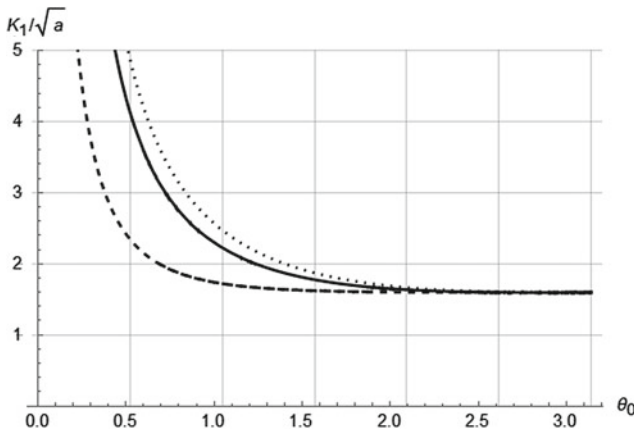


Fig. 28.2 Mode I SIF for the crack with faces loaded by the constant normal stresses versus the wedge angle

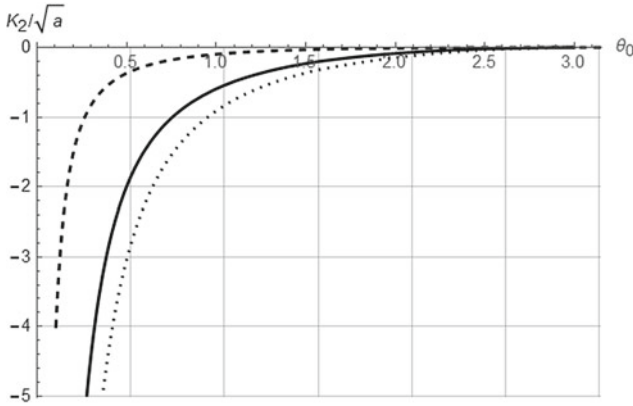


Fig. 28.3 Mode II SIF for the crack with faces loaded by the constant normal stresses versus the wedge angle

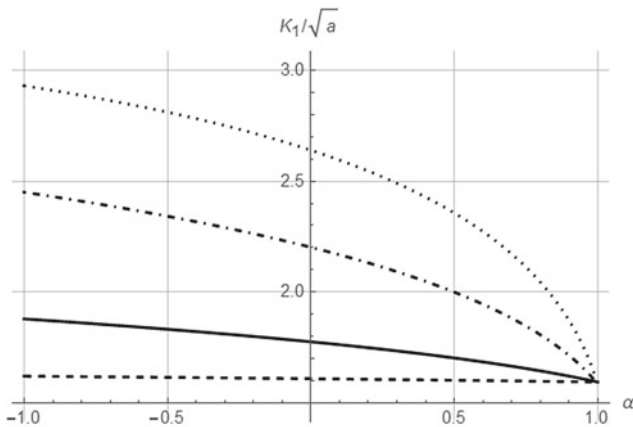


Fig. 28.4 Mode I SIF for the crack with faces loaded by the constant normal stresses versus the first Dundurs parameter α

It is seen from Fig. 28.2 that for $\theta \rightarrow \pi$ the value of K_1 approaches the value corresponding to a semi-infinite crack in a plane, whose faces are loaded with the normal stresses within interval a , the faster the large parameter α . The value corresponding to $\theta = \pi$ may be obtained from the solution for finite crack loaded symmetrically within finite intervals adjusted to the crack tips (Paris and Sih 2023) by a proper limit transition. This limiting value is

$$\frac{K_1}{\sqrt{a}\sigma_0} = \frac{2\sqrt{2}}{\sqrt{\pi}} \tag{28.46}$$

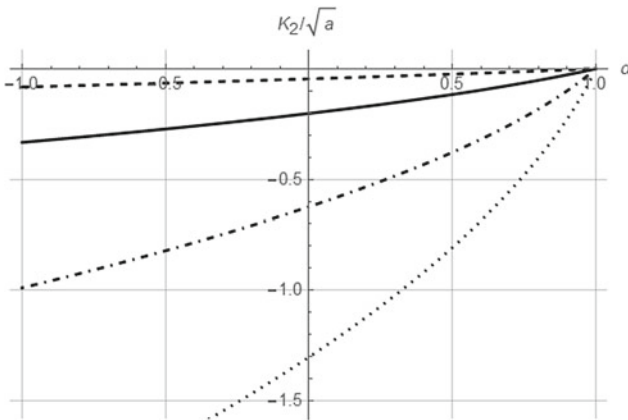


Fig. 28.5 Mode II SIF for the crack with faces loaded by the constant normal stresses versus the first Dundurs parameter α

28.8 Conclusion

A problem of an infinite wedge being in full contact with a half-plane everywhere except a finite region near the corner is considered. Both the wedge and half-plane are supposed to be linear elastic with, generally, different elastic constants: Young's moduli and Poisson's ratios. By using the Mellin transform, the problem has been reduced to a matrix Wiener-Hopf problem. For an arbitrary angle of the wedge and zero second Dundurs parameter, the matrix kernel of the problem allows factorization using Khrapkov's method. Thus a closed analytical solution has been obtained. The problem under consideration corresponds to one of particular cases of the problem for two contacting wedges allowing closed-form solution (Ustinov 2020), these cases being exactly the same as the ones considered by Khrapkov (1971a, b, c, 2001) for wedges of the same material. Loading of the crack faces with a uniform normal loading has been considered in more detail. Expressions for stress intensity factors for both opening and shear modes are obtained in terms of combinations of three single integrals of algebraic functions. For the wedge angle approaching to π , i.e. when the wedge unfolds to a half-plane, the values of SIFs tend to the values corresponding to a known solution for a plane with a semi-infinite crack. The obtained solution appears valuable for analyzing extreme cases of parameters.

Funding The work has been done under financial support of Russian State Assignment under contract No. -20-120011690133-1.

Acknowledgements The work has been done under the financial support of Russian State Assignment under contract No.-20-120011690133-1.

References

- Abrahams ID, Davis AMJ, Smith SGL (2008) Asymmetric channel divider in stokes flow. *SIAM J Appl Math* 68(5):1439–1463. <https://doi.org/10.1137/070703211>
- Abrahams ID, Davis AMJ, Smith SGL (2008) Matrix wiener-hopf approximation for a partially clamped plate. *Q J Mech Appl Math* 61(2):241–265. <https://doi.org/10.1093/qjmam/hbn004>
- Begley MR, Hutchinson JW (2017) The mechanics and reliability of films, multilayers and coatings. Cambridge University Press. <https://doi.org/10.1017/9781316443606>
- Bogy DB (1970) On the problem of edge-bonded elastic quarter-planes loaded at the boundary. *Int J Solids Struct* 6(9):1287–1313. [https://doi.org/10.1016/0020-7683\(70\)90104-6](https://doi.org/10.1016/0020-7683(70)90104-6)
- Bogy DB (1971) On the plane elastostatic problem of a loaded crack terminating at a material interface. *J Appl Mech* 38(4):911–918. <https://doi.org/10.1115/1.3408975>
- Bogy DB (1971) Two edge-bonded elastic wedges of different materials and wedge angles under surface tractions. *J Appl Mech* 38(2):377–386. <https://doi.org/10.1115/1.3408786>
- Dundurs J (1964) Edge-bonded dissimilar orthogonal elastic wedges under normal and shear loading. *J Appl Mech, Trans ASME* 36(3):650–651. <https://doi.org/10.1115/1.3564739>
- Erdogan F, Gupta GD (1976) Contact and crack problems for an elastic wedge. *Int J Eng Sci* 14(2):155–164. [https://doi.org/10.1016/0020-7225\(76\)90084-7](https://doi.org/10.1016/0020-7225(76)90084-7)
- Hutchinson JW, Suo Z (1991) Mixed mode cracking in layered materials. *Adv Appl Mech* 29:63–191. [https://doi.org/10.1016/S0065-2156\(08\)70164-9](https://doi.org/10.1016/S0065-2156(08)70164-9)
- Khrapkov AA (1971) Certain cases of the elastic equilibrium of an infinite wedge with a nonsymmetric notch at the vertex, subjected to concentrated forces. *J Appl Math Mech* 35(4):625–637. [https://doi.org/10.1016/0021-8928\(71\)90056-6](https://doi.org/10.1016/0021-8928(71)90056-6)
- Khrapkov AA (1971) Closed form solutions of problems on the elastic equilibrium of an infinite wedge with nonsymmetric notch at the apex. *J Appl Math Mech* 35(6):1009–1016. [https://doi.org/10.1016/0021-8928\(71\)90105-5](https://doi.org/10.1016/0021-8928(71)90105-5)
- Khrapkov AA (1971) The first basic problem for a notch at the apex of an infinite wedge. *Int J Fract Mech* 7(4). <https://doi.org/10.1007/bf00189109>
- Khrapkov AA (2001) Wiener-Hopf method in mixed elasticity theory problems. B.E. Vedeneev VNIIG Publishing House
- Kipnis LA (1979) A crack along the continuation of the face of a wedge enveloping a half-space. *J Appl Math Mech* 43(5):981–986. [https://doi.org/10.1016/0021-8928\(79\)90186-2](https://doi.org/10.1016/0021-8928(79)90186-2)
- Kipnis LA (1978) An interface crack between different media. *Prikl Mat Mekh (PMM)* 34(4):625–637
- Kuliev VD (1979) A crack with a finite branch in a piecewise-homogeneous elastic medium. *Soviet Phys Doklady* 246(6):1330–1333
- Noble B (1959) Methods based on the wiener-hopf technique for the solution of partial differential equations. *Phys Today* 12(9):50–50. <https://doi.org/10.1063/1.3060973>
- Paris PC, Sih GC (2023) Stress analysis of cracks. In: Fracture toughness testing and its applications, pp 30–3052. ASTM International. <https://doi.org/10.1520/stp26584s>
- Rogosin S, Mishuris G (2016) Constructive methods for factorization of matrix-functions. *IMA J Appl Math* 81(2):365–391. <https://doi.org/10.1093/imamat/hxv038>
- Sinclair GB (2004) Stress singularities in classical elasticity ii: asymptotic identification. *Appl Mech Rev* 57(5):385–439. <https://doi.org/10.1115/1.1767846>
- Sneddon IN (1979) The use of integral transforms. Tata McGraw-Hill Publication Co. Ltd., New Delhi
- Uflyand YS (1968) Integral transform in theory of elasticity, 2nd edn. Nauka, Leningrad
- Ustinov K (2019) On semi-infinite interface crack in bi-material elastic layer. *Eur J Mech—A/Solids* 75:56–69. <https://doi.org/10.1016/j.euromechsol.2019.01.013>
- Ustinov KB (2015) On separation of a layer from the half-plane: elastic fixation conditions for a plate equivalent to the layer. *Mech Solids* 50(1):62–80. <https://doi.org/10.3103/S0025654415010070>
- Ustinov KB (2020) Certain cases of elastic equilibrium of a composed wedge with an interface crack. *Math Mech Solids* 25(12):2199–2209. <https://doi.org/10.1177/1081286520924070>

- Ustinov K, Massabò R (2022) On elastic clamping boundary conditions in plate models describing detaching bilayers. *Int J Solids Struct* 248:111600. <https://doi.org/10.1016/j.ijsolstr.2022.111600>
- Zak AR, Williams ML (1963) Crack point stress singularities at a bi-material interface. *J Appl Mech* 30(1):142–143. <https://doi.org/10.1115/1.3630064>
- Zlatin AN, Khrapkov AA (1990) Elastic half-plane weakened by a crack parallel to its boundary. *Issledovaniya Po Uprugosti I Plastichnosti (Studies on Elasticity and Plasticity)* 16:68–75

Chapter 29

Static Thermomechanical Loading of Thermal Barrier Coatings: Compliance Functions



Andrey S. Vasiliev, Sergei M. Aizikovich, and Regina A. Bardakova

Abstract The paper addresses a modeling of a thermobarrier coating under thermal and mechanical loading. The coating consists of three layers of various thicknesses: metallic bond coat, thermally grown oxide and ceramic top coat. The surface of the coating is subjected to an arbitrary normal mechanical loading and thermal heating. A boundary value problem is obtained for construction compliance functions using the Hankel integral transformation. The compliance functions are obtained analytically for a homogeneous bond coat and numerically for a functionally graded bond coat. Illustrations of the properties of the compliance functions on each interface between the layers are presented for an example of a thermal barrier coating made of materials used in gas turbines. It is shown that graded properties and thickness of the bond coat sufficiently change the compliance functions. The results provide the basis for carrying out further research for the optimization of properties of the layer of thermal barrier coatings to reduce the stress concentration on the interfaces between the layers leading to delamination.

Keywords Thermal barrier · Coating · Contact · Thermoelasticity · Static thermomechanical loading · Analytical methods · Compliance functions

A. S. Vasiliev (✉) · S. M. Aizikovich · R. A. Bardakova
Laboratory of Functionally Graded and Composite Materials, Research and Education Center
“Materials”, Don State Technical University, 1 Gagrina sq., 344001 Rostov-on-Don, Russia
e-mail: andre.vasiliev@gmail.com

R. A. Bardakova
e-mail: regina-137@inbox.ru

© The Author(s), under exclusive license to Springer Nature Switzerland AG 2023
H. Altenbach and V. Eremeyev (eds.), *Advances in Linear and Nonlinear Continuum
and Structural Mechanics*, Advanced Structured Materials 198,
https://doi.org/10.1007/978-3-031-43210-1_29

29.1 Introduction

Thermal barrier coatings (TBCs) are the advanced layered systems which are used to provide thermal insulation to metallic components from the high temperature (Vaßen et al. 2010). They are widely used to increase the lifetime of the components of turbine engines (Wortman et al. 1989; Padture et al. 2002; Parker 1992) and usually consist of three layers: ceramic top coat (TC) with a significantly lower thermal conductivity than the metallic substrate, metallic bond coat (BC) and a thin interlayer of a thermally grown oxide (TGO). The BC is used to protect the substrate from oxidation and corrosion and improve the bonding between the substrate and top coat. The TGO layer forms as a result of oxidation of the BC during the high-temperature operating conditions. The TC is typically made of Y_2O_3 -stabilized ZrO_2 (YSZ) which possesses desirable properties for TBCs (Arnault et al. 1999; Chen 2006). It has one of the lowest values of thermal conductivity at an elevated temperature of all ceramics ($2.3 \text{ Wm}^{-1}\text{K}^{-1}$ at 1000°C) (Schlichting et al. 2001) and high thermal-expansion coefficient ($11.5 \cdot 10^{-6}\text{K}^{-1}$) (Vaßen et al. 2010). One of the most common causes of failure of TBCs is delamination, spallation and cracking in service owing to their poor bond strength and high residual stresses (Miller and Lowell 1982). The concept of functionally graded materials (FGMs) is used to mitigate these problems (Khor and Gu 2000; Schulz et al. 2003).

Mathematical modeling is one of the simplest and effective ways to study the influence of layer properties of TBCs on mechanical stresses and, thus, on one of the possible failure mechanisms. Contact problems of thermoelasticity can be used for that purpose. They are intensively studied by many authors in different formulations. One-dimensional contact problems for FGMs help one to study complex phenomena involving dynamic effects, wear, thermodynamic instability, etc. Barber (1969), Yi et al. (2000), Mao et al. (2017, 2018). An important feature of one-dimensional problems is the fact that their solutions can be obtained in an analytical form Zelentsov et al. (2022), Zelentsov and Mitrin (2019) using the Complex Analysis. Two-dimensional contact problems of thermoelasticity usually require the solution of singular integral equations which involves much more complex mathematical apparatuses. Thermoelastic quasi-static contact was studied taking into account fretting heat generation (Çömez and Güler 2022) including residual contact (Su et al. 2015), piezoelectric effect (Su et al. 2016; Çömez 2021), both in plane (sliding frictional contact) and axisymmetric (torsion) formulations (Liu et al. 2021). These problems are often solved using the semi-analytical methods such as collocation method (Erdogan and Gupta 1972) and the bilateral asymptotic method (Vasiliev et al. 2018). More complicated three-dimensional formulations are usually studied using numerical methods such as boundary element method (Ipatov et al. 2017; Igumnov et al. 2014, 2019) and finite element method (FEM) (Igumnov et al. 2019; Wang et al. 2018). Simulation of the mechanical behavior of thermal barrier coatings is also usually done using FEM only (Busso et al. 2009; Wang et al. 2014; Bäker and Seiler 2017).

The present paper addresses the construction of effective mathematical model of studying the mechanical behavior of TBCs using the approximated analytical approach (Vasiliev 2019). Thermoelastic half-space with a TBC under an arbitrary distributed thermal heating and normal mechanical loading is considered. The scheme of construction of a set of compliance functions is proposed. Analysis of these functions is important in the context of the solution of singular integral equations arising in the mixed problems of thermoelasticity for TBCs. It also makes it possible to evaluate the influence of the properties of each layer of TBCs on mechanical stresses on the interfaces between the layers.

29.2 Formulation of the Thermoelastic Problem

Let us consider a thermoelastic half-space with a thermal barrier coating of thickness H . Cylindrical coordinate system r, ϕ, z is used with the z -axis being normal to the surface of the half-space. Lamé parameters, thermal conductivity and thermal expansion coefficients of the TC, TGO and substrate are assumed to be constant and denoted by the symbols $\lambda_E^{(i)}, \mu^{(i)}, \lambda_T^{(i)}$ and $\alpha_T^{(i)}$. Hereinafter upper index (i) means that the quantity corresponds to a certain layer: (0) —TC, (1) —TGO, (2) —BC and (3) —substrate. The BC is assumed to be functionally graded (FG) with thermomechanical properties being the functions of z coordinate: $\lambda_E^{(2)}(z), \mu^{(2)}(z), \lambda_T^{(2)}(z)$ and $\alpha_T^{(2)}(z)$. Thicknesses of the TC, TGO and BC are denoted as $h^{(1)}, h^{(2)}$ and $h^{(3)}$. The depth of the interfaces between the layers are denoted by the following symbols: $H^{(0)} = 0, H^{(1)} = h^{(1)}, H^{(2)} = h^{(1)} + h^{(2)}$ and $H^{(3)} = H = h^{(1)} + h^{(2)} + h^{(3)}$. The surface of the coating is subjected to the normal mechanical loading $p_a(r)$ and thermal heating $q_a(r)$ in the circular area $0 \leq r \leq a$, stress free and thermally insulated outside this region. Thus, the following boundary conditions are satisfied:

$$\sigma_z|_{z=0} = \begin{cases} -p_a(r), & 0 \leq r \leq a \\ 0, & r > a \end{cases}, \lambda_T^{(0)} T'|_{z=0} = \begin{cases} -q_a(r), & 0 \leq r \leq a \\ 0, & r > a \end{cases}, \quad (29.1)$$

$$\tau_{rz}|_{z=0} = 0, r \geq 0$$

Perfect thermomechanical bonding on all interfaces between the layers of the TBC and substrate are assumed:

$$z = -H^{(i)} \quad u^{(i-1)} = u^{(i)}, w^{(i-1)} = w^{(i)}, T^{(i-1)} = T^{(i)}, \quad (29.2)$$

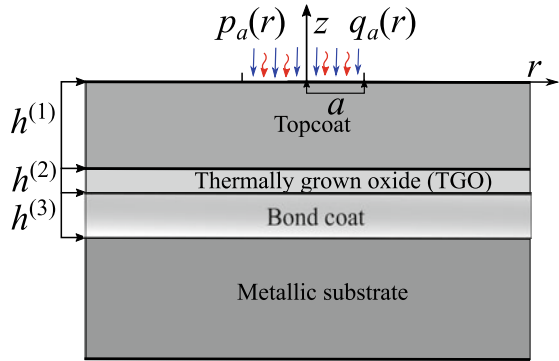
$$(i = 1, 2, 3) : \lambda_T^{(i-1)} T^{(i-1)'} = \lambda_T^{(i)} T^{(i)'}, \sigma_z^{(i-1)} = \sigma_z^{(i)}, \tau_{rz}^{(i-1)} = \tau_{rz}^{(i)}$$

Thermomechanical state of the half-space is described by the equilibrium equations and heat equation:

$$\frac{\partial \sigma_r}{\partial r} + \frac{\partial \tau_{rz}}{\partial z} + \frac{\sigma_r - \sigma_\phi}{r} = 0, \frac{\partial \sigma_z}{\partial z} + \frac{\partial \tau_{rz}}{\partial r} + \frac{\tau_{rz}}{r} = 0, \lambda_T \Delta T + \lambda_T' \frac{\partial T}{\partial z} = 0 \quad (29.3)$$

and Duhamel-Neumann’s law:

Fig. 29.1 The scheme of a TBC



$$\begin{aligned} \sigma_r &= (\lambda_E + 2\mu) \frac{\partial u}{\partial r} + \lambda_E \left(\frac{u}{r} + \frac{\partial w}{\partial z} \right) - kT, \sigma_\phi = \mu \frac{u}{r} + \lambda_E \left(\frac{\partial u}{\partial r} + \frac{\partial w}{\partial z} \right) - kT \\ \sigma_z &= (\lambda_E + 2\mu) \frac{\partial w}{\partial z} + \lambda_E \left(\frac{u}{r} + \frac{\partial u}{\partial r} \right) - kT, \tau_{rz} = \mu \left(\frac{\partial u}{\partial z} + \frac{\partial w}{\partial r} \right) \\ k(z) &= (3\lambda_E + 2\mu)\alpha_T(z) \end{aligned} \tag{29.4}$$

Vanishing of the displacements and temperature is also assumed:

$$\{u^{(3)}, w^{(3)}, T^{(3)}\} \rightarrow 0, z \rightarrow -\infty \tag{29.5}$$

The scheme of the problem is illustrated on Fig. 29.1.

29.3 Compliance Functions

Let us apply the Hankel integral transformation:

$$\begin{aligned} u(r, z) &= - \int_0^\infty \bar{u}(\alpha, z) J_1(\alpha r) \alpha d\alpha, \\ \{w, T\}(r, z) &= \int_0^\infty \{\bar{w}, \bar{T}\}(\alpha, z) J_0(\alpha r) \alpha d\alpha, \\ \{p_a, q_a\}(r) &= \int_0^\infty \{\bar{p}_a, \bar{q}_a\}(\alpha) J_0(\alpha r) \alpha d\alpha \end{aligned} \tag{29.6}$$

Equations (29.3) and (29.4) take the form of the following systems of ordinary differential equations (ODE):

$$\mathbf{A}^{(i)} \cdot \mathbf{x}^{(i)'} = \mathbf{x}^{(i)}, \mathbf{x}^{(i)} = (\bar{u}^{(i)}, \bar{u}^{(i)'}, \bar{w}^{(i)}, \bar{w}^{(i)'}, \bar{T}^{(i)}, \bar{T}^{(i)'})^T \tag{29.7}$$

Coefficients of these systems expressed by the matrix **A** are variable for the BC:

$$\mathbf{A}^{(2)} = \begin{bmatrix} 0 & 1 & 0 & 0 & 0 & 0 \\ \alpha^2 \frac{M^{(2)}}{\mu^{(2)}} & -\frac{\mu^{(2)'}}{\mu^{(2)}} & -\alpha \frac{\mu^{(2)'}}{\mu^{(2)}} & -\alpha \frac{\lambda_E^{(2)} + \mu^{(2)}}{\mu^{(2)}} & \alpha \frac{k^{(2)}}{\mu^{(2)}} & 0 \\ 0 & 0 & 0 & 1 & 0 & 0 \\ \alpha \frac{\lambda_E^{(2)'}}{M^{(2)}} & \alpha \frac{\lambda_E^{(2)} + \mu^{(2)'}}{M^{(2)}} & \alpha^2 \frac{\mu^{(2)'}}{M^{(2)}} & -\frac{M^{(2)'}}{M^{(2)}} & \frac{k^{(2)'}}{M^{(2)}} & \frac{k^{(2)}}{M^{(2)}} \\ 0 & 0 & 0 & 0 & 0 & 1 \\ 0 & 0 & 0 & 0 & \alpha^2 & -\frac{\lambda_T^{(2)'}}{\lambda_T^{(2)}} \end{bmatrix} \quad (29.8)$$

and constant for the TC ($i = 0$), TGO ($i = 1$) and substrate ($i = 3$):

$$\mathbf{A}^{(i)} = \begin{bmatrix} 0 & 1 & 0 & 0 & 0 & 0 \\ \alpha^2 \frac{M^{(i)}}{\mu^{(i)}} & 0 & 0 & -\alpha \frac{\lambda_E^{(i)} + \mu^{(i)'}}{\mu^{(i)'}} & \alpha \frac{k^{(i)'}}{\mu^{(i)'}} & 0 \\ 0 & 0 & 0 & 1 & 0 & 0 \\ 0 & \alpha \frac{\lambda_E^{(i)} + \mu^{(i)'}}{M^{(i)'}} & \alpha^2 \frac{\mu^{(i)'}}{M^{(i)'}} & 0 & 0 & \frac{k^{(i)'}}{M^{(i)'}} \\ 0 & 0 & 0 & 0 & 0 & 1 \\ 0 & 0 & 0 & 0 & \alpha^2 & 0 \end{bmatrix} \quad (29.9)$$

The following notation is used above: $M = (\lambda_E + 2\mu)$. Let us also seek the solution of these systems in the form of linear combinations over the Hankel transform of the applied mechanical and thermal loading:

$$x_k^{(i)}(\alpha, z) = -a_{k2}^{(i)}(\alpha, z)\bar{p}_a(\alpha) - a_{k3}^{(i)}(\alpha, z)\bar{q}_a(\alpha), k = 1, 3, 5 \quad (29.10)$$

Obviously, vectors $\mathbf{a}_j^{(i)} = (a_{kj}^{(i)})_{k=1}^6, j = 2, 3$ also satisfy the system (29.7), i.e.:

$$\mathbf{A}^{(i)} \cdot \mathbf{a}_j^{(i)} = \mathbf{a}_j^{(i)}, j = 2, 3 \quad (29.11)$$

Systems of ODE (29.11) for $i = 0, 1, 3$ have constant coefficients and can be solved analytically. Their solutions have the form:

$$\begin{aligned} a_{1j}^{(i)}(\alpha, z) &= (d_{j1}^{(i)} + \alpha z d_{j2}^{(i)})e^{\alpha z} + (d_{j3}^{(i)} + \alpha z d_{j4}^{(i)})e^{-\alpha z}, \\ a_{3j}^{(i)}(\alpha, z) &= (d_{j1}^{(i)} + (\alpha z - \frac{\lambda_E^{(i)} + 3\mu^{(i)'}}{\lambda_E^{(i)} + \mu^{(i)'}})d_{j2}^{(i)} + \frac{k^{(i)'}}{\alpha(\lambda_E^{(i)} + \mu^{(i)'})}d_{j5}^{(i)})e^{\alpha z} - \\ &\quad -(d_{j3}^{(i)} + (\alpha z + \frac{\lambda_E^{(i)} + 3\mu^{(i)'}}{\lambda_E^{(i)} + \mu^{(i)'}})d_{j4}^{(i)} + \frac{k^{(i)'}}{\alpha(\lambda_E^{(i)} + \mu^{(i)'})}d_{j6}^{(i)})e^{-\alpha z}, \\ a_{5j}^{(i)}(\alpha, z) &= d_{j5}^{(i)}e^{\alpha z} + d_{j6}^{(i)}e^{-\alpha z} \end{aligned} \quad (29.12)$$

Boundary conditions (29.1) and (29.2) after using Hankel transformations take the form:

$$\begin{aligned} z = 0 & : \mu^{(0)}(a_{2j}^{(0)} + \alpha a_{3j}^{(0)}) = 0 \\ (j = 2, 3) & : M^{(0)}a_{4j}^{(0)} - \alpha \lambda_E^{(0)}a_{1j}^{(0)} - k^{(0)}a_{5j}^{(0)} = \delta_{j2} \\ & \quad \lambda_T^{(0)}a_{6j}^{(0)} = \delta_{j3} \end{aligned} \quad (29.13)$$

$$\begin{aligned}
 z = -H^{(i)} & \quad a_{1j}^{(i-1)} = a_{1j}^{(i)}, a_{3j}^{(i-1)} = a_{3j}^{(i)}, \lambda_T^{(i-1)} a_{6j}^{(i-1)} = \lambda_T^{(i)} a_{6j}^{(i)}, \\
 (i = 1, 2, 3) : & \quad a_{5j}^{(i-1)} = a_{5j}^{(i)}, \mu^{(i)}(a_{2j}^{(i)} + \alpha a_{3j}^{(i)}) = \mu^{(i-1)}(a_{2j}^{(i-1)} + \alpha a_{3j}^{(i-1)}) \\
 (j = 2, 3) & \quad \begin{aligned} & M^{(i)} a_{4j}^{(i)} - \alpha \lambda_E^{(i)} a_{1j}^{(i)} - k^{(i)} a_{5j}^{(i)} = \\ & = M^{(i-1)} a_{4j}^{(i-1)} - \alpha \lambda_E^{(i-1)} a_{1j}^{(i-1)} - k^{(i-1)} a_{5j}^{(i-1)} \end{aligned}
 \end{aligned} \tag{29.14}$$

Here δ_{j2}, δ_{j3} are the Kronecker delta. Taking into account (29.5), one can obtain $d_{j3}^{(3)} = d_{j4}^{(3)} = d_{j6}^{(3)} = 0$. Thus, we have two boundary value problems ($j = 2, 3$) for the systems of ODEs (29.11), $i = 2$ and 21 boundary conditions (3 in Eq. (29.13) and 18 in Eq. (29.14) for $i = 1, 2, 3$) for each to obtain the unknown 6 coefficients in the ODE solutions and 15 coefficients $d_{jk}^{(i)} (k = 1, \dots, 6, i = 0, 1), d_{j1}^{(3)}, d_{j2}^{(3)}, d_{j5}^{(3)}$. If the BC is also homogeneous, i.e. $\lambda_E^{(2)}, \mu^{(2)}, \lambda_T^{(2)}, \alpha_T^{(2)}$ are independent of z , then vector-functions $\mathbf{a}_2^{(2)}$ and $\mathbf{a}_3^{(2)}$ can also be obtained analytically and have the form (29.12). For the case of FG BC, they can be obtained analytically only for some specific cases of the variation of properties in depth, for example, in the case of exponential variation of thermomechanical properties in depth. For the general FG materials, they have to be calculated numerically.

Let us introduce the following functions: $G_{kj} = a_{2k-1j}$. Then it is satisfied:

$$\begin{bmatrix} \bar{u} \\ \bar{w} \\ \bar{T} \end{bmatrix} = \begin{bmatrix} G_{11} & G_{12} & G_{13} \\ G_{12} & G_{22} & G_{23} \\ 0 & 0 & G_{33} \end{bmatrix} \begin{bmatrix} 0 \\ \bar{p}_a \\ \bar{q}_a \end{bmatrix} \tag{29.15}$$

It is convenient to introduce following notations:

$$\begin{aligned}
 L_{kj}^{*(i)}(\alpha) &= \alpha \Theta_{kj}^{(0)} G_{kj}^{(i)}(\alpha, H^{(i)}), \quad kj = 12, 22, 33 \\
 L_{kj}^{*(i)}(\alpha) &= \alpha^2 \Theta_{kj}^{(0)} G_{kj}^{(i)}(\alpha, H^{(i)}), \quad kj = 13, 23, \\
 L_{kj}^{*(i)}(\alpha) &= L_{kj}^{*(i)}\left(\frac{\alpha}{H}\right), \quad i = 0, 1, 2, 3
 \end{aligned} \tag{29.16}$$

$$\begin{aligned}
 \Theta_{22}^{(i)} &= \frac{E^{(i)}}{2(1-\nu^{(i)})^2}, \quad \Theta_{33}^{(i)} = \lambda_T^{(i)}, \quad \Theta_{23}^{(i)} = -\Theta_{13}^{(i)} = \frac{\lambda_T^{(i)}}{(1+\nu^{(i)})\alpha_T^{(i)}}, \\
 \Theta_{12}^{(i)} &= -\frac{E^{(i)}}{(1+\nu^{(i)})(1-2\nu^{(i)})}, \quad i = 0, 1, 3 \\
 \Theta_{22}^{(2)} &= \frac{E^{(2)}(-H)}{2(1-\nu^{(2)}(-H))^2}, \quad \Theta_{33}^{(2)} = \lambda_T^{(2)}(-H), \\
 \Theta_{12}^{(2)} &= -\frac{E^{(2)}(0)}{(1+\nu^{(2)}(0))(1-2\nu^{(2)}(0))}, \quad \Theta_{23}^{(2)} = -\Theta_{13}^{(2)} = \frac{\lambda_T^{(2)}(-H)}{(1+\nu^{(2)}(-H))\alpha_T^{(2)}(-H)}
 \end{aligned} \tag{29.17}$$

where E is Young’s modulus and ν is Poisson’s ratio which are related to the Lamé parameters by the following expressions:

$$E = \mu \frac{3\lambda_E + 2\mu}{\lambda_E + \mu}, \quad \nu = \frac{\lambda_E}{2(\lambda_E + \mu)} \tag{29.18}$$

Functions $L_{kj}^{(i)}(\alpha)$ characterize the relation between the Hankel transforms of the displacements and temperature on each interface and applied normal mechanical stresses and thermal heat on the surface. First index—1, 2 or 3—corresponds to the

radial, normal displacements and temperature respectively; second index—2, 3— corresponds to the type of applied loading—mechanical normal stresses or thermal heat. In the literature, these functions are called the compliance functions (Aizikovich and Aleksandrov 1982; Il’man and Privarnikov 1971). Obviously, they are closely related to the Hankel transforms of the Green functions. Constants $\Theta_{kj}^{(i)}$ describe the effective thermomechanical properties of each layer under the normal mechanical stresses and thermal heating. It was previously shown that the compliance functions have following properties (Volkov et al. 2020):

$$\begin{aligned} L_{kj}^{(0)}(\alpha) &= \frac{\Theta_{kj}^{(0)}}{\Theta_{kj}^{(3)}} + \alpha D_{kj} + O(\alpha^2), \alpha \rightarrow 0 \\ L_{kj}^{(0)}(\alpha) &\rightarrow 1, \alpha \rightarrow \infty \end{aligned} \tag{29.19}$$

Displacements and temperature can be obtained in the form of quadratures inverting the Hankel transformation:

$$\begin{aligned} u(r, H^{(i)}) &= \int_0^\infty \left(\frac{L_{12}^{*(i)}(\alpha)}{\Theta_{12}^{(0)}} \bar{p}_a(\alpha) + \frac{L_{13}^{*(i)}(\alpha)}{\Theta_{13}^{(0)}} \frac{\bar{q}_a(\alpha)}{\alpha} \right) J_0(\alpha r) d\alpha, \\ w(r, H^{(i)}) &= - \int_0^\infty \left(\frac{L_{22}^{*(i)}(\alpha)}{\Theta_{22}^{(0)}} \bar{p}_a(\alpha) + \frac{L_{23}^{*(i)}(\alpha)}{\Theta_{23}^{(0)}} \frac{\bar{q}_a(\alpha)}{\alpha} \right) J_0(\alpha r) d\alpha, \\ T(r, H^{(i)}) &= - \int_0^\infty \frac{L_{33}^{*(i)}(\alpha)}{\Theta_{33}^{(0)}} \bar{q}_a(\alpha) J_0(\alpha r) d\alpha \end{aligned} \tag{29.20}$$

Expression (29.20) is used to reduce the problems with mixed boundary conditions, such as contact problems, to the solution of singular integral equations with functions $L_{kj}^{(0)}$ being the kernel transforms. For example, function $L_{22}^{(0)}$ is the kernel transform of the integral equation arising in the solution of the elastic indentation problem (Vasiliev et al. 2018), and function $L_{33}^{(0)}$ is the kernel transform of the integral equation in the case of thermal heating of a circular area of the surface to a known temperature distribution (Volkov 2021). Function $L_{23}^{(0)}$ appears in an integral equation in the case of simultaneous thermomechanical loading. It should also be noted that the compliance functions for the axisymmetric problems considered in the present paper are exactly the same as for the plane contact problems (Vasiliev et al. 2017).

29.4 Numerical Results and Discussion

Let us consider a YSZ top coat, aluminum-containing bond coat, $\alpha - \text{Al}_2\text{O}_3$ thermally grown oxide and Ti64 substrate (Wright 1999). Material properties are presented in Table 29.1 (Vaßen et al. 2010; Wright 1999; Busso et al. 2009; Brandt et al. 1986; Shivakumar and Aradhya 2006; Ezugwu and Wang 1997). Let us consider homogeneous BC and two types of functionally graded BC with linear and exponential variation of all thermomechanical properties in depth (see Fig. 29.2):

Table 29.1 Properties of the considered TBC

| Layer | Young's modulus, GPa | Poisson's ratio | Thermal conductivity, $Wm^{-1}K^{-1}$ | Thermal expansion, $10^{-6}K^{-1}$ |
|-----------|----------------------|-----------------|---------------------------------------|------------------------------------|
| TC | 210 | 0.1 | 2.3 | 11.5 |
| TGO | 375 | 0.23 | 30 | 8.5 |
| BC | 200 | 0.3 | 16 | 14.5 |
| Substrate | 106 | 0.29 | 7.3 | 9.0 |

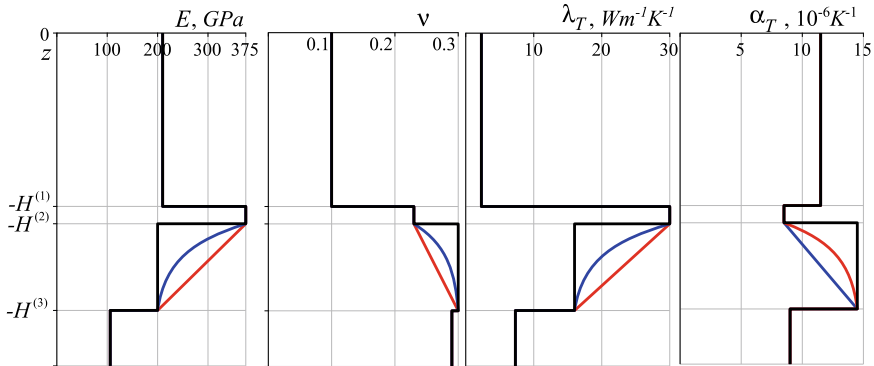


Fig. 29.2 Variation of thermomechanical properties in depth of the considered coatings

$$x^{(2)}(z) = x^{(0)} - (x^{(3)} - x^{(0)}) \frac{z+H^{(2)}}{H} \tag{29.21}$$

$$x^{(2)}(z) = \frac{(x^{(0)}e^{Kz} - x^{(3)})}{e^{Kz} - 1} - \frac{(x^{(0)} - x^{(3)})}{e^{Kz} - 1} \exp\left(\frac{K(z+H^{(2)})}{H}\right), K = -3 \tag{29.22}$$

Here $x^{(2)}$ is one of the following: $\{E^{(2)}, \nu^{(2)}, \lambda_T^{(2)}, \alpha_T^{(2)}\}$. Figures 29.3, 29.4 and 29.5 illustrate the compliance functions $L_{kj}^{(i)}(\alpha)$ for the homogeneous coating on all interfaces. The thicknesses of TC, TGO and BC are assumed to be 100, 10 and 50 microns. Functions $L_{13}^{(0)}$ and $L_{23}^{(0)}$ corresponding to radial and normal displacements appearing as the result of thermal heating are very close to each other while the same functions on different interfaces differ sufficiently. Functions $L_{22}^{(i)}, L_{23}^{(i)}$ and $L_{33}^{(i)}$ are monotonous and positive, $L_{12}^{(i)}$ is nonmonotonous on all interfaces, positive on the surface and sign-changing on other interfaces and $L_{13}^{(i)}$ is nonmonotonous and sign-changing only on the interface BC/substrate. Although the thickness of the TGO is small, the compliance functions on the interfaces TC/TGO and TGO/BC differ markedly especially $L_{12}^{(i)}$ and $L_{13}^{(i)}$.

Effect of the FG materials is illustrated in Figs. 29.6 and 29.7 on an example of $L_{kj}^{(2)}$. The biggest difference observed is for $L_{12}^{(2)}, L_{13}^{(2)}$ and $L_{23}^{(2)}$. Function $L_{23}^{(2)}$ for FG materials behaves nonmonotonically in contrast to a homogeneous coating. The influence of the thickness of BC on the compliance functions is illustrated in Figs. 29.8 and 29.9. No qualitative differences in the behavior of compliance functions were noted; however, there are significant quantitative differences.

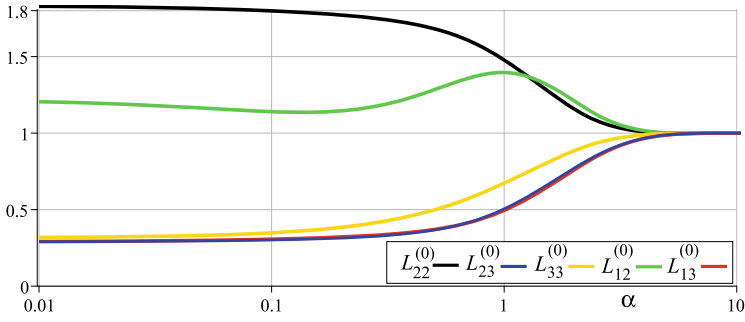


Fig. 29.3 Compliance functions $L_{kj}^{(0)}$ on the surface of the homogeneous coating

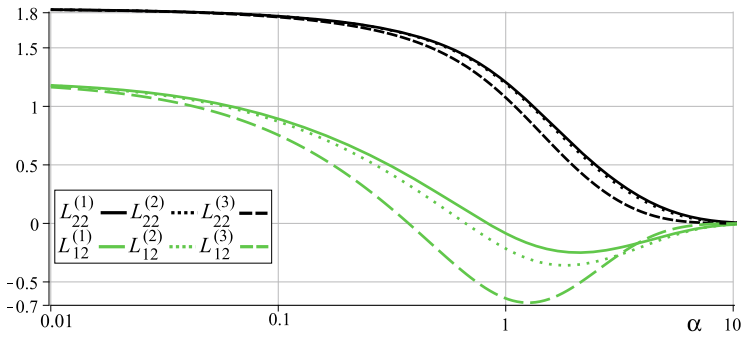


Fig. 29.4 Compliance functions $L_{12}^{(i)}$ and $L_{22}^{(i)}$, $i = 1, 2, 3$ on interfaces between the layers of the homogeneous coating

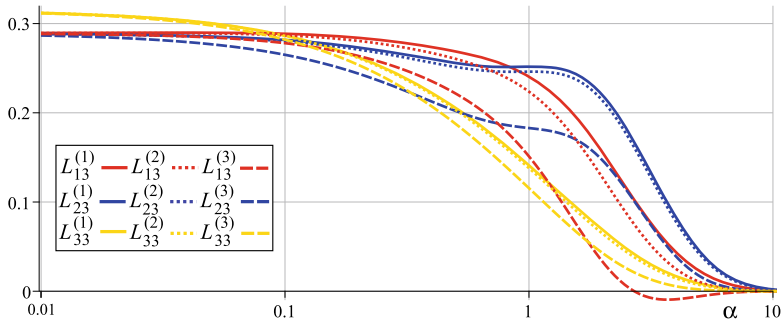


Fig. 29.5 Compliance functions $L_{13}^{(i)}$, $L_{23}^{(i)}$ and $L_{33}^{(i)}$, $i = 1, 2, 3$ on interfaces between the layers of the homogeneous coating

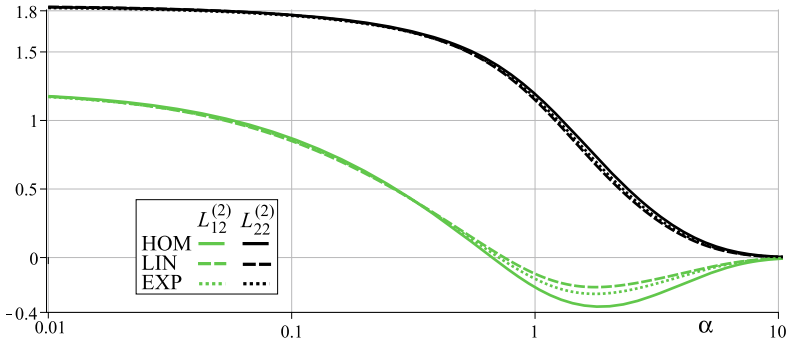


Fig. 29.6 Compliance functions $L_{12}^{(2)}$ and $L_{22}^{(2)}$ for the homogeneous FG coatings

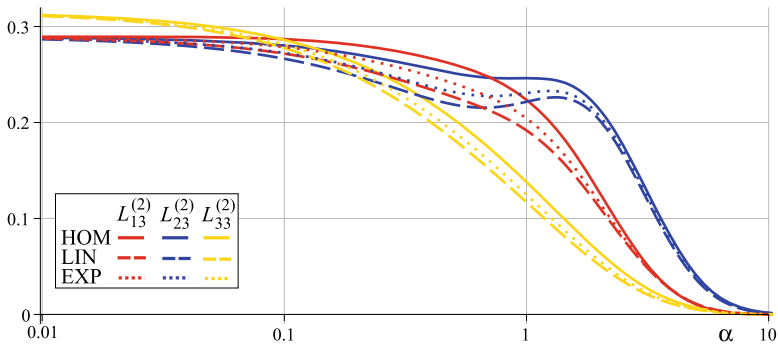


Fig. 29.7 Compliance functions $L_{13}^{(2)}$, $L_{23}^{(2)}$ and $L_{33}^{(2)}$ for the homogeneous FG coatings

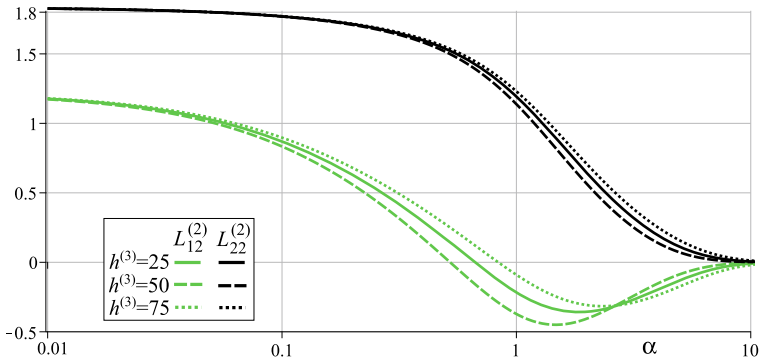


Fig. 29.8 Compliance functions $L_{12}^{(2)}$ and $L_{22}^{(2)}$ for the homogeneous coating with different BC thickness

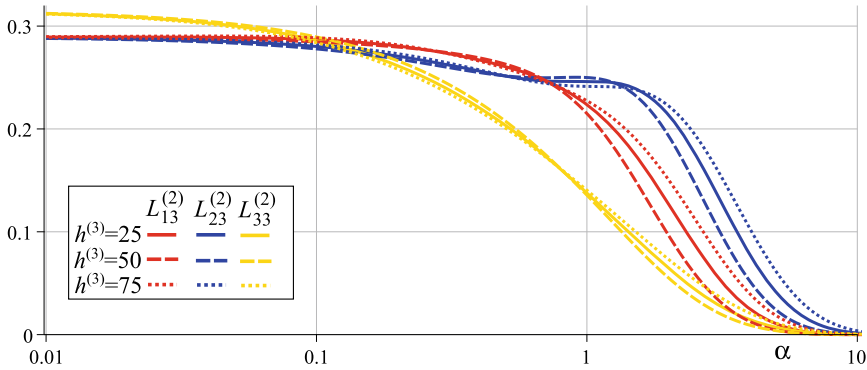


Fig. 29.9 Compliance functions $L_{13}^{(2)}$, $L_{23}^{(2)}$ and $L_{33}^{(2)}$ for the homogeneous coating with different BC thickness

29.5 Closure

Compliance functions for a thermoelastic half-space with a TBC under arbitrary thermomechanical loading are constructed. For the case of homogeneous bond coat, calculation of these functions is reduced to the solution of a system of linear algebraic equations. For the case of arbitrary functionally graded bond coat, they are calculated numerically from the solution of two-point boundary value problems for a system of ordinary differential equations with variable coefficients. The properties of the compliance functions are illustrated for each interface of the TBC for the case of homogeneous and functionally graded coatings. It is shown that the thickness of the bond coat and type of variation of properties in depth sufficiently change the compliance functions, especially the ones corresponding to the radial displacements. It means that the optimization of the thickness and properties of the bond coat can be effectively used to change the distribution of the radial displacements and shear stresses on the interfaces between the layer, thereby reducing the risk of delamination of the layers and failure of the TBC. The results of the paper will be used to obtain approximated analytical expressions for the stresses, displacements, temperature and thermal heat distribution appearing on the interfaces of the layered TBC under mechanical and thermal loading using the approaches developed earlier (Volkov et al. 2016; Vasiliev et al. 2018; Kudish et al. 2019).

Acknowledgements The study was supported by the Russian Science Foundation grant No. 19-19-00444, <https://rscf.ru/project/19-19-00444/>.

References

- Aizikovich S, Aleksandrov VM (1982) Properties of compliance functions for layered and continuously nonuniform half-space. *Soviet Phys Dokl* 27:765–767
- Arnault V, Mévrel R, Alperine S, Jaslier Y (1999) Thermal barrier coatings for aircraft turbine airfoils: thermal challenge and materials. *Revue de Métallurgie* 96:585–597. <https://doi.org/10.1051/metal/199996050585>
- Bäker M, Seiler P (2017) A guide to finite element simulations of thermal barrier coatings. *J Therm Spray Tech* 26:1146–1160. <https://doi.org/10.1007/s11666-017-0592-z>
- Barber JR (1969) Thermoelastic instabilities in the sliding of conforming solids. *Proc R Soc Lond A* 312:381–394. <https://doi.org/10.1098/rspa.1969.0165>
- Brandt R, Pawlowski L, Neuer G, Fauchais P (1986) Specific heat and thermal conductivity of plasma sprayed yttria-stabilized zirconia and NiAl, NiCr, NiCrAl, NiCrAlY, NiCoCrAlY coatings. *High Temp-High Press* 18:65–77
- Busso EP, Qian ZQ, Taylor MP, Evans HE (2009) The influence of bondcoat and topcoat mechanical properties on stress development in thermal barrier coating systems. *Acta Materialia* 57:2349–2361. <https://doi.org/10.1016/j.actamat.2009.01.017>
- Busso EP, Qian ZQ, Taylor MP, Evans HE (2009) The influence of bondcoat and topcoat mechanical properties on stress development in thermal barrier coating systems. *Acta Materialia* 57:2349–2361. <https://doi.org/10.1016/j.actamat.2009.01.017>
- Chen LB (2006) Yttria-stabilized zirconia thermal barrier coatings - a review. *Surf Rev Lett* 13:535–544. <https://doi.org/10.1142/S0218625X06008670>
- Çömez İ (2021) Thermoelastic receding contact problem of a layer resting on a half plane with frictional heat generation. *J Therm Stress* 44:566–581. <https://doi.org/10.1080/01495739.2021.1873082>
- Çömez İ, Güler MA (2022) Thermoelastic contact problem of a rigid punch sliding on a functionally graded piezoelectric layered half plane with heat generation. *J Therm Stress* 45:191–213. <https://doi.org/10.1080/01495739.2021.2009747>
- Erdogan F, Gupta GD (1972) On the numerical solution of singular integral equations. *Quart Appl Math* 29:525–534. <https://doi.org/10.1090/qam/408277>
- Ezugwu EO, Wang ZM (1997) Titanium alloys and their machinability-a review. *J Mater Process Technol* 68:262–274. [https://doi.org/10.1016/S0924-0136\(96\)00030-1](https://doi.org/10.1016/S0924-0136(96)00030-1)
- Igumnov LA, Amenitskii AV, Belov AA, Litvinchuk SYu, Petrov AN (2014) Numerical-analytic investigation of the dynamics of viscoelastic and porous elastic bodies. *J Appl Mech Tech Phys* 55:89–94. <https://doi.org/10.1134/S002189441401012X>
- Igumnov LA, Ipatov AA, Petrov AN, Litvinchuk SYu, Pfaff A, Ereemeyev VA (2019) A comparison of boundary element method and finite element method dynamic solutions for poroelastic column. In: Altenbach H, Müller WH, Abali BE (eds) *Higher gradient materials and related generalized continua*. Springer International Publishing, Cham, pp 121–134. https://doi.org/10.1007/978-3-030-30406-5_7
- Il'man VM, Privarnikov AK (1971) The effect of a system of punches on an elastic multilayer base. *Soviet Appl Mech* 7:602–606
- Ipatov AA, Igumnov LA, Belov AA (2017) Boundary element method in three dimensional transient poroviscoelastic problems. In: Parinov IA, Chang S-H, Jani MA (eds) *Advanced materials*. Springer International Publishing, Cham, pp 331–346. https://doi.org/10.1007/978-3-319-56062-5_28
- Khor KA, Gu YW (2000) Thermal properties of plasma-sprayed functionally graded thermal barrier coatings. *Thin Solid Films* 372:104–113. [https://doi.org/10.1016/S0040-6090\(00\)01024-5](https://doi.org/10.1016/S0040-6090(00)01024-5)
- Kudish II, Vasiliev AS, Volkov SS, Aizikovich SM (2019) Subsurface stressed state of functionally graded elastic solids involved in dry axially symmetric contacts. In: Altenbach, H., Belyaev, A., Ereemeyev, V., Krivtsov, A., Porubov, A. (eds) *Dynamical processes in generalized continua and structures*. advanced structured materials, p 103. https://doi.org/10.1007/978-3-030-11665-1_20

- Liu J, Ke L, Zhang C (2021) Axisymmetric thermoelastic contact of an FGM-coated half-space under a rotating punch. *Acta Mech* 232:2361–2378. <https://doi.org/10.1007/s00707-021-02940-7>
- Mao J-J, Ke L-L, Yang J, Kitipornchai S, Wang Y-S (2017) Thermoelastic instability of functionally graded coating with arbitrarily varying properties considering contact resistance and frictional heat. *Appl Math Model* 43:521–537. <https://doi.org/10.1016/j.apm.2016.11.013>
- Mao J-J, Ke L-L, Yang J, Kitipornchai S, Wang Y-S (2018) Thermoelastic instability of functionally graded materials with interaction of frictional heat and contact resistance. *Mech Based Des Struct Mach* 46:139–156. <https://doi.org/10.1080/15397734.2017.1319283>
- Miller RA, Lowell CE (1982) Failure mechanisms of thermal barrier coatings exposed to elevated temperatures. *Thin Solid Films* 95:265–273. [https://doi.org/10.1016/0040-6090\(82\)90019-0](https://doi.org/10.1016/0040-6090(82)90019-0)
- Padture NP, Gell M, Jordan EH (2002) Thermal barrier coatings for gas-turbine engine applications. *Science* 296:280–284. <https://doi.org/10.1126/science.1068609>
- Parker DW (1992) Thermal barrier coatings for gas turbines, automotive engines and diesel equipment. *Mater Des* 13:345–351. [https://doi.org/10.1016/0261-3069\(92\)90005-3](https://doi.org/10.1016/0261-3069(92)90005-3)
- Schlichting KW, Padture NP, Klemens PG (2001) Thermal conductivity of dense and porous yttria-stabilized zirconia. *J Mater Sci* 36:3003–3010. <https://doi.org/10.1023/A:1017970924312>
- Schulz U, Peters M, Fr-W Bach, Tegeder G (2003) Graded coatings for thermal, wear and corrosion barriers. *Mater Sci Eng: A* 362:61–80. [https://doi.org/10.1016/S0921-5093\(03\)00579-3](https://doi.org/10.1016/S0921-5093(03)00579-3)
- Shivakumar BP, Aradhya KSS (2006) Effect of temperature on mechanical and thermal properties for Ti-64/SiC MMC system with varying volume fractions-an fem investigation. In: Conference paper: national conference on engineering trends in thermal engineering, competitive manufacturing and management (TECM 2006), vol 1
- Su J, Ke L-L, Wang Y-S (2015) Two-dimensional fretting contact analysis of piezoelectric materials. *Int J Solids Struct* 73–74:41–54. <https://doi.org/10.1016/j.ijsolstr.2015.07.026>
- Su J, Ke L-L, Wang Y-S (2016) Fretting contact of a functionally graded piezoelectric layered half-plane under a conducting punch. *Smart Mater Struct* 25:025014. <https://doi.org/10.1088/0964-1726/25/2/025014>
- Vasiliev AS (2019) Penetration of a spherical conductive punch into a piezoelectric half-space with a functionally graded coating. *Int J Eng Sci* 142:230–241. <https://doi.org/10.1016/j.ijengsci.2019.06.006>
- Vasiliev AS, Volkov SS, Aizikovich SM (2018) Approximated analytical solution of a problem on indentation of an electro-elastic half-space with inhomogeneous coating by a conductive punch. *Dokl Phys* 63:18–22. <https://doi.org/10.1134/S1028335818010020>
- Vasiliev AS, Volkov SS, Aizikovich SM, Mitrin BI (2017) Plane contact problem on indentation of a flat punch into a transversely-isotropic half-plane with functionally graded transversely-isotropic coating. *Z Angew Math Phys* 68:4. <https://doi.org/10.1007/s00033-016-0746-8>
- Vasiliev A, Volkov S, Aizikovich SM, Litvinenko AN (2018) Indentation of an elastic half-space reinforced with a functionally graded interlayer by a conical punch. *Mater Phys Mech* 40:254–260. https://doi.org/10.18720/MPM.4022018_14
- Vasiliev A, Volkov S, Aizikovich SM (2018) Approximated analytical solution of contact problem on indentation of elastic half-space with coating reinforced with inhomogeneous interlayer. *Mater Phys Mech* 35:175–180. https://doi.org/10.18720/MPM.3512018_20
- Vaßen R, Jarligo MO, Steinke T, Mack DE, Stöver D (2010) Overview on advanced thermal barrier coatings. *Surf CoatS Technol* 205:938–942. <https://doi.org/10.1016/j.surfcoat.2010.08.151>
- Volkov SS (2021) Displacements of a surface of FGM-coated half-space heated in a circular area taking into account imperfect coating-substrate interface. *IOP Conf Ser: Mater Sci Eng* 1029:012062. <https://doi.org/10.1088/1757-899X/1029/1/012062>
- Volkov SS, Vasiliev AS, Aizikovich SM, Sadyrin EV (2020) Compliance functions for a thermoelastic FGM coated half-plane with incomplete adhesion between the coating and substrate. *J Phys: Conf Ser* 1474:012034. <https://doi.org/10.1088/1742-6596/1474/1/012034>

- Volkov S, Vasiliev A, Aizikovich SM, Seleznev NM, Leontieva AV (2016) Stress-strain state of an elastic soft functionally-graded coating subjected to indentation by a spherical punch. *PNRPU Mech Bull* 20–34. <https://doi.org/10.15593/perm.mech/2016.4.02>
- Wang T, Ma X, Wang L, Gu L, Yin L, Zhang J, Zhan L, Sun D (2018) Three-dimensional thermoelastic contact model of coated solids with frictional heat partition considered. *Coatings* 8:470. <https://doi.org/10.3390/coatings8120470>
- Wang L, Zhong XH, Yang JS, Tao SY, Zhang W, Wang Y, Sun XG (2014) Finite element simulation of surface micro-indentation behavior of yttria stabilized zirconia thermal barrier coatings with microstructural characteristic of columnar grains and sub-grains based on a nonlinear contact model. *Comput Mater Sci* 82:244–256. <https://doi.org/10.1016/j.commatsci.2013.09.034>
- Wortman DJ, Nagaraj BA, Duderstadt EC (1989) Thermal barrier coatings for gas turbine use. *Mater Sci Eng: A* 120–121:433–440. [https://doi.org/10.1016/0921-5093\(89\)90798-3](https://doi.org/10.1016/0921-5093(89)90798-3)
- Wright P (1999) Mechanisms governing the performance of thermal barrier coatings. *Curr Opin Solid State Mater Sci* 4:255–265. [https://doi.org/10.1016/S1359-0286\(99\)00024-8](https://doi.org/10.1016/S1359-0286(99)00024-8)
- Yi Y, Barber JR, Zagrodzki P (2000) Eigenvalue solution of thermoelastic instability problems using Fourier reduction. *Proc R Soc Lond A* 456:2799–2821. <https://doi.org/10.1098/rspa.2000.0641>
- Zelentsov VB, Lapina PA, Mitrin BI (2022) Wear of functionally graded coatings under frictional heating conditions. *Nanomaterials* 12:142. <https://doi.org/10.3390/nano12010142>
- Zelentsov VB, Mitrin BI (2019) Thermoelastic instability in the quasi-static coupled thermoelasticity problem dealt with the sliding contact with frictional heating. *Mech Solids* 54:58–69. <https://doi.org/10.3103/S0025654419010059>

Chapter 30

Sensitivity Analysis for Inhomogeneous and Prestressed Elastic Bodies



Alexander O. Vatulyan, Rostislav D. Nedin, and Victor O. Yurov

Abstract The research is devoted to the development of the theoretical foundations of a non-destructive acoustic method for identifying the laws of inhomogeneity of material characteristics and prestress fields of elastic bodies, depending on the probing loading and the frequency range. As additional data in the corresponding inverse coefficient problems, we consider the displacement field measured on a part of the body surface. The concept of sensitivity of field characteristics with respect to changes in variable elastic moduli, density and prestress tensor components, based on the use of Fréchet derivatives, is introduced, and formulas for its analysis are obtained. We present an example for inhomogeneous cylindrical rods, study sensitivity characteristics and give some recommendations for the choice of frequency ranges in the reconstruction of the law of axial initial stress inhomogeneity.

Keywords Inverse problem · Sensitivity · Fréchet derivative · Prestress · Elastic body · Inhomogeneity · Rod · Vibrations

30.1 Introduction

In view of the active use of structures made of new functionally graded materials (FGM) with complex inhomogeneous physical and mechanical properties, which are often prestressed, one of the urgent tasks is the development and refinement of

A. O. Vatulyan · R. D. Nedin (✉) · V. O. Yurov
Vorovich Institute of Mathematics, Mechanics and Computer Science, Southern Federal University, 8a Mil'chakova Str., 344090 Rostov-on-Don, Russia
e-mail: rdn90@bk.ru

A. O. Vatulyan
e-mail: aovatulyan@sfedu.ru

V. O. Yurov
e-mail: vyurov@sfedu.ru

Southern Mathematical Institute, Vladikavkaz Scientific Center of Russian Academy of Sciences, 53 Vatutina Str., 362025 Vladikavkaz, Russia

© The Author(s), under exclusive license to Springer Nature Switzerland AG 2023
H. Altenbach and V. Eremeyev (eds.), *Advances in Linear and Nonlinear Continuum and Structural Mechanics*, Advanced Structured Materials 198,
https://doi.org/10.1007/978-3-031-43210-1_30

545

deformation models. Modern FGM manufacturing technologies make it possible to create objects of complex geometry without using classical technologies, like casting, which requires additional production of molds. For the manufacture of FGM structural elements, high-temperature technologies are usually used (e.g., surfacing, sintering and work hardening), which is why, after cooling, the samples are often in conditions of prestress states that have a significant effect on their dynamic characteristics (Schajer 2013).

Recently, composite sandwich-FGMs have become increasingly popular, combining rigid layers and layers with a continuous graded structure. Due to the property of continuity of material characteristics, functionally graded sandwich structures can reduce a significant concentration of interfacial stresses between composite layers (Li et al. 2008). This type of composite structure has generated significant research interest from industry and academia (Li et al. 2019). Based on the theory of high-order shear deformation, the authors of Nguyen and Nguyen (2015) investigated the statics, buckling and vibrations of multilayer FGM beams. Based on the broken normal hypotheses and the Ritz method, Fazzolari (2016) presents an analysis of the stability of FGM sandwich panels.

In Dudarev et al. (2020), Vatulyan and Yurov (2021), the techniques for studying inverse problems of restoring the laws of inhomogeneity for material characteristics are proposed using the construction of an iterative process, at each step of which it is required to investigate a system of Fredholm integral equations of the first kind with smooth kernels; a numerical analysis is carried out for different objects. It should be noted that the order of the kernel norms in these equations can be different, which complicates the procedure for constructing a regularized solution, so it is advisable to perform additional analysis of the kernels depending on the loading and the frequency range. In connection with this circumstance and the need to analyze kernels, the concept of sensitivity has been introduced, which is quite widely represented in the literature when analyzing problems based on minimizing the residual functional. Sensitivity analysis is quite easy to carry out when the problem parameters are constant, and in the case of their variability, it is required to analyze operator relations in some function space. Based on this approach, some results of calculating the sensitivity characteristics for cylindrical rods within longitudinal and bending steady vibrations are given in Vatulyan and Yurov (2023).

The development of methods for measuring the level and structure of prestress is a fairly popular topic—a large number of studies have been devoted to it, and interest in it has increased significantly in recent years. Of certain practical importance is the study of the problems of determining prestress arising in the course of welding operations, hardening, heat treatment, shot peening and other technological processes (Schajer 2013). Several linearized approaches to modeling prestresses are given in Vatulyan et al. (2015), Nedin et al. (2017), which describe a number of methods for restoring the initial state in elastic bodies, including those made of functionally graded composites, on the basis on the acoustic sounding method. The proposed methods are mainly based on iterative-regularization schemes for solving the corresponding coefficient inverse problems. In Nedin et al. (2018), inverse problems on the reconstruction of prestress fields within the analysis of bending vibrations

of plates in the framework of Timoshenko's hypotheses were studied using several techniques. In Nedin et al. (2018), based on the general linearized formulation of the motion of an elastic prestressed body, the problem of radial oscillations of an elastic isotropic pipe is studied. The inverse problem of identifying an inhomogeneous prestress state is studied on the basis of additional data on the displacement function measured at the outer boundary in a certain frequency range. Yurov et al. (2020) investigates the problem for a finite cylinder under conditions of a complex initial stress state described by four non-zero components of the prestress tensor. Based on the perturbation method, formulas are derived that allow one to approximately find the changes in resonant frequencies caused by the presence of the components of the inhomogeneous prestress field. The influence of prestress levels on the change in natural frequencies is analyzed. In Nedin et al. (2022), the inverse problem of recovering three parameters of an inhomogeneous prestress field of a given structure is studied.

This study continues the development of theoretical foundations for identifying the laws of inhomogeneity of material characteristics and prestress fields of elastic bodies depending on the method of probing loading in the presence of the data on the measured boundary displacement fields in a certain frequency range. In order to improve the procedure for reconstructing the desired characteristics, a sensitivity analysis technique based on the use of Fréchet derivatives is proposed. An example of steady oscillations of the prestressed rod is considered. A sensitivity of the deformative characteristics with respect to the prestress is estimated, which makes it possible to reveal a recipe for the optimal probing loading when solving the corresponding inverse coefficient problems on restoring arbitrary laws of change in the inhomogeneous prestress distribution.

30.2 Vibrations of an Isotropic Elastic Inhomogeneous Body in the Presence of Prestresses

Using the principle of superimposing small deformations on finite ones, we shall consider small oscillations of an elastic prestress body of volume V bounded by the surface $S = S_u \cup S_\sigma$ under the action of a periodic load with the components $p_k e^{i\omega t}$, $k = \overline{1, 3}$, applied to the surface part S_σ in the actual configuration. The corresponding complete boundary-value problem after separating the time factor $e^{i\omega t}$ in the metric of the natural undeformed configuration takes the form Guz (2004), Vatulyan et al. (2015):

$$T_{ij,j} + \rho\omega^2 u_i = 0 \quad (30.1)$$

$$T_{ij} = \sigma_{ij} + u_{i,m} \sigma_{mj}^0 \quad (30.2)$$

$$\sigma_{ij} = \lambda \delta_{ij} u_{m,m} + \mu (u_{i,j} + u_{j,i}) \quad (30.3)$$

$$u_i|_{S_u} = 0, \quad T_{ij}n_j|_{S_\sigma} = p_i \tag{30.4}$$

Here, T_{ij} —the components of the linearized nonsymmetric first Piola-Kirchhoff stress tensor, u_i —components of small displacement vector, σ_{ij}^0 and σ_{ij} —components of symmetric initial and incremental stress tensors, ρ —density, ω —vibration frequency and n_i —components of the unit vector of the outer normal to the body surface; the surface part S_u is clamped. Taking into account the smallness of the initial deformation gradient, we assume that the change in the normal vector can be neglected in the transition from the initial configuration to the actual one. The statement (30.1)–(30.4) allows one to set arbitrary laws of change for the elastic modulus λ , μ and the density ρ depending on the coordinates allowing to describe an inhomogeneous material, for example, FGM.

Within the framework of this model, we shall consider the following two problems:

1. *Problem I—without prestress $\sigma_{ij}^0 = 0$, with variable elastic moduli and density*, for an inhomogeneous elastic body; (30.1)–(30.4) in this case take the classical form:

$$\sigma_{ij,j} + \rho\omega^2 u_i = 0 \tag{30.5}$$

$$u_i|_{S_u} = 0, \quad \sigma_{ij}n_j|_{S_\sigma} = p_i \tag{30.6}$$

where the stress tensor components σ_{ij} satisfy the constitutive relations (30.3).

2. *Problem II—with prestress*, in the framework of the statement (30.1)–(30.4). The presented model makes it possible to describe body oscillations in the presence of inhomogeneous prestress fields of various nature and given values of λ , μ and ρ .

30.3 General Structure of Relationships for Sensitivity Estimation

Consider two inverse problems of determining the following variable characteristics: (1) the elastic moduli λ , μ and the density ρ (3 functions); (2) the prestress tensor components σ_{ij}^0 (6 functions) when specifying the additional data on the measured displacement field in a certain frequency range $\omega \in [\omega_-, \omega_+]$. The inverse problem is reduced to a system of nonlinear operator equations, the solution of which is based on Newton’s operator method. In Dudarev et al. (2020), Vatulyan and Yurov (2021), Nedin et al. (2017), Nedin et al. (2018) and Nedin et al. (2018), methods for studying such inverse problems are proposed by constructing an iterative process, at each step of which it is required to investigate a system of Fredholm integral equations of the first kind with smooth kernels. A numerical analysis was carried out for different objects. Note that the order of the kernel norms in these equations, in general, can be different, which complicates the procedure for constructing a regularized solution, thus it is necessary to perform some preliminary analysis of the kernels depending

on the loading and the frequency range. For example, when studying the inverse problem for a cylinder, in case of probing by a tangential load along the lateral surface, the corresponding kernel by the Lamé parameter λ turns into zero, which makes its reconstruction impossible.

For a preliminary analysis of kernels, below we introduce the concept of sensitivity which is quite widely represented in the literature for operators with constant coefficients. In such a case, the inverse problem may be reduced to the minimization of the residual functional in finite-dimension space. However, in the case of variability of physical characteristics, it is required to derive additional boundary-value problems, introduce the corresponding Fréchet derivatives and analyze operator relations in some functional space. Let us turn to the formulations of Problems I and II described above.

Problem I

Consider the following subproblems.

(1) Sensitivity Characteristics with Respect to the Density ρ

Let us introduce the Fréchet derivatives $\xi_{ij}^\rho = \frac{\partial \sigma_{ij}}{\partial \rho}$ and $v_i^\rho = \frac{\partial u_i}{\partial \rho}$. It is easy to show that in terms of the introduced functions ξ_{ij}^ρ and v_i^ρ , the following equations hold:

$$\xi_{ij,j}^\rho + \omega^2 u_i + \rho \omega^2 v_i^\rho = 0 \quad (30.7)$$

Based on (30.6), the essential and natural boundary conditions for the functions σ_{ij} , ξ_{ij}^ρ , u_i and v_i^ρ take the form

$$v_i^\rho|_{S_u} = 0, \quad \xi_{ij}^\rho n_j|_{S_\sigma} = 0 \quad (30.8)$$

Let us multiply (30.5) by v_i^ρ and (30.7) by u_i , and integrate their difference over the volume V :

$$\int_V \left[\sigma_{ij,j} v_i^\rho - \xi_{ij,j}^\rho u_i - \omega^2 u_i u_i \right] dV = 0$$

Carrying out standard transformations using the Gauss-Ostrogradsky theorem and using boundary conditions (30.6), (30.8), we obtain

$$\int_{S_\sigma} p_i v_i^\rho dS - \int_V \left(\sigma_{ij} v_{i,j}^\rho - \xi_{ij}^\rho u_{i,j} + \omega^2 u_i u_i \right) dV = 0 \quad (30.9)$$

Let us show that the expression $\sigma_{ij} v_{i,j}^\rho - \xi_{ij}^\rho u_{i,j}$ turns into zero. To shorten the notation, we will use the generalized Hooke's law form $\sigma_{ij} = C_{ijkl} u_{k,l}$, where $C_{ijkl} = \lambda \delta_{ij} \delta_{kl} + \mu (\delta_{ik} \delta_{jl} + \delta_{il} \delta_{jk})$ represent the components of the elastic moduli tensor for isotropic case. According to the constitutive relations (30.3),

$\xi_{ij}^\rho = \frac{\partial \sigma_{ij}^\mu}{\partial \rho} = C_{ijkl} \frac{\partial \varepsilon_{kl}^\mu}{\partial \rho} = C_{ijkl} \varepsilon_{kl}^v$. Further, taking into account the symmetry of the tensors σ_{ij} , ξ_{ij}^ρ and C_{ijkl} , we have

$$\begin{aligned} \sigma_{ij} v_{i,j}^\rho - \xi_{ij}^\rho u_{i,j} &= \sigma_{ij}^\mu \varepsilon_{ij}^v - \xi_{ij}^\rho \varepsilon_{ij}^\mu = C_{ijkl} \varepsilon_{kl}^\mu \varepsilon_{ij}^v - C_{ijkl} \varepsilon_{kl}^v \varepsilon_{ij}^\mu = \\ &= C_{klij} \varepsilon_{kl}^\mu \varepsilon_{ij}^v - C_{ijkl} \varepsilon_{ij}^\mu \varepsilon_{kl}^v = 0, \end{aligned}$$

where $\varepsilon_{ij}^\mu = \frac{1}{2} (u_{i,j} + u_{j,i})$, $\varepsilon_{ij}^v = \frac{1}{2} (v_{i,j}^\rho + v_{j,i}^\rho)$. Thus, (30.9) takes the form

$$\int_{S_\sigma} p_i v_i^\rho dS - \omega^2 \int_V u_i u_i dV = 0 \tag{30.10}$$

(2) *Sensitivity Characteristics with Respect to the Lamé Parameter λ*

By introducing the functions of the Fréchet derivatives $\xi_{ij}^\lambda = \frac{\partial \sigma_{ij}}{\partial \lambda}$ and $v_i^\lambda = \frac{\partial u_i}{\partial \lambda}$, we get from (30.5)–(30.6) that

$$\xi_{ij,j}^\lambda + \rho \omega^2 v_i^\lambda = 0, \quad v_i^\lambda |_{S_u} = 0, \quad \xi_{ij}^\lambda n_j |_{S_\sigma} = 0 \tag{30.11}$$

Carrying out transformations similar to the previous subproblem, we obtain

$$\int_V [\sigma_{ij,j} v_i^\lambda - \xi_{ij,j}^\lambda u_i] dV = 0$$

whence, considering the boundary conditions (30.6), (30.11), we obtain

$$\int_{S_\sigma} p_i v_i^\lambda dS - \int_V (\sigma_{ij} v_{i,j}^\lambda - \xi_{ij}^\lambda u_{i,j}) dV = 0 \tag{30.12}$$

Taking into account that $\sigma_{ij} v_{i,j}^\lambda - \xi_{ij}^\lambda u_{i,j} = \sigma_{ij} \varepsilon_{ij}^v - \xi_{ij}^\lambda \varepsilon_{ij}^\mu = -\varepsilon_{kk}^\mu \varepsilon_{ii}^\mu$, we may rewrite (30.12) as

$$\int_{S_\sigma} p_i v_i^\lambda dS + \int_V \varepsilon_{kk}^\mu \varepsilon_{ii}^\mu dV = 0$$

or, using the strain tensor expressions ε_{ij}^μ in terms of displacement gradients,

$$\int_{S_\sigma} p_i v_i^\lambda dS + \int_V u_{k,k} u_{l,l} dV = 0 \tag{30.13}$$

(3) *Sensitivity Characteristics with Respect to the Shear Modulus μ*

Introducing similarly the function $\xi_{ij}^\mu = \frac{\partial \sigma_{ij}}{\partial \mu}$ and $v_i^\mu = \frac{\partial u_i}{\partial \mu}$, we get

$$\xi_{ij,j}^\mu + \rho\omega^2 v_i^\mu = 0, \quad v_i^\mu|_{S_u} = 0, \quad \xi_{ij}^\mu n_j|_{S_\sigma} = 0 \quad (30.14)$$

Carrying out similar transformations and considering the boundary conditions (30.11), we obtain

$$\int_{S_\sigma} p_i v_i^\mu dS - \int_V (\sigma_{ij} v_{i,j}^\mu - \xi_{ij}^\mu u_{i,j}) dV = 0 \quad (30.15)$$

Using $\sigma_{ij} v_{i,j}^\mu - \xi_{ij}^\mu u_{i,j} = \sigma_{ij} \varepsilon_{ij}^v - \xi_{ij}^\mu \varepsilon_{ij}^u = -2\varepsilon_{ij}^\mu \varepsilon_{ij}^u$, (30.15) takes the form

$$\int_{S_\sigma} p_i v_i^\mu dS + \int_V 2\varepsilon_{ij}^\mu \varepsilon_{ij}^u dV = 0$$

or

$$\int_{S_\sigma} p_i v_i^\mu dS + \frac{1}{2} \int_V (u_{i,j} + u_{j,i})(u_{i,j} + u_{j,i}) dV = 0 \quad (30.16)$$

Problem II

Let us now introduce the tensor functions of the fourth and third ranks $Q_{ij}^{sk} = \frac{\partial T_{ij}}{\partial \sigma_{sk}^0}$,

$v_i^{sk} = \frac{\partial u_i}{\partial \sigma_{sk}^0}$, fixing the indices $s, k = \overline{1, 3}$. Then from the linearized equations of motion (30.1), we obtain

$$Q_{ij,j}^{sk} + \rho\omega^2 v_i^{sk} = 0 \quad (30.17)$$

$$v_i^{sk}|_{S_u} = 0, \quad Q_{ij}^{sk} n_j|_{S_\sigma} = 0 \quad (30.18)$$

Performing transformations similar to those described for Problem I, on the basis of (30.1) and (30.17), we obtain

$$\int_S (T_{ij} v_i^{sk} - Q_{ij}^{sk} u_i) n_j dS - \int_V (T_{ij} v_{i,j}^{sk} - Q_{ij}^{sk} u_{i,j}) dV = 0 \quad (30.19)$$

Taking into account the conditions (30.4) and (30.18), the relation (30.19) takes the form

$$\int_{S_\sigma} p_i v_i^{sk} dS - \int_V (T_{ij} v_{i,j}^{sk} - Q_{ij}^{sk} u_{i,j}) dV = 0 \quad (30.20)$$

By using the generalized Hooke's law to shorten the notation, we have

$$Q_{ij}^{sk} = \frac{\partial}{\partial \sigma_{sk}^0} (\sigma_{ij} + u_{i,m} \sigma_{mj}^0) = \frac{\partial \sigma_{ij}}{\partial \sigma_{sk}^0} + \frac{\partial u_{i,m}}{\partial \sigma_{sk}^0} \sigma_{mj}^0 + u_{i,m} \frac{\partial \sigma_{mj}^0}{\partial \sigma_{sk}^0} = C_{ijkl} v_{k,l} + v_{i,m} \sigma_{mj}^0 + u_{i,s} \delta_{jk}$$

Then, using the symmetry of the tensors C_{ijkl} and σ_{mj}^0 , (30.20) transforms into

$$0 = \int_{S_\sigma} p_i v_i dS - \int_V [(C_{ijkl} u_{k,l} + u_{i,m} \sigma_{mj}^0) v_{i,j} - (C_{ijkl} v_{k,l} + v_{i,m} \sigma_{mj}^0 + u_{i,s} \delta_{jk}) u_{i,j}] dV$$

whence, returning to the original notation, we obtain

$$\int_{S_\sigma} p_i v_i^{sk} dS + \int_V u_{i,s} u_{i,k} dV = 0 \tag{30.21}$$

The obtained formulas (30.10), (30.13), (30.16) and (30.21) make it possible to evaluate the sensitivity in the models considered with respect to the corresponding functional parameters.

30.4 Sensitivity Characteristics for Problems I and II When Sounding by Concentrated Forces

Problem I Let $a_1 = \rho$, $a_2 = \lambda$ and $a_3 = \mu$, then $\xi_{ij}^{(m)} = \frac{\partial \sigma_{ij}}{\partial a_m}$ and $v_i^{(m)} = \frac{\partial u_i}{\partial a_m}$, $m = \overline{1, 3}$. We assume that in order to assess the sensitivity with respect to each of the three functions a_m , frequency sounding is implemented by means of the concentrated loads $p_i^{(m)} = P_i^{(m)} \delta(x - x^{(m)})$, applied to three different points on the surface of the body. According to the formulas from the previous section, we obtain the following sensitivity relations:

$$P_i^{(1)} v_i^{(1)}(x^{(1)}) = \omega^2 \int_V u_i u_i dV \tag{30.22}$$

$$P_i^{(2)} v_i^{(2)}(x^{(2)}) = - \int_V u_{k,k} u_{l,l} dV \tag{30.23}$$

$$P_i^{(3)} v_i^{(3)}(x^{(3)}) = - \frac{1}{2} \int_V (u_{i,j} + u_{j,i})(u_{i,j} + u_{j,i}) dV \tag{30.24}$$

Here, we note some properties of the quantities appearing on the right-hand sides of the relations obtained. On the right side of (30.22), there is a positive value, and (30.23) and (30.24) contain non-positive values. The expression on the right side of (30.23) vanishes if and only if the volumetric strain is zero (for example, during torsional vibrations of a cylinder). It follows from relations (30.23) that under loading for which there is no volumetric deformation, it is impossible to determine the modulus a_2 regardless of the frequency range. The expression on the right side of (30.24) vanishes if and only if all the strain tensor components are equal to zero.

Relations (30.22)–(30.24) make it possible to determine the sensitivity of the measured boundary functions with respect to variable elastic moduli and density under various types of probing concentrated loading and compare the responses for different inhomogeneity laws.

Problem II

In the case of probing with a concentrated force $p_i = P_i \delta(x - x^{(0)})$ applied to some point on the surface of the body $x_k = x_k^0$, from (30.21) we have

$$P_i v_i^{sk}(x^{(0)}) = - \int_V u_{i,s} u_{i,k} dV \tag{30.25}$$

The relation (30.25) makes it possible to determine the sensitivity of the measured boundary functions with respect to the prestress components, for certain probing modes, and to compare the responses for various inhomogeneity laws.

30.5 Sensitivity Analysis for Longitudinal and Flexural Vibrations of Rods

The results of calculating the sensitivity characteristics in the framework of Problem I for cylindrical rods within longitudinal and flexural steady-state vibrations are given in Vatulyan and Yurov (2023). Below, we consider several examples of estimating sensitivity functions for Problem II.

Example 30.1 Longitudinal Oscillation of Prestressed Rod

As an example, consider a uniaxial prestress state of tension or compression of a cantilevered beam, described by a single component $\sigma_{11}^0(x_1) = \sigma_0(x)$. The rod deformation hypotheses have the form $u_1 = u(x)$, $u_2 = 0$, $u_3 = 0$, where $u(x)$ is the longitudinal displacement. The probing is carried out by applying a longitudinal periodic load $p_1 = P_u/F$ at the free rod’s end, where F is the rod’s cross-sectional area, $V = [0, l] \times F$ and l is the rod’s length. The longitudinal displacement $u(l, \omega)$ is used as the additional data in the inverse problem. The only non-zero component of the third rank tensor $v_{isk}^0 = v_{111}^0$ we denote as v_u . The statement of the boundary-value problem on the longitudinal vibrations of the considered prestress rod has the

form Vatulyan et al. (2015):

$$((E + \sigma_0) Fu')' + \rho F \omega^2 u = 0 \tag{30.26}$$

$$u|_{x=0} = 0, \quad (E + \sigma_0) Fu'|_{x=l} = P_u \tag{30.27}$$

Based on (30.25) for the considered case and taking into account the indicated deformation hypotheses and the probing method, we have

$$P_u v_u|_{x=l} = - \int_V u_{1,1} u_{1,1} dV = - \int_0^l \int_F (u')^2 dF dx = - \int_0^l F (u')^2 dx,$$

which gives

$$P_u v_u|_{x=l} = - \int_0^l F (u')^2 dx, \quad v_u = \frac{\partial u}{\partial \sigma_0} \tag{30.28}$$

The relation (30.28) allows one to determine the sensitivity characteristic of the specified functions in relation to the axial distribution of the prestress $\sigma_0(x)$ when probing with a longitudinal load in a certain frequency range. Note that the right side of (30.28) coincides with the formula for the sensitivity characteristic with respect to the elastic modulus E in the problem on longitudinal vibrations of a rod without prestress (Vatulyan and Yurov 2023).

Example 30.2 Flexural Vibration of a Prestressed Rod

Let us consider the formulation of the problem on flexural vibrations of a prestress cantilever rod clamped by its left end. The rod deformation hypotheses are $u_1 = -x_3 w'(x)$, $u_2 = 0$ and $u_3 = w(x)$, where $w(x)$ represents the deflection function. As the additional data in the inverse problem, the deflection $w(l, \omega)$ or rotation angle $\theta(l, \omega)$ given at the free rod's end is used. The motion equation and the essential boundary conditions have the following form Vatulyan et al. (2015):

$$((E + \sigma_0) Jw'')'' - (F\sigma_0 w')' - \rho F \omega^2 w = 0 \tag{30.29}$$

$$w|_{x=0} = 0, \quad w'|_{x=0} = 0 \tag{30.30}$$

In the case of probing with transverse force $p_3 = P_w/F$ applied to the free rod's end, the natural boundary conditions take the form

$$(E + \sigma_0) Jw''|_{x=l} = 0, \quad ((E + \sigma_0) Jw'')' - F\sigma_0 w'|_{x=l} = P_w \tag{30.31}$$

in the case of probing by means of the bending moment M

$$(E + \sigma_0) J w''|_{x=l} = M, \quad ((E + \sigma_0) J w'')' - F \sigma_0 w'|_{x=l} = 0 \quad (30.32)$$

Based on (30.25), we express the sensitivity characteristic as

$$\begin{aligned} P_w v_{311}^0|_{x=l} &= - \int_0^l \int_F u_{i,1} u_{i,1} dF dx = - \int_0^l \int_F (x_3^2 (w'')^2 + (w')^2) dF dx = \\ &= - \int_0^l (J (w'')^2 + F (w')^2) dx \end{aligned}$$

hence,

$$P_w v_w|_{x=l} = - \int_0^l (J (w'')^2 + F (w')^2) dx, \quad v_w = \frac{\partial w}{\partial \sigma_0} \quad (30.33)$$

The relationship (30.33) makes it possible to determine the sensitivity characteristic of the rod with respect to some axial distribution of prestress $\sigma_0(x)$ when probing with a concentrated force in a certain frequency range. Similar sensitivity relation in terms of the rotation angle $\theta = w'$, when probing with a bending moment, will take the form

$$M v_\theta|_{x=l} = - \int_0^l (J (\theta')^2 + F \theta^2) dx, \quad v_\theta = \frac{\partial \theta}{\partial \sigma_0} \quad (30.34)$$

It is to be mentioned that the integrands of the sensitivity characteristics (30.28), (30.33) and (30.34) coincide with the expressions for the kernels of the Fredholm integral equations of the first kind, obtained when considering the inverse problems of prestress identification for the considered rods by linearizing the generalized reciprocity relation (Vatulyan et al. 2015). The generalized structure of this expression when determining (or estimating the sensitivity) prestress is given in the formula (30.25).

Consider a particular case of the statement (30.29)–(30.32), in which, due to the smallness of prestress with respect to the elastic modulus ($\sigma_0/E < 10^{-3}$), it is assumed that $E + \sigma_0 \approx E$. In this case, based on a simplified statement, using the technique for constructing sensitivity characteristics described in the previous section, it is easy to obtain the relations

$$P_w v_w|_{x=l} = - \int_0^l F (w')^2 dx, \quad M v_\theta|_{x=l} = - \int_0^l F \theta^2 dx \quad (30.35)$$

30.6 Numerical Experiments

This section presents computational experiments on estimating rods' sensitivity with respect to the uniaxial prestress state for longitudinal and bending vibrations based on the relations (30.33)–(30.35) in the framework of Problem II.

Additionally, an alternative way of calculating the sensitivity using the classical formula for the Fréchet derivative (Hutson and Pym 1980) is introduced according to

$$f(\sigma_0^* + \Delta\sigma_0) - f(\sigma_0^*) = v^* \Delta\sigma_0 + \eta(\sigma_0^*, \Delta\sigma_0), \quad \lim_{\|\Delta\sigma_0\| \rightarrow 0} \frac{\|\eta(\sigma_0^*, \Delta\sigma_0)\|}{\|\Delta\sigma_0\|} = 0 \tag{30.36}$$

Here, $v^* = f'_{\sigma_0^*}$ is the displacement sensitivity characteristic f with respect to some reference prestress state σ_0^* ; $\Delta\sigma_0$ —small prestress increment; $\|\eta(\sigma_0^*, \Delta\sigma_0)\|$ and $\|\Delta\sigma_0\|$ represent the norms in the corresponding normed spaces. It is possible to carry out a sensitivity analysis depending on the oscillation frequency in the vicinity of the zero prestress state by setting $f'_{\sigma_0^*}(\omega) \approx f'_0(\omega) = v(\omega)$:

$$f|_{\sigma_0=\Delta\sigma_0}(\omega) - f|_{\sigma_0=0}(\omega) = v(\omega)\Delta\sigma_0 + \eta(\Delta\sigma_0), \quad \|\eta(\Delta\sigma_0)\| / \|\Delta\sigma_0\| \rightarrow 0 \tag{30.37}$$

Note that since the prestress σ_0 is small compared to the elastic modulus E , the corresponding sensitivity during probing by the longitudinal force is close to zero. For flexural vibrations of the rod, the calculations were carried out based on dimensionless statements: a) when probing the rod with a transverse force (30.29)–(30.31); b) when probing with a bending moment (30.29)–(30.30) and (30.32), in case of a constant cross section ($F = F_0, J = J_0$). The following dimensionless complexes were used: $\xi = \frac{x}{l}, W = \frac{w}{l}, g(\xi) = \frac{E(\xi l)}{E_0}, r(\xi) = \frac{\rho(\xi l)}{\rho_0}, s = \frac{\sigma_0}{E_0}, \kappa^2 = \frac{\rho_0 \omega^2 l^2}{E_0}, \gamma = \frac{F_0 l^2}{J_0}, \tilde{P} = \frac{P_w l^2}{E_0 J_0}$ and $\tilde{M} = \frac{M l}{E_0 J_0}$. Using the introduced dimensionless notation, the sensitivity characteristics (30.33)–(30.35) for $\tilde{P} = 1, \tilde{M} = 1$ take the form

$$\tilde{v}_w|_{\xi=1} = - \int_0^1 [\gamma (W')^2 + (W'')^2] d\xi, \quad \tilde{v}_w = \frac{\partial W}{\partial s} \tag{30.38}$$

$$\tilde{v}_\theta|_{\xi=1} = - \int_0^1 [\gamma \theta^2 + (\theta')^2] d\xi, \quad \tilde{v}_\theta = \frac{\partial \theta}{\partial s} \tag{30.39}$$

For simplified formulations based on (30.35), we obtain

$$\tilde{v}_w|_{\xi=1} = -\gamma \int_0^1 (W')^2 d\xi, \quad \tilde{v}_\theta|_{\xi=1} = -\gamma \int_0^1 \theta^2 d\xi \tag{30.40}$$

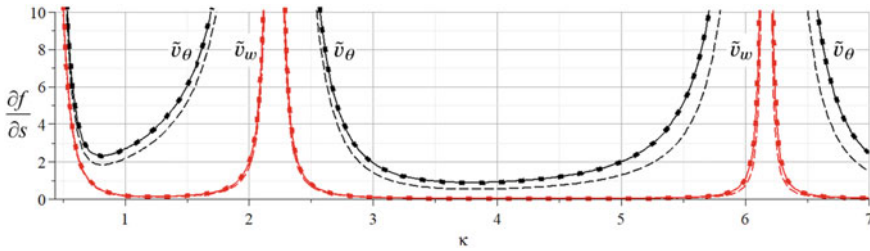


Fig. 30.1 Results of calculating the rod’s sensitivity characteristics \tilde{v}_w , \tilde{v}_θ with respect to prestress according to (30.37) (points); (30.38)–(30.39) (solid lines); (30.40) (dotted line)

Table 30.1 Sensitivities \tilde{v}_w and \tilde{v}_θ for different values of the dimensionless frequency parameter κ in the vicinity of the first three resonances $\kappa_1 = 0.352$, $\kappa_2 = 2.20$ and $\kappa_3 = 6.17$

| κ | 0.4 | 0.6 | 0.8 | 1.7 | 2 | 2.18 | 2.22 | 2.4 | 4 | 5.8 | 6.07 | 6.27 | 6.6 |
|--------------------|-------|------|------|------|------|-------|------|------|------|------|------|-------|------|
| \tilde{v}_w | 140.5 | 2.89 | 0.52 | 0.33 | 1.95 | 140.6 | 279 | 1.87 | 0.02 | 0.23 | 3.08 | 2.985 | 0.16 |
| \tilde{v}_θ | 247.7 | 4.82 | 2.32 | 10.2 | 49.6 | 3248 | 6325 | 39.4 | 0.91 | 15.2 | 192 | 181.3 | 9.29 |

Figure 30.1 shows the results of a comparative analysis of the sensitivity characteristics \tilde{v}_w and \tilde{v}_θ found according to (30.38)–(30.40) for the considered rod when probing with a transverse force and a bending moment. The problem parameters in the calculations were used as follows: $\gamma = 100$, $g = 1$, $r = 1$, $\tilde{P} = 1$ and $\tilde{M} = 1$.

Table 30.1 shows the sensitivity values \tilde{v}_w and \tilde{v}_θ calculated by formulas (30.38)–(30.39) in the vicinity of the first three resonant frequencies.

From the results shown in Fig. 30.1 and Table 30.1, we can conclude that bending moment probing leads to a significantly more pronounced dynamic response of the rod than axial force probing. Thus, when studying the inverse problem of identifying the law of inhomogeneity for the axial prestress component of a rod, it is advisable to perform frequency probing by the bending moment with the choice of oscillation frequencies in the vicinity of the first three resonances. Calculations over a wider frequency range have also revealed that the amplitude of sensitivity with respect to prestress for the rod during bending vibrations decreases in the regions between the resonances with increasing frequency; when considering longitudinal oscillations, there is no such a pattern.

30.7 Conclusion

Based on the introduced sensitivity concept for inhomogeneous bodies, formulas for the analysis of the desired material characteristics and prestress components for an arbitrary isotropic elastic body are proposed. The computational experiments on calculating the sensitivity characteristics for prestressed rods are carried out. The

recommendations are presented on the choice of sounding frequency ranges for cylindrical rods, inhomogeneous along the axial coordinate, when solving inverse coefficient problems on the basis of the longitudinal and flexural vibrations analysis.

Acknowledgements The study was supported by the grant from the Russian Science Foundation # 22-11-00265, <https://rscf.ru/project/22-11-00265/> Southern Federal University.

References

- Dudarev VV, Vatulyan AO, Mnutkin RM, Nedin RD (2020) Concerning an approach to identifying the Lamé parameters of an elastic functionally graded cylinder. *Math Meth Appl Sci* 43(11):6861–6870. <https://doi.org/10.1002/mma.6428>
- Fazzolari FA (2016) Stability analysis of FGM sandwich plates by using variable-kinematics Ritz models. *Mech Adv Mater Struct* 23(9):1104–1113. <https://doi.org/10.1080/15376494.2015.1121559>
- Guz AN (2004) Elastic waves in bodies with initial (Residual) Stresses. Kiev, A.S.K., p 672 (in Russian)
- Hutson V, Pym JS (1980) Applications of functional analysis and operator theory. Academic, p 432. [https://doi.org/10.1016/s0076-5392\(05\)x8032-8](https://doi.org/10.1016/s0076-5392(05)x8032-8)
- Li Q, Iu VP, Kou KP (2008) Three-dimensional vibration analysis of functionally graded material sandwich plates. *J Sound Vib* 311(1–2):498–515. <https://doi.org/10.1016/j.jsv.2007.09.018>
- Li W, Ma H, Gao W (2019) A higher-order shear deformable mixed beam element model for accurate analysis of functionally graded sandwich beams. *Compos Struct* 221:110830. <https://doi.org/10.1016/j.compstruct.2019.04.002>
- Nedin RD, Dudarev VV, Vatulyan AO (2017) Some aspects of modeling and identification of inhomogeneous residual stress. *Eng Struct* 151:391–405. <https://doi.org/10.1016/j.engstruct.2017.08.007>
- Nedin RD, Vatulyan AO, Bogachev IV (2018) Direct and inverse problems for prestressed functionally graded plates in the framework of the Timoshenko model. *Math Meth Appl Sci* 41(4):1600–1618. <https://doi.org/10.1002/mma.4688>
- Nedin RD, Vatulyan AO, Dudarev VV, Bogachev IV (2018) Detection of nonuniform residual strain in a pipe. *Int J Solids Struct* 139–140:121–128. <https://doi.org/10.1016/j.ijsolstr.2018.01.026>
- Nedin RD, Vatulyan AO, Yurov VO (2022) On estimating prestress state in an elastic cylinder. *Adv Struct Mater* 180:195–210. https://doi.org/10.1007/978-3-031-18393-5_12
- Nguyen TK, Nguyen BD (2015) A new higher-order shear deformation theory for static, buckling and free vibration analysis of functionally graded sandwich beams. *J Sandw Struct Mater* 17(6):613–631. <https://doi.org/10.1177/1099636215589237>
- Schajer GS (2013) Practical residual stress measurement methods. Wiley 560
- Vatulyan AO, Dudarev VV, Nedin RD (2015) Initial stresses: modeling and identification. Monograph Rostov-on-Don, SFedU Publishing House, p 206 (in Russian)
- Vatulyan AO, Yurov VO (2021) On the reconstruction of material properties of a radially inhomogeneous cylindrical waveguide. *Math Meth Appl Sci* 44(6):4756–4769. <https://doi.org/10.1002/mma.7067>
- Vatulyan AO, Yurov VO (2023) On estimation of sensitivity of model coefficients for inhomogeneous bodies. *Mechanics of Solids (Ob otsenke chuvstvitel'nosti koeffitsiyentov modeley dlya neodnorodnykh tel. Izvestiya Rossijskoj akademii nauk. Mekhanika tverdogo tela)* 3:135–145. <https://doi.org/10.31857/S0572329922600839> (in Russian)
- Yurov VO, Nedin RD, Vatulyan AO (2020) Oscillations of a non-uniform finite hollow cylinder under conditions of complex prestressed state. *Eng Struct* 221:111019. <https://doi.org/10.1016/j.engstruct.2020.111019>

Chapter 31

The Lowest Eigenfrequencies of an Immersed Thin Elastic Cylindrical Shell



Hazel Yücel, Barış Erbaş, Nihal Ege, and Julius Kaplunov

Abstract The plane strain time-harmonic motion of an immersed cylindrical elastic shell is considered. The revisit to this classical problem is motivated by modern technical applications, including the investigation of low-frequency band gaps arising at acoustic wave propagation through a periodic array of thin-walled cylinders. In this paper, the effect of the fluid is reduced to a mixed boundary condition along the outer face of the shell after the separation of the circumferential variable. The asymptotic analysis of the ordinary differential equations along a narrow interval results in approximate formulae for the lowest complex eigenfrequencies. It is demonstrated that their values are asymptotically smaller than the lowest eigenfrequencies of a shell with traction-free faces, and at leading order they do not depend on the shell density. At the same time, the fluid compressibility does not appear in the two-term asymptotic behaviour. Numerical examples for steel and aluminium shells immersed in water confirm that the imaginary parts of the sought-for frequencies are extremely small and may often be ignored in comparison with the contribution of structural damping.

H. Yücel

Department of Computer Engineering, Başkent University, Bağlıca Campus, 06790 Etimesgut, Ankara, Türkiye

e-mail: hazely@baskent.edu.tr

B. Erbaş · N. Ege

Department of Mathematics, Eskişehir Technical University, Yunus Emre Campus, 26470 Tepebaşı, Eskişehir, Türkiye

e-mail: berbas@eskisehir.edu.tr

N. Ege

e-mail: nsahin@eskisehir.edu.tr

J. Kaplunov (✉)

School of Computing and Mathematics, Keele University, Keele, Staffordshire ST5 5BG, United Kingdom

e-mail: j.kaplunov@keele.ac.uk

31.1 Introduction

Fluid–structure interaction problems for thin elastic shells were initially inspired by various engineering applications in the area of underwater acoustics; see the books (Veksler 2012; Kaplunov et al. 1998) and the general reference papers (Gaunaud and Werby 1990; Zarastvand et al. 2021), to mention a few. More recent efforts in this area are concerned with the modelling of modern materials, e.g., see Jin and Ren (2022), Li et al. (2013) and Hasheminejad and Rajabi (2007). In this case, the lowest eigenfrequencies of a thin cylindrical shell are of particular importance for the investigation of the main band gaps for the periodic arrays of cylinders immersed into acoustic media; see Krynkin et al. (2013) and also Krynkin et al. (2011), Shengjun et al. (2012). At the same time, such frequencies were not always within a special focus of the publications based on the canonical formulations for a single immersed shell. They usually studied a broader frequency band with several exceptions, including (de Loock et al. 2013) reporting on numerical and experimental results over the low-frequency region. Only very few developments on the subject presented explicit analytical results. Among them, we mention (Kaplunov et al. 1998, 1994) exposing robust asymptotic formulae for complex-valued scattering resonances, e.g., see Gaunaud and Brill (1984). However, the scope of the cited publications was mainly restricted to higher frequencies, for which the effect of the shell curvature was often less essential.

In this paper, we study the time-harmonic motion of a thin cylindrical shell immersed into a compressible fluid under plane strain assumptions. The consideration below generalizes the asymptotic analysis of 2D equations in elasticity in Ege et al. (2021), Ege et al. (2022) oriented to the evaluation of the lowest eigenfrequencies for a shell with traction-free faces. The alternative approach to the last problem was developed in Chapman and Sorokin (2017) starting from the full dispersion relation.

First, by using the Fourier series in the angular coordinate, we reduce the original fluid–structure interaction problem over an infinite domain to a 2D boundary value problem for a narrow annulus with mixed boundary conditions along its outer face and a traction-free inner one. The coefficients in the former involve appropriate Hankel functions satisfying the radiation conditions at infinity.

It is demonstrated that the presence of the fluid affects drastically the asymptotic order of the lowest eigenfrequencies of interest. As might be expected, they are much smaller than their counterparts for a free cylindrical shell calculated in Ege et al. (2021). Nevertheless, the scaling of the displacement and stress components appears to be the same as in Ege et al. (2021). A peculiarity of the considered problem consists in incorporating into the asymptotic techniques well established in the general shell theory; e.g., see Goldenveizer (1976), Kaplunov et al. (1998), the complex-valued series for the above mentioned coefficients in the boundary conditions containing Hankel functions.

A two-term asymptotic formula is derived for the real parts of the sought-for eigenfrequencies. The first term in this formula does not depend on the shell density,

while neither of them is influenced by fluid compressibility. The imaginary parts of the eigenfrequencies, due to the radiation of the vibration energy to infinity, are also evaluated explicitly. The approximate numerical values of the eigenfrequencies are calculated for steel and aluminium shells immersed in water.

31.2 Statement of the Problem

Consider an elastic cylindrical shell of thickness $2h$ with mid-surface radius R immersed in a compressible fluid; see Fig. 31.1. The shell is assumed to be thin, i.e., $\eta = h/R$ is a small geometric parameter. Specify the conventional orthogonal coordinates $\alpha_i, i = 2, 3$, in the form

$$\alpha_2 = R\theta, \quad \alpha_3 = h\zeta \tag{31.1}$$

where θ corresponds to the circumferential coordinate ($0 \leq \theta < 2\pi$) and ζ is the transverse coordinate ($-1 \leq \zeta \leq 1$ inside the shell and $\zeta \geq 1$ over the exterior domain).

The displacement and stress components $v_i(\theta, \zeta)$ and $\sigma_{ij}(\theta, \zeta)$ of the shell, $i, j = 2, 3$, and the acoustic pressure $p(\theta, \zeta)$ in the fluid can be presented as

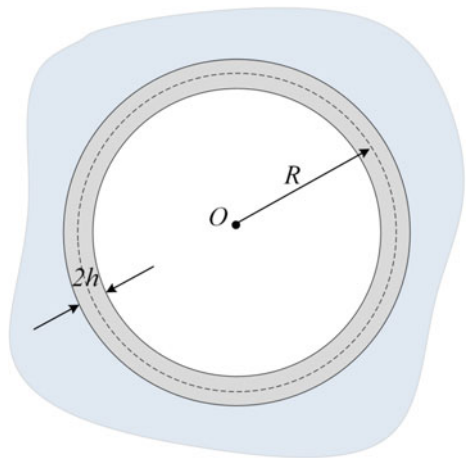
$$v_2 = u_2 \sin n\theta, \quad v_3 = u_3 \cos n\theta \tag{31.2}$$

and

$$\sigma_{22} = s_{22} \cos n\theta, \quad \sigma_{32} = s_{32} \sin n\theta, \quad \sigma_{33} = s_{33} \cos n\theta, \tag{31.3}$$

and

Fig. 31.1 Geometry of the problem



$$p = P(\zeta) \cos n\theta, \tag{31.4}$$

where $u_i(\zeta)$, $s_{ij}(\zeta)$ and $P(\zeta)$ denote unknown Fourier coefficients, and n is the circumferential wavenumber. Then, the plane strain equations of motion in linear elasticity, see, e.g., Ege et al. (2023), Kaplunov et al. (1998), become

$$\frac{\partial s_{32}}{\partial \zeta} - \frac{n\eta}{1 + \eta\zeta} s_{22} + \frac{2\eta}{1 + \eta\zeta} s_{32} + \eta\rho\omega^2 R u_2 = 0, \tag{31.5}$$

and

$$\frac{\partial s_{33}}{\partial \zeta} + \frac{n\eta}{1 + \eta\zeta} s_{32} - \frac{\eta}{1 + \eta\zeta} s_{22} + \frac{\eta}{1 + \eta\zeta} s_{33} + \eta\rho\omega^2 R u_3 = 0 \tag{31.6}$$

together with

$$s_{22} = \frac{E}{(1 - \nu^2)R} \frac{1}{(1 + \eta\zeta)} (nu_2 + u_3) + \frac{\nu}{1 - \nu} s_{33}, \tag{31.7}$$

$$\frac{E}{h} \frac{\partial u_3}{\partial \zeta} = (1 - \nu^2)s_{33} - \nu(1 + \nu)s_{22}, \tag{31.8}$$

and

$$s_{32} = \frac{E}{2(1 + \nu)R} \left(\frac{1}{\eta} \frac{\partial u_2}{\partial \zeta} - \frac{1}{1 + \eta\zeta} (u_2 + nu_3) \right). \tag{31.9}$$

Here, ω is the angular frequency, ρ is the mass density of the shell, E is Young’s modulus and ν is Poisson’s ratio; the time-harmonic factor $e^{i\omega t}$, where t is time, is omitted.

The fluid motion is governed by the Helmholtz equation ($\zeta \geq 1$)

$$\Delta P + \frac{\omega^2}{c_0^2} P = 0, \tag{31.10}$$

where c_0 is the sound wave speed, and the 2D Laplace operator is given by

$$\Delta = \frac{1}{R^2} \left(\frac{1}{\eta^2} \frac{\partial^2}{\partial \zeta^2} + \frac{1}{\eta(1 + \eta\zeta)} \frac{\partial}{\partial \zeta} - \frac{n^2}{(1 + \eta\zeta)^2} \right). \tag{31.11}$$

Next, we describe the fluid interaction through the contact conditions at $\zeta = 1$ (e.g., see Kaplunov et al. 1998), written as

$$s_{33} = -P, \quad s_{32} = 0, \tag{31.12}$$

and

$$u_3 = \frac{1}{h\rho_0\omega^2} \frac{\partial P}{\partial \zeta}, \quad (31.13)$$

where ρ_0 is the mass density of the fluid.

In addition, we assume that the inner surface of the shell $\zeta = -1$ is traction free. Thus,

$$s_{3i} = 0, \quad i = 2, 3. \quad (31.14)$$

As usual, the pressure P is subject to the radiation condition at infinity ($\zeta \rightarrow \infty$), given by

$$\frac{\partial P}{\partial \zeta} + i \frac{\omega}{c_0} P = o(\zeta^{-1/2}). \quad (31.15)$$

The fluid pressure satisfying the Helmholtz equation (31.10) over the region $\zeta \geq 1$, subject to the radiation condition (31.15), for the chosen time dependence $e^{i\omega t}$ can be written as

$$P = P_0 H_n^{(2)} \left(\frac{\omega R(1 + \eta \zeta)}{c_0} \right), \quad (31.16)$$

where $H_n^{(2)}(z)$ is the appropriate Hankel function; see Abramowitz et al. (1988).

Substituting the pressure (31.16) into the impenetrability condition (31.13) and taking into account the first of the boundary conditions (31.12), the two remaining boundary conditions may be combined in a single one such as

$$u_3 + s_{33} \frac{1}{\rho_0 c_0 \omega} \mathcal{H} = 0, \quad (31.17)$$

where

$$\mathcal{H} = \frac{(H_n^{(2)}(x))'}{H_n^{(2)}(x)} \quad (31.18)$$

at $x = \omega R(1 + \eta)/c_0$.

31.3 Asymptotic Scaling

Let us define the dimensionless displacement and stress components as

$$u_2 = Ru_2^*, \quad u_3 = Ru_3^* \quad (31.19)$$

and

$$s_{22} = E\eta s_{22}^*, \quad s_{32} = E\eta^2 s_{32}^*, \quad s_{33} = E\eta^2 s_{33}^* \quad (31.20)$$

where the starred quantities are assumed to be of the same asymptotic order. We also specify the dimensionless frequency by

$$\Omega = \eta^{-3/2} \frac{\omega R}{c_2}, \quad \Omega \sim 1 \tag{31.21}$$

with $c_2 = \sqrt{E/(2(1 + \nu)\rho)}$ denoting the shear wave speed in the shell material. It is worth noting that for a shell immersed in a vacuum, i.e., with both traction-free faces, the region of the lowest eigenfrequencies is observed at

$$\frac{\omega R}{c_2} \sim \eta, \tag{31.22}$$

e.g., see Ege et al. (2023), Ege et al. (2022). Thus, as might be expected, the presence of the fluid decreases the values of the lowest eigenfrequencies.

In addition, we have

$$\mathcal{H} = \eta^{-3/2} \mathcal{H}^* \tag{31.23}$$

where, according to Abramowitz et al. (1988, Eqs. 9.1.10 and 9.1.11),

$$\begin{aligned} \mathcal{H}^* = & -\frac{n c_*}{\Omega(1 + \eta)} - \frac{n - 2}{4(n - 1)c_*} \Omega \eta^3 (1 + \eta) + \dots \\ & - i \frac{\pi}{2^{2n-1} c_*^{2n-1} ((n - 1)!)^2} \Omega^{2n-1} \eta^{3n} (1 + \eta)^{2n-1} + \dots \end{aligned} \tag{31.24}$$

with $c_* = c_0/c_2$.

The equations of motion (31.5)–(31.9) may now be rewritten in dimensionless variables as

$$\frac{\partial s_{32}^*}{\partial \zeta} - \frac{n}{1 + \eta \zeta} s_{22}^* + \frac{2\eta}{1 + \eta \zeta} s_{32}^* + \frac{\eta^2 \Omega^2}{2(1 + \nu)} u_2^* = 0, \tag{31.25}$$

and

$$\frac{\partial s_{33}^*}{\partial \zeta} + \frac{n\eta}{1 + \eta \zeta} s_{32}^* - \frac{1}{1 + \eta \zeta} s_{22}^* + \frac{\eta}{1 + \eta \zeta} s_{33}^* + \frac{\eta^2 \Omega^2}{2(1 + \nu)} u_3^* = 0, \tag{31.26}$$

whereas the stress–displacement relations take the form

$$\eta s_{22}^* = \frac{1}{1 - \nu^2} \left(\frac{1}{1 + \eta \zeta} (n u_2^* + u_3^*) \right) + \frac{\nu}{1 - \nu} \eta^2 s_{33}^*, \tag{31.27}$$

$$\frac{\partial u_3^*}{\partial \zeta} = (1 - \nu^2) \eta^3 s_{33}^* - \nu(1 + \nu) \eta^2 s_{22}^*, \tag{31.28}$$

and

$$\eta^3 s_{32}^* = \frac{1}{2(1+\nu)} \left(\frac{\partial u_2^*}{\partial \zeta} - \frac{\eta}{1+\eta\zeta} (nu_3^* + u_2^*) \right). \quad (31.29)$$

In terms of the starred quantities, the conditions (31.14) and (31.17) take the forms

$$s_{32}^* = 0, \quad (\zeta = \pm 1), \quad s_{33}^* = 0, \quad (\zeta = -1) \quad (31.30)$$

and

$$\eta\Omega u_3^* - \frac{2(1+\nu)}{c_*\rho_*} \mathcal{H}^* s_{33}^* = 0, \quad (\zeta = 1) \quad (31.31)$$

where $\rho_* = \rho_0/\rho$.

In what follows, all starred quantities are expanded in asymptotic series as

$$f^* = f^{(0)} + \eta f^{(1)} + \eta^2 f^{(2)} + \dots, \quad (31.32)$$

while the dimensionless frequency is taken in the form

$$\Omega^2 = \Omega_0^2 + \eta\Omega_1^2 + \eta^2\Omega_2^2 + \dots. \quad (31.33)$$

31.4 Leading Order Approximation

At the leading order, by integrating equations (31.28) and (31.29) with respect to the thickness variable ζ , we have

$$u_3^{(0)} = U_3^{(0)} \quad \text{and} \quad u_2^{(0)} = U_2^{(0)} \quad (31.34)$$

where $U_3^{(0)}$ and $U_2^{(0)}$ are unknown constants. Taking into account (31.27), they are related by

$$U_2^{(0)} = -\frac{1}{n} U_3^{(0)}. \quad (31.35)$$

Then, by integrating equation (31.25) with respect to the thickness variable, we obtain

$$s_{32}^{(0)} = -n \int_{\zeta}^1 s_{22}^{(0)} ds. \quad (31.36)$$

Next, we deduce from the boundary condition (31.30) at $\zeta = -1$

$$\int_{-1}^1 s_{22}^{(0)} ds = 0. \quad (31.37)$$

It also follows from (31.26) that

$$s_{33}^{(0)} = - \int_{\zeta}^1 s_{22}^{(0)} ds \quad (31.38)$$

which results in $s_{33}^{(0)} = 0$ at $\zeta = \pm 1$, due to (31.37), agreeing with boundary conditions (31.30) and (31.31). The relations above do not allow calculating the leading order term Ω_0^2 in the asymptotic series (31.33). Therefore, we need to proceed to the next order approximation.

31.5 First Order Approximation

At the first order, we have from (31.28)

$$u_3^{(1)} = U_3^{(1)}. \quad (31.39)$$

Next, by integrating (31.29) in the thickness variable ζ , then using (31.35), we obtain

$$u_2^{(1)} = - \frac{1-n^2}{n} \zeta U_3^{(0)} + U_2^{(1)}. \quad (31.40)$$

Now, by integrating (31.27) along the thickness and employing (31.37), we arrive at the relation

$$U_2^{(1)} = - \frac{1}{n} U_3^{(1)}. \quad (31.41)$$

It also follows from (31.27), as a result of (31.41), that

$$s_{22}^{(0)} = - \frac{1-n^2}{1-\nu^2} \zeta U_3^{(0)}. \quad (31.42)$$

Substituting the latter back into (31.36) and (31.38), we respectively have

$$s_{32}^{(0)} = \frac{n(1-n^2)}{2(1-\nu^2)} (1-\zeta^2) U_3^{(0)}, \quad (31.43)$$

and

$$s_{33}^{(0)} = \frac{1-n^2}{2(1-\nu^2)} (1-\zeta^2) U_3^{(0)}. \quad (31.44)$$

Integrating (31.25) throughout the thickness of the shell and making use of equations (31.42) and (31.43), we find

$$\int_{-1}^1 s_{22}^{(1)} ds = \frac{2(1-n^2)}{3(1-\nu^2)} U_3^{(0)}. \quad (31.45)$$

We also deduce from (31.25) that

$$s_{32}^{(1)} = -n \int_{\zeta}^1 s_{22}^{(1)} ds + \frac{n(1-n^2)}{3(1-\nu^2)} (1-3\zeta+2\zeta^3) U_3^{(0)}. \quad (31.46)$$

Finally, Eq. (31.26) may be integrated along the thickness to give

$$\Omega_0^2 = \frac{4n(1-n^2)^2}{3\rho_*(1-\nu)} \quad (31.47)$$

taking into consideration the boundary condition

$$s_{33}^{(1)} \Big|_{\zeta=1} = \frac{\rho_*}{2(1+\nu)n} \Omega_0^2 U_3^{(0)}. \quad (31.48)$$

We also have

$$s_{33}^{(1)} = - \int_{\zeta}^1 s_{22}^{(1)} ds - \frac{(1-n^2)(1-\zeta) (3\zeta(1+\zeta) - n^2(2-\zeta-\zeta^2))}{6(1-\nu^2)} U_3^{(0)} + \frac{\rho_*}{2(1+\nu)n} \Omega_0^2 U_3^{(0)}. \quad (31.49)$$

31.6 Second Order Approximation

At the second order, by integrating equation (31.28) and using (31.42), we have

$$u_3^{(2)} = \frac{\nu}{2(1-\nu)} (1-n^2) \zeta^2 U_3^{(0)} + U_3^{(2)}. \quad (31.50)$$

Then, by integrating (31.29) and using Eqs. (31.34), (31.39) and (31.40), we obtain

$$u_2^{(2)} = - \frac{1-n^2}{n} \zeta U_3^{(1)} + U_2^{(2)}. \quad (31.51)$$

Next, integration of equation (31.27), taking into account relations (31.34), (31.39), (31.40) and (31.44), results in

$$U_2^{(2)} + \frac{1}{n}U_3^{(2)} = -\frac{\nu(1-n^2)}{2n(1-\nu)}U_3^{(0)}. \tag{31.52}$$

Substituting the latter back into (31.27), we obtain

$$s_{22}^{(1)} = -\frac{1-n^2}{1-\nu^2}\zeta U_3^{(1)} + \frac{1-n^2}{1-\nu^2}\zeta^2 U_3^{(0)}. \tag{31.53}$$

Now, Eqs. (31.46) and (31.49), taking into consideration (31.53), respectively become

$$s_{32}^{(1)} = \frac{n(1-n^2)}{2(1-\nu^2)}(1-\zeta^2)U_3^{(1)} - \frac{n(1-n^2)}{2(1-\nu^2)}\zeta(1-\zeta^2)U_3^{(0)}, \tag{31.54}$$

and

$$s_{33}^{(1)} = \frac{(1-n^2)}{2(1-\nu^2)}(1-\zeta^2)U_3^{(1)} + \frac{n(5\zeta^3 - 3\zeta - 2) + 4n^3(1-\zeta^3) - n^5(2-3\zeta + \zeta^3)}{6n(1-\nu^2)}U_3^{(0)} + \frac{\rho_*\Omega_0^2}{2n(1-\nu^2)}U_3^{(0)}. \tag{31.55}$$

Then, we derive from equation (31.25), subject to boundary conditions (31.30),

$$\int_{-1}^1 s_{22}^{(2)} ds = \frac{2(1-n^2)}{3(1-\nu^2)}U_3^{(1)} - \frac{1}{n^2(1+\nu)}\Omega_0^2 U_3^{(0)}. \tag{31.56}$$

Similarly, from equation (31.26) subject to boundary conditions (31.30) and (31.31), we have

$$\int_{-1}^1 s_{22}^{(2)} ds = \frac{2n^2(1-n^2)}{3(1-\nu^2)}U_3^{(1)} - \frac{2(1-n^2)^2}{3(1-\nu^2)}U_3^{(0)} + \frac{n+\rho_*}{n(1+\nu)}\Omega_0^2 U_3^{(0)} + \frac{\rho_*}{2(1+\nu)n} \left(\Omega_0^2 U_3^{(1)} + \Omega_1^2 U_3^{(0)} + \Omega_0^2 U_3^{(0)} \right). \tag{31.57}$$

Comparing the last two equations and using the expression for Ω_0^2 given by equation (31.47), we arrive at

$$\Omega_1^2 = -\frac{8(1-n^2)^2(1+n\rho_*+n^2)}{3\rho_*^2(1-\nu)}. \tag{31.58}$$

31.7 Discussion

Let us insert (31.47) and (31.58) in (31.33) to get a two-term approximate formula for the sought-for eigenfrequencies. It takes the form

$$\Omega^2 \approx \frac{4n(1-n^2)^2}{3\rho_*(1-\nu)} - \eta \frac{8(1-n^2)^2(1+n\rho_*+n^2)}{3\rho_*^2(1-\nu)}. \quad (31.59)$$

Using (31.21) and returning to the original variables we arrive at the dimensional counterpart of (31.59) given by

$$\omega \approx \sqrt{\frac{2Eh^3}{3(1-\nu^2)} \frac{(n^2-1)\sqrt{n}}{R^{5/2}\sqrt{\rho_0}}} \left(1 - \frac{1+n\rho_*+n^2}{\rho_*n} \frac{h}{R} \right). \quad (31.60)$$

It is remarkable that the leading order term of this formula does not depend on the shell density. At the same time, the fluid compressibility does not affect the lowest eigenfrequency at least up to first order corrections.

It follows from the derivation above that the imaginary parts of the eigenfrequencies of interest are placed outside the accuracy of formula (31.60) (or (31.59)). Nonetheless, below, we roughly evaluate them, ignoring the contribution of higher order terms associated with the real parts. To this end, we set

$$\Omega \approx \Omega_0 (1 + i\beta) \quad (31.61)$$

where $\beta \ll 1$ is a small parameter to be determined. Inserting the last ansatz into boundary condition (31.31) and taking into account (31.24), we obtain at the leading order

$$\beta \Omega_0^2 U_3^{(0)} - \frac{(1+\nu)n}{\rho_*} \frac{\pi}{2^{2n-1} c_*^{2n-1} ((n-1)!)^2} \Omega_0^{2n} \eta^{3n} s_{33}^{(1)} \Big|_{\zeta=1} = 0. \quad (31.62)$$

Then, substituting the value $s_{33}^{(1)}$ at $\zeta = 1$ from (31.48), we deduce that

$$\beta = \frac{\pi}{2^{2n} c_*^{2n} ((n-1)!)^2} \Omega_0^{2n} \eta^{3n}. \quad (31.63)$$

Numerical results are presented in Table 31.1 for aluminium and steel shells immersed in water. The densities and shear wave speeds are taken as 2790 kg/m³ and 3100 m/s for aluminium and 8030 kg/m³ and 3160 m/s for steel, whereas the density of water is 1000 kg/m³ with $c_0 = 1470$ m/s. As might be expected, the values of the imaginary part of the lowest eigenfrequencies are extremely small.

Table 31.1 Numerical values of the eigenfrequencies (31.47), (31.58), (31.59) and (31.63) for $\nu = 0.3$ and $\eta = 0.01$

| n | Ω_0^2 | | Ω_1^2 | | Ω^2 | | β | |
|-----|--------------|---------|--------------|---------------------|------------|---------|------------------------|-----------------------|
| | Al | Steel | Al | Steel | Al | Steel | Al | Steel |
| 2 | 95.65 | 275.31 | -1525.73 | -11604.5 | 80.39 | 159.26 | 3.55×10^{-8} | 3.17×10^{-7} |
| 3 | 1020.34 | 2936.69 | -21019.1 | -163084 | 810.15 | 1305.85 | 1.14×10^{-9} | 3.06×10^{-8} |
| 4 | 4782.86 | 13765.7 | -122991 | -967110 | 3552.95 | 4094.61 | 6.97×10^{-11} | 5.58×10^{-9} |
| 5 | 15305.1 | 44050.3 | -474704 | -3.76×10^6 | 10558.1 | 6382.01 | 7.78×10^{-12} | 1.86×10^{-9} |

31.8 Concluding Remarks

The asymptotic procedure typical for the general theory for elastic shells is adapted for a plane strain time-harmonic problem for a thin-walled hollow cylinder with mixed boundary conditions along its faces. The latter are established by separating the circumferential variable and expressing the solution of the Helmholtz equation over the exterior domain through appropriate Hankel functions. It is demonstrated that the lowest eigenfrequencies of a fluid loaded cylindrical shell occur at $\omega R/c_2 \sim \eta^{3/2}$, whereas for a shell with traction-free faces $\omega R/c_2 \sim \eta$. Thus, the latter are about $\eta^{1/2}$ times greater.

The obtained two-term asymptotic formula for the real parts of complex-valued eigenfrequencies does not involve the effect of the fluid compressibility. Moreover, the leading order term in this formula does not depend on the shell density. The imaginary parts of eigenfrequencies are also estimated. Numerical results presented for steel and aluminium shells immersed in water show that even very small structural damping may result in a greater contribution to the imaginary parts in question. The explicit asymptotic results presented in the paper may be used for validating the predictions based on various approximate theories for thin elastic shells, e.g., see Kaplunov et al. (1998), Kaplunov et al. (1994), Belov et al. (1998).

The proposed methodology allows various generalizations and extensions, including 3D problems, contrast problem parameters, including the case of the so-called light fluid loading, as well as FGM and viscoelastic shells. In addition, calculation of higher order terms in the asymptotic expansion for the real parts of eigenfrequencies, along with comparison with the exact solution of the initial plane strain problem, seem to be of interest.

References

- Abramowitz M, Stegun IA, Romer RH (1988) Handbook of mathematical functions with formulas, graphs, and mathematical tables
- Belov AV, Kaplunov JD, Nolde EV (1998) A refined asymptotic model of fluid-structure interaction in scattering by elastic shells. *Flow, Turbul Combust* 61(1–4):255–267
- Chapman CJ, Sorokin SV (2017) The deferred limit method for long waves in a curved waveguide. *Proc R Soc A: Math, Phys Eng Sci* 473(2200):20160900
- Ege N, Erbaş B, Kaplunov J (2021) Asymptotic derivation of refined dynamic equations for a thin elastic annulus. *Math Mech Solids* 26(1):118–132
- Ege N, Erbaş B, Kaplunov J, Noori N (2023) Asymptotic corrections to the low-frequency theory for a cylindrical elastic shell. *Zeitschrift für angewandte Mathematik und Physik* 74(2):43
- Ege N, Erbaş B, Kaplunov J, Noori N (2022) Low-frequency vibrations of a thin-walled functionally graded cylinder (plane strain problem). *Mech Adv Mater Struct* 1–9
- Gaunaurd GC, Werby MF (1990) Acoustic resonance scattering by submerged elastic shells. *Appl Mech Rev* 43(8):171–208
- Gaunaurd GC, Brill D (1984) Acoustic spectrogram and complex-frequency poles of a resonantly excited elastic tube. *J Acoust Soc Am* 75(6):1680–1693
- Goldenevizer AL (1976) Theory of thin elastic shells. Moscow, Izdatel'stvo Nauka, p 512. In Russian
- Hasheminejad SM, Rajabi M (2007) Acoustic resonance scattering from a submerged functionally graded cylindrical shell. *J Sound Vib* 302(1–2):208–228
- Jin Q, Ren Y (2022) Nonlinear size-dependent dynamic instability and local bifurcation of FG nanotubes transporting oscillatory fluids. *Acta Mechanica Sinica* 38(3):521513
- Kaplunov JD, Kossovitch LY, Nolde EV (1998) Dynamics of thin walled elastic bodies. Academic Press
- Kaplunov JD, Nolde EV, Veksler ND (1994) Asymptotic formulae for the modal resonance of peripheral waves in the scattering of an obliquely incident plane acoustic wave by a cylindrical shell. *Acta Acustica united with Acustica* 80(3):280–293
- Krynkin A, Umnova O, Taherzadeh S, Attenborough K (2013) Analytical approximations for low frequency band gaps in periodic arrays of elastic shells. *J Acoust Soc Am* 133(2):781–791
- Krynkin A, Umnova O, Sanchez-Perez JV, Boon Chong AY, Taherzadeh S, Attenborough K (2011) Acoustic insertion loss due to two dimensional periodic arrays of circular cylinders parallel to a nearby surface. *J Acoust Soc Am* 130(6):3736–3745
- Li L, Wen J-H, Cai L, Zhao H-G, Wen X-S (2013) Acoustic scattering from a submerged cylindrical shell coated with locally resonant acoustic metamaterials. *Chinese Phys B* 22(1):014301
- Shengjun X, Qiu C, Liu Z (2012) Acoustic transmission through asymmetric grating structures made of cylinders. *J Appl Phys* 111(9):094505
- Van de Loock J, Décultot D, Léon F, Chati F, Maze G, Rajaona DR, Klauson A (2013) Acoustic radiation of a submerged cylindrical shell in low frequency. *J Acoust Soc Am* 133(1):EL26–EL32
- Veksler ND (2012) Resonance acoustic spectroscopy, vol 11. Springer Science & Business Media
- Zarastvand MR, Ghassabi M, Talebitooti R (2021) Acoustic insulation characteristics of shell structures: a review. *Arch Comput Methods Eng* 28:505–523

Chapter 32

Grinding of Functionally Graded Coating Taking into Account Wear and Friction Heating



Vladimir B. Zelentsov, Polina A. Lapina, and Andrey L. Nikolaev

Abstract The processing of product materials by grinding is widely used in modern industry, both at the macro-, micro-, and even nano-level. Often the materials or coatings processed by grinding are inhomogeneous, multilayered, functionally graded in terms of the depth of processing. Material inhomogeneity complicates the processing process and can lead to emergency situations. Simulation of the grinding process makes it possible to study the signs of a developing emergency situation, to develop methods for its relief. For this purpose, the problem of grinding of a functionally graded coating with a rigid abrasive with a flat base shape moving at a constant speed over its surface is considered. During the movement of the abrasive, it settles into the coating material, taking into account wear and heating of the sliding contact from friction. Solutions to the problem are presented as convolutions from the abrasive introduction law and the original as a contour integral of the inverse Laplace transform. Analytical solutions made it possible to study the effect of the coefficient of functionally graded inhomogeneity on the main characteristics of the sliding contact: temperature, displacements, stresses, and wear of the functionally graded coating material with the same law of abrasive introduction. In order to control the grinding process, a method has been developed for selecting the law of abrasive introduction, which makes it possible to keep the values of the contact parameters (temperature, stresses, wear) within certain limits without creating emergency situations.

Keywords Functionally graded inhomogeneity · Thermoelasticity · Sliding contact · Wear · Heat generation from friction · Thermoelastic instability

V. B. Zelentsov · P. A. Lapina (✉) · A. L. Nikolaev
Research and Education Center “Materials”, Don State Technical University, 1 Gagarin Sq,
Rostov-On-Don 344000, Russia
e-mail: polina_azarova86@mail.ru

© The Author(s), under exclusive license to Springer Nature Switzerland AG 2023
H. Altenbach and V. Eremeyev (eds.), *Advances in Linear and Nonlinear Continuum and Structural Mechanics*, Advanced Structured Materials 198,
https://doi.org/10.1007/978-3-031-43210-1_32

573

32.1 Introduction

The problems of wear modelling grinding process of functionally graded coatings are actual problems of modern mechanics due to the need to optimize designs that include functionally graded coatings, and diagnose to prevent emergency situations. In microelectronics, semiconductor materials in the form of thin plates with a functionally graded inhomogeneity in depth are used. The thickness of such plates does not exceed 20–30 μm . The process of thinning of plates for microelectronics is carried out by grinding and polishing. The significant question is the determination of the influence degree of the properties of the functionally graded inhomogeneity of the workpiece material on the grinding process, the nature of the heating of the workpiece, the possibility of occurrence of thermoelastic instability of the contact, the acceleration or the deceleration of the grinding process, the grinding process control, etc.

Works (Guler and Erdogan 2007, Altenbach and Eremeyev 2009, Selvadurai and Katebi 2013, 2016, Tokovyy and Ma 2015, Vasiliev et al. 2017, 2018a, b, Alinia et al. 2016, Ma et al. 2016, Kudish et al. 2016, Zelentsov et al. 2016a) are devoted to mathematical modeling of the contact problems for bodies with functionally graded coatings. However, not enough attention is paid to the problem of modeling of wear or grinding of functionally graded coatings, there are several works in this direction (for example, Singh and Singh 2015). When solving wear problems, the Archard relations are most often used (Archard 1953). In Dow and Burton (1973), the Archard relation is used to study wear taking into account the conditions of heat generation from friction and the conditions for the occurrence of thermoelastic instability of a blade sliding along the surface of a half-space are also studied by the method of small perturbations. In Alexandrov and Annakulova (1990, 1992), the contact problem taking into account heat generation from friction and wear of the coating and the problem of mutual wear of coatings are considered. Works (Zmitrowicz 1987a, b) are devoted to the thermomechanical phenomena at the contact, taking into account friction and wear. A new direction in the development of the model of sliding contact between two elastic bodies, taking into account friction, wear, and heat generation has arisen, based on the principle of virtual energy and the basic laws of thermodynamics (Strömberg et al. 1996, Andrews et al. 1997). In Strömberg (1999), the finite element model implementation of such model in a two-dimensional formulation was performed. In Evtushenko and Pyryev (1997), Pyryev and Grilitsky (1996), Awrejcewicz and Pyryev (2002), Zelentsov et al. (2016b, 2017), the integral Laplace transform with the solution in the form of functional series over the poles of the integrands of contour quadratures of the inverse Laplace transform was used to solve contact problems of thermoelasticity in the course of wear process. The solution method makes it possible to establish the parametric boundaries of the thermoelastic instability of a sliding contact and to investigate the properties of the obtained solutions. In Belyakov and Nosko (2010), the contact problem of the sliding of an elastic coating over the surface of another one taking into account friction, wear, and heat generation from friction, is reduced to solving the differential equation

by the method of integral transformations, and the conditions of the thermoelastic stability of such a system are investigated. In Gu et al. (2000), quasi-static and dynamic unrelated contact problems of thermoelasticity on friction and wear of a rod were considered. In Papangelo and Ciavarella (2020a, b), the conditions of the occurrence of thermoelastic instability during mutual wear of surfaces made of different materials were considered. Due to the large number of parameters in the problems of wear and thermal friction contact, one-dimensional quasi-static problems were more often considered. In the listed works, the relationship between fields of strain and temperature was neglected, and the problems of uncoupled thermoelasticity were considered. In Zelentsov et al. (2019), the related problem of thermoelasticity of coating wear, taking into account the frictional heat generation in a quasi-static formulation, was considered.

32.2 Statement of the Problem of FGM Grinding

We consider the quasi-static contact problem of a rigid thermally insulated abrasive sliding with the constant velocity over the upper surface ($x = h$) of the elastic thermally conductive coating with the thickness h ($0 \leq x \leq h$). The lower surface of the coating adheres perfectly to a rigid substrate. The coating shear modulus varies in its depth and is represented by the function $\mu(x)$ ($0 \leq x \leq h$). When the abrasive slides, the coating wear takes place, which can also be considered as abrasive grinding of the coating surface. The frictional heat originated at the contact interface flows into the coating. From the initial time moment, the abrasive slides along the y axis and deforms the upper surface ($x = h$) of the elastic coating in the negative direction of the x axis according to the indentation law $\Delta(t)$. Before the initial time moment, the coating was resting and its temperature was zero (Zelentsov et al. 2022).

In the described problem formulation, the distributions of temperature, stresses, and displacements in the coating depend on the vertical coordinate x and time t and do not depend on the horizontal coordinate y (Evtushenko and Pyryev 1997, Pyryev and Grilitsky 1996, Awrejcewicz and Pyryev 2002, Zelentsov et al. 2016b, 2017). In this case, the stressed state of the coating is described by differential equations of linear elasticity in the quasi-static formulation and without taking into account body forces

$$\frac{\partial \sigma_{xx}}{\partial x} = 0, \quad \frac{\partial \sigma_{xy}}{\partial x} = 0, \quad 0 \leq x \leq h, \quad t > 0 \quad (32.1)$$

where $\sigma_{xx} = \sigma_{xx}(x, t)$, $\sigma_{xy} = \sigma_{xy}(x, t)$ are normal and tangential stresses in the coating.

Temperature distribution in the coating is presented using the heat equation

$$\frac{\partial^2 T}{\partial x^2} - \frac{1}{\kappa} \frac{\partial T}{\partial t} = 0, \quad 0 \leq x \leq h, \quad t > 0 \quad (32.2)$$

where $T(x, t)$ is the coating temperature, κ is the thermal diffusivity.

Stresses and displacements in the coating are related by Duhamell–Neumann law

$$\sigma_{xx} = \frac{2(1 - \nu)}{1 - 2\nu} \mu(x) \left(\frac{\partial u}{\partial x} - \frac{1 + \nu}{1 - \nu} \alpha T \right), \quad \sigma_{xy} = \mu(x) \frac{\partial w}{\partial x} \tag{32.3}$$

where $u(x, t)$, $w(x, t)$ are vertical and horizontal displacements in the coating, $\mu(x)$, ν , α are the shear modulus, Poisson’s ratio, coefficient of linear heat expansion of the coating material.

Equations (32.1) and (32.2) represent differential equations of linear uncoupled elasticity and describe thermoelastic state of the coating.

The boundary conditions are as follows ($t > 0$)

$$x = h \quad u(h, t) = -\Delta(t) + u_w(t) \tag{32.4}$$

$$\sigma_{xy}(h, t) = -f \sigma_{xx}(h, t) \tag{32.5}$$

$$x = 0 \quad u(0, t) = 0 \tag{32.6}$$

$$w(0, t) = 0 \tag{32.7}$$

where f is the coefficient of friction, $u_w(t)$ is the abrasive displacement due to the coating wear. We consider abrasive wear conditions (Pyryev and Grilitsky 1996) with linear wear rate, which can be represented in the integral form as

$$u_w(t) = -fVK^* \int_0^t \sigma_{xx}(h, \tau) d\tau, \quad t > 0 \tag{32.8}$$

where $\sigma_{xx}(h, t)$ is the compressive normal stress at the contact interface, K^* is the proportionality coefficient between the work of friction forces and the volume of removed material.

The boundary conditions for the heat Eq. (32.2) are as follows ($t > 0$)

$$x = h \quad K \frac{\partial T(h, t)}{\partial x} = Q(t) \tag{32.9}$$

$$x = 0 \quad K \frac{\partial T(0, t)}{\partial x} = k(T(0, t) - T_0) \tag{32.10}$$

where K is a coefficient of thermal conductivity of the coating material, k is a heat transfer coefficient, $Q(t) = fV(-\sigma_{xx}(h, t))$ is the amount of heat generated at the contact due to friction (Bowden and Tabor 1950). From (32.9) it follows that all the heat at the contact is formed due to friction.

Initial conditions for displacements and temperature in the coating are zero

$$u(x, 0) = w(x, 0) = T(x, 0) = 0 \tag{32.11}$$

32.3 Exact Solution of the Problem for an Arbitrary $\mu(X)$

We solve the problem using the Laplace integral transform (Ditkin and Prudnikov 1975).

$$T^L(x, p) = \int_0^\infty T(x, t)e^{-pt} dt, T(x, t) = \frac{1}{2\pi i} \int_{-i\infty+c}^{i\infty+c} T^L(x, p)e^{pt} dp, \tag{32.12}$$

$\text{Re } p < c, c > 0$

The index L in (32.12) denotes the Laplace transformation.

The temperature $T(x, t)$ in the coating is determined using the Laplace transformation, which is applied to the solution of the differential heat conduction Eq. (32.2). As a result of the Laplace transformation, the temperature of the coating material $T^L(x, p)$ is given by the formula

$$T^L(x, p) = A_1 sh \sqrt{\frac{p}{\kappa}} x + A_2 ch \sqrt{\frac{p}{\kappa}} x \tag{32.13}$$

where A_1, A_2 are arbitrary constants depending on the parameter p .

The vertical displacements $u(x, t)$ in the coating are determined from the first differential equation of elasticity theory (32.1). To solve Eq. (32.1), the integral Laplace transform (32.12) is used taking into account the first formula from (32.3). The Laplace transform of vertical displacements $u^L(x, p)$ is given by

$$u^L(x, p) = \frac{1 + \nu}{1 - \nu} \alpha \frac{1}{\sqrt{\frac{p}{\kappa}}} \left(A_1 ch \sqrt{\frac{p}{\kappa}} x + A_2 sh \sqrt{\frac{p}{\kappa}} x \right) - A_3 B(x) + A_4 \tag{32.14}$$

where A_1, A_2 are arbitrary constants from (32.13), A_3, A_4 are additional arbitrary constants depending on p . Function $B(x)$ is defined through the function $\mu(x)$ in the form

$$B(x) = \int_0^x \frac{d\xi}{\mu(\xi)}, 0 \leq x \leq h \tag{32.15}$$

where $\mu(x)$ is continuous and $\mu(x) \neq 0$ for all $x \in [0, h]$.

After applying the integral Laplace transform to the boundary conditions (32.4), (32.4), (32.9), (32.10) the constants $A_k, k = 1 - 4$ are determined

$$x = h \quad K \frac{dT^L(h,p)}{dx} = -fV\sigma_{xx}^L(h, p) \tag{32.16}$$

$$x = 0 \quad K \frac{dT^L(0,p)}{dx} = kT^L(0, p) \tag{32.17}$$

$$x = h \quad u^L(h, p) = -\Delta^L(p) + u_w^L(p) \tag{32.18}$$

$$x = 0 \quad u^L(x, p) = 0 \tag{32.19}$$

where

$$u_w^L(p) = -fVK^* \frac{\sigma_{xx}^L(h, p)}{p} \tag{32.20}$$

$$\sigma_{xx}^L(x, p) = \frac{2(1 - \nu)}{1 - 2\nu} \mu_1 \left(\frac{du^L(x, p)}{dx} - \frac{1 + \nu}{1 - \nu} \alpha T^L(x, p) \right) \tag{32.21}$$

Here $\mu_1 = \mu(h)$ is the value of the shear modulus at the upper coating boundary, $\Delta^L(p)$ is the Laplace image of the function $\Delta(t)$, representing abrasive displacement into the coating.

Substituting (32.13), (32.14), (32.20), (32.21) into the boundary conditions (32.16)–(32.19), we obtain a linear algebraic system from which the constants $A_k, k = 1 - 4$ are determined. After determination of $A_k, k = 1 - 4$, we obtain the transforms

$$T^L(x, p) = \frac{1 - \nu}{1 + \nu} \frac{\hat{V}}{\alpha h} \Delta^L(p) \frac{hB'(h)}{B(h)} \frac{N_T(x, z)}{R(z)} \tag{32.22}$$

$$N_T(x, z) = \sqrt{z} \left(\text{Bi}sh \sqrt{z} \frac{x}{h} + \sqrt{z} ch \sqrt{z} \frac{x}{h} \right) \tag{32.23}$$

$$u^L(x, p) = -\Delta^L(p) \cdot \frac{N_u^0(h, z)}{R(z)} \tag{32.24}$$

$$N_u^0(x, z) = zr(h, z) \frac{B(x)}{B(h)} - \hat{V} \frac{hB'(h)}{B(h)} (r(x, z) - \text{Bi}) \tag{32.25}$$

$$\sigma_{xx}^L(x, p) = \frac{2(1 - \nu)}{1 - 2\nu} \mu(x) \Delta^L(p) \frac{hB'(x)}{B(h)} \cdot \frac{N_\sigma^0(z)}{R(z)} \tag{32.26}$$

$$N_\sigma^0(x, z) = zr(x, z) \tag{32.27}$$

where

$$R(z) = zr(z) - \hat{V}\eta((1 - k_w)r(z) - \text{Bi}) \tag{32.28}$$

$$r(x, z) = \text{Bi} \, ch\sqrt{z}\frac{x}{h} + \sqrt{z}sh\sqrt{z}\frac{x}{h} \tag{32.29}$$

$$z = \frac{p}{\kappa}h^2, \text{Bi} = \frac{kh}{K}, k_w = \frac{1 - \nu}{1 + \nu} \frac{KK^*}{\alpha\kappa}, \hat{V} = \frac{fV\alpha}{K} \frac{2\mu(1 + \nu)h}{1 - 2\nu}$$

After substitution (32.23) into (32.20) the wear Laplace transform $u_w^L(p)$ takes the form

$$u_w^L(p) = k_w \hat{V} \frac{hB'(h)}{B(h)} \Delta^L(p) \frac{r(h, z)}{R(z)} \tag{32.30}$$

Performing the inverse Laplace transformation of the obtained transforms $T^L(x, p)$, $u^L(x, p)$, $\sigma_{xx}^L(x, p)$, we obtain solutions of the problem in the form of convolutions ($t > 0$)

$$T(x, t) = \frac{1 - \nu}{1 + \nu} \frac{\hat{V}}{\alpha h} \cdot \frac{hB'(h)}{B(h)} \int_0^t \Delta(\tau) f_T(x, t - \tau) d\tau \tag{32.31}$$

$$f_T(x, t) = \frac{1}{2\pi i} \int_{\Gamma} \frac{N_T(x, z)}{t_\kappa R(z)} e^{z\tilde{t}} dz \tag{32.32}$$

$$u(x, t) = - \int_0^t \Delta(\tau) f_u^0(x, t - \tau) d\tau \tag{32.33}$$

$$f_u^0(x, t) = \frac{1}{2\pi i} \int_{\Gamma} \frac{N_u^0(x, z)}{t_\kappa R(z)} e^{z\tilde{t}} dz \tag{32.34}$$

$$\sigma_{xx}(x, t) = - \frac{2\mu(h)(1 - \nu)\eta}{(1 - 2\nu)} \int_0^t \Delta(\tau) f_\sigma^0(x, t - \tau) d\tau \tag{32.35}$$

$$f_\sigma^0(x, t) = \frac{1}{2\pi i} \int_{\Gamma} \frac{N_\sigma^0(x, z)}{t_\kappa R(z)} e^{z\tilde{t}} dz \tag{32.36}$$

where $\tilde{t} = \frac{t}{t_\kappa}$, $t_\kappa = \frac{h^2}{\kappa}$.

When obtaining formula (32.35) from formula (32.26), it was taken into account that $\mu(x)B'(x) = 1$. The wear of the coating surface $u_w(t)$ is determined after inverse Laplace transformation $u_w^L(p)$ from (32.30).

$$u_w(t) = k_w \hat{V} \frac{hB'(h)}{B(h)} \int_0^t \Delta(\tau) f_w(t - \tau) d\tau \tag{32.37}$$

$$f_w(t) = \frac{1}{2\pi i} \int_{\Gamma} \frac{r(h, z)}{t_k R(z)} e^{z\bar{t}} dz \tag{32.38}$$

When studying the existence of contour quadratures (32.32), (32.34), (32.36), (32.38), the behavior of integrands is determined for large values of the integration variable ($\arg z = \pi/2, |z| \rightarrow \infty$):

$$N_T(x, z)R^{-1}(z) = O(z^{-1/2}), \quad 0 < x < h$$

$$N_u^0(x, z)R^{-1}(z) = \frac{B(x)}{B(h)} + O(z^{-1/2}), \quad 0 < x < h \tag{32.39}$$

$$N_\sigma^0(x, z)R^{-1}(z) = 1 + O(z^{-1/2}), \quad 0 < x < h$$

$$r(h, z)R^{-1}(z) = O(z^{-1})$$

Asymptotic relations (32.39) show that the integrands in (32.34) and (32.36) do not decrease at infinity (at $|z| \rightarrow \infty$), and the integrals are divergent and they are understood in a generalized sense (Brychkov and Prudnikov 1977). After regularization of quadratures (32.34), (32.36) and selection of the generalized component of the displacements $u(x, t)$ and stresses $\sigma_{xx}(x, t)$, they will be written in the form of the following formulas ($t > 0$)

$$u(x, t) = -\frac{B(x)}{B(h)} \Delta(t) - \int_0^t \Delta(\tau) f_u(x, t - \tau) d\tau, \quad 0 \leq x \leq h, \quad t > 0 \tag{32.40}$$

$$f_u(x, t) = \frac{1}{2\pi i} \int_{\Gamma} \frac{N_u(x, z)}{t_k R(z)} e^{z\bar{t}} dz \tag{32.41}$$

$$N_u(x, z) = N_u^0(x, z) - \frac{B(x)}{B(h)} R(z) \tag{32.42}$$

$$\sigma_{xx}(x, t) = -\frac{2(1 - \nu)}{(1 - 2\nu)B(h)} \left(\Delta(t) - \int_0^t \Delta(\tau) f_\sigma(x, t - \tau) d\tau \right), \quad 0 \leq x \leq h, \quad t > 0 \tag{32.43}$$

$$f_\sigma(x, t) = \frac{1}{2\pi i} \int_{\Gamma} \frac{N_\sigma(x, z)}{t_k R(z)} e^{z\bar{t}} dz \tag{32.44}$$

$$N_\sigma(x, z) = N_\sigma^0(x, z) - R(z) \quad (32.45)$$

where the integration contour $\Gamma = \{z : -i\infty + dt_\kappa, +i\infty + dt_\kappa\}$ is a straight line in the complex plane of the integration variable z parallel to the imaginary axis and spaced from it by a value dt_κ , which is chosen so that the integration contour passes to the right of all isolated singular points of the integrands.

Horizontal displacements $w(x, t)$ are determined from formulas (32.1), (32.5), (32.7) and have the following form

$$w(x, t) = -f B(x)\sigma_{xx}(h, t), \quad 0 \leq x \leq h, \quad t > 0 \quad (32.46)$$

The properties of integrands for calculating the corresponding quadratures make it possible to apply the methods of the theory of functions of a complex variable and study the obtained solutions for stability.

32.4 Poles of Integrands

To study the stability of the problem solutions obtained in the previous paragraph, it is necessary to study the dependence of the poles of the integrands in quadratures (32.32), (32.38), (32.41), (32.44) on the main parameters of the problem. The poles of the integrands are the zeros of the transcendental equation

$$R(z) = zr(h, z) - \eta \hat{V}((1 - k_w)r(h, z) - \text{Bi}) = 0, \quad |\arg z| < \pi, \quad |z| < \infty \quad (32.47)$$

in the complex plane $z = \xi + i\zeta$. Functions $R(z)$ and $r(x, z)$ are given in (32.38) and (32.29), where $\eta = hB'(h)/B(h)$. Equation (32.47) contains four dimensionless parameters of the problem ($k_w, \hat{V}, \text{Bi}, \eta$), which are expressed in terms of the dimensional physical, mechanical, and geometric parameters of the problem. In this case, the dimensionless parameter η , whose numerical value characterizes the functionally graded material of the coating, is added from $B'(h) = \mu^{-1}(h)$ and $B(h)$ from (32.15), for which, according to the mean value theorem, there is such a point $c \in [0, h]$, that the equality is true.

$$B(h) = \mu^{-1}(c)h, \quad c \in [0, h] \quad (32.48)$$

As a result, the parameter η is represented as a ratio of the average value of the shear modulus $\mu(c)$, $c \in [0, h]$ and the value of the shear modulus $\mu(h)$ on the contact surface of the functionally graded coating material:

$$\eta = \frac{\mu(c)}{\mu(h)}, \quad c \in [0, h] \quad (32.49)$$

32.5 Asymptotic Analysis of the Obtained Solutions

To determine the degree of influence of the dimensionless parameter η , as well as other parameters of the problem, an asymptotic analysis of the obtained solutions $T(x, t)$, $u(x, t)$, $\sigma_{xx}(x, t)$, $u_w(t)$ for small values of time t is carried out. The selected main parts $u(x, t)$ in (32.40), $\sigma_{xx}(x, t)$ in (32.43), taking into account the estimate of the convolution integrals, allow us to obtain the following asymptotic relations.

$$T(x, t) = \frac{1 - \nu}{1 + \nu} \frac{\hat{V}}{\alpha} \frac{B'(h)}{B(h)} \sqrt{\frac{t}{t_\kappa}} \Delta(t) + O(t^{3/2} \dot{\Delta}(t)) \text{ at } t \rightarrow 0 \quad (32.50)$$

$$u(x, t) = -\frac{B(x)}{B(h)} \frac{\Delta(t)}{h} + O(t^{1/2} \Delta(t)) \text{ at } t \rightarrow 0 \quad (32.51)$$

$$\sigma_{xx}(x, t) = -\frac{2(1 - \nu)}{(1 - 2\nu)B(h)} \Delta(t) + O(t^{1/2} \Delta(t)) \text{ at } t \rightarrow 0 \quad (32.52)$$

32.6 Features of Wear of the FGM Coating

The exact formulas for the main parameters on the sliding contact, such as temperature $T(x, t)$ (32.31), displacements $u(x, t)$ (32.33), stresses $\sigma_{xx}(x, t)$ (32.35) and wear $u_w(t)$ (32.37), were obtained in Sect. 32.3. The resulting formulas depend on an arbitrary shear modulus $\mu(x)$, $0 \leq x \leq h$.

Formulas for the coefficient of functionally graded inhomogeneity η and its components for elementary functionally graded laws of shear modulus $\mu(x)$ are presented in Table 32.1.

The numerical implementation of the obtained formulas for temperature, displacements, stresses, and wear is considered, when the shear modulus $\mu(x)$ of the functionally graded coating changes according to the parabolic law

$$\mu(x) = \mu_0 \left(a \left(\frac{x}{h} \right)^2 + b \frac{x}{h} + c \right) \quad (32.53)$$

$$a = 2 \left(\frac{\mu_1}{\mu_0} - 2 \frac{\mu_{1/2}}{\mu_0} + 1 \right), \quad b = - \left(\frac{\mu_1}{\mu_0} - 4 \frac{\mu_{1/2}}{\mu_0} + 3 \right), \quad c = 1$$

where $\mu_0 = \mu(0)$, $\mu_1 = \mu(h)$, $\mu_{1/2} = \mu(h/2)$. At the boundary with the rigid substrate at $x = 0$, the shear modulus is equal to μ_0 , at the contact of the coating with the rigid abrasive at $x = h$ it is equal to μ_1 , and in the middle of the coating it

Table 32.1 Formulas for the coefficient of functionally graded inhomogeneity η and its components for elementary functionally graded laws $\mu(x)$

| x | $\mu(x)$ | ε | $\frac{\mu_1}{h} B(x)$ | $\frac{\mu_1}{h} B'(x)$ | $\frac{\mu_1}{h} B(h)$ | $h B'(h) \frac{\mu_1}{h}$ | $\eta = \frac{h B'(h)}{B(h)}$ |
|-----------------------|---|-----------------------|---|---|---|---------------------------|--|
| $0 \leq x \leq h$ | μ_0 | 1 | $\frac{x}{\mu_0}$ | $\frac{1}{\mu_0}$ | $\frac{h}{\mu_0}$ | $\frac{h}{\mu_0}$ | 1 |
| $h - d \leq x \leq h$ | μ_1 | $\frac{\mu_1}{\mu_0}$ | $(\varepsilon - 1) \left(1 - \frac{d}{h}\right) + \frac{x}{h}$ | $\frac{1}{h}$ | $(\varepsilon - 1) \left(1 - \frac{d}{h}\right) + 1$ | 1 | $\frac{1}{(\varepsilon - 1) \left(1 - \frac{d}{h}\right) + 1}$ |
| $0 \leq x \leq h - d$ | μ_0 | | $\varepsilon \frac{x}{h}$ | $\varepsilon \frac{1}{h}$ | ε | ε | 1 |
| $0 \leq x \leq h$ | $\mu_0 + (\mu_1 - \mu_0) \frac{x}{h}$ | $\frac{\mu_1}{\mu_0}$ | $\frac{\varepsilon}{\varepsilon - 1} \cdot \ln \left 1 + (\varepsilon - 1) \frac{x}{h} \right $ | $\frac{\varepsilon}{h} \frac{1}{1 + (\varepsilon - 1) \frac{x}{h}}$ | $\frac{\varepsilon}{\varepsilon - 1} \ln \varepsilon$ | 1 | $\frac{\varepsilon - 1}{\varepsilon \ln \varepsilon}$ |
| $0 \leq x \leq h$ | $\mu_0 \exp(2dx)$ $d = \frac{1}{2h} \ln \frac{\mu_1}{\mu_0}$ | $\frac{\mu_1}{\mu_0}$ | $\frac{1 - \exp\left(-\frac{x}{h}\right)}{\varepsilon - \ln \varepsilon}$ | $\frac{\varepsilon}{h} \exp\left(-\frac{x}{h}\right)$ | $\frac{\varepsilon - 1}{\ln \varepsilon}$ | 1 | $\frac{\ln \varepsilon}{\varepsilon - 1}$ |
| $0 \leq x \leq h$ | $\mu_1 \cos\left(\left(1 - \frac{x}{h}\right)\gamma\right)$ $\gamma = \arccos \frac{1}{\varepsilon}$ | $\frac{\mu_1}{\mu_0}$ | $\frac{1}{2\gamma} \ln \left \frac{1 + \sin\left(\left(1 - \frac{x}{h}\right)\gamma\right)}{1 - \sin\left(\left(1 - \frac{x}{h}\right)\gamma\right)} \right + \frac{1}{2\gamma} \ln \left \frac{1 - \sin \gamma}{1 + \sin \gamma} \right $ | $\frac{1}{h} \frac{1}{\cos\left(\left(1 - \frac{x}{h}\right)\gamma\right)}$ | $\frac{1}{\gamma} \ln\left(\varepsilon + \sqrt{\varepsilon^2 - 1}\right)$ | 1 | $\frac{\arccos \frac{1}{\varepsilon}}{\ln\left(\varepsilon + \sqrt{\varepsilon^2 - 1}\right)}$ |

is equal to $\mu_{1/2}$. At $\mu_{1/2} = (\mu_1 + \mu_0)/2$, we obtain $a = 0$ and dependence (32.53) becomes linear.

Calculating the integral in (32.15) of the function (32.53), we obtain a formula for $B(x)$

$$B(x) = \frac{h}{\mu_1} \begin{cases} \frac{2\chi}{\sqrt{-D}} \operatorname{arctg} \frac{\sqrt{-D}}{\theta(x)} & D < 0 \\ \frac{\chi}{\sqrt{D}} \ln \left| \frac{1+\theta_-(x)}{1-\theta_+(x)} \right| & D > 0 \\ -4\frac{c}{b} \frac{\chi}{\theta(x)} & D = 0 \end{cases} \quad (32.54)$$

$$D = b^2 - 4ac, \chi = \frac{\mu_1}{\mu_0}, \theta(x) = 2c + b\frac{x}{h}, \theta_{\pm}(x) = \frac{2a_1}{b_1 \pm \sqrt{D}} \cdot \frac{x}{h}$$

Formula (32.54) allows to determine other characteristics of $\mu(x)$:

$$B'(x) = \frac{1}{\mu(x)} = \frac{1}{\mu_0 \left(a \left(\frac{x}{h} \right)^2 + b \frac{x}{h} + c \right)} \quad (32.55)$$

$$B'(h) = \frac{1}{\mu_0 \chi} \quad (32.56)$$

$$B(h) = \frac{h}{\mu_1} \begin{cases} \frac{2\chi}{\sqrt{-D}} \operatorname{arctg} \frac{\sqrt{-D}}{2c+b} & D < 0 \\ \frac{\chi}{\sqrt{D}} \ln \left| \frac{1+b^1}{1-b^1} \right| & D > 0 \\ -4\chi \frac{c}{b(2c+b)} & D = 0 \end{cases} \quad (32.57)$$

$$D = b^2 - 4ac, b^1_{\pm} = \frac{2a}{b \pm \sqrt{D}} b^1_{\pm},$$

Then the value η , characterizing the functionally graded coating material in the case of parabolic dependence (32.53), is written by the formula

$$\eta = \frac{hB'(h)}{B(h)} = \frac{h}{\mu_1 B(h)} \quad (32.58)$$

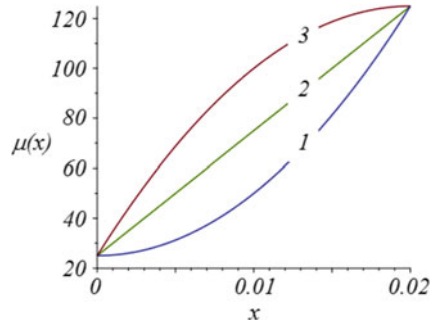
The law of introduction $\Delta(t)$ of the rigid abrasive into the coating is given in the form

$$\Delta(t) = \Delta_0(e^{\varepsilon t} H(1 - t) + H(t - 1)), t > 0 \quad (32.59)$$

where segment of introduction at $0 < t \leq 1$ is the active time segment of introduction, and segment of introduction at $t > 1$ is the passive one.

The problem is to study the influence of the parameter $\eta = \eta(\varepsilon)$ of the considered problem of thermoelasticity on wear by a rigid abrasive of an elastic strip of functionally graded material (aluminum with a gradient content of aluminum oxide), on the main characteristics of the contact (temperature $T(h, t)$, contact stresses

Fig. 32.1 Shear modulus $\mu(x)$ in the coating depth at various values $\mu_{1/2}$: 1 — 50, 2 — 75, 3 — 100 GPa



$p(t) = -\sigma_{xx}(h, t)$, wear of the coating $u_w(t)$, wear rate $\dot{u}_w(t)$). Functionally graded material is characterized by increased shear modulus $\mu_1 = \mu(h) = 125.0$ GPa at the contact and usual at the interface with the substrate $\mu_0 = \mu(0) = 25.0$ GPa, $\nu = 0.34$, $\kappa = 88.1 \cdot 10^{-6}$ m²/s, $\alpha = 22.9 \cdot 10^{-6}$ 1/K, $K = 209.3$ W/(m·K), $f = 0.47$, $h = \Delta_0 = 10$ mm. Three different values $\mu_{1/2} = \mu(h/2)$ are considered. At $\mu_{1/2} = 50$ GPa $\eta = 0.361287$, at $\mu_{1/2} = 75$ GPa $\eta = 0.497067$, at $\mu_{1/2} = 100$ GPa $\eta = 0.619564$. When $\mu_{1/2} = \mu(h/2)$ changing, $\mu(x)$ along the coordinate x illustrates in Fig. 32.1.

The coating is being worn out to the depth Δ_0 up to a point of time $t = t_w$ when the coating wear $u_w(t)$ equals to Δ_0 and the contact stress turns to zero ($p(t) = -\sigma_{xx}(h, t) = 0$). We call t_w the coating wear time by amount Δ_0 . Assuming the wear factor $K^* = 1.0 \cdot 10^{-11}$ m²/N, we obtain the values of dimensionless parameters $k_w = 0.511$ and $Bi = 10^5$ using formulas (32.29).

Tables 32.2 and 32.3 give the coating wear time t_w , together with maximum values of contact pressure $p(t)$ and temperature $T(h, t)$, depending on values of $\mu_{1/2}$ at sliding velocity $V = 2.5$ mm/s and $V = 5.0$ mm/s.

The regulation of the parameters of the functional dependence of the shear modulus $\mu(x)$ on the thickness of the coating allows you to accelerate or slow down the wear of the coating.

Table 32.2 Values of t_w , $\max_{t \in (0, t_w]} p(t)$, $\max_{t \in (0, t_w]} T(h, t)$ depending on the $\mu_{1/2}$ at $V = 2.5$ mm/s

| $\mu_{1/2}$, GPa | t_w , s | $\max_{t \in (0, t_w]} p(t)$, GPa | $\max_{t \in (0, t_w]} T(h, t)$, K |
|-------------------|-----------|------------------------------------|-------------------------------------|
| 50 | 192.3 | 0.142 | 4.600 |
| 75 | 128.9 | 0.196 | 6.292 |
| 100 | 93.3 | 0.246 | 7.749 |

Table 32.3 Values of t_w , $\max_{t \in (0, t_w]} p(t)$, $\max_{t \in (0, t_w]} T(h, t)$ depending on the $\mu_{1/2}$ at $V = 5.0$ mm/s

| $\mu_{1/2}$, GPa | t_w , s | $\max_{t \in (0, t_w]} p(t)$, GPa | $\max_{t \in (0, t_w]} T(h, t)$, K |
|-------------------|-----------|------------------------------------|-------------------------------------|
| 50 | 124.6 | 0.144 | 8.996 |
| 75 | 30.2 | 0.201 | 12.279 |
| 100 | 18.6 | 0.253 | 15.153 |

32.7 Grinding Process Control by Abrasive Settlement $\Delta(t)$

The process of controlling the wear-grinding of a strip of functionally graded material is primarily associated with the regulation of the temperature, contact stresses, wear time, that expand in the process of wear-grinding, to prevent emergency situations including the occurrence of thermoelastic instability of a sliding contact, etc. As a temperature controller, both at the contact and in depth, it is effective to use not only the change in the horizontal speed of the abrasive but also the order of settlement $\Delta(t)$ of the abrasive in the functionally graded material of the strip. To implement this, we use relation (32.31), which determines the temperature $T(x, t)$ in the strip through the law of abrasive settling $\Delta(t)$.

$$T(x, t) = \theta^{-1} \int_0^t \Delta(\tau) f_T(x, t - \tau) d\tau, \quad 0 \leq x \leq h, \quad t > 0 \tag{32.60}$$

where

$$f_T(x, z) = \frac{1}{2\pi i} \int_{\Gamma} \frac{N_T(x, z)}{t_\kappa R(z)} e^{z\tilde{t}} dz, \quad /, \theta = \frac{1 + \nu \alpha h}{1 - \nu \hat{V} \eta}, \quad z = p t_\kappa, \quad \tilde{t} = \frac{t}{t_\kappa} \tag{32.61}$$

$N_T(x, z)$ and $R(z)$ are given in (32.23) and (32.28).

If $T(x, t)$ in (32.60) is known in advance from any considerations, rules, experimental studies, then relation (32.60) turns into the Volterra integral equation (Polyanin and Manzhirov 2003) with respect to an unknown $\Delta(t)$ in the form

$$\int_0^t \Delta(\tau) f_T(x, t - \tau) d\tau = \theta T(x, t), \quad 0 \leq x \leq h, \quad t > 0 \tag{32.62}$$

To solve this equation, the Laplace transform (32.12) is used. As a result of applying the Laplace transform, we obtain that

$$\Delta(t) = \theta \int_0^t T(x, \tau) g_T(x, t - \tau) d\tau, \quad 0 \leq x \leq h, \quad /, \quad t > 0 \tag{32.63}$$

where

$$g_T(h, t) = \frac{1}{2\pi i} \int_{\Gamma} \frac{R(p t_\kappa)}{N_T(x, p t_\kappa)} e^{pt} dp \tag{32.64}$$

θ is given in (32.61). The resulting formula is also valid for $x = h$, that is, at the contact.

Often in practice, depending on the processing of a functionally graded material, it is necessary to control or limit contact stresses $p(t) = -\sigma_{xx}(h, t)$. To obtain a contact pressure sensor, we use the abrasive settlement $\Delta(t)$. For this purpose, formula (32.35) for $\sigma_{xx}(x, t)$ at $x = h$.

$$\sigma_{xx}(h, t) = -\theta^{-1} \int_0^t \Delta(\tau) f_{\sigma}^0(h, t - \tau) d\tau, \quad t > 0 \tag{32.65}$$

Where

$$f_{\sigma}^0(h, t) = \frac{1}{2\pi i} \int_{\Gamma} \frac{N_{\sigma}^0(z)}{t_{\kappa} R(z)} e^{z\tilde{t}} dz, \quad \theta = \frac{1 + \nu}{1 - \nu} \frac{1}{\eta\mu(h)}, \quad z = p t_{\kappa}, \quad \tilde{t} = \frac{t}{t_{\kappa}} \tag{32.66}$$

$N_{\sigma}^0(z)$ and $R(z)$ are given (32.27) in (32.28).

With a known or predetermined $\sigma_{xx}(h, t)$ relation (32.65) turns into the Volterra equation with respect to $\Delta(t)$

$$\int_0^t \Delta(\tau) f_{\sigma}^0(h, t - \tau) d\tau = \theta p(t) \tag{32.67}$$

$t > 0$

The solution of the integral Eq. (32.67) is determined by applying the Laplace transform (32.12) and has the form

$$\Delta(t) = \theta \int_0^t p(\tau) g_{\sigma}(h, t - \tau) d\tau \tag{32.68}$$

$t > 0$

where

$$g_{\sigma}(t) = \frac{1}{2\pi i} \int_{\Gamma} \frac{R(p t_{\kappa})}{N_{\sigma}^0(p t_{\kappa})} e^{pt} dp \tag{32.69}$$

θ is given in (32.66).

For grinding some functionally graded materials, it is necessary to use a delicate settlement of the abrasive into the material. To determine the delicate settlement, we use the formula (32.37) to determine the wear.

$$u_w(t) = \theta^{-1} \int_0^t \Delta(\tau) f_w(t - \tau) d\tau, \quad t > 0 \tag{32.70}$$

where

$$f_w(t) = \frac{1}{2\pi i} \int_{\Gamma} \frac{r(h, z)}{t_\kappa R(z)} e^{z\tilde{t}} dz, \quad \theta = \frac{1}{\eta k_w \hat{V}}, \quad z = p t_\kappa, \quad \tilde{t} = \frac{t}{t_\kappa} \tag{32.71}$$

$r(h, z)$ and $R(z)$ are given in (32.29) and (32.28).

With a known or predetermined abrasive settling $u_w(t)$ due to wear, relation (32.70) turns into the Volterra integral equation with respect to $\Delta(t)$

$$\int_0^t \Delta(\tau) f_w(t - \tau) d\tau = \theta u_w(t), \quad t > 0 \tag{32.72}$$

Applying the Laplace transform to solve the integral Eq. (32.70), we obtain

$$\Delta(t) = \theta \int_0^t u_w(\tau) g_w(t - \tau) d\tau, \quad t > 0 \tag{32.73}$$

where

$$g_w(t) = \frac{1}{2\pi i} \int_{\Gamma} \frac{R(p t_\kappa)}{r(h, p t_\kappa)} e^{pt} dp \tag{32.74}$$

θ is given in (32.71).

32.8 Conclusion

An exact solution to the problem of grinding of a functionally graded material for the main parameters of a sliding contact is constructed. The solution is presented in the form of Laplace convolutions from the law of abrasive settling into a functionally graded material and a function that characterizes the boundary value problem. On the one hand, this made it possible to investigate the behavior of the main contact parameters, such as temperature, stresses, wear, etc., depending on the law of abrasive settlement. On the other hand, this made it possible to obtain Volterra integral equations for determining the law of abrasive settling into a functionally graded material according to given limits of contact parameters. The foundations of the method of

stopping the possibility of emergency situations in the process of grinding have been laid.

Acknowledgements Zelentsov V. B. acknowledges the support of the grant of the RFBR (grant number 20-07-00949-a). Nikolaev A.L. acknowledges the support of the grant of the RSF (grant number 23-49-10062).

References

- Alexandrov VM, Annakulova GK (1990) A contact problem of thermo-elasticity with wear and heat release caused by friction. *Trenie Iznos* 11(1):24–28
- Alexandrov VM, Annakulova GK (1992) Interaction between coatings of a body with deformation, wear, and heat release due to friction. *Trenie Iznos* 13(1):154–160
- Alinia Y, Beheshti A, Guler MA, El-Borgi S, Polycarpou AA (2016) Sliding contact analysis of functionally graded coating/substrate system. *Mech Mater* 94:142–155
- Altenbach H, Eremeyev VA (2009) Eigen-vibrations of plates made of functionally graded material. *Comput Mater Continua* 9(2):153–177
- Andrews KT, Shillor M, Wright S, Klarbring A (1997) A dynamic thermoviscoelastic contact problem with friction and wear. *Int J Eng Sci* 35(14):1291–1309
- Archard JF (1953) Contact and rubbing of flat surfaces. *J Appl Phys* 24(8):981–988
- Awrejcewicz J, Pyryev Yu (2002) Thermoelastic contact of a rotating shaft with a rigid bush in conditions of bush wear and stick-slip movements. *Int J Eng Sci* 40(10):1113–1130
- Belyakov NS, Nosko AP (2010) Thermoelastic problem of friction of plane-parallel layers with allowance for nonstationarity of thermal processes. *J Frict Wear* 31(5):317–325
- Bowden FP, Tabor D (1950) *The Friction and Lubrication of Solids*. Oxford, London
- Brychkov YuA, Prudnikov AP (1977) *Integral Transformations of Generalized Functions*. Nauka, Moscow
- Ditkin VA, Prudnikov AP (1975) *Operational Calculus*. VishayaShkola, Moscow
- Dow TA, Burton RA (1973) The role of wear in the initiation of thermoelastic instabilities of rubbing contact. *J Lubr Technol* 95(1):71–75
- Evtushenko AA, Pyryev YuA (1997) Influence of wear on the development of thermoelastic instability of a frictional contact. *Izvestiya Rossiyskoy Akademii Nauk. Mekhanika Tverdogo Tela* 1:114–121
- Gu RJ, Kuttler KL, Shillor M (2000) Frictional wear of a thermoelastic beam. *J Math Anal Appl* 242(2):212–236
- Guler MA, Erdogan F (2007) The frictional sliding contact problems of rigid parabolic and cylindrical stamps on graded coatings. *Int J Mech Sci* 49(2):161–182
- Kudish II, Volkov SS, Vasiliev AS, Aizikovich SM (2016) Some criteria for coating effectiveness in heavily loaded line elastohydrodynamically lubricated contacts—part I: Dry contacts. *J Tribol* 138(2):021504
- Ma J, El-Borgi S, Ke LL, Wang YS (2016) Frictional contact problem between a functionally graded magneto-electroelastic layer and a rigid conducting flat punch with frictional heat generation. *J Therm Stresses* 39(3):245–277
- Papangelo A, Ciavarella M (2020a) The effect of wear on ThermoElastic Instabilities (TEI) in bimaterial interfaces. *Tribol Int* 142:105977
- Papangelo A, Ciavarella M (2020b) Can wear completely suppress thermoelastic instabilities? *J Tribol* 142(5):051501
- Polyanin AD, Manzhirov AV (2003) *Reference book on Integral Equations*. Fizmatlit, Moscow

- Pyryev YuA, Grilitsky DV (1996) The non-stationary problem of the frictional contact for a cylinder taking into account heat release and wear. *Appl Math Tech Phys* 37(6):99–104
- Selvadurai APS, Katebi A (2016) The Boussinesq–Mindlin problem for a non-homogeneous elastic halfspace. *Zeitschrift für angewandte Mathematik und Physik*, 67(3), <https://doi.org/10.1007/s00033-016-0661-z>
- Selvadurai APS, Katebi A (2013) Mindlin’s problem for an incompressible elastic half-space with an exponential variation in the linear elastic shear modulus. *Int J Eng Sci* 65:9–21
- Singh S, Singh R (2015) Wear modelling of Al-Al₂O₃ functionally graded material prepared by FDM assisted investment castings using dimensionless analysis. *J Manuf Process* 20(3):507–514
- Strömberg N (1999) Finite element treatment of two-dimensional thermoelastic wear problem. *Comput Method Appl Mech Eng* 177(3–4):441–455
- Strömberg N, Johansson L, Klarbring A (1996) Derivation and analysis of a generalized standard model for contact, friction and wear. *Int J Solids Struct* 33(13):1817–1836
- Tokovyy Yu, Ma C-C (2015) An analytical solution to the three-dimensional problem on elastic equilibrium of an exponentially-inhomogeneous layer. *J Mech* 31(5):545–555
- Vasiliev AS, Volkov SS, Aizikovich SM, Mitrin BI (2017) Plane contact problem on indentation of a flat punch into a transversely-isotropic half-plane with functionally graded transversely-isotropic coating. *Z Angew Math Phys* 68:1–18
- Vasiliev AS, Volkov SS, Aizikovich SM (2018a) Approximated analytical solution of contact problem on indentation of elastic half-space with coating reinforced with inhomogeneous interlayer. *Mater Phys Mech* 35(1):175–180
- Vasiliev AS, Volkov SS, Aizikovich SM (2018b) Approximated analytical solution of a problem on indentation of an electro-elastic half-space with inhomogeneous coating by a conductive punch. *Dokl Phys* 63(1):18–22
- Zelentsov VB, Mitrin BI, Aizikovich SM (2016a) Dynamic and quasi-static instability of sliding thermoelastic frictional contact. *Journal of Friction and Wear* 37:213–220
- Zelentsov VB, Mitrin BI, Lubyagin IA (2016b) Effect of wear on frictional heating and thermoelastic instability of sliding contact. *Comput ContinuumMechanics* 9(4):430–442
- Zelentsov VB, Mitrin BI, Lubyagin IA (2017) Wear resistance of coating materials under the frictional heating conditions. *J Frict Wear* 38(4):265–271
- Zelentsov VB, Mitrin BI, Lubyagin IA, Kudish II (2019) Diagnostics of wear thermoelastic instability based on sliding contact parameter monitoring. *IMA J Appl Math* 84(2):345–365
- Zelentsov VB, Lapina PA, Mitrin BI (2022) Wear of functionally graded coatings under frictional heating conditions. *Nanomaterials* 12(142), <https://doi.org/10.3390/nano12010142>
- Zmitrowicz A (1987a) A thermodynamical model of contact, friction and wear: I governing equations. *Wear* 114(2):135–168
- Zmitrowicz A (1987b) A thermodynamical model of contact, friction and wear: II constitutive equations for materials and linearized theories. *Wear* 114(2):169–197

Correction to: On Tensile Instability of Elastic Structures with Elastic Sliders of Different Stiffness



Vadim V. Eremeev and Polina A. Lapina

Correction to:
Chapter 8 in: H. Altenbach and V. Eremeyev (eds.),
Advances in Linear and Nonlinear Continuum and Structural Mechanics, Advanced Structured Materials 198,
https://doi.org/10.1007/978-3-031-43210-1_8

In the original version of the book, the following belated corrections have been incorporated: The author's name "Victor V. Eremeyev" has been changed to "Vadim V. Eremeev" in the Frontmatter and in Chapter 8. The book and the chapter have been updated with the changes.

The updated version of this chapter can be found at
https://doi.org/10.1007/978-3-031-43210-1_8

© The Author(s), under exclusive license to Springer Nature Switzerland AG 2023
H. Altenbach and V. Eremeyev (eds.), *Advances in Linear and Nonlinear Continuum and Structural Mechanics*, Advanced Structured Materials 198,
https://doi.org/10.1007/978-3-031-43210-1_33

C1